



30th International Conference on Electrical Contacts

7 – 11 Juni 2021
Online, Switzerland

Proceedings



Electrosuisse, Verband für Elektro-, Energie und Informationstechnik
Electrosuisse, Association pour l'électrotechnique, les technologies de l'énergie et de l'information
Electrosuisse, Associazione per l'elettrotecnica, la tecnica energetica e l'informatica
Electrosuisse, Association for Electrical, Energy and Information Technology

Our Sponsors

The Organizing Committee would like to express its thanks to the following companies having provided in such a large extent financial support for the conference arrangements.

Collini

Heraeus

ABB

ELESTA
Member of the PILZ Group

HITACHI **ABB**

HF HONGFA

Littelfuse

MODISON
THE SILVER PEOPLE

Panasonic
INDUSTRY

Allen-Bradley
by ROCKWELL AUTOMATION

SIEMENS
Ingenuity for life

STÄUBLI

TE

ATOTECH

COMSOL

DODUCO
CONNECTING IDEAS. CREATING SOLUTIONS.

EATON
Powering Business Worldwide

ECL Electrical Contacts Limited

ETA
ENGINEERING TECHNOLOGY

finder
SWITCH TO THE FUTURE

GIA

i²PS
Institute for International Product Safety

Kanton St.Gallen
Amt für Wirtschaft und Arbeit

PLANSEE

SAXONIA
TECHNICAL MATERIALS

Amphenol
ICC

DEHN

Empa

KME

Weidmüller

ELEKTRONIK
PRAXIS

Markt&Technik
DIE UNABHÄNGIGE HOCHSCHULE FÜR ELEKTRONIK

30th International Conference on Electrical Contacts

Proceedings

7 – 11 Juni 2021
Online, Switzerland

Proceedings

Publisher: Electrosuisse, Verband für Elektro-, Energie und Informationstechnik,
Fehraltorf, Switzerland – June 2021

Proceedings ICEC 2020

Edited by Hans Weichert, Program Chair

These complete proceedings are considered as open source documents. The Copyright of the documents in the proceedings remain with the authors. However the content of the papers may be used according to the license agreement as outlined in <https://creativecommons.org/licenses/by/4.0/deed.en>. If the material is copied, redistributed, remixed or transformed appropriate credit to the author must be given and changes of the text must be indicated.

Electrosuisse, Verband für Elektro-, Energie und Informationstechnik
Luppenstrasse 1, CH-8320 Fehraltorf
Phone +41 58 595 11 11
E-Mail info@electrosuisse.ch

ISBN 978-3-907255-11-7

Conference Chairman

Dr. Werner Jöhler

Littelfuse Inc.

Conference Committee

Dr.-Ing. Hans Weichert

Program chair

Dr.-Ing. Michael Gatzsche

Committee member

Jürgen Steinhäuser

Committee member/Promotion

Livia Russell

Project Manager

Günter Grossmann

Committee member

Mike Böning

Committee member

Dr. Dominique Freckmann

Committee member

Lars John

Web design/Promotion

Conference Administration

ICEC 2020

c/o Electrosuisse, Verband für Elektro-, Energie und Informationstechnik

Luppenstrasse 1

CH-8320 Fehraltorf

Switzerland

Phone +41 58 595 11 11

Email info@electrosuisse.ch

www.icec2020.com

The International Advisory Group

Prof. Hiroshi Inoue, Chairman

Japan

Prof. Dr.-Ing. Frank Berger, Vice Chairman

Germany

Dr. Thomas J. Schoepf, Secretary

Germany

Christian Kroepfl

Austria

Dr. R.S. Timsit, Past Chairman

Canada

Prof. Xingwen Li

China

Dr. Sophie Noël

France

Peter Jaeger

Netherlands

Dr. Magne Runde

Norway

Prof. Bogdan Miedzinski, PhD, DSc

Poland

Dr. Werner Jöhler, Past Chairman

Switzerland

Prof. Åsa Kassman Rudolphi

Sweden

Prof. John McBride

United Kingdom

Dr. Paul G. Slade, Past Chairman

USA

Prof. J.G.Zhang*

China

Prof. Dr.-Ing. Karl-Heinz Schroeder*

Germany

Piet van Dijk*

Netherlands

*member Emeritus

Chairman's Message

Welcome to the Participants of the Conference

When Switzerland was awarded the organization of the 30th International Conference on Electrical Contacts 2020 during the Advisory Group Meeting in Albuquerque in 2018 we were expecting to arrange a traditional conference.

We selected St. Gallen / Rorschach, a hidden pearl in the Eastern part of Switzerland, to hold the conference. St. Gallen is a University City with a long history going back to 612 A.D., Rorschach is beautifully located on one of the biggest alpine lakes in Europe, the Lake of Constance, maybe one of the most beautiful areas on Earth in the triangle between Switzerland, Germany and Austria. So far, the plans!

What we did not expect was the appearance of a small virus, which changed the situation globally within a few weeks, making traveling and bigger meetings impossible. In hope that we could have the 30th ICEC in a normal way, the conference was re-scheduled to 7-11 June 2021 after consulting the ICEC Advisory Group. Unfortunately, the global pandemic continued to affect people's lives and health across the globe in 2020 and 2021. To facilitate the exchange of the global Electrical Contact Community, while at the same time protecting health and safety of all participants, the Swiss Organizing Committee proposed to cancel the onsite conference and to take the ICEC 2021 to an online format, which was approved by the Advisory Group in late January 2021.

Hence, the 30th ICEC 2020 conference and exhibition will be held in a completely online way for the first time ever in 2021. We, as an Organizing Committee, are excited to be first in the 60-year history of the conference to create a new format, which was required due to the global pandemic situation. While we will miss the face-to-face interaction, the virtual format enables a broader group to participate at the conference. The "Hopin" Conference Software will provide an excellent platform

- For authors to present and discuss their work
- For sponsors to present their products and services
- For participants to interact with authors and sponsors

As Chairman, I would like to thank multiple people and organizations who helped to make this conference possible

- All Members of the Advisory Group especially the Program Chair Dr. Hans Weichert
- Electrosuisse for all the arrangements e.g. Livia Russel
- 64 experts who peer reviewed all papers
- All authors for submitting outstanding papers
- All sponsors who enabled the Conference

The Conference covers a wide range of topics. Besides the important areas of contact materials, switching devices and connectors many hot topics such as DC switching, arc fault detection, higher voltage in automotive applications, simulation and modelling as well as new technologies will be covered. We wish all of you interesting presentations, discussions and interactions with other participants and sponsors.

We are excited and welcome you virtually at the ICEC 2020 in Switzerland and wish you informative and enjoyable days.



Dr. Werner Johler

Chairman ICEC 2020 and Swiss Member of the Advisory Group ICEC

We kindly thank all reviewers

Christian	Affolter	Empa, Materials Science and Technology
Gerald	Andre	MERZ Schaltgeräte GmbH & Co + KG
Volker	Behrens	VDE Mitglied
Frank	Berger	TU Ilmenau
Christian	Bernauer	ASBESCO (India) Priv. Ltd.
Egon	Bolmerg	Heraeus Deutschland GmbH
Mike	Böning	Plansee Powertech AG
Christine	Bourda	METALOR TECHNOLOGIES ELECTROTECHNICS France
Isabell	Buresch	TE Connectivity
Zhuanke	Chen	Electrical Contacts Plus LLC
Henry	Czajkowski	Rockwell Automation
Christian	Franck	ETH Zurich
Dominique	Freckmann	TE Connectivity
Roman	Fuchs	HSR Hochschule für Technik Rapperswil
Michael	Gatzsche	Hitachi ABB Power Grids
Bernd	Gehlert	Heraeus Deutschland GmbH&Co.KG
Diego	Gonzalez	Leibniz Institute for Plasma Science and Technology
Sergey	Gortschakow	Leibniz Institute for Plasma Science and Technology
Lukas	Graber	Georgia Institute of Technology
Christian	Gregor	TE Connectivity
Günter	Grossmann	Empa, Materials Science and Technology
Makoto	Hasegawa	Chitose Institute of Science and Technology
Johannes	Herrmann	Collini AG
Engelbert	Hetzmannseder	Littelfuse
Christian	Hildmann	TU Dresden
Dave	Hillmann	Collins Aerospace
Hiroshi	Inoue	Akita University
Toni	Israel	TU Dresden
Peter	Jaeger	TE Connectivity
Werner	Johler	Littelfuse
Asa	Kassman	Uppsala University
Christian	Kroepfl	TE Connectivity
Tom	Kufner	Stäubli Electrical Connectors AG
Philip	Lees	Littelfuse
Manfred	Lindmayer	TU Braunschweig
Rod	Martens	TE Connectivity
Jean-Claude	Mauroux	Hitachi ABB Power Grids
John	McBride	University of Southampton
Ralf	Methling	Leibniz Institute for Plasma Science and Technology
Bogdan	Miedzinski	Wroclaw University of Science and Technology
Timo	Mützel	SAXONIA Technical Materials GmbH
Alex	Neuhaus	Frequentis AG
Sophie	Noel	GeePs/CNRS
Henrik	Nordborg	HSR University of Applied Sciences Rapperswil
Frank	Ostendorf	TE Connectivity
Daniel	Reitz	Rockwell Automation Switzerland GmbH
Magne	Runde	SINTEF Energy Research
William	Russell	TE Connectivity
Stephan	Schlegel	TU Dresden
Helge	Schmidt	TE Connectivity
Patrik	Schmutz	Empa, Materials Science and Technology
Clemens	Schrank	Sound Solutions Austria GmbH
John	Shea	Schneider-Electric
Paul	Slade	Consultant
Jian	Song	OWL University of Applied Sciences Lemgo

Jürgen	Steinhäuser	ELESTA GmbH
Ulrich	Straumann	Hitachi ABB Power Grids
Thomas	Strof	Maschinenfabrik Reinhausen GmbH
Roland	Timsit	Timron Scientific Consulting Inc.
Petrus	van Dijk	Consultant
Ashwin	Vijayasai	Inphi
Hans	Weichert	Consultant ICEC 2020
Wolfgang	Widl	University of Applied Sciences Wels / Upper Austria
Peter	Zeller	University of Applied Sciences Wels / Upper Austria
Xin	Zhou	Eaton Corporation

The History of ICEC Conferences

1961	Orono, USA
1964	Graz, Austria
1966	Orono, USA
1968	Swansea, U.K.
1970	Munich, Germany
1972	Chicago, USA
1974	Paris, France
1976	Tokyo, Japan
1978	Chicago, USA
1980	Budapest, Hungary
1982	Berlin, Germany
1984	Chicago, USA
1986	Lausanne, Switzerland
1988	Paris, France
1990	Montreal, Canada
1992	Loughborough, U.K.
1994	Nagoya, Japan
1996	Chicago, USA
1998	Nuremberg, Germany
2000	Stockholm, Sweden
2002	Zurich, Switzerland
2004	Seattle, USA
2006	Sendai, Japan
2008	Saint Malo, France
2010	Charleston, USA
2012	Beijing, China
2014	Dresden, Germany
2016	Edinburgh, United Kingdom
2018	Albuquerque, USA

Our Partners

The Organizing committee would like to express its thanks to the companies below having provided in such a large extent financial support for the conference arrangements .

Platinum Partners



Gold Partners



Member of the PILZ Group



THE SILVER PEOPLE



by ROCKWELL AUTOMATION



Ingenuity for life



Silver Partners



CONNECTING IDEAS. CREATING SOLUTIONS.



Powering Business Worldwide



Electrical Contacts Limited



ENGINEERING TECHNOLOGY



SWITCH TO THE FUTURE



Institute for International Product Safety



Amt für Wirtschaft und Arbeit



TECHNICAL MATERIALS

Bronze Partner



Supporters



Table of Contents

MONDAY | Session 1: Basic Contact Phenomena and Design

Circuit Control Development since the First International Conference on Electrical Contacts (1961 to 2020) <i>Paul Slade (Consultant)</i>	1
A novel experimental evaluation method of welding characteristics for contact materials <i>Xu Zhang (Harbin Institute of Technology), Wanbin Ren (Harbin Institute of Technology), Duanlin Jiang (G&A Electronics Ltd. Co.), Yinghua Fu (Chixi Technology Co.) and Yide Cai (Harbin Institute of Technology)</i>	9
Series Electric Plasma Discharges of Failing Contacts up to 10 A at Various Materials <i>Peter Zeller (University of Applied Sciences Upper Austria)</i>	16
Measurement and study of arc noise fluctuation by fast camera observations <i>Jean Baptiste Humbert (Univ Lorraine IJL CNRS), Patrick Schweitzer (Univ lorraine IJL CNRS), Serge Weber (Univ lorraine IJL CNRS) and Robert Hugon (Univ lorraine IJL CNRS)</i>	24
Electrically-functionalised nanoindenter integrated in-situ in a Scanning Electron Microscope : case studies <i>Fabien Volpi (SIMaP), Solène Comby-Dassonneville (SIMaP) and Marc Verdier (SIMaP)</i>	29
Session 2: Switching Behaviour A	
Recovery of Short AC Switching Arcs – An Old Principle Newly Investigated <i>Manfred Lindmayer (TU Braunschweig) and David Elmiger (Rockwell Automation Switzerland)</i>	37
Arc Re-striking Phenomena in Break Operations of AgSnO ₂ Contacts in Inductive DC Load Conditions up to 20V-17A under External Magnetic Field <i>Makoto Hasegawa (Chitose Institute of Science and Technology) and Seika Tokumitsu (Chitose Institute of Science and Technology)</i>	45
Effects of arc during mechanical bounces on contact material for different power supply frequencies <i>Asma Ramzi (Université de Rennes1), Erwann Carvou (Université de Rennes1) and Alexis Schach (Safran Group)</i>	52
Determination of dielectric recovery characteristic of a pyro switch in commutation circuit <i>Christian Drebenstedt (TU Ilmenau) and Michael Rock (TU Ilmenau)</i>	60
Influence of Load Current and Breaking Velocity on Arc Discharge at Breaking of Electrical Contacts <i>Koichiro Sawa (Nippon Institute of Technology), Kiyoshi Yoshida (Nippon Institute of Technology) and Kenji Suzuki (Fuji Electric FA Components & Systems Co., Ltd)</i>	68
Spectroscopic investigation of the DC-arc in gas filled contactors under external magnetic fields regarding the effects on the arc-plasma properties <i>Diego Gonzalez (Leibniz Institute for Plasma Science and Technology), Ralf Methling (Leibniz Institute for Plasma Science and Technology), Sergey Gortschakow (Leibniz Institute for Plasma Science and Technology), Steffen Franke (Leibniz Institute for Plasma Science and Technology), Shun Yu (TDK Electronics) and Frank Werner (TDK Electronics)</i>	74
Study of Arcing Processes in Circuit Breakers by Means of Spatially Resolved Magnetic Field Recordings <i>Christian Reil (Ostbayerische Hochschule Amberg-Weiden), Hans-Peter Schmidt (OTH - Technical University of Applied Sciences), Michael Anheuser (Siemens AG) and Frank Berger (Technische Universität Ilmenau)</i>	80

Session 3: Switching Behaviour B

Influence of electrode material properties on the anode phenomena in switching vacuum arcs <i>Sergey Gortschakow (Leibniz Institute for Plasma Science and Technology), Diego Gonzalez (Leibniz Institute for Plasma Science and Technology), Dirk Uhrlandt (Leibniz Institute for Plasma Science and Technology), Mike Boening (PLANSEE Powertech AG) and Sabine Boening (PLANSEE Powertech AG).</i>	87
Effect of contact materials process and test features on welding tendencies of vacuum interrupters during short time current test <i>Anthony Papillon (Schneider Electric), Jean-Pierre Meley (Schneider Electric) and Jean-Pierre Gauthier (Schneider Electric).</i>	95
The effect of WC/Ag contact material composition on chopping currents in MV contactors <i>Lavinia Scherf (ABB), Ralf-Patrick Sütterlin (ABB), Moritz Böhm (ABB Power Grids), Thierry Delachaux (ABB) and Thomas Schmölder (ABB).</i>	99
Investigations of the Possibility of Limiting the Hazard due to Internal Arc Faults in Medium Voltage Switchgears <i>Bogdan Miedzinski (Wroclaw university of Science and Technology), Bartosz Polnik (KOMAG Gliwice), Julian Wosik (KOMAG Gliwice), Grzegorz Wisniewski (Wroclaw University of Science and Technology), Marcin Habrych (Wroclaw University of Science and Technology) and Stanislaw Wapniarski (ELEKTROBUDOWA S.A.)</i>	105
Impact of pre-strike arc on contacts degradation after short circuit current making operation in medium voltage air load break switches <i>Naghme Dorraki (Norwegian University of Science and Technology (NTNU)), Marius Strand (Norwegian University of Science and Technology (NTNU)) and Kaveh Niayesh (Norwegian University of Science and Technology (NTNU)).</i>	111
Research on Arc Characteristics of Different Arc Extinguishing Medium Used in DC Contactor <i>Xuebing Yuan (School of Automation, Northwestern Polytechnical University) and Hu Zhao (School of Automation, Northwestern Polytechnical University)</i>	116
TUESDAY Session 4: Arc Interruption and Design	
PV Arc Fault Diagnosis and Modeling Methods: State of the Art and Perspectives <i>Xingwen Li (Xi'an Jiaotong University), Silei Chen (Xi'an University of Technology) and Jing Wang (Shenzhen Power Supply Bureau Shenzhen, P.R.China).</i>	121
Threshold Current of Arc-Free Commutation For Copper-Carbon Contact in a DC Hybrid Switch <i>Chomrong Ou (Department of Electrical and Electronic Engineering, Tokyo Institute of Technology), Huang Yinming (Department of Electrical and Electronic Engineering, Tokyo Institute of Technology) and Koichi Yasuoka (Department of Electrical and Electronic Engineering, Tokyo Institute of Technology).</i>	129
Hybrid DC switch with a Four-block Copper-Based Tungsten Contact <i>Yinming Huang (Tokyo Institute of Technology), Chomrong Ou (Tokyo Institute of Technology) and Koichi Yasuoka (Tokyo Institute of Technology).</i>	135
Investigation and optimization of a hybrid circuit breaker for low- and medium-voltage DC-Grids <i>Frederik Anspach (TU Braunschweig), Patrick Vieth (TU Braunschweig), Lars Claaßen (TU Braunschweig, Institute of Highvoltage Technology and Electrical Power Systems), Ernst-Dieter Wilkening (TU Braunschweig) and Michael Kurrat (TUBS).</i>	141
New Switching Technology for DC Grids <i>Wolfgang Hauer (Eaton Industrie Austria GmbH), Michael Bartonek (Eaton Industrie Austria GmbH) and Hartwig Stammberger (Eaton Industrie Germany GmbH).</i>	149

Switchgear Combination of Pyrotechnic Switch and Fuse <i>Arnd Ehrhardt (DEHN SE + Co KG) and Sven Wolfram (Technische Universität Ilmenau)</i>	157
Design of an electromechanical relay for 5G power supply application which withstand high lightning-stroke-current <i>Maosong Zhang (Ximen Hongfa Electroacoustic Co.,Ltd) and Yiqing Zhu (Ximen Hongfa Electroacoustic Co.,Ltd)</i>	162
Session 5: Connectors and Terminals	
Failure- and degradation mechanisms in plug connectors <i>Peter Jacob (Empa Swiss Fed Labs for Materials Testing and Research)</i>	166
Research on Ultrasonic Testing Technology for Wear Debris Caused by Fretting Wear of Electrical Connectors <i>Yanyan Luo (Hebei University of Technology), Pengyu Gao (Hebei University of Technology), Hong Liang (Maintenance Company of State Grid Tianjin Electric Power Company), Zihang Sun (Hebei University of Technology), Jingqin Wang (Hebei University of Technology), Jingying Zhao (Hebei University of Technology) and Jiaomin Liu (Hebei University of Technology)</i>	172
Study of vibration transfer in automotive connectors for understanding of fretting corrosion damage <i>Mack Mavuni (APTIV/UNIVERSITE DE RENNES 1), Erwann Carvou (UNIVERSTE DE RENNES 1) and Gregory Lalet (APTIV)</i>	178
Influence of PFPE lubricant modifications on tribo-electrical properties of a tin contact system <i>Marcel Mainka (Weidmüller Group), Thomas Wielsch (Weidmüller Group), Ralph Würtele (Klüber Lubrication) and Martin Dr. Schweigkofler (Klüber Lubrication)</i>	186
Durability of some asymmetrical contact pairs for connector application <i>Ana Torrealba (Laboratoire de Génie Electrique et Electronique de Paris), Sophie Noël (Laboratoire de Génie Electrique et Electronique de Paris), Antoine Fares Karam (Amphenol FCI), Aurore Brezard-Oudot (Laboratoire de Génie Electrique et Electronique de Paris), Damien Comte (Amphenol ICC), Anthony Franchini (Amphenol ICC) and Jeffrey Toran (Amphenol ICC)</i>	194
Investigation of the contact resistance as a function of the temperature for connectors and wire terminals <i>Tobias Dyck (WAGO Kontakttechnik GmbH & Co. KG) and Andreas Bund (Technische Universität Ilmenau)</i>	202
Session 6: Contact Materials and Design I A	
Contact Materials for Electromechanical Devices – Established Technologies and Improvements to Face Future Requirements <i>Volker Behrens (DODUCO Contacts and Refining GmbH)</i>	210
The Development of Sputtered Contact Systems Replacing Electroplated Systems in Reed Switch Applications <i>Philip Lees (Littelfuse), Eric Hafenstein (Littelfuse), Joshua Koeppel (Littelfuse) and Tony Spies (Littelfuse)</i>	219
Highly durable silver-based physically deposited contact finish for the application in socket connectors <i>Sönke Sachs (TE Connectivity), Helge Schmidt (TE Connectivity), Marjorie Myers (TE Connectivity), Michael Leidner (TE Connectivity), Waldemar Staborth (TE Connectivity) and Frank Ostendorf (TE Connectivity)</i>	226
An innovative silver-based coating system with high wear resistance for electrical connectors <i>Frédéric Hilty (Collini AG Switzerland) and Johannes Herrmann (Collini AG Switzerland)</i>	234
Investigations on cold welding and galling of various connector platings <i>Reinhard Wagner (Rosenberger Hochfrequenztechnik GmbH & Co. KG), Christian Dandl (Rosenberger Hochfrequenztechnik GmbH & Co. KG), Andreas Gruber (Rosenberger Hochfrequenztechnik GmbH & Co. KG), Reinhard Hogger (Rosenberger Hochfrequenztechnik GmbH & Co. KG) and Michael Eicher (Rosenberger Hochfrequenztechnik GmbH & Co. KG)</i>	241

A Cu/Sn Multilayer System and its Fretting Corrosion Behavior <i>Haomiao Yuan (Ostwestfalen-Lippe University of Applied Sciences and Arts) and Jian Song (Ostwestfalen-Lippe University of Applied Sciences and Arts)</i>	248
Silver Plating for Connectors – The right combination of new gal-vanic Silver processes and anti-tarnishes <i>Bernd Roelfs (Atotech Deutschland GmbH), Markus Hoerburger (Atotech Deutschland GmbH), Alexander Spoerrler (Atotech Deutschland GmbH) and Bruno Wibberg (Atotech Deutschland GmbH)</i>	254
WEDNESDAY Session 7: Contact Materials and Design II A	
Compatibility of Gold, Palladium and hard Silver based plating systems for connector applications <i>Antoine Fares Karam (Amphenol ICC), Anthony Franchini (Amphenol ICC), Ana Torrealba (Laboratoire de G enie Electrique de Paris, University Paris-Saclay), Damien Comte (Amphenol ICC), Aurore Brezard-Oudot (Laboratoire de Génie Electrique de Paris, CentraleSupélec), Sophie Noel (Laboratoire de Genie Electrique de Paris, CentraleSupélec), Doyle Anderson (Amphenol ICC) and Jeffrey Toran (Amphenol ICC)</i>	260
SnOx Gradient Composition Inside the Tin-plated Layer <i>Keiji Mashimo (Furukawa Electric), Atsushi Shimoyamada (Furukawa Electric) and Hirokazu Sasaki (Furukawa Electric)</i>	268
Alloy Development in the CuNiAl System for High Strength Materials <i>Miriam Eisenbart (fem Research Institute for Precious Metals and Metals Chemistry), Felix Bauer (fem Research Institute for Precious Metals and Metals Chemistry) and Ulrich Klotz (fem Research Institute for Precious Metals and Metals Chemistry)</i>	274
Special connector requirements call for specific contact coatings: new silver alloys show characteristics never seen before <i>Isabell Buresch (TE Connectivity Germany GmbH), Helge Schmidt (TE Connectivity Germany GmbH) and Sönke Sachs (TE Connectivity Germany GmbH)</i>	281
Tin Free Solutions Against Whisker Growth in Press-Fit Applications <i>Erika Crandall (TE Connectivity), Frank Ostendorf (TE Connectivity), Martin Bleicher (TE Connectivity), Helge Schmidt (TE Connectivity), Isabell Buresch (TE Connectivity) and Bart Kerckhof (TE Connectivity)</i>	289
Microstructural evolution of Ag/MeO contact materials and influence on mechanical properties <i>Yinglu Tang (ABB Switzerland), Tim Voegtlin (ETH Zurich), Sam Bodry (ETH Zurich) and Moritz Boehm (ABB Switzerland)</i>	297
On the correlation between performance, properties and microstructure of Ag/WC and AgW contact tips <i>Massimiliano Amato (ABB), Atanu Chaudhuri (ABB), Ato David (ABB), Cody Andelin (ABB), Carlene Jerram (ABB), Srinidhi Sampath (ABB) and Linda Jacobs (ABB)</i>	303
The Impact of Arcing (AC3) on the Contact Resistance Behavior of Ag/SnO2 <i>Timo Muetzel (SAXONIA Technical Materials GmbH), Christian Hubrich (SAXONIA Technical Materials GmbH) and Johannes Tasch (SAXONIA Technical Materials GmbH)</i>	311
Session 8: Sliding Contacts	
Effect on Brush Electrification Mechanism Associated with Various Ag Content of Ag Graphite Brushes. <i>Naoki Fukuda (Nippon Institute of technology), Yusuke Takada (Nippon Institute of technology), Koichiro Sawa (Nippon Institute of technology) and Takahiro Ueno (Nippon Institute of technology)</i>	317
Electrical and mechanical wear of a graphite brush having varying silver content in a slip-ring system <i>Takahiro Ueno (Nippon Institute of Technology), Naoki Fukuda (Nippon Institute of Technology) and Koichiro Sawa (Nippon Institute of Technology)</i>	323
Relationship between sliding surface roughness of slip ring and amount of brush wear in slip ring system <i>Yusuke Takada (Nippon Institute of Technology), Naoki Fukuda (Nippon Institute of technology), Koichiro Sawa (Nippon Institute of Technology) and Takahiro Ueno (Nippon Institute of Technology)</i>	329

Raman Spectroscopic Analysis of Carbon Film on Frictional Surface of Contact Wire <i>Yoshitaka Kubota (Railway Technical Research Institute)</i>	334
Tribology of electrical sliding contacts <i>Christian Holzapfel (Schleifring GmbH)</i>	339
Session 9: Automotive Applications	
Future of Electromechanical Switchgear <i>Frank Berger (Technische Universität Ilmenau)</i>	347
The silver anti-tarnish affecting the electrical stability of automotive terminals <i>Maxime Porte (Aptiv)</i>	355
Study on the Arc Erosion Characteristic and Mechanism of AgSnO ₂ Used in the Simulated Conditions of Automotive Relay <i>Li Jie (Fuda Alloy Materials Co., Ltd), Yan Xiaofang (Fuda Alloy Materials Co., Ltd) and Bai Xiaoping (Fuda Alloy Materials Co., Ltd)</i>	362
Thermal Equivalent Circuits: An Approach to Rate High-Power Connectors for Electric Mobility Applications <i>Michael Ludwig (TE Connectivity Germany GmbH), Michael Leidner (TE Connectivity Germany GmbH), Helge Schmidt (TE Connectivity Germany GmbH) and Frank Ostendorf (TE Connectivity Germany GmbH)</i>	370
Influence of the aging temperature on the hardness and the temperature-specific compressive yield point of bolted joints with copper and aluminium alloys conductors for vehicle electrical systems <i>Franck Stephane Djuimeni Poudeu (Mercedes-Benz AG), Michael Beilner (Mercedes-Benz AG) and Stephan Schlegel (Technische Universität Dresden)</i>	378
Modelling the switching behavior of pyrofuses for the protection of electric cars based on measurement data <i>Dietmar Haba (Hirtenberger Automotive Safety)</i>	385
Where would we be without contacts? Automotive trends and impact on electromechanical components <i>Uwe Hauck (TE Connectivity)</i>	392
THURSDAY Session 10: High and Low Power Contacts	
Qualification of Power Contacts in High-Voltage Products for IEC 115°C Limit Temperature <i>Michael Gatzsche (ABB Power Grids), Alberto Zanetti (ABB Power Grids) and Falk Blumenroth (ABB Power Grids)</i>	398
Recommendations for Testing the Short Circuit Behaviour of Power Plug-In Connectors <i>Toni Israel (Technische Universität Dresden), Stephan Schlegel (Technische Universität Dresden), Steffen Großmann (Technische Universität Dresden), Tom Kufner (Stäubli Electrical Connectors AG) and George Freudiger (Staubli Electrical Connectors AG)</i>	404
Calculations and metallographic investigations on the growth of Al ₂ O ₃ -layers in bimetallic contacts <i>Marcella Oberst (Technische Universität Dresden), Stephan Schlegel (Technische Universität Dresden) and Steffen Grossmann (Technische Universität Dresden)</i>	412
Volumetric erosion of a structured electrical contact surface using X-Ray Computed Tomography. <i>John McBride (University of Southampton), Thomas Bull (University of Southampton) and Kevin Cross (TaiCaan Technologies Ltd.)</i>	420
Silver based contact system enabling extremely low and stable contact resistance in mini thermal cut off devices <i>Werner Jöhler (Littelfuse Europe GmbH), Jack Bu (Littelfuse Electronics), Kevin Liang (Littelfuse Electronics) and Steven Hu (Littelfuse Electronics)</i>	428

Session 11: Environmental Effects, Diagnostics and Reliability

Research on the Corrosion Phenomenon of Iron Parts in the Internal Micro-environment of Relay
Qingxing Su (Testing Center of Xiamen Hongfa Electroacoustic CO.,LTD.), Changliu Jiang (Testing Center of Xiamen Hongfa Electroacoustic CO.,LTD.), Ningyi Lu (Testing Center of Xiamen Hongfa Electroacoustic CO.,LTD.) and Lei Yi (Testing Center of Xiamen Hongfa Electroacoustic CO.,LTD.)..... 436

Reliability Improvement of Gold Plated Contacts in Card Edge Connector of Power Cabinet
Yilin Zhou (Beijing University of Posts and Telecommunications), Mengqing Wang (Beijing University of Posts and Telecommunications), Nan Tian (Beijing University of Posts and Telecommunications) and Yunjie Shi (Beijing University of Posts and Telecommunications). 442

Influence of red phosphorous flame retarded plastic materials on relay contacts and electronic components
Dieter Volm (Panasonic Electric Works Europe AG), Bernhard Fauth (Panasonic Electric Works Europe AG) and Thomas Herrle (Panasonic Industrial Devices Europe GmbH)..... 450

The Effect of Relative Humidity on the Diffusion of Brass Elements Through Tin Plating
Bradley Schultz (TE Connectivity, Corporate Technology), Rodney Martens (TE Connectivity, Corporate Technology), Suvrat Bhargava (TE Connectivity, Corporate Technology) and Raymond Landon (TE Connectivity, Commercial Solutions Appliance Business Unit). 458

Session 12: Modeling/Simulation A

Simulations of switching devices with the example of a circuit breaker: the knowns, the unknowns, and the way ahead.
Henrik Nordborg, Roman Fuchs, Mario Mürmann (OST Eastern Switzerland University of Applied Sciences, Rapperswil, Switzerland) 466

Remarks Concerning Arc Roots in CFD Modeling of Switching Arcs
Manfred Lindmayer (TU Braunschweig). 474

Arc Evolution Process Considering the Motion of Moving Contact in DC Circuit Breaker
Jianning Yin (Xi'an University of Technology), Tian Tian (Xi'an Jiaotong University), Qian Wang (Xi'an University of Technology) and Xingwen Li (Xi'an Jiaotong University). 480

Surge protection device digital prototyping
Olga Schneider (DEHN SE + Co KG), Arnd Ehrhardt (DEHN SE + Co KG), Bernd Leibig (DEHN SE + Co KG), Sebastian Schmausser (DEHN SE + Co KG), Andrey Aksenov (Capvidia NV) and Elena Shaporenko (Capvidia NV)..... 486

Numerical arc simulations of radiatively-induced PMMA nozzle wall ablation
Roman Fuchs (HSR University of Applied Sciences Rapperswil)..... 494

Simulation-based Development of a Line Lightning Protection Device
Mario Muermann (IET Institute for Energy Technology, HSR University of Applied Science Rapperswil), Alexander Chusov (Streamer-Electric, St. Petersburg), Roman Fuchs (HSR University of Applied Sciences) and Henrik Nordborg (HSR University of Applied Sciences)..... 500

Research on virtual prototyping technology of dynamic characteristics for a type of hermetically sealed electromagnetic relay
Jiaxin You (Harbin Institute of Technology), Rao Fu (Harbin Institute of Technology), Xiangdong Feng (Harbin Institute of Technology), Bo Li (Harbin Institute of Technology) and Huimin Liang (Harbin Institute of Technology). 508

Robust and Efficient Software-based 3D Clearance and Creepage Analysis
Michael Martinek (e-laborate Innovations GmbH)..... 513

Investigations into the Mechanical Behaviour of Aluminium Conductors in Connectors for Plastic-Insulated High-Voltage Cables with large Cross-Sections using the Finite Element Method
Michael Hoischen (South Westphalia University of Applied Sciences), Shem George Varghese (South Westphalia University of Applied Sciences) and Robert Bach (South Westphalia University of Applied Sciences)..... 520

Session 13: Modeling/Simulation B

An improved method to identify the evolution of rough surface contact by the elliptical asperity <i>Wanbin Ren (Harbin Institute of Technology), Chao Zhang (Harbin Institute of Technology), Fubiao Luo (G&A Electronics Ltd. Co.) and Zhen Wei (G&A Electronics Ltd. Co.)</i>	526
Elastic Rough Surface Contact and the Root Mean Square Slope of Measured Surfaces <i>Robert Jackson (Auburn University), Yang Xu (University of Glasgow), Swarna Saha (Auburn University) and Kyle Schulze (Auburn University)</i>	534
Press-fit Whiskers Risk Assessment by Simulation <i>Marius Tarnovetchi (Continental AG), Francois Le-Rest (Continental AG) and Hans-Peter Tranitz (Continental AG)</i>	542
The mathematical model of a short arc at the blow-off repulsion of electrical contacts during the transition from metallic phase to gaseous phase <i>Stanislav Kharin (Kazakh-British Technical University)</i>	549
Optimization of current carrying connections under STC test conditions <i>Boguslaw Samul (ABB Power Grids Research), Joerg Ostrowski (ABB Corporate Research) and Remigiusz Nowak (ABB Power Grids Research)</i>	556
Series Arc Fault Modelling in Photovoltaic Resistive Systems <i>Silei Chen (Xi'an University of Technology), Xingwen Li (Xi'an Jiaotong University) and Jing Wang (Shenzhen Power Supply Bureau Shenzhen, P.R.China)</i>	562
Thermal simulation based on fluid-solid coupling method demonstrated on an Automotive Relay <i>Qiya Wang (Xiamen Hongfa Electroacoustic Co. , Ltd) and Zhengbin Zhang (Xiamen Hongfa Electroacoustic Co. , Ltd)</i>	568
Study on Thermoelastic Deformation of Bimetal Sheets in Miniature Circuit Breakers <i>Minglei Dai (Xi'an Jiaotong University), Yunkun Deng (Yunnan Electric Power Research Institute) and Xingwen Li (Xi'an Jiaotong University)</i>	575
FRIDAY Session 14: New Technologies	
SF6 alternative gases and future switching arc research <i>Christian Franck (ETH Zürich)</i>	581
Electric Arc Reconstruction from Magnetic Field <i>Jinlong Dong (Xi'an Jiaotong University), Luca Di Rienzo (Politecnico di Milano), Guogang Zhang (Xi'an Jiaotong University) and Jianhua Wang (Xi'an Jiaotong University)</i>	583
Model-based Design of Circuit Protection in DC Grids <i>Christian Strobl (E-TA Elektrotechnische Apparate GmbH)</i>	591
Influencing Factors for the Ultrasonic Compacting Process of Insulated Litz Wires for Electrical Drives <i>Johannes Seefried (Universität Erlangen-Nürnberg, Lehrstuhl FAPS), Andreas Riedel (Universität Erlangen-Nürnberg, Lehrstuhl FAPS), Andreas Lohbauer (Universität Erlangen-Nürnberg, Lehrstuhl FAPS), Hendrik Baessler (Universität Erlangen-Nürnberg, Lehrstuhl FAPS), Alexander Kuehl (Universität Erlangen-Nürnberg, Lehrstuhl FAPS) and Jörg Franke (Universität Erlangen-Nürnberg, Lehrstuhl FAPS)</i>	599
Experimental Setup of a Process Chain for Contacting Litz Wires for Electrical Drives <i>Andreas Riedel (Universität Erlangen-Nürnberg, Lehrstuhl FAPS), Johannes Seefried (Universität Erlangen-Nürnberg, Lehrstuhl FAPS), Alexander Schmidt (Universität Erlangen-Nürnberg, Lehrstuhl FAPS), Alexander Kuehl (Universität Erlangen-Nürnberg, Lehrstuhl FAPS) and Joerg Franke (Universität Erlangen-Nürnberg, Lehrstuhl FAPS)</i>	607

Investigations on Different Joining Techniques Regarding Current-carrying Joints with Normal Conducting Material and YBCO Coated Conductors at low temperatures
Katrin Baeuml (Schneider Electric) and Steffen Großmann (TU Dresden). 615

Analysis of HDMI 2.1 Mated Connector Contact Boundary Impedance Impacts on a High-speed Digital System Performance
Youngwoo Kim (Nara Institute of Science and Technology (NAIST)), Daisuke Fujimoto (Nara Institute of Science and Technology (NAIST)) and Yu-ichi Hayashi (Nara Institute of Science and Technology (NAIST))..... 623

Innovative switching concept to shutdown circuit currents in DC operating systems up to 1000VDC/30kA or 3600VDC/12kA based on ultrafast Powerfuse (PF) technology without outgasing.
Peter Lell (PyroGlobe GmbH)..... 628

Circuit Control Development since the First International Conference on Electrical Contacts (1961 to 2020)

Paul G. Slade, Consultant, Ithaca, U.S.A., paulgslade@verizon.net

Abstract

The paper reviews 60 years (1961 – 2020) development of circuit breakers, contactors, relays and switches. It also reviews the developments in measurement and analytical techniques that have enabled the further understanding of arc interruption and switching contact performance. The introduction of the high-speed oscilloscope in the early 1960s, for the first time, made possible observation of current and voltage down to the nano-second level. This led to a better understanding of arc formation, arc interruption and arc erosion. The scanning electron microscope introduced in 1965 permitted the detailed study of arc erosion effects. The addition of x-ray analysis in the early 1970's allowed a detailed analysis of elemental changes in contact surfaces. The development of advanced vacuum technology in the late 1960s enabled introduction of the sealed-for-life, power-vacuum interrupter for medium voltage distribution circuits. In the 1970s electronic sensors began to replace the electro-mechanical sensors to control circuit breakers, contactors and relays. Integrated circuit technology then was increasingly introduced into these sensors. Today there are many circuit breakers and other switches that can respond to many types of circuit conditions and determine the action to be taken. The personal computer (PC) first introduced in the 1980s began a revolution in the engineer's and scientist's world. Who remembers secretaries, the written letter and the slide presentation etc.? The PC became so powerful that in the 1990s circuit breakers and other types of switch could be designed at the engineer's desk top using 3-D drafting software. The introduction of finite element analysis (e.g. ANSOFT) and arc modeling software (e.g. FLUENT) has aided the advanced development of all switching devices. The MEMS (micro-electro-mechanical systems) switches were introduced in the late 1990s. In the future circuit breakers and other switches will continue to be used to switch and isolate electrical circuits in spite of the inroads of power electronic devices. They will become more compact and will also become more intelligent as more advanced sensor technology is introduced. The vacuum interrupter, now the prevalent technology for 5kV to 40.5kV circuits will start to dominate higher voltage circuits (72kV to 170kV). Perhaps even the MEMS switch will find a commercial application!

1. Introduction

Circuit control using electrical contacts has a long history dating back to the earliest days of electric power distribution at the end of the 19th century. Research symposia and conferences devoted to electric contact phenomena only began to be held in the 1950's. The first International Conference on Electrical Contacts was held in Orono Maine U.S.A., November 1961. At that time, it was called "The International Research Symposium on Electric Contact Phenomenon". It was a small beginning with only 25 papers and authors from only 6 countries (USA, Germany, Austria, Holland, UK and Japan). There were 14 papers on switching contacts, 4 on connectors, 4 on contact theory and 3 on sliding contacts. The instrumentation used to analyze the contact experiments was rather basic: volt and amp meters, slow sweep speed oscilloscopes, optical microscopes and photography using photographic film. None of the papers made reference to the computer.

2 The Decade 1961 to 1970

A new range of measurement tools were introduced in this decade. Some of them are shown in **Figure 1**. The oscilloscopes transitioned from tube electronics to transistors and had sub-nanosecond resolution. The screens were cathode ray tubes and polaroid introduced instant photography to capture the screen's data. High speed cameras using photographic film began to be a

feature in R&D laboratories. The most important instrument introduced in 1965 was the Scanning Electron Microscope that, for the first time, allowed a three-dimensional high-resolution image of the contact's surface.

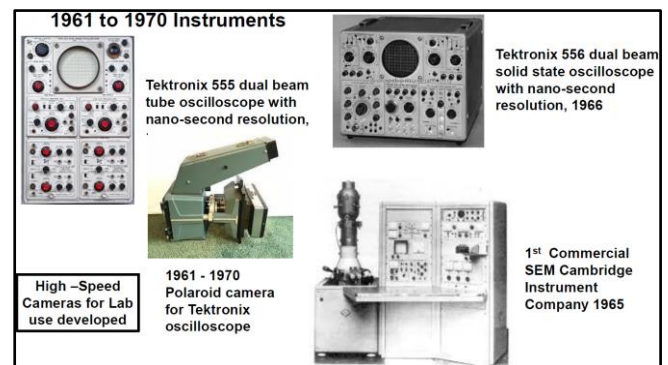


Fig. 1, New instrumentation 1961 -1970

There was a range of low voltage ($\leq 600V$) circuit breakers and contactors. Examples are shown in **Figure 2**. There was also a wide range of ac and dc and mechanical and magnetic relays for voltages less than 110V. The main contact materials used in these switch systems were Ag, Ag-W, Ag-Ni, Ag-CdO, and Ag-C.

In the late 1960's John Wafer and I developed an "Integral Motor Controller" that performed the switching function of a contactor as well as the circuit

protection function of a molded case circuit breaker [1]. In this development we calculated using a slide rule. The

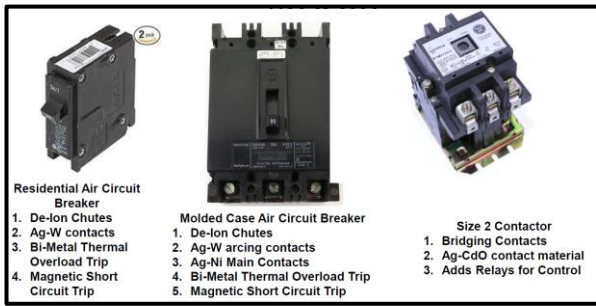


Fig. 2, Circuit switches and circuit protectors 1961-1970

design in Figure 3 was developed using our own intuition, the help of a skilled draftsman and a skilled machine shop operator.

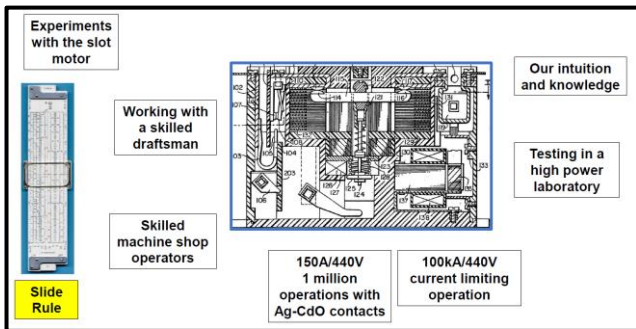


Fig. 3, The Integral Motor Controller

In this decade switching and control of distribution circuits (5kV to 38kV) was performed by two efficient circuit breakers; the minimum oil circuit breaker and the magnetic air circuit breaker [2]: see Figure 4.

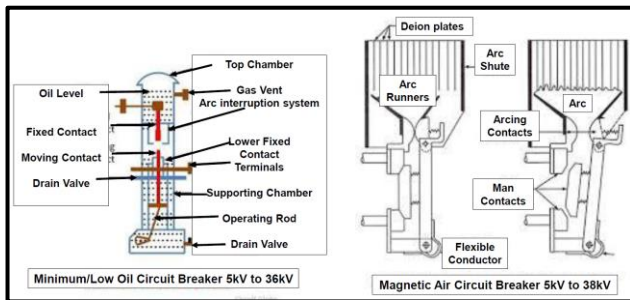


Fig. 4, Distribution Circuit Breakers 1961 to,1970

In the 1960's the General Electric Company (GE) announced the development of the power-vacuum interrupter: See Fig. 5. GE's design used a spiral contact to control the high current vacuum arc (Figure 6), Cu-Bi contacts that resisted welding in the vacuum environment and floating shields to prevent metal vapor coating the interior insulating walls. This general design became the benchmark for all future vacuum interrupter designs. Westinghouse also began its own development of the vacuum interrupter. They developed a superior contact material, Cu-Cr. They also introduced vacuum furnace pumping and sealing. Both became the standard

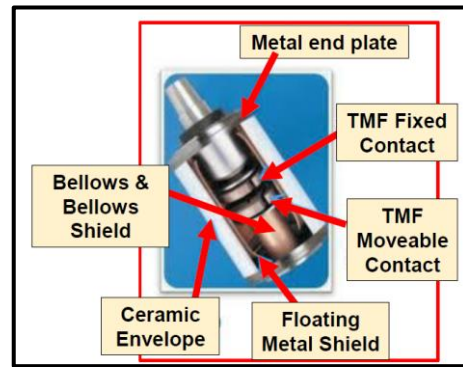


Fig. 5, The power vacuum interrupter

for all future power vacuum interrupters. Their goal in this decade was a vacuum interrupter capable of interrupting 12kA, 15kV with a diameter of 182 mm. Both companies engaged in significant R&D [3].

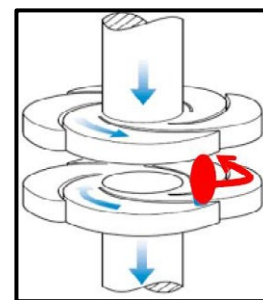


Fig. 6 The spiral contact (the transverse magnetic field contact [TMF])

The main frame computer started to be introduced and used by researchers in Universities and Industrial R&D Centers. These were very large systems and required installation in a large room: See Figure 7. The computer programs were punched on rectangular cards,

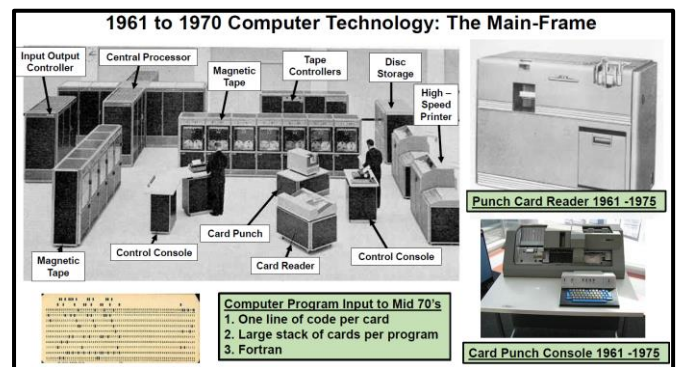


Fig. 7, The main frame computer

one code line per card. A large stack of cards was then fed into a card reader. Magnetic tape acted as the computer's memory. The room was staffed by a number of operators. The main engineering computer code was Fortran 4.

2 The Decade 1971 to 1980

In this decade the researcher's world began to be impacted by the rapid development of the integrated circuit which was initially developed in the late 1950s. In 1971 Hewlett Packard introduced the scientific calculator, **Figure 8**, that quickly replaced the slide rule. They sold millions at a price of \$395.00 equivalent of over \$3000.00 today!



Fig. 8, The HP 35 scientific calculator

Computer technology was also developing very rapidly. The card readers were replaced by direct input into main frame computers [4]. More user friendly computer programs were becoming available. Mini computers appeared that could do most of the work previously performed by the old main frames. The first artificial intelligence programs were written. Disc memory was introduced. Apple and Microsoft were start-up companies. And Xerox developed the mouse. **Figure 9** shows examples of a mini computer, an early word processor and the Apple II.



Fig. 9, The developing computer systems

Understanding of the impact of the electric arc on the performance of switching electric contacts continued to expand. The impact of the rupture of the molten metal bridge as the contacts open and the initial development of the arc in metal vapor and its transition to the arc burning in the ambient gas was recognized. It was observed that the interaction of silicone oils, greases and plastics with arcs resulted in high contact resistances. There was the initial development of the Ag-

SnO₂ contact material. The early compounds developed high contact resistances after frequent switching. Power vacuum interrupters began commercial production and the first vacuum circuit breaker sale occurred. The 12kA, 15kV vacuum interrupter now had a reduced diameter of 104mm. The axial magnetic contact design for vacuum interrupters that have to interrupt high-currents was developed. This allowed the high current vacuum arc to remain diffuse. **Figure 10** shows an example of a axial magnetic contact structure and the resulting diffuse vacuum arc [3].

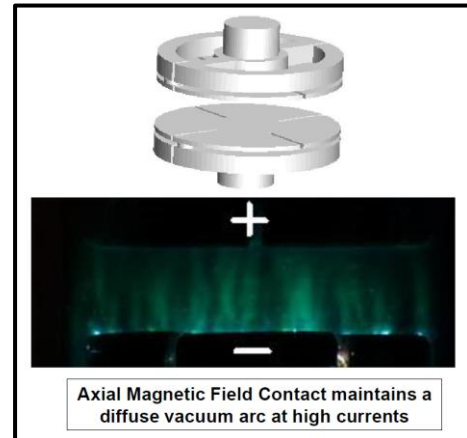


Fig. 10, The axial magnetic field vacuum interrupter contact and an image of the resulting high-current vacuum arc

3 The Decade 1981 to 1990

The modern age of computer technology really began in this decade. **Figure 11** illustrates the innovations seen.

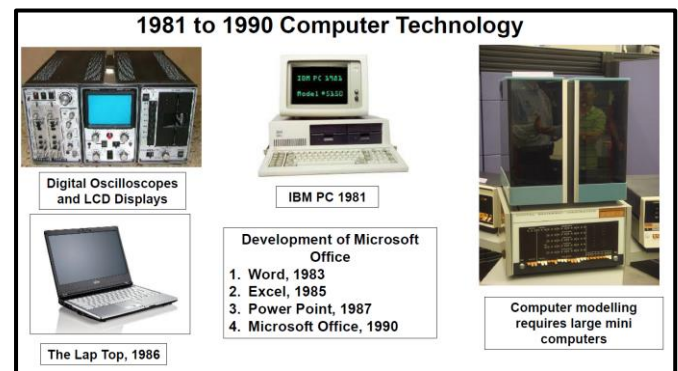


Fig. 11, The beginning of modern computer technology

The IBM PC brought computing to the desk top of scientists, engineers and the general public. The introduction of the LCD flat screen enabled the introduction of the portable lap-top computer. The large mini computer, for the first time, enabled solid modeling without the having to use a large main frame computer. One of the most important software developments in this decade was from Microsoft who introduced Word, Excel, Power Point and Office. Who now remembers typewriters, secretaries and conference

presentations that used photographic slides or overhead projectors?

The 1980s saw the introduction of a new generation of Molded Case Circuit Breakers. These had a current limiting ability and were capable of interrupting 100kA, 440V. They also incorporated electronic control for sensing overload and short circuit currents. Vacuum contactors for currents greater than 150A and circuit voltages less than or equal to 600V were introduced. DIN rail household circuit breakers gained general acceptance: See **Figure 12**.

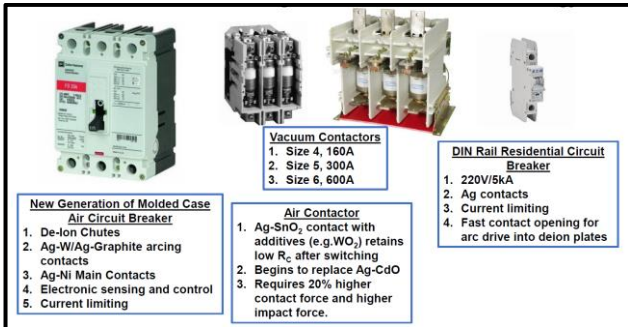


Fig. 12, The new low voltage circuit breaker and contactor developments

The recognition that Cd was an environmental hazard led to the realization that a replacement was required for the Ag-CdO contact. Continued research on improving the Ag-SnO₂ contact resulted in small additions of WO₂ or BiO₂. This permitted this contact to be used as a replacement of Ag-CdO as it no longer developed such a high contact resistance after a large number of switching operations. Also it was realized that 20% higher contact forces and higher impact were required for its use in contactors and relays.

By 1990 the installation of new minimum oil circuit breaker and magnetic air circuit breaker for distribution circuit protection was beginning to decline. The vacuum interrupter circuit breaker and the SF₆ puffer circuit breaker were taking their place. **Figure 13** shows that the vacuum circuit breaker had 50% of new circuit breaker installations by 1990.

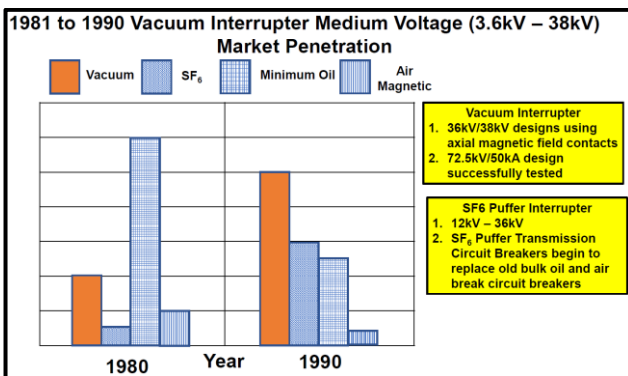


Fig. 13, The old circuit breaker technology for distribution circuits was being displaced by the new vacuum circuit breaker and the new SF₆ puffer breaker

4 The Decade 1991 to 2000

There was a significant development of engineering software for engineering design along with more powerful small computers in this decade: see **Figure 14**. The Sun work-station at the beginning of

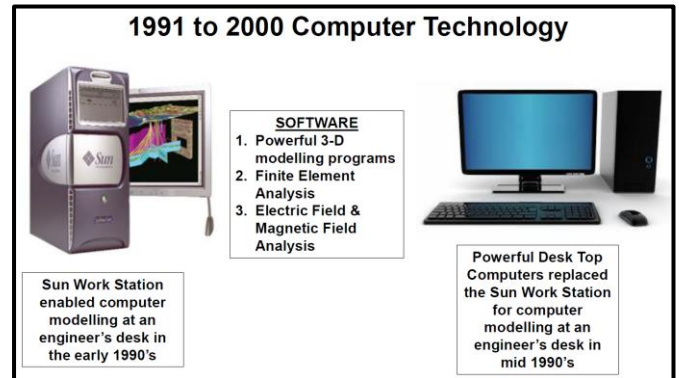


Fig. 14, The development of software and computer technology for the engineer and scientist

the decade enabled engineers to perform the work of a skilled draftsman using solid modelling software at their desks. The PC developed to such an extent that towards the end of the decade it made the Sun workstation obsolete. The user friendly Finite Element Analysis software enabled the engineer to perform electric and magnetic field analysis.

Integrated circuit technology continued to change the engineers' and scientists' world as shown in **Figure 15**. By Christmas 1990, Berners-Lee working at CERN

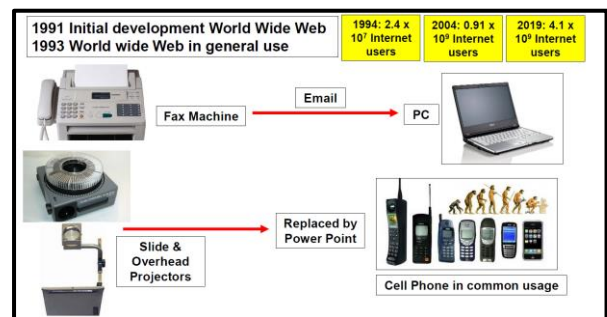


Fig. 15, The changes in communications

had built all the tools necessary for a working World Wide Web: In January 1991 the first Web servers outside CERN itself were switched on. The first web browser was available in 1992 and the use of the Internet gradually became an everyday phenomenon. By the end of 1994 there were 24 x 10⁶ users. Ten years later there were close to one billion users and last year there were 4.7 billion. Power Point figures replaced slides for all scientific and engineering presentations. Indeed, I could not have prepared this paper without the Internet and the Power Point software. The cell or mobile phone crept into our existence during this decade and email replaced the Fax machine for all correspondence except for those

that needed the utmost security. Who writes letters anymore?

There was a continued development of the Ag-SnO₂ contact material. Internally oxidized Ag-SnO₂-InO₂ was introduced and Ag-SnO₂ + additives gradually began to replace Ag-CdO in contactors and relay especially in Europe and Japan. Electronic sensing and control were added to contactors and relays. Some of the previous relays with switching contacts were replaced by electronic relays.

The R&D into the development of the vacuum interrupter led to really cost-effective designs. **Figure 16** shows the example of the size reduction and hence cost reduction of the 15kV/12.5kA vacuum interrupter.

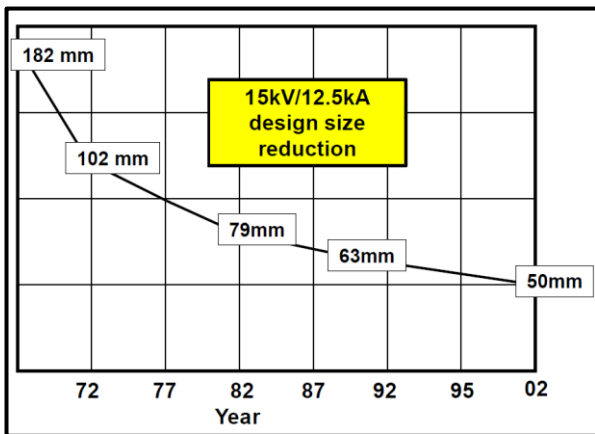


Fig. 16, The size and cost reduction of the 15kV/12.5kA vacuum interrupter from 1967 to 2002

The continued development of the Cu-Cr contact material, better understanding and control of the high-current vacuum arc with TMF and AMF contact structures and improved design of the floating shield all played a part in this size reduction. By 2000 the cost of a vacuum circuit breaker competed so well that it eclipsed the minimum oil circuit breaker for new distribution installations.

5 The Decades 2000 to 2020

The late 1990s saw the beginning of a revolution in photography and camera technology. The digital camera began to replace the use of photographic film. The digital images could now be uploaded directly to a computer and the internet. High-speed digital cameras also replaced the cameras that required photographic film. The use of these new cameras permitted direct study and analysis of the vacuum arc. In turn, it greatly aided the improvement of the design of high-current vacuum interrupter contacts. In 2002 the first digital camera was incorporated into the cell/mobile phone.

The advent of the hybrid and electric automobiles plus the expanded use of solar power generation called for new designs of higher voltage (up to 1500VDC), compact relays and circuit protectors. **Figure 17**

illustrates one way of achieving the high arc voltage to cause an artificial current zero in a dc circuit. This was achieved by using permanent, high-tesla magnets across bridging contacts. At present there is no coherent

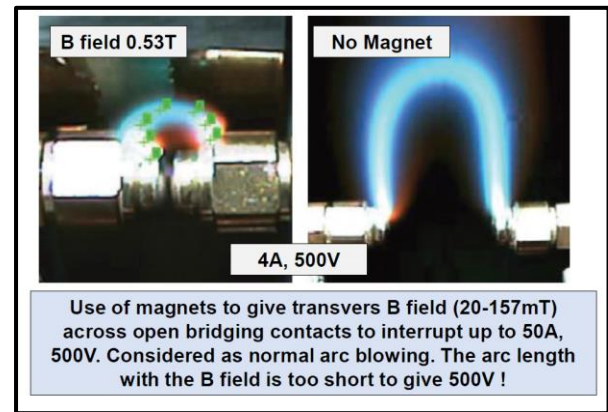


Fig. 17, The development of a high arc voltage using transverse magnetic fields across opening bridging contacts

theory of how the high arc voltage develops with such a short arc column. Commercial high-voltage relays now use a similar arrangement inside a hermetically sealed box containing a hydrogen atmosphere.

The market penetration of the vacuum circuit breaker shows a complete dominance as is shown in

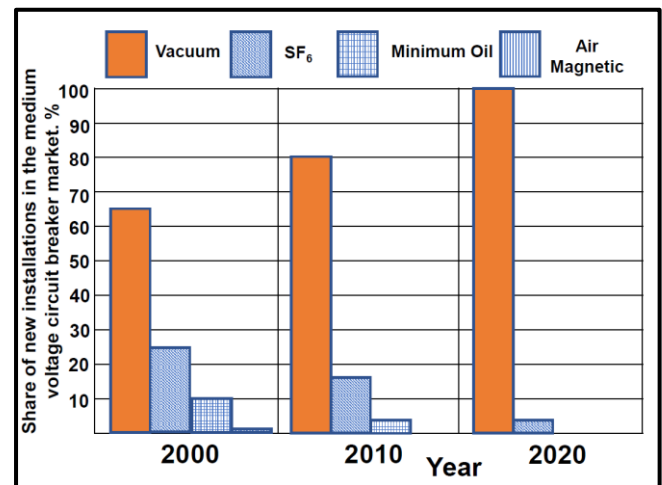


Fig. 18, The vacuum interrupter now has close to 100% share in the installation of distribution circuit breakers world-wide

Figure 18. While in the 1990s the SF₆ puffer interrupter was a strong competitor, the realization that SF₆ was a virulent green house gas led to its replacement by the environmentally neutral vacuum interrupter technology.

The integrated circuit sensing technology continued to be applied to circuit interruption devices. One excellent example is the Arc Fault Circuit Interrupter (AFCI) for household use. Its development was necessary, because the standard household circuit

breakers could only detect overload and short circuit currents [6]. It was realized that many household

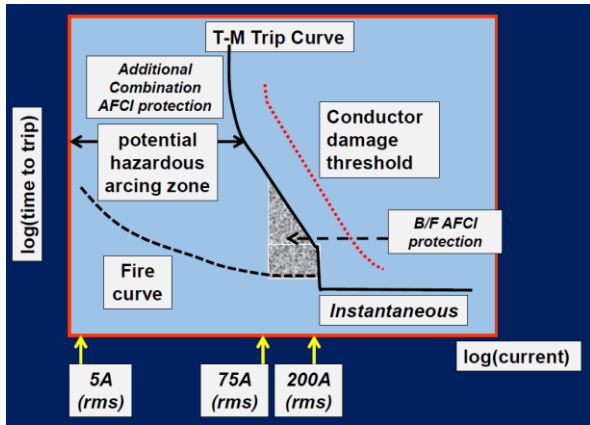


Fig. 19, The AFCI tripping curve showing the ability to detect low current faults

fires developed from low current arcs that went undetected by the standard household circuit breaker. Thus a new sensor was required using advanced intergrated circuit technology. The challenge when developing the sensor for the AFCI was to distinguish the low current arcing, a result of a disconnect in the household wiring, from normal arcing from relays that were used in many household appliances, e.g. the electric iron. An example of the trip curve is shown in **Figure 19**. The AFCI is now mandatory in all new house construction in the U.S.A.

One interesting development was the MEMS (micro electro mechanical system) switch [7].

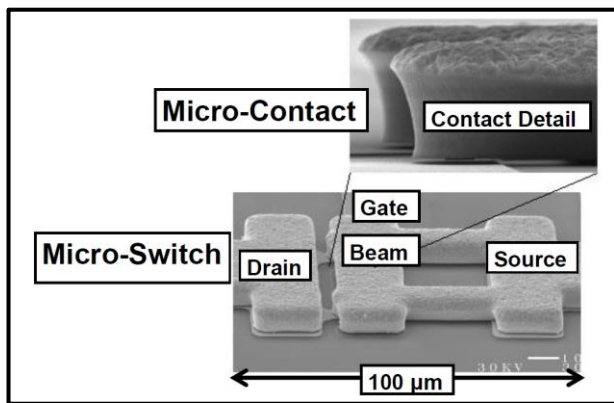


Fig. 20, The MEMS switch: note the dimensions

Figure 20 shows an example of a design that has the dimensions of about 100µm or 0.1mm. It was suggested that it would find a use in radar systems, high precision test equipment, cell phones, phase shifters, impedance matching networks and tunable filters. The major challenge was to find a suitable contact material that did not oxidize and also resisted welding. While R&D continues to perfect this device, as of 2020, no commercial MEMS switches have been marketed.

By 2020 the design engineer has complete control over new circuit breaker, contactor and switch

design and initial prototype development. The contrast from the way new prototypes were developed in the

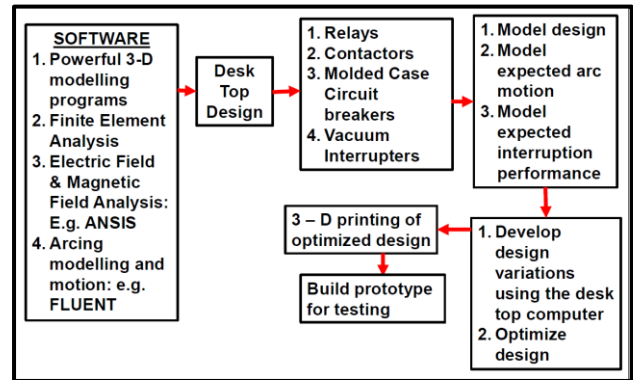


Fig. 21, The design and development for prototype interrupters from the engineer’s work station.

1960s as seen in **Figure 3** is enormous. **Figure 21** illustrates the way a design engineers has complete control from his work station. The software available even permits the engineer to model the electric arc and its motion as the contacts open. The solid modeling programs replace the need of a skilled draftsman. It is possible to estimate the new device’s performance before building a prototype. In the future 3-D printing will reduce the need for a skilled machinist for the first prototype model. The new designs will still have to be certified by testing at a recognized laboratory to UL, IEEE, and IEC standards before they are ready to be sold to potential users.

6 The Future, Post 2020

The addition of electronic sensing to circuit breakers, contactors and relays will only become more prevalent. **Figure 22** shows an example of the what can

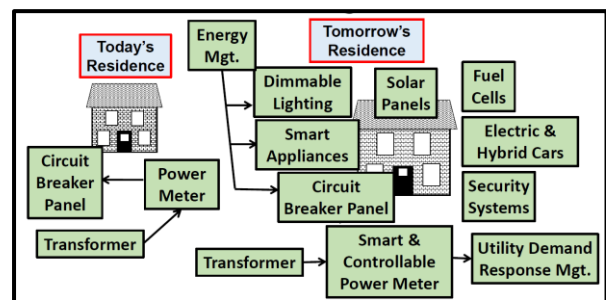


Fig. 22, The future of residential smart switching

be expected for new household construction. Smart switching will also have to be developed for the factory of the future. Here cogeneration using power generating stations, solar panels, wind turbines and fuel cells will have to be coordinated: see **Figure 23**.

The vacuum circuit breaker will continue to dominate the protection of distribution circuits (5kV – 40.5kV). As it will be necessary to reduce the downtime of these circuits, the vacuum recloser (a specialized version of the vacuum circuit breaker) will require

more. specialized sensing and communication capability [3]. Also the need to reduce the use of SF₆ the SF₆ puffer circuit breaker used for transmission circuits

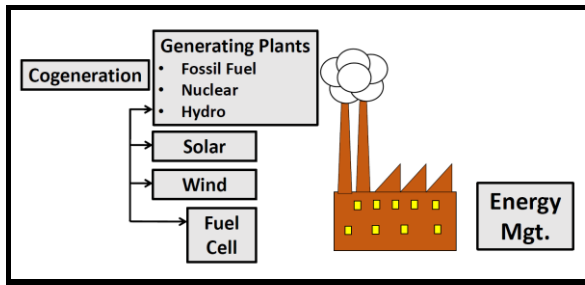


Fig. 23, The future of factory switching

(72.5kV – 750kV) will gradually be replaced by high-voltage vacuum circuit breakers. DC transmission of current, specially from off-shore wind turbine farms, will require the use of dc circuit breakers. Designs using vacuum interrupters are already being discussed [9].

There is, however, an elephant in the room (Figure 24) which will affect the future of switching



Fig. 24, The elephant in the room!

with electric contacts. This is the continued application of power semiconductors such as the IGBT (The integrated-gate bipolar transistor). This device is continuing to be developed and is capable of interrupting increased levels of current. It is also able to withstand higher circuit voltages. A single IGBT now has a current rating $\geq 1\text{kA}$ and a voltage rating $\geq 1\text{kV}$ [8]. It is capable of high speed switching for both ac and dc circuits. It can easily coordinate with electronic sensing circuits. Figure 25 gives some examples of solid-state interrupters

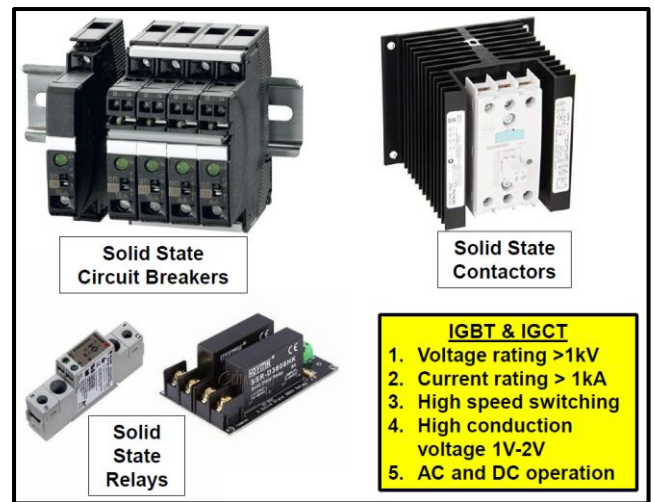


Fig. 25, Examples of solid-state circuit breakers, contactors and relays available in 2020.

They do have, however, two major disadvantages:

- 1) They require 1V to 2V across the semiconductor to conduct current
- 2) When open they do not have the complete circuit isolation of open contacts.

7 Conclusions

- 1) 60 years on from the 1st International Contact Conference has seen an increased understanding of switching contact science
- 2) In the past 60 years two major contact structures have been developed:
 - 1) Ag-SnO₂ + additives that is replacing Ag-CdO for air contactors and relays
 - 2) Cu-Cr that is the contact of choice for power vacuum interrupters
- 3) 60 years on from the 1st International Contact Conference the development of new switching devices using electrical contacts has been continuous:
 - 1) Circuit breakers, contactors and relays have now incorporated electronic sensing
 - 2) The vacuum interrupter is now the interrupter of choice for distribution circuit voltages (5kV – 40.5kV)
- 4) Solid-state switching devices are making inroads into traditional switch markets that use electrical contacts. They will occupy a larger niche market in the future, but will not entirely replace circuit breakers and other power switching systems using electrical contacts. Also, open electrical contacts will still be needed to provide total circuit isolation.

- 5) 2020 computer software has transformed the design, development and prototype manufacture of circuit breakers and other switching devices.
- 6) In 2020 computers, computer software and the instruments available for studying switching contacts and switching systems would have seemed like science fiction in 1961.

7 References

1. Slade, P., Wafer, J., “Modular Integral motor controller”, US Patent 4,025,883, May 1977
2. Lythall, R., The JSP Switchgear Book (7th Edition), pp. 418-465, 1972
3. Slade, P. The Vacuum Interrupter: Theory, Design and Application, (Pub CRC Press), 2007
4. https://en.wikipedia.org/wiki/History_of_computing_hardware
5. Sawa, K., Tsujimura, S., Motoda, S., “Fundamental characteristics of arc extinction by magnetic blow-out at dc voltages ($\leq 500\text{V}$) II”, Proc. IEEE Holm Conference on Electrical Contacts, pp. 154 – 159, Oct. 2015
6. Shea, J, “Arc faults and electrical safety”, Electrical Contacts: Principles and Applications (2nd Edition), (Pub. CRC Press), Editor Slade, P., pp. 849 – 879, 2014
7. Toler, B., Couto, R., McBride, J. “Low current and high frequency miniature switches: microelectromechanical systems (MEMS), metal contact switches”. Electrical Contacts: Principles and Applications (2nd Edition), (Pub. CRC Press), Editor Slade, P., pp. 703 – 730, 2014
8. https://en.wikipedia.org/wiki/Insulated-gate_bipolar_transistor
9. Jovicic, D., Tang, G., Pang, H., “Adopting circuit breakers for high-voltage dc networks”, IEEE Power and Energy Magazine, Vol. 17, No. 3, pp. 82 EEE Power and Energy Magazine, Vol. 17, No. 4, pp. 56 – 66, July/Aug. 82 – 93, May/June 2019

technology; the vacuum interrupter. In his career at the R&D Center he held a number of technical management positions culminating in the position of Chief Scientist for the Westinghouse Industrial Group. When Westinghouse sold its Distribution Equipment Division to the Eaton Corporation, he joined Eaton’s Vacuum Interrupter Product operation as manager of Vacuum Interrupter Technology, where he had complete responsibility for the R&D and for new vacuum interrupter designs. Since his retirement from Eaton in 2007 he has been an independent consultant for vacuum interrupter technology, electrical contacts and circuit interruption. His email address is: paulgslade@verizon.net

Dr Slade has over 50 years’ experience in the application of electric contacts for switching electric current. His research has covered many aspects of electric contact and arcing phenomena in vacuum, air and SF₆. He has published over 130 technical papers in archival journals and scientific conferences. He is also the holder of 23 US patents. He is the major contributor and editor of the 2nd edition of the book “Electrical Contacts: Principles and Applications”. He authored the book “The Vacuum Interrupter: Theory, Design and Application”. He is the recipient of the IEEE Ragnar Holm Scientific Achievement Award and of the German VDE Albert Keil Pries for his contributions to the science of electrical contacts. He is a fellow of the IEEE.



Paul G Slade received his BS and PhD in Physics from the University of Wales, Swansea, U.K. and an MBA from the University of Pittsburgh, Pennsylvania, U.S.A. He joined a group of scientists at the Westinghouse R & D Center who, at that time, were developing a new electric circuit interruption

A novel experimental evaluation method of welding characteristics for contact materials

Xu Zhang¹, Wanbin Ren¹, Duanlin Jiang², Yinghua Fu³, Yide Cai¹

1. School of Electrical Engineering and Automation, Harbin Institute of Technology, Harbin, 150001, China

2. G&A Electronics Ltd. Co., Guilin, 541002, China

3. Chixi Technology Co., Nanchang, 330000, China

Email: renwanbin@hit.edu.cn

Abstract

Contact welding failure considerably influences the electrical lifetime and reliability of electromechanical switching devices. Also, the welding characteristics correlate closely with physical properties of contact materials, contact force, current level and duration. In this paper, a novel experimental method for reoccurring the welding phenomenon between two closed contacts is proposed. And the welding force and associated welding trace are measured simultaneously. Furthermore, the effects of current load and static contact force on the welding characteristics of different contact materials (Ag, Cu, AgSnO₂ and AgNi) are investigated explicitly. Finally, a modified mathematical model for calculating threshold welding current of elastic contact is proposed.

Key words: Contact welding, welding force, welding trace, contact force, threshold welding current.

1 Introduction

As known, contact welding can occur if a high enough current passes through closed contacts and causes the contact spot to melt [1]. The excessive welding force for switching contact in such state can lead to the contacts failed to open and must, therefore, be addressed.

Slade [2-4] did a lot of theoretical research and experimental verification work to determine the ability of vacuum circuit breakers to withstand short circuit current, and concluded that the threshold welding current of butt contact is directly related to current load, static contact force and material properties. In addition, Tslaf [5] proposed a thermal conduction model for cross bar contacts, and pointed out that the weldability of different contact materials is determined by coefficient η_w , which depends only on melting temperature, resistivity and heat conductivity. Kharin *et al.* [6] established a mathematical model of contact welding for AC current half-wave, and proposed the calculation method of welding area considering the softening contact zone.

Moreover, much efforts have been devoted to the experimental research of the contact welding characteristics. Borkowski *et al.* [7] reported an automated test stand for testing contact welding at a high current load, which can measure contact voltage and welding force synchronously. Slade *et al.* [4] experimentally investigated the effect of short circuit

current on the welding of closed contacts in vacuum circuit breakers for contact force of 1.3-2.1kN and current of 20kA, and concluded that the increase of contact force and/or the reduced of current duration could reduce the welding probability. Chalyi *et al.* [8] examined the effect of short-duration pulsed current on closed contact for contact force of 100N and 300N, and found that the welding force increased with the increase of pulsed current.

Nevertheless, power electromechanical relays have been designed to withstand inrush overload current in recent years. So, it is urgent to know the influencing factors of welding force of contact material. However, the threshold welding current of silver metal oxide materials and further associated welding characteristic for contact force of tens of mN remain unexamined.

The objective of this paper is to design a novel experimental evaluation method of welding characteristics, which can reoccur the welding phenomenon between two closed contacts, and in situ measure the welding force and welding traces synchronously. In Section II, the designed novel test rig and experimental conditions are introduced, then the typical transient waveforms of contact force and the pictures of the welding trace and associated welding area are given explicitly. In Section III, the effect of the current duration, initial contact force, material properties and contact current on the welding characteristics are studied experimentally. Finally, a modified mathematical model for calculating threshold welding current of elastic contact is proposed.

2 Experimental Details

2.1 Description of the test rig

In general, the test rig allows researching the welding behaviors of contact materials under different contact force and inrush current load. It was designed to fulfill the following goals, i.e.:

- Variable initial contact forces, inrush current levels, current duration, and breaking velocity to achieve the contact welding condition simulation of materials.
- Synchronization of data with electric actuator to allow measurement of welding force and welding trace in situ during contact breaking process.
- Electrical endurance tests with different operation modes, including MO (only making with load, breaking without load), BO (only breaking with load, making without load) and M&B (making and breaking both with load).

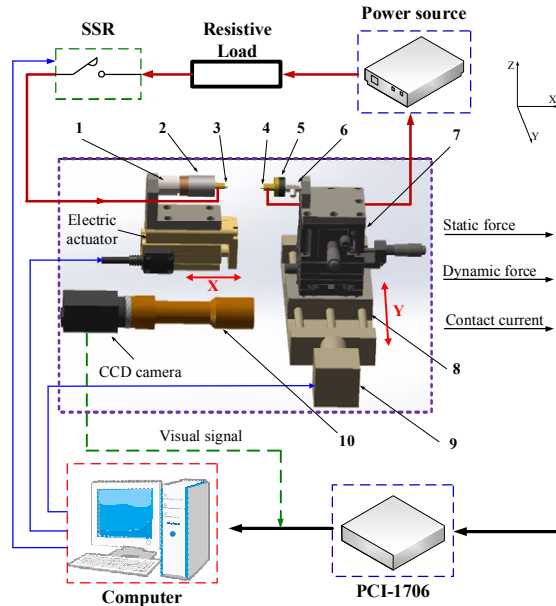


Fig.1 Schematic plot of the new designed test rig (1. Strain transducer 2. Flexible joint 3. Movable contact 4. Stationary contact 5. Insulation block 6. Dynamic force transducer 7. Multi-axis stage 8. Axis ‘Y’ LTS 9. Stepper motor 10. Telecentric lens)

A schematic diagram of the test rig is shown in Fig. 1. The test rig consists of four main units, including mechanical structure, measurement module, optical module and PC. The measurement of welding force is realized by a piezoelectric dynamic transducer (209C11, PCB, USA) with the upper frequency limits of 30kHz and the force resolution of 0.09mN. The initial contact force is measured by the strain transducer (FA404-2kg, FIBOS, China), which provides a resolution of 1mN. The contact current is measured by hall current sensor, which has the resolution of 50mA. The horizontal actuation of the movable contact is obtained by the electric actuator (RCA2, IAI, Japan). The actuation of the stationary

contact in ‘Y’ direction is obtained by means of a precision slider that is pushed by a stepper motor (42HB40, Leadshine, China). The optical module allows in situ observation of the contact surface morphology, which includes a color charge-coupled device (CCD) camera (MV-SUB1600C-T, Mindvision, China) with the pixel of $1.34\mu\text{m} \times 1.34\mu\text{m}$ and a telecentric lens with 2mm depth of field. The captured photograph could be read from USB3.0 interface of camera, which is connected with a personal computer. All above signals including contact current, dynamic force and static contact force are acquired by the commercial DAQ system (PCI1706, Advantech, Taiwan), which has a measurement resolution of 16 bits and a sampling frequency of 250 kHz. The instrument is interfaced to an industrial computer through PCI bus. Data acquisition and logging process are controlled by LabVIEW software.

Fig.2 shows a schematic of the excited current passing through the closed contact for producing welding. The contact current I_0 and current duration t_0 could be adjusted by power source and solid state relay respectively.

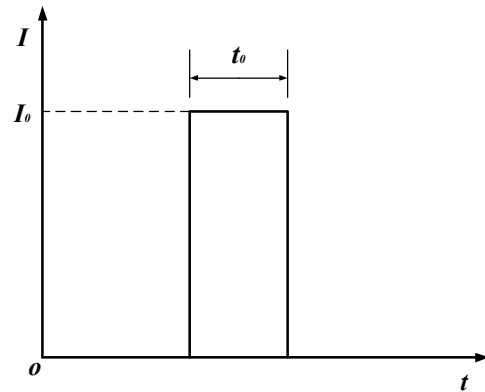


Fig.2 Illustration of the excited current passing through the closed contact for producing welding.

The experimental sequence was:

- The position of the stationary contact was adjusted to the central axis by the multi-axis stage. Then the electric actuator was used to control the movable contact to approach the stationary contact at the speed of $10\mu\text{m/s}$, until the contact force reaches the experimental setting value.
- The contact current I_0 was controlled by the solid state relay to pass through the closed contacts for the required current duration t_0 .
- The current was switched off and two minutes later the electric actuator was used to control the contacts to break at the required speed, and the dynamic force and contact displacement were measured simultaneously.
- The stationary contact was moved in ‘Y’ direction to the CCD camera view by means of a precision slider that is pushed by a stepper motor. Then the contact surface morphology and associated welding trace were observed.

2.2 Experimental conditions

The contact materials are Ag (99.99%), Cu (99.99%), AgSnO₂ (88/12) and AgNi (90/10). The movable contacts are cone-shaped, and stationary contacts are plane-shaped, and the Rhino-3D of experimental samples are shown in Fig.3. The samples are degreased using alcohol and distilled water in an ultrasonic cleaner, dried and carefully mounted in the test rig. The details of the experimental conditions are listed in Table1.

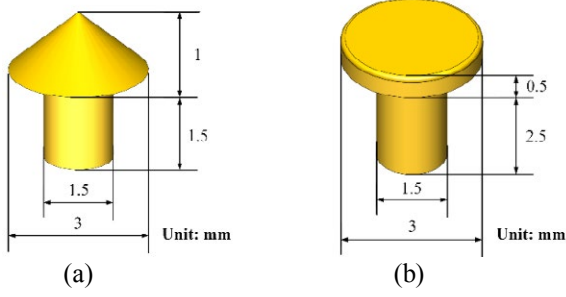


Fig.3 Rhino-3D of samples. (a) Cone. (b) Plane.

Table 1 Experimental conditions

Environment	Ambient temperature
Contact Material	Ag, Cu, AgSnO ₂ , AgNi
Contact Current	60-160A
Current Duration	1-2000ms
Initial Contact Force	20-800mN
Maximum opening Velocity	30mm/s
Resistance	0.1Ω

2.3 Measurement of welding force

The typical example of measured dynamic force transducer signal and actuator position waveforms during contact breaking is illustrated in Fig.4.

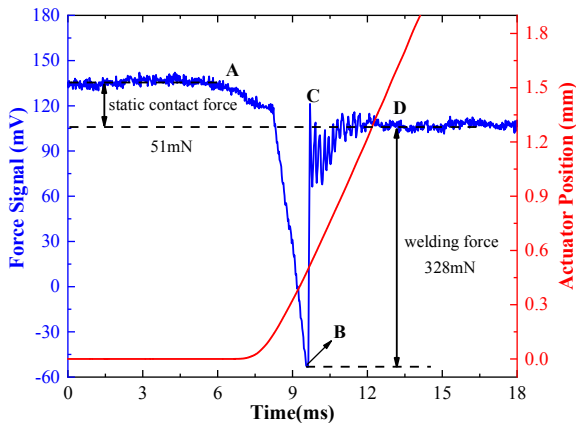


Fig.4 Typical waveforms of dynamic force transducer and actuator position during the contact breaking process (Contact current:140A, Contact force:50mN).

There is an obvious continuously drop in the force signal from 'A'(134.5mV) to 'B'(-53.3mV) and the associated actuator position increases from 0 to 0.4mm

simultaneously, and then the force signal increases to the steady value of 'D'(109.1mV) after 3ms fluctuation. The transducer has non-zero voltage signal output when it is not stressed, and the voltage 'D' is selected as a reference, we define the difference of two electrical potentials ('B' and 'D') as the maximum welding force and the voltage potential difference between 'A' and 'D' represents the static contact force. Taking the sensitivity of the force transducer is 2.022mN/mV [9], the maximum welding force is measured as (109.1+53.3) mV × 2.022mN/mV = 328mN, and the associated static contact force is (134.5-109.1) mV × 2.022mN/mV = 51mN.

2.4 Welding trace and associated area

Fig.5 shows the representative surface morphology of AgSnO₂ contact material for breaking contact current of 140A, current duration of 500ms and initial contact force of 50mN. Fig.5 II is a zoomed-in view of welding trace in the centre of Fig.5 I, and the crescent shaped area surrounded by the green dotted line is the welding area.

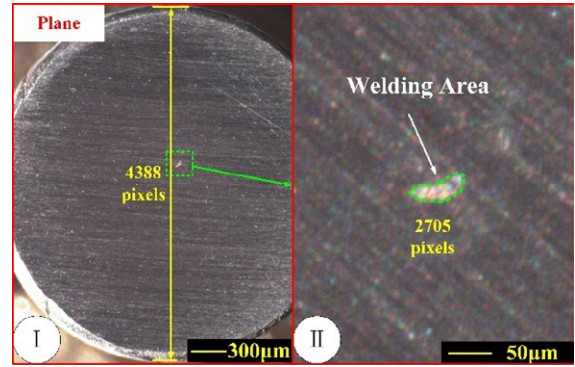


Fig.5 Photographs of contact obtained from CCD camera (Welding force: 328mN).

As shown in Fig.5, the contact diameter (3mm) corresponds to the pixel value 4388. Thus, the length of a single camera pixel l is calculated as $l=3/4388=6.837 \times 10^{-4}$ mm, and the area of a single pixel is equal to the square of the pixel length l , that is, $a=l^2=4.674 \times 10^{-7}$ mm². The area surrounded by green dotted lines is measured as 2705 pixels. Hence, the welding area A_w can be written as $A_w=2705 \times a=1.264 \times 10^{-3}$ mm².

The SEM images of the sample in Fig.5 are shown in Fig.6. I and III in Fig.6 are movable contact and corresponding stationary contact separately. The zoomed-in view of contact region are shown in Fig.6 II and IV, and the welding traces in both figures are surrounded by green dotted lines. As shown, the welding area is crescent shaped and consists of two parts, and welded fractures and cracks are observed. Nevertheless, no obvious material transfer is found in welding area of movable and stationary contacts and therefore leads to weak welding force, only 328mN.

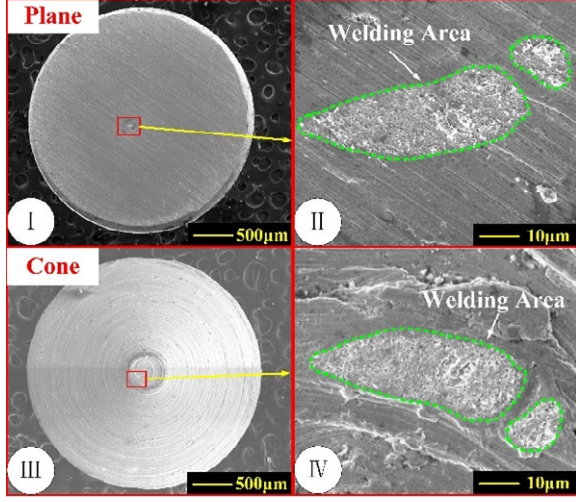


Fig.6 SEM pictures of contacts after experiment (Contact current: 140A, Contact force: 50mN)

The standard length of $10\mu\text{m}$ in Fig.6 II corresponding to the pixel value 102, so the length of a single camera pixel l and the associated area a are $9.8 \times 10^{-5}\text{mm}$ and $9.61 \times 10^{-9}\text{mm}^2$ respectively. The sum of the two parts in Fig.6 II, 109898 pixels and 18307 pixels, is the welding area, which is equal to $1.232 \times 10^{-3}\text{mm}^2$. In contrast to the welding area obtained by SEM, the difference of welding area is 2.6%.

3 Results and Discussion

3.1 Effect of current duration

The average value and error band of welding force are graphed versus the values of current duration for constant current of 140A and initial contact force of 50mN in Fig.7.

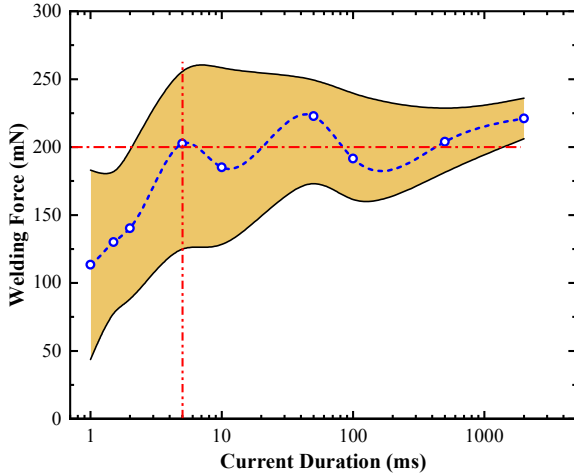


Fig.7 Variations in welding force as a function of current duration (Contact material: Ag)

As the current duration increases from 1ms to 5ms, the average of welding force increases from 113mN to 203mN. While the current duration is longer than 5ms, the variation in current duration has negligible impact on the welding force, which suggests that the welding force tends to be stable with increasing current duration.

Also, the standard deviation of the welding force decreases from 69.7mN to 14.9mN with the increase of the current duration from 1ms to 2s, which indicates that the current duration considerably influences the fluctuation range of the welding force.

The contact melting and welding is formed by Joule heat due to the passage of high current through constriction. The melting heat of contact material Q_m can be expressed as the difference between the heat production Q_p and the heat dissipation Q_d , where Q_p is

$$Q_p = I^2 R_c t \quad (1)$$

where I is the contact current, R_c is contact resistance and t is the current duration. According to (1), the heat production Q_p is proportional to the current duration t , therefore increasing the current duration t will increase melting heat Q_m and result in a strong welding phenomena, on the assumption that the heat dissipation Q_d would be constant. However, the welding force is independent of the current duration when the current duration is longer than 5ms, as shown in Fig.7. The exact reason for this is speculated to be connected with the relationship between material hardness H and temperature T [1]:

$$H = H_0 [1 - \beta(T - T_0)] \quad (2)$$

$$F_c = A_c H \quad (3)$$

With the use of (2) and (3), the A_c can be expressed as:

$$A_c = \frac{F_c}{H} = \frac{F_c}{H_0 [1 - \beta(T - T_0)]} \quad (4)$$

Where H_0 is the hardness at ambient temperature T_0 , β is a constant dependent upon the contact material, F_c is the initial contact force and A_c is the contact area.

Admittedly, the high temperature T is always associated with the longer current duration t . According to (4), the variation features in temperature T determine the contact area A_c , which is inversely proportion to the corresponding contact resistance R_c , on the assumption that the contact force F_c would be constant. So the long current duration t leads to the low contact resistance R_c , suggesting that the heat dissipation Q_d increases and heat production Q_p decreases (according to (1)) with increase of current duration t . The relationship between heat dissipation Q_d , heat production Q_p and current duration t indicates that the heat production Q_p and heat dissipation Q_d will reach a balance with increase of current duration t . Therefore, the welding force remains unchanged after the current duration longer than 5ms.

3.2 Effect of initial contact force

Fig.8 shows the distributions of welding area and welding force in terms of initial contact force for contact current of 140A and current duration of 500ms. As shown, the increase of the initial contact force causes the welding area and welding force decreases

monotonously from $1.73 \times 10^{-3} \text{mm}^2$ to 0 and 408mN to 0 respectively.

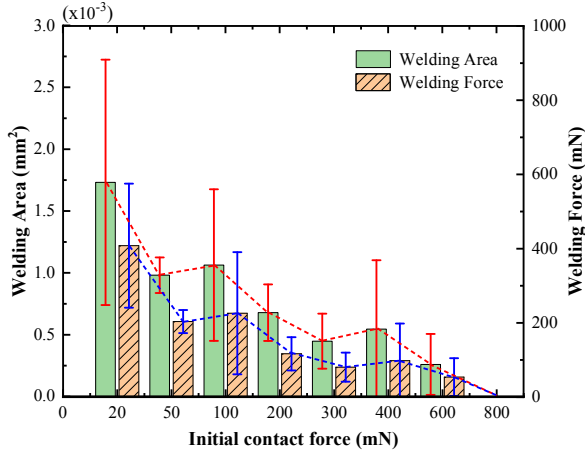


Fig.8 Variations in welding area and welding force as a function of initial contact force (Contact material: Ag)

If the contact resistance R_c could be equivalent to the constriction resistance, which is written by [1]

$$R_c = \frac{\rho}{2a} = \frac{\sqrt{\pi}\rho}{2\sqrt{A_c}} \quad (5)$$

Where ρ is the resistivity of contact material, a is the radius of contact spot. According to (3) and (5), it is reasonably believed that the high initial contact force F_c could increase the contact area A_c and reduce the contact resistance R_c . Therefore, the strong initial contact force is always accompanied by low heat production Q_p and weak welding phenomenon.

3.3 Effect of material

Fig.9 shows the welding area and welding force of Ag, Cu, AgSnO₂ and AgNi for contact current of 140A, current duration of 500ms and initial contact force of 50mN.

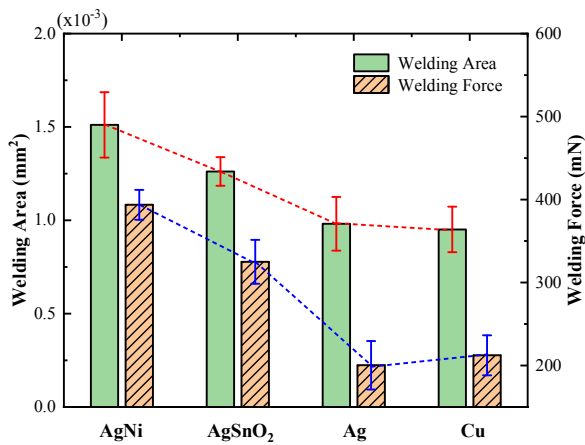


Fig.9 Welding area and welding force for Ag, Cu, AgSnO₂ and AgNi

As shown, the strong welding force always relates to large welding area, and the average of welding force of

Ag, Cu, AgSnO₂ and AgNi are 201mN, 212mN, 325mN and 394mN, and the associated welding area are $0.98 \times 10^{-3} \text{mm}^2$, $0.95 \times 10^{-3} \text{mm}^2$, $1.26 \times 10^{-3} \text{mm}^2$ and $1.51 \times 10^{-3} \text{mm}^2$, respectively. Due to the tensile strength of the materials is not the same, the ratios of welding force to welding area are significantly different in Fig.9. It should be noted that the welding area of Ag is slightly larger while the welding force is weaker than that of Cu.

3.4 Effect of load current

Fig.10 shows the variation of welding area and welding force as a function of contact current of Ag, Cu, AgSnO₂ and AgNi for initial contact force of 50mN and current duration of 500ms.

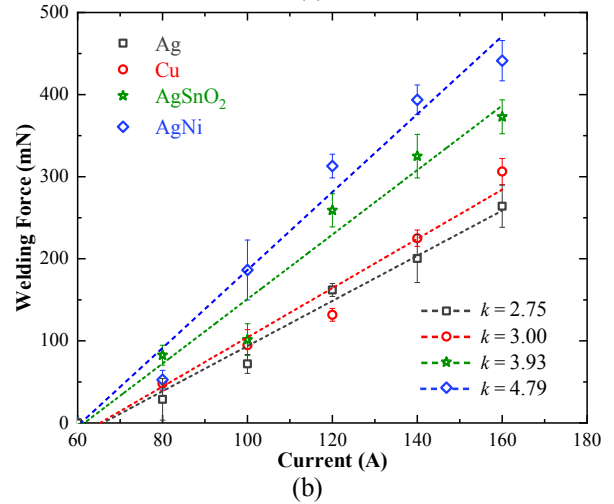
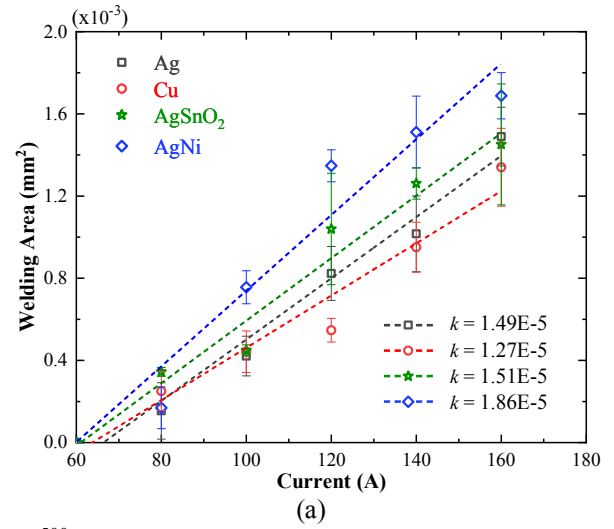


Fig.10 Variations in welding area and welding force as a function of current for Ag, Cu, AgSnO₂ and AgNi. (a) Welding area. (b)Welding force.

The results for AgNi show that there is a significant linear correlation between welding area, welding force and contact current. As shown, the increase of the contact current causes the welding area increases from 0 to $1.77 \times 10^{-3} \text{mm}^2$ and the associated welding force increases linearly from 0 to 441mN, and the slope is

$1.86 \times 10^{-5} \text{ mm}^2/\text{A}$ and $4.79 \text{ mN}/\text{A}$ respectively. Also, the welding area and welding force of Ag, Cu and AgSnO_2 increase linearly with the current. We defined the intersection of fitting slope and x-axis as threshold welding current, then the threshold welding current of Ag, Cu, AgSnO_2 and AgNi are calculated as 66A, 64A, 62A and 61A respectively.

According to [2], the threshold welding current of material depends on the properties of the contact material, and the threshold welding current I_w can be expressed as:

$$I_w = \frac{U_m}{R} \quad (6)$$

Where U_m is the melting voltage of material, R is contact resistance. Substituting (3) into (5), the radius of contact spot is given by:

$$a = \sqrt{\frac{F_c}{\pi H}} \quad (7)$$

The resistivity ρ_T for a contact spot at a high temperature T than the ambient temperature T_0 can be written by:

$$\rho_T = \rho_0 \left[1 + \frac{2}{3} \alpha (T - T_0) \right] \quad (8)$$

Where ρ_0 is the contact material's bulk resistivity and α is the temperature coefficient of resistivity. If the blow-off force is considered, the total force holding the contacts together is:

$$F_c = F - 4.45 \times 10^{-7} I_w^2 \quad (9)$$

Substituting (3), (5) and (7)-(9) into (6):

$$I_w = \frac{2U_m \sqrt{F_c}}{\left[\{0.1\pi H_0 \rho \left[1 + \frac{2}{3} \alpha (T_1 - T_0) \right] \}^2 + 1.78 \times 10^{-6} U_m^2 \right]^{1/2}} \quad (10)$$

Where T_1 is a temperature close to, but lower than the melting temperature. Table 2 shows the relevant physical properties of Ag, Cu, AgSnO_2 and AgNi.

Table 2 Physical properties [1,2,10]

	Ag	Cu	AgSnO_2	AgNi
U_m [V]	0.37	0.44	0.57	0.37
ρ [$\Omega \cdot \text{mm}$]	1.59×10^{-5}	1.65×10^{-5}	2.0×10^{-5}	1.92×10^{-5}
α [$10^{-3}/\text{K}$]	3.8×10^{-3}	3.9×10^{-3}	3.1×10^{-3}	3.5×10^{-3}
T_i [K]	1234	1356	1873	1233
H_0 [N/mm ²]	300-700	400-900	600-1000	500-1100

Taking the initial contact force F_c as 50mN, the ambient temperature T_0 as 293K, then the range of threshold welding current I_w of Ag, Cu, AgSnO_2 and AgNi are calculated and plotted in Fig.11. As shown, the maximum welding current of Ag, Cu, AgSnO_2 and AgNi are 230A, 216A, 183A and 181A respectively. High threshold welding current required suggests hard to weld, so the Ag is most difficult to weld and the welding force of Ag, Cu, AgSnO_2 and AgNi is inversely proportion to the threshold welding current. It indicates that the welding force of Ag is the weakest, whereas the welding force of AgNi is the strongest,

which shows a good agreement with the results in Fig.10 (b).

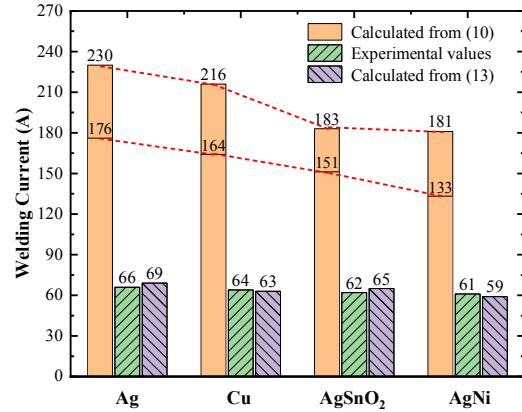


Fig.11 Comparison between the calculated values and experimental values for AgNi, AgSnO_2 , Ag and Cu. (Contact force: 50mN)

It is noted that, the threshold welding current calculated from equation (10) in Fig.11 deviates obviously from the experimental results. The exact reasons for these differences are speculated to be connected with the relationship between contact radius a and contact force F_c . Considering that the contact radius a in (7) is calculated based on plastic deformation, which is not suit to the case of low contact force. The relationship between contact radius a and contact force F_c of tens of mN should be elastic deformation. The contact radius a under elastic deformation is described as

$$a = \sqrt[3]{\frac{F_c}{E}} r \quad (11)$$

Where E is the modulus of elasticity and r is the radius of sphere. Substituting (5), (8), (9) and (11) into (6):

$$I_w = \frac{2U_m \sqrt{\frac{F - 4.45 \times 10^{-7} I_w^2}{E}} r}{\rho_0 \left[1 + \frac{2}{3} \alpha (T_1 - T_0) \right]} \quad (12)$$

$$I_w^3 + 4.45 \times 10^{-7} \frac{r}{E} \left(\frac{2U_m}{\rho_0 \left[1 + \frac{2}{3} \alpha (T_1 - T_0) \right]} \right)^3 I_w^2 - \frac{Fr}{E} \left(\frac{2U_m}{\rho_0 \left[1 + \frac{2}{3} \alpha (T_1 - T_0) \right]} \right)^3 = 0 \quad (13)$$

Table 3 Modulus of elasticity [1,2]

	Ag	Cu	AgSnO_2	AgNi
E [GPa]	79	115	86	84

Table 3 shows the modulus of elasticity for Ag, Cu, AgSnO_2 and AgNi. Taking the initial contact force F_c as 50mN and the radius of sphere r as 200 μm , then the calculation results of threshold welding current from (13) are shown in Fig.11. As shown, the threshold welding current of Ag, Cu, AgSnO_2 and AgNi are 69A, 63A, 65A and 59A, respectively. In contrast to the experimental results, the calculation errors of (14) are

4.5%, 1.6%, 4.8% and 3.3%. Therefore, the calculated values of threshold welding current I_w from (13) are in good agreement with the experimental values.

The relationship between welding area and welding force of Ag, Cu, AgSnO₂ and AgNi for contact current of 0-160A, current duration of 500ms and initial contact force of 50mN is shown in Fig.12.

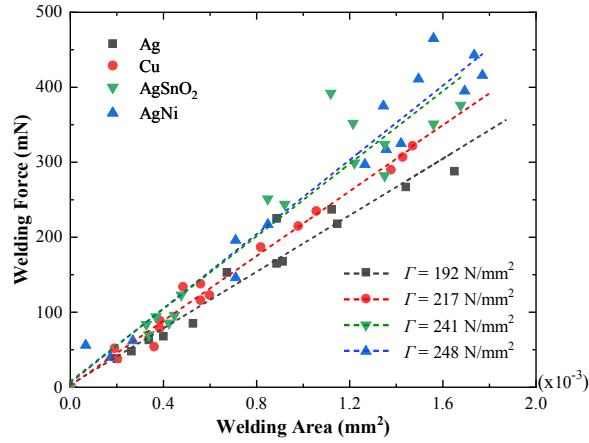


Fig.12 The relationship between welding area and welding force for Ag, Cu, AgSnO₂ and AgNi

As shown in Fig.12, all of the recorded welding area are distributed within the range $0-2 \times 10^{-3} \text{mm}^2$, and there is a clear trend that the average of welding force increases with the increase of welding area.

According to [1], the welding force F_w is given by

$$F_w = \Gamma A_w \quad (14)$$

where Γ is the material tensile strength. Hence, the fitting slope in Fig.12 represents the material tensile strength Γ . As shown, the tensile strength of Ag, Cu, AgSnO₂ and AgNi are 192 N/mm², 217 N/mm², 241N/mm² and 248N/mm², respectively.

Furthermore, the relationship between welding force, welding area and contact current can be obtained by introducing the threshold welding current and tensile strength:

$$A_w = k(I - I_w) \quad (15)$$

$$F_w = k\Gamma(I - I_w) \quad (16)$$

For initial contact force of 50mN, the coefficient k and the tensile strength Γ are shown in Table 4.

Table 4 Characteristic parameters

	Ag	Cu	AgSnO ₂	AgNi
k [mm ² /A]	1.49×10^{-5}	1.27×10^{-5}	1.51×10^{-5}	1.86×10^{-5}
Γ [N/mm ²]	192	217	241	248
I_w [A]	69	63	65	59

4 Conclusions

A novel experimental evaluation method of welding characteristics, which allows to accurate, real time and in situ welding force, welding trace, contact current, current duration and contact force measurement was described. It is found that the welding trace can be accurately captured by using CCD camera combined

with a telecentric lens. The preliminary results showed that the welding phenomena tends to be stable with the increase of current duration, and the welding area and associate welding force are significantly affected by the contact force. Furthermore, the measured welding force of Ag is the weakest, whereas the welding force of AgNi is the strongest for the contact current of 60-160A. Finally, the threshold welding current calculation based on the elastic deformation contact is more suitable for low contact force situation.

ACKNOWLEDGMENT

The authors express their gratitude for the kind support provided by The National Natural Science Foundation of China (Contract Number 51377029 and 51777039).

References

- [1] Paul G. Slade. *Electrical contacts principles and applications*. New York, NY, USA: CRC, 2014.
- [2] Paul G. Slade, "The Current Level to Weld Closed Contacts," in *Proc. 59th IEEE Holm Conf. Elect. Contacts*, Newport, RI, USA, 2013.
- [3] Paul G. Slade, "The threshold welding current for large area closed contacts with 'n' points of contact for short duration, high fault currents," in *Proc. 60th IEEE Holm Conf. Elect. Contacts*, New Orleans, LA, USA, 2014.
- [4] Paul G. Slade, E. D. Taylor and R.E. Haskins, "Effect of short circuit current duration on the welding of closed contacts in vacuum," in *Proc. 51st IEEE Holm Conf. Elect. Contacts*, Chicago, IL, USA, 2005.
- [5] A. Tslaf, "A Thermophysical Criterion for the Weldability of Electric Contact Material in a Steady-State Regime," *IEEE Transactions on Components, Hybrids, and Manufacturing Technologies*, vol. 5, no. 1, pp. 147–152, Mar. 1982
- [6] S.N. Kharin, M.M. Sarsengeldin and S. Kassabek, "The Model of Melting and Welding of Closed Electrical Contacts with Softening Contact Zone," in *Proc. 64th IEEE Holm Conf. Elect. Contacts*, Albuquerque, NM, USA, 2018.
- [7] P. Borkowski and E. Walczuk, "Computerized measurement stands for testing static and dynamic electrical contact welding," *Measurement*, vol. 44, no. 9, pp. 1618–1627, Nov. 2011.
- [8] A. M. Chalyi, V.A. Dmitriev and M.A. Pavleino, "On Peculiarities of Welding and Destruction of the Surface of High-Current Layered Contacts by Pulsed Currents," *Surface Engineering and Applied Electrochemistry*, vol. 54, no. 1, pp. 96–102, Jan. 2018.
- [9] PCB, 209C11 Datasheet, www.pcb.com/Products.aspx?m=209C11.

Series Electric Plasma Discharges of Failing Contacts up to 10 A at Various Materials

Peter Zeller, University of Applied Sciences Upper Austria, Wels, Austria, peter.zeller@fh-wels.at

Abstract

Latest, efficient and cost competitive power electronics products are providing the technology to realise future DC powered energy supply. Apart from a number of advantages of DC systems (lower power losses compared to AC systems, no capacitive losses, etc.), one challenge of DC systems is to treat arc faults. Especially series arcing can be very stable and has to be detected by appropriate approaches in order to avoid long lasting and very stable plasma discharges. In literature, the analyzation of the spectrum of either the system current or - voltage is introduced. The aim of this work is to investigate whether such an approach will provide a reliable method to detect series contact faults in general with a special focus on the feedback of plasma discharges to the signal noise across a failing contact. Experiments in a current range from 1 A to 10 A at low inductive (0 mH) and high inductive (4 mH) loads were performed. The failing contact was filmed by means of a colour high speed camera. The voltage signal was split into subsequent 1 ms observation intervals, where the spectrum was processed by a standard FFT algorithm. Defining a harmonic content (HC) value (square root of the sum of the quadratic amplitudes of the single harmonics) and an arbitrary HC trigger level, the failing contact could be detected with a good performance for copper (96% to 97% correct detections) and aluminium (97% to 98% correct detections), whereas the detection rate for brass and steel was poor. These results are corresponding to the plasma discharge phenomena (glowing contact and arc): any deflection from the stable plasma discharge equilibrium by plasma root displacement, contact material eruptions, etc. cause detectable noise. The permanent disturbance of the plasma by the effects listed before are strongly correlated with the contact material performance. Future work should cover the transfer of results for this specific detection method for more realistic circuits and sensor locations, as well as the improvement of the detection algorithm by multiple subsequent trigger processing.

1 Introduction

The enormous progress of power electronics technology with respect to power density, energy efficiency, reliability, and costs provides the basics for a transition of the traditional AC power supply approach into a DC approach [1]. DC grids provide numerous advantages compared to AC grids such as no extra losses caused by reactive power, no capacitive current losses, and no skin effect. However, DC systems require more attention with respect to insulation and protection technology. One specific fault situation is electric arcing caused by series or parallel faults. In DC systems, very stable and long lasting arcs may be observed because of the lack of no natural current zero conditions (as in AC systems), which will be required for the arc plasma to cool down, lose its fault current carrying ability and finally lead to the interruption of the affected electric circuit. Furthermore, series arcing (caused by failing contacts) may not be detected by classical protection approaches such as fuses or miniature circuit breakers, because any series fault is acting as an extra series circuit resistor, which will cause the electric current to drop instead of increasing the current up to relevant trigger values, required by any protection device. As a consequence, new approaches for detecting any failing contact should be developed for future DC networks.

In literature, a very promising approach of analysing the noise, caused by instable arc plasma, is introduced and intensively investigated for AC systems [2-4]. Here, the reigniting of the arc after current zero generates a detectable noise (harmonics) which can easily be detected by various fast Fourier transformation algorithms. [2-4] is also proposing spectrum analyses approaches for DC systems. However, less DC harmonics will be generated compared to AC applications because of the lack of natural arc re-ignition. This could cause sophisticated processing of the spectrum of any current or voltage signal and appropriate trigger algorithms. Furthermore, such a trigger approach has to work for all typical kinds of materials and configurations of the grid as well as for all operational current and voltage values, in order to reduce the need of intensive adjustment of such trigger systems by expensive experts for different applications. The goal should be the availability of protection devices with low of adjustment effort. As a consequence, intense and basic research is required to analyse the origin of noise in the voltage and current signal caused by an electric series arc under various parameters like contact material and equivalent circuit values like Thevenin resistor or inductive loads. Subsequently, research activities were initiated in order to carry out basic investigations with respect to the noise generated by electric arcs between failing contacts. Domestic applications should be considered only.

Therefore, the current range was limited to a maximum value of 10 A.

As a basic assumption for the research, it was assumed that the failing contact is defined as the occurrence of an electric arc or at least a too high voltage drop between two electrodes of an almost infinite small contact gap.

Furthermore, the detection of a failing contact should be realized with existing sensors of the applications (power electronics units) and should not require any extra installation of additional sensors. However, for the investigations published in this paper, the current and voltage noise across the contact should be directly investigated in a first step. It should be analysed whether the failing contact will cause significant noise at all, before complex algorithms have to be developed and implemented into the signal processing units of power electronics devices or loads of DC systems.

1.1 Basic circuit

For the investigations, a very simple and very basic circuit was introduced (**Fig. 1**). It consisted of a DC source (open loop voltage U_S , Thevenin resistance R_{Th} , Thevenin inductance L_{Th}), an ohmic / inductive load (R_L , L_L), and a contact with a voltage drop across the contact $u_C(t)$ as a function of time. Most real circuits can be reduced to such a basic arrangement.

Introducing the equations for the relation between the voltage drop at the components and the current $i(t)$ in the loop Kirchhoff's voltage law leads to equation (1). Analysing equation (1), any random noise in either the current $i(t)$ or the voltage drop across the contact or the circuits components can be generated by the contact only.

$$U_S = u_C(t) + i(t)(R_{Th} + R_L) + \frac{di(t)}{dt}(L_{Th} + L_L) \quad (1)$$

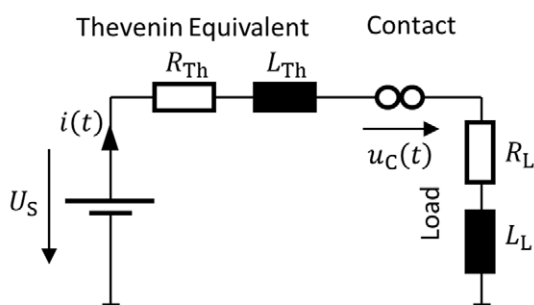


Fig. 1 Basic circuit with a Thevenin source, a series contact, and an ohmic inductive load.

Therefore, the processes and effects of the discharge at the failing contact and any random deflection from a natural “multi physics equilibrium” of the discharge will generate noise in the electric circuit. This is an important difference to any AC application. As mentioned above, it is assumed that a failing contact is defined as the presence of electric arc plasma between the contact electrodes. At AC, the re-ignition of the electric arc after current zero will cause noise naturally. This is the

most relevant reason why arc fault interruption via noise detection at DC is much more sophisticated compared to AC situations.

In order to become more specific with the meaning of the term “multi physics equilibrium”, a short introduction into the relevant arc physics principles shall be given in the next chapter.

1.2 Arc physics / origin of noise

It is assumed that slow (aging) processes causes the failing of the contact. As a consequence, short arcs between electrodes of low gap distance are considered in further discussions. The feedback of the electric plasma discharge to the electric system may be described by analysing the electric arc characteristic's equation (2). The voltage drop across the contact gap u_C is the sum of the cathode drop u_{Ca} , the anode drop u_{An} , and the voltage drop in the very short plasma column $u_P(i)$ [5]. While the cathode and anode drop could be assumed as constant (current independent; defined as the minimum arc voltage in [5]), the plasma column voltage drop is strongly influenced by the conductivity of the plasma volume and the plasma structure / extension. Very short arcs contain evaporated and ionised electrode metal mainly. The temperature of the plasma defines the number of free (by ionization processes generated) charge carriers [6]. The mobility and the number of free charge carriers influence the conductivity. Therefore, the plasma temperature, -composition, -density, and -geometry are the main parameters influencing the voltage drop in the plasma column region.

$$u_C = f(i) = u_{Ca} + u_{An} + u_P(i) \quad (2)$$

Based on the considerations above, any disturbance of the thermal equilibrium or the change of the geometry of the plasma volume will cause a change of the plasma voltage $u_P(i)$ and could therefore be identified as the main responsible origin of noise. As a consequence it is expected, that the specific contact material property exposed to an electric arc (such as boiling behaviour) is influencing the generation of noise significantly. In combination with the conclusion out of equation (1) any series arc detection based on FFT algorithms must be affected by the choice of the contact material. Hence the specific effects of initiating any arc instability are one of the specific focus of the research documented in this paper.

2 Experiments

In order to cover a wide range of possible (real) parameters, a variation of the inductivity in the circuit (sum of the single inductors in the circuit **Fig. 1**) and a variation of the current from 1 A up to 10 A in one ampere steps were combined for the single experiments according to **Table 1**. It was the goal to investigate the interaction in between the electric arc and the DC source only. Hence the sum of the two series resistors

was assumed as 0Ω no extra ohmic resistor was introduced to the circuit.

Material	Current	Inductor
Copper	1...10 A	0 H, 4 mH
Aluminium		
Brass (MS58)		
Steel		

Table 1 Set of parameters for the experiments, for all parameter combinations four single experiments have been carried out; the current value was adjusted from 1 A up to 10 A in 1 A steps for every material and inductor combination.

With each specific set of parameters, four single experiments were carried out.

2.1 Test equipment

With the test equipment (**Fig. 2**), automated test sequences could be performed. The equipment consisted of two series interconnected commercial DC sources (power electronics) operated in constant current / constant voltage mode. The maximum voltage of the source was adjusted to 600 V. Since the voltage drop at small contact gaps is close to the minimum arc voltage (typically 10 V to 15 V for the applied contact materials) the DC sources had been operated in constant current mode mainly. In case of any random interruption of the circuit by the opened contact, the power supplies switched to constant voltage mode. The voltage and current control was defined by the implemented control algorithm of the supplier.

The pair of contacts (materials see **Table 1**) was opened by means of a computer controlled stepper motor drive at one contact piece. A pneumatic piston at the other contact piece provided a constant contact force of 5 N. The voltage was measured by means of a differential voltage probe with a limiting frequency of 100 MHz. A hall probe current sensor was applied to measure the current with a limiting frequency of 2 MHz.

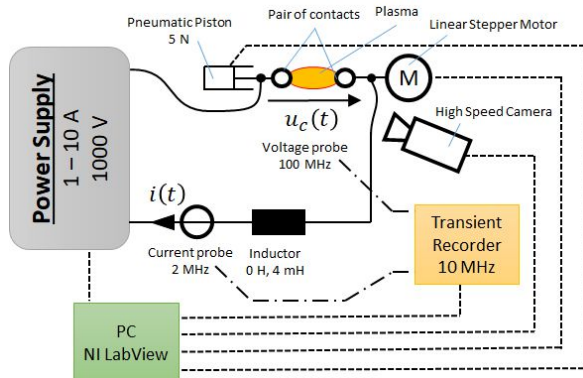


Fig. 2 Measurement equipment of the experiment; voltage sensor: differential probe, limiting frequency 100 MHz; current sensor limiting frequency 2 MHz; signal recording a transient recorder (sampling frequency 10 MHz); colour filming of the plasma with 10000 to 20000 frames per second.

The voltage and current signal have been recorded with a transient recorder for 0.4 s (maximum memory of the instrument) with the (maximum) sampling frequency of 10 MHz. The data was transferred to a personal computer via a glass fibre transmission. A high-speed camera integrated into the systems (triggered by the transient recorder) filmed the contact plasma with frame rates of 10000 and 20000 frames per second. A tele lens (210 mm focal length) attached with extension tubes (30 cm total length) to the camera provided close-up images of the contact opening process. The whole setup was steered via a personal computer by a specific developed control software. An inductor (4 mH) introduced for some experiments influenced the dynamics of the power supply control.

2.2 Test routine

The power supply was switched on at initially closed contacts. After all switching transients had been faded out the contact separation was initiated. While operating the stepper motor the contact voltage was measured continuously. At 6 V contact voltage, the stepper motor stopped, and the transient recorder started to record both, the voltage and the current signal. Consequently, the voltage and current were measured at a very small contact gap imitating a failing of a pair of contacts by a long term ageing effect or slowly contact force degeneration.

3 Measurement results

3.1 Signals, arc structure, and noise

For a better understanding of the effects at the opening contact gap, the obtained raw signals will be discussed in the following chapters.

3.1.1 Low inductive circuit

For all results, introduced in this section, no series inductor was added to the circuit (see **Table 1**, 0 H).

3.1.1.1 Copper contacts

As a representative result, **Fig. 3** shows the voltage and current versus time plots at a short circuit current value of 6 A. Up to the time of 0.025 s, the contact was closed and the voltage drop rises slightly because of the increase of the contact resistance due to the dropping contact force immediately before the contact separation (see **Fig. 3**, time period between 0 s and the vertical indicator “Beginning of contact separation”).

At 0.025 s the contact starts to fail (see **Fig. 3**, “Beginning of contact separation”). The voltage rises up to a value of roughly 1 V. An electric arc can be detected after 0.04 s (see **Fig. 3**, “Beginning of arcing”) which is indicated by a contact voltage in between a range of 14 V up to 18 V, which represents the minimum arc voltage and an extra voltage drop along the plasma channel bridging the pair of contacts according to the discussions in chapter 1.2. The voltage noise caused by

the electric arc causes a corresponding current noise which cannot be compensated by the controller of the power supply

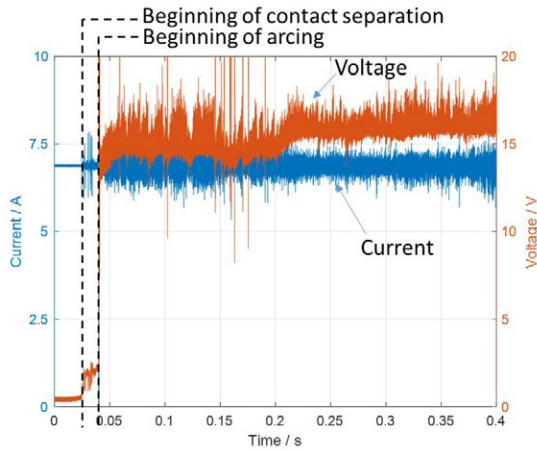


Fig. 3 Measurement result for copper electrodes at 6 A short circuit current, and 600 V open loop voltage.

For further considerations, the voltage signal was post processed via a standard Fast Fourier Transformation (“FFT”, see Fig. 4). The FFT was applied for the whole recording period of 0.4 s at once. As indicated by the spectrum plot Fig. 4, the amplitudes of the harmonics drop beginning with an initial value of 2.8 V down to a value roughly three orders lower at a frequency of 10 kHz (compared to the initial value). Considering any typical measurement resolution of 10 bit (typical measurement resolution of an analogue to digital converter for medium performance signal processors or micro controllers), considering any spectrum content exceeding 10 kHz is not reasonable any more (with respect to future industrial applications of an arc detection system). Therefore, the spectrum content exceeding 10 kHz was not considered for further spectrum analysis. It has to be emphasized that the limiting frequencies of the measurement equipment were sufficient enough for resolving the spectrum up to 10 kHz.

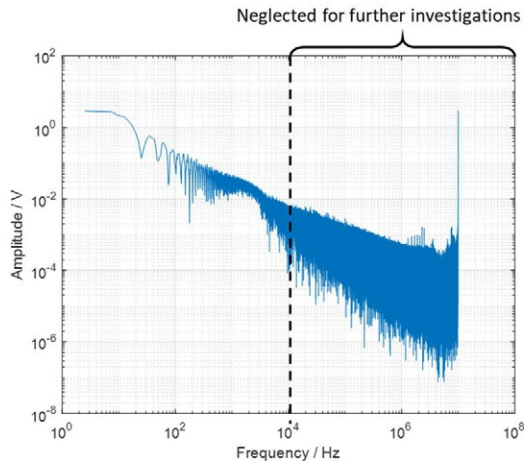


Fig. 4 Frequency spectrum of the voltage signal corresponding to Fig. 3.

Performing an FFT for the total recording time of 0.4 s is not an appropriate approach for any industrial arc detection procedure. Effective protection systems should provide a trigger delay less than 0.4 s. Hence it was assumed that a typical signal measuring period could be 1 ms. As a consequence, the whole voltage signal of Fig. 3 was scanned for every 1 ms interval subsequently (“subsequent FFT”).

Fig. 5 shows the plot of the spectrum (y- and z- coordinate indicated by “Frequency / Hz” and “log(Amplitude) / log(V)” up to a frequency of 10 kHz for the subsequent 1 ms time intervals (x-coordinate). For the considered specific data introduced in Fig. 3 and Fig. 4, the subsequent FFT yields a good correlation of the spectrum content with the presence of any arc (indicated by the voltage step according to the indication in Fig. 3). After 0.04 ms the spectrum content rises significantly (see Fig. 5, “Inception of noise”), which is corresponding with the arc activity in the recordings shown in Fig. 3.

For a direct correlation of the spectrum with the recorded voltage and current signals in a time plot, an auxiliary value, the “(total) harmonic content” (HC) of the spectrum (up to 10 kHz) was calculated according to equation (3).

$$HC = \sqrt{\sum_{i=2}^N u_i^2} \quad (3)$$

Note that the DC component of the spectrum was not considered in equation (3) (the summation starts with the second element of the FFT result) in order not to influence the result by the absolute level of the voltage (assuming the noise of the arc should be considered only). The HC values for subsequent 1 ms time intervals are plotted time correlated to the recorded voltage and current in Fig. 6. As indicated in Fig. 6, for this specific single experiment the correlation of the HC level with the appearance of an electric arc is excellent.

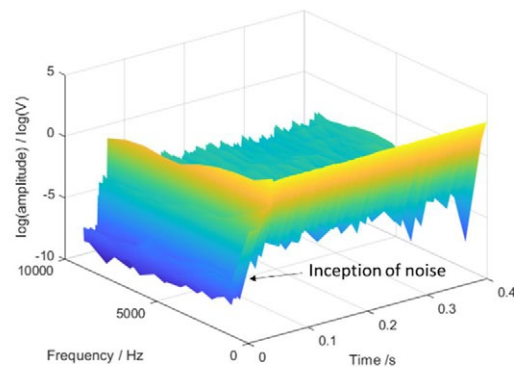


Fig. 5 Frequency spectrum for subsequent 1 ms time periods of the voltage signal corresponding to Fig. 3.

Taking a closer look to the voltage signal in the time range in between the begin of the contact separation and the begin of the electric arc (see Fig. 3 “Beginning of contact separation” and “Beginning of arc”) an electric arc is indicated by the HC level in Fig. 6. However,

the voltage drop of roughly 1 V is far below the minimum arc voltage of an electric arc between copper electrodes (see chapter 1.2). For a more detailed investigation of the processes in the contact gap, a high speed film of the contact surface while separating the contact was performed (see Fig. 7 and Fig. 8).

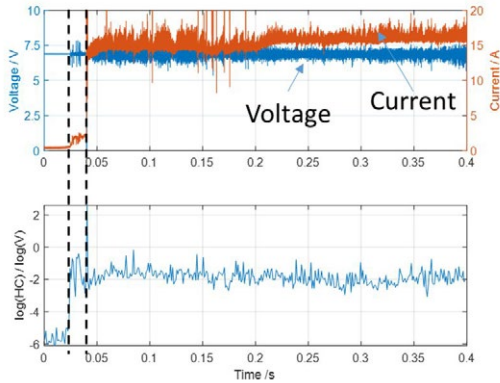


Fig. 6 Correlation of subsequent 1 ms period spectrum HC corresponding to Fig. 3.

An Analysis of the result of the filmed phenomenon in the contact gap strongly indicates that the phenomenon can be addressed as a glowing contact plasma discharge (see the selected single frame in Fig. 7). It must be emphasized that the roots of the discharge did not originate at the narrowest gap of the geometry.

The phenomenon of a glowing contact has been described as glowing contact phenomenon by [7] already. Glowing contacts have been observed at contacts with oxide layers at the electrodes surface only (see Fig. 7, “Oxide layers”).

Analysing the corresponding high-speed film, a very stable (stationary) discharge with respect to plasma displacement / mobility was observed (see Fig. 8, film strip at the left side).

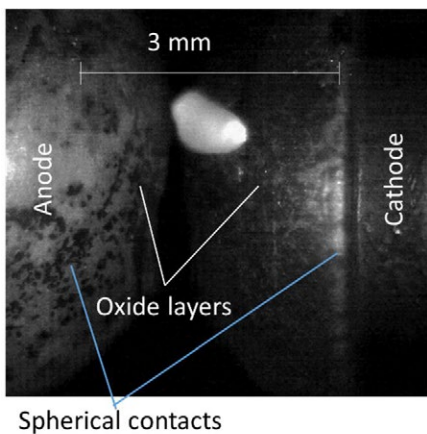


Fig. 7 Single frame of the opening contact between copper electrodes at 6 A current level.

While most of the plasma volume is almost stationary, the cathode arc root shows a moderate mobility (see film strip in Fig. 8, left side). Analysing the voltage signal across the contact (see Fig. 8, middle diagram, the corresponding time points of the single plasma images

are indicated), an almost constant medium level superimposed by a small noise band was measured. This results in a very low amplitude level in the FFT spectrum (see Fig. 9). Comparing the spectrum of the total signal of the arc (see Fig. 5) with those of the glowing contact (see Fig. 9), the amplitudes of the spectrum of the glowing contacts are lower than that of the fully developed arc approximately by one order.

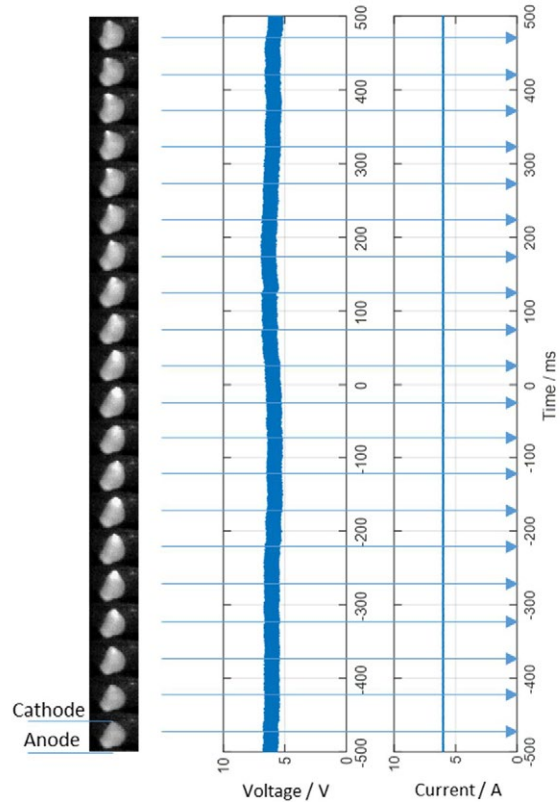


Fig. 8 High speed film of an opening contact between copper electrodes at 6 A current level; single frames (left diagram, anode bottom plasma root, cathode top plasma root) corresponding to the recorded voltage (middle diagram) and current (right diagram), rising time value from the bottom up to the top of the diagram; time point of the exposure indicated by horizontal lines.

In contradiction to glowing contacts, electric arcs show higher mobility (see Fig. 10). The arc displaces continuously or spontaneously respectively. In the period with high arc mobility, the voltage signal shows corresponding steps. (see Fig. 10, left side, “High arc mobility”).

3.1.1.2 Aluminium contacts

For different contact material, very different the arc structure and arc effects where observed. As an example at aluminium electrodes the gross mobility of the arc is low, however massive eruptions of electrode material cause massive disturbances of the plasma region which results in rapid displacements of parts of the arc plasma volume (see Fig. 11, left side, film strip, time

interval between 3 ms and 20 ms, the arc plasma is influenced by heavy electrode material eruption). In case of eruptions and deflected / displaced plasma a very noisy voltage signal can be observed (see Fig. 11, recorded voltage signal, time periods 3 ms to 20 ms and 40 ms to 50 ms). Comparing the FFT results yield from copper contacts with that from aluminium contact results it is clearly indicated that aluminium shows a higher noise activity compared to that of copper contacts (see Fig. 12).

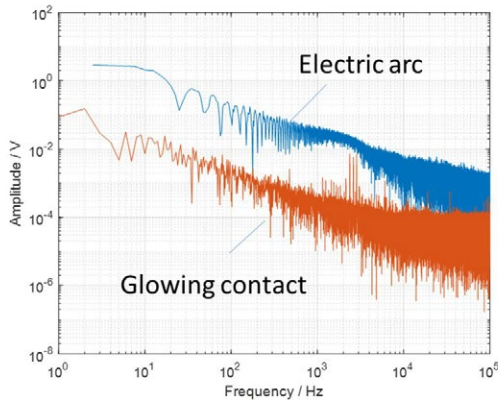


Fig. 9 Spectrum of the voltage of the glowing contact (corresponding to Fig. 7 and Fig. 8) and the electric arc (corresponding to Fig. 3 and Fig. 5).

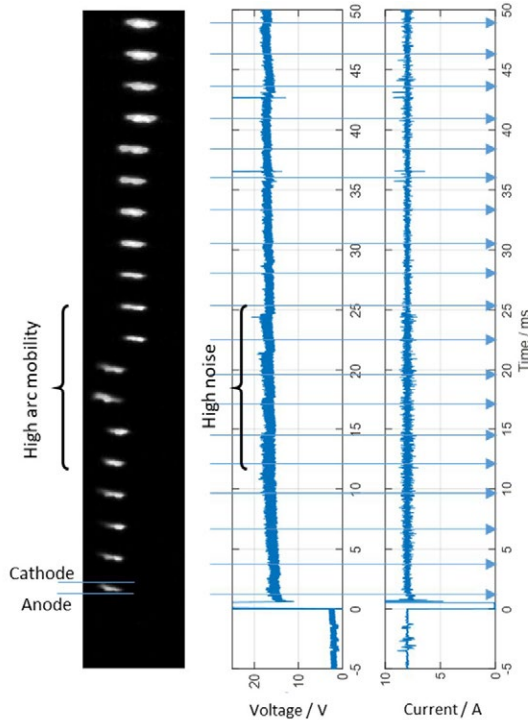


Fig. 10 High speed film: electric arc between copper electrodes at a current of 8 A.

3.1.2 High inductive circuit

The recorded voltage and current signals with a series inductor of 4 mH (see Table 1) are shown in Fig. 13. The transition speed of the current (affected by the internal but unknown control algorithm of the DC power

supply) in case of a voltage fluctuation is limited in case of a series inductor. An attenuated oscillation of the current can be detected in case of any rapid voltage change (see voltage step at the time point of the failing contact). Such an oscillation was not detected for experiments without a series inductor (compare the current signal at the moment of the arc formation voltage rise in Fig. 3 and Fig. 13).

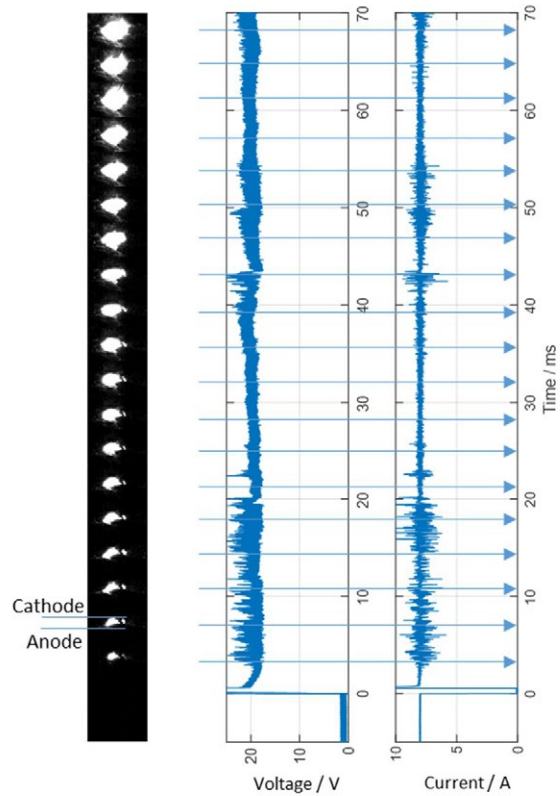


Fig. 11 High speed film: electric arc between aluminium electrodes at a current of 8 A.

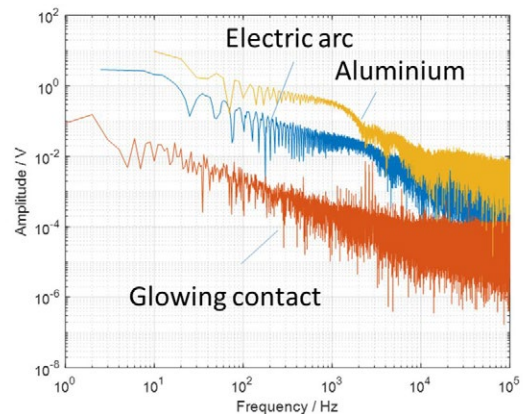


Fig. 12 Comparison of the spectrum measured at copper (glowing contact: corresponding to Fig. 7 and Fig. 8; electric arc corresponding to Fig. 10) and aluminium (corresponding to Fig. 11) contacts.

It is obvious that such specific oscillations, caused by the series inductor and the interaction with the power supply, influence the spectrum response of such a circuit: In case of the specific DC power supply applied

for this specific experiments extra harmonics had been observed in the frequency range between 400 Hz and 7 kHz (see Fig. 14, compare the signal generated with an inductor of 4 mH “Inductor 4 mH) and no inductor “Inductor 0 mH”).

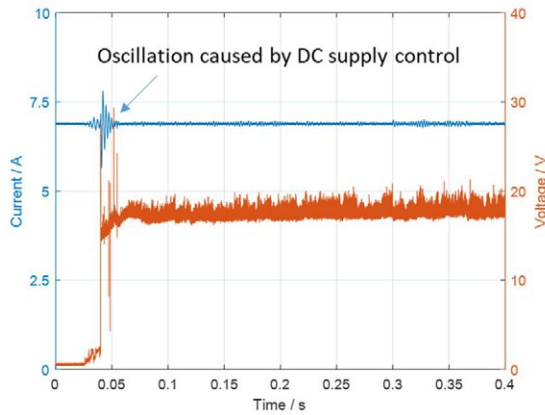


Fig. 13 Voltage and current recording at copper contacts with a series inductor of 4 mH according to Fig. 2 (“4 mH”) at a current of 7 A.

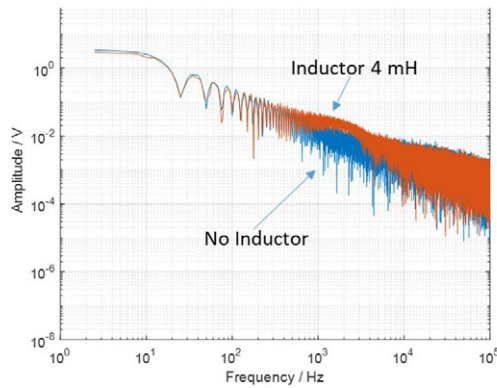


Fig. 14 Comparison of the spectrum response with a series inductor of 4 mH (corresponding to Fig. 12) and no series inductor (corresponding to Fig. 3).

4 Post processing / arc detection

For further and automated post processing of the subsequent 1 ms interval spectra (HC) in the current range between 1 A and 10 A (according to Table 1) the decimal logarithm of the HC and voltage level were split into decimal logarithmic classes between $-4 \log(V)$ and $2 \log(V)$ with a resolution of $0.01 \log(V)$. The logarithmic scaling was selected to yield a better visualization of the signals. For all recorded signals and all subsequent 1 ms intervals it was counted how frequent the HC and voltage level occurred in one specific interval of the classification. A similar approach is well known and very common for the visualization of partial discharge measurement results in high voltage systems.

All 1 ms intervals with a current value lower than 0.5 A had been neglected for the counting of the HC classes: it is assumed that a lower current value cannot cause any dangerous power loss at a failing contact. The counts are plotted in a count pattern plot (see Fig. 15).

Analysing the result in Fig. 15, the correlation between the counts and voltage levels exceeding the value of 1 V is very strong: If the voltage at the contact exceeds 1 V, the counts increase significantly up to a level of $10^{-2} \log(V)$, hence an arbitrary trigger level of $HC = 10^{-2} \log(V)$ was introduced.

By introducing this arbitrary trigger level (indicated in Fig. 15 “Noise trigger level for arc detection”), it can be concluded that only a few counts will be found above the trigger level and a voltage below a level of 1 V. Such counts are wrong indications of a failing contact. Since these wrong indications are the minority of the counts, it can be concluded that the failing contact can be detected with a good reliability.

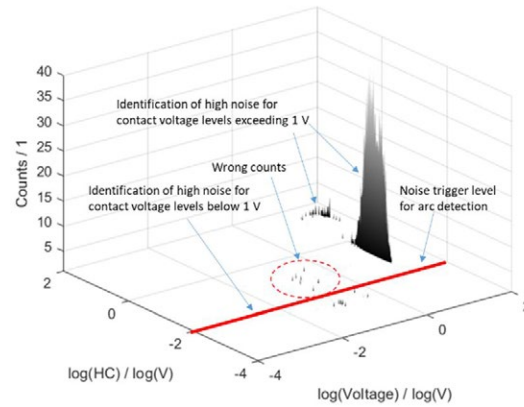


Fig. 15 Counts versus the HC and voltage classes for all experiments with copper and no series inductor according to Table 1.

Classification	Voltage level / V	Current level / A	HC level / V
Correct	> 1	> 0.5	> 10^{-2}
Wrong, no current	> 1	< 0.5	> 10^{-2}
Wrong with arc	> 1	> 0.5	< 10^{-2}
Wrong no arc	< 1	-	> 10^{-2}

Table 2 Applied classifications for all 1 ms observation intervals of all performed experiments according to Table 1.

Based on these considerations, the correct number of arc detections had been counted for all experiments (covering all inductor, material, and current configurations according to Table 1). For all these parameter variations, the 1 ms observation intervals were assigned to the classification listed in Table 2. By these specific classifications, it is possible to calculate the hit rate of the correct detection of a failing contact. In Table 3, the results of all counts for all classifications (correct hits and incorrect hits according to Table 2) are listed.

The results indicate a good hit rate for copper and aluminium. The detection performance for brass is moderate, while the rate for steel is extremely poor. This is correlating to the very stable arcing phenomena observed for those materials (not documented in this paper, but observed by analysing the corresponding film material). Whereas at these two bad performing materials (brass and steel), the wrong counts without the presence of an arc are moderate low the number of not

detected arcs is contributing mainly to the bad detection performance. These results are clearly indicating a strong material influence of the contact material onto the performance of arc detection systems based on FFT approaches.

	Inductor	Level	Total counts	Wrong			Correct	
				with arc	no arc	no current	Correct Hits	
Copper	No	100	23541	0	545	309	22687	96%
	Yes	100	11970	3	332	41	11594	97%
	Total	100	35511	3	877	350	34281	97%
Aluminum	No	100	23541	233	359	214	22735	97%
	Yes	100	11970	39	223	21	11687	98%
	Total	100	35511	272	582	235	34422	97%
Brass	No	100	23541	399	511	126	22505	96%
	Yes	100	11970	1225	221	54	10470	87%
	Total	100	35511	1624	732	180	32975	93%
Steel	No	100	23541	3666	365	75	19435	83%
	Yes	100	11970	3574	181	88	8127	68%
	Total	100	35511	7240	546	163	27562	78%

Table 3 Correct and wrong detections within the subsequent 1 ms observation intervals for all experiments (parameter variations listed in Table 1).

5 Discussion and conclusions

5.1 Plasma phenomena

5.1.1 Glowing contacts

The glowing contacts observed at some specific experiments are in accordance with the observations reported in [7]. Based on the view number of observations of the glowing contacts covered by the experiments of this paper, there is an indication if the copper oxide layers are required to enable such a phenomenon. This is in agreement with the observations from the high-speed films: Only in the presence of oxide layers glowing contacts were observed, brand new contacts never show such a phenomenon. From the high-speed films, a spontaneous (but moderate) moving cathode spot can be observed. This could indicate that this phenomenon requires the presence of oxide layers: if the arc root is located in the vicinity of an oxide layer, the electron work function is decreased and the plasma discharge can be sustained at a low total voltage drop across the contact (below the minimum arc voltage). This would also mean, that the oxide layer is responsible for the low cathode drop. Because of the high current (power) density the oxide layer must be evaporated, and the cathode plasma root has to be displaced in order to find a new centre for electron emissions. Such an effect could explain the origin of cathode plasma root displacement of Fig. 8.

5.1.2 Electric arc

The high-speed films, combined with the voltage and current plots clearly indicate that any disturbance of the plasmas (thermal) equilibrium causes noise in the voltage and the current across the electric contact.

This disturbance may be caused by contact material eruption or arc root displacement. Hence, there is a direct correlation of any signal noise with the contact material as assumed in chapter 1.2).

5.2 Influence of the electric circuit to the signal noise

As expected, and indicated by the measurement results the electric circuit affects the spectrum of the voltage and current signal. As a consequence, any failing contact detection approach must be designed in a very robust way, considering all possible and realistic circuits. This seems to be a challenging drawback of failing contact detection systems based on spectrum analyses, all possible network configurations and sensor positions have to be considered.

5.3 Fault detection

The post processing of the signals by means of subsequent processing of the harmonics content of 1 ms observations intervals leads to a good detection performance for copper and aluminium and poor to low performance for brass and steel contacts. The performance could perhaps be improved by more sophisticated approaches. One approach could be to consider more than one subsequent HC level. If more than one of these single levels are not indicating a failing contact the protection switch should not be triggered.

6 Acknowledgements

The author wants to acknowledge the contribution to this work by the staff members of the Electrical Engineering department of the University of Applied Sciences of Upper Austria, especially Christian Gruberbauer, Bsc., Christoph Diendorfer Msc, Sebastian Gomes, Bsc..

7 Literature

- [1] T. Kaipia, P. Salonen, J. Lassila, J. Partanen: Application of low voltage DC-distribution systems-a techno economical: Cired, 19th International Conference on Electricity Distribution, 2007
- [2] G. Artale, A. Cataliotti, V. Cosentino, G. Privitera: Proc. IEEE International Instrumentation and Measurement Technology Conference (I2MTC), 2014
- [3] J. McCormick, M. Walz, J. Engel, P. Thiesen and E. Hetzmanseder: Arc-Fault Circuit Interrupters: Proc. of the Conference on Advances in Aviation Safety, 2000
- [4] B. Pahl, T.J. Schöpf, X. Zhou, E.Hetzmanseder: Arc faults in residential electrical systems, VDE Fachberichte, 2009
- [5] W. Rieder: Plasma und Lichtbogen, Vieweg, 1967
- [6] F. Karetta, M. Lindmayer: Simulation of the gasdynamic and electromagnetic processes in low voltage switching arcs, IEEE Transactions on Components Packaging and Manufacturing Technology Part A, 1998
- [7] J.J. Shea, Glowing Contact Physics: Proc. 52nd IEEE Holm Conference on Electrical Contacts, 2006

Measurement and study of arc noise fluctuation by fast camera observations

HUMBERT Jean-Baptiste, SCHWEITZER Patrick, WEBER Serge, HUGON Robert
University of Lorraine, Institute Jean Lamour (IJL), UMR7198, Nancy, F-54000, France,
e-mail: patrick.schweitzer@univ-lorraine.fr

Abstract

As part of this work, we seek to study more precisely the formation of an arc and its behaviour at the opening of a circuit in conditions close to those of avionics (altitude, atmosphere, etc.). Our work is carried out on an HVDC 270VDC type electrical network at various pressures. The phenomenon is observed by a PHOTRON FASTCAM SA5 model 775K-M3 camera at a rate between 20000 and 100000 frames per second. Our observations show a repetitive behaviour in electrical measurements (current and arc voltage) depending on the experimental conditions. In this paper, we propose an analysis of the noise oscillation phenomenon present in an arc of moderate intensity (<20A) through a fast camera study and then a diagnostic method of the phenomenon observed by camera only from the measurement of line current.

measurement of the line current (part 4). The electrical noise oscillations is used to develop methods of protection against electrical faults.

1 Introduction

Protection against arc-type electrical faults is essential in electrical distribution networks for avionics. False contact, aging, wear, vibration, corrosion, oxidation are all reasons that can get a power supply harness to an arc fault. Indeed, this type of fault can cause major damage: fire, arc-tracking, destruction of cables or equipment, explosion, loss of aircraft control and crash [1-3]. In the context of this work, we seek to study more precisely the formation of an arc and its behaviour at the opening of a circuit under experimental conditions close to those encountered in an airplane (pressure temperature variations). The detection of a fault based on an electrical signature specific to the arc is delicate. However, the electrical measurements (U/I) of a faulty network often show fluctuations both in its mean impedance value and in the noise level (especially outside the established regime). It is by this means that many studies on electrical fault protection exploit these stochastic phenomena (RMS value, variance, filtering, wavelet, etc.) [4-9]. For electrical protection, we propose a study of the phenomenon of impedance oscillation, which is perceptible in many publications [10], [11] but less exploited. In the case of arc furnaces, the main problem lies in the regulation of the reactive power initiated by a flicker phenomenon [12-14] perceptible in the laboratory in discharge lamps. In this paper, we propose an analysis of the noise oscillation phenomenon present in an arc of moderate intensity (<20A) through a fast camera study (part 3). Then a diagnostic method of the phenomenon is observed by camera only from the

2 Experimental test bench and data analysis

Our work is focused on the study of the behaviour of arcs on a 270VDC HVDC type electrical network at pressures ranging from ambient pressure to 120hPa corresponding to a variation in altitude from sea level to 15'000 meters. Figure 1 illustrates our experimental device which is composed of a continuous power supply (CHROMA 62000H series and/or ETsystem 4kW), a resistive load (LANGLOIS 4kW). The arc fault is created by the separation of the contact between two copper electrodes.

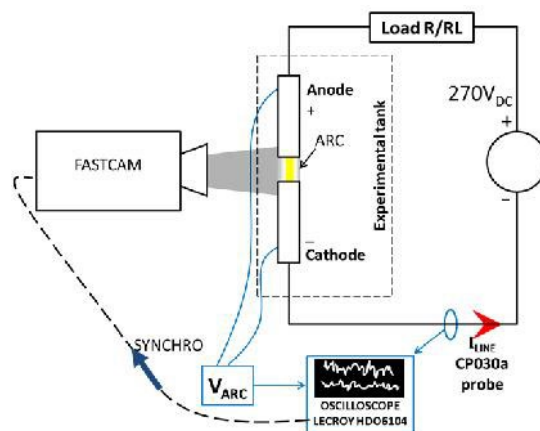


Fig. 1 Experimental test bench

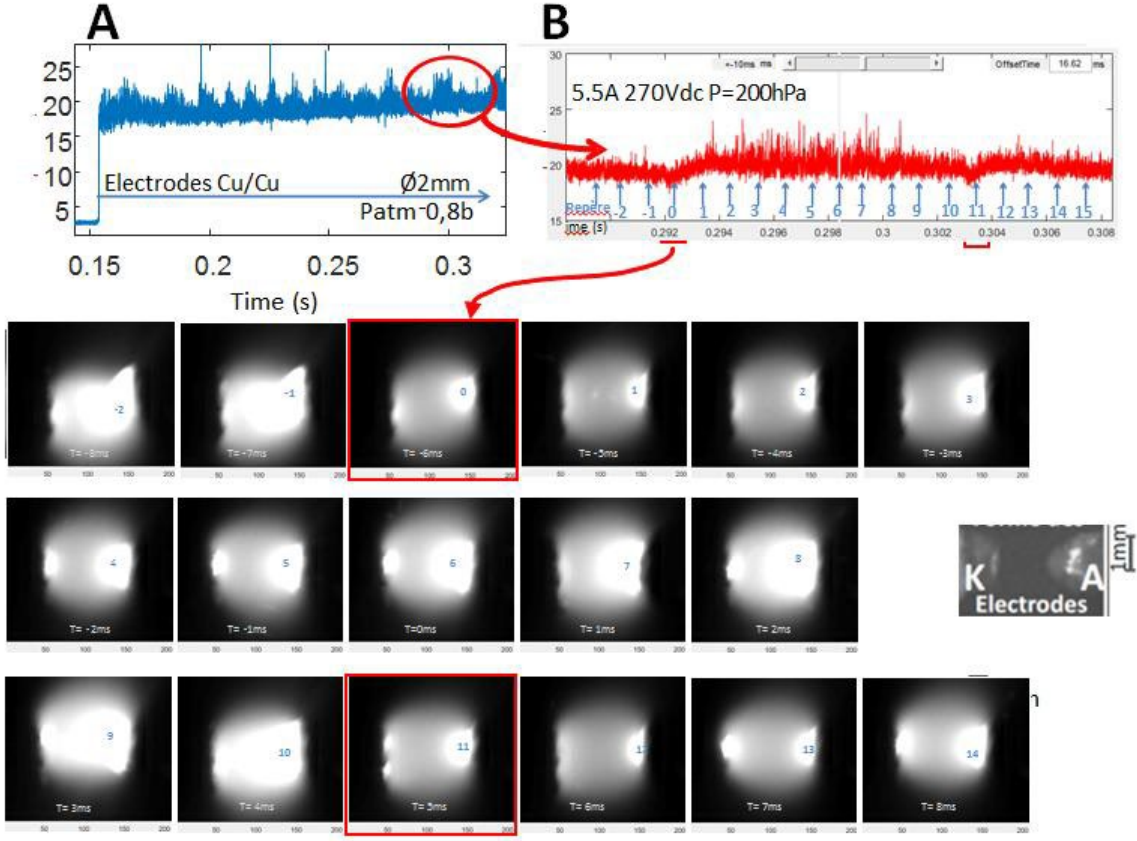


Fig. 2 Evolution of the arc voltage and the discharge

The measurement of the electrical signals is collected by an HDO6104 oscilloscope at a rate of 1MHz using a Lecroy CP030a probe (Accuracy: $\pm 1\%$, max bandwidth: 70MHz at 1mA/div, 100kHz at 1A/div) for the line current and a differential probe TESTEC TTS19010 1:100 with a bandwidth of 70MHz (Accuracy: $\pm 2\%$, Voltage Rating VAC:7000V) for the potential difference between the electrodes during an arc.

The arc is observed by a PHOTRON FASTCAM SA5 model 775K-M3 camera at an acquisition rate between 20'000 and 100'000 frames per second (fps). The triggering of the camera is controlled by the trigger of the oscilloscope according to a threshold depending on the voltage contact during the arcing process (higher than 10V). Using Matlab, the images acquired by the camera are synchronized with the oscilloscope signals. The synchronization of the images is checked by the concordance between the optical and electrical events (arc start, extinction, disturbances).

2.1 Analysis of the luminosity of the discharge

The evolution of the anode luminosity is quantified by the average sum of the luminosity amplitudes measured by the fast camera between the 2 electrodes. This measurement takes into account the whole discharge (arc foot on the cathode, luminescent column of the arc and anode zone).

We estimate its average value by calculating the following value:

$$R_{lumi} = \frac{1}{N} \sum_{i=y-\frac{N}{2}}^{y+\frac{N}{2}} A(I) \quad (1)$$

With: A is the intensity of the pixel, y the vertical position of the discharge, Window height (N=30 pixels).

The window width is fixed experimentally to 200 pixels for testing the feasibility of the method.

2.2 Analysis of the electrical luminosity of the discharge

The evolution of the electrical noise of the arc (voltage or current) is evaluated by the analysis of sliding variance using the equation :

$$VAR(Varc(k)) = \frac{1}{n_{ms}} \sum_{i=(k-1)N_{ms}}^{i+n_{ms}} (Xn(i) - \overline{Xn(i)})^2 \quad (2)$$

Xn= Voltage (or line current) signal, k = Analysis window number, N = Number of points in the analyzed window, n_{ms}= Shifting between 2 successive analysis windows

3 Observations

3.1 Analysis of video and electrical signals

The arc fault is produced under the following circuit conditions: Valim 270VDC, low pressure p ≅ 500hPa, load RL=48Ω 105μH. Under these experimental conditions, the arc produces a repetitive variation of the noise amplitude (visible on the arc voltage Figure 2 A). Part of this ripple is visualized using the high-speed camera to understand the phenomenon. The trace in Figure 2 B represents the correspondence between the electrical measurements and the video observation.

The measurements show that for the time reference point '0', the amplitude of the Varc noise is about 1.5V peak-to-peak with an average voltage of 18.85V. At benchmark '1' the average gap field increased by about 0.4V. From this moment, a zone of strong luminescence extends from the anode to the cathode. This zone never seems to touch the cathode. However at image '10', the luminescent zone of the anode returns to its initial state in 1 to 2 ms. The gap voltage reaches the value of 18.9V. This development cycle of the anode zone is then repeated several times.

It can be seen that during the growth of the anodic luminescent zone, the arc foot is very mobile on the cathode. These movements may be the cause of the increase in noise on the electrical signal. On the other hand, the increase in average resistance suggests that the anode zone change in length the flow of electrons. A comprehensive study is required to conclude.

3.2 Gap brightness evolution measurement

The study of the brightness of the gap according to equation (1) makes it possible to estimate the tem-

poral evolution of the phenomenon. This evolution is showed on Figure 3 (Rlumi versus time), which shows a periodic increase in light intensity. This increasing ramp is completed by a sudden decrease (about 1ms) before renewing a relatively linear growth.

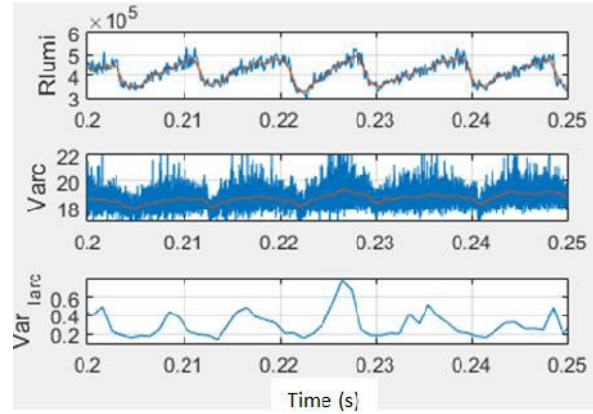


Fig. 3 Measurement of brightness and electrical levels of the discharge

4 Electrical diagnosis.

4.1 Pressure influence

The study of the influence of pressure from similar experiments (gap between 0.8mm and 1mm, equivalent electrode geometry, 270VDC, initial load 48Ω, etc.) is represented by the spectrograms of Figs 4 to 6.

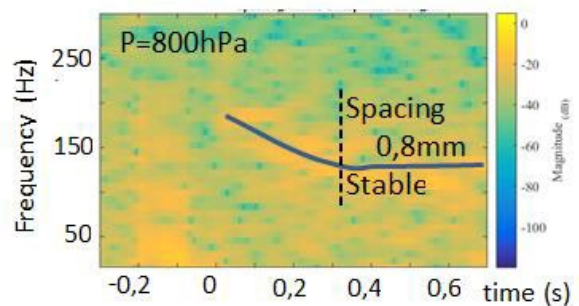


Fig. 4 Spectrogram fluctuations – P = 800hPa

The spectrograms represent the spectral components that make up the signal by sliding FFT. It can be seen from these measurements that in the first few moments after the arc is established the flicker rate is approximately 125 Hz at 800 hPa, 70 Hz at 500 hPa and 50 Hz at 200 hPa.

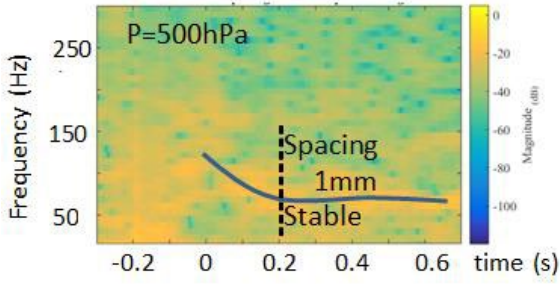


Fig. 5 Spectrogram fluctuations – P = 500hPa

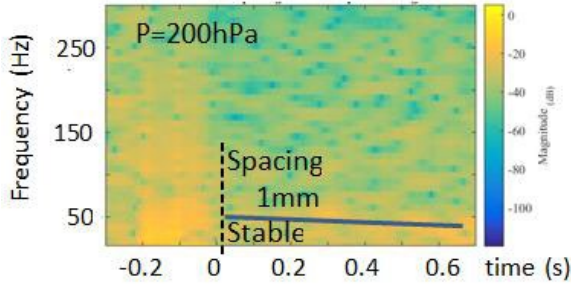


Fig. 6 Spectrogram fluctuations – P = 200hPa

These results show that:

- the behaviour of the arc is strongly linked to pressure condition
- the fluctuations rate increase with pressure.

4.2 Signal fluctuations at atmospheric pressure

The observation of noise fluctuations in the measured electrical signals is mainly observed when the pressure falls and is difficult to observe at atmospheric pressure.

pheric pressure should have a rate higher than 125Hz (800hPa).

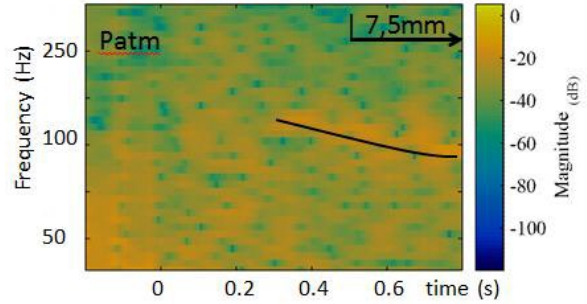


Fig. 8 Arc noise spectrogram – P atm

However, by our observations it was not possible to detect a fluctuation at 1mm (reference $A \cong 1\text{mm}$ - Figure 7). This noise oscillation is however perceptible (increasing) when the gap increases (gap of about 7.5mm B, C mark Figure 7). The spectrogram (Figure 8) then shows an oscillation rate close to 150Hz for a spacing of 7.5mm under ambient atmospheric pressure.

5 Conclusion

In this work, we observed the evolution of the electrical characteristics of a serial arc when the pressure of the surrounding environment decreases. Fast camera permits us to observe a phenomenon of arc flicker, associated with arc presence. That phenomenon occurs repeatedly and can also be pointed out in electrical current measurements. Our measurements put also in evidence that these fluctuations are highly dependent on the pressure. Future works will be devoted to fast camera measurements and more generally optical characterization, in order to develop a reliable arc fault detector based both on electrical and physical measurements.

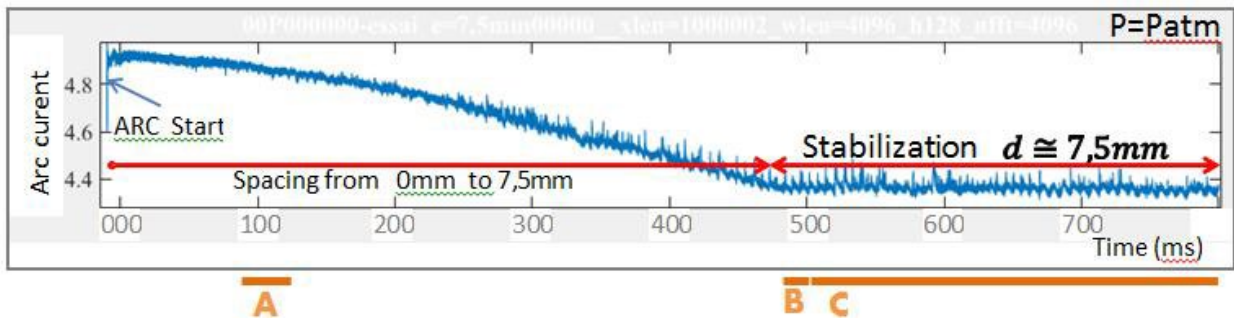


Fig. 7 Line current on a resistive load (48 ohms)

According to the observations carried out in depression (from 200 to 800hPa), the fluctuations at atmos-

This bi-disciplinary study should allow us to set off a detector operating under severe conditions (pressure, temperature, vibrations, etc).

6 Literature

- [1] Johnson, J.; Armijo, K.: Parametric study of PV arc-fault generation methods and analysis of conducted DC spectrum. 2014, pp. 3543–3548
- [2] El Bayda, H.; Valensi, F.; Masquere, M.; Gleizes, A.: Energy losses from an arc tracking in aeronautic cables in DC circuits. *IEEE Trans. Dielectr. Electr. Insul.* Vol. 20, No 1, 2013, pp.19–27
- [3] Haeberlin, H.; Real M.: Arc Detector for Remote Detection of Dangerous Arcs on the DC Side of PV Plants. 22nd European Photovoltaic Solar Energy Conference, Milano, Italy, 2007
- [4] Mackay, L.; Shekhar, A.; Roodenburg, B.; Ramirez-Elizondo, L.; Bauer, P.: Series arc extinction in DC microgrids using load side voltage drop detection. *IEEE First International Conference on DC Microgrids (ICDCM)* 2015, pp. 239–244
- [5] Faifer, M.; Ottoboni, R.; Rossi, M.; Toscani, S.; Grasseti, R.: A method for the detection of series arc faults in DC aircraft power networks. *IEEE International Instrumentation and Measurement Technology Conference (I2MTC)* 2013, pp. 778–783
- [6] Yao, X.; Herrera, L.; Wang, J.: A series DC arc fault detection method and hardware implementation. *Twenty-Eighth Annual IEEE Applied Power Electronics Conference and Exposition (APEC)* . 2013, pp. 2444–2449
- [7] Seo, G.S.; Kim, K. A.; Lee, K.C.; Lee, K.J.; Cho, B.H. A new DC arc fault detection method using DC system component modeling and analysis in low frequency range. *IEEE Applied Power Electronics Conference and Exposition (APEC)*. 2015, pp. 2438–2444
- [8] Wendl, M.; Weiss, M.; Berger, F.: HF Characterization of Low Current DC Arcs at Alterable Conditions. *International Conference on Electrical Contacts*. 2014, pp. 1–6
- [9] Wang, Z.; Balog, R. S.: Arc Fault and Flash Signal Analysis in DC Distribution Systems Using Wavelet Transformation. *IEEE Trans. Smart Grid* Vol. 6, no 4, 2015, pp. 1955–1963
- [10] Yao, X.; Herrera, L.; Wang, J.: Impact evaluation of series dc arc faults in dc microgrids. 2015 *IEEE Applied Power Electronics Conference and Exposition (APEC)* .2015, pp. 2953–2958
- [11] Johnson J.; Pahl B.; Luebke, C.; Pier T.; , Miller T.; Strauch J.; Kuszmaul, S.; W.: Photovoltaic DC Arc Fault Detector testing at Sandia National Laboratories. *Conference Record of the IEEE Photovoltaic Specialists Conference* 2011, pp. 003614–003619
- [12] Haruni, A. M. O.; Muttaqi, K. M.; Negnevitsky, M.: Analysis of harmonics and voltage fluctuation using different models of Arc furnace. *Australasian Universities Power Engineering Conference*, 2007, pp. 1–6
- [13] Manchur G.; Erven, C. C.: Development of a model for predicting flicker from electric arc furnaces. *IEEE Trans. Power Deliv.* Vol. 7, No 1, 1992, pp. 416–426
- [14] Schwieger, J.; Wolff, M.; Baumann, B.; Manders, F.; Suijker, J.: Characterization of Discharge Arc Flicker in High-Intensity Discharge Lamps. *IEEE Trans. Ind. Appl.* Vol. 51, No 3, 2015, pp. 2544–2547

Electrically-functionalised nanoindenter integrated *in-situ* in a Scanning Electron Microscope : case studies

F. Volpi^{a*}, S. Comby-Dassonneville^a, C. Boujrout^a, M. Rusinowicz^a, G. Parry^a, M. Braccini^a, S. Iruela^a,
A. Antoni-Zdziobek^a, Y. Champion^a, F. Charlot^b, R. Martin^b, F. Roussel-Dherbey^b, L. Maniguet^b,
J. Fouletier^c, E. Siebert^c, D. Pellerin^d, M. Verdier^a

^a Univ. Grenoble Alpes, CNRS, Grenoble INP - SIMaP - 38000 Grenoble, France

^b Univ. Grenoble Alpes, Grenoble INP - CMTC - 38000 Grenoble, France

^c Univ. Grenoble Alpes, Univ. Savoie Mont Blanc, CNRS, Grenoble INP - LEPMI - 38000 Grenoble, France

^d Scientec / CSInstruments - 91940 Les Ulis, France

*Corresponding author : fabien.volpi@grenoble-inp.fr

Abstract

Fundamental understanding and quantitative characterization of electron transport mechanisms between two solids brought into mechanical contact require the development of a dedicated multifunctional device. In this article, we report original measurements and analyses based on a nanoindenter coupled with fine electrical measurements *in-situ* a Scanning Electron Microscope (SEM). After a description of the experimental set-up, we report quantitative results on resistive-nanoindentation performed on metallic systems with increasing complexity. Starting from a model case (Au single crystal, a noble metal), a procedure is developed, numerically modelled and further applied to a complex rheology structure (200 nm Au thin film plastically deformed against an elastic substrate) to demonstrate the quantitative monitoring of contact area. Then a two-phase AgPdCu alloy is used to illustrate the benefit of local characterisation performed under SEM imaging. The effect of interfacial layer (probably a native oxide film) on the electrical response is discussed. Finally, we present local impedance spectroscopy characterisation of a 10nm-thick alumina layer on aluminium substrate. The conductance through alumina during mechanical compression is discussed in terms of electrochemical processes.

1 Introduction

The understanding and the quantitative analysis of the electro-mechanical processes involved at the interface between two solids are of crucial interest for both academic and applied purposes [1,2]: electric connectors for electrotechnics and automotive applications, intermittent contacts in mechanical switches (at both macro- and micro-scales), microelectronics,... The development of scanning probe microscopy (SPM) triggered the experimental study of these phenomena at small-scale [3,4,5], but only the coupling of electrical measurements with instrumented indentation (independent load and displacement measurements) provided the precise control and monitoring of both contact mechanics and electrical conduction [6]. Initiated by the monitoring of phase transformation under pressure [7,8,9], resistive-indentation has then been extended to the study of other phenomena: native oxide fracture [10,11,12,13], MEMS operation at small scales [14,15] and contact area computation during nanoindentation tests [16,17]. In the past decades, numerous efforts have been made to further expand the capabilities of nanoindentation [6], such as real-

time imaging [18,19], coupling with multifunctional characterisation tools [20,21] and high temperature measurements [22].

The present article reports the development and the application of a home-made multifunctional characterisation device based on a commercial nanoindentation head. This device combines mechanical and electrical characterisations, and can be integrated *in-situ* in a Scanning Electron Microscope (SEM). Quantitative electrical characterisations cover resistive and capacitive measurements (focus is made on resistive measurements in this paper). *In-situ* SEM integration allows precise positioning of local nanoindentation tests (with a precision better than 100nm) as well as the positioning of electrically-coupled nanoindentation maps. The electrochemical reactions occurring at oxidised surfaces are also explored by impedance spectroscopy.

2 Experimental details

The experimental set-up combines different commercial instruments, with customized adapter systems. Fig. 1 presents the Infra-Red view of the set-up once integrated within the SEM chamber.

The nanoindentation head is a commercial actuator (InForce 50 actuator from Nanomechanics Inc / KLA-Tencor), displaying a maximum load of 50mN and a static load resolution below 0.1 μ N. This force-controlled actuator enables continuous stiffness measurement (CSM) through locked-in detection of displacements induced by oscillatory loads superimposed to the main load signal. This CSM mode gives access to the continuous extraction of both hardness and elastic modulus during indentation [23]. A fast mapping technique is also available, allowing high-speed nanoindentation tests (\sim 1 indent per second). The indentation tip is fixed on a 1.5 cm-long extension. All the experiments presented in this paper have been performed with boron-doped diamond (BDD) tips with resistivity in the range of [0.2-2] Ω .cm (with either Berkovich, cube-corner or flat-punch shapes). Electrical contacts to the tip are made with thin copper wires connected to fixed sockets. Actuator and sample displacements are performed with linear positioners from SmarAct GmbH. Typical travel ranges are at the cm-scale with a \sim 1 nm resolution. An overall frame stiffness larger than 10^6 N/m has been extracted, thus validating the overall mechanical behavior.

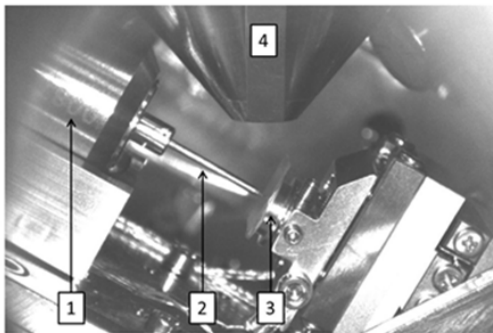


Fig. 1. Infra-Red view of the set-up once integrated within the SEM. (1 = Nanoindenter head, 2 = Extender + tip, 3 = Specimen, 4 = SEM column)

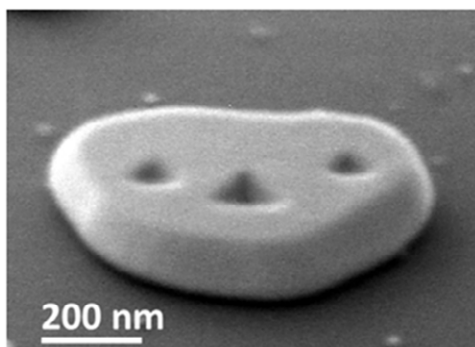


Fig. 2. Illustrations of the set-up performances. Gold crystallites after three individual indents (without tilt-correction).

The SEM apparatus used was a Field Emission Gun (FEG) GEMINI SEM 500 from Zeiss [24]. The arrangement of the analytical tools within the SEM chamber has been optimized to improve the observa-

tion angle during indentations. In standard conditions, the specimen surface was scanned under a 60° tilt angle, that was software-corrected during experiments. The SEM-integration allows positioning of indents with a precision better than 100nm. As an illustration, Fig. 2 presents a $0.75\mu\text{m}$ -large gold island (obtained by dewetting of a gold film on sapphire substrate) after a ‘smiley pattern’ obtained with three indents.

Resistance measurements were conducted with a ResiScope apparatus from CSI/Scientec. Originally developed for conductive-atomic force microscopy [25], this device is optimised for real-time and self-compliant resistance measurements. It ranges from 100 Ω to 1 T Ω , with acquisition rates up to 1kHz. Impedance spectroscopy measurements were also performed for the characterisation of thin oxide layers: an LCR-meter (Agilent 4980) was used, with a sensitivity better than 1nS for admittance measures at 2MHz.

3 Resistive-nanoindentation of metals

The electrical resistance which is measured during a resistive-nanoindentation test is the sum of several resistances in series (Fig. 3-a): the tip resistance, the interface resistance (oxide, capping layer,...) and the sample resistance. In the case of metallic samples, the latter resistance is negligible. In standard resistive-nanoindentation experiments, the overall resistance tends to decrease as the tip penetrates the sample (Fig. 3-b). This trend is driven by the combination of several mechanisms: (1) as the tip penetrates the sample, the tip-to-sample contact area increases, thus decreasing the overall contact resistance, (2) the interfacial layer (usually insulating) tends to crack, thus allowing direct local tip-to-metal contacts and (3) the spreading resistance through the tip tends to decrease.

3.1 Resistive-nanoindentation on pure metals: effect of a native oxide

The behaviours of three pure metals have been compared: a noble metal (Au) and two natively-oxidised metals (Al and Cu). The two latter were covered with their native-oxide layers characterised by different conduction mechanisms: alumina displays ionic conduction only, while copper oxides display both electronic and ionic conduction. All samples were (111)-oriented bulk single crystals.

A set of resistive-nanoindentation experiments (Resistance-Depth curves) performed with a Berkovich tip under different biases (from 0.5 to 10V) is shown in Fig. 3-b,c,d. On Au, all curves are clearly superimposed, suggesting an ideal ohmic contact (which is confirmed by current-voltage characteristics, not shown here). This behaviour will be quantitatively analysed in Part 3.2. On the contrary, the two oxidised

metals display drastically different behaviours: much larger resistances are measured (up to 6 orders of magnitude larger with aluminum) and highly-non-linear behaviour is observed. The lower dispersion observed on copper (compared to aluminum) is a signature of the electronic conductivity in copper-oxides, while oxido-reduction reactions are supposed to be the cause of the highly-dispersed data on aluminum (discussed in Part 3.4).

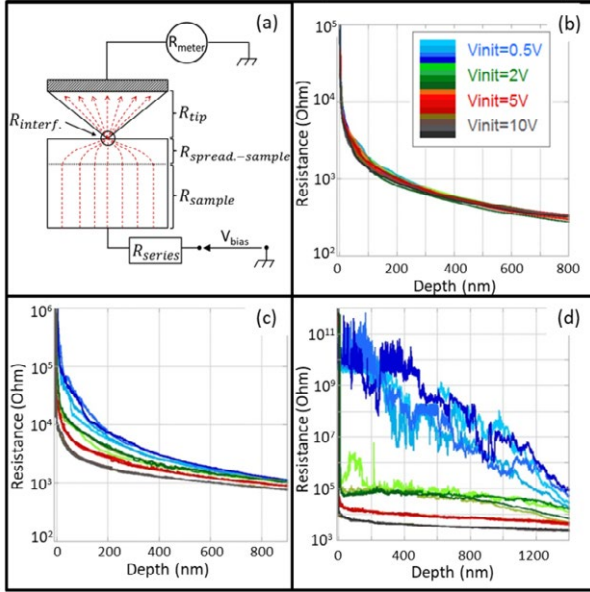


Fig. 3. Resistive-nanoindentation illustrations. (a) Schematic of the resistance contributions. Set of resistive-nanoindentation tests on Au (b), Cu (c) and Al (d).

3.2 Resistive-nanoindentation on noble metals

3.2.1 Experiments

In the case of noble metals, the absence of interfacial layer leads to measure the tip resistance only (Fig. 4-a). Under this condition, the measured resistance can be simply given by (1) (for more details, see [26]):

$$R_{measured} = A + B/(h_c + h_0) \quad (1)$$

A and B are two constants that depend only on the experimental set-up (tip geometry and resistivity, series resistance,...) but not on the specimen (A and B have to be determined experimentally during the calibration step, see below). h_0 is the length of the tip defect (unavoidable rounded apex of the tip). Even though expression (1) relies on strong approximations (self-similar shape of the tip, homogeneous distribution of current lines through the contact,...), it is verified experimentally (Fig. 4). In order to validate this approach, a finite element (FE) modelling of this experiment was carried out.

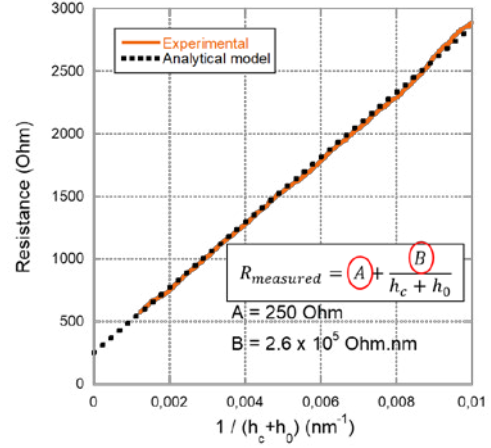


Fig. 4. Linear fitting of resistive-nanoindentation data according to Equation 1.

3.2.2 Finite-Element Modelling

FE modelling was performed in 2D axisymmetric (Fig. 5-a). The commercial FE software ABAQUS®/Standard was used. The indenter was a Berkovich tip defined as an elastic body and built from an experimental area function (fused silica reference sample using Oliver and Pharr method). The sample (Au) was defined as an elasto-plastic cylinder with a 10 μ m radius and height. The mechanical behavior of Au was modeled by a Hooke's law for the elastic part ($E = 77.2$ GPa ; $\nu = 0.42$) and by a Hollomon power law for the plastic part which has the following form:

$$\sigma_{Plastic} = K \epsilon_{plastic}^n \quad (2)$$

where K and n are constants which were used as fitting parameters in order to reproduce the experimental Load-Depth curves (see Tab. 1).

Concerning the electrical coupling, the electrical conduction in the tip and in the sample was modeled using a pure ohmic law with an electrical conductivity extracted from previous works [27].

The two parts were meshed with axisymmetric deformation element CAX3T. Frictionless mechanical contact was defined by default. During loading, a displacement of 1 μ m along the vertical direction z was applied to the top surface of the tip. For the electrical boundary conditions, a 10V bias was applied between the top surface of the tip (0V) and the bottom surface of the sample (10V). Post treatment using a Python subroutine made it possible to extract load, penetration depth, contact depth, contact area and electrical resistance.

Without any advanced fitting process, the FE-modelled Resistance-Depth curves show remarkable match with the experimental data (Fig. 5-b). And the linear dependence of resistance with the reciprocal of the contact depth (Equation 1) is numerically confirmed (Fig. 5-c). This is explained by the homothetic distribution of current lines through the contact interface at the periphery of the contact [26].

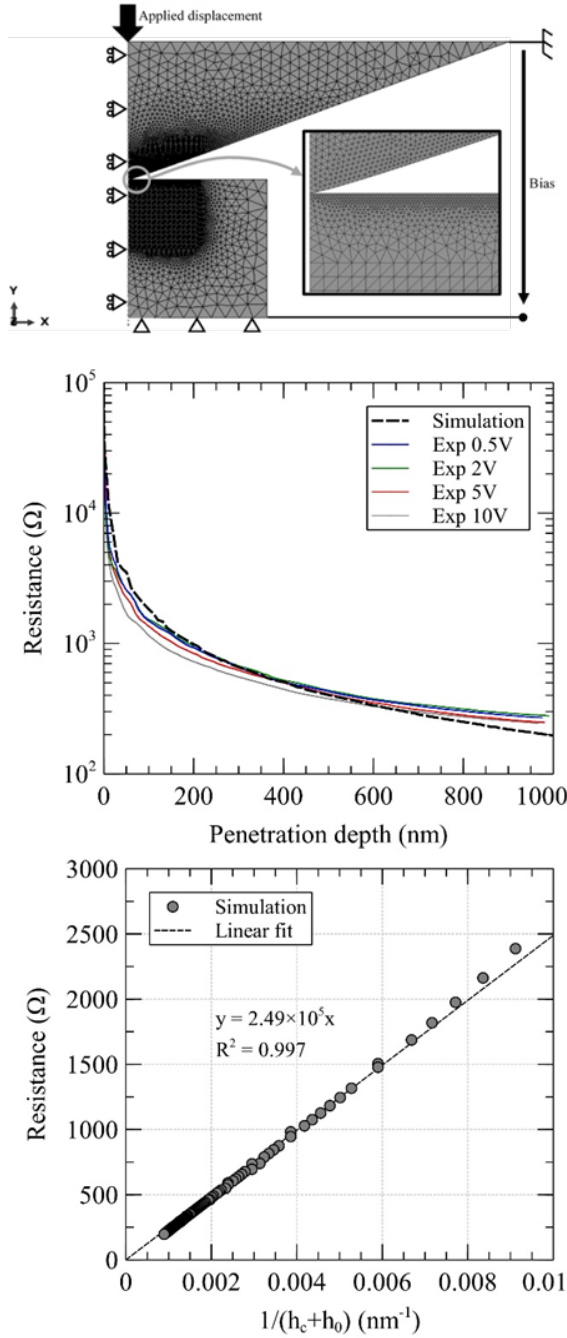


Fig. 5. Numerical modelling. (a) System model. (b) Comparison of simulated and experimental resistive-nanoindentation tests. (c) Linear fitting of simulated resistive-nanoindentation data.

Tab. 1. Parameters of the Hollomon law describing the plastic behaviour of bulk gold, fitted to the experimental data.

Parameter	σ_y	K	n
Value	100 MPa	230 MPa	0.1

3.2.3 Application to the real-time monitoring of contact area

The real-time monitoring of resistance during nanoindentation is of particular interest for the quantitative analysis of nanoindentation tests. Indeed, the simultaneous computation of sample Young's modulus and hardness relies on a precise knowledge of the contact area A_c . However even for the simplest cases of homogeneous semi-infinite specimens, the determination of A_c is strongly affected by pile-up or sink-in phenomena that occur at the contact periphery (Fig. 6). The actual contact area may then be misinterpreted by 20-30%. The standard methods widely used to extract contact area require analytical models based on material rheology assumptions [28,29]. On the contrary, the direct monitoring of contact area by resistive-nanoindentation should bring supplementary inputs for the quantitative analysis of indentation tests. Some attempts to combine micro- or nano-indentation to resistive measurements to quantitatively analyse the indentation process have been reported [16,17] but the monitoring of contact area was not processed.

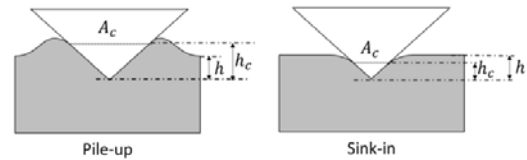


Fig. 6. Effect of material rheology on contact area and contact depth. The penetration depth h is the depth reached by the tip from the initial specimen surface, while the contact depth h_c describes the contact height of the tip with the specimen.

One of the bottleneck steps for the quantitative analysis of resistive-nanoindentation tests is the appropriate analytical description of the electrical measurement chain.

This description being established, the experimental extraction of the contact area can be processed through a 3-step procedure:

- Step 1: The tip geometry is determined from direct AFM characterisation. This step generates the tip "shape function" that relates the projected contact area to the contact depth h_c .
- Step 2: An electrical calibration is carried out (on a gold bulk single crystal for instance), aiming at the determination of the A and B constants (see (1)). As A and B depend only on the experimental set-up, a one-to-one analytical correspondence is then established between the electrical resistance and the contact depth (independently of the specimen).
- Step 3: The contact area monitoring of any oxide-free specimen can then be performed. Using the tip shape function (step 1), the contact area is finally determined from the contact depth values (step 2) for this specimen to be characterized.

This procedure has been applied and validated on a 200 nm-thick polycrystalline gold film deposited on a sapphire substrate. Such a composite geometry is a model case of complex rheology which is depth-dependent and where no analytical model exists. To do so, resistive-nanoindentation tests with various final penetration depths have been performed. For each test, post-mortem AFM measurements have been conducted to compare the contact area to the one monitored by our procedure. Fig. 7 shows an excellent agreement between our predictions and the effective areas. For comparison, the contact area computed from the standard Oliver-Pharr method [28] (based on sink-in assumption) is also reported showing a ~50% discrepancy. Such a precise monitoring of the tip-to-sample contact area has been reported for the first time in literature in [26].

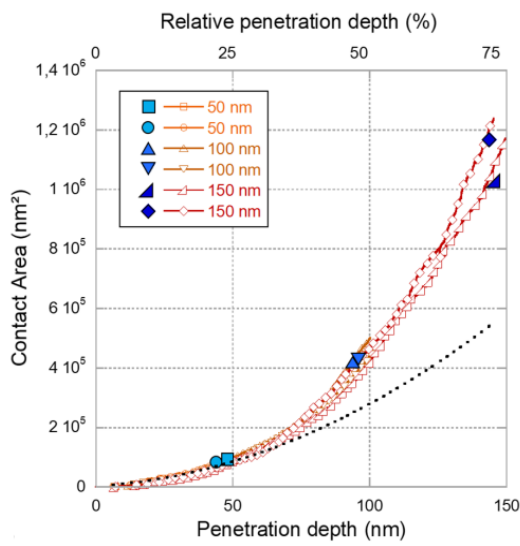


Fig. 7. Contact area against penetration depth on the Au thin film. Comparison of the computed data (open markers) with the corresponding post-mortem AFM measurements (solid markers). Predicted contact area from Oliver and Pharr model in dotted line.

3.3 Resistive-nanoindentation of multi-phased alloys

As already mentioned, the integration of this resistive-nanoindentation set-up within the SEM allows precise positioning of the spot to analyze as well as the electro-mechanical mapping of a specimen surface. These two advantages are illustrated through the study of an AgPdCu alloy designed to combine high conductivity and large yield strength. Fig. 8 presents an SEM view of the sample after a local indent performed on the Ag-rich phase (lightest contrast in the SEM image). The darkest domain is constituted of Cu-rich phases. Fig. 9 (a)-(b) collect the resistance and hardness measurements obtained over 28 indents on the two domains. These electrical and mechanical data clearly discriminate the Ag- and Cu-rich phases. The Cu-rich domain appears as more conductive than the Ag-rich

one, but it also appears as harder. The higher resistance of the Ag-rich domain can be attributed either to a larger intrinsic resistivity, to a more resistive native-oxide or to different material rheologies.

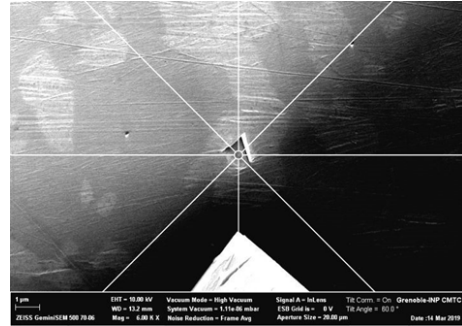


Fig. 8. SEM view of an indent left after local testing of the Ag-rich phase. The white triangle at the bottom of the image is the indenter tip.

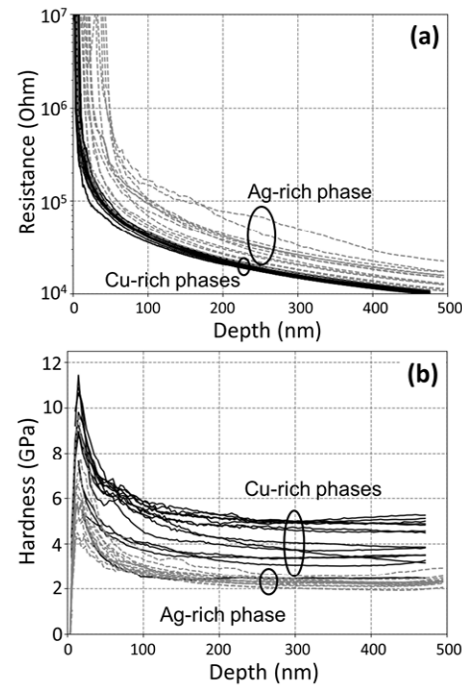


Fig. 9. Electrical and mechanical data from 28 indents performed in both Ag- and Cu-rich phases. (a) Resistance and (b) Hardness evolutions with indentation depth. Hardness data were extracted from Oliver-Pharr model [26].

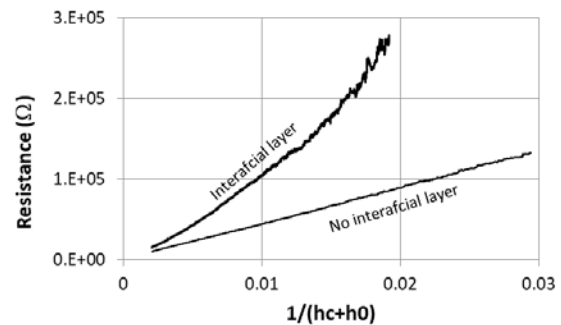


Fig. 10. Evolution of resistance against $1/(h_c+h_0)$ on two distinct indents.

The plotting of resistance against $1/(h_c+h_0)$ (according to Equation 1) is shown in Fig. 10. It clearly discriminates the ideal indents (linear dependence) from those affected by an interfacial layer (non-linear dependence), most-likely an oxide layer. This behaviour supports the need for a deeper analysis of oxide-covered metals.

3.4 Resistive-nanoindentation of oxide-covered metals

In the case of oxidised metals, the electrical resistance is essentially controlled by the conduction mechanisms through the oxide layer. A set of experiments have been performed on a 10nm thick alumina film deposited by Atomic Layer Deposition onto an aluminum substrate.

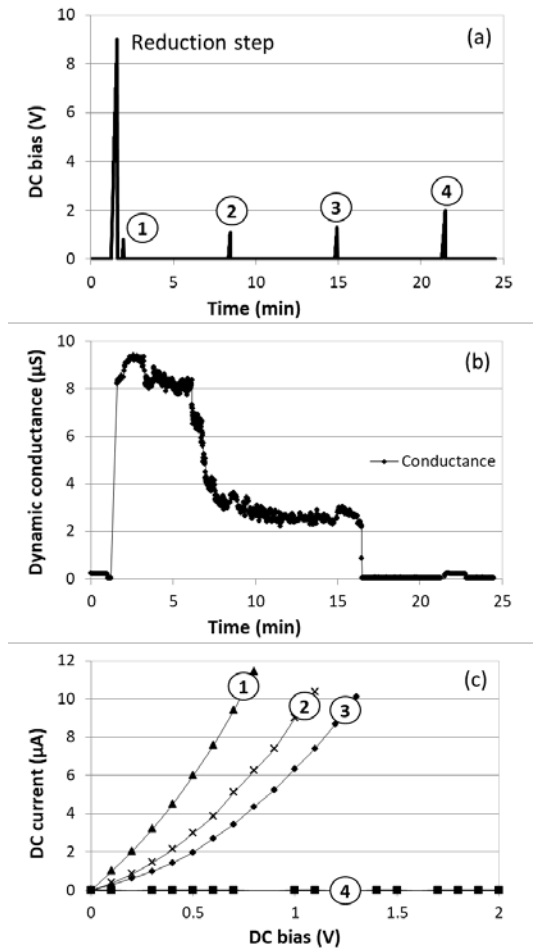
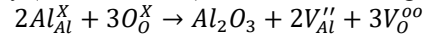


Fig. 11. Characterisation of a 10nm-thick alumina film (under mineral oil). (a) Timeline of the test protocol. (b) Evolution of the dynamic conductance during test. (c) Current-Voltage characteristics during alumina recovery.

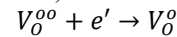
For these experiments, compression tests were performed with a $5\mu\text{m}$ large flat-punch tip. The tip was set into contact with the alumina surface with a low load ($100\mu\text{N}$, leading to an applied stress close to 5 MPa). Once the contact set, impedance-

spectroscopy measurements were performed with an LCR-meter. The experiment timeline was the following (Fig. 11-a): a large voltage scan (referred as “Reduction step”) was first applied in order to reduce locally the alumina film, then dynamic conductance and capacitance were monitored continuously under 0 V, while small voltage scans were performed every 5 min to monitor the alumina recovery (voltage scans 1 to 4). After the “Reduction step”, the conductance is seen to increase drastically (Fig. 11-b).

Alumina is a pure ionic conductor exhibiting a Schottky (and/or Frenkel) disorder, according to:



When a DC current passes through the layer, electrode reactions take place at both alumina interfaces. At the diamond tip side, a possible cathodic reaction could be the reduction of oxygen. In order to check this hypothesis, the experiments were performed either at room atmosphere or with the alumina surface immersed into a mineral oil drop (thus preventing any interaction with atmospheric oxygen). Similar results were obtained in both conditions, thus showing that this reaction can be put aside. Consequently, this “Reduction step” is attributed to the reduction of oxygen vacancies according to the following reaction (formation of F-centres):



Considering the Gibbs energy of formation of alumina (circa -1000 kJ/mol), the cathodic voltage to be applied for electron injection into alumina is higher than -2.5 V/O_2 . The difference to the large voltage applied at the “Reduction step” (8-10 V) is due to the Ohmic voltage drop through the highly insulating alumina layer.

After the “Reduction step”, the alumina layer becomes an electronic conductor, and its conductance remains high for more than 15 min (up to 1h for some tests). The four current-voltage scans (Fig. 11-c) clearly confirm the decrease of DC-conductance, and the final recovery of alumina insulation (scan 4).

It is to be noted that the electric field applied to the alumina layer at the “Reduction step” (8-10 MV/cm) is comparable to the breakdown electric field of alumina films. However in the present case, the change-over in conduction state (from insulator to conductor) is reversible. This reversibility has already been reported for instance in alumina nanocapacitors [30].

The control of the oxide layer conductivity will be further explored by complementary experiments: doping of alumina (with a mixed-conductive oxide like copper oxide), exploration of negative biases, kinetics of recovery in open-circuit conditions,...



Fig. 12. Numerical modelling of an alumina/aluminum stack under resistive-nanoindentation.

Numerical simulations are in progress in order to describe the mechanical and electrical behaviour of this alumina layer under mechanical stress. Fig. 12 reports exploratory results, where high radial tensile stresses are identified at the tip apex and periphery (see insets).

4 Conclusion

An experimental set-up dedicated to the coupling of local electrical and mechanical characterisations is presented. This set-up combines a nanoindentation head to fine electrical measurements *in-situ* in a scanning electron microscope. The ability of the set-up to characterise the contact with oxide-free or oxidized metals is shown. First the ability to monitor quantitatively the contact area all along a nanoindentation test is demonstrated. Then a two-phase metallic system is characterized through individual local indents. Finally the electrical behaviour of an oxide layer is analysed and described on the basis of electrochemical processes. Numerical modelling of the experiments is used to support the understanding of the overall system behaviour.

5 Acknowledgment

This work has been performed with the financial support of the Centre of Excellence of Multifunctional Architected Materials "CEMAM" n° ANR-10-LABX-44-01. The CEMAM program is funded by the French Agence Nationale de la Recherche (ANR).

The authors thank the technical team of SIMaP lab (B. Mallery, S. Massucci, N. Vidal) for its support, the CMTC platform (physico-chemical characterization platform of Grenoble INP), as well as members of CSI/Scientec company (Les Ulis, France) for their support for the functionalization of the nanoindentation head: L. Pacheco, A. Lecoguiec and S. Poulet.

5 Literature

- [1] R. Holm. "Electrics Contacts, Theory and Applications", Springer, 2000.
- [2] M. Braunovic, V.V. Konchits, N.K. Myshkin, "Electrical Contacts, Fundamental, Applications and Technology", "BRAU", CRC Press, 2007.
- [3] G. Binnig, C. F. Quate, and Ch. Gerber, "Atomic Force Microscope", Phys. Rev. Lett. 56, 930, 1986.
- [4] W. Vandervorst, M.Meuris, European patent 466274, 1992
- [5] P.Eyben, W.Vandervorst, D.Alvarez, M.Xu, and M.Fouchier, "Probing Semiconducteurs Technology and Devices with Scanning Spreading Resistance Microscopy", in "Scanning Probe Microscopy Electrical and Electromechanical Phenomena at the Na Probing", Springer, 2007.
- [6] H. Nili, K. Kalantar-Zadeh, M. Bhaskaran, S. Sriram, "In situ nanoindentation: Probing nanoscale multifunctionality", Prog Mater Sci. 58, 2013.
- [7] D. R. Clarke, M. Kroll, P. D. Kirchner, R. F. Cook, B. J. Hockey, "Amorphization and Conductivity of Silicon and Germanium Induced by Indentation" Phys. Rev. Lett. 60 2156-2159, 1988.
- [8] G. M. Pharr, W. C. Oliver, R. F. Cook, P. D. Kirchner, M. Kroll, T. R. Dinger, "Electrical resistance of metallic contacts on silicon and germanium during indentation", J. Mater. Res. 7 961-972, 1992.
- [9] S. Ruffell, J. E. Bradby, J. S. Williams, O. L. Warren, "An in situ electrical measurement technique via a conducting diamond tip for nanoindentation in silicon", J. Mater. Res. 22 578-585, 2007.
- [10] J. B. Pethica, D. Tabor, "Contact of characterised metal surfaces at very low loads: Deformation and adhesion", Surf. Sci. 89 189-190, 1979.
- [11] D. D. Stauffer, R. C. Major, D. Vodnick, J. H. Thomas, J. Parkern, M. Manno, C. Leighton, W. W. Gerberich, "Plastic response of the native oxide on Cr and Al thin films from in situ conductive nanoindentation", J. Mater. Res. 27 685-693, 2012.
- [12] H. H. Nguyen, P. J. Wei, J. F. Lin, "Electric contact resistance for monitoring nanoindentation-induced delamination", Adv. Nat. Sci.: Nanosci. Nanotechnol. 2 015007-1-4, 2011.
- [13] T. Shimizu, T. Horie, N. Watanabe, J. Miyawaki, S. Fujii, Y. Yamagata, T. Kondo, M. Onuma, "The investigation of electrical contacts using newly designed nano-indentation manipulator in scanning electron microscope", Proc. 60th IEEE Holm Conf. Elect. Cont. 403-406, 2014.
- [14] P. Y. Duivivier, V. Mandrillon, K. Inal, C. Di-ppedale, S. Deldon-Martoscia, J. P. Polizzi, "Investigation of the Electrical Resistance of Au / Au Thin Film Micro Contacts", Proc. 56th IEEE Holm Conf. Elect. Cont. 58-64 Time Dependence, 2010.
- [15] B. Arrazat, P. Y. Duivivier, V. Mandrillon, K. Inal, "Discrete Analysis of Gold Surface Asperities Deformation under Spherical Nano-Indentation Towards Electrical Contact Resistance Calculation", Proc. 57th IEEE Holm Conf. Elect. Cont.1-8, 2011.
- [16] L. Fang, C. L. Muhlstein, J. G. Collins, A. L. Romasco, L. H. Friedman, "Continuous electrical in situ contact area measurement during instrumented indentation", J. Mater. Res. 23 2480-2485, 2008.
- [17] D. J. Sprouster, S. Ruffel, J. E. Bradby, D. D. Stauffer, R. C. Major, O. L. Warren, J. S. Wil-

- liams, “Quantitative electromechanical characterization of materials using conductive ceramic tips”, *Acta Mater.* 71 153-163, 2014.
- [18] Rabe R, Breguet JM, Schwaller P, Stauss S, Haug FJ, Patscheider J, et al, “Observation of fracture and plastic deformation during indentation and scratching inside the scanning electron microscope”, *Thin Solid Films*, 469–470:206–13, 2004.
- [19] Wall MA, Dahmen U, “Development on an in situ nanoindentation specimen holder for the high voltage electron microscope”, *Microsc Microanal* ; 3:593–4, 1997.
- [20] Sridhar S, Giannakopoulos AE, Suresh S, Ramamurty U. “Electrical response during indentation of piezoelectric materials: a new method for material characterization”, *J Appl Phys*, 85:380–7, 1999.
- [21] Rar A, Pharr GM, Oliver WC, Karapetian E, Kalinin SV. “Piezoelectric nanoindentation”, *J Mater Res* ;21:552–6, 2006.
- [22] Schuh CA, Packard CE, Lund AC. “Nanoindentation and contact-mode imaging at high temperatures”, *J Mater Res*; 21:725–36, 2006.
- [23] W. C. Oliver and G. M. Pharr, “Measurement of hardness and elastic modulus by instrumented indentation: Advances in understanding and refinements to methodology”, *J. Mater. Res.*, Vol. 19, No. 1, Jan 2004.
- [24] L. Maniguet, F.Roussel, R.Martin, E.Djurado, M.C.steil, E.Bichaud, A.LeGo, M. Holzinger, S.Cosnier, J.M.Chaix, and C.Carry, “Fuel cells and ceramic-characterizing real-worlds sample with a feseem ready for challenges”, *Microscopy and Analysis*, 21:47, 2015.
- [25] F. Houzé, R.Meyer, O.Schneegans, and L.Boyer, “Imaging the local electrical properties of metal surfaces by atomic force microscopy with conducting probes”, *Applied Physics Letters*, 69:19751977, 1996.
- [26] S.Comby-Dassonneville, F. Volpi, G. Parry, D. Pellerin, M. Verdier, “Resistive-nanoindentation: contact area monitoring by real-time electrical contact resistance measurement”, *MRS Communications*, Vol. 9 (3), 1008-1014, 2019
- [27] <https://tel.archives-ouvertes.fr/tel-01897366>
- [28] W. C. Oliver, G. M. Pharr, “An improved technique for determining hardness and elastic modulus using load and displacement sensing indentation experiments”, *J. Mater. Res.* 7 1564-1582, 1992.
- [29] J. L. Loubet, M. Bauer, A. Tonck, S. Bec, B. Gauthier-Manuel, “Mechanical Properties and Deformation Behavior of Materials Having Ultra-Fine Microstructures : Nanoexperiments with a surface force apparatus”, in: M. Nastasi, D. M. Parkin, H. Gleiter (Eds.), “Mechanical Properties and Deformation Behavior of Materials Having Ultra-Fine Microstructures”, Kluwer Academic Publisher 429-447, 1993
- [30] Belkin, A., Bezryadin, A., Hendren, L. et al. “Recovery of Alumina Nanocapacitors after High Voltage Breakdown”. *Sci Rep* 7, 932, 2017

Recovery of Short AC Switching Arcs – An Old Principle Newly Investigated

Manfred Lindmayer, TU Braunschweig/D and David Elmiger, Rockwell Automation Switzerland, Aarau/CH
M.Lindmayer@tu-braunschweig.de; delmiger@rockwellautomation.com

Abstract

It has been known from Slepian since 1928 that the recovery of AC arcs burning between simple contacts without additional quenching aids depends on the formation of a thin space charge sheath in front of the new cathode after polarity change. Already in the 1950s/1960s it has been found that arcs of sub-millimeter length behave superior in comparison with longer gap distances. In his 1968 thesis Schmelzle in addition to systematic experiments treated this phenomenon theoretically, and found that there exists an immediate recovery voltage after polarity reversal, followed by a further increase due to flattening of the temperature gradient between the cooler cathodic contact and the still hot column. Based on this theory, new simulations were now carried out using the COMSOL® Multiphysics program. Additionally to arcs in the contact center, arcs on contact edges were considered. This theoretical work was accompanied by switching experiments. In both ways it is shown that the shorter the gap length the faster the withstand voltage increases. This is due to the better column cooling by the closer counter-electrode. Arc roots on edges are characterized by a slower growth of the sheath thickness around the edge, leading to a deteriorated quenching behavior. The application of this interruption principle lies in AC arcs in currents between a few Amperes and a few hundred Amperes, such as smaller contactors, or auxiliary switches.

1 Problem, Objectives

It has been known since Slepian in 1928 that AC arcs after polarity reversal exhibit an immediate withstand voltage of a few hundred Volts, and that a growing space charge sheath in front of the new cathode is responsible [1, 2]. Shortly later this was confirmed by probe measurements [3]. Already in the 1950/1960s it was found that arcs of sub-millimeter length perform better in this respect in comparison with arcs of several millimeters to centimeters [4-6]. The better cooling of the arc column toward the colder contacts was thought to be responsible for this effect. In his thesis from 1968 Schmelzle [8] investigated many different silver-based contact materials with respect to their recovery behavior after current zero with consequent polarity change. Additionally, he derived a theoretical model of this effect, similar to Paschen's breakdown model, and compared the results with the experiments. This model is taken as the basis for newer simulations with better approaches to the properties of contact materials as well as the plasma of the arc column. Again, in an industrial switching laboratory, interruption experiments were carried out for comparison with the simulation results.

2 Schmelzle's Theory of Arc Recovery after Current Zero

2.1 General

Following, the new cathode is only denominated cathode. Schmelzle [8] considers the temperature

profile between the relatively cold cathode at current zero (500 K - 1800 K) and the hot column. According to [7] this is ≈ 5000 K, rather independent of the previous AC current. Starting with a sharp temperature step, the transition becomes smoother with time by heat conduction. The degree of ionization x_i is strictly coupled to the local temperature, see **Fig. 1**.

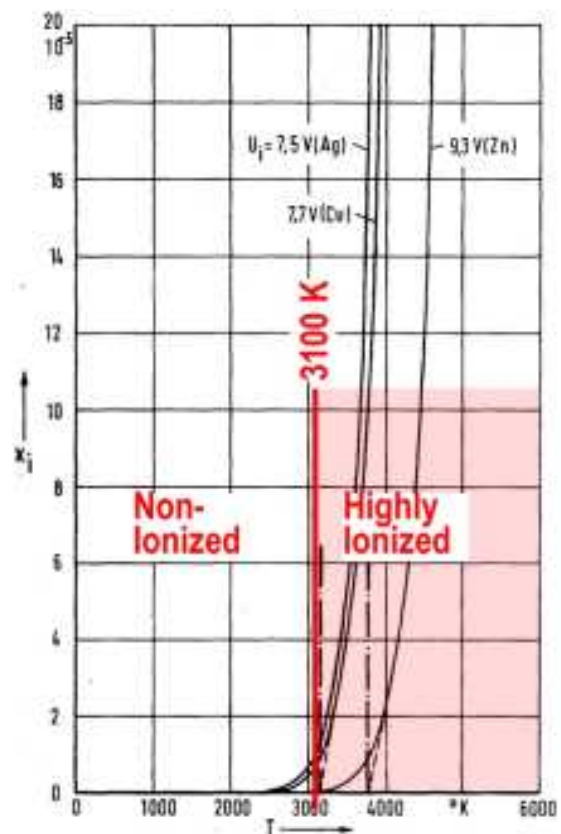


Fig. 1 Ionization Degree x_i of Metal Plasmas as a Function of Temperature T [8]

Schmelzle idealizes this into a highly ionized region above the temperature T_{Limit} , which lies at 3100 K for Ag, and a non-ionized region below. A positive space charge sheath of thickness d is formed under the influence of the transient recovery voltage (TRV). This sheath, which takes the whole TRV, grows with time.

The ignition condition (Pachen's Law) reads

$$\ln\left(\frac{1}{\gamma_i} + 1\right) = \int_0^d \alpha \cdot dx \quad (1)$$

γ_i is the secondary emission coefficient of electrons at the cathode, α the ionization coefficient in the sheath d . α is often described as a function of the local field strength E :

$$\alpha = Ap \cdot \exp\left(-\frac{Bp}{E}\right), \quad (2)$$

Where p is the pressure, and A and B depend on the gas. Due to the lack of data for the plasma mix of metal vapor and air, the values of air,

$$A = 14.6 \frac{1}{\text{cm} \cdot \text{Torr}}, \quad B = 365 \frac{\text{V}}{\text{cm} \cdot \text{Torr}} \quad (3)$$

are taken here. The pressure is $p = 760$ Torr.

Schmelzle uses findings by Tajev [9] that prove a correlation between the secondary emission coefficient and the work function U_A :

$$\gamma_i = \frac{0.115}{U_A/V} \quad (4)$$

He further postulates that the work function U_A behaves in the same way as the cathodic electron emission due to temperature T_C and electric field E_C there. Then U_A depends on T_C :

$$U_A(T_C) = \frac{2kT_C}{e} \cdot \ln \frac{T_C}{T_0} + \frac{T_C}{T_0} U_A - f(E_C) \quad (5)$$

The last term is negligible. k = Boltzmann Constant, e = electron charge.

Together with the field distribution within the sheath, we finally get Schmelzle's ignition condition:

$$\ln\left(\frac{1}{\gamma_i(T_C)} + 1\right) = Ap \int_0^d \exp\left(-\frac{Bp}{\frac{3U_F}{2d}\sqrt{1-\frac{x}{d}}}\right) dx \quad (6)$$

U_F is the recovery voltage, synonyms are breakdown voltage, withstand voltage, or reignition voltage. Equ. (6) is depicted in **Fig. 2** with γ_i on the vertical axis and U_F as parameter. The colored horizontal lines mark γ_i for different cathode temperatures. From this, other V-shaped curves of $U_F = f(d)$ and $U_F = f(t)$ can be derived, where t is the cooling time after current zero.

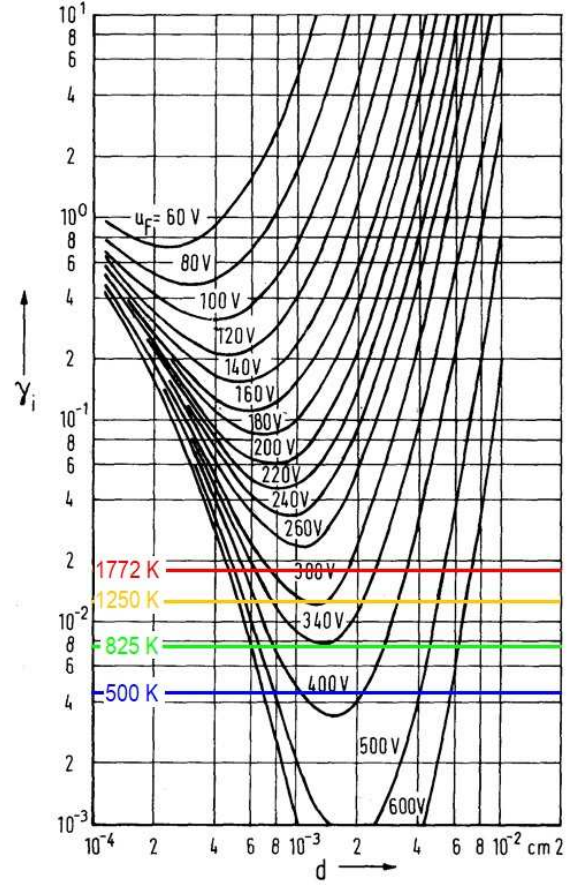


Fig. 2 V-Shaped Curves Representing Equ. (6)

2.2. Some Results from [8]

The simulations in [8] were partly carried out with simplified data for the electrode materials and the plasma of the arc column. In a first step the temperature at the contact surface was calculated analytically by assuming the metallic contact as a semi-infinite ball. The arc spot radius was kept constant for each current in such a way that the maximum temperature just touched the boiling temperature of Ag. The current shape was half-sinusoidal. After 10 ms arcing time, the second step was the 1D cooling of the plasma column toward the cathode. Average values from air were taken for the thermal properties. **Fig. 4** is an example of calculated recovery voltage U_F vs. the frequency f_E of the TRV, which is inversely proportional to the time after current zero.

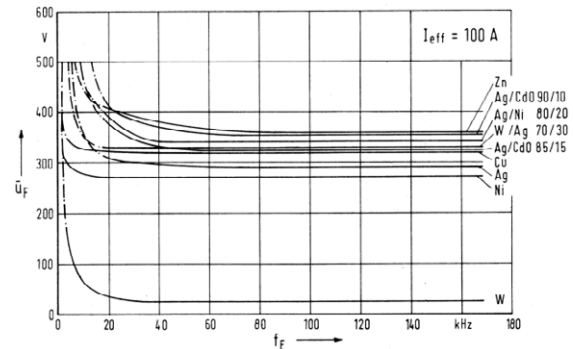


Fig. 4 Calculated Recovery Voltage U_F vs. Frequency f_E of TRV [8]

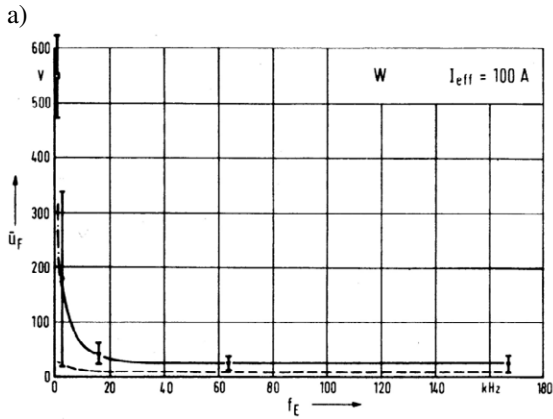
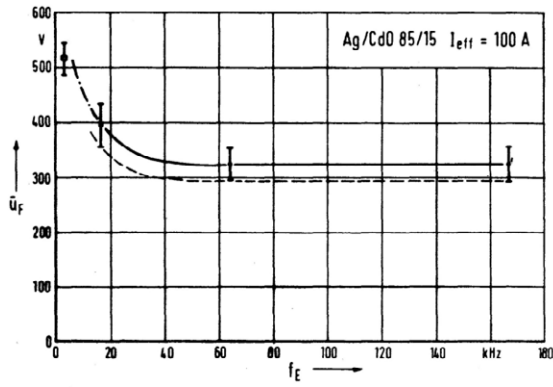


Fig. 5 Calculated Recovery Voltage U_F vs. Frequency f_E of TRV [8]
a) Ag/CdO 85/15 b) W

The constant U_F values at high frequencies mean that there is an immediate recovery voltage at current zero ($t=0$). Comparison of the calculated voltages with experimental results in **Fig. 5** shows that there is also a reasonable accordance between theory and experiment with respect to different contact materials.

3 Simulation Setup

For the simulations in this work a 3D contact geometry was set up, see **Fig. 6**. The contact tips of 3 mm x 3 mm x 0.5 mm of AgSnO₂ are mounted on a copper support of 0.8 mm thickness, whose exact shape is irrelevant because heat does not penetrate so much into the support to influence the situation on the contact surface. Only one quarter is modeled and symmetry conditions applied. The arc length L is varied from 0.2 mm to 4 mm. Three different positions of the arc root (= arc spot) are used for the simulations:

- (C) Spot in the contact **C**enter
- (M) Spot in the **M**iddle of the contact edge
- (O) Spot at an **O**uter edge of the contact

Full, half, or quarter circles are used for the shapes of these spots. In a first simulation step only the temperature development of the metallic parts is simulated. From [10, 11] a constant current density of $2 \cdot 10^8$ A/m² for AgSnO₂ is taken for the full circle in position (C). This means that the diameter d_{Spot} varies with time as the current varies. Together with the Equivalent Anode Voltage $V_{eqA} = 9$ V [11] a constant power density $p = 1.8 \cdot 10^8$ W/m² acts on the contact surface. For the half circle (M) the double, for the quarter circle the fourfold value is used. It can already be stated here that the current and power density, respectively, only play a minor part, since the applied model of vaporization erosion keeps the surface temperature at boiling temperature relatively long. This model, described in detail in [12], takes into account all relevant enthalpies of AgSnO₂ 8.7. Those of other oxide content are nearly identical.

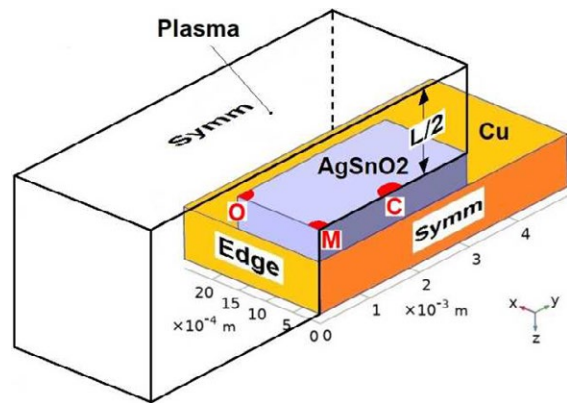


Fig. 6 Simulation Geometry

The arc current was modified in two ways, the RMS value of the $f = 50$ Hz current, as well as the arcing time t_v before the current zero moment.

$$i(t) = \hat{i} \cdot \max\{0, \sin[2\pi f \cdot (t + 10\text{ms} - t_v)]\} \quad (7)$$

Fig. 7 shows this current evolution in principle.

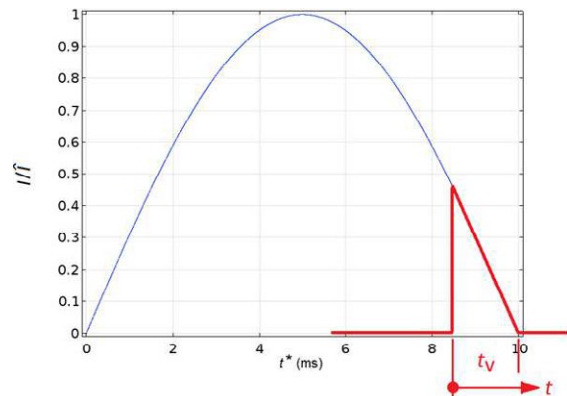


Fig. 7 Current Evolution, here $t_v = 1.5$ ms

The RMS current was varied between 16 A and 250 A.

Free cooling for several hundred microseconds is achieved by running the total computation time longer than the arc time t_v .

In a second step, only the cooling and sheath growth in the plasma volume is simulated. Because the exact shape of the arc column is not known, the initial temperature of the whole plasma volume is set to 5000 K [7]. The temperatures of the metallic parts from the first step are used as boundary conditions of the plasma volume, the other boundaries thermally insulated. Due to the lack of better plasma data, those of Cu are taken [13]. All simulations are carried out with the Muliphysics Program COMSOL® [14].

4 Simulation Results

4.1 General

First, to get a correlation between the growing sheath thickness d and the recovery voltage U_F , Equ. (6) and Fig. 2 are taken as a basis. When we take the temperature T_C as parameter, we obtain the V-shaped Paschen Curves of Fig. 8.

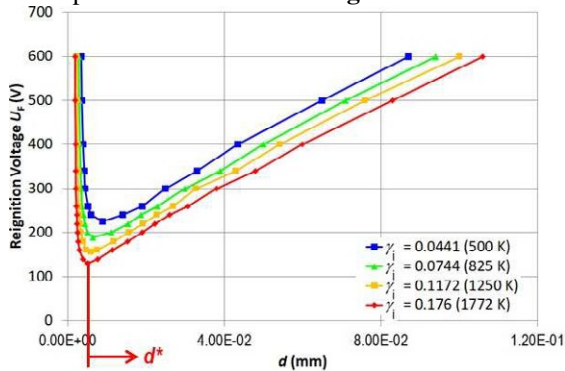


Fig. 8 Paschen Curves derived from Equ. (6) and Fig. 2

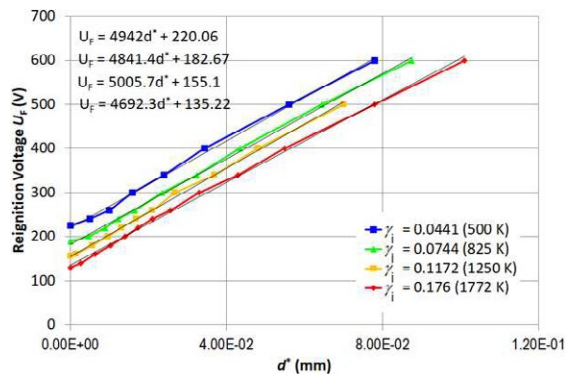


Fig. 9 Recovery Voltage U_F as a Function of Cathode Temperature T_C and of Sheath Thickness d

They show a so-called Paschen Minimum, a nearly linear rise to the right, and a strong increase with infinite values to the left. Those are physical nonsense, because there is always a path where the

minimum breakdown voltage is active. There are two practical ways to get around this problem. The first is to shift the thickness scale to d^* as shown in Fig. 8, the second to restrict all U_F values below the temperature-dependent minimum. This is, however, irrelevant because the Paschen Minimum is already reached after $> 1 \mu s$ cooling time, and there is not much difference between d and d^* . In Fig. 9 the correlation used in the simulations is depicted. It can be described by the equation

$$\frac{U_F}{V} = 2420 \cdot \left(\frac{T_C}{K}\right)^{-0.385} \quad (8)$$

4.2 Arc Position in Contact Center

Fig. 10 shows the simulated temperatures in the arc root center for different arcing times t_v and an additional free cooling time of 500 μs . The round dots mark the moments of current zero. For longer t_v (> 2.5 ms) they are nearly constant ≈ 1800 K, below they fall to ≈ 800 K.

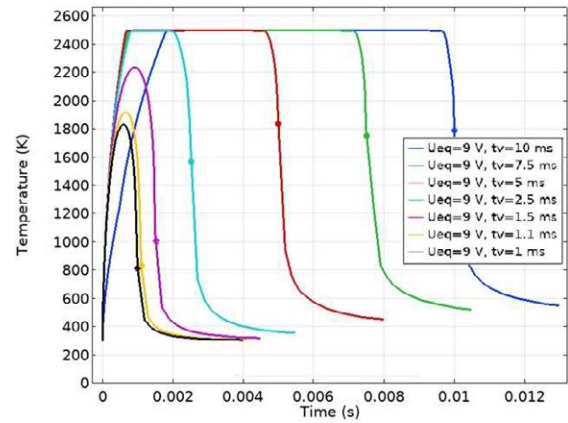
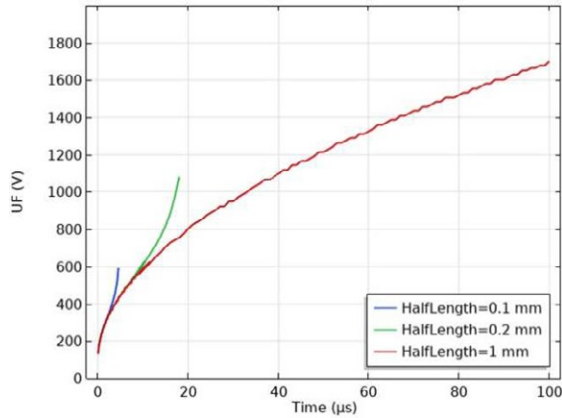


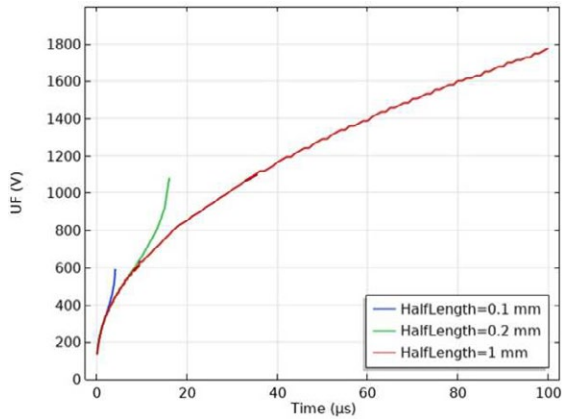
Fig. 10 Temperatures in the Arc Root Center; Current $I_{RMS} = 150$ A

During free cooling the sheath thickness in the arc spot area grows rather homogeneously, with the limit T_{Limit} parallel to the contact surface, see also Fig. 13 at $t = 5 \mu s$, position d1. In Fig. 11 the resulting recovery voltages U_F are plotted for different half lengths $L/2$, and for both $t_v = 10$ ms and $t_v = 1$ ms. First, we see that there is no influence of t_v . because the temperature difference at t_v (Fig. 10) does not influence the evolution of sheath thickness much.

We first look at $L/2 = 1$ mm. U_F starts with somewhat below 200 V at $t = 0$ (“Immediate Recovery Voltage”), to rise degressively with time. All $L/2 > 1$ mm are identical with 1 mm. For $L/2$ below 1 mm, however, U_F deviates from this evolution. Rising starts earlier and runs steeper for lower arc length and contact distance, respectively. This is in perfect agreement with old results [4-6], and is explicable by better cooling to the counter contact.



a)



b)

Fig. 11 Recovery voltage U_F as a Function of Cooling Time after Current Zero. $I_{RMS} = 150$ A
a) $t_v = 10$ ms, b) $t_v = 1$ ms

Fig. 12 shows the effect of the RMS current over a wide range on U_F . There is nearly no influence, because the spot surface temperatures, due to the realistic erosion model, are nearly identical, and so are the minimum sheath thicknesses.

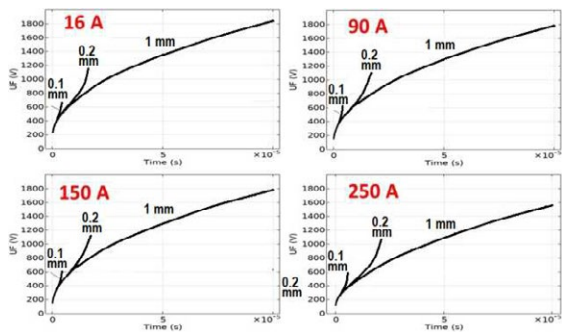


Fig. 12 Effect of RMS Current on the Recovery Voltages U_F ; Parameters $L/2$

4.3 Arc on Contact Edges

Rather independent of the shape of the arc spots and the current density there, the temperatures in the hottest points, the circle centers, are nearly identical to those of **Fig. 10**. The difference lies in the evolution of the minimum sheath thickness d .

Fig. 13 shows the growth of this thickness at two different times after current zero. In the parallel area between the contacts the growth happens with a nearly constant thickness d_1 , while the thickness d_2 at the edge is always smaller. The breakdown always happens at the edge, and is determined by $d = d_2$.

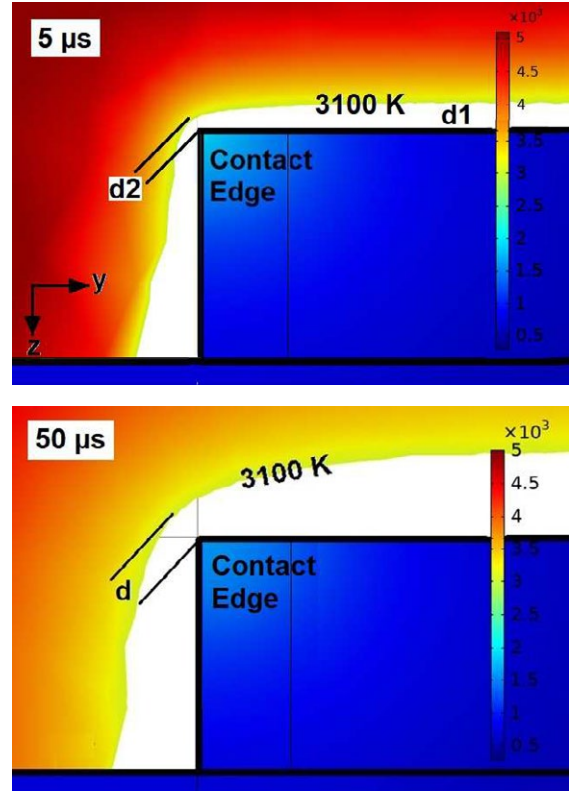


Fig. 13 Example of Growth of Sheath Thickness d around a Contact Edge
Arc Spot (M), $I_{RMS} = 150$ A, $t_v = 10$ ms, $L/2 = 1$ mm

In **Fig. 14** the recovery voltages U_F are drawn for the arc position (M), again with $L/2$ as parameters. There is a clear influence of L in that U_F is higher for shorter arcs, but different from the central arc position (C), **Figs 11, 12**, there is no length-dependent deviation from an initially common course.

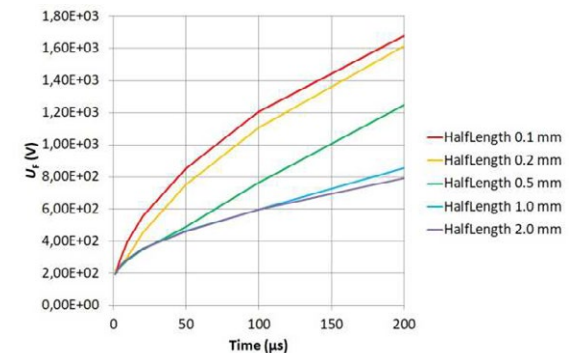


Fig 14 Recovery Voltage U_F as a Function of Cooling Time after Current Zero. $I_{RMS} = 150$ A, $t_v = 10$ ms, Parameter $L/2$.

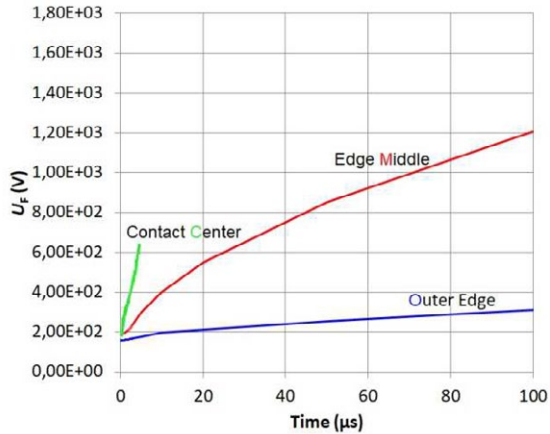


Fig. 15 Recovery Voltage U_F for Different Arc Positions. $I_{RMS} = 150$ A, $t_v = 10$ ms, $L/2 = 0.1$ mm

The last simulation result is a comparison of recovery voltages U_F for the three different arc root positions, **Fig. 15**. At $t = 0$ they all start at a similar immediate recovery voltage. Then there is a very clear sequence in faster rise from (O) as the worst, via (M) to (C) as the best case. The cooling and the expansion of sheath thickness off the cathode is best when the cooling arc root is a plane, see also **Fig. 13**. This is the case when the arc exists in the contact center (C).

5 Experimental Setup

In addition to the simulation work, switching tests were carried out with the aim to determine the recovery voltage as a function of recovery time. The principle is to measure the breakdown voltage for different frequencies of the Transient Recovery Voltage TRV. This approach was also used by Schmelzle [8]. The TRV frequencies directly correlate to the steepness dU of the TRV. Therefore, different time instants of the air gap's recovery voltage can be investigated through frequency adjustment.

Fig 16 shows the 3-phase control unit used for tests. The control unit accommodates 3 switching elements. Through a microcontroller unit MCU the switching elements can be controlled individually. Additionally, the arc time of the switching elements can be controlled. Per actual test only one switching element opened with arc, and the other two remained closed. Therefore, the one that opened was tested. The thyristor of the test facility finally turned off the 3-phase current once the recovery voltage of the switching element under test was measured. The switching elements were replaced once all three were tested.

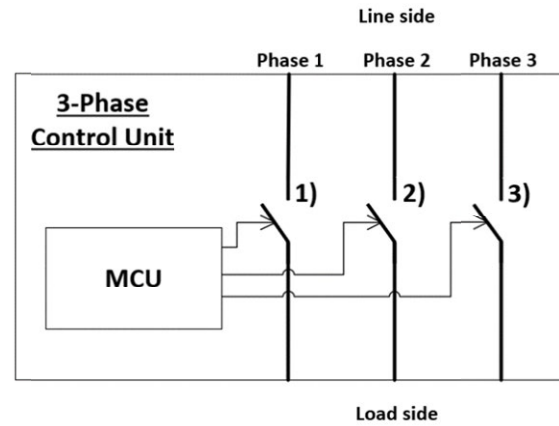


Fig. 16 3-Phase Control Unit

The switching elements were single break designs with 1 pair of $AgSnO_2$ contacts. The exact contact material composition is unknown. The shape is squared with 3×3 mm length and a height of 0.8 mm. The air gap between the contacts is 0.8 mm in fully open state. Additionally, samples with 0.35 mm gap were tested. High speed movies showed an opening speed of 1 mm / ms. The movable contact becomes fully stable after 4.5 ms from first contact opening instant. Therefore, for arc times ≥ 5 ms the contacts are fully opened and settled.

Table 1 shows the test ratings. The overshoot factor of the TRV was 1.6 for all the tests. The TRV frequencies however are different for 90A and 16A test current. Limited adjustability for 16A was possible since the load itself was already significantly damped.

The voltage peak of the TRV is roughly 1.3 kV which is the measuring range of the test set-up. For 90 A two switching elements were tested and 20 cycles per switching element and TRV frequency were performed. For 16A three switching elements were tested, and the cycle number per test was increased to 50. The break time between switching cycles was 30 s.

Test voltage:	768V RMS
Power factor:	0.40 – 0.45
TRV overshoot factor:	1.6

RMS Test currents and respective TRV frequencies

90A:	10, 20, 30 kHz
16A:	10, 13 kHz

Table 1 Test Ratings

Fig. 17 shows the test circuit which is in line with the low-voltage switchgear standard IEC 60947-1 (common part). The switching elements are shown as SE1...3. The load consists of the resistor $R_{L1...3}$ and the series air core inductors $X_{L1...3}$. In parallel to the load impedance are the damping resistors $R_{D1...3}$

and capacitors $C_{D1...3}$. These allow to adjust the overshoot and frequency of the TRV. The calibration procedure was also according to IEC 60947-1 except that the TRV frequency and overshoot values were according to **Table 1**. A calibration generator G was used and connected at the points CON1...3. These connections were removed after the TRV was adjusted. The currents $A1...3$ and voltages across the contacts $V1...3$ were measured with a transient recorder with 10 MHz sampling rate.

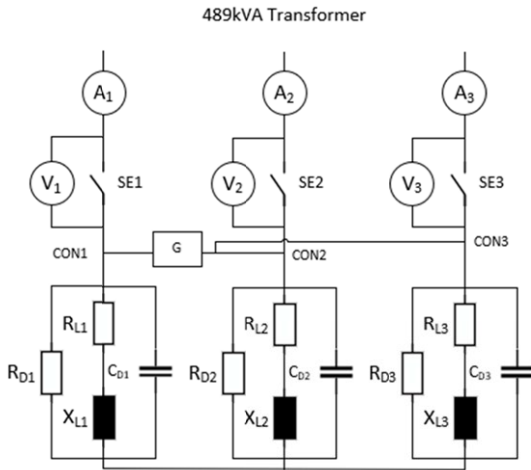


Fig. 17 Test Circuit

6 Results of Switching Tests

6.1 Breakdown detection

The breakdown voltage and recovery time were detected automatically with a script written in the TranAX (measurement software) formula editor. **Fig. 18** shows an example of a detection. U_{reg} is the recovery voltage and t_{reg} the time till breakdown.

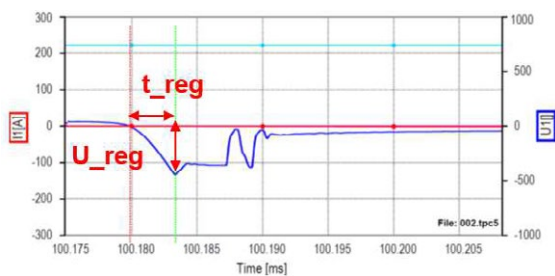


Fig. 18 Breakdown Example

6.2 Test results 90 A

Figs. 19 and 20 show the recovery voltages as a function of recovery time. The geometrical mean of each test frequency shows the recovery trend. For 9 ms arc time the recovery voltage starts with 350 V after 5 μ s and rises with 175 V / 10 μ s. For

5 ms arc time the recovery voltage starts with 410V after 5 μ s and rises with 205 V / 10 μ s (**Fig. 19**). A slightly better recovery was therefore observed for 5 ms compared to 9 ms.

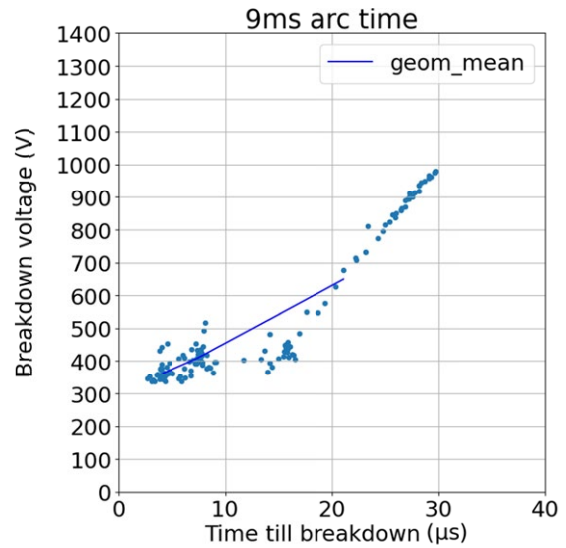


Fig. 19 Breakdown Voltage as a Function of Recovery Time for 9 ms Arc Time and 90 A Test Current

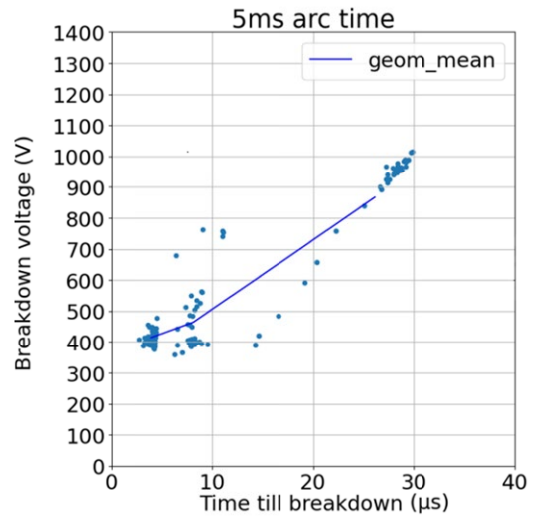


Fig. 20 Breakdown Voltage as a Function of Recovery Time for 5 ms Arc Time and 90 A Test Current

Fig. 21 shows the boxplot comparison of the tests with 0.8 mm air gap and 0.35 mm air gap. The results with 0.8 mm gap show more variation as the 1st and 3rd quartile indicate. The median of the 0.8 mm air gap is 350 V. The median of the reduced gap is at almost 500 V. The visual inspection of the samples showed that for 0.8 mm gap the arc spot was mainly at position (O) of **Fig. 6** whereas for 0.35 mm gap (M) and (O) were observed. Overall, the gap comparison supports the theory of increased recovery voltages for short gaps and arc spot in the contact center.

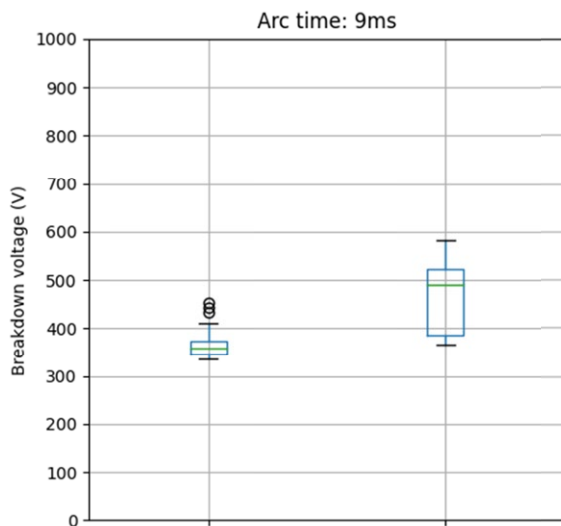


Fig. 21 Gap Comparison at 30 kHz TRV Frequency. Left 0.8 mm Air Gap, Right 0.35 mm Air Gap

6.3 Test Results 16 A

Fig. 22 shows the results for 16 A Test Current. After 12 μs most of the values lay around 1020 V (P1). After 23 μs the value center increases to 1100 V (P2). However significantly lower values with a range of 600 – 950 V (P3) were also observed. The arc spots of contact samples from region P1 / P2 and P3 were compared through a visual erosion check. As for the 16 A results, the comparison showed that samples which tended to region P3 had the arc spot at (O) whereas samples of region P1 and P2 tended to position (C) and (M). This observation is in line with the simulation results as well as the 90 A gap comparison results.

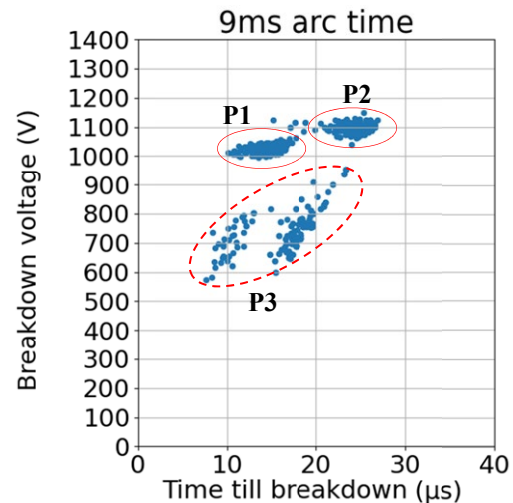


Fig. 22 Breakdown Voltage as a Function of Recovery Time for 9 ms Arc Time and 16 A Test Current

7 Summary and Conclusion

The 3D simulations of the recovery voltage U_F confirms the long-known effect of faster recovery after current zero for arcs with short contact distances in the sub-millimeter range. This is in agreement with the results from switching experiments. New findings, also confirmed by the experiments, are that the recovery of arcs with their roots standing on contact edges is inferior to that of arcs in the contact center. In addition to excess arc erosion, this is a second detrimental effect of arc roots sticking to contact edges. These theoretical findings are supported by the results of additional switching tests. The practical consequences for switching systems based on the mechanism of cathodic sheath recovery have been used for a long time: At least one ball-shaped contact to ensure arc ignition and existence in the center, and to avoid magnetic blow fields that might move the arc roots to the rim of the contacts.

8 Literature

- [1] Slepian, J.: Extinction of an A.C. Arc. Trans. AIEE (1928), pp 1398-1407.
- [2] Slepian, J.: Theory of the Deion Circuit Breaker. Trans. AIEE (1929), pp 523-527.
- [3] Timoshenko, G.: Die Lichtbogenwiederzündung als Durchschlag in stark ionisierten Gasen. Zeitschrift für Physik 84 (1933), pp 783-793.
- [4] Nöske, H.: Untersuchungen an kurzen Wechselstromlichtbögen in Luft. Zeitschrift für Angewandte Physik (1958), pp 327-336 and 382-393.
- [5] Berndt, H.: Über die Löschung des Wechselstromlichtbogens bei kleinen Trenngeschwindigkeiten der Kontaktstücke. Elektrie (1961), pp 124-128.
- [6] Burghardt, G.: Der Einfluss der wiederkehrenden Spannung auf das Löscherhalten kurzer Wechselstromlichtbögen in Niederspannungsprüfkreisen. PhD Thesis TH Hannover, 1963.
- [7] Weinzierl, G.: Die Temperatur von Lichtbogen-Entladungstrecken nach der Stromunterbrechung. Elektrie 19 (1965), pp 359-362 and 448-452.
- [8] Schmelzle, M.: Grenzen der Selbstlöschung kurzer Lichtbogenstrecken bei Wechselstrombelastung. PhD Thesis TU Braunschweig, 1968.
- [9] Tajev, I.S.: Theoretische Bestimmung der wiedererlangten Festigkeit eines Kontaktpaltes. Elektrische Kontakte, Verlag Energija, 1964.
- [10] Lindmayer, M., Sun, M.: Arc Stress and Erosion Losses of Contact Materials at Currents up to 1000 A. 16th Int. Conf. on Electrical Contacts, Loughborough/UK 1992.
- [11] Lindmayer, M.: Remarks Concerning Arc Roots in CFD Modeling of Switching Arcs. 30th Int. Conf. on Electrical Contacts, Rorschach/CH, 2020, postponed to 2021.
- [12] Lindmayer, M.: Simulation von Erwärmung, Abbrand und mechanischer Beanspruchung elektrischer Kontakte beim Schalten. 20. Fachtagung "Kontaktverhalten und Schalten" Karlsruhe 2009. VDE-Fachbericht 65, pp 147-153, VDE-Verlag Berlin 2009.
- [13] Murphy, T. (CSIRO): Data of Cu plasmas. Private communication between T. Murphy and J. Riss (2011).
- [14] COMSOL AB, Stockholm (2018). Introduction to COMSOL Multiphysics and Documentation within COMSOL 5.

Arc Re-striking Phenomena in Break Operations of AgSnO₂ Contacts in Inductive DC Load Conditions up to 20V-17A under External Magnetic Field

*Makoto Hasegawa and Seika Tokumitsu, Chitose Institute of Science and Technology, Chitose, Japan

*hasegawa@photon.chitose.ac.jp

Abstract

Arc re-striking phenomena of break arcs are sometimes observed with applied external magnetic field even at small or middle load levels. In this study, AgSnO₂ contacts were operated to break an inductive DC load circuit of 14V-7A, 14V-12A, 20V-7A, or 20V-17A with an applied external magnetic field of about $B=120\text{mT}$ at contact opening speeds of 1 to 200mm/s. Movements of break arcs were observed with a high-speed camera, while arc voltage/current waveforms were also obtained. Arc energy was later calculated based on the obtained voltage/current waveforms. Arc re-strikes were likely to be observed with larger load current levels and faster contact opening speeds. The number of arc re-strikes was sometimes two or more. Arc energy calculations revealed that the total arc energy from ignition to extinction reached almost the same level irrespective of re-striking incidents. Thus, occurrence of the arc re-striking phenomena during break operations of inductive DC load currents up to 20V-17A is believed to be influenced by the amount of energy to be supplied into a contact gap and to be consumed as arc energy. Even when arc is blown out of a contact gap due to an applied external magnetic field, arc re-strikes may occur and repeat until a certain amount of arc energy is finally consumed.

1 Introduction

Re-striking or re-ignition phenomena of break arcs are sometimes observed when breaking a load current with a mechanical switching device. In the authors' previous investigations [1-4] on switching of DC inductive loads with an AgSnO₂ contact pair under application of an external magnetic field, re-striking or re-ignition phenomena were sometimes observed, although the switching operations were done even in relatively light load conditions up to 20V-17A. In other words, re-striking or re-ignition phenomena of break arcs with an applied external magnetic field can be observed even at small or middle load levels.

Arc re-striking or re-ignition phenomena have been already studied and reported. However, such previous reports were in different load conditions and/or operating conditions from the authors' conditions.

With respect to the phenomena in AC switching, Hauer and Xin Zhou [5] studied arc re-ignition processes during standardized 10kA/600V single-phase short circuit interruption tests with Molded Case Circuit Breakers (MCCBs), and reported the two different re-ignition phenomena. The first category was "instantaneous re-ignition", in which an arc re-ignites immediately after the current-zero point and a short circuit current continues to flow in reverse polarity. The second category was "delayed re-ignition", in which arc re-ignition takes place with a certain time period after the current-zero point. Slade [6] described in detail about arc re-

striking phenomena in capacitor switching with vacuum interrupters. Slade and Tayler [7] further investigated influences of emission currents from a cathode contact on occasional late or delayed re-strike after capacitor switching with vacuum interrupters.

In addition, arc re-striking or re-ignition phenomena have been also reported in DC switchings under application of an external magnetic field.

For example, Xue Zhou et al. [8] reported arc re-ignitions in a bridge-type Cu contact pair when breaking a DC resistive 270V-200A, based on arc current measurements and arc image observations. They suggested that a uniform magnetic field with a proper density would reduce arc re-ignitions. Xue Zhou et al. [9] also reported occurrences of re-striking by multiple-arcs and re-ignition led by swirl motion of arcs, based on arc voltage measurements and arc image observations during breaking experiments of a DC resistive 50A at 280-730V with a bridge-type Cu contact. They further reported [10] arc re-striking phenomena in the breaking experiments of a DC resistive 50A at 300-800V with a bridge-type Mo30%-Cu70% alloy contact pair based on arc voltage measurements and arc image observations, indicating that the arc re-strike phenomena can be categorized into two types (i.e., a contact-contact type and an arc-contact type) based on observed arc voltage waveforms. Multi-arcs striking phenomena were also reported by Ono et al. [11-12] when breaking a DC resistive 10A current at up to 450V with an Ag contact pair, although they called the phenomena as re-ignition.

Irrespective of the above-mentioned previous studies, re-striking or re-ignition phenomena of break arcs with an applied external magnetic field in small or middle load regions have not been reported in detail. Their better understanding, for example on their occurrence conditions, will be advantageous for realizing better performances and reliabilities of mechanical relays. Thus, in this paper, arc re-striking or re-ignition phenomena to be observed in break operations of AgSnO_2 contacts in an inductive DC load circuit up to 20V-17A with an applied external magnetic field of about 120mT at contact opening speeds of 1mm/s to 200mm/s were studied in view of arc energy levels [13-14].

2 Experimental Conditions and Procedures

2.1 Experimental setup

The experimental setup in this study was the same as that in the authors' recent studies [1-4]. **Fig.1** shows pairs of AgSnO_2 contacts (Ag88%- SnO_2 12%, prepared by internal oxidation with no additives) used in this study. Both stationary (right in Fig.1) and movable (left in Fig.1) electrodes were of solid rivet-type with a head thickness of about 1mm and a head diameter of about 3mm. The head of the stationary electrode was attached onto a metal plate (18mm x 6mm), while the head of the movable electrode was attached onto a spring plate (also 18mm x 6mm) made of phosphor bronze.



Fig. 1 Stationary (right) and movable (left) electrodes in this study.



Fig. 2 Experimental setup in this study.

Fig.2 shows a photo of the experimental setup employed in this study.

The switching mechanism included a motorized stage driven by an AC servo motor. The motorized stage was placed onto a stable metal platform on which one electrode of a test contact pair was also fixed as a stationary

electrode via a certain attachment jig. Another electrode was mounted onto the motorized stage as a movable electrode. Switching operations of the contact pair were realized via movements of the motorized stage by controlling the AC servo motor through instructions from a PC program.

The inductive load circuit in this study included an inductive component of about 5.7 mH. It was not intended to realize any specific applications, but rather, it was intended to mitigate influences of unregulated inductive components in the circuit (e.g., stray inductance components due to wirings) by employing such an intentional inductive component. No specific control for the load current flow was employed during the switching operations, resulting in both break and make discharges. Among them, only break arc discharges were investigated in this study.

In order to externally apply a magnetic field, a piece of neodymium magnet (with 0.5 cm in height and 1.5 cm in diameter) was placed at about 0.5 cm away from the contact gap position. With such a placement, the resultant magnetic flux density at the contact gap was measured to be about 120 mT, although it was not able to confirm whether or not the magnetic flux density was uniform in the contact gap.

Table 1 summarizes the experimental conditions.

Table 1 Experimental conditions.

Contact material	Ag(88%)- SnO_2 (12%)
Load circuit	DC inductive (L=5.7mH) (time constant = 2 to 5 ms)
Load conditions	14V-7A, 14V-12A, 20V-7A, and 20V-17A
Ambient environment	laboratory air (no control)
Contact opening speed	1, 10, 50, 100, 200 mm/s
Final contact gap	about 2 mm
External magnetic field	about 120 mT @ contact gap

2.2 Measurement and observation procedures

Before the test, the surfaces of both electrodes of a test contact pair were polished with #1000 sandpaper and then wiped with methyl alcohol. Thereafter, the contact pair was mounted onto the switching mechanism with the movable electrode as an anode and the stationary electrode as a cathode. At the closed position, the movable anode electrode was slightly pushed backward by the mating stationary cathode electrode, thereby resulting in slight bending of the spring plate (an electrode assembly arm for the movable anode electrode) due to its elasticity. This may cause some

wiping between the electrode surfaces as is usual in commercial relays.

In each of the test conditions, four arc voltage waveforms across the separating contacts, as well as corresponding arc current waveforms, upon contact opening were recorded with a digital storage-scope (Yokogawa DL1620). Arc movement was also observed and recorded simultaneously with a high-speed camera (Photron FASTCAM MiniAX200). Recorded movies of the arc movements, as well as the arc voltage/current waveforms, were later analysed.

3 Experimental Results

3.1 Occurrence tendencies of arc re-striking phenomena

In the following descriptions, the term “re-strike” or “re-striking” will be used without any specific distinctions from the term “re-ignition”, different from the several other researchers’ previous references as mentioned in the above.

Whether arc re-strike was occurred or not was determined based on the measured arc voltage waveforms. **Fig.3(a)** shows exemplary arc voltage/current waveforms without any re-strikes, while **Fig.3(b)** and **Fig.3(c)** show the waveforms with one or several arc re-strikes. In each of these figures, the voltage waveform (the blue traces) finally became constant at the power supply level, while the current waveform (the orange traces) finally reaches zero. The black-colored vertical line at around the timing of rapid increase in the arc voltage waveform before the final extinction corresponds to the arc blown-out timing, as determined from the respective corresponding high-speed movies. It should be noted that due to limitation of the measurement range of the digital storage-scope employed, the arc voltage waveforms are flattened at about 80V in these figures.

From the waveforms as shown in Fig.3(a), in the case without re-striking phenomena, the arc current was likely to already be relatively small when the magnetic arc blown-out occurred. The arc current then rapidly decreased during the arc blown-out in a short period of time. On the other hand, with one or more arc re-strikes, the arc blown-out occurred when the arc current was still at relatively a high level, and thus decrease in the arc current during the arc blown-out was likely to take a longer period of time, as shown in Fig.3(b) and Fig.3(c).

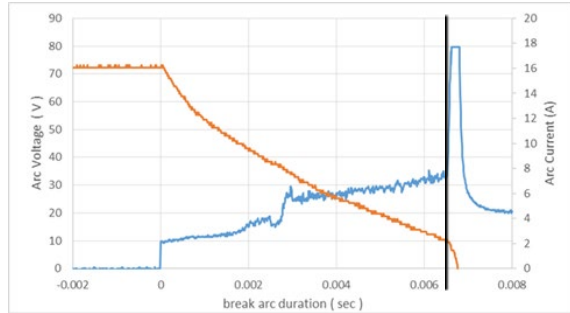
Although not perfectly confirmed, a full contact gap was not yet reached upon re-striking.

The observed results on occurrence tendencies of arc re-striking phenomena are summarized in **Table 2**.

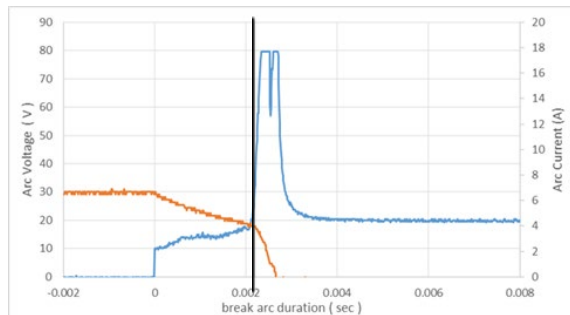
In this table, the mark “x” means that arc blown-out (and arc re-strikes) was not observed among the respec-

tive four observations. The number “0” means that although arc blown-out occurred, no arc re-strikes were observed among the four observations.

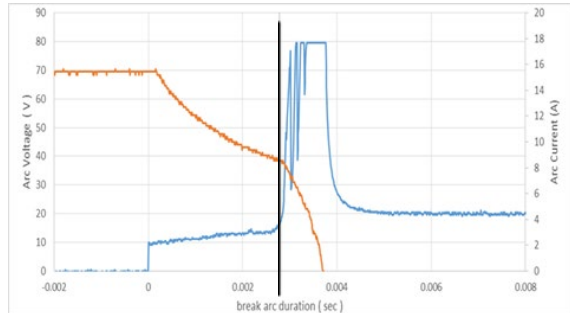
The other numbers indicate the averages of observed arc re-striking phenomena among the four observations. For example, in the 14V-7A@50mm/sec condition, the number “0.25” means that only one re-strike was observed among the four observations.



(a) without any arc re-strikes (20V-17A@50mm/s)



(b) with one arc re-strike (20V-7A@200mm/s)



(c) with several arc re-strikes (20V-17A@50mm/s)

Fig. 3 Exemplary observed arc voltage/current waveforms with/without arc re-striking phenomena.

Table 2 Occurrence tendencies of arc re-striking phenomena.

Contact opening speed	Load conditions			
	14V 7A	14V 12A	20V 7A	20V 17A
1mm/sec	x	x	x	0.25
10mm/sec	x	0.25	x	3
50mm/sec	0.25	2.75	0.25	2.25
100mm/sec	0.5	2.25	0	1.75
200mm/sec	0	2.5	0.25	2.5

These summarized results show that re-striking phenomena were likely to be observed with larger load current levels such as at 14V-12A and 20V-17A. Furthermore, in those conditions, multiple re-strikes were observed at faster contact opening speed levels. In the other two load conditions (14V-7A and 20V-7A), arc re-striking phenomena were likely to be observed only at faster contact opening speeds.

3.2 Arc energy comparisons between the cases with or without arc re-striking phenomena

Among the respective conditions indicated in Table 2, at least one arc re-strike was observed in each of every four observations in the following conditions:

- 14V-12A @ 50mm/s;
- 14V-12A @ 100mm/s;
- 14V-12A @ 200mm/s;
- 20V-17A @ 10mm/s; and
- 20V-17A @ 200mm/s.

On the other hand, in the following four conditions, both of the cases with/without arc re-striking phenomena were observed among the respective four observations:

- 20V-7A @ 200mm/s;
- 20V-17A @ 1mm/s;
- 20V-17A @ 50mm/s; and
- 20V-17A @ 100mm/s.

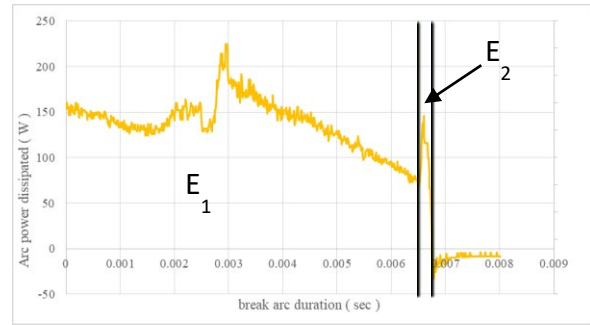
Thus, these four conditions were picked up for the purpose of make comparisons between the cases with or without arc re-strikes. The observed results of arc re-striking phenomena are summarized in **Table 3**.

Table 3 The number of observed arc re-strikes.

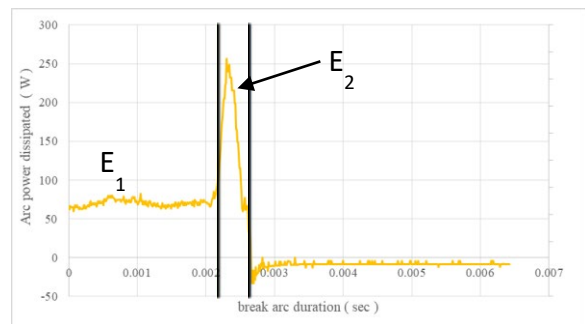
	Operating conditions															
	20V-7A 200mm/sec				20V-17A 1mm/sec				20V-17A 50mm/sec				20V-17A 100mm/sec			
	1	2	3	4	1	2	3	4	1	2	3	4	1	2	3	4
Re-strike (yes: O no: X)	O	X	X	X	X	X	X	O	O	X	O	O	X	O	O	O
Number of re-strikes	1	/	/	/	/	/	/	1	2	/	4	3	/	4	1	2

Based on the measured arc voltage/current waveforms as shown in Fig.3, arc energy (in other words, power dissipated) was calculated as the product of the arc voltage and the arc current. The thus-obtained exemplary arc energy waveforms are shown in **Fig.4(a)** and **Fig.4(b)**, respectively. In both of these figures, the vertical line at around the timing of rapid increase before the final extinction indicates the arc blown-out timing corresponding to the black-colored vertical line in Fig.3. Furthermore, another vertical line corresponds to the arc extinction timing also determined from the respective corresponding high-speed movies.

In the calculated arc energy waveforms as shown in Fig.4, an arc energy value (E1), which corresponds to the section from the initial arc ignition to the magnetic blown-out timing, and an arc energy value (E2), which corresponds to the section from the magnetic blown-out timing to the final arc extinction, were respectively obtained. In other words, the value E2 corresponds to the arc energy during the magnetic arc blown-out period, and energy during arc re-striking phenomena is included in the arc energy value E2.



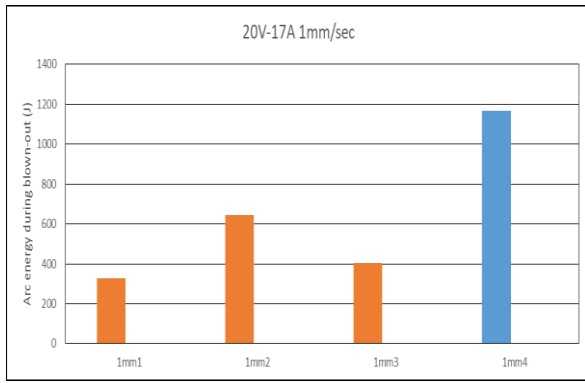
(a) without any arc re-strikes (20V-17A@50mm/s) (corresponding to Fig.3(a))



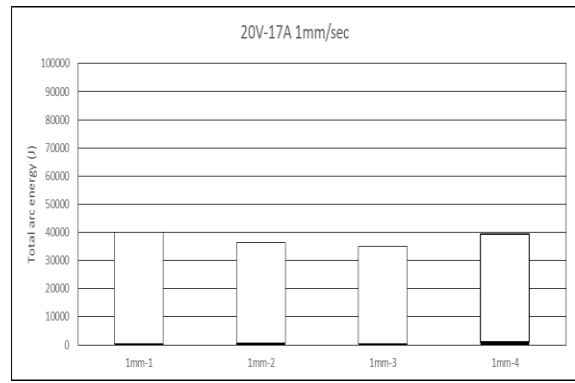
(b) with arc re-strikes (20V-7A@200mm/s) (corresponding to Fig.3(b))

Fig. 4 Exemplary arc energy waveforms with/without arc re-strikes.

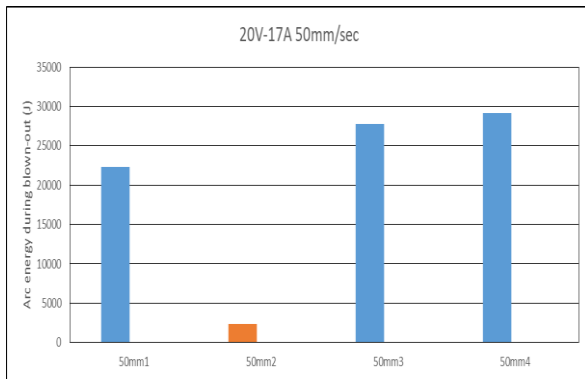
Fig.5 shows the values E2 in the magnetic arc blown-out period in the respective four observations for each of the four operating conditions indicated in Table 3. In **Fig.5(a)** and **Fig.5(b)** which correspond to the cases with the relatively slow opening speed levels of 1mm/s or 50mm/s, large differences in the energy vales E2 during the magnetic arc blown-out period can be recognized among with or without arc re-striking phenomena. In contrast, however, in **Fig.5(c)** and **Fig.5(d)** which correspond to the cases with the relatively faster opening speed level of 100mm/s or 200mm/s, the energy values E2 during the magnetic arc blown-out period reached almost the same level irrespective of whether or not arc re-striking phenomena occurred.



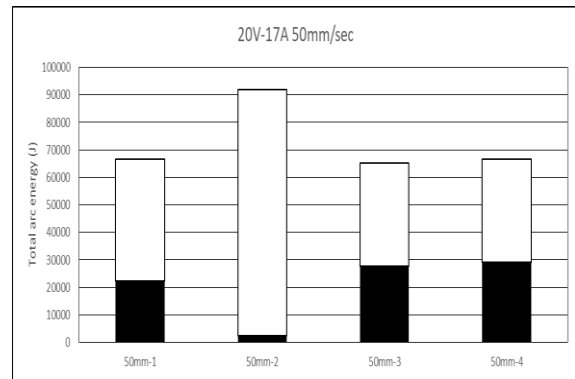
(a) 20V-17A@1mm/s



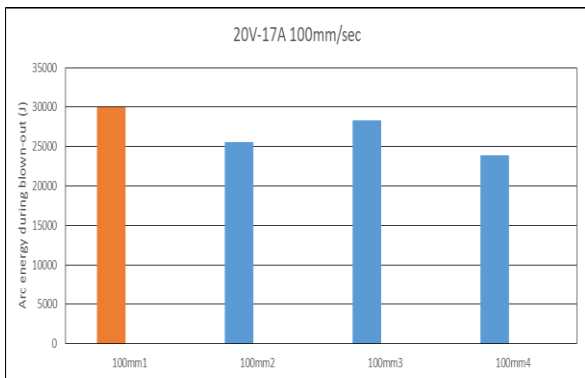
(a) 20V-17A@1mm/s



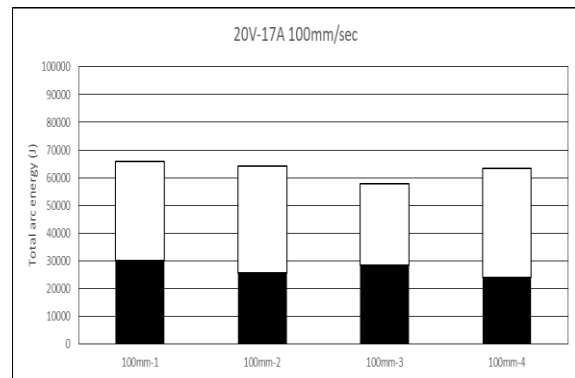
(b) 20V-17A@50mm/s



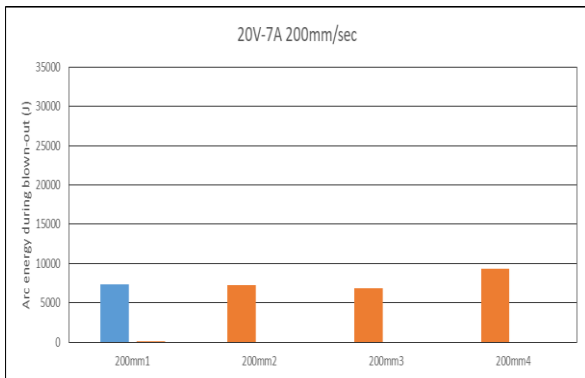
(b) 20V-17A@50mm/s



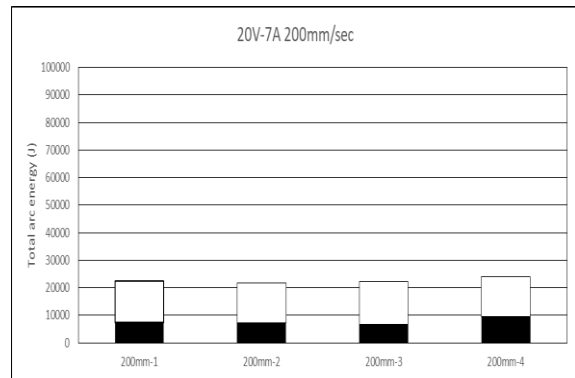
(c) 20V-17A@100mm/s



(c) 20V-17A@100mm/s



(d) 20V-7A@200mm/s



(d) 20V-7A@200mm/s

Fig. 5 Comparisons of the arc energy values E_2 during the magnetic arc blown-out period. (Blue-colored bars correspond to the cases with re-striking, while orange-colored bars correspond to the cases without re-striking.)

Fig. 6 Comparisons of the total arc energy values (E_1+E_2) from the initial arc ignition to the final arc extinction with/without arc re-striking phenomena. (White-colored bar portions correspond to E_1 values and black-colored bar portions correspond to E_2 values, respectively)

Fig.6 shows total arc energy values in the respective four observations for each of these four operating conditions.

The total arc energy for each of the four observations reaches almost the same level in each of these operating conditions, irrespective of whether or not arc re-strike was observed, and irrespective of the number of actually observed arc re-strikes. In other words, even if arc is blown out of a contact gap due to an external magnetic field, arc would not completely disappear until the supplied energy is finally consumed with one or more re-striking incidents.

4 Discussions

Referring again here to Fig.5(a) and Fig.5(b) where in the cases without any arc re-strikes, the arc energy values (E2) consumed during the magnetic arc blown-out period were smaller than those in the cases with arc re-strikes. In such cases, Fig.6(a) and Fig.6(b) show that relatively large arc energy was consumed (as E1) in the period from the initial arc ignition to the magnetic arc blown-out timing. As a result, the total arc energy (E1+E2) shown in Fig.6(a) and Fig.6(b) reached almost the same level among the respective four observations in each of these two conditions, irrespective of occurrences of arc re-strikes.

Therefore, with slower contact opening speeds, it will be possible to say that even if the magnetic arc blown-out occurs earlier, one or several arc re-strikes will occur so as to consume the remaining energy.

It should be noted that in Fig.6(b), the total arc energy in the second observation (corresponding to the case without any arc re-strikes) exhibited relatively a large amount. For this specific case, a time period from the initial arc ignition to the magnetic arc blown-out timing was relatively long, resulting in the arc energy E1 to be consumed in this period becoming larger, resulting in a larger total arc energy level.

Referring further to Fig.5(c) and Fig.5(d), the energy values E2 consumed during the magnetic arc blown-out period reached almost the same level irrespective of whether or not arc re-striking phenomena occurred. Even in such cases, the total arc energy (E1+E2) shown in Fig.6(c) and Fig.6(d) reached almost the same level among the respective four observations in each of these two conditions, irrespective of occurrences of arc re-strikes.

Thus, from the results obtained in this study, it may be possible to say that at least in the operating conditions investigated in this paper, even when a break arc is magnetically blown out, the arc will not completely extinguish until the energy supplied into the contact gap is finally consumed while experiencing one or more re-striking phenomena. Consumption of the supplied energy at the contact gap can be one of possible factors influencing occurrence of arc re-strikes.

5 Conclusions

Switching operations with AgSnO₂ contacts in an inductive DC load circuit of 14V-7A, 14V-12A, 20V-7A, or 20V-17A with an applied external magnetic field of about 120mT at contact opening speeds of 1mm/s to 200mm/s were conducted, and break arc phenomena were studied.

(1) Arc re-striking phenomena were likely to be observed with larger load current levels and faster contact opening speeds. The number of arc re-strikes was some-times two or more, especially when a load current value was larger and a contact opening speed was faster.

(2) Arc energy was calculated from the measured arc voltage and current waveforms. The thus calculated results of arc energy revealed that the total arc energy from ignition to extinction reached almost the same level irrespective of arc re-striking incidents.

(3) Thus, occurrences of arc re-striking phenomena in break operations of inductive DC loads up to 20V-17A are influenced by the amount of energy that is supplied into and to be consumed at a contact gap. Even when arc is blown out of a contact gap due to an external magnetic field, arc re-strikes may occur and sometimes repeat until the supplied energy is finally consumed.

Relationships between re-striking phenomena and contact performances such as total break arc durations are not yet made clear. It is also not yet made clear whether or not the first re-striking incident occurs at the same current level. Further investigations will be required, for example, with different levels of an external magnetic field and/or in different load conditions, in order to realize further understandings of arc re-striking phenomena.

6 Acknowledgment

The authors thank Tanaka Kikinzoku Kogyo Co., Ltd. for supplying contact samples used in this study. The authors also thank Photron Ltd. for their courtesy of letting us use their high-speed camera for this study.

7 Literature

- [1] M. Hasegawa and S. Tokumitsu, "Break arc duration characteristics of AgSnO₂ contacts under magnetic field application with contact opening speeds in the range up to 200mm/s in DC load conditions", Proc. 62nd IEEE Holm Conf. on Electrical Contacts (Holm2016), pp.119-124, Oct. 2016.

- [2] S. Tokumitsu and M. Hasegawa, "Effective shortening of break arc durations of Ag and several Ag-based contacts in DC load conditions with increased contact opening speeds and external magnetic field", Proc. 29th Intl. Conf. on Electrical Contacts (ICEC2018) and 64th IEEE Holm Conf. on Electrical Contacts (Holm2018), pp.87-94, Oct. 2018.
- [3] S. Tokumitsu and M. Hasegawa, "Relationships between break arc behaviors of AgSnO₂ contacts and Lorentz force to be applied by an external magnetic force in a DC inductive load circuit up to 20V-17A", IEICE Trans. Electronics, Vol.E102-C, No.9, pp.641-645, Sept. 2019.
- [4] S. Tokumitsu and M. Hasegawa, "Arc movement investigations of break arcs of AgSnO₂ contacts under applied external magnetic field in inductive DC load conditions", Proc. 65th IEEE Holm Conf. on Electrical Contacts (Holm2019), pp.95-100, Sept. 2019.
- [5] W. Hauer and Xin Zhou, "Re-ignition and post arc current phenomena in low voltage circuit breaker", Proc. 27th Intl. Conf. on Electrical Contacts (ICEC2014), pp.398-403, June 2014.
- [6] P. G. Slade, "The vacuum interrupter: Theory, Design, and Application" CRC Press, pp.363-372, 2008.
- [7] P. G. Slade and E. D. Taylor, "Emission currents and late restrikes after switching capacitors using vacuum interrupters", Proc. 29th Intl. Conf. on Electrical Contacts (ICEC2018) and 64th IEEE Holm Conf. on Electrical Contacts (Holm2018), pp.229-234, Oct. 2018.
- [8] Xue Zhou, Xinglei Cui and Guofu Zhai, "Study on arc behaviors at opening a 270 V resistive circuit by bridge-type contacts under magnetic field", IEICE Trans. Electron., vol.E96-C, no.9, pp.1124-1131, Sept. 2013.
- [9] Xue Zhou, Xinglei Cui, Mo Chen and Guofu Zhai, "Experimental study on arc behaviors of a bridge-type contact when opening a resistive load in the range of from 280 VDC to 730 VDC", Proc. 60th IEEE Holm Conf. on Electrical Contacts (Holm2014), pp.341-347, Oct. 2014.
- [10] Xinglei Cui, Xue Zhou, Mo Chen, Kai Bo and Xi-yuan Peng, "Experimental research on re-strike phenomenon occurring during high-voltage direct-current breaking process under transverse magnetic field", Proc. 61st IEEE Holm Conf. on Electrical Contacts (Holm2015), pp.187-190, Oct. 2015.
- [11] H. Ono, J. Sekikawa and T. Kubono, "Arc duration of break arcs magnetically blown-out in a DC 450 V resistive circuit", IEICE Trans. Electron., vol.E95-C, no.9, pp.1515-1521, Sept. 2012.
- [12] H. Ono and J. Sekikawa, "Arc length of break arcs magnetically blown-out at arc extinction in a DC450V/10A resistive circuit", IEICE Trans. Electron., vol.E96-C, no.9, pp.1132-1137, Sept. 2013.
- [13] S. Tokumitsu and M. Hasegawa, "Arc energy calculation during re-striking phenomena in break operations of AgSnO₂ contacts in inductive DC load conditions up to 20V-17A with different contact opening speeds", Proc. 7th Intl. Conf. on Reliability of Electrical Products and Electrical Contacts (ICREPEC2019), pp.18-22, Nov. 2019.
- [14] S. Tokumitsu and M. Hasegawa, "Arc movement observation of DC inductive break arcs of AgSnO₂ contacts up to 20V-17A under external magnetic field application", IEICE Technical Report, EMD2019-47, Dec. 2019 (in Japanese language).

Effects of arc during mechanical bounces on contact material for different power supply frequencies

Asma Ramzi, Université de Rennes1, SAFRAN Group, Rennes, France, asma.ramzi@univ-rennes1.fr
Erwann Carvou, Université de Rennes 1, Rennes, Institut de Physique de Rennes, UMR CNRS 6251 France, erwann.carvou@univ-rennes1.fr
Alexis.Schach, SAFRAN Group, Montreuil, France, alexis.schach@safrangroup.com

Abstract

During a make operation in an electromechanical switching device, an electrical arc could occur because of mechanical bounces and can cause serious damages, such as contact welding and electrodes erosion. The characteristics of this arc are influenced by several parameters such as the level of voltage and current, the load of circuit, the nature of contact materials and, a parameter that we will focus on, the voltage frequency.

Indeed, for frequencies equal or greater than 50 Hz, the current can go through zero several times during typical mechanical bounce. The energy transferred to the electrodes, which will condition the welding, depends on the total arc duration, and so on the reignition of the arc.

In order to investigate this phenomenon, the contacts welding in relation with the re-ignition of arc have then been studied for different frequencies. The make tests were done for 115 Vrms/750 Arms with a mechanical bounce of 2 ms, with different frequencies 50 Hz/ 400 Hz/ 500 Hz and with AgSnO₂ contact material and silver contacts as reference. The welding characteristics, such as welding occurrence and force were measured as a function of arc characteristics (voltage/current/energy).

Finally, this investigation showed the importance of the voltage frequency on contactors reliability.

1 Introduction

Switching devices like contactors play an important role in an electrical network. In the area of aeronautics, an ongoing evolution of electrical network is taking place to improve the performance of the vehicles. Therefore, the number of electrical contactors has increased. Consequently, from a statistical point of view, it could cause more deficiencies such as overheating and contact welding.

Welding phenomenon is one of the most important issues which could take place at the contacts closure [1], [2]. It could damage the switch and consequently influence the safety and driveability of the vehicle. Therefore, for a better understanding of this phenomenon, it was the subject of multiple studies [3–8] in which the authors tried to show the influence of different parameters on it such as arc energy, material nature and contact force.

In the present study, contact-welding and their characteristics have been studied in different power supply frequencies, 50 Hz, 400 Hz and 500 Hz, as well as the bounce arc characteristics. AgSnO₂ contacts have been used for this study. They are well known by their anti-welding aspect [2], [8–10]. Pure Silver contacts have been used as a reference.

The electrical current, the contact material nature, the kinematic of the contact, are well known to have significant effect on welding characteristics [1], [2]. By having an effect on arc characteristics, voltage frequency, which influence arc duration may also have an influence on contact welding. The purpose of this work is to

determine how AC current may influence the welding phenomenon.

An approach of the problem indicates that high frequency would lead to short arcs [11] and consequently weak welding. Indeed, a short arc injects less thermal energy on the arc spot, thereby decreasing the amount of molten zone. However, this study showed that this approach is too simplistic.

2 Experimental part

2.1 Welding test bench

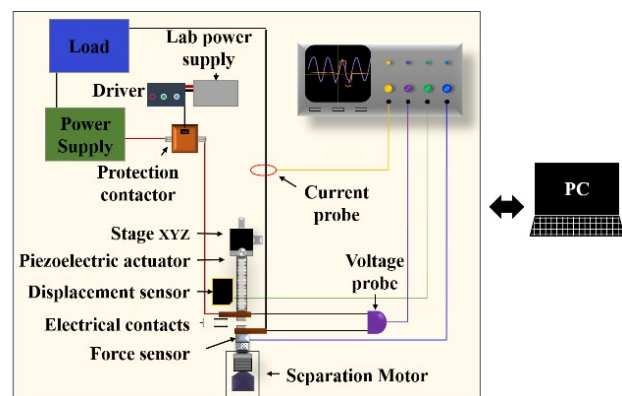


Fig.1 Scheme of the testing equipment for make tests

Based on the model of Morin et al [8], an experimental test bench has been designed to characterize the bounce arc and the contact welding (Figure 1).

In this test bench, a piezoelectric actuator, fixed on the anode, reproduces a controllable mechanical bounce during the electrodes closing, which helps to eliminate nearly the different softness and damping effect of the contact material.

The displacement motor applies a chosen contact force, which is adjusted thanks to the force sensor. This force sensor fixed on the cathode also measures the supplementary force required to separate the contacts in case of sticking, called welding force. The contacts are considered definitely stuck when the welding requires an effort superior to the pulling force of the displacement motor equal to 100 N.

The arc voltage and current are measured by probes. The laser displacement sensor is placed behind the piezoelectric actuator. It allows to check the profile of the bounce. These measuring instruments are connected to an oscilloscope. Figure 2 shows an example of acquired data by the oscilloscope. These data allow to determine the arc duration, the arc energy and the height of the bounce.

All the instrumentations allowing data acquisition (motor, power supply, oscilloscope, voltmeter, displacement sensor, force sensor) are connected by USB bus and controlled by a computer.

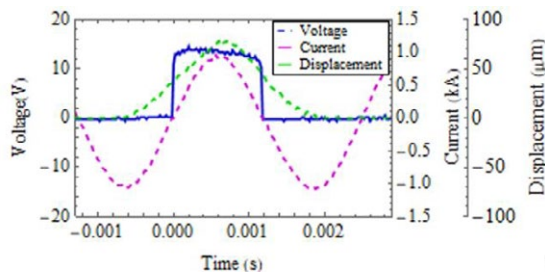


Fig. 2 Voltage and current of a bounce arc and the height of the bounce during a make test.

Table 1 shows the mechanical and electrical conditions of the tests.

Source voltage	115 Vrms
Current	750 Arms
Load type	Resistive
Contact force	6 N
Welding force lower limit	2 N
Atmosphere	Ambient air
Bounce height	80 µm
Bounce duration	2 ms
Number of Bounces	1
Motor pull capacity	100N

Table.1 Tests conditions for bounce arc

2.2 Samples Material

Silver-based contacts are the most frequently used on electrical switching devices. The addition of tin oxide

provides an anti-welding effect, by facilitating the welding fracture.

The samples used for these tests are tips with two types of materials: pure Silver and AgSnO₂ (10 wt.% SnO₂). The electrodes have curved surfaces with a radius of 300 mm. The diameter of those samples is 16 mm.

3 Results and discussion

3.1 Welding force vs voltage frequencies

Table 2 summarizes the results of welding phenomenon obtained from the make tests. It shows the maximum welding force, the welding occurrence rate, and the average welding force of Silver and AgSnO₂ samples for the test frequencies 50 Hz, 400 Hz and 500 Hz.

Frequency [Hz]	Sample Code	Contact Material	F _s max [N]	F _s mean [N]	Welding rate [%]
50	S50	Silver	>100	>100	100
	AS50	AgSnO ₂	76.8	13.5	91.7
400	S400	Silver	80	12.2	81.5
	AS400	AgSnO ₂	68	13.7	90
500	S500	Silver	83	17	90.5
	AS500	AgSnO ₂	78	15.39	92

Table.2 Contact welding characteristics

F_{s,max} corresponds to the strongest welding that the separation motor could break. When the contacts are definitely stuck (F_{s,max}>100), the number of tests stops.

For the test done with the frequency 50 Hz, the silver sample S50 has been stuck definitely since the first operation. On the other hand, for silver samples S400 and S500 a number of 450 and 240 cycles were carried out respectively.

Concerning AgSnO₂ samples, the definitive sticking has been reached after 400 cycles for AS50, 500 cycles for AS400 and 100 cycles for AS500. This shows that the service lifetime of the contacts is not related linearly to the voltage frequency.

Moreover, except for the case of the sample S50, the average welding forces of S500 and AS500 (500 Hz) are the highest besides the average welding forces of the rest of the samples.

Figure 3 highlights the visualisation of the welding force trending, and the maximum force for each period of Silver and AgSnO₂ contacts tested at different frequencies: 50 Hz, 400 Hz and 500 Hz.

For AgSnO₂ contacts (AS50, AS400 and AS500) the impact of ageing is considerably notable on the welding force, it increases according to the service time. Nevertheless, cases of strong welding over 60 N are exceptionally observed in the beginning of the contacts lifetime. Contrary to the silver contacts (S400 and S500), there is a fluctuation of welding force throughout all their lifetimes.

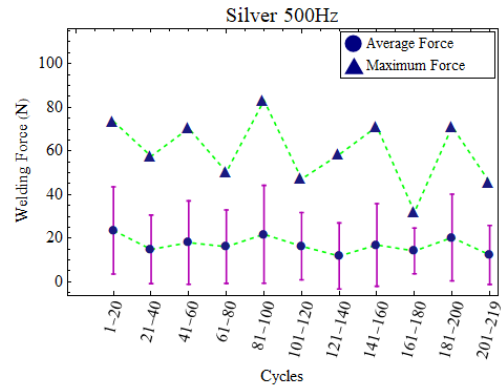
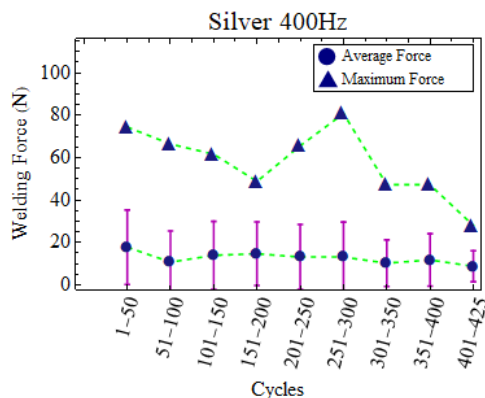
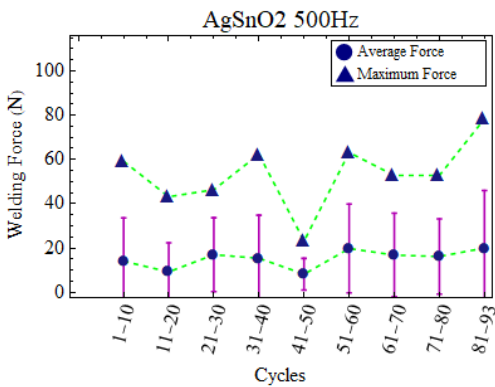
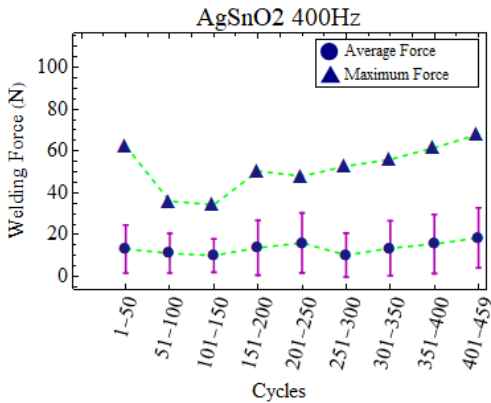
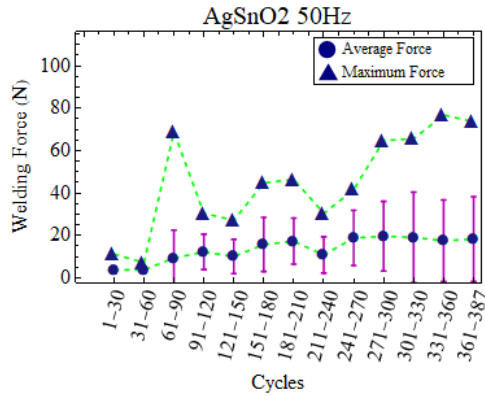
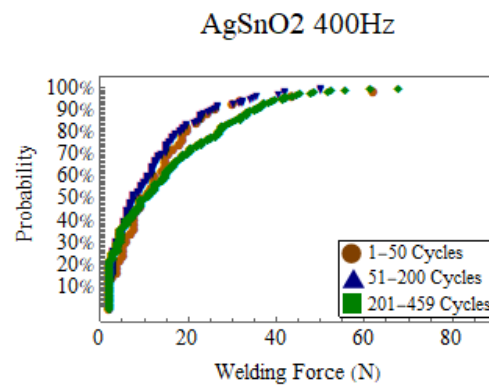
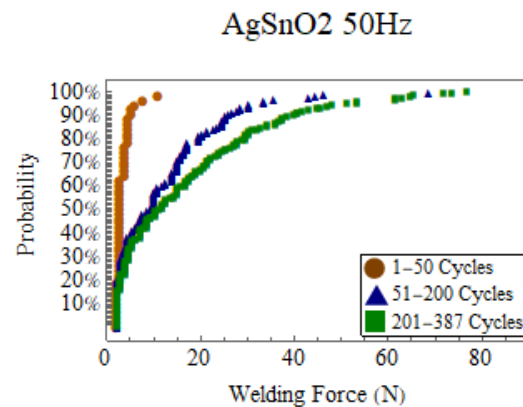


Fig. 3 Welding average force vs. test cycles

Furthermore, Figure 4 presents the cumulative distribution curves of welding force versus different lifetime periods (the beginning, the middle and the end). It shows that despite that contact ageing has a slight impact on the welding force, AgSnO₂ and silver samples have an opposed behaviour with time.

AgSnO₂ sample starts by the occurrence of small welding forces and ends by occurring high ones. In the other hand, it is observed that for the Silver samples during the first periods, the occurrence of high welding force is greater than the rest of the contacts lifetime.



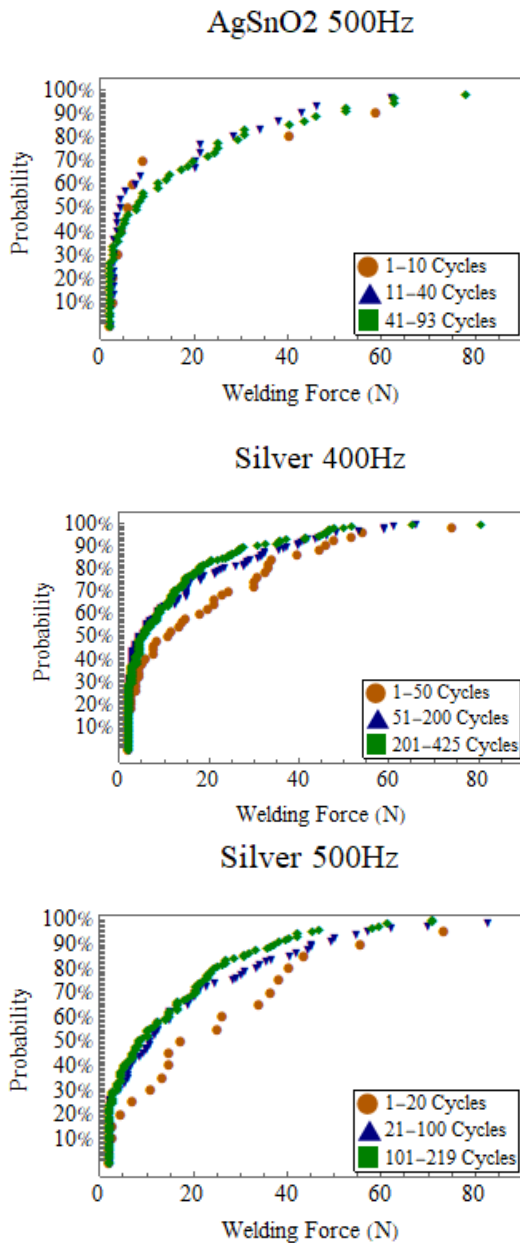


Fig. 4 Cumulative distribution of welding force for different lifetime periods

In order to understand this welding behaviour, the arc characteristics (duration and reignition) and the arc energy are presented in Figure 6-7 and 8 respectively.

3.2 Arc duration vs voltage frequencies

The bounce arc could stay ignited till the definitive contacts close, which means that the arc duration is equal or less than the bounce duration. Nonetheless, the definitive arc extinction could be conditioned by the voltage frequency.

In the literature, the arc ignition requests a power supply voltage greater than 12 volts and a current above 400 mA for Silver [2], [11]. Hence, the maximal arc duration is depending on the frequency. Therefore, under this approach, the arc duration could not be higher than the half-period of the voltage waveform. Figure 5 below

shows the maximum arc duration that could have occurred following this approach.

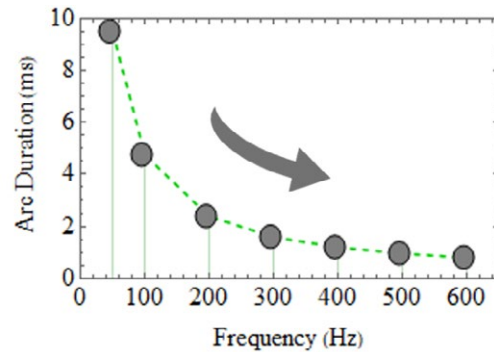
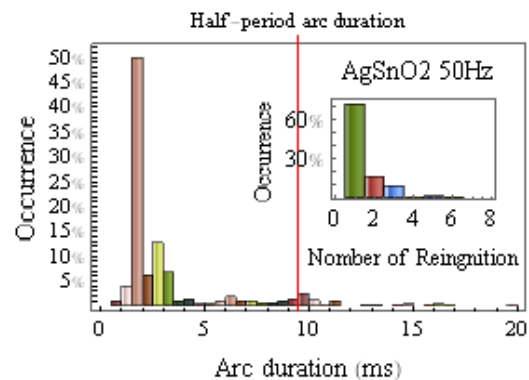


Fig. 5 Arc durations during a voltage half-period waveform vs. voltage frequency for 115 Vrms

Nevertheless, at all the tested frequencies, 50 Hz, 400 Hz and 500 Hz, the arc durations were measured and part of them exceeded the half-period duration of the voltage waveform of each frequency as shown in Figure 6. The occurrence of reignition is showed also in the same figure. As observed in these figures, the reignition number increases by increasing the voltage frequency. This explains the observed long arc durations for AS400 and AS500. This phenomenon takes place for the majority of tests. It could depend not only on the frequency of the current but also on the nature of contact materials and the condition of contact surface. Actually, the arc reignition may happen because of a residual plasma existing in the contact gap [12], this reignition causes a splashing of melted metal, which helps to increase the melted surface and consequently increase the welding occurrence. Figure 7 shows two examples of arc reignition for 50Hz and 500Hz and an example where the arc extinguishes after the first ignition.

Beyond the phenomenon of reignition, towards the end of tests, the contacts became very rough. This leads sometimes to a mechanical perturbation, which leads to create small bounces after the main applied one.



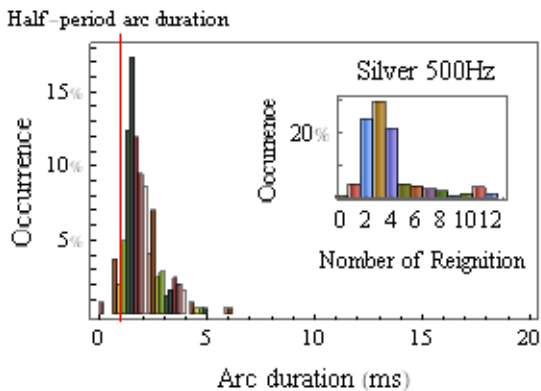
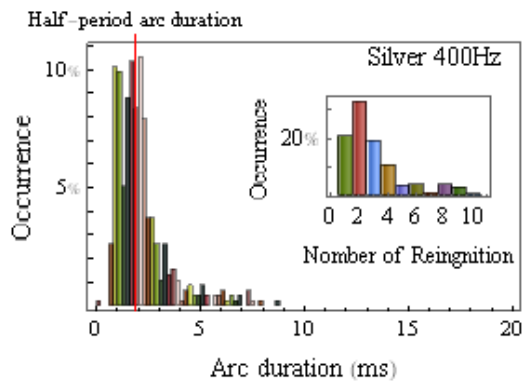
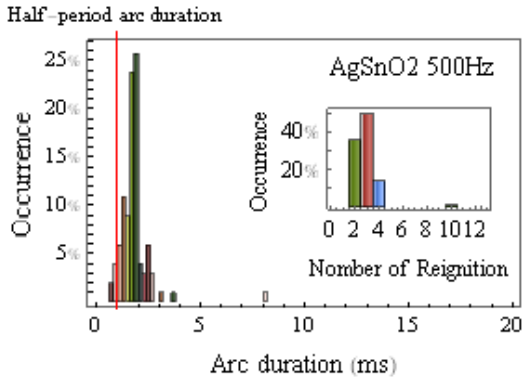
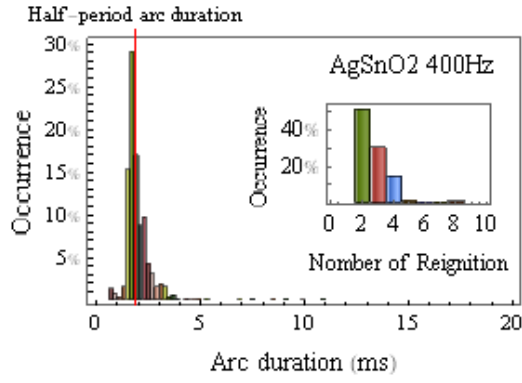


Fig. 6 Bounce arc duration occurrence vs. voltage frequency

The longer arc duration may also be caused by evaporated and molten contact material, this could be influenced by several factors such as the material structure and the pressure, but it is still a complex phenomenon requesting a precise investigation and understanding.

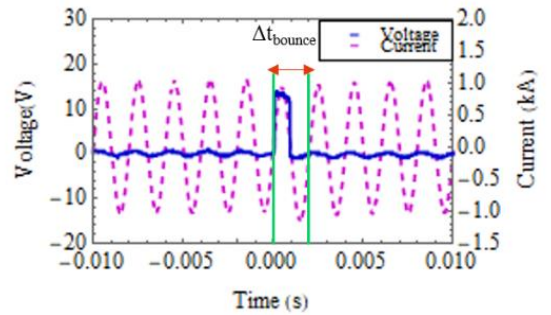
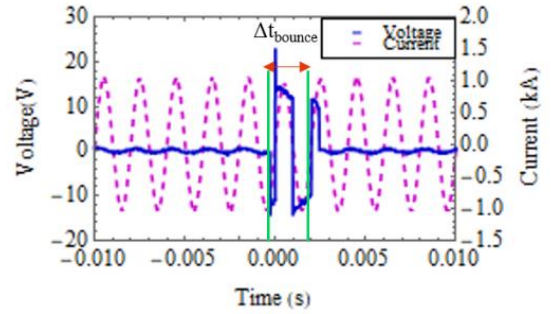
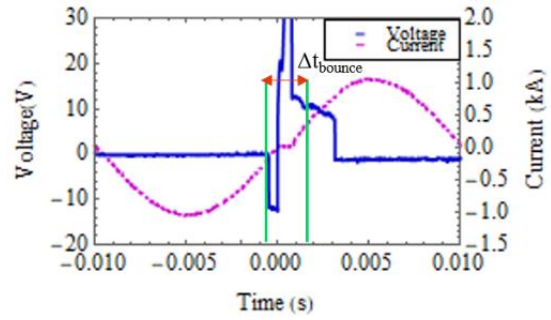


Fig. 7 a) & b) Example of reignition phenomenon at 50 Hz and 500 Hz respectively c) one ignition at 500 Hz

3.3 Bounce arc energy vs voltage frequencies

The arc energy W_{arc} has an important impact on the welding characteristics, the energy dissipated during arc time is [13] :

$$W_{arc} = \int_{\Delta t_{arc}} u i dt \quad (1)$$

u : the voltage across the contact gap

i : the current flowing through the contact

The bounce arc energies measured during the make tests are presented in Figure 8. The dependence of these energies with respect to the contact lifetime follow approximately the one of the welding force shown in Figure 3.

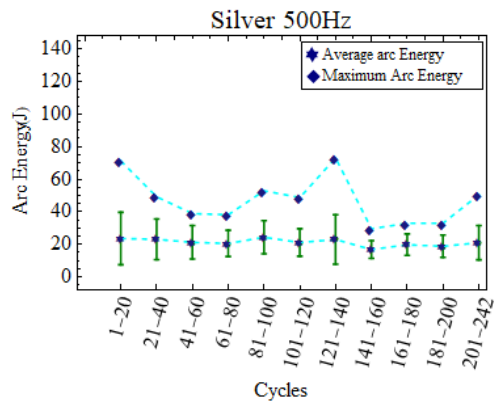
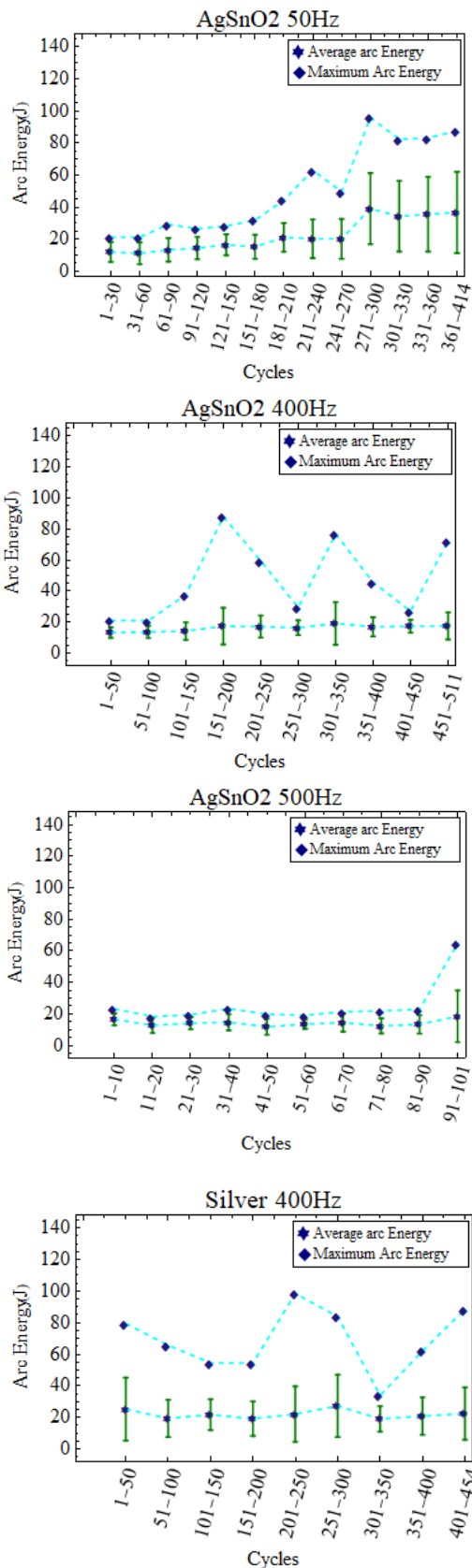


Fig. 8 Bounce arc energy vs. test cycles

The bounce arc energies are proportional to the arc duration, to the current level and the voltage level. In this case, the increasing of energies for AgSnO₂ samples especially in 50 Hz is explained by the damage of the contacts surfaces. This deformation increases the number of asperities, which provokes other arcs and implicitly increases the arc energy values (Figure 9). In addition, the high current (750 Arms) helps to maintain the arc longer and expand the arc duration.

3.4 Contact materials after the make test

After going through several arcing tests, a major change is observed on the contacts surfaces. Those damages are depending on the arc energy and the material nature as explained before.

Figure 9 shows the condition of those surfaces after the make tests

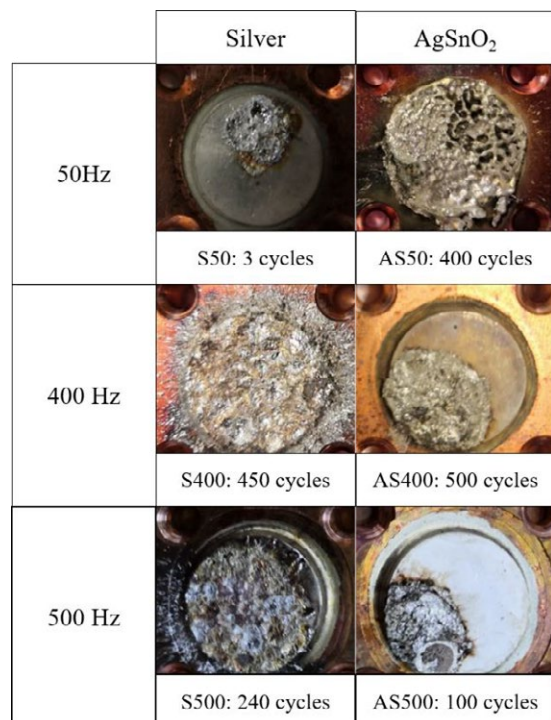
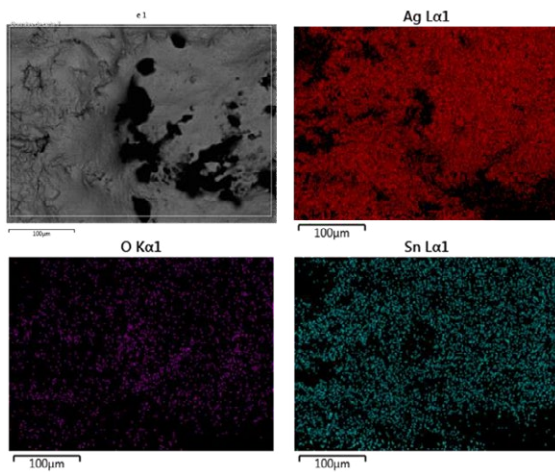


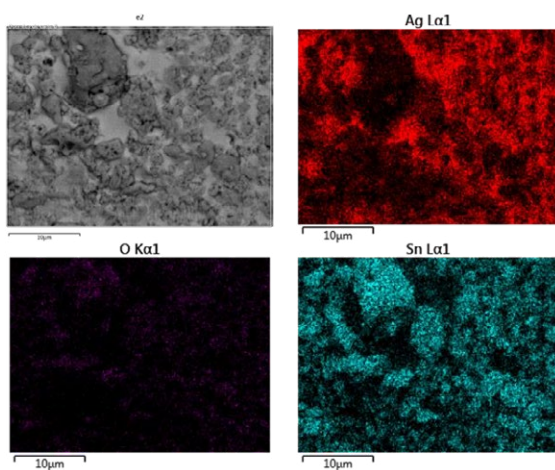
Fig. 9 Contacts surfaces after the make tests

The presence of pores on the surfaces of AgSnO_2 samples is referred to the presence of the metallic oxide on the contact material, they are created by gaseous bubbles of the metallic oxide in the silver matrix. This aspect is considered as an anti-welding mechanism [14]. The diameter of these pores varies between 1 mm and 10 μm . In addition to this, it is noticed that the arcs have reached all the surface of AgSnO_2 sample AS50 which is not the case for AgSnO_2 AS400 and AS500. Thus when the probability of arc occurrence increases on a small part of the sample, this leads to a local severe degradation, which could accelerate the occurrence of strong welding. Furthermore, Rieder et al. demonstrated that the more the molten zones of each electrode meet perfectly the more the welding force becomes higher [15]. This could explain the difference of the samples lifetimes.

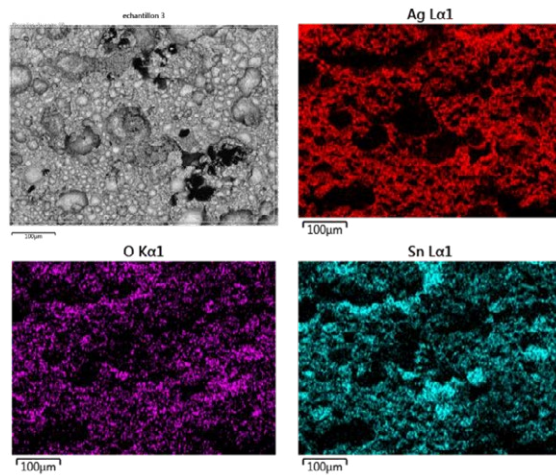
The silver samples are damaged differently from the AgSnO_2 ones. On their surfaces, a severe erosion had taken place by splattering the droplets of molten metal as observed on the surface of the contact holder.



a) MEB AgSnO_2 50 Hz



b) MEB AgSnO_2 400 Hz



c) MEB AgSnO_2 500 Hz

Fig. 10 Microstructure of AgSnO_2 sample with SEM – EDS. a) AS50 - b) AS400 - c) AS500

Figure 10 shows the surface roughness of AgSnO_2 contacts after finalizing the make tests, the images are obtained by using SEM. The EDX analysis have been used to show the chemical elements repartition on the contacts surfaces. It is found that the elements still almost homogenous even after all the arcing cycles. Furthermore, the tin oxide is more concentrated in the edges of the pores especially on the samples tested with 400 Hz and 500 Hz.

4 Conclusion

In this work, making tests were carried out for 115 V/ 750 Arms with different frequencies; 50 Hz, 400 Hz and 500 Hz. The purpose of this study was to analyse the effect of the voltage frequency on the bounce arc and the contacts welding characteristics.

According to an analytical approach, it was expected that increasing the voltage frequency could help to reduce the bounce arcs duration and consequently decrease the rate of welding occurrence and the welding force. However, the obtained results show that the voltage frequency has an indirect effect on welding characteristics because of the arc reignition.

That is, the arc reignition expands the arc durations and implicitly increases the arc energies. It has also an impact on the condition of contact surface. The number of arc reignition, characteristics of arc energy and the degradation of contact surface lead to high welding forces and increase the welding occurrence.

The results of this work open up further studies for the understanding of the physical interaction of arc reignition with the contact materials and its effects on their reliability in different electrical, mechanical and atmospheric conditions.

5 Literature

- [1] R. Holm, *Electric Contacts theory and applications*, Fourth edition. Germany, 2000.
- [2] P. G. Slade, *Electrical Contacts: Principales and Applications*, 2^e éd. 2014.
- [3] H. Cinaroglu, V. Behrens, and T. Honig, « Application of a New Ag/SnO₂ contact material in AC-contactors », *IEEE Holm Conference on Electrical Contacts*, 2017, p. 215-220.
- [4] C. Leung, E. Streicher, and D. Fitzgerald, « Welding behavior of Ag/SnO₂/contact material with microstructure and additive modifications in Electrical Contacts ». *Proceedings of the 50th IEEE Holm Conference on Electrical Contacts and the 22nd International Conference on Electrical Contacts*, 2004, p. 64-69.
- [5] A.R. Neuhaus, W.F. Rieder, and M. Hammerschmidt, Influence of arc duration and current on contact welding in low power switches». *Proceedings of the 48 IEEE Holm Conference on Electrical Contacts*, 2002.
- [6] Z. Chen and G. Witter, « Dynamic welding of silver contacts under different mechanical bounce conditions », in *Electrical Contacts, 1999. Proceedings of the 45 IEEE Holm Conference on*, 1999, p. 1-8.
- [7] X. Zhang, Z. Zheng, W. Ren, and Z. Zhou, « An Experimental Investigation of Dynamic Welding Mechanism of Contacts Used in Low Current Switching Devices », in *2018 IEEE Holm Conference on Electrical Contacts*, oct. 2018, p. 488-494.
- [8] L. Morin, N. B. Jemaa, D. Jeannot, J. Pinard, and L. Nedelec, « Make arc erosion and welding in the automotive area ». *Proceedings of the 45 IEEE Holm Conference on Electrical*, oct. 1999, p. 9-16.
- [9] F. Hauner, D. Jeannot, and K. McNeilly, « Advanced AgSnO₂ Contact Materials with High Total Oxide Content », p. 452-456, 2002.
- [10] E. YEE KIN CHOI, E. CARVOU, A. VASSA, N. BENJEMAA, and J.B. MITCHELL, « Optimisation of material erosion and welding performance by metal oxides and magnetic particles », Dresden, Germany, p. 61-66, 2014.
- [11] E. Carvou and N. Ben Jemaa, « Experimental Studies on Arc Duration in Ac Voltage Supply », France, p. 7-12, 2008.
- [12] Nozomi MIKI and Koichiro SAWA, « Arc Extinction Characteristics in Power Supply Frequencies from 50Hz to 1MHz », ICEC, 2008 France, p. 13-18.
- [13] C. Poulain and J. Devautour, « Parametric Study of the dynamic welding of Power Electrical Contacts », in *Proc. 19th Int. Conf. Elect. Contact*, 1998, p. 343.
- [14] T. Mutzel, M. Bender, and R. Niederreuther, « The effect of material composition on dynamic welding of electrical contacts », in *Holm Conference on Electrical Contacts (HOLM), 2013 IEEE 59th*, 2013, p. 1-7.
- [15] W. F. Rieder and A. R. Neuhaus, « Short Arc Modes Determining Both Contact Welding and Material Transfer », *IEEE Trans. Compon. Packag. Technol.*, vol. 30, n° 1, p. 9-14, mars 2007.

Determination of dielectric recovery characteristic of a pyro switch in commutation circuit

Christian Drebenstedt, Technische Universität Ilmenau, Ilmenau, Germany, christian.drebenstedt@tu-ilmenau.de
Michael Rock, Technische Universität Ilmenau, Ilmenau, Germany, michael.rock@tu-ilmenau.de

Abstract

Pyrotechnic switches are used for overcurrent protection, e.g. in low-voltage DC circuits (battery disconnectors). At fault current interruption, arc voltage built up by the switch must be sufficiently high to drive the current to zero (DC switching principle). Compared to AC interruption, the switch does not experience a transient recovery voltage (TRV). With increasing breaking capacity, comparatively large construction volumes are necessary. Possible reduction in design effort of the switch is found by using the commutation principle where the pyrotechnic switch is integrated as commutation switch in the low-impedance main current path.

This publication presents an experimental method for recording the dynamic dielectric recovery characteristics of a pyrotechnical switch for commutation circuits. An electrically equivalent network without a switch-off element in the commutation path was installed in the synthetic test circuit and stressed with currents up to 10 kA. From the moment of successful commutation by the pyrotechnical switch, the switch was loaded with voltages up to 4 kV using an RC circuit for recording the dynamic dielectric recovery characteristic. With the resulting dielectric recovery course and the verification of the switching capacity required for successful commutation, an optimally adapted switch-off element can be selected for realizing the overcurrent protection device based on the commutation principle.

1 Introduction

Traditional devices to protect in case of overcurrent in low voltage networks are fuses, circuit breakers and miniature circuit breakers. In circuit breakers, the detection of a fault current is usually done with electromechanical tripping units, and the current is also interrupted electromechanically.

Fuses, current limiting circuit breaker and miniature circuit breakers are able to interrupt high fault currents within a few milliseconds. Big circuit breakers with rated currents up to several thousand amperes usually need at least several 10 ms, if not intentionally time-delayed to provide selectivity.

In some cases these traditional protection measures are not sufficient, especially if

- the equipment to be protected does not have sufficient current carrying capacity for the let through current remaining until interruption, or
- protection against the effects of electric arcs is required, which can cause considerable damage to equipment and hazards to persons already in a very short time [1].

Therefore, protection devices are required which can interrupt the fault current in much shorter time. Semiconductor switches can interrupt currents in a very short time, but do not have the isolation distance in the off-state, which is often required for safety reasons.

In such cases pyrotechnical switches are increasingly used (e.g. to protect the battery systems in electric vehicles), which are one-time switches in normally closed condition [1] [2] [3].

In the case of the interruption of a fault current in a DC circuit, the switching arc voltage built up by the switch must be sufficiently high to bring the current to zero.

With increasing demands on the breaking capacity of the switch, relatively large construction volumes are required. One possibility to reduce the design effort for the switch can be the use of the generally known commutation principle as described in [1] and [2].

With this solution the pyrotechnical switch is integrated as a commutation switch in the low-impedance main current path, which is designed for carrying the operating current. When the fault occurs, which means a much higher current than the operating current, the pyrotechnical switch is activated with the help of a suitable fault detection. Due to the functionally very short switching time and the directly following significant voltage build-up, the fault current is completely commutated into the higher-impedant commutation path. Due to the higher impedance of this path, the fault current is limited and is subsequently switched off by a conventional switching device with a low current carrying capacity and short interruption time.

The switching capacity to be applied by the pyrotechnical switch during the commutation process is low compared to a complete switch-off. For the final interruption of the fault current in the commutation path, the integrated conventional switching device (e.g. fuse) builds up a high counter-voltage (switching voltage). The total voltage from the product of the current and the impedance of the commutation path and the switching voltage of the conventional switching device stresses the open switching path of the pyrotechnical switch (comparable to the transient voltage in AC circuits). For the safe and fast interruption of fault current, the dynamic voltage build-up by the switching device in the commutation path needs to be adapted to the time dependent dielectric recovery of the pyrotechnical switch immediately after completion of the commutation process.

Therefore, the task is to determine precise element combinations for each application in order to successfully interrupt both small (several 100 A) and large residual currents of up to several 10 kA which may occur in low voltage networks.

Due to the comparatively high commutation and switch-off speed, such overcurrent protection is possible for both DC and AC networks.

1.1 Setup of an interruption installation on the basis of commutation principle

Figure 1 shows the equivalent circuit diagram of the commutation circuit described in this article. The total current i_0 represents the operational current which has to be carried continuously or the fault current to be interrupted in case of a failure. The total current is divided between both paths of the commutation circuit. Due to the dimensioning of these paths the larger part i_1 of the total current flows through the commutation switch with pyrotechnic switch, which can be triggered. The equivalent impedance Z_1 of the main path is nearly fully determined by the geometry of the path of the closed pyrotechnical switch. A smaller part i_2 of the current flows through the commutation path, which contains the interruption device, which is shown here as a fuse. Additionally other elements (e.g. resistors) can be installed to increase the equivalent impedance of the commutation path Z_2 .

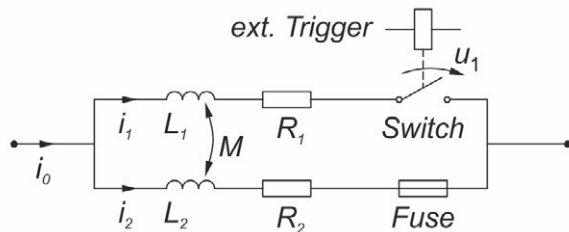


Fig. 1 Commutation circuit with main current path (1) containing triggerable pyrotechnic switch and commutation path (2) with its fuse.

By appropriate choice of the impedance ratio Z_1/Z_2 the load of the commutation path and therefore of the fuse can be reduced while the pyrotechnic switch is closed.

So a small cross section of the fuse-element can be chosen, which improves the response behaviour and the switching capacity of the fuse [4].

For the investigations presented here a commercial pyrotechnical switch was used as the test object, which is intended for DC networks in conjunction with electrochemical accumulators. The switch has a breaking capacity of 250 A at 400 V (2000 A at 32 V) and purely resistive load.

1.2 Description of the load of the commutation switch

The choice of the pyrotechnical switch in relation to the switching capacity and the dielectric recovery characteristic determines the possible elements of the complete commutation circuit.

The switching capacity of the switch determines whether the commutation process is successful. The following three parameters must be considered: The instantaneous value of the fault current I_0 at initiation of the commutation process determines together with the impedance of the commutation circuit the minimum voltage level to be built up by the switch U_{commu} [5]:

$$U_{commu} > I_0 * (Z_1 + Z_2)$$

Furthermore, the voltage must be present for the entire commutation time t_{commu} . The duration is essentially determined by the time constant of the commutation circuit τ_{commu} , which is calculated as follows:

$$\tau_{commu} = \frac{L_1 + L_2 - 2M}{R_1 + R_2}$$

In addition to the impedances of the individual paths, which can each be broken down into an ohmic (R) and an inductive (L) component, the magnetic coupling of the two paths via the common mutual inductance M plays an important role for in determining the time constant and the resulting commutation time.

Thus the maximum size of the impedance Z_2 and the possible impedance ratio are limited by the course of the commutation voltage and the self-impedance of the commutation switch, which essentially corresponds to Z_1 .

The current i_0 is assumed to be impressed during the very short commutation period. After successful commutation and until the response of the interruption device (fuse), the now open switching path of the pyrotechnical switch has to withstand the voltage of the commutation path (u_1 in **Figure 1**), which is determined by the total fault current i_0 , which now flows completely through the impedance Z_2 . In most cases the voltage stress is lower than the commutation

voltage built up previously. The load on the switching path is therefore estimated as non-critical.

Since there is no further energy input into the arc gap after the current zero crossing (CZ), the gas temperature drops over time. The conductivity in the switching path decreases. Also the contact distance still increases further. Both processes increase the process of the dielectric recovery.

When the switch-off element, corresponding to **Figure 1** a fuse, is tripped, a significant voltage build-up occurs in the commutation path, which still has to be withstood by the open switching path of the commutation switch. Any re-ignition of the switching path in the commutation switch must be prevented in any case. Therefore, at any time after CZ, the dielectric strength of the switching path must be higher than the applied voltage.

The influence of the fuse on the voltage stress on the switching path of the commutation switch is significant. The form of dynamic voltage stress depends on the choice of fuse, on its response time and switching characteristics.

If the time characteristic of the switching voltage of the fuse were known, the qualification of the commutation switch by means of a synthetic test circuit similar to the switching capacity test of high-voltage circuit breakers according to [6] could be applied, for example in the form of the Weil-Dobke circuit.

To find the optimum combination of impedance ratio, commutation switch and interruption device, knowledge of the switching capacity and, above all, the dynamic dielectric recovery characteristic of the commutation switch is of decisive importance.

The further described investigations do not serve to evaluate the switching capacity or the dynamic dielectric recovery of this specific switch, but are only intended to present the developed investigation method.

2 Test setup to determine the dielectric recovery characteristic

2.1 Method for determining dynamic dielectric recovery characteristic

Different methods are known to record the dielectric recovery characteristics. A selection is discussed in [7]. The methods differ in the number of recorded measuring points per switch-off operation and in the voltage load of the switching path after CZ.

For a multiple sampling of the dynamic dielectric recovery during a switch-off process, a method using a saw tooth oscillation generated by a capacitor connected in parallel to the switching path was presented in [8] (similar to **Figure 4**). The capacitor is short-circuited when the switch is closed or the arc resistance is low. Immediately following CZ, the capacitor is

charged by a DC voltage source with a in series-connected high-impedance charging resistor. If the instantaneous value of the voltage applied across the open contact gap exceeds the present strength, the gap is ignited and the capacitor discharges abruptly. After the voltage drop, the process of charging starts again. A typical course of the voltage across the open contacts is shown in **Figure 2**. With a sufficiently high density of sampling points (ignitions of the switching path), an approximated dynamic dielectric recovery characteristic curve can be derived from the voltage maxima achieved for each switch-off process.

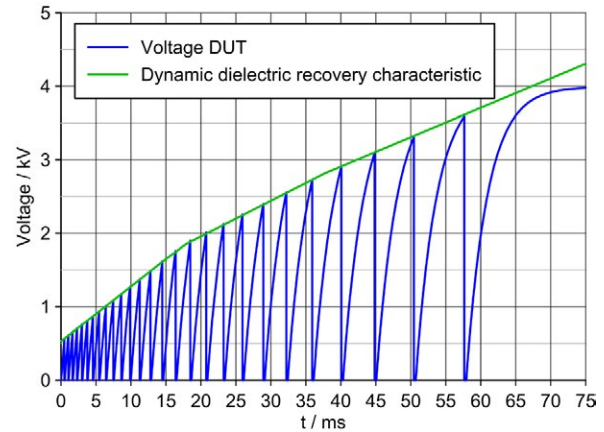


Fig. 2 Voltage course obtained by the method of [8] at no-load disconnection to derive the dynamic dielectric recovery characteristic.

Selecting the charging voltage, the charging resistor and the capacitance parallel to the switching path, the steepness of voltage rise and thus the possible density of the sampling points can be adjusted. It should be noted that with each discharge, energy is introduced into the switching path again. Any influence on the residual conductivity of the switching path must be excluded or minimized, otherwise the recorded characteristic curve will be distorted according to [7].

For the test arrangement, the maximum voltage stress of the switching path should be adjustable. It is assumed that the parallel fuse can be a commercial product for a nominal system voltage of 400 V or 690 V and an overvoltage category IV assigned to it. According to the insulation coordination [9] it is permissible that the fuse generates a maximum voltage of 8 kV itself. Accordingly, a power electronic DC voltage source with a maximum voltage of up to 10 kV was selected.

Due to the fast switching and commutation process by the pyrotechnical switch within a few 10 μ s, a very fast sampling directly after CZ is preferred. This is achieved by adjusting the time constant of the RC element used. With selectable charging voltages of $U_{DC} \leq 10$ kV and the aim of a low energy input to the switching path during each ignition process, the capacitance parallel to the switching path must be minimal. In contrast to other investigations [7] [8], a separate parallel capacitor is not used here. Instead, the capacitance

of the RC high-voltage probe, which is arranged in parallel to the test object and used to measure the voltage curve across the switching path, is used. Its input capacitance corresponds to $C_{V1} = 3$ pF. A high-voltage resistant charging resistor $R_{HV} = 100$ k Ω is used to limit the charging current of the DC source and to set the time constant. This results in a theoretical time constant of $\tau_{HV} = 0.3$ μ s for the charging process.

In order to check the applicability of the selected parameters and to test the circuit, the circuit was built up and a single pyrotechnic switch was used as the device under test (DUT). An attempt was made to record a dielectric recovery characteristic. Since the pyrotechnic switch was not initially stressed by a current from a load circuit, the obtained curve in **Figure 3** shows the dielectric strength at no load. After contact separation, a rapidly repeating sequence of a saw tooth shaped voltage curve occurs, with an amplitude between 400 V and 500 V. As the contact distance increases, the voltage maxima are increasing. In the range of approx. 28 μ s to 35 μ s, the last breakdown of the switching path occurs and the voltage applied across the switching path then rises to approx. 4.6 kV. Due to the high steepness of the charging current and a low inductance of the circuit, overshooting occurs. The voltage oscillates following the externally applied charging voltage of 4 kV, which is permanently maintained by the DUT. The process of contact movement is not yet complete at this point. However, the voltage applied is no longer sufficient to cause a further ignition at the contact position.

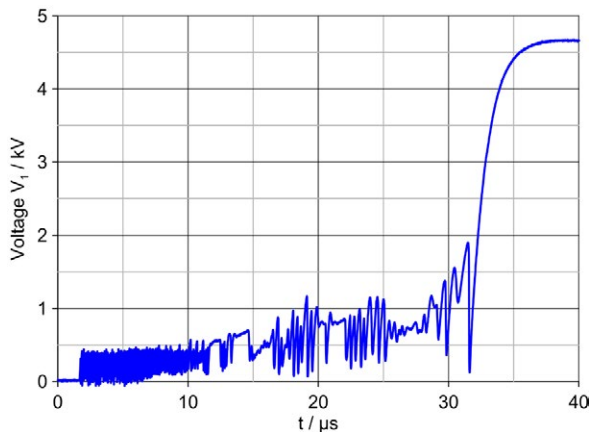


Fig. 3 Dielectric strength of the pyrotechnic switch (DUT) in no-load test (no-load characteristic).

For the last charging processes time constants τ_{HV} were determined in the range of 1.2 μ s to 1.25 μ s. The deviation from the previously calculated time constant can be explained by the equivalent circuit, hereinafter referred to as the voltage circuit, shown in **Figure 4**. In addition to the input capacitance C_{V1} of the high-voltage probe V_1 , the intrinsic capacitance C_{DUT} of the open switching path of the DUT plays a decisive role. With open contacts 6.3 pF was measured for C_{DUT} . Other existing parasitic capacitances are not taken into account.

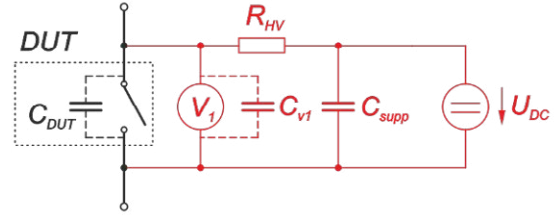


Fig. 4 Voltage circuit for recording the dynamic dielectric recovery characteristic of the DUT.

The DC source was set up locally separate from the test object for safety reason. To compensate the inductive influence of the long supply lines and to minimize the influence of the internal controller of the source, a supporting capacitor with $C_{supp} = 5$ nF was used at the input of the DUT and the RC element.

2.2 Experimental setup of the commutation circuit to obtain the dynamic dielectric recovery characteristic

The dynamic dielectric recovery characteristic is obtained from the combined loading of the commutation switch by a commutation process carried out by itself and the subsequent loading with the test voltage. Correspondingly, the voltage circuit from **Figure 4** shown above is integrated into the circuit in **Figure 5**.

The test current i_{HSG} is injected into the model of the commutation circuit by a half-sinusoidal generator (HSG, 50 Hz, $U_{charge} = 10$ kV, $I = 15$ kA) from an RLC circuit via a controllable make switch (MS). In the commutation current path with the current i_2 , a fixed substitute impedance Z_2 is used. The switch-off element, which causes the actual voltage stress on the DUT, is not integrated here. The main current path with current i_1 consists of the voltage circuit (red) described above and the commutation switch (DUT) to be tested. A disconnecting switch (DIS) is installed in series to the DUT as a decoupling element to separate the DUT from the high current circuit after successful commutation.

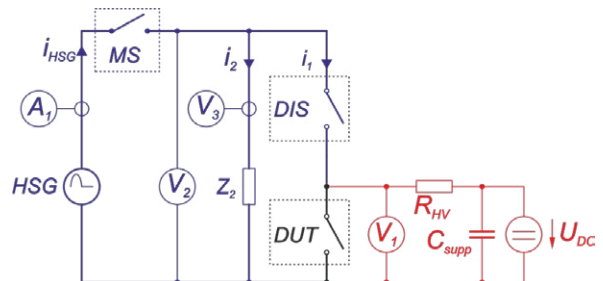


Fig. 5 Equivalent circuit diagram of test arrangement with high current circuit (blue) and voltage circuit (red).

As shown in **Figure 5**, essentially variables are recorded to determine the dynamic switching and dielectric recovery characteristics of the DUT. A high voltage probe V_2 is used to measure the total voltage across the commutation circuit. With the high voltage probe V_1

the voltage across the DUT during commutation and during the subsequent dielectric recovery is measured after CZ. For the measurement of the total current i_{HSG} a wide range current transformer A_1 is used. The partial current i_2 is measured indirectly by recording the output voltage V_3 on a self-built Rogowski coil, which is characterized by very small geometric dimensions and a very low self integration. Furthermore, the tripping signals for the switch under test (DUT) and the disconnecting switch are recorded. For the recording of the measured data a digital storage oscilloscope was used.

2.3 Selection of disconnecting switch

With the solutions described in [7] or [8] for determining the dielectric recovery characteristics at switching elements (e.g. switches, spark gaps), the test current from the high current circuit is interrupted. Following a disconnecting switch is opened to prevent a new current flow driven by the high current circuit during a possible subsequent re-ignition of the clearance between open contacts. This can be inserted theoretically at any point of the high current circuit.

In contrast a commutation is induced by the DUT here. The test current then continues to flow through the commutation path parallel to the DUT with the impedance Z_2 . In order to avoid a back-commutation the disconnecting switch (DIS) must be integrated into the main current path according to **Figure 5**. The required characteristics of the disconnecting switch (DIS) are:

- Minimum current carrying capacity corresponding to the desired test current with a current magnitude of up to 15 kA over a period of 10 ms.
- Low contact resistance and ideally negligible self-inductance, as otherwise the impedance of the main circuit Z_1 is adversely affected. (This results in a small dimension of the DIS).
- Low variance in time to contact separation with $\Delta t_{\text{open}} < 10 \mu\text{s}$ for a time-precise decoupling of the DUT with connected voltage circuit from the remaining current circuit directly after CZ.
- The DIS should theoretically only operate after successful commutation through the DUT, so the DIS does not need to have any switching capacity. However, the build-up of the dielectric strength after triggering should be faster than in the DUT, as otherwise a proper decoupling from the current circuit is not obtained.
- According to the installation locations of DUT and DIS in relation to the voltage circuit (**Figure 5**), the DIS must have a very low intrinsic capacitance C_{DIS} in open condition. This capacitance is via Z_2 connected in parallel to C_{DUT} and C_{V1} and thus influences the time constant τ_{HV} of the voltage circuit.

Different options for a disconnecting switch were examined and evaluated. Electromechanical switchgear showed a too large variance in time to contact separation and a too low dielectric strength after no-load opening due to

the comparatively low contact separation velocity. Mostly large dimensions causes a comparatively high self-inductance. Triggerable spark gaps with a high extinguishing capacity influenced the course of the test current in the main current path and showed disadvantages in the dielectric strength after CZ. Extinguishing diodes would be the means of choice, since they theoretically extinguish automatically in a circuit without external control. However, the available diodes had too large inherent capacitances so the time constant of the voltage circuit τ_{HV} was increased undesirably. Based on these considerations, a pyrotechnical switch of the same design as the test object itself was used as the DIS in the tests shown here.

A direct current of 5 A was used to trigger the pyrotechnic drive in the DUT and DIS. A programmable microcontroller was used to provide the trigger signal and to control the sequence with the HSG at an exact time. Prior to this, the inherent delay of the used devices were determined. The pyrotechnical switches showed an average time to contact separation of about $230 \mu\text{s} \pm 15 \mu\text{s}$ in no-load operation.

Despite the low variance in time to contact separation, the following problems arise when controlling the DIS: For an ideal decoupling of the current circuit to the DUT, the DIS should open in the instant of CZ. Since the commutation time varies in an unknown manner with each operation, even under identical preconditions, it is difficult to determine the time offset of the command. Probably the greater influence is the variance in time to contact separation of the used pyrotechnical switches. In the worst case, the error in the contact separation is about $30 \mu\text{s}$. This is considerable high with an expected commutation time of a few $10 \mu\text{s}$.

If the contact separation of the DIS is too early, a resulting voltage built up will influence the commutation process. If the DIS is tripped too late, the dielectric strength in the DUT might be higher. Then a no-load characteristic of the DIS would be recorded by the voltage circuit. To differentiate between the cases that may occur, it is essential to evaluate the voltage across both switches. The voltage characteristic curve from the previously performed no-load tests helps for the evaluation of the measurement.

2.4 Commutation circuit for determining dielectric recovery characteristic

The main current path is formed by connecting two identical pyrotechnic switches in series (**Figure 5**). Since these are commercial components, the influence of the switch internal conductor paths is limited. An attempt has been made to keep the effective length and the resulting impedance Z_1 of the main current path as small as possible. For this purpose, a copper connection module was attached to each of the two open ends, which is used to contact the main current path with the circuit and with the auxiliary current path.

As a replacement for the switch-off element, the commutation path contains only a resistance element which consists of 3 parallel round wires each with a diameter of $d = 2$ mm made of the non-magnetic material NiCr 80:20. The arrangement of these wires was chosen with regard to the following criteria: The resulting impedance Z_2 should be selected close to the impedance of the real switch-off element installed in the future (e.g. fuse). Furthermore, the mechanical and thermal loads occurring during the tests must be withstood.

According to the relationship between the time constant of the commutation circuit τ_{commu} and the effect of the self- and mutual inductances between the main and commutation current path, it is evident that a better magnetic coupling can partially compensate the effect of the self-inductances given in (see 1.2). The two paths have been moved together as far as possible to achieve maximum coupling. It is taken into account that a real switch-off element (e.g. fuse) can still be integrated in the bypass path without great design effort.

The resistance of the main current path was determined by measurement with $R_1 = 1,15$ m Ω and that of the commutation path with $R_2 = 22$ m Ω . The comparably small inductances could not be measured. Using the geometries, the self-inductance of the main current path was estimated to be $L_1 = 100$ nH, the self-inductance of the commutation current path to be $L_2 = 250$ nH and the mutual inductance to be $M = 35$ nH.

3 Determination of dielectric recovery characteristic

3.1 Description of typical experiments

Following five experiments are presented, each carried out with the same type of pyrotechnical switch and the same arrangement. The load current of the commutation circuit was varied in the range of 2 kA up to 10 kA with sinusoidal wave shape and frequency of 50 Hz.

The trigger signal to the DUT was set shortly after the peak of current. A typical course of the measured signals is shown in **Figure 6** and enlarged in time base for the commutation process in **Figure 7** for the experiment #2.

The current distribution between main and commutation current path is almost solely determined by the resistance ratio R_1/R_2 until start of commutation. Commutation is initiated at an instantaneous value of 4 kA and is successfully completed after 36 μ s. Contact separation of the DIS takes place 3 μ s before CZ, so that the latter has a supporting effect for a short time but with little influence when the current in the main current path is interrupted. The shape of the voltage measured at V_1 across the DUT corresponds to the no-load characteristic (see **Figure 3**). The time constant of the charging pulses was determined to $\tau_{\text{HV}} = 1,57$ μ s and is almost the same as for the no-load characteristic. It can be assumed that here the dielectric strength of the

DIS corresponds to the character of the measured voltage. Thus, the dielectric strength of the switching path of the DUT should be comparable or higher despite the previously applied breaking capacity.

The stress of the switching contact gap by the voltage circuit is withstood successful within approx. 0.4 ms after CZ. Subsequently, partial drops in the voltage across the switching gap down to 2.2 kV are detected. Both the voltage drop and the subsequent charging characteristic show RC behavior with significantly increased time constant in the range of $\tau_{\text{HV}} \approx 230$ μ s. This time constant is not determined by the test circuit. Rather, an increase in conductivity in the switching gap of the DUT can be assumed. What causes the change in conductivity can only be speculated. In any case, this effect occurred with all pyrotechnical switches under stress, which realized commutation at high current.

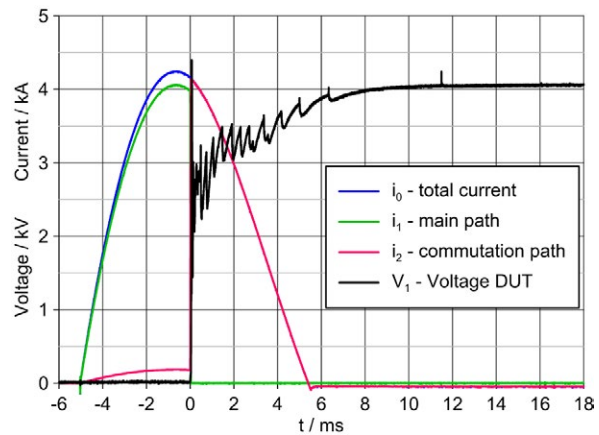


Fig. 6 Characteristic time courses for experiment #2.

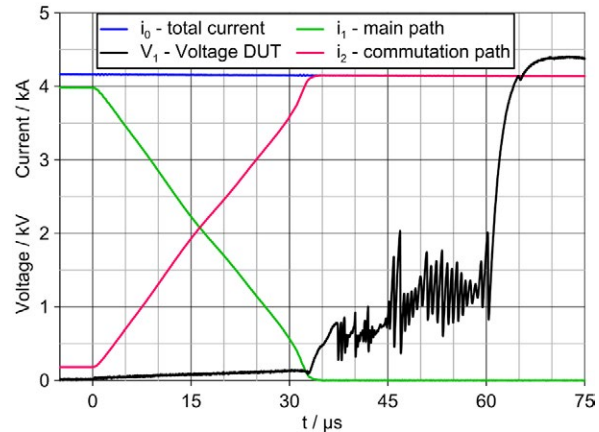


Fig. 7 Characteristic time courses for experiment #2 enlarged in time base for the commutation process and following voltage stress by voltage circuit.

3.2 Comparison of measurement results

The recorded time courses are qualitatively the same for all experiments. In **Table 1** the parameters that are decisive for commutation are listed. In addition to the instantaneous value of the total current I_0 and the commutation time t , the charge Q converted during the commutation process and the Joule integral I^2t were evaluated.

The product of the charge Q and the electrode drop voltage is responsible for the heating of the arc root, whereby the heating promotes thermos-field emission. Due to the short duration of the commutation of a maximum of 46 μs , an adiabatic heating at the root point can be assumed. The Joule integral I^2t is the extent of energy converted in the arc column, which is largely responsible for the ionization of air and for the conductivity of arc.

Tab. 1 Characteristic parameters for the commutation process in 5 experiments.

Experiment	#1	#2	#3	#4	#5
\hat{I}_0 / kA	2	4	7	10	10
$t / \mu\text{s}$	29.6	36.0	42.9	42.0	45.6
Q / As	0.04	0.08	0.15	0.22	0.24
$I^2t / \text{kA}^2\text{s}$	0.06	0.22	0.73	1.64	1.77

Basically, it can be assumed that with an increasing flowed charge Q or a higher converted Joule integral I^2t , the conditions for rapid dielectric recovery after CZ deteriorate, since higher residual conductivity in the switching gap can be assumed. For this purpose, the determined dynamic dielectric recovery characteristics for the tests 1 to 5 are shown in **Figure 8**. Contrary to expectations, the characteristics are close together despite the significantly different energy conversion. It can therefore be assumed that the energy conversion in the examined current range has no significant influence. The dielectric recovery characteristics are only determined by the repeated partial re-ignition of the switching gap starting in the range of 0.3 ms to 0.6 ms after successful commutation.

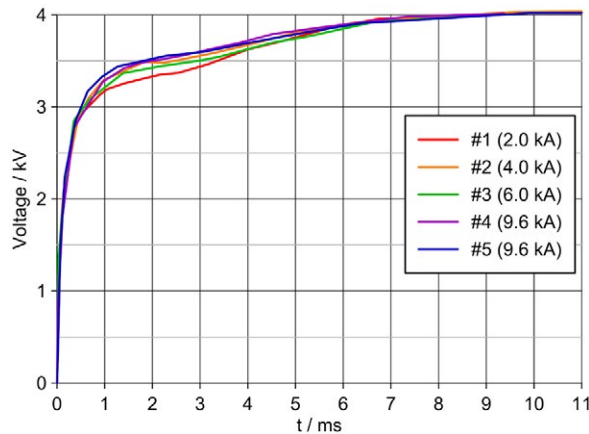


Fig. 8 Derived dynamic dielectric recovery characteristics for the examined pyrotechnic switch under various load currents.

For setting up a model for simulate the commutation behaviour the evaluation of the arc voltage, which is built up by the commutation switch as a function of time and the current to be commutated, would be interesting. For practical reasons of contacting the high-voltage probe above the device under test, however, voltages over the conductor path of the switch and additional magnetic couplings into the measuring loop [10] are partially measured. Therefore the actual arc voltage was calculated from the measured currents and

impedances, derived from the geometry and material parameters. The calculation method will not be discussed further here.

With the help of the measuring arrangement presented here, it is basically possible to investigate and characterize the behavior of the commutation switch based on pyrotechnical drive. The relationships obtained with the aid of the measurements can be used as a basis and comparison for a possible physical modelling of a pyrotechnical switch for commutation processes.

4 Summary

This paper presents an experimental method which allows the recording of the dielectric recovery characteristic of a pyrotechnical fast acting switch for commutation circuits. For this purpose, an electrically equivalent network without a switch-off element was installed in a specifically adapted synthetic test circuit and stressed with currents of up to 10 kA. From the moment of successful commutation the dynamic dielectric recovery characteristic was recorded using a saw tooth shaped voltage curve with amplitudes up to 4 kV.

With the verification of the switching capacity required for commutation and the derived dynamic dielectric recovery characteristic, an optimally adapted switch-off element can be selected for the final implementation of an overcurrent protection device based on the commutation principle.

In case of searching for a suitable fuse as a switch-off element its characteristic behavior must be determined first. Comparatively high current amplitudes with high steepness are commutated into the fuse before current limitation. The delayed tripping behaviour of the fuse after commutation and the subsequent voltage build-up over time must be known. Corresponding investigations were carried out and will be presented in a later publication.

For the selection of the pyrotechnical switch, a suitable fuse and the determination of the optimum impedance ratio, an electrical network model is available which simulates the characteristic behaviour of the commutation switch with pyrotechnical drive and the fuse as a switch-off element.

The resulting solutions based on the commutation principle with a commutation switch with pyrotechnical drive can be used in both AC and DC networks. Depending on the speed of fault detection, the prospective short-circuit current can be significantly higher than the 10 kA examined here.

5 Literature

- [1] Ouaida, R.; Berthou, M.; Tournier, D.; Depalma, J. F.: State of art of current and future technologies in current limiting devices, First International Conference on DC Microgrids (ICDCM), Atlanta, USA, 7. – 10. June 2015, (pp. 175-180), IEEE
- [2] Ouaida, R.; Palma, J. F. de; Gonthier, G.: Hybrid Protection based on Pyroswitch and Fuse Technologies for DC Applications, Symposium de Genie Electrique, June 2016, Grenoble, France. hal-01361696
- [3] Bergmann, S.: Pyrotechnic switch for battery of battery system used in motor car, has electronic circuit whose control output end is connected with electrically activated pyrotechnic igniter while control input end is connected with shunt, DE201210214835, 2014, Robert Bosch GmbH, Samsung SDI Co Ltd
- [4] Johann, H.: Elektrische Schmelzsicherungen für Niederspannung: Vorgänge, Eigenschaften, technischer Einsatz, Springer-Verlag, Berlin Heidelberg, 1982
- [5] Beer, F.: Über Ausgleichsvorgänge an Vor- und Hauptkontaktsystemen elektrischer Schalter, Wissenschaftliche Zeitschrift der Elektrotechnik, Band 2, Heft 3, 1963
- [6] IEC 62271-101:2012: High-voltage switchgear and controlgear - Part 101: Synthetic testing
- [7] Müller, O.: Dielektrische Wiederverfestigung von Gasentladungsstrecken bei Wechselstromlichtbögen unter besonderer Berücksichtigung des Elektrodenmaterials, PhD thesis, Ilmenau, 1965
- [8] Ozaki, Y.: Study on the Dielectric Recovery Characteristics of the Lightning Arrester Spark-Gaps, ETJ of Japan, Vol. 5, 3/4, 1960, pp. 94-97
- [9] IEC 60664-1:2007: Insulation coordination for equipment within low-voltage systems - Part 1: Principles, requirements and tests
- [10] Drebenstedt, C.; Rock, M.: Grundlegende Betrachtung zur Spannungsmessung bei Impulsstrom, 13. VDE/ABB-Blitzschutztagung, Aschaffenburg, Germany, 24. – 25. October 2019, VDE-Fachbericht 76, pp. 98-106, VDE Verlag, Berlin, 2019

Influence of Load Current and Separation Velocity on Arc Discharge at Breaking of Electrical Contacts

Koichiro Sawa, Nippon Institute of Technology, Miyashiro-cho, Japan, sawa@sd.keio.ac.jp
 Kiyoshi Yoshida, Nippon Institute of Technology, Miyashiro-cho, Japa, yoshida@nit.ac.jp
 Kenji Suzuki, Fuji Electric FA Components & Systems Co., Ltd, Konosu-shi, JAPAN,
 suzuki-knj@fujielectric.com

Abstract

DC interruption is more difficult than AC interruption even at DC low voltage. So, magnetic blow-out is usually used to quickly extinguish arc discharge. However, magnetic blow-out is less effective at low current so, the arc duration becomes the maximum at lower current called “critical load current”. In the previous paper, this phenomenon was examined in the current range of 1 to 30 A with the source voltage of DC 100 V and at the magnetic flux density of 0, 5 and 10 mT with the breaking velocity of 100 mm/s.

In this report the above phenomenon is examined at the breaking speed of 25, 50 and 100 mm/s with the magnetic flux density of 10 mT and the same voltage and current conditions as the previous report.

Consequently, the same phenomenon of maximum arc duration at lower current is found at three velocities. In addition arc energy is examined and Lorentz force working on arc column is discussed

Keywords— electrical contacts, arc discharge, arc duration, arc energy, magnetic blow-out, separation velocity

1 Introduction

Micro-grid systems including solar cell generation and EV are expected to be more popular and DC power supply systems are increasing in near future. In these systems it is indispensable to switch on or off current. However, it is well-known that switching-off dc current is more difficult than ac [1]. Therefore, switching in hydrogen atmosphere and /or magnetic blow-out are effective and widely used [2].

Magnetic blow-out has been used in large ac current switching and its effectiveness is well-known. Recently many papers have been published to show the effect of magnetic blow-out in large dc current interruption [3-8].

The authors have reported the effect of magnetic blow-out for dc current up to 30A and voltage less than 500 V [9,10]. In these researches arc duration at small current interruption was confirmed to be longer than that at large current interruption [9]. That is supposed to be because Lorentz force decreases at small current. In this paper the arc duration is investigated at the current range from 1 to 30A and the separation velocity of 25, 50 and 100 mm/s with the source voltage of 100 V and the magnetic flux density of 10 mT. Consequently, the arc duration is confirmed to increase at the current less than 20A at each velocity of 25, 50 and 100 mm/s for both contacts of Ag and W.

2 Experimental setup

Figure 1 shows the top view of an experimental set-up used in this test. The contacts move horizontally, and a

magnet is put above those. Figure 2 shows the configuration of the magnet and contacts and the relation between their distance and magnetic flux density. Three curves in the figure show the magnetic flux density at the center, its right-hand edge and its left hand edge of the magnet, respectively. They are confirmed to be almost the same value in the case of 10 mT.

An experimental circuit is resistive as shown in Figure 3. Table 1 shows experimental conditions. Silver and

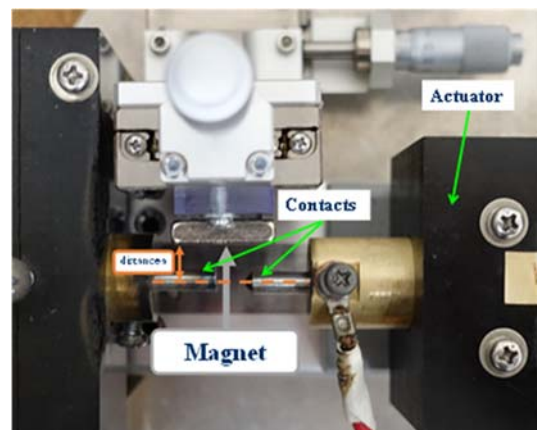


Fig.1 Switching setup and blow-out magnet.

Table 1 Experimental conditions.

Source voltage	DC 100 V
Closed circuit current	30, 20, 10, 5, 3, 1 A
Load	Non-inductive resistor (50 Ω)
Contact materials	W, Ag
Separation velocity	25, 50, 100 mm/s
Magnetic flux density	10 mT
Measurement number	5 times at each current

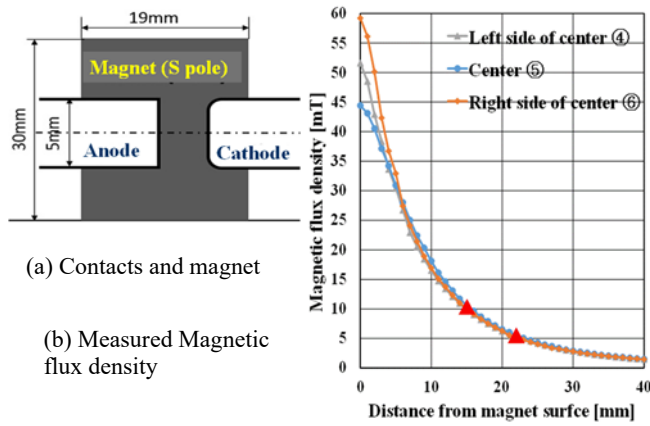


Fig.2 Magnet configuration and measured magnetic flux density.

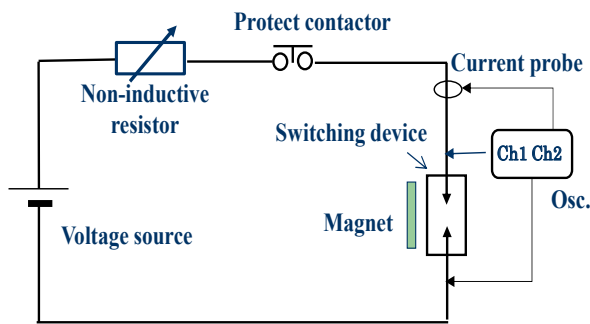


Fig.3 Resistive circuit used in the test.

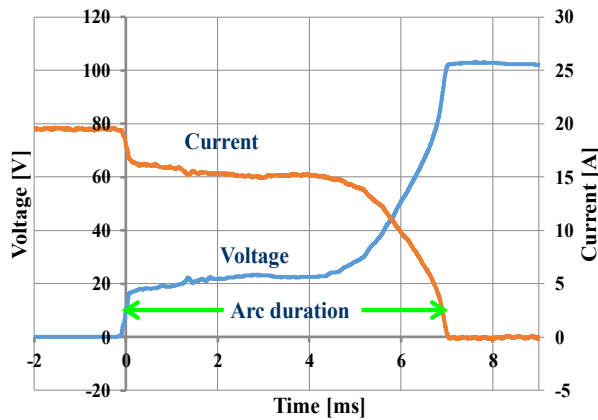


Fig.4 An example of arc voltage and current waveform.

tungsten are used as contact materials, and the separation velocity is 25, 50 and 100 mm/s with the magnetic flux density of 10 mT. Contact voltage and current waveforms are measured by an oscilloscope GW Instek GDS-3502 and current probe Tektronix A6303. The arc behavior at breaking contacts is observed by a high-speed camera. A typical waveform of arc voltage and current is shown in Figure 4 and the arc duration is obtained.

3 Results and discussion

3.1 Arc duration and arc energy

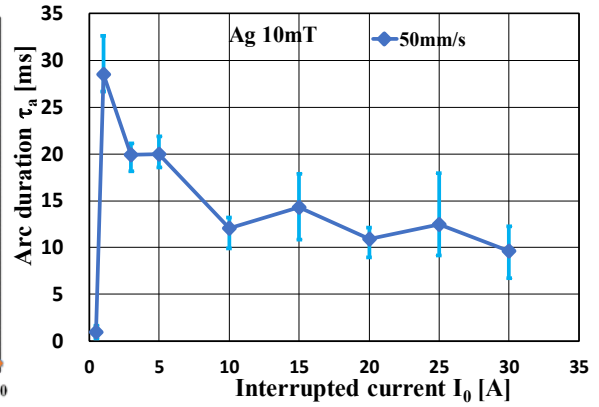


Fig.5 Arc duration vs. interrupted current.

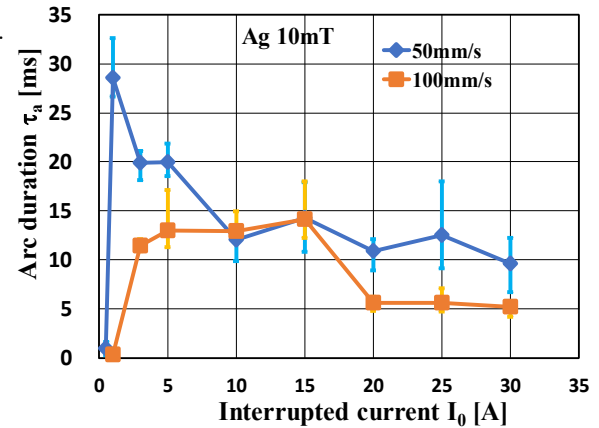


Fig.6 Comparison of arc duration at the velocity of 100 mm/s (Ag).

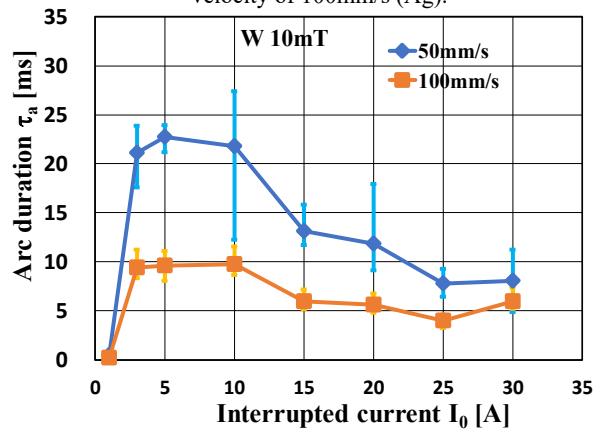


Fig.7 Comparison of arc duration at the velocity of 100 mm/s (W).

Figure 5 shows the relation between arc duration and interrupted current at the separation speed of 50 mm/s and the magnetic flux density of 10 mT for Ag contacts. Error bars show maximum and minimum duration among five measurements, Arc duration is found to increase as the interruption current decreases. This result is compared with the previous one at the separation speed of 100 mm/s [16] as shown in Figure 6. From this figure the arc duration at 50 mm/s is longer than that at 100 mm/s, but both are similar for the increase of arc duration at small current. And the arc duration becomes less than 1 ms at the current of 0.5 A which is close to the minimum arc current of 0.4 A for Ag contacts. The results for W contacts are shown in Figure 7.

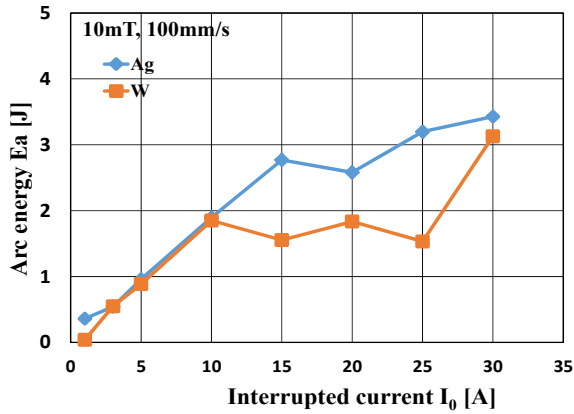


Fig.8 Arc energy vs. interrupted circuit. (Ag and W at 100mm/s).

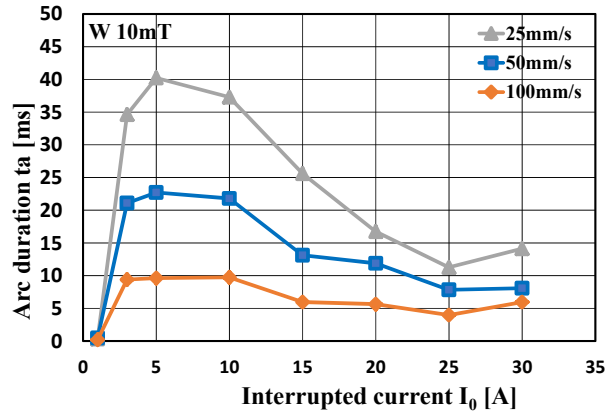


Fig.10 Dependence of arc duration on separation velocity (W, 10mT).

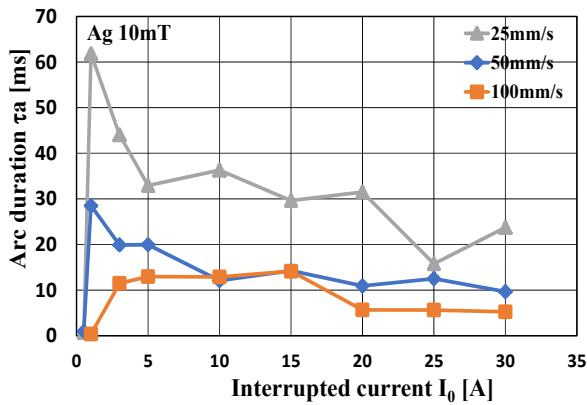


Fig.9 Dependence of arc duration on separation velocity (Ag, 10mT).

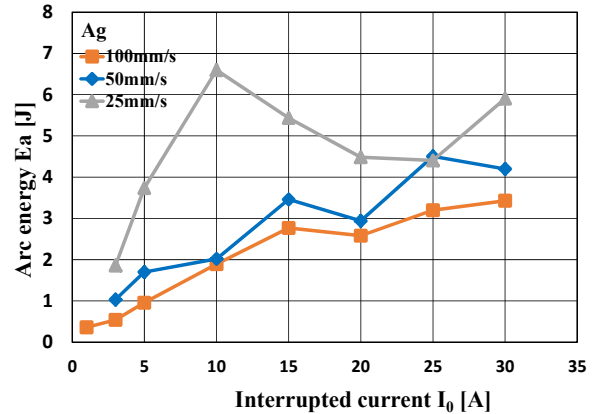


Fig.11 Dependence of arc energy on separation velocity (Ag, 10mT).

Further, though the arc duration at 50 mm/s is generally longer than that at 100mm/s, both durations are almost the same at the current of around 10-15 A for Ag contacts. In addition, based on the data of arc voltage and current, arc energy can be calculated by the following equation;

$$E_a = \int_0^{\tau_a} v_a i_a dt \quad (1)$$

where v_a : arc voltage, i_a : arc current, τ_a : arc duration.

Figure 8 shows arc energy vs. interrupted current with 10 mT and 100 mm/s for Ag and W contacts. From this result, though the arc duration is longer at small current, arc energy goes up with current increase for Ag and W contacts at the separation speed of 100 mm/s. However, the situation is different at lower velocities as mentioned later.

3.2 Effect of separation velocity on arc behaviours

Figure 9 shows the arc duration of three velocities where the result at 25mm/s is added to Fig.6. As expected, the arc duration at 25 mm/s becomes more longer, and it rapidly goes down around 0.1 A. The velocity of 25 mm/s is one-fourth of 100 mm/s and the

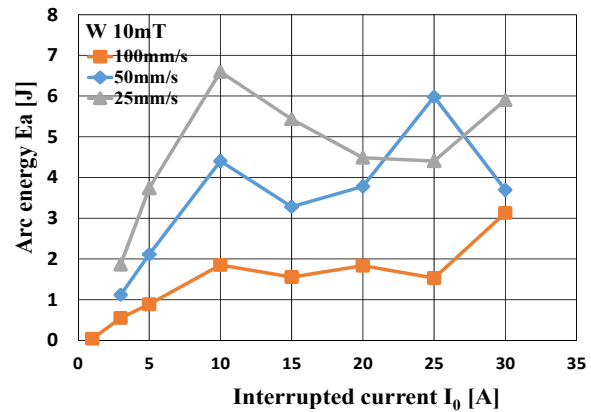
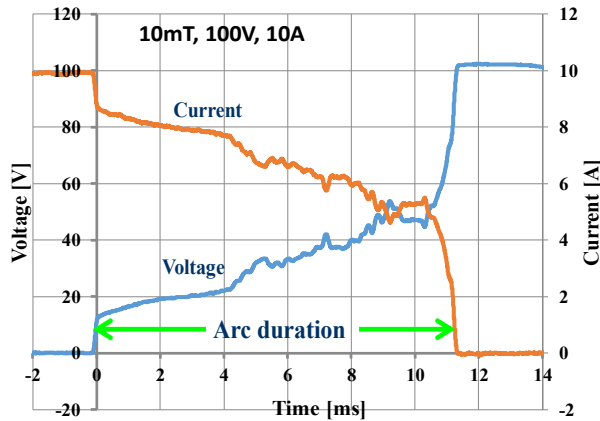


Fig.12 Dependence of arc energy on separation velocity (W, 10mT).

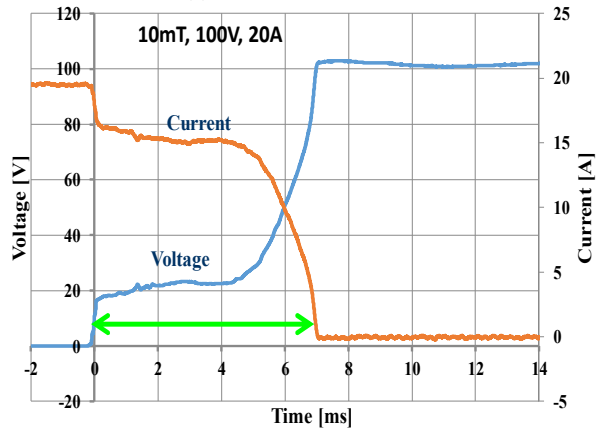
arc duration becomes three or four times as long as that at 100 mm/s.

Figure 10 shows the dependency of arc duration for W contacts on the separation velocity. The velocity dependency is not large at the current above 20 A, while it becomes large below 20A. The arc duration at 25 mm/s is almost four times as long as that at 100 mm/s.

Then the dependency of arc energy on separation velocity is examined. Figures 11 and 12 show the dependency for Ag and W contacts, respectively. From these results, the maximum energy of the separation velocity of 25 mm/s is shown at the current less than 30 A for both contact materials. This fact is important



(a) Current 10A



(b) Current 20A

Fig.13 Arc voltage and current waveform.

for design and usage of switching devices for dc current.

On the other hand, the arc energy increases as the current goes up at both velocities of 50 and 100 mm/s for both contact materials. Moreover, for Ag contacts the difference in energy at each velocity of 50 and 100 mm/s is small.

3.3. Lorentz force

Above results show that arc duration increases at low current for all separation velocities. The reason is discussed here. **Figure 13** shows waveforms of arc voltage and current for both currents. One is for 10 A where the arc duration is long and the other is for 20A where it is shorter than that at 10 A. Its bottom waveform shows that the arc voltage rapidly increases around 5 ms and that the arc is extinguished around the time of 7 ms. On the other hand the arc voltage gradually increases, but it is not extinguished even over 10ms. Eventually the arc duration reaches 11 ms.

In case of 20 A, the current where the arc voltage rapidly increases is about 15 A. On the other hand, in case of 10 A, the voltage waveform goes up a little when the arc current decreases to around 7.5 A, but the arc voltage does not rapidly increase and the arc is sustained until 11 ms.

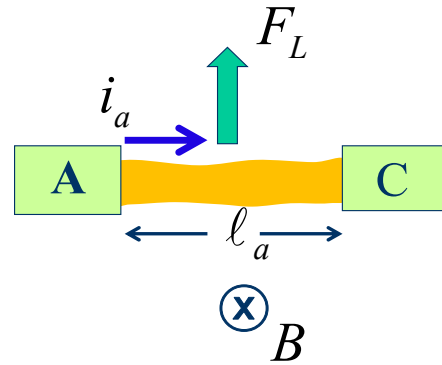


Fig.14 A model of Lorentz force working on arc column.

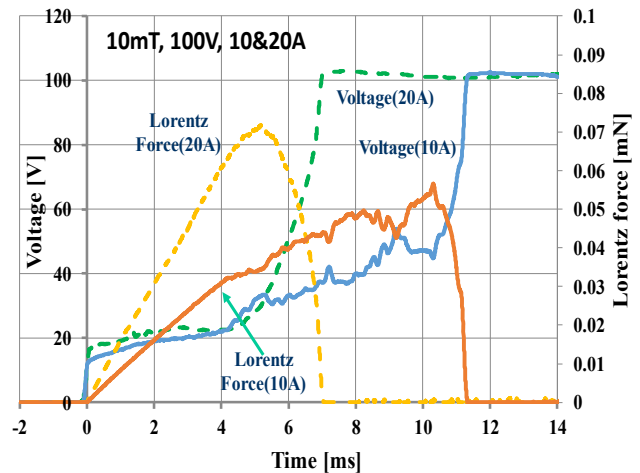


Fig.15 Time dependence of Lorentz force during arc ignition.

With magnetic blow-out, arc column is pulled out by Lorentz force which is generated by the interaction of current and magnetic flux density. Then arc column becomes longer and arc quickly disappears.

The Lorentz force works on the arc column as shown in **Figure 14**, and can be calculated by the following equation.

$$F_l = (i_a \times B) \ell_a \quad (2)$$

where i_a : arc current, B : magnetic flux density, ℓ_a : arc length.

The arc length is calculated by separation speed multiplied by time. The Lorentz force working on arc column is calculated by Equation (2), and its time dependence is shown in **Figure 15**. In this figure solid line is for the current of 10 A and dashed line for 20 A.

From this figure, in case of 20 A, the arc column is pulled out of the gap at the time of 4.5 ms, that is, at the Lorentz force of about 0.065 mN and the arc rapidly increases in voltage to disappear. The arc duration is about 7 ms.

In case of 10 A, the arc column seems to be pulled out at the time of 4.5 ms, that is, at the Lorentz force of around 0.02 mN, and gradually increases without rapid increase. Finally the Lorentz force goes up at 0.055 mN and the arc rapidly increases in voltage to disappear.

Its duration is about 11 ms which is much longer than that of 20 A.

In both cases of 10 and 20 A, the arc column is pulled out of the gap at the time of around 4.5 ms, and afterward it becomes like circular in shape as shown in **Figure 16**. So, the calculation of Lorentz force becomes more complicated as discussed later.

Figure 16 shows the relation between arc voltage and arc column image as a function of time for 10 A. The arc column stays in the gap until 4ms and is pulled out from the gap at about 5 ms. Then, the arc column is not quickly enlarged in length and finally rapidly enlarged around 10 ms to disappear. In addition, the arc voltage is observed to be little changed when the column is pulled out.

Figure 17 shows the case of 20 A. The arc column stays in the gap until about 4ms and is pulled out around 5 ms similar to the case of 10 A. However, the arc column is found to be rapidly enlarged just after pulled out, different from the case of 10 A. So, the arc duration is about 6 ms much shorter than 10 ms of 10 A.

Magnetic blow-out is effective to shorten the arc duration. The above results show that the arc column is pulled out at about 5ms for both currents of 10 and 20 A. However, the Lorentz force is 0.035 mN for 10 A and 0.07 mN for 20 A. There is no common threshold value of the Lorentz force above which the arc column is pulled out for different current. The conditions for the arc column to be pulled out should be discussed in more detail.

As mentioned just before, when the arc column is pulled out of the gap, the shape is like circular as shown in **Figure 18(a)**. The arc column is pulled out and both cathode and anode spots are also moved from the contact gap. So, the calculation of Lorentz force become more complicated.

Then, the Lorentz force is calculated, based on a simplified model of the arc column as shown in **Figure 18(b)**, where the arc column is approximated to be a semicircle of the radius r . Lorentz force working on a minute length on the circle is expressed as follows;

$$\Delta F_l = (\mathbf{i} \times \mathbf{B})r\Delta\theta \quad (3)$$

The component of y-direction (upward) is as follows;

$$\Delta F_{ly} = iBr\Delta\theta \sin\theta \quad (4)$$

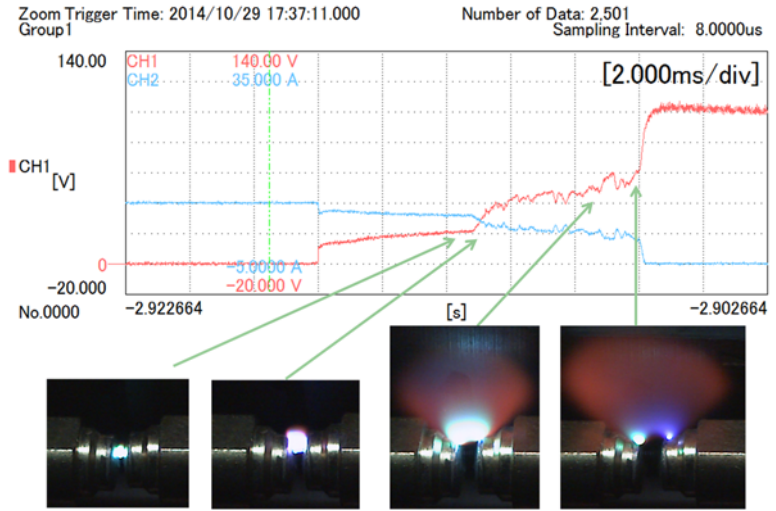


Fig.16 Arc images and Time dependence of Lorentz force during arc ignition.

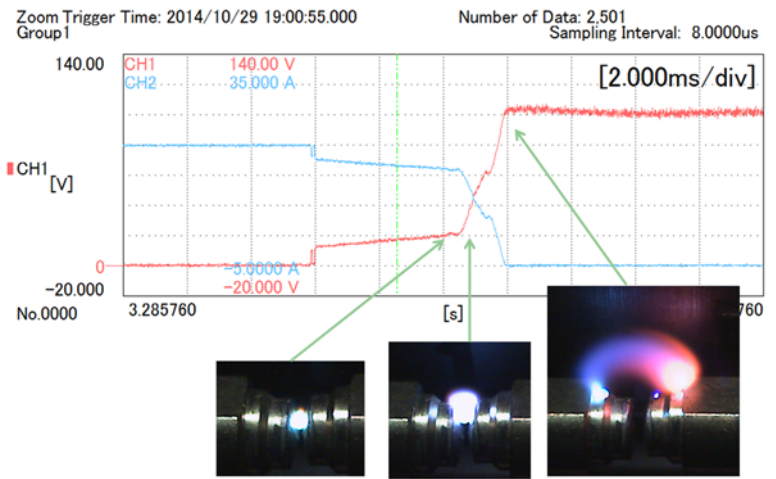


Fig.17 Arc images and Time dependence of Lorentz force during arc ignition (20A).

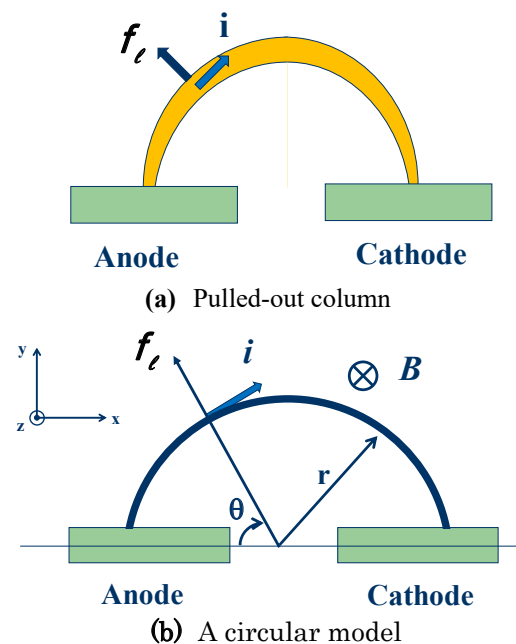


Fig. 18 A model for calculation

Then, the total y-direction force on the semicircle (pull-up force) is calculated as follows;

$$F_{\ell_y} = \int_0^\pi iBr \sin \theta d\theta = iB2r \quad (5)$$

Here, $2r$ is equal to the length projected on x-axis of the semicircle, which is longer than the gap length. Therefore, Lorentz force calculated by Equation (2) is smaller than that by Equation (5).

It means that Lorentz force after the arc column is pulled out has to be more accurately calculated, that is, after the time of 4.5 ms in Fig.15. This is one of future issues.

4 Conclusions

In this paper, the fundamental behaviour of breaking arc is investigated at the source voltage of 100 V and the current range from 1 to 10 A with the separation velocities of 25, 50 and 100 mm/s for the magnetic intensity of 10mT. From measured voltage and current waveforms arc duration and energy are obtained, and the followings can be made clear;

- (a) For both Ag and W, the arc duration becomes longer at smaller current at all velocities of 25, 50 and 100 mm/s, like the previous report.
- (b) As expected, the arc duration is longer at low velocity than that at high velocity, and the maximum duration at each velocity is almost in inverse proportion to the velocity.
- (c) For both velocities of 50 and 100 mm/s, arc energy decreases as the current goes down, though the arc duration has a maximum at lower current than 30 A. On the other hand, for 25 mm/s the maximum energy appears at the current less than 30 A
- (d) The force which pulls out arc column seems to be Lorentz force. However, the arc is not pulled out at the same Lorentz force for different current. In this test the arc column is pulled out of the gap at almost the same arc time, about 5ms for 10 and 20 A. But the arc column is not rapidly enlarged for 10 A and its arc duration is longer than that of 20 A.

It is a future issue to make a model that explains in terms of Lorentz force why arc duration becomes longer at small current. Further there is another theory of the effect of magnetic flux density on arc extinction [11]. It should be considered for future discussion.

5 References

- [1] P.G. Slade: Electrical contacts, Marcel Dekker, Inc., 2013
- [2] J. F. Trittle, "Air-break magnetic blow-outs for contactors and circuit breakers both A-C. and D-C.," AIEE Trans. Vol.41, pp.257-266, 1922
- [3] W. Rieder, "Interaction between magnet blast arcs and contacts," Proc. the 28th IEEE Holm Conf. on electrical contacts, pp. 3-10, 1982
- [4] K. Poeffel, "Characteristics of break arcs driven by external magnetic field in a DC42V resistive circuit," IEEE Trans. Plasma Science PS-8, pp.443-448, 1980
- [5] R. Michal, "Theoretical and experimental determination of the self-field of an arc," Proc. the 26th IEEE Holm Conf. on electrical contacts, pp. 265-270, 1980
- [6] J. Sekikawa, T. Kubono, "Characteristics of break arcs driven by external magnetic field in a DC42V resistive circuit," Proc. the 54th IEEE Holm Conf. on electrical contacts, pp. 21-26, 2008
- [7] K.Sawa, M.Tsuruoka, S. Yamashita, "Fundamental Arc Characteristics at DC Current Interruption of Low Voltage(<500V).", 27th International Conference on Electrical Contacts, Dresden, pp.662-667, 2014
- [8] K.Sawa, M.Tsuruoka, M.Morii, "Fundamental Characteristics of Arc Extinction by Magnetic Blow-out at DC Voltages (<500V)", Proc. the 60th IEEE Holm Conf. on electrical contacts, pp. 144-149, 2014
- [9] K.Sawa, S.Tsujimura, S. Motoda, "Fundamental Characteristics of Arc Extinction by Magnetic Blow-out at DC Voltages (<500V) II," Proc. the 61th IEEE Holm Conf. on electrical contacts, pp. 154-159, 2015
- [10] J.W.McBride, P.A.Jeffery, P.M.Weaver, "Electrode processes and arc form in miniature circuit breakers.", Proc. the 44th IEEE Holm Conf. on electrical contacts, pp. 93-99, 1998
- [11] John J. Shea, Elissa Heckman, and José C. Suárez Guevara2, "DC Arc Properties in a DC Magnetic Field.", Proc. the 64th IEEE Holm Conf. on electrical contacts, pp. 195-202, 2018

Spectroscopic investigation of DC-arcs in gas filled contactors under external magnetic fields regarding the effects on the arc-plasma properties

Diego Gonzalez¹, Ralf Methling¹, Sergey Gortschakow¹, Steffen Franke¹, Shun Yu², Frank Werner²

¹. Leibniz Institute for Plasma Science and Technology

². TDK Electronics

Greifswald, Germany, diego.gonzalez@inp-greifswald.de

Abstract

The spectral characteristics of switching DC-current arcs in hydrogen containing gas mixtures under several bar pressure was investigated using a model chamber and optical emission spectroscopy. The switching device consists of a model of a real double breaker DC-contactor with copper contacts. High-speed imaging and spectroscopy permit to observe and to characterize the properties of the switching arc plasma. The experiments show the influence of the external magnetic fields on the resulting arc voltage and on the current-limiting performance of the switching device. Strong widened H-alpha and H-beta lines characterize the arc-plasma.

1 Introduction

1.1 General considerations

The market for fully hybrid and most recently for fully electrically driven cars has been growing considerably during the last ten years.

The consequently enhancing of battery power, current rating and voltage both, demands switching devices capable of withstand the higher switching conditions regarding cycles and operations number as well as current interrupting capability.

To comply this task, gas filled contactors – GFC are the usual alternative, since they have a high reliability, are compact and provide enough current limiting performance. To this regard have shown Shiba, Kaneko and co-workers [1] results regarding DC- switching devices using H₂/N₂. Their work indicates that this gas mixture, especially in the proportion of 80% H₂ to 20% N₂, provides a higher electric strength and shorter arcing times compared to air at the same filling pressure (1 bar). In addition, the combined effect of the H₂/N₂ mixture and magnetic arc blowing reduces further the arcing time.

Sawa, Suzuki and co-workers [2], investigated the effect of pressure and working gas on the switching behaviour of GFC. They considered H₂, N₂, He, and air setting working pressures between 0.5 bar and 4 bar. Their analysis of resulting arc voltage, current characteristics, and arcing time for 100 V and 30 A DC relays indicates that shorter arcing times shall be obtained using H₂. Longer times were observed using N₂, air, and He, respectively. In particular, the arcing time using He was up to 7 times longer than with H₂. They found also out, that the arc duration was inversely proportional to

the working pressure. The influence of pressure was much more evident for arc currents higher than 20 A independently of filling gas.

According to Eidinger and Rieder [3] the interaction of electric arcs with external magnetic fields regarding its application for arc extinction have been considered since 1879. In particular, the elongation and displacement of the arc due to resulting Lorentz-forces are the most evident and used effects of the interaction.

The advantages of magnetic blowing were reported by Schrank, Gerdinand and co-workers [4] through investigations using DC circuit breakers with operating voltages around 330 V DC in air. Also results of Volm [5] point to the enhancing of switching performance for 1000 V and 40 A air relays through magnetic blowing combined with out-gassing from polymer inserts.

In addition to the reported changes of geometry and arc displacement because of external magnetic fields, also changes on the electric conductivity of the plasma can be expected. [6], which is caused by the increased number of collisions of the ions in the presence of the external magnetic fields.

Recent results of simulations of Shea and co-workers [7] have shown that the voltage increase is supported by an enhanced cooling effect through the mass-flux perturbations induced by the interaction with the external magnetic field. The increased convective energy losses over the arc column cause a reduction of the arc temperature and consequently a further reduction of the electrical conductivity of the plasma.

1.2 Intended work

The purpose of the investigation reported here was to characterize switching arcs of gas-filling contactors using H₂/N₂ mixture. The main topics of interest were to

observe the arc dynamics under the combined influence of pressure and external magnetic field, the resulting arc geometry and the characteristic spectral distribution and species in order to determine plasma properties like temperature and radial distribution.

2 Methodology

2.1 Experimental setup

The observation of the characteristics of switching arcs in gas-filled contactors is limited by the required housing. Especially the use of H_2 as filling gas demands gas-tight vessels. These are normally made of non-transparent alumina ceramics surrounded by a polymer casing, which supports the magnets and further connecting parts, provides fixing terminals and allows for mechanical protection against shocks. In order to provide an optical access to the contacts and switching chamber it is mandatory to modify the standard casing but this poses additional challenges for a gas-tight operation. In addition, the replacement of some components would be limited.

For an optical access to the arc-chamber it was therefore decided to construct a model switch (Fig. 1) using a polymethyl methacrylate (PMMA) housing. It replicates the geometry of the real device. Since all the additional parts, including the mechanics, are those of the real device the model switch shall perform exactly as the real application.

Besides the obtained optical access for a high-speed imaging, the used PMMA provides good transmission properties in the visible and near infrared wavelength range, which makes possible to apply optical emission spectroscopy (OES) to study the properties of the arc plasma.

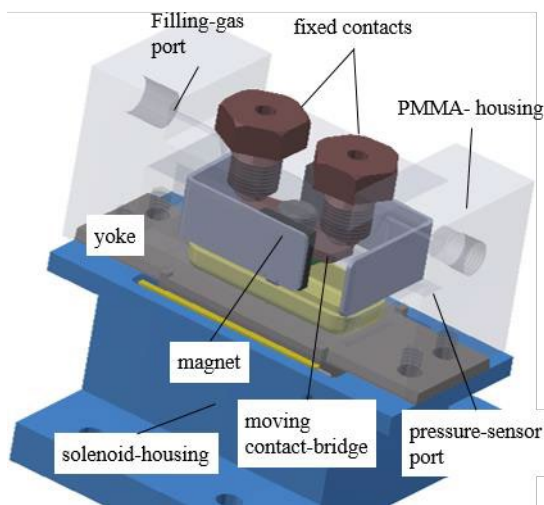


Fig. 1 CAD-schematic of the model switch

Further characteristics of the experimental setup are as follows: The contact-bridge and fixed contacts are

made of copper. A 12 V DC solenoid exerts the bridge translation (travel and over-travel). The internal volume of the arc chamber is about 20 cm^3 . The constructed device is gas-tight and withstands filling pressures of up to 7 bar. The filling gas was a mixture of H_2/N_2 in a proportion of 80 to 20 % and purity of 5.0. In order to convert the arc current and voltage signals to measurable values, a Pearson 1423 current monitor and a Tektronix 6015A voltage probe were used, respectively. In addition, the dynamic change of pressure inside the chamber during arcing was measured via a piezoelectric sensor model PCB 105C. The reduced electrical signals were then acquired with a Tektronix oscilloscope model DPO 4054. The experimental setup is depicted in Fig. 2.

For the experiments, we set a pressure of 5 bar for the filling gas. Before filling prior experiments, the remaining air inside the model chamber was drained by a membrane pump until the pressure reached 150 mbar. Through filling to the intended pressure (5 bar) and re-drain three consecutive times, it was expected that no important amount of remaining air would affect the experimental results (max. 150 mbar out of 5 bar). To prevent possible influence of gas contamination due to interaction between arc and PMMA wall, the filling gas was regularly changed.

2.2 DC-Current source

The current source consists of 10 CL-groups connected in a transmission line like configuration (Fig. 2). The delivered current pulse has an almost rectangular shape. Depending on the value of the individual inductivities, the pulse duration varies from about 5 ms up to 28 ms. According to the selected charging voltage it is possible to deliver currents up to 10 kA.

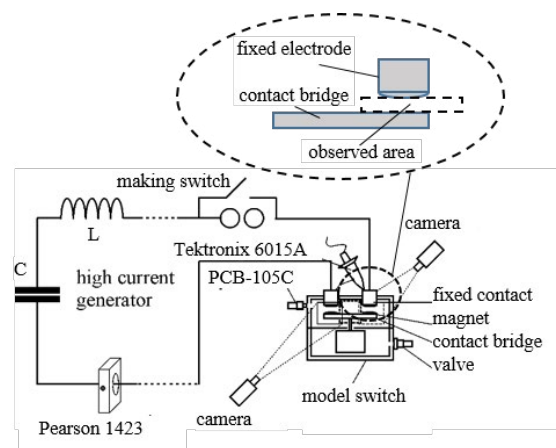


Fig. 2 Schematics of experimental setup

The experimental results presented in this paper were obtained using the configuration for the 28 ms-pulse and charging voltages of 500 V. The amplitude of the corresponding current was of 80 A. Since the circuit configuration of the 28 ms-pulse involves a relative

high effective inductivity of 64 mH, the used currents show a near impressed nature.

2.3 Spectroscopy and high-speed imaging

The spectral distribution of the arc radiation was firstly determined with a compact fibre spectrometer (AvaSpec-ULS2048), working in the wavelength range from 300 to 1000 nm with a temporal resolution of 1-2 ms. For further experiments an imaging 1/2 m spectrometer (Roper Acton) combined with a PI-Max4 ICCD-camera (Princeton Instruments) was used. The line of sight of the spectrometers was oriented nearly along the same line of view as the cameras and perpendicular to the selected field-of-view (upper side of Fig. 2). The absolute intensity calibration of the spectrometer detector was performed by means of a tungsten strip lamp (OSRAM Wi 17/G) in units of spectral radiance. The dynamic behaviour of the arc was recorded using high-speed cameras of the series Y4 and Y6 from Integrated Design Tools. The sampling rates were set to 3900 fps (Y6) and 5000 fps (Y4). The exposure time was of 1 μ s. In some experiments, metal interference filters (MIF) with a full width at half maximum - FWHM of about 10 nm for the H alpha line at 656 nm and for the Cu-line at 525 nm were placed in front of the lenses of the high-speed cameras.

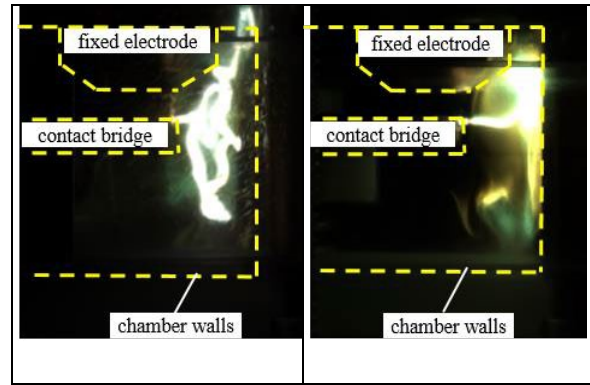


Fig. 3 Images of the arc with (left) and without (right) external magnetic field. High-speed camera exposure time 1 μ s, 3900 fps.

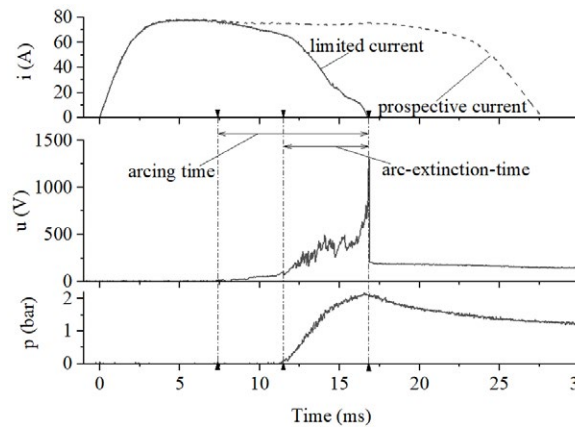


Fig. 4 Example of recorded current, arc-voltage and pressure signals from a switching operation.

3 Results and discussion

3.1 Dynamic characteristic of the Arc

Due to the combined influence of pressure and magnetic field shows the arc a highly arbitrary and dynamic behaviour. In particular, a comparison of images of the arc with (Fig. 3 left) and without (Fig. 3 right) external magnetic field indicates the strong influence of the arc field interaction.

As Fig. 3 (right) shows, without external magnetic field the self-induced Lorentz-force acts just enhancing the radius of the arc-loop, which is limited by the vessel walls. Electrode effects at the arc roots appear to dominate the arc-geometry so that plasma jets of the arc-root at the contact-bridge and fixed contact would impinge directly the wall.

With the external magnetic field, the resulting Lorentz-force acts in different directions, interacting with the arc in a more dynamic way.

The Fig. 3 (left) presents a remarkably example of the interaction. The arc is being elongated and twisted several times, occupying a higher part of the available volume in the vessel.

3.2 Electric arc behaviour

In order to evaluate the corresponding switching performance for a given condition, we defined an arcing time and an arc-extinction-time (Fig. 4).

The arcing time considers the elapsed time between the first contact opening and the arc extinction. The arc-extinction-time is the elapsed time during which the combined effects of elongation, due to Lorentz-forces, and turbulent convective gas flow inside the arc chamber cause a considerable voltage increase. During this time, the arc shows a strong oscillating behaviour, which is also reflected on abrupt changes of the voltage signal. From several measurements a mean value of arc-extinction time around 2 ms for the 80 A arc was determined.

Because of the highly dynamic behaviour, it is also possible that the arc will be driven to the region near the gap so that its length will be shortened again. Due to the shorter length, the arc voltage reduces suddenly to values of some 50 V, comparable to those during ignition. This interrupts temporally the current limiting behaviour of the device. Since the arc current is limited and driven to zero, its extinction usually occurs before the capacities of the current source are fully discharged. The voltage signal remains thus at a level greater than zero until the grounding system is activated.

The trend of the pressure rising corresponds to that of the arc-voltage and is defined by the arc-extinction-time. At the beginning of the switching processes, no

considerable pressure changes are observed. The increase on pressure starts only after the arc voltage rises considerably. This indicates that a considerable volume gas heating requires that the arc reach a certain length. After current zero the pressure decays slowly, since the cool-down process of the heated gas occurs through convection.

3.3 Arc spectrum

In order to overcome the difficulties posed by the dynamic behaviour of the arc, experiments using OES to complement the high-speed imaging were necessary. This permits to obtain images providing the actual geometry of the arc together with the corresponding spectral distribution. A characteristic overview spectrum of the 80 A arc is presented in Fig. 5. It was acquired with the fibre spectrometer, i.e. without spatial resolution and integrating over rather long exposure time. Strongly broadened H_α (656 nm) and H_β (486 nm) lines dominate the spectrum.

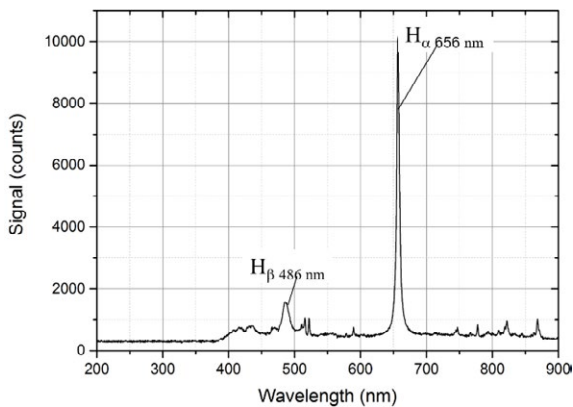


Fig. 5 Spectral distribution of the switching 80 A arc in H_2/N_2 .

In order to override the effect of the intense atomic hydrogen lines, the detector of the spectrometer was also operated with over-exposition (Fig. 6). As a result, the H_γ line as well as further species of nitrogen from the filling gas and copper from the electrodes could be observed. In addition, several lines indicating carbon and oxygen atomic species in the plasma were detected, too. They result from ablative arc processes on the PMMA walls as well as on the additional polymer supporting components of the device. Since for real devices no ablative arc-wall interaction is expected, an extrapolation of the obtained plasma properties to real devices is only partially valid.

3.4 Plasma properties

The overview spectra indicates that the optical emission is dominated by the atomic lines of hydrogen although other components were found as nitrogen from the filling gas, copper from the electrodes, and carbon

and oxygen from the camber wall. The obtained spectral distributions of the arc were further evaluated by imaging spectroscopy to obtain information of the plasma properties. Since the main interest refers to the plasma of the filling gas, we used the high-speed images to select the spectra of the cases in which the arc was burning far from the chamber walls but not directly between the electrodes. Fig. 7 shows an example of (a) the selected video camera image and (d) the corresponding calibrated 2D-spectrum in the wavelength range around the atomic hydrogen lines H_β and H_γ . In Fig. 7d also the contours of the electrodes were marked as well as the line of spectral observation that was focused onto the entrance slit of the spectrometer, i.e. the spatial dimension of the imaging spectrum.

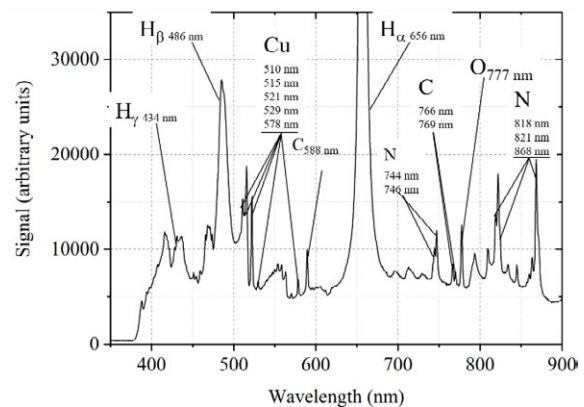


Fig. 6 Spectral distribution of the switching 80 A arc in H_2/N_2 overriding the effect of the H_α line.

For the determination of the plasma properties, the H_β line at 486 nm was used. While spatial integration over the arc diameter mainly yields a spectral radiance with improved signal-to-noise ratio (Fig. 7b), the spectral integration over the H_β line (Fig. 7c) provides the line integral for each side-on position that can be used to obtain the emission coefficient for this line. Therefore, inverse Abel transformation has to be carried out to convert side-on intensities to radial intensities. This procedure demands rotational symmetry of the arc. While in many applications with more or less “stable” arcs such a symmetry can be assumed, moving arcs, e.g. driven by magnetic forces, usually show a distinct deviation from rotational symmetry: One side has a steeper edge due to these forces while the opposite side is characterized by a wider profile. In Fig. 8a, the side-on line integrals of Fig. 7c are shown in detail together with two cases: On the one hand, the fit was carried out for the right, smaller and steeper side (red, dotted). On the other hand, an average of both sides was considered, covering the whole width of the arc (blue, dashed). The according emission coefficients obtained by inverse Abel transformation are given in Fig. 8b. Using the computed plasma composition with a self-programmed algorithm for a 5 bar H_2/N_2 mixture and assuming local thermodynamic equilibrium (LTE) per-

mits to obtain the H_{β} line emission coefficient depending on the temperature based on NIST transition probabilities. Finally, comparison of measured and calculated emission coefficients gives the radial distribution of the arc temperature (Fig. 9). The two curves for the right and the both sides are not a sign of disagreement but should be regarded as a measure of the parameter range for the “real” temperature distribution inside the arc column. The central temperature is around 15 000 K and decreases to 10 000 K within only 1-2 mm and to 8 000 K within about 3 mm. This strongly indicates a rather narrow arc cross section with temperatures that are high enough for significant contribution to the electrical conductivity of the arc. The used gas mixture and pressure causes strong constriction of the arc that is enhanced by the magnetic forces and fast movement. Comparing this result with the corresponding values of voltage and considering the obtained results for other intervals of time, it becomes clear that the arc elongation is not the only one effect responsible for the increase of the voltage. The relatively low conductivity due to moderate arc core temperature and small arc diameter must be considered.

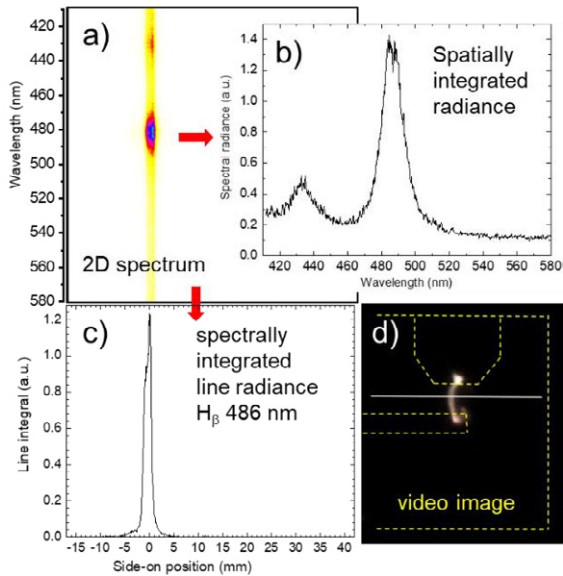


Fig. 7 a) 2D spectrum for a 80 A switching arc in H_2/N_2 mixture by 5 bar, b) spatially integrated radiance, c) spectrally integrated radiance of the H_{β} -line, d) high-speed image of the arc corresponding to the acquisition time of the spectrum along the line of sight between fixed contact and contact bridge.

Whereas the above analysis was carried out for spectra that are dominated by the emission of hydrogen atoms, it should be mentioned that in some cases completely different spectra were observed. In particular, for the instants were the arc nears the chamber walls (Fig. 10), the H_{β} (486 nm) and eventually the H_{γ} (434 nm) line emission is superimposed by the much stronger pattern of the Swan bands. This band structure is emitted by C_2 molecules and characterized by an increase towards

higher wavelengths with a maximum and abrupt decrease of intensity at the band-heads at 438.2 nm, 473.7 nm, 516.5 nm, and 563.6 nm. The Swan bands have been widely investigated by laser-induced optical breakdown spectroscopy (LIBS) of graphite targets [10,11] and can be applied to estimate (rotational) temperatures of the gas by comparison with spectra simulation. Recently it could be shown that both optical emission as well as absorption spectra of high-current arcs with strong wall erosion can be dominated by Swan band structures, depending on the energy input and gas flow [12]. In the example shown in Fig. 10, the arc profiles with Swan bands emission were found to be much broader than for the hydrogen-dominated arcs.

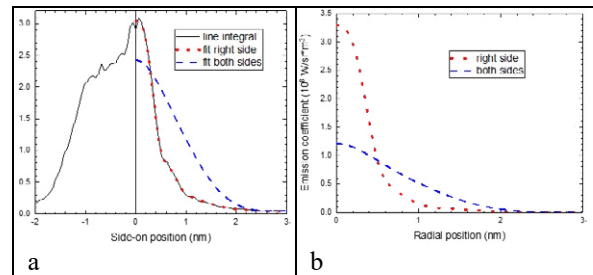


Fig. 8 a) Spectrally integrated radiance of the H_{β} -line 486 nm and fits for the right of the arc (red, dotted) and both sides (blue, dashed), b) Corresponding emission coefficient profiles after Abel inversion.

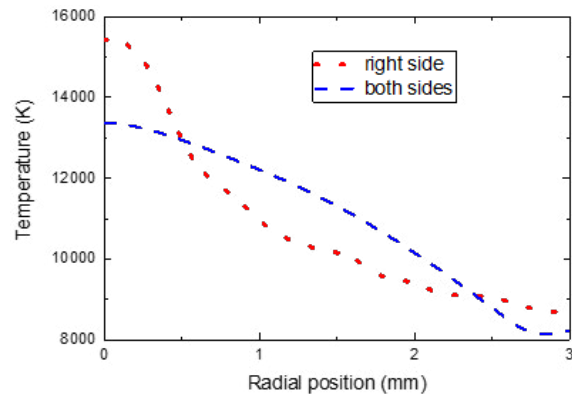


Fig. 9 Determined temperature profiles for the two fits introduced in Fig. 8 for the 80 A switching arc in H_2/N_2 mixture by 5 bar.

The radial profile of the arc temperature cannot be determined yet due to necessity of two-dimensional inverse Abel transformation and limitations by signal-to-noise ratio. However, from the spectra it can be assumed that the core temperatures probably will be lower. Estimations concerning the electrical conductivity lack of composition calculation for this plasma. Here, the production of different carbon-containing molecules like C_3 , C_4 that are known to be responsible for the C_2 production by photo defragmentation [10]

have to be taken into consideration as well as oxygen-containing molecules, atoms, and ions.

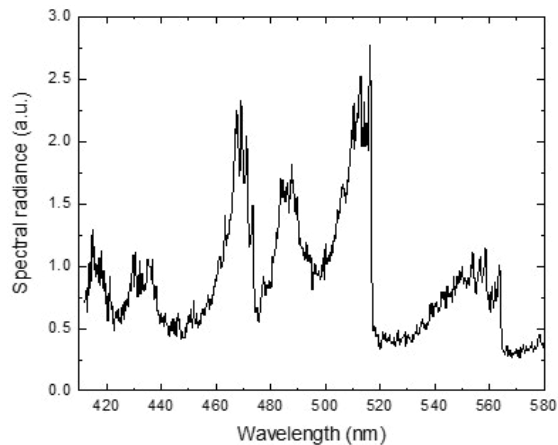


Fig. 10 Spatially integrated radiance profile for the 80 A switching arc in H_2/N_2 by 5 bar showing the typical spectral profile of Swan bands.

4 Summary

The radiative characteristic of DC switching arcs in H_2/N_2 mixtures by 5 bar filling pressure in a switch model was investigated.

In order to allow for the observation of the arc dynamics and for the determination of the arc spectrum a containment of the filling gas for the model switch was realized using a PMMA chamber.

The spectrum of the switching arc in H_2/N_2 mixtures by 5 bar filling pressure shows dominating atomic line emission of hydrogen. The temperature profile for the 80 A arc by 5 bar was determined using imaging spectroscopy around the H_β line at 486 nm. Narrow profiles with central temperatures of about 15 000 K and a decrease to 10 000 K within 1-2 mm were obtained. This strongly indicates a rather narrow arc cross section with temperatures that are high enough for significant contribution to the electrical conductivity of the arc.

5 Literature

[1] Y. Shiba, Y. Morishita, S. Kaneko, S. Okabe, H. Mizoguchi, and S. Yanabu, "Study of DC Circuit breaker of H_2-N_2 Gas Mixture for High Voltage," *Electrical Engineering in Japan*, 174(2):1407–1413, 2011. 239

[2] K. Sawa, K. Yoshida, K. Suzuki, and K. Takaya, "Influence of sealed gas and its pressure on arc discharge in electromagnetic contactor," *IEEE Holm Conference on Electrical Contacts*, pp. 236–241, 2017.

[3] W. Rieder and A. Eidinger, "Das Verhalten des Lichtbogens im transversalen Magnetfeld (Magnetische Blasung)," *Archiv für Elektrotechnik*, 43(2):94–114, 1957.

[4] C. Schrank, F. Gerdinand, E.-D. Wilkening, and P. Meckler. Breaking performance of a circuit breaker influenced by a permanent magnetic field at dc voltages up to 450 v. *Proceedings of the ICEC-ICREPE*, pp. 236–241, 2012.

[5] D. Volm and F. Winkler. Development of a compact relay for high voltage switching of up to 1000 v and 40 A. *International Conference on Electrical Contacts*, 27:144–148, 2014.

[6] D. Gonzalez, R. Methling, S. Gortschakow, St. Franke, and D. Uhrlandt, "Spectroscopic investigation of DC-arcs between parallel rails under the influence of external magnetic fields", *IEEE Holm Conference on Electrical Contacts*, Sept. 2019, pp. 115-121. ISSN: 2158-9992.

[7] J. Shea, E. Heckman, and J. Suarez Guevara, "DC Arc Properties in a DC Magnetic Fields," 64th *IEEE Holm Conference on Electrical Contacts/29th International Conference on Electrical Contacts*, 64(1):195–202, 2017.

[8] S. Gortschakow, D. Gonzalez, S. Yu, and F. Werner, "3D-Analysis of low-voltage gas-filled DC-switch using a simplified arc model," *Plasma Physics and Technology* 6(1):65–68, 2019, doi:10.14311/ppt.2019.1.65

[9] D. Gonzalez, S. Gortschakow, S. Yu, and F. Werner; "Investigation of the arc characteristics of switching DC-arcs on hydrogen containing gas mixtures," *Plasma Physics and Technology* 6(1):69–72, 2019, doi:10.14311/ppt.2019.1.69.

[10] S. S. Harilal, Riju C. Issac, C. V. Bindhu, V. P. N. Nampoori and C. P. G. Vallabhan, "Optical emission studies of C2 species in laser-produced plasma from carbon," *J. Phys. D: Appl. Phys.*, 30, 1703-1709, 1997.

[11] J. J. Camacho, L. Diaz, M. Santos, D. Reyman, and J. M. L. Poyato, "Optical emission spectroscopic study of plasma plumes generated by IR CO2 pulsed laser on carbon targets," *J. Phys. D: Appl. Phys.*, 41, 105201, 2008.

[12] R. Methling, St. Franke, N. Götte, S. Wetzeler, and D. Uhrlandt, "Analysis of C2 Swan Bands in Ablation-Dominated Arcs in CO2 Atmosphere," *Plasma Physics and Technology* 6(1):82–86, 2019, doi: 10.14311/ppt.2019.1.82.

Study of Arcing Processes in Circuit Breakers by Means of Spatially Resolved Magnetic Field Recordings

Christian Reil, OTH-Technical University of Applied Sciences, Amberg, Germany, ch.reil@oth-aw.de
Hans-Peter Schmidt, OTH-Technical University of Applied Sciences, Amberg, Germany, hp.schmidt@oth-aw.de
Michael Anheuser, Siemens AG, Amberg, Germany, michael.anheuser@siemens.de
Frank Berger, Technische Universität Ilmenau, Ilmenau, Germany, frank.berger@tu-ilmenau.de

Abstract

Magnetic field measurements performed on a circuit breaker in order to study the switching arc processes are presented. Characteristic for these measurements is the spatial two-dimensional recording of the magnetic field with simultaneous high temporal resolution. A sensor head was developed for this purpose, which records the magnetic flux density in an area of 42 mm x 60 mm with a spatial resolution of 12 x 24 measuring points. A highly integrated sensor chip based on the Hall effect was used for the design. The configurability of this sensor chip makes it possible to adapt the time resolution to the measurement task, always in compromise with the amplitude resolution and the number of field components to be measured. Measurements with a sampling rate of 80 kHz were conducted. Also, with the sampling rate reduced to 25 kHz, three axis measurements could be performed. By combining two sensor heads into one measuring system, it was possible to perform simultaneous measurements at the two contacts of a low-voltage circuit breaker with double breaker. As a result, both slow and fast changes in the magnetic field caused by the arcing process were recorded and visualized. The changes in the field distribution measured with the two sensor heads correlated well with the respective arc voltage. With the help of such magnetic field measurements, study of the arcing processes in low-voltage switchgear should be made possible without interference of the arc itself.

1 Introduction

Continuous development is required in the field of switchgears. The increasing demands of current and future electrical distribution grids are driving this development. To be mentioned here are the change from a purely unidirectional to a bidirectional supply structure, the increasing spread of direct current networks or the use of new storage technologies. Continuous improvement of the performance of protective devices such as low-voltage circuit breakers is essential to ensure that they meet upcoming challenges. The arc behaviour during the switching operation is crucial for the switching performance of a breaker. By modifying the contacts and the breaking chamber, the arc behaviour can be optimized.

The use of a high-speed optical camera enables observation of the arc during a switching process lasting only a few milliseconds. This diagnosis method requires an optical access into the breaking chamber. Since low-voltage circuit breakers are usually designed with a moulded case, modifications are necessary to gain optical access. Therefore special laboratory samples are used with housings that are transparent, have cut-outs [1], holes or optical fibres inserted into their housing wall [2].

Such modifications to the laboratory samples make it impossible to rule out influences on the arcing behaviour. Especially the application of other materials in the switching chamber can in turn influence the arcing process. For example, the different gas emission characteristics of the transparent material introduced can change the flow and pressure conditions inside the chamber and thus the behaviour of the arc.

2 Literature on Magnetic Switchgear Diagnosis

With magnetic field measurements, it is possible to test switching devices without influencing the switching behaviour itself. Blaise Pascal University in France published work on this subject between 1990 and 2008. Three different concepts were presented. First, they presented a method called "Magnetic Camera" [3] [4] [5]. Based on a simplified model switch, up to 88 pickup coils attached to the outside of the switch detect the magnetic field. The arc was modelled as a polygon line between the electrodes divided into segments. A nonlinear system of equations based on the law of Biot-Savart was established. The movement of the arc was reconstructed by inversion and thus e.g. the re-ignition of the arc could be investigated. In a more advanced method, referred to as "Inverse Method", up to 14 Hall effect sensors were used instead of micro coils

to detect the magnetic field [6] [7]. The reconstruction was also based on a non-linear system of equations. The influence of the quenching plate configuration, the contact material and the circuit chamber material were investigated. In addition, the current commutation during re-ignition was examined in more detail by modelling two arcs using two separate polygon lines. In a third method, called "Deconvolution Method", the arc was modelled as narrow volume elements between the electrodes instead of a polygon line [8]. The homogeneous current density in each of these elements was reconstructed by inverting a linear system of equations. This method was combined with the "Inverse Method" to investigate the commutation of the current from the moving contact to the electrode. All three methods have in common the use of a simplified model switch, the restriction of the arc movement to two dimensions and the use of Biot-Savart not considering magnetic materials.

Reichert and Berger [9] were also able to determine the arc root movement with pickup coils arranged alongside arc rails. The influence of the current in the rails on the magnetic field measurement was excluded by the arrangement of the coils.

Ghezzi et al [10] theoretically described the current density reconstruction in vacuum circuit breakers by magnetic field inversion. With the help of methods such as singular value decomposition, regularization and temporal filtering, the reconstruction was improved. However, it turned out that this method is only capable of a rough reconstruction of the course of the arc. An exact determination of e.g. the shape of the arc's roots is therefore not possible.

At Jiaotong University in Xi'an, China, a magnetic field sensor array with 8 x 8 Hall effect sensors was presented and used to investigate the influence of quenching plates and ferromagnetic inserts on the arc movement [11] [12]. The sampling rate of the sensors was 20 kHz. Further work describes the reconstruction of three-dimensional current density distributions from magnetic field measurements [13]. The model is based on a simplified switching chamber. A paramagnetic behaviour of the quenching plates and eddy currents in the quenching plates and busbars are considered. In addition, the influence of a real sensor on the reconstruction was examined [14]. The averaging of the magnetic field over the active sensor surface, the tilting and errors in the sensor positioning are taken into account.

3 Measuring System

In order to be able to study fast arcing processes with the help of the magnetic field, a measuring system is required that combines a spatially resolved measurement with a high temporal resolution. Due to the fast

arcing process lasting only a few milliseconds, a sampling rate of several kilohertz is required. Commercial measuring devices are available for spatially high-resolution two-dimensional measurements of magnetic fields [15] [16]. However, the sampling rates of about 1 Hz to 100 Hz of these systems are too low for the intended application. For this reason, we developed and built our own magnetic field measurement system particularly designed for this purpose. The developed measuring system consists of several sensor heads, for synchronous measurement at multiple positions. Currently five sensor heads are available to take the measurements. Each sensor head records the magnetic field in a rectangular area, which is equipped with individual sensor ICs (integrated circuits).

3.1 Sensor Technology

For the measurement system, we use the highly integrated sensor IC FH5401 from Fraunhofer IIS [17]. This sensor chip combines six Hall effect sensors, a temperature sensor, the analog and digital signal processing and a sequence control in one IC package. The Hall effect sensors are arranged in two spatially separated measuring points called pixel cells with three sensors each for the three spatial directions as shown in Fig. 1. A vectorial detection of the magnetic field is therefore possible. The IC is controlled via a serial peripheral interface (SPI). Due to the configurable sequence control, adaptation to different measuring tasks is possible. For example, you can choose which of the integrated sensors are used and the sampling rate and resolution at which they operate. The integrated temperature sensor allows compensation of the temperature-dependent gain of the Hall effect sensors.

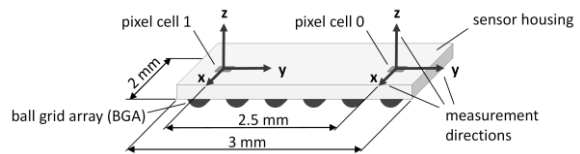


Fig. 1 Packaging of the FH5401 sensor IC.

The two configurations "Single Axis" and "Three Axis" were used for the measurements shown in this paper. Table 1 lists the data of both configurations. Both use only one measuring point in the IC to achieve the high sampling rates. The "Single Axis" configuration uses only one Hall effect sensor in the IC, which allows a high sampling rate of 80 kHz. The "Three Axis" configuration uses three Hall effect sensors in one measuring point instead. This allows us to record the magnetic flux density in magnitude and direction. Further configurations are possible. Considerable options include increasing the sampling rate to over 100 kHz or using both measuring points in the IC at a reduced sampling rate.

TABLE 1. USED CONFIGURATIONS FOR FH5401.

	Single Axis	Three Axis
Axis:	Bz	Bx, By and Bz
Sampling rate:	80 kHz	25 kHz
Range:	± 50 mT	± 50 mT
Resolution:	160 μ T	270 μ T

3.2 Sensor Head

The main components of the sensor head are the sensor board and a control board. The sensor board is equipped with 288 FH5401 sensor ICs. These ICs are arranged in a rectangular 12 x 24 array. The sensor array covers an area of 42 mm x 60 mm, resulting in spatial resolution of 3.5 mm in x-direction and 2.5 mm in y-direction. The sensor board is connected to the control board via board-to-board connectors to form a single unit. The main component of the control board is an FPGA (field programmable gate array), which simultaneously controls and reads out all sensor ICs and temporarily stores the measured data. A plastic housing ensures the targeted airflow from the mounted fan to the sensor board. The rear of the sensor board is cooled to prevent overheating of the sensor ICs on the front of the board. The complete sensor head can be positioned as a unit on the object to be measured. A PC controls the sensor head using a USB interface.

3.3 Measuring Procedure

A command sequence is loaded from the PC into the FPGA to prepare a reading. The command sequence is specific to a sensor IC configuration. Thus, separate sequences are required for the "Single Axis" and the "Three Axis" configurations. After the acquisition duration has been set, you can start the measurement. An auxiliary board to which all camera heads are connected synchronizes the start of the measurement. In addition, this board provides the connection of the peripherals for igniting a thyristor and the control of an auxiliary trigger. After completing the measurement, the magnetic field data temporarily stored in the FPGA is transferred to the PC. There the offset and temperature-dependent gain correction is carried out.

4 Measurements on a Circuit Breaker

4.1 Measurement Setup

The arcing processes in a circuit breaker are studied by performing simulated switch-off operations of a device. The test specimen was a low-voltage circuit breaker with a rated current of 250 A and a rotary double-breaker system. An outer phase of the three-phase device was tested. A test setup was built to conduct the

measurements, which is shown in Fig. 2. With the contact system initially closed, the switchgear is subjected to a semi-sinusoidal current waveform with an amplitude of up to 3 kA and a duration of 10 ms. This is achieved by discharging a capacitor bank via a choke designed as an air-core coil. During this discharge, the circuit breaker is then remotely tripped by an auxiliary release and the contact system opens. The current flow, driven by the capacitor voltage and the choke, creates an electric arc between the contacts. The time at which the device is tripped can be varied according to the phase of the current.

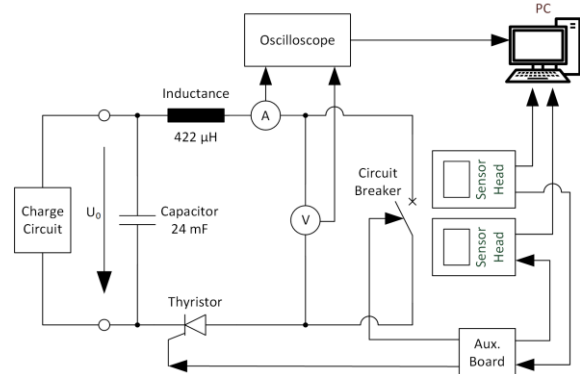


Fig. 2 Schematic of the test setup.

During the arcing process, two sensor heads mounted on the outer wall of the switch detect the magnetic field. Fig. 3 shows the arrangement. The measuring plane is aligned parallel to the contact system. The two measuring areas are each positioned at the height of the quenching plate arrangement of the two breakers of the double breaker system, as shown in Fig. 4. This should allow observation of the arc interaction with the quenching plates, with the focus on the outward and inward movement of the arc. In addition to the flux density, the current and voltage are also measured. A tap on the moving contact piece measures the voltage for both breaker points.

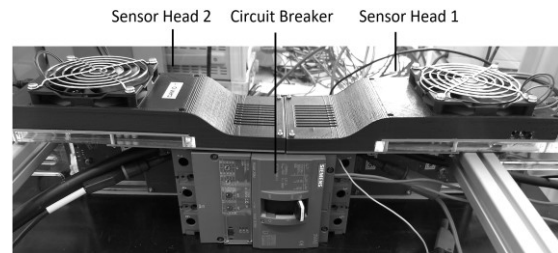


Fig. 3 Picture of the measurement setup.

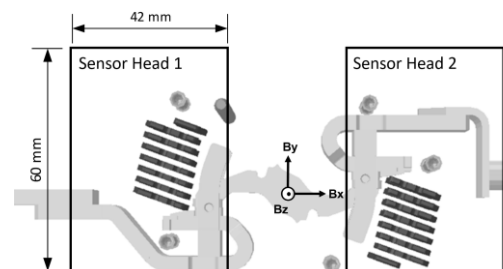


Fig. 4 Location of the measurement areas of the two sensor heads.

4.2 Single Axis Measurement

Fig. 5 shows the current and voltage curve of a measurement. The current reaches a maximum of 1.4 kA. The voltage was measured for both contacts of the double breaker. At $t = 1.3$ ms the switch opens, which is indicated by an arising voltage across the contacts. The two voltage curves differ mainly by the many high-frequency peaks and drops in the voltage across contact 2 (u_2). In contrast, only a few but larger voltage drops can be observed at contact 1 (u_1).

The magnetic flux density in the z-direction was measured with the single axis configuration at a sampling rate of 80 kHz during the entire simulated switch-off process. The lower part of Fig. 5 shows a section of the voltage waveforms. Here, the time points of the magnetic field measurements for a range of 225 μ s are shown. **Fig. 6** shows the recorded field distributions at these times for both sensor heads. Each pixel in the images represents the measured value of a sensor IC. The field distributions of the two heads show changes during the observed period, each locally limited. The field changes result from the change of the current path within the switching device, which is generated by the opening of the contacts and by the arc movement. Sensor head 1 shows a slow change in the field distribution, which is expressed by a one-time change in the sign of the flux density. A shift in the current density distribution within the switching chamber relative to the sensors can cause such a change in sign. Sensor head 2, on the other hand, detects many fast changes, each of them happening in a few samples. These findings correlate well with the voltage curves, as sensor head 1 is positioned near contact 1 and head 2 near contact 2. Rapid changes in the field always occur with sudden voltage drops.

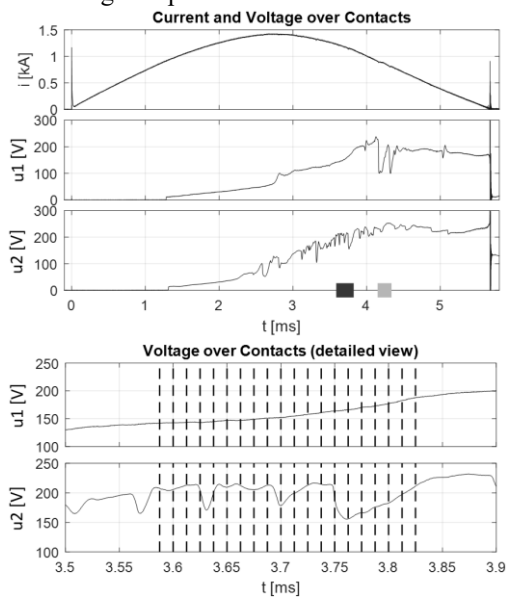


Fig. 5 Current and voltage over contact 1 (u_1) and 2 (u_2) during single axis measurement (rectangles on the t axis: investigated periods. bottom: detailed view with marked sampling points of the magnetic field).

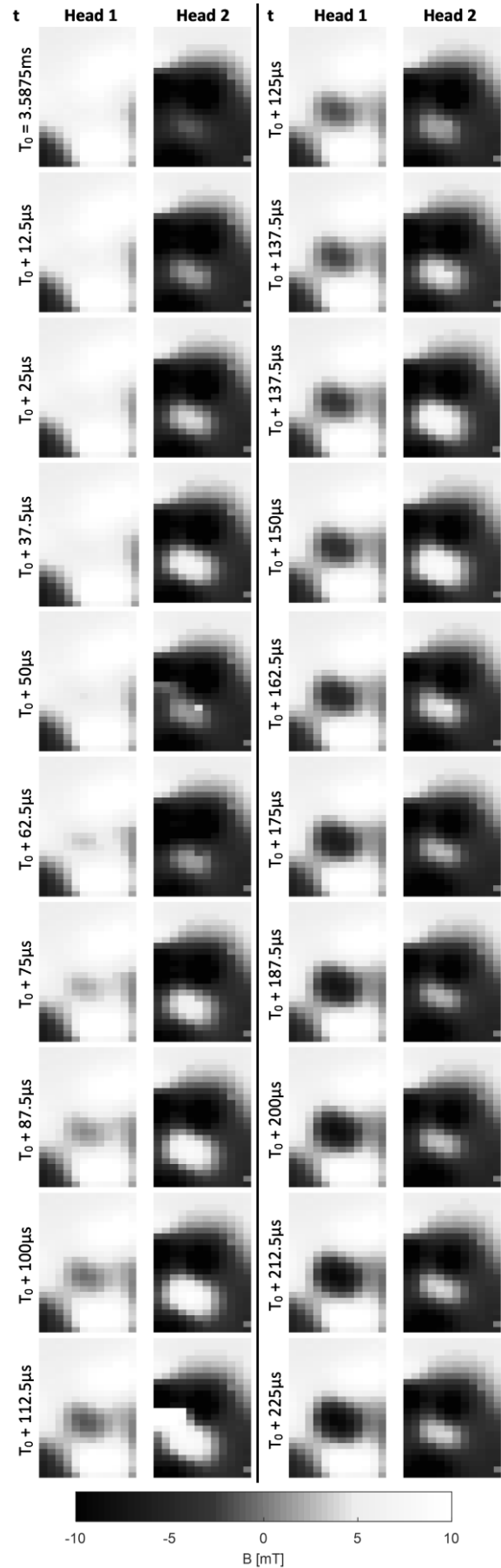


Fig. 6 Magnetic field distribution in z-direction of sensor head 1 and 2 from $t = 3.5875$ ms to $t = 3.825$ ms.

Fig. 7 shows a different timeframe of the same single axis measurement. It is noticeable that the voltage across contact 1 now shows large drops. In the field distributions from sensor head 1 shown here, the voltage drops correlate well with changes in the field. In the magnetic field at $T_1 + 12.5 \mu\text{s}$ a strong deflection of some nearby sensors is noticeable, which occurs at the time of a sudden voltage drop. This voltage drop indicates a very fast arcing process. Therefore, it is possible that sensor IC internal effects or interactions with the circuit board cause the deflections shown in the field. Further investigations are necessary to investigate this.

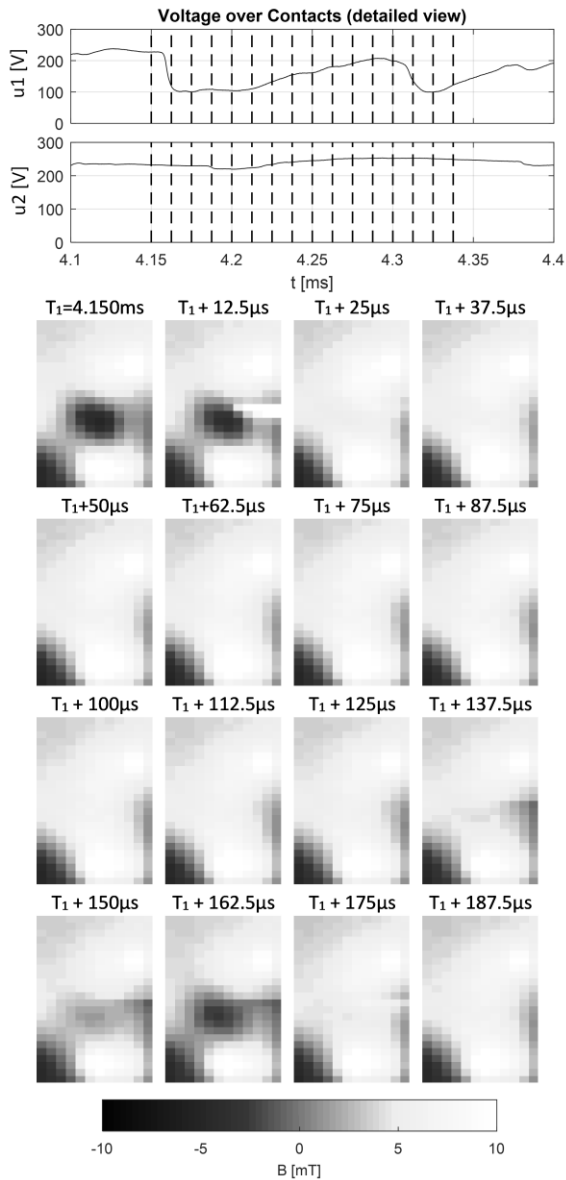


Fig. 7 Magnetic field distribution B_z of sensor head 1 from $t = 4.150 \text{ ms}$ to $t = 4.3375 \text{ ms}$.

4.3 Three Axis Measurement

Fig. 8 and **Fig. 9** show the result of a second measurement. The use of the three axis configuration enables the magnetic flux density to be measured in all directions in space. Here the sensor ICs read the field with a sampling rate of 25 kHz. **Fig. 8** shows current and voltage. Larger peaks and dips in the voltages are limited temporally to about $500 \mu\text{s}$ each. **Fig. 9** shows the field distribution at four successive points in time for each spatial direction, for both sensor heads. A larger change, happening abruptly between two samples, can only be observed on sensor head 1. The two samples were taken once before and once after a drop of voltage u_1 .

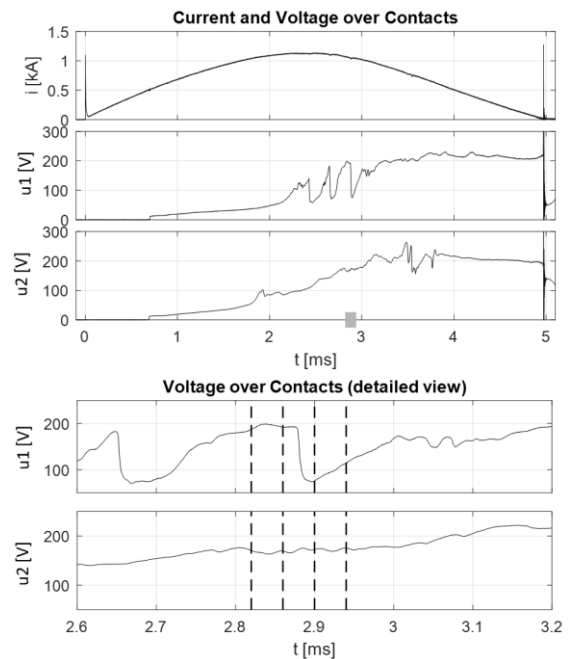


Fig. 8 Result of the three axis measurement (current and voltage).

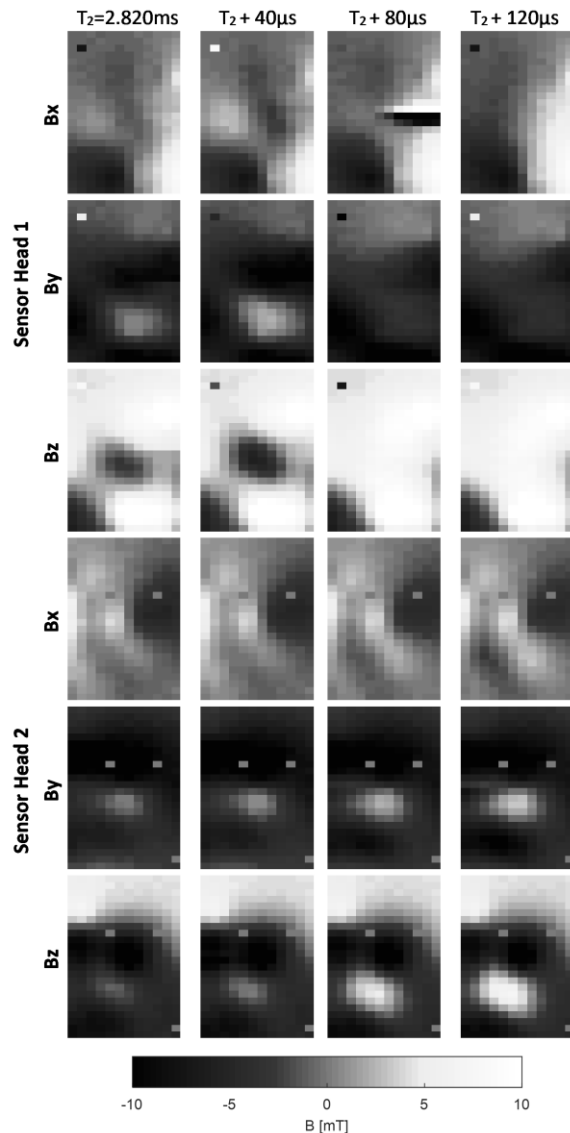


Fig. 9 Result of the three axis measurement (magnetic flux density distribution for the three directions and the two sensor heads).

4 Conclusion

Magnetic field measurements on a circuit breaker during a simulated switch-off process are shown. We used a specially developed magnetic field measuring system. The system is able to detect a field distribution locally resolved with a high sampling rate. Fast as well as slow events showed up in the visualized field distributions. An adaptation of the measuring system to the specific task is possible by using different sensor IC configurations. As shown, a reduction of the sampling rate to 25 kHz allows three axis magnetic field measurements. Using two sensor heads allowed measurements near each contact of the double breaker. The two field distributions measured, correlate well with the corresponding voltage of the contact.

The next step will be a simultaneous measurement of the electric arc with a high-speed optical camera and the magnetic field with the measuring system presented here. Therefore, the presented measuring system shall be verified, supported by numerical magnetic field simulations.

5 Literature

- [1] Beckert, T.; Erven, W.; Meyer, J.: Charakterisierung von DC-Schaltlichtbögen – Löschverhalten und Effekte. 25. Albert-Keil-Kontaktseminar Oct. 2019
- [2] Shin, D.; Golosnoy, I. O.; Bull, T. G.; McBride, J. W.: Experimental study on the influence of vent aperture size and distribution on arc motion and interruption in low-voltage switching devices. 4th International Conference on Electric Power Equipment - Switching Technology (ICEPE-ST), 2017, pp. 213-217
- [3] Mercier, M.; Laurent, A.; Velleaud, G.; Gary, F.: Study of the movement of an electric breaking arc at low voltage. *J. Phys. D: Appl. Phys.* 24, 1991, pp. 681-684
- [4] Laurent, A.; Gary, F.; Cajal, D.; Velleaud, G.; Mercier, M.: A magnetic camera for studying the electric breaking arc. *Meas. Sci. Technol.* 4 1043-9, 1993
- [5] Debollut, E.; Cajal, D.; Gary, F.; Laurent, A.: Study of re-strike phenomena in a low-voltage breaking device by means of the magnetic camera. *J. Phys. D: Appl. Phys.* 34, 2001, pp. 1665–1674
- [6] Brdys, C.; Toumazet, J.; Velleaud, G.; Laurent, A.; Mercier, M.; Servant, S.: Determination of the Re-Ignition Parameters by Means of Magnetic Diagnostic. 1998
- [7] Toumazet, J.; Brdys, C.; Cajal, D.; Gary, F.; Laurent, A.; Arnoux, C.: Influence of the electrical contact materials on the circuit breaker performances. ICEC 2008
- [8] Cajal, D.; Brdys, C.; Toumazet, J.; Gary, F.; Laurent, A.: Current density determination by means of a coupling of two inverse problems using magnetic data. Application to the current transfer phase in a low-voltage model breaker. ICEC 2008
- [9] Reichert, F.; Berger, F.; Rümpler, C.; Stamberger, H.; Terhoeven, P.: Experimental studies of the arc behaviour in low voltage arc rail arrangements supporting numerical simulations. IEEE Holm Conference on Electrical Contacts, 2006, pp. 34-39
- [10] Ghezzi, L.; Piva, D.; Di Rienzo, L.: Current Density Reconstruction in Vacuum Arcs by Inverting Magnetic Field Data. *IEEE Transactions on Magnetics*, vol. 48, no. 8, 2012 pp. 2324-2333
- [11] Qie, S.; Zhang, G.; Xu, Y.; Zhang, Z.; Geng, Y.; Wang, J.: Study of the arc motion characteristics

- of low-voltage circuit breaker based on magnetic sensor array. 4th International Conference on Electric Power Equipment - Switching Technology (ICEPE-ST), Xi'an, 2017, pp. 221-225
- [12] Xu, Y.; Zhang, G.; Dong, J.; Qie, S.; Zhang, Z.; Geng, Y.; Wang, J.: A switching arc plasma measurement experimental system using a magnetic sensor array. 4th International Conference on Electric Power Equipment - Switching Technology (ICEPE-ST), 2017, pp. 872-875
- [13] Dong, J.; Zhang, G.; Geng, Y.; Wang, J.: Current Distribution Reconstruction in Low-Voltage Circuit Breakers Based on Magnetic Inverse Problem Solution Considering Ferromagnetic Splitters. IEEE Transactions on Magnetics, vol. 54, no. 10, 2018, pp. 1-9
- [14] Dong, J.; Zhang, G.; Geng, Y.; Wang, J.: Influence of Magnetic Measurement Modeling on the Solution of Magnetostatic Inverse Problems Applied to Current Distribution Reconstruction in Switching Air Arcs. IEEE Transactions on Magnetics, vol. 54, no. 3, pp. 1-4, March 2018
- [15] Magcam: Magcam MiniCube3D. [online]. Available: <https://www.magcam.com/product/Minicube3D>. [Accessed 05-Jan-2020]
- [16] Matesy GmbH: cmos-magview – the Magnetic Field Camera. [online]. Available: <https://matesy.de/en/products/magnetic-field-visualization/cmos-magview-magnetic-field-camera,-viewer-and-measurement-device>. [Accessed: 05-Jan-2020]
- [17] Fraunhofer IIS: [online]. Available: <https://www.iis.fraunhofer.de/en/ff/sse/sens/leist/magnetfeldsensorik.html>. [Accessed: 05-Jan-2020]

Influence of electrode material properties on the anode phenomena in switching vacuum arcs

Sergey Gortschakow, Leibniz Institute for Plasma Science and Technology, Greifswald, Germany, sergey.gortschakow@inp-greifswald.de

Diego Gonzalez, Leibniz Institute for Plasma Science and Technology, Greifswald, Germany, diego.gonzalez@inp-greifswald.de

Dirk Uhrlandt, Leibniz Institute for Plasma Science and Technology, Greifswald, Germany, uhrlandt@inp-greifswald.de

Mike Boening, PLANSEE Powertech AG, Seon, Switzerland, Mike.Boening@plansee.com

Sabine Boening, PLANSEE Powertech AG, Seon, Switzerland, Sabine.Boening@plansee.com

Abstract

Powder metallurgical manufactured CuCr electrodes made from materials with different Cr morphology have been studied under the AC current load up to 6.5 kA. Special attention was paid to the appearance of various anode modes. Arc dynamics has been acquired by high-speed camera. NIR spectroscopy was used for determination of the time- and space-resolved anode surface temperature. Broadband absorption spectroscopy was applied for determination of the vapour density with respect to different anode modes. Existence ranges of various anode modes, as well as the results of anode surface temperature and Cr I density measurements for two electrode materials are presented and discussed.

1 Introduction

Vacuum interrupters (VI) are environmental friendly alternative to SF₆ switches at medium and high-voltage levels. Applications of this type of circuit breakers are permanently growing and give a rise for continuing research. The high-current operation of VI is accompanied by remarkable metal vapour generation, which can occur also after the current interruption when the electrode surface temperature is high enough. Sufficiently high vapour density promotes the arc reignition in the presence of transient recovery voltage. Control over the density of neutral species close to the current zero crossing is, therefore, of great importance. The anode is the main source of neutral vapour in case of switching vacuum arcs. The anode activity is especially high when the high-current anode modes occur. **Figure 1** presents the typical anode modes observed in the experiment [1, 2]. The appearance of those modes depends on the electrode distance, arc current, arc duration and anode surface temperature [1, 2, 3]. Thus, the intense mode usually is typical for arc ignition stage, the diffuse mode occurs at comparably low currents and the anode spot (type 1 or type 2) has been obtained when the anode surface becomes melted. The last anode mode, the anode plume, was found at the conditions of significant anode melting and appears usually close to the current zero crossing. The plume consists of neutral vapour [2, 4] and moves toward the cathode creating a conducting channel. Therefore, it is highly desirable to avoid the anode spot mode. This

could be achieved by the choice of electrode material, which provides for example lower surface temperature or decreased vapour density.

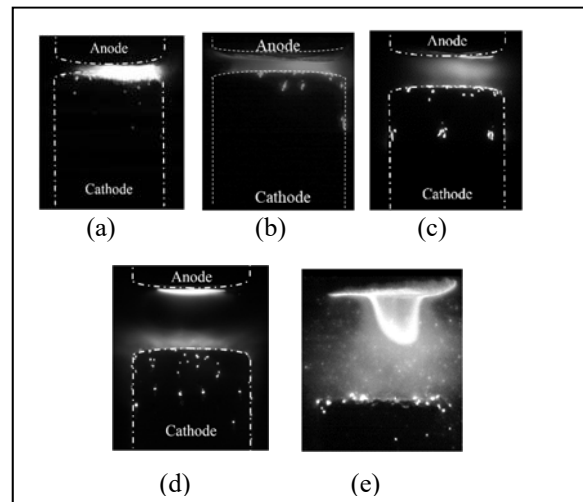


Fig. 1 Images of vacuum arc discharge during different high-current anode modes: (a) intense, (b) diffuse, (c) footpoint, (d) anode spot, (e) anode plume. Anode on the top, cathode on the bottom.

Some research work was done in the past to identify the optimized parameters such as Cr content [5, 6, 7] and particle size [5, 8, 9]. However, the results are not directly comparable due to the differences in both manufacturing parameters and experimental conditions. In order to get a full picture about possible switching behaviour of certain contact material, as much parameters as possible have to be acquired simultaneously.

Powder metallurgical manufactured CuCr electrodes made from materials with different Cr morphology have been studied under typical switching operation conditions. Special attention was paid on the appearance of various anode modes. Existence ranges of various anode modes, as well as the results of anode surface temperature and Cr I density measurements for various electrode materials are presented and discussed.

The comprehensive characterization of high-current anode phenomena was done by simultaneous application of electrical and optical diagnostics which comprises registration of arc voltage and current behaviour, observation of anode mode transitions, measurements of anode surface temperature, as well as determination of vapour density after current interruption. Details are given in Section 2.

2 Experimental setup and diagnostics

2.1 Studied materials

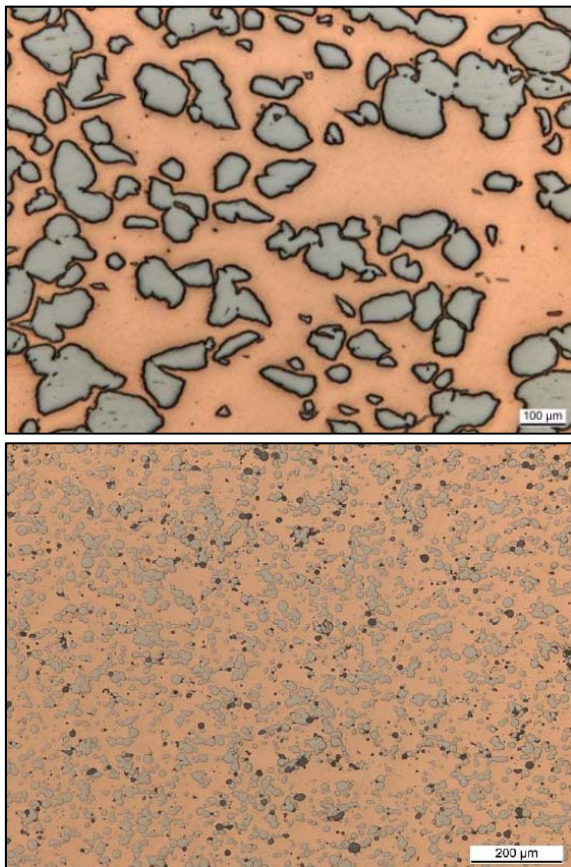


Fig. 2 Images of material structure top – Material I, bottom - Material II, magnification 200x. Grey spots - Chromium, black- Alumina

Two different materials with 25 wt% Cr, but different Cr particle size distributions further denoted as Material I and Material II have been studied. Both

materials are aluminothermic Chromium – material I is a standardised medium grain size powder whereas material II is a finer sieving fraction with a significantly higher level of alumina impurities related to the brittle behaviour of the ceramic component (**Figure 2**). The contact materials were manufactured by powder metallurgy at Plansee Powertech AG. Cu- and Cr-powders were mixed, cold compacted and subsequently sintered under protective atmosphere, slightly below the melting point of Cu.

The electrodes had a diameter of 20 mm and a height of 10 mm.

2.2 Power source

The current pulses were provided by a high-current generator [10]. AC operation with a current range 380 A- 6500 A has been used. The arc duration was varying between 3 and 9 ms.

2.3 Vacuum chamber

A vacuum chamber with optical access described in [10] has been used in the experiments. It contains four optical viewports allowing for simultaneous acquisition of several optical signals. As in the real applications, the electrodes are moved by an actuator with an opening speed of about 1 m/s. For simplification of optical diagnostics the fixed electrode was powered as the anode and the grounded cathode was moving.

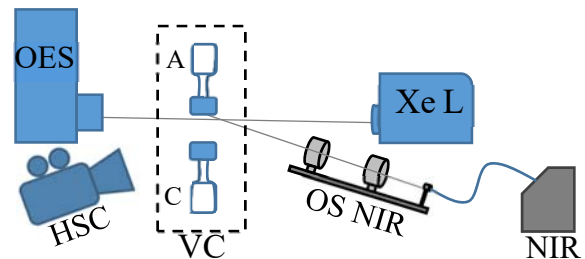


Fig. 3 Schematic representation of experimental setup with a vacuum chamber VC, electrode system (A- anode, C- cathode) and used optical diagnostics: compact NIR spectrometer (NIR) with optical fibre and collimator (OS NIR), system for absorption measurements – Xenon flash lamp (Xe L) and optical emission spectroscopy system (OES), high-speed camera (HSC).

2.3 Applied diagnostics

Electrical and optical diagnostics has been applied for characterisation of arc behaviour. Arc dynamics has been acquired by high-speed camera (**Figure 3**). NIR spectroscopy was used for determination of the time-

and space-resolved anode surface temperature. Broadband absorption spectroscopy was applied for determination of the vapour density with respect to different anode modes.

2.3.1 Electrical diagnostics

Arc current and arc voltage have been measured by corresponding probes. Pearson current monitor model 1330 was used for determination of current evolutions. The arc voltage was acquired by Tektronix high voltage probe P6015A. The signals have been registered by the transient recorder HBM GEN7t.

2.3.2 Arc images

The arc dynamics has been registered by high-speed camera IDT Motion Pro Y4 with a frequency of 10000 fps and exposure time between 2 μ s for high currents and 5 μ s for low currents. Typical arc images are shown in Figure 1.

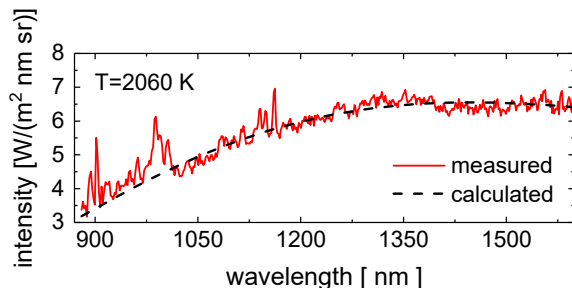


Fig. 4 Example of temperature evaluation using NIR spectrum.

2.3.3 Techniques for surface temperature determination

Determination of the anode surface temperature has been performed by two complementary methods. The NIR spectroscopy was used for measurements of the cooling dynamics after current zero. Using the optical system (OS NIR in Fig. 3) the measuring spot of ca 1 mm in diameter was adjusted to the supposed position of highest temperature. Hamamatsu NIR spectrometer C1142GA with the spectral range 900 – 1650 nm and temporal resolution of 1.5 ms (exposure time 200 μ s) have been used for spectra registration. After the acquisition the spectra have been processed according to the routine presented in [11] in order to determine the temperature. An example of temperature evaluation is shown in **Figure 4**. During the active phase the enhanced high speed camera techniques has been used to acquire the qualitative evolution of the surface temperature. A metal interference filter with the central wavelength of 891 nm and FWHM of 10 nm has been used to block the plasma radiation. The anode surface images were acquired than by a second high-speed camera (IDT MotionPro Y4) with 10000 fps at an exposure time of 100 μ s. The absolute temperature

was calculated by calibration at the position of NIR measurements at the instant close to current zero crossing. More details about used diagnostic techniques can be found in [2].

2.3.4 Absorption spectroscopy

Broadband optical absorption spectroscopy (OAS) was used for determination of chromium vapour density after extinction of arc plasma (after current zero). This technique is based on evaluation of absorption spectra in the wavelength range where the resonance lines of material of interest are present.

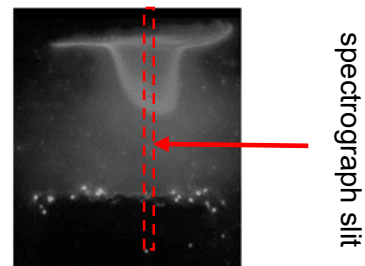


Fig. 5 OAS evaluation position. Anode on the top, cathode at the bottom. The dashed line marks the projection position of spectrograph slit.

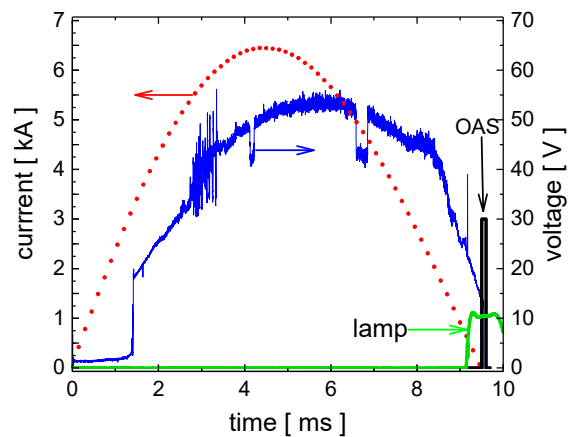


Fig. 6 Signal sequence for OAS diagnostics.

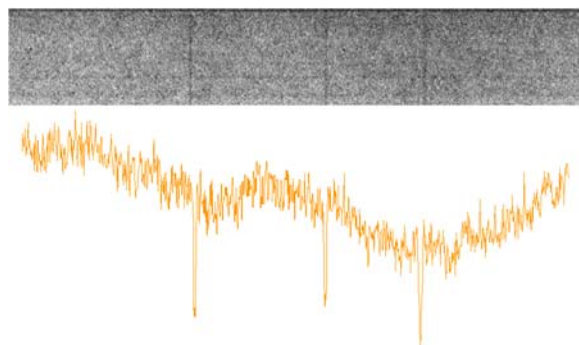


Fig. 7 2D image of the spectrograph in the range of Cr I resonance lines (top) and averaged absorption spectrum (bottom). Cr I lines (from the left to the right) 425.43, 427.78, and 428.97 nm.

A rectangular-shape pulsed high-intensity Xenon lamp is used as a background radiation source. It emits a Planck-like radiation of 12 000 K with a maximum power of 1MW [12]. The Xenon lamp is positioned on the right side window of the vacuum chamber (Fig. 2). Its radiation is directed through the electrode system on the optical axis and coupled to the spectrometer entrance slit that is placed at the opposite window. By using a deflecting and a focusing mirror, the electrode gap is observed along a line perpendicular to the electrode surfaces. The radiation is spectrally dispersed using the Andor Technology Ltd. Shamrock 750 spectrograph (Czerny–Turner type) with a 0.75m focal length equipped by an intensified charge coupled device camera (Andor iStar). The position of the spectrograph slit is presented by dashed-dotted line shown in **Figure 5**.

The method and corresponding theory together with the experimental setup are described in more detail in [2] and [13]. Spectral interval 423–431 nm was chosen to study the Cr I density, which contains spectral lines of different resonance transitions of 425.43, 427.78, and 428.97 nm [14].

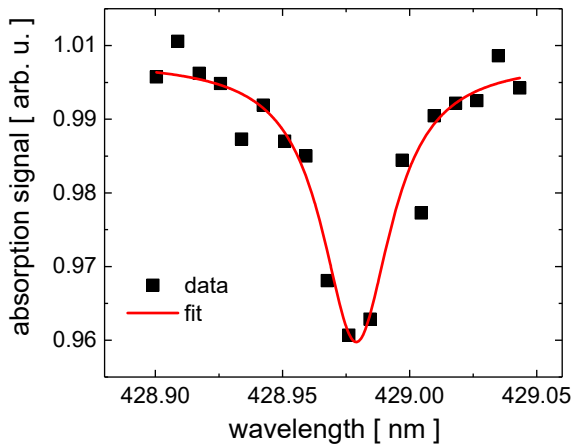


Fig. 8 Example of Cr I 428.9 nm line fit procedure.

Figure 6 shows the operation sequence applied for OAS measurements. Absorption spectra have been acquired immediately after current zero crossing with a delay about 100 μ s, which was necessary for plasma decay. Xe lamp started about 9.5 ms and reached its maximum intensity close to the instant of acquisition time. An example of high-resolution spectra is presented in **Figure 7**. The anode and cathode are at the top and bottom of the figure, respectively. The light grey background corresponds to the continuum radiation emitted by the Xenon lamp. Three darker narrow vertical lines shown on the top of Fig. 4 correspond to the absorption by three resonance lines of Cr I at 425.43, 427.78, and 428.97 nm. The relative intensities of the plasma transmission and the background light source integrated along the wavelengths are shown in Fig. 6 (bottom). The signal is averaged over a horizontal stripe of approximately 5 mm in the axial direction in the front of anode.

Figure 8 presents an example of data processing for the Cr I line 428.9 nm. The preparation routine includes dark signal correction and Lorentzian fit of obtained signal. Finally, the area under the absorption signal was determined, which gives the value of optical depth τ . The lower state population density N_l in the absence of plasma radiation (after current zero) can be determined from the optical depth as follows [2]:

$$\int_0^{\infty} \tau(\lambda) d\lambda = \int_0^{\infty} \ln\left(\frac{I_0}{I}\right) d\lambda = \frac{\pi e^2 \lambda_0^2 D N_l f_{lu}}{4\pi \epsilon_0 m_e c^2} \quad (1)$$

Here, ϵ_0 is the permittivity of free space, m_e is the electron mass, c is the speed of light in vacuum, e is the elementary charge, f_{lu} is the oscillator strength, λ_0 is the center wavelength of the considered transition, I_0 denotes undisturbed radiation the background light source, I is the radiation measured after absorbing material and D is the absorption length.

Detailed information regarding the broadband absorption spectroscopy method and spectroscopic constants for the selected lines, including wavelength, transition probability, and oscillator strength can be found in [2].

2.4 Electrode surface conditioning

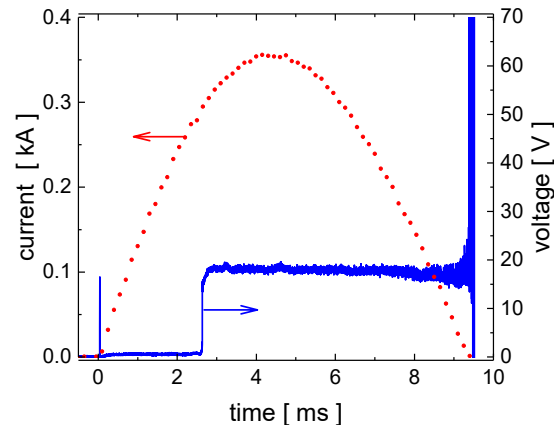
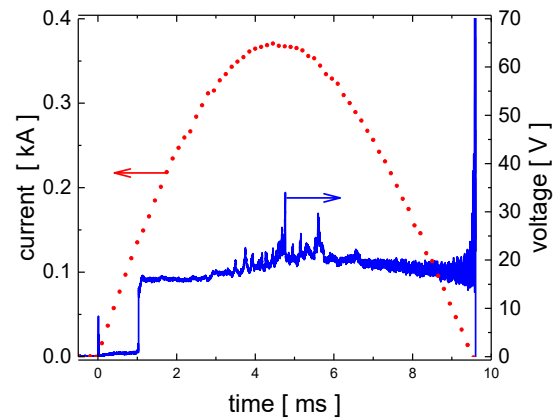


Fig. 9 Example of arc current and voltage behaviour during the conditioning cycle. Top – new electrodes, bottom - conditioned electrodes.

Prior to the measurements the electrode surface must be cleaned from adsorbed particles, the lubricant rests of machining processing, dielectric layers, water etc. The cleaning procedure was performed in several steps. First, the electrodes were processed in ultrasonic bath with distilled water and grease removing fluid. In the next step, the surface was cleaned by acetone and isopropanol. Finally, after the mounting inside the vacuum chamber, low-current arc discharges were applied for conditioning of the surface.

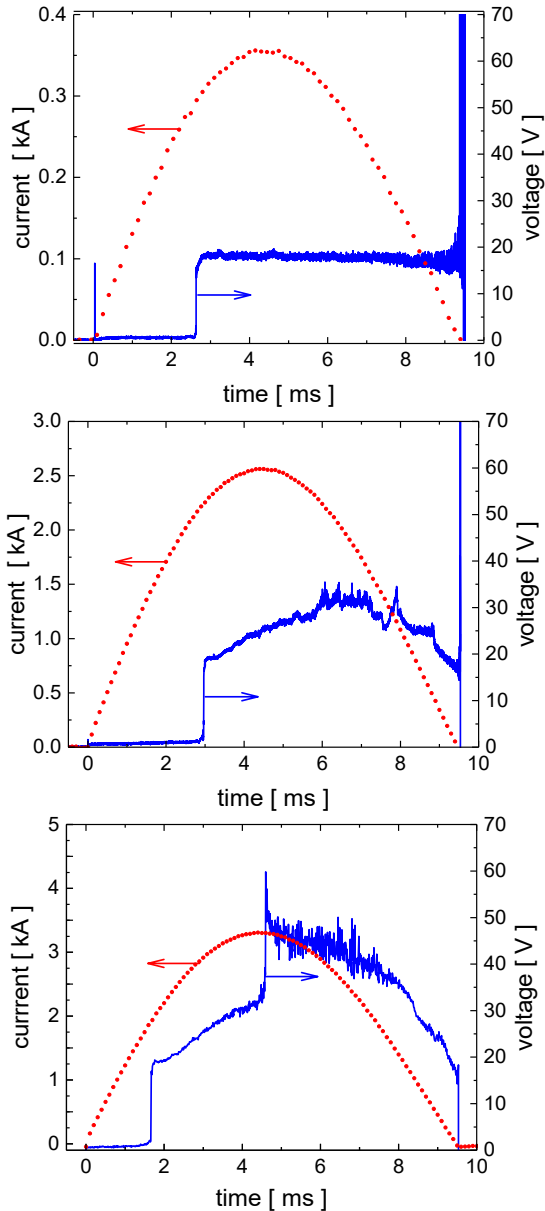


Fig. 10 Characteristic voltage behaviour in case of diffuse anode attachment (top), footpoint or anode spot 1 mode (middle) and anode spot type 2 (bottom).

Figure 9 shows the temporal evolution of the current and voltage during the conditioning cycle. The stepwise increase of the arc voltage denotes the instant of the electrode separation (arc ignition). Typical arc duration was between 6.5 and 9 ms. First shots with the new electrodes show certain instabilities in the voltage

behaviour which are connected with stochastic spot formation on the electrode surface at the positions of adsorbed impurities. The high-speed videos confirm the unstable arc root positions in this case. After typically 10 shots the voltage curve becomes more smooth indicating the end of conditioning process. The arc glow becomes more diffuse and the cathode spots are uniformly distributed over the surface.

3 Results and discussion

3.1 Anode modes existence range

Distinguishing between different high current anode modes is based on evaluation of the arc images and the shape of the arc voltage. **Figure 10** shows three characteristic cases of arc voltage. A diffuse arc attachment is accompanied by a stable voltage course. Small voltage fluctuations (from instants after 6 ms in Fig. 10 middle) point to appearance of localized arc attachment, which is characteristic for footpoint mode or anode spot type 1. Finally, a pronounced voltage jump occurs when an anode spot of type 2 is formed (instant of 4.3 ms in Fig. 10 bottom).

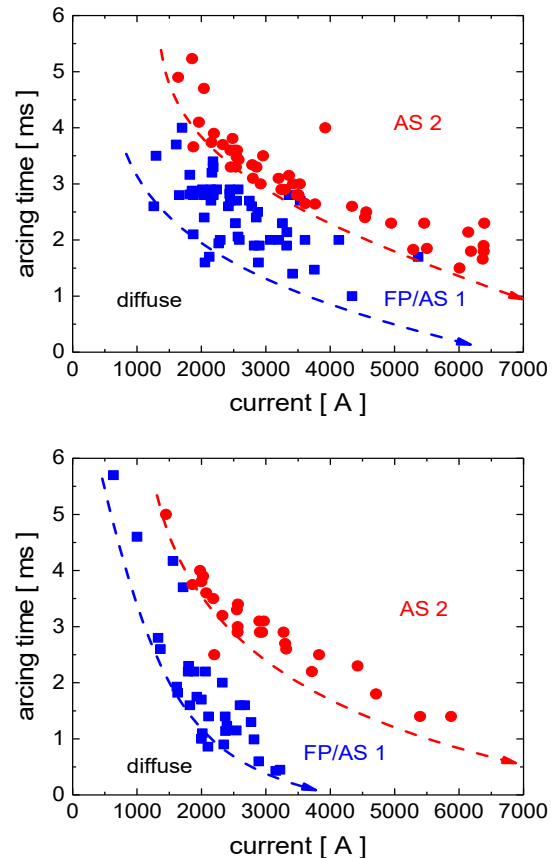


Fig. 11 Anode mode existence diagrams for Material I (top) and Material II (bottom). Dashed curves show supposed boundary between different modes: diffuse, footpoint/anode spot 1 (FP/AS 1), anode spot type 2 (AS 2).

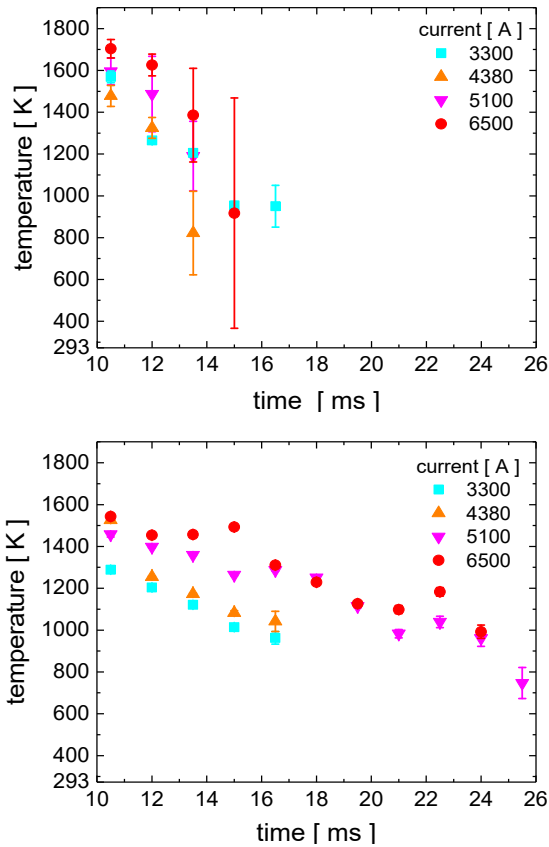


Fig. 12 Evolution of anode surface temperature obtained from NIR measurements for Material I (top) and Material II (bottom).

The electrodes made of both materials and conditioned according to the routine described in Sec. 2.4 have been loaded by variable current in the range 380 A – 6500 A between 1 and 3 times. During the analysis of high speed images and voltage courses the time of first appearance of corresponding mode after the arc ignition and related current have been evaluated. Since during a single shot various modes transition can occur, some shots give the information for several pairs current/arc duration. The results of this analysis are presented in **Figure 11**. The footpoint mode is usually a forerunner for the anode spot type 1 mode. In many cases, it is also difficult to identify the exact instant (and current) of mode transition between footpoint and anode spot type 1. Therefore, corresponding cases are summarized together in the diagrams, so that three typical existence ranges are distinguished. The diffuse attachments occurs when the current is rather low at long arc duration or also in the cases when the arc duration is short and the current is high. An increase of the current is accompanied by a mode change to footpoint or anode spot type 1 mode. In the case of Material II this transition takes place at lower current values when the arc duration is long. Furthermore, in the experiments with a short arc duration the diffuse arc for Material II was never obtained for the currents higher than 3000 A. Also, the transition to the anode spot type 2 mode requires less current at the same arc

duration in case of Material II. In general, the arc constriction occur at lower current resp. lower arc duration for Material II comparing to Material I.

3.2 Surface temperature

Temporal evolutions of anode surface temperature after current zero crossing are presented in **Figure 12**. Initial temperature varies between about 1300 K and 1700 K. Its value increases when the maximum arc current is higher. Material I shows higher starting temperatures at comparable experimental conditions. In case of Material II the temperature decay is nearly linear with time. The signals for Material I exhibit a strong noise for currents higher than 3300 A due to significant anode activity in form of anode plume. The anode plume was not obtained in case of Material II at the present experimental conditions. Despite to lower initial temperature Material II needs longer time for cooling. After about 10 ms the temperature decreases by about 25% of its value at current zero. Thus, the expected predicted time to reach the room temperature is about 20 - 30 ms in case of Material I and about 35 - 45 ms in case of Material II.

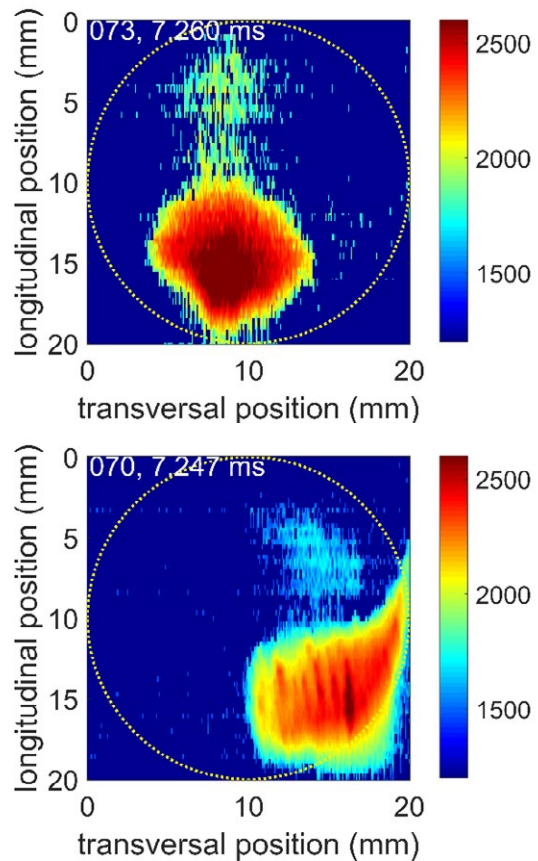


Fig. 13 2D surface temperature plots for the instant 7.25 ms in case of maximum current of 6500 A. Top – anode made from Material I, bottom – Material II.

Figure 13 presents a comparison of 2D anode surface temperature distribution at the instant 7.25 ms in case

of maximum current of 6500 A for both studied materials. In general, the temperature in case of Material II was lower also during the active phase of the discharge. For the presented instant, the maximum temperatures were about 2430 K and 2280 K for case of Material I and Material II correspondingly. Such behaviour could be partially explained by increased spot area in comparison to Material I. The anode spots on the anode made from Material II tends to occupy the lateral surface, while the spot in case of Material I had the position, which approximately coincides with the ignition point of the arc.

3.3 Vapour density after CZ

Results of absorption measurements for Cr I vapour density after current zero crossing are shown in **Figures 14 and 15**.

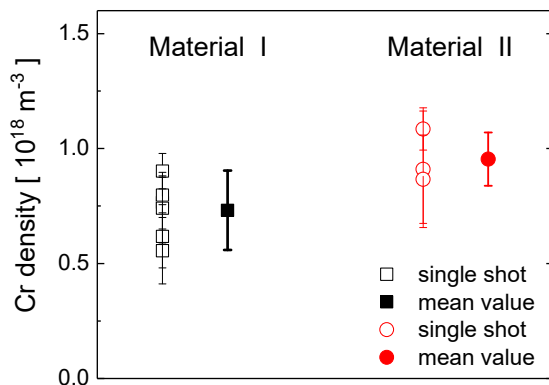


Fig. 14 Cr I density close to the instant of current zero crossing in case of maximum current of 6500 A. Empty symbols – single shot results; full symbols - from several measurements.

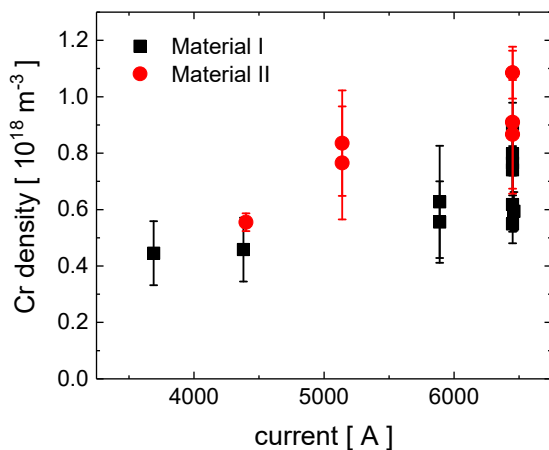


Fig. 15 Dependence of Cr I density close to the instant of current zero crossing on the maximum arc current.

Due to low spectral intensity the acquisition of only one spectrum per shot was possible. Therefore, several measurements at similar experimental conditions have been performed.

Despite the lower surface temperature, the vapour density is higher in case of Material II. It amounts to about 10^{18} m^{-3} , while the value for Material I is about $7.4 \times 10^{17} \text{ m}^{-3}$.

The vapour density remains higher for Material II in the current range 3500 – 6500 A (Figure 15). For the lower current values the sensitivity of AOS system was not enough to resolve the absorption spectra. Higher evaporation rate in case of Material II is probably caused by finer Cr grain structure and lower thermal conductivity which is influenced by smaller Cr and alumina particles distributed in the copper matrix [15, 16] promoting a thinner and broader melting bath.

4 Conclusions

Powder metallurgical manufactured CuCr electrodes made from materials with different Cr morphology have been studied under typical switching conditions. Existence ranges of various high-current anode modes were determined. Material I shows a broad range of diffuse attachment, while the arc constriction and formation of anode spots in case of Material II takes place at lower currents and shorter arc duration. Anodes made from Material I show higher surface temperature and more constricted anode spots. The surface temperature in case of Material II is lower, but the parameters as spot area, cooling time and Cr I vapour density after current interruption are higher, which make this material less favourite for switching applications at considered experimental conditions.

5 Literature

- [1] Miller, H. C.: Anode modes in vacuum arcs: Update, IEEE Trans. Plasma Sci., Vol. 45, No. 8, Aug. 2017, pp. 2366 – 2374
- [2] Khakpour, A.; Popov, S.; Franke, St.; Kozakov, R.; Methling, R.; Uhrlandt, D.; Gortschakow, S.: Determination of Cr density after current zero in a high-current vacuum arc considering anode plume. IEEE Trans. Plasma Sci. Vol. 45, No. 8, Aug. 2017, pp. 2108–2114
- [3] Kimblin, C. W.: Anode Voltage Drop and Anode Spot Formation in dc Vacuum Arcs. J. Appl. Phys. Vol. 40, No. 4, Mar. 1969, pp.1744-1752
- [4] Batrakov, A. V.; Popov, S. A.; Schneider, A. V.; Sandolache, G.; Rowe, S. W.: Observation of the Plasma Plume at the Anode of High-Current Vacuum Arc, IEEE Trans. Plasma Sci. Vol. 39 2011, pp. 1291 - 1295
- [5] Rieder, W. F.; Schusseck, M.; Glätzle, W.; Kny, E.: The Influence of Composition and Cr Particle Size of Cu/Cr Contacts on Chopping Current, Contact Resistance, and Breakdown Voltage in Vacuum Interrupters. IEEE Trans. Compon.,

- Hybrids, *Manuf. Technol.* Vol. 12, 1989, pp. 273-283
- [6] Li, W.; Thomas, R. L.; Kirkland Smith R.: Effects of Cr Content on the Interruption Ability of CuCr Contact Materials. *IEEE Trans. Plasma Sci*, Vol. 29, 2001, pp. 744-748
- [7] Xiu, S.; Yang, R.; Xue, J.; Wang, J.; Wang, J.: Microstructure and properties of CuCr Contact Materials with Different Cr Content. *Trans. Nonfer. Met. Soc. China* 21, 2011, pp.389-393
- [8] Wang, Y.; Ding, B.: The Preparation and Properties of Microcrystalline and Nanocrystalline CuCr Contact Materials. *Trans. Compon., Packaging, Manuf. Technol.*, Vol. 22, 1999, pp. 467-472
- [9] Devismes, M.; Schellekens, H.; Picot, P.; Olive, S.; Henon, A.; Ponthenier, J.; Boutillier, M: The Influence of CuCr25 Characteristics on the Interruption capability of vacuum Interrupters. *IEEE, XXIst Intern. Symp. on Discharges and Electrical Insulation in Vacuum, Yalta, Crimea, Sept. 2004*, pp.359-362
- [10] Methling, R.; Gorchakov, S.; Lisnyak, M.; Franke, St.; Khakpour, A.; Popov, S.; Batrakov, A., Uhrlandt, D.; Weltmann, K.-D.: Spectroscopic investigation of high-current vacuum arcs. in *Proc. 26th Int. Symp. Discharges Elect. Insul. Vac.*, Sep. 2014, pp. 221–224.
- [11] Methling, R.; Steffen Franke, St.; Gortschakow, S.; Abplanalp, M.; Sütterlin, R.-P.; Delachaux, Th.; Menzel, K. O.: Anode surface temperature determination in high current vacuum arcs by different methods. *IEEE Trans. Plasma Sci.*, Vol. 45, No. 8, Aug. 2017, pp. 2099 - 2107
- [12] Günther, K.; Radtke, R.: A proposed radiation standard for the visible and UV region, *J. Phys. E* Vol. 8, 1975, pp. 371 – 376
- [13] Gortschakow, S.; Khakpour, A.; Popov, S.; Franke, St.; Methling, R.; Uhrlandt D.: Determination of Cr density in a high-current vacuum arc considering anode activity. *Plasma Phys. Technol.*, Vol. 4, No. 2, 2017, pp. 190–193
- [14] Gortschakow, S.; Popov, S.; Khakpour, A.; Schneider. A.; Methling, R.; Franke, St.; Uhrlandt, D.: Cu and Cr density determination during high-current discharge modes in vacuum arcs. in *Proc. 28th Int. Symp. Discharges Elect. Insul. Vac.*, Greifswald, Germany, Sep. 2018, pp. 181–184
- [15] Klinski-Wenzel, K.; Kowanda, C.; Rettenmaier, T.; Heilmaier, M.; Hinrichsen, V.; Mueller, F. E. H.: Microstructural Features of Switched Cu-Cr Surface Melt Layers. *Proc. of 18th Plansee seminar*, 2013, pp. 1-10 (available at https://www.plansee-com.azureedge.net/fileadmin/user_upload/RM50_Microstructural_Features_of_Switched_Cu-Cr_Surface_Melt_Layers.pdf)
- [16] Hauf, U.; Feilbach, A.; Böning, M.; Heilmaier, M.; Hinrichsen, V.; Müller, F. E. H.: Investigation of the Heat Affected Volume of CuCr Contact Material for Vacuum Interrupters. *Proc. XXVII ISDEIV, Souzhou, China, Sept. 2016*, pp. 137-140

Effect of contact materials process and test features on welding tendencies of vacuum interrupters during short time current test

Anthony Papillon, Jean-Pierre Meley, Jean-Pierre Gauthier, Schneider Electric, Grenoble, France, anthony.papillon@se.com

Abstract

Single phase short time current test at 40 kA were performed on various vacuum interrupters with different test parameters. Welding force between contact was measured by tensile test means. The influence of contact material process and contact structure were investigated. Furthermore, the influence of certain test parameters link to the circuit breaker design were also analysed.

1 Introduction

Vacuum interrupters are used in the whole range of medium voltage switchgear. The used contact material depends mainly on the application (i.e. contactor, switch, circuit breaker). For circuit breaker application Cu-Cr pseudo alloy are used with a Cr content between 25 and 50 wt%. Cu-25wt%Cr is commonly known for its very good short circuit performances [1] [2] [3]. However, materials with such amount of copper have a rather high welding tendency due to low melting point of copper compared to temperature encountered during arcing phase. Therefore, vacuum circuit breaker drive should deliver a shock energy high enough to break all type of welds. Welding can occur on two type of tests:

- Making on short circuit current. The prearc before contact touch creates liquid copper that will solidify once contact are closed and can create strong welds
- Short time current test (STC) where short circuit current is maintained for several seconds (between 2 and 4 s depending on the standards). During the first ms, there is a first high peak current that could reach 2.5 to 2.6 times the short circuit current. During this peak the current constriction at contact spot location (Figure 1) creates a repulsion force. This repulsion force is well known and considering the simplified geometry of Figure 1, it is given by [4] [5] :

$$F_B = \frac{\mu_0 i^2}{4\pi} \log\left(\frac{R}{a}\right) \quad (1)$$

Where μ_0 is the permeability of vacuum, i the current, R the contact radius and a , the estimated spot

radius. This spot radius can be calculated from Holms contact law [6] and gives:

$$a = \sqrt{\frac{F}{H\pi}} \quad (2)$$

Where F is the applied contact force and H the material hardness.

This model gives a first rough estimation of repul-

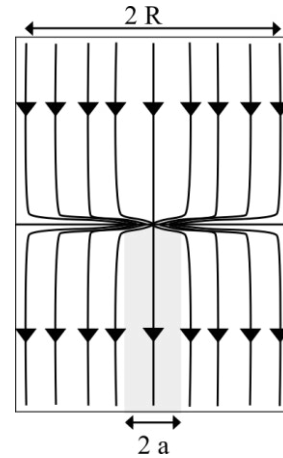


Figure 1 Illustration of a simplified model of two cylindrical conductor of radius R in contact with the force F applied creating the central contact spot of radius a

sion force. However, this simple model doesn't consider the effect of some parameters. For example, Kulas et al. estimated the effect of an off-centre contact spot on the repulsion force [7]. Approaching the conductor edge, the calculated repulsion force increases up to more than 15 % of the value in the centre. Other parameters such as the contact materials nature and the contact geometry to magnetically influence the arc behaviour can also have significant effect on this value.

This work focusses on the experimental study of several key parameters of the Vacuum Circuit Breaker (VCB) design on this repulsion force. The effect of the contact manufacturing process, the arc control type (Axial Magnetic Field: AMF vs

Radial Magnetic Field: RMF) and the use of a damping system on the test bench were analysed, discussed and compared to the above-mentioned simple model (equation (1)).

2 Materials and method

2.1 Contacts and vacuum interrupter (VI) preparation

Two type of electrical contacts with same composition (25wt%Cr, rest Cu) were obtained from two processes:

- Solid state sintering (SSS)
- Vacuum casting (VC)

Those processes lead to different microstructures and properties (Figure 2 and Table 1)

Solide state sintering consist in powder mix compression and sintering close to copper melting point (< 1358 °K). The Cu matrix and the Cu/Cr interphase contain some porosity. Vacuum casted microstructure consists in dendritic formations of Cr inside a Cu matrix. The Cr grain size is quite smaller (around 20 μm) compared to the one of sintered Cu/Cr contacts (50 to 100 μm). Its porosity level is very low as casting defects are well controlled.

	SSS	VC
Porosity (%)	$2 < P < 5$	< 1
Conductivity (MS/m)	30	30
Hardness (Hv)	60-80	90-100

Table 1 Material properties of solide state sintered and vacuum casted electrical contacts

Vacuum interrupters (VI) used for the test campaign are commercial references for $31,5$ kA I_{sc} / $17,5$ kV Ur. VIs with radial magnetic field (RMF) and axial magnetic fields (AMF). Contacts diameter is 60 mm for both cases. Figure 3 shows the geometry of both types of

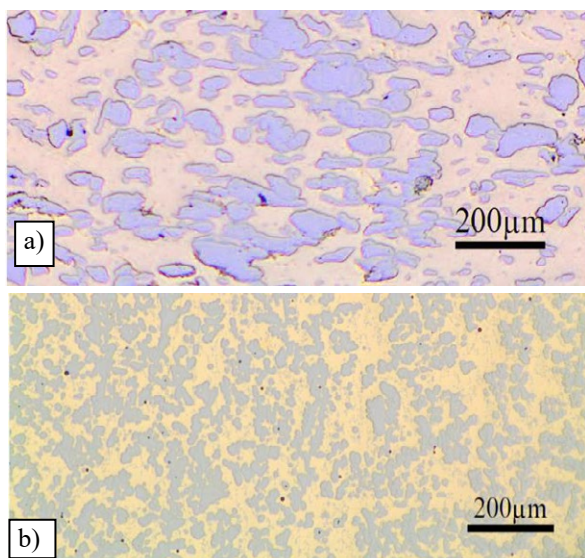


Figure 2 Microstructure of Cu25%Cr contact materials a) solid state sintered; b) vacuum casted

AMF and RMF contacts. VI were assembled by brazing in a vacuum furnace. The contact surfaces were subsequently conditioned by doing several low voltage/3 kA breaking operations. No voltage conditioning was applied as no high voltage withstand is required during STC tests.

2.2 Power test conditions

A low voltage capacitor bench was used to generate the 95 kA of the test at 50 Hz.

2.3 Test bench

VIs were mounted on a specific test bench shown in Figure 5. Current conduction is done using sliding contacts not inducing any additional electrodynamic force during peak current tests. Contact force is applied with a mechanical jack and controlled with a piezoelectric stress sensor ranging between -1000 daN (traction) and $+1000$ daN.(compression). A contact pressure spring is used to be in mechanical conditions close to the one encountered in vacuum circuit breakers. The voltage drop on the VI is measured during the current flow.

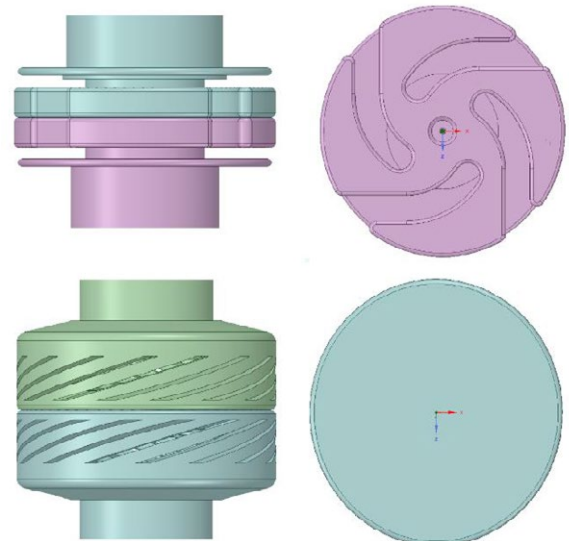


Figure 3 Contact designs a) RMF with helix shape contac tip and contact screens, b) AMF with disk contact ship and "coil" to create the axial magnetic field

Any contact separation can be detected as the arc resistance is much higher than contact resistance. Therefore, during the repulsion, a voltage pulse can be observed as shown in Figure 4.

2.4 Tensile measurement

Tensile measurements were done using the piezoelectric stress sensor on the test bench. Tensile force was applied using the mechanical jack.

3 Results and discussion

Test were done three time at each contact force value starting by the higher value (i.e. lower risk of repulsion) and decreasing of 50 daN until popping was de-

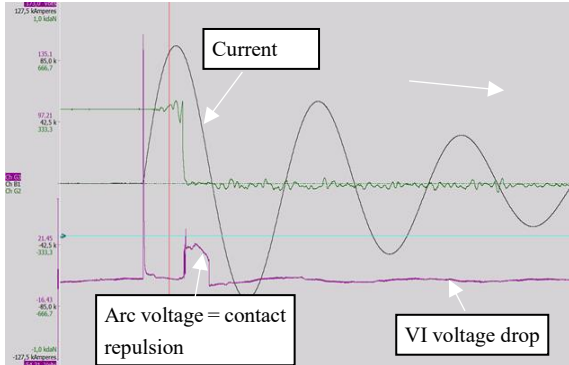


Figure 4 Example of oscillogram of peak current test where repulsion occurred

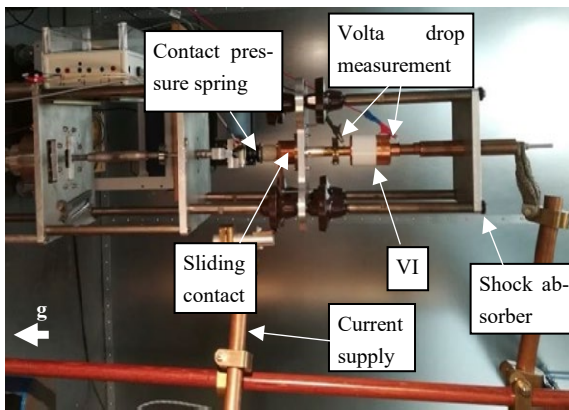


Figure 5 Picture of the test bench used for the two test campaigns

tected or welding force was over 1000 N (sensor limit). Repulsions is indicated by a cross while no repulsion is indicated by a dot (Figure 6). We can observe that no repulsion occurred at contact force above F_B ($F_B \sim 2300$ daN for 95 kA). First welding and repulsion occurred at 200 daN. This is in accordance with the estimated repulsion force from the model mentioned in the introduction.

3.1 Effect of contact material

Comparing contact materials, we could expect larger repulsion force with casted contact than with sintered one as its hardness is 20-40 % lower and F_B is proportional to $\log(H)$. First welding occurred at the same contact force value. However, repulsion occurred at higher contact force with casted contact compared to sintered (Figure 6). This is therefore in accordance with our expectations. Welding force was much higher for sintered contact, but this is due to a longer repulsion time (3,8 ms vs 1,0 ms). Indeed, we could also expect

a higher unwelding force of casted contact. Due to its porosity content and bad interface between Cu and Cr, sintered contact should have a lower fracture strength than casted contact. Therefore, when a strong weld occur, sintered contact requires less energy to create a fracture in the bulk than casted contact. Microstructure of broken welds in the bulk of sintered materials and in the welding interface of casted materials can be found on Böhm et al. work [8] which is in accordance with this expectation.

3.2 Effect contact geometry

From Figure 6, we can see that VI using AMF arc control show no repulsion at 200 daN. Repulsion and welding only occur at 150 daN. This can be explained by the attraction of the coils which increase the contact

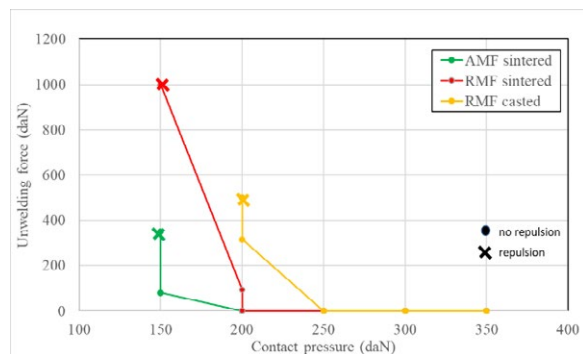


Figure 6 Unwelding force vs contact force of RMF Cu25Cr contact from two process and of AMF contact

pressure during peak current. FEA transient simulations were done at peak current in order to estimate the difference of repulsion force between AMF and RMF. Simulations were done with supposed same contact spot size calculated with Holm formula. However, dif-

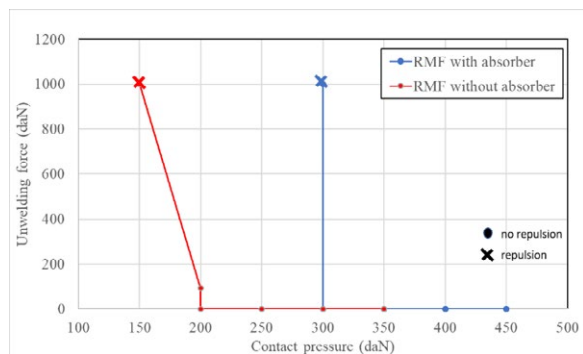


Figure 2 Unwelding force vs contact force of VIs with RMF arc control with and without shock absorber

ferent spot location (edge for AMF vs close to centre for RMF) were used as arc control geometry are different. Repulsion force was found around 15 % inferior with AMF compared to RMF. Therefore, the repulsion force for AMF is just below 200 daN which is in accordance with our experimental observations.

3.3 Effect of bench mechanical damper

Two configurations of test bench were also compared. One with a shock absorber (10 mm thick rubber plate as shown in Figure 5) placed between the top of the bench and the columns, initially used to reduce bouncing. The other configuration without shock absorber. From Figure 2, repulsion is observed at higher contact force and above the calculated repulsion force. High-speed camera was used to detect bench deformation during the test. Deformation of the rubber was observed during the peak current allowing a gap between contacts and leading to contact repulsion. The repulsion force is supposedly not above the 300 daN applied contact force but it is high enough to deform the rubber and create a gap between the contact. The contact force where repulsion is observed is here twice the value without absorber. Its effect is therefore larger than the one of contact material or arc control type. It shows that the circuit breaker should be rigid enough to avoid this phenomenon at high contact force.

4 Conclusion

This study focused on the effect of several parameters on the repulsion force during peak current. It appeared that with the same material composition, there is only a slight difference of behaviour between vacuum casted and solid-state sintered Cu-25wt%Cr materials. However sintered material might be a better choice as they require a slightly lower contact force and mainly because the unwelding force should be lower than with casted material.

It was also observed that using RMF arc control is leading to a higher repulsion force than AMF arc control with embodied coils. Those coils are attracting each other during the peak current which increases the contact force.

The most noticeable effect was finally the mechanical properties of the CB. A large rigidity is needed to avoid any deformation that could lead to contact separation. However, this goes against the required damping of the circuit breaker structure in order to limit contact bouncing during CB closing. Therefore, developing a vacuum circuit breaker is a matter of finding the good balance between those parameters.

Despite its simplifying assumptions, the model mentioned in the introduction is in accordance with the experimental observation of this work. It is therefore a useful tool to estimate the needed contact force depending on the short circuit current rating.

5 Literature

[1] E. Huber, K. Fröhlich und R. Grill, «Dielectric recovery of copper chromium vacuum interrupter

contacts after short-circuit interruption,» *IEEE Transactions on Plasma Science*, Bd. 25, Nr. 4, pp. 642-646, 1997.

- [2] W. Li, R. Thomas und R. Kirkland Smith, «Effects of Cr content on the interruption ability of CuCr contact materials,» *IEEE Transactions on Plasma Science*, Bd. 29, Nr. 5, pp. 744-748.
- [3] J. Sato, T. Watanabe, T. Seki, H. Somei und M. Honma, «Effect of Cr content in CuCr contact material on the interrupting ability of VCB,» *Proc. of ECASA, Xi'an*, 1997.
- [4] A. Snowdon, «Studies of electrodynamic forces occurring at electrical contacts,» *AIEE Transactions*, Bd. 80, pp. 24-28, 1961.
- [5] D. Piccoz, P. Teste, R. Andlauer, T. Leblanc und J. Chabrierie, «The repulsion of electrical contact crossed by short circuit currents,» *Proceeding of the 44th IEEE Holm Conference on Electrical Contacts*, pp. 129-135, 1999.
- [6] R. Holm, *Electric contact*, Berlin: Springer-Verlag, 2000.
- [7] S. Kulas, L. Kolimas und M. Piskala, «Electromagnetic forces on contact,» *43rd International Universities Power Engineering Conference*, 2008.
- [8] M. Böhm, P. Morin, T. Schmörlzer, D. Gentsch und R. A. Simon, «A simple test method for the welding degradation of arcing contacts,» *27th International Conference on Electrical Contacts*, 2014.

The effect of WC/Ag contact material composition on chopping currents in MV contactors

Lavinia M. Scherf¹, Ralf-Patrick Sütterlin¹, Moritz Böhm², Thierry Delachaux¹, Thomas Schmölzer³

¹ ABB Schweiz AG, Baden-Dättwil, Switzerland

² ABB Power Grids Switzerland AG, Zürich, Switzerland,

³ ABB AG, Ratingen, Germany

Email: lavinia.scherf@ch.abb.com

Abstract

Vacuum contactors often employ tungsten carbide-silver (WC/Ag) contact materials due to their low chopping currents and high welding resistance. For cost reasons, it would be desirable to replace silver by copper or other metals with high electrical conductivity. This, however, decreases the vapor pressure of the contact material which generally results in increased chopping currents. In this work, various material compositions with lower silver contents were prepared and their current chop behaviour was tested inside commercial vacuum interrupters. Statistical evaluation of the test results shows that material compositions with increased tungsten carbide content or containing a finely dispersed additive present lower chopping currents than expected based on their silver contents. Vacuum interrupter resistivity measurements suggest that the tested contact material formulations do not impact contact resistance significantly. These findings show that clever material design enables silver-reduced WC/Ag materials which still provide the low chopping currents necessary for application in vacuum contactors.

1 Introduction

Vacuum contactors are typically used to switch electric motors and to control electrical circuits with a high number of operations. Unlike vacuum interrupters (VI) for circuit breakers, this application requires a much larger number of operational cycles. WC/Ag composite materials are typically used as contact materials, in which WC provides the high welding resistance and Ag the low contact resistance required for the long device lifetimes [1].

A typical phenomenon in vacuum interruption is current chopping: when the AC current approaches current zero, the vacuum arc becomes unstable and then extinguishes suddenly. In vacuum contactors, large chopping currents I_c are undesirable as they can induce large voltage surges that may cause dielectric failure of downstream motors or transformers in the grid. Actual chopping currents I_c depend heavily on the contact material and vary with current level and the surge impedance of the circuit [2]. In addition, they are statistically distributed.

WC/Ag contacts exhibit very low I_c , enabling vacuum contactors to switch loads without any additional surge protection devices. It is well established that this favourable performance originates from low thermal conductivity and high vapor pressure of the material [3] [4].

In contact materials with a low thermal conductivity, the arcing heat is dissipated from the cathode spot more slowly, providing more evaporated contact material to keep the low current arc stable. In WC/Ag contacts, WC exhibits the lower thermal conductivity. Thus, increasing the WC:Ag ratio in VI contacts was observed to correlate with a lower chopping current [5] [6].

Similarly, high vapor pressure materials stabilize low current arcs by providing evaporated contact material at lower temperatures. Thus, pure Ag metal exhibits much lower I_c than Cu metal due to its higher vapor pressures, while thermal conductivities are similar [7] [8].

However, due to the high and volatile price of silver, more cost-effective alternatives to WC/Ag are being considered. From a technical and economic perspective, only Cu is suitable as a conductive alternative for Ag. Thus, WC/Cu contacts have been tested in vacuum contactors by Behrens and Temborius [6] [9]. They both found that WC/Cu exhibits significantly larger chopping currents than WC/Ag due to the lower vapor pressure of Cu compared to Ag.

We have now studied the chopping currents of WC/Ag-type contacts with lower Ag contents. The latter was achieved by partially replacing Ag by Cu and other metals or by increasing the WC:Ag ratio. In addition, the effect of a finely dispersed additive in WC/Ag-type contacts was investigated.

2 Contact Materials

2.1 Compositions

As a reference, we chose commercial contacts **1** with a composition of 60 wt. % WC and 40 % Ag that are widely used in vacuum contactors. To analyze the effect of changing the vapor pressure of the contact materials, different fractions of Ag were replaced by Cu in compositions **2-5** while keeping the mass ratio refractory material:conductor constant at 60:40. To evaluate the impact of changing thermal conductivity, a WC-rich composition **6** with 70 % WC was chosen. Furthermore, we prepared contact material **7** containing a finely dispersed additive in addition to the WC/Ag-base composition. All selected material compositions are listed in **Table 1**.

The limited densification of WC/Ag based materials when manufactured by liquid phase sintering is improved by the addition of 3 wt. % Co to the materials from this process. Since Co is barely soluble in Ag or Cu, this addition does not have drastic effects on electrical conductivity.

WC/Ag-type contacts were produced by powder metallurgical processes, starting from powders of the contact material components. Some contacts were prepared by liquid infiltration, others using a simple liquid phase sintering process [10]. The sintered materials were machined to the required contact shape and finally assembled inside commercial vacuum interrupters.

2.2 Characterization

Different contact material compositions do not only affect chopping currents in the vacuum interrupter but can also have effects on contact resistance. Thus, material hardness (Emco test M1C010 hardness tester) and bulk conductivity (Institut Dr. Förster Sigmatest 2.069 eddy current probe) were measured to verify that the selected compositions are suitable for contact material application. The results of these measurements are listed in **Table 1**.

The effect of contact resistance was additionally estimated by measuring vacuum interrupter resistivities after each of 50 switching operations, using a Micro ohmmeter MO 2A (Rasmus & Kühne, Dresden, Germany).

3 Chopping Current Testing

Chopping currents of vacuum interrupters containing the experimental contact materials were measured using a dedicated test setup pictured in **Figure 1**. It was designed for high test repetition rates to be able to account for the statistical distribution of chopping currents.

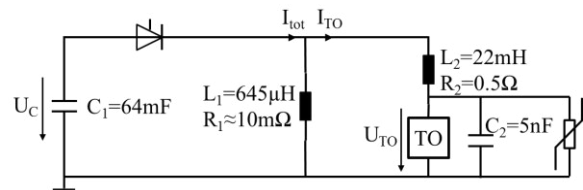


Fig. 1 Circuit diagram of the setup used for I_c testing. TO indicates the test object which is located in a current path parallel to the main circuit.

The test setup is similar to the one described in [11] and is based on a synthetic circuit. A capacitor bank C_1 charged to 400 V is used as the power source. When the thyristor is switched on, it discharges the stored energy through L_1 and R_1 and produces a resonance circuit with 50 Hz sine voltage and the corresponding current, supplying one halfwave of a total current I_{tot} of 1.7 kA. With a parallel current path containing an additional inductance L_2 and the test object, the test current I_{TO} was tuned to a peak of 65 A, corresponding closely to the root mean square current of 45 A as used by Czarnecki et al. [11]. Although current and voltage are similar to their setup, our setup exhibits a smaller parallel capacitance of 5 nF (vs. 26 nF in [11]), so that we can expect slightly larger chopping currents for comparable materials. The parallel metal oxide varistor (clipping voltage of 1.8 kV) is used as a safety element in case of major faults in the test objects and stayed passive during the investigations.

Table 1 Contact materials used to investigate the effects of material composition on chopping currents.

Material	Composition (wt.%)	conductivity (MSm ⁻¹)	hardness (HV10)	production technique
1	WC60 Ag40	19.0	250	infiltration, commercial reference
2	WC60 Ag37 Co3	14.1	324	liquid phase sintering
3	WC60 Ag32 Cu5 Co3	13.1	304	liquid phase sintering
4	WC60 Ag27 Cu10 Co3	12.7	300	liquid phase sintering
5	WC60 Ag10 Cu30	19.6	387	infiltration
6	WC70 Ag27 Co3	11.2	405	liquid phase sintering
7	WC60 Ag17 Cu20 Co3 add. 0.1	12.1	308	liquid phase sintering

For accurate measurements of I_c , the current and voltage across the test object were measured using a Pearson 110A probe (Pearson Electronics, Palo Alto, US) and a differential probe with a ratio of 1:200 and a maximum bandwidth of 25 MHz (Teledyne LeCroy), respectively.

Initial testing with several VIs containing commercial contact materials showed high reproducibility between different devices. Each contact material was tested repeatedly to ensure reasonable statistics with at least 92 valid measurements observed for every material (cf. Table 2).

4 Results and Discussion

4.1 Contact Resistance

Bulk conductivity and hardness of the materials can be considered to gauge effects on contact resistance. According to Table 1, bulk conductivity is highest for materials **1** and **5** that were produced by infiltration, whereas the materials produced by liquid phase sintering exhibit lower bulk conductivities.

Soft surfaces are beneficial for contact resistance as they facilitate deformation of surface asperities, leading to larger contact surfaces. Here, the commercial reference material **1** is most promising, while WC-rich material **6** shows the highest surface hardness values.

In an attempt to quantify the effects of contact resistance, the resistivities of several vacuum interrupters containing experimental materials were measured. **Figure 2** shows that VI resistivities can vary significantly between different VIs assembled with the same contact material. These variations are often larger than those between VIs with two different contact materials.

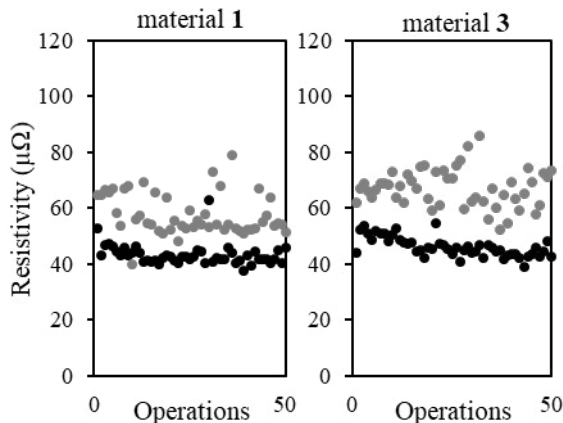


Fig. 2 Experimental resistivities of two vacuum interrupters containing contact material **1** and two devices containing contact material **3**.

Thus, VI resistivity measurements can give only limited information on the contact resistance of different contact materials. However, since none of the VIs containing experimental materials exhibited dramatically

increased resistivity, we do not expect large issues regarding contact resistance from any of the materials.

4.2 Chopping Currents

Figure 3 shows the measured chopping currents exemplarily for one of the tested materials. As expected, the chopping currents of individual chops are statistically distributed and do not follow any trend across an increasing number of shots. This is true for all tested materials and suggests that the compositions of the contact materials remain unchanged during I_c testing (cf. inset in **Figure 4**).

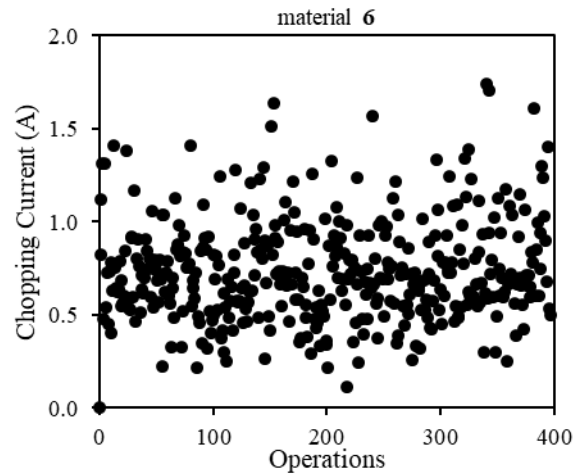


Fig. 3 Chopping currents for one experimental contact material.

Figure 4 shows that the distribution of I_c is typically rather smooth and asymmetric. Thus, we performed χ^2 tests on the experimental datasets for four different material compositions to identify a suitable probability function for modelling the statistical distribution of chopping currents. The χ^2 tests revealed that log-logistic distribution functions best fit the experimental data.

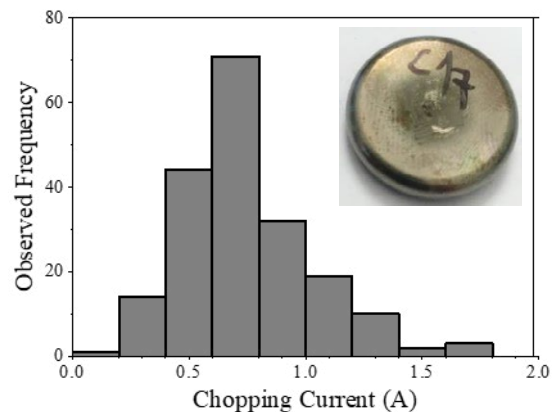


Fig. 4 Representative probability density function (bottom) found for one type of material in one vacuum interrupter. Inset: photograph of an experimental contact after chopping current testing.

Table 2 Parameters describing the statistical distribution of experimental chopping currents for the tested contact materials: Total number of measurements N_{tot} , average and median I_c as well as the number of chopping events with $I_c > 3$ A were determined directly from the experimental data, while the parameters α (median) and s (spread) were derived from the corresponding log-logistic probability functions.

	Composition (wt. %)	N_{tot}	Average I_c (A)	Median I_c (A)	$N_{I_c > 3 \text{ A}}$	α (A)	s (A)
1	WC60 Ag40	400	0.938	0.913	0	0.874	0.276
2	WC60 Ag37 Co3	376	1.380	1.348	1	1.297	0.244
3	WC60 Ag32 Cu5 Co3	313	1.569	1.502	7	1.492	0.190
4	WC60 Ag27 Cu10 Co3	188	1.666	1.586	0	1.594	0.174
5	WC60 Ag10 Cu30	175	1.850	1.699	10	1.733	0.194
6	WC70 Ag27 Co3	400	0.792	0.742	0	0.750	0.204
7	WC60 Ag17 Cu20 Co3 add.0.1	92	1.335	1.326	0	1.295	0.174

Log-logistic distribution functions are characterized by a rather heavy right tail, corresponding to significant probabilities of large chopping current events. This distribution is described by the following cumulative distribution function:

$$F = \frac{x^\beta}{\alpha^\beta + x^\beta}$$

Here, the parameter $\alpha > 0$ is a scale parameter and the median of the distribution. The parameter β is a shape parameter signifying a unimodal distribution if $\beta > 1$. β is the inverse of the spread of the distribution s , so that the dispersion of the distribution increases with increasing s . Fitting the parameters of this function to the experimental results for all experimental materials, allowed the determination of the parameters of the I_c distribution (**Table 2**).

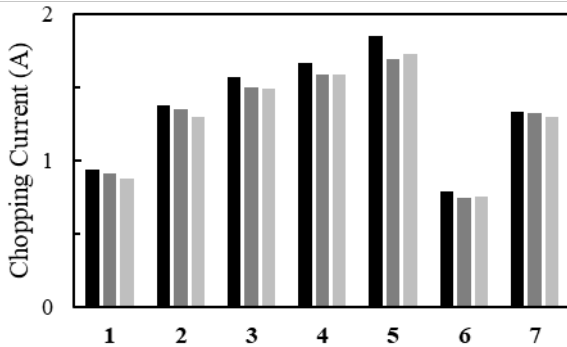


Fig. 5 Average (black) and median (dark grey) I_c from the experimental datasets of the tested contact materials compared to the scale parameter α of the corresponding probability density functions (light grey), also representing the median of the distributions.

The average and median chopping currents as measured for materials 1-7 are plotted in **Figure 5**, along with the parameter α of the corresponding log-logistic distribution functions. Due to the asymmetric distribution of chopping currents, the median I_c of the experimental datasets is always somewhat smaller than the average. The scale parameter α of the fitted probability density functions corresponds well to the medians of

the experimental data, so that this value will be used for comparisons throughout this paper.

Material **1** is the commercial WC60 Ag40 material and exhibits a comparatively low median I_c of 0.91 A in our test setup. From materials **1** to **5**, where more and more Ag is replaced by Cu and Co, I_c increases gradually. Already the presence of the sintering aid Co (3 wt. %) in material **2** induces a significant increase in I_c . This behaviour can be explained by the lower vapor pressures of Co and Cu.

Material **7** exhibits a moderate median I_c of 1.33 A, comparable with that of material **2**. This is quite surprising, considering their very different compositions (cf. Table 1). Even though large amounts of Ag are replaced by Cu and Co in material **7**, the additive-containing contact material still performs similarly to Cu-free material **2**.

The WC-rich material **6** exhibits the lowest chopping currents of all materials. Here, the high WC content is expected to lower the thermal conductivity of the contact material, improving the chopping behaviour.

4.3 Vapor Pressure Correlation

The gradual replacement of Ag by Cu (and Co) in materials **1** to **5** enables a more quantitative understanding of the relationship between vapor pressure and I_c . Since the thermal resistances of Ag and Cu are comparable, the vapor pressures of these two elements should be the main cause for different chopping currents in the same test setup.

Thus, we plotted chopping currents against estimated vapor pressures at 2400 K (close to the boiling point of Ag) for all materials (**Figure 6**). Assuming ideal mixtures of the metal matrix elements in the liquid phase, the vapor pressures were calculated according to Raoult's law as the sum of the vapor pressures of the components weighted by their respective mole fraction.

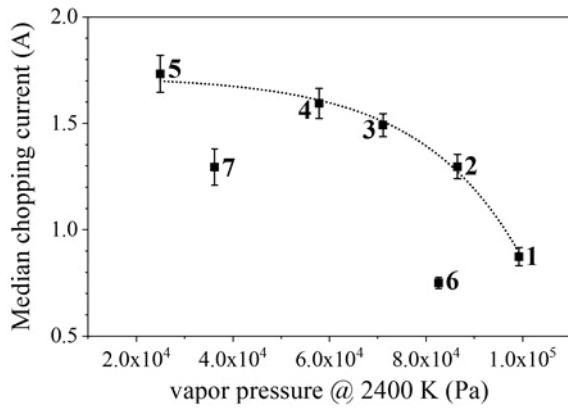


Fig. 6 Median chopping current (from the distribution functions) against estimated vapor pressure at 2400 K: Except for materials **6** and **7**, all data points were fitted with an exponential function that shows good agreement with the experimental data.

Figure 6 shows an exponential correlation of median I_c to vapor pressure for materials **1** to **5**. This relation is rather unfavourable for vacuum contactor applications, as slight deviations from the reference WC60 Ag40 compositions towards cheaper components already have a large detrimental effect on chopping current.

The chopping currents for materials **6** and **7** clearly deviate from the exponential correlation, presenting options for decreasing chopping currents independent of changing vapor pressures.

For material **6** (WC70 Ag27 Co3) this is easily explained by the WC-rich composition that is expected to increase the thermal resistance of the material. However, the high WC content also makes for harder contact materials with lower bulk electrical conductivity (cf. Table 1). Thus, the improved chopping behaviour of material **6** likely comes at the cost of increased contact resistance inside VIs. Consequently, the optimum balance of chopping current and contact resistance can be obtained by adjusting the WC:Ag ratio in electrical contacts for vacuum contactors accordingly.

For material **7**, the case is not so clear. This material contains small amounts of a finely dispersed additive, which might affect thermal resistance or other properties like the work function, which have been proposed to impact the chopping currents of contact materials [7] [12]. If this is the case, then the addition of such finely dispersed material presents a way to reduce chopping currents of Ag-reduced contact materials.

4.4 Probability of Large Chopping Currents

For application in vacuum contactors, individual current chops with very high I_c are most problematic as the induced voltage surges can damage downstream loads. Consequently, the suitability of a contact material for a

specific contactor application does not depend on its average or median I_c , but on the probability of chops occurring above a certain, potentially damaging chopping current.

Thus, the suitability of different contact materials should not only be evaluated using average, median or even maximum I_c from a limited number of tests. Ideally, one would evaluate the probability of current chops with damagingly large I_c for the specific application to select an appropriate contact material. Exemplarily, the obtained probability density functions for materials **1**, **2** and **7** are plotted in **Figure 7**.

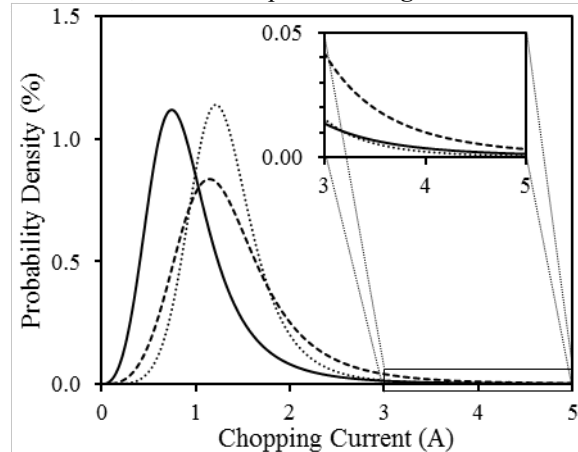


Fig. 7 Log-logistic probability density functions for the chopping currents of materials **1** (solid line), **2** (dashed line), and **7** (dotted line) as determined from the experimental datasets.

For our materials evaluation, we arbitrarily selected 3 A as a cut-off for allowable I_c . Using the probability density functions of the tested materials, the probability for critical chopping currents above 3 A can now be determined (s. **Figure 8**).

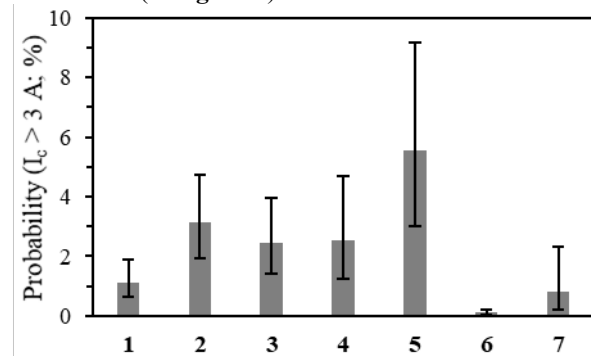


Fig. 8 Probability of current chops with $I_c > 3$ A for VIs containing the tested contact materials. Error bars signify 95 % confidence intervals. The data was calculated from the respective probability distributions.

The confidence intervals for the probability of large current chops are rather large, so that an unambiguous ranking of the tested contact materials is not reasonable. However, it is obvious that partial substitution of Ag by Cu and Co in materials **2-5** increases the likelihood of critical current chops significantly. The lowest

probability for large current chops is observed for the WC-rich material **6**. These results follow the trend observed for the respective average chopping currents.

Interestingly, the probability of critical current chops in VIs with contact material **7** is also very low, comparable to that of reference material **1**. For our scenario, material **7**, which contains only 17 wt. % Ag, would thus be as suitable as the commercial WC60 Ag40 material. This promising result originates from the rather narrow distribution of chopping currents (s. inset in Figure 7).

5 Conclusions

The chopping currents of different WC/Ag-type contact materials in vacuum interrupters were evaluated to identify opportunities to reduce the content of expensive Ag. Partial replacement of Ag by Cu (and small amounts of Co) increases I_c significantly, observing an exponential correlation to estimated vapor pressures. Cu-containing materials with lower vapor pressures could however exhibit better interruption capability [6], allowing a contact material selection according to an optimal balance of chopping current and interruption capability.

Two of the tested materials present possible strategies towards Ag-reduced contact materials with low chopping currents. Increasing the WC:Ag ratio decreases the thermal conductivity of the material and thus lead to lower I_c . As this compositional change comes at the expense of poorer contact resistance, this approach is limited. Nevertheless, adjusting the WC:Ag ratio towards an optimal balance of chopping current and contact resistance may be worthwhile.

A WC:Ag-type contact material containing a finely dispersed additive also presented surprisingly low chopping currents. Further investigations are necessary to clarify which mechanism enables this behaviour. Although the average chopping current of the latter material is still significantly higher than that of standard WC60 Ag40 contacts, a statistical analysis of the experimental results shows that the probability for the occurrence of critically large chopping currents is similar. Our results suggest that vacuum contactors containing a contact material with a Ag content of only 17 wt. % could exhibit the same low risk for damaging surge voltages as traditional WC60 Ag40.

6 Literature

- [1] Slade, P. G.: *The Vacuum Interrupter: Theory, Design, and Application*. Boca Raton: Taylor & Francis Group, LLC, 2008
- [2] Smeets, R. P. P.; Kaneko E.; Ohshima, I.: *Experimental Characterization of Arc Instabilities and Their Effect on Current Chopping in Low-Surge Vacuum Interrupters*. IEEE Trans. Plasma Sci. vol. 20 (1992) no. 4, pp. 439 - 446
- [3] Lee T. H.; Greenwood, A.: *Theory of the cathode mechanism in metal vapor arcs*. J. Appl. Phys. vol. 32 (1961) no. 5, pp. 916 - 923
- [4] Lee, T. H.; Greenwood A.; Polinko, G.: *Design of Vacuum Interrupters to Eliminate Abnormal Overvoltages*. Trans. Am. Inst. Electr. Eng., Part 3 vol. 81 (1962) no. 3, pp. 376 - 382
- [5] Ochi S.; Miyamoto S.; Koga H.; Kan, N.; Harada, T.; Ito, T.; Koyama K.; Yamade, S.: *The Effect of contact material composition of AgWC and Axial Magnetic Field intensity on interrupting capability and chopping current*. XXIIInd International Symposium on Discharges and Electrical Insulation in Vacuum. Matsue, 2006, pp. 285 - 288
- [6] Temborius, S.; Lindmayer M.; Gentsch, D.: *Properties of WCAg and WCCu for Vacuum Contactors*. IEEE Trans. on Plasma Sci. vol. 31 (2003) no. 5, pp. 945 - 952
- [7] Slade, P. G.: *Advances in Material Development for High Power, Vacuum Interrupter Contacts*. IEEE Trans. Compon., Packag., Manuf. Technol., Part A vol. 17 (1994) no. 1, pp. 96 - 106
- [8] Frey, P.; Klink, N.; Michal R.; Saeger, K. E.: *Metallurgical Aspects of Contact Materials For Vacuum Switching Devices*. IEEE Trans. Plasma Sci. vol. 17 (1989) no. 5, pp. 734 - 740
- [9] Behrens, V.; Honig T.; Kraus, A.: *Tungsten and Tungsten Carbide Based Contact Materials Used in Low Voltage Vacuum Contactors*. Proceedings of the 45th IEEE Conference on Electrical Contacts. Pittsburgh, 1999, pp. 105 - 110
- [10] German, R. M.: *Phase Diagrams in Liquid Phase Sintering Treatments*. J. Met. vol. 38 (1986) no. 8, pp. 26 - 29
- [11] Czarnecki L.; Lindmayer, M.: *Chopping Current and Quenching Capability of Low-Voltage Vacuum Arcs*. IEEE Trans. Compon., Hybrids, Manuf. Technol. vol. 8 (1985) no. 1, pp. 157 - 162
- [12] Czarnecki L.; Lindmayer, M.: *Experimental and theoretical investigations of current chopping in vacuum with different contact materials*. Proceedings of the 13th International Conference on Electrical Contacts. Lausanne, 1986

Investigation of the Possibility of Limiting the Hazard due to Internal Arc Faults in Medium Voltage Switchgear

Bartosz Polnik, Julian Wosik, Institute of Mining Technology KOMAG, Gliwice, Poland, bpolnik@komag.eu
Grzegorz Wisniewski, Marcin Habrych, Bogdan Miedziński, Wrocław University Of Science and Technology,
Wrocław, Poland, bogdan.miedziński@pwr.edu.pl

Stanisław Wapniarski, ELEKTROBUDOWA S.A., Konin, Poland, eskwap@op.pl

Abstract

This paper proposes and discusses a method of fast quenching of arc faults, inside the switchgear, by forced transformation into solid three-phase faults with earth. This is achieved through the use of an independent system of three open vacuum chambers connected in an earthed star and included in the medium voltage network. This system is activated (closed) under the influence of the increased internal gas pressure of the switchgear (due to the electric arc) over the respective value. The results of laboratory tests of the effectiveness of such a system during simulated arc faults in a medium voltage network of 6kV are presented and discussed. Appropriate practical conclusions are formulated.

1 Introduction

Medium voltage switchgear belong to the most widely used power equipment in industry, municipal services and transport. There has been a tendency for several years to build them in metallic housing to meet the electric arc protection requirements [1]. Due to economic reasons they are currently made as hermetic and compact small sized. The small dimensions reduce the costs of the structure and allow for location the switchgear inside much smaller and therefore cheaper space. The small size of the modern switchgear structure results from the much smaller geometrical dimensions of the basic components and the denser filling of the space with apparatus (busbars, disconnectors, current and voltage transformers as well as fuses, earthing switches, support and bushing insulators, drives, etc.). However, high density of electrical apparatuses inside individual shielding compartments, can lead, under some conditions, to an increased probability of high-current internal short circuits. The most common reasons are due to:

- human errors (prefabrication stage, tools left after maintenance and/or repairing),
- design errors,
- structural defects of the apparatus as a result of both aging and insulation degradation,
- long-lasting overloads,
- internal and/or external (atmospheric) overvoltages,
- unintentional leaving of the loosed electrical connections after measuring on cables,
- animals

It should be underlined that for such compact structure of the switchgear bay the increased heat generation and internal gas pressure under internal arc faults are key

factors [2-5]. However, for correctly designed structure and carefully selected equipment the damage during internal solid faults is not dangerous. But, such faults are seldom and are quickly switched off due to high short circuit current value. Besides, switchgear are subjected to short-circuit capacity tests according to standards [6]. Their ability to conduct short-time withstand current (thermal resistance) and peak rated withstand current in anticipated operating conditions (dynamic strength) are checked. The most serious problems occur during transient faults with intermittent arcs (e.g. earth faults) [7-10]. The thermal damage and /or destruction of the bay can occur along with the dynamic damage of the switchgear housing. It is of course related to value and time of the short-circuit current flow therefore, on amount of energy released in the arc column. This usually results in long-term shutdown of the bay or switchgear from operation. In recent years, many ways have been developed to reduce the effects of the internal short-circuit with electric arc. Of course, they usually come down to shortening the short-circuit current flow time and limiting its value. The use of the common circuit breakers results in long duration of the internal faults (protection operation time + circuit breaker time) of around 60-100 ms, despite the use of optoelectronic arc detection. It doesn't live up to expectations. So, a more effective and faster solution is needed.

This paper proposes and discusses a method of fast quenching of an arc fault ,inside the switchgear, by transforming it into a solid three-phase fault with earth. This is achieved through the use of an independent system of three open vacuum chambers connected in an earthed star and joined to medium voltage networks. The system has been developed using vacuum chambers for a required MV value and is activated (closed)

under the influence of the increased internal gas pressure of the switchgear (due to the electric arc) over the respective value. This solid 3-phase fault can be then effectively detected by protections (including optoelectronic) and quickly tripped by switches. The results of laboratory tests of the effectiveness of such a system during simulated arc faults in a medium voltage network (6 kV) are presented and discussed. Appropriate practical conclusions are formulated.

2 Study of the effects of the internal faults in distribution switchgear at permanent and heavy arc short circuits

2.1 High current solid faults

High-current solid short-circuits, that are relatively rare, create, for correctly selected apparatus for short-circuit conditions, a relatively low danger. Of course, provided that they are turned off in a sufficiently short time by circuit protections and switches. The threat for the switchgear is mainly related to thermal and dynamic strength [4,11]. Before commissioning, the switchgear is subjected to appropriate short-circuit capacity tests [6,12]. The authors for testing selected a switchgear with the following rated data $U_n=12$ kV, $I_n=1250$ A. For solid short-circuits the withstand short-circuit current is equal to 25 kA for 3 s. Whereas, during the heavy arcing faults duration of the flow time of the same (25 kA) current value is reduced to 0.3 s. View of an example switchgear selected for testing on the test stand is shown in **Figure 1**.



Fig. 1 View of distribution switchgear on the test stand

Electrical diagram of the system for testing the ability of the switchgear to conduct short-time withstand current and withstand peak short-circuit current is shown in **Figure 2**.

During the tests, currents in the main circuits were measured and recorded. After tests, the state of the main elements, equipment and the circuit breaker was inspected. Examples of the measured short-circuit current waveforms when checking the ability of the

switchgear to conduct short-time short-circuit current and withstand peak current are shown in **Figure 3**. The proper selection of apparatus for short-circuit conditions and a small amount of heat released in the main current circuit during permanent short circuits testify that the switchgear is not damaged and is suitable for further operation.

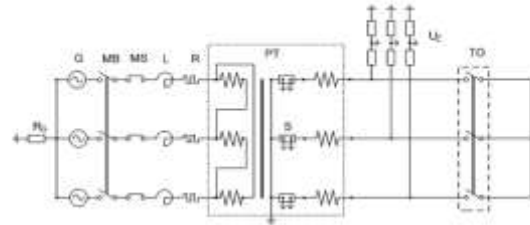


Fig. 2 Diagram of the test circuit to check the ability of the switchgear to conduct short-time withstand current and withstand peak short-circuit current (TO-tested object, G-generator 350 MVA, PT-transformer)



Fig. 3 Registered short-circuit currents under testing the ability to conduct short-time withstand current and withstand peak current

2.2 Heavy current arc short-circuits

The effects of internal arc faults are much more dangerous. As a result, the short-circuit current duration must be significantly reduced. The degradation of the switchgear and its components results from both the high arc temperature and the increase in pressure of the surrounding gas (usually air). Therefore, thermal damage/destruction of the insulation, evaporation of metallic parts, perforation of the casing or its deformation (especially in switchgear with a high degree of IP protection) apparatus damage, etc. may occur. This usually leads to long-term shutdown of the switchgear. Therefore, there is an urgent need to limit these effects by reducing the amount of thermal energy released in the arc column. Shortening of the arc duration by quick shutdown using the circuit breakers, gives poor results. It is due to a rather long tripping resultant time. This time consists of a short-circuit protection operation time of 20-40 ms, the operating time of the circuit breaker 40-100 ms and additional time due to grading of short-circuit protection what is from several hundred ms to 1 s. In extended power systems can reach up to 2.5 s. Under these conditions, the total breaking time of the arc fault can reach several hundred ms and even more. Thus, the arc energy can lead to irreversible damage of the switchgear. For this reason, it is so important to know the phenomenon of electric arc so that you can effectively counteract this damage.

The most common switchgear use so-called solid-air insulation. According to the literature, an arc burning in these conditions is a free arc. Its parameters are influenced by environmental conditions (air) and electrode material [4,9,13].

Ignition of the arc requires a sufficient number of electric charge carriers (electrons, ions) inside the inter-electrode space. In order for the electric discharge to take the form of an electric arc, the conditions for minimum voltage and current must be met. Therefore, the voltage must be higher than ignition value ($u > u_z$) and the current –over the discharge limit current ($I > i_g$). For example, these values are as follows [4, 13]:

- for iron electrodes (Fe) $u_z = 13-15$ V, $i_g = 0.3-0.5$ A,
- copper (Cu) $u_z = 12$ V, $i_g = 0.4$ A,
- silver (Au) $u_z = 12$ V, $i_g = 0.4$ A.

The radial temperature distribution in the arc column for two different gases is shown as an example in **Figure 4** [3]. The outer surface of the arc column is called the covering. Its temperature is around 1000°C (this is the value at which gas dissociation practically disappears).

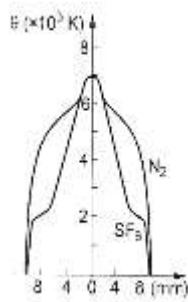


Fig. 4 Radial temperature distribution in an arc column [7]

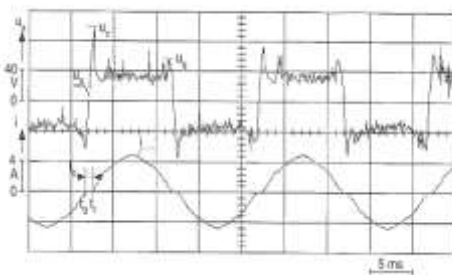


Fig. 5 Current and arc voltage waveforms (in resistive circuit), U_z -ignition value, (t_z-t_g) -power-off time

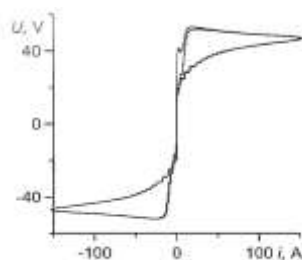


Fig. 6 Dynamic characteristics of the AC arc

For example, **Figure 5** shows the current and arc voltage waveforms, whereas, **Figure 6** - the dynamic characteristics of the AC arc respectively.

The arc column composed of a core and a covering for analytical purposes, is most often represented in the form of a cylinder whose diameter results from the balance of forces acting inside it. The discharge environment is a plasma consisting of electrons and ions (usually positive) and non-ionized particles (atoms, molecules and macromolecules of the substance). Outside, the plasma remains an inert gas. This environment can be analyzed in scales:

- microscopic,
- macroscopic.

For a microscopic scale, the analysis concerns the properties of particles and their interactions, taking into account the electric and magnetic fields. The purpose is to describe the paths of particle movement, their collisions and the energy processes that occur at the time, which makes it possible to determine the statistical distribution of the degree of dissociation, recombination ionization and the emission of spot components.

Whereas, for a macroscopic scale, the analysis concerns observation of the gas in an average way because the plasma is treated as a continuous medium for which the equations of mass, momentum and energy conservation of particles [2,8,9,13] are valid. After considering the interaction of electric and magnetic fields, such models are called magnetohydrodynamic models. The physical processes occurring in the arc column in the gas are determined by the electrical, thermal and flow properties of the gas. They are characterized by the concentration of " n " ions, density " ρ ", free path " l ", electrical conductivity " G_a ", thermal conductivity " λ ", specific heat " c_p " and " c_v " (at constant pressure and volume), specific enthalpy " h ", dynamic viscosity " η ", and sound speed " V_d ", which depend on the pressure " p " and temperature " Θ ". Most gases, including nitrogen and oxygen, which are the main components of air, occur in the form of diatomic molecules (N_2 , O_2).

Diffusion occurs when at ambient temperature during collisions of molecules instead of elastic collisions, the molecules break down into atoms, (if the kinetic energy of the molecule is greater than the chemical bonding energy). The degree of gas dissociation X_d and the degree of ionization of gas X_j are determined by the Saha equations.

- gas dissociation degree:

$$\left[\frac{X_d^2}{(1-X_d^2)} \right] p = C_1 \Theta^{1.5} e^{-\frac{w_d}{k\Theta}} \quad (1)$$

- gas ionization degree:

$$\left[\frac{X_j^2}{(1-X_j^2)} \right] p = C_2 \Theta^{2.5} e^{-\frac{w_j}{k\Theta}} \quad (2)$$

where: p - gas pressure, w_d - dissociation energy (9.78 eV for N₂), Θ - temperature, k - Boltzman constant (1.38×10^{-23} Ws/K), $\Theta_d = 7000$ K for N₂, $\Theta_d = 4000$ K for O₂.

Power delivered to the electric arc:

$$P_{a,t_g-t_d} = \frac{U_{av}}{t_g - t_d} \int_{t_d}^{t_g} |i_a| dt = U_{av} I_{ar,t_g-t_d} \quad (3)$$

Energy provided to the electric arc:

$$W_{a,t_g-t_d} = U_{av} \int_{t_d}^{t_g} |i_a| dt = U_{av} Q_{a,t_g-t_d} \quad (4)$$

I_{ar} - average arc current value, U_{av} - equivalent arc voltage, where:

$$U_{av,t_g-t_d} = \frac{\int_{t_d}^{t_g} u_a i_a dt}{\int_{t_d}^{t_g} |i_a| dt} \quad (5)$$

The energy processes in the arc are described by equations (3) - (5) [2,4,7].

When considering air as a perfect gas enclosed in a sealed compartment of the switchgear in which an arcing short circuit can be expected, the air temperature will increase approximately [2,13]:

$$d\Theta = \frac{1}{c_v \gamma V_g} dW \quad (6)$$

where:

c_v - specific heat of an air in a constant volume, γ - air density.

This increase of temperature $d\theta$ results in the increased gas pressure Δp by about

$$\Delta_p(t) = k_t \frac{\kappa - 1}{V_g} W_a \quad (7)$$

where:

k_t - heat transfer coefficient depending on the electrode material [4], κ - adiabat coefficient, V_g - volume of the compartment, $W_a(t)$ - energy generated in the arc according to (4).

Tests of resistance to internal arc faults were performed for the same 12 kV switchgear. Arc faults were initiated as in **Figure 8**. Due to the safety of the personnel in the switchgear a special shield called the arc flash indicator as seen in **Figure 7** was used.

The effect of an internal arc fault in the tested 12 kV switchgear can be observed in **Figure 9** whereas the measured current waveforms in **Figure 10**.



Fig. 7 View of the arc flash indicators used for the test



Fig. 8 View of the modelled arc initiation



Fig. 9 View of the switchgear during internal arc fault test

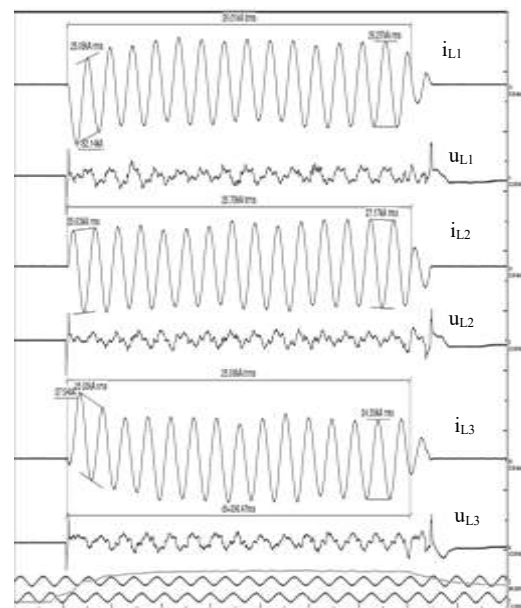


Fig. 10 Current and voltage waveforms during a three-phase internal arc fault in a distribution switchgear (25 kA, $t_z = 300$ ms)

3 Proposed method to reduce the effects of the heavy current internal arcing

Analyzing the effects of internal short-circuits in medium voltage distribution switchgear under solid (metallic) and arc short-circuits, it was found that short-term metallic short circuits implemented in laboratory conditions, do not cause significant damage to the switchgear. The rated duration of the short circuit during these tests did not exceed $t_2 \leq 3$ s. According to [7] for LV switchgear, the extent of damage under heavy current internal arcing should be considered as dependent on the value and duration of the short-circuit current (energy generated in the arc). The scope of necessary repair work due to this is also specified. For the arc duration below 100 ms (with energy released in the arc up to 100 kJ), no significant damage was found except this of sooting. To bring the switchgear back to service only cleaning the apparatus from sediment is required. Considering the above statements, one should strive to quickly eliminate arc faults or to transform them into short-lasting solid short circuits with a small amount of released energy. The quick-disconnection methods known from the literature, apart from the relatively long operation time of the circuit breakers, require constant monitoring of the circuit by various types of protections and triggering systems as well as maintaining them in continuous efficiency and periodic control.

In this paper is recommended a very fast passive system for converting an arc fault, especially phase-to-phase, into the solid fault. For this purpose, a system of 3 fast earthing devices connected in a star was used. They are based on appropriately adapted vacuum circuit breaker chambers whose view for one phase is illustrated in **Figure 11**. After the quick earthing switch is activated (under the influence of an increased gas pressure inside the switchgear volume) the electric arc is extinguished. The flowing solid earth fault current gives long enough time to switch it off by short-circuit overcurrent protection and circuit breaker. This solution is approved for use by international regulations [14].

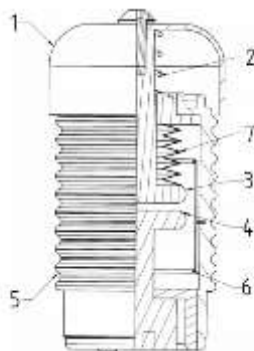


Fig. 11 View of one phase of a fast earthing device; 1-cylinder with spherical surface, 2-return spring, 3-movable contact, 4-stationary contact, 5-insulating sleeve, 6-metal shield, 7-bellows

The vacuum switch chamber used was placed inside the insulating sleeve 5. The movable contact of the vacuum chamber 3 is normally kept in the open position by the pulling spring 2. This spring rests on one end with the insulating body of the vacuum chamber 5 and the other with the nut on the end of the rod being the moving contact extension. The movable contact is connected by a flexible cable to the respective phase. Terminal of the stationary contact 4 is connected to a grounding rail. The stationary and movable contacts are located inside a metallic sleeve connected to the elastic sealing bellows. The metallic sleeve protects the walls of the vacuum chamber against direct deposition of metal vapours from the contacts. The increase in the gas pressure under an arc fault (according to (7)) results in a shock wave, which gives the force closing the contacts. To obtain the appropriate axial contact force, a cylinder closed on one side with a spherical surface 1 (piston effect) was mounted on the plunger. The spherical surface of this cylinder makes it possible to provide a closing force value capable to overcome the resistance of the back pulling spring of the movable contact. It is performed. Regardless the direction from which the shock wave originates, i.e. regardless of where the short circuit occurs inside the switchgear. Compared to earlier solutions, this system is much simpler in structure and cheaper to operate. Appropriate tests were performed to check the effectiveness of the proposed system. The arc fault in the switchgear was initiated by means of the arc initiation wire as shown in **Figure 8**. Short-circuit currents and voltages in all phases as well as the gas pressure occurring in the connection compartment of the switchgear were measured and recorded. The results are shown for the example in

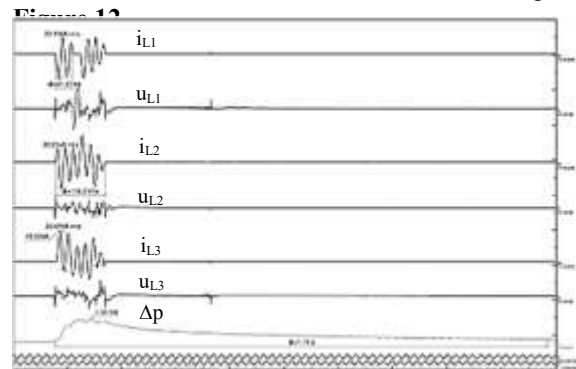


Fig. 12 Current and voltage waveforms as well as the gas pressure inside the connecting compartment under three-phase arc fault inside the switchgear equipped with an earthing device

The arc fault was transformed into a metallic fault and quickly tripped by the circuit breaker. The whole process took less than 100 ms. During the switchgear inspection, no damage to the electrical apparatus and cables was found except for weak, easy to remove sooting at the fault initiation site.

4 Conclusions

The proposed method in the paper to reduce the effects of internal arc faults inside medium voltage switchgears by transforming them into solid earth faults and clearing by commercial protections and switches has proved to be very effective. As a result the irreversible damages to electrical apparatus by an electric arc are eliminated. Fast clearing of the effects of short-term arc faults allows also to avoid power outages and eliminates therefore financial losses related to the costs of replacement / repair of electrical apparatus and due to interruptions in power supply to consumers.

5 Literature

- [1] Yamagiwa, T., & Twomey, C. (2019). Mixed Technology Switchgear (MTS) Substations. *Substations*, 487-506
- [2] Xia, H., Guan, Y., Yu, Z., Cai, S., Wang, X., Peng, Z., Huang, Z. (2019). Temperature rise test and analysis of high current switchgear in distribution system. *The Journal of Engineering*, 2019(16), 754-757
- [3] Xu, K., Cao, P., Gao, K., & He, Y. (2019, March). Model Establishment and Analysis of Grounding Circulation of Gas Insulated Metal-Enclosed Switchgear Enclosure. In *2019 IEEE Asia Power and Energy Engineering Conference (APEEC)*, pp. 69-74, IEEE
- [4] Slade, P. G. (Ed.). (2017). *Electrical contacts: principles and applications*. CRC press
- [5] Liao, X., Zhou, X., Bo, K., & Zhai, G. (2018, October). 3-D Hydrodynamic Model of Metal Droplet Sputtering and Molten Pool Formation Under Electric Arc. In *2018 IEEE Holm Conference on Electrical Contacts*, pp. 56-60, IEEE
- [6] PN-EN 62271-200: 2012. High-voltage switchgear and control equipment. Part 200: AC switchgears in metal enclosures for rated voltage above 1 kV up to 52 kV inclusive (public IEC60466: 1987)
- [7] Partyka R. Study of the effects of arc faults in enclosed switchgears. Gdańsk University of Technology Publisher. Gdansk 2006. (in polish)
- [8] Bucca, G., Collina, A., & Tanzi, E. (2017). Experimental analysis of the influence of the electrical arc on the wear rate of contact strip and contact wire in ac system. In *Advances in Italian Mechanism Science* (pp. 449-456). Springer, Cham.
- [9] Yan, H. Y., Song, L. M., Zhang, R. H., & Jia, L. X. (2018). Experimental Research on Current-carrying Efficiency of Arc under Different Polarities.
- [10] Panetta S., Design of arc flash protection system using solid state switch, photo detection, with parallel impedance. 2013 IEEE IAS Electrical Safety Workshop. IEEE, 2013.
- [11] Giere, S., Heinz, T., Lawall, A., Stiehler, C., Taylor, E. D., & Wethekam, S. (2019). Control of Diffuse Vacuum Arc Using Axial Magnetic Fields in Commercial High Voltage Switchgear. *Plasma Physics and Technology*, 6(1), 19-22.
- [12] ref. IEC 60529: 1989: Degrees of protection provided by enclosures (IP Code).
- [13] Koch B., Maksymowicz J. : Arc protection of enclosed switchgears and arc faults simulation. Warsaw University of Technology Publishing House, Warsaw 2007.(in polish)
- [14] Patent Description PL 224958: Super fast earthing switch of short-circuit arc

Impact of pre-strike arc on contacts degradation after short circuit current making operation in medium voltage air load break switches

Naghme Dorraki, Norwegian University of Science and Technology (NTNU), Trondheim, Norway,

naghme.dorraki@ntnu.no

Marius Strand, Norwegian University of Science and Technology (NTNU), Trondheim, Norway,

mstran@stud.ntnu.no

Kaveh Niayesh, Norwegian University of Science and Technology (NTNU), Trondheim, Norway,

kaveh.niayesh@ntnu.no

Abstract

Medium voltage load break switches are required to perform a number of making operation while passing of short circuit current that could be more than tens of kiloamperes. Using air-filled devices as an alternative to SF₆, which is a high impact greenhouse gas, makes the switch more environmentally friendly but leads to more challenging making operation due to higher arcing times and dissipated energies between the contacts. In this case, the pre-strike arc could lead to contacts welding and degradation, which is highly undesirable. This paper reports on an investigation of the pre-strike arc impact on erosion and welding of copper/tungsten (20/80) arcing contacts during short-circuit making operations. For this purpose, a synthetic test circuit consisting of a high current source in combination with a high voltage one is used. Experiments are conducted for different operation voltages, while the short circuit current is kept constant at 22 kA. Mass loss measurement and visual inspection of eroded/welded contacts are examined with regard to pre-strike arc impact on their degradation. The contacts are welded by three times repeating the test at operation voltage of 20 kV and short-circuit current of 22 kA and failed to re-open. Besides, an increase in the contacts' mass loss with arcing time is observed while the making current is constant. This is an indication that the pre-strike arc energy highly impacts the switch reliability and service life.

1 Introduction

Considering the crucial role of Load Break Switches (LBS) in Medium Voltage (MV) distribution networks, high reliable operation of MV-LBS is required [1, 2]. An MV-LBS must be able to interrupt load currents and close under fault conditions. Making of short circuit current results in fault current flow through the contacts while closing. Although MV-LBS are designed to carry fault currents of tens of kiloamperes up to few seconds in the closed position, we should consider that the current flow starts before contacts full touch moment when arc formation makes a bridge between the contacts, which will deteriorate the contacts' surfaces. The local electric field strength between the contacts increases while closing, which causes a breakdown in the insulation gas and arc burning before contacts' touch. The short circuit current flows through the pre-strike arc causes high energy dissipation between the contacts, which are partly absorbed by contact surfaces leading to their melting and evaporation. Closing the contacts with melted surfaces could lead to welding the contacts to each other and failure to re-open, which is

one of the main reasons for failure in this type of switches. The stresses applied to the contact are expected to be higher during making operation compared to current interruption because of higher arc energy dissipation between the contacts [3]. The dissipated energy between contacts could be limited by arcing time, which is dependent on the dielectric strength of the insulation gas. Although SF₆ supports the design of compact, low cost, and reliable MV-LBS due to high dielectric strength, it has a high environmental impact, which put an end to using SF₆ in gas-insulated switchgear. Regarding cost-effective and environmentally friendly insulation gas, air or air mixtures could be an alternative to SF₆ [4]. However at the pressure of one bar, air with dielectric strength of 3 kV/mm causes higher arcing time compared to SF₆ with dielectric strength of 8.9 kV/mm at same making test condition which makes the switch operation even more challenging.

From the aspect of arcing contact erosion, several theoretical and experimental investigations have been done [5-7]. Simulation models have been developed based on arc-metal contacts interface to explain arc behavior under the injection of particles and metal vapors [8, 9]. Several parameters have been calculated,



Fig 1. Electrical contacts made of W/Cu (80/20). Pin is the fixed contact (cathode) and split tulip is the dynamic one (anode).

such as contacts surface temperature, material transfer rate, arc temperature, thermal and electrical conductivity [10, 11].

It has been shown that the erosion mechanism at high current is different from the low current. Several factors affect the electrical contacts erosion in switching operation such as arc energy, arcing time, gap distance, closing velocity, contacts shape, and material properties [12]. Besides, there is still a lack of understanding of the impact of pre-strike arc on contacts erosion during making operation in fault conditions.

In this work, we focus on the impact of the pre-strike arc on the contacts degradation during making operation. A spring-type drive test object and a synthetic test circuit are employed. Arc electrical characterizations and mass loss measurement are used to find a meaningful relationship between the pre-strike arc parameters and the contacts degradation.

2 Experimental set-up

For the test type switch, the stationary contact is a pin with a diameter of 10 mm, and the dynamic one is a split tulip with an outer diameter of 20 mm and an inner diameter slightly less than 10 mm. The contacts are shown in figure 1. The pin is the anode and the split

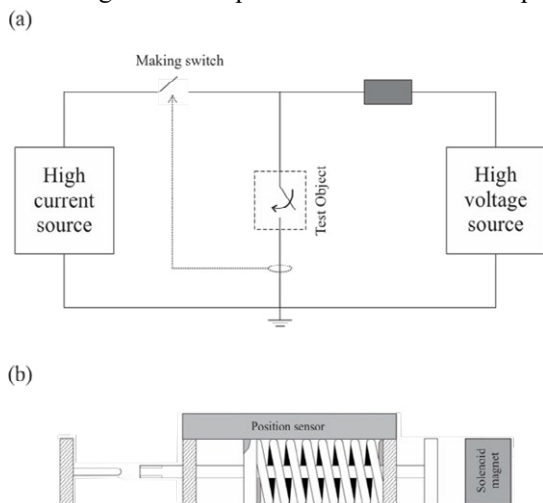


Fig 2. Schematic of the synthetic circuit (a), and the test-object.

ring is the cathode with an inner diameter slightly smaller than the pin to provide fully touch of the contacts in closed position. The contacts are made of copper-tungsten (20/80), and the closing velocity is 3 m/s. The closing speed and the material type are chosen not to differ too much from the commercial product. The test circuit is a synthetic making circuit based on the IEC 62271 standard [13]. The circuit includes two parts; high current and high voltage sources. The high voltage circuit supplies the test voltage for dielectric breakdown while the switch is closing. Once the breakdown happens, a signal is sent to the high current source to initiate the flow of the transient making current. A schematic of the synthetic circuit is shown in figure 2 (a). The test object is a spring-type switch with axisymmetric arcing contacts. The synchronization between the time of breakdown by the synthetic circuit and closing the test object is achievable through the time setting for the release of the dynamic contact by a solenoid magnet (figure 2 (b)) A sensor records the position of the dynamic contact over time, making it possible to record the arcing time and length while contacts are closing. A Pearson current probe measures the arc current and a 6015A Tektronix voltage probe measures the arc voltage. To avoid the interference of electromagnetic noises, an optical system transmits the measured data to record them.

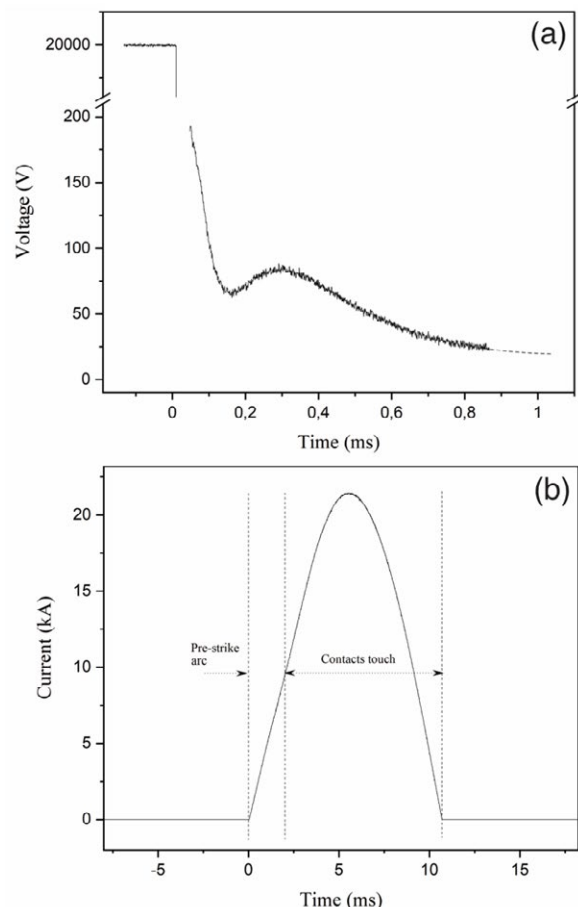


Fig 3. Arc voltage at 20 kV test voltage(a) and 50 Hz half-cycle short circuit current (b).

To make different arcing times to investigate the impact of pre-strike arcing on the contacts erosion and welding, two test voltages of 10 kV and 20 kV are applied to the test object with a short circuit current of 22kA. The fault currents duration has a tolerance of one to two milliseconds because of inaccuracy in the control system for the synthetic circuit. The difference does not make significant changes in the pre-strike arc current since di/dt is approximately constant in all the tests.

In order to figure out how long the eroded contacts can withstand fault conditions, each test has been repeated on the same set of samples until they weld to each other. The arcing time and mass loss are measured after each test. Figure 3 shows a typical arc voltage and current waveforms. The voltage waveform shows a sharp fall from the dielectric breakdown voltage at 20 kV to arc voltage, which is in the order of tens of volts. The first $50\mu s$ of the voltage fall is neglected due to interference with electromagnetic noises caused by air breakdown. Because of limitation on oscilloscope bandwidth, the arc voltage is measured for the first millisecond of arc burning while expecting to decay slightly to 13 V, which is the minimum voltage drop across the plasma sheath in front of the contacts [12, 14]. Figure 3 (b) shows the 50 Hz half-cycle of sinusoidal current with an amplitude of 22 kA. The waveform is divided into two parts. The pre-strike arc burns for 2.2 ms, while the current rises to ~ 9 kA. The rest of the current passes through the contacts when they are in touch.

For the sake of accuracy in the obtained results, each test has been repeated for three different samples. The contacts were cleaned after each test, and the mass loss was measured with an accuracy of 0.00001 gr.

3 Results

A summary of results including number of tests at two test voltages of 10 and 20 kV with constant fault current of 22 kA is shown in Table 1. The results show an increase in mass loss with pre-strike arcing time by repeating the test at each specific sample. The highest arcing time is measured for samples 02 and 03 for the third time of repeating the test (3rd-Table 1), which is about four milliseconds and resulted in welding of the contacts. The pre-strike arcing current rises to ~ 20 kA before the contacts' touch.

At the test voltage of 10 kV, the results show the mass loss is higher for the second time of repeating the test than the third time. Even for the test voltage of 20 kV, there is a slight difference between the mass loss for the second and third times of repeating the tests. This is an indication of arc ignition at different spot of the contact's surface.

Visual inspection of the pin's eroded area at different test conditions is taken to clarify the difference in mass loss changes. Figure 4 shows the pin's eroded surface

for the first and the second samples of each test voltage. The arc ignites at a random spot on the contact's surface by air breakdown. At the test voltage of 10 kV, arc hits the same spot in case of sample one, while for sample two at the second time of repeating the test, two spots close to each other are observed in the side view of the contacts, and eroded surface is larger compared to sample one at the second time of repeating the test. Therefore, hitting at the same spot for arc ignition causes higher mass loss, which could be a reason for electric field enhancement at sharp points or more conductive area due to aggregated molten copper compared to the rest of the contact's surface.

For the test voltage of 20 kV, the contact is eroded for more than 50 % of the first test's surface area. The mass loss at this test condition is more than ten times higher than the test voltage of 10 kA. For the second time of repeating the test, the erosion almost covered the whole contact's surface. After the third time, the contact's surface is totally burnt for sample one, and some deformation on the contact's shape is observed on the side view of the pin. The third time of repeating the test for sample two at test voltage of 20 kV and short-circuit current of 22 kA, causes the contacts to weld and fail to re-open.

Table 1. The arcing time and mass loss for each test and repeated for three times for test voltage of 10 kV and 20 kV with constant fault current of 22 kA.

Breakdown Voltage:		Number of tests		
10 kV		1st	2nd	3rd
Sample 01	Arcing time (ms)	1.13	1.37	1.37
	Mass loss (mg)	6.62	35.19	32.08
Sample 02	Arcing time (ms)	1.15	1.32	1.37
	Mass loss (mg)	7.32	13.99	24.08
Sample 03	Arcing time (ms)	0.98	1.41	1.47
	Mass loss (mg)	3.96	53.28	28.64

Breakdown Voltage:		Number of tests		
20 kV		1st	2nd	3rd
Sample 01	Arcing time (ms)	2.5	3.35	2.855
	Mass loss (mg)	67.44	203.68	104.59
Sample 02	Arcing time (ms)	2.18	2.73	4.45
	Mass loss (mg)	69.71	86.8	334.47
Sample 03	Arcing time (ms)	2.62	2.62	3.58
	Mass loss (mg)	65.46	128	336.01

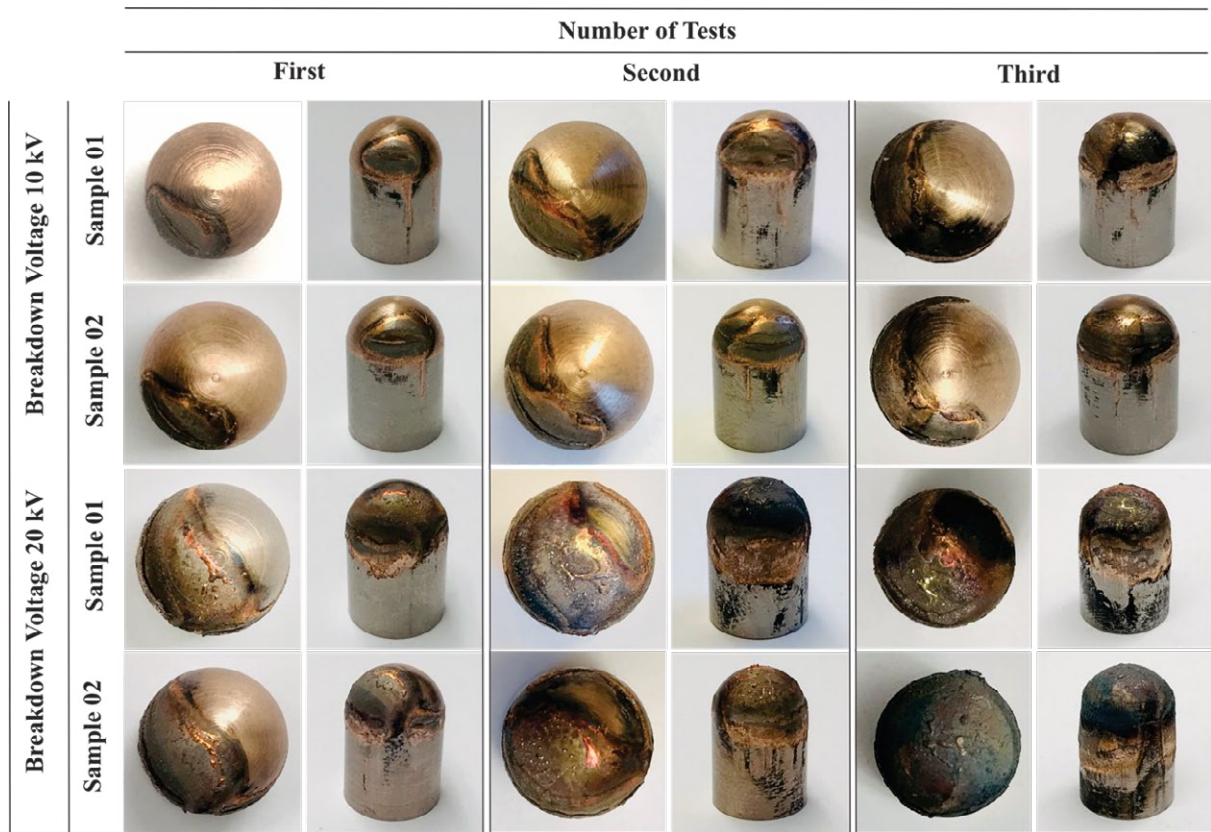


Fig 4. Eroded contacts' surface after each three times repeating the test at test voltage of 10 kV and 20 kV when a short circuit current of 22 kA passed through the contacts.

4 Discussion

Making operation of MV-LBS under fault condition is the main failure reason of the switch. The switching behavior at different pre-strike arcing times with the same short circuit current has shown the interaction between the arc and the contacts could have a deteriorating impact on switch service life by heating up the contacts surfaces to melting and evaporation points and occasionally welding them to each other in the closed position, as has occurred after three times of repeating the test at the voltage of 20 kV and fault current of 22 kA. At test voltage of 10 kV, although the contacts could withstand a couple of times more than the eroded contacts at 20 kV, we should take into account that gradual erosion of the contacts could lead to shortening the length of the contacts that would cause failure in current interruption.

Mass loss measurement is a proper method to get an approach on the contacts' erosion and prediction of the switch failure, though it needs a dedicated assessment of the results. At test voltage of 10 kV, the second time of repeating the test shows higher mass loss compared to the third time. It can be seen in figure 4 for the contacts surface erosion at 10 kV that the arc did not ignite at same spot by dielectric breakdown. For contacts with smaller front area, the arc could initiate from the same spot each time, enhancing the erosion and shortening the switch service life. Therefore, the

size of the contacts plays a crucial role in enduring longer under fault conditions.

Regardless of the eroded area impact on pre-strike arcing time, the mass loss for different arcing time is plotted in figure 5. The results show an increase in pre-strike arcing time causes higher mass loss and erosion of the electrical contacts. Higher arcing time does not necessarily lead to higher energy dissipation between the contacts since the increase in arc current in the order of kiloamperes follows by a slight decrease in arc voltage. However, higher arcing time means more time for heat conduction between the arc and the contacts to melt and evaporate the metal surfaces. In the closed position, the melted metals cool down and could weld the contacts to each other.

The obtained results indicate that the rate of contact erosion caused by making operation is increasing with increasing arcing time which is mainly because of partly absorption of dissipated arc energy by contacts' surfaces. Therefore, if the contacts are in full-touch in the closed position, the erosion only depends on the pre-strike arc time and energy, not the amount of short-circuit current. Therefore, the influential factors and involved parameters in the switch operation should be designed to decrease the impact of pre-strike arc to improve the switch service life.

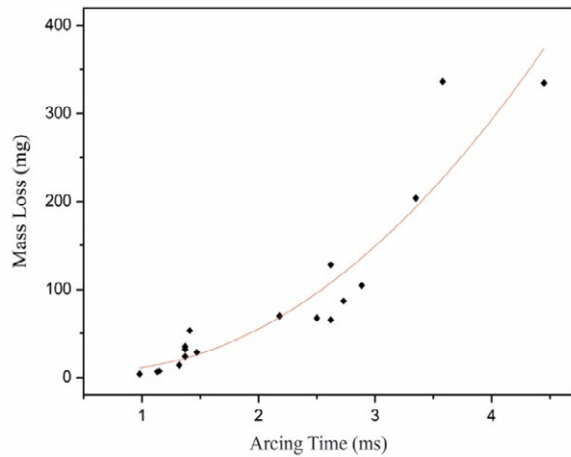


Fig 5. Mass loss as a function of arcing time when the short circuit current is kept constant (22 kA)

5 Conclusion

The electrical arcing contacts erosion/welding in an MV-LBS during making operation was investigated to understand the impact of the pre-strike arc before the contacts touch on switch failure. Experiments were conducted for test voltages of 10 kV and 20 kV, while the 50 Hz half-cycle sinusoidal short circuit current with peak of 22 kA was kept constant.

The results showed switch failure to re-open after three times repeating the test on the same set of contacts at test voltage of 20 kV. Further, an increase in mass loss with arcing time at the same current proved the impact of pre-strike arc on the contacts erosion/welding.

This work should be continued by further studies on optimizing the switch design and finding the interrelation between different parameters involved in switch operation like the speed of closing and the contacts material to minimize the impact of pre-strike arc on the contacts welding.

Acknowledgment

The Norwegian Research Council, grant number 269361, financially supported the work. The authors would like to thank Bård Ålmos and Dominik Häger from NTNU for technical supports.

References

[1] K. Niayesh and M. Runde, *Power Switching Components*. Cham, Switzerland: Springer, 2017.
 [2] M. Seeger, "Perspectives on research on high voltage gas circuit breakers," *Plasma Chemistry and Plasma Processing*, vol. 35, no. 3, pp. 527-541, 2015.

[3] M. Mohammadhosein, K. Niayesh, A. A. S. Akmal, and H. Mohseni, "Impact of Surface Morphology on Arcing Induced Erosion of CuW Contacts in Gas Circuit Breakers," in *2018 IEEE Holm Conference on Electrical Contacts*, 2018: IEEE, pp. 99-105.
 [4] N. S. Støa-Aanensen, M. Runde, E. Jonsson, and A. Teigset, "Empirical relationships between air-load break switch parameters and interrupting performance," *IEEE Transactions on Power Delivery*, vol. 31, no. 1, pp. 278-285, 2016.
 [5] J. Tepper, M. Seeger, T. Votteler, V. Behrens, and T. Honig, "Investigation on erosion of Cu/W contacts in high-voltage circuit breakers," *IEEE transactions on components and packaging technologies*, vol. 29, no. 3, pp. 658-665, 2006.
 [6] T. Schoenemann, "Comparing investigations of the erosion phenomena on selected electrode materials in air and sulfurhexafluoride," in *Electrical Contacts-1996. Proceedings of the Forty-Second IEEE Holm Conference on Electrical Contacts. Joint with the 18th International Conference on Electrical Contacts*, 1996: IEEE, pp. 115-120.
 [7] E. Hetzmannseder and W. Rieder, "The influence of bounce parameters on the make erosion of silver/metal-oxide contact materials," *IEEE Transactions on Components, Packaging, and Manufacturing Technology: Part A*, vol. 17, no. 1, pp. 8-16, 1994.
 [8] A. Kadivar and K. Niayesh, "Two-way interaction between switching arc and solid surfaces: distribution of ablated contact and nozzle materials," *Journal of Physics D: Applied Physics*, vol. 52, no. 40, p. 404003, 2019.
 [9] J. L. Zhang, J. D. Yan, and M. T. Fang, "Electrode evaporation and its effects on thermal arc behavior," *IEEE Transactions on Plasma Science*, vol. 32, no. 3, pp. 1352-1361, 2004.
 [10] S. Franke, R. Methling, D. Uhrlandt, R. Bianchetti, R. Gati, and M. Schwinne, "Temperature determination in copper-dominated free-burning arcs," *Journal of Physics D: Applied Physics*, vol. 47, no. 1, p. 015202, 2013.
 [11] P. Stoller, E. Panousis, J. Carstensen, C. Doiron, and R. Färber, "Speckle measurements of density and temperature profiles in a model gas circuit breaker," *Journal of Physics D: Applied Physics*, vol. 48, no. 1, p. 015501, 2014.
 [12] P. G. Slade, *Electrical contacts: principles and applications*. Boca Raton, FL, USA: CRC press, 2017.
 [13] IEC 62271-101, "High-Voltage Switchgear and Controlgear-Part 101: Synthetic Testing", S. IEC, 2006.
 [14] J. Lowke, "Simple theory of free-burning arcs," *Journal of physics D: Applied physics*, vol. 12, no. 11, p. 1873, 1979.

Research on Arc Characteristics of Different Arc Extinguishing Gases Used in DC Contactor

Xuebing Yuan, School of Automation, Northwestern Polytechnical University, Xi'an, China, yxb@nwpu.edu.cn

Hu Zhao, School of Automation, Northwestern Polytechnical University, Xi'an, China, hzhao@nwpu.edu.cn

Abstract

In recent years, the new energy fields such as electric vehicles, photovoltaic power generation and electric aircraft develop so rapidly that DC contactor demand has been increasing dramatically. Under the development trend of high voltage and large current for contactor, it is more difficult to improve the arc extinguishing performance only from the structural design. It is necessary to study the performance and selection of different arc extinguishing gas. However, the various arc extinguishing gases, their mixing ratio and their arc quenching characteristics are not quite clear. In this paper, the arc properties of insulation gases such as H₂, N₂, CO₂, air, and different mixture ratio of N₂-H₂ have been researched through experimental tests. The results are as follows: The thermal conductivity of H₂ arc is high, which is good for energy dissipation when small current, however, the N₂ arc is more unstable, which is benefit for dissipation when large current. Better comprehensive 20%N₂ has better comprehensive properties including arcing time, heat dispersion and heat recovery rate than others.

1. Introduction

The new energy fields such as electrical vehicles, photovoltaic power generation and electric aircraft, require greater electrical power for their increasing direct current (DC) loads and drive, therefore, the high voltage cables and electrical devices up to 500V_{DC} are reconsidered and redesigned. In the future even higher supply voltage, as high as 1000V_{DC}, will be used in electrical system for higher energy efficiency and lighter weight. The DC high voltage contactors and protector devices are necessary components in the system to carry out the distribution and the protection of the electrical energy.

The increasing voltage has serious influence on the interrupting capability and electrical life of contactor and circuit breaker. As the voltage increases, the arc is difficult to extinguish so that contact erosion even contact welding will be more severe [1]-[4]. It is difficult to be extinguished for DC arc for its property of no natural zero. It is of great significance to extinguish the arc and shorten the arc time as soon as possible to protect load and whole electrical system.

Usually, the lengthening of the arc and increasing the arc voltage are main effective methods to shorten arc duration and extinguish arc. In DC contactor, the bridge-type contact system to double the arc voltage and applying a magnetic field near the electrodes to drive and bend the arc are widely used in the industry. Liu XY et al. researched the influence of external transverse magnetic field on the characteristics of the low pressure direct current arc [2]. Sekikawa et al. measured the breaking arc duration in a 450V_{DC}/10A resistive circuit when driven by transverse magnetic field

with permanent magnets [3]. X. Zhou et al. presented arc behavior of three kinds of bridge-type contacts switched at resistive load in range of 300V_{DC} to 750V_{DC} and their experimental research [6]-[8]. Besides, high power DC contactors are always sealed with different arc extinguishing gas for cooling arc and increasing arc voltage. Yuji Shiba et al. tested the arc break characteristics at voltage 25V_{DC}-600V_{DC}, current 30A-250A, gas pressure 0.1Mpa, in sealed inflatable equipment, and got conclusion that the H₂ had higher arc voltage and 80%H₂-20%N₂ was most effective mixture ratio [9]. Niu CP et al. researched different gases and gas pressure through setting a test equipment of DC contactor, and got variation patterns of arc voltage, arc current, duration time and arc energy of different gas and pressure to arc characteristics [10]. Wu J et al. made transparent sealed arc extinguishing device to simulate interrupting tests at 270V_{DC} filling H₂-N₂ mixture, and got result that the interrupting capability of H₂ mixture was better than N₂ mixture [11]. Bo Kai et al. researched arc dwelling and restriking characteristics in DC high power relay, simulated arc dwelling behaviour during bridge type contacts opening process for high power relays [12]-[13].

However, the previous research did not give more kinds of gases for arc extinguishing, the arc physical parameters of gases used in DC high power contactors were less analyzed comparatively. In this paper, the arc characteristics of the arc extinguishing gases: air, N₂, He, H₂-N₂ mixture, N₂, have been researched. The arc voltage, arc current, arc duration, arc current peak, arc heat flux and arc extinction voltage are comparatively analyzed. The most effective mixture and proper ratio for DC high power contactor arc extinguishing are suggested. This research paper will be helpful for under-

standing arc extinguishing mechanism and arc characteristics of different gases filled in DC high power contactors. It is also helpful for designing higher voltage and current rating DC contactors.

2. Experimental Methods

The simplified equipment for tests consists of sealed cavity, gas filling devices, DC high power contactor and measuring equipment, power supply and load. The DC high power contactor consists of one movable contact and two static contacts that are all made from pure copper, and control structure by speed motor. The contactor is no sealable case in this research which is different from commercial products. Because more kinds of gases for arc extinguishing can be filled easily into cavity surrounding the contacts. Because this paper is focused on arc characteristics of different gases when breaking, then the LC power is used for its simple and adjustable properties. The arc voltage is measured by using a high voltage probe, the arc current is sensed by current sensor, and the data is recorded by an oscilloscope. Arc images are taken by using high-speed camera. **Figure 1** shows the arrangement of the experimental devices.

The high speed camera used in experiments is Photron's FASTCAM Mini AX100 with performance 1024*1024 pixels at 4,000fps.

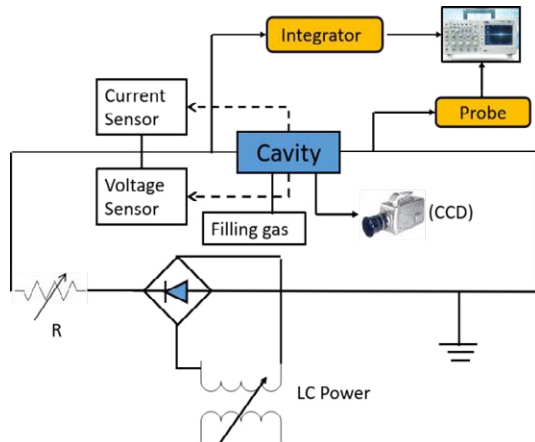


Figure 1 Simplified experimental devices

3. Experiment Results and Analysis

In order to analyze arc characteristics of DC high power contactors in several kinds of gases, firstly their arc shapes are taken by High speed camera when contactor being opened; secondly the arc voltage and current data is acquired by oscilloscope and then analysed comparatively.

3.1 Arc shape in different gases

The arc extinguishing gases include air, N_2 , H_2 , 20% H_2 -80% N_2 , 50% H_2 -50% N_2 , 80% H_2 -20% N_2 , 50%He-50% N_2 . Their various arc shapes are taken by the high speed camera when contactors being opened. The images of the arc shapes captured at the same time are shown as in **Figure 2**. The arc shapes and arc stability of several gases are different from each other through comparing the images, and the gases have influence on arc voltage and heat dissipation performance. From the whole arc behavior comparison, the dynamic arc behavior including arc starting, arc elongating and arc extinguishing can be observed clearly.

The sealed DC high power contactor was uncased, then put into the sealed cavity. Different gases including air, N_2 , H_2 , 20% H_2 -80% N_2 , 50% H_2 -50% N_2 ,80% H_2 -80% N_2 and 50%He-50% N_2 were filled into cavity after vacuum. Arc characteristics tests were carried out breaks, their arc voltage and current data was acquired with probe and current sensor then recorded by oscilloscope.

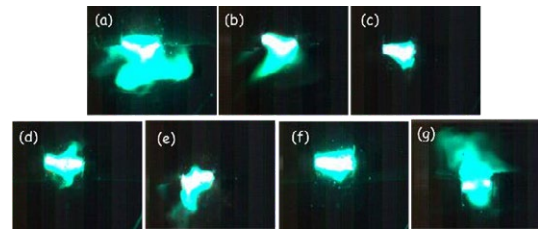


Figure 2 Several gases arc shapes when contactors being open(a)air, (b) N_2 , (c) H_2 , (d)20% H_2 -80% N_2 , (e)50% H_2 -50% N_2 , (f)80% H_2 -20% N_2 , (g)50%He-50% N_2

3.2 Arc characteristic analysis of different gases

Then the test data is drawn as **Figure 3** and **Figure 4**. From the **Figure 3**, the arc voltage and current waveforms are quite similar, which indicates the arc extinguishing property is almost the same. The arc characteristics of 50%He-50% N_2 and 50% H_2 -50% N_2 are different, because the 50% H_2 -50% N_2 has higher arc exit-voltage as shown in circle in **Figure 3**, which is helpful for increasing the probability of successful interruption. The He is an inert gas, which has stable property and poor ionization capacity, therefore, the arc extinguishing performance of 50% H_2 -50% N_2 is better than that of 50%He-50% N_2 . The **Figure 4** is shown arc voltage and current of different mixing ratios of H_2 and N_2 . By contrast, the peak of arc extinguishing exit-voltage increases with the H_2 ratio goes up. Accordingly, the arc duration is also gradually shortened.

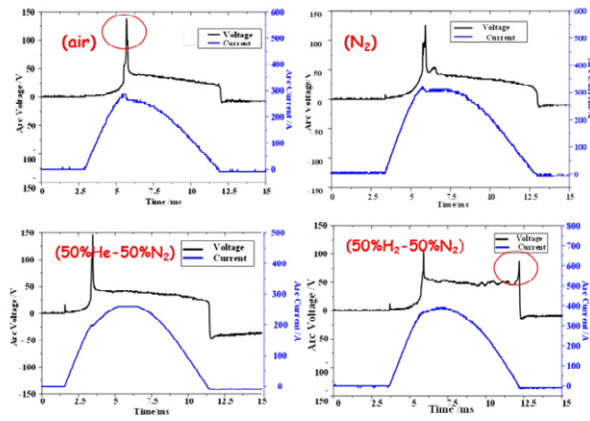


Figure 3 Arc Voltage and Current of air, N₂, 50%He-50%N₂ and 50%H₂-50%N₂

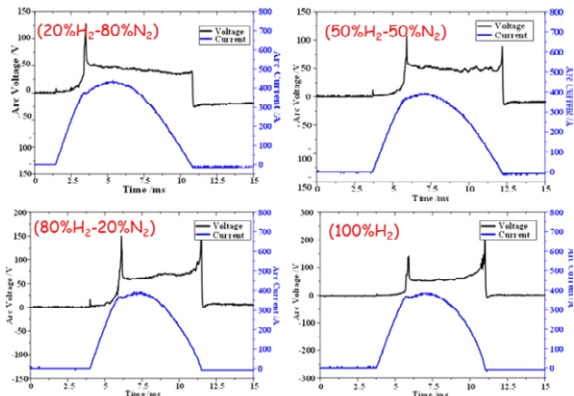


Figure 4 Arc Voltage and Current of 20%He-80%N₂ and 50%He-50%N₂, 80%He-20%N₂ and H₂

The arc duration is critical for breaking and electrical life. The arc duration comparison of these gases as shown in **Figure 5**. As H₂ ratio goes up, the arc duration of H₂-N₂ mixture gas reduces obviously as black line. By contrast, the He-N₂ mixture gas has longest arc duration, followed by the N₂. Even if air, its arc duration is shorter than He-N₂ mixture gas.

The arc current peaks comparison of these gases are shown as **Figure 6**. The peak of air is minimum, and followed by N₂, the main reason is related to the conductivity and physical parameters. The heat flux(Joule Integral, I²t) of these gases has a similar pattern as arc current peak, which both reveals the arc extinguishing properties and gases limiting capacity. In addition, the heat flux has closely related with motion feature of drive speed.

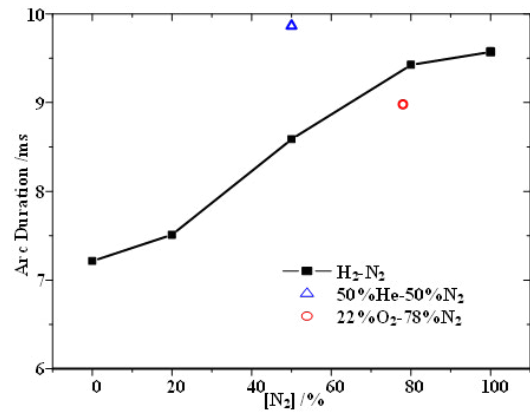


Figure 5 Arc duration comparison of different gases

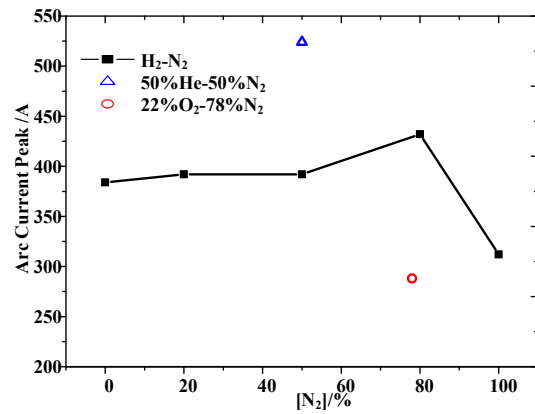


Figure 6 Arc current peak comparison of different gases

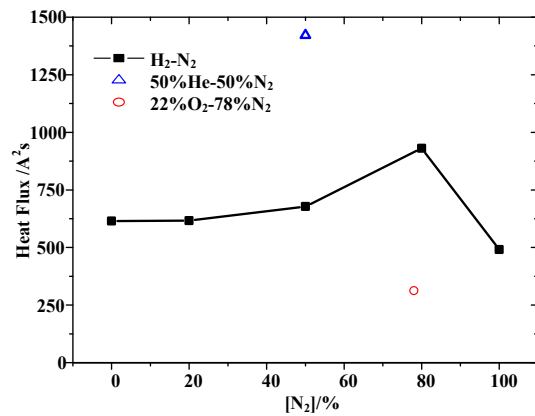


Figure 7 Arc heat flux of different gases

The arc exit-voltage comparison of these gases as show in **Figure 8**. With the H₂ ratio goes up, the arc exit-voltage of H₂-N₂ mixture gas increases obviously, it has an opposite pattern with arc duration. The air, N₂ and He-N₂ mixture have lowest arc exit-voltage. And the arc exit-voltage characterizes the thermal recovery property of the gas.

The first peak of arc voltage first decreases and then increases with H₂ ratio increasing. And there is a minimum value at 50%H₂-50%N₂. The He-N₂ mixture and H₂ have a maximum value of first arc voltage peak.

The arc time constant of different gas has great dispersion as in **Figure 9**, and it is difficult to distinguish the difference between gases.

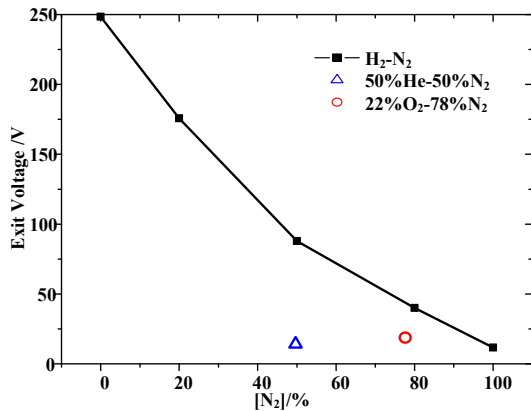


Figure 8 Arc exit-voltage of different gases

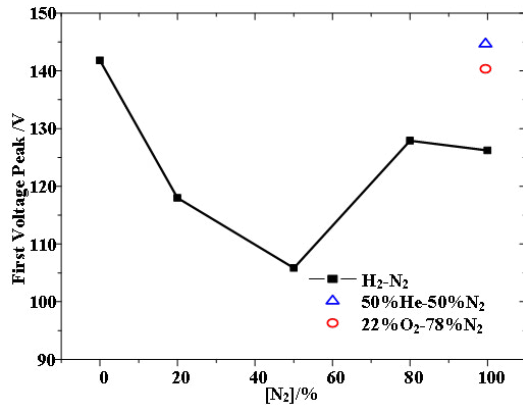


Figure 9 First voltage peak of different gases

The arc energy dissipation coefficient comparison of these gases is shown as **Figure 10**. When the conductance increases, the arc energy dissipation coefficient grows significantly. The H₂ has highest arc energy dissipation coefficient, He-N₂ mixture has lowest arc energy dissipation coefficient, followed by N₂.

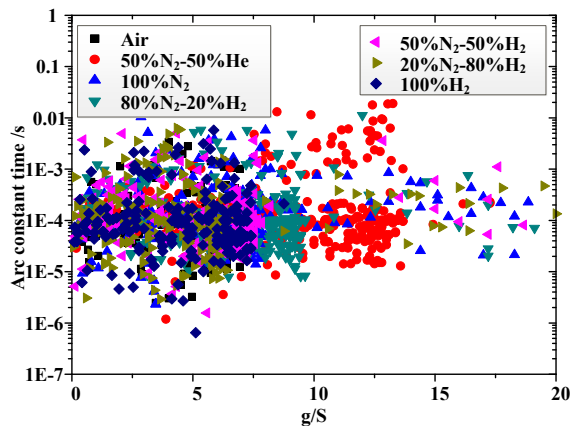


Figure 10 Arc time constant of different gases

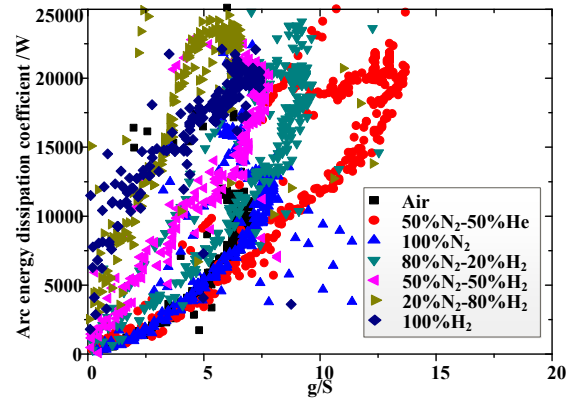


Figure 11 Arc energy dissipation coefficient of different gases

4. Conclusion

The arc characteristics of different gases in DC high power contactors through a simplified equipment, have been investigated. The gases used for extinguishing arc include air, N₂, H₂, 20%H₂-80%N₂, 50%H₂-50%N₂, 80%H₂-20%N₂, 50%He-50%N₂. The parameters of arc voltage, arc current, arc duration, arc current peak, arc heat flux, arc exit-voltage, first voltage peak, arc time constant and arc energy dissipation coefficient have been analyzed, whose variation is revealed among several gases. The main conclusions are listed as follows:

- 1) The arc shapes of different gases have large difference, and their stability has obvious variation, which will have influence on arc voltage and heat dissipation.
- 2) As the H₂ ratio goes up, the arc duration of H₂-N₂ mixture gas decreases obviously, and the He-N₂ has longest arc duration, followed by N₂.
- 3) As the H₂ ratio goes up, arc exit-voltage of H₂-N₂ mixture gas increases significantly, the arc energy dissipation coefficient increases obviously, H₂ is the highest, He-N₂ is the worst, followed by N₂.
- 4) In general, the performance of H₂ and 80% H₂-20%N₂ is the best in terms of heat dissipation capacity, heat recovery rate and arc duration. However, considering that the insulation strength of H₂ is relatively low and N₂ is relatively high, it is recommended to select a mixture ratio 80%H₂-20%N₂ for commonly used DC high power contactors. That is consistent with the research of SHIBA Y in paper [9].

In future, with energy storage industry, electrical truck and bus, and photovoltaic power generation developing, the higher power and voltage DC contactors increase rapidly in demand. The ratio of the N₂ of H₂-N₂ mixture gas helps to improve the voltage level accordingly, for example, 1000V_{DC} and 1500V_{DC} high power contactors. The contactor with higher voltage

(1000V_{DC}) will be deeply researched. And the arc characteristics at inductive and capacitive loads will also be studied.

This paper acknowledges the Fundamental Research Funds of the Central Universities (NO.3102020ZDHKY04)

Reference

- [1] Y. Liu, Z. li and K. Wang, Experimental study on arc duration under external transverse magnetic fields in a DC 580 V circuit, Proceedings of 26th International Conference in Electrical Contacts, pp.30-34, 2012.
- [2] Liu XY, Liu SX and Cao YD. Research on the influence from outside magnetic field to the characteristics of the low pressure direct current arc[C]. The 7th international conference on electromagnetic field problems and applications, 2016:488-489.
- [3] H. One, J. Sekikawa, Arc Length of Break Arcs Magnetically Blown-Out at Arc extinction in a DC450V10A Resistive Circuit, IEICE Transactions on Electronics, vol.E96-C, no.9, pp.1132-1137, 2013.
- [4] Liang H, Liu D, Zhou X, et al. Arc Behaviors of Three Kinds of Bridge-type Contacts when Opening a Resistive Load in Range of from 300VDC to 750VDC[C]//2018 IEEE Holm Conference on Electrical Contacts. IEEE, 2018: 81-86.
- [5] H. One, J. Sekikawa, and T. Kubono, Arc duration of breakarcs magnetically blown-out in a DC 450 V resistive circuit, IEICE Transactions on Electronics, vol.E95-C, no.9, pp.1515-1521, 2012.
- [6] X. Zhou, X. L. Cui, and G. F. Zhai, Study on arc behaviors at opening a 270V resistive circuit by bridge-type contacts under magnetic field, IEICE Transactions on Electronics, vol.E96-C, no.9, pp.1124-1131, 2013.
- [7] Zhou X, Cui X, Chen M, et al. Experimental study on arc behaviors of a bridge-type contact when opening a resistive load in the range of from 280VDC to 730 VDC[C]//2014 IEEE 60th Holm Conference on Electrical Contacts (Holm). IEEE, 2014: 1-7.
- [8] Liang H, Liu D, Zhou X, et al. Arc Behaviors of Three Kinds of Bridge-type Contacts when Opening a Resistive Load in Range of from 300VDC to 750VDC[C]//2018 IEEE Holm Conference on Electrical Contacts. IEEE, 2018: 81-86.
- [9] SHIBA Y, MORISHITA Y, KANEKO S, et al. Study of DC circuit breaker of H₂-N₂ gas mixture for high voltage[J]. Electrical Engineering in Japan, 2011, 174(2): 9-17.
- [10] Niu CP, Xiong QC, Xu D, et al. Experimental Study on Arc Breaking Characteristics of High-power DC Contactor in Different Gases[J]. High Voltage Engineering, 2019,45(11):3481-3486.
- [11] XIN C, WU J, LIU B, et al. Plasma characteristics of DC hydrogen-nitrogen mixed gas arc under high pressure[J]. IEEE Transactions on Plasma Science, 2014, 42(10): 2722-2723.
- [12] Bo K, Zhou X, Zhai G. Investigation on arc dwell and restriking characteristics in DC high-power relay[J]. IEEE Transactions on Plasma Science, 2017, 45(6): 1032-1042.
- [13] Bo K, Zhou X, Zhai G. Simulation of Arc Dwelling Behavior During Bridge-Type Contacts Opening Process for High-Power Relay[J]. IEEE Transactions on Components, Packaging and Manufacturing Technology, 2018, 8(6): 975-981.

PV Arc Fault Diagnosis and Modeling Methods: State of the Art and Perspectives

Xingwen Li

State Key Laboratory of Electrical
Insulation and Power Equipment
Xi'an Jiaotong University
Xi'an, P.R.China
xwli@mail.xjtu.edu.cn

Silei Chen

School of Electrical Engineering
Xi'an University of Technology
Xi'an, P.R.China

Jing Wang

Shenzhen Power Supply Bureau
Shenzhen, P.R.China

Abstract

The global photovoltaic (PV) power capacity is growing exponentially. However, the undetected arc faults would pose a severe fire hazard to PV systems, so various advanced diagnosis techniques have been proposed especially in the last few years. This talk presents a comprehensive review of state-of-the-art techniques for arc fault diagnosis and modeling methods in PV systems, and the development trend of future diagnosis methods is also discussed. Diagnosis methods viewed from physical and electrical signals of PV arc faults have been proposed for a few decades. Their capabilities and limitations are discussed, compared, and summarized in detail. By acquiring electromagnetic radiation and sound characteristics of arc faults, diagnosis methods based on physical signals have the advantage of the accurate identification. However, these methods show limitations for large-scale PV systems due to the increasing interference factors in the exposed environment. Through signal processing methods such as time-domain methods, fast Fourier transform and time-frequency transforms, much more works focus on diagnosis methods based on electrical signals. Recently, diagnosis methods with good switching noise and system transition immunity have been introduced. For instance, the existing Db9-based features would cause nuisance trip for the arc fault detection in grid-connected PV systems. The Rbio3.1-based features are proposed to achieve better arc fault recognition ability. Since the field testing is costly and time consuming, precisely modeling arc faults becomes more critical. Different types of arc fault models including dynamical state model, stationary state model, and high-frequency component model have been reviewed and compared. In addition, future trends about PV arc fault diagnosis methods are outlined. It is predicted that facing more complex arc fault conditions, the data processing chip development and machine learning based classifier are of great significance to improve the detection accuracy of diagnosis methods. Also, the detection reliability of diagnosis methods would be significantly improved without increasing the computation time significantly.

1 Introduction

The renewable energies have drawn a great attention recently. Many researches prove that photovoltaic (PV) energy power systems occupy an important share in the future electricity for the unlimited and clean features of the solar power [1][2]. The Paris agreement and the large-scale installed PV capacity around the world fully demonstrate the powerful driving force for PV power generation system [3][4]. In order to ensure the electrical safety of new energy dc system, American electrical law NEC690.8 stipulates that PV system voltage greater than 80V must be equipped with the arc fault circuit interrupter (AFCI) [5]. In 2011, underwriters laboratories developed the corresponding standard UL1699B for evaluating the effectiveness of dc arc fault detection methods in PV systems [6][7]. In 2013, the international electrotechnical commission formulated IEC 62606 named an international standard for dc

arc faults detection of electrical appliances [8][8]. The European Union proposed to achieve zero energy consumption in commercial buildings by 2020. It set up a project "DC Components and Grid" (DCC+G) in 2012, including arc faults protection within the $\pm 380V$ grid [9][3]. Under this background, the PV arc fault detection has become one of the hot issues to be studied.

There are two common types of arcs in life. One is called normal arc, usually occurring in the plug or the normal circuit break. The duration of these operations is relatively short. Besides, the time and location of the normal arc could be predicted with the known installation location. Therefore, the normal arc usually would not cause damage to the line or equipment, nor would it easily cause electrical fire. The other one is arc fault, which is almost irregular and damaged. Because the location and time of arc faults occurred in the system cannot be determined in advance, the arc faults have the characteristics of randomness, chaos and intermittently, which increases the difficulty of detection.

Arc faults are classified according to their topological relationship with the PV system shown in 0. Factors such as internal aging or external wear and tear could lead the obvious break to the current path by loosening the connector or damaging the insulation. However, traditional protection devices like circuit breakers or fuses are not able to trip the fault and isolate the faulty loop facing this kind of smaller faulty current. In this case, the arc fault occurs as a part of the path, called the series arc fault. Due to the numerous connectors in PV systems, series arc faults occur more frequently than other kinds of arc fault. Factors such as internal thermal cycling or external animal bite lead to brittle fracture to form additional independent discharge paths. This kind of arc fault is called the parallel arc fault as an additional load in the circuit. However, due to the inherent safety distance between the PV panels and strings, the generation probability of parallel arc faults is small. Besides, the current generated by this kind of arc fault usually could be protected by traditional protection devices such as the overcurrent protection device and residual current device.

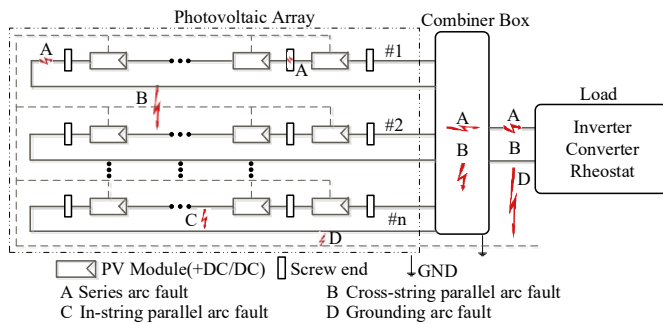


Figure 1.1 Arc fault classification in photovoltaic systems (In some PV systems, DC/DC converters are connected to PV modules to achieve the maximum power output)

Because the series arc fault cannot be detected by the existing protection devices, the developed high temperature ionized gas exists continuously. The released heat can ignite the combustible material around and spread to burn the system components, eventually causing the power failure and fire accidents [10][11]. Most of PV systems are installed on the roofs of buildings, occurred fire becomes even dangerous when the heat stored in ordinary PV system polymers such as polycarbonate, nylon 6.6 and PET is enough [12]. Due to the large number of components, connectors and cables existing in PV systems, the duration, propagation speed and occurrence scale of PV arc faults are not easy to control. Moreover, the existence of outdoor irradiance makes PV array continuously inject energy into arc faults. Under the joint action of photocurrent independence, PV arc faults have stable combustion environment. Therefore, the fire prevention of PV arc faults is difficult. The occurred fire accident is easy to destroy all the PV modules on the power station and buildings completely. In addition, arc faults also consume the output power of the system, reducing the operation efficiency of the system. And they can transmit the electricity to the system device and support electrification, causing electric shock even life threats to personnel in contact with the device. In addition to the thermal damage, arc fault can also cause different kinds

of damages to the human body, such as the explosion pressure damage, hearing damage, radiation damage [13].

This paper focuses on PV arc faults viewed from their diagnosis and modeling methods. In section II, diagnosis methods are summarized from their sampling signal type in detail. In section III, arc fault models are reviewed from the model extracting idea. In section IV, future diagnosis methods are discussed due to the rapid development of data processing chip and machine learning technology.

2 Diagnosis methods of PV arc faults

2.1 Physical signal based PV arc fault diagnosis method

Based on the multi-dimensionality of the arc fault emission, a dual-sensor system consisting of electromagnetic and sound sensors is used. In addition, the time of arrival (TOA) to each sensor is also obtained through the signal processing method, so that the precise identification of the arc fault is achieved in PV systems [14].

A fourth-order Hilbert curve fractal antenna is used to detect the electromagnetic radiation (EMR) characteristics of PV arc faults. Viewed from the spectrum of electromagnetic radiation signal, the characteristic frequency of PV arc fault is around 39 MHz. Compared with the switch operation, PV arc fault behaves higher characteristic frequency and longer pulse interval [15]. Another advantage of EMR based detection method is that malfunctions of fault-like conditions would be effectively avoided. Steady patterns such as the structural similarity index (SSIM) and 6-dB bandwidth bins (6-dB BWBs) are proposed to extract PV arc fault features, accurately distinguishing PV arc faults from fault-like operations [16].

2.2 Electrical signal based PV arc fault diagnosis method

Based on physical signal of arc faults, arc fault detection algorithm is able to be simplified for decreasing fault-like interference consideration. Relying on the special sensor, physical signal based arc fault detection methods have shortcomings such as limited detection range and narrow application scope. However, interference factors are extremely increased in PV systems for their exposed environment [17]. Therefore, the electrical characteristics are chosen as the sampling signal in most PV arc fault researches.

2.1.1 Time-domain based arc fault diagnosis method

Time-domain diagnosis methods are usually described as a mathematical equation, directly outputting one-dimensional detection variable value.

PV arc faults would distort the loop current signal in time domain including sudden changes and irregular fluctuations, which are obtained by the Euler method and variance analysis

[18][19]. Euler method focuses on current changes between two adjacent time windows while variance analysis focuses on the current fluctuation in a certain time window. In the steady-burning arc stage with the constant arc gap length, the variance analysis could still show arc fault differences for the arc instability nature. Involving the calculation of the time window, Euler method and variance analysis could be turned into the current change rate and range value [20][21]. In grid-connected PV systems with a single-phase inverter, the Tsallis entropy is applied to analyze the arc fault current. Focusing on the time-domain randomness nature of arc faults, the arc fault occurrence is identified as soon as arc fault periods are found over 3 times within 0.5s [22].

2.1.2 FFT based arc fault diagnosis method

To improve the arc fault detection accuracy, the arc fault spectrum is conducted to acquire more useful information in most literatures.

Fast Fourier transform (FFT) is a basic spectrum analysis method. Belonging to the frequency-domain method, the FFT analysis should be conducted for the normal and arc fault current separately. In PV resistive systems without extra strong switching noises, arc fault noises are relatively pure. After the arc fault occurrence, the amplitude of arc fault current spectrum would increase compared with that of normal current [23].

In grid-connected PV systems, the arc fault spectrum also generally shows an increased amplitude pattern. However, the arc fault and normal state would display the serious overlap in the frequency band of switching frequency and its related harmonics for inverter interferences. While containing these information, the detection variable would become insignificant so that the misoperation would appear [24]-[27]. Compared with normal current sensors including current probe, current transformer and hall sensor, the magnetoresistance (TMR) sensor is designed to acquire more obvious arc fault spectrum under many influence factors [28].

The determination of the arc fault occurrence time is the key task for the arc fault detection algorithm. But FFT is a global transformation, only giving a kind of information before or after the transform. Then it cannot reflect the time-varying changes of the PV arc fault spectrum. Therefore, the FFT analysis is destined to failure of grasping when PV series arc fault occurs, which cannot be used directly for the arc fault detection.

2.1.3 Time-frequency-domain based arc fault diagnosis method

It is necessary to consider the time-frequency-domain analysis methods to simultaneously obtain both time and frequency information of the PV arc fault current. Most decomposition coefficients cannot be directly used as arc fault characteristics. Besides, clear detection variables are also required to reduce the two-dimensional result. Then the extracted detection variables could achieve the state judgment process. Therefore,

it is necessary to extract detection variables to process the time-frequency coefficient.

Accompanied with the Rectangular window, the FFT analysis analyzes the input current signal window by window, turning into the STFT analysis. Involving the transient arc state, it is possible for the STFT analysis to identify the arc fault as earlier as possible. All-phase FFT (APFFT) is applied to acquire the frequency response of arc fault current in a certain cycle [29]. Then a window by window mode is used to obtain the whole analyzed results for different current states. Detection variables including average value, maximum value, addition value are combined with the STFT analysis [29][31]. Before conducting the transform analysis, some software based filter methods including Kalman filter are recommended to improve the detection accuracy [32]. After the filter effect of the Hamming window, more obvious arc fault features and better detection results could be acquired [2].

The STFT analysis with the rectangular window based arc fault detection algorithm is implemented by using DSP. The PV current signal is obtained by a high frequency current transformer, filtered by a band-pass infinite impulse response (IIR) digital filter. After analyzing the characteristics of the signal frequency band, the arc fault state is identified by comparing the threshold value. It is pointed out that the fault-like malfunctions of commercial detection devices could be conquered [33][34].

The basic idea of short time Fourier transform (STFT) is to acquire locally stationary current signal for the FFT analysis. Through a time window sliding on the time axis, the local analysis in the time domain is realized. However, it's found that the window function limits the time width and frequency width, leading to difficulties of achieving the optimal time resolution and frequency resolution at the same time. Wavelet transform (WT) also has good time-frequency localization properties, which can convert the time-domain current to plenty information in the time-frequency domain. It has a higher frequency resolution and a lower time resolution in the low frequency part while it has a higher time resolution and a lower frequency resolution in the high frequency part. In the arc fault detection field, two kinds of WT analysis are often used. As shown in 02.1, discrete wavelet transform (DWT) uses low-pass and high-pass filters to divide only the approximate signal decomposed by the original current. Wavelet packet decomposition (WPD) simultaneously applies two filters to divide the approximate and detail signals obtained by the previous layer. For the WPD analysis, the high-frequency information has higher resolution and more appropriately divided information [35].

Selecting a proper mother wavelet is the most difficult problem, which is a key factor affecting the PV arc fault detection effectiveness. In the research of the arc fault detection, Daubechies wavelet family have the outstanding performance in detecting the discontinuity of arc fault signals [36][37]. Most existing arc fault detection researches usually use it as the mother wavelet in PV resistive systems. Db4 wavelet is used to extract three detection variables, realizing the parallel arc fault detection in PV resistive systems [38]. The optimization of the Daubechies wavelet family is

conducted to obtain better arc fault detection results in the PV resistive system. Compared with Db3, the frequency response of Db9 has a more pronounced cut-off frequency. Although Db19 has more wavelet coefficients, it does not provide the same significant improvement compared with Db9. Considering better approximation results and fewer mathematical operations, Db9 is recommended as the eclectic mother wavelet in the Daubechies family [39]. Capacitors are brought to the PV system as a current sensor. For the high-pass effect of capacitors, the high frequency components of the arc fault current could be directly acquired to detect the PV arc faults. Through the DWT analysis based on Db9, the time-frequency distribution of the capacitor current is acquired. Then the polarities, amplitudes, and integrals of the distribution are used as the key attributes to distinguish PV series arc faults from fault-like conditions [40]. However, the arrangement and cost of extra capacitors are a difficult problem in the large-scale PV power station.

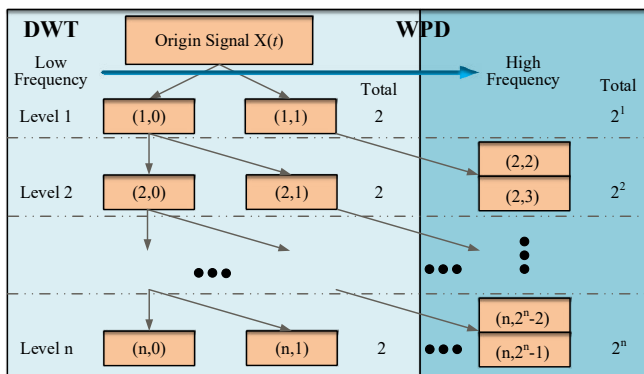


Figure 2.1 Different analysis architectures between DWT and WPD [35]

From the above time-frequency distribution results in PV resistive systems, the arc fault would show the increased spectrum amplitude. However, different arc fault behaviors would appear in PV systems with the inverter or dc-dc converter operating. In frequency bands containing the switching frequency and its harmonics, the relatively weak arc fault noise would be interfered by the strong switching noise. Then the arc fault spectrum amplitude shows the similar level to the normal spectrum, forming the constant amplitude pattern shown in Fig. 2.2. While these frequency bands are adopted, which would lead to the failure problem of the arc fault detection in grid-connected PV systems. While the angle between the injected switching noise and the arc fault signal is proper, Db9 wavelet based detection variables begin to show a decreasing amplitude pattern shown in Fig. 2.2. These seriously overlapping detection variables would appear in higher frequency bands, eventually causing failure tripping under arc fault conditions. Therefore, a proper mother wavelet is investigated for PV systems with the power electronic equipment.

The precise arc fault occurrence time and the obvious arc fault state separation are the key factors for the accurate arc fault detection. The symmetric property of the mother wavelet is beneficial to the singularity detection of arc faults. The

biorthogonality property and vanishing moment could display the arc salient disturbances more clearly. Having better performance in these three properties, the Rbio3.1-based features are recommended to achieve the PV arc fault detection. Then the Rbio3.1 is able to give more arc fault occurrence time discovery pulses and better arc fault separation degree. As shown in Fig. 2.3, Rbio3.1 can achieve the significant improvement in arc fault detection effects compared with the same calculation process of Db9. For different factors such as switching frequencies, inverter types, and inverter stages, Rbio3.1 successfully changes the constant or even decreasing amplitude pattern to the desired increasing amplitude pattern. Meanwhile, this feature improvement ability may not appear under fault-like conditions. Therefore, the Rbio3.1 wavelet can grasp more obvious arc fault features, which would significantly improve the detection accuracy of arc faults [41].

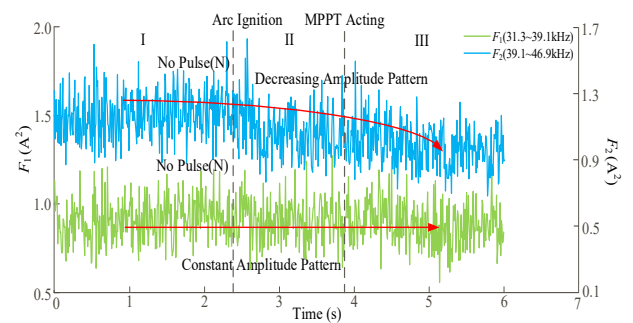


Figure 2.2 Detection variable results using the Db9-based WPD analysis [35]

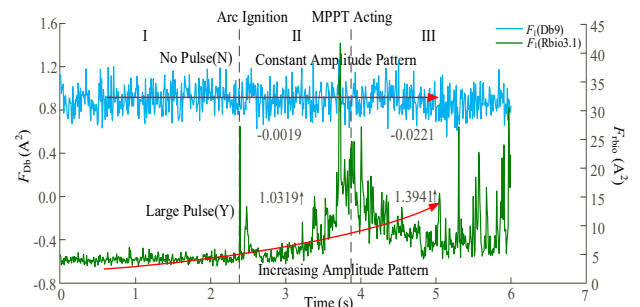


Figure 2.3 The effectiveness improvements of the detection variable result using the Rbio3.1-based WPD analysis [35]

For both two linear time-frequency transforms, corresponding parameters including the window type, mother wavelet type and the time window length are demanded to be optimized, achieving the best identification results. The STFT analysis has the less calculation load than the WT analysis. Therefore, most signal processing chips choose the STFT analysis to implemented. It is also found that the low-frequency characteristics of the STFT analysis is better while high-frequency characteristics of the WT analysis is better [42]. There are many other kinds of the time-frequency-domain analysis methods except two transforms claimed above. For instance, the variational mode decomposition (VMD) is adopted to extract the characteristic frequency band of the PV arc current, which could conquer the modal aliasing and

endpoints effects. Then the detection variable based on Shannon entropy is used as a combination [43].

3 PV arc fault models

Since the field testing is costly and time consuming, precisely modeling arc faults becomes more critical. In addition, the establishment of the arc model is very important to grasp the relationship between the arc faults and the system, to simulate the electrical signals of the arc faults under special conditions, to elaborate the essential characteristics and generation mechanism of the arc faults, and to explain the macroscopic phenomena of the arc faults. Because the characteristics of the arc faults may be affected by the fault location and current level, the arc fault data obtained from the real system is limited. Therefore, a more complete arc fault database can be established by using arc fault model for simulation analysis, and diverse arc fault conditions can be developed to help develop arc fault detection algorithm.

For the arc fault modeling, it is difficult to obtain helpful electrical signals from magnetic field simulation [44]. The simulation from the circuit angle could obtain the relevant electric signals of arc fault directly. The arc fault could be modeled as a circuit component in PV system, which gives satisfactory fitting results with the current less than 10A [45]. Erhard divided the arc faults into three parts including anode fall region, cathode fall region and arc column. Results show that a series arc fault could influence the operating point of the PV system [46]. At present, there are mainly three following types of arc fault models.

3.1 Dynamical state model

Mayr model assumes that the arc is a cylindrical gas channel with a constant diameter, and the energy dissipation from the arc gap is constant [47]. Energy dissipation depends on the effect of heat conduction and radial diffusion. In other words, the temperature of the arc changes with the radial distance and time from the arc axis. The expression for Mayr model is as follows:

$$\frac{1}{g} \frac{dg}{dt} = \frac{1}{\tau} \left(\frac{i_{arc}^2}{P} - 1 \right) \quad (1)$$

where g is arc conductance, i_{arc} is arc current, τ is arc time constant, P is static cooling power. And the Mayr model is suitable for the case of small current, and it is used to analyze the dynamic characteristics of current crossing zero.

Cassie model assumes that the shape of an arc is a cylinder of highly ionized gas and free electrons [48]. The arc column has a constant temperature and current density, and its diameter varies with the change of current. It assumed that the arc voltage was constant, and the energy dissipation was caused by forced convection. In addition, the power loss of the arc was proportional to the cross-sectional area of the arc column. Based on the above assumptions, the following formula is obtained:

$$\frac{1}{g} \frac{dg}{dt} = \frac{1}{\tau} \left(\frac{u^2}{u_c^2} - 1 \right) \quad (2)$$

where g is arc conductance, τ is arc time constant, u_c is constant arc voltage, u is the arc voltage. Cassie arc model is more suitable for high levels of current.

In addition, some other physical-based arc model such as improved Cassie and Mayr models can also be used for arc simulation of PV systems [49]-[51]. But the parameters selection of physical-based arc model is a difficult problem, complex models are often difficult to simulate. A black-box parameter determination method is proposed. Its effectiveness is verified by the Schwarz model in experiments [52]. The non-linear least squares is proposed to identify the parameters and optimize the arc model [53]. The Cassie model is used to simulate the arc fault in the DC resistive system. However, this study only displays the simulated arc fault noise below 5 kHz, which does not involve the simulation of high-frequency arc fault characteristics [39].

3.2 Stationary state model

The V-I model considers the static characteristics of the air arc. This model is described by the empirical model obtained by fitting a large amount of experimental arc voltage and current data. The applicable range of arc current and gap is different for each V-I model [54]-[56]. In terms of the arc fault current and gap range specified in UL1699B, the Paukert model is an acceptable choice. Moreover, the arc gap was added to the Paukert model, realizing the better fitting performance.

In 1993, Paukert proposed an arc model with the arc current ranged from 0.3A to 100kA and the electrode gap widths ranged from 1 to 200mm [57]. This model is divided into two equations, one is for arc current less than 100A and the other is for arc current greater than 100A. In 2014, considering the influence from the arc gap length, modified Paukert arc model is proposed with the electrode gap widths ranged from 1.016mm to 3.048mm [58]. This model gives a more accurate description of the arc with small gap widths, the modified equation is as follows:

$$V_{arc} = \frac{A + BL}{I_{arc}^{C+DL}} \quad (7)$$

where A, B, C, D are constants, L is the gap widths.

In recent years, there are also some models to describe the behavior of arc voltage and current by using equations. Uriarte found that the arc voltage and current are approximated with the hyperbola, so an arc model suitable for dc microgrid is proposed [59][58]:

$$v_{gap} = v_q + e_{gap} \quad (8)$$

$$v_q = V_{dc} \left(\frac{1}{2} + \frac{1}{2} \tanh(\alpha(q-1)) \right) = V_{dc} \left(\frac{e^{2q\alpha}}{e^{2\alpha} + e^{2q\alpha}} \right) \quad (9)$$

$$e_{gap} = \frac{1}{2}(a + bx_{gap})(\tanh(\lambda q) - \tanh(\lambda(q-1))) \quad (10)$$

$$q = \frac{x}{x_{gap}} \quad (11)$$

where v_{gap} is the arc voltage, v_q is the hyperbolic-tangent component, e_{gap} is the electromotive force (EMF) pulse term, V_{dc} is the average dc voltage before fault, α is a variable related to the slope of v_q , a , b , λ are the variables related to e_{gap} , x_{gap} is the electrodes width when the arc quench, x is the electrodes width. There's a similar equation for arc current i_{gap} in the model. According to the experimental and simulation results, this model is suitable for transient simulations of the arc voltage, current and power.

3.3 High-frequency component model

The V-I characteristic model only shows the evolution of the dc component, without the unique high-frequency arc behavior. However, the plasma discharge process in the arc fault channel will cause the high frequency components in the arc fault current signal. The collision between molecules in the plasma channel and coulomb shows the randomness of the arc faults, forming the high frequency components dominated by molecular collision. At present, there are many arc fault detection methods based on frequency domain characteristics. Thus it is of great significance to establish an accurate high-frequency variation arc model.

Zero-mean noise is added to the arc model to describe the frequency characteristics of the arc [60]-[62]. The arc noise equation is as follows:

$$\xi(x) = \frac{1}{\sigma\sqrt{2\pi}} \exp\left(-\frac{x^2}{2\sigma^2}\right) \quad (14)$$

where σ is the standard deviation. Terzija verified the feasibility of using gaussian distribution to describe the randomness of arc current. Furthermore, the distribution was proved to be quantitatively correlated with the level of dc component of arc current [63].

It is found that PV arc faults have broadband characteristics [24]. Random functions are used to describe the frequency characteristics of an arc [64]. Researchers found that the frequency characteristic of the arc was similar to pink noises [65]. And pink noise was added to the arc simulation of the PV system [22][66]. Because the power spectral density of the pink noise is inversely proportional to the frequency of the signal, a high-frequency variation arc model based on pink noise is proposed [42]. A digital filter is designed to generate pink noise from white noise, the equation is as follows:

$$H(z) = \frac{1 + 0.5z^{-1} - 0.125z^{-2} + 0.063z^{-3} - 0.036z^{-4} - 0.026z^{-5} + 0.007z^{-6} - 0.005z^{-7}}{1 - 0.5z^{-1} - 0.125z^{-2} - 0.063z^{-3} - 0.036z^{-4} + 0.026z^{-5} + 0.007z^{-6} + 0.005z^{-7}}$$

A modified pink noise is used to describe the arc noise, the equations are proposed as [67]:

$$S(f) = \frac{c_1}{\ln(v)} + c_2 \quad (15)$$

$$c_1 = \frac{20 \log_{10}(\sqrt{f_c}) \ln(2) \ln(v)}{\ln\left(\frac{v}{2}\right)} \quad (16)$$

$$c_2 = 20 \log_{10}(w) - \frac{20 \log_{10}(\sqrt{f_c}) \ln(2)}{\ln\left(\frac{v}{2}\right)} \quad (17)$$

$$v = a_2(f_c^{b_2} - 1) + 2 \quad (18)$$

where f_c is the cut-off frequency, w is the white noise, $S(f)$ is the magnitude of the power spectral density (PSD) curve, c_1 and c_2 are the parameters associated with the cut-off frequency and DC value of the PSD, a_2 is the parameter associated with the steepness of the slope before the cut-off frequency, b_2 is the parameter associated with the moving tendency of the modified pink noise, v is the slope at frequencies before the cut-off frequency. This high-frequency variation arc model could change the slope and cut-off frequency of the PSD and other parameters to generate several different arc fault noise characteristics.

4 Discussion and conclusion

Nowadays, rapid developments of the PV industry make the PV system more complex, which poses new challenges to the arc fault detection. Many system factors including switching noises, branch connection form, cable length would affect the PV arc fault detection, forming various PV arc fault conditions [68][69]. Then the obtained arc fault conditions are limited from the experiments. Considering the accurate detection of the unknown arc fault and fault-like conditions, the future algorithm is recommended to adopt machine learning based fusion methods. Then this arc fault detection algorithm could achieve more applicable scenarios and higher detection accuracy.

In the future, the frequently-used data processing chip may have larger data storage capacity and higher calculation speed. Then this kind of chip could realize the fast calculation of the complex time-frequency transform and machine learning methods. Then the detection accuracy and application scope of PV arc faults could be significantly improved. Without increasing computation time, the detection reliability of the designed hardware is highly enhanced.

5 Acknowledgement

This work was supported by the Key Science and Technology Project of China Southern Power Grid Corporation (090000KK52180116).

6 Literature

- [1] F. Dincer, "The analysis on photovoltaic electricity generation status, potential and policies of the leading countries in solar energy," in *Renewable & Sustainable Energy Reviews*, vol. 15, no. 1, pp. 713-720, Jan 2011.
- [2] S. Chen, X. Li, and J. Xiong, "Series arc fault identification for photovoltaic system based on time-domain and time-frequency-domain analysis," in *IEEE Journal of Photovoltaics*, vol. 7, no. 4, pp. 1105-1114, Jul 2017.
- [3] J. Rogelj *et al.*, "Paris Agreement climate proposals need a boost to keep warming well below 2 degrees C," in *Nature*, vol. 534, no. 7609, pp. 631-639, Jun 30 2016.
- [4] K. H. Solangi *et al.*, "A review on global solar energy policy," in *Renewable & Sustainable Energy Reviews*, vol. 15, no. 4, pp. 2149-2163, May 2011.
- [5] D. S. Pillai *et al.*, "Extended analysis on line-line and line-ground faults in PV arrays and a compatibility study on latest NEC protection standards," in *Energy Conversion and Management*, vol. 196, pp. 988-1001, Sep 15 2019.
- [6] National Fire Protection Association. *NFPA 70: National electrical code*. NationalFireProtectionAssoc, 2011..
- [7] T. Zgonena, L. Ji, and D. Dini. "Photovoltaic DC arc-fault circuit protection and UL Subject 1699B," *Photovoltaic Module Reliability Workshop*, Golden, CO, 2011..
- [8] International Electrotechnical Commission. "General requirements for arc fault detection devices," *International Electrotechnical Commission: Geneva, Switzerland*, 9 July 2013.
- [9] T. Awoniyi. *Transition to DC distribution grids*. MS thesis. UiT Norges arktiske universitet, 2017.
- [10] W.-S. Moon *et al.*, "Ignition characteristics of residential series arc faults in 220-V HIV wires," in *IEEE Transactions on Industry Applications*, vol. 51, no. 3, pp. 2054-2059, May-Jun 2015.
- [11] D. J. Hoffmann, E. M. Swonder, and M. T. Burr, "Arc faulting in household appliances subjected to a fire test," in *Fire Technology*, vol. 52, no. 6, pp. 1659-1666, Nov 2016.
- [12] K. M. Armijo *et al.*, "Characterizing fire danger from low-power photovoltaic arc-faults," *2014 IEEE 40th Photovoltaic Specialist Conference (PVSC)*, Denver, CO, 2014, pp. 3384-3390.
- [13] L. B. Gordon and L. Cartelli, "A complete electrical hazard classification system and its application," *2009 IEEE IAS Electrical Safety Workshop*, St. Louis, MO, 2009, pp. 1-12.
- [14] C. Vasile and C. Ioana, "On the multi-modal sensing of electrical arcs," *2017 IEEE Sensors Applications Symposium (SAS)*, Glassboro, NJ, 2017, pp. 1-5.
- [15] Q. Xiong *et al.*, "A novel dc arc fault detection method based on electromagnetic radiation signal," in *IEEE Transactions on Plasma Science*, vol. 45, no. 3, pp. 472-478, Mar 2017.
- [16] S. Zhao *et al.*, "A series dc arc fault detection method based on steady pattern of high-frequency electromagnetic radiation," in *IEEE Transactions on Plasma Science*, vol. 47, no. 9, pp. 4370-4377, Sep 2019..
- [17] Y. Ma *et al.*, "DC fault arc identification and detection analysis of photovoltaic power generation system," *2018 International Conference on Robots & Intelligent System (ICRIS)*, Changsha, 2018, pp. 63-65..
- [18] S. Chen *et al.*, "Hardware implementation of series arc fault detection algorithm for different DC resistive systems," *2019 IEEE Holm Conference on Electrical Contacts*, Milwaukee, WI, USA, 2019, pp. 245-249..
- [19] S. Chen and X. Li, "PV series arc fault recognition under different working conditions with joint detection method," *2016 IEEE 62nd Holm Conference on Electrical Contacts (Holm)*, Clearwater Beach, FL, 2016, pp. 25-32..
- [20] Y. Gao *et al.*, "An innovative photovoltaic DC arc fault detection method through multiple criteria algorithm based on a new arc initiation method," *2014 IEEE 40th Photovoltaic Specialist Conference (PVSC)*, Denver, CO, 2014, pp. 3188-3192.
- [21] J. Johnson and J. Kang, "Arc-fault detector algorithm evaluation method utilizing prerecorded arcing signatures," *2012 38th IEEE Photovoltaic Specialists Conference*, Austin, TX, 2012, pp. 1378-1382.
- [22] N. L. Georgijevic *et al.*, "The detection of series arc fault in photovoltaic systems based on the arc current entropy," in *IEEE Transactions on Power Electronics*, vol. 31, no. 8, pp. 5917-5930, Aug. 2016.
- [23] Y. Cao *et al.*, "Arc fault generation and detection in DC systems," *2013 IEEE PES Asia-Pacific Power and Energy Engineering Conference (APPEEC)*, Kowloon, 2013, pp. 1-5.
- [24] C. Strobl and P. Meckler, "Arc faults in photovoltaic systems," *2010 Proceedings of the 56th IEEE Holm Conference on Electrical Contacts*, Charleston, SC, 2010, pp. 1-7.
- [25] C. Luebke *et al.*, "Field test results of DC arc fault detection on residential and utility scale PV arrays," *2011 37th IEEE Photovoltaic Specialists Conference*, Seattle, WA, 2011, pp. 1832-1836..
- [26] G. Artale *et al.*, "Experimental characterization of series arc faults in AC and DC electrical circuits," *2014 IEEE International Instrumentation and Measurement Technology Conference (I2MTC) Proceedings*, Montevideo, 2014, pp. 1015-1020.
- [27] J. Johnson *et al.*, "Differentiating series and parallel photovoltaic arc-faults," *2012 38th IEEE Photovoltaic Specialists Conference*, Austin, TX, 2012, pp. 720-726..
- [28] W. Miao *et al.*, "Arc-faults detection in PV systems by measuring pink noise with magnetic sensors," in *IEEE Transactions on Magnetics*, vol. 55, no. 7, pp. 1-6, July 2019, Art no. 4002506..
- [29] M. Li *et al.*, "Series arc fault detection in DC microgrid using hybrid detection method," *IECON 2018 - 44th Annual Conference of the IEEE Industrial Electronics Society, Washington, DC, 2018*, pp. 265-270..
- [30] G. Seo, J. Ha, B. Cho and K. Lee, "Series arc fault detection method based on statistical analysis for dc Microgrids," *2016 IEEE Applied Power Electronics Conference and Exposition (APEC)*, Long Beach, CA, 2016, pp. 487-492..
- [31] S. Chen *et al.*, "A synthetic method for photovoltaic series arc fault detection with different loads and its identification" *28th International Conference on Electric Contacts*, Edinburgh, 2016, pp. 379-384.
- [32] M. Ahmadi, H. Samet, and T. Ghanbari, "Kalman filter-based approach for detection of series arc fault in photovoltaic systems," in *International Transactions on Electrical Energy Systems*, vol. 29, no. 5, May 2019, Art. no. e2823.
- [33] J. Gu *et al.*, "Design of a DC series arc fault detector for photovoltaic system protection," in *IEEE Transactions on Industry Applications*, vol. 55, no. 3, pp. 2464-2471, May-June 2019.
- [34] M. I. Fitrianto *et al.*, "Identification and protection of series DC arc fault for photovoltaic systems based on fast Fourier transform," *2019 International Electronics Symposium (IES)*, Surabaya, Indonesia, 2019, pp. 159-163.
- [35] S. Chen *et al.*, "Wavelet-based protection strategy for series arc faults interfered by multicomponent noise signals in grid-connected photovoltaic systems," in *Solar Energy*, vol. 183, pp. 327-336, May 1 2019.
- [36] W. K. Ngui *et al.*, "Wavelet analysis: mother wavelet selection methods," in *Applied Mechanics and Materials*, vol. 393, pp. 935-8, 2013 2013..
- [37] I.-S. Kim, "On-line fault detection algorithm of a photovoltaic system using wavelet transform," in *Solar Energy*, vol. 126, pp. 137-145, Mar 2016.
- [38] C. He, L. Mu and Y. Wang, "The detection of parallel arc fault in photovoltaic systems based on a mixed criterion," in *IEEE Journal of Photovoltaics*, vol. 7, no. 6, pp. 1717-1724, Nov. 2017..
- [39] Z. Wang and R. S. Balog, "Arc fault and flash signal analysis in DC distribution systems using wavelet transformation," in *IEEE Transactions on Smart Grid*, vol. 6, no. 4, pp. 1955-1963, July 2015.
- [40] Q. Xiong *et al.*, "Detecting and localizing series arc fault in photovoltaic systems based on time and frequency characteristics of capacitor current," in *Solar Energy*, vol. 170, pp. 788-799, Aug 2018.
- [41] S. Chen and X. Li, "Experimental study and feature improvement of DC series arc faults with switching noise interference," *2018 IEEE Holm*

- Conference on Electrical Contacts*, Albuquerque, NM, 2018, pp. 135-142.
- [42] S. Chen *et al.*, "Time-frequency distribution characteristic and model simulation of photovoltaic series arc fault with power electronic equipment," in *IEEE Journal of Photovoltaics*, vol. 9, no. 4, pp. 1128-1137, July 2019.
- [43] S. Lu *et al.*, "Application of the variational mode decomposition-based time and time-frequency domain analysis on series DC arc fault detection of photovoltaic arrays," in *IEEE Access*, vol. 7, pp. 126177-126190, 2019.
- [44] Q. G. Reynolds, R. J. Jones, and B. D. Reddy, "Mathematical and computational modeling of the dynamic behaviour of direct current plasma arcs," in *Journal of the Southern African Institute of Mining and Metallurgy*, vol. 110, no. 12, pp. 733-742, Dec 2010.
- [45] J. Andrea *et al.*, "Simulation of arcing fault in PV panel network," *2018 IEEE Holm Conference on Electrical Contacts*, Albuquerque, NM, 2018, pp. 329-335.
- [46] F. Erhard, B. Schaller and F. Berger, "Field test results of serial DC arc fault investigations on real photovoltaic systems," *2014 49th International Universities Power Engineering Conference (UPEC)*, Cluj-Napoca, 2014, pp. 1-6.
- [47] O. Mayr, "Beitrag zur Theorie des Statischen und des Dynamischen Lichthogens," in *Archiv für Elektrotechnik*, vol. 37, no. 12, pp. 588-608, 1943.
- [48] A. M. Cassie, "Theorie Nouvelle des Arcs de Rupture et de la Rigidité des Circuits," in *Cigre Report*, vol. 102, pp. 588-608, 1939.
- [49] A. Sawicki, "About using of modified Cassie models to simulate impact of arc column length disturbances on the work of electrical devices," in *Przegląd Elektrotechniczny*, vol. 88, no. 9A, pp. 107-110, 2012 2012.
- [50] A. Balestrero *et al.*, "Black box modeling of low-voltage circuit breakers," in *IEEE Transactions on Power Delivery*, vol. 25, no. 4, pp. 2481-2488, Oct. 2010.
- [51] F. Bizzarri and A. Brambilla, "Brushing up on the urbanek black box arc model," in *IEEE Transactions on Circuits and Systems I: Regular Papers*, vol. 65, no. 5, pp. 1675-1683, May 2018.
- [52] M. Walter and C. Franck, "Improved method for direct black-box arc parameter determination and model validation," in *IEEE Transactions on Power Delivery*, vol. 29, no. 2, pp. 580-588, April 2014.
- [53] K. Park *et al.*, "Parameter identification of dc black-box arc model using non-linear least squares," in *The Journal of Engineering*, vol. 2019, no. 16, pp. 2202-2206, March 2019.
- [54] R. F. Ammerman *et al.*, "DC-arc models and incident-energy calculations," in *IEEE Transactions on Industry Applications*, vol. 46, no. 5, pp. 1810-1819, Sept.-Oct. 2010.
- [55] W. B. Nottingham, "A new equation for the static characteristic of the normal electric arc," in *Trans. Amer. Inst. Elect. Eng.*, vol. 42, pp. 302, 1923.
- [56] A. D. Stokes, W. T. Oppenlander, "Electric arcs in open air," in *Journal of Physics D-Applied Physics*, vol. 24, no. 1, pp. 26-35, Jan 14 1991.
- [57] J. Paukert, "The arc voltage and the resistance of LV fault arcs," *Seventh International Conference on Switching Arc Phenomena. Part 1: Conference Materials*, pp. 49-52, 1993.
- [58] X. Yao *et al.*, "Characteristic study and time-domain discrete-wavelet-transform based hybrid detection of series DC arc faults," in *IEEE Transactions on Power Electronics*, vol. 29, no. 6, pp. 3103-3115, June 2014.
- [59] F. M. Uriarte *et al.*, "A DC Arc Model for Series Faults in Low Voltage Microgrids," in *IEEE Transactions on Smart Grid*, vol. 3, no. 4, pp. 2063-2070, Dec. 2012.
- [60] M. B. Djuric and V. V. Terzija, "A new approach to the arcing faults detection for fast autoreclosure in transmission systems," in *IEEE Transactions on Power Delivery*, vol. 10, no. 4, pp. 1793-1798, Oct. 1995.
- [61] V. V. Terzija and H. J. Koglin, "On the modeling of long arc in still air and arc resistance calculation," in *IEEE Transactions on Power Delivery*, vol. 19, no. 3, pp. 1012-1017, July 2004.
- [62] X. Yao, L. Herrera and J. Wang, "Impact evaluation of series dc arc faults in dc microgrids," *2015 IEEE Applied Power Electronics Conference and Exposition (APEC)*, Charlotte, NC, 2015, pp. 2953-2958..
- [63] V. V. Terzija, M. Popov, V. Stanojevic and Z. Radojevic, "EMTP simulation and spectral domain features of a long arc in free air," *CIRED 2005 - 18th International Conference and Exhibition on Electricity Distribution*, Turin, Italy, 2005, pp. 1-4.
- [64] G. Seo *et al.*, "A new DC arc fault detection method using DC system component modeling and analysis in low frequency range." *2015 IEEE Applied Power Electronics Conference and Exposition (APEC)*, Charlotte, NC, 2015, pp. 2438-2444.
- [65] J. Johnson *et al.*, "Photovoltaic DC arc fault detector testing at Sandia National Laboratories," *2011 37th IEEE Photovoltaic Specialists Conference*, Seattle, WA, 2011, pp. 3614-3619.
- [66] S. Lu, B. T. Phung and D. Zhang, "Study on DC series arc fault in photovoltaic systems for condition monitoring purpose," *2017 Australasian Universities Power Engineering Conference (AUPEC)*, Melbourne, VIC, 2017, pp. 1-6.
- [67] C. J. Kim, L. Brad and B. Roy, "DC arc fault model superimposing multiple random arc noise states on an average model." *2019 20th Workshop on Control and Modeling for Power Electronics (COMPEL)*, IEEE, 2019.
- [68] J. Johnson and K. Armijo, "Parametric study of PV arc-fault generation methods and analysis of conducted DC spectrum," *2014 IEEE 40th Photovoltaic Specialist Conference (PVSC)*, Denver, CO, 2014, pp. 3543-3548.
- [69] J. Johnson *et al.*, "Using PV module and line frequency response data to create robust arc fault detectors," *26th European International Conference on Photovoltaic Solar Energy*, 2011, pp. 3745-3750.

Threshold Current of Arc-Free Commutation For Copper-Carbon Contact in a DC Hybrid Switch

Chomrong Ou, Huang Yinming, and Koichi Yasuoka,
Tokyo Institute of Technology, Department of Electrical and Electronic Engineering, Tokyo, Japan
ou@hv.ee.e.titech.ac.jp

Abstract

Hybrid DC switches (HDCSs) have attracted considerable attention due to the low on-state loss and fast current interruption. With low current interruption, there is no arc generation between the contacts. However, arc discharge occurs between the contacts after the contact opens for a high circuit current. Arc discharge erodes the surface of the contacts and decreases the insulation strength between the contacts. This paper presents a new configuration of contacts that can increase the threshold current for arc-free commutation. The contact has a cuboid shape with a join of copper and carbon. When the contacts are in the closing position, the copper and carbon materials of the contacts come in contact. When the contacts start opening, the contact spots of the copper start decreasing until rupture, but carbon, which has a higher resistivity than copper, still remains in contact. With a higher resistance of the contacts, the current is further commutated to the semiconductor device until the current at the contacts becomes low. After the contacts rupture, the low surge voltage from the inductance in the circuit cannot ignite arc discharge. Thus, arc-free commutation can be achieved.

Keywords– Hybrid DC switch, copper-based carbon contact, arc discharge, threshold current, arc-free commutation.

1 Introduction

Arc can be longer for DC interruption than AC interruption [1], [2], [3]. Arc discharge in electric contact is a harmful phenomenon which erodes the surface of contacts and decreases the insulation strength between the contacts [1-3]. The arc discharge from DC current interruption can be longer than that of AC current interruption [4-5]. Hybrid DC switches (HDCSs) comprising of a parallel connection with **contacts serving as mechanical switch (MS)** and a semiconductor device are an effective solution due to the low on-state loss and rapid current interruption [6-7]. HDCSs overcomes the drawbacks of conventional mechanical switches (MSs) and semiconductor devices. **The HDCSs is used with microgrid with voltage level of a few kV.** MSs have a low contact resistance but suffers from long-duration arc when the contact opens, which results in serious contact erosion and a short lifespan. Semiconductor switching devices interrupt the current rapidly without an arc, but they have a high on-state resistance and low thermal capacity. This causes considerable power loss and requires a greater amount of space.

Figure 1 shows the circuit diagram of an HDCS that is used DC voltage distribution below 2 kV. The HDCS has a **mechanical switch (MS)** connected in parallel with a SiC-MOSFET and a metal-oxide varistor (MOV). Figure 2 shows the effect of current interruption in the HDCS. During normal operation, a circuit current from the DC source flows through **MS** to the load at position (1). When the current needs to

be interrupted in the case of faults, the contacts are separated, and simultaneously, the SiC-MOSFET turns on at position (2). Then, the current is commutated to the SiC-MOSFET, the commutated from the contacts to the SiC-MOSFET device. After the entire SiC-MOSFET carries the current for a while so that the contact has enough gap to prevent breakdown caused by the surge voltage after the SiC-MOSFET turns off at position (3). The surge voltage occurs between the contacts and potentially leads to breakdown between the contacts if the dielectric strength of the gap is not enough. Then, the surge decreases to the system voltage because the MOV absorbs the remaining current in the circuit.

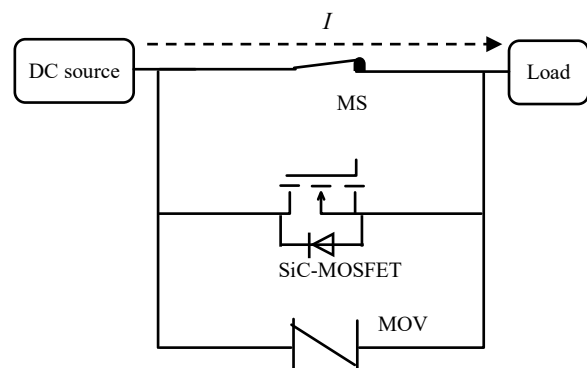


Fig. 1 Circuit diagram of a hybrid DC switch.

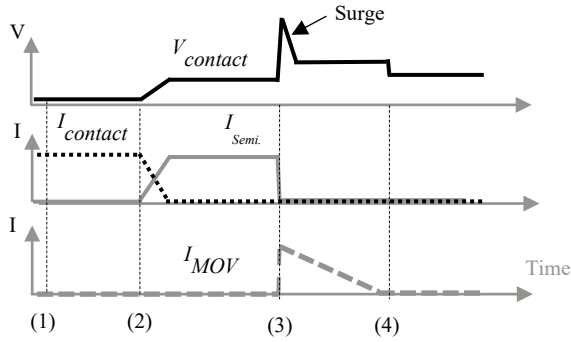


Fig. 2 Operating diagram of a hybrid DC switch.

In previous researches, the contact material was found to have an influence on the arc-free commutation in the hybrid DC switch [8-10]. For experiment on the effect of the contact material, the authors compared the threshold current of arc-free commutation of a pair of copper contacts with a pair of tungsten contacts. The copper and tungsten contacts could commutate the current up to 120 A and 300 A, respectively, without arc discharge. Copper-based tungsten (Cu-W) contacts that had tungsten material on top of the copper contact could commutate current up to 400 A without arc discharge. The current was fed by voltage up to 20 V. Although Cu-W contacts showed threshold current up to 400 A with arc-free commutation, the contact resistance at the closing contacts was high compared to that of copper contacts. This results in power loss during normal operation of the switch. Therefore, we propose a new design of the contact, which has low contact resistance during normal operation and increases the threshold current of arc-free commutation.

2 Experimental Setup

Figure 3 shows a circuit diagram of the HDCS used in the experiments. A DC power supply was connected in parallel with a switch S , a SiC-MOSFET (Cree, CAS325M12HM2), and a MOV (Panasonic, ERZE14A431). The circuit current was generated from a DC power supply having a current rate of 800 A. In the experiment, we used a pair of contact as shown in Fig. 4. The left contact was made from a copper cuboid, and a joint of carbon plate was inserted on top of the cuboid as shown in Fig. 4(a). The joint was made by a high conductive paste (Cr-3520, KAKEN TECH) under cueing of 150 °C for 30 minutes and 180 °C for 60 minutes. The thickness of the carbon plate was 1 mm. The right contact was made from copper and had the same shape as that shown in Fig 4(b). The upper side of the right contact had a hole 3 mm in diameter. The right contact was fixed by a tungsten rod that was inserted into the hole of the right contact. The lower side of the right contact was attached to a coil compression spring (AP065-010-0.9, Showa Spring) with maximum force of 26 N. The maximum load of the spring was 26 N. The direction of spring force was leftward. The right

contact was the ground and was moveable. The left contact was the anode, and it was fixed with a stepping motor as shown in Fig. 5. The left contact was moved by the stepping motor towards the right for closing the contact and towards the left for opening the contact. The spring force could push the lower part of the right contact by 15° in the clockwise. A direct current of up to 800 A was fed through the circuit. The closing force was 40 N. For the contact opening operation, we turned on the SiC-MOSFET at the same time when the left contact started moving to the left direction at a speed of 200 mm/s. When the contacts started separating, the contact area between the copper material of the left contact and the right contact decreased, but the carbon material still remained in contact due to the force of the spring. When the left contact moved further, the contact area of the carbon decreased and was completely ruptured. Then, we turned off the SiC-MOSFET after the contact opened for 20 ms.

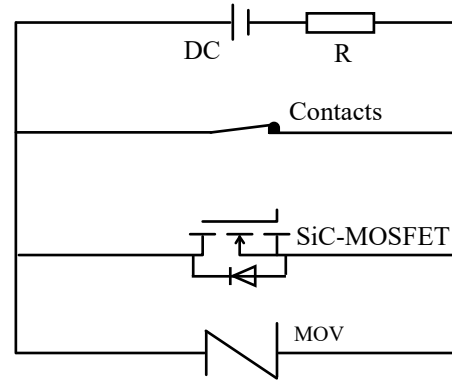


Fig. 3 Experimental circuit diagram of hybrid DC switch.

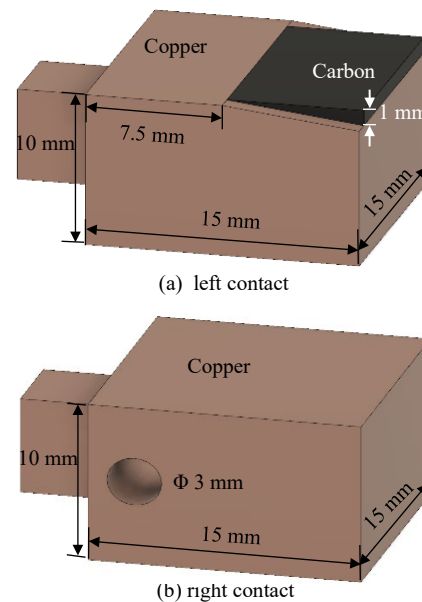


Fig. 4 Configuration of the right and left contacts.

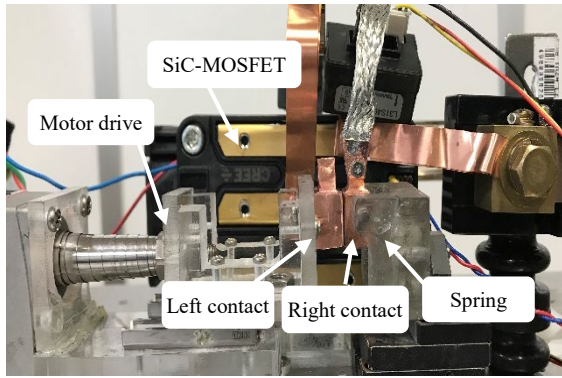


Fig. 5 Actual experimental setup of hybrid DC switch.

3 Experimental Results

3.1 Contact Resistance

Figure 6 shows the average value of contact resistance in this work (Cu-C contacts) with tungsten (W) contacts and copper-tungsten (Cu-W) contacts for currents from 100 to 400 A with closing force of 47 N for all currents. The contact resistance of tungsten contacts is the highest for all currents. The contact resistance of Cu-W is between the contact resistances of tungsten and Cu-C contacts, and it decreases with increasing current due to the softening and expand of the contact a-spots when a large current and contact closing force were applied in the contacts. For Cu-C contacts, the contact resistance was low for all values of current because the current flows through the copper of the left contact, which has low resistivity.

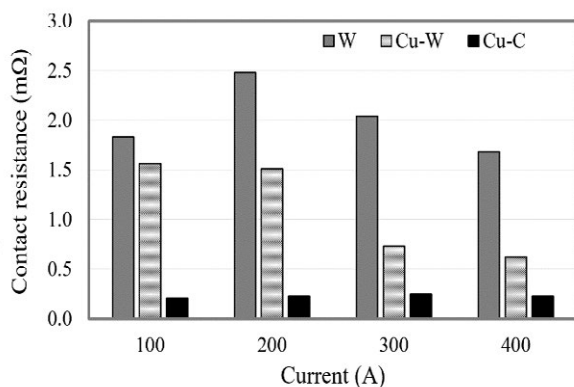


Fig. 6 Contact resistance of tungsten, Cu-W, and Cu-C contacts [12].

3.2 Threshold Current for Arc-Free Commutation

Figure 7 shows the voltage and current waveforms with arc-free commutation for 700 A. Before the contact separation at approximately 2 ms, the circuit current

flowing through the contacts is 700 A, and the contact voltage is slightly above 0 V. After the contacts start separating, the contact voltage increases with time, and the contact current decreases accordingly. The decrease in contact current indicates that a partial current is flowing to the SiC-MOSFET. Then, a pulse suddenly occurs at approximately 7.6 ms, and the contact current drops rapidly. After the pulse, the contact voltage increases further and the contact current decreases to zero at 11 ms. The main cause of current commutation is the increase in contact resistance. Fig. 8 shows the image of contacts during separation in the commutation phase from Fig. 7. During the initial contact closing, the copper and carbon materials of the left contacts are in contact with the right contact as shown in Fig. 8(a). The contacts have much lower resistance than that of the SiC-MOSFET. Therefore, almost all of the circuit current flows through the contacts. After the contacts start separating, the contact force is released and the contact area of the copper material of the left contact decreases with time but this does not happen for the carbon material. Then, the copper in the left contact ruptures at 7.6 ms as shown in Fig. 8(b). Owing to the large differential resistivity of carbon and copper as shown in Table 1, the resistance of the contact in

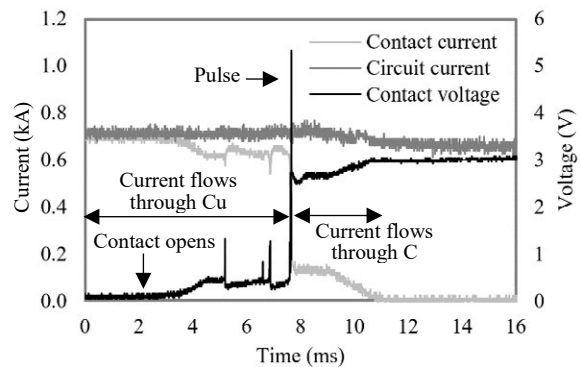


Fig. 7 Contact voltage and current waveforms of the arc-free commutation of copper-carbon contact for 700 A.

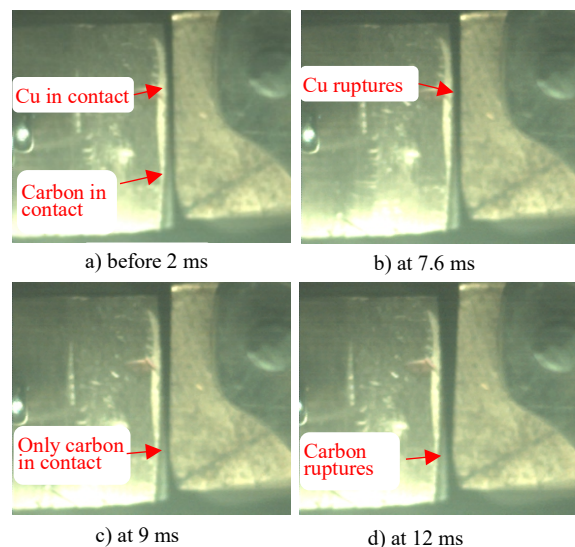


Fig. 8 Image of contact opening in commutation phase.

Table 1.
Properties of contact materials [11]

Material	Resistivity ($\Omega\cdot\text{m}$)	Temp. Coeff. (K^{-1})
Copper	1.8×10^{-8}	4×10^{-3}
Carbon	3.5×10^{-5}	-5×10^{-13}

creases significantly and commutates the circuit current to the SiC-MOSFET. The entire current is not commutated to the SiC-MOSFET; a partial current still flows through the carbon, which is still in contact with the right contact due to force of the spring as shown in Fig. 8(c). Afterward, the contact current drops further when the contact area of the carbon decreases until rupture, and the current at the contact is almost zero. After the rupture, there is no surge voltage because of the small $L(di/dt)$.

Figure 9 shows the contact resistance calculated from equation (1).

$$R_C = R_{SiC} \frac{I - I_c}{I_C} \quad (1)$$

where R_{SiC} is the resistance of the SiC-MOSFET, and I and I_C are the circuit current and contact current, respectively.

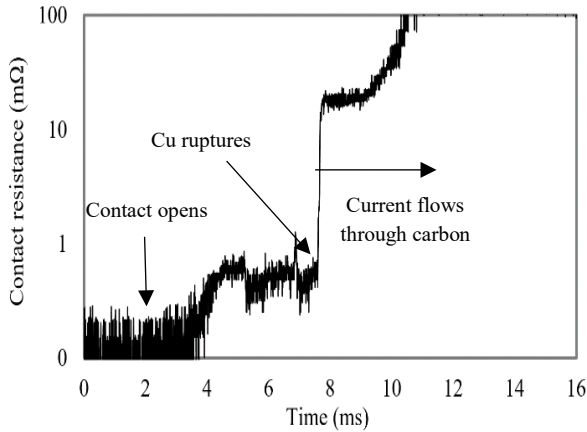


Fig. 9 Contact resistance calculated from Fig. 7.

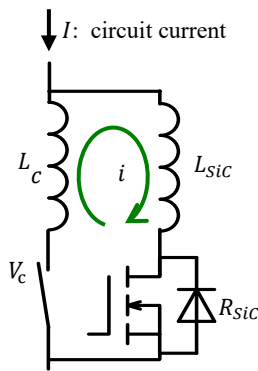


Fig. 10 Circuit diagram of loop circuit between the contacts and the SiC-MOSFET.

We simplified the calculation of the contact resistance by neglecting the inductance in the circuit. In our experiment, R_{SiC} is 4 m Ω . The values of circuit current and contact current are taken from Fig. 7. From Fig. 9, the calculated contact resistance is about 0.2 m Ω , and it increases up to 0.8 m Ω at 7.6 ms when the copper of the left contact ruptures. Then, the resistance promptly increases to 40 m Ω . The prompt increase in resistance causes the contact current to decrease rapidly, which creates the pulse at 7.6 ms. The pulse was due to the inductance and derivation of current with respect to time, $L(di/dt)$ in the loop circuit between the contacts and the SiC-MOSFET as shown in Fig. 10. However, the surge does not cause arc generation because the surge voltage does not reach the critical voltage to generate arc discharge. When the carbon is absent, the current drop at the contacts is larger, which causes a larger surge voltage that can generate an arc discharge. To generate arc discharge, a contact voltage of at least the minimum arc voltage is required. The minimum arc voltage of copper is 12.19 V [13]. When we increased the circuit current to 800 A, the surge voltage reached the critical voltage, generating an arc discharge. Fig. 11 shows an example of the current commutation with an arc discharge of 800 A. With increase in current to 800 A, the current drop is higher than 700 A, at the copper ruptures. Then, the $L(di/dt)$ generates a high surge voltage that generates an arc discharge at 8.67 ms. A light emission from the arc discharge was found between the contacts. The arc trace is found at the copper part of the left contact as shown in Fig. 12

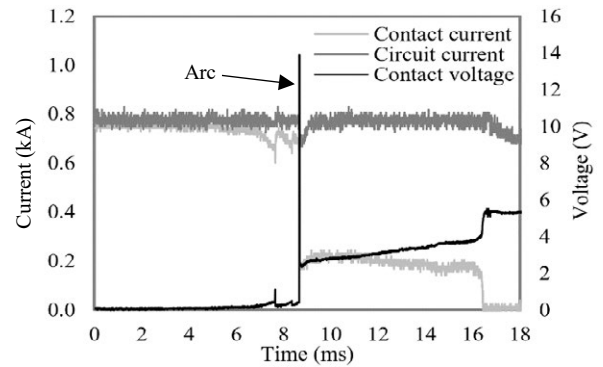


Fig. 11 Current commutation of copper-carbon contact for 800 A.

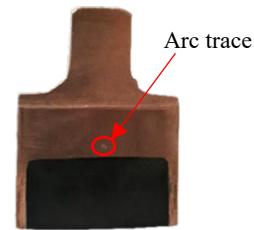


Fig. 12 Arc traces from experiment of Cu-C contacts.

3.3 Current Interruption

Figure 13 shows the contact voltage and current waveforms for 700 A current interruption. The contact opens at approximately 15 ms, and the entire circuit current is transferred to the SiC-MOSFET at 22 ms. Afterward, we turned off the SiC-MOSFET at 35 ms. After turning off, the circuit current dropped to zero, while a pulse voltage of approximately 300 V was induced. The pulse is caused by the rapid drop in the circuit current. However, this voltage does not ignite an arc or cause a breakdown because the SiC-MOSFET can withstand a voltage of up to 1.2 kV and the contacts have an air gap of approximately 2 mm, which has enough dielectric strength to prevent arc discharge or breakdown. The interruption time can be shortened by decreasing the degree of inclination of the right contact, separation speed, and turning-off time of the SiC-MOSFET.

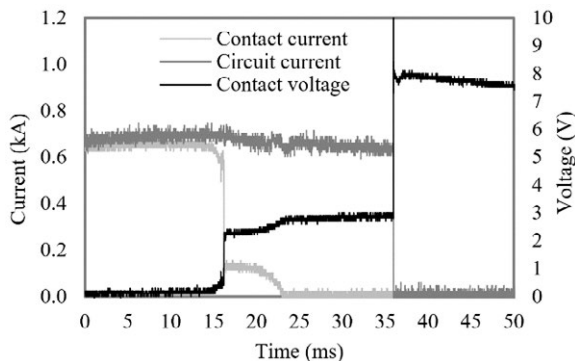


Fig. 13 Contact voltage and current during current interruption of Cu-C at 700 A.

3.4 Current Interruption

Figure 14 shows the voltage and current waveforms for the contact closing at 700 A. From 0–4 ms, the contacts were in separated position, and the SiC-MOSFET was turned on. Therefore, approximately 300 A flows through the SiC-MOSFET. From 4 ms, the carbon material of the contact starts to come in contact with the right contact. The circuit current increases with time because the contact area of carbon increases with increasing contact force when the left contact moves toward the right. From 16.5 ms, the copper material of the left contact is in contact with the right contact. Owing to the low resistivity of copper, majority of the circuit current flows through the contacts. Although the current increases rapidly, a surge voltage was not found between the contacts. In a conventional switch, arc discharges are found due to the bouncing contact when a strong contact force is applied to close the contacts [14]. With an additional spring, the contacts do not bounce and an arc discharge is not found.

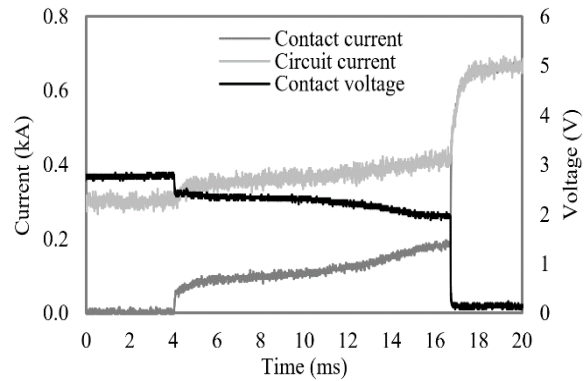


Fig. 14 Voltage and current waveforms for closing contacts.

4 Conclusion

A join of copper and carbon contact can interrupt current up to 700 A with arc-free commutation. Because the copper and carbon of the left contact are in contact with the right contact during normal operation, the contact resistance is low. The copper-carbon contact can commutate current up to 700 A without arc discharge because the carbon material of the left contact has a high resistance to commutate almost the entire current to the SiC-MOSFET. However, an arc discharge is found at the copper material of the left contact when we increase the current higher than 700 A due to the current drop at the contact is large that causes large difference between the copper and carbon materials. To increase further threshold current for arc-free commutation, a material having a resistivity between that of copper and carbon should be inserted to prevent rapid drop in contact current. Although the interruption time is about 20 ms, the interruption time can be improved by increasing the separation speed of the contact driven by the stepping motor, the inclination of the right contact, or the turning-off time of the SiC-MOSFET. With a spring force, the bouncing arc does not occur.

ACKNOWLEDGEMENT

This work was supported by JSPS KAKENHI Grant Number JP18H01420. The authors would like to thank Japan International Cooperation Agency – JICA.

REFERENCES

- [1] Z. Zaluchi and J. Kutzner, "Dielectric strength of a vacuum interrupter contact gap after making current operations," *IEEE Trans on Diel. and Elec. Insu.*, vol. 10, no. 4, pp. 583–589, Aug. 2003.
- [2] C. Ou, R. Nakayama, S. Zen, K. Yasuoka, "Influence of a short-duration arc on the erosion and dielectric strength of narrow air gap contacts in a hybrid Dc switch," *IEEE Trans. on Comp., Pack. and Manu. Tech.*, vol. 9, no. 6, pp. 1068–1074, June 2019.

- [3] T. Qin, E. Dong, G. Liu and J. Zou, "Recovery of dielectric strength after DC interruption in vacuum," *IEEE Trans. Diel. and Elec. Insu.*, vol. 23, no. 1, pp. 29–34, Feb. 2016.
- [4] R. Ma, M. Rong, F. Yang, Y. Wu, H. Sun, D. Yuan, H. Wang and C. Niu, "Investigation on arc behavior during arc motion in air DC circuit Breaker," *IEEE Trans. Plas. Scie.*, vol. 41, no. 9, pp. 2551–2560, Sep. 2013.
- [5] K. Sawa and M. Tsuruoka and S. Yamashita, "Fundamental arc characteristic at DC current interruption of low voltage(<500V)," in *Proc. 27th Inte. Conf. on Elec. Cont.*, Jun. 2014, pp. 662–667.
- [6] Y. Bingjian, G. Yang, W. Xiaoguang, H. Zhiyuan, C. Longlong and S. Yunhai, "A hybrid circuit breaker for DC-application," in *Proc. 2015 IEEE First Inter. Conf. on DC Micr. (ICDCM)*, Jun. 2015, pp. 187–192.
- [7] A. Mokhberdorani, O. G. Bellmunt, N. Silva and A. Carvalho, "Current flow controlling hybrid DC circuit breaker," *IEEE Trans. Powe. Elec.*, vol. 33, no. 2, pp. 1323–1334, Feb. 2018.
- [8] K. Yasuoka, Y. Tsuboi, T. Hayakawa, N. Nozomi, "Arcless commutation of a hybrid DC breaker by contact voltage of molten metal bridge," *IEEE Trans. on Comp., Pack. and Manu. Tech.*, vol. 8, no. 3, pp. 350–355, March 2018.
- [9] M. Chen, K. Nakayama, S. Zen, K. Yasuoka, "Study on Cu-W cold contact materials with arc-less current commutation in a hybrid DC switch," in *Proc. 2018 IEEE Holm Conf. on Elec. Cont.*, Octo. 2018. pp. 166–171.
- [10] S. Zen, T. Hayakawa, K. Nakayama and K. Yasuoka, "Development of an arcless DC circuit breaker using a mechanical contact and a semiconductor device," in *Proc. 2017 IEEE Holm Conf. on Elec. Cont.*, Sep. 2017. pp. 249–252.
- [11] R. Holm, "Electric Contacts: Theory and Application," 4th edit., Berlin, Germany: Springer-Verlag, 1967.
- [12] K. Yasuoka, Y. Yamada and M. Chen, "Contact Resistance and Arc-free Commutation Current of Tungsten-clad Copper Contacts for a Hybrid DC Switch," 019 IEEE Holm Conference on Electrical Contacts, Milwaukee, WI, USA, 2019, pp. 359-362.
- [13] P. G. Slade, "Electrical Contacts: Principles and Application," 2th edit., New York, CRC Press, Taylor & Francis Group, 2014.
- [14] K. Yoshida, S. Shimotsuma, K. Sawa, K. Suzuki, K. Takaya, "Various characteristics of electromagnetic contactor when arc discharge are generated only make arc," in *Proc. 2016 IEEE Holm Conf. on Elec. Cont.*, Octo. 2016. pp. 215–221.

Hybrid DC switch with a Four-block Copper-Based Tungsten Contact

Yinming Huang, Chomrong Ou, Koichi Yasuoka
Tokyo Institute of Technology, Tokyo, Japan, ming@hv.ee.e.titech.ac.jp

Abstract

For DC switches, the most promising topology is the hybrid DC switch, in which the circuit current commutates from mechanical contacts to a semiconductor device after the opening of the contacts. During the commutation period the contact temperature continues to increase, and once the temperature exceeds the boiling temperature of the contact metal, metal vapor generates between the contacts and hence leads to arc discharge. The threshold current of arc-free commutation can be increased by using tungsten contacts, however, a concentration of the contact current limits the maximum arc-free current. A new structure of four-block contacts has been developed to avoid the current concentration by splitting the contact current and heat. With heat being distributed, the temperature on the surface of the contact is lowered significantly, this will provide the contact with a larger arc-free current. We evaluated the four-block structure of contacts by numerical simulations and experiments up to DC 400 A.

Key words – Hybrid DC switch, arc-free commutation, Cu-W clad electrical contact

1 Introduction

Recently, the DC system has been intensively studied due to the increasing requirement of renewable energy such as solar and wind power. Those needs for load supplied by direct currents such as electric cars and electric trains are also showing significance [1]. One of the key components of the DC system is the circuit breaker because the direct current has no regularly zero crossing, and the arc generated between the mechanical contacts cannot be easily eliminated comparing to alternating current. In order to solve this problem, the most frequently used structure is the hybrid DC circuit switch, which contains a mechanical switch for on-state and a solid-state semi-conductor switch for commutation, as shown in **Fig. 1**. In recent year, the researches on hybrid DC switch are making progress. A DC hybrid circuit breaker with ultra-fast contact opening and integrated gate-commutated thyristors(IGCTs) was designed to interrupt 1.5 kV/ 4 kA within 300 μ s [2], a 270 V hybrid DC switch with capability of arc free commutation up to 100 A has been designed [3].

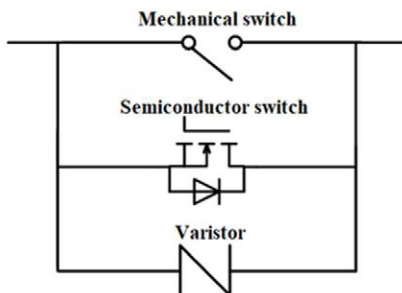


Fig. 1 Configuration of hybrid DC switch

One promising semiconductor device that could be applied in the hybrid DC circuit breaker is a SiC (Silicon-Carbide) MOSFET, which has a low on-state resistance. Its characteristic makes the current commutate at a lower voltage, and hence possible to commutate with no arc generation within a certain value of current, which is determined by the specific value of the contact material. The previous experiment has indicated an arc-free commutation of DC 300 V, 200 A, using tungsten contacts [4]. The contact erosion by arc can be avoided with arc-free commutation, therefore, the life of the contact greatly increases. However, in order to face the actual application in the DC system, a larger current limit is of vital importance.

To increase the current limit, the contact material of higher boiling temperature is required to raise the arc-free commutation current. Tungsten is a promising material that can sustain 2.1 V of contact voltage without arc generation. This value is largest among all metal materials, and the relation between the contact voltage and the maximum surface temperature is given as the following equation [5].

$$T_{max} = \sqrt{\frac{V_c^2}{4L} + T_0^2}$$

, where the highest temperature in the contact area T_{max} [K], the voltage between contacts V_c [V], Lorenz number L , the room temperature T_0 .

However, the resistance of tungsten is relatively large comparing to the normally used contact material copper, this can cause large on-state energy losses.

In **Fig. 2**, the waveforms of contact voltage in the previous experiment for arc-free commutation with different contact designs are given.

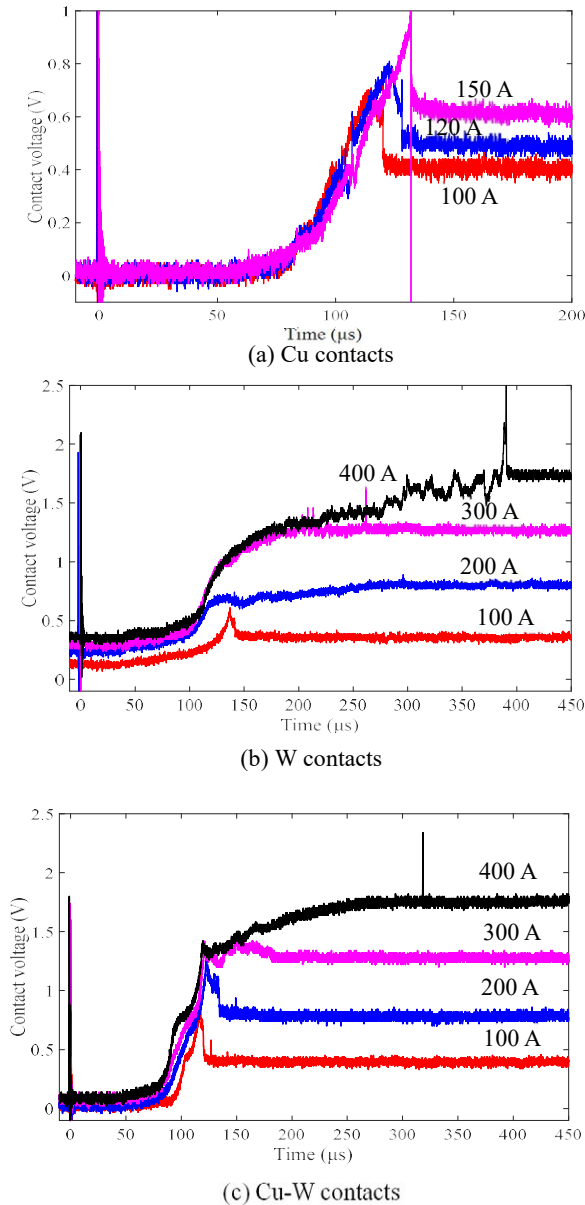


Fig. 2 Contact voltage in commutation phase [6]

In Fig. 2, the contact voltage increased as the contacts began to separate, arc discharges during this period was indicated by surges of current. Therefore, according to Fig. 2, the maximum no arc commutation current of Cu, W, and Cu-W contacts are 120A, 300A, 400A respectively.

In this paper, a new structure of the Cu-W contacts is introduced, comparing to the previous contact using copper as substrate and a thin, flat tungsten clad as the contact area, the new structure of the contact separated the flat tungsten clad to four small blocks with each block shaped as square of 1.5 mm of length. This new structure allows current to conduct at multiple points rather than concentrate at one point. With current being separated, the temperature on the surface of the contact can be lowered significantly, thus, this will provide the contact with a larger on-state current limit and ability to achieve the commutation without arc generation under larger current.

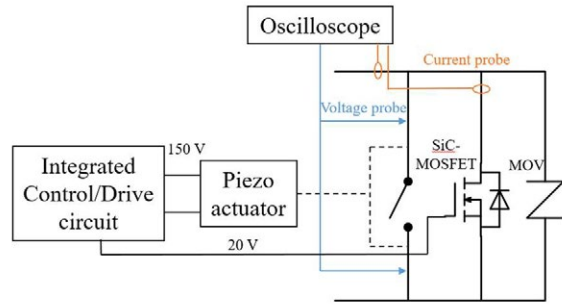


Fig. 3 Structure of Hybrid DC switch for experiment

2 Experimental methods

2.1 Hybrid DC switch and contacts

The hybrid DC switch used in the experiment is shown in Fig. 3. The mechanical part of the hybrid DC switch used the copper-clad contact and a magnified piezoelectric actuator to exert the movement of the contact. The actuator model APF710 manufactured by Thorlabs, controlled by 150 V of voltage and applies force to the contact of approximately 50N.

The model of SiC-MOSFET used in the hybrid DC switch is CAS325M12HM2 made by Wolfspeed, Inc., 1200 V, 444 A, 3.7mΩ of on-state resistance according to its date sheet. The model of varistor used is ERZV20D391, which has a varistor voltage of 390 V and maximum clamping voltage is 650 V. The experiment focused mostly on the commutation, therefore the varistor used has a relatively low clamping voltage.

The figure of contact is shown in Fig. 4 where Fig. 4a shows the previous Cu-W clad structure and Fig. 4b shows the new designed Cu-W 4-block structure. Both structures have a cylinder shape copper with a 10 mm diameter and a 14 mm length as the substrate. However, the previous Cu-W clad contact has a flat 1 mm length cylinder tungsten as the top layer while the new Cu-W block structure replaces the top layer with 4 small blocks. The Cu-W clad contacts were manufactured by Metal Technology Company by using the brazing method, the new Cu-W block structure contacts are made by using wire electrical discharge machining (WEDM).

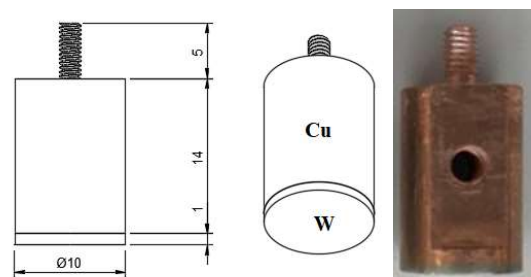


Fig. 4a Previous Cu-W clad structure

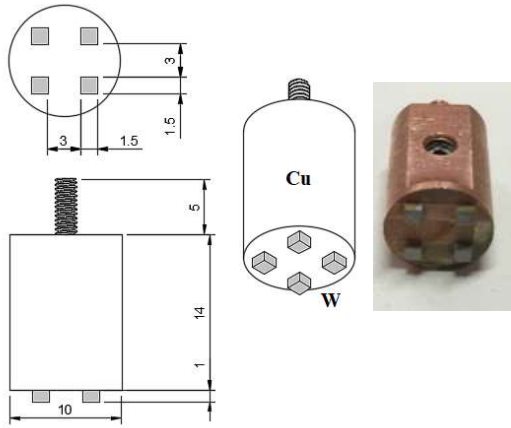


Fig. 4b New Cu-W block structure

2.2 Simulation method

The simulation was achieved by COMSOL multiphysics 5.4 with the three-dimensional joule heating time-dependent study, including the heat transfer, electric potential, electric magnetic heating, and other physics. Two types of contacts have been put into the simulation as shown in Figs. 5a and b.

Determining the exact contact area is difficult by experiment so the solution used is to estimate the contact area by contact voltage in the experiment which is 0.41 V [6], and therefore apply the same contact area to the simulation. The contact area in the simulation was approximately 0.027 mm^2 for the previous Cu-W clad structure shown in Fig. 4a. For the new designed Cu-W 4-block structure, the total contact area remained unchanged as 0.027 mm^2 except for separated into four same parts with 0.006 mm^2 each and distributed at the same distance. This simulation is the ideal model of the new Cu-W block structure shown in Fig. 5b as it assumed the contact area of each block are completely the same and the current flows through each block's contact area averagely.

The mesh has been refined in the contact area specifically to acquire better results as well as fitting the small contact area. To compare the characteristic of each structure, the other parameters are set as the same.

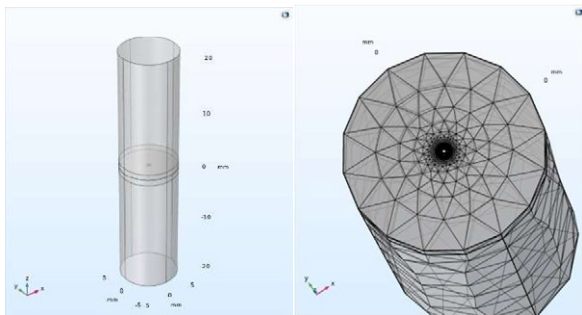


Fig. 5a Cu-W clad geometry and contact area mesh

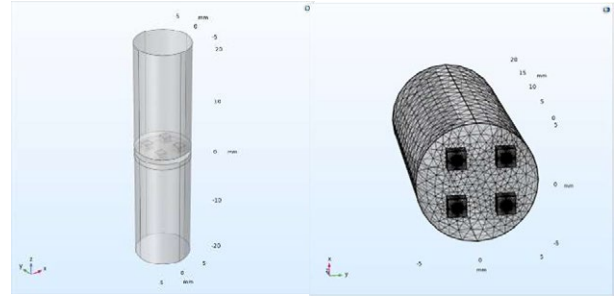


Fig. 5b Cu-W block geometry and contact area mesh

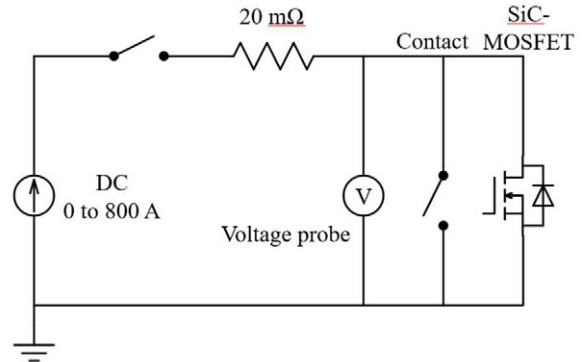


Fig. 6 Commutation experimental circuit

2.3 Experimental circuit

The commutation experimental circuit is shown in Fig. 6. The circuit includes a DC power source with current can be ranged from 0 to 800 A, the maximum output voltage was 20 V. The power source was connected to the DC switch through a resistor of 20 mΩ. The DC switch used in the experiment is the one shown in Fig. 3 with the varistors were removed since only the commutation phase is of interest.

3 Experimental results and discussion

3.1 Contact resistance

The contact resistance of on-state was calculated by four-terminal sensing by using the circuit of Fig. 6,

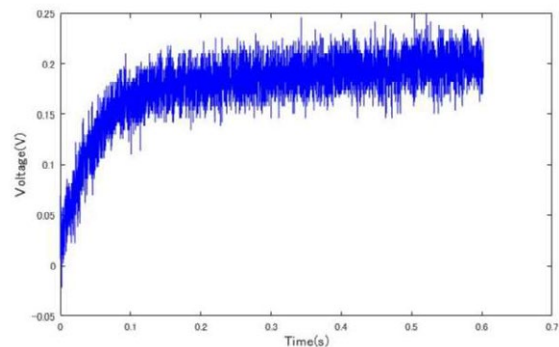


Fig. 7 Contact voltage detected under 300 A

while the SiC-MOSFET was turned off and the contacts were closed by a contact force of 50 N. The voltage probe was attached to the copper part of the contact near the through hole in Fig.4b. A current probe was also placed to monitor the contact current.

The result of the new designed 4-block structure contacts is shown in Fig. 7. The current increased to 300 A at around 0.15 s and kept almost constant. The contact voltage was approximately 200 mV at under 300A. The time of current conducting was short, therefore, the resistance influence by heat can be ignored. The voltage probe was attached to the copper and is close to the contact area, so the voltage drop by the probe connection was also small enough to be ignored as well. As a result, the contact resistance was roughly 0.67 mΩ, which was the same value as the value measured with the previous Cu-W clad structure contact.

Considering the contact force is certain, the total contact area of the 4-block structure and the Cu-W clad structure should be the same. In case of a clean metal contact, contact resistance R_c is simply considered as a constriction resistance, which is calculated by the equation below, where ρ is resistivity, and a is the radius of contact area [5].

$$R_c = \frac{\rho}{2a}$$

As a result of the contact resistance experiment, it showed that the total resistance of the new Cu-W 4-block contacts have the same contact area as the previous Cu-W clad structure and the resistance is basically the same.

3.2 Simulation results

The simulation result was carried out by using COMSOL, including the comparison of the 4-block Cu-W contact with the previous Cu-W clad contact under the same current value and with the same contact area, the temperature of the 4-block Cu-W contact under different current value. In addition, a model of 4-block Cu-W contact with only 2 points conduct was made to study the relationship between the maximum temperature and the number of conduct points.

The heat distribution simulation result of the previous Cu-W clad contact, the 4-block Cu-W contact with 2 points connected and the 4-block Cu-W contact with all four points connected under 450 A of current are shown in Fig. 8. The simulation was time-dependent and the figure was taken 1 s after the current started conducting.

As shown in Fig. 8, for the Cu-W clad contact, the temperature of the contact area reached 1600 K after 1 s passed. For the new 4-block structure contact with two points conducted, the peak temperature was 533 K by the simulation with all conditions were set the same as the previous Cu-W clad contact and the total contact

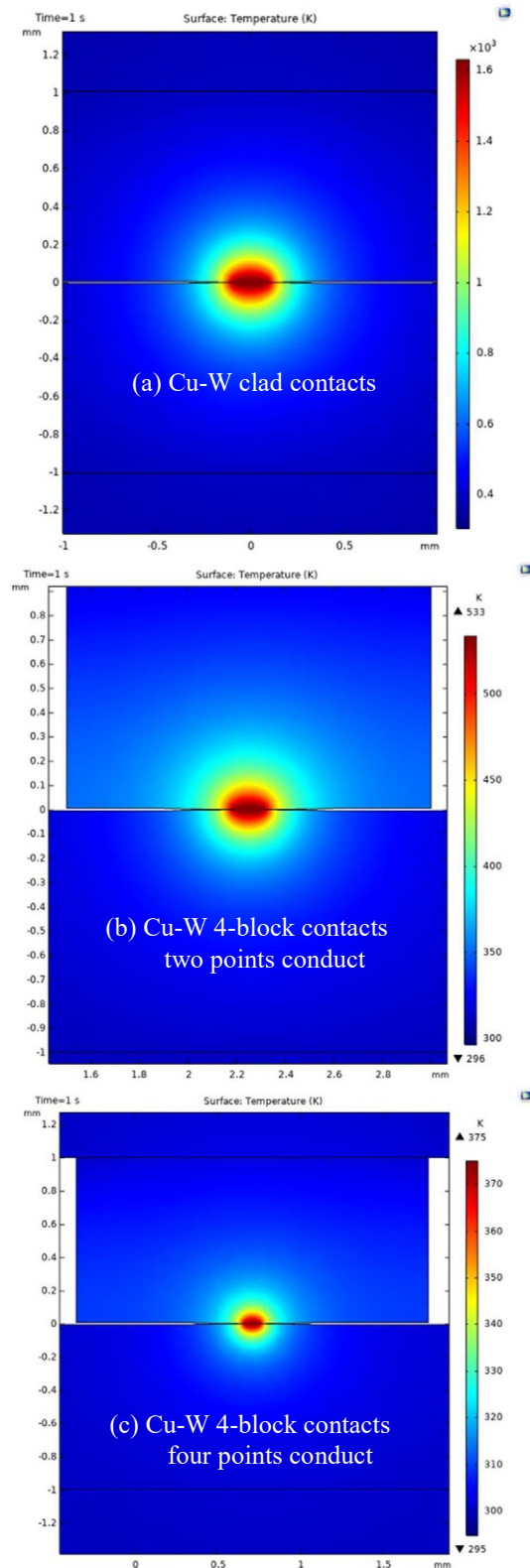


Fig. 8 Heat distribution simulation under 450 A area was the same as well. The 4-block structure with four points conducted had a temperature of 375 K with all conditions unchanged and the total contact area the same as well.

The comparison of maximum contact temperature of different types of contact under the current of 450 A is shown in Fig. 9. It shows that the temperature

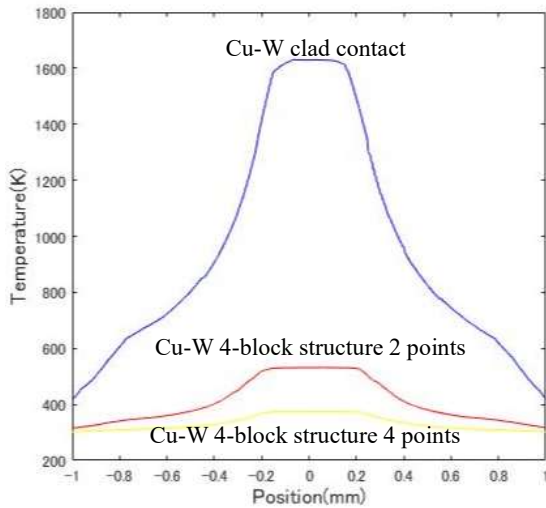


Fig. 9 Comparison of contact area temperature

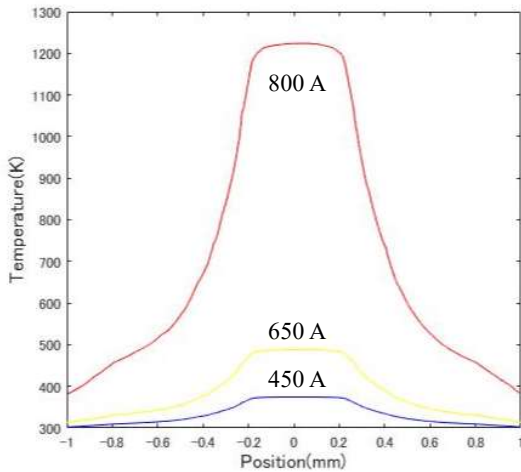


Fig. 10 Contact temperature under different current

decreased significantly as the points of contact increased with the total contact area unchanged. As a result, if the total contact area can be divided into multiple parts and all the parts are distributed with no heat interference to each other, the contact temperature can be decreased significantly.

If the contact temperature can be decreased, the contact would be able to sustain higher current and the arc ignition can be suppressed by paralleling with SiC-MOSFET. The simulation result of the 4-block contact under higher current is shown in Fig. 10. The result shows the contact temperature under the current of 450 A, 600 A, and 800 A. The temperature of the 4-block contact reached the same level as the previous Cu-W clad contact under 450 A when the current was over 800 A, the current limit of the 4-block contact was significantly higher. This result shows that with the 4-block structure contact, a higher no arc generation current limit level can be expected.

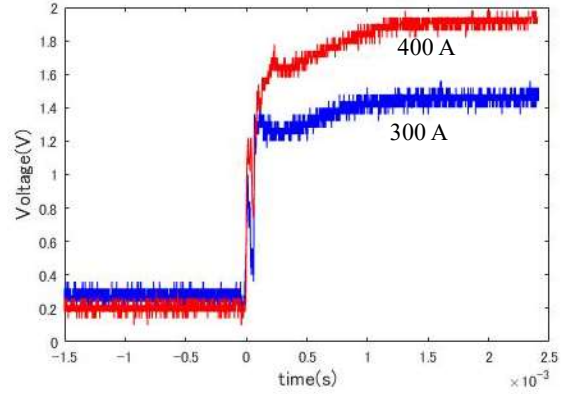


Fig. 11 Commutation experiment contact voltage

3.3 Commutation experiment result

The result of the commutation experiment using the experiment circuit shown in Fig. 6 is shown in Fig. 11. During the on-state, the current flowed through the contact and the SiC-MOSFET was off. The commutation started as the SiC-MOSFET was on and the contact began separating, the current commutated gradually from the contact to SiC-MOSFET as the contact area became smaller and the contact voltage increased. The commutation phrase was complete after the contacts were completely separated, and the current commutated completely from the contact to SiC-MOSFET. If there is no arc generation during the commutation, the no arc commutation is realized.

Fig. 11 shows no surge of arc as a result of current of 300 A and 400 A, however, the arc was observed as the current exceeded 400 A and arc erosion was observed on the surface of the contact. The result of the no arc current limit level is similar to the previous Cu-W clad contact as it also has a no arc commutation limit level of over 400 A.

The arc erosion as the current exceeded 400 A was observed at only one block out of four, which indicated that the current only conducted in one during the commutation instead of all four blocks. There were two reasons for this phenomenon. Firstly, the total contact area of the Cu-W clad was not separated into four averagely which led to different resistance of each block and hence the current was conducted majorly in one block. The second reason is that the separation time of each block is not the same which means that three blocks separated prior to the separation of one block, this focused the current at one point instead of four during the commutation.

4 Conclusion

In this study, the Cu-W clad structure contact and its new design, as well as the application in DC switch were investigated. The results were carried out by simulation and experiment. The simulation used COMSOL multiphysics with the joule-heating model.

The Cu-W clad structure and the new Cu-W 4-block structure were compared by simulation, the simulation result shows a promising advance of the new structure, and the potential to increase the no arc commutation current limit level. The experiment of the contact used in DC switch for commutation was also introduced, the Cu-W clad structure was able to sustain a current of over 400 A with no arc generation during the commutation, the new 4-block structure made no significant difference comparing to this value due to the different time of separation of each block and the different contact area of each block. The study showed that if the contact is manufactured ideally and the separation time of each block is completely the same, a higher arc-free commutation current can be expected. The WEDM method was used for the manufacture of the contact in our study and the cost and difficulty were relatively large. However, it's possible to simply joint the copper with the small tungsten block to achieve the manufacturing in real industry production with low cost and difficulty.

ACKNOWLEDGEMENT

This work was supported by JSPS KAKENHI Grant Number JP18H01420.

5 Reference

- [1] K. Yukita, T. Takeda: Technical Trends on the Development of DC Power System. The Journal of The Institute of Electrical Engineers of Japan. Vol. 135, No. 6, pp. 366-369, 2015 (in Japanese)
- [2] J. M. Meyer, A. Rufer: A DC hybrid circuit breaker with ultra-fast contact opening and integrated gate-commutated thyristors (IGCTs). IEEE Transactions on Power Delivery, vol.21, no.2, pp.646-651, 2006.
- [3] P. J. Theisen, S. Krstic: 270-V DC Hybrid Switch, Transactions on Components, Hybrids, and Manufacturing Technology. Vol. CHMT-9, No. 1, MARCH, 1986.
- [4] K. Yasuoka, Y. Tsuboi, T. Hayakawa, and N. Takeuchi: Arcless Commutation of a Hybrid DC Breaker by Contact voltage of Molten Metal Bridge. IEEE Trans. CPMT, vol. PP, no.99, pp.1-6,2017.
- [5] R. Holm: Electric Contacts, 4th edition. Springer Verlag, 1967.
- [6] Y. Yamada, M. Chen, S. Zen, K. Yasuoka: Hybrid DC switch using CU-W clad contact, in Proc. 11st Inte. Work. on High. Volt. Enge., Nov. 2018.

Investigation and Optimization of a Hybrid Circuit Breaker for Low- and Medium Voltage DC-Grids

F. Anspach, P. Vieth, L. Claaßen, D. Bösche, E. -D. Wilkening, M. Kurrat, TU Braunschweig- elenia Institute for High Voltage Technology and Power Systems, Braunschweig, Germany, f.anspach@tu-bs.de

Abstract

In previous investigations the result was found that the hybrid switch is the most suitable switchgear topology for low- and medium voltage DC-grids. The hybrid switch has the best performance in all operation modes except in the short circuit range. The investigations are part of the research project Smart-Modular-Switchgear-II. In this contribution the focus is set to the optimization of the hybrid switching performance. Therefore, the switch-off behaviour of two types of hybrid switches were investigated to determine the optimization potential. The hybrid switches were investigated in a current range from 10 A up to 600 A and three ohmic-inductive time constants were used: 0 ms, 1 ms and 3 ms. The highest optimization potential was detected in the improvement of the actuator. The new actuator causes a reduction of the switch-off time from 30 ms to 8 ms. Further results of the switch-off performance will be discussed in detail to describe the impacts to the switching process.

1 Introduction

1.1 Motivation

DC-Systems in all voltage levels are an essential part of research projects for years. Main topics are clearing of a fault, multi terminal DC-Grids, insulation properties. The focus in the high voltage level is on the energy transmission on land or sea. In the low and medium voltage sections the focus is on the efficiency to connect renewable energy sources and industrial applications, for example electrical drives. Here sources and loads often use a common DC-Bus [1]. The connection points and transmission to the AC-Grid is centralized and minimized. As a result the effectiveness of the whole system increases. [1–4]

This publication is based on results of the project Smart Modular Switchgear-II (SMS-II). In SMS-II three main research topics are focussed: DC-Grids, Switchgear and grid protection coordination. In SMS-II a multi-level DC-Grid with a 3 kV medium voltage (MVDC) and two low voltage levels (LVDC) (380 V, 1 kV) are installed. The modular grid design enables different experimental setups in accordance to the common DC-Grid applications. The grid protection coordination detects, characterizes, localizes and generates the switching commands. The switchgear interrupts nominal loads, overloads and clears short circuit current faults on each voltage level in the DC-Grid. The switching process mainly determines the duration of the interruption process. The duration of fault detection, characterisation and localization is 2 ms. This is short in comparison to the switchgear delay time (DT) and the current interruption time. Furthermore, low power dissipation (closed contacts) and high number of

switching cycles are important properties of DC-Switchgear (DCS). Therefore, the optimization of a Hybrid Circuit Breaker (HCB) is addressed in this publication. Few publications deal with the optimization of HCBs. In [5, 6] the interaction of the power electronic (PE) with the other switchgear components are improved and a method to run the control unit and the PE without an external supply is presented. In [7] the improvement of the mechanical switchgear is shown, which limits the maximum fault current and reduces the stress of the PE. In order to the mentioned works, this publication determines further optimization potentials and focuses the actuator delay time.

1.2 Process of Hybrid Circuit Breaker optimization

The HCB optimization process is displayed in **Figure 1**. Simultaneously the V-model shows the structure of this publication. The solid line of the key points describes finished process steps, the dashed lines represents the development tasks discussed in this publication and the chain-dotted line the planned future process. The first step in this contribution is the

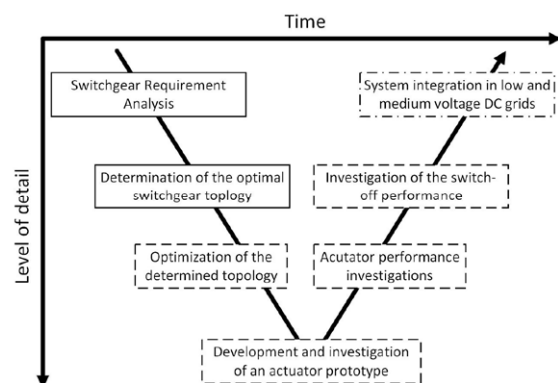


Fig. 1 Switchgear investigation process of SMS-II

switchgear requirement analysis. The second step is the **determination of the optimal switchgear topology.** The results are given in a previous publication of the project SMS-II [8]. The result is that the HCB is the most suitable switchgear topology for the application in this project. Based on this result two HCB's for LVDC (1 kV) grids are developed (Chapter 2). In the third step of the investigation process the **optimization of the determined topology** is conducted. Therefore, both types of HCBs are investigated in the laboratory and the results are analyzed and compared (Chapter 3). The highest optimization potential is detected in the contact actuator. Based on that result the V-model is designed for the actuator optimization. Fourth step is the **development and investigation of an actuator prototype.** Chapter 4 shows the preliminary investigations and the development of the new actuator concept. The process step **actuator performance investigations** includes the investigation of the new actuator connected to the contact system without electrical load (Chapter 4.2). In Chapter 5 the following part of the V-model **investigation of the switch-off performance,** the impact of the new actuator concept to the switch-off performance is investigated and compared with the investigations in **optimization of the determined topology.** The **switchgear integration in low and medium voltage DC Grids** conclude the HCB optimization process. The last process step is not part of this publication, but will be presented in future contributions.

2 DUTs and test set up

2.1 DUTs

2.1.1 Hybrid Universal Power Switch

The Hybrid Universal Power Switch (HUPS) was developed in the research project Universal Power Switch (UPS). There the mechanical switching chamber and the power electronic of HUPS were connected to realize the hybrid switchgear concept. Due to new referenced requirements of SMS-II the concept was improved on the basis of UPS for the application in SMS-II. The switch-off performance of the mechanical switching chamber of the HUPS in short circuit current faults is investigated and the results are shown in [9] and [10]. In **Figure 2** the construction of the HUPS is shown. The detection unit verifies, whether an arc is existing. In case of an arc the control unit is enabled. The performance data of the HUPS are given in **Table 1**. In Table 1 is given, that the maximum switching capacity of the power electronics is 600 A. The minimum current to guarantee the full function of the mechanical switching chamber is > 400 A. In this case the power electronics is the switching element if $0 \text{ A} < I < 600 \text{ A}$ and the mechanical is active if $I > 600 \text{ A}$. Finally, there is an adequate overlap considered

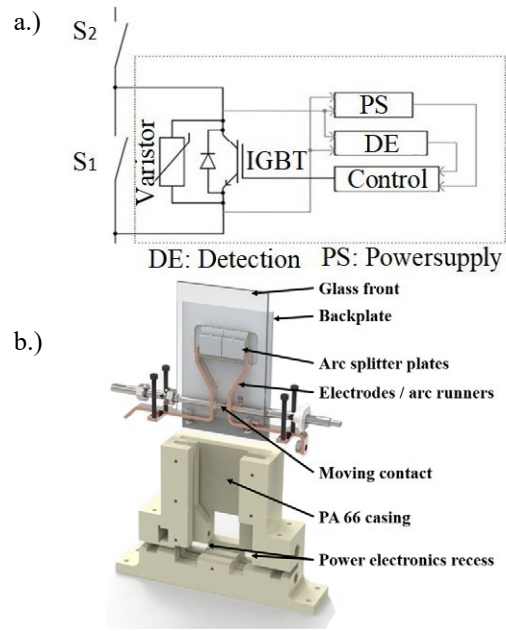


Fig. 2 Construction design of the HUPS [9]:
a.) Circuit diagram HUPS
b.) 3D-Model of the HUPS switch part S₁

Parameter	Value
Nominal voltage U_N	500 V DC
Nominal current I_N	100 A
Switch off capability	3 kA, $U_N = 550 \text{ V}$, $\tau = 1 \text{ ms}$
Polarity	Bidirectional
Contact resistance	$< 400 \mu\Omega$
Contact Material	AgSnO ₂
Actuator delay time	Max. 28,23 ms
Plasma ejection	observed
Hybrid switching limit	Max. 600 A (bidirectional)
Over voltage protection	Varistor (1 mA, 510 V)

Table 1: Performance data HUPS

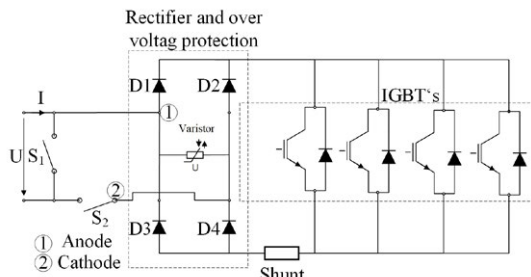
The actuator delay time is defined as the time delay between setting the switching command until the first actuator movement.

2.1.2 High Voltage Relays 10

The High Voltage Relay 10 (HVR10) was developed by the project partner Elektro Technische Apparate (E-T-A), it has only a power electronic switch. The HVR10 is currently tested in the 1kV SMS-II DC-Grid. The mounted mechanical switching chambers only provide the commutation process (S1), ensure the galvanic disconnection in the currentless state (S2) and ensure the efficient current flow (S1), when the contacts are closed (**Figure 3**). The mechanical switches are not able to switch currents in the SMS-II DC-Grid. The detailed performance data are in given in **Table 2**.

Parameter	Value
Nominal voltage U_N	1000 V DC
Nominal current I_N	300 A
Switch off capability	1 kA, $U_N = 1000$ V, $\tau = 0,3$ ms
Polarity	Bidirectional
Contact resistance	359,39 $\mu\Omega$
Contact Material	AgSnO ₂
Actuator delay time	Max. 8,14 ms
Plasma ejection	Not observed
Hybrid switching limit	Max. 1000 A (bidirectional)
Over voltage protection	Varistor (1 mA, 1200 V)

Table 2: Performance data HVR10



b.)

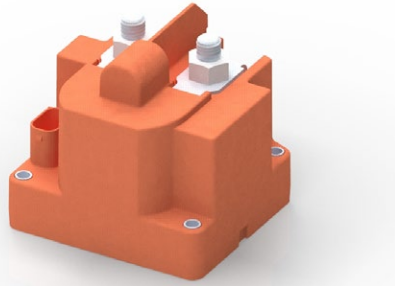


Fig. 3 Construction of the HVR10:
a.) Circuit diagram HVR10
b.) Photograph of the HVR10

2.2 Test setup

The switch-off investigations to optimize the determined hybrid topology (see Fig. 1) are conducted in the DC laboratory of the TU Braunschweig. In **Figure 4** the electrical circuit is given.

Instrument	Data
Transient recorder	HBM Gent3
Measurement satellite	HBM HV6600
Probe (DC-voltage)	Tek P5100 100x
Probe (arc voltage)	PMK PHV 100:1
Shunt (I_{total})	HILO TEST ISM 200/0,25 m Ω
Shunt (PE current)	HILO TEST ISM 50/5 5 m Ω
Linear potentiometer	Novotechnik T75

Table 3: Measurement equipment

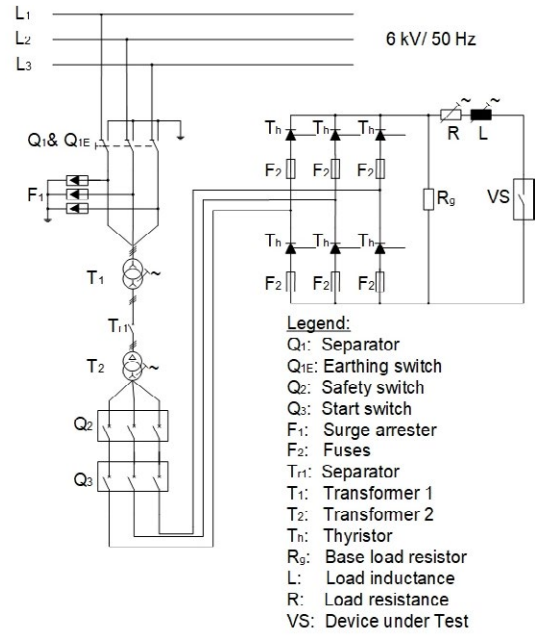


Fig. 4 Diagram of the DC laboratory

The test setup supplies a maximum voltage of 561 V(RMS) and a maximum current of 4,6 kA(RMS). Different AC voltage levels can be adjusted with the transformer windings on the secondary stage. The firing angle of the rectifier is $\alpha = 5^\circ$. With the adjustable components R and L the test current and time constant can be varied. The switches Q_2 and Q_3 are used to start and stop the experiments. The performance data of the applied measurement instruments is shown in **Table 3**. The sampling rate was 1 MS/s.

In **Figure 5** the measurement equipment of table 3 is assigned to the measurement positions.

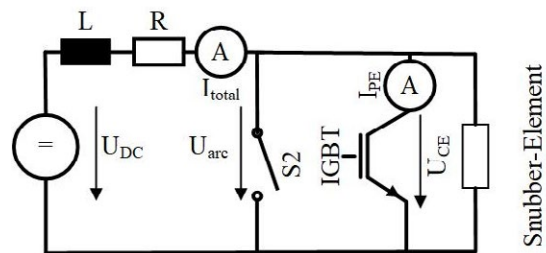


Fig. 5 Measurement equipment assigned to the measurement positions

3 Determination of the Optimization potential

3.1 Design of Experiments

The determination of the optimization potential is based on the comparison of the HUPS and the HVR10 in all operating modes of DC- Grids. The open circuit

test voltage in all investigations is 500 V. Investigations in the 1 kV SMS-II test grid show, that short circuit currents do not exceed 600 A, when the system power is limited to 150 kW [11]. The conclusion that fault currents in the given DC-grid will be switched exclusively in hybrid mode is in a first approach allowed. Therefore, high short circuit currents in the kilo ampere range are no part of this research. The 10 A test scenario represent the part load operation mode. The 100 A test current represents the nominal operation mode in DC-Grids. The 400 A and 600 A tests represent the overload and the beginning of the short circuit current range. The ohmic-inductive time constant is chosen in orientation to Koepf and Boesche [12, 6]. The reliability of the statistical analysis is secured with ten measurements each test case. The complete design of experiments is given in **Table 4**.

Prospective test current I_P in A	Time constant $\tau = L/R$ in ms
10	0, 1
100	0, 1, 3
400	0, 1, 3
600	0, 1, 3

Table 4: Design of experiments

3.2 Results and Comparison

In **Figure 6** a switch-off oscillogram of the HUPS is given. The displayed measured values are given in the circuit diagram of Figure 5. The current interruption process is divided in five phases, which are described in Figure 6. The phases are connected with following transition effects (see **Table 5**):

Transition	Effect
I-II	Arc formation
II-III	Switch on PE
III- IV	Switch off PE
IV-V	Complete dissipation of the inductive energy

Table 5: Transitions effects

The switch-off oscillograms of the HVR10 can be classified with the same procedure.

Based on the oscillogram different properties of the switch-off process are analysed to determine the optimization potentials. Properties are the maximum arc voltage, arc power, arc and PE energy consumption and the switch-off time (SOT). In **Figure 7** the SOT and their subdivisions are displayed. The actuator DT is excluded. The HVR10 interrupts the current in all test cases faster than the HUPS. The differences are also visible in the colorized subdivisions. The conductivity time (Phase IV) of the varistor of HUPS is in all investigations longer. The reason is given in the different varistor properties of the HUPS and the HVR10 (Table 1 and 2). The varistor of the HVR10 dissipates the in-

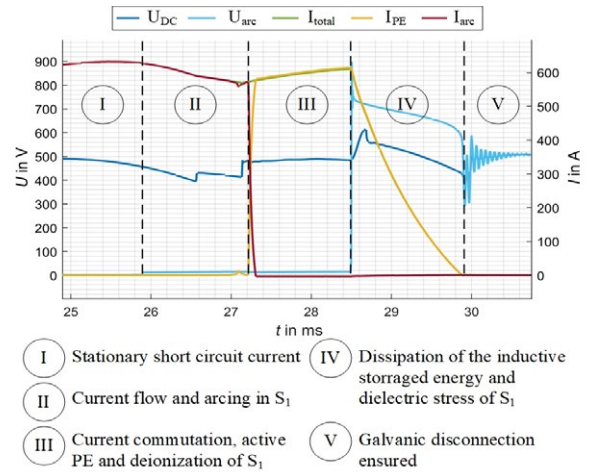


Fig. 6 Switch-off oscillogram HUPS; $I_P = 600$ A, $U_{DC} = 460$ V, $\tau = 1$ ms

ductive energy faster. Within the phases II-III the following discrepancies were found. The duration of phase II of the HUPS is 2,5 ms. In comparison the period of phase II of the HVR10 is only few micro seconds. The reason is the difference of the power supply of the switchgear control unit. The HVR10 uses an external 24 V power supply. In contrast the HUPS uses the arc energy [5]. The inductive coupling and energy transmission cause the time difference. Furthermore, the parallel mechanical switch S_1 of HVR10 is a double breaker. In consequence the necessary commutation voltage is reached earlier. The duration of phase III is determined of the minimum deionization time (DI) of the parallel switch S_1 . Arc restrikes caused by the dielectric stress in phase IV have to be avoided. The deionization process is currently a subject in different switchgear projects. The power electronic on-time of the investigated switchgear is predefined and obviously higher than the DI. The DI of the HVR10 is 1,2 ms and of the HUPS is 1,29 ms. Finally, there is a further discrepancy between the switchgear, but simultaneously an optimization potential, too. The differences summed up result in a difference in the SOT of 4 ms. The last and powerful difference is the actuator DT. The HVR10 show an actuator DT of 8,14 ms and the HUPS a time of 28,23 ms, all previous mentioned differences and optimization potentials have a small

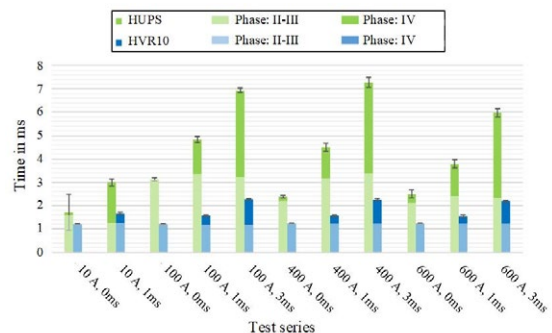


Fig. 7 Comparison of the switch-off time

impact in comparison to the actuator DT. The reduction of the actuator DT has the highest optimization potential.

4 Development and investigation of an actuator prototype

4.1 New Actuator and functional concept

Thomson coil actuators are fast actuators, their application in switchgear is introduced in [13]. The concept enable high accelerations and low DTs. In contrast to the referenced publication, there is no attempt to design a new actuator, instead the application of the principle to already existing actuators should be clarified. In **Figure 8** the test setup for actuator tests is shown. The development is performed in orientation to [13].

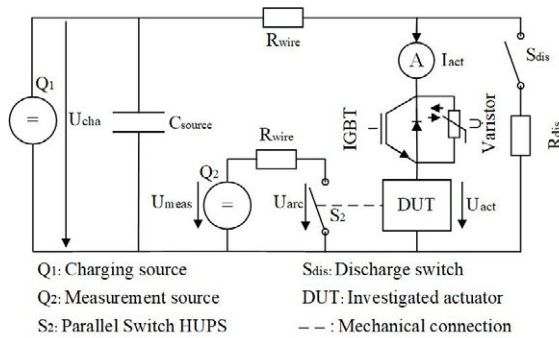


Fig. 8 Actuator test setup

In **Table 6** the functional principle is presented.

Process step	Action
I	All switches and IGBT open Charging of C_{source} to the test voltage
II	IGBT turned on Discharge of C_{source} to the DUT DUT is active S_2 is moved
III	IGBT turned off Varistor active
IV	All switches open Grounding of the test setup with S_{dis}

Table 6: Functional principle of the actuator test setup

The test set up enables different actuator voltages. The actuator is determined from the difference between the control signal to the IGBT and the change of the arc voltage U_{arc} . It should be mentioned, that the output current of the source Q_2 is limited to 0,1 A. In consequence the influence of arc effects in the switchgear S_1 can be neglected.

Different available actuator types were investigated in the test setup. In **Figure 9** a comparison of two actuator types is given. The DT of both actuators are plotted over the actuator voltage. The actuator of the HVR10

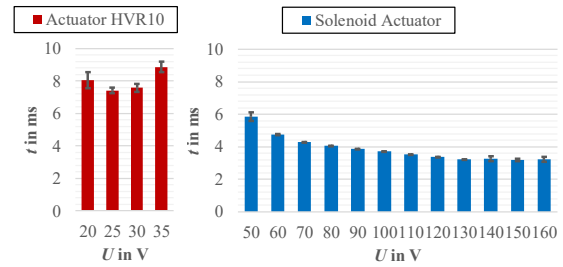


Fig. 9 Comparison of two actuator types

is a bistable actuator. The actuators only consume energy during the position change process. The steady position is ensured with a magnetic circuit. Details are given in [14]. The actuator of the right diagram in **Figure 9** is a solenoid actuator. The open position is held by a return spring. For the movement and to hold the closed position of the actuator energy is necessary. The DT of the actuator of HVR10 is shortest at 24 V, which corresponds to the nominal drive voltage. Higher and lower voltages result in longer DTs. Voltages higher than 35 V cause a dielectric failure in the insulation. In comparison the DT for the solenoid actuator decreases with increasing actuator voltage. The maximal dielectric strength is reached at 160 V. The conclusion that solenoid actuators show the best properties under high actuator voltages and high actuator pulse currents to reduce the DT is valid.

4.2 Investigation of the actuator delay time and velocity

Based on the result of 4.1 a solenoid actuator with a higher dielectric strength is chosen. In **Table 7** the properties of the tested actuator are given.

Parameter	Value
Dielectric Strength	1000 V (V_{RMS})
Nominal actuator voltage	24 V
Coil Resistance	36,9 Ω
Windings	2680

Table 7: Properties solenoid acuator-282367-027 Ledex [15]

In **Figure 10** the implementation of the new actuator is shown.

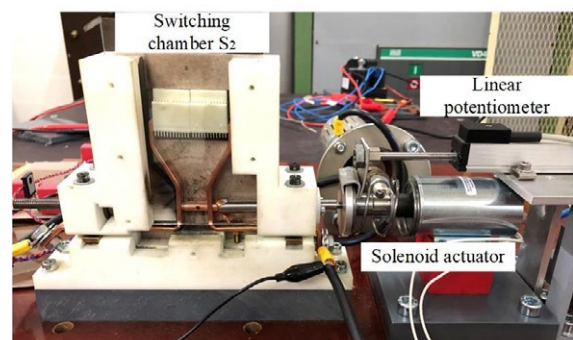


Fig. 10 Implementation of the new actuator in the existing HUPS arrangement

The switchgear actuator combination is connected to the actuator test circuit (Figure 8). The actuator delay is investigated under different actuator voltages. In Figure 11 the results are displayed.

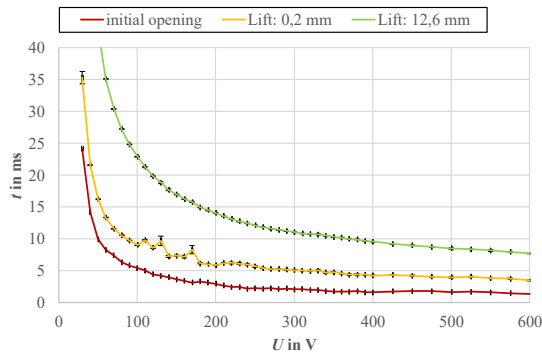


Fig. 11 Investigation of the actuator DT of the new solenoid actuator

Based on the mentioned fact, that arc effects can be neglected in the given actuator test setup, the initial opening marks the start of the contact movement. Further on, the DT for a travel of 0,2 mm is visualized, because that opening distance is necessary to generate a sufficient arc voltage to activate the PE and guarantee the commutation process of the HUPS. The travel 12,6 mm is equal to 90 % of the maximum lift. The 90 % travel is chosen, because the measurement signal of the linear potentiometer is overlaid with mechanical oscillations in the end position. The 90% measuring point ensures comparable results. The results show that the DT decreases in all analysed positions with increasing voltages. The rate of change reduces in the range of higher voltages. Therefore, actuator voltages higher than 600 V are not investigated. Finally, the new actuator is successfully implemented in the switchgear and the advantage of the optimization are validated. The new actuator is faster than the actuators of HVR10 and HUPS in Chapter 2. The mentioned DTs in Chapter 2 correspond to the measuring curve *initial opening* of Figure 11. The new actuator is five times faster than the HVR10 and almost twenty times faster than the pneumatic actuator of the HUPS.

5 Investigation of the switch-off performance

5.1 Selection of the appropriated actuator parameters

In this chapter the impact of the new actuator to the switching performance is presented. First the appropriated actuator parameters are declared. As mentioned in the previous chapter the rate of change is reduced for high actuator voltages. Therefore, the actuator voltage is set to 500 V. The DT is only 0,2 ms higher compared to 600 V actuator voltage. 500 V are chosen, because

the supply of the actuator out of the grid is possible. In Figure 12 a proposal is given.

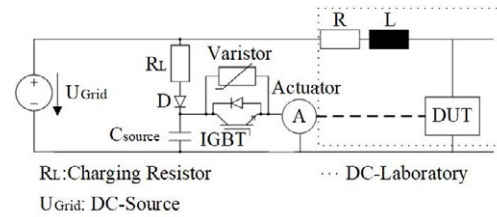


Fig. 12 Proposal of a direct supplement of the actuator out of the DC

The dotted line frame represents the DC-Laboratory shown in Figure 4. The Diode D prevents that the Capacitor C_{Source} injects a current in the fault current, which was detected in the DUT. The actuator, the IGBT and Varistor have the same function as shown in Figure 8. Finally, that equivalent circuit diagram is a proposal and is not tested yet. The principle is probably applicable to all DC-Grids. The requirement is, that the grid voltage does not exceed the dielectric strength of the actuator. Therefore, in this publication 500 V actuator voltage is chosen.

5.2 Investigation of the switch off behaviour

The test currents are 100 A and 600 A with ohmic-inductive time constants of 0 ms and 3 ms. The 10 A study is excluded. The arc sometimes extinguished caused by energy consumption of the control electronics. The function of the control electronics is described in 2.1.1. The 400 A test is neglected, because the assumption was made, that if the 100 A and 600 A tests are successful the 400 A test is probably, too. Finally, the nominal current (100 A) and the maximum hybrid switch capacity (600 A) are determined.

In Figure 13 a switch-off oscillogram of the HUPS with the new actuator is given.

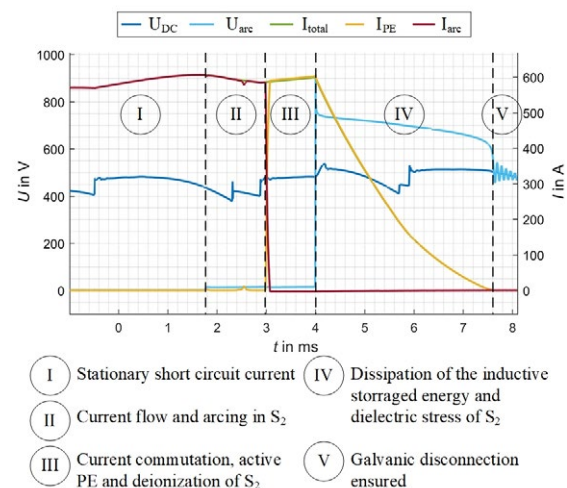


Fig. 13 Switch-off oscillogram HUPS with new actuator; $I_P = 600$ A, $U_{DC} = 460$ V, $\tau = 3$ ms

The HUPS in addition with the new actuator interrupted the shown test load and all other test loads successfully. The mentioned phases of the hybrid switching process exist and are visible (Table 5). In **Table 8** the means of the maximum arc voltages and the arc and PE energies of all test cases are summarized.

Test case	E_{arc} in J	$E_{PE} + Var$ in J	U_{arcmax} in V
100 A, 0 ms	1,91	1,47	804,74
100 A, 3 ms	1,87	100,05	823,37
600 A, 0 ms	9,60	32,40	861,64
600 A, 3 ms	10,44	593,74	917,61

Table 8: Means of E_{arc} , E_{PE} and U_{arcmax}

The arc energies of the 100 A investigations are similar and independent of the time constant. The difference of the arc energies within the 600 A investigations is almost 10%. That is caused by a floating potential inside the control electronics. After the investigations the root cause of the difference is solved. The energy consumption of the power electronics and the varistor is increasing with rising currents and time constants. Furthermore, the voltage increases due to the reasons mentioned above. Finally, it can be noted that the implementation of the new actuator is functional.

5.3 Comparison of the Hybrid Switchgear topologies

In the previous section the successful implementation of the new actuator concept is shown. In this section the comparison of the new results with the previous results of Chapter 3.2 is shown. In **Figure 14** the SOTs in connection with the DTs are compared.

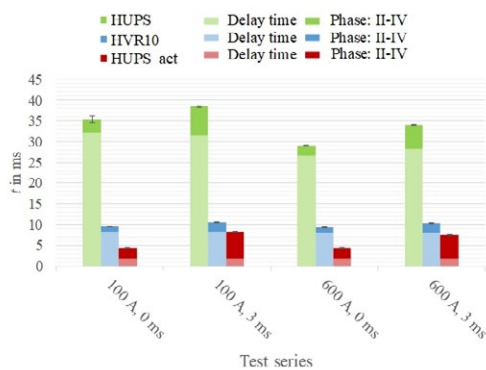


Fig. 14 Comparison of the SOTs and DTs

The HUPS with the new actuator is marked with the abbreviation $HUPS_{act}$. The $HUPS_{act}$ is the here tested fastest switchgear. The main impact is the short DT. The time *Phase: II-IV* of the HVR10 is the shortest in all test cases. Especially the divergence is evident in the ohmic-inductive investigations. The main reason is the different varistors used. Finally, the objective is to shorten the DT and in order to reduce the whole interruption time. The comparison shows that this intention

is successfully realized. Simultaneously it has to be recognized that there is no positive influence to the hybrid switching process (Phase I-V). The influence is shown in **Figure 15**.

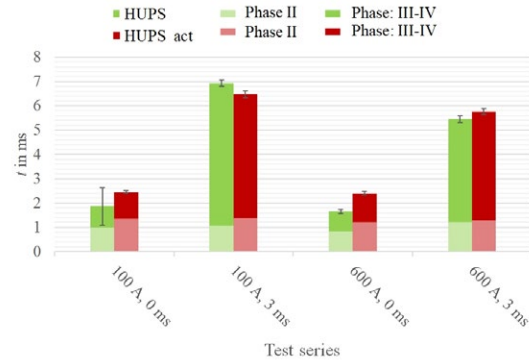


Fig. 15 Comparison of the section times HUPS and $HUPS_{act}$

The figure comparing the section times of the HUPS and $HUPS_{act}$ during the current interruption. The DT is neglected in the figure. The comparison shows that the HUPS interrupts the current faster than the $HUPS_{act}$. The case 100 A and 3 ms is an exception. The case is part of ongoing research. In all test cases it is recognisable, that the arc time of the $HUPS_{act}$ is longer in comparison to the arc time of the HUPS. The reason of the difference is visible in **Figure 16** and marked with the numeration 1.

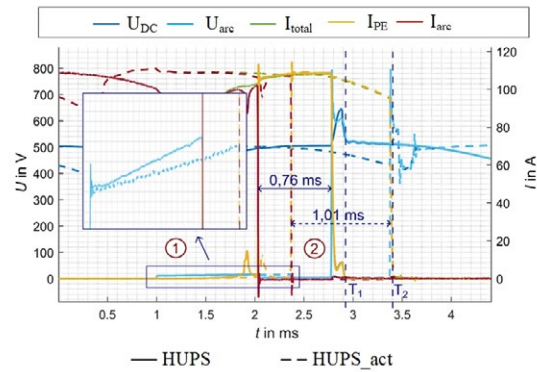


Fig. 16 Comparison of Phase I-V in an oscilloscope $I_P = 100$ A, $U_{DC} = 460$ V, $\tau = 0$ ms

The phase II is extended in the zoom window. The arc voltage of the HUPS and arc voltage of the $HUPS_{act}$ are visible. The arc voltage of the HUPS rises faster. Therefore, the HUPS reached phase III earlier, because the condition is an arc voltage above 15 V. The 15 V condition is marked with the red vertical lines in the zoom window. The different rising speeds are caused by the different initial speeds of the actuators. The initial actuator speed of the HUPS is higher in comparison to the $HUPS_{act}$. The initial speed of the in the $HUPS_{act}$ tested solenoid actuator is lower, because the active force is small with extended anchor [15]. In consequence of the different arc time the energy entry is also different. The second reason for the elongated SOT, which based on the described phenomenon is the

difference in the minimum PE on-time. The section and the on-times are marked with 2 in Figure 13. The PE minimum on-time to avoid arc restrikes of the HUPS_act is 1,01 ms. The PE on-time of the HUPS is 0,25 ms shorter. As also mentioned the reason is the lower energy entry. Remarkable is that the relation of the times which is needed to reach the 15 V and the PE on times is the same. In both cases the relation is 0,75. The correlation has to be investigated detailed in future. Finally, the two delays extend the SOT of the HUPS_act. In **Table 9** the advantages and the disadvantages of the new actuator are summarized.

Advantages	Disadvantages
<ul style="list-style-type: none"> - High overload capacity - Short delay time - Shortened total interruption time 	<ul style="list-style-type: none"> - Higher power electronic on time necessary - Lower initial velocity

Table 9: Dis- and advantages of the new actuator

6 Summary and Outlook

The publication presents a method to optimize a hybrid circuit breaker. The approaches and results are given and explained. The comparison of two hybrid switchgear show, that the highest optimization potential is the improvement of the actuator delay time. The application of the Thomson coil principle to solenoid actuators show a remarkable reduction of the delay time. The short delay time reduces the overall interruption time as shown in the switch off performance investigations. Nevertheless, it must be noted that there are disadvantages. The higher power electronic on time and the lower initial velocity are detected in the switch off oscillograms. Simultaneously these points are new optimization potentials, which are investigated in future. Further on, a procedure to determine the minimal necessary power electronics on time effectively and the connection of the actuator speed and the power electronics on time will be investigated. Finally, all optimization potentials and new findings should be considered in the design process of the 3 kV switchgear of SMS-II.

Literature

- [1] Borcherdig; Austermann; Kuhlmann *et al.*: Concepts for a DC Network in Industrial Production. *In: 2017 IEEE Second International Conference on DC Microgrids (ICDCM).*
- [2] Klosinski; Bösche, D.; Ross *et al.*: Hybrid Circuit Breaker-based Fault Detection and Interruption in 380V DC Test-setup. *In: Conference Transscript-HOLM, 2018.*
- [3] L'Abbate; Chiumeo; Gandolfi *et al.*: Overview of HVDC and MVDC developments and studies in Italy. *In: 2020 AEIT International Annual Conference (AEIT), 2020.*
- [4] Neidhardt; Lerch; Wiesinger *et al.*: Long-Term Tests of a DC Gas Insulated Transmission Line (DC GIL) embedded in Temporally Flowable Backfill: Soil-Mechanical and Thermic Interaction. *In: VDE Hochspannungstage, Vol. 1 (2020), pp. 518-524.*
- [5] Bösche, D.; Wilkening, E.-D.; Köpf, H. *et al.*: Breaking Performance Investigation of Hybrid DC Circuit Breakers: An Experimental Approach, 2015, 117-122.
- [6] Bösche, D.; Wilkening, E.-D.; Köpf, H. *et al.*: Hybrid DC Circuit Breaker Feasibility Study. *In: IEEE Transaction on Components, Packaging and Manufacturing 7, 2017, 7, pp. 354-362.*
- [7] Zhou, X.; Feng, Y.; Shen, Z.J. *et al.*: Hybrid DC Molded Case Circuit Breaker Technology. *In: 2020 IEEE 66th Holm Conference on Electrical Contacts and Intensive Course (HLM), pp. 157-164.*
- [8] Anspach, F.; Claafßen, L.; Wilkening, E.-D. *et al.*: Overview about different DC-circuit breaker topologies and comaparison of their switch-off performance. *In: VDE High Voltage Technology 2020; ETG-Symposium, pp. 453-459.*
- [9] Claafßen, L.; Anspach, F.; Wilkening, E.-D. *et al.*: Investigation of a mechanical switch within a hybrid circuit breaker in DC grids. *In: IEEE 66th Holm Conference on Electrical Contacts (2020), pp. 123-130.*
- [10] Alija; Wilkening, E.-D.; Kopp, T. *et al.*: Switching Characteristics of hybrid low voltage DC circuit breaker. *In: 22nd International Conference on Gas Discharges and Their Applications-Conference Transcript.*
- [11] Anspach, F.; Claafßen, L.; Kurrat, M.: Transient fault behavior analysis in LVDC-Grids in a 1000 V modular laboratory setup and under consideration of passive and active components. *In: The 4th IEEE International Conference of DC Microgrids.*
- [12] Köpf, H.: Schalten von Gleichströmen in automobilen HV-Bordnetzen bis 500 V, unter Berücksichtigung der Lichtbogenwanderung im Doppelkontaktsystem. Braunschweig, TU Braunschweig- Carolo Wilhelmina, Thesis, 2018.
- [13] Wu, Y.; Wu, Y.; Rong *et al.*: A New Thomson Coil Actuator: Principle and Analysis. *In: IEEE Transactions on Components, Packaging and Manufacturing Technology, 11. November 2015, pp. 1644-1655.*
- [14] Schulze, S.: Relais-Technologien für Gleichspannungen bis 1500V. Dresden, TU Dresden, diploma thesis (unpublished), 2011.
- [15] Ledex: Datasheet- Ledex Size 150M Pull Tubular Solenoids -38mm Dia. x 64mm.

New Switching Technology for DC Grids

Wolfgang Hauer, Eaton Industries GmbH, Vienna, Austria, WolfgangHauer@eaton.com
Michael Bartonek, Eaton Industries GmbH, Vienna, Austria, MichaelBartonek@Eaton.com
Hartwig Stammberger, Eaton Industries GmbH, Bonn, Germany, HartwigStammberger@eaton.com

Abstract

This paper discusses hybrid switching technology in general and the practical implementation in particular. A novel low voltage DC hybrid circuit breaker (HCB) and its components are introduced. The HCB is rated for up to 100 A / 700VDC and can interrupt currents with a rise rate up to 5 A/ μ s. Particular attention was given to the power stage of the HCB including the ultra-fast bypass relay and the semiconductor switch. Its design considerations are discussed. The mechanical construction of the bypass relay and the current commutation process from the bypass relay to the semiconductor switch are emphasized. Short circuit interruption and selectivity test results which were performed at an industrial DC model installation in the course governmental funded DC-Industrie project are discussed.

1 Introduction

Several pilot projects and plants in the field of industry, infrastructure and commercial building showed successfully that the utilization of DC micro grids has progressed beyond the nursery stage [1], [2], [3]. The benefits compared to AC are obvious: improved reliability due to easier implementation of distributed energy generation such as photovoltaics (PV), chemical storage and capacitors; improved efficiency due to elimination of rectifiers on every single appliance and simple use of energy recuperation; cost savings due to reduced conductor cross section (higher nominal voltage, no reactive power losses), and enhanced flexibility due to micro energy management control. Energy management demands monitoring and remote-control functions which traditional electromechanical circuit breakers, do not provide or only at prohibitive costs. The time has therefore come for new concepts for switching and protection devices. There are basically two technologies known that meet these requirements: solid state switching and hybrid switching. The paper focuses on the hybrid switching technology.

2 Hybrid Switching Technology

The hybrid switching technology has already been known for a long time [4] but has been limited to individual concept studies, prototypes and special applications. Due to the evolution of power semiconductor technologies regarding reduced power losses, increased current carrying capacity, as well as reduced size and cost, hybrid switching becomes attractive from a commercial point of view.

2.1 Introduction to hybrid switching

Basically, a hybrid switch or hybrid circuit breaker is made up of an electro-mechanical relay connected in parallel with a semiconductor switch such as IGBTs and, MOSFETs. The basic schematic of such a hybrid switch is shown in **Figure 1**. Besides the electro-mechanical relay – hereafter called *bypass relay* –, the semiconductor switch and the overvoltage protection device, a galvanic separation relay is connected in series to establish isolation between line- and load-side if required.

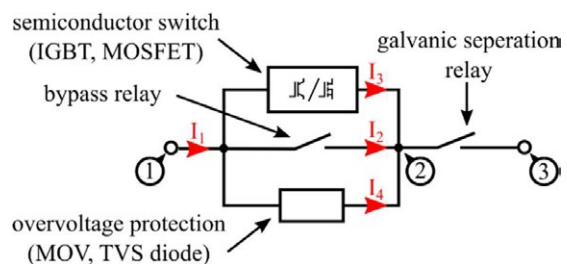


Fig. 1 Basic schematic of a hybrid breaker. The current I_1 to I_4 correspond to the total current through the hybrid breaker, current through bypass relay, current through semiconductor switch and current through overvoltage protection device as shown in Figure 2.

During normal on-state operation both relays are closed, and the semiconductor is switched off so that the load current flows via the mechanical contacts. Only during switching the semiconductor takes over the load current. At switch-on operation the semiconductor is switched on first, taking over the current flow. Subsequently the bypass relay is closed, and the current commutates to this parallel branch avoiding electrical stress on the contacts; the semiconductor is switched off once the bypass relay is closed.

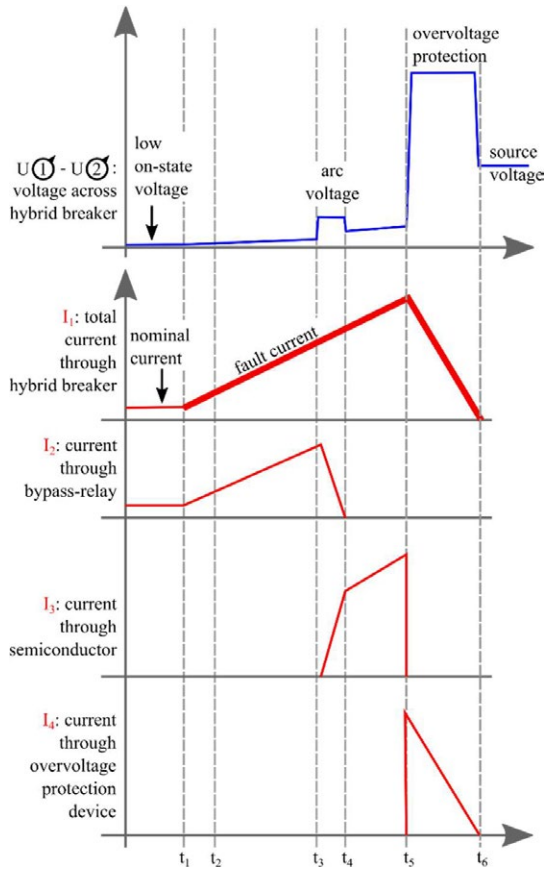


Fig. 2 Typical current-voltage waveforms of a hybrid circuit breaker during switch off operation. Here, t_1 indicated the start of the short circuit, t_2 is the detection time, t_3 ...start of commutation, t_4 ...end of commutation, t_5 ...semiconductor switches off, t_6 ...short circuit is cleared

However, at switching off operation the situation is different, especially at fault (overload and short circuit) condition as indicated in **Figure 2** Here, the current through the hybrid circuit breaker I_1 and its components (I_2 - I_4) as well as the voltage across the hybrid breaker (U_1 - U_2) are shown. Assuming the breaker is in on-state and is to be switched off due to a short circuit event. At the beginning the nominal current flows via the bypass relay with its contact resistance of about $100 \mu\Omega$ to $200 \mu\Omega$. Therefore, the voltage drop across the breaker is very small. At t_1 a short circuit event occurs, the current increases rapidly with a rise rate depending on the internal and line inductance (one to double-digit A/ μ s). For DC applications, due to the resistive-capacitive nature of DC grids, an additional inductance (air coil) is usually connected in series to the hybrid switch/breaker to limit the rise rate of the current to a maximum allowable limit. The current still flows via the contacts of the bypass relay and is limited by the external and internal line impedance as well by the contact resistance only. A certain time period ($t_1 - t_2$) is needed to analyse the current, whether there is a fault event (short circuit or overload) or a transient

(short term) inrush current event. The breaker shall only interrupt for fault events. If a short circuit is detected (t_2) the bypass relay driver applies a trigger signal to the relay. Since the bypass relay is an electro-mechanical system it is subject to intrinsic delays due to mass inertia of moving parts. Hence, the contact bridge of the relay starts to move a certain delay time ($t_2 - t_3$) after being energized. At the same time (t_2) the semiconductor is switched on. Because the On-resistance R_{ON} of the semiconductor is approx. 10 – 1000 time higher than the resistance of an electromechanical contact, almost the whole current flows via the contacts of the bypass relay during this period. R_{ON} depends mainly on the semiconductor technology, the max. allowed supply voltage and the number of parallel connected semiconductor devices.

The contacts of the bypass relay eventually separate (t_3), and a molten metal bridge is drawn between them [5]. This bridge represents an additional serial resistance so that the voltage across the bypass relay increases. As the bridge is elongated further it becomes unstable. At the moment of bridge rupture an arc is formed, and the cathode-anode-fall voltage is added to the voltage across the bypass relay [6]. The commutation of the current from the bypass relay to the semiconductor becomes significant once the voltage across the relay (i.e. the arc voltage U_{arc}) is in the same order of magnitude as the voltage drop caused by the On-resistance (saturation voltage).

Between times t_4 and t_5 the full current flows via the semiconductor and the contacts of the bypass relay separate further. Once the contacts have gained a sufficient distance (t_5) to establish the necessary dielectric strength to avoid a dielectric break down caused by the recovery voltage, the semiconductor is switched off. The current commutates to the overvoltage protection device which can be a MOV (Metal-Oxide Varistor) or a TVS (Transient Voltage Suppressor) diode. It limits and dissipates any overvoltage originating from energy stored in line and stray inductances. Finally, after the current was driven to zero, the galvanic separation relay opens and establishes isolation between the line and the load side. This sequence is also performed at normal switch-off operation. The switch-on sequence is in reverse order, meaning the galvanic separation relays are closed first (current-less). Afterwards the semiconductor is turned on so that the load current flows. At the same time the bypass relay is switched on, but due to the mass inertia it takes some time before the current commutates to the relay.

2.2 Practical implementation

The practical implementation of the hybrid switch as depicted in Figure 1 (excluding the galvanic separation relay) is shown in **Figure 3**. It features the bypass relay placed on top of the IGBT module and two MOVs connected sideways next to the relay. This assembly unit shown, hereafter called power stage, was designed for DC application with rated voltages of 650 VDC, rated

currents up to 45 A and a maximum allowed current rise rate of 5 A/ μ s. This corresponds approximately to a 50 Hz sinusoidal short circuit current of 15 kA peak. It is also applicable to 230/400 VAC.

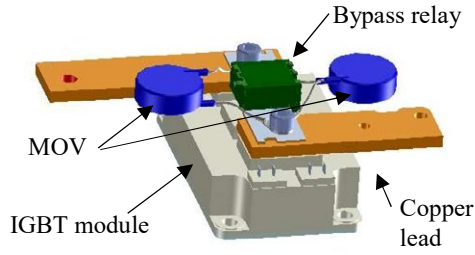


Fig. 3 Practical implementation of the hybrid switch

Special care must be taken when designing the mechanical and electrical parallel connection of the IGBT module, bypass relay and MOV about minimizing the loop inductance since this determines the commutation time [7]. Therefore, the bypass relay was mounted directly on the output terminals of the IGBT module and the MOVs were connected to it with the shortest achievable lead lengths in order to minimize the area of the commutation loop.

The limiting factor of this hybrid switching technology to be applicable for circuit protection is the maximum current carrying capacity of the bypass relay and the maximum forward surge (on-state) current (I_{FSM}) of the semiconductor switch during short circuit condition. It is directly related to the switch-off time ($t_1 - t_5$, see Figure 2). The faster the breaker can be switched off, the lower is the current at switch-off.

The fault detection time ($t_1 - t_2$) can be reduced to a limited extent only, because a certain time is needed to analyse the current characteristics in order to distinguish between an inrush current and a short circuit event. Otherwise misinterpretation will lead to nuisance tripping.

The contact opening time ($t_2 - t_5$) of the bypass-relay has the most significant impact on the I_{FSM} of the semiconductor. It depends mainly on the mechanical design of the bypass relay. Since commercial relays with the required nominal current and voltage reach at best a minimal contact opening time of greater than 5 ms, which is too slow to be used for hybrid switching, a new superfast bypass relay design, capable of fully opening its contacts within 500 μ s, was developed.

2.2.1 Bypass Relay

The bypass relay was designed not only to carry the full nominal current of up to 100 A but also temporary overloads according to the IEC60898-1 tripping characteristic B and C. Therefore, an appropriate contact area and contact forces had to be considered for its design. On the other hand, the mass moment of inertia of the moving part (armature, contact bridge) was minimized

to maximize the contact opening speed and thus decrease the contact opening time. A rotational symmetric design of the contact bridge is the most appropriate choice as illustrated in **Figure 4**. It shows a double break system with two contacts per pole in a) closed and b) open position. The relay was designed as a magnetically latched, bi-stable system, meaning that no energy is needed to keep the relay in the two stable end positions (on/off). Only during the switching process power is needed, thus saving energy and reducing the relay temperature. In a first step a bypass relay with a nominal current of 45 A was developed and tested. In a second phase a 100 A relay was developed. Due to the higher current carrying capacity, the contact bridge was designed in a more massive way. Thus, the contact opening time increased to 320 μ s compared to 200 μ s of the 45 A relay.

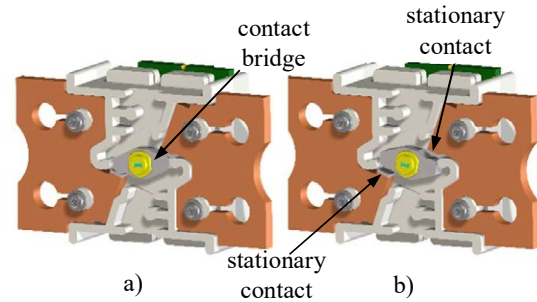


Fig. 4 Mechanical layout of the bypass relay a) in closed position and b) in open position

It was also designed to allow a high number of electrical switching cycles, a necessary feature for every-day power switching in a power management application. The general requirements of the bypass relay are listed in **Table 1**.

Parameter	Value	
Nominal voltage	400VAC/700VDC	
Nominal current	45 A	100 A
Contact resistance	< 200 $\mu\Omega$	
Delay time	< 200 μ s	< 325 μ s
Contact opening time	< 320 μ s	< 500 μ s
Electrical lifetime @ I_n	> 10000 cycles	
Mechanical lifetime	> 100000 cycles	

Table 1: Technical specification bypass relay

To demonstrate the superfast contact opening, the contact bridge movement as a function of time is shown in **Figure 5**. Here, the coils of the relay are energized at $t = 0 \mu$ s. After a delay time of about 190 μ s the contacts start to separate. This time is needed for acceleration of the moveable masses and to overcome the overtravel of the contacts. The distance needed to establish the required dielectric strength of 1 mm total contact gap (0,5 mm per pole) is reached at $t = 320 \mu$ s (i.e. the contact opening time). An overshoot of about 37%

in respect to the contact end position of 0,7 mm can be observed. The contact motion is not axially symmetric, as indicated by the two different gap measurements. This is because the pivot point of the armature is not rigidly mounted. The average opening speed of the contacts was 4.5 m/s during the first 200 μ s after contact separation (from $t = 200 \mu$ s to 400 μ s). First electrical endurance tests (acc. to EN60947-2) reveal that the delay time remains stable at $(200 \pm 10) \mu$ s for the entire life time of 10000 switching cycles. As the delay time critically influences the short circuit behaviour, these results also indicate a stable interruption capability over the observed life time.

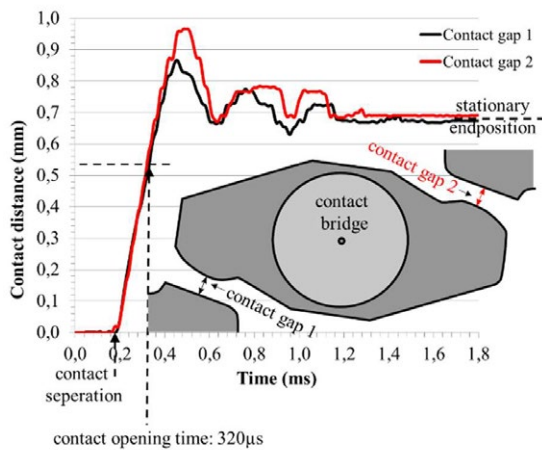


Fig. 5 Contact opening of the bypass relay

2.2.2 Semiconductor Switch

Since this hybrid switching technology requires the semiconductor to be activated during the switching process only, focus in selecting the semiconductor technology was put on the surge current carrying capacity rather than on the on-state resistance/losses. Thus, the IGBT technology is the most appropriate choice. An IGBT module from Semikron [8] was selected. It is not only more tolerant against overloads but also features a higher collector-to-emitter voltage, required for future-proof DC applications (up to 1400V), compared to power MOSFETs. The schematics of the module in Figure 6 shows two Trench IGBTs including fast, soft freewheeling diodes connected back-to-back. It can be used in AC grids as well as in DC grids with interconnected prosumers (feed & back-feed).

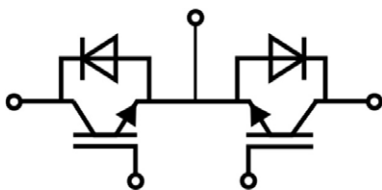


Fig. 7 Schematics of the IGBT module

2.2.3 Current commutation

The process of current commutation from the bypass relay to the IGBT is shown in Figure 7. The short circuit is initiated at $t = 0,07$ ms. The current increases with a rate of approximately 5 A/ μ s and is mainly carried by the bypass relay. The IGBT is already switched on. At $t \approx 0,3$ ms commutation takes place. The current is transferred to the IGBT. For another 100 μ s the IGBT carries the full short circuit current before it is switched off. The peak current, the IGBT was subjected to, was about 1700 A.

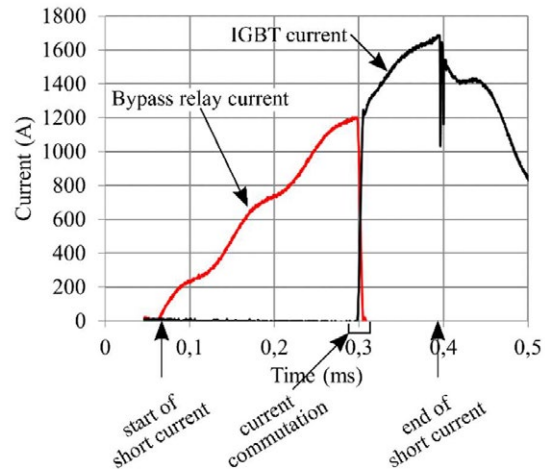


Fig. 6 Current commutation at a short circuit interruption

A detailed view of the commutation process at $t \approx 3$ ms is shown in Figure 8. Additionally, to the currents through the bypass relay and the IGBT, the voltage across the hybrid power stage is illustrated. The separation of the first contact pair occurs at $t \approx 0,298$ ms indicated by the step in the voltage across the power stage of about 10 V. This voltage step marks the start of commutation. The current through the relay decreases simultaneously with increasing current through the IGBT. Such a voltage step after contact separation usually represents the ignition of an arc and is mainly caused by the cathode- and anode-fall voltage [9]. According to literature, the expected cathode-anode-fall voltage at a given contact material (here Ag) is between 18 to 20 V [10]. This is almost double the measured voltage step of 10 V. Therefore, an arc phenomenon appears unlikely at present. Another explanation of the voltage step may be a molten metal contact bridge drawn between separating contacts. The voltage drop then depends on the boiling voltage of the contact materials involved.

However, the voltage stays relatively stable for about 1 μ s. An elongating contact bridge would cause voltage increase due to increasing length of the bridge with simultaneous decrease of the bridge cross section resulting in a continuous increase of the bridge resistance and voltage drop respectively.

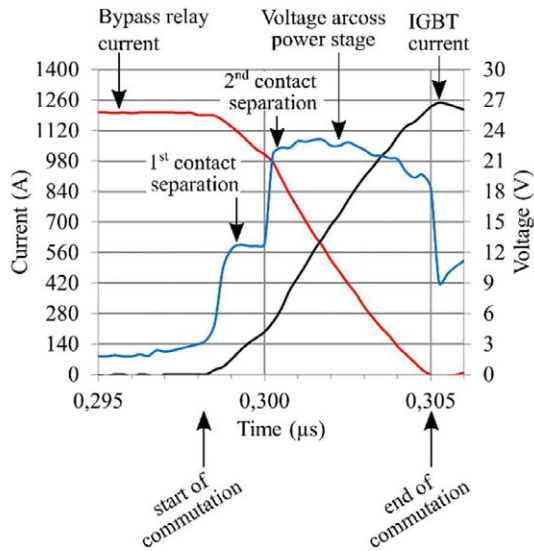


Fig. 8 Detailed view of the current commutation

Whether the elongation of approx. $4,5 \mu\text{m}$ within this $1 \mu\text{s}$ period has an influence on the bridge resistance or an arc phenomenon causes the step voltage will be part of further investigations. The second contact separation can be observed $1 \mu\text{s}$ after the first, indicated by another voltage step of about 10 V . Again, the voltage remains relatively stable at about 22 V for $5 \mu\text{s}$. Due to the increased voltage across the power stage, the slew rate of the currents increases, accelerating the commutation. It is mainly limited by the loop inductance of the power stage. At $t = 0,305 \text{ ms}$ the commutation is completed. The total commutation time is $7 \mu\text{s}$.

3 Hybrid Switching Technology

The Hybrid circuit breaker was designed for up to $45 \text{ A}/700 \text{ VDC}$. The block diagram of the complete hybrid circuit breaker (HCB) is shown in **Figure 9**. The power stage connected in series with a monostable galvanic separation relay protects the plus pole against overload and short circuit events. The minus pole provides galvanic separation by a monostable relay only. The relays and IGBT module are controlled via adequate drivers by a processing unit. It also controls the user interface (display and operating elements) and the communication interface for remote control. A fault detection unit identifies abnormal grid conditions and switches off the breaker accordingly. The external powered power supply generates the different required voltage levels.

Like a conventional low voltage circuit breaker, the HCB primarily serves to protect electrical power systems in the case of fault event. Besides the overload and short circuit protection with adaptive and current depending tripping characteristic, it features also undervoltage ($< 400 \text{ V}$) and overvoltage ($> 800 \text{ V}$) protection. Due to the hybrid switching concept the HCB allows an improved switching behaviour compared to

state-of-the art electromechanical circuit breaker designs (e.g. 10000 operations under load). After further system optimizations it could possibly exhibit a contactor-like switching function at nominal current.

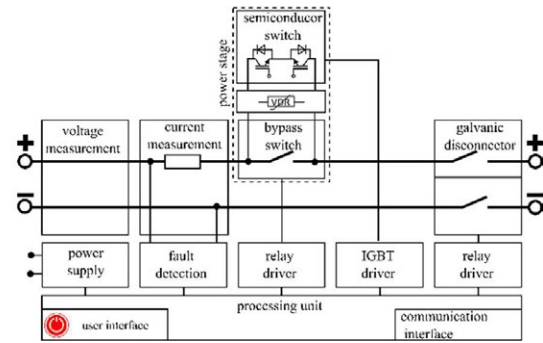


Fig. 9 Block diagram of hybrid circuit breaker (HCB).

The complete assembled hybrid circuit breaker is illustrated in **Figure 10**. Here, only the IGBT module of the power stage can be seen because the bypass relay is covered by the IGBT. Two isolation relays for galvanic separation, the electronic PCBs of the power supply, measurement unit and micro controller are shown as well. On the top of the housing a manual ON/OFF switch and a display, can be found.

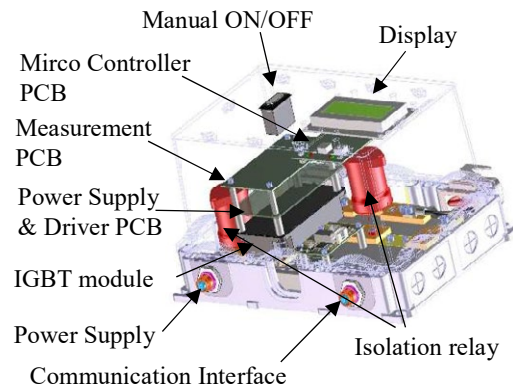


Fig. 10 Hybrid circuit breaker

The top view of the hybrid breaker is given in **Figure 11**. It has two dedicated power connectors, one for the DC bus and one connected to the load. The current flows, indicated by the dashed red line, from the bus connector via the current measurement shunt, the power stage and the isolation relay to the load connector. At the minus pole only, the current flows from the bus side via the galvanic separation relay to the load side (indicated by the solid black line).

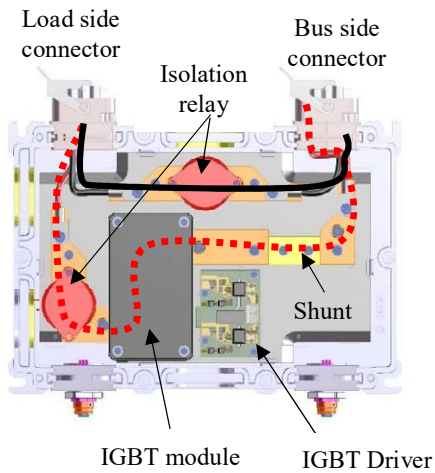


Fig. 11 Top view of the hybrid circuit breaker

4 “DC-Industrie”

The development of the hybrid circuit breaker was part of a German governmental funded project called “DC-Industrie” where about 20 companies and research institute joined forces to establish an open DC-Grid concept for industrial facilities. Goal of the project was to demonstrate smart DC-grids in industrial model applications which were previously powered by AC.

Figure 12 shows the block diagram of the industrial DC grid. Devices and applications which form a logical unit are grouped into load zones (LZ). A bidirectional active frontend rectifier (LZ1) serves as link to the AC grid and provides a nominal system voltage of 650 V on the DC bus side. Additional load zones are an electrical storage unit (LZ2), and different electric drives (LZ3 – LZ5). All load zones are connected to the DC bus via a so-called DC-branch.

4.1 DC-branch

The DC-branch combines the functionality of fault protection, load isolation, monitoring, communication and pre-charging. The detailed block diagram of the DC-branch is shown in Figure 13. The fault protection, fault isolation and monitoring are taken over by the HCB. Communication is provided by the HCB in combination with a ProfiNet gateway (not shown in the figure). A 140 μH inductance connected at the plus side of the bus limits the current rise rate to a maximum of $4,6\text{A}/\mu\text{s}$ at 650V bus voltage. A manual service switch (required under IEC 60947-3) decouples the load side from the DC Bus in case of maintenance work.

A pre-charging unit, consisting of a contactor and a PTC resistor (R_V), charges back-up and input capacitors of a load zone. If the bus voltage is reached, the hybrid breaker is closed bypassing the pre-charging unit and directly connecting the zone to the DC bus. A PLC (not shown in the figure) provides the sequence control of the pre-charging process.

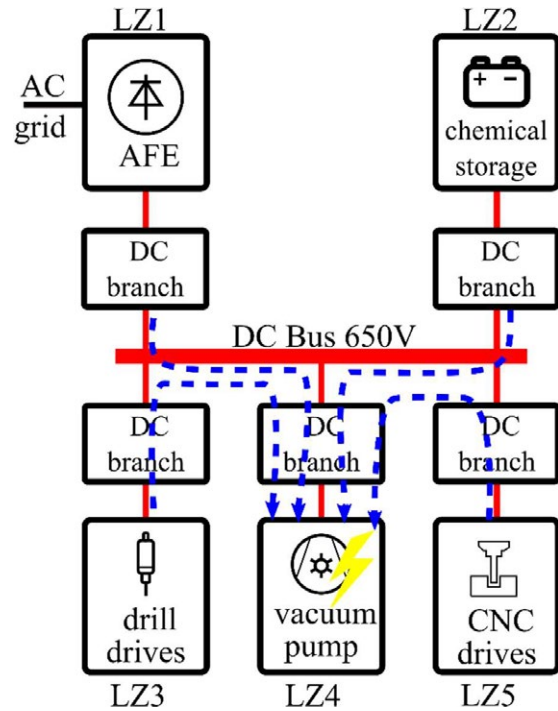


Fig. 12 Block diagram of the DC Industrie grid topology [1]

These DC branches have been developed in close collaboration with project partner Weidmüller [11], (pre-charging, further measurement and communication functions). The circuit breaker functionality was provided by Eaton.

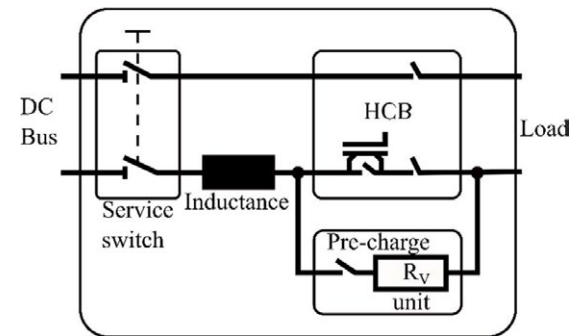


Fig. 13 Block diagram of the DC branch

The concept of the DC-branch enables full control of the DC production grid by a SCADA system allowing smart grid applications, such as real-time energy flow management, demand side management, load shading, identifying location and extent of power losses, outage prevention, condition- and performance-based maintenance, to be implemented.

4.2 Selectivity test

By means of a model installation the selectivity performance of the DC production grids shall be demonstrated. The model installation is a woodworking machine from Homag [12] where all the drives were modified for DC operation. The block schematics of the model installation is shown in figure 12. A 50 kW AFE serves as a power feed (LZ1). In addition, a 21 kWh Li-NMC battery storage (LZ2) is connected to the DC bus. LZ3 represents a 15 kW spindle/drilling motor drive, LZ4 a 12 kW vacuum pump drive and LZ5 represents the CNC-axes drives (31 kW in total).

A selectivity test is performed as follows: In a load zone, for example LZ4 (see Figure 12) a short circuit is intentionally created causing the corresponding DC-branch (HCB) to interrupt the fault current. During the fault all unaffected load zones feed into the faulty load zone meaning that a rather high current can flow in reverse direction out of the load zone. Selectivity is achieved if a fault in the load zone LZ4, is cleared by the upstream DC-branch, while all other load zones remain unaffected. **Figure 14** shows the voltages (upper graph) and currents (lower graph) measured at the DC branch of LZ1, LZ2, LZ3 and LZ4 during a selectivity test. No measurements were taken from LZ5. LZ4 is protected with a 20 A nominal current HCB. The prospective short circuit current was set to 600 A (30 times the nominal current). The fault current in LZ4, indicated by the red line in the lower graph, starts to flow at t_0 and rises within 1,05 ms to 320 A. At that time (t_1) the HCB clears the fault indicated by the drop of the current to zero within 65 μ s. Note, that a current flow into a load zone is defined as positive whereas a current flow out of the load zone is defined negative. As expected, the major portion of the fault current originates from the AFE (LZ1) and the battery storage (LZ2). A negative current was measured at LZ3 (green line, lower graph) indicating a reverse current out of the zone, feeding the faulty zone. During this period ($t_0 - t_1$) the voltage in LZ4 decreases from initially 600 V to 450 V. Afterwards, it decreases further due to the discharge of the input capacitors. The voltage measurement reveals that other load zone voltages were only influenced insignificantly by the fault event. A voltage drop of max. 10 % of the DC bus voltage (600 V) was observed. This result proves that selectivity is achieved because none of the other load zones were disconnected from the DC bus due to the fault event.

In conclusion, in 80 % of the test cases selectivity was achieved. In other cases, the short-circuit current was 60 times the nominal current of the HCB. It causes the DC bus voltage to breakdown below the minimum bus voltage of 400 V so that all load zones switched off due to undervoltage detection. This failure mode emphasized the importance of back-up capacitors with low internal inductance which are capable to stabilize the bus voltage by providing enough energy fast.

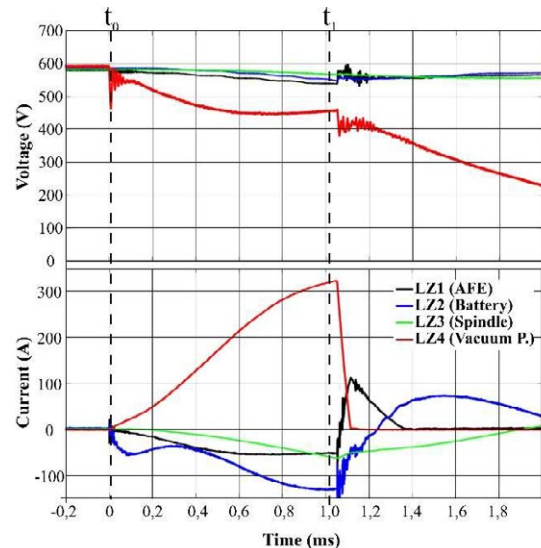


Fig. 14 Voltage and current measured at different load zones during a short circuit interruption test.

5 Conclusion

The results of the research clearly demonstrate the functionality and feasibility of an innovative power electronics-based circuit breaker with enhanced feature set. By using a hybrid switching approach with a dedicated superfast bypass relay, which enables a current commutation to a power electronic switch in case of a fault and also provides low power dissipation during normal operation, an excellent DC switching behaviour could be proven. Integrated galvanic separation relays provide the required safety related functions needed for maintenance purposes. An off-the-shelf IGBT module was deployed for hybrid circuit breaker (HCB) prototypes leaving room for future miniaturization efforts. The HCB prototypes have been implemented into a novel DC grid for industrial production/assembly application at a bus voltage of 650 VDC. Testing within a dedicated demo-grid ensured that selectivity between different parallel load zones could be established in case of a fault at branch level, increasing the energy availability within the full industrial application.

6 Acknowledgment

The authors gratefully acknowledge financial support by the German Federal Ministry of Economic Affairs and Energy (BMWi) via grant numbers 03ET7558A to N (Project acronym: “DC-INDUSTRIE”).

Parts of the presented work have been funded and supported by Austrian Klima- und Energiefonds/KLIEN and Austrian Research Promotion Agency/FFG (“DC and the future in power management”, project number 865677).

7 Literature

- [1.] dc-industrie.zvei.org, 'Das Forschungsprojekt „DC-INDUSTRIE“', [Online], [Accessed: 24.Jan.2020].
- [2.] <https://www.zuid-holland.nl>, 'Highway N470 produces Energy ', [Online], [Accessed: 20.Jan.2020].
- [3.] <https://www.rvo.nl>, 'DC-flexhouse'', [Online], [Accessed: 24. Jan.2020]
- [4.] Anshuman, S.; Georgios, D.: A Survey on Hybrid Circuit-Breaker Topologies., IEEE Trans. on Power Delivery, Vol. 30, pp. 627-641, Apr. 2015
- [5.] Koren P.P.; Nahemow M.D.; Slade P.G.: The molten metal bridge stage of opening contacts., IEEE Trans. on Parts, Hybrids and Packaging Technology, Vol. PHP-11, No. 1, pp 4 – 10, Mar. 1975
- [6.] Slade P.G.; Nahemow. M.D.: A photographic study of the initiation of the drawn arc., In Proceedings of the International Conference on Electrical Contacts, pp 285 – 288, May 1970.
- [7.] Kenan A.; Bartonek M.; Weichselbaum K.: Power Module for Low Voltage DC Hybrid Circuit Breaker IEEE Transaction on DC Microgrids, May 20-23, 2019
- [8.] Semikron, SKM400GM12T4 datasheet, Rev. 1, 03.09.2013
- [9.] Rieder W.: Plasma und Lichtbogen. Friedr. Vieweg & Sohn GmbH, Braunschweig, 1967.#
- [10.] Hemmi R, Yokomizu Y., Matsumura T.: Anode-fall and cathode-fall voltages of air arc in atmosphere between silver electrodes, Journal of Physics, Vol. 36, No. 9, pp 1097--1106, Apr,2003
- [11.] www.weidmueller.de, [Online], [Accessed: 24. Jan.2020]
- [12.] www.homag.com, [Online], [Accessed: 24. Jan.2020]

Switchgear Combination of Pyrotechnic Switch and Fuse

Arnd Ehrhardt, DEHN SE + Co KG, Hans-Dehn-Straße 1, 92318 Neumarkt, Germany, arnd.ehrhardt@dehn.de

Sven Wolfram, Technische Universität Ilmenau, Gustav-Kirchhoff-Str. 1, 98693 Ilmenau, Germany, s.wolfram@tu-ilmenau.de

Abstract

The article presents the combination of a low-voltage fuse with a pyrotechnic switch in a compact design. Different circuit concepts will be discussed, and their scope of application demonstrated with the aid of simulations and experiments based on two sample arrangements. Besides having a passive over-current protective characteristic, both arrangements allow active triggering and fast disconnection. The protective behaviour of both variants from the over-current to the short-circuit range is described for purely passive behaviour and especially for active triggering.

1 Introduction

The massive modification of power supply networks, which is currently underway among other places new demands on over-current protective devices. As numerous power generators feed electricity into the grid, the flow of power in the distribution network is no longer just unidirectional, but frequently bidirectional. The source characteristics of numerous electricity generators and new regulating mechanisms for controlling power flow reduce short-circuit currents in the grid. Both effects influence the tripping conditions for over-current protective devices in the power grid.

Fuses have the advantage over switches of being smaller whilst possessing a very high short-circuit breaking capacity, strong current limitation as well as a corresponding-low total clearing integral. Both, ambient temperature and the installation conditions are impacting the tripping behaviour of fuses, especially under small over-currents. This effect may yield to critical clearing times in modern networks with high content of renewables producing low short circuit currents. Koprivsek [1] proposed a short circuiter integral to the fuse to enhance the maximum fault current. However, this requires conventional networks with a high short-circuit power. A summary of different approaches is provided in [2].

Switches, on the other hand, generally have the advantage that the over-current characteristics are easily adjusted and can be remotely controlled. However, in networks with active power control, the passive protective characteristic of over-current protective devices often only plays a role when this control function fails. This means that in such cases, similar to with high short-circuit currents, the one-off switching function in combination with external controllability is adequate.

The design targets for our own concept of a simple “one-off switching device” for low-voltage applications (nominal voltage 230 V AC) were:

- a) high passive short-circuit breaking capacity
- b) full-fledged time/current characteristic of an over-current protective device
- c) additional external triggering feature with a disconnection time less than 30 ms
- d) high dielectric strength after disconnection
- e) high capacity to carry impulse current, especially lightning currents (25 kA 10/350 μ s)
- f) nominal current up to approx. 250 A

A simple series connection of a fuse and a switch was selected for the test arrangement. The switch is integrated into the fuse.

In the first experiments, this basic concept is examined in detail in two different test arrangements. The two test arrangements differ, especially with regard to the function and arrangement of the switches.

2 Configuration and components of the test arrangements examined

Both test arrangements were set up on the basis of the individual parts of a capsule fuse size 22 x 58. The arc quenching medium selected was conventional compacted silica sand. To achieve the desired high impulse current resistance, two parallel copper fuse elements with modulation were routed, as far as possible, straight through the housing. The nominal current of the double fuse element is 250 A. The fuse can carry lightning impulse currents with an amplitude of 25 kA (impulse shape 10/350 μ s with $I^2t = 156 \text{ kA}^2\text{s}$). Thus, a configuration was selected by which the nominal current and impulse current are at the upper limit, resulting

in maximum requirements on the switching capacity. Realisation of the active switching function was achieved by integrating a very simple pyrotechnic switch in a fuse filled with silica sand.

2.1 Structure and description of the test samples according to test arrangement 1

Figure 1 shows the principle structure of a test sample according to test arrangement 1. The pyrotechnic switch for radially cutting the fuse element with the aid of an insulated cutting blade is located in the middle of the fuse. The sand-filled part of the fuse link (fuse part) is split into two sections. Each of the two fuse parts holds half the restricted sections of the fuse element required to disconnect the short-circuit current.

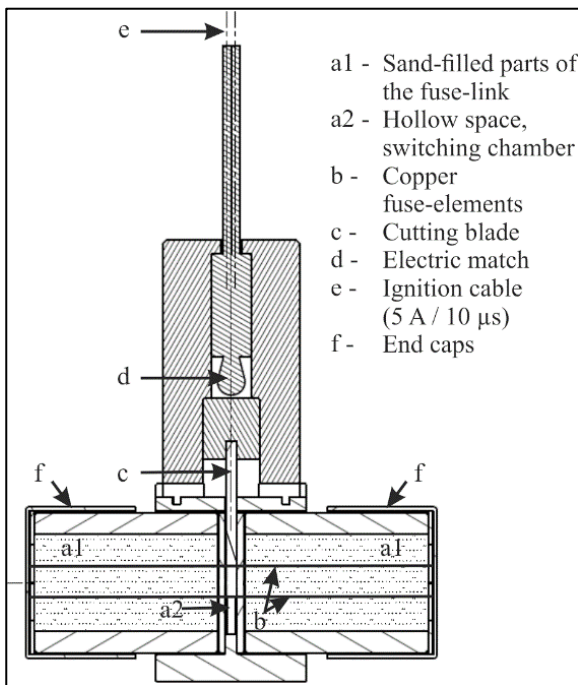


Fig. 1 Test sample according to test arrangement 1

Between the fuse parts a1 is a hollow space a2 through which the fuse elements b are guided. In this chamber, the fuse elements have an additional restricted section, which is dimensioned in such a way that it does not trigger at the usual total clearing integral of the fuse when short-circuit currents are interrupted. A single fuse element with such a restricted section in the centre is shown in **Figure 2a**. This special restricted section does not melt in the entire time/current range with the usual passive function of the fuse. It merely reduces the power required for cutting.

The time/current behaviour of the sample arrangement was simulated with FEM calculations of transient impulse current loads up to 1 h current. **Figure 2b** shows the temperature rise of the fuse element when impulse current flows through it [3]. A simple simulation model for optimising the cutting blade, the force required and the stroke path is shown in **Figure 2c**. To determine the

separation distance, the model is supplemented with the walls of the hollow space a2 in addition to the blade and the fuse element.

An insulated cutting blade is guided in the hollow space between the two fuse parts and cuts through the special restricted section when the electric match is actuated. The fuse parts with silica sand filling are separated from the hollow space by a wall thinner than 1 mm in such a way that no quenching agent can penetrate the hollow space. This ensures that the force required to operate the cutting blade is low. The total width of the hollow space is narrower than 5 mm. When the cutting device is actuated, the severed fuse elements are crushed between the insulated blade and the walls made of insulating material which separate the fuse parts. This results in the arrangement of an isolating gap switch for the arc that may arise. If the intrinsic switching capacity of the pyrotechnic switch is exceeded, an arising arc can extend along the fuse element to the fuse parts filled with silica sand. In this case, the arc is also safely quenched.

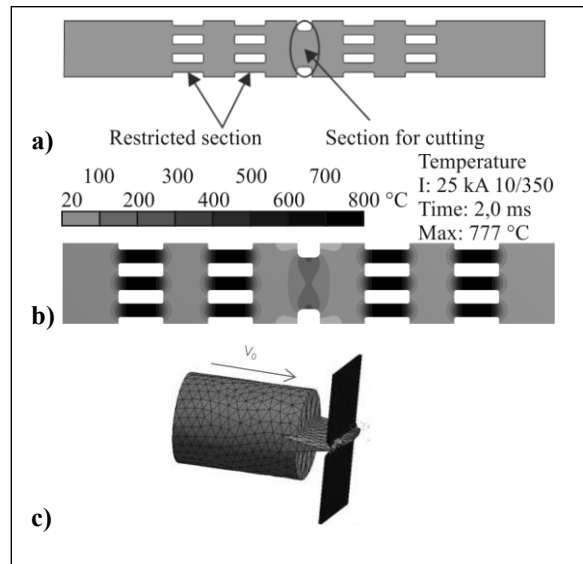


Fig. 2 a) Fuse element with additional restricted section
b) Calculated maximum temperature at 25 kA, pulse shape 10/350 μ s
c) Simulation model of the cutting process

2.2 Structure and description of the test samples according to test arrangement 2

The housing of the sample fuses was split into two cavities. In the first cavity of the switching chamber, the fuse elements are surrounded by silica sand. All the restricted sections of the fuse elements can also be found in this cavity. There is no silica sand in the second cavity and the cross-section of the fuse elements there is undiminished. The two cavities are separated by a plate through which the fuse elements are loosely routed. In the cavity with no silica sand, the fuse elements are

fixed to a moving piston. The piston can be moved axially by several millimetres within the housing by an internal electric match. When the piston moves, both fuse elements break, and a separation point is formed in the fuse element within the switching chamber which equals the stroke length of the piston and is surrounded by silica sand. The parts of the fuse elements moved by the piston are deformed in the cartridge without silica sand.

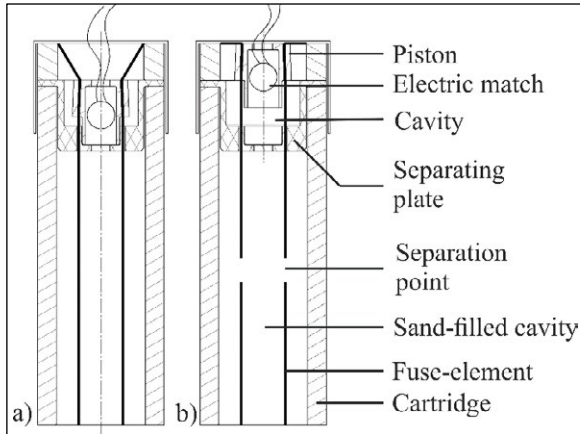


Fig. 3 Sample fuse according to test arrangement 2
a) in normal state
b) after active disconnection

The arrangement in the cavity without silica sand thus corresponds to a switching mechanism. The fuse and the interruption section of the "one-off switch" are both located in the cavity filled with silica sand. **Figure 3a** shows such a basic arrangement in the conductive, or rather, normal state. **Figure 3b** shows the state after movement and breaking of the fuse elements following an active actuation of the electric match. Several measures are necessary to achieve a defined separation point and a defined isolating distance in minimal space. The tensile force acts on all restricted sections of the entire fuse element. Taking into account the heating up of the fuse element at nominal current and overcurrent, there is a considerable expansion in the order of several millimetres before the fuse element interrupts. The interruption takes place at one of the defined restricted sections of the fuse element. **Figure 4a** shows the elongation (> 6 mm) calculated for one of the two fuse elements with restricted sections without a temperature rise before breaking. If, for example, an isolating distance of 6 mm is to be reliably achieved in addition to tearing, a linear stroke of more than 12 mm is required. To combat these disadvantages, a further restricted section is introduced in the fuse elements, see **Figure 4b**. This additional restricted section has a much lower residual cross-section than the other restricted sections. It is, however, very short. This design means that the elongation required to break the fuse element under force is very small and is almost entirely limited to the additional restricted section. The stroke of the piston is,

therefore, almost identical with the minimum isolating distance.

The force required to break the restricted section can be reduced by more than a third. The influence of the additional restricted section on the time/current characteristic and the switching behaviour of the fuse is therefore imperceptible.

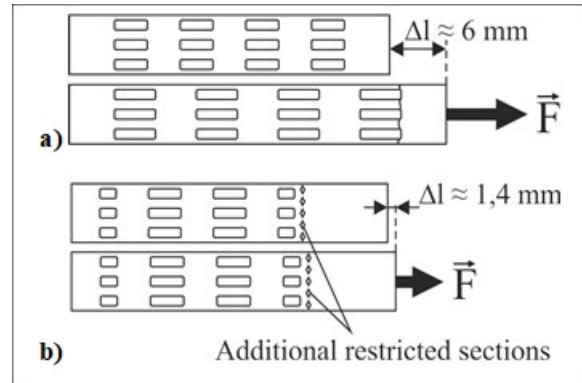


Fig. 4 **a)** Calculated change in length up to elongation fracture
b) Calculated change in length up to elongation fracture with additional restricted sections

Figure 5a, 5b show the rise in temperature in the restricted section when loaded with impulse current in comparison to one of the other restricted sections. The characteristic allows this restricted section to be positioned almost anywhere in the fuse elements. However, the additional restricted section should be far enough away from the plate separating the cavities with and without silica sand to ensure that, when activated, the safe interruption of overload currents is possible in a single break.

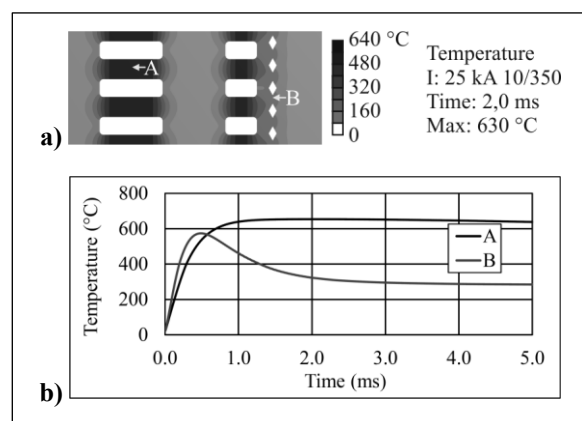


Fig. 5 **a)** Calculated temperature distribution ($^{\circ}\text{C}$) at the fuse-element after 2 ms at 25 kA, pulse shape 10/350 μs
b) Calculated temperature/time curve for points A and B

3 Mode of operation

3.1 Passive operation

The time/current characteristic of the model configuration according to test arrangements 1 and 2 was simulated with FEM calculations of transient impulse current loads of up to 1h current. **Figure 6** shows the temperature rise of the fuse element with the additional restricted section as per test arrangement 2 in case of an overload current with a pre-arcing time of approx. 30 ms.

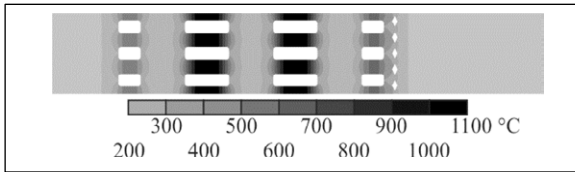


Fig. 6 Calculated temperature rise ($^{\circ}\text{C}$) after 30 ms at $I_p = 3 \text{ kA}$

Figure 7 compares the calculated and experimentally determined time/current characteristic in the current range from approx. 600 A to 50 kA. The curves of time/current behaviour are almost identical for both test arrangements. Figure 7 also shows the time/current characteristic of a conventional NH fuse.

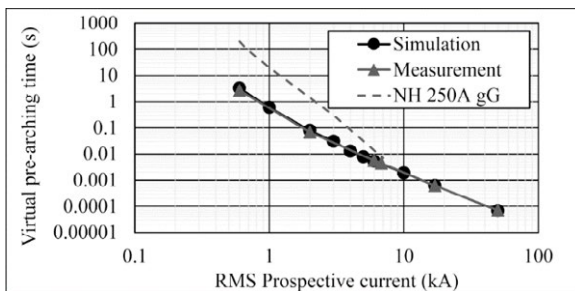


Fig. 7 Comparison of the measured with the calculated passive time/current characteristic

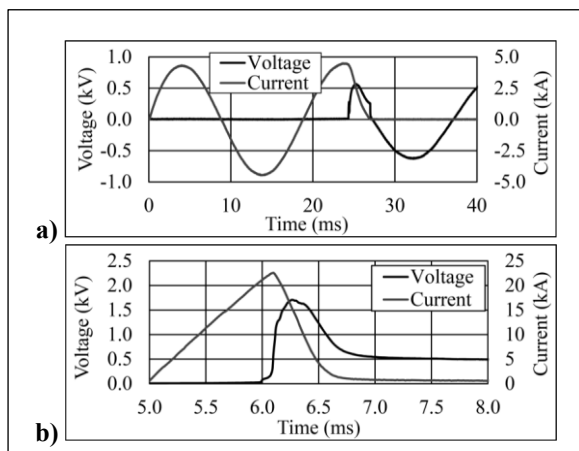


Fig. 8 Measured voltage/current curve at:
a) $I_p = 3 \text{ kA}$ ($U_C = 440 \text{ V}$; $\cos\phi = 0.87$)
b) $I_p = 50 \text{ kA}$ ($U_C = 440 \text{ V}$; $\cos\phi = 0.23$)

There is a sufficiently good congruence between simulation and measurement in both test arrangements. The passive switching behaviour with test samples of test arrangements 1 and 2 was examined at 440 V in the current range of 600 A to 50 kA. **Figure 8a** shows the current and voltage curves at a prospective load of 3 kA and **Figure 8b** at 50 kA for test samples of test arrangement 2. With regard to the passive switching behaviour, the two examined test arrangements 1 and 2 hardly differ, so that a separate representation has been omitted.

3.2 Active operation

In addition to the passive operation, the operation of functional samples of test arrangements 1 and 2 with active control of the pyrotechnic switch in the event of overload currents was also investigated. Here, the triggering time T_{Delay} and the time until both fuse elements break T_{PreArc} are relevant. The sum of both times is the whole time delay T_V . This time determines the maximum current load that must be mastered with active triggering. If the passive melting time is shorter than the delay time, the fuse switches purely passive. In the event of short-circuit currents, several or all restricted sections of the fuse elements respond. In this case, an active shutdown is not necessary and also not sensible. The triggering time must therefore not be less than 20-30 ms. At the same time, this enables safe fault detection and evaluation with a low error ratio and is fast enough for many applications.

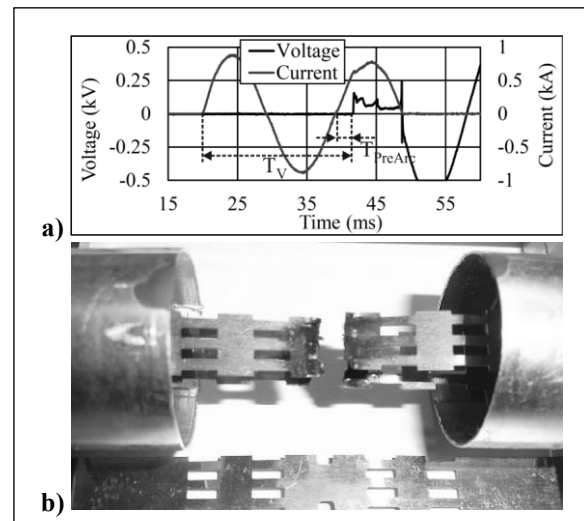


Fig. 9 **a)** Measured voltage/current curve at $I_p = 600 \text{ A}$ ($U_C = 440 \text{ V}$; $\cos\phi = 0.92$)
b) Burn-off area after disconnection

Figure 9a shows the disconnection of a current of 600 A for a sample of test arrangement 1. The current load of 600 A is switched off by the switch itself as a result of the current zero. In **Figure 9b** the burn-off area is small and without silica sand residue. **Figure 10a** shows the disconnection of a current of approx. 3 kA for a sample of test arrangement 2.

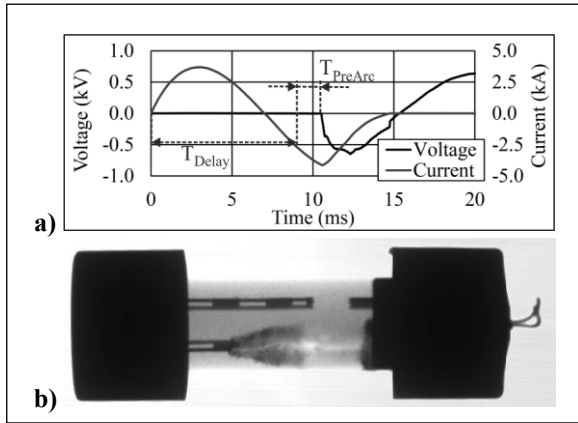


Fig. 10 a) Measured voltage/current curve at $I_P = 3 \text{ kA}$ ($U_C = 440 \text{ V}$; $\cos \phi = 0.86$)
b) X-ray photograph after disconnection

As a basic principle, short-circuit currents of about 3 kA and higher are only switched passively in the given test configuration. For the test in Figure 10a, the arrangement had already been modified to allow accelerated operation. The test current in Figure 10a and the switching capacity achieved for the sample fuse therefore exceed the maximum capacity required. The X-ray photograph in Figure 10b show the basic behaviour of the fuses in test arrangement 2. Due to the rapid pulling movement, an arc is only generated in the fuse element which disconnects last. This arc is also rapidly extended by the movement, whereby the fulgurite contains few electrically conductive particles (bright).

4 Discussion of the results

In Figure 11 the realistic active curve of the model fuse alongside the passive time/current characteristic for both test arrangements is shown. This diagram clearly shows that safe disconnection is possible within a total current range more than 30 ms using the configuration examined. In case of a longer tripping delay or lack of activation / high short-circuit currents, the configuration has the time/current behaviour of the fuse.

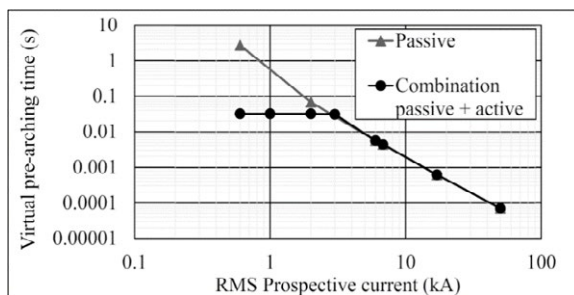


Fig. 11 Time/current characteristic of the switch gear combination

The switching capacity of the simple pyrotechnic switch and combination with the passive protective characteristic of the fuse thus allow safe and unin-

terrupted operation of the series connection in both active and passive mode of operation in both arrangements.

After the switching loads which were mastered by active and passive functions, the rated impulse withstand voltage was tested for the model configuration [4]. This revealed that in case of active tripping the impulse withstand voltage was always more than 6 kV, regardless of the current load. The tested sample arrangement thus reliably prevents a renewed current flow through the fuse even at higher voltages after disconnection.

A sufficiently precise simulation of the time/current characteristic of the fuse element could be achieved for both test arrangements examined. The mechanical interruption at the additional narrow point of the fuse element by cutting (arrangement 1) and pulling (arrangement 2) can be optimized through simulation. The two test arrangements examined offer the opportunity to achieve the self-defined objectives a) to e) such as listed in section one (introduction).

5 Summary

It has been demonstrated that higher switching capacities and lower clearing integrals, similar to fuses of comparable size, can be achieved via the additional “triggering” function. The disconnection time when controlled externally is comparable with that of remotely operated switching devices. In case of failure of the triggering function, the fuse still at least fulfils the standard protective function of a normal passive fuse against over-current and short-circuits. In addition, the test arrangements can conduct high transient impulse current without interruption. Safe, active disconnection is independent of the current load, i.e. from zero current up to the short-circuit current range, whereupon a higher and more defined withstand voltage is achieved than with passive fuses. The active triggering function can be implemented using simple monitoring devices and without an additional power supply.

6 Literature

- [1] Koprivsek, M.: Triggered fuse. In 10th ICEFA, Sept. 2015, pp 69–78
- [2] Bessei, H.: Smart fuses for smart grids: Considerations about the need, potential product features and feasibility. In 10th ICEFA, Sept. 2015 pp. 79–86
- [3] Rochette, D.: Modelling of the pre-arcing period in hbc fuses including solid-liquid-vapour phase changes of the fuse element. In 64th IEEE Holm Conference on Electrical Contacts, September 2007, pp. 87-93
- [4] IEC 60664-1 Insulation coordination for equipment within low-voltage supply systems - Part 1: Principles, requirements and tests, 2007

Design of an electromechanical relay for 5G power supply application which withstand high lightning surge current

Maosong Zhang, Yiqing Zhu, Xiamen Hongfa Electroacoustic Co.,ltd, Xiamen, China, tech@hongfa.com

Abstract

Electromechanical relay which connect 5G base station with the power supply should have DC load switching ability and be able to withstand the impact of lightning surge current. Based on the theoretical analysis this paper introduces the principle of how to break the arc in the contact system of a relay, the principle of how to protect the application when the lightning current occurred and the description of overall design of relay, especially the design of the contact system. The design of the electromechanical relay can meet the requirement of main technical performance of 5G power supply applications, and be able to withstand 10kA lightning surge current in series and 20 kA lightning surge current in parallel shown in the design validation.

1 Introduction

With the development of mobile communication technology, the fifth generation mobile communication technology (5G) has been commercialized. Compared with 4G, the number of 5G base stations is greatly increased and widely distributed. Because of the efficiency, the power supply voltage increased from 48Vdc to 240Vdc, which will be even higher in the future. Due to the outdoor working characteristics of most base stations, they have to withstand a lot of lightning strikes, which will be a great impact on the power supply.

The relay which connecting the power supply to the base station, the load switching capacity must be increased to 240 Vdc. Apart from that it must be able to withstand the impact of lightning surge current, fulfill reliable insulation between the base station and the power supply, protect the power supply and the base station when necessary.

The traditional electromechanical relay can only break the DC load of about 3A/48Vdc, and explosion or contact welding failure may occur when lightning current pass through. In order to meet the application requirements of 5G power supply, it requires high power electromechanical relay with higher voltage DC load switching ability and lightning protection function.

2 Design principles of switching Higher Voltage DC load

When the relay breaks the DC circuit in the atmosphere and the voltage exceed 10V, the arc will be generated between the contacts. The AC circuits can naturally extinguish arcs because of zero crossing. But the

DC circuit can only wait for the arc to be long enough to break it, the relationship between DC current and voltage corresponding to different contact gaps which can extinguish the arc reliably^[1] is as figure 1. For example, it needs more than 20 mm contact gap to break the 240Vdc and 5A circuit. That large contact gap couldn't be achieved by traditional electromechanical relay.

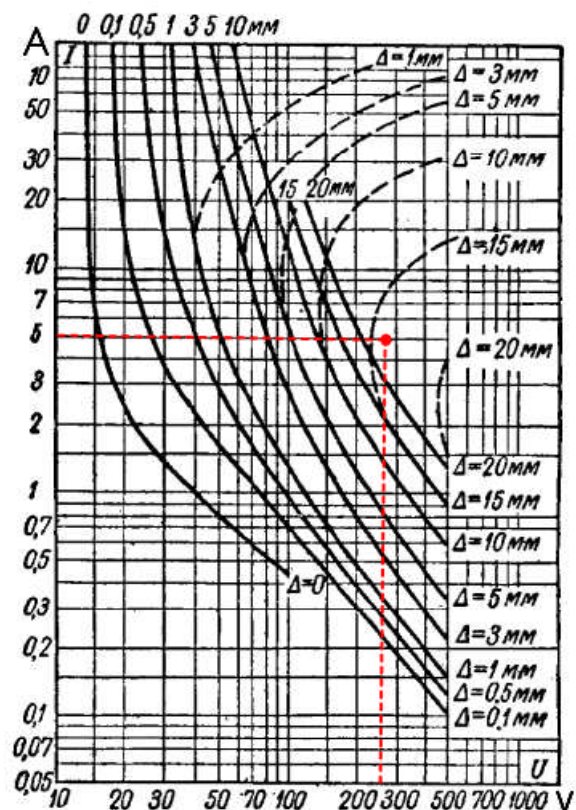


Fig.1 The relationship between DC current and voltage corresponding to different contact gaps^[1]

There are some typical methods to help to break the arc.

Encapsulate the contact parts of relay in a closed cavity, which is vacuum or filled with SF₆ gas. The SF₆ gas and high vacuum have high insulation and strong arc extinguishing ability. But it is cost intensive to seal the contact parts for lifetime.

By designing the arc extinguishing chamber with about 15 metal blades the arc voltage will be increased - due to several shorter arcs between the metal blades, adding the anode and cathode voltage (about 20Vdc) for each metal blade – till it exceeds the level of the power supply voltage. This design needs a lot of space, which will enlarge the size of the relay.

Lengthening the arc by using additional walls out of insulation material can bend and extend the arc till it extinguishes. This design also needs some extra space.

Using an additional magnet will lengthen the arc and move the arc from the contact area cooling it down rapidly through the electrodynamic effect of external magnetic field. Compare with other methods it is easier to realize at a limited space.

3 Design principles of handling Lightning surge Current

3.1 Theoretical analysis

When a current pass through the conductor, a magnetic field is created around it, and other current-carrying conductors in the magnetic field are subjected to generate an electrodynamic force. The magnitude of the force is related to the spacing between the current-carrying conductors and the magnitude of the current. Because the electrodynamic force is proportional to the square of the current, when lightning surge current occurs, the electrodynamic force will be as much as tens times or even hundreds of times as much as that of the normal operation, which will cause mechanical damage to the equipment.

The main electrodynamic force acting on relay contacts are Lorentz force^[2] and Holm force^[3]. From the basic principle of the electromagnetic field, when current flows through a "U" shape circuit, the opposite direction of the current carrying conductor generates a repulsive force, that is called Lorentz force. As shown in figure 2.

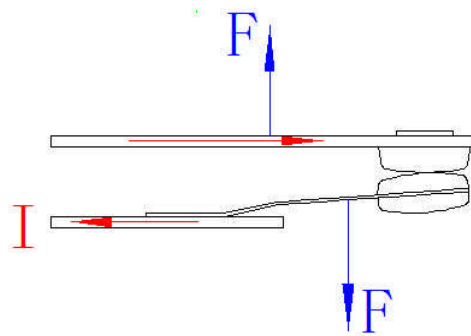


Fig. 2 Schematic diagram of Lorentz force

The Holm force is due to the constriction of the electrical current when being forced through a small, effective contact area. The contacts do not touch over the entire apparent contact area but in fact, due to the rough and uneven surface of the contacts, touch only a few relatively small points. When the contacts are separated, the Holm force disappears. As shown in figure 3.

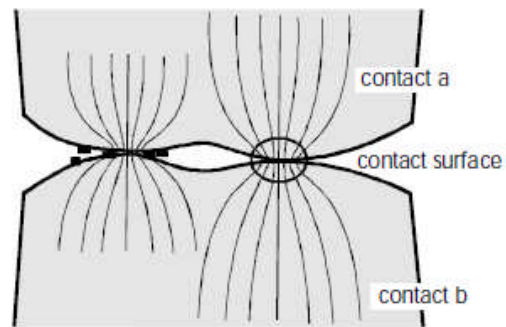


Fig. 3 The principle of Holm force

3.2 Design principles of handling Lightning surge Current

By changing the shape of the current loop, the force generated by the current itself acts as an additional contact force in closing direction, see Figure 4. This "reverse loop contact" principle is well known for the contact design in high voltage disconnectors.^{[4][5]}

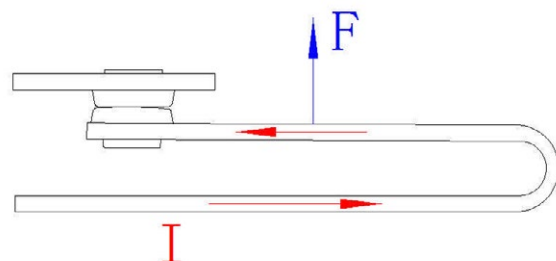


Fig. 4 Design of the contact system to a "U" shape to generate an additional contact force

4 Design of the electromechanical relay applied to 5G power supply

4.1 Technical requirements of 5G power supply:

2 poles normally open contacts;

Contact gap ≥ 2.6 mm;

Lightning-proof current capability: In series contact 10 kA; In parallel contact 20 kA; (according to IEC 61000-4-5:2005^[6])

Load capacity: 25 A 225 Vdc ; 14 A 400 Vdc

4.2 Design Principles

4.2.1 Overall design structure of the relay

Overall structure of the electromechanical relay against lightning surge current is show in Figure.5.

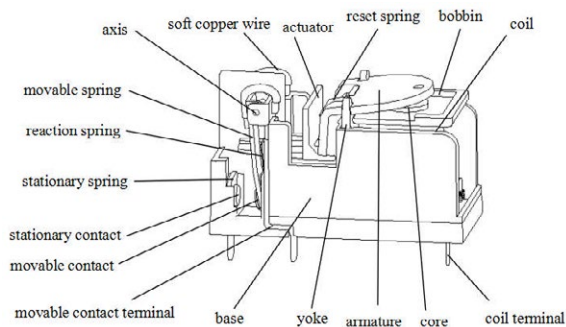


Fig. 5 Overall structure of high power electromechanical relay against lightning surge current (release position)

The above figure is the inside structure of an electro-mechanical relay. It is composed of magnetic circuit system, contact system and base. The contact system including the following parts:

- The movable contact is fixed on the movable contact spring. The movable contact spring can rotate around its axis.
- The rigid movable spring and the rigid movable contact terminal were connected by the soft copper wire make it a “U” shape circuit.
- The reaction spring is mounted on the back of the rigid movable spring to generate the contact force when moved by the armature.
- The reset spring opens the contacts when the coil voltage is below the release voltage.

4.2.2 Design principles of handling higher voltage DC current load by using magnetic blow-out

A magnet is placed under the contact system. The DC current flows in the direction shown in figure 6, an arc will occur when the movable and static contacts are separated. According to the left hand rule, the arc will move outside under the magnetic field of the magnet, thus prolonging the arc and extinguishing the arc.

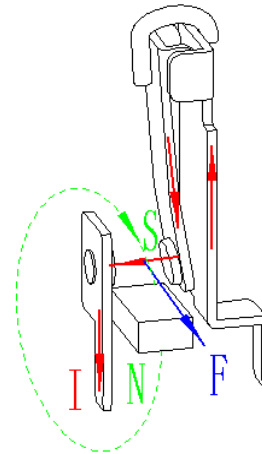


Fig. 6 Magnetic blow-out

4.2.3 Design of contact system for Lightning-proof current

When the lightning surge current occurs, the Holm force will be produced and will cause the contacts to be disconnected, which may impact the electro-dynamics stability of the electromechanical relay. As show as figure.7 when the lightning surge current pass through the “U” shape movable contact parts, the Lorentz force (increasing the pressure of the movable contact on the static contact) will counteract the Holm force, so that the contacts can maintain close status.^[7]

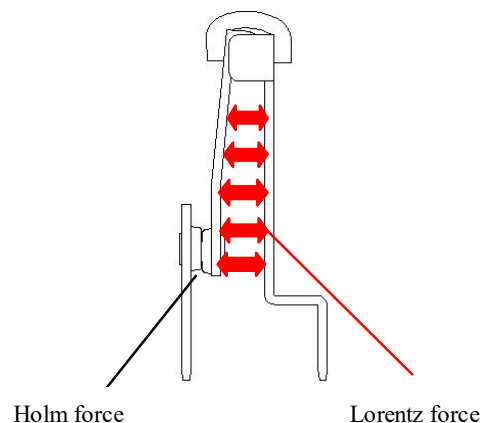


Fig. 7 The schematic of the Holm force and the Lorentz force

The Lorentz force generated by the peak current of lightning surge current is very large, which may cause the permanent deformation of the spring. To avoid this kind of failure, the movable spring is set to be rigid, use pure copper material with excellent performance of electrical and thermal conductivity. Because the rigid movable spring couldn't be deformed, the reaction spring is designed to provide contact force. The reaction spring does not participate in the conductive heat conduction circuit and will not overheat or lose its elasticity. So it can provide a stable contact force during the long-term operation of the relay.

4.3 Experimental verification

4.3.1 Lightning current experiment

Ambient temperature : room temperature

Energized condition : initially energized by rated voltage, and reduce to 50% rated voltage after 100 ms

Contact load: waveform as shown in figure 8, 2 poles in series connection 10 kA, forward and reverse 5 times; 2 poles in parallel connection 20 kA, forward and reverse 5 times, totally 20 times.

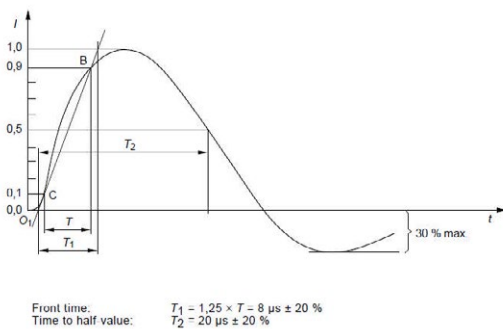


Fig. 8 Lightning current waveform

Failure criterion: contact welding is not allowed during the experiment, and the functional parameters is within the specification.

Test Result: Pass.

4.3.2 Electrical endurance test

Sample after lightning surge current experiment

Ambient temperature: 85 °C

Energized condition: rated coil voltage

Load 1: 2 poles in series connection, 225 Vdc 25 A, 1 s on, 9 s off, 5000 cycles

Load 2: 2 poles in series connection, 400 Vdc 14 A, 1 s on, 9 s off, 5000 cycles

Failure criterion: contact welding is not allowed during the experiment, and the functional parameters is within the specification.

Test Result: Pass.

5 Conclusion

This paper introduces the structure of an electromechanical relay. Base on theoretical analysis, design an “U” shape circuit by connecting the rigid movable spring and the rigid movable contact terminal to create the Lorentz force, which can counteract the Holm force due to the huge lightning surge current. Use magnetic blow-out structure to switch the higher voltage DC current. According to the experiment result, this relay can withstand 10kA lightning surge current in series and 20 kA lightning surge current in parallel, and it is reliable to switch 25 A 225 Vdc and 14 A 400 Vd.c, it can meet the main technical requirements for 5G power supply. This paper has reference value for the design of high power electromechanical relay which is used to withstand short circuit current.

6 Literature

- [1] M.I.Witenberg (author), Fu Zhizhong(translator), “Design of Electromagnetic Relay for automatic device and Communication equipment”, POSTS & TELECOM PRESS, Beijing, 1964, pp. 632
- [2] Hendrik Antoon Lorentz, Electro Magnetic Force, 1895
- [3] R.Holm, Electric Contacts, 4th edition, Springer-Verlag, Berlin, Heidelberg etc., 1967, 3rd print 2000
- [4] https://mindcoretech.com/Brochure_ADB.pdf Aluminium Double Break Disconnect Switch 38 to 500kv / 600 to 4000A, MindCore Technologies, 1845 Jean-Monnet Terrebonne (Quebec) J6X 4L7 Canada
- [5] http://nepa-ru.com/Coelme_files/disconnectors/tcb/02_web_double_break_stc_en.pdf STC 72.5 - 550 kV Twist Motion Double Break disconnecter, COELME, Via G. Galilei, 1/2 - 30036 Santa Maria di Sala (VE) - Italia
- [6] IEC 61000-4-5 (2005) Electromagnetic compatibility (EMC) — Part 4-5 : Testing and measurement techniques — Surge immunity test
- [7] Ji Guoce, Su Xiuping, Zhang Ziyong, Qiao Yanhua, “Research on Electrodynamics Force of Magnetic Latching Relay”, DIANQI YU NENGXIAO GUANLI JISHU, Vol.23, 2017:2

Failure- and degradation mechanisms in plug connectors

Jacob, Peter, Empa Duebendorf, Switzerland

Abstract

Plug connectors are frequently the root cause of failures on system level. The spectrum of failures include connector weakness, surface contaminations, fretting, arcing, isolation problems and a series of secondary failures especially on printed circuit boards (PCBs) like bending, heat transfer to PCB lines and also borderline specification issues. When discussing about plug connector failures, the electrical and physical environment of the connector needs to be included into root cause investigation, since the amount of damage significantly depends on these "secondary" factors, too.

1 Introduction

In many cases, failures in plug connectors end up in catastrophic burning damage. In the recent years and under a certain pressure of miniaturization in the whole scope of electronics, many connectors were specified in a rather borderline manner. On the user side, at the same time no or only few derating has been designed in the connector applications – driven by competition- and cost reasons. In consequence, failures root-caused by plug connectors got more and more into the focus of failure analysis and failure anamnesis on system level. This paper is an updated and extended version of a former paper on the topic, which I have published in 2016 [1] (but not dealing with the relay sections in the abovementioned paper).

2 Failure signatures

Like a transistor in on-state, a contact has a power loss, too - resulting from the voltage drop on the contact multiplied with the current flow. If a plug connector suffers degradation, the voltage drop will increase and with it, the power loss, too. This power converts directly to a very locally "point shape" heat source which initiates various degradation mechanisms, which have all one subject in common: They accelerate themselves and initiate further failure mechanisms needing higher activation energy by further increasing the voltage drop and the power loss. Fig. 1 shows the most frequent ways of failure development in plug connectors as an overview. It highlights, that at the end of the failure development, either a complete open results or the situation escalates in arcing and/ or burning – at least, as long as no electric fuse stops the ongoing supply of energy.

As an example for PCB connectors, fig. 2 shows a principle drawing indicating the most frequent potential failure root causes.

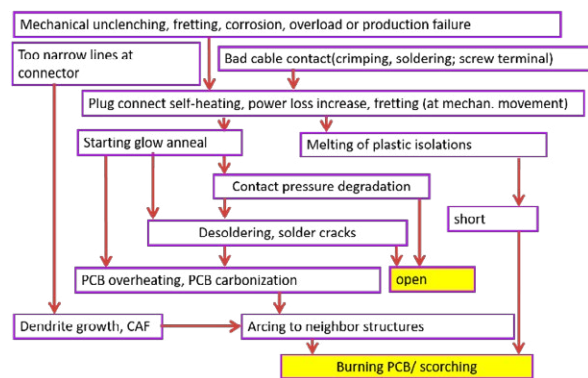


Fig. 1 Development of failures in plug connectors

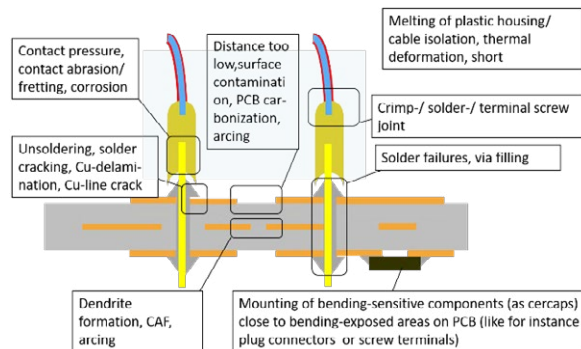


Fig. 2 Frequent failure types in a PCB connector

2.1 Arcing

Another issue that applies especially to connectors on PCBs is the narrow layout at the connector, where the neighbourhood between PCB lines become closest. For instance, in case of electronic switching power supplies, high voltage lines sometimes are not kept in enough distance to ground or low-voltage lines. If in such case, additional heating applies by any reason (including wearout of the connector), the PCB starts to become locally dark (and carbonized) – resulting in a loss of isolation capability. Then, subsequent arcing is

only a question of time. Therefore, already in the design phase, not only the current and voltage load capability needs to be obeyed but the pin-to-pin and line-to-line (on PCB) isolation need to be considered.

Once the ignition of arcing has happened, a plasma discharge based on ionized gas molecules applies which needs by far less voltage than it was needed for ignition: only about 10 V are enough to maintain the arcing. Arcing is not only limited to a missing distance between high- and low-potential PCB lines and connector pins but may also apply as a late secondary effect of heat generation due to contact degradation: If, for instance the solder joint of a related pin is circular broken, the small gap may be "bridged" by arcing (fig. 3). The same may apply if the isolation between two pins of a connector starts to melt and deforms the pin arrangement towards shorting. Finally yet importantly, any thermal stress-induced deformation of the connector that results in a small gap disconnection may become a source of arcing.



Fig.3 Arcing damage in the PCB at the connector

2.2 Contact degradation by chemistry

In some applications, electronics is hermetically sealed in a small cabinet and the cabinet is exposed to extreme sunshine and other climatic changes. Under such circumstances, the inner temperature may reach even 100°C. Already above 80°C, outgazing of chemistry starts for instance from lacquers of wires from transformers, relays or coils, outgazing from plastics and component housing can start and provide isolating nanolayers on relay contacts and connectors. The presence of additional humidity may even generate aggressive and/ or corrosive chemistry as for instance sulphuric acid. While in relays or switches, such effects provide a rapid degradation or even functional failures, plug connectors usually don't fail rapidly from these effects but suffer significant long-term degradation. This applies especially for low signal appliances with only few mA or less of current at low voltage.

Beyond this, it needs to be mentioned that connectors, relays and switches provide an ideal microclimate incubator [2]

The use of contact chemistry as contact spray, grease etc. may also become a basis of chemical induced degradation processes [3].

2.3 Degradation of contact pressure

This is one of the most frequent beginnings of contact degradation in plug connectors. The construction characteristics of a female plug connector with respect to the generation of contact pressure is one of the most important topics, which, however, frequently is not taken into account.

Cheap constructions use simply bended fork female contacts as shown in fig. 4. Such contacts are not useful if a plug connector is connected and disconnected frequently or when it is used for high power applications. In case of frequent plugging/ unplugging, a beginning contact pressure degradation accelerates itself rapidly: When reaching high temperature, the contacting metal may start to glow slightly. This heating reduces both contact pressure and the elastic recovery of the contact forks significantly and irreversibly.

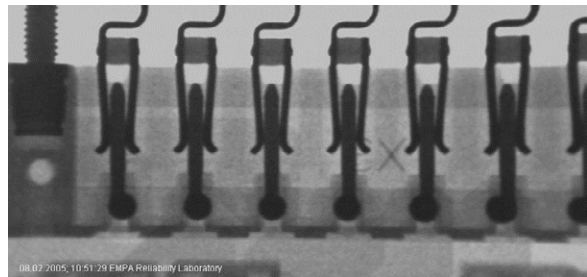


Fig. 4 Fork contacts of a connector (X-ray image). The fork material itself makes the contact pressure.

A better, but more expensive solution is the use of separate spring clips around the contacting forks or cylindrical contact systems with pressure-enhancing spring mechanisms. Advantages of such solutions are multiple contact points, a better heat distribution and a more constant contact pressure over long times. Fig. 5 shows a frequent and simple example of such solution, the 4mm banana plug connector.



Fig. 5 Banana plug connector with an integrated contact spring in the male plug (arrow). It provides a multi-contacting in the cylindrical female connector at the right hand side.

2.4 Contact metal degradation

In this chapter, we discuss degradation mechanisms of the contact metal surface. Usually the contact surfaces are coated by metals like e.g. gold, silver or nickel in order to make the contacts more robust against chemi-

cal attacks and to reduce the contact resistance. However, this is not always an effective resp. sufficient precaution, as we will see in the next two subchapters.

2.4.1 Corrosion

The presence of humidity promotes corrosion and electrolytic transfer of materials. Fig. 6 gives an overview

Metal Corroding \ Contact Metal	Magnesium & alloys	Zinc & alloys	Aluminium & alloys	Cadmium	Steel-carbon	Cast Iron	Stainless steels	Lead, tin and alloys	Nickel	Brasses, nickel silvers	Copper	Bronzes, cupro-nickels	Nickel copper alloys	Nickel-Chrome-Mo Alloys	Titanium	Graphite, gold, platinum
Magnesium & alloys	X	X	X	X	X	X	X	X	X	X	X	X	X	X	X	X
Zinc & alloys		X	X	X	X	X	X	X	X	X	X	X	X	X	X	X
Aluminium & alloys			X	X	X	X	X	X	X	X	X	X	X	X	X	X
Cadmium				X	X	X	X	X	X	X	X	X	X	X	X	X
Steel-carbon				X	X	X	X	X	X	X	X	X	X	X	X	X
Cast Iron					X	X	X	X	X	X	X	X	X	X	X	X
Stainless steels					X	X	X	X	X	X	X	X	X	X	X	X
Lead, tin and alloys						X	X	X	X	X	X	X	X	X	X	X
Nickel							X	X	X	X	X	X	X	X	X	X
Brasses, nickel silvers					X	X	X	X	X	X	X	X	X	X	X	X
Copper						X	X	X	X	X	X	X	X	X	X	X
Bronzes, cupro-nickels								X	X	X	X	X	X	X	X	X
Nickel copper alloys													X	X	X	X
Nickel-Chrome-Mo Alloys														X	X	X
Titanium															X	X
Graphite, gold, platinum																X

Fig. 6 Galvanic corrosion risk of different metal contacting partners. Graphic from [6]

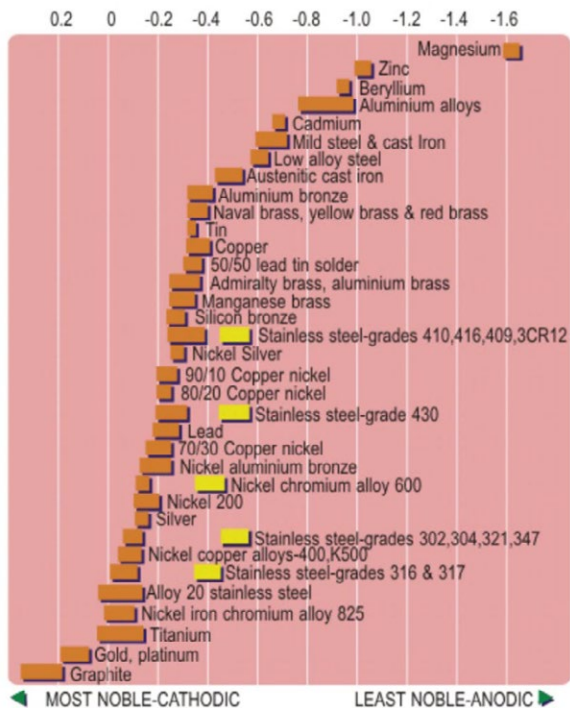


Fig. 7 Less noble metal surfaces suffer enhanced corrosion attacking. Top scale: Volt vs std. hydrogen sat. Cu/CuSO₄, Calomel electrode (proportional to Galvanic Series of Metals)

on galvanic corrosion in connectors, showing the compatibility of various contact metallization surfaces. In

general, less noble metal surfaces suffer enhanced corrosion attack by environmental impacts as humidity or aggressive gases (but of course some have other disadvantages), see fig.7.

Many connectors are chemically coated with oxide inhibitors or anti-oxidant coatings in order to protect the contact partners when they are stored for a long time before first field application. The compatibility of such chemistry with the contact finish metal should be carefully reviewed with respect to their potential to promote chemical or electrolytic attacks to contacting surfaces.

2.4.2 Fretting

Fretting is also a frequent failure mechanism in plug connectors. The initial triggering is a micro-vibration or repeating micro-movements between the contacting metal surfaces. Fig. 8 shows the steps of fretting degradation:

In a first step (a), the surface metal (and small surface nanolayers) are locally abraded. In consequence, an oxide film grows on the underlying metal surface. The electric contact still exists, since continuous micro movements as described locally destroy the oxide film. In step (b), the non-oxidized parts of the surface suffer again oxidation, thus isolating the oxide gaps in the metal surface again. The electrical contact behaviour becomes intermitting and from the sides, the oxide undergrows the contact points.

Steps (c) and (d) show the ongoing of this process, ending up in a closed oxide layer, so that no electric contact at all will exist anymore.

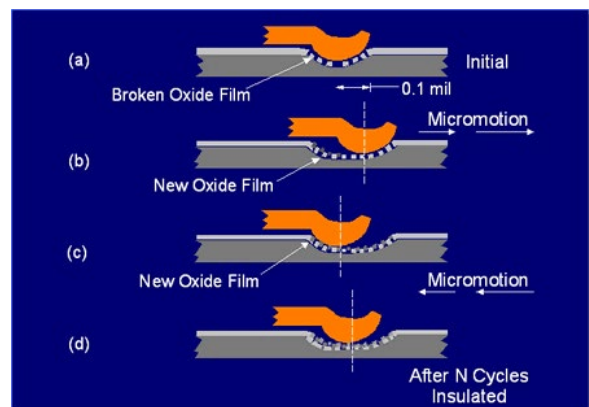


Fig. 8 Fretting development steps. Image from [5] and [6]

2.5 Plug connectors to flex prints

These interconnects nearly include an own class of failures. In most applications, the flexprint frequently suffers movements. In order to keep the resulting forces away from the plug connector itself, a kind of bending- and strain-relief is made by a stiff material, which strengthens the flexprint at its ends with the related connector plugs (usually made as simple contact

forks). This approach, however, shifts the bending stress during movements from the ends of the flexprint to the ends of the stiff material plates, to which the flexprint is glued. At these positions and in priority at the end lines of the flexprint, the copper lines frequently suffer significant bending problems, which finally may result in copper line micro crack opens of the flexprint. (Fig. 9)

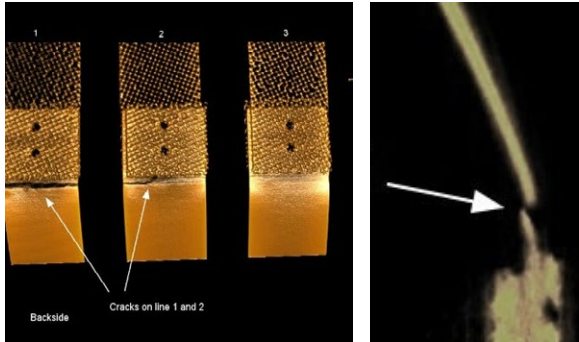


Fig. 9 Cracks in flexprint, especially when leaving the stiff part of the connector and in priority at the end of the flexprint. Top X-ray view (left), side view (right)

Another failure mechanism has been observed in flex print connector forks, which were mechanically fixed by a cement. This cement suffered some post vulcanisation, which included a small increase in cement volume, such pressing the contact fork away from the flexprint surface. A total open resulted after the hardening as fig. 10 shows.

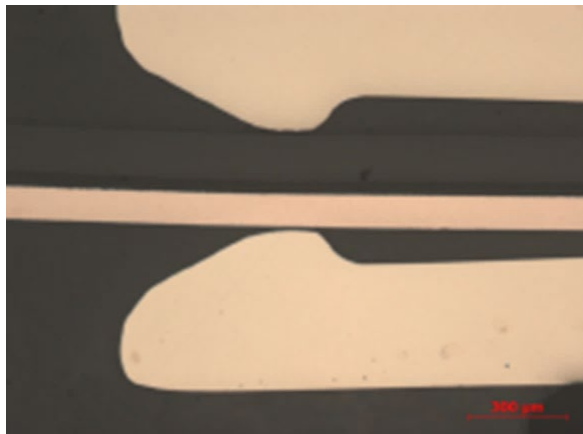


Fig. 10 Flex print connector fork, lifted from the contact tongue by cement post-vulcanization. Courtesy of RoadMicrotec

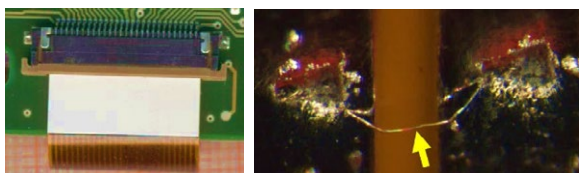


Fig. 11 Plugged flex print connector (left); whisker short grown from footprint-to footprint on the tin part

of the plug (grown when plugged into the female connector under functional operation). Images: Courtesy of Gert Vogel

In addition, short-circuiting tin-whiskers have been observed on tin surfaces of flexprint connectors where the passivation ends. They are promoted by humidity and electric potential difference. In some cases, they start and end at contact footprints on the tin surface, as shown in fig. 11.

2.6 Borderline specification and missing derating

In nearly all electronic components, this topic is a highlight in failure analysis root cause findings. Decades of miniaturization and economization steps in electronics didn't pass by traceless in the design and construction of plug connectors. However, the specifications were not adapted accordingly. Experienced electronic engineers, even electronic hobbyists, and ham radio amateurs have a good stomach feeling on cable cross sections and contact sizes and shapes versus current load capability. Plug connectors of the same size and class that once were specified for a continuous DC current load of 1A in the 1970ies are actually sometimes rated up to 4A continuous load. If this current applies for long time, the contact housing may begin melting and the ongoing disastrous degradation starts rather early. On top of this, sometimes specifications are written in a manner that supports misunderstanding. For instance, if we talk about the maximum current, we probably do not mean necessarily the same thing. It can mean also:

- the peak current in extraordinary situations
- the maximal allowed continuous current
- the current which is only reached for a short time after switching on the equipment
- the maximal allowed continuous current, but only if the connector is plugged/ unplugged few times
- the maximal allowed continuous current, even if the connector is plugged/ unplugged frequently
- one of the currents above, but with restrictions to environmental conditions as temperature, humidity, pressure or vibration.

Therefore, for industrial electronics, catalogues and specifications should only be a rough guideline for component selection. In case of industrial electronics component design-in, it becomes more and more mandatory to have a previous, recorded and signed application discussion with a qualified product application engineer of the vendor with respect to all specified (or non-specified but application-important) data of relevance.

On the other – the user's side – frequently any derating is frequently missing due to economic/ cost reasons or due to forces towards competitive-driven miniaturization. In general, a 30% current derating should be designed-in due to reliability reasons and – considering the operational voltage, including possible voltage

spike amplitudes, useful distances and isolations between neighbour lines and pins need to be observed.

2.7 Plug connector cable terminals

In some cases, connector failures were based on the terminal connect to related cables. The focal point here are non-soldered terminal joints. Fig. 12 and 13 show examples as insufficient crimping (where no micro welding has happened) and low-cost crimping through



Fig. 12 Insufficient crimping. Image: Courtesy of RoodMicrotec

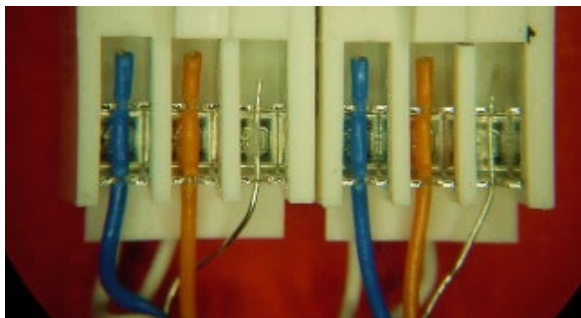


Fig. 13 Cable crimping through the isolation. Image: courtesy of RoodMicrotec

the cable isolation. The latter is used in most telecommunication connectors, where only low signal currents flow and no risk of arcing or fire exists. In some cases, insufficient pull-reliefs ended in a wearout of the terminal joints or damaged cable isolations, finally ending up in plug-internal shorts or leakage – frequently in an intermitting manner.

2.8 Other failure mechanisms

Plug connectors on PCBs can introduce a **bending stress onto PCBs**, which frequently is not compatible with bending-sensitive components around. In principle, this applies for many components in SMT (surface mount technology), in special ceramic capacitors are at risk of suffering cracking-induced shorts and MLF/QFN packages may suffer severe solder cracking. It has been frequently observed that ceramic capacitors

were placed directly underneath terminal connectors in order to block RF ingress from outside. After cracking, ceramic capacitors need some time until an internal crack converts to an evident electric short. This explains why many related failures are root-caused at much earlier time than the failure appears. Fig. 14 shows a typical example. Bending stress in assembly processes, excessive vibration loads during production or in dedicated application can cause field-failures at much later time. It is mandatory to strictly observe ceramic capacitor placement rules as described in [4] and to prevent PCB-bending by plugging/ unplugging by using enough support- and fixing points.

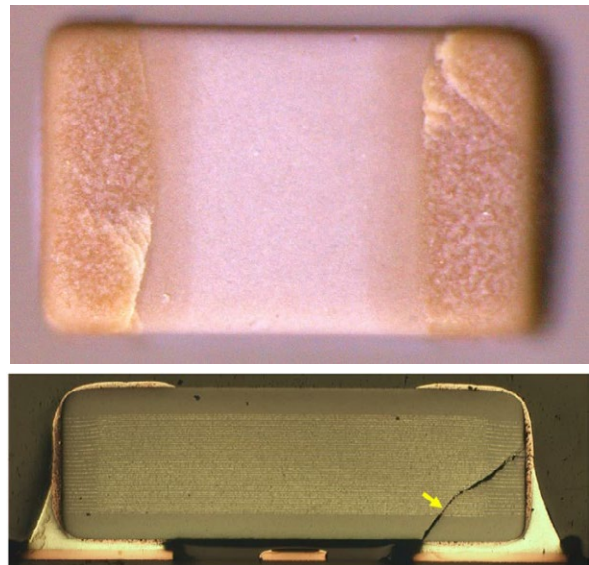


Fig. 14 Cracking of a ceramic capacitor, e.g. caused by PCB-bending when plugging a PCB connector. In most cases, the cracks are hidden under the solder caps, which need to be chemically removed (top image). Bottom image (courtesy of RoodMicrotec): Cross sectional view of a hidden crack.

A special attention should be paid to **the plug connector housing material**. It needs not only to be stable enough to withstand forces during plugging or unplugging but also to withstand thermal stress in case of a connector used for high current load. In many cases, the thermal-induced deformation of a plug-connector is the starting point of a degradation chain with the milestones “housing deformation” – “contact bending” – “increased power loss” – “glowing contact springs” – “lack of isolation due to molten housing plastics” – “arcing” – “fire on PCB”. A heat-resisting housing material would be useful for at least prevent from shorting, arcing and fire.

A completely other, indirect failure mechanism is **ESD (electrostatic discharge)**, which can be introduced via the plug connector. This happens frequently in the assembly lines of big systems as cars, locomotives or power plants. Long cable trees with pre-confectioned plug connectors charge themselves by transportation processes and thereafter are plugged to ESD-sensitive

electronic circuitry, which thereafter suffers ESD damage. Although this failure is not a real plug connector degradation, it needs to be listed here as a construction weakness: To prevent from this problem, the ground pin of the plug connector should be constructed in a manner that the ground pin of PCB and plug contact each other at first. If this is observed, any electrostatic charge is discharged to the ground without creating damage within the electronics attached to the other pins. To achieve, the most simplest approach is to make the ground pin a little bit longer than the other pins so that it will make the first contact in any case.

3 Discussion

The descriptions of the various failure mechanisms can be categorized into direct and indirect failure root causes. The direct ones deal with the connector itself as housing, contact metals, dimensioning/ rating & derating, construction issues etc. while the indirect ones deal with stress effects which are effective to neighbored bending-sensitive components as for instance ceramic capacitors, QFN-packaged devices etc.

A reliable plug connector needs to observe both direct and indirect aspects. In addition, it needs to be considered how many plugging and unplugging cycles should be expected – and under which conditions (forces, PCB bending, ESD risks) this happens.

However, the main point is that the specifications for plug connectors need to be critically scrutinized, especially in case of a planned current load close to the limits of specification. At least in case applications with high reliability requests, a significant derating should take place and also the construction of the connector (contact pressure wearout) should be selected carefully. General hints for risk assessments, derating and their inclusion into standards (and including technical specifications) are provided in the IEC Guide 51 [7]. This effects both system users (derating!) as well as connector manufacturers (specification guard band tests). However, in any case the final responsibility for the selection of connectors is at the side of the system manufacturer, who carefully needs to estimate whether type, size and construction of a plug connector copes with the application under worst case conditions.

4 Conclusion

This paper reached its goal if it has sensitized the reader to the fact that plug connectors deserve more attention with respect to reliability, current and/ or voltage overload, construction, critical viewing on specifications and taking derating into account.

A variety of different failure mechanisms and their slow development have been described, highlighting that many of them may cause severe incidents up to a complete fire destruction of the whole system in which

they are used. In case of low signal transmission through plug connectors, a useful material selection and a careful reviewing of the operational environment conditions are of high importance, since even small corrosion or isolation layers may suppress a proper contact.

5 Acknowledgement

The author wants to acknowledge for many helpful discussions with internal and external colleagues in failure analysis. Special thanks is given to Jürgen Gruber of RoodMicrotec, to Gert Vogel (former Siemens Germany, meanwhile retired) and to my Empa colleague Günter Grossmann. These colleagues also provided some of the photographs used in this paper.

6 Literature

- [1] Jacob, P., "Failure mechanisms and precautions in plug connectors and relays", *Microelectronics Reliability*, Vol. 64, September 2016, pp.693-698
- [2] Vogel, G. "Creeping Corrosion of Copper on Printed Circuit Board Assemblies", *Microelectronics Reliability*, Vol. 64, September 2016, pp.650-655
- [3] Ditroia, G, Lai, R., Woo, K., Zahlman, G., "Connector Theory and Application – A Guide to Connection Design and Specification", 5th edition, Burndy LLC, 2018, see https://hubbellcdn.com/ohwassets/HCE/burndy/PDFs/connectortheory_20180411.pdf
- [4] Vogel, G. „Avoiding Flex Cracks in Ceramic Capacitors – Analytical tool for a reliable failure analysis and guideline for positioning cercaps on PCBs”, *Microelectronics Reliability*, Vol. 55, September 2015, pp. 2159-2164
- [5] Mroczkowski, B. "Connector Degradation Mechanisms" in <https://www.connectorupplier.com/connector-degradation-mechanisms-corrosion-part-i/>, June 2007
- [6] Grossmann, G., "Degradation in der Verbindungstechnik" presentation at the Empa Seminar 2010, Dübendorf, Empa Dübendorf, Switzerland
- [7] IEC Guide 51, "Safety aspects – Guidelines for their inclusion in standards", Third edition 2014-04-01, <https://www.sis.se/std-917199>

Research on Ultrasonic Testing Technology for Wear Debris Caused by Fretting Wear of Electrical Connectors

Luo Yanyan*, Gao Pengyu*, Liang Hong**, Sun Zihang*, Wang Jingqin*, Zhao Jingying*, Liu Jiaomin*

*State Key Laboratory of Reliability and Intelligence of Electrical Equipment,
Hebei University of Technology, Tianjin, China, e-mail: luoyy@hebut.edu.cn

**Maintenance Company of State Grid Tianjin Electric Power Company,
Tianjin, China, e-mail: lianghong0507@163.com

Abstract

An ultrasonic testing method was used to detect fretting wear behavior of electrical connectors. The specimens used in this study were contacts of type-M round two-pin electrical connectors. The experiments consisted of running a series of vibration tests at each frequency combined with one g levels. During each test run, by an electrical connector fretting wear ultrasonic detection system, the attenuation of reflected wave energy of ultrasound was monitored as a performance characteristic, which is induced by the wear debris generated by the fretting wear of electrical connectors. The results exhibit that vibration frequency, vibration acceleration and vibration times all have positive cumulative effect on debris generation on the contact surface of contacts. There are more debris accumulated in the root area of the contact pin. The fretted surface is examined using SEM analysis to assess the surface profile and extent of fretting damage, and the observed results are basically consistent with the ultrasonic test results.

Key words: electrical connector, fretting wear, Ultrasonic testing technology, debris, surface topography

1 Introduction

Electrical connector is one of the important interface components used to realize electrical and signal on-off. It is widely used in aerospace, national defense, electronic communication and other fields. The electrical connector is subject to various environmental stresses during storage and use. Various factors affect the contact pin and contact jack, causing friction and relative displacement of the contact parts. As a result, the performance of the electrical connector is gradually degraded or even the function fails.

Domestic and foreign scholars' research on the fretting wear of electrical connectors mainly includes three aspects: 1) In terms of testing, domestic and foreign scholars mainly complete the high-precision fretting test benches, such as the fretting test bench of the Electrical Contact Teaching and Research Office of Beijing University of Posts and Telecommunications [1], Shin-ichi Wada's six-degree-of-freedom vibration test system [2], micro-motion test bench designed by scholars such as Ito [3]. 2) In terms of performance degradation research, D. Gagnon and other scholars studied fretting wear and found that compared with contact materials, the fretting amplitude has a more significant effect on the contact failure of the contact. The contact resistance of the contact material has the same variation law [4].

Tetsuya Ito and other scholars have obtained when researching the influencing factors of fretting, the contact resistance will change with the change of the tin plating thickness and contact pressure of the contact [5]. Ren Wanbin and others conducted fretting wear tests using an electric shaker, studied the changes in contact resistance and surface topography under different fretting environments, and used the fretting wear failure analysis method to derive the fretting wear failure mechanism [6]. 3) In terms of detection, most of them use the micro-range measurement method to indirectly obtain the effect of fretting wear on contact performance [7-9]. At the same time, scholars performed simulation analysis on electrical connectors. George T. Flowers and others used ABAQUS simulation software to study the fretting wear of electrical connectors. By establishing a joint finite element model of fretting corrosion rate and critical vibration level, correspondence between the contact pressure and the fretting rate under fretting conditions can be obtained [10]. Yasuyuki Ishimaru carried out a simulation study on the contact resistance of electrical connectors under fretting wear, and found that the contact resistance increases with the vibration times, which is basically consistent with the experimental results [11]. In the micro-wear detection of electrical connectors, most of them reflect their wear by simulating or indirectly measuring their contact pressure and contact resistance, while ultrasonic testing shows the contact wear by visually reflecting the size of the signal. Therefore, It is

significant to carry out ultrasonic inspection of micro-wear of electrical connectors.

Ultrasonic testing is a commonly used non-destructive testing technology. It realizes the qualitative and quantitative detection of internal or surface defects of the test object based on the change of the acoustic characteristics (absorption, scattering, reflection) after the ultrasonic wave propagates in the test object [12-14]. Ultrasonic testing technology has functions such as defect location and distributed defect detection, which can meet the requirements for the detection of wear debris inside the electrical connector. Therefore, this article chooses the ultrasonic method to detect the fretting wear of the electrical connector [15-16].

2 Experimental details

2.1 Test Specimens

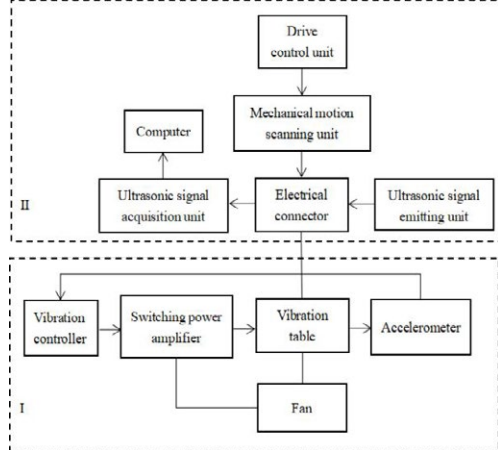
The Type-M circular double-pin electrical connector in this study is a kind of cable connectors, used in machine tool, their contacts are about 10mm in diameter, made of brass (HPb59-1 grade: Cu, 60%; Pb, 1.9%; Ni, 1%; Fe, 0.5% and balance zinc) and plated Au-Ni coating. The photo of the specimen can be seen in Fig. 1.



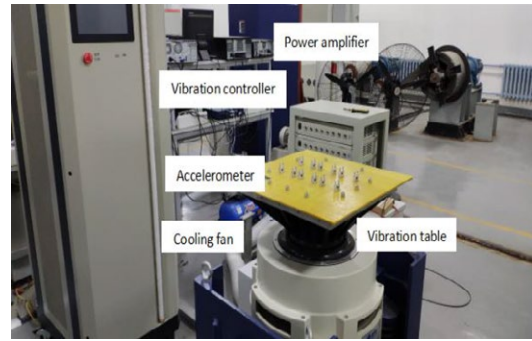
Fig. 1 The contacts specimen of electrical connector

2.2 Test Device

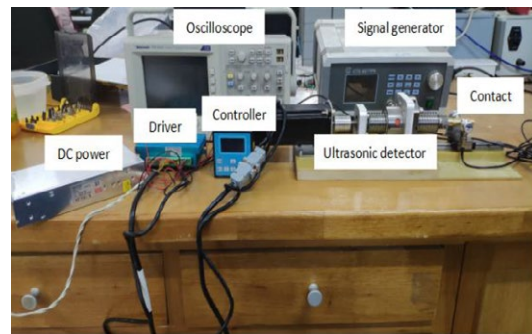
As shown in Fig. 2, the electrical connector fretting wear ultrasonic testing test device designed in this test includes two parts: a fretting table driving mechanism and an ultrasonic testing mechanism (Figs. I and II).



(a) Structure diagram



(b) Fretting drive platform



(c) Ultrasonic testing platform

Fig. 2 Schematic and physical diagram of the test device

The driving mechanism applies the corresponding control commands through the vibration controller, and the control current is amplified by the power amplifier to drive the vibration of the vibration table. The acceleration sensor is used to monitor the vibration acceleration and adjust it in real time. The cooling fan is used for heat dissipation of the vibration table and the power amplifier.

When the ultrasonic detection mechanism detects, the signal of the controller drives the stepping motor to run through the driver, which drives the ball screw connected to it to rotate, so that the contact parts of the electrical connector can rotate at a uniform speed and move stepwise in the axial direction. The ultrasonic probes fixed on both sides of the contact are to test the electrical connector at different positions, and the detected test data is transmitted to the PC connected to it.

Due to the limitation of the size of the electrical connector contacts and the ultrasound probe, the probe can detect 4 positions while rotating the contact once, and can detect 6 positions in the axial direction. Expanding the outer surface of the contact can see that the ultrasound probe detects a total of 24 areas. The number is shown in Fig. 3. The split groove in the middle of the pin divides the detected contact surface into area A and area B.

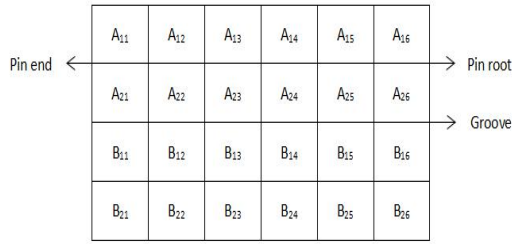


Fig. 3 Division diagram of ultrasonic probe detection area

2.3 Test scheme

The purpose of this test is to investigate the fretting wear of electrical connectors under different vibration conditions. The test excitation conditions in this paper include vibration frequency, vibration acceleration, and vibration times, as shown in Table 1. The test consisted of 6 groups, with 4 specimens in each group. The specimen is vibrated under different conditions. The difference between the original ultrasonic value and the detection signal value of each area when the specimen vibrates 1,000,000 times and 600,000 times is tested.

According to relevant standards, all tests are performed under environmental conditions (temperature: 15-35 °C; relative humidity: 20% -80%; atmospheric pressure: 73-106kpa).

After the test, in order to analyze the characteristics of the wear area of the specimen and the distribution of wear debris, the contact areas A and B of the specimen pins and their ends, middle and roots were respectively observed by SEM. The specific observation locations are shown in Fig. 4.

Table 1 Vibration excitation conditions of electrical connectors.

Test group	Vibration frequency (Hz)	Acceleration acceleration (m/s ²)	Specimen No.
I		4g	1-4
II	100	8g	5-8
III		12g	9-12
IV		4g	13-16
V	150	8g	17-20
VI		12g	21-24

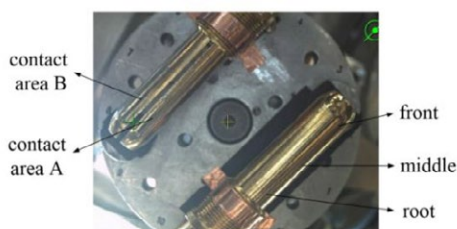


Fig. 4 Schematic diagram of SEM observation position

3 Results and discussion

In this paper, ultrasonic testing is performed on the electrical connectors that have not been subjected to vibration. Because there is no fretting wear between the pin and the jack, and the surface is in good contact, the shape and amplitude of the ultrasonic signals in each sub-region detected by the ultrasonic probe are basically the same. The results show the various positions have the same contact conditions before the tests.

3.1 Effect of vibration frequency

Fig. 5 is a histogram of the changes in the detection value of the 6# specimen (100Hz, 8g) and 19# specimen (150Hz, 8g) after 600,000 vibrations. The calculation shows that the relative change in the detection value of the frequency from 100Hz to 150Hz is 48.46%.

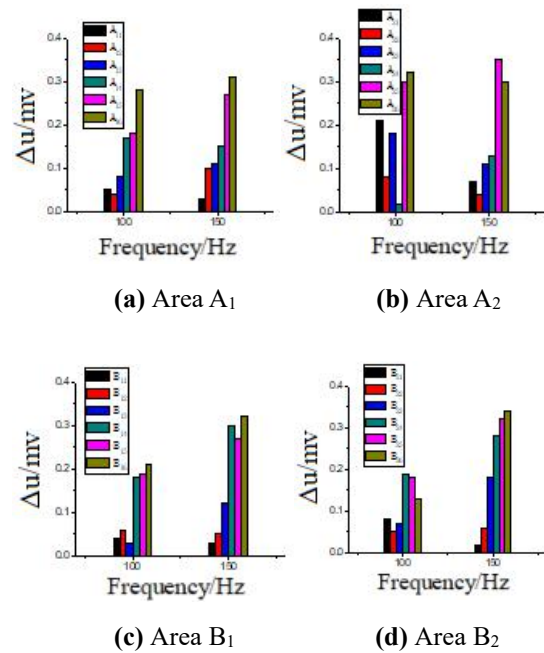


Fig. 5 Ultrasonic detection values at various detection points under different vibration frequencies

It can be seen from Fig. 5 that when the vibration acceleration and vibration times are the same:

(1) With the increase of the vibration frequency, the amount of wear debris accumulation between contact surface of the pin and jack generally increases, and only some areas have reduced wear debris, which may be caused by the wear debris migration during the fretting wear process.

(2) The rate of wear debris accumulation in different parts of the contact area between the pin and the jack

is different. The wear debris accumulates fastest at the root of the pin and the slowest at the end.

According to the theoretical analysis, an increase in frequency will cause the surface temperature of the contact to rise, promote the chemical reaction between the surface metal and the atmosphere, and strengthen the mechanism of action, thereby accelerating fretting corrosion and fretting wear.

3.2 Effect of vibration acceleration

Fig. 6 is a histogram of the detection values of 3# specimen (100Hz, 4g), 8# specimen (100Hz, 8g), and 10# specimen (100Hz, 12g) after 800,000 vibrations. The calculation shows that the relative change of the detected value of the acceleration from 4g to 12g is 81.35%.

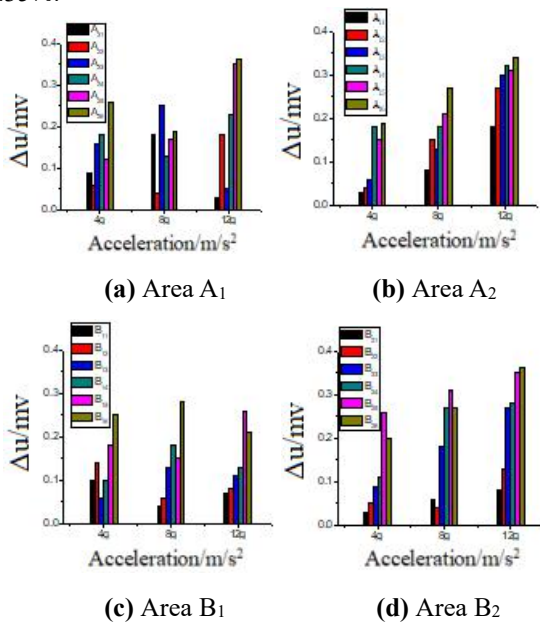


Fig. 6 Ultrasonic detection values at various detection points under different vibration accelerations

Fig. 6 shows that when the vibration frequency and vibration times are the same:

(1) With the increase of vibration acceleration, the accumulation of abrasive debris between contact surface of the pin and jack generally increases gradually.

(2) The degree of wear of the root area of the pin is relatively serious, especially when the vibration acceleration reaches 12g, a large amount of abrasive debris is accumulated around the circumference of the root of the pin, which affects the contact performance of the electrical connector.

When the vibration acceleration increases, the amplitude also increases, which causes the relative movement amplitude of the pin and the jack to increase, the form of material wear also changes from adhesive wear to slip wear. The heat generation rate at the center of the wear area increases significantly, and thermal effect will soften the microscopic surface

coating and fall off from the base metal layer, forming a tendency to accumulate to the edge of the wear scar, the more severe the fretting wear.

3.3 Effect of vibration times

Fig. 7 shows the histogram of the detection value of 21# specimen (150Hz, 12g) under different vibration times. The calculation shows that the relative change in the detected value from 400,000 to 600,000 times is 41.27%, and the relative change from the 600,000 to 1,000,000 times is 84.30%.

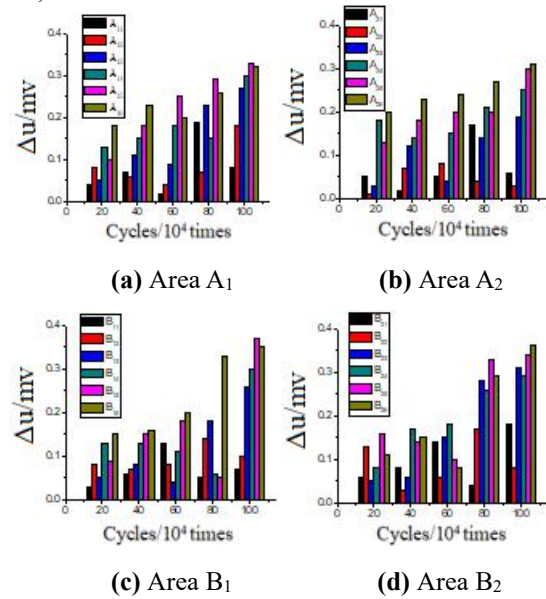


Fig. 7 Ultrasonic detection values at various positions under different vibration times

Fig. 7 shows when the vibration frequency and vibration acceleration are the same:

(1) As the vibration times increase, the total amount of abrasive debris accumulated between the contact area of contact pin and the jack gradually increases; and the amount of abrasive debris accumulation in the sub-regions (such as B₂₅, A₂₂, B₁₁, etc.) increases or decreases, it can be speculated that during the fretting wear, the abrasive debris migrates.

(2) The accumulation of wear debris has a non-linear relationship with the vibration times. From 200,000 to 600,000 times, the cumulative increase rate of wear debris is slow. After 600,000 to 1,000,000 times, the accumulation rate of wear debris is obvious faster.

According to the theoretical analysis, during the vibration process, with the increase of the vibration times, the stress relaxation phenomenon of the electrical connector contacts will occur, and the contact between the pin and the jack will also be transformed from elastic deformation to plastic deformation, and the contact surface will be broken. Chips and abrasions gradually accumulate, resulting in reduced electrical contact performance. Fig. 8 shows the pin surface topography of the B₁ area of 21# specimen.

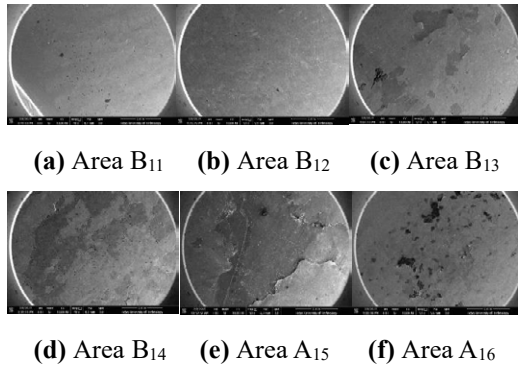


Fig. 8 Surface profile of the pin of the 21# specimen

Fig. 8 shows that the pins B₁₁ and B₁₂ of the 21# specimen are basically free of impurities, while a small amount of plating has fallen off in the areas B₁₃ and B₁₄. The contact surface has become uneven, and the entire surface film layer has fallen off in the area B₁₅. There are both protrusions and pits on the microscopic surface of the area B₁₆. The protrusions may be the film layer scraped off and accumulated on the surface of the pin. The pits are caused by the continuous grinding of abrasive debris on the surface of the contact, which further causes the top surface of the pin damage.

In general, the more abrasive debris accumulates toward the root area of the pin, the gold-plated layer on its contact surface comes off, and the base metal is continuously oxidized when exposed to the air, causing non-conductive substances to increase between the contact areas, reducing the effective conductive area, which may cause the contact resistance exceeds the threshold and intermittent failure occurs.

3.4 Effect of comprehensive factors

A comprehensive analysis of the effects of vibration frequency and vibration acceleration on the fretting wear performance of electrical connectors shows that with increasing frequency and acceleration, the accumulation of abrasive debris will increase, and the fretting wear will become worse. When the vibration frequency is increased from 100Hz to 150Hz, the detection value does not change much, and the fluctuation range remains below 10%. When the vibration acceleration gradually increases, the detection value changes significantly, and the fluctuation amplitude can reach about 30%, especially within the range of 8g to 12g, the amplitude of the change reaches the maximum, which indicates that the vibration acceleration has a great impact on the fretting wear performance of the electrical connector, and its impact is far greater than the vibration frequency.

Table 2 shows the corresponding detection values under different vibration conditions, and its value is the average value of the detection values of the four

specimens in each group in the A₁₆ area. Table 2 shows that the detection value is 0.31 at 100Hz and 12g, and the detection value is 0.27 at 150Hz and 8g. The low-frequency and high-acceleration is more abrasive than the high-frequency and low-acceleration conditions, and the wear is more serious. The influence of vibration acceleration is more significant under multiple factors.

During the vibration process, the oxide film layer and the contaminated film layer on the contact surface tend to rub off, the conductive contact spots will be extruded from the film layer and increase, but the contact resistance will decrease. In the early stage of vibration, the change of performance depends on the reduction of contact pressure and the cleaning effect of the contact surface film by the vibration. Their influence on the contact resistance is opposite, and the final effect depends on the contrast of their effects. However, with the increase of vibration times or the strengthening of the vibration force, the wear phenomenon will become more and more serious, the proportion of wear to promote the increase of contact resistance will gradually increase, and the contact performance will gradually degrade.

Table 2 Ultrasonic detection value of A₁₆ area under various vibration conditions

Frequency (Hz)	Acceleration (m/s ²)	Detection value (mv)
100	4g	0.20
	8g	0.24
	12g	0.31
150	4g	0.23
	8g	0.27
	12g	0.34

4 Conclusion

This test analyzes the effects of the vibration times and vibration conditions on the generation and distribution of wear debris on electrical connector contacts. The result shows:

- (1) When the vibration conditions are the same, as the vibration times increase, the degree of wear of the electrical connector contacts will also increase, and the changes in the contact areas A and B of the electrical connector will be similar. During the fretting wear process, the demarcation points of the two stages of the abrasion of the electrical connector contacts are 400,000 and 1,000,000 respectively.
- (2) The abrasive debris will migrate between different parts of the contact area. The vibration of high-frequency and high-acceleration has a more significant effect on the distribution of abrasive debris in the electrical connector contacts. When the

vibration times and the acceleration are the same, as the vibration frequency increases, the degree of wear between the contacts of the electrical connector also increases. With the increase of the vibration frequency, the difference in the wear debris distribution in the contact area A and B of the contact also becomes larger. When the vibration times and the frequency are the same, as the vibration acceleration increases, the degree of wear between the contacts of the electrical connector also increases. With the increase of the vibration acceleration, the wear debris distribution in the contact area A and B of the contact is basically the same. Therefore, it can be considered that vibrations times, the vibration frequency and the vibration acceleration all have a certain effect on the degree of wear of the contact, and the vibration frequency has a more significant effect on the wear debris distribution of the contact. This is basically similar to the change rule of SEM test results.

(3) The difference between Δu on the sub-region can reflect the distribution of wear debris in the contact area to a certain extent, but cannot distinguish two different states: large-area corrosion and large-scale peeling of the coating. Compared with large-area plating peeling, the value of Δu is more sensitive to the accumulation of abrasive debris, but the detection accuracy of the ultrasonic detector is not high for areas with slight wear or scattered debris distribution.

(4) The test results can well reflect the wear of the contact pin, and the wear debris distribution in different contact areas of the contact pins can be identified. The ultrasonic fretting wear detection method and device designed in this test can provide certain research ideas for the prediction of the wear debris distribution law of electrical connectors.

Acknowledgments

This work was supported by the Natural Science Foundation of Hebei Province (E2018202156).

References

- [1] Lu Na, Xu Liangjun. Design of Micro-motion Contact Resistance Test System [C]. The 3rd International Conference on Reliability and Electrical Contact of Electrical Products. 2009: 262-266.
- [2] Shin-ichi Wada, Koichiro Sawa. Degradation Phenomenon of Electrical Contacts by 3-D Oscillating Mechanism[C]. Proceedings of 54th IEEE Holm Conference on Electrical Contacts. 2008:284-293.
- [3] Tetsuya Ito, Masato Matsushima. Factors Influencing the Fretting Corrosion of Tin Plated Contacts[C]. Proceedings of the 52th IEEE Holm Conference on Electrical Contacts. 2006:267-272.
- [4] Gagnon D, Braunovic M. Effect of Fretting Slip Amplitude on the Friction Behaviour of Electrical Contact Materials[C]. Proceedings of the 51st IEEE Holm Conference on Electrical Contacts, 2005:186-195.
- [5] Tetsuya Ito, Masato Matsushima. Factors Influencing the Fretting Corrosion of Tin Plated Contacts[C]. Proceedings of the 52nd IEEE Holm Conference on Electrical Contacts, 2006:267-272.
- [6] Ren Wanbin, Wang Peng, Ma Xiaoming, et al. Experimental study on fretting wear characteristics of gold-plated copper contact materials for connectors [J]. Transactions of the China Electrotechnical Society, 2013, (12): 120.
- [7] Zou Jibin, Sun Guiying, Qi Yulin, et al. Friction test system for micro load [J]. Chinese Journal of Tribology, 1998,18 (4): 369-372.
- [8] Yu Zhenglin, Wu Yihui, Liu Zhihua, et al. Light reflection micro-friction tester [J]. China Mechanical Engineering, 2005, 16 (14): 1299-1302.
- [9] Li Xiaobing, Liu Ying, Guo Jilin, et al. Research progress of micro-friction test technology [J]. Lubrication and Sealing, 2006, (7): 178-181.
- [10] George T. Flowers, Fei Xie, Bozack M, et al. Modeling Early Stage Fretting of Electrical Connectors Subjected to Random Vibration[J]. IEEE Holm Conference on Electrical Contacts, 2003, 28(4): 45-50.
- [11] Yasuyuki Ishimaru, Keiji Mashimo, Kyota Susai. Computational Modeling for Fretting Simulation[C]. Vancouver CANADA: Proceeding of the 55th IEEE Holm Conference on Electrical Contacts, 2009, 141-146.
- [12] Cawley P. The rapid nondestructive inspection of large composite structures[J]. Composites, 1994, 25(5): 351-357.
- [13] Meo M, Polimeno U, Zumpano G. Detecting damage in composite material using nonlinear elastic wave spectroscopy methods[J]. Applied composite materials, 2008, 15(3): 115-126.
- [14] Thompson R B, Lopez E F. The effects of focusing and refraction on gaussian ultrasonic beams[J]. Journal of Nondestructive Evaluation, 1984, 4(2): 107-123.
- [15] Honarvar F, Sheikhzadeh H, Moles M, et al. Improving the time resolution and signal to noise ratio of ultrasonic NDE signals[J]. Ultrasonics, 2004, 41(9): 755-763.
- [16] Nandi A K, Mampel D, Roscher B. Blind deconvolution of ultrasonic signals in nondestructive testing applications[J]. IEEE Transactions on Signal Processing, 1997, 45(5): 1382-1390.

Study of vibration transfer in automotive connectors for understanding of fretting corrosion damage

M. Mavuni^{1,2}, E. Carvou¹, G. Lalet²

¹Université de Rennes1, France
Institut de Physique de Rennes UMR CNRS 6251
35042 Rennes cedex – France

² APTIV, France
Z.I. des Longs Réages - BP50025 | 28231 Epernon Cedex | France
* E-mail : mack.mavuni-nzamba@univ-rennes1.fr

Abstract-- Fretting corrosion damage is caused by a relative motion of contact pairs surfaces subjected to external mechanical vibrations. Indeed, global mechanical excitation on a whole connector may cause relative displacement on contact area and then to fretting degradation. This work experimentally investigates the global relative motion in 1-way automotive connectors with many components (11 parts). Therefore, a methodology is presented, that allows to study the whole connector movement in order to analyze the relative influence on connector components. To understand the fretting degradation at the actual contact interface, a test bench and a methodology were set up to perform these relative motion measurements using a 3D laser vibrometer. We first focus to understand induced motion through different connector components from wires to male and female terminals as well as male and female holdings motions caused by vibrations. Then the whole connector relative movements were deduced from the measured displacements in three-dimensions, on components such as housing, terminals and wire. Furthermore, the experiment results were compared with the frequency response, obtained from modal analysis modeling. So, from the previous comparison, the specific damaged frequencies domains were detected. Finally, the relative displacements of the electrical contact zone are deduced and if effectively fretting corrosion may appear.

Keywords: Fretting corrosion, automotive connectors, vibration, modal analysis, modeling

1. Introduction

The automotive environment in which electrical connectors are located is characterized by high vibrations that can reach acceleration up to 80 g within the range from 5 Hz to 2 kHz frequency [1]. The vibration induced by automotive environment is transferred on different connectors [2], particularly on

the wire and housing and then transferred to the terminals. This leads to relative micro displacements at the interface of male and female parts, inducing fretting-corrosion which strongly, influence its electrical conductance and then voltage fluctuation. Therefore, an increase in contact resistance is considered as an indication of the electrical contact failure [3].

To achieve a reliable device, electrical connector must meet certain vibration specifications requirements to ensure continuous conduction without being damaged by fretting corrosion [1], [4].

To minimize the relative displacement on electrical interface and so fretting corrosion, designers develop electrical connectors consisting of many components, with different mechanical properties. In fact, each component is meticulously chosen as it plays a specific role. For example, the female inner casing component, that has loaded female terminal for limiting his movement, the silicone component for damping and absorbing vibration-induced, or the lock spring for mechanical interlock of connectors etc. [5]. Unfortunately, these connectors are not exempted from failure.

The occurrence of fretting corrosion is difficult to predict. Many investigations have been done in order to determine a threshold fretting damage [6-9]. Bouzera [8],[10] concluded that the fretting is indeed worst when the relative displacement between the terminals, at contact point, reach a certain threshold value. Fu, et al. [11] found that the relative displacement measured at the contact interface, increasing when the vibration amplitude increases. Park, et al. [12] review and summarize previous work on fretting corrosion in electrical contacts. They summarize and list the most important parameters for fretting corrosion. Besides, the motion of cables also may have an effect on the electrical contact during vibration test since it can induce additional stresses for such vibration test [13].

In 2017, Carvou and al. [2] proposed a new methodology for measuring relative displacement, inside a connector, by using a non-contact 3D laser vibrometer. This approach allows a better

understanding of dynamical behavior of electrical connector under vibration. They found that relative motions depend not only on the vibration of excitation, but also on the way these movements are mechanically transferred. Thus, proper instrumentation and testing methods are also inevitable for obtaining fretting corrosion conditions in experimental test [14].

This paper presents development of this previous investigation that consider the transfer of vibrations, at three dimensions, into the automotive connectors and cable which leads on fretting corrosion.

To be sure, after attempting to design a mechanically stable connector, of its reliability, it is necessary to validate new designs by making qualification tests aimed to detecting if the connector is susceptible to present fretting corrosion during his lifetime.

Combining various experimental test and modal analysis modeling, we will attempt to answer two fundamental questions:

- How exactly is the vibration transferred on the contact zone, in three dimensions, for a given vibration excitation?
- Which frequency domain will cause the maximum relative displacement between contact surfaces?

A test bench was designed to measure the motions at various points of connector components and wire. Then, absolute and relative displacements were deduced at different frequencies. Furthermore, the experimental results were compared with the frequency response obtained from modal analysis modeling. Finally, specific damaged frequencies domains were determined.

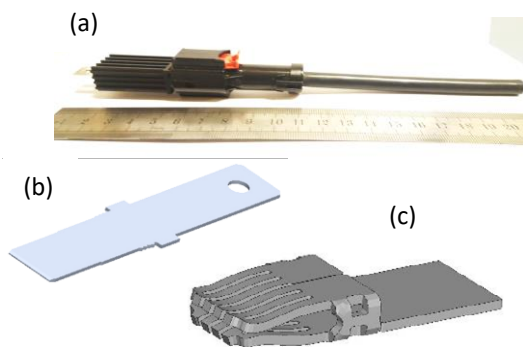


Fig. 1: (a) Automotive connector, (b) Pin, (c) Socket

1.1. The sample connector

The connector to be tested is 1-way automotive connector manufactured by Aptiv. This connector consists of 11 parts were the main ones are insulating housings, contact pair (pin and socket) and spring lock (see Figure 1). The female part consists of 12 contact points symmetrically distributed (Figure 1c). The

contact force is between 20 – 30 N. This force is distributed on the two sides of the male part joining two female parts at 6 contact zones on each.

The connector surface is plated with silver and the substrat connector material is copper, on which an electrolytic nickel interlayered was deposited in order to limit copper diffusion. Many works report that a connector with silver plating coatings could make the fretting corrosion less significant [15], [16]. The table below provides more details about connector characteristics.

Parts	Thickness [mm]	Density [kg.m ⁻³]	E [GPa]
Pin housing	-	1470	2.7 - 9.2
Female housing	-	1470	2.7 - 9.2
Male terminal	1	8819	125 - 130
Female terminal	0.5	8819	125 - 130
Cable	-	4157	4 - 56
Seals	-	1000	1 – 3

Table 1: Material and dimensional proprieties of model components

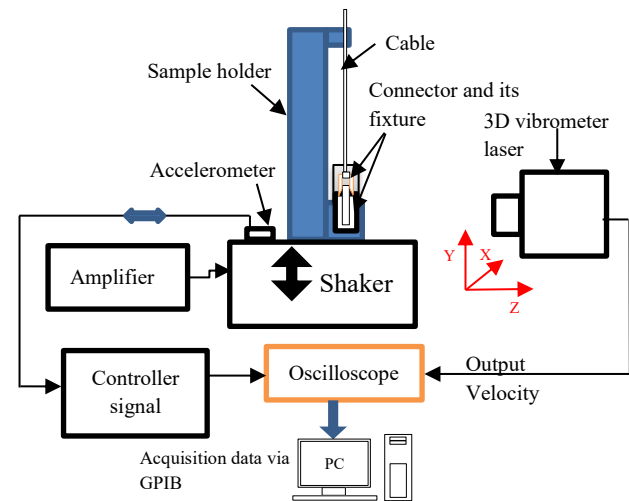


Fig. 2: Schematic diagram of the test bench (lateral view).

2. Experimental set up

In order to study the effects of vibration on the connector, a vibration bench test was built and set up with the aim of to be as close as possible of automotive vibrations environments conditions. The input vibration excitation is produced by using an electrodynamic shaker driven by an accelerometer. A schematic diagram of the experimental test setup is shown in Figure 2. A sample holder, on which the connector is mounted, was specially designed and

afterwards it is rigidly fixed on shaker head which is displayed in Figure. 3. The connector fixed on sample holder is in testing equipped with a male and female housing and a cable length of 145 mm. the male housing was fixed to limit his movement in two directions perpendicular to electrical contact insertion. Furthermore, the cable was clamped. By doing so, the connector system will be able to follow the motion of the shaker head.

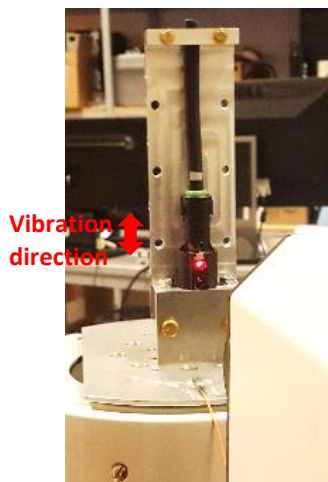


Fig. 3: Fixture and vibration direction (front view)

This fixation configuration is required by the automotive manufacturer in accordance to standard tests described in [1] and [4]. The excitation direction is axial (Y-axis), is chosen parallel to the direction of the electrical contact insertion as illustrated in Figure 3. The parts inside the housing are accessible by making holes, small enough in order to avoid modification of the mechanical properties of the connector [10]. Series of tests were done in order to investigate mechanical behavior of this automotive connectors subjected to axial vibration excitation. An acquisition data program has been developed on a computer to collect data from oscilloscope via GPIB bus.

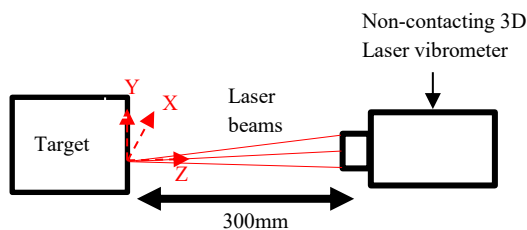


Fig. 4: Principle of measurement geometry by using CLV-3D laser vibrometer

3. Measurement of displacements

The displacement measurements of the different samples are carried out using one non-contacting 3D-Laser vibrometer by reflecting laser beam on a specified target surface. This equipment allows measuring simultaneously, at a single-point targeted all three velocity components on a vibrating structure (Figure 4). The output is an analog voltage signal, which are proportional to the velocity amplitude of the target [10]. Figure 5 shows the measuring locations of the male and female parts through holes. The displacement measurements of the different parts are deduced by integrating the velocity measured by the vibrometer.

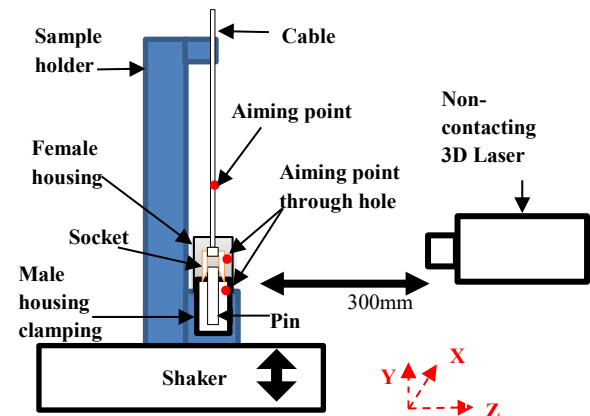


Fig. 5: Located measuring displacement through the holes (red dots)

For an axial vibration applied i.e. in the direction of the insertion of the connector (aka the Y-axis), the absolute displacements of the sample holder, female housing, female terminal, male terminal and the cable were measured in 3-axis. We assume that the sample holder movement amplitude is the reference movement with the respect to the movement amplitude of the other components.

4. Measured relative displacement

The fretting corrosion damage is governed by the relative displacement of the contact pairs. Ideally, the relative displacement between two contact points should be measured simultaneously but this requires duplicating expensive equipment (one 3D laser vibrometer per piece). Our experimental set-up consists of only one 3D laser vibrometer. This causes a phase's problem between two measurement points. To solve this issue, we used the signal phase of the accelerometer as reference time and we corrected our signal accordingly:

- i. By subtracting the reference phase from the phase of the measured signal

ii. Then we will hence extract from previous measurements the relative displacements of the male part with respect to the female part as described by Carvou et al. [2], Fu et al.[11].

5. Modeling and simulation of the frequency response of the connector system

5.1 Modal analysis

A modeling and simulation, with finite element analysis (FEA), for modal analysis, has been conducted on the connector (include the cable) in order to identify the terminal natural frequencies and its vibration modes. We assume that if one of these natural frequencies is close to the car engine frequencies, then there is a potential risk for the connector integrity [17]. Modal analysis is run with frequencies sweep from 5 Hz to 2 kHz, by using LS-DYNA Software[18]. The modeling and FE simulation approach proposed in this paper is shown in Figure 6.

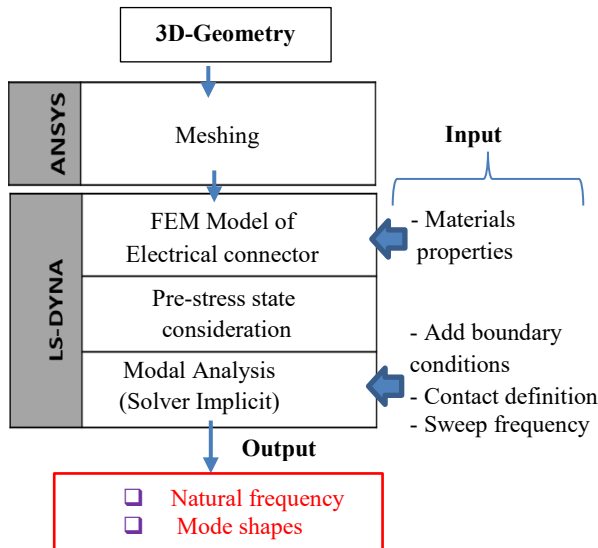


Fig. 6: FEA Simulation process of modal analysis of electrical connector

The material properties (such as Young's modulus E , and density) were given in Table 1. The connector is meshed using the hexahedral elements. The mesh is refined around the terminals contact interface.

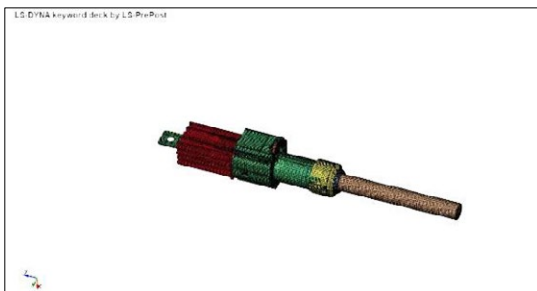


Fig.7: Views of connector with its finite element mesh

6. Results and Discussion

Using the test configuration described above, a series of experiments and modal analysis simulation were performed to investigate the dynamic behavior of the automotive connector subjected to axial vibration input. First, for characterizing experimentally the response of the sample during a vibration test, sine sweep is a fast and useful method for determining eigen or dominating frequencies of the connector [19]. We measured the transfer function of different components to determining resonant peak and vibration modes, seen in Figure 8. The transfer function of the connector sample is determined by comparing the output response at the component to the input vibration amplitude from the shaker head.

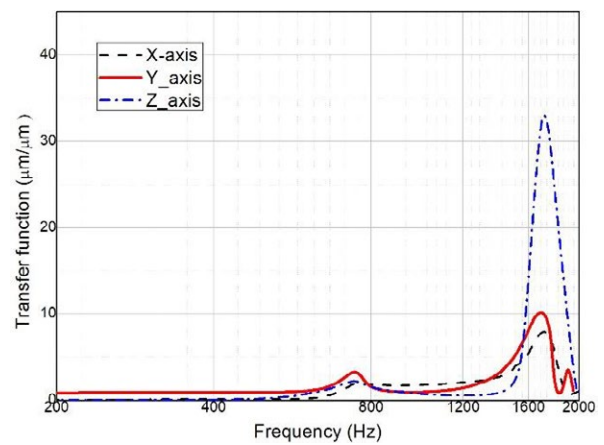


Fig. 8.a: Experimental results showing the transfer function for the Female housing

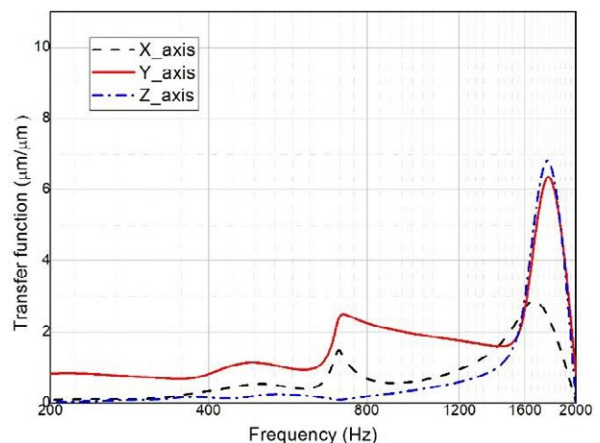


Fig. 8.b: Experimental results showing the transfer function for the Male housing

A sine sweep applied on the connector/cable system produce a motion that will be transferred on electrical contact. The frequencies of he applied vibration ranges from 5 Hz to 2 kHz with a fixed acceleration 1 G (9.8 m/s^2) and the sweep rate is 0.1 oct/min. Figure 8.a and Figure 8.b show the transfer function that were obtained, in three axis, for different vibration amplitude

for the female and male housing, respectively. We can observe that for the low frequency domain, the transfer function value is 1 in the vibration direction (aka Y) because the input amplitude is equal to the output amplitude. However, the transfer function value is around 0 for the perpendicular axis (X and Z axes) to the vibration direction. It is logical because the input amplitude in vibration direction is to larger than the output amplitude in X and Z axes. The value of transfer function has a significant change at the frequencies between 1600 Hz and 1800 Hz. For the female housing, two natural frequencies have been detected (Figure 8.a). At 1650 Hz according Y and Z axes, and at 1770 Hz according X-axis. Regarding the male housing, two natural frequencies were detected at 1700 Hz for the X and Y axes and at 1650 Hz for X-axis (Figure 8.a).

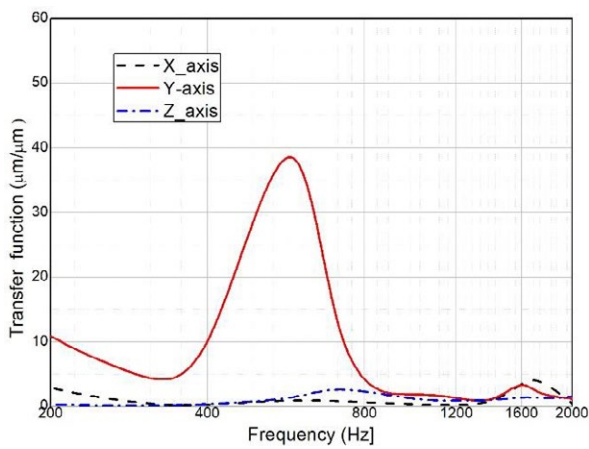


Fig. 9.a: Experimental results showing the transfer function for the Female terminal

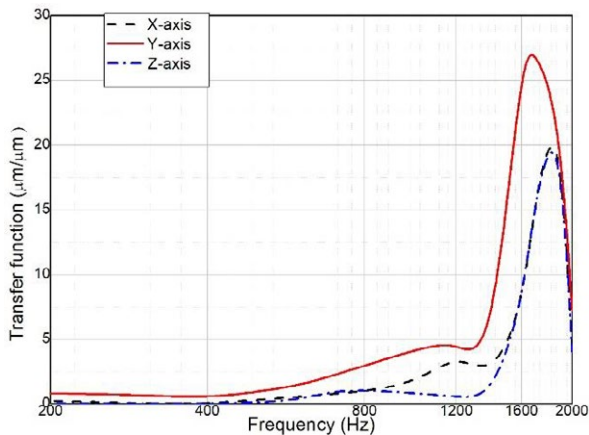


Fig. 9.b: Experimental results showing the transfer function for the Male terminal

Experimental results of transfer function measured on the terminals are illustrated in Figure 9.a and Figure 9.b. For the female terminal (socket), the peak became more pronounced at approximately 600 Hz in the insertion direction of the connector (Y-axis) (Figure 9.a). In fact, around 1600 Hz the peak is lower in Z and

X axes. Regarding the male terminals (Pin), the natural frequencies were detected at 1650 Hz in Y-axis and at approximately 1770 Hz for Z and X axes.

FEA simulation of modal analysis was carried out with the same boundaries conditions as the experimental fixing. LS-DYNA software was used with an implicit solver assuming that the problem was linear static. From simulation, two modes were extracted between 5 Hz and 2 kHz to identify natural frequencies of the connector system. The table provides three modes from simulation and experiment results.

Mode shapes	Natural Frequencies [Hz]	
	experimental	Simulation
1	1650	1568
2	1770	1754
3	1600	-

Table 2: Identified natural frequencies between 5 Hz and 2 kHz

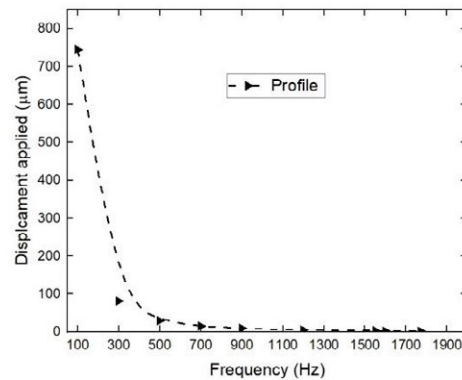


Fig. 10: A standard vibration profile

Thus, two natural frequencies were computed from modal analysis simulation, at 1568 Hz for mode 1 (Z-axis) and at 1754 Hz for mode 2 (X-axis). We can observe a low difference between the results, of natural frequencies, obtained from experimental and simulation. Two reasons allow explaining this. First, it can be related to the difference between the mass of real connector and the 3D model's mass used in simulation. Furthermore, it may due to the contact parameters defined between each component in FEA simulation.

6.1 Effect of vibration with fixed acceleration with varying amplitudes and frequencies

During this test, the vibration acceleration is fixed at 15 G. The objective of this type of test was to highlight the most damaging domain for this connector. A standard vibration 15 G profile (Figure 10) is used to scan ranges of frequency with varying amplitude in order to determine the mechanical response of the system.

The vibration excitation was applied in inserting connector direction (aka Y-axis). The Figure 11 shows the absolute displacement, measuring in three axes, for different connector components.

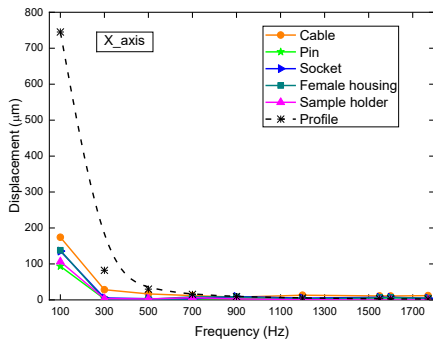


Fig. 11.a: Spectrum of the absolute displacement in X-axis

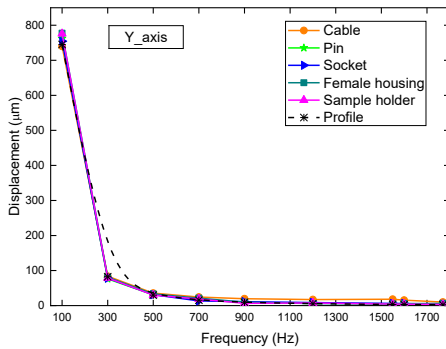


Fig. 11.b: Spectrum of the absolute displacement in Y-axis

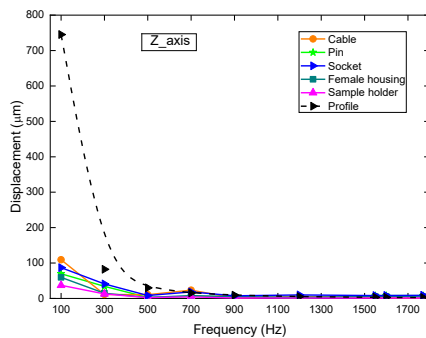


Fig. 11.c: Spectrum of the absolute displacement in Z-axis

The absolute displacement measurements of the different samples are deduced by integrating the velocity measured by the 3D vibrometer. As shown in Figure 11.a, 11.b and 11.c, all the components present the same shape of the curve as the vibration profile, in three axes. For vibration in X-axis (Figure 11.a), the cable presents the highest displacement amplitude, and

then the vibration is transferred from the cable to the socket. The pin follows the sample holder's motion. Regarding vibrations in the direction of insertion (aka Y-axis), the Figure 11.b shows that the connector system follows exactly the vibration profile with the same input displacement amplitude. For vibration in Z-axis, displacements follow each other in a rough way, seen in Figure.11.c.

The relative displacement of the contact interface induced by engine vibration is one of the most significant causes for the fretting corrosion phenomenon. We will thus extract from previous measurements the relative displacements of the male part with respect to the female part. The results are presented in Figure 12 for the three axes, X, Y and Z.

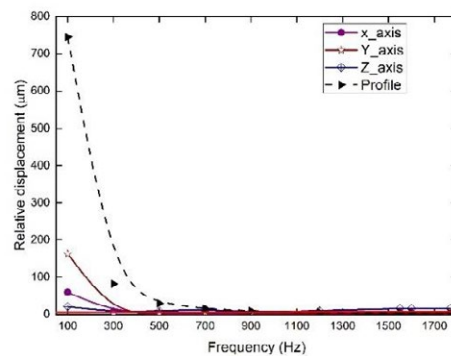


Fig. 12: Spectrum of the relative displacement

For the three axes, X, Y and Z, the relative displacements between pin/socket are relatively important in low frequency domain (between 100 Hz and 300 Hz) for the highest applied amplitude. However, the relative motions measuring at high frequency domain are relatively small for X and Y axes. For Z-axis, we can see that the relative motion is around 18 µm greater than the fretting damage threshold [9]. We therefore see that the measurements of the relative motion between the connector components allow us to determine the vibration conditions for which relative motion of contact zone is greater than 5 µm, then to avoid a critical frequency range when using connectors [10], [7].

To summarize, the methodology and the vibration amplitude used in this paper for this type of connectors, made it possible to determine the frequency domains of vibration to avoid. First the low frequencies, due to their very large vibration amplitude. But also the high frequencies, which have been identified as the natural frequencies for these types of connectors. Outside these domains, whatever the amplitude of vibration, there is a good probability that relative displacement at the contact interface of Pin / socket will remain less than 5

µm. Subsequently, it will be difficult to be able to trigger the fretting corrosion mechanisms.

7. Conclusions

This study shows how the vibration is transferred to the different connector parts. It may thereby induce motion and fretting damage to the contact interface. The main results are as follows.

- 1) An experimental methodology has been proposed, allowing for in-situ measurement through a 1-way connector under range of vibration. This methodology is generalizable for another type of connector.
- 2) For the transfer function, the peak of natural frequencies was only found at the high frequency domain, in the three axes X, Y and Z. The transfer function values were smaller at the low frequency domain.
- 3) The simulation results are correlated with the experimental behavior of the connector parts. Two mode shapes were detected between the results obtained with the FEA simulation of modal analysis and experimental test. A slight difference was observed between the results of natural frequency obtained in simulation and experiment test.
- 4) Hence, the important conclusion is that fretting corrosion may appear in both low frequency and high frequency domains.

Future work will include

- Establish a correlation between previous results and the contact resistance changes under the most dominating frequencies
- Investigation of fretting corrosion in low frequency and high frequency domains, over long operating time.
- Investigate relative motion by using FEA simulation of vibration for validating the model

REFERENCES

- [1] LV 214-3 Motor Vehicle Connectors; Test Sequences, 2010.
- [2] E. Carvou, J. Labbé, L. L. Marrec, C. Plouzeau and F. L. Strat, "A Phenomenological Model of Vibrations Transfer in Connectors for Fretting Corrosion Phenomena," 2018 IEEE Holm Conference on Electrical Contacts, Albuquerque, NM, 2018, pp. 381-386.
- [3] S. E. Mossoues et al., "Analysis of temporal and spatial contact voltage fluctuation during fretting in automotive connectors," ICEC 2014; The 27th International Conference on Electrical Contacts, Dresden, Germany, 2014, pp. 1-5.
- [4] PSA Peugeot-Citroën, "connectors general requirements," Standard B217050.
- [5] Performance specification for automotive electrical connector systems SAE/USCAR, February 2013.
- [6] H. Yang and G. Flowers, "Threshold of Axial Vibration Induced Fretting in Electrical Connectors," 2013 IEEE 59th Holm Conference on Electrical Contacts (Holm 2013), Newport, RI, 2013, pp. 1-10.
- [7] G. T. Flowers, Fei Xie, M. Bozack and R. D. Malucci, "Vibration thresholds for fretting corrosion in electrical connectors," Proceedings of the Forty-Eighth IEEE Holm Conference on Electrical Contacts, Orlando, FL, USA, 2002, pp. 133-139.
- [8] A. Bouzera fiabilité de la connectique sous sollicitation de vibrations mécanique. PhD thesis, Université de Rennes 1, 2012.
- [9] A. Bouzera, E. Carvou, N. Ben Jemaa, R. El Abdi, L. Tristani, and E.M. Zindine. Minium fretting amplitude in medium force for connector coated material and pure material. 56th IEEE Holm Conference on Electrical Contacts, pages 101–107, 2010.
- [10] J Labbé, Détection et étude de microdéplacement des contacts sous contrainte vibratoire et leurs conséquences sur les matériaux et revêtements des connecteurs automobiles, Phd thesis, Rennes, 2017.
- [11] R. Fu et al., "Vibration-Induced Changes in the Contact Resistance of High Power Electrical Connectors for Hybrid Vehicles," in IEEE Transactions on Components, Packaging and Manufacturing Technology, vol. 2, no. 2, pp. 185-193, Feb. 2012.
- [12] Y. W. Park, J. P. Jung, and K. Y. Lee, "Overview of fretting corrosion in electrical connectors," Int. J. Automot. Technol., vol. 7, no. 1, pp. 75–82, 2006.
- [13] A. Bouzera, E. Carvou, Influence of cable vibrations on connectors used in automotive application, Journal of Electrical and Electronics Engineering.
- [14] Clarence W. de Silva, Vibration and Shock Handbook, 2005.
- [15] J. F. Bruel, P. Smirou, and A. Carballeira, "Gas environment effect on the fretting corrosion behavior of contact materials," in Proc. 14th Int. Conf. Electr. Contacts, 1988, pp. 219–223.
- [16] F. Hubner-Obenland and J. Minuth, "A new test equipment for high dynamic real-time measuring of contact resistances," in Proc. 45th IEEE.
- [17] Yahya, O. and Miled, H., "Modeling of the Impact of Ultrasonic Welding of Harness on the Terminals Integrity," SAE Technical Paper 2014-01-0224, 2014.

- [18] Dynaplus Licence supplier, www.dynasplus.com.
- [19] Yashan Xing and Weilong XuSignal, “Analysis of Fretting Damages on Electrical Connector Systems,” Karlskrona, June 2017.

Influence of PFPE lubricant modifications on tribo-electrical properties of a tin contact system

Marcel Mainka, Weidmüller Group, Detmold, Germany, marcel.mainka@weidmueller.com
Thomas Wielsch, Weidmüller Group, Detmold, Germany
Ralph Würtele, Klüber Lubrication, Munich, Germany
Dr. Martin Schweigkofler, Klüber Lubrication, Munich, Germany

Abstract

The influence of PTFE-additivated PFPE-based lubricants on tribology, contact resistance and wear behaviour of tin surfaces was examined. For this purpose, different modifications of PFPE lubricants were systematically investigated in a comparative manner, whereby both macro- and microtribological tests were carried out. The results prove a significant reduction of the friction coefficients as well as of the macro-tribological wear in the contact area by the use of the examined lubricants, so that a higher lifetime and reliability of the contact system can be achieved. The micro-tribological tests showed a significant reduction and delay of friction corrosion effects. Overall, however, differences between variants of the lubricants can be demonstrated. The results clearly show that when selecting a suitable lubricant, not only the value of the friction coefficient and the contact resistance must be considered as target values, but also, for example, wear volumes, wear mechanisms and the resulting appearance of the contact areas.

1 Introduction

1.1 Motivation

Due to constantly growing tribo-electrical requirements for industrial connectors, their suppliers are challenged to continuously improve the performance of contact systems. The ongoing miniaturization of connectors leads to an increasing spatial density of contacts and correspondingly to an increasing power density, while the requirements for mechanical properties such as contact forces as well as both insertion and withdrawal forces often remain almost unchanged. Overall, a low contact resistance remaining constant over time and a high wear resistance over the lifetime of the contact system are also required. This makes it necessary to optimize the tribology of contact systems while maintaining electrical properties in order to keep insertion and withdrawal forces at a low level over the lifetime of a contact system and to prevent wear defects as far as possible. A central role of the solution approaches is played by the contact surface of the contact partners, whose tribological and electrical behaviour has a significant influence on the performance of an electrical contact. The use of Ag or Au as contact surface is often not economically viable due to the high and volatile noble metal prices, so that a tribological optimization of Sn contact surfaces comes into focus. This optimization can be realized by micro-alloying or micro-structuring Sn surfaces [1], new coating systems such as Ni-Ag-Sn with a specifically adjusted intermetallic Ag₃-Sn phase [2][3] or the usage of lubricants [4][5].

1.2 Fundamentals

Lubrication of electrical contacts has been used almost since the emergence of electrical contacts in order to meet the above-mentioned various requirements in an economically viable and technically applicable approach. The application of lubricants can reduce both friction and wear mechanisms resulting in higher lifetime of electrical contacts. In addition, suitable lubricants can protect the electrical contact against environmental influences and contamination due to reduced reaction rates, thus further increasing performance. However, it should always be noted that a lubricant shall not deteriorate the mechanical, electrical and material properties of the electrical contact system. All in all, this results in a wide requirement profile which must be taken into account when investigating and selecting lubricants:

low volatility in application / thermal and chemical reaction stability against environment (liquids and gases) and materials in the contact system / good adhesion with adequate wetting behaviour / protection of the electrical contact area against environment and wear / no significant impairment of electrical contact or electrical properties by friction polymerisation, separation of contacts or embedding of wear particles / non-toxic / low costs / detectability[4][5]

The friction coefficient of a lubricated contact system mainly depends on the viscosity of the lubricant η , the relative speed v and the contact pressure of the contact partners p , whereby these influencing variables can be

summarized as so-called Stribeck parameter $\eta v p^{-1}$. Basically, three qualitative functional areas can be identified using this parameter. Area A in Fig. 1 corresponds to low values of the Stribeck parameter and is characterized by high friction coefficients with dominating interface effects, since the lubricant cannot separate the contact partners sufficiently. For high values of the Stribeck parameter (area C), hydrodynamic effects predominate, resulting in comparatively low friction coefficient. The transition area B between interfacial and hydrodynamic effects is called *elastic-hydrodynamic* or *mixed friction* area. It can easily be seen that at given pressures and speeds, viscosity in particular is the decisive influencing variable for optimizing the tribological performance of a contact system [6].

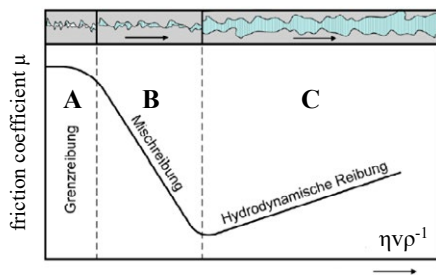


Fig. 1 Dependency of friction coefficient and Stribeck parameter [8].

In addition to the tribological behaviour of a contact system, the contact resistance is a decisive target variable. For lubricated contacts, three areas can also be identified here, which are determined by the characteristics of the microscopic interface. For area A, the lubricant is displaced from the contact area so that a metallic contact is present resulting in the smallest possible contact resistance. Within area C the contact areas of both partners completely separated by a (thin) lubricant film, so that the flow of electrical current can only take place via tunnel effects. Thus, significantly higher contact resistances than for area A can be observed, whereby the resistances increase exponentially with the thickness of the lubricant film.

The transition area B is characterized by the fact that the contact area contains both metallic contacts and areas with a thin lubricant film resulting in intermediate contact resistance values. Detailed theoretical considerations of the contact resistances of the described areas can be found in [7].

The correlation of the areas A to C for the friction coefficient and the contact resistance is obvious. The central aim of the systematic investigation of lubricants for electrical contact systems is therefore to select a suitable combination of viscosity, contact pressure and speed in order to minimize both the contact resistance and the friction coefficient as far as possible, considering the other requirements mentioned above.

2 Experimental

2.1 Specimens

Subject of the investigations is a tin contact system from an existing connector family of the Weidmüller Group. Both flat (contact blade) and rider (contact arm of a socket contact) have a tin surface with a thickness of $1.9 \pm 0.10 \mu\text{m}$ on a Cu base material. The normal force is about 2 N per contact arm. The contact area of the rider has an elliptical geometry with radii of 1 mm in the mating direction and 1.5 mm transverse to the mating direction.

For the contact system under investigation, the lubricant group of PTFE (polytetrafluoroethylene) - additivated PFPE (perfluoropolyethers) has already been identified as the most suitable and implemented in the production process (*medium 0*). This is due to its chemical inertness, excellent temperature stability and good tribological behaviour [7]. In the past, intense systematic studies on PFPE-lubricated tin surfaces have been carried out, in particular by S. Noël et al. [9,10,11].

Name	PTFE system	base oil viscosity [mm ² /s]	base oil structure
medium 0	reference (o)	400 (o)	branched (x)
medium 1	reduced (↓)	400 (o)	branched (x)
medium 2	reference (o)	200 (↓)	branched (x)
medium 3	reference (o)	200 (↓)	linear (l)
medium 4	reference (o)	600 (↑)	linear (l)
medium 5	reference (o)	600 (↑)	branched (x)

Tab. 1 Properties overview of the tested lubricants

Within the scope of the present study, the influence of varying PTFE additivation, base oil viscosities and base oil structures on the triboelectric properties in the fields of micro- and macro-friction was systematically investigated in order to optimize the tribological and electrical behaviour in the best possible way. For this purpose, the current series status (*medium 0*) and five alternative lubricants (*media 1 to 5*) were investigated (Tab. 1), whereas contact pressures and speeds were kept constant for each tribological testing collective.

2.2 Tribological tests

The tribological investigations were carried out on a self-designed tribometer, which under control of the normal force allows the simultaneous measurement of friction force, relative displacement and contact resistance by means of the dry circuit method. Rider and flat were loaded by means of "soft touch" starting from a normal force of 400 mN in order to avoid damage to the contact partners by the loading process.

For each friction path, the average values of both friction coefficient and contact resistance were calculated for the sliding friction area, providing the data for the comparative analysis.

Macro-tribological tests were carried out over 100 paths with a friction path of 2 mm at a speed of 24 mm/min, considering both standards and product requirements. Five tests were carried out for each lubricant. Micro-tribological tests were carried out over 10.000 paths with a friction path of 100 μm at a frequency of 2 Hz. Here, three tests were carried out for each lubricant.

2.3 Analysis of contact areas

Both the optical appearance and the topography of the contact areas was examined by means of confocal 3D laser scanning microscopy, whereby, in addition to the optical and topographical appearance, the wear volume and wear area were also analysed. The ratio between wear volume and wear area was calculated, which corresponds to the average wear depth.

3 Results and discussion

3.1 Macro-tribology

For the medium 0 (**Fig. 2**) the friction track width is about 250 μm , whereby abrasive wear is visible. At the ends of the friction paths, tin deposits can be seen, an alternating transfer of wear material is not visible. The contact area of the rider appears to be covered by tin oxides.

During an initial phase, which is characterized by flattening effects of the contact partners and running-in behaviour of the lubricant, the friction coefficient drops from 0.30 to less than 0.20 within five friction paths. The friction coefficient then remains at a level of between 0.20 and 0.25. The contact resistance increases successively starting after 5 friction paths from approx. 3 m Ω to approx. 10 m Ω . This course is due to the initial metallic contact and the subsequently increasing disturbance of the electrical contact through the formation of wear particles, embedding of PTFE particles in the tin matrix and the transition to mixed friction. Based on wear volume and wear area an average wear depth of approx. 1.1 μm has been calculated (see **Fig. 8**).

Medium 1 (**Fig. 3**) corresponds to medium 0 in terms of base oil type and base oil viscosity but has a reduced PTFE additivation.

Both the wear mechanisms and courses of contact resistance as well as friction coefficient are similar to medium 0. During the initial 10 friction paths the friction coefficient reduces from 0.30 to a constant level of about 0.25. After approx. five friction paths the contact resistance increases successively, caused by the same effects as explained before for medium 0. Both wear volume and wear area as well as the resulting average wear depth are similar to medium 0 (see **Fig. 8**).

All in all, medium 1 can practically be considered to be identical to medium 0, so that no tribo-electric differences result from the different PTFE additivation.

Medium 2 (**Fig. 4**) differs from medium 0 solely in its reduced base oil viscosity. The type of base oil and the PTFE additivation are identical to medium 0.

The friction track width is slightly reduced to 200 μm . As seen at medium 0 abrasive wear is also visible, but the abrasion appears more pronounced in the form of individual paths. Both tin deposits at the ends of the friction paths and a coverage of the rider by oxides are detectable, too. The initial friction coefficient of 0.30 reduces significantly to a low and almost constant level of 0.15 within five friction paths. Subsequently the contact resistance rises to a local maximum of approx. 14 m Ω after 40 paths and then decreases again to approx. 8 m Ω . This course is due to the disturbance of the initial metallic contact by the formation of wear particles. Most probably the less base oil viscosity leads to a smaller lubricant film thickness, which results in increased wear and thus in a more pronounced increase of contact resistance by wear particles present in the contact area. The better flow characteristic of the base oil then supports the transportation of wear particles out of the contact area after approx. 40 paths, and consequently the contact resistance decreases.

Compared to medium 0 the wear area is reduced by approx. 10 %, while the wear volume is approx. 30 % more (see **Fig. 8**), resulting in an average increase of the wear depth by approx. 50 % up to 1.6 μm .

The reduced base oil viscosity of medium 2 shows a worse tribo-electric behaviour compared to medium 0. The smaller lubricant film thickness causes more wear particles to emerge, which reduce the friction coefficient, but increase the tendency to abrasive wear and leads to contact resistances that vary over the friction cycles.

Medium 3 (**Fig. 5**) differs from medium 0 in its reduced base oil viscosity and different, linear base oil structure. The PTFE additivation is identical.

The friction track width is again reduced to approx. 200 μm . Both tin deposits at the ends of the friction paths and a coverage of the rider by oxidation products are also present. During the initial five friction paths the friction coefficient drops significantly from 0.20 to an almost constant, low level of about 0.10. Compared to medium 2, the additional reduction in the friction coefficient by the changed base oil structure can be seen. The contact resistance increases successively to a local maximum of approx. 20 m Ω between 30 and 60 paths and then decreases to approx. 10 m Ω . The first increase of the contact resistance can be explained by the same effects as for the previous media (initial metallic contact and subsequent formation of wear particles). Due to the reduced base oil viscosity and the linear base oil structure, the wear is increased compared to media 0 and 2 since a poorer spatial separation of the contact partners occurs, resulting in a more pronounced increase of contact resistance.

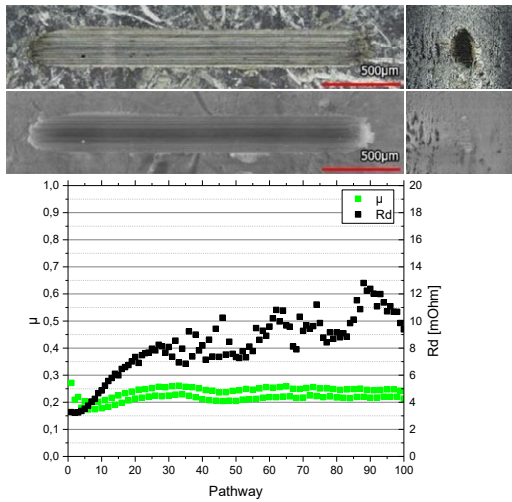


Fig. 2 Test results for *medium 0* showing both light microscopy and topography images with $-7.5/+7.5 \mu\text{m}$ scaling (black/white) as well as courses of friction coefficient and contact resistance.

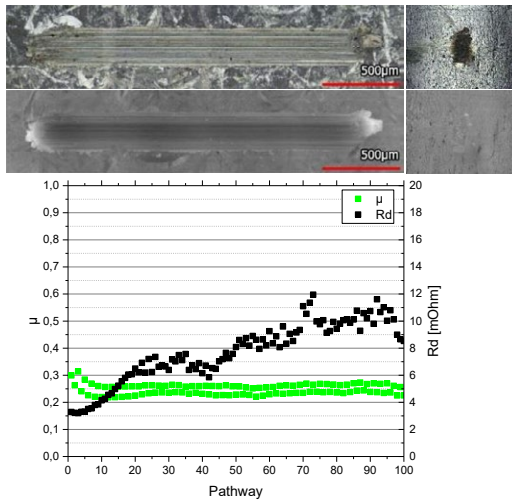


Fig. 3 Test results for *medium 1* showing both light microscopy and topography images with $-7.5/+7.5 \mu\text{m}$ scaling (black/white) as well as courses of friction coefficient and contact resistance.

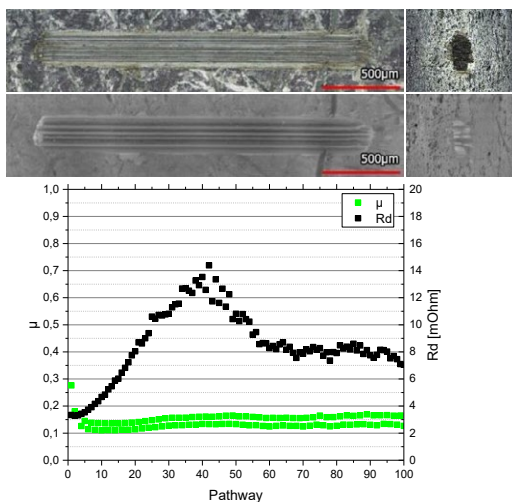


Fig. 4 Test results for *medium 2* showing both light microscopy and topography images with $-7.5/+7.5 \mu\text{m}$ scaling (black/white) as well as courses of friction coefficient and contact resistance.

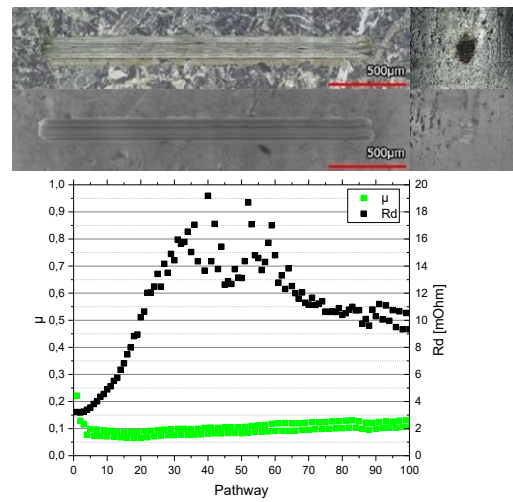


Fig. 5 Test results for *medium 3* showing both light microscopy and topography images with $-7.5/+7.5 \mu\text{m}$ scaling (black/white) as well as courses of friction coefficient and contact resistance.

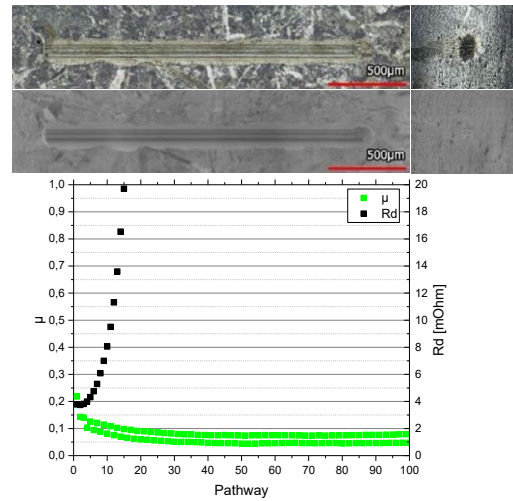


Fig. 6 Test results for *medium 4* showing both light microscopy and topography images with $-7.5/+7.5 \mu\text{m}$ scaling (black/white) as well as courses of friction coefficient and contact resistance.

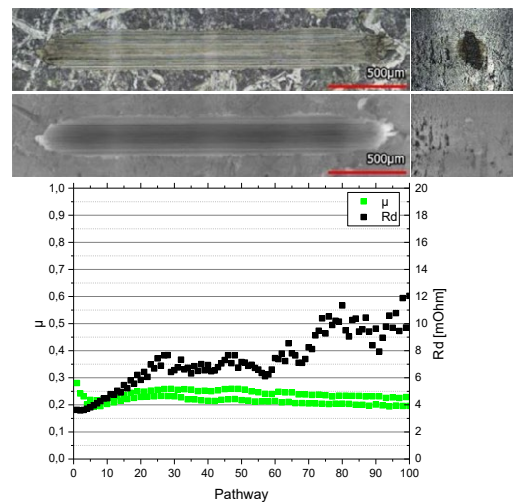


Fig. 7 Test results for *medium 5* showing both light microscopy and topography images with $-7.5/+7.5 \mu\text{m}$ scaling (black/white) as well as courses of friction coefficient and contact resistance.

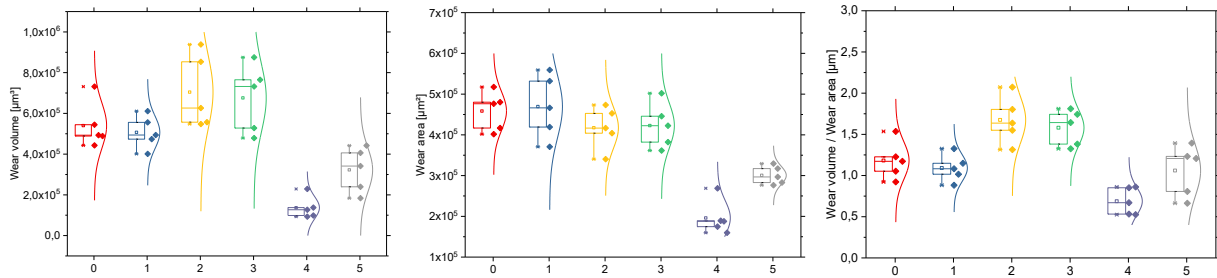


Fig. 8 Comparative illustration of values regarding wear volume, wear area and ratio of both values (corresponds to the average wear depth) for the investigated lubricants. Beside the individual data their respective distribution is indicated. The presented data were acquired for the flats.

The ongoing abrasive wear and the displacement of the wear particles out of the contact area causes the contact resistance to drop again after approx. 60 paths, while the friction coefficient gradually increases with the wear.

The wear area is approx. 10 % less than with medium 0, while the wear volume is approx. 25 % more. This results in a 40% increase of the average wear depth to 1.5 µm. The reduced base oil viscosity and the changed base oil structure of medium 3 shows a worse tribo-electric behaviour compared to medium 0. The friction coefficient might be reduced by increased formation of wear particles, but this leads to an increased, significantly varying contact resistance. Especially in comparison to medium 2 the influence of the changed base oil structure on the formation of wear particles (which disturb the electrical contact) is clearly recognisable by the height of the resistance maximum.

Medium 4 (**Fig. 6**) differs from medium 0 in its linear base oil structure as well as in an increased viscosity level, while the PTFE additivation is identical.

The friction track width is reduced to approx. 110 µm. The abrasive wear appears to be significantly concentrated to a small area compared to medium 0. Both tin deposits at the ends of the friction paths and a coverage of the rider by oxidation products are detectable, too. The initial friction coefficient drops from 0.20 to an almost constant and low level of 0.07 within five friction paths. This extremely low level in particular is due to the changed base oil structure (compare to medium 5 below). The contact resistance rises abruptly from approx. 4 mΩ to more than 20 mΩ during five friction paths and remains at a high level. After initial flattening of the micro-roughness, the changed base oil structure leads to an increased formation of wear particles, which, as third bodies, together with the more pronounced hydrodynamic frictional conditions of the higher base oil viscosity, then hinder the electrical contact. No decrease of the contact resistance could be detected, since the wear particles are not displaced from the contact area because of the high viscosity of the base oil.

The wear area is reduced by approx. 57 % compared to medium 0, while the wear volume is reduced by approx. 75 %. As a result, the average wear depth decreases by approx. 40 % to 0.6 µm (see Fig. 8).

The increased base oil viscosity in combination with the linear base oil structure of medium 4 shows a significantly worse electrical behaviour compared to medium 0. Although the wear is spatially reduced, more wear particles appear to be produced which cannot be displaced from the contact area and subsequently cause massively increased contact resistances.

Medium 5 (**Fig. 7**) differs from medium 0 by an increased viscosity level, while both the PTFE additivation and the base oil structure are identical.

The wear mechanisms are comparable to medium 1. Besides tin deposits at the end of the friction paths tin oxides can be found on the rider. Due to flattening effects of the contact partners and the running-in behaviour of the lubricant, the friction coefficient drops within 5 friction paths from 0.30 to an almost constant level of about 0.20. Even though the base oil viscosity of medium 5 is higher compared to medium 0, the friction coefficient behaves identically. By direct comparison to medium 4 (**Fig. 6**), the influence of the base oil structure to the friction coefficient can be recognized: despite comparable base oil viscosities and PTFE additivation, there are massive differences in the friction coefficient for media 4 and 5. The contact resistance increases successively from about 5 friction paths from approx. 3 mΩ to approx. 10 mΩ. This course is due to the metallic contact initially present as a result of the flattening effects and the successively increasing disturbance of the electrical contact through the formation of wear particles, embedding of PTFE particles in the tin matrix and the transition to mixed friction. The wear area is reduced by approx. 34 % compared to medium 0, while the wear volume is reduced by approx. 40 %. As a result, the average wear depth decreases by approx. 5 % to 1.0 µm (see Fig. 8).

Despite the increased base oil viscosity, the triboelectric behaviour of medium 5 is identical to that of both medium 0 and medium 1.

3.2 Micro-tribology

For medium 0, the contact area of the flat still appears metallic after 10,000 frictional movements (**Fig. 9**). Fretting corrosion products can be detected around both the contact areas of flat and rider. The appearance of the contact partners after the micro-friction tests demonstrates that the formation of fretting corrosion is inhibited by the lubricant, although instable contact resistance is noted from about 5,000 frictional paths onwards. This can be attributed to the ongoing formation of wear particles in the contact area. The friction coefficient initially rises to over 0.2, which is due to the flattening of roughness peaks and the running-in process of the contact area. Due to the successive formation of wear particles as third bodies as well as the embedding of PTFE particles in the tin matrix, the friction coefficient then decreases to approx. 0.1.

Medium 1 (**Fig. 10**) corresponds to medium 0 in terms of base oil type and base oil viscosity but has a reduced PTFE additivation.

The optical appearance of the contact areas for medium 1 is identical to medium 0. The contact area of the flat appears metallic after 10,000 frictional movements. Fretting corrosion products can be detected around the contact area of both flat and rider. Due to the modified PTFE additivation the inhibition of the emergence of fretting corrosion products appears to be enhanced for medium 1, resulting in an electrical contact without obvious disturbances. Due to the running-in of the contact partners and embedding of PTFE particles into the tin matrix, the friction coefficient decreases at the beginning of the tests. The contact resistance is stable with only a slight increase. caused by the formation of fretting corrosion products as third bodies in the contact area, which simultaneously reduces the friction coefficient.

Medium 2 (**Fig. 11**) differs from medium 0 solely in its reduced base oil viscosity. The type of base oil and the PTFE additivation are identical to medium 0.

As for medium 0, for both rider and flat fretting corrosion products can be found around a metallic contact area, here with a circular shape of the representative specimen. Due to running-in of the surfaces and initial embedding of PTFE particles in the tin matrix, the friction coefficient drops at the beginning of the tests. The ongoing increase in contact resistance and the decrease of the friction coefficient is more pronounced than for medium 1, since a thinner lubricating film is formed because of the reduced base oil viscosity. This favours the formation of wear particles that as a result reduce the friction coefficient as third bodies and simultaneously increase the contact resistance.

Medium 3 (**Fig. 12**) differs from medium 0 in its lower base oil viscosity and linear base oil structure. The PTFE additivation is identical.

Contact partners are showing an increased coverage with fretting corrosion products. The formation of fretting corrosion products is much less inhibited compared to media 1 and 2. By direct comparison these media, this can be mainly traced back to the linear base oil structure, which encourages the formation of fretting corrosion products (compare section 3.1). As a result, after running-in of the contact partners and the initial embedding of PTFE particles in the tin matrix, the friction coefficient quickly reaches a low level due to the presence of wear particles as third bodies in the contact area. Due to precisely these fretting corrosion products, the contact resistance of the sliding friction area increases progressively.

Medium 4 (**Fig. 13**) differs from medium 0 regarding the linear base oil structure as well as an increased viscosity level, while the PTFE additivation is identical.

As seen at medium 3 the coverage with fretting corrosion products in the contact areas is increased. Again, the formation of fretting corrosion products is poorly inhibited compared to media 1 and 2. This is especially due to the linear base oil structure, which encourages the formation of fretting corrosion products. Also, the friction coefficient drops quickly to a low value after running-in of the contact partners and embedding of PTFE particles in the tin matrix, due to the presence of third bodies in the contact area. But these fretting corrosion products also lead to a progressive increase of the contact resistance. The increase is more pronounced compared to medium 3, since medium 4 has a higher base oil viscosity, which makes it less probable to displace the wear particles out of the contact area (compare section 3.1).

Medium 5 (**Fig. 14**) differs from medium 0 by an increased viscosity level, while both PTFE additivation and base oil structure are identical.

The appearance of the contact areas for medium 5 is identical to medium 0. For both flat and rider, a metallic contact area can be found which is surrounded by wear particles. The lubricant inhibits fretting corrosion within the contact area, whereas the inhibition is more pronounced than for medium 0 due to the increased base oil viscosity. Because of the running-in of the contact partners, the friction coefficient initially decreases. The contact resistance remains stable. Due to the formation of fretting corrosion products as third bodies in the contact area, only a slight increase of the contact resistance with a simultaneous reduction of the friction coefficient is present.

Overall, the triboelectric behaviour in the field of micro-friction is primarily determined by the formation and retention of fretting corrosion products in the contact area, whereby clearly different characteristics of the triboelectric behaviour of the lubricants can be observed.

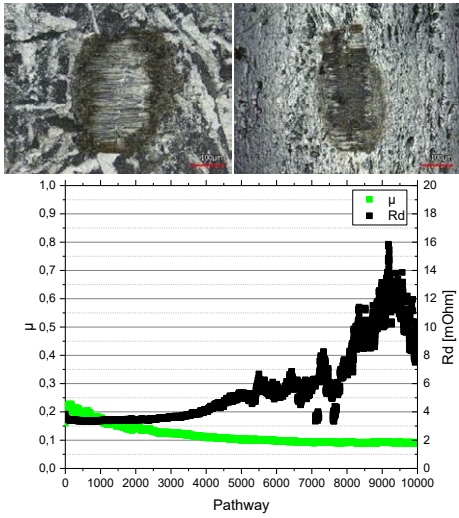


Fig. 9 Test results for the *medium 0* showing both light microscopy and courses of friction coefficient and contact resistance.

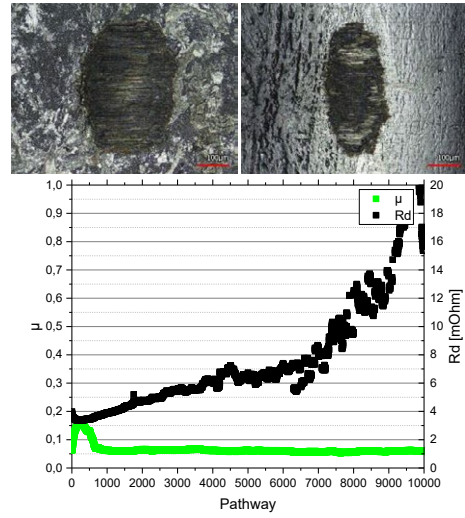


Fig. 12 Test results for the *medium 3* showing both light microscopy and courses of friction coefficient and contact resistance.

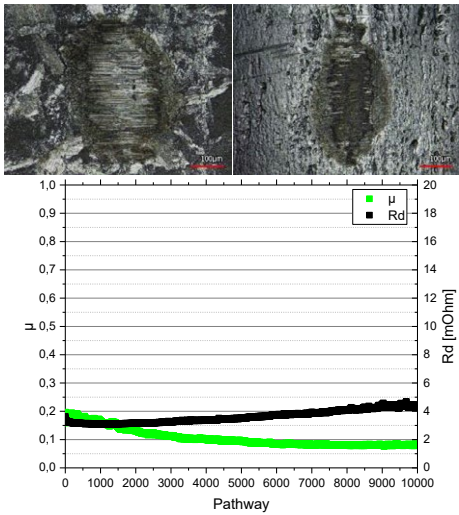


Fig. 10 Test results for the *medium 1* showing both light microscopy and courses of friction coefficient and contact resistance.

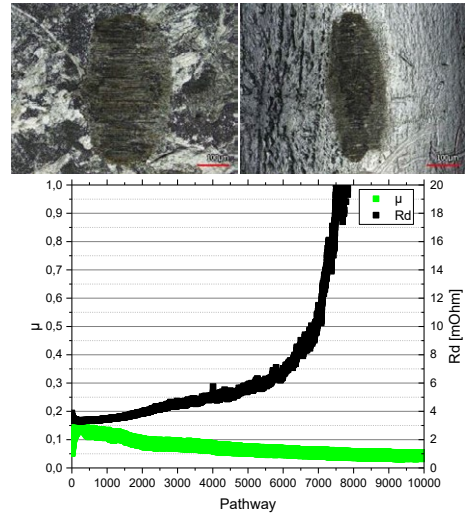


Fig. 13 Test results for the *medium 4* showing both light microscopy and courses of friction coefficient and contact resistance.

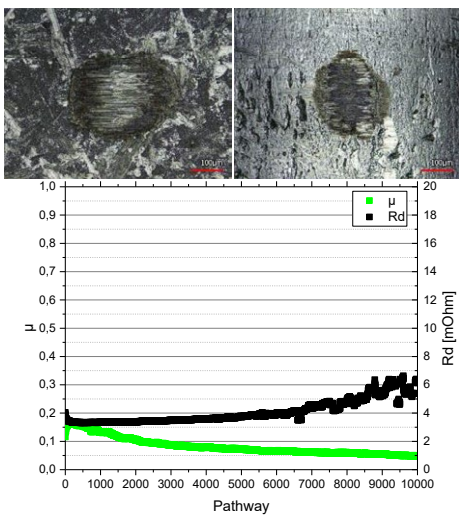


Fig. 11 Test results for the *medium 2* showing both light microscopy and courses of friction coefficient and contact resistance.

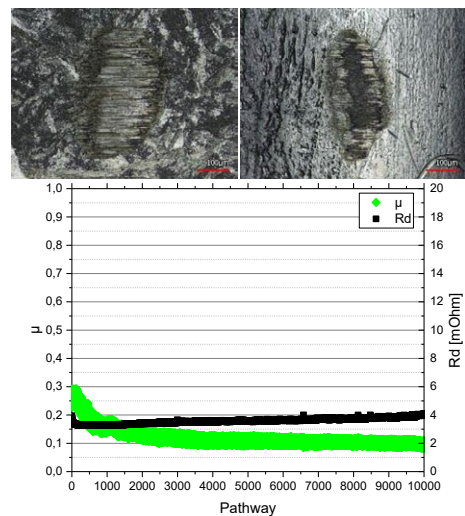


Fig. 14 Test results for the *medium 5* showing both light microscopy and courses of friction coefficient and contact resistance

4 Conclusion

The test results show that for an optimization of the triboelectric performance of the contact system using PTFE-additivated PFPE media, a detailed, comparative investigation of different modifications and their resulting effects is necessary. A suitable combination of the investigated lubricant properties cannot only reduce the friction coefficients and thus the insertion and withdrawal forces in the application, but also reduce wear, especially for macro-friction, thus increasing the lifetime and reliability of the contact system. Regarding micro-friction, a significant reduction or delay of frictional corrosion effects can be achieved.

Overall, dependencies of the triboelectric behaviour of the contact system on the base oil viscosity, the base oil structure and the PTFE additivation can be recognized (**Tab. 2**).

Based on the macro- and micro-tribological investigations, the main improvements compared to medium 0 can be achieved either via

- (I) a change in the PTFE additivation with both identical base oil viscosity and base oil structure (medium 1), **or alternatively**
- (II) an identical PTFE additivation and base oil structure with an increase of the base oil viscosity (medium 5)

For these variations, wear can be reduced with simultaneously improved tribological and comparable electrical behaviour.

A change in base oil structure (media 3 and 4) shows to be disadvantageous regarding the contact resistance due to an increased formation of wear particles. Additionally, a reduction of the base oil viscosity (media 2 and 3) shows to be disadvantageous regarding average wear depths due to thinner lubricant films. The characteristic conflict of interests between tribological and electrical optimization of a contact system becomes apparent: A low friction coefficient results from a high spatial separation of the contact partners through thicker lubricant films and/or third bodies, but simultaneously the contact resistance increases because of the very same influencing factors.

Medium	PTFE additivation	base oil viscosity	base oil structure	friction coefficient	average wear depth	contact resistance
0	o	o	x	o	o	o
1	↓	o	x	o	o	+
2	o	↓	x	+	-	o
3	o	↓	l	+	-	-
4	o	↑	l	++	+	--
5	o	↑	x	o	o	+

Tab. 2 Qualitative overview of the test results with qual. evaluations + (better) / o (similar) / - (worse). The lubricant properties are characterized qualitatively, too.

Overall, the results of the investigations confirm the necessity of a differentiated and comparative investigation of the properties of lubricating media and their influence on the tribo-electric properties of an electrical contact system. It is not advisable to change or implement a lubricant without the need to do so, since the influence on the decisive target variables such as contact resistance for different tribological stresses must be considered in order to avoid undesired performance loss.

When introducing or changing the lubrication of a contact system, steps beyond the basic investigations are also necessary. Besides, the application of the lubricant and its detectability has to be considered. Furthermore, product tests must be carried out to ensure the successful functioning of the lubrication, considering environmental influences and ageing.

5 Literature

- [1] Leidner, M.: Verbesserung der tribologischen und elektrischen Eigenschaften von Zinn-Kontaktflächen durch Partikel/Schmierstoff-Einbettung mittels Laser-Texturierung. Symp. Connectors, Lemgo 2017
- [2] Wielsch, T.: Potential neuer hochleistungsfähiger Beschichtungen für Steckverbindersysteme – es muss nicht immer „edel“ sein. Symp. Connectors, Lemgo 2015
- [4] Slade, P.: Electrical Contacts – Principles and Applications. CRC Press, Boca Raton 1999
- [3] Buresch, I.: Der Schlüssel zur richtigen Kombination: Die 3 Elemente Ag - Sn - Ni. Kontaktflächen für außergewöhnliche Anforderungsprofile. Symposium Connectors, Lemgo 2019
- [5] Vinaricky, E.: Elektrische Kontakte, Werkstoffe und Anwendungen. Springer, Berlin 2013
- [6] Antler, M.: The lubrication of gold. Wear 6 (1963) pp 44-65
- [7] Braunovic, M.: Electrical Contacts - Fundamentals, Applications and Technology. CRC Press, Boca Raton 2007
- [8] Braun, D.: Größeneffekte bei strukturierten tribologischen Wirkflächen. Dissertation, KIT, Karlsruhe 2015
- [9] Noël, S.: Electrical and tribological properties of hot-dipped tin separable contacts with fluorinated lubricant layers. Proc. Holm Conf. (1999) pp 225-235
- [10] Noël, S.: Lubrication mechanisms of hot-dipped tin separable electrical contacts. Proc. Holm Conf. (2001), pp 197-202
- [11] Noël, S.: A New Mixed Organic Layer for Enhanced Corrosion Protection of Electric Contacts. Proc. Holm Conf. (2004) pp 274-280

Durability of some asymmetrical contact pairs for connector application

A. Torrealba^{1,2}, S. Noël¹, A. Brézard Oudot¹

¹ Université Paris-Saclay, CentraleSupélec, CNRS, Laboratoire de Génie Electrique et Electronique de Paris, 91192, Gif-sur-Yvette, France
Sorbonne Université, CNRS, Laboratoire de Génie Electrique et Electronique de Paris, 75252, Paris, France

A. Fares Karam², D. Comte², A. Franchini², J. Toran³

²Amphenol ICC, Besançon, France.
³Amphenol ICC, Etters, PA, USA

Abstract

Reliability of connectors is still a major concern for end users in many applications. One way to improve it is to optimize the surface coatings deposited on base substrates. Although gold remains the most widely used contact plating material, many alternative coatings have been developed in the past or recent years. Among these alternatives are silver final coatings and gold flash over palladium-nickel plated alloy. The properties of these two platings have been mainly investigated in symmetrical configurations where male and female contacts have similar deposits. In this work, asymmetrical configurations - where platings on male and female contacts are dissimilar - are studied. Wear behaviour was investigated with friction and fretting tests. The aim was to characterize the role of the various layers on the wear performances of contacts. Contact resistance behaviours were measured and correlated to the wear tracks investigated with various techniques such as SEM, EDS and 3D-Profilometry. It is shown that in some cases dissimilar final coatings on male and female contacts can significantly improve durability.

1. Introduction

The development of electrification and of connected consumer devices is causing an exponential rise of the number of connectors used and produced worldwide. Historically gold has been the best metal to meet all connector needs. However in view of its cost other alternatives have been developed, such as various palladium alloys [1] [2] in the 80s and hard silver [3]. The concerns were mainly frictional polymer and tarnish film formation for these two types of coatings respectively.

Numerous studies have been done to determine the performance in terms of fretting and wear resistance of all the coatings used in the connector industry, such as the study of the fretting and wear resistance of nickel [4], tin coatings [5] or a new alternative, gold capped silver (GCS) [6]. Gold flash over palladium nickel and the hard silver with (or without surface post-treatment and lubrication) have been used successfully for particular applications. Literature shows that in general palladium nickel alloy has good wear resistance [7] but low fretting resistance [8], while silver coatings have good fretting resistance [9] but low wear resistance. Antler's seminal work on connectors has shown in [10] that dissimilar contact pairs could be very detrimental to wear and fretting behaviour. More recently in [11] Lin et al. have shown that the fretting

resistance of PdNi is improved when in an asymmetric Au (1.2 μm) versus PdNi contact.

In this paper the wear and fretting resistance of two multilayer plating systems are studied: hard pure silver plating on nickel and a gold flashed palladium-nickel on a nickel layer. The four possible configurations were tested for friction and fretting properties since the degradation modes are known to be different. The aim of the study is to bring some insight on the wear mechanisms and to determine if it is possible to improve the performance of each coating by using asymmetrical contacts.

2. Samples and experimental set-ups

2.1 Samples

A hemisphere (cap) of 1.4 mm radius was stamped on CuSn₆ substrates before the electrodeposition of the coating. All the samples (caps and flats) were plated on industrial reel-to-reel plating lines in order to obtain a better reproducibility and all had a 1.3-1.6 μm nanocrystalline Ni first coating. The multilayers studied are described in Table 1. The PdNi alloy coating is called GXTTM; it consists of 80% w/w Pd and 20% w/w Ni deposited from a low ammonia plating bath. A cobalt hardened gold flash of about 50 to 80 nm was deposited on the top. The hardness was measured with a nanoindentation tester

at 0.1 gf and found to be between 400 HV and 420 HV. The GXT™ coatings will be referred to as GXT for simplicity. Care was taken in the measurement with the X Ray fluorescence spectroscopy (XRF Fisher XDVμ model) of the Pd and Ni concentrations in the PdNi coatings. A low free cyanide silver plating bath with no alloying was used for the silver coatings. Plating parameters were adapted to obtain hard silver deposit with average hardness between 120 and 130 HV. These AGT® coatings will be referred to as nAGT because they are not lubricated. All the hardness measurements were carried out under 0.1 g load with a NHT³ Anton Paar nanoindenter. The CuSn₆ substrates hardness was 230 HV with a Young modulus of 120 GPa.

GXT		nAGT	
Thickness (μm)		Thickness (μm)	
Au	0.05 - 0.08	Ag	Cap 4.5 - 5.0
PdNi	0.70 - 0.80		Flat 2.5 - 3.0
Ni	1.30 - 1.50	Ni	1.3 - 1.5
CuSn ₆	350	CuSn ₆	350

Table 1 : Thickness and composition of the GXT and nAGT plating systems.

2.2 Experimental set-ups

Contacts were submitted to durability tests. The evaluation of a coating pair was based on the electrical properties (contact resistance Rc), the friction properties (friction coefficient μ not shown here) and wear properties after several numbers of cycles.

2.2.1 Durability and fretting tests

The durability testing was done with a Bruker UMT3 universal tester fitted with a mechanical reciprocating module. The stroke was set at 2 mm (peak to peak) under a 1 N normal load and a speed of 125 mm/min (0.53 Hz). The contact resistance and the tangential force were measured continuously every 0.1 s. The mean values of 10 measurements were calculated.

The fretting tests were performed with a dedicated device (electro-dynamic shaker [4]) working at constant displacement. The conditions were: d=50 μm peak to peak displacement, 10 Hz and normal load 1 N. The contact radius calculated with the Hertz formulation is 25μm for the studied substrate. The tests were carried out at ±25μm, in order to be in fretting gross slip mode and not in reciprocating sliding mode. During the test, the voltage drop in the contact was measured with an acquisition card (333 10³ samples/s), the DC current value set at 20 mA and voltage limit at 250 mV. The

mean values of 500 measurements per cycle were calculated. All experiments were done at room temperature (23°C) and 55% relative humidity.

Contacts will be referred to as coating1/coating2, the first being the cap and the second the flat through all the paper.

2.2.2 Characterizations

3D images, profiles and wear volumes were measured by a Bruker Contour GT-X 3D Optical Profiler. The wear volumes calculations took into account positives volumes due to transfer and negative ones due to deformation and particles ejection; the following formula was used:

$$V_{cap} = |V_{cap}^- - V_{cap}^+| \text{ and } V_{flat} = |V_{flat}^- - V_{flat}^+|$$

$$V_{wear} = |V_{cap}^- - V_{cap}^+| + |V_{flat}^- - V_{flat}^+|$$

Scanning electron microscope (SEM) images were obtained with a ZEISS EVO MA10 microscope fitted with an Oxford Instruments Xmax probe for Energy Dispersive X-ray Scanning (EDS) analysis for the identification of the chemical elemental composition of selected surfaces. The analyses were done at 15 KeV, the depth of analysis was therefore less than 1 μm.

3. Results and discussion

3.1 Durability experiments

3.1.1 Symmetrical contacts

The evolution of Rc and of the wear were studied as a function of number of friction cycles n. Figure 1 shows Rc(n) curves for the symmetrical contacts nAGT/nAGT and GXT/GXT up to 1200 cycles. All the experiments were performed several times and were repeatable; a representative curve is giving in the following text for all the runs.

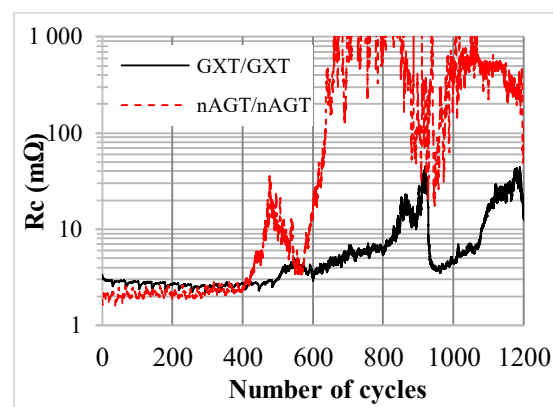


Fig. 1: Durability of nAGT/nAGT and GXT/GXT contacts

The behaviour of the nAGT/nAGT contacts is described first. An initial contact resistance (R_{c1}) of 2.4 m Ω is measured, the values then remain low and stable during the first 400 cycles (~ 2 m Ω). After these 400 cycles there is a rapid increase of R_c to a value of about 30 m Ω at 480 cycles. This indicates the beginning of a degradation of the silver layer; after a decrease R_c drastically increases over a value of 1 Ω .

The composition of the wear tracks were analysed for different numbers of cycles 150, 250, 430 and 1200 cycles. Figure 2 shows the EDS chemical maps of the wear tracks pasted over the SEM images of the contact. The compositions calculated for the depicted wear tracks are plotted in figure 3. At 150 friction cycles the wear track is still fully covered with silver ([Ag]=96 and 88 at% for the cap and flat). At 250 cycles Ni starts to be exposed ([Ni]=21 and 46 at% for the cap and flat) and becomes more predominant at 430 cycles ([Ni]=25 and 55 at% for the cap and the flat). The atomic percentage of O is also more important (32 and 14 at% for the cap and flat), which correlated to the beginning of the electrical disturbances. Finally, at 1200 cycles the cap and flat are worn and oxidized through to the copper substrate ([Cu]=14 and 7 at%; and [O]=38 and 19 at% for the cap and flat respectively) while R_c values are very high (~ 100 m Ω).

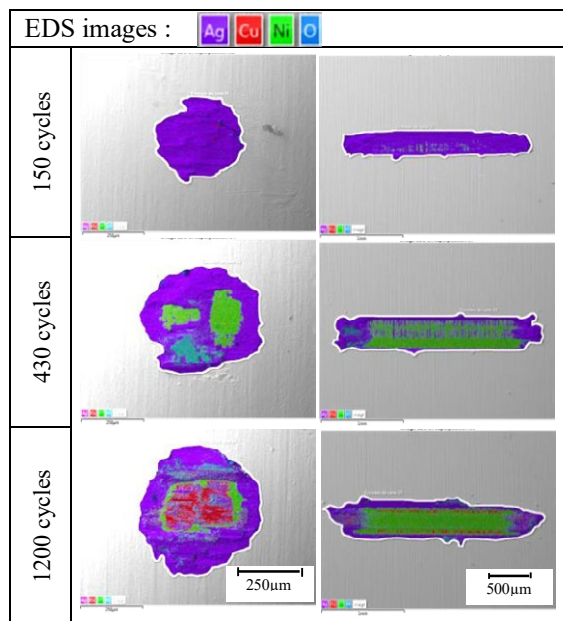


Fig. 2: EDS composition images of nAGT/nAGT contacts for different numbers of friction cycles. Left nAGT caps, right nAGT flats. The white line shows the region used for the composition calculation.

Profilometric measurements and wear volume calculations showed there was a small transfer of silver from the flat to the cap at 150 friction cycles. Beyond that, the cap and the flat are more and more

worn out and at 1200 friction cycles, the wear depth reach 4 μm for the flat and 10 μm for the cap.

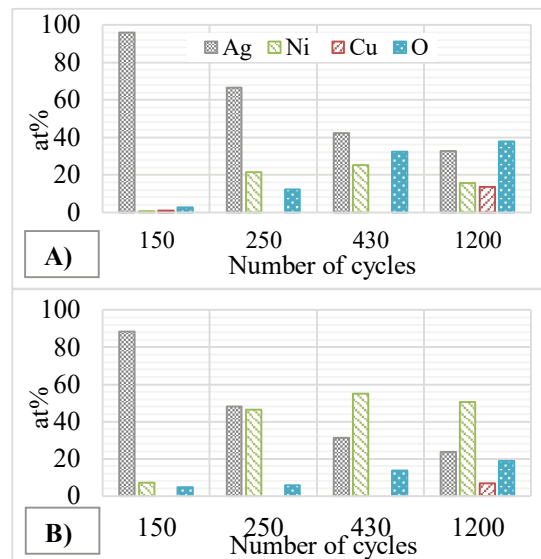


Fig. 3: Chemical composition (%at) of the wear tracks showed in figure 2 : caps A) and flats B)

The beginning of the increase of R_c at 430 cycles corresponds to the thinning of Ag and exposure of Ni. The experiments show that as long as the surface of contact involves an average composition of 57 at% of Ag, the contact resistance remains stable.

The second multilayer studied is a symmetrical GXT/GXT contact. Figure 1 shows the variation of R_c as a function of durability friction cycles. R_c values are low and stable (~ 2.5 m Ω) till 500 cycles, they start to increase slowly up to 850 cycles (10 m Ω). After 850 cycles the values vary between 5 m Ω and 40 m Ω . The durability properties of GXT/GXT is thus observed to be better than that of nAGT/nAGT

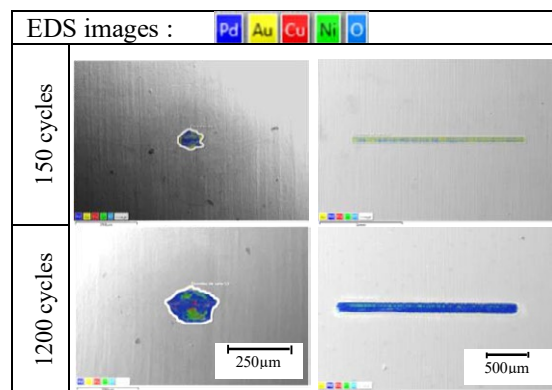


Fig. 4: EDS composition images of GXT/GXT contacts for different numbers of friction cycles. Left GXT caps, right GXT flats

The SEM images in figure 4 show the composition of the wear tracks for the friction tests of GXT/ GXT contacts stopped at different numbers of cycles.

During the first 150 cycles Au is not removed. As the number of cycles increases, the percentage of gold decreases ([Au]=7 and 10 at% at 600 cycles for the cap and the flat respectively) and PdNi is more exposed ([Pd]=26 and 41 at% for the cap and the flat respectively) (figure 5).

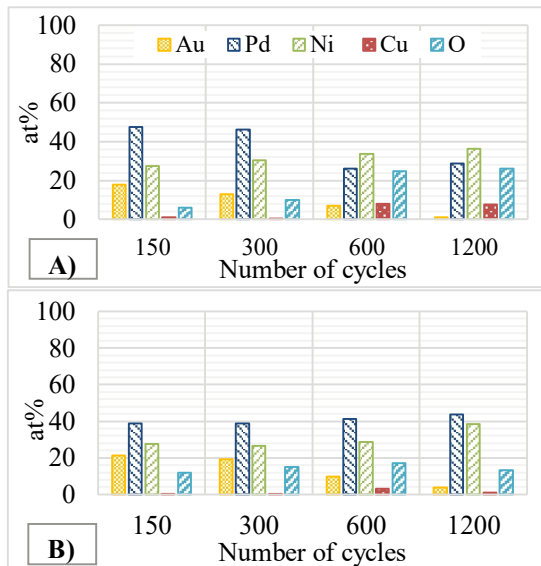


Fig. 5: Chemical composition (%at) of the wear tracks shown in figure 4: caps A) and flats B)

The composition graphs of figure 5 can be correlated to the Rc evolution: Rc values remain stable and low as long as the mean interface composition involves more than 20 at% of Au. As this percentage decreases, PdNi and Ni are exposed and Rc values start to increase.

Comparing the size of the wear tracks on the caps after 150 cycles for the two types of contacts shows that the nAGT/nAGT track is 14 times larger than the GXT/GXT one due to the difference in hardness (125HV/ 420 HV respectively) and the following wear modes.

For the two symmetrical contacts studied we have two totally different wear modes. The multilayer nAGT/nAGT shows adhesive wear with a more severe degradation. When the silver in the wear track is removed and displaced to the edges of wear area, the nickel underlayer is exposed and the contact resistance increases from 2 mΩ to 1 Ω after nearly 480 cycles. For the GXT/GXT multilayer there is abrasive wear, with a much smaller worn surface with a contact resistance that gradually increases but without ever reaching 50 mΩ.

3.1.2 Asymmetrical contacts

For an applicative point of view it was important to investigate the behaviour of contacts with dissimilar platings involving the two described above.

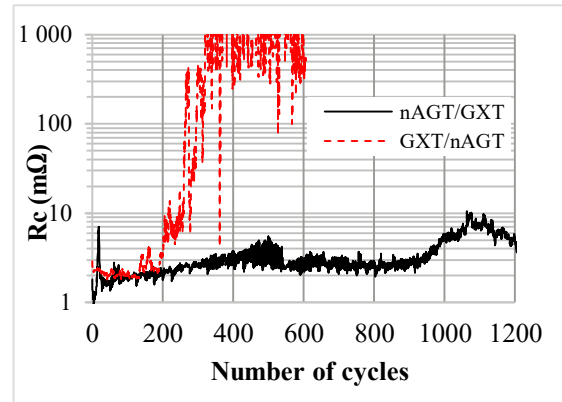


Fig. 6: Durability of nAGT/GXT and GXT/nAGT contacts

The behaviour of GXT/nAGT is described first. Figure 6 shows the initial Rc value is 2.9 mΩ, it stays stable for the first 120 cycles (~ 2 mΩ) and then increases drastically after 300 cycles (Rc=1 Ω at 320 cycles).

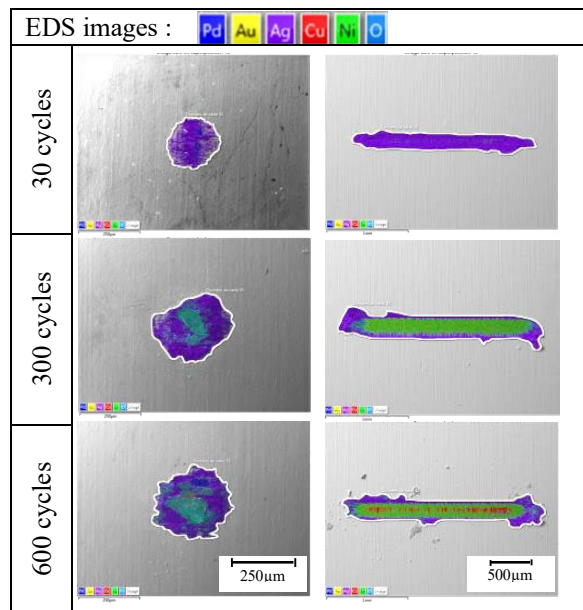


Fig. 7: EDS composition images of GXT/nAGT contacts for different numbers of friction cycles. Left GXT caps, right nAGT flats

Figure 7 shows the composition maps of nAGT flats and GXT caps. After 30 cycles Ag is transferred from the flat to the cap while the flat remains covered with 57 at% Ag. At 300 cycles the flat is mostly composed of Ni which is also detected on the cap in an oxidised form. Figure 8 confirms that there is 18 at% of Ni and 52 at% of O on the cap and 60 at% of Ni and 8 at% of O on the flat. At that stage a drastic change of Rc is observed. The percentage of gold on the cap

has decreased to 1 at%: the contact is no longer Ag-Ni vs. Au-PdNi but Ni vs. PdNi.

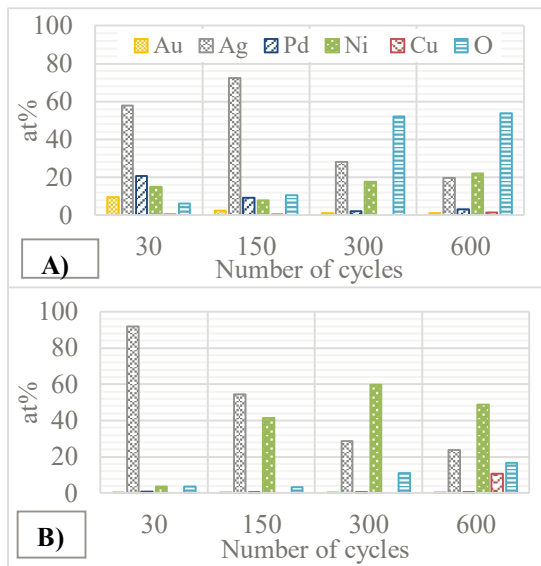


Fig. 8: Chemical composition on the wear tracks shown in figure 7: caps A) and flats B)

Figure 9 shows the 2D profiles of the flats at the corresponding wear stages and the maximum wear depths d_z . After 30 cycles $d_z = 2.8 \mu\text{m}$ which is about the thickness of the Ag layer; at 300 cycles $d_z = 3 \mu\text{m}$ and for 600 cycles $d_z = 4 \mu\text{m}$. The wear volumes calculated from the 3D measures (not shown here) showed that the wear volume on the caps were always positive.

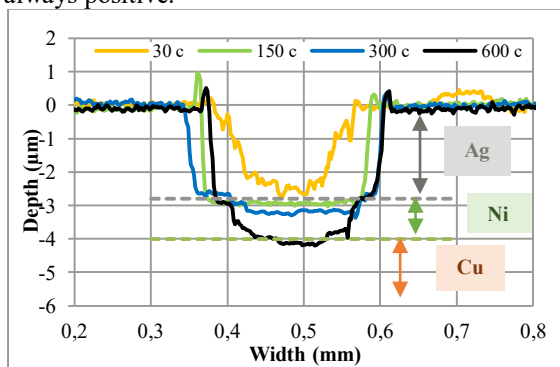


Fig. 9: 2D profiles of the nAGT flats after 30, 150, 300, 600 cycles (GXT/nAGT contacts)

The beginning of the increase of R_c at 300 cycles corresponds to the thinning of Ag and exposure of Ni on the flat. Experiments show that as long as the contact surface involves an average composition of at% Ag higher than that of Ni, the contact resistance remains stable.

The behaviour of the nAGT/GXT contact shown in figure 6 is very different. After an initial R_c value of $1.9 \text{ m}\Omega$ a small peak at around $7 \text{ m}\Omega$ is recorded followed by a stabilized value of $2.5 \text{ m}\Omega$. After 850 friction cycles the R_c increases, but remains below

$10 \text{ m}\Omega$. For all the experiments carried out this peak was present during the first 40 cycles; it corresponds to the beginning of Ag transfer on the flat. 3D profiles of the GXT flats (not shown here) stopped during the peak showed that Ag is first transferred to the top of the delamination waviness of the flat. After 90 cycles Ag is spread homogeneously on the flat and $R_c = 2 \text{ m}\Omega$.

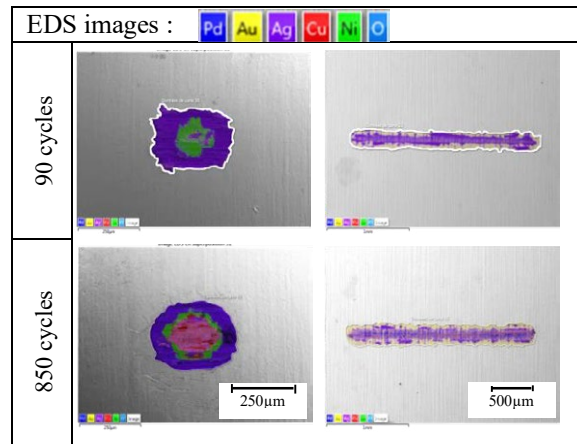


Fig. 10: EDS composition images of nAGT/GXT contacts for different numbers of friction cycles. Left nAGT caps, right GXT flats

The compositions maps of figure 10 shows that at 90 cycles Ag the cap is worn and that Ni is exposed on the cap. At 850 cycles a zone in the middle of the cap seems to be composed of Ni on the outside and a mixture of Cu, Au and Ag in the middle.

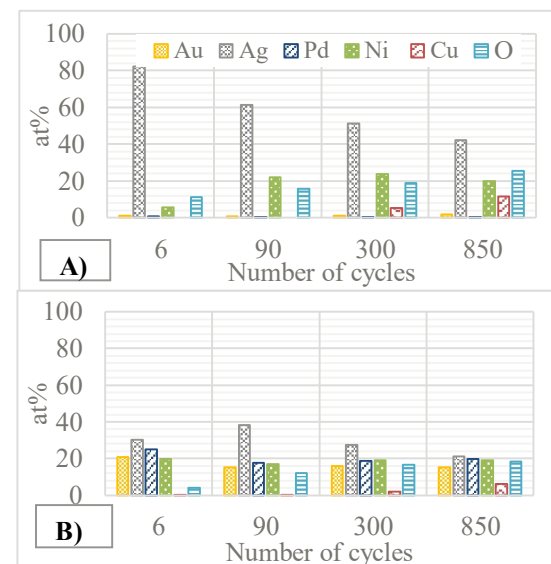


Fig. 11: Chemical composition on the wear tracks shown in figure 10: caps A) and flats B)

From the compositions of figure 11 a wear mechanism can be proposed. At the very beginning of the friction test (6 cycles) some Au of the GXT flat is transferred to the cap but mainly Ag from the cap is transferred to the flat ($[\text{Ag}] = 36 \text{ at}\%$ at 90 cycles). Then the concentration of Ag decreases with

the number of cycles on the cap and flat. After 850 cycles [Cu] reaches 11 and 6 at% for the cap and flat respectively. An analysis focussed on the centre of the cap wear scar did not show any O. It can be observed that at all the stages the GXT flat wear tracks show some Au (probably located on the side on the wear tracks). These two observations are correlated to the stable and low values of Rc measured during the 850 cycles.

3.2 Fretting experiments

Fretting behaviour of Ag/Ag contacts has been described in several works [9] [12] as well as that of Au flashed PdNi [8] [1] [13]. The first type of contacts (soft/soft) shows minor fretting degradation while the second one (hard/hard) shows a severe one; the severity of this latter one depends of the thickness of the gold flash and the contact pressure.

The same four pairs have been submitted to fretting tests (described above) in order to investigate the fretting behaviour of hard/soft and soft/hard contacts.

3.2.1 Dissymmetric contacts

Figure 12 shows the electrical behaviour during 150 000 cycles for the two asymmetrical pairs.

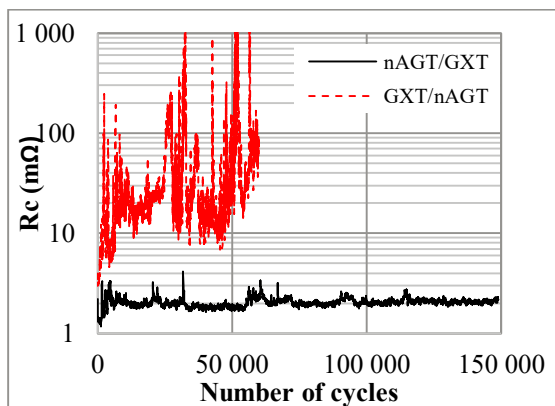


Fig. 12: Fretting behaviours of nAGT/GXT and GXT/nAGT contacts

The behaviour of the GXT/nAGT contacts is described first. For 600 cycles the Rc values stay constant and low ($\sim 3\text{m}\Omega$); they then increase and vary strongly.

Figure 13 shows the EDS images in the wear scars and figure 14 the compositions of this wear tracks. At 200 cycles (during the low Rc plateau) Ag from the flat is transferred to the cap; Ni is exposed on the flat and becomes lightly oxidized.

After 1000 cycles the compositions of the tracks are similar to those after 200 cycles. The strong increase

in Rc has started but the values are still below 10 mΩ. For higher numbers of cycles less Ag is observed inside the wear tracks of the cap and flat. Rc values are high and fluctuate. After 60 000 cycles severe wear is observed and both cap and flat tracks are composed of O, Ni, Cu and small amounts of Ag.

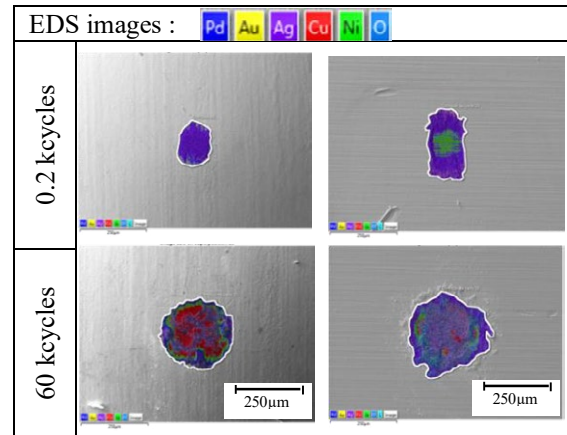


Fig. 13: EDS images of GXT/nAGT for different numbers of fretting cycles. Left GXT caps, right AGT flats

Comparing the wear scars after 10 000 fretting cycles (corresponding to a distance of 1m) to those after 300 friction cycles (distance 1.2m) it can be seen that the wear of the fretting test is more severe. Cu starts to be exposed for the fretting test, while for the friction test flat and cap are still coated with Ag at more than 25 at%.

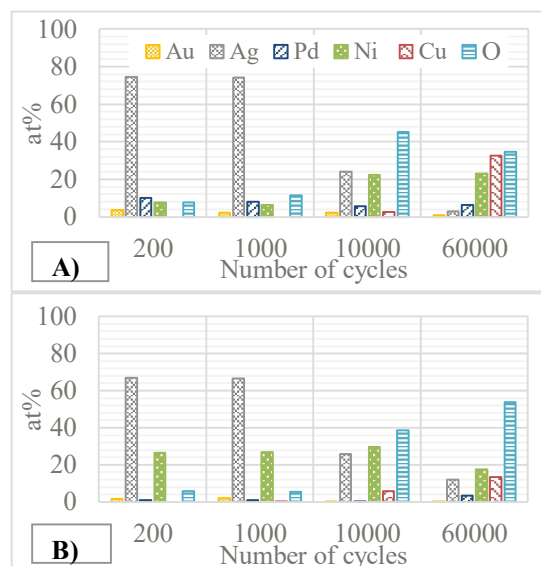


Fig. 14: Chemical composition (%at) of the wear tracks shown in figure 13: caps A) and flats B)

Although Rc values increase rapidly and vary widely, they are lower than with GXT/GXT contacts due to the presence of Ag in the interface. The beginning of the increase of Rc corresponds to an [Ag] below 25 at% on average.

Finally the most interesting case is the nAGT/GXT contact. Figure 12 shows that during the whole test the contact resistance values never reach 10 mΩ. Rc starts at 2.1mΩ, then during 1 400 cycles there is a plateau at 1.5mΩ, then an increase to about 2 mΩ and finally a plateau of stable values lasting 150 000 cycles.

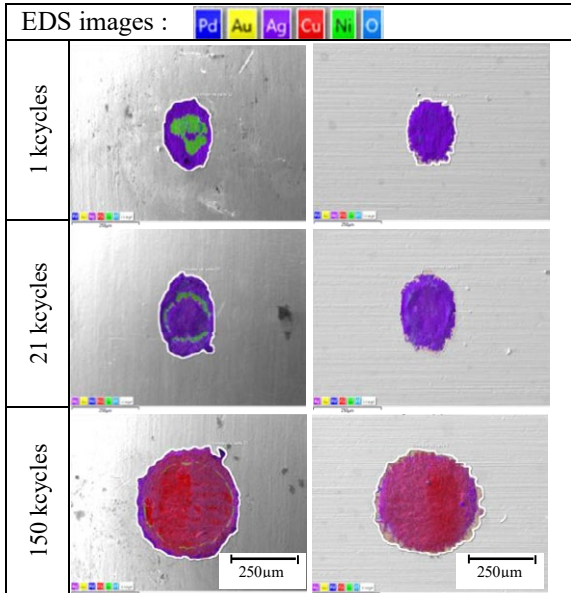


Fig. 15: EDS images of nAGT/GXT for different numbers of fretting cycles. Left nAGT caps, right GXT flats.

The EDS images in figure 15 show that Ag from the cap is transferred to the flat, exposing Ni. The compositions in figure 16 indicate that the percentage of Ag remains between 36 and 52 at% on the cap and between 40 and 76 at% on the flat during 21 000 cycles. After 150 000 cycles the wear tracks of both the cap and the flat are composed of Cu, O and some Ag.

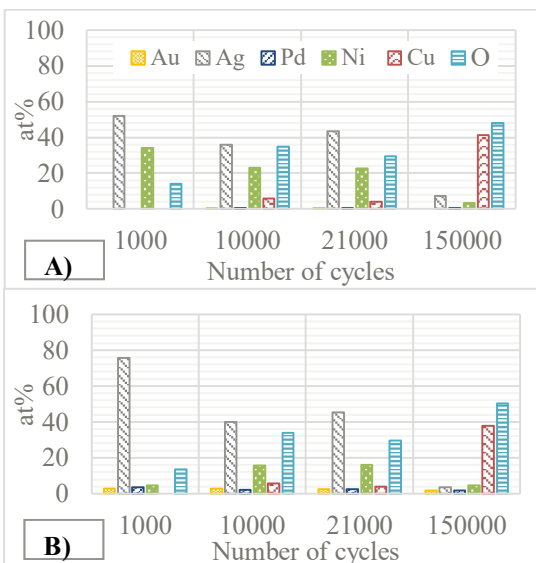


Fig. 16: Chemical composition (%at) of the wear tracks shown in figure 15: caps A) and flats B)

Figure 17 displays the 2D profiles of the nAGT cap and the GXT flat after 150 000 cycles. The cap has been worn by the hard GXT flat and the remaining scar is 5 μm deep. Transferred material 5 μm high can be seen on the flat. Oxygen is detected in rather high quantities on the cap and the flat due to the presence of Cu and Ni. Nevertheless at this stage the measured contact resistance is 2.8 mΩ probably due to the presence of Ag on the periphery of the wear scars.

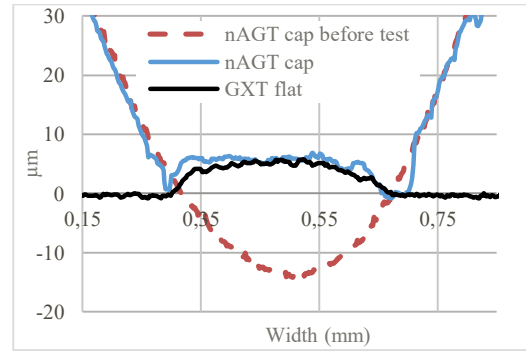


Fig. 17: 2D profiles of the nAGT/ GXT contact after 150000 fretting cycles

Figure 18 shows the wear volumes of the cap and flat. Negative volumes represent displaced matter and ejected matter and positive ones represent displaced matter and transfer. These wear volumes are almost constant during the first 100 000 cycles. After that a very large increase of the cap wear volume (900 10³ μm³) is observed. It is due to the filing of the Ag top of the cap by the hard flat. Simultaneously some transfer of silver on the flat occurs as seen in figure 17.

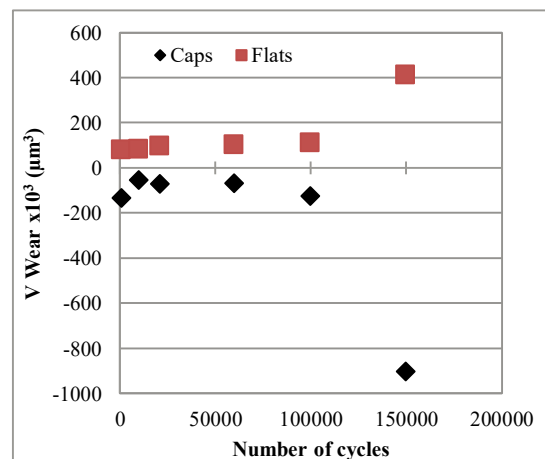


Fig. 18: Wear volumes of the caps and flats for nAGT/GXT contacts

The fretting results have shown that dissimilar contacts involving one Ag and one GXT contact behave differently whether the Ag or the GXT is on the cap. In the conditions of this study, an Ag coating on the cap allows very low and stable Rc values

because of the beneficial transfer of the silver from the cap to the flat.

4. Conclusion

Durability tests of four configurations of contacts were investigated. Soft (AGT) cap on soft (AGT) flat, hard (GXT) cap on hard (GXT) flat and mixing the two for disymmetric contacts. It was shown that:

- With the soft/soft configuration strong wear of the soft Ag coating occurred, leading to an Ag/Ni contact interface, the beginning of Rc increase and finally to a Cu/Ni interface giving high Rc.

- With the hard/hard configuration the 50 nm flashed Au remained long enough in the interface for the Rc to increase slowly with Rc < 10mΩ after more than 800 cycles.

- For the hard cap on soft flat strong wear is recorded, Ag transferred to the cap and finally the contact interface becomes Ni/Cu leading to a very fast Rc increase. This is the worse case of the study.

- Finally the soft/hard configuration gave very long lasting low Rc because of low wear with some transfer of the flashed Au on the cap and some transfer of the Ag to the flat. An unexpected “alloy-type” Ag-Au-Cu acted as a third body during friction.

These results were compared to fretting experiments and summarized in table 2.

	N friction cycles for Rc > 10mΩ	N fretting cycles for Rc > 10mΩ
nAGT/nAGT	450	1800
GXT/GXT	850	1000
GXT/nAGT	220	1200
nAGT/GXT	-	-

Table 2: Number of friction and fretting cycles for Rc > 10 mΩ.

Friction of GXT/GXT contacts lasts twice longer than nAGT/nAGT. Using a GXT cap on nAGT (asymmetrical GXT/AGT) degrades the behaviour as compared to the symmetrical contacts. Using a nAGT cap on GXT flats ensures low Rc values. Fretting duration of GXT/GXT is 1.8 smaller than that of nAGT/nAGT. Using a GXT cap on AGT multiplies by 1.3 the fretting duration as compared to GXT/GXT contacts. Finally using a nAGT cap on GXT (asymmetrical nAGT/GXT) no Rc increase due to fretting was recorded for 150 000 cycles. This study has shown that the transfer of a soft relatively

“noble” metal such as silver on a hard surface acted as a solid lubricant diminishing fretting degradation.

REFERENCES

- [1] Antler, M.: Fretting of electrical contacts: An investigation of palladium mated to other materials. *Wear*, 81, 1982, pp.159-173.
- [2] Antler, M.: The application of palladium in electronic connectors. *Platinum Metals Rev.*, 26,3, pp.106-117.
- [3] Myers, M.: The performance implications of silver as a contact finish in traditionally gold finished contact. *Proc. IEEE Holm Conference 2009, Vancouver, Canada, 2009*, pp.307-315.
- [4] Noël, S.; Correia, S.; Alamarguy, D.; Gendre, P.: Fretting behaviour of various intermetallic compounds in electrical contacts: influence on reliability. *Wear*, 271, 2011, pp. 1515 – 1523.
- [5] Trinh, K. E.; Tsipenyuk, A.; Varenberg, M.; Rosenkranz, A.; Souza, N.; Mucklich, F.: Wear debris and electrical resistance in textured Sn-coated Cu contacts. *Wear*, 344-345, 2015, pp.86-98.
- [6] Fares-Karam, A.; Anderson, D.; Toran, J.: Performance evaluation of the new gold capped silver (GCS) plating systems for connectors contact applications. *Proc. 28th ICEC2016, 2016, Edinburgh, U.K.*, pp.81-86.
- [7] Myers, M: Comparison of hard Au versus hard Au flashed PdNi as a contact finish. *Proc. IEEE Holm Conference 2010, Charleston, U.S.A. 2010*, pp.49-57.
- [8] Morse, C.; Aukland, N. R.; Hardee, H. C.: A statistical comparison of gold and palladium-nickel plating systems for various fretting parameters. *Proc. IEEE Holm Conference, Montreal, Canada, 1995*, pp.33-51.
- [9] Song, J.; Schinow, V.: Correlation between friction and wear properties and electrical performance of silver coated electrical connectors. *Wear*, 330-331, 2015, pp. 400-405.
- [10] Antler, M.: Electrical effects of fretting connector contact material: a review. *Wear*, 106, 1985, pp.5-33.
- [11] Lin, X. Y.; Luo, G.; Liangjun, X.: Fretting property of asymmetrical metal contact pairs. *Proc. 26th ICEC2012, 2012, Beijing, China*, pp.213-220.
- [12] Laporte, J.; Perrinet, O.; Fouvry, S.: Prediction of the electrical contact resistance endurance of silver plated coatings subjected to fretting wear, using a friction energy density approach. *Wear*, 330-331, 2015, pp.170-181.
- [13] Murata, H.; Imada, Y.; Honda, F.; Nakajima, K.: Effect of fretting on de electroplated Pd-Ni contacts. *Wear*, 162-164, 1993, pp.339-346.

Investigation of the contact resistance as a function of the temperature for connectors and wire terminals

Tobias Dyck, WAGO Kontakttechnik GmbH & Co. KG, Minden, Germany, tobias.dyck@wago.com
Andreas Bund, Technische Universität Ilmenau, Department of Electrochemistry and Electroplating, Ilmenau, Germany, andreas.bund@tu-ilmenau.de

Abstract

The hardness of coating materials such as tin or gold is temperature-dependent, so the contact area and thus the contact resistance change depending on the temperature. Contact resistance measurements are carried out on hard gold- and tin-coated connector contacts at elevated temperatures. It is shown that the contact resistance decreases significantly with increasing temperature. Tests are also being carried out with solid and stranded copper wires. In addition to the hardness, foreign layers on the copper conductors have a further influence on the contact resistance.

1 Theoretical background

The contact resistance depends on the real contact area. The contact area in turn is a function of the contact force and the hardness of the surface. [1] Because the hardness of metals decreases with increasing temperature (Fig. 1) there is also a temperature-dependence between contact resistance and temperature.

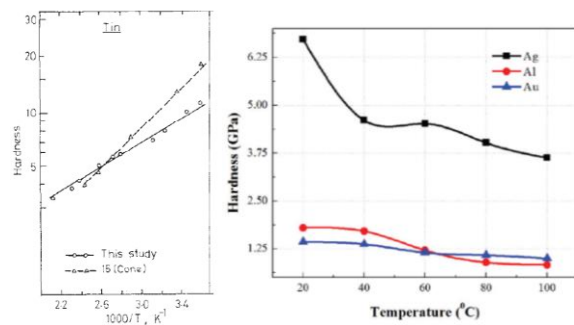


Fig. 1 Change in the hardness of tin depending on the temperature. (left) [2] Change in the hardness of aluminium, silver and gold depending on the temperature. (right) [3]

Foreign layers lead to a reduction in the real contact area and thus to an increase in the contact resistance. [1] With regard to bare copper conductors, it is obvious that copper forms an oxide layer in the presence of air. Apart from the oxide layer, there are other foreign layers on copper conductors that originate from the production process. Copper strands are drawn to the required diameter using drawing emulsions. Dispersing agents are used when the insulation is extruded. Also ingredients of the wire insulation like plasticizers can evaporate [4] and even form oily residues [5].

Microscopic examinations of copper conductors show transparent contamination layers on the surface (Fig. 2). With the use of IR spectroscopy substances like phthalate esters, amide waxes and plasticizers can be detected. [6,7]

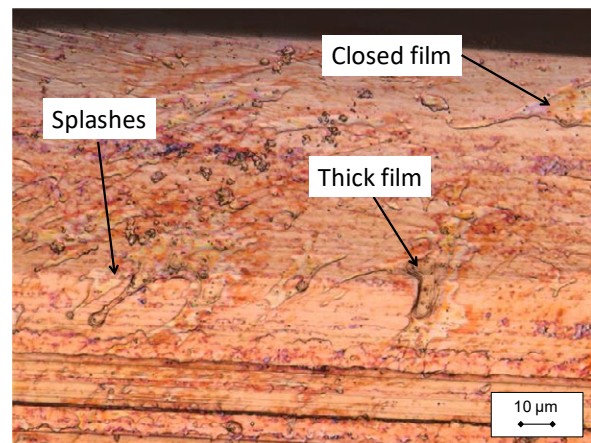


Fig. 2 Micrograph of inhomogeneous distributed contaminations on a conductor surface. [6]

2 Experimental setup

2.1 Connector investigations

For the experimental investigations copper contacts with hard gold and tin coatings are used (Fig. 3 and Tab. 1). A contact force of 3 N is used for all tests. The test setup is shown in Fig. 4 and Fig. 5.

Because tin forms thin oxide layers, which can influence the contact resistance, tests are also carried out with wear stressed contacts (Tab. 1). This is done by performing one wear cycle with a track length of

10 mm after applying the contact force of 3 N. After the wear cycle the contacts are separated from each other for a short moment to release the cold-welded contacts. The separation and subsequent contacting takes place within a few seconds in order to avoid re-oxidation of the contact surfaces. The electrical measurement takes place in the middle of the wear track.

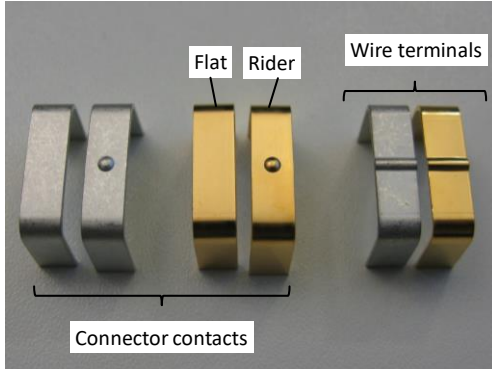


Fig. 3 Photograph of gold- and tin-coated contact geometries. The spherical radius of the connector contacts is 1.5 mm, the contact radius of the wire contact is 1.0 mm. The base material is Cu-HCP.

For reaching the target temperature of about 100 °C, in addition to the contact resistance there are two further heat sources installed by placing steel plates between the contacts and the supply lines (Fig. 4). The connection resistances are about 10 mOhm and the contact resistance about 1 mOhm, so that most of the heat is generated at the feed-in points (Fig. 4). Indirect heating should prevent the contact point from overheating.

During the experiment the current is increased in 5 A steps (0.1 A, 5.0 A, 10.0 A ... 25 A) and is held for 900 seconds for each step. The voltage drop is measured as a four-wire measurement (Fig. 4).

The following instruments and sensors are used for all measurements: A data acquisition system Keithley DAQ6510 / 7700 is used for measuring the voltage drop. As power source a TOELLNER TOE 8951-40 is used. For the temperature measurement thermocouples type J (Fe-CuNi) are used.

Tab. 1 Test plan for investigations with connector contacts. A contact force of 3 N is used. For each parameter combination five measurements are carried out.

Coating	Preparation	Current range
1.2 μm AuCo / 2.2 μm Ni	Unstressed	0.1 – 25 A
11.1 μm Sn (matte)	Unstressed	0.1 – 25 A
11.1 μm Sn (matte)	Stressed	0.1 – 25 A

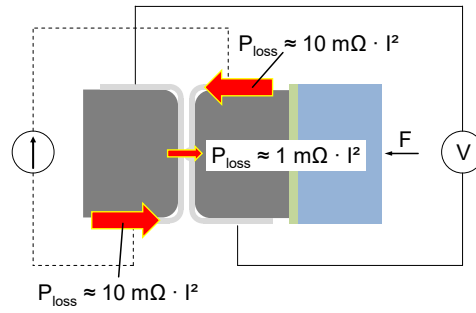


Fig. 4 Schematic representation of the test setup for carrying out contact resistance measurements at elevated temperatures for connector contacts.

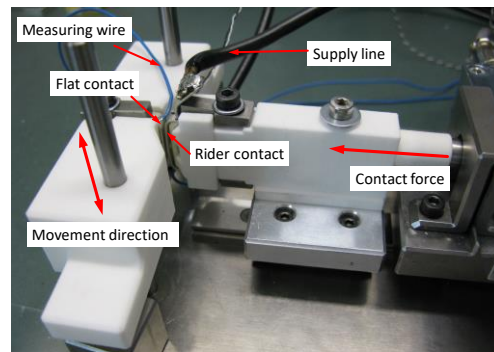


Fig. 5 Photo of the experimental setup for the investigation of connector contacts. The clamping devices are made of polyamide. The contact force is set by a screw mechanism and measured by a force sensor. The wear cycles are carried out manually.

2.2 Wire terminal investigations

The wire terminal investigations (Tab. 2) are performed with solid and stranded wires with a cross-section of 6 mm² (Fig. 6) and with gold- and tin-coated contacts (Fig. 3). The test setup is shown in Fig. 7 and Fig. 8. A contact force of 10 N is applied, which is generated by a steel weight (Fig. 8).

For tests with cleaned wires (Tab. 2) the conductor is abraded and wiped off with an ethanol-impregnated fiber cloth. The experiments are started immediately after cleaning the conductor.

The current is increased in 5 A steps (0.1 A, 5.0 A, 10.0 A ... 35 A) during the experiment. For each step the set current is held for 900 seconds. The voltage drop is measured as a four-wire measurement (Fig. 7).

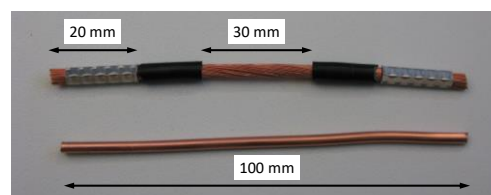


Fig. 6 Photograph of wire samples (6 mm²). The ends of the stranded wire (top) are crimped and in the middle a defined length is stripped. The solid conductor (bottom) is stripped over the entire length.

Tab. 2 Test plan for contact resistance with wire terminals. A contact force of 10 N is used. For each parameter combination three measurements are carried out.

Coatings	Wire type	Preparation	Current
1.0 μm AuCo / 3.1 μm Ni and 8.2 μm Sn (matte)	6 mm ² solid	Uncleaned and cleaned	0.1 A
	6 mm ² solid	Uncleaned and cleaned	0.1 A – 35 A
	6 mm ² stranded	Crimped, uncleaned	0.1 A
	6 mm ² stranded	Crimped, uncleaned	0.1 A – 35 A

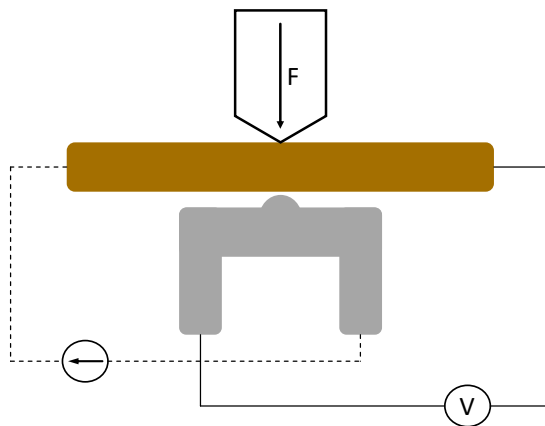


Fig. 7 Schematic representation of the test setup for carrying out contact resistance measurements at elevated temperatures for wire terminals. [7]

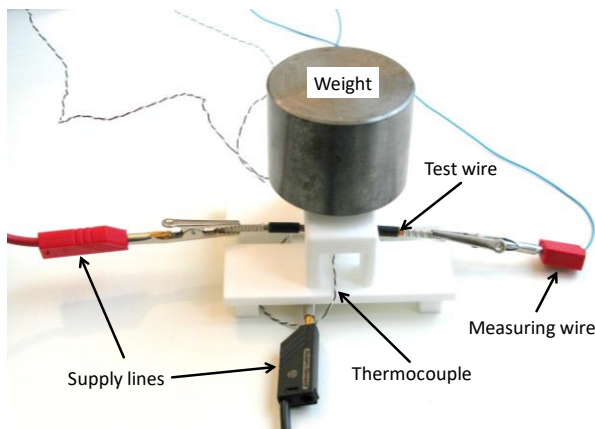


Fig. 8 Photograph of the experimental setup for the investigation of wire terminals. Two thermocouples are placed directly under the contact. The higher temperature is used for the evaluation. Alligator clips are used to contact the conductor and the wire terminal.

3 Results und discussion

3.1 Experimental investigation of connector contacts

The effect of a decreasing hardness of the coating on the contact resistance is examined by carrying out tests at elevated temperatures. The result for a 1.2 μm AuCo / 2.2 μm Ni coating (**Fig. 9**) shows that the contact resistance decreases with increasing temperature. The average from five measurements is 0.31 mOhm for the initial value (at ambient temperature) and for the final value 0.22 mOhm (at 100-110 °C). The contact resistance at maximum temperature is on average 71 % of the initial value at ambient temperature.

With the 11.1 μm Sn (matte) coating (**Fig. 10**) the contact resistance already decreases significantly depending on the time, even at low temperatures (< 40 °C). This behavior can be explained by the flow of the tin and the existing tin oxide layer. Since the oxide layer was not penetrated by a relative movement, the existing oxide layer leads to higher initial values compared to the gold coating (Fig. 9). After the contact force is applied, the tin begins to flow and the oxide layer is penetrated depending on the time. With increasing temperature the contact resistance continues to decrease because, on the one hand, the contact area increases, on the other hand, the oxide layer is penetrated further. The average of five measurements is for the initial value 1.56 mOhm and for the final value 0.21 mOhm (at 104-120 °C). The contact resistance value at maximum temperature is on average 13 % of the initial value at ambient temperature.

Another experiment was carried out with the 11.1 μm tin coating (Fig. 11), whereby the contacts are stressed by one wear cycle before starting the measurement. The wear cycle simulates a mating cycle of a connector and leads to a removal of the oxide layer.

The behavior is now comparable to that of the gold plating. The average from five measurements is for the initial value 0.23 mOhm and for the final value 0.14 mOhm (at 97-111 °C). The contact resistance at maximum temperature is on average 61 % of the initial value at ambient temperature. The change in resistance is solely due to the decreasing hardness of the tin and the increasing real contact area.

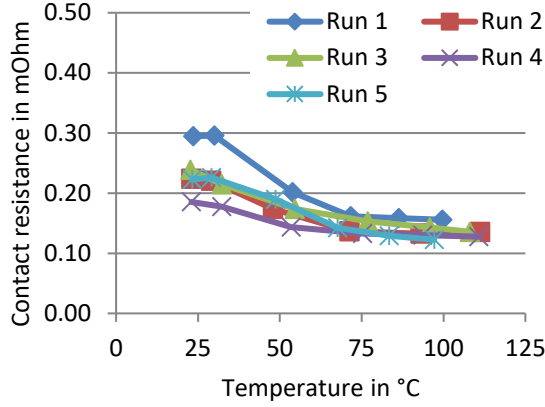


Fig. 9 Test result of the temperature and time-dependent contact resistance behaviour of 1.2 μm AuCo / 2.2 μm Ni coated contacts (unstressed). Current: 0.1 – 25 A. Contact force: 3 N.

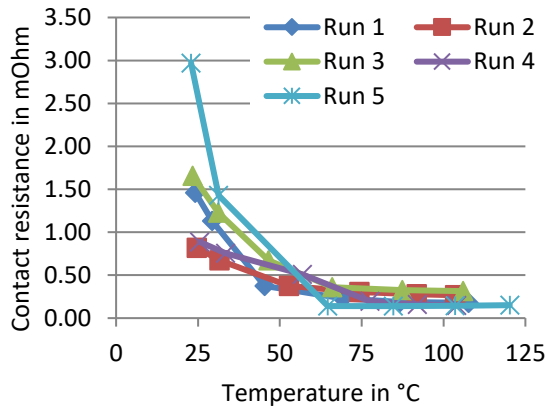


Fig. 10 Test result of the temperature and time-dependent contact resistance behaviour of 11.1 μm Sn (matte) coated contacts (unstressed). Current: 0.1 – 25 A. Contact force: 3 N.

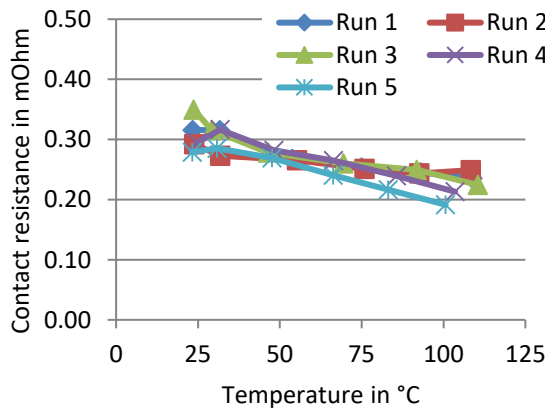


Fig. 11 Test result of the temperature and time-dependent contact resistance behaviour of 11.1 μm Sn (matte) coated contacts (stressed). Current: 0.1 – 25 A. Contact force: 3 N.

3.2 Discussion of the contact physical effects

In the following the temperature-dependent contact resistance behavior for oxide-free contacts should be explained using an analytical approach.

The constriction resistance R_c depends on the specific electrical resistance of the contact material ρ and the contact radius a (Eq. 1). [1]

$$R_c = \frac{\rho}{2a} \quad (1)$$

The contact area A is calculated with the hardness H of the contact material and the contact force F (Eq. 2).

$$A = \frac{F}{H} \quad (2)$$

Because the radius of the contact geometry a is much larger than the thickness of the coating, the real contact area can be simplified to a circular area (Eq. 3).

$$A = a^2\pi \quad (3)$$

With Eq. 2 and Eq. 3 there is a dependence of the contact radius a on the contact force F and the hardness H (Eq. 4).

$$a = \sqrt{\frac{F}{H\pi}} \quad (4)$$

If now Eq. 1 and Eq. 4 are used, an expression for the constriction resistance R_c dependent on the specific electrical resistance of the contacting material ρ , the contact force F and the hardness H is obtained (Eq. 5).

$$R_c = \frac{\rho}{2\sqrt{\frac{F}{H\pi}}} \quad (5)$$

With Eq. 5 and the available temperature-dependent hardness values for gold and tin (Fig. 1) now should be estimated how much a hardness change affects the contact resistance. When interpreting, it must be taken into account that the hardness values are measured on a pure gold layer and not on a hard gold layer. It is also possible that the coating thickness and the substrate material influence the temperature-dependent development of the hardness.

The calculated results (Tab. 3) are in good agreement with the test results (Fig. 9 and Fig. 11). Experimental for the gold-coated contacts a change in contact resistance of 15-36 % (calculated: 20 %) was measured. For the tin-coated contacts with one wear cycle for removal of the oxide-layer a change of 31-47 % (calculated: 30 %) was measured.

Tab. 3 Calculation of constriction resistances depending on the hardness of gold and tin (Fig. 1).

Coating	Hardness	Constriction resistance
Gold	$H_{(100\text{ }^{\circ}\text{C})}$ $\approx \frac{2}{3} H_{(20\text{ }^{\circ}\text{C})}$	$R_{c(100\text{ }^{\circ}\text{C})} \approx \frac{\sqrt{6}}{3} R_{c(20\text{ }^{\circ}\text{C})}$ $\approx 0.8 R_{c(20\text{ }^{\circ}\text{C})}$
Tin	$H_{(110\text{ }^{\circ}\text{C})}$ $\approx \frac{1}{2} H_{(20\text{ }^{\circ}\text{C})}$	$R_{c(110\text{ }^{\circ}\text{C})} \approx \frac{\sqrt{2}}{2} R_{c(20\text{ }^{\circ}\text{C})}$ $\approx 0.7 R_{c(20\text{ }^{\circ}\text{C})}$

3.3 Experimental investigation of wire terminals

3.3.1 Measurements with gold-coated contacts and uncleaned solid wires

The results for uncleaned solid conductors on a 1.0 μm AuCo / 3.1 μm Ni coated contact at ambient temperature (Fig. 12) show a wide spread of the initial values (3-11 mOhm). The reason are inhomogeneous distributed foreign layers on the surface of the conductor (Fig. 2) [6,7]. The contact resistances decrease over time, since the displacement of the foreign layers from the contact area is presumably time-dependent. The contact resistance after a time of 120 minutes is on average 3.24 mOhm and 51 % of the initial value (6.33 mOhm).

At elevated temperatures and the same test time of 120 minutes, there is a significantly greater drop in contact resistance (Fig. 13). The contact resistance after a period of 120 minutes / at the highest temperature is on average 0.45 mOhm and 5 % of the initial value (9.22 mOhm).

In order to eliminate the influence of the time-dependent plastic deformation of the roughness peaks and other temperature-independent effects in the first seconds of contacting, the change in the contact resistance can be examined from a defined point in time or a defined temperature. In this case (Fig. 13) the average contact resistance at maximum temperature is about 11 % of the contact resistance at 30 $^{\circ}\text{C}$.

Compared to the experiment with the gold-coated connector contacts (Fig. 9), the change in resistance is much more pronounced. The cause for the higher initial resistances compared to the gold on gold contact situation are foreign layers on the copper conductor. The reason for the greater reduction in contact resistance is only to a small extent the change in the hardness of the coating; the main cause is probably a temperature-dependent change of the foreign layers, e.g. changes in viscosity, decomposition or evaporation. It can be concluded that with uncleaned conductors, the time and temperature each have an important influence on the contact resistance.

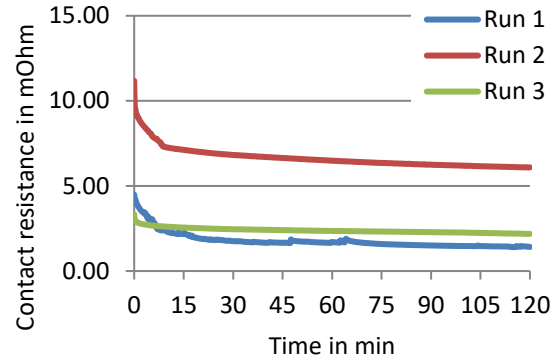


Fig. 12 Test results for uncleaned solid copper wires (6 mm²) with 1.0 μm AuCo / 3.1 μm Ni coated contacts. Current: 0.1 A. Contact force: 10 N.

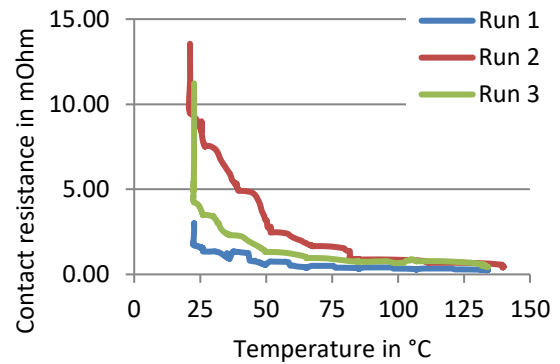


Fig. 13 Test results for uncleaned solid copper wires (6 mm²) with 1.0 μm AuCo / 3.1 μm Ni coated contacts. Current: 0.1 – 35 A. Contact force: 10 N.

3.3.2 Measurements with gold-coated contacts and cleaned solid wires

In another test series with gold-coated contacts, cleaned conductors are used.

The initial contact resistances for cleaned conductors (Fig. 14) are significantly lower than for uncleaned conductors (Fig. 12). A significant decrease in the values can be observed just within the first seconds (Fig. 14), which can be explained by a time-dependent plastic deformation of the roughness and thus an increase in the real contact area. The average initial contact resistance is 0.29 mOhm and after a time of 120 minutes 0.19 mOhm.

For elevated temperatures (Fig. 15) the average contact resistance at maximum temperature is about 92 % of the contact resistance at 30 $^{\circ}\text{C}$. The effect is probably weaker than with the gold on gold contact situation (Fig. 10), mainly because the contact force is significantly higher at 10 N. With the higher contact force, the initial contact area is already relatively large and the potential for growth of the area is lower due to the decreasing hardness of the coating.

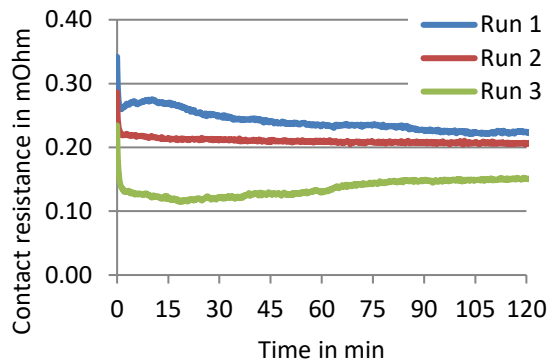


Fig. 14 Test results for abraded and ethanol cleaned solid copper wires (6 mm²) with 1.0 μm AuCo / 3.1 μm Ni coated contacts. Current: 0.1 A. Contact force: 10 N.

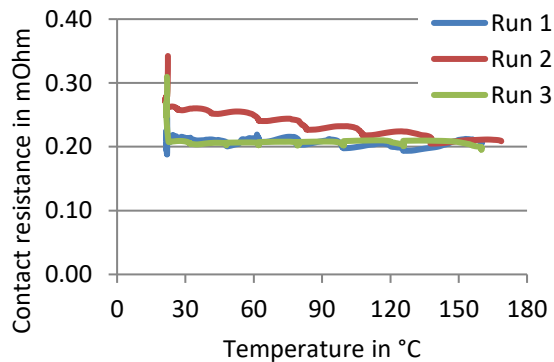


Fig. 15 Test results for abraded and ethanol cleaned solid copper wires (6 mm²) with 1.0 μm AuCo / 3.1 μm Ni coated contacts. Current: 0.1 – 35 A. Contact force: 10 N.

3.3.3 Measurements with tin-coated contacts and uncleaned solid wires

For another test series 8.2 μm Sn (matte) coated contacts are used (Fig. 3). The same conductors are used as in the previous series of tests, so that the results are comparable.

The test results at ambient temperature for tin-coated contacts and uncleaned conductors (Fig. 16) show differences and similarities in comparison with the results of gold-coated contacts (Fig. 12). First of all, it should be noted that the initial values are significantly lower (on average 0.85 mOhm). This is probably due to the fact that the real contact area is significantly larger than that of the gold-coated contacts due to the low hardness of tin and the higher layer thickness. In addition, there is also a time-dependent drop in the contact resistance, so that the values after 120 minutes are on average 53 % (0.45 mOhm) of the initial contact resistance. The results largely correspond to those of the gold-coated contacts.

When heated by current (Fig. 17), the contact resistance decreases with increasing temperature, similar to the tests with gold-coated contacts (Fig. 13). The average contact resistance at maximum temperature (0.21 mOhm) is about 24 % of the initial contact resistance (0.87 mOhm) and 48 % of the contact resistance at 30 °C (0.44 mOhm).

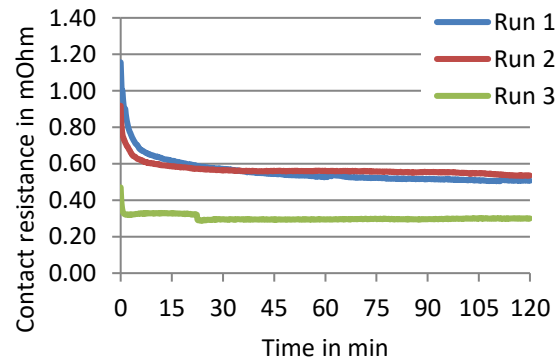


Fig. 16 Test results for uncleaned solid copper wires (6 mm²) with 8.2 μm Sn (matte) coated contacts. Current: 0.1 A. Contact force: 10 N.

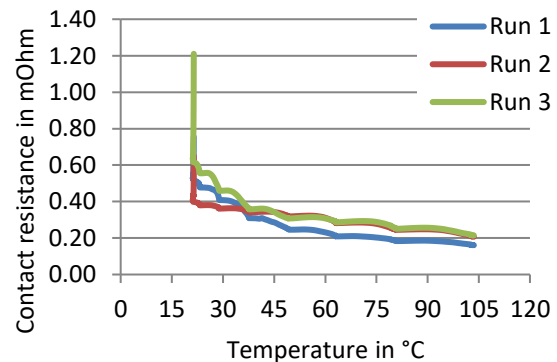


Fig. 17 Test results for uncleaned solid copper wires (6 mm²) with 8.2 μm Sn (matte) coated contacts. Current: 0.1 – 35 A. Contact force: 10 N.

3.3.4 Measurements with tin-coated contacts and cleaned solid wires

The experiment with cleaned conductors and tin-coated contacts (Fig. 18) shows very low contact resistances from the beginning. There is no significant change in contact resistance during the test period. After a test time of 120 minutes, the mean value is 0.16 mOhm and thus in the same range as in the tests with the gold-coated contacts (Fig. 14). To a certain extent, this result contradicts the statement from the previous investigations that the size of the contact area is the cause of the significantly lower initial values of tin coatings. The advantage of the tin coatings seems to be particularly evident in the case of contaminated conductors. However, there may be an interaction between the soft tin layer and the foreign layers

on the copper conductors. It is conceivable that when the conductor penetrates the tin layer due to the relative movement between the conductor and the tin material, foreign layers are displaced from the contact area and thus the conductor is “cleaned”. Further investigations are necessary at this point in order to explain the processes exactly.

At elevated temperatures (Fig. 19) there is after the initial phase even a slight increase in the values compared. The decreasing conductivity of the tin layer predominates the growing contact area, since the relatively high contact force of 10 N has largely exhausted the potential for growth of the contact area. Further investigations are also necessary here.

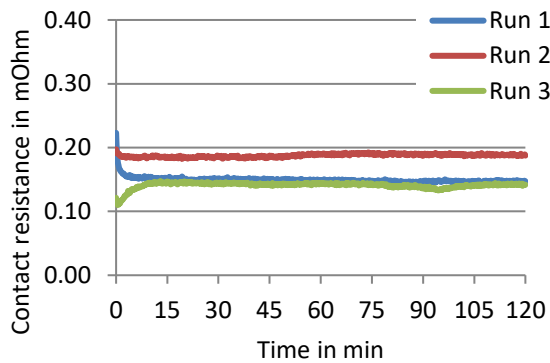


Fig. 18 Test results for abraded and ethanol cleaned solid copper wires (6 mm²) with 8.2 μm Sn (matte) coated contacts. Current: 0.1 A. Contact force: 10 N.

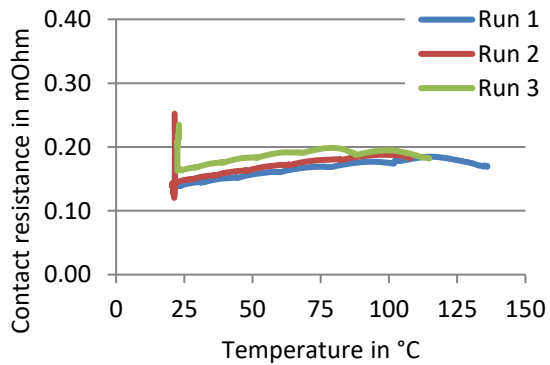


Fig. 19 Test results for abraded and ethanol cleaned solid copper wires (6 mm²) with 8.2 μm Sn (matte) coated contacts. Current: 0.1 – 35 A. Contact force: 10 N.

3.3.5 Measurements with gold-coated contacts and stranded wires

Tests are carried out with stranded wires. Cleaning of the conductors was not carried out in all experiments. With gold-coated contacts there is a time-dependent reduction in contact resistance at ambient temperature (Fig. 20). So far, the behavior is the same as solid conductors. However, the curves are less smooth (see

Run 2 in Fig. 20). This can be explained by the fact that during the test individual strands of the wire reorient. The reorientation creates new contact points that may initially have foreign layers, which is why the contact resistance increases. Because the distribution of the contact force within the contact system is more favorable after the reorientation, a resistance level is reached after a certain time, which is below the level before the reorientation. The average values after 120 minutes are 60 % (2.24 mOhm) of the initial values (3.77 mOhm). The time-dependent change is comparable to that of the solid uncleaned conductors (Fig. 12 and Fig. 17).

At elevated temperatures (Fig. 21) the contact resistance decreases significantly. The average value at maximum temperature is 16 % (0.60 mOhm) of the initial value (3.70 mOhm) and 36 % of the value at a temperature of 30 °C (1.65 mOhm). In summary, there is also for stranded conductors a time- and temperature-dependence of the contact resistance.

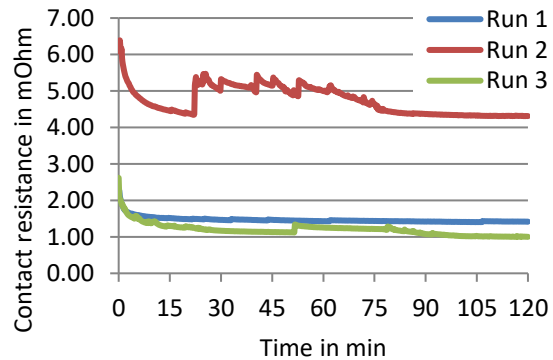


Fig. 20 Test results for stranded (crimped) copper wires (6 mm²) with 1.0 μm AuCo / 3.1 μm Ni coated contacts. Current: 0.1 A. Contact force: 10 N.

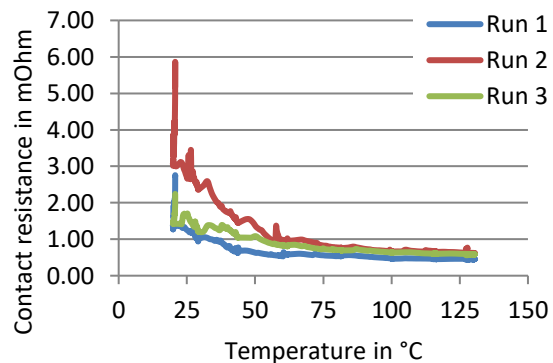


Fig. 21 Test results for stranded (crimped) copper wires (6 mm²) with 1.0 μm AuCo / 3.1 μm Ni coated contacts. Current: 0.1 – 35 A. Contact force: 10 N.

3.3.6 Measurements with tin-coated contacts and stranded wires

According to the results for solid conductors, also for stranded wires the initial values for tin-coated contacts (Fig. 22 and Fig. 23) are much lower than for gold-coated contacts (Fig. 21 and Fig. 22). The contact resistance decreases with time at ambient temperature (Fig. 22). The average final value is 60 % (0.58 mOhm) of the initial value (0.96 mOhm). It appears that in the tests carried out at ambient temperature (Fig. 22) there was no strong reorientation of the individual strands, since the curves are smooth.

At elevated temperatures (Fig. 23) the average contact resistance at maximum temperature is 60 % (0.52 mOhm) of the initial value (0.86 mOhm) and 68 % of the value at a temperature of 30 °C (0.77 mOhm). The change in resistance due to the effect of temperature hardly differs from the change at ambient temperature (Fig. 22). Because the tin layer may “clean” the contaminated copper wires, the temperature influence is significantly less pronounced than with a gold coating (Fig. 21). With gold-plated contacts the current heating in turn leads to a displacement of the foreign layers from the contact area.

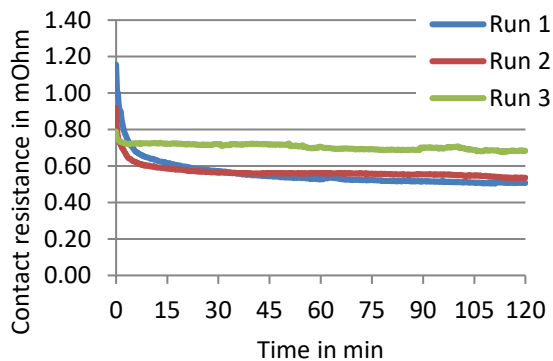


Fig. 22 Test results for stranded and crimped copper wires (6 mm²) with 8.2 μm Sn (matte) coated contacts. Current: 0.1 A. Contact force: 10 N.

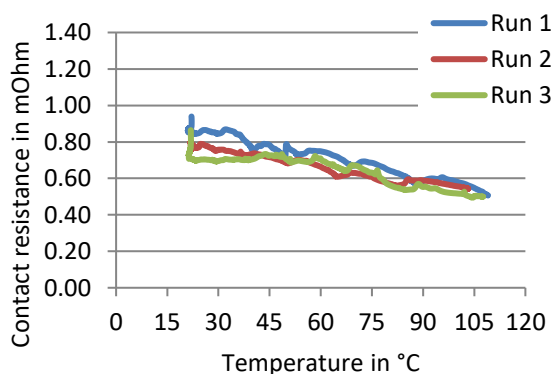


Fig. 23 Test results for stranded and crimped copper wires (6 mm²) with 8.2 μm Sn (matte) coated contacts. Current: 0.1 – 35 A. Contact force: 10 N.

4 Summary

It could be shown for connector contacts that the contact resistance decreases significantly with increasing temperature (Fig. 9-11). In the case of tin coatings, the oxide layer must be taken into account. If the oxide layer is not initially penetrated by wear or high contact forces, the drop in contact resistance is particularly strong. The decrease in contact resistance can be explained by the fact that the hardness of the coating material decreases (Fig. 1). The test results could be confirmed by calculations (Tab. 3). The calculations could be improved by taking into account the temperature-dependent specific electrical resistance of the coating material and the change in the layer thickness.

In addition, tests for the contact resistance at wire connections were carried out (Fig. 12-23). Tin-coated contacts show significantly lower initial values at ambient temperature for uncleaned solid and stranded conductors. With gold-coated contacts and uncleaned conductors, the temperature-dependent drop in contact resistance is particularly pronounced. The foreign layers on the copper conductor presumably have a particularly strong effect and there may be an interaction between the foreign layer and the coating. In order to better understand the temperature-dependent effects, further investigations are needed.

5 Literature

- [1] R. Holm: Electric Contacts, Springer-Verlag Berlin Heidelberg, 1967 (reprint 2000).
- [2] H. D. Merchant et al.: Hardness-temperature relationships in metals. *Journal of Materials Science*, Volume 8, 1973, pp. 437-442.
- [3] V. V. Merie et al.: Atomic force microscopy analyses on metallic thin films for optical MEMS. 5th International Conference on Powder Metallurgy & Advanced Materials, Cluj-Napoca, Romania, 2017, pp. 125-133.
- [4] W. F. Garland: Effect of decomposition products from electrical insulation on metal and metal finishes, *Electrical Insulation Conference*, 1965, pp. 56-60.
- [5] Schneider Electric: Data Bulletin. Oily Residue Found in Electrical Distribution and Control Equipment, Schneider Electric USA, 05/2011.
- [6] T. Dyck, A. Bund: The Influence of Contaminated Copper Wires on the DC Joule Heating of Connectors. *IEEE Xplore digital library*, 2018, pp. 17-23.
- [7] T. Dyck, A. Bund: Influence of the Bead Geometry and the Tin Layer on the Contact Resistance of Copper Conductors. *IEEE Transactions on Components, Packaging and Manufacturing Technology*, Vol. 8 (10), 2018, pp. 1863-1868.

Contact Materials for Electromechanical Devices – Established Technologies and Improvements to Face Future Requirements

Volker Behrens, Doduco Contacts and Refining GmbH, Pforzheim, Germany
BehrensVolker@web.de

Abstract

With electromechanical devices as connectors and switchgear, the contact material used is a crucial component to fulfill technical and commercial requirements. With connectors and switches for information technology, contact surface layers with thicknesses in the μm range are used in very most cases. Due to arcing with switching operations in power engineering applications, thin layers are not sufficient – thus, contact material thicknesses ranging from some hundred μm up to some cm are applied. The present paper gives an overview regarding different contact material families for power engineering as silver/nickel, silver/refractory, copper/tungsten, silver/metal oxide, and silver graphite, including the different physical mechanisms leading to their specific switching behavior. On the background of climate change and measures to reduce greenhouse gas emissions, the generation and use of electrical power undergo remarkable changes. Thus, switching devices have to meet modified or new tasks as switching of highly energy-efficient electric motors, more demanding DC applications, and combinations of electromechanical and solid-state switching devices. This paper discusses possible consequences for contact materials to fit better to these changing requirements.

1 Introduction

Electromechanical switching devices have to manage different tasks – in the closed condition, they have to carry the current, they open the electric circuit with a break operation, ensure galvanic isolation between the voltage source and load in off state, and close the electric circuit with a make operation.

Switching for power engineering is associated with the formation of arcs on make and break. There is a remarkable diversity of switching devices in the field as contactors, relays, disconnectors, load switches, or circuit breakers. They are designed for specific needs in the transmission, distribution, or use of electrical energy. Their design is tailored to meet the requirements of the electric circuit defined by the main parameters voltage (AC or DC, rated voltage, and surge), current (on make, rated current, break current, overcurrent, and short circuit current), and AC power factor or DC time constant. From the application side and the standards there are additional requirements as frequency of operations, service life, environmental conditions, and legal restrictions.

Accordingly, there are various contact materials with tailored properties to fulfill these devices' specific tasks in their appropriate applications. [1, 2, 3]

With the very most low voltage power engineering switching devices the contact system works in ambient air. Additionally, the contact system has to manage make and break operations with arcing, current conduction in the closed condition, and insulation in open

condition. In other words, contact tips are exposed to oxygen from the ambient air, to elevated temperatures in the a-spots during steady state current, and to high temperatures due to arcing causing melting, splashing, and evaporation of contact material on make as well as on break operations.

Silver (Ag) is a primary compound for electrical contacts because of its excellent electrical conductivity combined with its precious metal property resulting in no formation of stable silver oxide layers during switching operations in the air.

But pure silver and silver alloys show disadvantages especially with arcing contacts:

- silver is soft. Thus the mechanical impact on make operations can cause severe deformation.
- due to the low viscosity of the molten silver and silver alloys droplets can be splashed easily, resulting in high material loss and thus reduced service life
- arcing on make due to bouncing or pre-ignition can cause severe contact welding

To solve these disadvantages, dispersion of non-soluble particles in the silver or silver alloy matrix as a second phase is commonly applied. Due to dispersion hardening, these particles increase the hardness of the contact material as manufactured as well as after arcing, they increase the viscosity of the molten contact surface by the action of the arc, and they reduce the forces required to break sticking contacts due to embrittlement of the contact material.

A wide variety of dispersion particles are used as additives to silver to tailor contact materials (CM) to fulfill specific requirements in switching applications. Among them are metal particles as nickel (Ni), tungsten (W), or molybdenum (Mo), oxide particles as tin oxide (SnO₂), zinc oxide (ZnO) or cadmium oxide (CdO), carbide particles as tungsten carbide (WC) or molybdenum carbide (Mo₂C), and carbon (C) in different allotropes. As a consequence of their physical and chemical properties at temperatures present at the arc foot points, their reactions with the ambient air and molten silver, their interaction with the switching arc, and other properties, a wide variety of silver-based heterogeneous contact material is achieved.

The composite contact material families in the field of low voltage power engineering are

- Silver / Nickel (Ag/Ni)
- Silver / Tungsten (Ag/W) and Silver / Tungsten Carbide (Ag/WC)
- Silver / Metal Oxide (Ag/MeO):
 - Silver / Tin Oxide (Ag/SnO₂)
 - Silver / Zinc Oxide (Ag/ZnO)
 - Silver / Cadmium Oxide (Ag/CdO)
- Silver / Graphite (Ag/C)
- Silver with combinations of additives, e.g., Ag/WC/C, Ag/Ni/C

In addition, in low voltage applications with pretravel contact systems tungsten-based contact materials as pure tungsten or tungsten/copper (W/Cu) can be used [4].

To prevent global climate change from reaching tipping points, it needs to substantially reduce anthropogenic carbon dioxide (CO₂) emissions [5]. Measures required include the transformation of electrical power generation from power plants using fossil fuels to renewable power production as photovoltaic (PV) and wind turbines, increased efficiency in power transmission and power consumption, and reduction of CO₂ emissions with industrial production, mobility, and heating.

The task of decarbonization will expand electricity's role in our lives as we see it for example with e-mobility, PV, and local DC networks. These changes require overall a huge amount of innovations and optimizations - including switching devices.

This paper deals with the question whether these changes can affect the use of state-of-the-art contact materials and trigger further development.

2 Contact Materials (CM)

Powder metallurgy (p.m.) techniques are applied to manufacture very most heterogeneous contact materials [6]. There different technologies starting with powder production, powder conditioning, blending techniques, and compaction to manufacture the CM.

With silver/metal oxide CM, there is an additional production technique based on internal oxidation (i.o.) of non-precious additives in silver alloys [7, 8, 9].

2.1 Silver / Nickel (Ag/Ni)

For most switching applications exceeding currents in the range of 5 A fine silver or silver alloys as fine-grain silver (AgNi 0,15) are not recommended because of contact sticking on make. To overcome this issue Ag/Ni CM is a well-established solution for switching currents in the range of 5 to 200 A.

Ag and Ni are two metals with very low mutual solubility in solid state and a clear difference in melting temperature (Ag: 962 °C, Ni: 1455 °C) [10]. Under arcing conditions this difference leads to solid Ni particles dispersed in the molten silver pool in a wide temperature range. This mechanism increases the viscosity of the melt and in turn, reduces contact material losses.

The other important mechanism with Ag/Ni contact material is related to the constitution of the phase diagram Ag and Ni, see fig. 1. While the maximum solubility of Ni in solid Ag is limited to 0.15 % by weight (wt.%), the solubility of Ni in molten Ag increases with temperature as shown in the Ag-Ni phase diagram (fig. 1, phase L₂ indicated by a circle).

As the maximum temperature of molten silver is limited by boiling (2212 °C), it can be estimated that the maximum solubility of Ni in molten silver is in the range of 15 wt.%.

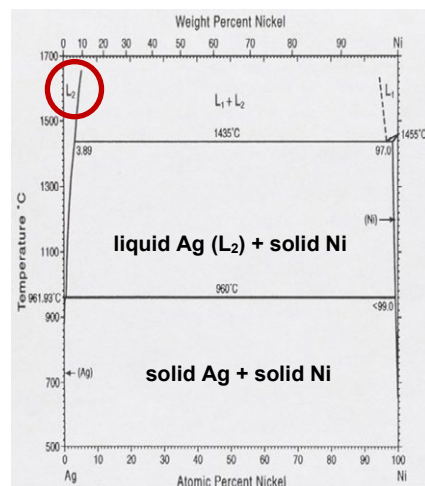


Fig. 1 Phase diagram of Silver – Nickel [10]

The p.m. manufacturing technique most applied for Ag/Ni contact material is blending Ag and Ni powders, followed by compaction of a billet and extrusion to get a wire or a strip [11, 12]. This deformation leads to an elongation of Ni particles to Ni fibers and thus to anisotropic microstructure of Ag/Ni.

For that, it is needed to differentiate Ag/Ni CM properties depending on the orientation of said Ni fibers relative to contact tip surface (parallel (||) or perpendicular (⊥)).

Fig. 2 and 3 show etched microsections of Ag/Ni10 after electrical test in a model switch (1000 break operations, $I=115A$, $U=230V$ AC) with Ni fiber orientations \perp and \parallel respectively [11]. Switching surface and thus the thermal impact of the arc is on top, numbers indicate different areas: (1) material as manufactured; (2) material next to switching surface molten by the arc and re-solidified; (3) Ni fibers due to extrusion process.



Fig. 2 Microsection of Ag/Ni 10 \perp after model switch test [11], for details refer to the text.

It is interesting to see that with extrusion direction \perp the Ni fibers stay rooted in the solid matrix while the top protrudes into the melt. This slows down the solution of Ni in the Ag melt while Ni fibers with extrusion direction \parallel (fig. 3) are easily stirred in the melt and solved. Moreover the difference in Ni content solved in liquid Ag affects the directional re-solidification: there are columnar Ag crystals with fig. 2 while Ag grains in fig.3 are more irregular.

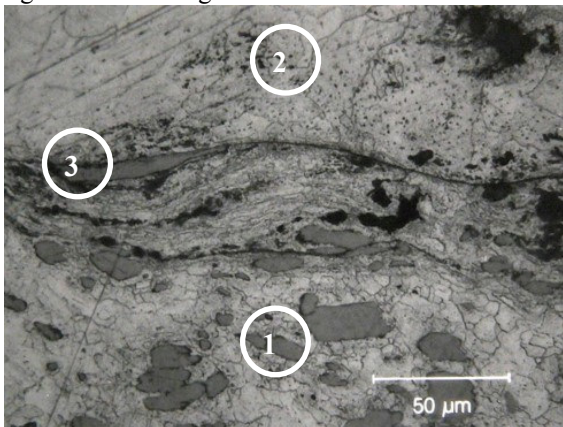


Fig. 3 Microsection of Ag/Ni 10 \parallel after model switch test [11], details see text

After the extinction of the arc the molten contact material cools down rapidly with the precipitation of fine Ni particles. As Ni is a non-precious metal and switching occurs in ambient air, Ni particles oxidize and form NiO particles. This leads to some increase in contact resistance [11, 12] with service life.

Increasing the Ni content in Ag/Ni exceeding 10 wt.% leads to changes in electrical properties. Ag/Ni15 shows only a slight increase in contact resistance but

advantages with erosion and welding forces, while further increase leads to substantially higher contact resistances [13]. Increasing Ni content to 20 wt.% or more has a severe impact on contact resistance. Molten silver cannot solve all of the Ni. Consequently, the formation of larger Ni (and after oxidation NiO) areas and NiO surface layers appear as shown in Fig. 4.

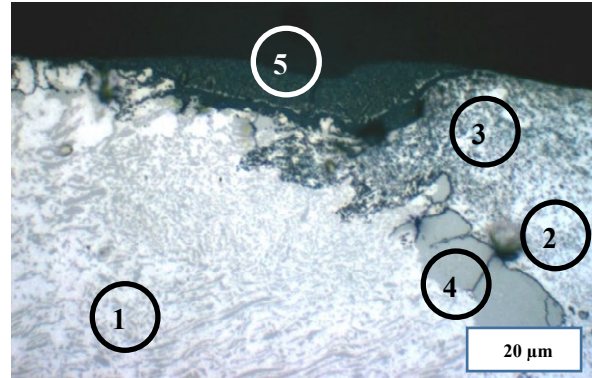


Fig. 4 Microsection of Ag/Ni 20 \parallel after service life test (fluorescence lamp load) in a wall switch [14].

- (1): Ag/Ni20 material as manufactured
- (2): molten material with Ni precipitation
- (3): as (2) with subsequent oxidation of Ni
- (4): Ni area due to Ni content exceeding the solubility limit
- (5): NiO layer at the contact surface

Typical Ag/Ni 10 to Ag/Ni 20 contact material applications are relays, switches, and small contactors with rated currents up to app. 10 to 20 A. The limiting switching property of Ag/Ni contact material at higher currents is sticking forces exceeding the device's opening forces.

Application of Ag/Ni with Ni contents in the range of 30 to 40 wt.% is in circuit breakers as mating contact materials to Silver/Graphite (Ag/C).

From the commercial side Ag/Ni contact material has the advantage of good workability and can be brazed or welded directly to contact carriers [3].

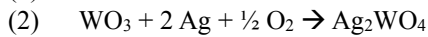
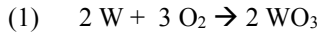
To reduce the welding force of Ag/Ni CM for relay or small switches to a certain extent, a small amount of graphite in the range up to 0.5 wt% can be added.

2.2 Silver / Tungsten (Ag/W)

As with Ag/Ni CM, silver/tungsten (Ag/W) uses metal as an additive to improve the switching properties of pure silver. But comparing Ag/W with Ag/Ni there are three essential differences.

- a. Ag and W have no mutual solubility, neither in solid nor in liquid phase [10].
- b. The melting temperature of W (3422 °C) exceeds the boiling temperature of Ag (2212 °C) [15] by far.
- c. As Ni, W is oxidized in the air. But in contradiction to NiO, tungsten oxide (WO_3) continues to react with Ag and O forming silver

tungstates [16].



These differences between Ag/Ni and Ag/W result in remarkable differences in switching behavior.

With that, the arc burning on the contact surface leads to boiling Ag while W is still solid. Because boiling is a process consuming most of the arc foot energy, W is cooled and thus protected from severe erosion in the initial erosion phase. This mechanism leads to low contact erosion rates of Ag/W contact materials even at high short circuit currents [17].

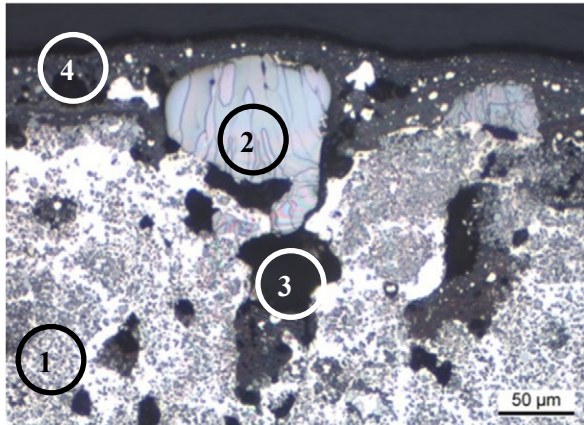


Fig. 5 Microsection of Ag/W 50 contact material after 7000 operations (200 A at 230 V AC) [18]

- (1) Ag/W 50 as manufactured
- (2) pure W, molten and re-solidified
- (3) remaining porosity from boiling silver
- (4) surface layer of WO_3 and silver tungstates

Fig. 5 shows this surface layer formation.

Despite WO_3 loss due to evaporation caused by its high vapor pressure, silver tungstate formation leads to heavy non-conductive surface layers after arcing and is responsible for high contact resistance.

The effect of tungsten cooling by boiling matrix metal without additional oxidation can be observed with tungsten/copper (W/Cu) contact material when used under a protective atmosphere as sulfur hexafluoride (SF_6). The primary erosion mechanism is quite similar to Ag/W as the boiling temperature of copper (app. 2400°C) is also substantially below the tungsten's melting temperature [19]. Fig. 6 shows a microsection of W/Cu25 after short circuit arcing in a High Voltage Circuit Breaker (HVCB). Note the dense tungsten surface layer caused by a small Ni additive in this W/Cu CM facilitating W particles' sintering.

Typical applications of Ag/W with W contents ranging from 40 to 80 wt.% are different types of low voltage circuit breakers.

The manufacturing technique for Ag/W material is p.m. of individual tips based on blending, pressing a green, sintering, and subsequent infiltration with silver. Several countermeasures are in the field to overcome high contact resistance and associated high over-temperatures under steady state current conditions.

These are from the breaker design side sufficient high contact forces, high mechanical impact on make and sliding movement during make operation to break the brittle non-conductive surface layers.

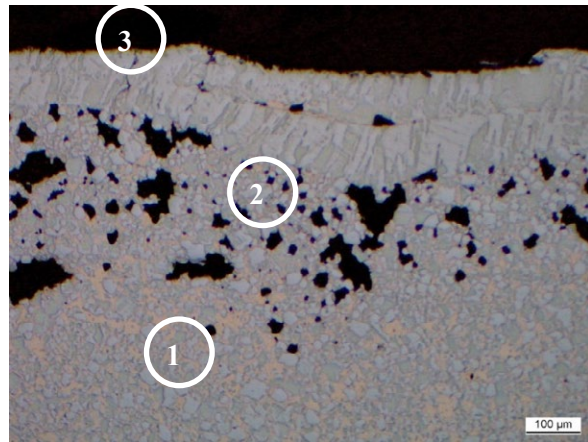


Fig. 6 W/Cu 25 after short circuit arcing in a HVCB with SF_6 atmosphere.

- (1) W/Cu contact material as manufactured
- (2) high porosity area due to partial evaporation of Cu, the remaining W forms a skeleton
- (3) W surface layer formed by W melting and re-solidification after evaporation of most of Cu at the very surface

An asymmetric contact material combination with silver/graphite (Ag/C) on the stationary contact is also often applied.

Using silver/tungsten carbide (Ag/WC) instead of Ag/W leads in many applications to reduced contact erosion, especially with high short circuit currents. WC grain size and additives like Fe, Co, and Ni are important factors to optimize Ag/WC contact material. Manufacturing and joining techniques of Ag/WC are basically the same as with Ag/W [20].

Contact material somehow between Ag/WC and Ag/C are combinations of all three components: silver / tungsten carbide / graphite (Ag/WC/C) [21]. Due to the graphite content, neither the process step infiltration nor direct welding or brazing to the contact carrier are possible. Thus manufacturing technique is a two-layer contact tip with a silver backing. After blending the compounds Ag + WC + graphite, the two-layer green is pressed (die compaction), followed by sinter and re-press steps.

Despite substantial differences in switching properties arc erosion and contact resistance, the two silver/metal contact materials Ag/Ni and Ag/W have a similar issue: a limited resistance against sticking and welding.

Especially with Ag/Ni in contactors, relay, and switches sticking and welding defines the application limit with higher currents and triggers to step forward to another family of contact materials: silver plus metal oxide.

2.3 Silver / Metal Oxide

With relay, switches, and contactors designed for rated currents exceeding 20 A and switching currents exceeding 200 A, using Ag/Ni contact material is often not possible due to sticking forces between contacts caused by make operation. For these applications, silver with metal oxide additives is used widely. Metal oxides added are tin oxide (SnO_2), zinc oxide (ZnO), cadmium oxide (CdO), and more seldom Fe_2O_3 .

Among the silver/metal oxide contact material family, the replacement of Ag/CdO for environmental reasons is a long-lasting story since the 1970s. While most of Ag/CdO has been substituted in Europe, it is still used in Asia and the Americas [8, 22].

Particles from metal oxides mentioned above are hard, brittle, and not soluble, neither in solid nor in molten silver. Compared to silver/metal contact material, the adhesion forces between silver matrix and oxide particle are lower, leading to embrittlement of silver/metal oxide composite material. As a consequence, opening forces required to break welded contacts are reduced. This mechanism allows higher make currents for a given switch design with silver metal oxide contact material instead of Ag/Ni.

On the other hand, oxide particles' behavior in the molten silver pool during arcing needs special attention. The main influencing properties of oxide particles are thermal stability, decomposition and evaporation temperature, wettability by molten silver, and the tendency for oxide agglomeration and coagulation forming oxide layers in or on the contact surface after arcing.

To prevent oxide agglomeration, the formation of oxide layers and associated oxide depleted regions at contact surfaces after arcing a sufficient wettability of oxide particles by molten silver is required. Especially for Ag/ SnO_2 contact material, various oxide additives such as CuO , MoO_3 , WO_3 , Bi_2O_3 , and Ag_2MoO_4 are applied to ensure good contact properties [23, 24, 25]. For DC applications, two other switching properties are essential: low DC material transfer [26] and good arc running behavior [27, 28].

While most Ag/ SnO_2 materials are manufactured by p.m. technique applying extrusion to get strip or wire material also die compaction is in the field. With this technique, sintering additives can contribute to gain sufficient final density [29].

To braze or weld silver/metal oxide tips on a contact carrier, a silver underlayer is required. With extruded material, this underlayer can be applied by cladding or co-extrusion, with die-compaction two-layer press-sinter-repress technology is used.

Applying die compaction enables Ag/ SnO_2 material with higher total oxide contents compared to extruded Ag/ SnO_2 . Ag/ SnO_2 with oxide contents exceeding 20 wt.% leads to CM with low welding forces suitable for CB applications [18].

Silver zinc oxide (Ag/ ZnO) material is used for smaller switches as wall switches. As with Ag/ SnO_2 , additives can be used to tailor Ag/ ZnO switching properties [14]. Oxide particles in the silver matrix in the 100 nm and below size range are gained by applying the internal oxidation technique instead of p.m. . To make this process work, in most cases the addition of indium is needed leading to a final composition Ag/ $\text{SnO}_2/\text{In}_2\text{O}_3$. Compared to p.m. Ag/ SnO_2 i.ox. material can show advantages with inductive automotive DC loads [9].

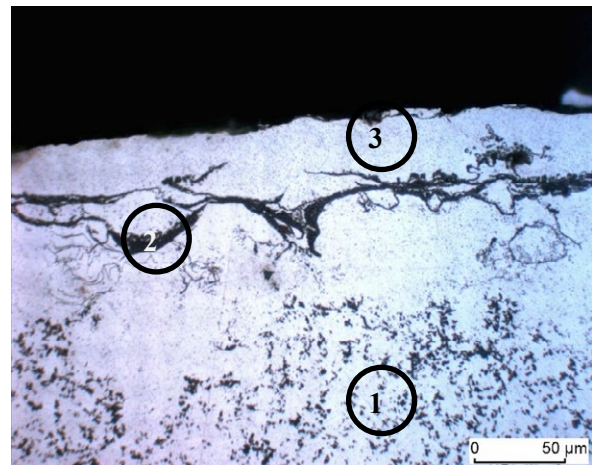


Fig 7 Microsection of Ag/CdO 10 contact material after 100 operations at 1460 A / 115 V AC revealing the formation of oxide agglomeration due to arcing [30]

(1) contact material as manufactured ..(2) oxide agglomeration (3) oxide depleted region

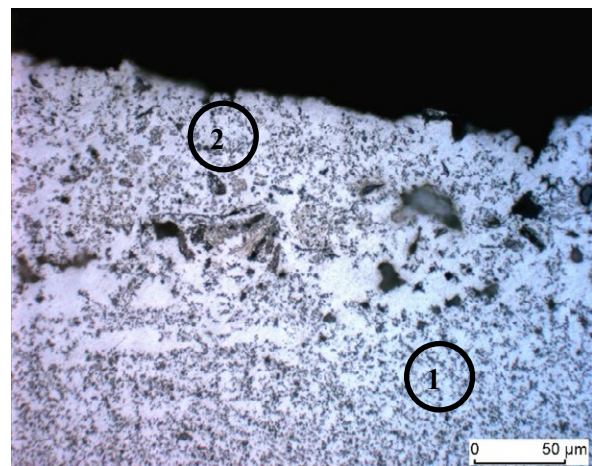


Fig 8 Microsection of Ag/ SnO_2 12 with Ag_2MoO_4 additive with stable microstructure at the surface after arcing, same conditions as fig. 7 [30].

(1) contact material as manufactured (2) contact surface region after melting and re-solidification

Limitation for silver/metal oxide contact material in regard to make currents is typically in the range of 5 to 8 kA. Thus especially for circuit breakers, as molded case circuit breaker (MCCB) contact material with better resistance against contact welding is required.

2.4 Silver / Carbon (Ag/C)

Silver with carbon addition is a family of contact materials tailored for applications in circuit breakers with safety functionality. With these switching devices as MCB, MCCB, and RCCB, welding of contacts is inadmissible. Thus contact material with the lowest welding forces is needed. Due to nihil adhesion forces between solid silver and carbon and no carbon wetting by molten silver, Ag/C is a brittle material with low hardness.

As carbon has different allotropes as charcoal, coal, carbon black, natural and artificial graphite, carbon and graphite fibers, carbon nanotubes (CNT), and graphene, there are many different species of Ag/C contact material in the field [31].

2.4.1 Silver / Graphite

In most commercial Ag/C contact material, graphite or mixtures of different graphite types are used [32].

The excellent low welding forces are attributed to the material as manufactured and become even better after arcing in air. The reasons are chemical reactions of C with oxygen (O₂) and nitrogen (N₂) leading to C particles burn out. These reactions lead to gaseous reactants as CO and CO₂ blowing out of the contact surface. Thus the remaining Ag/C surface after arcing consists of pores and pure silver [33, 34]. This mechanism leads to very low welding forces due to the high porosity in the contact surface and excellent low contact resistances due to soft and pure silver. But this blowout mechanism also causes disadvantages of the Ag/C contact material family. Contact erosion is high leading to reduced service life, and contact material vapor condensation on walls needs countermeasures in device design against low dielectric strength.

Manufacturing technology for Ag/C material is powder metallurgy applying die compaction or, in most cases extrusion technology. As with silver metal oxide CM, Ag/C cannot be brazed or welded directly to a contact carrier. Again an additional back layer of silver is required. Two-layer die compaction, strip surface decarbonization after extrusion, or co-extrusion with Ag/C on a silver backing are wide-spread technologies.

Like Ag/Ni, the extrusion process with Ag/C leads to an elongation of C and Ag particles resulting in anisotropic material and properties.

The formation of porosity in the Ag/C contact surface due to arcing reflects the original grain orientation leading to pore orientation perpendicular (⊥) or parallel (∥) to the contact surface. Figures 9 and 10 show this for silver graphite contact material with 3 wt.% of graphite. Fig. 9 is a microsection of extruded Ag/C contact tips with the extrusion direction perpendicular to the contact surface, and pores accordingly orientated perpendicular to the surface with columns of molten

and re-solidified silver. Silver columns are well attached to Ag/C original material.

Fig. 11 shows a similar situation for extruded Ag/C material with the extrusion direction parallel to the switching surface. Here silver columns and pores are oriented parallel to the contact surface – and with silver columns just slightly connected to the Ag/C original material.

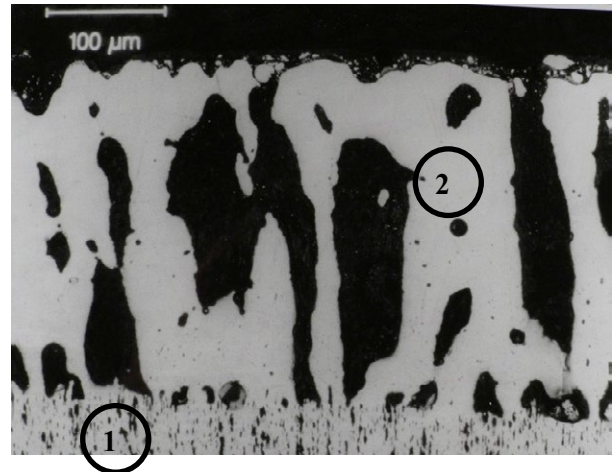


Fig. 9 Microsection of extruded Ag/C 3 after arcing (peak current 1,1 kA, 230 V AC), extrusion direction perpendicular (⊥) to contact surface [35]

- (1) Ag/C contact material as manufactured, tiny black dots are graphite particles
- (2) Contact surface area after arcing with silver columns and pores (black areas between silver columns, filled with plastic mounting material)

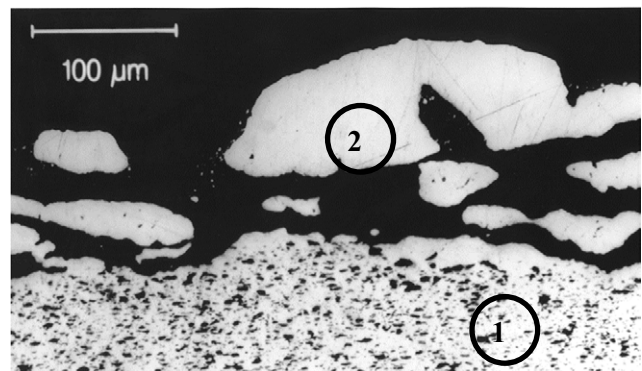


Fig. 10 Microsection of extruded Ag/C 3 after arcing (peak current 1,1 kA, 230 V AC), extrusion direction parallel (∥) to contact surface [35]

- (1) Ag/C contact material as manufactured, tiny black dots are graphite particles
- (2) Contact surface area after arcing with silver columns and pores (black areas between silver columns, filled with plastic mounting material)

As a consequence of these mechanisms, extrusion orientation relative to the switching surface has a substantial influence on the switching behavior of Ag/C material. Ag/C ⊥ has the advantage of lower contact erosion, while Ag/C ∥ has lower welding forces.

C content, allotrope and C particle size, and manufacturing parameters as deformation ratio also substantially influence Ag/C contact performance [31, 36].

As contact erosion of Ag/C is high compared to other CM, Ag/C is often used on the stationary contact in circuit breakers, while for the movable contact more erosion-resistant materials as Ag/Ni, Ag/SnO₂, Ag/W, or Ag/WC are applied.

Fig. 11 shows such an asymmetric contact material combination in an RCCB. Ag/C contact material with its porous surface structure after arcing enabled the CB to break the weld.

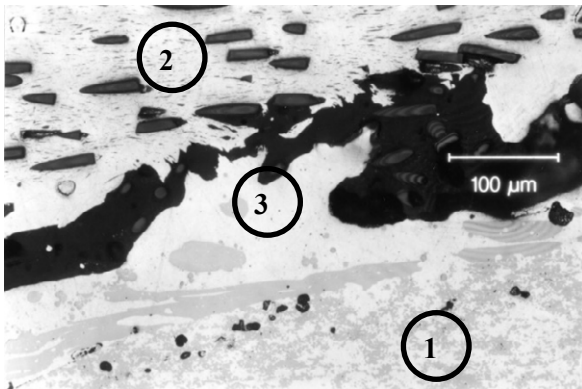


Fig. 11 Microsection of a broken weld in an RCCB after short circuit make test with asymmetric contact material combination [35]

- (1) Ag/Ni40
- (2) Ag/C 3,8, graphite content consists of fine graphite powder and coarse graphite fibers
- (3) Broken weld

2.4.2 Ag/C with CNT and Graphene

With the discovery and technological production of carbon allotropes as carbon nanotubes (CNT) and graphene, these substances gained a lot of R&D attention for electrical and energy-related R&D [37].

The excellent electrical conductivity of CNT and graphene can be an advantage for power engineering electrical contact materials.

Thus, Ag/C material based on or with the addition of CNT or graphene found some attention [31, 38, 39, 40] in the field of arcing contacts. As new research showed improvements to overcome the issue of inhomogeneous distribution of CNT in a metal matrix [41, 42] it will be interesting to see how these allotropes can contribute to Ag/C contact material optimization for commercial applications.

2.4.3 Ag/Ni/C and Ag/WC/C

Three-component contact materials try to combine the specific advantages of binary CM. With the addition of

graphite to Ag/Ni or Ag/WC, the resistance against welding of these materials is reduced substantially, while the contact erosion is reduced compared to the equivalent Ag/C material. Typical applications are MCCB and ACB. Due to graphite content, Ag/WC/C cannot be manufactured by die compaction with subsequent infiltration process as Ag/WC. The typical manufacturing technique of these p.m. composite materials is die compaction with press-sinter-repress operations. A silver backing as a second layer for brazing or welding is needed for these tips.

As with Ag/C and Ag/WC, contact and switching properties can be adjusted by varying powder properties and manufacturing parameters [21].

3 Some ideas on future CM optimizations and developments

State-of-the-art contact materials are highly sophisticated functional materials that fulfill today's requirements for power engineering switching tasks in an excellent way. Nevertheless - contact material development or optimization will continue driven by different tasks as

1. manufacturing cost reduction for CM
2. evaluation of cost reduction potentials from reduced CM silver content
3. Environmental concern and legal restrictions regarding hazardous substances in CM
4. CM optimization to enable cost reduction for the switching device
5. Shifting or new requirements for switching devices due to changing electrical loads and requirements

Topics 1. and 2. are just daily business and are not discussed here.

Topic 3 was an important motivation for CM innovations over the past 30 years to replace Ag/CdO. Today, many commercial and approved Ag/SnO₂ and Ag/ZnO species are well established in the market. Thus no or just minor adaptations are expected in the future.

Reduction of the total cost of switching devices (topic 4) includes decreasing the size while maintaining technical properties as rated current. In turn, overtemperature during steady state current becomes more critical. As the voltage drop over the closed contact is a significant heating source, CM with low/optimized contact resistance while maintaining other required switching properties can lead to advantages.

With topic 5, there are different shifts in the application requirements for switching devices on hand.

For most of them, only little is known up to now regarding the detailed load parameters and requirements. In addition, the performance and possible limitations of

state-of-the-art CM in said applications are to be evaluated.

- a. LED loads
Loads with LED lamps show increased inrush currents leading to higher sticking and welding probabilities of contacts. Details of LED loads in the field show substantial scatter and experience with CM in the market for these applications just started to rise [43].
Silver/metal oxide contact material with reduced welding forces could be advantageous.
- b. A demand for CM with improved anti-welding behavior could also rise for DC-DC power converters.
- c. The use of high-efficiency motors leads to increased inrush currents [44], and therefore could be advantageous for contact materials with reduced welding forces.
- d. Using electromechanical contactors combined with solid-state contactors or variable frequency drives leads to short arcing, especially with break. Thus the contact surface is affected differently compared to conventional motor loads. This difference in arc impact on the contact surface could lead to differences in surface microstructure evolution and could foster CM optimization.
On the other hand, CM erosion could be reduced substantially leading to reduced contact material volumes for these applications.
- e. Increasing use of DC switching devices and DC circuit breakers with voltage up to 1500 V DC will rise the demand for CM with excellent arc running behavior. It is possible that CM with a shorter time of reduced arc motion (TRM) and improved arc running velocity can contribute to decrease DC break arc duration.
- f. The potential of CNT and graphene additives to silver or silver-based CM is not evaluated in depth up to now. It would be interesting to learn whether or not these carbon allotropes can contribute to future improvements of CM.

4 Literature

- [1] P. Slade (ed.), *Electrical Contacts: Principles and Applications*, 2nd edition, CRC Press, Boca Raton, 2014.
- [2] E. Vinaricky (ed.), *Elektrische Kontakte, Werkstoffe und Anwendungen*, 3rd edition, Springer, Berlin, Heidelberg, 2016.
- [3] Doduco GmbH: *Data Book of Electrical Contacts*, 3rd edition, Stieglitz Verlag, Mühlacker, 2012.
- [4] E.Johansson, A.Andersson, G.Johansson, and M. Johansson: ‘Breaking Performance of a Novel DC Contactor’, Proc. 29th ICEC, Albuquerque, 2018, pp. 483-487.
- [5] Intergovernmental Panel on Climate Change (IPCC): 5th Assessment Report (2013/2014), 5th AR, Synthesis Report (2014)
https://www.ipcc.ch/site/assets/uploads/2018/02/SYR_AR5_FINAL_full.pdf
5th AR, WG 1: The Physical Science Basis (2013)
https://www.ipcc.ch/site/assets/uploads/2018/02/WG1AR5_all_final.pdf
- [6] V.Behrens and W.Weise, Contact Materials, in: Landolt-Börnstein, Group VIII, Vol. 2, Subvol. A, Part 1: Metals and Magnets, Springer Verlag, Heidelberg, Berlin, 2003, pp. 10-1 – 10-29.
- [7] A. Shibata, “Silver-Metal Oxide Contact Material by Internal Oxidation Process,” Proc. 7th ICEC, Paris (1974), pp 214-220.
- [8] Ch.Leung and V.Behrens: ‘A review of Ag/SnO₂ Contact Material and Arc Erosion’, Proc. 24th ICEC, St.Malo (2008), pp. 82-87.
- [9] O.Lutz, V.Behrens, S.Franz, Th.Honig, J.Heinrich, I.Aichele. and B.Benedikt, Silber/Zinnoxid-Kontaktwerkstoffe auf Basis der inneren Oxidation für AC- und DC Anwendungen, VDE-Fachbericht **65**, VDE Verlag, 2009, pp. 167-176.
- [10] T.B.Massalski (ed.): *Binary Alloy Phase Diagrams*, II Ed., 1990, 1.
- [11] V.Behrens, R.Michal, N.Minkenber, K.E.Saeger, B.Liang, and W.Zhang: Erosion Mechanisms of Different Types of Ag/Ni 90/10 Materials, Proc. 14th ICEC, Paris (1988), pp. 417-422.
- [12] V.Behrens, R.Michal, J.N. Minkenber, and K.E. Saeger: Abbrand und Kontaktwiderstandsverhalten von Kontaktwerkstoffen auf Basis von Silber-Nickel, *e&i* **107** (1990), pp. 72-77.
- [13] H.Wang and H.Yuan: ‘Investigation on the Electrical Properties of AgNi Contact Materials with Various Ni Content’, Proc. 63rd IEEE Holm Conf., Denver (2017), pp. 221-224.
- [14] O.Lutz, V.Behrens, M.Finkbeiner, Th.Honig, and D.Späth: ‘Ag/CdO-Ersatz in Lichtschaltern’, VDE Fachbericht **61** (2005), pp. 165-173.
- [15] W.M.Haynes (ed.): *Handbook of Chemistry and Physics*, 95th Edition, CRC Press, Boca Raton, London, New York, 2014.
- [16] P.Slade, “Variations in Contact Resistance Resulting from Oxide Formation and Decomposition in Ag-W and Ag-WC-C Contacts Passing Steady Currents for Long Time Periods”, Proc. 31st IEEE Holm Conf., Boston (1985), pp. 3-17.
- [17] Walczuk, E., Borkowski, P., Kaliszuk, K. and Frydman, K.: “Effect of composition and microstructure on the arc erosion and contact resistance of W-Ag composite materials at high currents”, Proc. 20th ICEC, Stockholm (2000), pp. 259-266.
- [18] J.Röhberg, Th.Honig, N.Witulski, M.Finkbeiner, and V.Behrens, Performance of Different Silver/Tin Oxide Contact Materials for Applications

- in Low Voltage Circuit Breakers, Proc. 55th IEEE Holm Conf., Vancouver (2009), pp. 187-194.
- [19] J.Tepper, M.Seeger, T.Votteler, V.Behrens, and Th.Honig: Investigation on Erosion of Cu/W Contacts in High Voltage Circuit Breakers, IEEE Trans. CPT, vol. 29 (2006), pp. 658-665.
- [20] T.Mützel, B.Kempf: ‚Neue Erkenntnisse zum Schaltverhalten von SilberWolframkarbid Kontaktwerkstoffen‘, VDE Fachbericht **69**, VDE Verlag, Berlin, 2013, pp. 35-42.
- [21] S.Allen, E.Streicher, C.Leung: Electrical Performance of Ag-W-C and Ag-WC-C Contacts in Switching Tests, Proc. 20th ICEC, Stockholm (2000), pp. 109 - 114.
- [22] V.Behrens, Th.Honig, O.Lutz, and D.Späth: Substitute Contact Material for Silver/Cadmium Oxide in AC Applications in the Low Current Range, Proc. 23rd ICEC, Sendai (2006), pp. 294-299.
- [23] Bourda C; Jeannot D; Pinard J; Ramoni P.: Properties and Effects of Doping Agents used in AgSnO Contact Materials, Proc. 16th ICEC, Loughborough (1992), pp. 377-382.
- [24] F. Heringhaus, P. Braumann, A. Koffler, E. Susnik, and R. Wolmer, “Quantitative Correlation of Additive Use and Properties of Ag-SnO₂-based Contact Materials“, Proc. 21st ICEC, Zürich (2002), pp. 443-446.
- [25] A. Koffler, P. Braumann, B. Kempf, “The influence of manufacturing process, metal oxide content, and additives on switching behavior of Ag/SnO₂ in DC- and AC relays (2)”, Proc. 23rd ICEC, Sendai (2006), pp. 288-293.
- [26] Th.Schöpf, V.Behrens, Th.Honig, and A.Kraus: ‘Substitute for Palladium Copper in DC Flasher Relay’, Proc. 48th Int. Relay Conf., Lake Buena Vista (2000), pp. 5.1 – 5.6 .
- [27] H.Manhart, W.Rieder, and C. Veit: ‘Arc Mobility on New and Eroded Ag/CdO and Ag/SnO₂ Contacts’, Proc. 34th IEEE Holm Conf., San Francisco (1988), pp. 47-56.
- [28] M.Ommer, U.Klotz, D.Gonzales, F.Berger, and B.Wielage: ‘Arc behaviour and material deterioration of silver based composites used for electrical contacts’, Proc. 56th IEEE Holm Conf., Charleston (2010), pp. 494-503.
- [29] E.Streicher, C.Leung, R.Bevington, and S.Allen: Press-Sinter-Repress Ag/SnO₂ contacts with Lithium and Copper Sintering Additives for Contact Applications, Proc. 47th IEEE Holm Conf., Montreal (2001), pp. 27-34.
- [30] C.Bernauer, T.Kuntze, V.Behrens, T.Honig: Substitution of Silver/Cadmium Oxide in High Voltage Disconnectors, Proc. 51st IEEE Holm Conf., Chicago (2005), pp. 42 – 47.
- [31] P. Borkowski, E. Walczuk, D. Wojcik-Grzybek, K. Frydman, D. Zasada: Electrical Properties of Ag-C Contact Materials Containing Different Allotropes of Carbon, Proc. 56th IEEE Holm Conf., Charleston (2010), pp. 167-175.
- [32] V.Behrens, T.Honig, A.Kraus, E.Mahle, R.Michal, K.Saeger: Test Results of Different Silver/Graphite Contact Materials in Regard to Applications in Circuit Breakers, Proc. 41st IEEE Holm Conf., Montreal (1995), pp. 393–397.
- [33] E.Vinaricky and V.Behrens, Switching Behavior of Silver/Graphite Contact Material in Different Atmospheres in Regard to Contact Erosion, Proc. 44th Holm Conf., Arlington (1998), pp. 292-300.
- [34] E.Vinaricky and V.Behrens, “Welding Behaviour of Closed Contact Material Combinations of Silver/Graphite against Copper with and without Electrodynamic Lift off in Different Atmospheres”, Proc. 19th ICEC, Nürnberg (1998), pp. 301-305.
- [35] V.Behrens, Silber/Nickel und Silber/Grafit – zwei Spezialisten auf dem Gebiet der Kontaktwerkstoffe, METALL **61** (2007), pp. 308-312.
- [36] T.Mützel and R.Niederreuther: Development of Contact Material Solutions for Low-Voltage Circuit Breaker Applications (2), Proc. 57th IEEE Holm Conf., Minneapolis (2011), pp. 117-122.
- [37] Rdest, M. and Janas, D.: Carbon Nanotube Films for Energy Applications. Energies **2021**, 14, 1890. <https://doi.org/10.3390/en14071890>
- [38] J.Jačimović, L.Felberbaum, E.Giannini, and J.Teyssier: Electromechanical properties and welding characteristics of Ag/MoS₂, Ag/WS₂, Ag/CNTs and Ag/CdO materials for high-DC current contact applications, Proc. 27th ICEC, Dresden (2014), pp. 132-137.
- [39] P.Wang, Z.Wei, M.Shen, H.Pan, J.Fu, and L.Chen: In-situ Synthesized Silver-graphene Nanocomposite with Enhanced Electrical and Mechanical Properties, Proc. 63rd IEEE Holm Conf., Denver (2017), pp. 225-228.
- [40] H.Chen, P.Weng, and J.Hernandez: Study of Silver-graphene Tungsten Material For Low Voltage Electrical Contact, Proc. 65th IEEE Holm Conf., Milwaukee (2019), pp. 142-148.
- [41] K.Aristizabal; A.Katzensteiner, A.Bachmaier, F.Mücklich, and S.Suarez: Microstructural evolution during heating of CNT/Metal Matrix Composites processed by Severe Plastic Deformation-[www.nature.com/scientificreports/\(2020\)10:857, https://doi.org/10.1038/s41598-020-57946-3](https://doi.org/10.1038/s41598-020-57946-3)
- [42] .S.Suarez, R.Puyol, Ch.Schäfer, and F.Mücklich: Carbon Nanotube-reinforced Metal Matrix Composites as Novel Electrodes for Low-voltage Switching Applications: A Surface Degradation Analysis, Proc. 65th IEEE Holm Conf., Milwaukee (2019), pp. 135-140.
- [43] T.Mützel and Ch.Hubrich: ‘Contact Material Solutions for LED Lamp Applications’, Proc. 64th IEEE Holm Conf., Albuquerque (2018), pp. 159-165.
- [44] A.Krätzschmar: Update der Anforderungen an Motorstarter aus normativer Sicht, VDE Fachbericht **73**, 2017, VDE Verlag, Berlin, pp. 201-216.

The Development of Sputtered Contact Systems Replacing Electroplated Systems in Reed Switch Applications

Philip Lees, Littelfuse, Boston, MA, USA PLees@Littelfuse.com
Eric Hafenstein, Littelfuse, Lake Mills, WI, USA, EHafenstein@Littelfuse.com
Joshua Koeppel, Littelfuse, Lake Mills, WI, USA, JKoppel@Littelfuse.com
Tony Spies, Littelfuse, Lake Mills, WI, USA, TSpies@Littelfuse.com

Abstract

The application of materials to contact areas of reed switches is accomplished by either electroplating or sputtering techniques. In general, electroplated contact materials have been used for higher voltage and higher power (30-100 watts) applications and sputtered coatings for lower voltage and lower power, (5-20 watts) applications. The material stack for electroplated reed switch contacts was a top layer of ruthenium (Ru), an intermediate layer of rhodium (Rh) and a base layer of gold (Au). This base layer of gold is plated from a cyanide bath. Safety, regulatory and environmental concerns, surrounding the cyanide bath prompted the exploration of sputtered material stacks to replace the electroplated stacks. It was found that traditional material stacks of Ru over molybdenum (Mo) could not meet the performance characteristics of the electroplated stack whereas substituting copper (Cu) for gold (Au) showed promising results. The introduction of a Cu base layer under an intermediate Mo layer or directly under a top layer of Ru significantly improved life expectancy for all but the most demanding electrical loads.

Key Words: Reed switch, switching contact materials, electroplating, sputtering

1 Introduction

The components of a reed switch are reeds and a glass tube. The reed is manufactured from a low expansion magnetic alloy integrating the flexing member or web with a solderable lead. The contact material is selectively applied to the contact areas on the tip of the web. A glass enclosure is either evacuated or filled with an inert gas and sealed around the leads. Reed switches are actuated by a magnetic field. Reed switch designs are characterized by narrow contact gaps (5-50 micrometers) and light contact loads. A picture of a reed switch and the details of a reed are shown in **Figure 1**.

The selective application of materials to contact areas of reed switches is accomplished by either electroplating or sputtering techniques. The material stack for electroplated reed switch contacts is a top layer of ruthenium (Ru), an intermediate layer of rhodium (Rh) and a base layer of gold (Au).

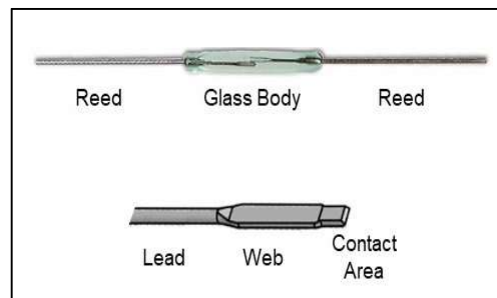


Fig. 1. Reed switch and closeup of a reed.

The plating sequence is gold strike, functional gold, rhodium and ruthenium. The gold strike promotes adhesion of subsequent deposits through prevention of immersion plating. Immersion plated deposits from electrolytic solutions are loosely adhered to the substrate material. The thicker, functional gold layer protects the reed material from corrosive attack by the fumes from the rhodium bath. The rhodium layer provides a hard surface forestalling wear and ruthenium is the contact material.

The material stack for sputtered reed switch contacts is a thin adhesion layer to promote adhesion between the intermediate layer and the reed, intermediate layer and the contact material. A typical stack would be a titanium adhesion layer, a molybdenum intermediate layer and a ruthenium contact layer.

Figure 2 contains representations of the plated and sputtered material stacks.

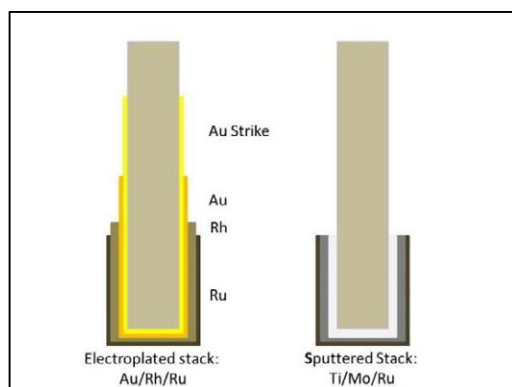


Fig. 2. Representations of plated and sputtered material stacks.

Reed Switches fail in one of two ways: the switch will fail to open when expected (stick) or it will fail to close when expected (miss). For the evaluations conducted in this study, a stick is defined as the voltage across the switch, when it should be open, $\leq \frac{1}{2}$ of the open circuit voltage or 0.7V, whichever is less. A miss is defined as the contact resistance across the switch, when the switch is closed; either 2% of load resistance or 2 Ω whichever is greater [1]. The first failure, stick or miss, for each switch is recorded and then analyzed. To generate acceptable reliability predictions testing is conducted until at least 50% or more of the sample group has failed.

2 Material Design and Sample Preparation

2.1 Material Design

The first stack consideration was the production standard of Ru over Mo. Variations of this stack are used for the preponderance of reed switches produced by Littelfuse. The Ru layer ranges from 0.5 to 1.1 microns and the Mo layer is determined by subtracting the Ru thickness from the required magnetic gap.

A sputtered stack analogous to the electroplated Au/Rh/Ru was developed substituting Cu for Au and Mo for Rh. The primary consideration was improved thermal conductivity for the high-power applications. Individual layer thicknesses from the electroplated Au/Rh/Ru system were mirrored in the sputtered Cu/Mo/Ru stack for the initial screening tests.

Ru only samples, sputtered at various thicknesses were included for both conductivity and durability considerations.

Finally, as a contingency plan, an electroplated, cyanide free Au/Rh/Ru stack was evaluated in case the sputtered systems did not meet the electroplated system parametric and/or expected life requirements.

2.2 Test Vehicles

The test vehicles were production switches with 10 W and 100 W ratings. The switches are structurally and mechanically different. The 10W switch has a beam length of about 7 mm and the length of the glass tube about 20 mm [2]. The 10W switch will close when the applied magnetic field is in the range of 20-25 Ampere-turns (AT). The 100W switch has a beam length of about 19 mm and the length of the glass tube is about 50 mm [3]. The 100W switch will close when the applied magnetic field is in the range of 60-70 AT. Nitrogen was introduced during sealing as the inert gas.

2.3 Sample Preparation

All samples were prepared on production equipment using DC Magnetron sputtering. A KDF Model 954i four target machine was used [4]. Layer thickness was controlled using a calibration program that calculates sputter time based on thickness results from individual targets processed at a specific traverse speed and a defined number of passes. A Bowman model BA100 XRF coating thickness measurement system was used to determine individual layer thicknesses [5]. After sputtering the switches were assembled on automatic assembly machines to the targeted AT values. The glass enclosure was filled with nitrogen during sealing.

3 Results and Discussion

3.1 Life Test Evaluation

Two-parameter Weibull distributions were used to analyze the sample failure data. [6,7] The two parameters obtained from the regression fit are: the Weibull Scale parameter – Eta (η) and the Weibull Shape parameter – Beta (β). The Weibull scale parameter is a measurement of the spread in the distribution of the data analyzed. It is also known as the characteristic life of the data analyzed and corresponds to the time at which 63.2% of the

samples have failed. In this study, the screening criteria for life is the predicted number of cycles at which 10% of the product should fail: **B(10)**. The Weibull shape parameter is a measurement of the slope or failure rate of the data. A slope less than 1.0 indicates that the product has a decreasing failure rate, typical of infant mortality or a product failing during “burn-in” period. A slope equal to 1.0 indicates that the product has a constant failure rate. A slope greater than 1.0 indicates an increasing failure rate, typical of products that are wearing out.

Figure 3 depicts Weibull plots for the 100W switch at rated power. Fig. 3(a) is the plot for the electroplated stack and Fig 3(b) the sputtered stack

The calculated B(10) life for the electroplated stack was 590 cycles and the sputtered stack 9,100. The slope for the electroplated stack is less than one indicating a decreasing failure rate and typical of infant mortality. The slope for the sputtered stack is greater than 1, indicating an increasing failure rate and typical of wear.

3.2 Electrical Test Parameters

Initial life test screening was conducted using 20VDC and 500mA for the 10W switch and 33V DC and 3 A for the 100W switch. All loads, AC and DC were resistive. Littelfuse has found that testing switches at rated power enables the reduction of a large sample matrix to the most promising within a few weeks.

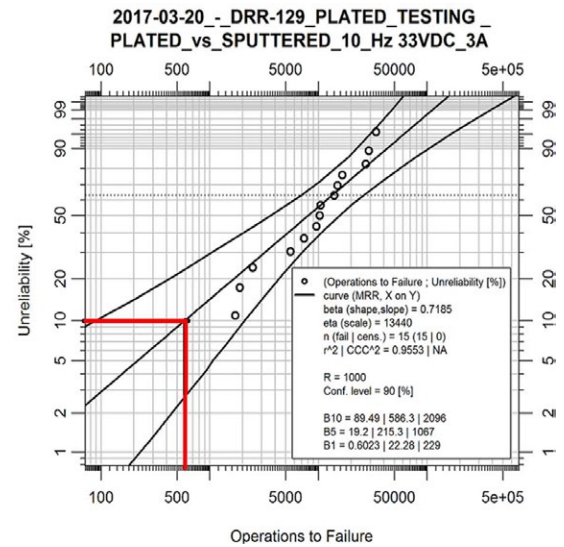
3.3 Life Test Results

The sample matrix consisted of electroplated controls for 10W and 100W switches, Cu-Ru stack for both power ratings, standard Mo-Ru, Ru only and Cu-Mo-Ru for the 10W switch and cyanide free Au electroplated for the 100W switch.

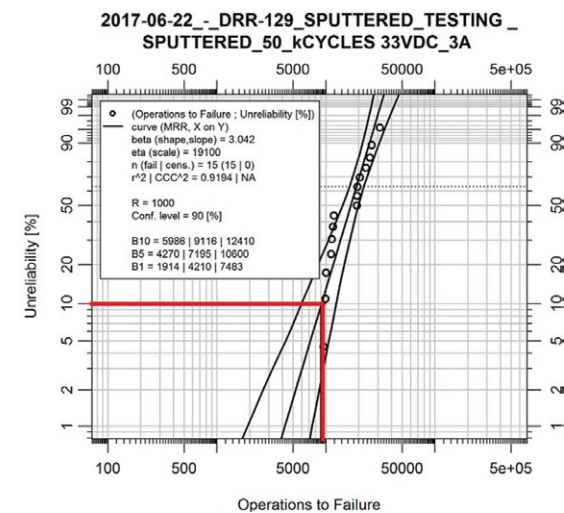
All failures, regardless of stack coating process, were “sticks.” No contact resistance failures were recorded.

The complete sample matrix and life test results are contained in **Table I**. The results in Table I indicate that electroplated coating on the 10W switch has a B(10) life three times that for the best sputtered stacks.

The opposite is true for the 100W switch. The B(10) life of the sputtered stack is nearly three times that of the electroplated stack.



(a) Electroplated



(b) Sputtered

Fig. 3. Weibull plots for 100W switch at rated power. Fig. 3 (a) electroplated stack. B(10) = 590 cycles and $\beta = 0.72$. Fig. 3 (b) sputtered stack. B(10) = 9,100 and $\beta = 3.04$.

Table I. Initial Sample Stacks for Screening.	10 W Switch B(10) Life	100 W Switch B(10) Life
Standard Electroplated: 0.8 μ Au / 1.4 μ Rh / 0.5 μ Ru	3,115,000	
Standard Electroplated: 1.15 μ Au / 1.27 μ Rh / 0.5 μ Ru		3,600
0.08 μ Ti / 2.29 μ Cu / 0.08 μ Ti / 0.5 μ Ru	46,000	10,800
0.15 μ Ti / 1.5 μ Mo / 2.0 μ Ru	650,000	
0.5 μ Ti / 2.5 μ Ru	376,000	
0.5 μ Ti / 3.8 μ Ru	1,042,000	
Cyanide-Free Electroplated: 1.15 μ Au / 1.27 μ Rh / 0.5 μ Ru		12,100*
0.08 μ Ti / 0.66 μ Cu / 0.08 μ Ti / 1.4 μ Mo / 0.5 μ Ru	1,015,000	

*Replicate run failed due to poor adhesion between cyanide free Au and the reed

One of the advantages of the cyanide based Au plating bath is that the cyanide gold strike bath prevents immersion plating and thus promotes excellent adhesion. The cyanide free electroplated system relies on additives to prevent immersion plating. These additives have a limited bath life. The effect of additive bath life manifested during a replicate plating run. The gold would not adhere to the nickel-iron reeds. Consequently, the cyanide free Au electroplated system was eliminated from further consideration.

As stated above, all failures were “sticks.” To combat stickiness, the thickness of web in the 10W switch was increased from 262 microns to 287 microns. This increase in stiffness counters the stick adhesion force opposing the opening the switch. Samples switches with the thicker reed web were manufactured to the specified 20-25 AT range in order to maintain the same contact force. Both the Mo / Ru and Cu / Mo / Ru stacks were evaluated. The life test results are contained in

Table II.

Table II. Modified Beam Sample Stacks for Screening. Web thickness was increased from 262 to 287 microns.	10 W Switch B(10) Life
0.15 μ Ti / 1.5 μ Mo / 2.0 μ Ru	1,279,000
0.08 μ Ti / 0.66 μ Cu / 0.08 μ Ti / 2.0 μ Mo / 0.5 μ Ru	2,988,000
0.08 μ Ti / 0.66 μ Cu / 0.08 μ Ti / 1.4 μ Mo / 1.0 μ Ru	2,589,000

Looking at both Tables I and II reveals some trends for the 10W switch. First, increasing the beam thickness significantly increased mean life. Second, Mo under Ru is more beneficial than just increasing Ru. Finally, Cu under Mo / Ru is more beneficial than just Mo under Ru. Based on the initial results in Tables I and II, additional voltage-current combinations were evaluated for the 0.66 μ Cu / 2.0 μ Mo / 0.5 μ Ru stack and thicker beam for the 10W switch and 2.29 μ Cu / 0.5 μ Ru for the 100W switch. Electroplated switches were run as controls. The material stack for the 10W switch was 0.8 μ Au / 1.4 μ Rh / 0.5 μ Ru and that for the 100W switch was 1.15 μ Au / 1.27 μ Rh / 0.5 μ Ru. Life test results are summarized in **Table III**. Data represent averages of at least 2 runs.

All failures, regardless of stack coating process, were “sticks.” No contact resistance failures were recorded.

3.3.1 10 W Switch Trends

In DC testing the B(10) life for both electroplated and sputtered switches decreased as the voltage increased and current decreased. In general, the characteristic life of electroplated switches exceeded that of sputtered switches. In AC testing, the characteristic life of electroplated switches was an order of magnitude larger than that of the sputtered switches. None the less, the B(10) life of the sputtered switch met design criteria.

Table III. Specified B(10) life targets and calculated results from expanded testing of electroplated and sputtered stacks.					
10W Results	20VDC, 500mA		1000VDC, 1mA	120VAC, 100mA	240VAC, 50mA
Target	$\geq 2,000,000$		$\geq 1,000,000$	$\geq 2,000,000$	$\geq 2,000,000$
Electroplated	2,900,000		1,200,000	24,600,000	14,900,000
Sputtered	2,400,000		868,800	2,800,000	2,400,000
100W Results	33VDC 3A	400VDC 2mA		120VAC 1A	240VAC 200mA
Target	$\geq 9,000$	$\geq 7,000,000$		$\geq 20,000$	$\geq 5,000,000$
Electroplated	590	6,500,000		34,300	5,500,000
Sputtered	9,600	5,600,000		48,600	5,900,000

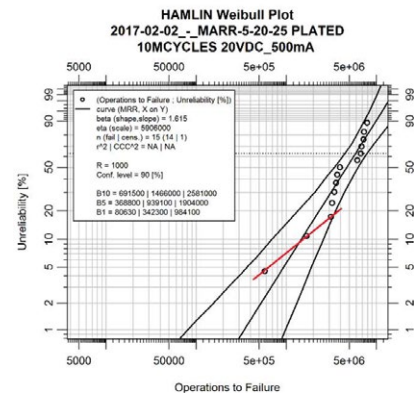
3.3.2 100 W Switch Trends

In DC and AC testing, the B(10) life of the electroplated switches increased as voltage increased and current decreased. A similar trend was observed for the sputtered switches. The B(10) life for the sputtered switches was comparable to that of the electroplated switches. As with the 10W switches, the B(10) life of the sputtered switches met design criteria.

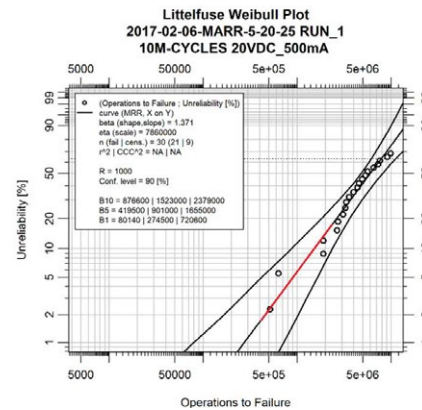
3.3.3 Weibull Slope Features

Figure 4 depicts Weibull plots for the 10W switches tested at 20VDC and 500mA.

The B(10) life for both electroplated and sputtered stacks was approximately 1.5 million cycles. The average slope for the electroplated stack is 1.6 and that for the sputtered 1.4 indicating an increasing failure rate. Closer examination of Fig 4(a) reveals three distinct regions with two different slopes. It appears that the initial slope based on the first three points, is less than one, indicating infant mortality. The slope abruptly changes to a value much greater than one indicating a change in failure mechanism from infant mortality to wear. Conversely, in Fig. 4(b), the data points around the extrapolation line appear to be randomly located above and below the line. The average slope is greater than one, indicating that wear is the primary failure mechanism. A detailed examination of the behavioral differences between electroplated and sputtered stacks is beyond the scope of this paper.



(a) Electroplated



(a) Sputtered

Fig. 4. Typical Weibull plots for 10w switch. Fig. 4 (a) electroplated stack with an initial slope of less than 1 (red line) and Fig. 4 (b) sputtered stack with initial points randomly dispersed around the calculated slope line.

Table IV summarizes the slopes obtained from Weibull plots for both power ratings and coating process.

The data in Table IV indicate that after DC testing the Weibull slopes for electroplated stacks are less than those for the sputtered stacks. Further, the slopes for both coating technologies decreased as the voltage increased. After AC testing, the Weibull slopes for both electroplated and sputtered stacks increased as the voltage increased. The proportional increase for the electroplated stacks was much larger than that for the sputtered stacks; 10W switch, 3.1 for the electroplated compared to 1.36 for the sputtered and 100W switch, 5.71 for the electroplated compared to 1.61 for the sputtered. Additional investigations are necessary to determine the mechanisms supporting these behaviors.

3.4 Contact Resistance Results

Sticking behavior and contact resistance levels were examined for the sputtered 10W switch exhibiting early sticks during switching a resistive load at 20V and 500mA. Typical results are shown in **Figure 5**. Each interval corresponds to 10,000 operations. The partial graph was extracted from test data to demonstrate effects just before, during and after the first stick. Initially, contact resistance fluctuated between 60 mΩ and 170 mΩ until the onset of sticking. After the onset of sticking, the contact resistance rose to about 350 mΩ and remained at this level for the duration of the test. The reed switch was torn down after testing and the reed contact areas were examined using both light microscopy and SEM with EDS. A pip and corresponding crater, typical of DC switching, were detected on opposing reeds. The pip corresponds to the cathode and the crater the anode. SEM micrographs of the pip and crater are shown in **Figure 6**.

Table IV. Weibull slopes for 10W and 100W, electroplated and sputtered switches				
10W Switch				
	20VDC, 500mA	1000VDC, 1mA	120VAC, 100mA	240VAC, 50mA
Electroplated	≈ 0.50*	<< 0.50*	0.73	2.30
Sputtered	3.00	0.92	2.80	3.80
100W Switch				
	33VDC, 3A	400VDC, 2mA	120VAC, 1A	240VAC, 200mA
Electroplated	0.80	0.25	2.80	16.0
Sputtered	3.90	1.04	2.80	4.60

*Slope estimated by graphical methods using initial failure data.

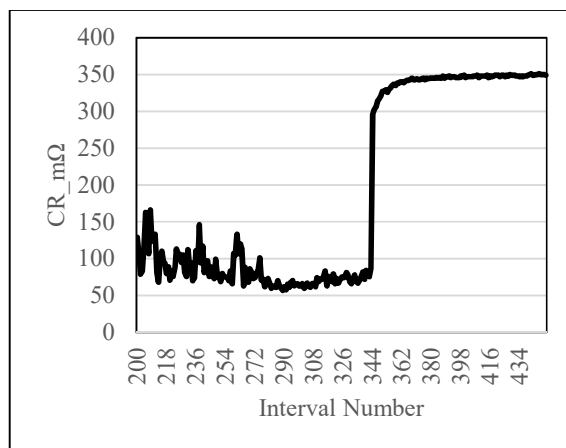


Fig. 5. Contact resistance just before, during and after the first stick for sputtered 10W switch tested at 20VDC and 500mA.

EDS analysis revealed that the composition at the peak of the pip and bottom of the crater were that of the Ni-Fe expansion alloy. No Ru, Mo, Cu or Ti were detected in these areas. At the end of test the material on both contact surfaces was the Ni-Fe alloy. The electrical resistivity of Ru is reported by Johnson Matthey [8] as 6.16 μΩ cm. National Electronic Alloys [9] reports that the electrical resistivity of Alloy 52 Ni-Fe is 260 Ohm-cir-mil/ft which converts to 43 μΩ cm. The contact resistance changes illustrated in Fig. 5 are readily explained in terms of EDS results and electrical resistivity values.

As wear progressed, the composition of the contact surfaces changed causing an increase in contact resistance. Once the contact surface composition stabilized to Ni-Fe, the contact resistance stabilized, albeit at a higher level, for the remainder of the test.

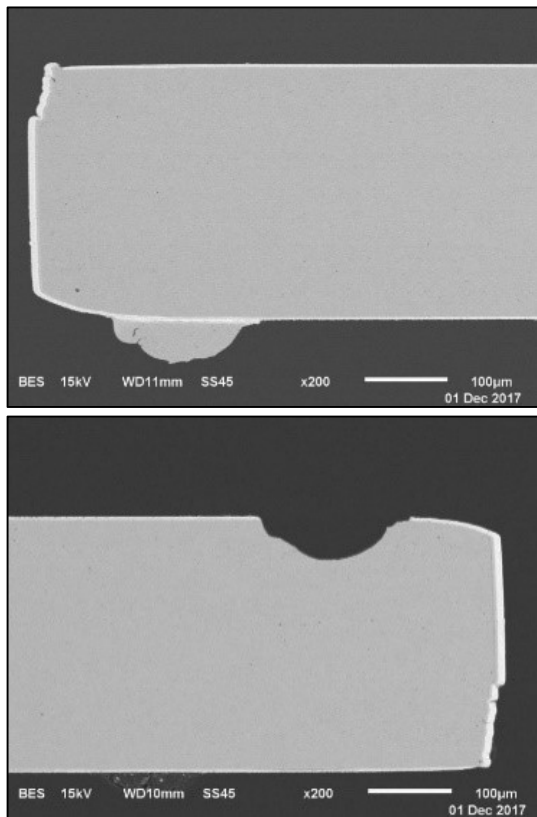


Fig. 6. SEM micrographs of the pip (upper) and crater (lower) developed after testing a 10W sputtered switch at 20VDC and 500mA.

4 Conclusions

1. Electroplated switches for the most part exhibited early failures.
2. Sputtered switches for the most part, exhibited “wear out” failures.
3. For the 10W switch, the calculated life of the electroplated switches was greater than that of the sputtered switches. The differences were much greater after AC testing.
4. For the 100W switch, the calculated life for both electroplated and sputtered switches were of the same order of magnitude and comparable.
5. During DC testing, the 10W switch displayed decreasing life with increasing voltage and decreasing current.
6. During DC testing the 100W switch displayed increasing life with increasing voltage and decreasing current.

7. Given the different geometries of the two test vehicles, the differences in DC switching behavior suggest an interaction between mechanical design and contact material microstructure. Further study is required to understand this implied interaction.
8. During AC testing both the 10W and 100W switches displayed increasing life with increasing voltage and decreasing current.
9. For the 10W switch, increasing the web thickness by about 10% minimized early sticks, allowing for the development of a sputtered Cu/Mo/Ru stack to replace the electroplated Au/Rh/Ru stack.
10. For the 100W switch, no modifications were required and a sputtered Cu/Ru stack was developed to replace the electroplated Au/Rh/Ru stack.
11. Both the sputtered 10W stack and the 100W stack met specified life targets after a battery of AC and DC life tests.

5 Acknowledgement

The authors would like to acknowledge Dr. Werner Johler for project support and manuscript review.

6 References

1. EIA/NARM RS-421-A, *EIA/NARM Standard for Dry Reed Switches*, March 1983
2. MVSR-20 19.7mm Reed Switch Data Sheet
3. DRS-50 50.8mm High Power Reed Switch Data Sheet
4. KDF 900i Product Series Brochure, <https://www.kdf.com/wp-content/uploads/2016/03/900i-Series.pdf>
5. Bowman B Series XRF Brochure, <https://bowmanxrf.com/>
6. IEC 61649:2008, *Weibull analysis*
7. IEC 61810-2:2017, *Electromechanical elementary relays, Part 2: Reliability*
8. *Johnson Matthey Technol. Rev.*, 2016, **60**, (3), 179
9. www.nealloys.com/pdf/nickle-iron-periodic-table

Highly durable silver-based physically deposited contact finish for the application in socket connectors

Sönke Sachs¹, Helge Schmidt¹, Marjorie Myers², Michael Leidner¹, Waldemar Stabroth¹, Frank Ostendorf¹
TE Connectivity, ¹Bensheim, Germany, ²Harrisburg, United States of America
ssachs@te.com

Abstract

Increasing electrical contact performance requirements in the Automotive industry, especially with respect to vibration resistance, mating force levels, mating cycle durability, and temperature exposure stability lead to a need to develop new contact finishes that exhibit performance qualities superior to that of the standard contact finishes available in the market. A newly developed high-performance selective AgCu contact finish appropriate for copper alloy substrates is presented here which is made using a non-aqueous physical application process. This selective AgCu finish exhibits a low coefficient of friction of 0.2-0.3, excellent wear resistance, enhanced vibration stability performance, an absence of cold-welding effects, and exceptional resistance to delamination; all while maintaining a stable and reliable electrical contact resistance. Analyses will be presented that show that these enhanced functional contact properties are based on the Ag/Cu gradient composition and the fine-grained crystalline nature of the finish material. Product level testing demonstrates the advantages of the new finish, compared side-by-side with standard electroplated silver finishes.

1 Introduction

Ever present increases in precious metal prices and environmental performance requirements push the limitations of contact material performance and cost. With industry design requirements trending towards continued miniaturization and increasing pin counts, meeting connector mating force limitations and greater temperature and vibration requirements will only become more difficult. Contact finishes with properties exceeding that of the existing standard ones will be needed.

Today, standard electroplating processes are widely used for applying contact finishes to separable connector contact interfaces [1]–[3]. While overall very successful, electroplating processes involve the use of aqueous chemistries and impose limitations of material choices and compositions. Physical vapor deposition (PVD) techniques offer a viable alternative process method to electroplating methods for applying contact finishes [4]. With PVD, multiple layers can be applied using a great variety of chemical compositions, such as mixtures of non-alloying elements or as amorphous layers [1]. This high degree of freedom with respect to composition and structure allows new strategies to overcome the inherent limitations of existing finishes. However, high deposition rates and selectivity are difficult to achieve with PVD techniques.

Regarding contact materials, besides hot-dipped Sn, electroplated Au, Ni, Sn finishes, electroplated Ag based finishes are commonly used in the automotive

industry, especially for applications which require greater current carrying capabilities, higher operating temperatures, and/or more severe vibration levels [5]. However, using electroplated Ag finishes can have some inherent disadvantages in that they typically exhibit high mating force, limited mating cycle durability, and can require passivation/environmental protection. Potential cold-welding effects and extended excessive thermal exposure delamination effects can occur. If required by the application specifics, these shortcomings can be mitigated by applying one of a few available specific Ag alloy electroplatings, e.g. AgPd [6], [7].

Another approach was followed here where a high-performance Ag based finish is created and selectively applied to a copper alloy base metal substrate using a physical deposition process, which consists of two steps: application of material by a printing process and fast melting of the applied material [8].

In the first part of this paper, the structure and composition of this finish are introduced and discussed. The second part directly compares the connector level functionality of this new finish to a benchmark electroplated silver finish. The connectors used for this comparison were designed specifically for a high-temperature and high-vibration environment automotive application.

2 Finish Composition and Structure

2.1 Materials

The selective AgCu contacts were produced using both CuNiSi and CuSn0.15 base metal contact strip. CuSn0.15 substrate material was used to make the lab testing geometry samples to execute lab level evaluations. CuNiSi substrate material was selected because that is the substrate material specified for the receptacles chosen for the product evaluations. This alloy is required to be able to meet the electrical and mechanical connector performance requirements of the connector geometries.

The contact surface materials were directly applied to the base material using this physical deposition technique. **Fig. 1** shows a photograph of such a sample with selectively deposited contact and crimp finishes, only applied to the regions where they are functionally needed in the targeted product (areas 1 (separable interface) and 3 (crimp area)). This coated contact strip can then be post-formed into an electrical receptacle contact. The greyscale image shows clearly the rectangular areas, where the finishes were selectively applied. The remaining area of the surface remains without finish and shows the copper alloy base material appearance (area 2).

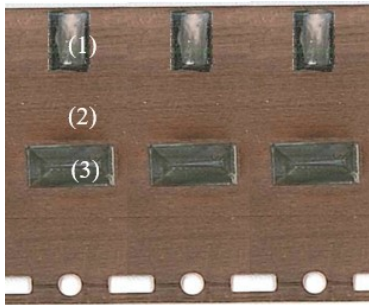


Fig. 1 Sample material with applied contact finish: (1) silver contact finish with an area of approximately $1.5 \times 3.0 \text{ mm}^2$, (2) CuNiSi base material, (3) tin finish for the crimp area.

2.2 Composition and Structure

Scanning Electron Microscope (SEM) images taken at a higher magnification of the selective AgCu contact area are shown in **Fig. 2**. While the edges appear uneven in places, the middle of the contact finish zone is homogenous and smooth. The surface roughness of the finish is $R_a = 0.2 \mu\text{m}$ which is comparable to that of the substrate material. The backscattered contrast image 2 b) shows the micrometer and sub-micrometer sized structures at the surface.

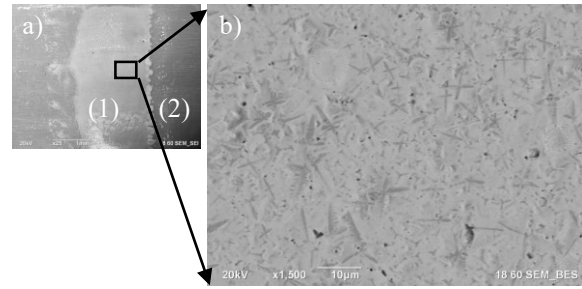


Fig. 2 Scanning electron microscope (SEM) pictures of the contact finish: a) overview of the whole contact area, b) magnified SEM picture in backscattered mode of the finish surface.

More detailed information about the specific structure of the finish can be seen in **Fig. 3**. The ion-polished cross-section image shows the three main phases of the finish: a nano-crystalline top layer with a thickness of about $2\text{-}3 \mu\text{m}$, an intermediate layer with a larger grain structure morphology, and in this case, the CuSn0.15 base layer. The backscattered contrast shows the distinct concentration profile of the selective AgCu contact material through the thickness of the deposit which has a high silver concentration near the surface which transitions to a lower silver concentration adjacent to the substrate bulk material.

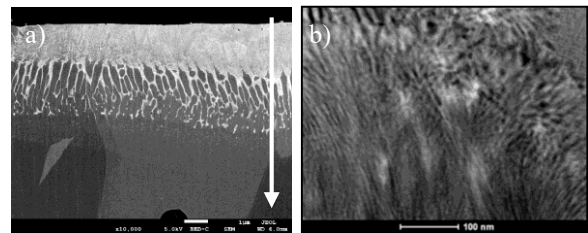


Fig. 3 Structure of the finish shown in cross-section images: a) Ion-polished cross-section imaged in SEM backscattered mode. b) Transmission electron microscope picture of the structure of the top layer.

This finding is corroborated by the glow discharge optical emission spectroscopy (GDOES) results shown in **Fig. 4**. At the surface, the finish has a silver concentration of about 65 % and a copper concentration of about 25 %. In a transition between the surface and a depth of about $5 \mu\text{m}$, the silver concentration continuously decreases and the copper concentration continuously increases until a $> 95 \%$ copper level is measured, as would be expected for the CuSn0.15 base material. Small amounts of carbon and oxygen are also detected, especially near the surface. While the oxygen originates from formation of thin surface oxides, the carbon was added intentionally to the material formulation.

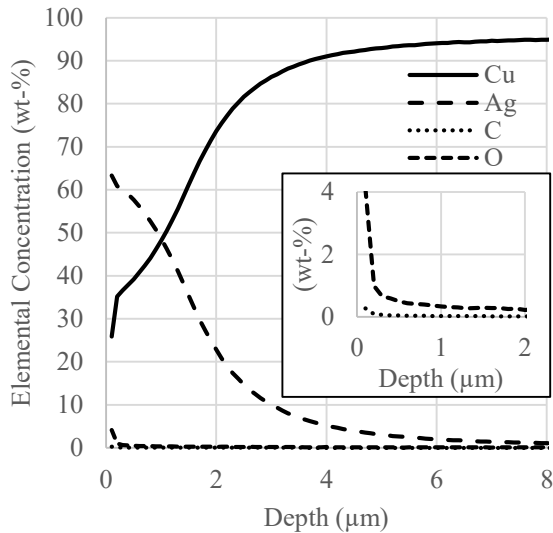


Fig. 4 Glow discharge optical emission spectroscopy (GDOES) data of the finish composition, measured across a 5 mm circular spot diameter of the sample. The inset graph shows the increased carbon and oxygen concentrations near the surface.

The cross-section and GDOES data show that the finish is not deposited as a traditional layered structure with clear interfaces, but that considerable mixing between the copper alloy base material and the applied silver material is introduced and a gradient composition is created by the process. The near-surface layer has a fine-grain structure which is fine enough to be hard to resolve in the ion-polished cross-section image in **Fig. 3 a**). This is clearly shown in the high-resolution TEM image in **Fig. 3 b**) which shows that its fine grained structure is significantly smaller than the 100 nm image scale bar. Nano-indentation measurements reveal a hardness of the selective AgCu finish of HV 200-240, compared to HV 80-110 for the reference electroplated Ag finish.

Overall, the finish is composed of a nano-scale structured silver-copper (AgCu) mixture near the surface with a larger grain structure transition zone adjacent to the bulk of the base material. The overall elemental composition is similar to that of powder metallurgy processed AgCu contact material. The difference is that it has a much smaller grain structure than any powder-metallurgy generated AgCu material. This small grain structure results in a significantly higher hardness of the finish, compared to standard electroplated Ag.

3 Contact Properties

The composition and microstructure of this selectively applied AgCu material determines its resistivity and wear properties and thus the performance as an electrical contact material. Its performance was first tested

using standard interface geometry test samples: AgNi10 contact rivet probes versus the AgCu finished 30x30 mm² CuSn0.15 flat contact surfaces. After that testing, connector product samples were built for testing. **Fig. 5** shows samples with different sized AgCu contact areas in three different states: the as-deposited/untreated state, after 1000 h of 150 °C temperature exposure, and after Mixed Flowing Gas (MFG) exposure -as per DIN IEC 60068-2-60: 0.2 ppm SO₂, 0.01 ppm H₂S, 0.2 ppm NO₂, 0.01 ppm Cl₂, 25 °C, relative humidity 75%, 21 days. Compared to the untreated sample in **Fig. 5 a**), the high-temperature exposed sample in **Fig. 5 b**) shows discoloration of the copper base material. The 21 day MFG sample in **Fig. 5 c**) shows slight discoloration of the copper base material and the finish areas.

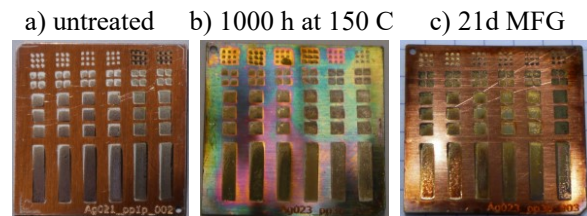


Fig. 5 Photographs of 30x30 mm² samples with contact coating areas between 0.5x0.5 mm² and 3x10 mm² for a) an untreated freshly coated sample, b) a sample after temperature exposure and c) a sample after mixed flowing gas (MFG) test.

3.1 Static Contact Resistance

Fig. 6 shows curves of the normal force dependent static (no wipe) contact resistance (CR), compared side-by-side with a comparable 3 μm electroplated Ag over CuSn0.15 finished flat. The contact resistance of the AgCu finish is inherently higher than that of the standard electroplated Ag finish, e.g. 0.42 mΩ vs. 0.12 mΩ at a normal force of 5 N. In the same graph, static resistances after mixed flowing gas exposure is also shown. Due to formation of surface films (see the color change in **Fig. 5 c**) the static CR values are slightly higher than in the initial as-deposited state, but still functional like the pre-exposed surface static CR.

3.2 Coefficient of Friction

In addition to the contact resistance, the coefficient of friction (COF) of the AgCu finish was measured. The graph in **Fig. 7** shows measured COF values of ~0.2 for the AgCu finished samples which is much lower than the value of the standard electroplated Ag sample with COF values of 0.7-0.9. Even after thermal aging and MFG exposure, the samples have low COF values of < 0.4. In comparison, the standard Ag electroplated sample shows only lower values after temperature exposure due to the formation of lubricious silver-sulfide films [5].

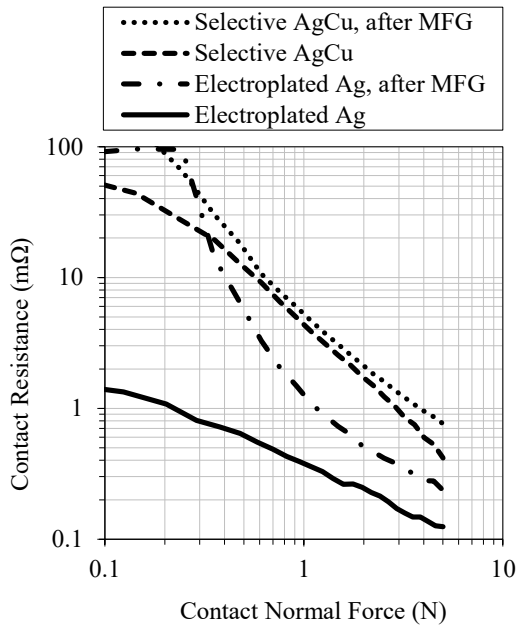


Fig. 6 Static contact resistance measurements from a probe/flat test sample geometry. AgNi10 rivets were used as probe contacts. The curves display median values of 5 measurements which were performed on different spots on the samples using dry-circuit conditions (max. 20 mV, 100 mA). Electroplated Ag contact resistances are shown as reference.

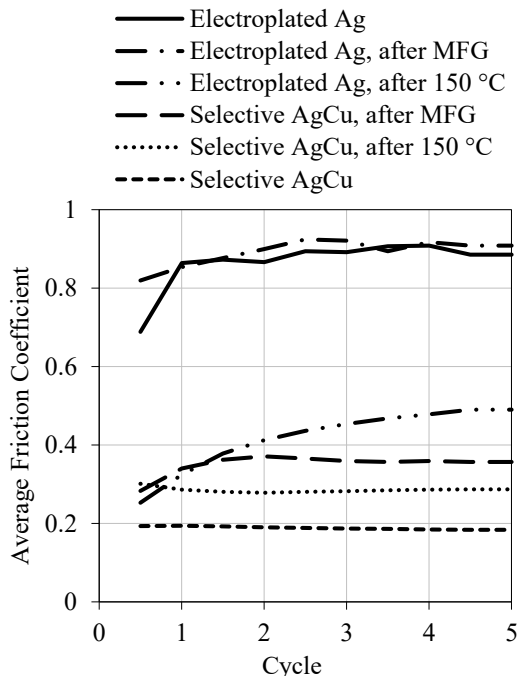


Fig. 7 COF data for the AgCu finish and standard Ag electroplated silver samples in the as-deposited state and after mixed flowing gas and high-temperature exposure. The coefficient of friction was measured for 5 back and forth motion cycles over a distance of 1 mm with an applied normal force of 2 N. The probe contact was an AgNi10 relay contact rivet.

3.3 Temperature Stability

The stability of the selective AgCu contact finish upon temperature exposure was tested by exposing the finish to 180 °C for 1000 h. **Fig. 8** shows side by side, surface and cross-section SEM image taken before and after this thermal exposure. After exposure, a discontinuous partial dark surface film forms on the surface which can be identified as a thin copper oxide layer. This film migrates across the surface laterally from the edges of the finish. This copper oxide layer can also be seen in the cross-section view and has a thickness of 0.1-0.3 μm. The structure of the finish itself does not change considerably with the thermal exposure. Light microscopy analysis of the finish and wear tracks reveal no signs of delamination of the finish.

Contact resistances were measured before exposure (1.5 mΩ at 2 N normal force), after exposure in the mated state (1.1 mΩ at 2 N normal force), and after exposure after a disturbance wipe of 0.1 mm was done (1.5 mΩ at 2 N normal force). The lack of the resistance increase in the mated state shows that no excessive copper oxide layer builds up at this interface and that the contact areas are protected against oxidation in the mated state to a certain extent. Additionally, the formed copper oxide layer can be easily displaced by a wiping motion, allowing a metallic contact even after oxide growth. In addition, the AgCu structure does not show indications of copper diffusion through the fine-grain AgCu top layer. There was no significant increase of the grain size observed. A possible explanation for that is that the added small amounts of carbon stabilize the small-size grain structure.

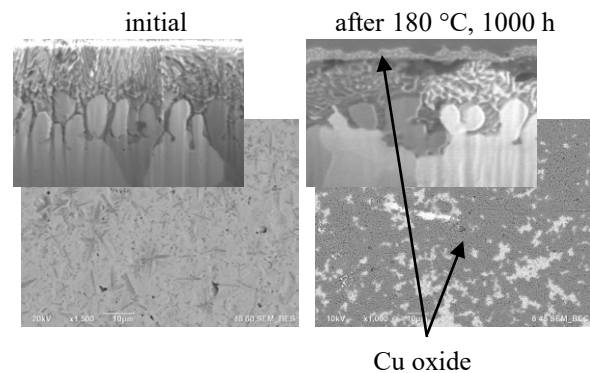


Fig. 8 Cross section SEM images of the selective AgCu contact finish before (left) and after exposure to 180 °C, 1000 h (right). The dark areas in the surface SEM image and the light grey coloured layer which are indicated by the arrows shows copper oxide layers.

4 Performance in Connector Applications

In addition to testing of the selective AgCu contact finish in the probe/flat test geometry, material strip for socket contacts was coated and the samples were tested side-by-side with reference standard electroplated Ag production samples as a benchmark. Two automotive contact receptacle contact geometries were selected for these evaluations:

- a 1.2 mm wide tab receptacle contact (10 N nominal normal force per contact) where the standard contact finish is electroplated Ag over Ni, with passivation
- a 0.5 mm wide tab receptacle contact (2 N nominal normal force per contact) where the standard product contact finish is an electroplated hard AgSb₂ over Ni

In the case of the selective AgCu material, the finish is deposited prior to the stamping and forming of the contact geometries. In contrast, the standard electroplated contacts require electroplating to be done after the contact geometries are formed. Both these two types of receptacle connectors were tested using their respective standard electroplated Ag header type tabs.

4.1 Insertion and Withdrawal Forces

The comparatively low COF of this selective AgCu finish makes it a capable candidate for low insertion force/higher pin count applications. Therefore, the receptacle contacts with this finish were tested for up to 20 mating/durability cycles as mated to standard electroplated silver counter contacts, and compared to the performance of the standard electroplated silver finished receptacles and header tab combination. Contrasting 20 cycle contact interface testing results (selective AgCu vs. electroplated Ag receptacle finish mated to standard electroplated Ag tabs) for the 1.2 mm tab contact interfaces are shown in Fig. 9. Clearly, the lower COF of the selective AgCu finish results in lower insertion and extraction forces than the electroplated Ag finish. In addition, the mating forces are more stable across the 20 mating cycles.

Similar data is shown in Fig. 10 as a function of the maximum mating force per cycle. The selective AgCu receptacle results stay constant over 20 cycles. Conversely, the higher values of the standard electroplated Ag receptacle show insertion forces that increase from the first cycle to the second cycle. The decreasing forces after the second cycle are an indication of progressing wear damage.

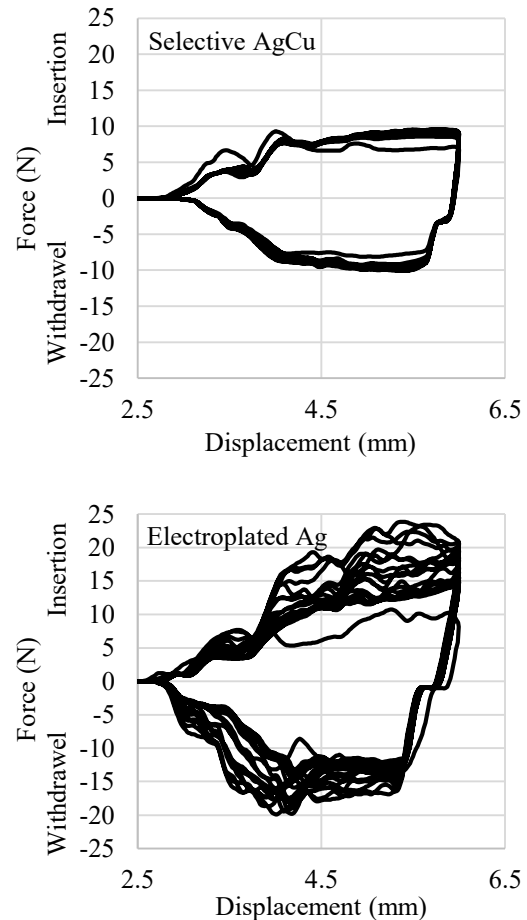


Fig. 9 Insertion and withdrawal forces of the first 20 mating cycles for the selective AgCu contact finish and the standard electroplated Ag finish using a 1.2 mm mating tab width receptacle contact.

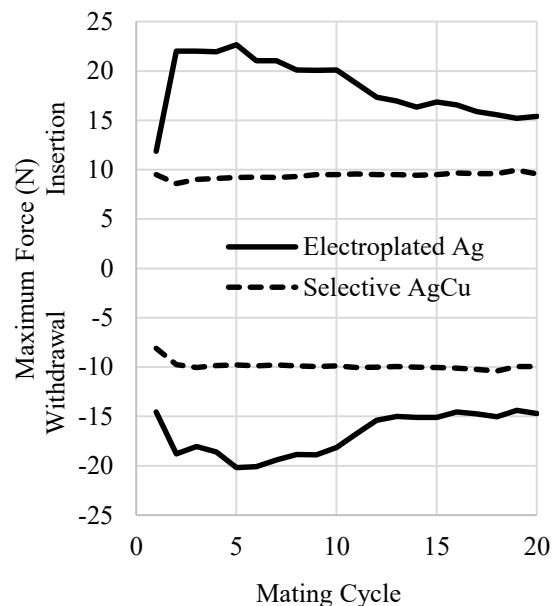


Fig. 10 Maximum values of the insertion and withdrawal forces per cycle from Fig. 8 using the 1.2 mm mating tab width receptacle contact. The contact normal force of two contact points was 10 N each.

Similar contrasting data is shown in **Fig. 11** for the 0.5 mm tab width receptacle contact for 50 mating cycles, comparing receptacle performance of selective AgCu to the standard electroplated hard AgSb₂ contact finish. In this case, the hard nature of both finishes exhibits similar maximum forces for the first cycle. The selective AgCu finish, however, exhibits constant forces up to 25 cycles before evidence of progressive wear becomes evident. Conversely, indications of wear damage initiation is exhibited by the electroplated hard AgSb₂ finish just after the first cycle.

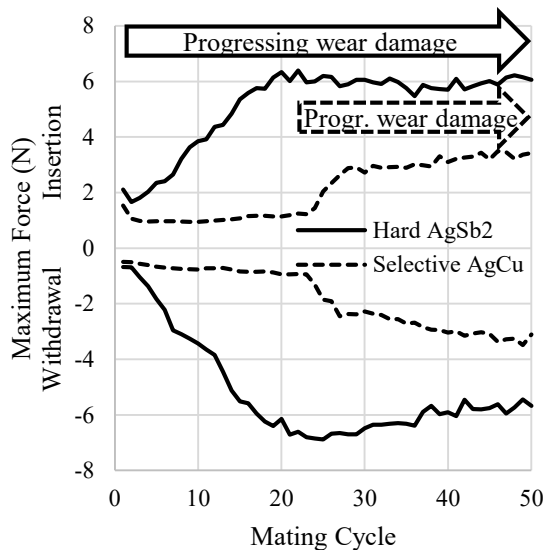


Fig. 11 Maximum values of the insertion and withdrawal forces per cycle for the 0.5 mm tab width receptacle contact system. The contact normal force of one contact point was 2 N.

This finding is corroborated by an analysis of the contact points after 50 mating cycles, as depicted in **Fig. 12**. The dark area in the middle of the image of the AgSb₂ receptacle contact surface shows wear-through to the nickel underplating. In contrast, the image of the selective AgCu receptacle contact surface does not show any wear-through and the contact surface finish remains intact through the 50 cycles. Furthermore, though the opposing electroplated Ag tab contact surfaces have clear wear tracks, they do not show wear through to the Ni underplate.

Surface analysis of the contact surfaces of the 1.2 mm receptacles and tabs show comparable results: partial wear-through on the reference electroplated Ag receptacle contact surface and no wear-through on the selective receptacle contact AgCu surface and on the tab surfaces.

4.2 Cross-Compatibility with Standard Platings

Comparable mating cycling have also been done for these receptacles as mated to electroplated hard Au and hot-dipped Sn tabs to evaluate the cross-compatibility of the selective AgCu finish with these other standard

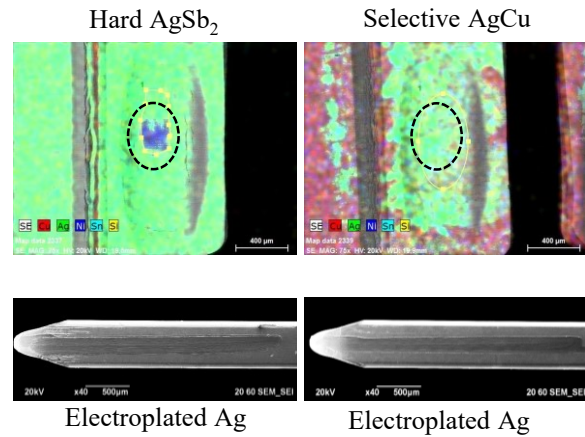


Fig. 12 Elemental contrast SEM images of the contact surfaces after 50 mating cycles. The contact point on the receptacle side (top pictures) is indicated by the oval dashed line. The bottom pictures show the 0.5 mm electroplated silver tab contact after 50 cycles.

finishes. For the case of the 1.2 mm receptacle, they exhibited a maximum mating forces of 9-11 N, when mated with the hard Au finished tabs (comparable to the values in **Fig. 10**). No wear-through of the finishes was detected even after 50 mating cycles. When mated with hot-dipped tin coated tab contacts, the performance was comparable to a hot-dipped tin coated receptacle/tab combination.

4.3 Vibration and Micromotion Tests

The mechanical stability of the finish was further evaluated using vibration testing. Generally, the selective AgCu finish exhibited improved vibration resistance and showed no, or at least less, wear damage than the standard electroplated finishes.

Micromotions at the contact interface, such as is induced by mechanical vibrations or thermal cycling, were tested using a driven micromotion test method for mated 0.5 mm tab/receptacle interfaces. The evaluation of the contact resistance over the cycles is shown in **Fig. 13**. While the CR of the selective AgCu contact finish stays constant over 1500 tested cycles, the CR of the electroplated AgSb₂ sample already starts to increase after < 100 cycles.

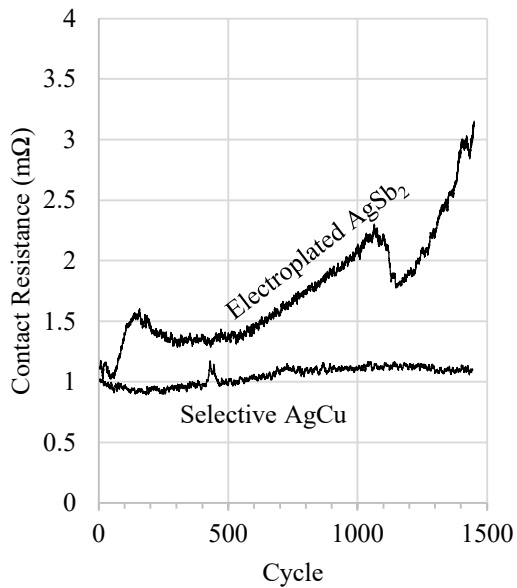


Fig. 13 Micromotion measurement of the 0.5 mm wide tab selective AgCu vs. standard AgSb₂ finished receptacles. The contacts were displaced 0.1 mm with a frequency of 1.5 Hz and the contact resistance was monitored continuously.

4.4 Contact Resistance and Current Carrying Capability

The resistance of the 1.2 mm receptacle-tab connection (1.15 mΩ for two parallel contact points, including the bulk structure of the connector) was just slightly higher than the contact resistance of 1.04 mΩ of a comparably measured standard electroplated mated interface. Even after temperature exposure to 180 °C for 3000 h, the resulting contact resistance of 3.8 mΩ was still in an acceptable range. The higher contact resistance of the selective AgCu finish resulted in a 3 % smaller current carrying capability of the connector compared to the electroplated silver finish.

5 Conclusions

The composition and structure of the selective AgCu contact finish are the foundation for the enhanced performance as a contact material. The fine-grain structure of the mixed Ag and Cu and the added small amount of carbon form a durable and hard material which is especially well-suited for applications with high mechanical load. The contact resistance is slightly higher than that of pure Ag due to the hardness of the material and the Cu within the layer. The nature of the bonding of the contact material with the substrate material results in great resistance to delamination. The fine grain

structure is resistant to recrystallization with temperature exposure.

Overall, there are performance advantages inherent to using this finish for connector application receptacles as mated to standard electroplated Ag tabs:

- A low coefficient of friction of 0.2 – 0.3
- Improved mating cycle durability as compared to standard electroplated Ag, e.g. up to 50 cycles with 10 N normal force vs. 10 cycles for the reference electroplated Ag receptacles
- Suitability for high vibration environments
- Hardness in the range of HV 200-240
- No passivation required
- No cold-welding
- No delamination at high temperatures
- Suitable for temperatures of 180 °C up to 1000 h
- Survives forming operation without cracking (no pre-forming and post plating required)
- Cross-compatible to standard electroplated Sn, HAL-Sn, Ag, Au finishes
- Highly selective contact surfaces possible

In conclusion, this contact material produced using a non-aqueous physical deposition process exhibits superior performance to available standard finishes. This is due to the well-engineered composition and structure.

6 Literature

- [1] M. Braunovic, N. K. Myshkin, and V. V. Konchits, *Electrical contacts: fundamentals, applications and technology*. CRC press, 2006.
- [2] E. Vinaricky, *Elektrische Kontakte, Werkstoffe und Anwendungen*. Heidelberg: Springer-Verlag, 2002.
- [3] H. Endres, *Praxishandbuch Steckverbinder*, 1st ed. Würzburg: Vogel Business Media, 2018.
- [4] G. Herklotz, E. Bolmerg, H. Eligehausen, B. Gehlert, and K. Witting, "Application of sputtered layers in contact technology," presented at the Thirty-Sixth IEEE Conference on Electrical Contacts, and the Fifteenth International Conference on Electrical Contacts, 1990, pp. 182–192, doi: 10.1109/HOLM.1990.113012.
- [5] M. Myers, "The Performance Implications of Silver as a Contact Finish in Traditionally Gold Finished Contact Applications," in *Proceedings of the*

55th IEEE Holm Conference on Electrical Contacts, 2009, pp. 310–318.

- [6] M. Myers, “Connector Level Performance Evaluation of a New High Speed Reel to Reel Electroplated Silver Palladium Alloy Contact Finish,” presented at the 27th International Conference on Electrical Contacts, Dresden, 2014.
- [7] F. Talgner, “Novel Silver-Palladium Electrolyte for Electrical Contacts,” presented at the 27th International Conference on Electrical Contacts, Dresden, 2014.
- [8] H. Schmidt, M. Leidner, and S. Sachs, “Method for Manufacturing at Least One Functional Area on an Electric Contact Element Such as a Switching Contact or a Plug Contact,” WO2012136614.

Acknowledgments

The authors thank Felix Greiner, Shallu Soneja, Gokce Gulsoy, Yiliang Wu, Martin Hottes, Barry Matthews, and Dave Sarraf for fruitful discussions and their support.

Disclaimer

While TE has made every reasonable effort to ensure the accuracy of the information in this paper, TE does not guarantee that it is error-free, nor does TE make any other representation, warranty or guarantee that the information is accurate, correct, reliable or current. TE reserves the right to make any adjustments to the information contained herein at any time without notice. TE expressly disclaims all implied warranties regarding the information contained herein, including, but not limited to, any implied warranties of merchantability or fitness for a particular purpose.

The dimensions in this paper are for reference purposes only and are subject to change without notice. Specifications are subject to change without notice. Consult TE for the latest dimensions and design specifications.

TE Connectivity and TE are trademarks owned or licensed by the TE Connectivity Ltd. family of companies.

An innovative silver-based coating system with high wear resistance for electrical connectors

Dr. Frédéric Hilty, Collini AG, Dübendorf, Switzerland, fhilty@collini.eu
Dr. Johannes Herrmann, Collini AG, Dübendorf, Switzerland, jherrmann@collini.eu

Abstract

Due to the very high electrical and thermal conductivity, silver-plated materials are widely used as electronic contact materials with medium corrosion resistance. Silver is typically applied on plug-in connectors with a thickness of 2–5 μm with or without an intermediate nickel layer. However, the number of mating cycles is limited due to the low wear resistance, which needs to be improved. This publication describes a novel coating system consisting of a wear- and corrosion-resistant base layer with a thin silver top-coating. This layered structure shows a clearly improved sliding and wear resistance behavior with a low contact resistance. At the same time, cost reduction is achieved by significantly reducing the use of precious metals. In this paper, the performance and limitations of this silver coating system compared with classic soft and hard silver coatings will be shown.

1 Introduction

Silver has the best electrical and thermal conductivity of all metals and has therefore become very important in electrical engineering. Silver-plated materials are used as contact materials with medium corrosion resistance [1]. However, the number of mating cycles is limited due to the low wear resistance, which needs to be improved. In addition, silver surfaces tend to tarnish on contact with various harmful gases (SO_2 , H_2S , HCl). Silver sulphide or silver chloride is formed on the surface [2,3]. AgCl is an electrical insulator and therefore massively increases the contact resistance. Ag_2S , on the other hand, is a semiconductor and has almost no influence on the electrical resistance but can impair solderability. In addition, silver surfaces show a tendency to cold welding, which can lead to the contacts getting stuck. To avoid the problems mentioned above, silver surfaces have been provided with passivation layers for many years. These are either organic (often thiol compounds) or inorganic (e.g. Sn or Cr) based. By selecting a suitable passivation, the coefficient of friction through sliding can be reduced and thus increase the wear resistance. However, for reasons of contact resistance, this protective layer is so thin that it is already worn through after a few mating cycles. Nevertheless, it supports the running-in of the plug contact in the critical first cycle, which is of decisive importance for its service life.

Additionally, base materials are usually copper-based. This element is well known for its ability to diffuse into silver, which impairs the solderability and bondability of the contact layer. In order to minimize this behaviour, an intermediate layer is deposited as a diffusion barrier. This is usually Ni with a layer thickness of 2–4 μm .

The aim of this study is to identify and test silver coating systems with the following properties: (1) Comparable contact properties such as the standard silver coating for plug-in contacts (2–4 μm nickel / 2–5 μm silver), (2) improved wear resistance due to lower coefficient of friction in the contact pairing and (3) lower precious metal usage (costs). A known possibility to realize a better wear resistance is to use hard silver instead of soft silver with similar coating thickness. Another approach is the combination of the soft silver with a hard barrier layer such as nickel phosphorus, which is known to significantly improve the wear behaviour of corresponding contact layer systems with AuCo [4]. These non-magnetic intermediate layers can be applied at similar costs to nickel [5] and have a high resistance to wear and corrosion with a phosphorus content > 11% [6]. The nickel phosphorus layer there-

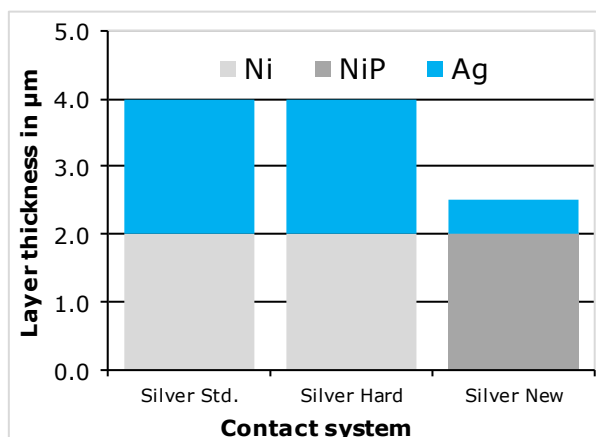


Fig. 1 Layer structure of various silver contact systems for plug-in contacts

fore serves as corrosion, diffusion and wear protection. Silver ensures low contact resistance even at layer thicknesses < 1 μm . This can also significantly reduce

the amount and therefore the costs of the precious metal. The layer structure of the coating system in comparison with classical silver and hard silver coatings is shown in **Figure 1**.

2 Experimental

The wear behaviour of real plug-in contacts is simulated using the pin-on-disc method. As shown in **Figure 2**, a ball is moved linearly back and forth on a plate under the influence of the contact force from above. This is done on a fixed path with a defined path length and a certain speed.

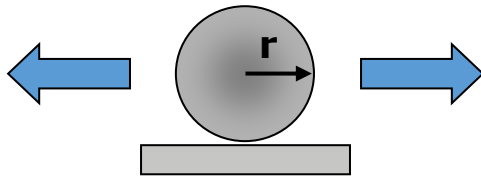


Fig. 2 Schematic setup for ball-on-plate

The wear resistance of a material equals to the number of wear cycles before the contact layer is worn through. At this point, the contact system is considered to have failed according to IEC 62271-1. The layer thickness therefore represents a wear buffer. Besides this parameter, the wear resistance additionally depends on the contact force as well as the contact radius of the material.

2.1 Experimental setup

The tribological examination was carried out on a specially designed tribometer [7] as shown in **Figure 3**. The contact plates are mounted on a table, which is moved linearly back and forth by a motor. The contact partner (ball or bar) is fixed to a nickel-plated stainless-steel holder.

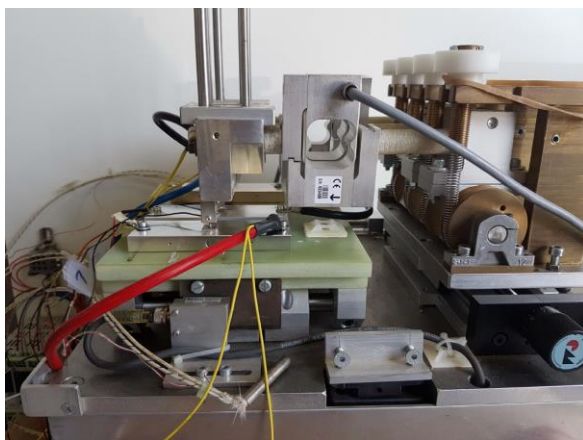


Fig. 3 Tribometer for experimental setup

The contact force can be variably adjusted from 1 to 10 N by means of weights. In this test apparatus, 3 contact pairs can be examined simultaneously, whereby the friction force is measured independently of each other using separate force sensors. For the measurement of the contact resistance, the current flows serially through the 3 measuring positions and the potential is tapped by a 4-point measurement directly at the contact plate and the contact ball or bar. The coefficient of friction is measured continuously as the ratio of normal force to friction force and the contact resistance is measured with a short stop after every 10 cycles to ensure perfect contacting. The measuring current is 10 (ball) or 50 A (bar), respectively. The samples tested are listed in **Table 1**. Both contact partners (plate and ball) were made of brass and coated with the same layer system. Hard silver is an alloy of silver with approx. 1% antimony. The hardness depends on the Sb content and is in the range of 140-200 HV.

Tab. 1 List of tested samples

Sample name	Coating system	Passivation
Silver Standard	2 μm Ni / 2 μm Ag	Thiol-based
Silver Hard	2 μm Ni / 2 μm Ag	Thiol-based
Silver New	2 μm NiP / 0.5 μm Ag	Thiol-based

The samples were examined at contact forces ranging from 1 to 7 N with or without lubricant. To show the influence of the contact geometry, different contacts (ball or bar) with contact diameter or width ranging from 1 to 3 mm were tested. The material wear was determined after 100, 500, 1000 and 3000 cycles. The evaluation of the wear tracks on the plate was carried out using a laser profile meter. The maximum track depth was examined and the cross-sectional area of the respective friction track evaluated. Thus, with the known track length, the wear volume (mm^3) can be calculated. Since both the contact force and the total path length (which equals to the number of cycles multiplied by the ball displacement per cycle) are known, the wear coefficient (mm^3/Nm) can be determined. As shown in **Figure 4**, the diameter of the ablated spherical surface was visualized under the Keyence VHX-6000 light microscope and determined as a circle by means of approximation.

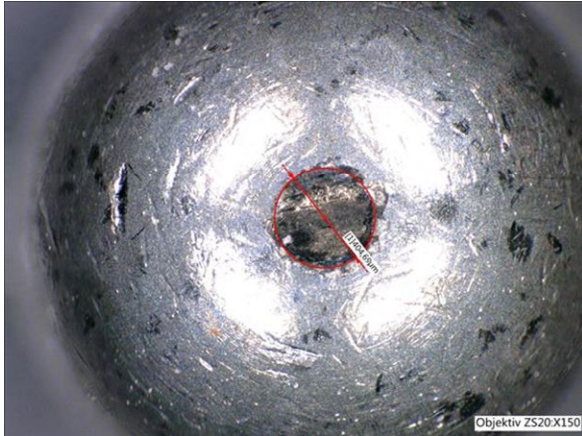


Fig. 4 Exemplary wear of the contact ball under the microscope.

According to **Figure 5**, The wear depth h can be calculated as follows using the sphere equation:

$$h = r - \sqrt{r^2 - a^2} \quad (1)$$

Here, a represents the calotte radius and r the contact radius. At this point it should be mentioned that the evaluation under the microscope takes place with a certain uncertainty. Often the wear surface cannot be clearly defined and is also not perfectly round. These results should be evaluated with caution.

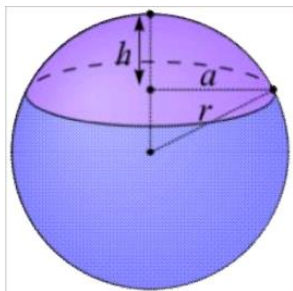


Fig. 5 Sphere model

In order to test the corrosion resistance of the contact system, the samples underwent 100 wear cycles and were afterwards exposed to 10 ppm H₂S for 4 days according to EN 60068-2-43:2003. The samples were then again subjected to 100 wear cycles and the measurement progress of the contact resistance and the coefficient of friction was monitored in order to see if there was a significant increase of these parameters.

3 Results and Discussions

The wear resistance of the novel coating system over 1000 wear cycles at a Force F of 1 N is shown in **Figure 6**. The measurement was performed at room temperature with a contact diameter d of 3 mm and a wear track l of 4 mm, therefore 1 cycle equals 8 mm. The initially low coefficient of friction of approx. 0.3 remains constantly low at 0.4-0.5 after a slight increase over the entire measurement period. Due to the hard barrier layer, this value is lower compared to the pairing of soft silver contacts [8]. The contact resistance at the beginning is approx. 2 mΩ and remains constantly low with a value smaller than 3 mΩ through the whole measurement. The slightly increased electrical resistance compared to the standard silver coating (2 μm Ni / 2 μm Ag) is due to the nickel phosphorus barrier layer. This nickel alloy has a significantly lower specific electrical conductivity than nickel or silver, respectively. This circumstance needs to be taken into account when replacing silver coatings for high voltage applications.

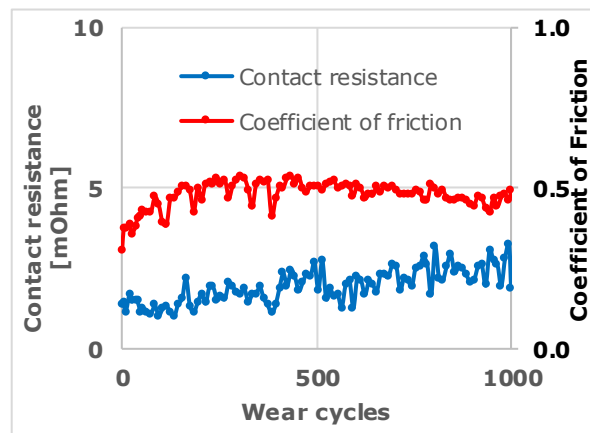


Fig. 6 Contact resistance and coefficient of friction of the investigated novel coating system as a function of the number of wear cycles at a contact force of 1 N, a contact diameter of 3 mm (ball) and a wear track of 4 mm.

The comparison of the wear resistance of different silver coating systems is shown in **Figure 7**. Due to the higher wear load, the ball (shown as circle) was always worn through before the plate (shown as square), therefore becoming the limiting factor. The standard silver coating was worn through after approx. 20-50 and hard silver after approx. 100 cycles. The alloy with antimony therefore provides an increased wear resistance, which can also be found in the literature [9]. The investigated contact system, on the other hand, was worn through after approx. 500 cycles despite the lower layer thickness. This corresponds to a factor of 10 compared to the standard silver coating for plug-in contacts.

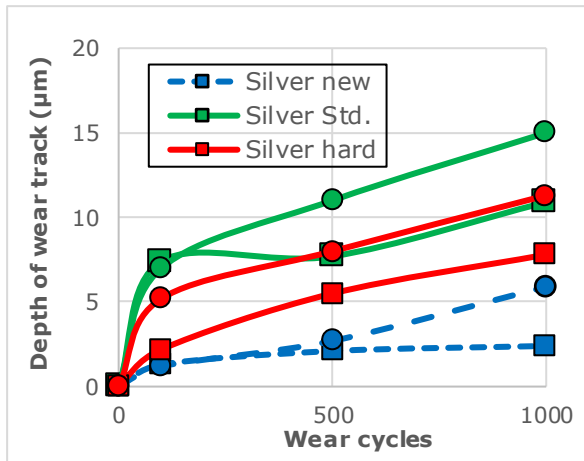


Fig. 7 Wear resistance of various silver coating systems at a contact force of 1 N, a contact diameter of 3 mm (ball) and a wear track of 4 mm.

In all samples, the diffusion barrier (nickel or nickel phosphorus) is significantly harder than the silver layer. The soft silver is displaced into the recesses of the harder material, thus acting as a lubricant and simultaneously maintaining a low contact resistance. With a higher precious metal layer thickness, this effect lasts longer because more silver is present. On the other hand, it has been shown that this effect was already observed for the targeted layer build-up with a very low silver layer thickness of 0.5 µm.

The dependence of the wear resistance from the contact radius is shown for the investigated contact system in **Figure 8**. A smaller contact radius leads to a faster increase of the ratio between the diameter of the removed calotte and the contact ball, resulting in a higher wear depth. Additionally, the friction track on the plate becomes narrower and correspondingly deeper. Both effects lead to an earlier abrasion of the contact layer.

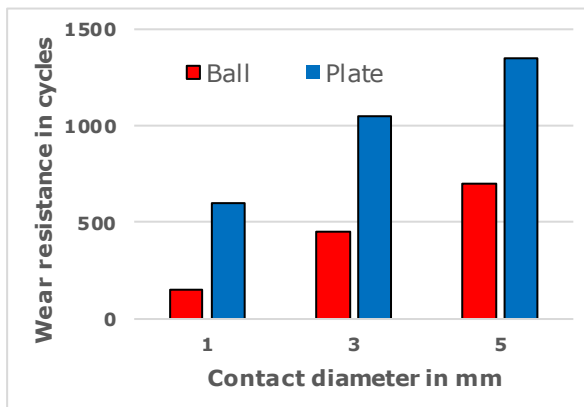


Fig. 8 Wear resistance of the novel coatings system as a function of contact diameter at a contact force of 1 N, a temperature of 20 °C and a wear track of 4 mm (1 cycle = 8 mm).

According to Holm, a higher contact force leads to a lower contact resistance due to the higher surface pres-

sure [10]. At the same time, a higher contact force results in increased abrasion, which leads to lower wear resistance of the novel coating system as shown in **Figure 9**.

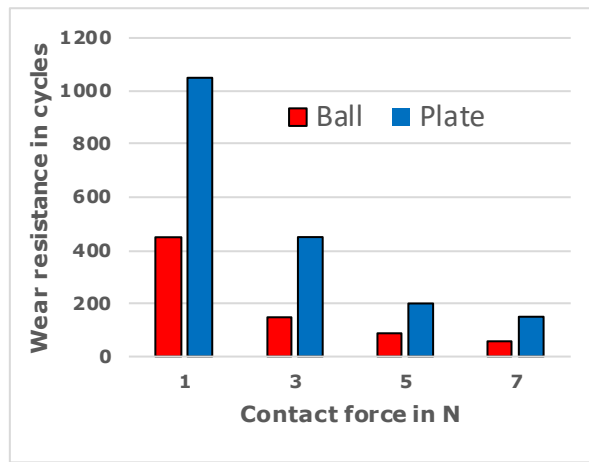


Fig. 9 Wear resistance of the novel coating system as a function of contact force at a temperature of 20 °C, a wear track of 4 mm (1 cycle = 8 mm) and a fixed contact diameter of 3 mm.

3.1 Influence of lubrication

In the following chapter, the influence of lubrication on the wear behaviour will be shown. The use of a lubricant reduces the coefficient of friction and, due to the gentle sliding motion, also the wear coefficient. Both factors lead to an increase of the wear resistance by at least a factor of 100. The influence of the lubricant on the examined novel coating system regarding the coefficient of friction and the contact resistance as a function of wear cycles is shown in **Figure 10**. In this experimental setup, a plate was paired with a contact bar, which has a sliding length of 4 mm and a contact width of 1 mm at the relevant contact surface. Thus, this contact partner experiences a cylindrical abrasion.

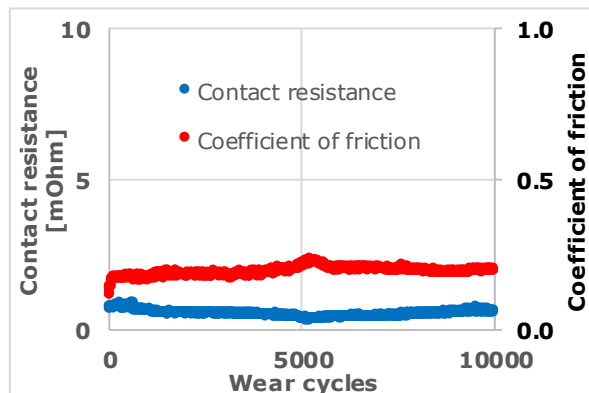


Fig. 10 Contact resistance and coefficient of friction of the investigated novel coating system with lubricant as a function of the number of wear cycles. The measurement was performed at a contact force of 7 N, a wear track of 30 mm and with a contact bar as counterpart to the plate (instead of a ball).

The measurement was carried out at 20 °C and at a contact force of 7 N. The wear track was 30 mm. Therefore 1 cycle equals to 60 mm, at an average speed of 20 mm/s. The coefficient of friction remains constantly low throughout the entire measurement at a value of approx. 0.2. The same behaviour also applies to the contact resistance, which has not increased significantly even after 10000 cycles. The average value is approx. 0.5 mΩ.

By evaluating the abrasion on the plate and the bar, the wear coefficient for the novel coating system with lubricant can be calculated, which is in the range of 1 to 4 times $10^{-15} \text{ m}^3/\text{Nm}$. Assuming a constant coefficient of wear, the wear resistance for real plug-in contacts can be estimated.

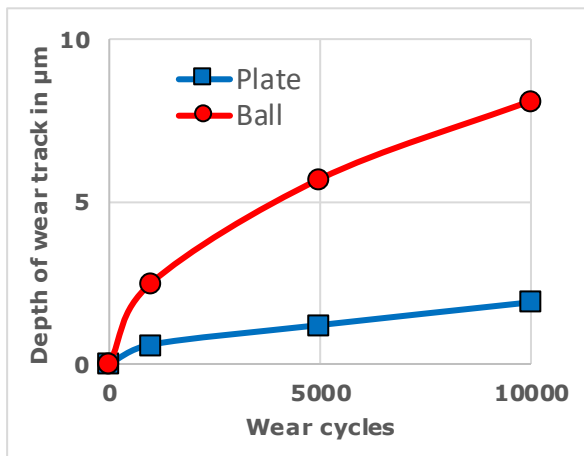


Fig. 11 Estimation of the wear resistance of the novel coating system with lubricant at a high contact force of 7 N, a contact diameter of 3 mm (ball) and a wear track of 4 mm.

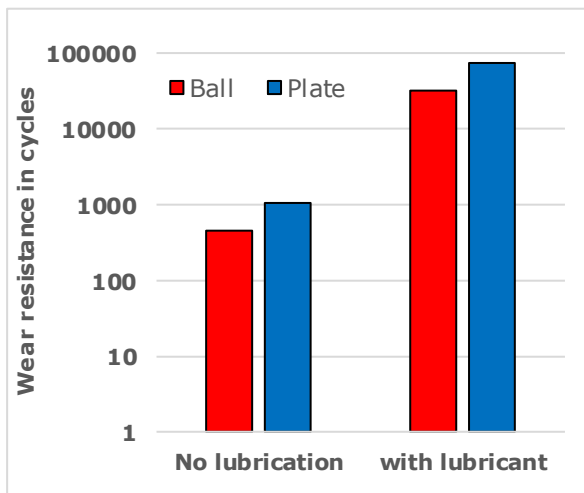


Fig. 12 Estimation of the wear resistance of the novel coating system with lubricant compared to samples without lubricant at a contact force of 1 N, a contact diameter of 3 mm (ball) and a wear track of 4 mm.

A wear track of 4 mm with a contact diameter of 3 mm is assumed. The wear resistance at high (7 N) and low contact force (1 N) is shown in **Figure 11** and **Figure 12**, respectively. The use of a lubricant therefore increases the wear resistance of the examined novel coating system by almost a factor of 100.

3.2 Crossability

As a rule of thumb, the pairing of contact systems with the same or similar hardness leads to a higher wear resistance. This is achieved by equal wear of both contact partners. In order to verify this statement, the wear behavior of a contact pairing of the investigated coating system with the soft silver was investigated. The contact partner to the plate was coated with 12 µm soft silver without a nickel barrier layer. All samples were provided with a lubricant. The measurement was performed with a contact diameter of 3 mm, a contact force of 7 N, a wear track of 4 mm and at a temperature of 20 °C. The wear resistance of this pairing is shown in **Figure 13**. In this test arrangement, soft silver with a coating thickness of 12 µm provided the same resistance of the contact ball as 2.5 µm of the new coating system. However, this was only possible due to the much higher layer thickness as a buffer for wear. Regarding the plate, the contact pairing of different coatings leads to a slightly lower wear resistance. This is due to the pairing of two contact systems with different hardness.

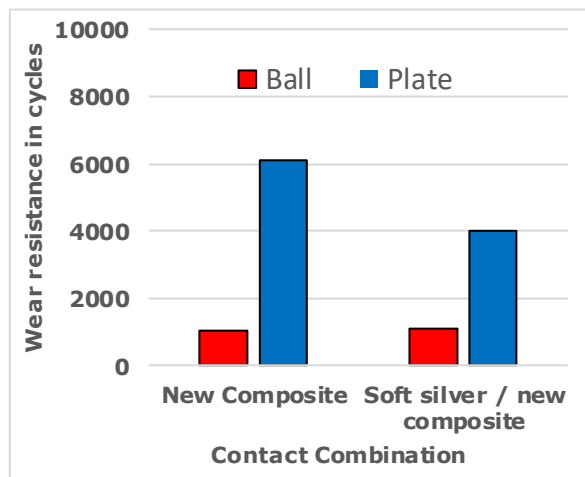


Fig. 13 Comparison of the wear resistance of soft silver combined with the new coating system against the homogeneous contact pairing of the latter. All samples were provided with a lubricant. The measurement was performed at a contact force of 7 N, a contact diameter of 3 mm (ball) and a wear track of 4 mm.

3.3 Corrosion resistance

The measurement progress of the contact resistance and the coefficient of friction for the novel coating system before and after ageing in H₂S gas (10 ppm for 4 days) are shown in **Figure 14**. The wear measurement was performed at a temperature of 20 °C, with a wear track of 30 mm and at a contact force of 1 N. The diameter of the ball was 3 mm.

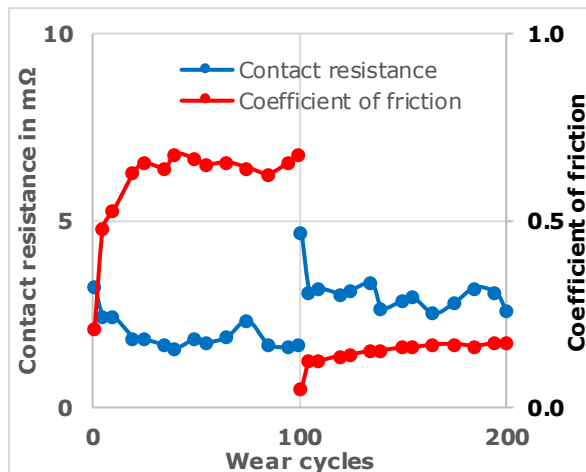


Fig. 14 Contact resistance and coefficient of friction of the novel contact system before (cycles 1 to 100) and after ageing in H₂S gas (cycles 101 to 200). The wear measurement was performed at a contact force of 1 N, a contact diameter of 3 mm (ball) and a wear track of 30 mm.

In the first cycles after exposition to the harmful gas, a slightly increased contact resistance is observed, which is caused by the formation of sulphides. However, this sulphide layer is already removed after a few wear cycles and the contact resistance decreases again. This measured quantity does not exceed the limit value of 5 mΩ at any time, so that a perfect contact is always available. The coefficient of friction, on the other hand, decreases drastically after exposition to H₂S. This is due to the sliding effect of the formed sulphides (Ag₂S). Additionally, it should be noted that the initial coefficient of friction was higher than expected (approx. 0.4), which is believed to be caused by a rougher sample surface.

4 Conclusions

Compared to standard silver coatings, the wear resistance of the investigated contact system has been increased by a factor of 10. Depending on the contact geometry, this equals up to approx. 500 and with lubrication up to approx. 30000 plug-in cycles. This is achieved with good corrosion resistance and up to 75% reduced precious metal usage at the same time. However, the inclusion of a nickel phosphorus base layer also has some side effects. There is a slightly increased overall electrical resistance due to the lower electrical

conductivity of this nickel alloy. This effect is especially crucial when replacing silver coatings in high voltage applications. In addition, nickel phosphorus is much harder and more rigid than nickel or silver, respectively. Therefore, the overall ductility of the contact system is lowered.

At this point it must be mentioned that the tribometric experiments can only be regarded as a model of reality and are not able to reproduce it completely. On one side, vibrations in the apparatus (especially at the mounting of the contact ball) promote wear, on the other hand there is a delayed increase of the contact resistance due to the short test duration. The increase of this measured quantity occurs multiple wear cycles later after the failure of the contact system, since the oxidation of the base material (copper or copper alloy) also takes some time. The wear resistance of different coating systems should therefore be mainly rated relative to each other. In practice, it has been shown, that this novel layer combination can deliver 1000 mating cycles with low contact resistance and without system failure. The contact geometry naturally plays an important role here, especially the contact radius in particular is decisive for wear resistance. With a constant wear coefficient, the wear track is narrower and deeper with smaller radii. The contact layer is therefore worn through earlier and the wear resistance decreases.

In summary, this novel coating system shows a significantly improved sliding and wear behaviour than conventional silver coatings with a low contact resistance. At the same time, costs can be reduced by significantly reducing the use of precious metals. This coating system therefore represents an attractive alternative with high wear resistance compared to classical soft and hard silver coating systems.

6 Literature

- [1] Charman, D.H.; Users Guide to the correct use of electrical contacts; ERA Report 90-0405R, 1990.
- [2] Abbot, W.H.; The effects of test atmosphere conditions on the contact resistance of surface films on silver; Proc. International Conference on Electrical Contacts, 1982, 294-296.
- [3] Hisakado, T.; Effects of surface roughness and surface films on contact resistance, *Wear*, 44, 1977, 345-359.
- [4] Herrmann, J.; Braun, H.A.; TRIBOR – an innovative coating system for electrical contacts and connectors; ICEC: 19th International Conference on Electric Contact Phenomena, 1998, 173-179.
- [5] Kreye, H.; Schenzel, J.; Puipe, J. Cl.; Vanhumbeeck, J.; Ide, G.; *Metall-oberfläche* 43, 2, 1990
- [6] Vanhumbeeck, J.; Ide, G.; Puipe, J. Cl.; *Metall-oberfläche* 43, 9, 1990.

- [7] Hagen, B.; Kufner, T.; Freudiger, G.; Basic Investigation on tribological systems for design optimization of connectors in electrical power engineering; Karlsruhe, 24. Albert-Keil-Kontaktseminar 2017.
- [8] Vinaricky, E.; Elektrische Kontakte, Werkstoffe und Anwendungen; Berlin, Springer-Verlag, 2002.
- [9] Krastev, I.; Petkova, N.; Zielonka, A.; *J. Appl. Electrochem.* 32, 2002, 811.
- [10] Holm, R.; Electrical Contacts; Berlin, Springer-Verlag, 2000.

Investigations on cold welding and galling of various connector platings

Reinhard Wagner, Christian Dandl, Andreas Gruber, Reinhard Hogger, Michael Eicher
Rosenberger Hochfrequenztechnik GmbH & Co. KG, Fridolfing, Germany
reinhard.wagner@rosenberger.com

Abstract

Unintended cold welding of contact spots as well as galling are frequent issues for electrical connectors, leading to very high disengagement forces and damage of platings when connectors are disconnected. Particularly silver-plated connectors are affected by these phenomena. Thus, a test bench has been developed in order to investigate the cold welding and galling behaviour of various connector platings. The test bench consists of contacts with ball-on-flat geometry that can be loaded with various normal forces. The contacts are moved against each other in order to determine the displacement force as a function of the displacement distance. Therefore, both static friction as well as dynamic friction can be investigated with this test bench. Furthermore, the experimental setup can also be subjected to accelerated aging tests. Initial results for the frictional behaviour of various connector platings are presented.

1 Introduction

Adhesive wear caused by cold welding and galling is a serious problem for electric connectors. Particularly silver-plated connectors are strongly affected by these phenomena, leading to very high disengagement forces and damage of connector platings when being unmated.

Cold welding is a form of adhesive wear. It is caused by the localized formation of bonds between the solid contact surfaces. The formation of cold welds is promoted by the presence of pristine metal surfaces without oxide layers or contaminations. On the one hand, cold welds are desirable for closed contacts as they decrease the contact resistance, while on the other hand they are undesired if the contact should be disconnected, as they lead to high disengagement forces and damage of the contact surface.

Similarly, galling is considered as a form of nonabrasive adhesive surface damage, characterized by protrusions raising above the original surface. In most cases, it includes material transfer from one surface to the other, extensive plastic deformation, and the presence of torn material on at least one surface [1]. According to the ASTM Technical Committee on Wear and Erosion, galling is defined in the ASTM standard G40 as “a form of surface damage arising between sliding solids, distinguished by macroscopic, usually localized, roughening and creation of protrusions above the original surface; it often includes plastic flow, material transfer or both” [2].

These processes are particularly critical for silver-plated contacts, where wear phenomena associated with cold welding and similar processes have been

studied extensively under fretting conditions [3, 4]. In this study, we investigate the displacement force as a function of the displacement distance under conditions which resemble the unmating process of a connector. In contrast to other studies, special emphasis is put on a spatially resolved measurement of the displacement force, enabling the differentiation between static and dynamic effects.

2 Experimental

2.1 Test bench design

A new test bench has been developed in order to investigate cold welding and galling behaviour of individual contact spots. The test bench is shown in **Figure 1**.

The test bench has a star-like design, enabling the examination of 20 individual contact spots within one test run, and it is rotatable around its central axis. It consists of a lower part, where displaceable disc-shaped samples with knobs (base material CuZn37, 14 mm diameter, 0.8 mm thickness), plated with different platings, are placed on immobile PTFE blocks. The displaceable disc-shaped samples protrude the PTFE blocks on the exterior side. The immovable PTFE blocks (which are screwed onto the base plate) are arranged in two different levels in order to facilitate the spatial arrangement. The upper part of the test bench contains the counter contacts, i.e. plated spheres (base material CuSn6, three mm diameter), which are fastened by a nut and connected to leaf springs that are assembled to a central axis. Thus, the contact situation resembles a *ball-on-flat* geometry. The contact force is applied by using weights which are put onto the central axis; the force is passed to individual contact spots via leaf springs.

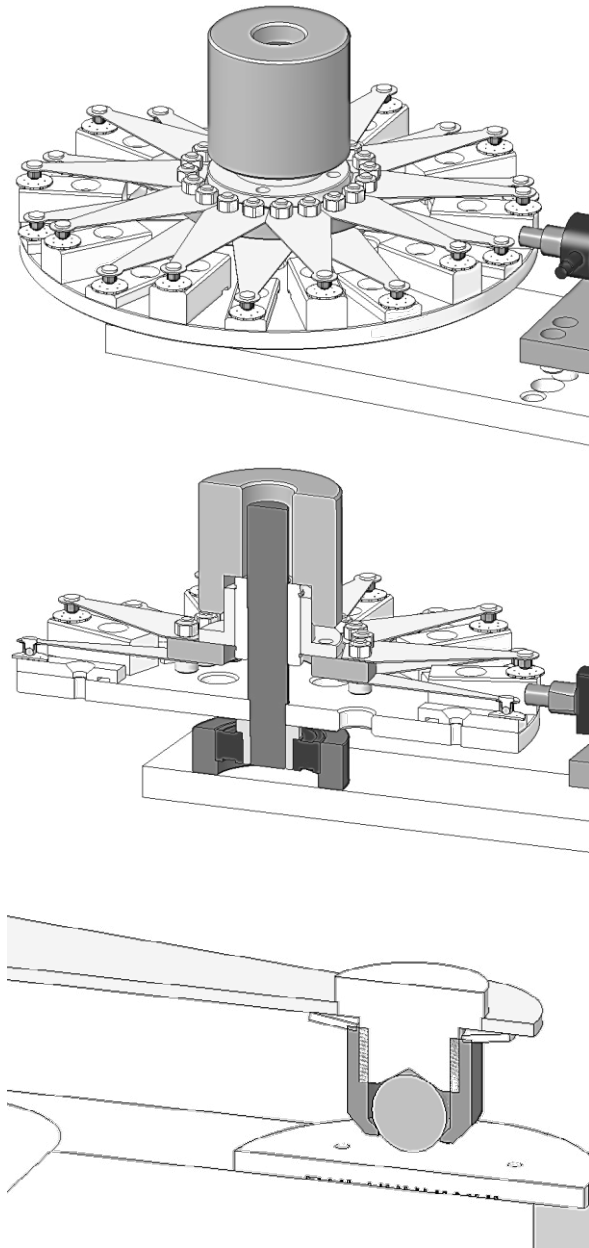


Fig. 1 Test bench. a) Schematic view of complete test bench; b) cross section; c) cross section detail of contact spot with plated sphere contacting disc-shaped sample.

The operating principle of the test bench is schematically illustrated in **Figure 2**, representing the lower level. For the radial displacement of the plated disc-shaped samples towards the central axis, a step motor with an integrated load cell is placed on a mounting adjacent to the star-shaped test bench. The disc-shaped samples, which are contacted by the immovable spheres and protrude the fixed PTFE block, are moved towards the centre of the desk bench, i.e. in radial direction, with a speed of 1 mm/s. Simultaneously, the tangential force required for the movement, furthermore referred to as displacement force, is measured by a load cell and recorded with a frequency of 2400 Hz; thus, it is possible to determine the static friction force

as well as the dynamic friction force as a function of the displacement distance. It has to be noted that the displacement force is the sum of the frictional force between the immobile sphere and the displaceable disc-shaped sample ($F_{R_Contact}$) plus the frictional force between the disc-shaped sample and the immobile PTFE block ($F_{R_Disc_PTFE}$). For the investigation of the cold welding and galling behaviour of contacts, mainly the frictional force between the fixed sphere and the displaceable disc-shaped sample ($F_{R_Contact}$) is of interest. The contribution of $F_{R_Disc_PTFE}$ to the total displacement force is discussed in section 4.

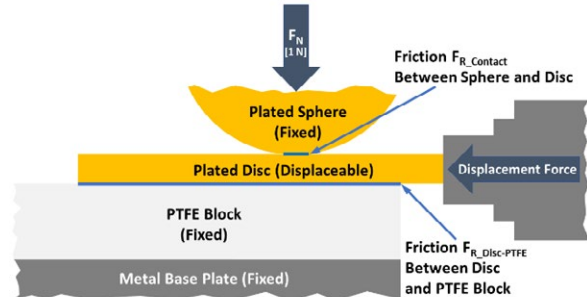


Fig. 2 Schematic illustration of the operating principle of the test bench.

2.2 Samples

Disc-shaped samples with knobs (base material CuZn37, 14 mm diameter, 0.8 mm thickness) as well as bronze spheres (base material CuSn6, three mm diameter) have been plated with common connector finishes by barrel plating. Silver plated samples have received an anti-tarnish post-treatment by a Sn immersion process. The different layer systems including their nominal layer thicknesses are shown in **Table 1**.

System	Base Layer	Underplate	Top Layer
Gold-Flashed Nickel	Cu (2 μm)	Electroless Ni High-Phos (2 μm)	Hard Au (0.1 μm)
Nickel	Cu (2 μm)	-	Duplex Ni (4 μm)
Tin	Cu (2 μm)	Ni (2 μm)	Sn (4 μm)
Silver	Cu (2 μm)	-	Ag (4 μm)

Tab. 1 Plating layer systems investigated in this study

2.3 Experimental conditions

In this study, only homogeneous contact material pairings have been investigated. Samples have been installed in the setup by placing the disc-shaped samples on the PTFE blocks and mounting the spheres in the sample holder. Afterwards, the star-

shaped upper part has been put gently on the lower part in a way that the spheres contact the discs without any wiping motion. Finally, a defined load has been put on the central axis in order to apply a normal force on the contact. In this study, all contacts were affected by a normal force of 1 N. Unless otherwise stated, the measurement of the displacement force has been carried out immediately after assembling. In order to test all 20 samples of an individual setup, the test bench has been rotated carefully in order to move every sample to the step motor without inducing any unintended displacement of individual contacts before the measurement. The experimental setup, assembled with silver-plated samples (with Sn immersion anti-tarnish post-treatment), has also been subjected to an accelerated aging test in mated condition by uninterrupted storing in a heating chamber at 175°C for 250 h, 500 h, and 1000 h, respectively. Individual experiments for different exposure durations have been performed independently. For each experiment, new samples have been used. The test setup has been allowed to cool down in the heating chamber to ambient temperature. Afterwards, the measurement has been performed in the heating chamber carefully without moving the test bench in order to avoid any disturbance of the closed contacts. After the displacement force of all samples had been measured, the upper part was lift-off vertically without any lateral movement. On both sides of the contacts, the wear tracks resulting from the experiment have been examined by confocal laser scanning microscopy (Keyence VK-X 100 series).

3 Results

For all contact pairs investigated, characteristic measurements displaying the displacement force as a function of the displacement distance are shown below. In addition, **Table 2** provides an overview about the median values of the static friction (i.e. the maximum of the displacement force at the initial phase of movement) as well as the dynamic friction (average of the displacement force after passing the initial maximum caused by static friction).

A boxplot displaying the summaries of static displacement forces (static displacement forces of individual measurements, 20 samples per experiment) and dynamic displacement forces (dynamic displacement forces of individual measurements, 20 samples per experiment) of investigations on gold-flashed nickel contacts, nickel-plated contacts and tin-plated contacts is shown in **Figure 3**.

Again it is pointed out that these values are not equivalent to the coefficient of friction of contact materials, as the displacement force does not only include friction resulting from displacement of the mated samples (i.e. friction between plated spheres and plated discs), but also friction resulting from the movement of the disc-shaped samples on the PTFE block.

Contact Pair	Displacement Force [N]	
	Static Friction	Dynamic Friction
Gold-flashed Nickel	0.39	0.31
Nickel	0.30	0.25
Tin	1.32	0.89
Silver before aging	0.42	0.30
Silver - 175°C/250h	1.58	1.37
Silver - 175°C/500h	1.64	1.73
Silver - 175°C/1000h	2.07	1.69

Tab. 2 Static and dynamic friction values (medians of 20 individual samples for each plating) of various connector platings derived from the measurement setup described above at a normal force of 1 N

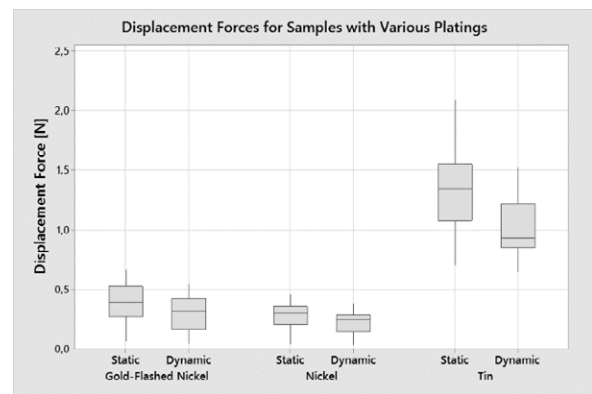


Fig. 3 Boxplot showing displacement forces for both static and dynamic friction of individual measurements of contact arrangements with various platings.

3.1 Gold-flashed nickel samples

For gold-flashed samples with nickel high-phos plating, the static friction showed an average of 0.39 N (median), while the median of dynamic friction was around 0.31 N, being relatively constant over the whole sliding distance. A typical graph of the displacement force versus the displacement distance for gold-flashed nickel samples is shown in **Figure 4**. No distinct wear tracks were observed under the microscope.

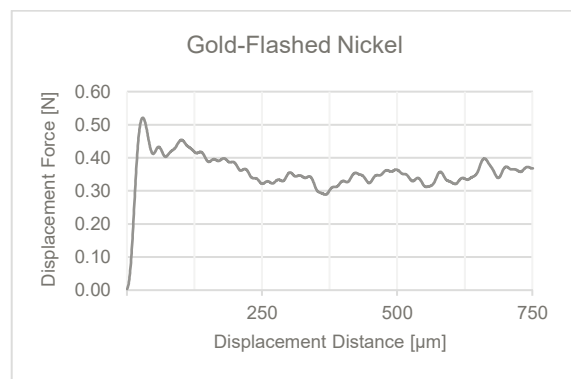


Fig. 4 Representative graph showing displacement force vs. displacement distance for a gold-flashed nickel contact arrangement.

3.2 Nickel-plated samples

Nickel-plated samples plated with a duplex nickel system revealed a static friction of 0.30 N (median) and a dynamic friction of 0.25 N (median). A typical graph of the displacement force versus the displacement distance for nickel samples is shown in **Figure 5**. Similar to gold-flashed nickel-plated samples, no distinct wear tracks were observed during confocal laser scanning microscopy.

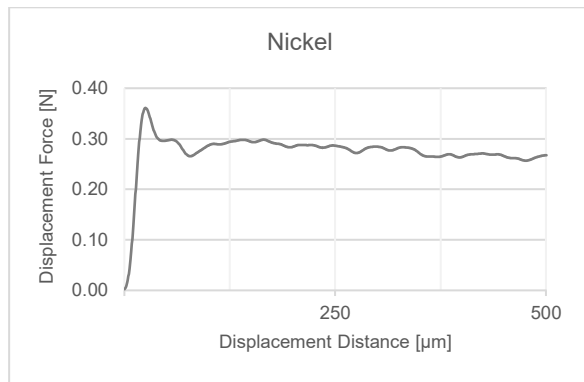


Fig. 5 Representative graph showing displacement force vs. displacement distance for a nickel-plated contact arrangement.

3.3 Tin-plated samples

In contrast to the samples mentioned above, tin-plated samples show drastically higher friction, with a pronounced maximum at the initial stage of the displacement that can be attributed to static friction (median 1.32 N), followed by a plateau representing dynamic friction with a median of 0.89 N, as shown in **Figure 6**. Confocal laser scanning microscopy showed pronounced wear tracks on the disc-shaped samples with numerous protrusions above the original surface within the wear track, which is considered as characteristic feature of galling. A typical wear track of a tin-plated sample is shown in **Figure 7** and **Figure 8**. Furthermore, significant wear has also been observed on the rider, i.e. on the plated sphere.

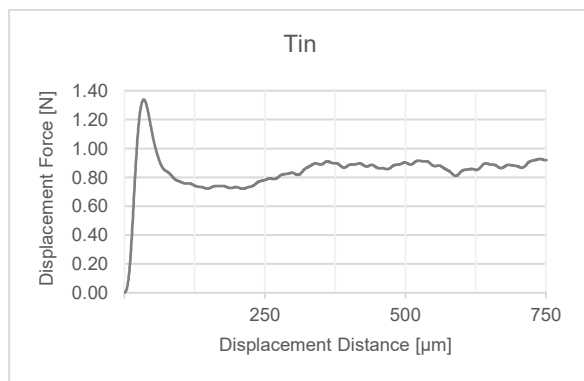


Fig. 6 Representative graph showing displacement force vs. displacement distance for a tin-plated contact.

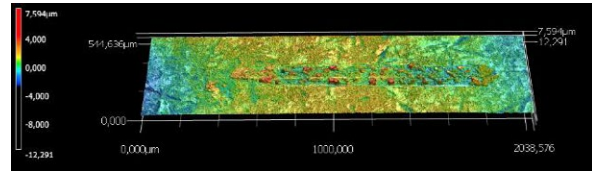


Fig. 7 Topography model of the wear track on a tin-plated disc-shaped sample (400% vertical exaggeration).

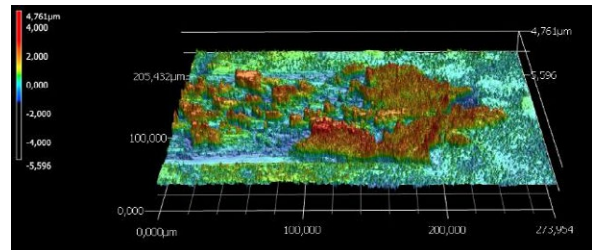


Fig. 8 Topography model of the terminal point of a wear track on a tin-plated disc-shaped sample (400% vertical exaggeration).

3.4 Silver-plated samples

3.4.1 Measurements performed immediately after mating

Fresh silver-plated samples with tin immersion anti-tarnish post treatment revealed a static friction of 0.42 N (median) and a dynamic friction of 0.30 N. A typical graph of the displacement force versus the displacement distance for silver-plated samples is shown in **Figure 9**. While wear tracks on the flat sample were only weakly pronounced, distinct cold welding and galling features have been found on the spheres, see **Figure 10**, as well as on the terminal point of the wear track, where the contact has been unmated by a vertical lift-off.

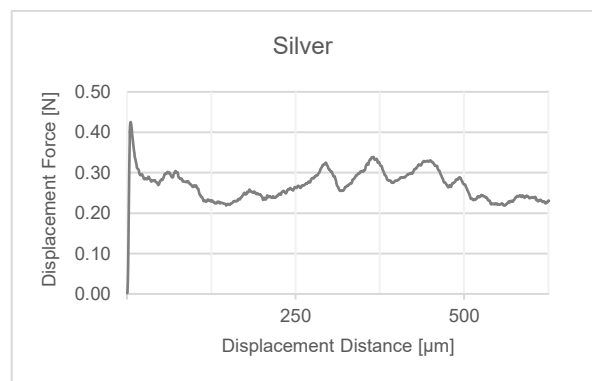


Fig. 9 Representative graph showing displacement force vs. displacement distance for a silver-plated contact arrangement.

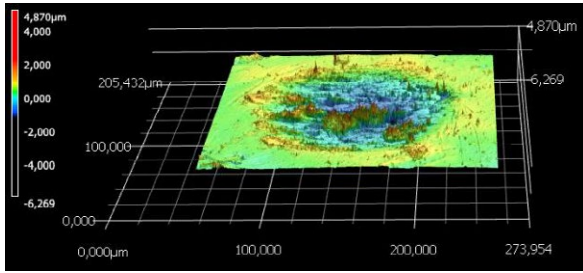


Fig. 10 Topography model of wear on a silver-plated sphere (400% vertical exaggeration).

3.4.2 Measurements performed after accelerated aging of mated contacts

Accelerated aging of silver-plated samples with tin immersion anti-tarnish post treatment in mated condition has been performed by storing the assembled setup at 175°C for 250 h, 500 h, and 1000 h, respectively. The measurements have been performed on individual samples, i.e. measurements after different exposure durations have not been performed on the same sample surface, as the contact spot would have been disturbed by the measurement. The accelerated aging led to a significant increase of the displacement force as well as to a notable change of the general shape of the curve displaying the displacement force vs. displacement distance.

After 250 h exposure at 175°C with a load of 1 N per contact spot, the static friction increased to 1.58 N (median), while the dynamic friction was around 1.37 N (median). After 500 h, the median values of static and dynamic friction increased to 1.64 N and 1.73 N, respectively; and after 1000 h, the median values of static and dynamic friction were around 2.07 N and 1.69 N, respectively. A boxplot displaying the summaries of static displacement forces (static displacement forces of individual measurements, 20 samples per experiment) and dynamic displacement forces (dynamic displacement forces of individual measurements, 20 samples per experiment) of experiments with silver-plated contacts is shown in **Figure 11**.

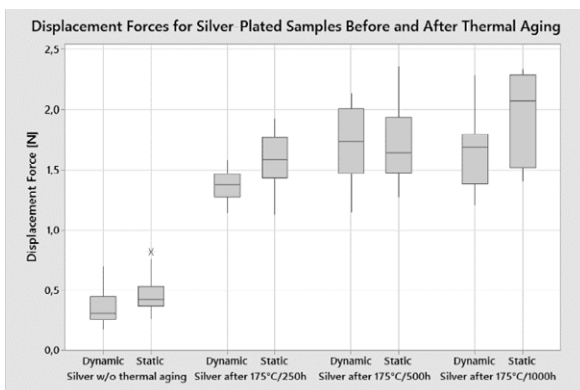


Fig. 11 Boxplot showing displacement forces (both static and dynamic friction) of individual samples for silver-plated contacts before and after aging in mated condition for 250 h, 500 h, and 1000 h, respectively.

In contrast to other measurements, the highest displacement forces after aging are not at the beginning of the movement (i.e. at the initial phase, caused by static friction), but rather randomly distributed over the movement phase. The graph of the displacement force vs. displacement length shows several individual maxima and an irregular shape of the curve, without features like a dominant static friction peak at the beginning followed by a rather constant displacement force during the movement. Typical curves for 250 h, 500 h, and 1000 h are shown in **Figure 12**, **Figure 13**, and **Figure 14**, respectively.

Surfaces of samples that have been subjected to accelerated aging by storage at 175°C show features that indicate signs of aging. Confocal laser scanning microscopy showed the presence of wear tracks on both contact partners. Contrary to tin-plated samples, protrusions within the wear track were less pronounced, but there was a notable material transfer to the terminal point of the wear track, see **Figure 15**.

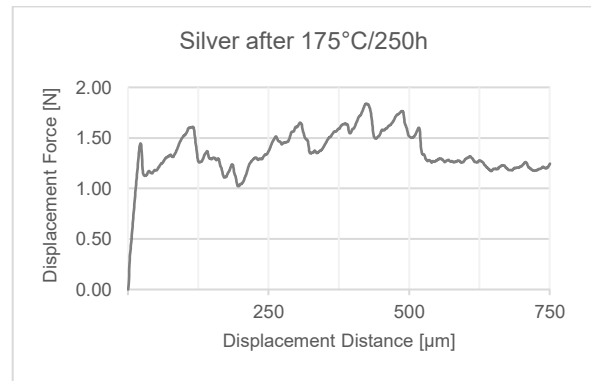


Fig. 12 Representative graph showing displacement force vs. displacement distance for an arrangement with silver-plated contacts after exposure to 175°C for 250 h in mated condition.

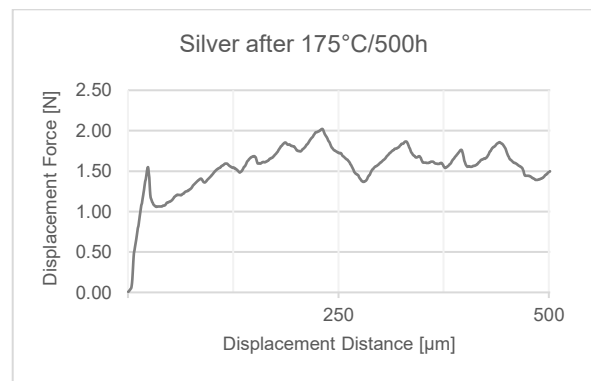


Fig. 13 Representative graph showing displacement force vs. displacement distance for an arrangement with silver-plated contacts after exposure to 175°C for 500 h in mated condition.

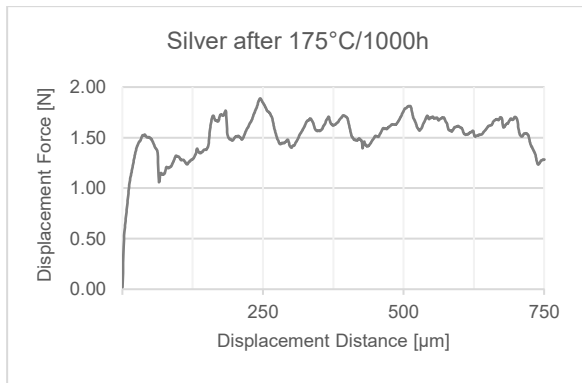


Fig. 14 Representative graph showing displacement force vs. displacement distance for an arrangement with silver-plated contacts after exposure to 175°C for 1000 h in mated condition.

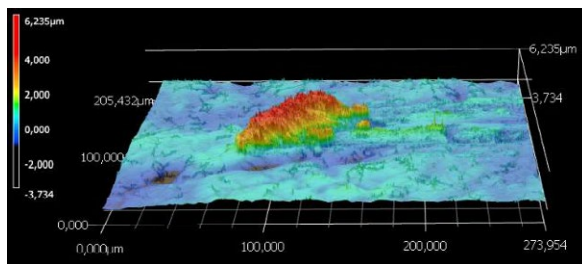


Fig. 15 Topography model of the terminal point of the wear track on a silver-plated disc-shaped sample after aging for 1000 h at 175°C in mated condition (400% vertical exaggeration).

4 Discussion

For gold-flashed nickel, nickel, tin, and silver contacts before aging, the shapes of the curves illustrating the displacement force as a function of the displacement distance are well in accordance with the widely accepted model, displaying an initial friction maximum due to static friction, followed by a +/- constant plateau at a lower displacement force that can be attributed to dynamic friction. Confocal laser scanning microscopy of tin-plated samples show distinct features of galling and cold welding that were not observed for other samples. It stands to reason that the comparatively soft tin plating facilitates the formation of such phenomena. Silver-plated samples that have been subjected to an accelerated aging in mated condition show a very interesting feature. It is well-known that connectors where both contact partners are plated with silver can show very high unmating forces, particularly if the contacts have been mated for a longer time and/or been exposed to elevated temperatures. In this study it was shown that the friction of such contacts is not only high at the very beginning of the movement, i.e. where a high coefficient of friction due to cold welds that formed between mated contacts might be expected. Instead, the friction remains high or even increases during the movement, so the dynamic friction during the

displacement might be even higher than the static friction at the beginning of the movement. For silver-plated contacts that have been subjected to accelerated aging in mated condition, the maximum values of the displacement force are observed frequently not at the beginning of the movement. In this case, the shape of the graph of the displacement force versus displacement length resembles a stick-slip movement. This phenomenon has already been mentioned in literature, stating that a sliding movement between two metallic surfaces is in most cases not a steady motion, but it is rather divided into more or less pronounced phases of adhesion and sliding, resulting in a stick-slip motion [5, 6].

As cold welding is particularly promoted by the presence of pristine metal surfaces without oxide layers or other contaminations, noble metals such as silver are particularly affected by this phenomenon. The influence of the anti-tarnish post-treatment prevents the formation of notable cold welds in the beginning, but after storage, the protective effect disappears.

It has already been mentioned that the values for static and dynamic friction, derived from displacement forces shown above, are not equivalent to coefficients of friction for contact materials shown in literature, as in this study, also the friction between the PTFE block and the disc-shaped samples has to be taken into consideration. Test measurements with silver-plated disc-shaped samples on PTFE blocks (i.e. without the upper part of the test bench, thus, only representing the frictional force between the moveable disc-shaped sample and the immobile PTFE block) revealed a coefficient of friction of ~0.12 for silver-plated samples on PTFE. Additional experiments showed that the coefficient of friction between other platings and PTFE is similar. Furthermore, the difference between static and dynamic friction is <0.05. If the contribution of friction between the disc-shaped samples and the PTFE block is taken into account (i.e. considering $F_{R_Disc_PTFE}$ as annotated in section 2.1), the resulting coefficients of friction for the metal/metal contacts are well in accordance with characteristic values for individual contact material pairings.

5 Conclusions

It was shown that the new test bench design presented in this study is capable to investigate the cold welding and galling behaviour of different connector platings. It particularly enables the analysis of the displacement force (i.e. friction) as a function of the displacement distance in order to study the friction properties of connector platings with model geometries. Furthermore, the test bench can be subjected to elevated temperatures, enabling the application of accelerated aging

tests for the investigation of the friction properties of aged connector platings in mated condition. Initial results on the cold welding and galling behaviour of different connector platings revealed notable results particularly for silver-plated contacts subjected to aging in mated condition. It was shown that the friction increases drastically after aging and the maximum friction of such samples does not occur at the beginning of the movement, but rather a high coefficient of friction is present during the whole movement. These results support the need of further investigations with this kind of test setup.

6 Literature

- [1] Hummel, S. R., & Helm, J. (2010). Repeatability Estimation in Galling Resistance Testing. *Journal of Tribology*, 132(4), pp. 044504-1 – 044504-5.
- [2] ASTM Committee G02 on Wear and Erosion (2008). Standard Terminology Relating to Wear and Erosion. *G40-05, Annual Book of ASTM Standards*, ASTM, Philadelphia, Vol. 03.02.
- [3] Kassman, Å., & Jacobson, S. (1993). Surface damage, adhesion and contact resistance of silver plated copper contacts subjected to fretting motion. *Wear*, 165(2), pp. 227 – 230.
- [4] Rudolphi, Å. K., & Jacobson, S. (1996). Gross plastic fretting—examination of the gross weld regime. *Wear*, 201(1-2), pp. 255 – 264.
- [5] Vinaricky, E., Faber, M., Huck, M., & Bahrs, W. (2016). Gleitender Kontakt. In *Elektrische Kontakte, Werkstoffe und Anwendungen* (pp. 191-222). Springer Vieweg, Berlin, Heidelberg.
- [6] Braunovic, M., Myshkin, N. K., & Konchits, V. V. (2006). *Electrical contacts: fundamentals, applications and technology*. CRC press.

A Cu/Sn Multilayer System and its Fretting Corrosion Behavior

Haomiao Yuan, Jian Song*

Precision Engineering Laboratory, Ostwestfalen-Lippe University of Applied Sciences and Arts
32657 Lemgo, Germany

* Corresponding author: jian.song@th-owl.de (J. Song)

Abstract

A plating is generally applied on the base material of electrical contacts, in order to extend their lifetime and achieve higher performance. Tin is a widely used plating material because of its good corrosion resistance and commercial benefit. However, the tin plating can also be oxidized. If relative motion is inevitable, a thick oxide layer can form, causing electrical failure after long-term operation. In order to extend the application of tin platings in electrical contacts, an inexpensive method regarding lifetime extension is much in demand. In this paper, a system with a Cu/Sn multilayer, fabricated with a galvanic process, is developed to prolong the lifetime of tin plated electrical contacts. With the assistance of design of experiments (DoE), the influence of the number of Cu/Sn layers, the plating time of the Cu and Sn layer and the use of the Ni layer as an underlayer on the lifetime of the electrical contacts is investigated. It is revealed that the lifetime of the multilayer system is significantly improved compared to the conventional single layer tin plating. Consequently, application range of tin platings can be greatly extended.

1 Introduction

The development of cyber-physical systems, such as autonomous and networked vehicles and smart factories, increases the demands on highly reliable and long-lifetime electrical contacts to connect the large quantity of terminals in the system. Initially, gold was used as the plating material for electrical connectors, because it can provide a low and stable contact resistance for the majority of applications during their service life [1]. However, since the mid 1970's, the price of gold has not only increased but also become unstable, which has led to the consideration about the necessity of using gold and the development of alternatives [2]. Tin or tin alloy plating is thought to be a good candidate [2-6]. However, the tin surface can also be oxidized. Fretting corrosion is one of the critical failure mechanisms of tin plated electrical contacts, if relative motion between the contact parts is inevitable during the operation. As a result, the lifetime of tin plated electrical contacts is much shorter than gold plated electrical contacts [7]. In order to extend the application of tin plating, it is of great importance to develop an inexpensive method to fabricate tin plating which has a long lifetime.

In our previous study, it was found that a longer lifetime in the fretting corrosion test can be more feasibly achieved with thinner tin plating [8] and bare copper base material has a longer lifetime in the fretting corrosion test than tin plated electrical contacts under certain operating conditions [9]. However, bare copper has an insufficient corrosion resistance, and thus tin plating is used as a passivating

layer to provide a good protection against corrosion [10]. This initiates the design of a Cu/Sn multilayer system to take advantage of the Sn and Cu surfaces for better performance against corrosion and fretting corrosion. The basic concept is to repeat the thin layers of copper and tin to form a multilayer system. By generating this kind of multilayer system, Cu-Sn intermetallic compound can be formed, and the hardness of the plating can be increased [11]. The wear of the surface will be slowed down, and the wear debris is as a result reduced. If there is less wear debris in the contact interface, the oxidation of the wear debris will also be inhibited. As each layer of the plating is thin, the amount of intermetallic compound is also controlled, so that the negative influence of too thick intermetallic compounds on the contact resistance can be limited. Moreover, introducing a nickel underlayer can assist in obtaining a smoother surface, it is also involved in the plating system, and the influence of the nickel underlayer is investigated. In this paper, the fabrication of the Cu/Sn multilayer system is realized with a galvanic process. The scopes of this study are:

- If a Cu/Sn multilayer system could improve the fretting corrosion performance
- If the copper or tin layer should be used as the first layer
- The optimum combination of parameters: the number of Cu/Sn layers, the use of a Ni underlayer and the plating duration of the Cu and Sn layers

For the purpose of a systematic study, the design of experiments (DoE) is employed. In this study, the potential of prolonging the lifetime of non-noble materials plated electrical contacts using the

multilayer system is demonstrated. The average lifetime of the multilayer systems is compared to the single tin plating. Based on this study, the preferred multilayer systems are recommended for the future study.

2 Experimental

2.1 Samples

The samples consist of a sphere/plane configuration. The radius of the spherical parts is 4.5 mm. The base material is stamped from copper sheets. The total surface of a contact pair is approx. 0.012 dm². The plating is fabricated with a galvanic process as demonstrated in Section 2.4.

2.2 Preliminary experiment

The aim of the preliminary experiment is to determine the first deposition layer for the Cu/Sn layers. Two tests are conducted to find out, whether the tin layer or the copper layer should be used as the first deposition layer. These plating systems with the same number of tin layers are listed in Table 1. The results are demonstrated in Section 3.1. Based on the result of the preliminary experiment, the copper layer is used as the first deposition layer, since a longer mean lifetime is achieved. Further experiments will use the copper layer as the first layer to start the Cu/Sn layers in the multilayer plating.

Table 1 Plating systems to determine the first deposition layer

Plating system	Plating time for Cu layer [s]	Plating time for Sn layer [s]
Cu/Sn/Cu/Sn	60	88
Sn/Cu/Sn	60	88

2.3 Design of parameter matrix for fabrication

The parameter matrix to fabricate the multilayer system is designed with the assistance of the DoE to conduct a systematic investigation of the influence of the parameters on the lifetime of the produced electrical contacts. The Taguchi algorithm is used. The parameters are the number of Cu/Sn layers, the plating time for each nickel layer, for each copper layer and for each tin layer. The resultant plating systems are listed in Table 2.

2.4 Plating procedure

The plating procedure is schematically illustrated in Fig. 1. During one implementation of the plating process, three contact pairs are clamped to the sample holder. In order to prepare for galvanic plating, the

samples are firstly degreased in an alkaline bath to remove the oil on the sample surfaces applied during the stamping of the samples. Then a pickling process in a sulfuric acid solution is used to neutralize the remaining alkaline substances, followed by rinsing in water.

Afterwards, the layers are deposited according to the parameter matrix in Table 2. The nickel plating is plated in the bright nickel bath manufactured by Katewe. The electrolyte is heated to 35 °C and the temperature is maintained during the plating process. The current density is 1.5 A/dm², corresponding to a current input of 55 mA. The copper plating is deposited in a copper bath SLOTOCOUP CU 50 manufactured by Dr.-Ing. Max Schlötter GmbH & Co. KG. The Cu plating is fabricated at room temperature. The current density is 2 A/dm², resulting in a current input of 74 mA. The tin layer is galvanically plated in the electrolyte tin bath SLOTOTIN 60 manufactured by Dr. Ing. Max Schlötter GmbH & Co. KG. The electrolyte is heated to 35 °C and the temperature is kept stable during the plating process. The current density is 2 A/dm², corresponding to 74 mA current input. After each deposition, the surface is rinsed in distilled water for 30 s.

By varying the plating time, different plating thickness can be obtained. Experiments were conducted to obtain the build-up rate of each layer. The build-up rate for the nickel, copper and tin layers is about 0.17 µm/min, 0.3 µm/min and 0.34 µm/min, respectively. Thus, the thickness of nickel, copper and tin layers should be in the range of 0.5~1 µm, 0.1 ~ 0.5 µm and 0.1 ~ 0.5 µm, respectively. As a reference, samples with single tin plating of 1 µm on the copper base material are fabricated.

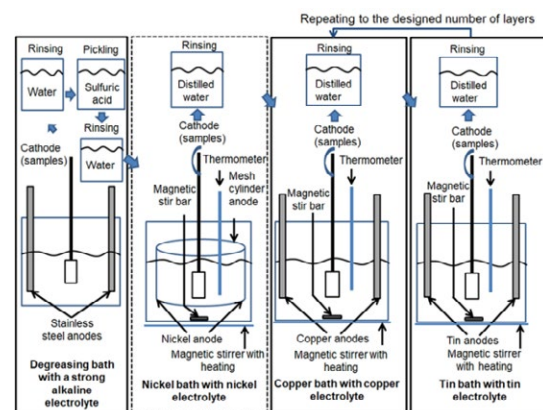


Fig. 1 Schematic illustration of the plating procedure to fabricate the multilayer system

Table 2 Plating systems according to DoE

Variation	Number of Cu/Sn layer	Plating time for each Ni layer [s]	Plating time for each Cu layer [s]	Plating time for each Sn layer [s]	Plating system
1	2	-	20	18	Cu/Sn
2	2	173	60	53	Ni/Cu/Sn
3	2	347	100	88	Ni/Cu/Sn
4	4	-	60	88	Cu/Sn/Cu/Sn
5	4	173	100	18	Ni/Cu/Sn/Cu/Sn
6	4	347	20	53	Ni/Cu/Sn/Cu/Sn
7	6	-	100	53	Cu/Sn/Cu/Sn/Cu/Sn
8	6	173	20	88	Ni/Cu/Sn/Cu/Sn/Cu/Sn
9	6	347	60	18	Ni/Cu/Sn/Cu/Sn/Cu/Sn

2.5 Wear and fretting corrosion test

The wear and fretting corrosion test device illustrated in Fig. 2 is used to measure the lifetime of the electrical contacts. The normal force in the test is 2 N; the peak to peak fretting amplitude is 50 μm . The temperature is room temperature, and the fretting frequency is 1 Hz. The termination criterion is the electrical contact resistance reaching 300 m Ω . For each variation of plating, three pairs of specimens are tested.

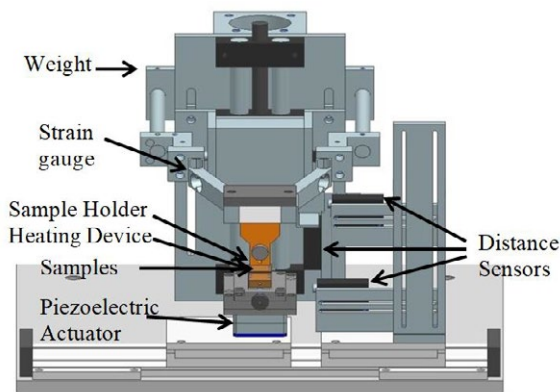


Fig. 2 Schematic illustration of the wear and fretting corrosion test device

2.6 Characterization of the element distribution of the multilayer

After the wear and fretting corrosion test, the element distribution on the cross-section of the layers is analyzed. The samples are cut by a focused ion beam

(FIB) outside of the wear scar, and the cross-section of the multilayer system is observed using a scanning electron microscope (SEM), Zeiss NEON[®] 40. The element distribution on the cross-section is measured with an energy-dispersive X-ray spectroscopy (EDS), UltraDry EDS Detector from Thermo Fisher Scientific, using the X-ray Linescans mode.

3 Results and Discussion

3.1 Preliminary experiments for the determination of the first layer

In Fig. 3 the mean lifetime of the plating system “Cu/Sn/Cu/Sn” and “Sn/Cu/Sn” with the plating parameters in Table 1 is illustrated. With the Cu as the first deposition layer, a longer mean lifetime is more likely obtained. Thus, Cu is used as the first layer in the stack of Cu/Sn layers.

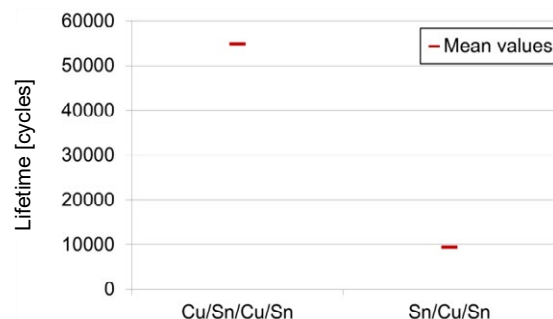


Fig. 3 Comparison of the mean lifetime of plating system “Cu/Sn/Cu/Sn” and “Sn/Cu/Sn” with the same plating parameters in Table 1

3.2 Potential of improving lifetime using multilayer system

The potential of improving lifetime using multilayer system is shown in Fig. 4. The lifetime of the multilayer system increases greatly compared to that of the conventional single tin layer on the same base material of copper. Considering the costs and the performance, the best results are achieved with the Variation 4 (Cu/Sn/Cu/Sn) and Variation 5 (Ni/Cu/Sn/Cu/Sn) structures. It should be noticed that the scattering of the lifetime is large, but it can be reduced by optimization and stabilization of the galvanic process. For this purpose, a large number of plated samples are required, which is beyond the scope of this study.

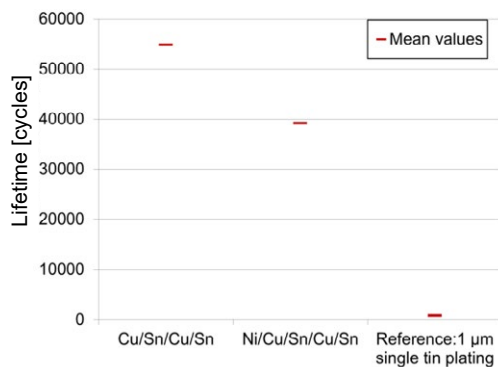


Fig. 4 Comparison of the mean lifetime of multilayer systems and the lifetime of conventional single tin plating

3.3 Element distribution of the multilayer

The element distribution of multilayer Variation 4 (Cu/Sn/Cu/Sn) is measured on the cross-section of the multilayer with EDS. The result is illustrated in Fig. 5. Two tin content peaks are found along the measuring line, corresponding to the tin layers. Meanwhile copper content valleys can be observed. The simultaneous presence of tin and copper indicates the formation of the Cu-Sn intermetallic compound. The Linescan shows the variation of copper and tin content on the multilayer, but it cannot characterize the thickness of the multilayer. The reason for this is the Linescan measurement spot is larger than the thickness of the layer. Based on the EDS result, the multilayer system is successfully fabricated.

3.4 Wear scars of the multilayer system

The wear scars of the multilayer system from the Variation 4 (Cu/Sn/Cu/Sn) are observed with a digital microscope. As a reference, the tin single layer plating

of 1 μm is also analyzed. The wear scars are shown in Fig. 6. According to the microscopies, the size of the wear scars does not show large difference. The single tin plating is totally black and no color from the base material of copper is observed. This is the typical indication for the fretting oxidation of tin. The edge of the wear scar is smooth. On the contrary, though the most part of wear scar of the multilayer system Variation 4 (Cu/Sn/Cu/Sn) is black, the color from copper can be observed, indicating the mixture of tin and copper and their oxides in the contact area. The edge of the wear scars is no longer smooth.

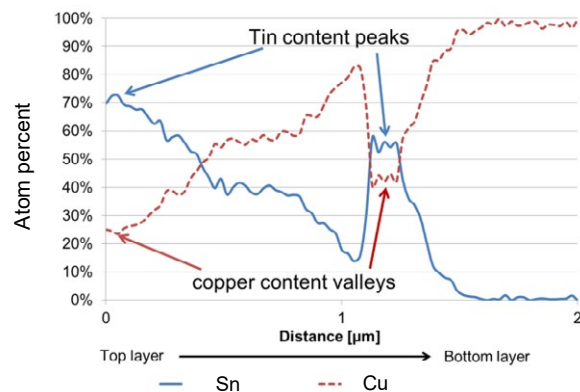
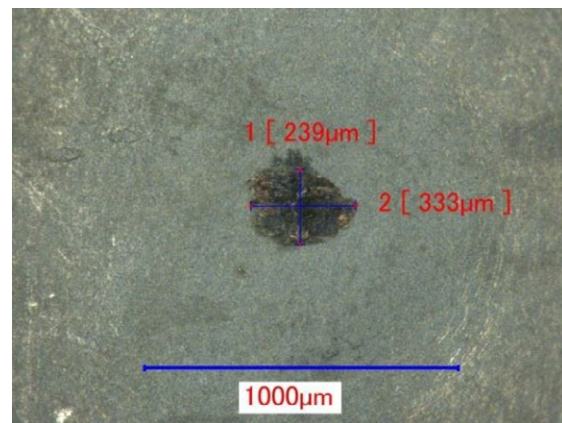
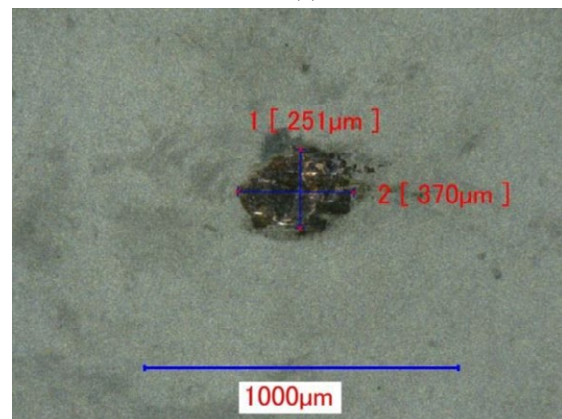


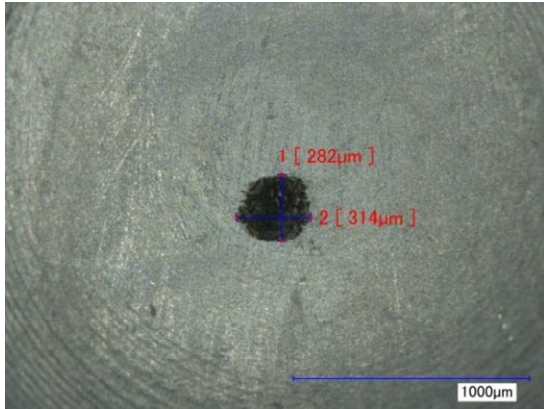
Fig. 5 Element distribution on the cross-section of the multilayer Variation 4 (Cu/Sn/Cu/Sn, Sn is the top layer), measured by EDS in X-ray Linescans mode



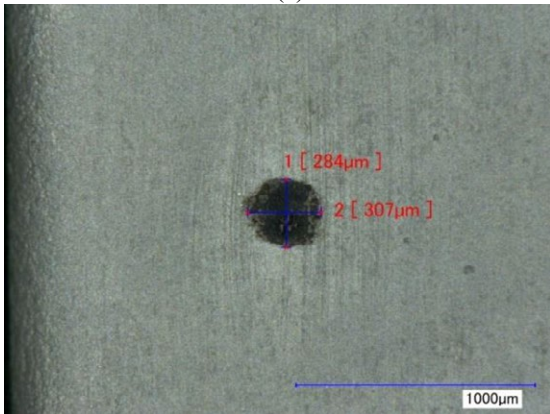
(a)



(b)



(c)



(d)

Fig. 6 Wear scars of multilayer system and the single layer tin plating: (a) wear scar on the spherical part Variation 4 (Cu/Sn/Cu/Sn); (b) wear scar on the flat part Variation 4 (Cu/Sn/Cu/Sn); (c) wear scar on the spherical part with 1 μm single tin plating; (d) wear scar on the flat part with 1 μm single tin plating

3.5 Influence of plating parameters in the galvanic process on the lifetime of electrical contacts

In this study, the mean lifetime of each plating system is used to find the influence of the plating parameters of the plating system on the lifetime of the electrical contacts and to provide the directions for further investigation. The influence of the number of Cu/Sn layers, along with the plating time for the nickel layer, the copper and the tin layer on lifetime is analyzed and illustrated in Fig. 7. Based on the mean lifetime of each plating system, it is found that an increase in the number of Cu/Sn layers can assist in prolonging the lifetime of the electrical contacts; however, after the number of Cu/Sn layers exceeds four, the lifetime of electrical contacts with six Cu/Sn layers is not further improved compared to the lifetime of the four-layer-system. The use of nickel as the underlayer and the plating time for the nickel layer in the testing range do not show clear influence on the lifetime of

the electrical contacts. At a moderate plating time for the copper layer and a short plating time for the tin layer in the testing range, a longer lifetime is more likely to be achieved. The influence grade of each plating parameter is ranked in Table 3. As a consequence, it is recommended to optimize the plating time of tin layer at first, in order to obtain a longer lifetime. The long lifetime is achieved with both four-layer-system and six-layer-system. Since the cost for the galvanic process is roughly proportional to the number of layers, four-layer-system is preferred.

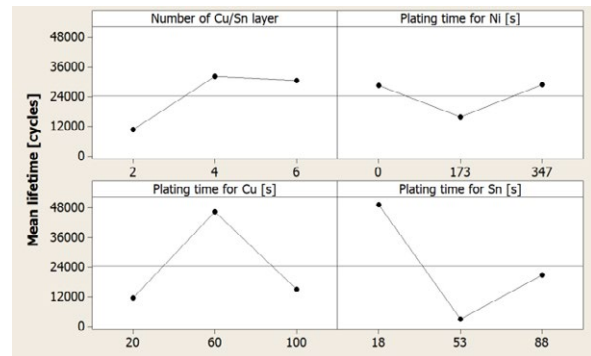


Fig. 7 Influence of plating parameters on the lifetime of the multilayer system

Table 3 Ranking of the influence of the plating parameters in the fabrication on the average lifetime of the multilayer system

	Number of Cu/Sn layers	Plating time of nickel layer	Plating time of copper layer	Plating time of tin layer
Ranking	3	4	2	1

4 Conclusion and Outlook

In this paper, a novel Cu/Sn multilayer system is developed using the galvanic process in order to combine the good fretting corrosion behavior of copper and high corrosion resistance of tin. The potential to improve the lifetime of electrical contacts with non-noble plating by applying a multilayer system is investigated and validated by the results. The influence of the plating parameters in the galvanic process on the lifetime of the multilayer system is examined. Based on the results, by using a short plating time for the tin layer and a moderate plating time for the copper layer in the testing range, it is more likely to obtain a plating system with a longer lifetime. With a higher number of Cu/Sn layers, it is possible to achieve a longer lifetime; however, when exceeding four Cu/Sn layers, the lifetime of

electrical contacts does not increase further. Considering that the cost for the galvanic process is roughly proportional to the number of layers, four-layer-system is preferred. The use of nickel as an underlayer and the plating time for the nickel layer in the testing range do not show clear influence on the lifetime of the electrical contacts. Since the plating time for the tin layer has the greatest influence on the lifetime of the multilayer system, it is recommended to optimize the plating time of tin at first in order to achieve a long lifetime for the multilayer system.

We have observed that some variations of the multilayer systems display a large scatter with regard to lifetime in the wear and fretting corrosion tests. Thus, it would be worthwhile to carry out further research on the production of multilayer systems in order to optimize their stability. A corrosion test is also planned to examine, whether the developed multilayer system has a sufficient corrosion resistance.

5 Acknowledgment

This study is partly financed by the German Federal Ministry for Economic Affairs and Energy (BMWi, IGF, 20139 N).

6 Literature

- [1] AMP: Golden Rules: Guidelines for the Use of Gold on Connector Contacts. Technical Report of AMP Incorporated, Harrisburg, PA, USA, 1996
- [2] Whitley, J.H.: Reflections on contacts and connector engineering. Proceedings of 33rd IEEE Holm Conference on Electrical Contacts, 1987, pp. 1-7
- [3] Sankara Narayanan, T.S.N.; Park, Y.W.; Lee, K.Y.: Fretting-corrosion mapping of tin-plated copper alloy contacts. *Wear* 262 (2007), pp. 228–233
- [4] Sankara Narayanan, T.S.N.; Park, Y.W.; Lee, K.Y.: Fretting corrosion of lubricated tin plated copper alloy contacts: Effect of temperature. *Tribology International* 41 (2008), pp. 87–102
- [5] Park, Y.W.; Sankara Narayanan, T.S.N.; Lee, K.Y.: Fretting corrosion of tin-plated contacts: Evaluation of surface characteristics. *Tribology International* 40 (2007), pp. 548–559
- [6] Evans, C.: Connector finishes: tin in place of gold. *IEEE Transactions on Components, Hybrids, and Manufacturing Technology* 3 (1980)3, pp. 226–232
- [7] Yuan, H.; Song, J.; Koch, C., Silbernagel, E.; Schinow, V.: Tribological Properties and Fretting Performance of Gold, Silver and Tin Coatings. Proceedings of XXX International Conference on Surface Modification Technologies (SMT30), 29th June–1st July, 2016, Milan
- [8] Yuan, H.; Song, J.; Schinow, V.: Fretting corrosion of tin coated electrical contacts: the influence of normal force, coating thickness and geometry of sample configuration. Proceedings of the 62nd IEEE Holm Conference on Electrical Contacts, 9th-12th, October, 2016, Clearwater Beach, FL, USA
- [9] Yuan, H.; Song, J.; Schinow, V.: A modification of the calculation model for the prediction of the wear of silver-coated electrical contacts with consideration of third bodies. Proceedings of the 64th IEEE Holm Conference on Electrical Contacts, 14th-18th, October, 2018, Albuquerque, NM, USA, pp. 310–316
- [10] Song, J.; Wang, L.; Zibart, A.; Koch, C.: Corrosion Protection of Electrically Conductive Surfaces. *Metals* 2 (2012), pp. 450–477
- [11] Timsit, R.S.; Antler, M.: Tribology of electronic connectors: contact sliding wear, fretting, and lubrication, in Slade, P.G. (Ed.), *Electrical contacts: principles and applications*, 2nd ed., CRC Press, Boca Raton, 2013, pp. 276.

Silver Plating for Connectors - The right combination of new galvanic Silver processes and anti-tarnishes

*Dr. Bernd Roelfs, Markus Hoerbinger, Alexander Spörrer and Bruno Wibberg, Atotech Deutschland GmbH, Erasmusstr. 20, 10553 Berlin, Germany, bernd.roelfs@atotech.com

Abstract

Silver is the final finish material for connectors when transmission of either high current densities or frequencies is paramount. Its unmatched conductivity and comparable moderate price make it a viable alternative to Nickel Gold or Palladium finishes. Silver deposits must achieve certain requirements. The contact resistance of the deposit should be close to pure silver but hardness values should be significantly larger than pure silver and ideally not degrade during thermal budget as most Ag deposits do. Ag layers should not contain poisonous or harmful additives at best

We are presenting in this paper a combination of a newly modified non-cyanide Ag electrolyte Argalux NC mod with selected anti tarnishes based on either organic additives or Cr(III) solutions.

1 Introduction

Silver is the metal finish of choice for many upcoming connector applications e.g. for hybrid electric vehicles. This is the consequence of the excellent thermal and electrical conductivity and the price evolution of alternative materials as Au and Pd (see Fig 1). Silver is currently about a 100 times cheaper than Pd and 80 times cheaper than Au [1].

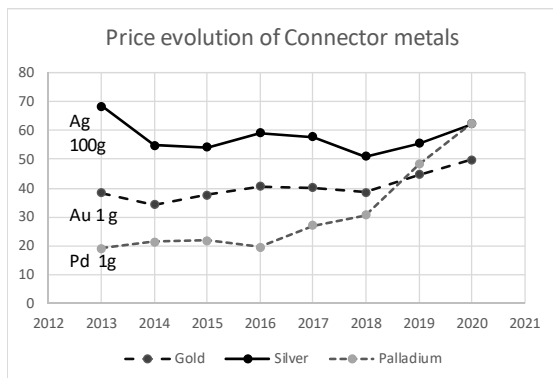


Fig. 1 Price evolution in of connector metals: Prices are given for fabricated materials in €/1 g except for Ag €/100 g.

Silver finishes are being used for battery chargers, battery connections to converters etc.. and must withstand high temperatures, vibration and corrosive media and exhibit certain physical properties as low contact resistance and high hardness over the time. Since pure

Ag layers do not fulfil all these requirements it is necessary to either modify the Ag layers either by adding certain additives or by using specific anti-tarnishes to protect them.

Thus, it is essential to choose the right Anti-tarnish for silver. This paper will discuss the influence and the decision criteria on both the Ag layer and the Anti-tarnish including a newly developed Anti-tarnish based on Cr. Fig. 2 demonstrates the schematic built-up of a typical connector, which complies of Ni diffusion barrier on the Cu ally base material, a relatively thick silver layer of varying thickness and three different anti-tarnishes.

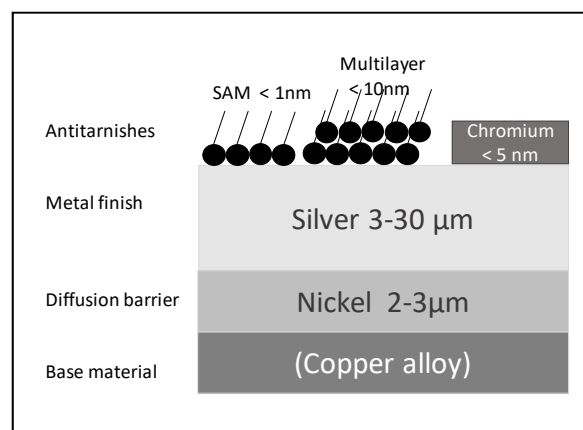


Fig. 2 Typical built up for a connector with 3 different anti-tarnishes i) organic ad layer based on a self assembled monolayer, ii) organic multilayer and iii) a chromium adlayer..

2 Silver plating

2.1 Electrolyte systems

The majority of commercialized Ag electrolytes is based on Ag-Cyanide. Ag-Cyanide is readily soluble in contrast to other Ag-salts, prevents Ag from precipitation and enables extremely high current densities of more than 100 A/cm². As a consequence, these electrolytes are used for high throughput manufacturing in Reel-to-Reel plating lines. These electrolyte can be applied for semi bright to mirror bright depositions covering a variety of applications such as lead frame plating, LED plating [2] and connector plating [3,4].

On the other hand there are only a few non-cyanide Ag electrolytes on the market based on Ag nitrate with reduced Ag concentration, thus reduced current densities of about 0.5-1 A/dm². Consequently these electrolytes are mainly used in barrel and rack plating machines. Target for us was to increase the productivity of this electrolyte type.

2.2 Test results

We improved our latest non-cyanide Ag electrolyte and managed to increase the Ag content from just 15 g/l Ag to 30 g/l. This in turn allows to double the applied CD from 0.5-1.0 ASD up to about 2 ASD. This converts to a plating speed of 1.2-1.5 μm/min. The improved electrolyte has no restrictions in the Ag thickness, 30 μm or more are accessible. Table 1 summarises the old and the modified version

Topic	Cyanide free Ag electrolyte	Modified cyanide free Ag electrolyte
Ag content g/l	15	30
CD A/cm ²	0.5 -1.0	1.0-2.0
Deposition speed μm/min	0.62 at 1 ASD	1.25 at 2 ASD
Max Thickness	6 μm	>30 μm

Table 1: comparison between the old and the modified NC Ag electrolyte (AgNO₃ based).

The deposition properties of the cyanide and non-cyanide based electrolytes differ significantly.

Table 2 gives an overview on the different properties. Main difference between a non-cyanide and cyanide electrolyte is the inherent hardness. This is one of the key factors for the usage of Ag electrolytes.

The modified CN free electrolyte has a constant and stable hardness of > 130 HV, independent of the bath age and storage time. Samples measured after half a year exhibit the same hardness values as freshly prepared ones. This is significantly higher than the pure or high speed versions of Ag hardness showing just about 70 HV which is in line with previous results documented in [3]. Hardness has been measured according

to ISO 14577-1 as indentation hardness and calculated to Vickers hardness.

Contact resistance tests have been conducted according to EN IEC 512 with parameters 10 mA/20 mV/5cN.

Process	Chemistry	Current Density ASD	Hardness (HV)	Contact resistance (mOhm)	Contact resistance (mOhm) After 1h at 200°C
CN free mod	CN Free	0.5-2.0	130 – 140	1.7	1.7
Pure Ag	High CN	2-50	70 – 80	2.6	1.4
High Speed Ag	Low CN	20 -300	70 – 120	1,7	1,7
Hard Ag	CN with hardener	0.2-1.2	160 – 210	2.3	2.3

Table 2: Comparison between different Ag electrolytes.

The hardness values can be modified with the help of specific hardeners as it is done for the hard Ag electrolyte in table 2. This comes on cost of an increase of the contact resistance. Moreover, the hardener type deposits tend to recrystallize already at moderate temperature of about 120°C and hardness may decrease [3].

The Cyanide free Ag deposit does not have a hardener component inside.

The purity of the Cyanide free deposit is as follows:

Mass fraction %	Carbon	Sulfur	Nitrogen
Mod. CN free Ag No hardener	0.087	<0.0005	0.020
CN electrolyte No hardener Pure Ag	0.009	<0.0005	<0.0005

The mod Cyanide free containing electrolyte is rated as ASTM B700 type 2B whereas a CN containing electrolyte without hardener is rated as ASTM B700 type 1A.

The difference is mainly based on the different crystal structure as can be seen from fig 3.

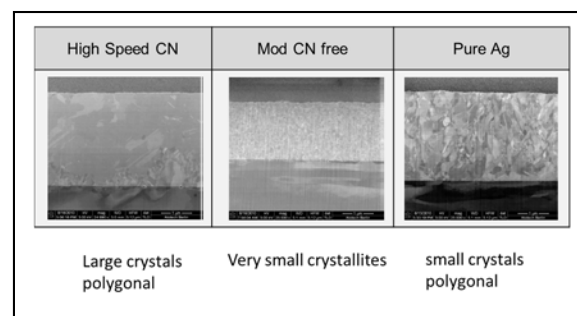


Fig. 2 SEM pictures of Ag plated layers from cyanide and CN free electrolytes (mid)

Both cyanide based system show a regular polygonal structure with comparably large crystallites, whereas the cyanide free Ag deposit shows a nanocrystalline structure with crystallites <100nm. The increasing hardness from the cyanide deposits to the non cyanide electrolyte is in line with the reduction of crystal size observations from other authors and fits well to the general Hall-Petch relationship [5,6]

The combination of a high inherent hardness, the low contact resistance, improved productivity and the non-hazardous character of the formulation is standing out to our knowledge and should make this Ag process a very interesting alternative to the standard cyanide type systems.

3 Anti-tarnishes

3.1 Tarnishing

Tarnishing of silver surface starts immediately after deposition and is strongly depending on the corrosive environment. Typical tarnishes effects are visible as colour changes to yellow or even black and are the consequence of sulphide or sulfur dioxide exposition. Thin layers of the semiconducting Ag₂S may not harm the technical properties but thicker sulphide layer may lead to enhanced corrosion, degrading solderability and an increase in contact resistance [7]. Effective anti-tarnishes have to minimize the formation of Ag₂S or AgSO₄ layers. Thus, we applied in the following tests

- K₂S Test (2 %)
- Thioacetamide test (DIN EN ISO 4538)
- Kesternich test (DIN EN ISO 6988)
- Contact resistance measurement (EN IEC 512)

with and without heat treatment of 1 h at 200°C.

3.2 Anti-tarnish Processes

The following anti-tarnishes have been tested (see table 3). There are 3 organic anti-tarnishes included two of which are based on thiols known to form self assembled mono or multilayers [8] and two chromium anti-tarnishes. The system plated from a Cr(VI) electrolyte has been used as a reference system. The system based on a Cr(III) electrolyte has been newly developed. Reach and RoHS conformity of that process and deposit has been confirmed.

All test have been done with a CuSn base material plated with a 5 µm thick layer of Ag from the non-cyanide electrode mentioned in Chapter 2.2 without any Ni intermediate layer.

Type	No	Description	CD [A / dm ²]
Organic:	AT-1	Water-based, hydrophobic Thiol Emulsion, multilayer	0.5 (optional)
	AT-2	Water-soluble Thiol monolayer	None
	AT-3	Org. Si-Polymer	None
Metallic:	AT-4	Cr coating Cr(VI)	1-5
	NEW: AT-5	Cr coating Cr(III)	6-18

Tab. 3 Overview about tested anti-tarnishes AT-1-5. All proprietary anti-tarnishes were used according to their data sheet.

3.3 Test results

3.3.1 Tarnishing test

Thioacetamide TAA test were performed acc. to DIN EN ISO 4538 in a 20l Glass desiccator at RT for 24 h with sodium-acetate 70% humidity and 50 mg/dm² Thioacetamide.

K₂S test were performed with a 2 % solution of K₂S and parts were dipped in for 15 min before and after heat treatment for 1 h at 200°C.

Kesternich test were done after RT storage and storage at 110° and 200 °C for one hour.

All test were optically evaluated. Colour change to slight yellowish has been rated as pass whereas as colour changes to yellow, red, brown or even black were rated as fail.

Example for test results are given in fig 3 and 4.

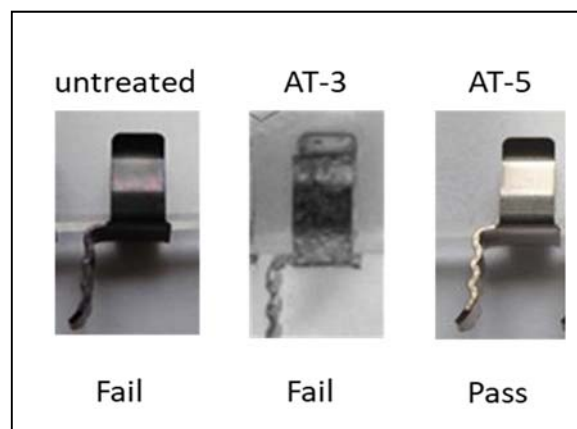


Fig. 3 Silver parts after TAA tests treated without Anti-tarnish, with AT-3 and with AT-5

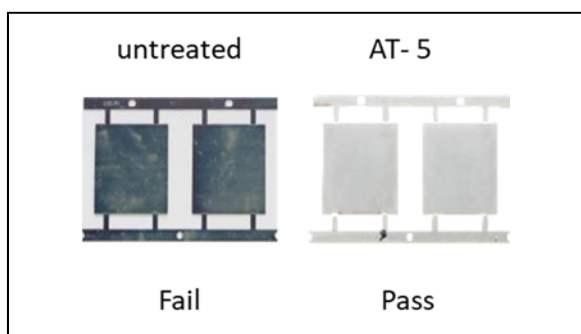


Fig. 4 Silver parts after K_2S test without Anti-tarnish (l) and with AT-5 (r) after 1 h at $200^\circ C$

No	Description	TAA Test	K_2S Test RT	K_2S after 1h $200^\circ C$	Kesternich 1 h $200^\circ C$
Ref.	No AT	fail	fail	fail	fail
AT-1	Thiol multilayer	pass	pass	fail	pass
AT-2	Thiol monolayer	pass	fail	fail	fail
AT-3	Si based polymer	fail	fail	fail	fail
AT-4	Cr coating Cr(VI)	pass	pass	pass	pass
AT-5	Cr coating Cr(III)	pass	pass	pass	pass

Tab. 4 Results from TAA, K_2S and Kesternich test for different anti-tarnishes.

Tab. 4 summarizes the test results with the different anti-tarnishes and its reference without any anti-tarnish. The silicon based anti-tarnish and the reference failed in all tests.

The multilayer thiol AT-1 gives a better performance than the monolayer thiol type AT-2 but fails at elevated temperatures. This is in line with Thermal Gravimetric Analysis TGA we performed on AT 1- and AT-2 layers which show that decomposition of the organic thiol adlayers starts at $160^\circ C$.

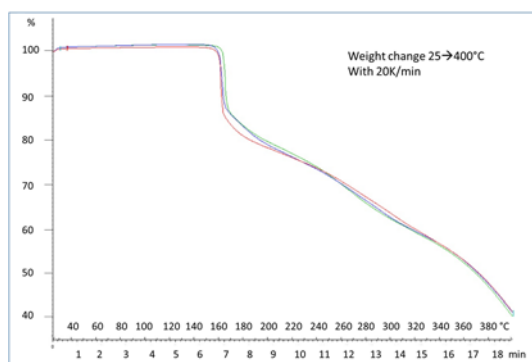


Fig. 5 TGA from the thiol monolayer based anti-tarnish showing decomposition at $160^\circ C$

Only the chromium based anti-tarnishes AT-4 and AT-5 pass all tests without any discoloration or stains. Kesternich tests results are reported after storage at $200^\circ C$ since here significant differences were visible.

The results from table 4 do not mean that AT-3, the silicon based AT-3 does not have any tarnishing effect. AT-3 covered Ag surfaces survives milder sulphide test 5 min in 5% Na_2S (not shown here) at RT and the TAA test for 2 h where none treated silver fails. A ranking based on the anti-tarnish effectivity would result in:

Anti-tarnish effectivity:

Chromium based Anti-tarnish > Thiol Multilayer >> Thiol Monolayer > Si- Polymer > none

3.3.2 Contact Resistance test

Contact resistance tests have been conducted according to EN IEC 512 with parameters 10 mA/20 mV/5cN, 8 measurement points from each sample. Measurements were conducted with sample storage at both at RT and 1h at $200^\circ C$ storage. For most samples additional tests after Pressure Cooker Test PCT have also been performed.

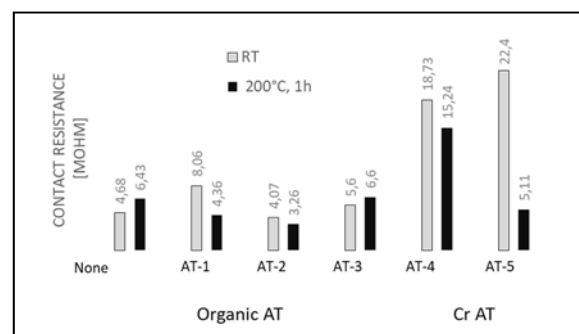


Fig. 6 Contact resistance of Ag plated parts treated with different Anti-tarnishes.

For some samples there is a significant difference between the RT and the 1h at $200^\circ C$ storage, esp. for the Chromium treated samples.

Samples treated with Chromium from Cr (VI) show a significantly higher contact resistance even after heat treatment in contrast to the samples treated with the Cr(III) electrolyte. The samples with the Cr(III) treatment show a comparable contact resistance to the organic Anti-tarnishes after a short exposure to heat which has been confirmed by independent test from customers.

The difference between the two different Cr anti-tarnishes is yet not fully understood and subject to further investigations. There is no thickness difference between the two Cr anti-tarnishes in this experiment, both system deliver a mean Cr thickness of only 2 nm (calculated from the Ah and an assumed current yield of 25%). Structural investigations on both systems will follow.

There is also a slight difference between the Multilayer thiol and the monolayer thiol based anti-tarnish. The multilayer based anti-tarnish shows a slightly higher contact resistance if stored at RT but declines after heat treatment probably due to partial decomposition.

3.3.3 Solderability test

The solderability performance of the two best performing anti-tarnishes has been investigated by the wetting performance of the different anti-tarnish covered Ag samples

Samples were silver plated with the non-cyanide version without a Nickel intermediate and test done according to IPC/EIA J-STD-003 WAM1&2: wetting of >95 % of the area is rated as good.

Solder bath: Sn96.5Ag3.0Cu0.5

Flux: Flux for lead-free soldering according to IPC/EIA J-STD-003C WAM1&2

Dipping device: Dip tester LPK

Fluxing time: 10 s

Soldering time: 10 s

Immersion rate: 25 mm/s

Sample	Wetting Performance
Not treated	Good
AT-1 Multilayer thiol	Good
AT-5 Cr from Cr(III)	Dewetting

Tab. 5 Wetting performance of Ant-tarnished Ag layers

The good results for the thiol covered surface is in line with wetting balance measurements [9] with a lead free SnAgCu solder (SAC) at 245°C and R-flux.

Measured is the time to zero $T(0)$ and the max.-force $F(\max)$ that is attained to the sample. For the multi-layered thiol AT-1 we measured a $T(0)$ to 0.3 sec and $F(\max)$ to 0.55 mN/mm whereas the Chromium type anti-tarnish showed a similar value for $T(0)$ of 0,33 s and a slightly lower but still acceptable $F(\max)$ of 0,44 mN/mm.

More investigations on solderability of chromium anti-tarnishes are under way to better understand significant factors that influence the solderability performance on the anti-tarnish.

3.4 Comparison

The choice of the right anti-tarnish for silver depends on a mixture of environmental requirements, tarnishing effectivity, solderability and contact resistance demands.

	Case 1	Case 2	Case 3	Case 4
Green approach	None RoHS	RoHS compatible	RoHS compatible	RoHS compatible
Tarnishing effectivity	Best: well suited for high T and harsh environment	Best: well suited for high T and harsh environment	Good: for normal environment conditions	Low: suited for manufacturing process protection
Temp. stability	> 200°C	>200°C	< 160°C	<160°C
Solderability	Case to case	Case to case	Very good	Very good
Contact resistance	Increase of >50 %	Change < 10 % (after heat treatment)	Change < 10 % (after heat treatment)	Change < 10 % (after heat treatment)
Recommended Anti-tarnish AT	AT from Cr(VI)	AT from Cr(III)	AT Thiol Multi layered	AT Thiol mono layer
Remarks	Not accepted in EU	Withstands probably T up to 500°C	Will reduce the coefficient of friction.	

Tab. 6 Comparison between different types of anti-tarnishes

An anti-tarnish based on a monolayer of Thiol is the choice for an in-process protection during manufacturing and short storage times with a focus on good solderability. The next level would be achievable with a multilayer thiol on cost of a slight increase of the contact resistance. Self-assembled layers of thiols are known to change the coefficient of friction [3] [10][11] depending on factors as monolayer vs multilayer, molecular structure and humidity and this has to be taken into account for the application.

4 Summary

We have shown that only the combination of the silver electrolyte and the subsequent anti-tarnish will result in the desired performance. A modified cyanide free Ag electrolyte with an inherent high hardness and low contact resistance has been presented as well as the most effective anti-tarnish based on RoHS compatible Cr(III) system.

5 Literature

- [1] https://www.agosi.de/ek/ek.php7front-end/showshow_jahre/de
- [2] Zhang et al. „Study on Ag-plated Cu Lead Frame and Its Effect to LED Performance under Thermal Aging. IEEE Transactions on Device and Materials Reliability. 14. 1022 - 1030. 10.1109/TDMR.2014.2360081.
- [3] H. Schmidt, “Oberflächen von Steckverbindern, Praxishandbuch Steckverbinder P. 205-244
- [4] M. Myers, “Overview of the use of Silver in Connector applications”, <https://electro-lurgy.com/wp-content/uploads/2015/06/Use-of-Silver-in-Connector-Applications-M-Myers.pdf>
- [5] X.Y. Quin et al. “The microhardness of nanocrystalline silver”, Nanostructured materials, 1995 Vol 5, 1, p. 101-110

- [6] <https://www.sciencedirect.com/topics/materials-science/hall-petch-strengthening>
- [7] S. Nineva et al. "New posttreatment process with enhanced technical performance: corrosion protection for electronic contacts", *Jahrbuch Oberflächentechnik* 2016, 72 p.52-59.
- [8] A. Ulman, "self-assembled monolayers of thiols", *Thin Films* Vol. 24 1998 Academic Press.
- [9] F. Xu et al., "To quantify a Wetting Balance Curve", electronics.macermidenthone.com/application/files/4514/9865/4439/IPC_Wetting_balance_paper-12-14-15-RM_FX_RM.pdf
- [10] B. Bushan et al. "Nanotribological properties and mechanisms of alkylthiol and biphenyl thiol self-assembled monolayers studied by AFM" *Phys. Rev. B* 63, 245412
- [11] B. Bushan "Nanotribology and Nanomechanics, An Introduction" Springer ISBN-10 3-540-24267-8, Chapter 18

Compatibility of Gold, Palladium and hard Silver based plating systems for connector applications

Antoine Fares Karam¹, Anthony Franchini¹, Ana Torrealba², Damien Comte¹, Aurore Brézard-Oudot²,
Sophie Noel², Doyle Anderson³, Jeffrey Toran³

¹Amphenol ICC, Besancon, France. ³Amphenol ICC, Etters, PA, USA.

²Université Paris-Saclay, CentraleSupélec, Sorbonne Université, CNRS, Laboratoire de Génie Electrique et Electronique de Paris, Gif-sur-Yvette, France

Plating systems of electrical contacts are key technologies for connectors in terms of electrical and mechanical reliability performance. Au/Ni is historically the reference plating system and Au/PdNi/Ni is widely used since 1986. More recently, plating systems like Au/Ag/Ni, Au/NiW, AgPd/Ni and AgSb/Ni were also introduced. Nevertheless, published scientific literature, concerning tribological compatibility of these various plating systems, is limited. This research work is a simplified approach to study compatibility, in terms of durability & wear, between Au/Ni, AuPdNi/Ni, Au/Ag/Ni and AgSb/Ni under different contact pressures or normal forces. Durability and frictional wear testing were performed. Various surface analysis techniques were used to analyze wear tracks and investigate wear mechanisms as well as their impact on contact resistance. Results show that terminal contact pressure range is a key parameter to take into account when mating two different platings.

1 Introduction

Electronic connectors and overall interconnect applications have historically used gold plating (**Au/Ni**) as the main plating for male/female interfaces. Gold presents the advantages of being an excellent conductive material, of being a noble metal with excellent corrosion resistance and of presenting naturally a very low coefficient of friction making it an excellent solid lubricant. Nevertheless, the economical constraints and sometimes, some technical limitations have lead, widely, to the development and use of alternative platings. Gold Flash over Palladium-Nickel (**GF-PdNi**) was developed in the late 1970's [1] and commercialized starting 1986 [2] in order to obtain a much lower cost plating as well as a higher durability (resistance to mating and unmating cycles) metallic layer. GF-PdNi presented also the advantage of being a lower porosity deposit showing better resistance to corrosion and showed better compatibility for high temperature applications. All these advantages offset its lower resistance to fretting corrosion compared to gold and final connector users had the choice of these two platings according to their technical requirements. These two platings are considered fully compatible: This means that when a connector is plated with Au/Ni, it can be mated to its counterpart which is plated with GF-PdNi, without excessive wear-through precious metal layer. In the mid 1990's the Automotive industry started developing conventional silver plating especially for some power applications. Although conventional silver is known to have a low hardness, low young modulus and a poor coefficient of friction, its excellent conductivity (it has practically the lowest resistivity among

precious metals) and its moderate cost offset all its disadvantages. Silver plated connectors were historically rated for 50 mating/unmating cycles only. A lot of development work followed in the mid 2000's and new silver plating stacks and deposits were developed with pure silver showing much higher hardness and Young moduli. Several alloyed silver processes were also developed with deposits showing relatively very high hardness such as silver-antimony (AgSb) and silver-palladium (AgPd) [3,4]. Researchers developed improved organic or inorganic anti-tarnishing solutions as silver is naturally subject to sulfidation. Improved post-treatments were also developed such as new contact lubricants or low coefficient of friction grafted molecules. The objective was to extend silver usage to electronic connectors where more than 50 mating/unmating cycles are required, as gold and palladium prices have shown to be extremely volatile and unpredictable. We have seen, for example, AgSb plated connectors developed and commercialized, by several connector manufacturers, for Hybrid and Electrical vehicles where several thousands of mating/unmating cycles are required. This was unimaginable initially when considering silver plating. We have also seen gold over hard silver (**GCS**) plated electronic and power connectors [5,6] commercialized, when gold plated over silver engineering usage was limited, for decades, to special electrical switches [7] applications and special aerospace connectors.

1.1 Compatibility of various plating systems

Now that all these different plating systems are on the market, we are facing many cases where these plating systems are mated to each other on the same type of connectors. As already mentioned, conventional gold

plating (Au/Ni) is known to be compatible with GF-PdNi and it has been produced and used since nearly 35 years for billions of connectors. Thus, it was important to study further the compatibility of these different platings especially when Au/Ni and GF-PdNi are mated with GCS (Au/Hard Pure Silver/Nickel) and GCSb (Gold over Hard Silver-Antimony Alloy/Nickel). In the remainder of this article, GCS and GCSb acronyms will be used to designate these alternative plated stacks. From one side, silver based platings were historically used in Automotive connectors, where we have usually relatively large connector contacts with relatively high normal forces. From another side, Au/Ni and GF-PdNi are historically mainly used for relatively mid-size and low size connectors contacts with relatively moderate or much lower normal forces. We have examined the contact pressure (Hertz Stress) for 88 connector families commercialized by the top twenty connector manufacturers. These 88 connectors families mean in practice thousands of connector models as usually every connector family could cover up to twenty+ versions of connectors which all use the same contact system and the same contact constriction model between male and females. The output of this preliminary statistical examination, shown in Table 1, should not be considered exhaustive, but simply to identify trends. The result was very interesting as most (> 75%) of automotive connectors are using electrical contacts with a Hertz stress ranging between 200 MPa and 700 MPa while the absolute majority of electronic connectors (> 90%) are using contacts with Hertz stress ranging between 600 MPa and 1400 MPa.

So, we need to validate that the plating systems which are proven systems in automotive, are compatible, in terms of resistance to wear, with electronic applications where contact pressures are quite different. Although some scientists believe that contact pressure complexity is a barrier to its usage as a parameter in

mated, avoiding excessive precious metals wear of plated headers or receptacles.

1.1.1 Connector contact pressure calculation background

In practice, the huge development of digital electronic applications coupled to miniaturization requirements, have lead connector designers to reduce regularly the geometrical dimensions of electrical contacts while keeping constant the normal forces which are recommended by international standards. Most of these normal forces were specified in 1980's when there was much less miniaturization. The electronic connectors application went through highly accelerated miniaturization in the past 15 years while for automotive industry, this miniaturization was much slower. The current development of autonomous vehicles will probably change this quite quickly. In all cases, we can say that we are using today electronic connectors with much higher contact pressures compared to the 1970's and 1980's, while the trend in plating is to reduce the plating thicknesses for precious metals. Gold thickness of 1.27µm (50µin) and 2.0µm (80µin) were a standard in the early 1990's while today we use gold thicknesses ranging between 0.25µm (10µin) and 0.76µm (30µin) most of the time. So, this is another reason to validate compatibility between different plating systems under different contact pressures. This work shows the compatibility between Au/Ni, GF-PdNi, GCS and GCSb to ensure up to 250 mating cycles of intermateability, without excessive wear, under Hertz Stress ranging between 400 and 1300 MPa.

1.1.2 Contact pressure calculation

The Hertz theory is used to calculate the apparent contact area when two solids are pressed one against the other, provided the part geometries as well as the Young modulus and the Poisson coefficient are known. The Hertz theory assumes that the material deformations are elastic, and the contact area is small compared to the size of the solids. Without going deeply into Hertz theory it is important to note the fundamental equations. If we have two solid spheres having an elastic contact under a normal force (F), the spheres are characterized by their radii (R₁) and (R₂), their Young moduli (E₁) and (E₂) and Poisson coefficients (ν₁) and (ν₂). The contact area is a disc of radius "a". From a mathematical point of view, the problem is equivalent to the case of a sphere of radius R and Young modulus E pressing onto a plane of infinite rigidity, R and E being given by:

$$\frac{1}{R} = \frac{1}{R_1} + \frac{1}{R_2} \quad \frac{1}{E} = \frac{1-\nu_1^2}{E_1} + \frac{1-\nu_2^2}{E_2} \quad (\text{EQ1})$$

The calculation was published by Hertz in 1882 where "a" is : $a = \sqrt[3]{\frac{3FR}{4E}}$ (EQ2)

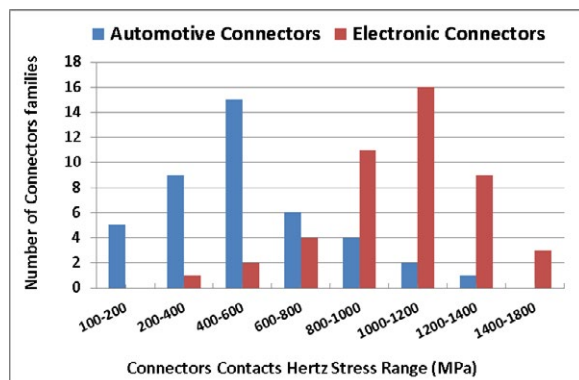


Fig.1 : Distribution of electrical contacts Hertz stress for 88 connectors families (2011-2019)

contact design [8,9], today the digital computing and numerical simulation capabilities are enormous and allow us to bypass these limitations. We also need to determine the conditions where these different plating systems perform the best (compatibility) when cross-

The local contact pressure at a distance “r” from the centre of the disc is given by:

$$p(r) = \frac{3F}{2\pi a^2} \left(1 - \frac{r^2}{a^2}\right) \quad (\text{EQ3})$$

The average contact pressure is:

$$p_m = \frac{F}{\pi a^2} = \frac{2}{3} \sqrt[3]{\frac{6FE^2}{\pi^3 R^2}} \quad (\text{EQ4})$$

The maximum stress within the material is in the range of:

$$0.3p_{\max} \approx 0.15 \frac{F}{a^2} \quad (\text{EQ5})$$

Those calculations assume that the deformation of the materials are purely elastic, which is not always the case in real world applications, especially for normal forces and contact geometries generating very high contact pressures. These equations consider that the surface state is perfect while in real contacts we have always certain level of roughness although it could be extremely low. Plated layers could also go through partial plastic deformation during mating and unmating cycles [10]. Thus, it is commonly noted that a contact pressure calculation for connectors is valid for a certain specific moment and certain surface state. In other words, the contact pressure we are calculating is between male and female contacts before durability testing. We call that the nominal initial contact pressure. During durability cycles, wear occurs in the contact area resulting in Hertz stress variation, probably due to modifications in contacts spot size because of elasto-plastic or, eventually, plastic deformation [10,11]. For simplification, we always refer to the initial nominal contact pressure. Finally, Hertz stress equations consider only the 2 solids which are homogeneous material with well-defined Young Modulus. For connectors, we use plated base material and to be more representative of reality, we measure and calculate the composite Young Modulus of the total plated stack using a nanoindentation technique [11]. This methodology is commonly used as it gives more accurate Hertz stress values, which takes into account the barrier underlayer plating (nickel in our case) as well as the final precious metal(s) layers.

2 Experimental

Durability testing was simulated in the laboratory using a tribometer and validated, in most of cases, on real connector contacts. The tribometer with continuous low-level electrical contact resistance (LLCR) measurements is a Bruker UMT3 universal mechanical tester equipped with a mechanical reciprocating module. A flat real connector header contact or a flat plated specimen were fixed on this lower module. The upper module has special hemispherical coupon with different radii (between 0.8mm and 1.6mm) allowing to simulate different connector terminals receptacle geometries under different contact pressures.

A 4-wire system was used to measure ‘dry circuit’ contact resistance (Rc). A typical plated hemisphere and a schematic representation of the Rc measurement principle are shown in Figure 2. All durability tests were done according to EIA-364-09C standard. A stroke length of ±2mm and a sliding speed of 25mm/min were used. All platings were deposited using reel-to-reel plating lines including the flat and the hemispherical lab samples.

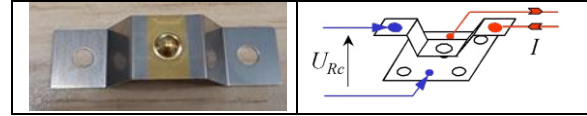


Fig.2 : Typical plated hemisphere used for durability simulations and wiring setup

The base material used was a commonly used C70250 (CuNiSiMg) alloy with 43% IACS conductivity. All samples and contacts went through electrochemical alkaline degreasing followed by electropolishing before plating a ductile (26%) 1.5µm ±0.25µm nanocrystalline nickel. All gold layers used an electroplated cobalt-hardened gold. Thick gold (Au/Ni) layer thicknesses were nominally 0.76µm ±0.1µm while flash gold layer thicknesses were 0.07µm ± 0.015µm. The Palladium-Nickel (PdNi) layer was plated using a low ammonia plating bath to ensure low stress PdNi layer, containing 80%Pd and 20%Ni nominal. The PdNi layer thickness was 0.69µm ± 0.16µm on contact area. The hard pure silver layers had a thickness of 3.2µm ± 0.7µm. The silver-antimony (AgSb) layers thicknesses were 2.9µm ±0.4µm and were plated at 10 A/dm² current density. They contained ~3% of Antimony (Sb). A Fischer XDV-µ polycapillary X-Ray fluorescence spectrometer (XRF) with 25µm spot diameter, was used to measure all plating thicknesses and verify base material composition. All samples were lubricated using a PerFluoroPolyEther (PFPE) lubricant. Scanning Electronic Microscopy (SEM) morphological analyses were performed using a ZEISS EVO MA-10 SEM at 15 kV operating voltage, equipped with an Oxford Instruments XMax EDS probe fitted with a 50mm² detector. Plated stack composite Young modulus and composite hardness were determined using an Anton Paar NHT3 nanoindenter.

3 Results

In this paper we have included the compatibility between Au/Ni and GF-PdNi as reference systems. We have performed 250 mating/unmating simulation cycles on hemisphere/flat setup under different contact pressures. The compatibility between these two plating systems with GCS and GCSb plating systems were studied. We provide typical observations, analysis and SEM micrographs to illustrate the methodology of investigation, but we cannot show each individual result in this short article, given the large number of plating combinations evaluated.

3.1 GF-PdNi and Au/Ni platings

Typical results under 700 MPa are shown in table 3.1 where we can see the optical images of the interface surfaces as well as the SEM/EDS elemental mapping of gold and palladium. After 250 mating cycles, when 0.76 μ m of Au/Ni plated on flat, we can see gold transfer to the 0.76 μ m GF-PdNi plated hemisphere. This local over-thickness of gold explains the dark area in the palladium elemental map at the center of hemisphere where Pd is masked by Au. We can see clearly that no excessive wear is observed and no nickel underlayer is exposed, demonstrating in this case the full compatibility and intermateability of the these two plating systems.



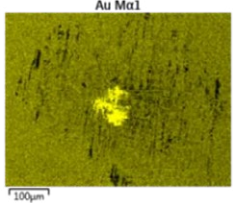
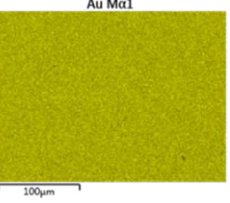
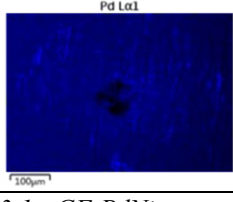
700 MPa	0.76 μ m GF-PdNi Hemisphere	0.76 μ m Au/Ni Flat
Optical		
Au EDS Mapping		
Pd EDS Mapping		N/A

Table 3.1: GF-PdNi compatibility with Au/Ni at 700 MPa of contact pressure

In practice, we always notice that, when hemispheres are plated with 0.76 μ m GF-PdNi and flats are plated with 0.76 μ m of Au/Ni, these two systems are perfectly compatible even at extremely high contact pressure such as 1300 MPa or even 1400 MPa. This is what is expected of such high durability GF-PdNi plating. To illustrate an incompatible case, table 3.2 shows the surface wear after 250 durability cycles for a hemisphere plated with Au/Ni and a flat sample plated with GF-PdNi, under 1300 MPa, which is a very high nominal initial contact pressure. Visually speaking, we could say that surfaces are acceptable as optically we still observe the golden color on the hemisphere. But we start seeing some greyish shades. That indicates that we are close to the nickel underlayer. EDS elemental mapping shows that the remaining yellow golden color is the result of an extremely thin layer of gold, probably less than 15~20nm thickness. In fact,

we are starting to expose the nickel underlayer that is quite visible with EDS mapping. A quick examination of the flat samples shows that we have gold transfer from the hemisphere to the flat GF-PdNi surface which shows gold over-thickness in some areas on the wear track. The exposed nickel underlayer, calculated using an image treatment software, is less than 10% of the total contact area. This value of 10% of exposure is the maximum limit defined by Telcordia GR-CORE-1217 standard concerning the wear-through of contacts noble metallization of separable contact interfaces [12].



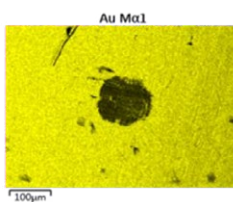
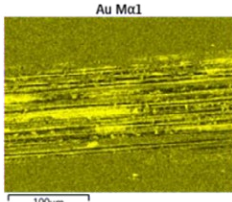
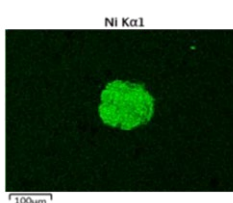
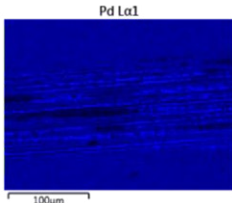
1300 MPa	0.76 μ m Au/Ni Hemisphere	0.76 μ m GF-PdNi Flat
Optical		
Au EDS Mapping		
Ni or PdNi EDS Mapping		

Table 3.2 : GF-PdNi compatibility with Au/Ni at 1300 MPa of contact pressure

Mechanically speaking, we can say that at 1300MPa of nominal Hertz stress, the 0.76 μ m Gold plating on female contact is incompatible with 0.76 μ m GF-PdNi for 250 mating/unmating cycles. Indeed, we are starting to have excessive wear. One could argue that remaining excessively thin gold layer could be acceptable, because if we examine the evolution of contact resistance (R_c) during these 250 mating cycles, shown in Figure 3, we can notice that R_c is extremely stable and quite low during the entire experiment. This is a positive element in favor of accepting a final residual gold layer of a few nm of thickness. Nevertheless we can also estimate that such final thin gold layer is not enough to protect the electrical contacts against corroding and aggressive atmospheric contaminants or pollution gases. Consequently, we can consider that under 1300MPa of Hertz stress, these two platings are incompatible, or, 1300MPa is the maximum contact pressure for compatibility. To re-establish this compatibility, we should either reduce the maximum

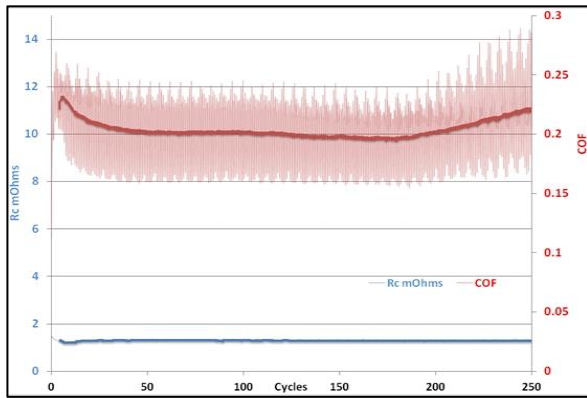


Fig.3 : Contact resistance and coefficient of friction evolution during 250 durability cycles between Au/Ni hemisphere and PFPE lubricated GF-PdNi flat under 1300 MPa of contact pressure.

number of mating/unmating cycles (durability limits), change connector contact design to reduce nominal contact pressure, reduce normal loads if this is possible or increase the precious metal layer thicknesses.

3.2 Au/Ni and GCS platings

To illustrate the wear behavior of a hard pure silver based plating system, we used the GCS plating which has a gold flash layer on top surface to protect silver. It is important to note that the Young modulus for a GCS plating is around 110~115 GPa which is much higher than the Young modulus of pure soft silver plating which is in the range of 85~90 GPa. We expect better shear resistance of GCS plating during durability cycling. But GCS still has a lower Young modulus than Au/Ni plating which is in the range of 160~170 GPa. It is also much lower than the modulus of GF-PdNi plating which is between 245 and 255 GPa. Consequently, for a constant normal force, when using a gold plated hemisphere, replacing the GF-PdNi on the flat surface by GCS plating will reduce the contact pressure by 200~300 GPa. This means, that it is extremely difficult to reach, in real GCS plated connectors, such 1300 MPa of Hertz stress. In practice, a contact pressure of 1000 MPa is considered as extremely high for a silver based plating system. This is also what explains that for automotive silver plated connectors, we use high normal forces which are practically not allowed to be used for gold plating. These high normal forces provide enough contact pressure to break the blackish silver sulfides (Ag_2S), formed on silver surface, and retrieve the excellent electrical conductivity of silver plating. Table 3.3 shows the results, after 250 durability cycles, between a hemisphere plated with $0.76\mu m$ of Au/Ni and a flat plated with GCS, at 700 MPa. Visually we see significant wear tracks and quite large contact area on the gold plated hemisphere. When performing elemental mapping on the hemisphere, we can notice silver transfer from the flat surface, which is expected knowing that silver plating is usually sub-

jected to galling. The presence of a contact lubricant has significantly reduced such galling in this case, compared to what is historically observed with non-lubricated silver plating. This silver transfer on the hemisphere partially masks the signal of the gold layer where we can see a non-yellow (black) spot. We say partially, because EDS mapping of elemental nickel shows few nickel spots from the nickel underlayer

700 MPa	0.76 μm Au/Ni Hemisphere	GCS Flat
Optical		
Au EDS Mapping		
Ag EDS Mapping		
Ni EDS Mapping		

Table 3.3 : Au/Ni compatibility with GCS at 700 MPa of contact pressure

This limited worn gold zone constitutes less than 5% of the total measured contact area and it was not systematically observed. We have shown, on purpose, the worst case for pedagogical illustration. A quick examination of the flat sample shows that we are still on the hard silver layer, in all cases, and there is never wear-through to the nickel underlayer. A silver layer thickness measurement using micro-XRF shows that only 60% to 70% of silver was worn after 250 mating cycles at 700 MPa. Using GCS and Au/Ni plating seems to be a robust option provided that we respect certain Hertz stress rules. In other experiments, mating GF-PdNi to GCS has shown also to give excellent results, even better than traditional Au/Ni plating, ensuring a very high durability plating couple. In practice, we notice that mating a silver plating contact to a non-silver plated contact gives better durability results

than when it is mated to itself because we have less galling and more abrasion [13], which is the most frequent wear mechanism of silver.

3.3 Au/Ni and GCSb platings

GCSb in this study is a variant of GCS plating. We use a silver-antimony (AgSb) alloy instead of pure hard silver. This AgSb alloy is known to have much higher composite hardness up to 180 Vickers compared to hard pure silver limited to 120~135 Vickers. We measured its Young modulus and it is in the range of 150 GPa. The presence of an alloying element will slightly increase the silver electrical resistivity but we still observe very low electrical contact resistance between hemisphere & flat, as shown in Fig.4 under different contact pressures. Rc remains stable and very low at 900 MPa while at 400 MPa and 700 MPa, we notice a 3 mΩ average increase, as we have fewer contact spots when we reduce Hertz stress. These 3mΩ could be significant for some power connector applications. This is an additional reason to study and select the appropriate contact pressure when using different plating systems on male and female contacts.

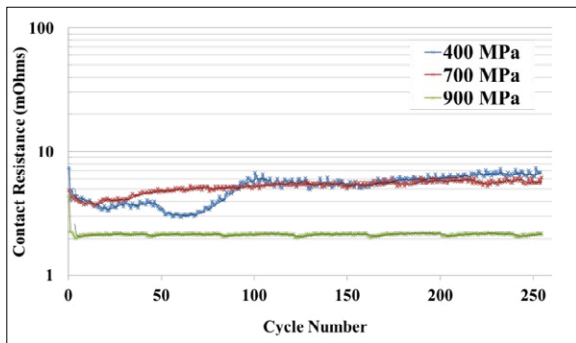
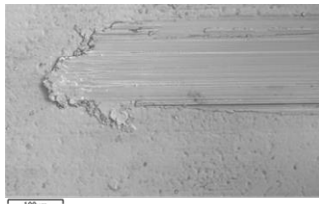
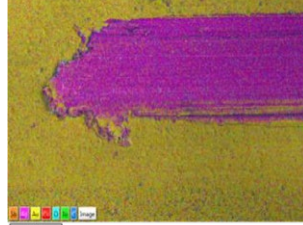

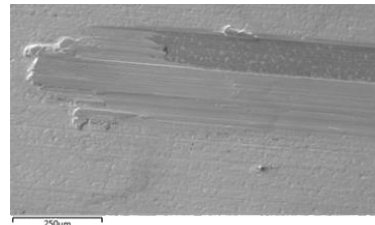
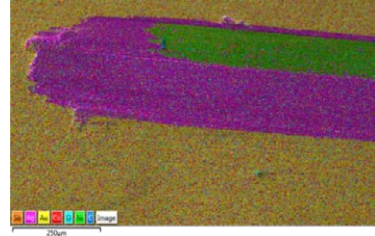


Fig.4 : Contact resistance evolution vs. durability cycles between Au/Ni hemispheres & GCSb flats

This GCSb variant indeed provides better durability in several cases given that we have better resistance to shear vs. pure silver, as well as higher hardness silver. It has been proven that the ratio between hardness and Young Modulus is much more correlated to wear extent than hardness alone [14,15] and consequently this is an important difference with GCSb. Table 3.4 presents the surface wear after 250 durability cycles, at 900 MPa of Hertz stress between a hard Au/Ni plated hemisphere and a GCSb plated flat. The optical high resolution photo of hemisphere shows that gold plating is almost not scratched and the little whitish color is the result of silver transfer from flat to hemisphere. Concerning flat GCSb plating, the elemental analysis micrograph shows that gold is removed but the AgSb layer is practically intact and no wear-through is observed to the nickel underlayer. We may think, at this stage, that with a harder Silver alloy with superior Young modulus, we may be able to use very high contact pressures, observed in many miniaturized connectors nowadays.

900 MPa	0.76μm Au/Ni Hemisphere vs. GCSb plated flat (Au/AgSb/Ni)
SEM Micrograph of GCSb flat	
EDS Mapping on GCSb flat	
3D Photo : Gold plated hemisphere	
Table 3.4 : Au/Ni compatibility with GCSb (Au/AgSb/Ni) at 900 MPa of contact pressure	

Unfortunately, even when alloying silver (Ag) with antimony (Sb), we still observe silver galling occurring, if we try to work in such high Hertz stress range. Table 3.5 shows the SEM micrograph of the GCSb surface after 250 mating cycles under nominal contact pressure of 1200 MPa.

1200 MPa	0.76μm Au/Ni Hemisphere vs. GCSb plated flat (Au/AgSb/Ni)
SEM Micrograph of GCSb flat	
EDS Mapping on GCSb flat	
Table 3.5 : Au/Ni compatibility with GCSb (Au/AgSb/Ni) at 1200 MPa of contact pressure	

We notice significant silver wear on the track. EDS mapping shows that nickel underlayer is exposed. Given the limited number of wear debris around the wear track, we are probably again under a galling wear mechanism coupled to limited abrasion. We have flakes of Silver detached from the surface of flat.

Unfortunately, alloying Ag with Sb and applying a lubricant does not completely offset the galling mechanism. Under such high contact pressures, the lubricant layer between male and female contacts becomes extremely thin and inefficient to reduce the intrinsically high coefficient of friction. The flash gold on top of AgSb is playing the role of a solid lubricant, same as for GF-PdNi, but it is gradually worn during the 250 durability cycles. The maximum durability cycles before wear-through, under different contact pressures, will be published separately.

3.4 Compilation of results & discussion

After showing above several examples of the investigation methodology, tables 3.6, 3.7 and 3.8 show the compilation of all obtained results from a wear compatibility point of view. When the intermateability result case is highlighted in green, this means that no wear-through of noble metal layer down to the nickel underlayer was observed on both flat and hemisphere contacts. When the case is highlighted in red, it is not advised to mate these 2 plating systems together under the specific mentioned contact pressure given we have significant wear down to non-noble barrier underlayer. When the intermateability case is highlighted in dual green-orange color or only in orange, it means that we have slight wear, less than or close to the tolerable 10% of contact area, specified by the Telcordia standard. We consider that this is the maximum contact pressure which we could adopt according to application specifications. Table 3.6 shows that 0.76µm Au/Ni plating is fully compatible with GF-PdNi up to 1200 MPa of contact pressure, and we start seeing wear-through down to the Ni layer of Au/Ni plated hemisphere starting 1300 MPa.

All Samples are lubricated	0.76µm Au/Ni Plated Hemisphere ; 250 durability cycles										
	Contact Pressure Range										
Flat Plating	400	500	600	700	800	900	1000	1100	1200	1300	1400
0.76µm GF-PdNi	Green										
0.76µm Au/Ni	Green										
GCS	Green										
GCSb	Red										

Table 3.6 : Compatibility of Au/Ni when plated on hemisphere with 3 other plating systems according to various contact pressures

In practice, this value shows also to be the limit for 250 mating cycles intermateability for Au/Ni plating with itself. It is interesting to note that when the flat is plated with GF-PdNi, this plating did not show any damage as we have gold transfer from the 0.76µm thick layer on hemisphere to the flat. When the flat is plated with similar Au/Ni plating, the gold transfer is mutual and we could observe Nickel exposed spots randomly on both hemisphere and flat. This is a known electroplated gold wear mechanism but in our case, the transfer phenomena seems to be significantly increased under high contact pressures. When mating a Au/Ni plated hemisphere to a GCS plated flat, the compatibility of these two systems is limited up to 700MPa only and 800MPa is considered as the inflec-

tion point where we should not mate these plating systems together. We have significant silver transfer from flat to hemisphere. What was not expected is the transfer of gold from hemisphere to GCS plated flat and we observed the first significant nickel underlayer exposure of Au/Ni layer at 800 MPa. Lubricant is known to reduce galling and flaking extent for metallic coatings, but it seems that gold and silver solid solution is formed under the pressure accelerating the transfer (wear) of gold on hemisphere. When plating GCSb, these two systems are compatible till 900MPa. Nevertheless, we observe in this case more conventional debris on both sides, showing that we have different wear mechanisms between GCS and GCSb. Alloying silver with 3% of Sb (Antimony) is generating quite a different plating system. When examining Table 3.7, we immediately notice that when using a GF-PdNi plated hemisphere vs. Au/Ni plated flat, we have an improvement in wear compatibility between these

All Samples are lubricated	0.76µm GF-PdNi Plated Hemisphere ; 250 durability cycles										
	Contact Pressure Range										
Flat Plating	400	500	600	700	800	900	1000	1100	1200	1300	1400
0.76µm GF-PdNi	Green										
0.76µm Au/Ni	Green										
GCS	Green										
GCSb	Red										

Table 3.7 : Compatibility of GF-PdNi when plated on hemisphere with 3 other plating systems according to various contact pressures

All Samples are lubricated	GCS Plated Hemisphere ; 250 durability cycles										
	Contact Pressure Range										
Flat Plating	400	500	600	700	800	900	1000	1100	1200	1300	1400
0.76µm GF-PdNi	Green										
0.76 µm Au/Ni	Green										
GCS	Green										
GCSb	Red										

Table 3.8 : Compatibility of GCS when plated on hemisphere with 3 other plating systems according to various contact pressures

platings. GF-PdNi vs. GF-PdNi shows in this case its higher durability, technically speaking, compared to other plating systems. Using GF-PdNi plating on hemispheres allows us to use GCS plating on flats up to 1000 MPa before we observe adhesive wear on these flats. When plating the flat with GCSb, compatibility with GF-PdNi is up to 1100 MPa and then we start observing abrasive wear. Above 1200MPa, we observe additional oxidation wear beyond abrasion debris which may be the result of localized frictional heat generation [13] at such high Hertz stress for these two high stiffness platings. Nevertheless, this remains a hypothesis as durability tests were conducted at moderate sliding speed of 25mm/min and frictional heat generation is theoretically minimized. Further investigations are ongoing to understand the mechanisms of such oxidation. The results in table 3.8 show that when using GCS on the hemisphere, the maximum contact pressure which can be used is 1000MPa when mating to a 0.76µm Au/Ni plating or GCSb on flat samples. This is already a very high contact pressure for a silver based plating. It is interesting to notice that when using GF-PdNi flat samples vs. GCS

on hemisphere, we have much less wear, for GCS evidently, compared to the opposite configuration discussed above. When the flat is plated with GF-PdNi, the maximum contact pressure to be used is 800MPa while it was 1000MPa in the opposite case. The continuous solicitation of GCS plating, during 250 durability cycles, when plated on hemisphere (simulating female contacts), leads to continuous galling and transfer of silver from hemisphere to flat, resulting in faster nickel underlayer exposure which is not desirable for corrosion resistance issues. Another important observation is the maximum 700MPa contact pressure when GCS is mated to itself. We have in this case maximum galling, although attenuated by lubrication. Nevertheless, 700MPa with both parts plated with GCS is obtained with normal forces which could generate a contact pressure higher than 1000MPa if the plating would have been GF-PdNi or Au/Ni on both parts. In other words, using GCS as a plating system is still very interesting from an electrical and economical point of view, provided that connector contact designer would forecast this since the beginning. All the plating systems investigated above have various hardness and Young moduli and many results were unexpected. All this suggests and confirms that hardness is not the main major parameter influencing wear evolution [16]. Again, it seems that the ratio of hardness to Young's modulus correlates much more accurately to the wear behaviour on multi-layered coatings. The existing mathematical relationship between this ratio (hardness/Young Modulus) and the wear observed on our real connectors and the tribological hemisphere/flats will be presented elsewhere.

4 Conclusions

We have presented in this investigation work, the compatibility ranges for different plating systems according to the nominal initial contact pressure of sphere/flat contact configuration, up to 250 durability (mating/unmating) cycles. The objective was to offer connector designers some guidance when developing a connector with several plating options, as compatibility, in terms of wear resistance, will vary according to defined normal force and thus contact pressure. This work covered traditional gold plating, the historical GF-PdNi alternative plating, as well as 2 other silver based platings which are used now in the industry. Using asymmetrical platings (different platings on male and female contacts) allows higher performance and in some cases it can simultaneously reduce plating costs.

5 Further inquiries

Antoine FARES KARAM
Amphenol FCI, 2 Rue LaFayette, Besançon, France.
E-Mail: antoine.fares-karam@fci.com

6 Literature

- [1] Bare J.; Graham A.: Wear resistance characterization for plated connectors. Proc. IEEE Holm Conf. on Electrical Contacts, 1985; pp. 147-155
- [2] A Abys J.; Straschil H.: The electrodeposition and material properties of Palladium-Nickel alloys. Metal Finishing, July 1991, pp.43-52
- [3] Nobel, F.I.: Electroplated Palladium Silver Alloys. Proc. 12th Conf. Electrical Contact Phenomena, Chicago, 1984, pp.137-154
- [4] Myers, M.; Schmidt, H.: Connector Level Performance Evaluation of a New High Speed Reel to Reel Electroplated Silver Palladium Alloy Contact Finish. Proc. 27th ICEC Conference, Germany, 2014, pp.96.
- [5] Fares Karam, A.; Anderson, D.: Overview of FCI new AGT Plating System. Proc. 3rd Tricoa Finishair Congress, Besançon, France, 2013.
- [6] Fares Karam, A.; Anderson, D; Toran, J: Performance evaluation of the new Gold Capped Silver (GCS) plating system. Proc. 28th ICEC Conference, Edinburgh, UK, 2016, pp.81-86
- [7] Johler, W; Reider, W.: Reliability of Silver Contacts with and without Gold Plating. Proceedings of the 35th Relay Conference, Stillwater, OK, USA, 1987, Rep. No. 8, 11s.
- [8] Mroczkowski R.: Concerning "Hertz Stress" as a Connector Design Parameter: a Negative Vote. Proc. 24th Ann. Conn.Interconn. Technology Seminar, Oct. 1991
- [9] Fluss H.S.: Hertzian Stresses as A Predictor of Contact Reliability, Connection Technology, Dec. 1990, pp 12-21
- [10] Van Dijk P. : Contacts Spots, Proc. ICEC Conference, 2000, pp. 135-140
- [11] Tinvisut K.; Branter H.P.: Determination of mechanical properties of thin films and substrates from indentation tests, Philosophical Magazine A, 2002, Vol. 82, No.10, pp.2013-2029
- [12] Telcordia GR-1217-CORE: Generic Requirements for Separable Electrical Connectors Used in Telecommunications Hardware. Issue 2, December 2008, section 6.1.10
- [13] Koji K.; Koshi A.: Wear Mechanisms. Modern Technology Handb., Chap.7, CRC Press, 2001
- [14] Pintaude G.: Introduction of the Ratio of the Hardness to the Reduced Elastic Modulus for Abrasion. Tribology: Fundamentals and Advancements; Chap. 7, pp.217-230
- [15] Wangyang N.; Grummon D.: Effects of the ratio of hardness to Young's modulus on the friction and wear behavior of bilayer coatings. App. Phys. Lett., 2004, Vol.85, No.18, pp. 4028-4030
- [16] Aadarsh M.: Analysis of relation between friction and wear. Int. J. Mech. Eng. & Rob. Res. 2014, Vol. 3, No. 3, pp. 603-606

SnO_x Gradient Composition Inside Tin-oxide Layer

Keiji Mashimo¹, Atsushi Shimoyamada¹ and Hirokazu Sasaki¹

¹Furukawa Electric, Advanced Technologies R&D Laboratories.

Abstract

The natural oxide film that forms on tin is approximately 20 nm at most, but it may be less than 10 nm on a newly plated surface. Basically, knowledge of the characteristics of oxide films is a prerequisite for calculating the electrical contact resistance. However, for most real connectors, the initial film structure is broken during the connecting action. Therefore, knowledge of the exact characteristics of oxide films has not been considered to be an important factor when designing connectors. An attempt was made to calculate the electrical contact resistance of tin-plated terminals using analytical models. The construction of such computational analytical models requires knowledge of the exact properties of the oxides. In our previous paper, the electronic structure of natural oxide films was investigated using soft X-ray absorption near-edge structure (XANES) spectroscopy. In this paper, the gradient composition of natural oxide films is mainly described by the depth profile of the natural oxide films on the tin-plated layer. The depth profiles were investigated by X-ray photoelectron spectroscopy (XPS). It was assumed that oxides of valence II and IV were the main inclusions in the film. XPS results showed that there was much more SnO₂ than SnO near the surface at the initial stage.

1 Introduction

The need to understand the altering state about the terminal surfaces that affect the contact resistance motivated this study. This knowledge is required for computational analysis. As fretting degradation advances in the contact area on the surface of connector terminals, the percentage of the oxide increases. Although the sizes and volume of the wear particles change, the main cause of the contact resistance seems to be the volume fraction of the oxides [1-3]. On the other hand, the thickness of the natural oxide film exposed to air increase without touching or sliding. While the thickness change was measurable, the composition of the film was not clear. It may be altered as a function of depth because the diffusion of oxygen is supposed to make a ramped composition. Thus, it is hard to define the thickness of the films. The measured results indicate just the amount of oxides.

Several analysis methods were used to investigate the composition of the plated tin surface. In previous papers, the valence of SnO_x at the surface of plating at the initial stage and the sputtered SnO₂ film were measured using XPS [4] and Mössbauer spectroscopy [5], respectively. In those cases, at least two valences (II and IV) of oxygen were included in the oxide films. In those papers, the depth profiles of the oxide films with respect to the valences were not performed. Another paper previously published describes the inside of the fretting debris after sliding, SnO was dominant [1]. This result was analyzed with scanning transmission electron microscope (STEM) and electron diffraction. In general, these results were not sufficiently

accurate for the computational analytical models. In the previous methods (with small scale laboratory size facilities), the peak separation of valences II and IV was not perfect due to the insufficient amount of oxides. We also decided to use a synchrotron radiation beam for soft X-ray absorption near-edge structure (XANES) spectroscopy which is usually in large scale facilities. From the XANES data, the valence state and symmetry of the atomic level in the specimens were obtained [6-13]. Although the method was expected to be highly accurate, applying it to thin natural oxide films is still challenging [14]. In this paper, the depth profiles of XPS analysis were performed. The gradient composition of SnO_x was detected. Basically, the valence II and valence IV of SnO_x is mixed. Near the surface, the former ingredient increases and the latter one decreases as depth increase.

2 Experimental Methods

2.1 Prepared specimens

Three specimens with different aging periods after the plating process were prepared: twelve-year-old (No.1), two-year-old (No.2) and one-week-old (No.3). A schematic view of the specimens is shown in **Fig. 1**. The backing plate was Cu-alloy which is undercoated with Cu. After the plating process, a post-heating process (reflow) was applied. The samples were kept in a laboratory. In the area where the lab is located, the average outdoor ambient temperature and relative humidity is around 7 °C and 75%, respectively. The minimum and maximum temperatures were around -15 °C and 30 °C, respectively. The temperature and humidity in the laboratory were not accurately controlled. However,

in the day time, the room temperature was controlled at around 18 °C–26 °C.

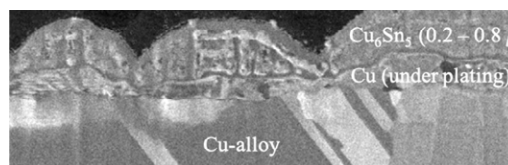


Fig. 1 Cross-sectional view of the specimens.

2.2 XPS Setups

The specification of the XPS setups is as follows. The X-ray source used was a monochromatic Al-K α line. It can be applied for Li to U atoms. Its accuracy is 0.1 atomic % minimum. The x-ray spot has a diameter of 100 μ m. The XPS measurement was combined with argon ion sputtering for depth profiling.

3 Results and Discussions

3.1 Measured Spectra

Figures 2 to 4 show the measured Sn 3d spectra with various sputtering cycles. The pseudo-Voigt function was used for curve fitting.

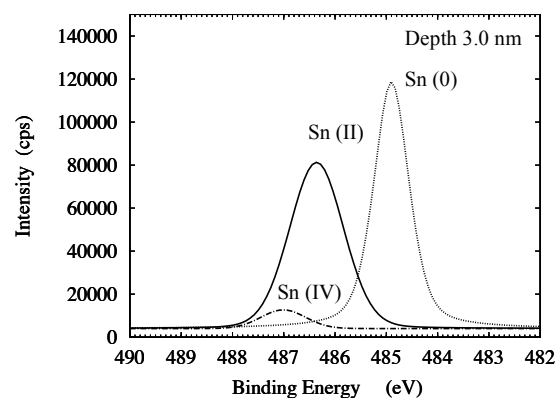
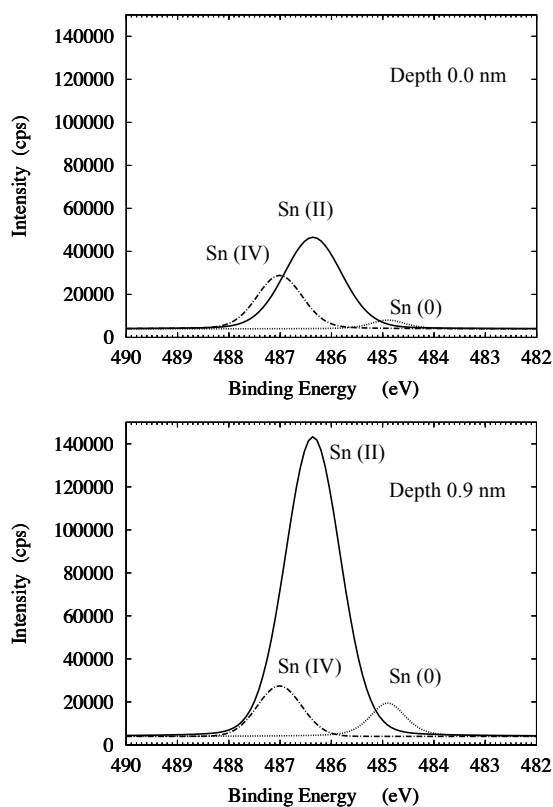


Fig. 2 XPS of Sn 3d spectra for specimen No. 1.

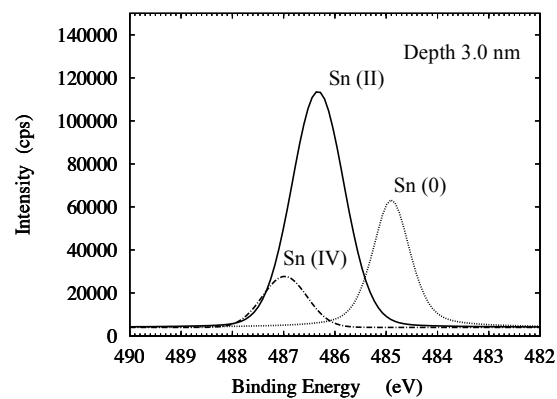
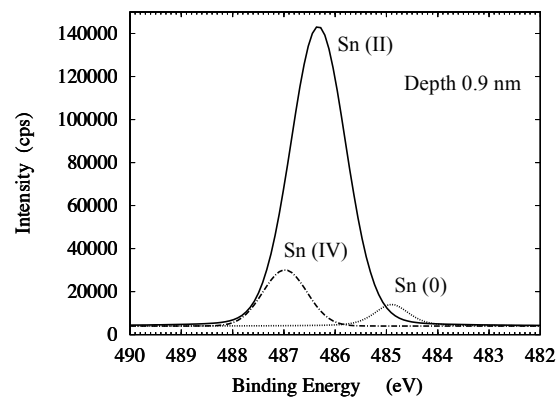
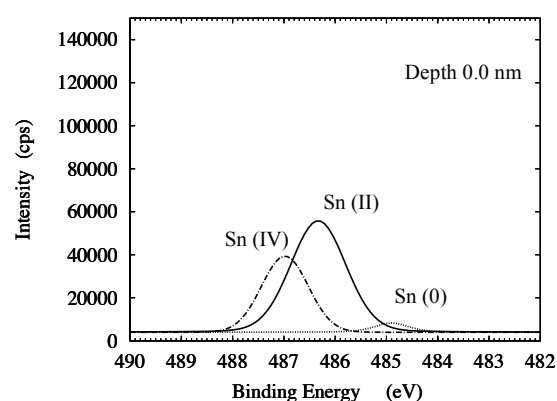


Fig. 3 XPS of Sn 3d spectra for specimen No. 2.

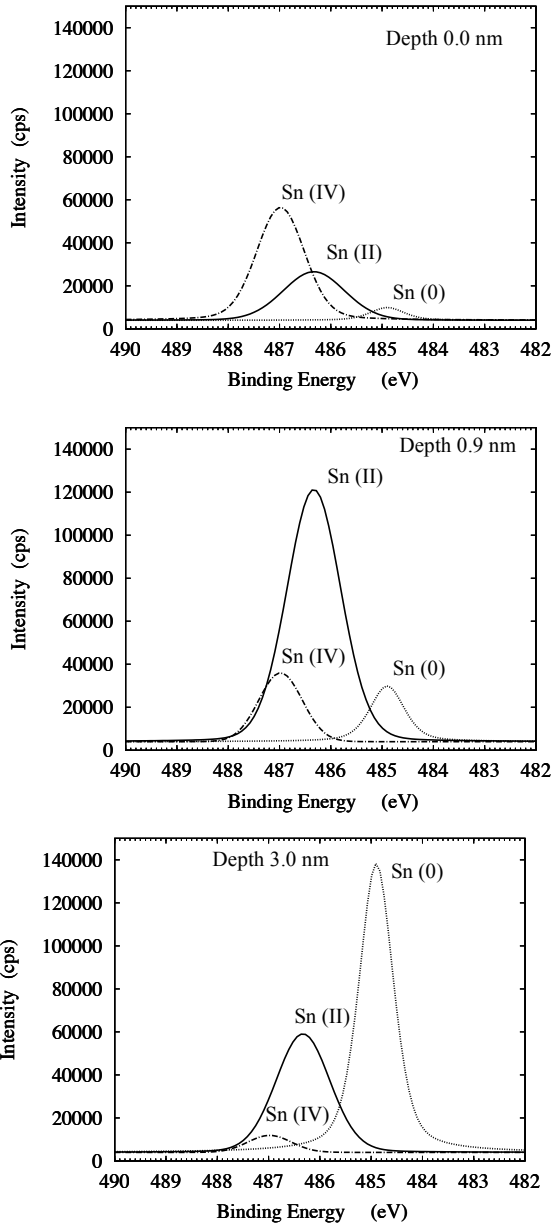


Fig. 4 XPS of Sn 3d spectra for specimen No. 3.

In particular, the Sn (IV) peak was prominent near the surface of the No. 3 sample. On the other hand, the maximum of Sn (II) peaks in all samples was observed at a depth of approximately 1 nm (equivalent to SiO₂). The O 1s spectra were also measured (See Fig. 5). In this case, an additional component was indicated by a peak at 532 eV. According to Akgul et al, (2013) [15], this component is due to the absorbed OH⁻ group. The 532 eV peaks were prominent only at the surface in all cases. The other two peaks corresponded to the peaks of the Sn 3d spectra. Precisely, several amounts of Sn (II) and/or Sn (IV) at the surface in these fitting must be due to the hydroxides of tin.

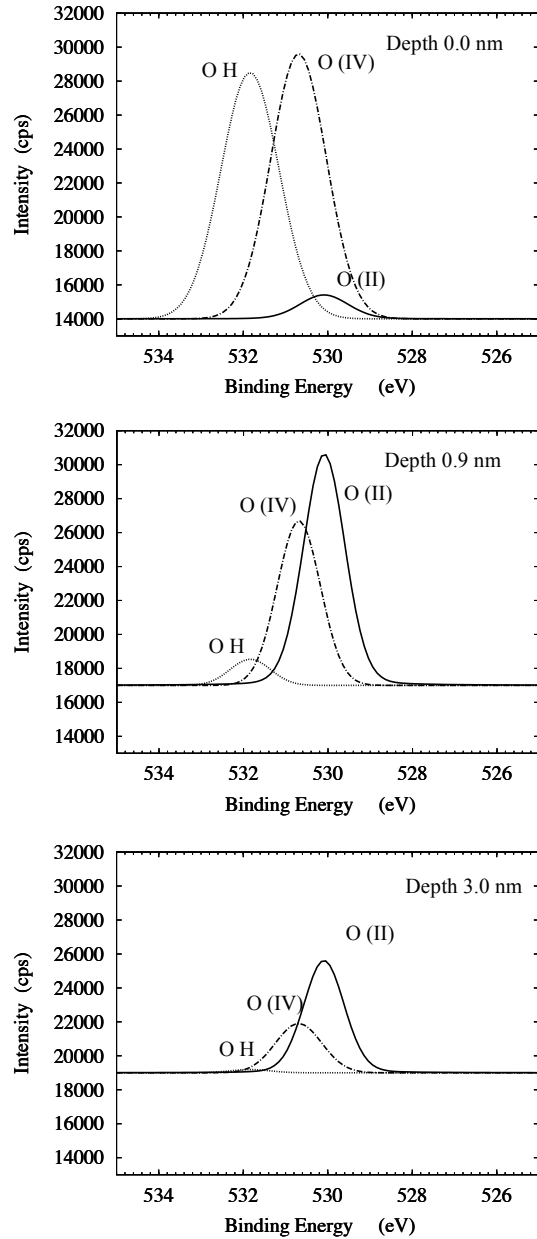


Fig. 5 XPS of O 1s spectra for specimen No. 3.

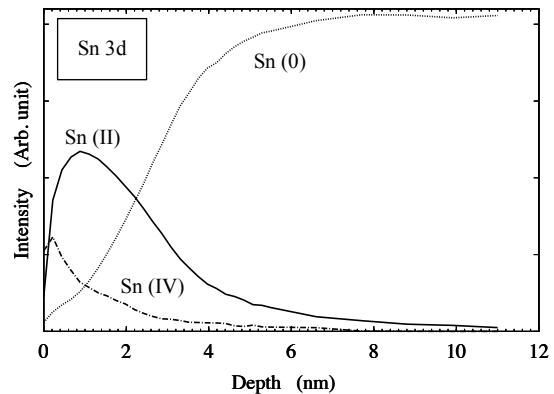


Fig. 6 Raw profile of Sn 3d spectra for specimen No. 3.

3.2 Depth Profiles

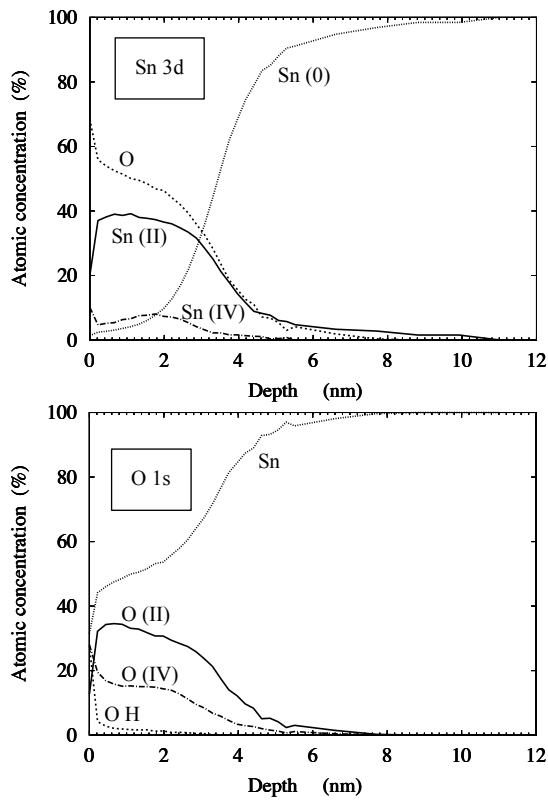


Fig. 7 XPS depth profile (No.1).

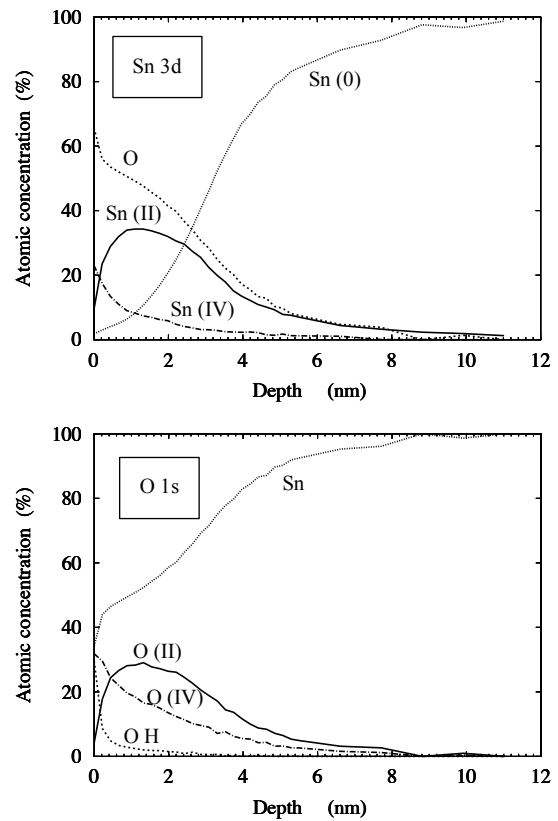


Fig. 9 XPS depth profile (No.3).

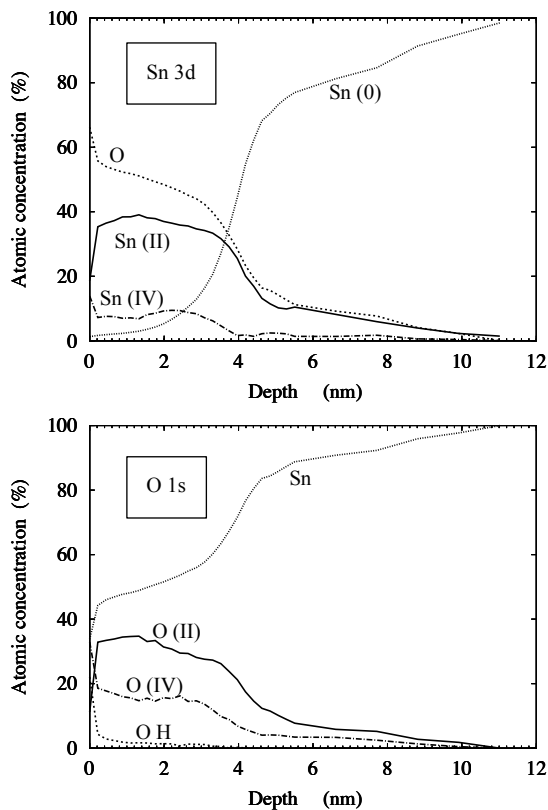


Fig. 8 XPS depth profile (No.2).

The depth profiles of valence II and IV tin oxides are shown in Figs. 6 to 9. In Fig. 6, raw intensity is used. The values of depth are converted values equivalent to SiO_2 .

The differences between the old (No.1 and No.2) samples and the new sample (No.3) are as follows. First, the former has a plateau for the SnO_x profile, but the latter does not. Second, the volume of Sn(IV) is larger near the surface of the latter sample than the former.

The hydroxide profile is not significantly different among all samples.

3.3 Discussions

In this study, the native oxide films before contact action were investigated by XPS. In the practical use of connectors, the oxide films are repeatedly destroyed and reformed. The sliding action induces plastic flow [16], and as fretting progresses, the volume of oxide in the plating layer increases. Figure 10 shows the estimated mean value of the native oxide composition in each specimen. After fretting degradation has progressed, the ratio of SnO_{1-x} and SnO_{2-x} is most likely to have these values (4:1 to 6:1).

In practical situations, oxides are continuously produced as fretting degradation progresses. The growth rate of SnO_{1-x} is slow. Therefore, the aging effect does not directly affect the material. In other words, the use

of aged materials does not make a significant difference in the electrical properties related to the contact resistance profile. This scenario is true as long as the aging condition is mild enough to prevent matrix damage.

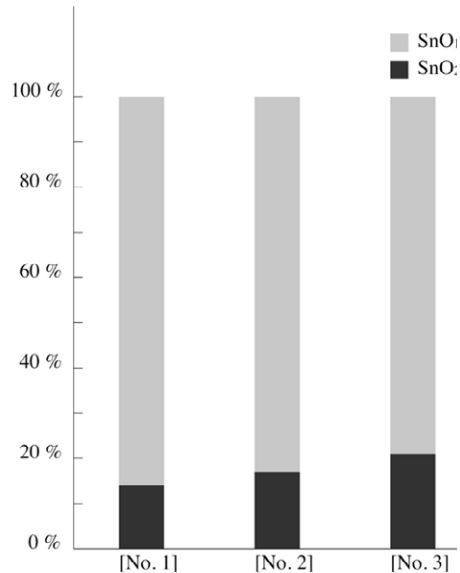


Fig. 10 Mean value of the oxide composition.

4 Conclusion

Native oxide films on plated tin were investigated by XPS spectra. The measured results indicate that the samples aged at room temperature from 1 week to 12 years are composed of SnO_{2-x} and SnO_{1-x} mixture. From the depth profile of Sn 3d and O 1s spectra, the difference between the old and new samples was detected. The hydroxide profiles among the three samples were similar to each other. The compositions of SnO_{2-x} and SnO_{1-x} were estimated from the depth profiles. In the aged samples, the ratio of SnO_{1-x} increases (0.15 to 0.20 approximately).

5 Literature

- [1] K. Mashimo, S. Yamazaki, A. Shimoyamada, H. Nishikubo, Y. Hori, and H. Sasaki, Microstructure of Fretting Debris on Tin-plated Terminals, Proceedings of the 62nd IEEE Holm Conference on Electrical Contacts, 2016, pp. 141-145.
- [2] K. Mashimo, H. Nishikubo, Y. Ishimaru, Y. Okuno, and S. Kawata, Prediction of Wear Volume on Sliding Contacts using Cellular Automata, Proceedings of the 61st IEEE Holm Conference on Electrical Contacts, 2015, pp. 408-413.
- [3] K. Mashimo, H. Nishikubo, Y. Ishimaru, Y. Okuno, and S. Kawata, Fretting analysis of tin-coated terminals under rotational motion, Proceedings of the 60th IEEE Holm Conference on Electrical Contacts, 2014, pp. 282-288.
- [4] K. Mashimo, Y. Saita, and Y. Ishimaru, Automatic Construction of a Computational Model for a Three-Dimensional Resistance Network, Proceedings of the 56th IEEE Holm Conference on Electrical Contacts, 2010, pp. 334-339.
- [5] K. Mashimo, and Y. Ishimaru, Electrical Contact Resistance Presumption about Tin-Coated Copper-Alloy Contacts Using RF Sputtered SnO_x Thin Films, Proceedings of the 58th IEEE Holm Conference on Electrical Contacts, 2012, pp. 270-274.
- [6] V. V. Bolotov, P. M. Korusenko, S. N. Nesov, S. N. Povoroznyuk, and R. V. Shelyagin, XANES and XPS Studies of Processes Initiated by High Vacuum Annealing in SnO_x/MWCNT Composite Layers, Physics of the Solid State, Vol. 55, No. 6, 2013, pp. 1289-1293.
- [7] O. M. Özkendir, Y. Ufuktepe, Electronic and structural properties of SnO and SnO₂ thin films studied by X-ray-absorption spectroscopy, Journal of Optoelectronics and Advanced Materials, Vol. 9, No. 12, 2007, pp. 3729 - 3733.
- [8] T. F. Baumann, S. O. Kucheyev, A. E. Gash, J. H. Satcher, Jr., Facile Synthesis of a Crystalline, High-Surface Area SnO₂ Aerogel, Advanced Materials, Vol. 17, 2005, pp. 1546-1548.
- [9] S. Gautam et al, X-ray spectroscopy study of Zn_xSn_{1-x}O₂ nanorods synthesized by hydrothermal technique, Thin Solid Films, Vol. 546, 2013, pp. 250-254.
- [10] H. Kurata et al, Electron-energy-loss near-edge structures in the oxygen K-edge spectra of transition-metal oxides, Physical Review B, Vol. 47, 1993, pp. 13763-13768.
- [11] Georg Hähner, Near edge X-ray absorption fine structure spectroscopy as a tool to probe electronic and structural properties of thin organic films and liquids, Chem. Soc. Rev., Vol. 35, 2006, pp. 1244-1255.
- [12] J. J. Rehr, R. C. Albers, Theoretical approaches to x-ray absorption fine structure, Reviews of Modern Physics, Vol. 72, No. 3, 2000, pp. 621-654.
- [13] X. T. Zhou et al, Time-resolved x-ray excited optical luminescence from SnO₂ nanoribbons, Appl. Phys. Lett., Vol. 89, 2006, pp. (213109-1) - (213109-3).
- [14] K. Mashimo, Y. Hori, and S. Yamazaki, A XANES Study of Natural Oxide Films on Plated Tin, Proceedings of the 64th IEEE Holm Conference of Electrical Contacts, 2018, pp. 130-134.
- [15] Funda Aksoy Akgul et al, Structural and electronic properties of SnO₂, Journal of Alloys and Compounds, Vol. 579, 2013, pp. 50-56.

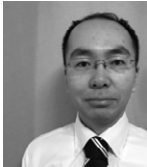
- [16] J.A. Schneider and A.C. Nunes, Jr., Characterization of Plastic Flow and Resulting Microtextures in a Friction Stir Weld, *Metallurgical and Materials Transactions B*, Vol. 35, 2004, pp. 777-783.

Biography



Keiji Mashimo received his Ph. D. degree in computer science from Okayama University, Japan in 2006 and also his B. Sc. degree in physics from Tohoku University, Japan, in 1982.

Since 1982, he has been working as a research engineer at Furukawa Electric Co., Ltd. His research areas include numerical simulations of material properties and artificial intelligence.



Atsushi Shimoyamada received his B. S. in physics in 2003 from he received his Tokyo University of Science, the M. S. and Ph. D. degree in materials science in 2005 and 2008, respectively,

from the University of Tokyo. He joined Furukawa Electric Co., Ltd. in 2009. His research interest involves microstructure analysis in metals and semiconductors using TEM, STEM, and spectrum imaging techniques.



Hirokazu Sasaki received his B.S. in physics in 1996 from Hiroshima University, his M.S in physics in 1998 from the University of Tokyo and Ph.D. degrees in materials engineering in 2011 from the University of Tokyo.

In 1998, he joined Furukawa Electric Company, Ltd., where he has been engaged in electron microscopy. His current research interest involves electric potential analysis in semiconductor using several electron phase imaging techniques.

Alloy Development in the CuNiAl System for High Strength Materials

Miriam Eisenbart, fem Research Institute, Schwaebisch Gmuend, Germany, eisenbart@fem-online.de
Felix Bauer, fem Research Institute, Schwaebisch Gmuend, Germany, bauer@fem-online.de
Ulrich E. Klotz, fem Research Institute, Schwaebisch Gmuend, Germany, klotz@fem-online.de

Abstract

In recent years a new high throughput alloy development method based on diffusion couples has been introduced [1]. Based on the findings of an extensive study on 35 Cu-based alloy systems, the ternary alloy system Cu-Ni-Al has been identified as a promising base for the development of new high strength materials with possible applications as contact materials. On bulk materials samples, the precipitation hardening process was studied in detail and revealed peak hardness values of more than 300 HV. Tensile tests have shown that the material reaches more than 10 % strain to rupture. Ongoing research now focuses on improving the alloy composition in order to enhance the electric conductivity by fine tuning the Ni : Al ratio and by introducing further alloying elements and, thus, a second species of precipitates in the hardening mechanism.

1 Introduction

Precipitation hardenable Cu-alloys often show an excellent combination of hardness and electric conductivity. This is based on the combination of the particle strengthening mechanism and a relatively pure copper matrix with only a small amount of residual dissolved alloying elements. Their application is widespread. The Cu-Be alloying system comprises materials with a particularly beneficial combination of high strength and high conductivity. Since the application of Cu-Be alloys warrants certain precautions during manufacturing in order to prevent possible health hazards for human workers, the development of new alloys with comparable characteristics is imperative.

In recent years, a new alloy development strategy was introduced that provides an alloy screening method based on diffusion couples [1]. The method uses base alloys which can be solution annealed at a certain high temperature. The diffusion-welded couples are kept at high temperature for a period of time, e.g. 2 weeks, until a broad chemical diffusion zone is established. The samples are then quenched from the solution annealing temperature and subsequently heat treated at temperatures between 350 and 500 °C, which is a typical temperature range for precipitation hardening in copper alloys. The samples are subsequently investigated with EDS and micro-hardness measurements resulting in alloy libraries with information on hardenability as a function of chemical composition. 35 Cu-based systems have been evaluated using this method.

The systems Cu-Al-Sn-Ti, Cu-Mn-Sn-Ti as well as Cu-Co-Fe-Ti [1] [2] [3] have been published so far based on this method. One particularly interesting alloying system that emerged from these efforts is the Cu-Ni-Al system [4].

Since diffusion couples only reveal limited information on mechanical properties and electric conductivity, bulk sample material was cast and thermo-mechanically treated to test the macroscopic and microscopic properties of individual alloy compositions. To this end, ternary Cu-Ni-Al alloys as well as quaternary compositions were chosen. The latter alloy compositions were engineered with a fourth metallic element “Me” partially substituting the aluminum content in the base Cu-Ni-Al alloy following the formula $\text{CuNi}_{15}\text{Al}(5\text{-X})\text{Me}(\text{X})$ (at.%). The elements chosen in this study were Me = Si, Sn, Ge, Ti, Zn. The alloying compositions are henceforth given in weight %. The ternary alloys comprised a Ni content of between 8 % and 18 % and an Al content of 1 % to 3 % (rounded to integers). The molar Ni : (Al+Me) ratio has been kept as constant as experimentally possible. The following **Table 1** lists the chemical composition of the alloys as determined by Glow Discharge Optical Emission Spectroscopy (GDOES) analysis. Each value is given as a mean value of two individual measurements, taken at both ends of the cast bolt. The Ni : (Al+Me) ratio is given in atom-% to reflect the stoichiometric ratio of possible precipitates.

Table 1: Chemical composition of the investigated alloys as measured by GDOES

Alloy	Ni [wt.%]	Al [wt.%]	Me [wt.%]	Cu [wt.%]	Ni/(Al+Me) [at.%]
CuNi14Al1Si0.6	14.12	1.30	0.62	balance	3.42
CuNi14Al1Sn3.4	13.73	1.28	3.34	balance	3.09
CuNi14Al1Ge1.2	13.82	1.30	1.17	balance	3.66
CuNi13Al2Ti0.4	13.05	2.00	0.41	balance	3.01
CuNi15Al1Zn1.7	14.57	1.17	1.70	balance	3.59
CuNi8Al1	8.32	1.29		balance	2.96
CuNi11Al2	11.28	1.75		balance	2.95
CuNi15Al2	13.55	2.21		balance	2.82
CuNi18Al3	17.73	2.83		balance	2.88

2 Material and Method

The alloys were melted via induction heating in an inert atmosphere and cast into copper molds with rectangular shaped cavities (150*18*8 mm). Following this rapid solidification, a homogenizing treatment was conducted in order to dissolve possible micro segregation zones. This treatment was performed at 900 °C for 12 h in vacuum. The treatment in vacuum successfully suppressed the formation of oxide layers on the surface, but necessitated a slow cooling to room temperature inside of the furnace. A second heat treatment under nitrogen flux was hence applied at 885 °C for 30 minutes followed by quenching in water at room temperature in order to achieve a solution-annealed state (SAS).

The rectangular bolts were relatively soft (70-100 HV1 depending on the alloy composition) and could be easily cold rolled (CR) into alloy sheets. The alloys were sufficiently ductile to endure a reduction of up to 80 % without developing cracks. At a sheet thickness of 2 mm, the sheets were again solution annealed and cold rolled to 1 mm, resulting in a final 50 % thickness reduction. The subsequent heat treatment was performed at 455 °C, 500 °C and 550 °C, respectively. Hardness and electrical conductivity measurements were recorded as a function of heat treatment duration time. The heat treatment for 1 h was performed in a salt-bath furnace, longer heat treatments for up to 1000 h were done in air. Peak hardness conditions were chosen for tensile test specimens. SEM investigations of the precipitates were performed as well. The equilibrium precipitation behavior, namely precipitation volume and type, was simulated using ThermoCalc® software employing the database TCCU2.

The electrical conductivity was measured using a Sigmascope® SMP350 which employs eddy current testing at 120 kHz.

The microstructure was recorded using a Zeiss Gemini SEM and an ESB detector in order to show material contrast in the images. The images were recorded with a very low acceleration voltage of 2 kV in order to record only information from very

superficial sample volumes. This prevents superposition of precipitates from deeper material layers in the images.

3 Results

3.1 Ternary alloys

The ternary alloys showed a fast response to heat treatment, even after 1 h already a large increase in hardness was recorded compared to the cold rolled state **Figure 1**. For a heat treatment at 500 °C unanimously the peak hardness was achieved after approx. 10 h. The heat treatment at 455 °C resulted in comparable hardness values only after approx. 200 h. A heat treatment at 550 °C was shown to result in no further increase of the hardness compared to the lower temperatures. The hardening behavior according to Figure 1 reveals a high stability against overaging at 455 °C. At 500 °C, the hardness diminishes only after more than 100 h significantly, while at 455 °C, no significant overaging even after more than 1000 h can be observed. Only a heat treatment at 550 °C resulted in more pronounced overaging. A higher Ni+Al content results in a larger precipitation volume and, hence, an increased potential for precipitation hardening according to ThermoCalc® simulations [1]. The precipitate species was dubbed FCC_L12#2 by the ThermoCalc® software and is, in fact, the well-known Ni₃Al, or γ' , intermetallic phase that is responsible for the excellent strength of Ni-based superalloys [5].

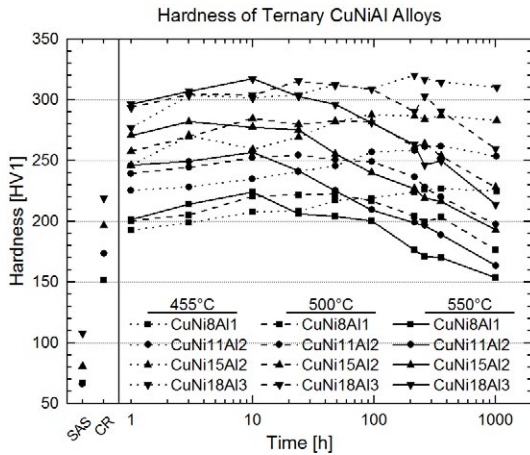


Figure 1: Influence of chemical composition and annealing temperature on the precipitation behavior of Cu-Ni-Al alloys at three different temperatures.

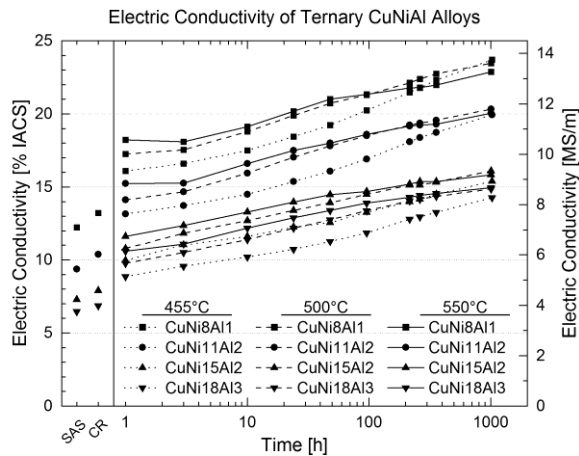


Figure 2: Influence of the chemical composition and the annealing temperature on the electric conductivity.

The experimental results confirm these simulations, for higher alloy contents, a higher hardness could be achieved. CuNi8Al1, for example, achieved 220 HV1 after 10 h at 500 °C. CuNi15Al2 achieved 285 HV1 after the same treatment and CuNi18Al3 even 300 HV1. The drawback of highly alloyed compositions is their electric conductivity, which follows the opposite trend with 12 %IACS for CuNi18Al3 and 19 %IACS for CuNi8Al1 (500 °C, 10 h). The electric conductivity follows an upwards trend during the entire heat treatment and does not seem to be closing in on saturation after 1000 h (**Figure 2**). While at 500 °C and 550 °C some retardation of the conductivity development is apparent after long annealing times, at 455 °C no significant slowing is observed and the lower temperature conductivity surpasses the higher temperature conductivities for some alloys. The nature of the precipitates was confirmed by XRD measurements to be Ni_3Al (not shown here).

3.2 Quaternary alloy compositions

Adding a fourth element to the alloy can have an impact on the precipitation behavior as well as on the overall achievable hardness. The addition of Sn, Si and Ti resulted in a higher hardness than similar ternary Cu-Ni-Al alloys, but the precipitation kinetics were enhanced as well (**Figure 3**). These alloys achieve the peak hardness values already after 1 h heat treatment at 455 °C. While the Ti containing alloy still shows the same stability against overaging as the ternary alloys, the Si and Sn containing compositions overage faster. This is particularly valid for the Si containing alloy. The alloying of Zn and Ge, respectively, does not improve but rather diminishes the hardness.

The electric conductivity shows some interesting deviations from the ternary alloys. The Si containing composition is especially noteworthy. The conductivity rises faster than that of the other alloys.

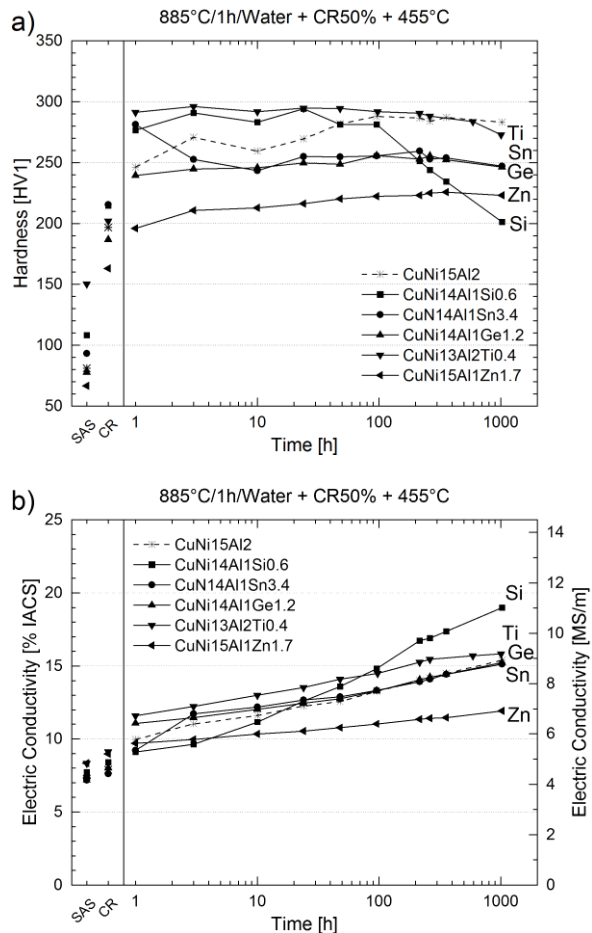


Figure 3: Development of hardness (a) and electric conductivity (b) of quaternary alloy compositions at 455 °C as a function of time. A comparable ternary alloy composition is plotted with dashed line.

3.3 Mechanical Properties

Exemplary tensile test measurements for the ternary alloys after a heat treatment for 216 h at 455 °C are shown in **Figure 4**. For each alloy, at least two samples were tested with very similar results. They showed a high tensile strength, which is in good accordance with the results from hardness measurements. Additionally they also comprise a high ductility of up to 10 % plastic strain and more for the alloy CuNi18Al3 with the highest tensile strength and even larger plastic strain values for the less alloyed compositions. The yield strength values were measured to be between 560 MPa and 909 MPa. Overall, the ternary alloys showed a similar behavior in the tensile test with a constant decrease in strength and increase in plastic strain as the content of alloying elements is reduced.

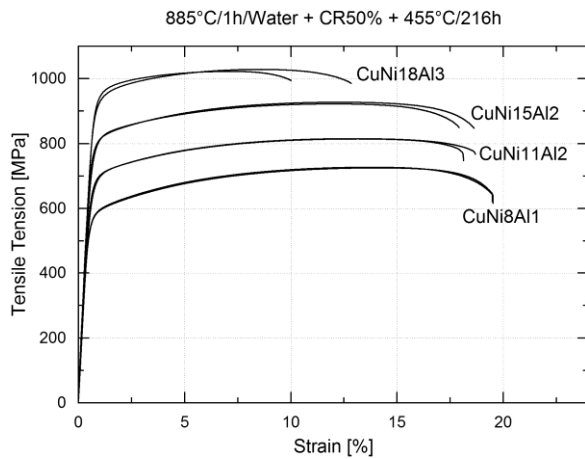


Figure 4: Tensile test results of ternary alloy compositions after a heat treatment at 455 °C for 216 h

The quaternary alloys on the other hand showed deviations of the deformation behavior in the tensile testing curves (**Figure 5**). While the Zn and Ge alloyed compositions still behaved similar to the ternary alloys, Si and Sn largely reduced the ductility. Ti increased the yield strength significantly. During plastic deformation of the Ti alloyed composition no further strengthening was detected, but rather softening occurred. **Table 2** and

Table 3 show the values of the mechanical properties for two different heat treatments. The tensile test results after a heat treatment for 10 h at 500 °C are very similar to the ones after a heat treatment for 216 h at 455 °C.

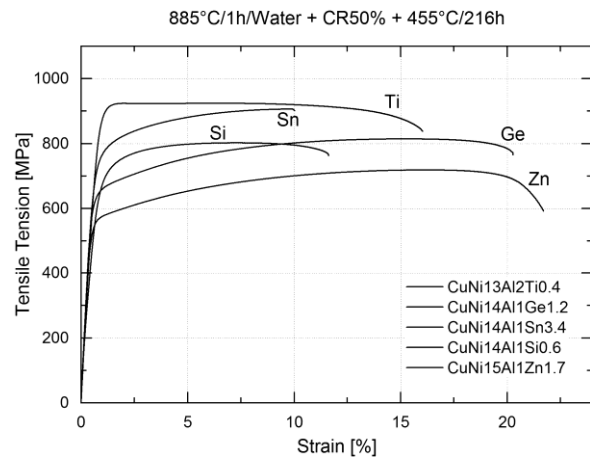


Figure 5: Tensile test results of quaternary alloy compositions after a heat treatment of 216 h at 455 °C

3.4 Investigation of the microstructure

The investigation of the microstructure, namely the quantification of the precipitate development as a function of time and temperature, is ongoing. For the alloy CuNi15Al2, preliminary results can be seen in **Figure 6** and **Figure 7**. For a heat treatment at 500 °C for 10 h, an overall homogeneous distribution of precipitates was recorded. Only occasionally, coarser discontinuous precipitation phenomena were observed at grain boundaries (Figure 7). Even after heat treatment duration for 1000 h at 455 °C, a homogenous distribution of precipitates could be observed (Figure 7). The diameter of the precipitates was significantly smaller than 100 nm. Again, discontinuous precipitation occurred along grain boundaries. This phenomenon was more pronounced than in the 500 °C/10 h sample of the same alloy.

Regarding the quaternary alloys, the most noticeable influence on the microstructure was observed for Si and Ti additions. While Si promoted a much more pronounced discontinuous precipitation behavior, Ti largely reduced the grain size.

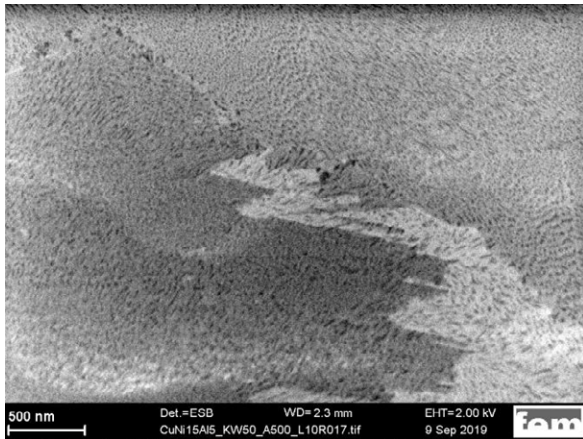


Figure 6: Microstructure of the alloy CuNi15Al2 after 10 h at 500 °C: homogeneous precipitate distribution

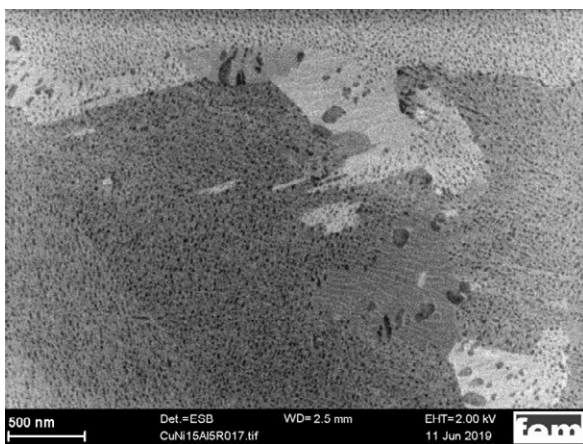


Figure 7: Microstructure of CuNi15Al2 after a heat treatment for approx. 1000 h at 455 °C: homogeneously distributed precipitates and coarser discontinuous precipitates concentrated predominantly at some grain boundaries

4 Discussion and Outlook

Despite the fact that as early as 1921 a scientific investigation into the Cu-Ni-Al system was published by A. A. Read [6], the number of scientific papers concerning this system today is small, even more so for the alloy range reported here. Important contributions to the understanding of the system were done by W.O. Alexander [7], who described the phase diagram, and H. Böhm [8], who identified the precipitates as Ni_3Al . Similar as the γ' -precipitates in nickel based superalloys, these precipitates are responsible for the superior mechanical properties of this alloy system. Presumably, the ordered $L1_2$ -structure of these precipitates and their coherent orientation to the Cu-matrix govern the mechanical behavior. Cutting of ordered precipitates by dislocations would cause an anti-phase boundary, which increases the internal energy of the system. Therefore, dislocation tend to cross slip or to climb

over the precipitates rather than cutting them. This sustains further dislocation movement and thereby increases strength.

The heat treatment employed in this study causes the precipitation of such Ni_3Al precipitates, which promotes strengthening. As a positive side effect of the precipitate development, the Cu-matrix is depleted in Ni and Al and thus its electric conductivity is enhanced. Our results show, that the enhancement of the electric conductivity has still not reached saturation by the end of the 1000 h heat treatment. A possible explanation could be that the precipitation process has not reached equilibrium yet and the precipitation volume is still growing at this point of the process. While we qualitatively observed some Ostwald ripening in the SEM pictures, we can conclude from the hardness measurements that the heat treatment at 455 °C has not resulted in overaging, which is an encouraging result regarding the thermal stability of the precipitates and the robustness of the precipitation treatment in industrial production. Further optimization of the heat treatment to speed up the precipitation process will be required.

The tensile tests proved a high residual ductility even in peak hardened condition, which is also very promising for the technical application of this alloy system as a high strength wrought Cu alloy. While the electric conductivity leaves something to be desired at this point of the research, the results show that there is potential for an improvement of the conductivity in the future. Especially at lower annealing temperatures, more of the dissolved alloying elements seem to be precipitated, leading to higher conductivity values at conditions closer to the equilibrium state. This observation is in good agreement with the simulated molar content of precipitate phase [1] where it is clear that maximum precipitation volumes are expected below 400 °C. Regarding the introduction of further alloying elements, silicon seems to accelerate the enhancement of electric conductivity significantly. A possible explanation of this effect could be that a second precipitate species is introduced. For example Shen et al. [9] showed the presence of Ni_2Si precipitates in a CuNi10Al3Si0.8 alloy after a precipitation treatment, so the Ni_2Si precipitation species is a likely candidate in our alloy system as well. Ochiai et al. [10] report that in the Ni_3Al intermetallic phase, some Ni positions can also be inhabited by Cu atoms. Since the molar ratio of Ni : Al or Ni : (Al+Me) was kept at approx. 3, some residual Ni might be left dissolved in the copper matrix in favor of Cu atoms in the Ni_3Al phase. The residual Ni might readily be available to produce Ni_2Si precipitates, thereby leaving a much cleaner Cu matrix behind and hence resulting in higher conductivity values. Figure 8 and Figure 9 show simulated ternary and quaternary phase diagrams in the copper-rich corner of the CuNiAl and CuNiAlSi alloy system, respectively. The investigated alloy

compositions are depicted in the plots. According to the calculation, the ternary compositions are located in the two-phase region with a Cu solid solution matrix material and Ni₃Al precipitates.

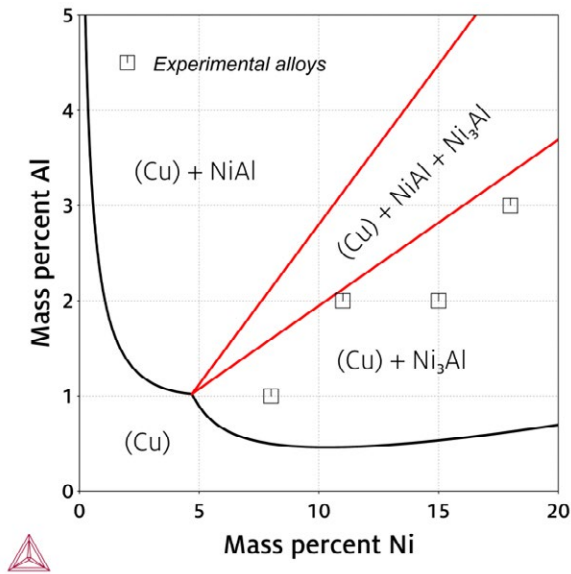


Figure 8: Simulated isothermal plot of the equilibrium phases of the CuNiAl system in the copper rich corner at 500 °C including the compositions of the experimental alloys. The plot was calculated using the ThermoCalc® Software and the TCCU2 database.

In the case of the alloy system CuNiAlSi, more phases are predicted. According to the simulation, our experimental alloy CuNi14Al1Si0.6 is located in the three-phase region, where the matrix consists of Cu solid solution and Ni₃Al as well as Ni₁₉Si₆ precipitates are present. An XRD measurement on a sample of alloy CuNi14Al1Si0.6 aged at 455 °C for 1024 h did not yield a conclusive result on the presence of a nickel-silicide phase, it did however reveal the presence of Ni₃Al. Further investigations, for example TEM-experiments, would be necessary to prove the presence of a second precipitate phase, but based on the literature and the calculation shown here, it seems possible that a nickel silicide phase is precipitated in

the CuNi14Al1Si0.6 alloy.

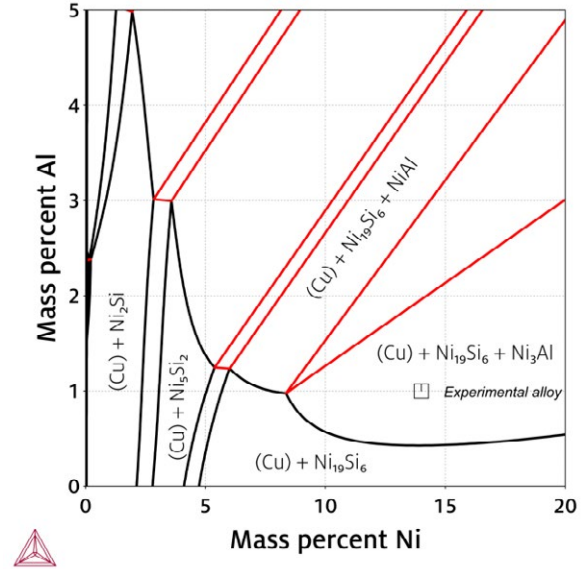


Figure 9: Simulated isothermal plot of the equilibrium phases of the CuNiAlSi system at a Si-content of 0,62 wt.% in the copper rich corner at 500 °C including the compositions of the experimental alloys. The plot was calculated using the ThermoCalc® Software and the TCCU2 database.

The scientific description of the exact precipitate development is currently under investigation and crucial for the optimization of the alloy composition. The minimum duration for the heat treatment to achieve peak hardness values depends on temperature and alloy composition. Higher amounts of alloying elements result in higher precipitation volumes and, as would be expected, to higher achievable hardness values. Judging from the results shown here, a heat treatment for 10 h at 500 °C seems to be beneficial for technical applications, although preliminary results suggest that higher degrees of initial cold rolling might further optimize the results. Adding Sn, Si or Ti can influence the response to heat treatment significantly.

Table 2: Tensile test results for a heat treatment at 500 °C and 10 h

Alloy	R _m [MPa]	R _{p0.2} [MPa]	A [%]
CuNi14Al1Si0.6	821 ± 15	632 ± 40	4.5 ± 1.4
CuNi14Al1Sn3.4	948 ± 1	823 ± 9	7.8 ± 0.5
CuNi14Al1Ge1.2	819 ± 4	622 ± 2	22.0 ± 0.5
CuNi13Al2Ti0.4	934 ± 2	850 ± 15	17.0 ± 0.8
CuNi15Al1Zn1.7	702 ± 5	511 ± 5	18.9 ± 2.0
CuNi8Al1	712 ± 1	536 ± 4	21.2 ± 0.5
CuNi11Al2	790 ± 5	641 ± 7	18.4 ± 2.6
CuNi15Al2	914 ± 3	755 ± 2	20.0 ± 0.5
CuNi18Al3	1002 ± 2	889 ± 15	13.8 ± 2.0

Table 3: Tensile test results for a heat treatment at 455 °C and 216 h

Alloy	R _m [MPa]	R _{p0.2} [MPa]	A [%]
CuNi14Al1Si0.6	802	566 ± 22	11.2 ± 0.3
CuNi14Al1Sn3.4	904 ± 3	715 ± 4	8.2 ± 1.2
CuNi14Al1Ge1.2	816 ± 2	630 ± 3	20.7 ± 0.4
CuNi13Al2Ti0.4	921 ± 4	819 ± 1	16.5 ± 0.3
CuNi15Al1Zn1.7	718 ± 1	547 ± 5	20.9 ± 1.2
CuNi8Al1	726 ± 1	562 ± 1	19.8 ± 0.5
CuNi11Al2	815 ± 1	657 ± 5	18.6 ± 0.4
CuNi15Al2	925 ± 3	768	18.5 ± 0.4
CuNi18Al3	1025 ± 3	909 ± 3	11.2 ± 1.5

5 Literature

- [1] F. Bauer, M. Eisenbart and U. E. Klotz, "Entwicklung von hochfesten Cu-Ni-Al Legierungen," *Metall* 73, p. 428–431, 2019.
- [2] R. Bürgel, H. Maier and T. Niendorf, *Handbuch Hochtemperatur-Werkstofftechnik*, Vieweg + Teubner, 2011.
- [3] A. Read and R. Greaves, "The Properties of some Nickel-Aluminium-Copper Alloys," *Journal of the Institute of Metals*, pp. 57-84, 1921.
- [4] W. Alexander and D. Hanson, "Copper-rich Nickel-Aluminium-Copper Alloys. Part I. - The Effect of Heat-Treatment on Hardness and Electrical Resistivity," *Journal Inst. Metals*, pp. 83-99, 7 9 1937.
- [5] H. Böhm and W. Leo, "Entmischungsvorgänge beim Zerfall übersättigter Kupfer-Nickel-Aluminium Mischkristalle," *Acta Metall.* 12 (1964) , pp. 966-968, 1964.
- [6] L. Shen, Z. Li, Y. Zha, Y. Wang, Q. Dong and M. Wang, "Phase transformation behavior of Cu–10Ni–3Al–0.8Si alloy," *Materials Chemistry and Physics*, pp. 421 - 428, 2016.
- [7] S. Ochiai, Y. Oya and T. Suzuki, "Alloying behaviour of Ni3Al, Ni3Ga, Ni3Si and Ni3Ge," *Acta Metallurgica*, pp. 289 - 298, 1984.
- [8] K. Ratschbacher, U. E. Klotz and M. Eisenbart, "Diffusion samples as a high-throughput screening method for alloy development," *Materials Science and Technology*, pp. 1-8, 2018.
- [9] U. E. Klotz, M. Eisenbart, K. Ratschbacher and F. Bauer, "Entwicklung von hochfesten Cu-Legierungen im System Cu-Ni-Al," in *VDE e.V. (Ed.), Kontaktverhalten und Schalten: 25. Albert-Keil-Kontaktseminar*, Berlin, VDE VERLAG, 2019, pp. 57-63.
- [10] U. E. Klotz, M. Eisenbart and K. Ratschbacher, "Neuartige Screeningmethode zur Legierungsentwicklung auf Basis von Diffusionspaaren," *Metall*, pp. 345-348, 2018.

Special connector requirements call for specific contact coatings: new silver alloys show characteristics never seen before

Dr. Isabell Buresch*¹, Dr. Helge Schmidt**, Sönke Sachs**

TE Connectivity Germany GmbH
73499 Wört* / 64625 Bensheim**, Germany

¹isabell.buresch@te.com

Abstract

Requirements for electrical contact surfaces in automotive connectors undergo a tremendous change when having a look on new applications like electric engine connections, charger terminals for charging E-vehicles, electrical lighting terminations etc.. New silver alloys show exceptional temperature stability combined with a higher hardness. Therefore, they are more stable over lifetime and ensure a consistent property profile. In comparison to pure silver coatings, critical changes in the microstructure do not occur. Metallurgical and physical processes within the coating and its interfaces, which are typically observed during harsh environment qualifications and as a result significantly affecting the performance, are successfully suppressed by these new silver alloys. The present study demonstrates contact coatings solutions like low alloyed silver-coatings (Ag) and Ag-Sn Multi-layer coatings for use in the newer and harsher applications required for automotive connectors in comparison to pure silver surfaces. Depending on the composition, they can also replace noble metal coatings.

1 Introduction

The standard contact surfaces for connector contacts in automotive applications at elevated temperatures between 130 – 160 °C today are pure Ag-coatings with a nickel-underlayer when using Ag above 140°C.

In addition, Ag-coatings are the favored solution for high vibration load and power applications. Beside this Ag shows the best cost/performance relation and for metals the highest electrical conductivity. Nickel (Ni) is the simplest and most effective barrier layer. The disadvantages of pure Ag-films are the tendency to cold welding, tarnishing as well as the propensity towards material migration. Special passivation solutions to overcome these disadvantages are available, but their effectiveness is limited and a high and/or uncontrolled amount or thickness of these chemicals or the metal film can cause severe electrical problems.

Several investigations with pure Ag-coatings after aging at temperatures above 160°C result in a decrease in coating hardness due to recrystallisation. Above 180°C oxygen is diffusing along the grain boundaries in the Ag-coating leading to an inner oxidation of the underlayers like Ni or Copper (Cu) resulting in foreign oxide film formation and peeling [1, 2] (**Figure 4**).

The trend for higher temperatures in the contact point of connector contacts is driven by a higher packaging

densities and high currents as seen in electric vehicles as well as ongoing miniaturisation. Maximum temperatures up to 180-200°C for over 1000h are being demanded for automotive applications, meaning solutions must be developed. The mating cycle requirement for standard applications is >50 and for charger terminals > 10.000 which then call for more robust coatings.

Simple modifications of Ag-coatings with alloying small amounts of Sb, Ni, Cu, Te or organic additives result in so called “hard-Ag-coatings”. These hard-Ag variants are available today. The goals of these low- or micro alloyed surfaces are to increase the film hardness (**Table 1**) and the wear resistance. They can withstand high vibration load. What is not achievable with these measures is the mitigation of the recrystallisation process and therefore the hardness stability at elevated temperatures, the cold-welding behavior and the tendency for tarnishing. An additional passivation film is almost always necessary. The problem of the diffusion of oxygen along the grain boundaries is also not solved with these hard-Ag variants.

Hard-Ag	Hardness HV
Ag	(30)-90
AgSb2	130-170
AgTe2	100-120
AgNi0,15	70-100
AgCu3	130-160
Ag bright	80-130
Ag (org. add.)	80-110
AgPd 1-8	80-310

Tab. 1: Coating hardness of hard-Ag films in the as plated condition (load indentation measurement).

Some years ago, ideas to implement an “oxygen trap” in combination with an underlayer like Ni were leading to sandwich-coatings which were optimized over time [2,3,4]. Contact surfaces often use the element tin (Sn) which is highly oxygen-affine and offers in combination with Ag and Ni, depending on their coating thicknesses and the kind of combination, a lot of possibilities. Sn reacts with Ag and Ni and forms different intermetallic phases, which help to obtain a wide variety of coating properties, fulfilling certain requirements for different applications, including: good temperature stability at temperatures up to 200°C for E-mobility applications, reduced whisker risk in press-fit connections for nearly all PCB-types and a higher wear resistance for components with up to 50 mating cycles. The key factors for these behaviors are due to the above mentioned intermetallics in combination with the thickness of the coatings, correlations and sequences of the multilayers or an alloy / co-deposition of the elements as well as additional temper processes after plating [3].

The precondition for forming chemically stable composite coatings during the production processes is depositing the correct stoichiometric matrix or depositing the correct layers in sequence or/and thickness of the elements, followed by a temper process such as reflow, which matches with the element correlations conditions. Temper processes, whether inline or in a separate oven, and especially when selective, are challenging and depend on the melting temperature and component/part design.

Electroplating, being the favored selective plating technology, allows the deposition of nearly all noble metals as single layers. Layer systems with Palladium (Pd), such as NiPd or Pd/Ni/Ag, are well known for decora-

tive parts and electronic components. Micro alloyed alloy-coatings like the hard-silver variants or AuCo will be used in several applications.

Pure Pd is in use for decorative features, in electronic applications Pd is well known as a flash or a really effective barrier layer. Sandwich layers like Ni/Pd/Au are used in Leadframe applications as whisker reducing and bondable surfaces [5]. AgPd is implemented with 30-50%Pd as a contact material in relays and switches. Pd shows a good resistance against sulfidation and electromigration. Alloys with a high Pd-content tend to polymerize (brown-powder effect), which can induce high transition resistance.

The goal of the solution described in this paper is to deposit a high temperature resistant, low alloyed hard-Ag coating, which offers all advantages to pure Ag and eliminates the negative effects of pure Ag and Pd. The main coating properties for connector contacts like contact resistance and the mating cycle / wear behavior will be compared to the above mentioned sandwich layer coatings.

2 Fundamental

The hardening mechanisms of metals include dispersion hardening, solid solution hardening, precipitation hardening, fine grain hardening and hardening by forming. For coatings fine grain, solid solution, diffusion and dispersion hardening as well as in some cases also hardening by additional forming will be used. Diffusion hardening is a possibility specially for sandwich layers with appropriate layer combinations in addition with reflow or other temper processes.

By combining the elements Ni, Sn and Ag, hardening can be achieved by forming a solid solution during the code position of the elements with or without a temper process or by initiating diffusion between the layer sequences. The various intermetallic phases are then responsible for the hardening mechanisms [3].

Coatings with intermetallic layers show mostly a high hardness, sometimes 2-10 times harder than the individual element layers. This is often combined with a kind of brittleness, so forming after plating is not recommended. Intermetallic phases show a good chemical resistance and a high melting point. They are very stable and therefore suitable for use at elevated temperatures. Unfortunately, the electrical conductivity is lower in comparison to pure metals and the solderability usually bad. The temper processes used to initiate the diffusion processes affect wider areas over the part or strip and therefore, also areas which ideally shouldn't be exposed like partially Sn-coated regions or Ni/Au(Co) coatings. This was the reason to search for

other solutions which don't need this additional heating step.

The use of Pd as an element in coatings for electromechanical components has been known for a long time. Pd belongs to the group of Pt-metals. It is very corrosion resistant in air and acids and will be therefore used as a flash or diffusion barrier [5].

Electroplated Pd is well known for its tendency to form micro cracks at higher coating thicknesses, which is caused by its high absorption capacity for hydrogen and the combined phase transition. In combination with Ag, Pd forms a gapless solid solution (**Figure 1**). This allows a deposition in nearly every composition and increases the hardness without any additional temper process. This is the reason why this alloy system is suitable for selective plating. Pd has one disadvantage: it decreases the electrical conductivity of Ag with an impact on the contact resistance (**Figure 2**), which has to be taken into consideration, especially depending on the application and the contact normal force when choosing the alloying element content.

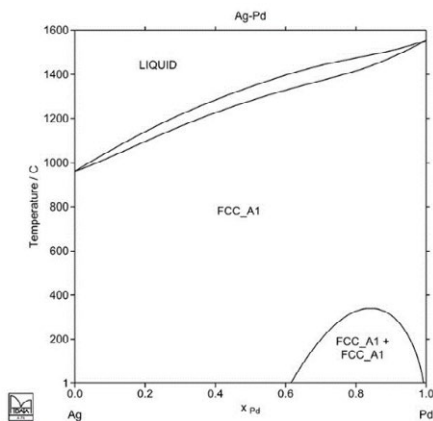


Fig. 1: Phase Diagramm Ag-Pd [6].

The challenge is to create an electrolyte composition with the 2 elements and additives, which is stable in its tolerated range without any ageing phenomena, and which has suitable and economic process parameters with high performance:

- Almost identical electrical behaviour like Ag
- Better temperature stability without recrystallisation, softening and O₂-diffusion
- Low insertion forces without passivation / no cold welding and galling
- No tarnishing without passivation
- Better wear resistance and therefore higher max. mating cycles
- Good performance in mixed paired connectors

- Cross compatibility with Ag, Au, Sn, NiPd/Au-flash
- No significant cost increase compared to hard-Ag
- Better vibration resistance including fulfilling SG4-vibration level and higher

In 2014 a new electrolyte for the deposition of AgPd-alloy coatings in the range between 4-10%Pd was developed [7, 8, 9].

Due to cost reasons a very thin AgPd-coating thickness was achieved which involves an additional Ni intermediate layer to fulfil the mating cycles specifications.

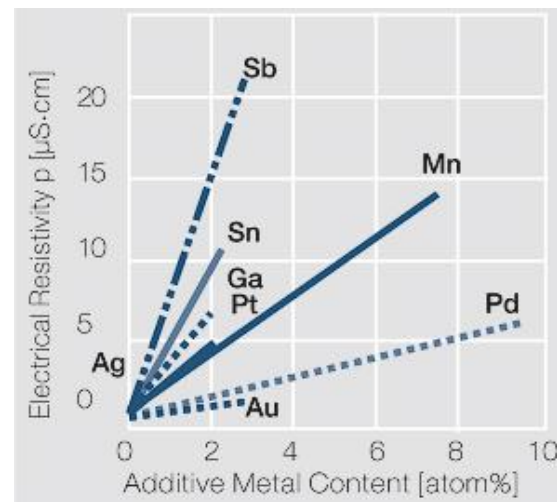


Fig. 2: Ag-alloys and the influence of different alloying elements on the electrical resistance [10].

The price increase for Pd has been severe during the last years and geometric / design related deposition effects during reel-to-reel plating with the first AgPd-electrolyte resulted in the decision to optimize the AgPd-electrolyte. An additional goal was also to reduce metal cost which means a new electrolyte with less Pd-content in the coating.

3 Coating properties

The tribological behaviour of a coating combined with the electrical properties are most important for connector contacts. These along with the adhesion are strongly related to the coating microstructure, crystallization structure and layer sequence. For Ni/Ag/Sn-multilayer coatings the layer thickness ratio, the sequence and the temper condition for the diffusion process are additional influencing factors. For co-deposited alloy-coatings these are the electrolyte formulation, the alloying content and the plating parameters.

3.1 Microstructure of coatings

Sandwich-layers like Ni/Ag/Sn and Ni/Sn/Ag differentiate in the top-layer, which can be manipulated by temper processes (Figure 3). The results are different surface microhardnesses, different coefficients of friction and behaviour in various atmospheres.

A free thin Sn top-layer in the combination with Ni/Ag/Sn acts as a „metallic“ lubricant to reduce the coefficient of friction and ensures low contact resistance values. On the other hand, free tin increases the whisker risk and shows a tendency for fretting corrosion, which limits the use under vibration load.

By varying the reflow-conditions the Sn-film can be reduced to small single Sn-islands embedded in the Ag₃Sn-intermetallic. This situation reduces the fretting behaviour and the whisker risk.

In the layer sequence Ni/Sn/Ag the typical Ag-surface properties correspond with the Sn-intermediate layer, which acts as an oxygen-catcher. Oxygen can no longer penetrate through the whole layer sequence and therefore inhibits peeling-off (Figure 4). Due to diffusion induced recrystallisation (DIR) of the AgSn-intermetallic phases, Sn is diffusing along the grain boundaries of Ag and blocks the oxygen. The typical recrystallisation and grain coarsening for Ag at elevated temperatures cannot be eliminated by this measure. Passivation to avoid cold welding is still necessary.

Both layer combinations ensure a higher stability at elevated temperatures up to 180°C due to the formation of the Ag₃Sn- and Ni₃Sn₄-intermetallic during an additional temper process. Ag₃Sn as a top-layer is diffusion resistant against oxygen and shows a stable grain structure at higher temperatures.

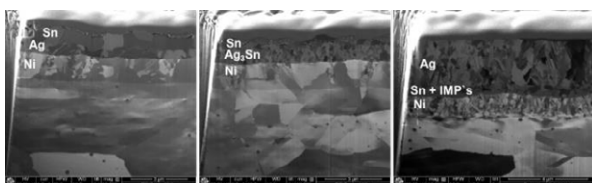


Fig. 3: Layer structure and microstructure of multilayer coatings: a) Ni/Ag/Sn initial, b) dto. after reflow, c) Ni/Sn/Ag initial.

The co-deposition of Ag with an additional element in low concentrations like Sb, Te, Ni or Cu are well known as hard-Ag coatings. Depending on the element the hardness of the coating in the initial condition can be increased up to 180 HV. This hardness increase is not durable since recrystallisation and grain coarsening of Ag cannot be stopped with these elements.

The deposition of a low-alloyed AgPd-coating with a Pd-content <4% shows even a high hardness up to 200 HV and a nanocrystalline crystallization structure but does not change its behaviour up to temperatures of 200°C (Figure 5). Here, an additional passivation is not necessary. The new developed electrolyte provides a good throwing power and reproduces the base material's topography.

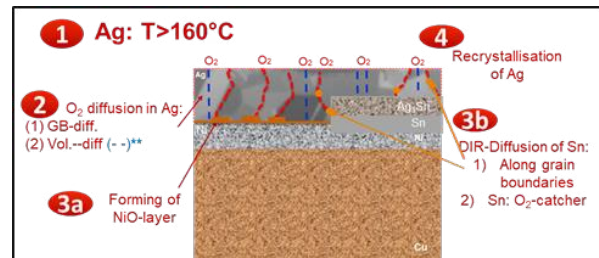


Fig. 4: Diffusion mechanisms in Ni/Ag- and Ni/Sn/Ag-coatings at 180°C [1].

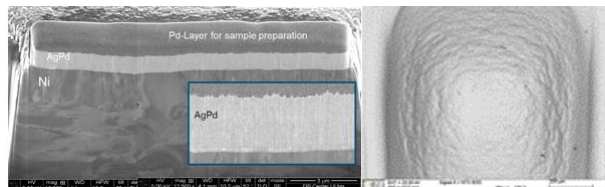


Fig. 5: Crystallization structure and surface microstructure of a hard-AgPd coating on a formed contact dome.

3.2 Coating hardnesses

The coating microhardness is an important factor influencing the contact resistance and wear resistance during mating-/unmating cycles and under vibration load. Using a Ni/Ag/Sn-sandwich coating the portion of free tin and the ration Sn: Ag as well the Ag-layer thickness in combination with the reflow parameters are all critical. They are responsible for the formation of the Ag₃Sn-IMP and the portion of residual free tin, which defines the surface properties in the application and during use. The relevant parameters in an AgPd-alloy coating include the Pd-content and the amount of additives and grain refiner and the coating thickness. The hardening effect of the Ag-matrix by alloying with Pd is more effective in comparison to the diffusion hardening with Sn and results in comparable values already at only >4 w% Pd.

3.3 Electrical Behavior

The coating hardness, the surface roughness and topography, the contact normal force, the coating composition with its contamination film, the contact design and

the contact pairs are all responsible for the contact resistance behaviour.

Standard Ag-coatings and hard-Ag coatings show a wide range of variations in their contact resistance values in the as plated condition depending on the used electrolytes and qualities (**Figure 6**). During temperature load, within the typical temperature range used today, the difference in between the single qualities increases. The reasons for this behaviour are the tendency for recrystallisation and softening beside the various additives, as well as the grain refiner and the varying electrolyte chemistry of the manufacturer. Organic additives and some of the alloying elements are diffusing during the aging process to the top of the surface and as a result increasing the contact resistance in a significant way (fig. 6b). The necessity for a clear definition of a hard-Ag coating will be essential.

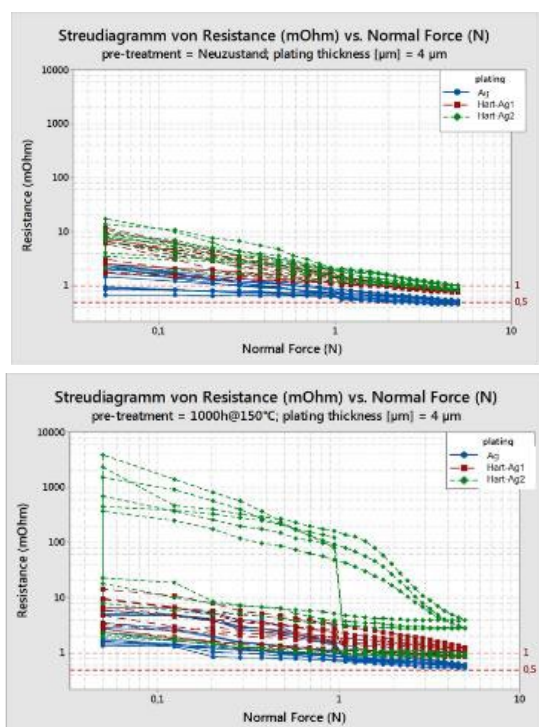


Fig. 6: Static contact resistance of different Ag-coatings measured under dry-circuit conditions (4-point resistance method with rider-on-flat samples).

Alloy-hardened coatings and diffusion hardened multi-layer surfaces show a totally different behaviour. In the initial condition pure single metal-films, like Sn and Ag, have the better electrical behaviour in comparison to their alloyed variants. Intermetallic layers, which are precisely adjusted or grown during use at elevated temperatures, even with their high hardness and specific crystal structure, have some disadvantages compared to alloyed / codeposited coatings (**Figure 7**). Contact resistance values of AgPd-coatings are leveling during temperature load at a low level compared to the initial condition, independent of the coating thickness. The

reason for this behaviour can be due to a grain-reorientation or a small softening effect; grain growth or a kind of recrystallisation could not be seen here.

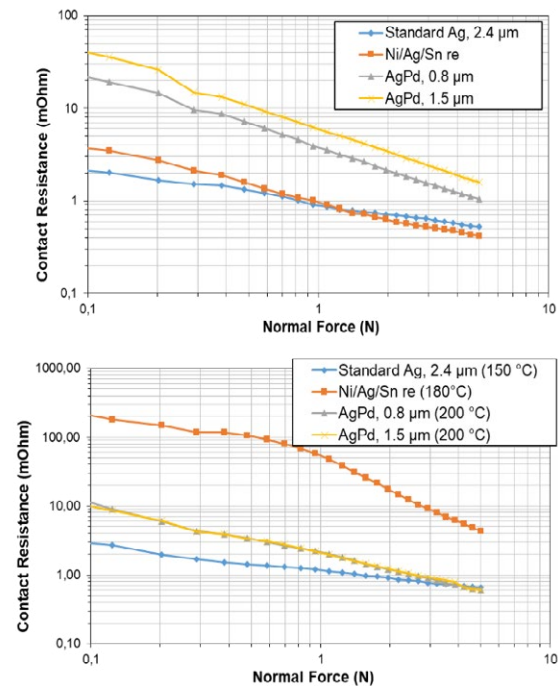


Fig. 7: Contact resistance values of Ag-based coating systems in the initial condition and after 1000h aging measured under dry-circuit conditions with rider-on-flat samples paired with pure Ag.

Serial production requires reproducible coating properties and therefore constant process parameters, especially the current density and agitation. Both are the most influencing parameters for the variation and absolute value of the contact resistance and alloy-element content (**Figure 8**) during co-deposition of two or more elements. Background for this statement is the current density depended incorporation of Pd, the crystallization structure and the roughness of the surface coating. The impact on the process parameters shows the run of the contact resistance over the contact normal force, which correlates with the Pd-content. Selective plating on prestamped parts requires therefore a considerable process effort and specific agitation conditions.

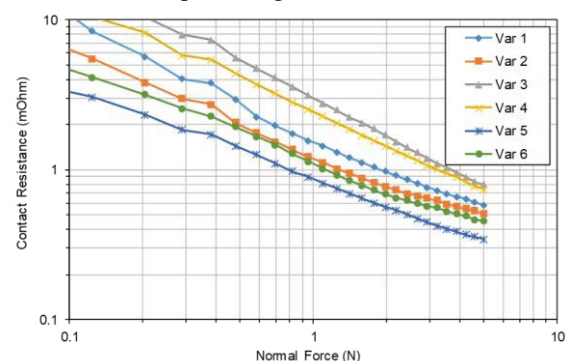


Fig. 8: Variation of contact resistance of AgPd-surfaces with a content of 0,8% (Var.1) up to 4 weight% Pd depending on the chosen plating parameters in the initial condition.

3.4 Wear behavior

The mating- and unmating behaviour and therefore the tribological properties are essential for the first mating cycle / in the initial condition and during life time. Their characteristics were evaluated and compared with pure Ag using rider-on-flat samples with a contact normal force of 2N and 1mm wipe. The contact pairing was always with Ag. During the test the coefficient of friction and the contact resistance over the number of cycles was monitored.

Using the sandwich layer Ni/Ag/Sn with an appropriate reflow process, the top layer Sn acts as a thin metallic lubricant during the first cycles: the coefficient of friction is reduced compared to pure Ag- and Sn-coatings (**Figure 9a**). Within a Sn-coating thickness range up to 0,5 μ m the coefficient looks very stable, however, not so the electrical behaviour: within the first cycles we see low values – but as the mating cycles increase, the contact resistance increases as well, depending on the free Sn-layer thickness, which suggests the formation and agglomeration of abrasive Sn-oxide particles at the contact dome and wear through. These particles will be removed from the wear track after >20 cycles combined with a decrease of the resistance value (**Figure 11**). Using a higher free Sn-film on top results in a comparable contact resistance value to pure Ag-coatings (fig. 9b). The free tin is therefore the relevant parameter for the wear induced electrical behaviour.

Hard-Ag coatings alloyed with Pd are desirable because of their reduced stable coefficient of friction. The contact resistance level correlates even under mechanical load with the Pd-content and can be below the Ag-level (fig. 9c+d). Further influencing factors are the crystallization performance which correlates also with the Pd-content and the roughness due to the high hardness (**Figure 10**).

The wear resistance and the friction coefficient are comparable to higher alloyed AgPd-coatings, Au-flash-PdNi- and hard-Au-films [11].

In contrast to pure Ag-layers, all tested AgPd-coatings achieve an improved friction behaviour. This means that the cold-welding effect known from pure, unpassivated Ag (fig. 9e), can always be eliminated by implementing a low Pd-content. The wear induced electrical behaviour will be influenced by the Pd-content.

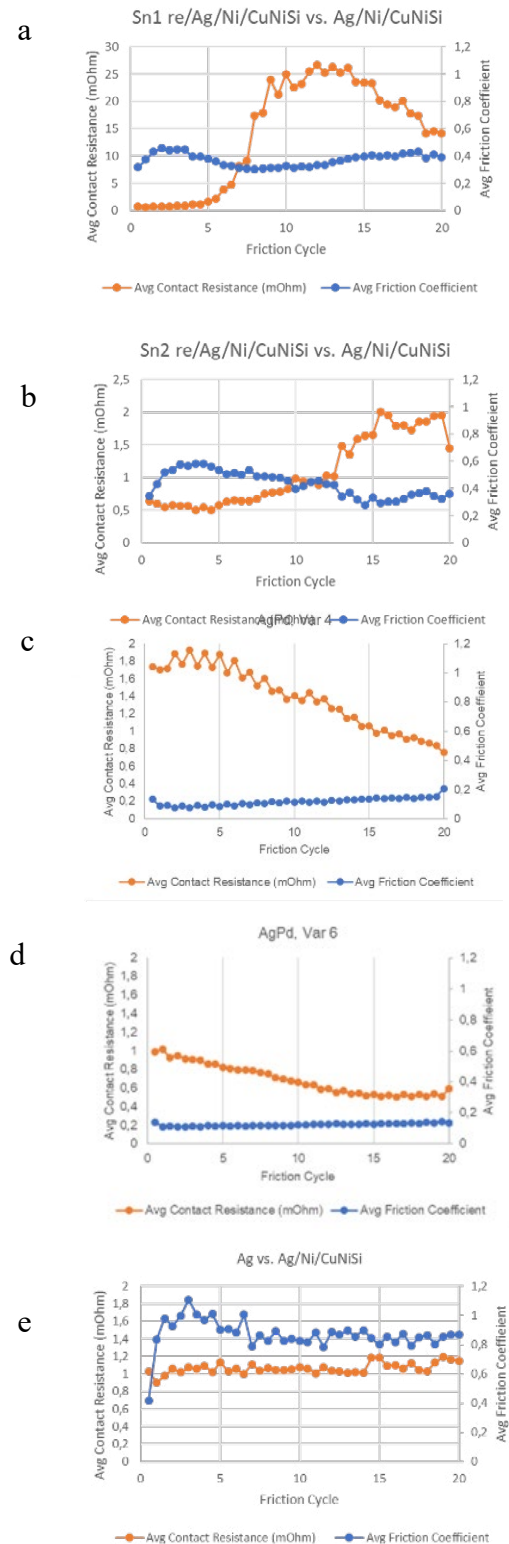


Fig. 9: Contact resistance and coefficient of friction over number of cycles for different coating systems in the initial condition paired with pure Ag non-passivated.

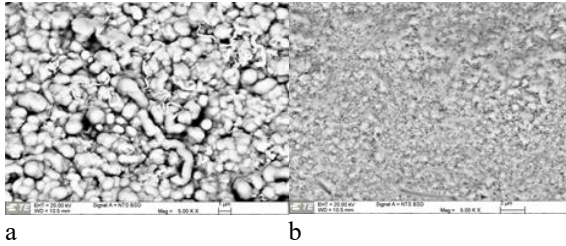


Fig. 10: Surface structure of AgPd-coatings a) variant 4 and b) variant 6.

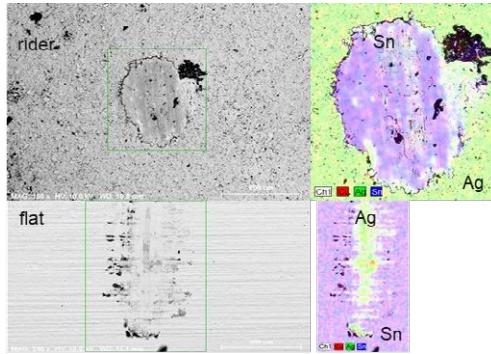


Fig. 11: Ni/Ag/Sn reflow top surface with free Sn in the initial condition: contact dome and the wear effect after 20 cycles.

4 Outlook and challenges

4.1 Low-alloyed hard-Ag-coatings

Some initial statements can already be made even though not all investigations with a specific contact have been completed:

- the low alloyed hard-AgPd-coatings when paired with pure Ag in the initial condition show a similar behaviour compared to the former developed higher alloyed AgPd-coatings with 8-10%Pd.
- the primary property contact resistance behaves similar to pure Ag in the initial condition and after temperature load as well as in a simulated mating test.
- the wear performance of AgPd could be drastically improved as the cold-welding effect is eliminated and the coefficient of friction decreased by a factor of ~ 5 compared to pure Ag.
- the low alloyed AgPd-coating is suitable for high temperature applications up to 200°C; diffusion of oxygen into the coating or recrystallization do not occur (**Figure 12a**). A minor reduction of the contact resistance at high temperatures without grain coarsening is related to the low Pd-content and as a result, the reduced mechanical stabilizing effect.
- the high microhardness of the AgPd-film requires a minimum contact normal force of 2N.

4.2 Sandwich coatings

The layer sequence of the pure metal's Ni/Ag/Sn with Ni as a barrier layer can be combined in two ways:

1. With Sn as an oxygen-catcher in between Ni and Ag forming the Ag_3Sn -intermetallic layer and eliminating the O_2 -diffusion along the grain boundaries of the Ag with all its associated negative effects (fig. 12b). One disadvantage of this diffusion hardened multi-layers; or more specific, the additional reflow processes is, that this can effect selective plated areas, for example other existing coatings such as Sn or Ni/Au (Co), in a negative way. New developments using a laser for local heat treatment can extend the advantages of this coating system to a wide range of products.
2. With the layer sequence Ni/Sn/Ag with Ag as the top surface, the necessity for passivation and the temperature induced recrystallization is always present. The max. application temperature is limited to 180°C when stable contact properties during lifetime usage are required.
3. When using the layer sequence Ni/Ag/Sn, the challenge is the exact ratio of Ag to Sn, so that after the reflow process the presence of single Sn-islands remain on top of a hard Ag_3Sn -layer to reduce the fretting behaviour and to ensure a stable and low contact resistance level under mechanical load. For high vibration loaded application the layer sequence Ni/Sn/Ag is therefore preferred.

From the literature it is well known that electrical current at high current densities can increase the growth rate of the intermetallic phases [12]. This means that at the interface migration effects occur, which will be influenced by temperature and current flow.

In high current applications like in E-vehicles or power engineering, this effect has to be taken into consideration and investigated for each situation. According to the conditions, the coating thicknesses of the combined films have to be defined to ensure a stable functionality.

The challenges for all coating systems are the deposition of the combined elements in the right stoichiometric ratio, as well as the small film tolerances in combination with the appropriate temper-/ reflow parameters for sandwich layers. The electrolyte composition, its additives, the possible selectivity settings and the bath agitation show all a comparable sensitivity. Low fluctuations can have a significant effect on the electrical and mechanical behaviour of the resultant film.

The use of connector contacts at elevated temperatures up to 200°C requires not only high-performance coatings, however also a base material, which fulfills the more severe demands for relaxation resistance as well as mechanical and electrical load. For this purpose, the Cu-semi finished industry is encouraged to deliver their contribution.

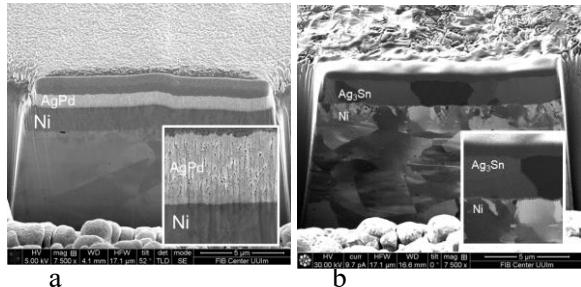


Fig.12: Microstructure of different coating systems after 1000h: a) Hard-AgPd at 200°C, b) Ni/Ag/Sn at 180°C.

5 Literature

- [1] W.Zhang, H. Schmidt: “Galvanische Silberbeschichtungen für Hochtemperaturanwendungen im Automobil”; DGO 7. Expertenworkshop, Berlin 2018.
- [2] I. Buresch: “Oberflächenbeschichtungen für Steckverbinderkontakte bei höheren Einsatztemperaturen“, 24. Fachtagung Albert Keil Kontaktseminar 2017, VDE Karlsruhe.
- [3] I. Buresch, H. Schmidt: Der Schlüssel zur richtigen Kombination: Die 3 Elemente Ag-Sn-Ni – Kontaktflächen für außergewöhnliche Anforderungsprofile; Tagungsband der GMM-Fachtagung 7. Symposium Connectors – Elektrische und optische Verbindungstechnik 2019, VDE/VDI-Gesellschaft.
- [4] T. Wielsch, F. Ernst, I. Buresch: Tribologische und oberflächenanalytische Untersuchung eines neuen hochleistungsfähigen Schichtsystems für Steckverbinder; Jahrbuch Oberflächentechnik 71, 2015, Leuze Verlag, S. 43.
- [5] O. Kurtz, J. Barthelmes, R. Rütter: Ultradünne Palladiumschichten zur Kosteneinsparung in der Elektronikindustrie; PLUS 4/2013, S.841.
- [6] MTDATA, National Physical Laboratory; <http://resource.npl.co.uk/mtdata/phdiagrams/agpd.htm>.
- [7] M. Myers; H. Schmidt: Connector level performance evaluation of a new high-speed reel to reel electroplated Silver Palladium alloy contact finish; 27th International Conference on Electrical Contacts, 2014 Dresden, VDE-Verlag.
- [8] F. Talgner; U. Manz; S. Berger u.a.: Novel Silver-International Conference on Electrical Contacts, 2014 Dresden, VDE-Verlag.
- [9] F. Talgner, M. Myers, H. Schmidt: Galvanisch Silber-Palladium als Kontaktoberfläche; PLUS 9/2017, S. 1611
- [10] Electrical Contacts WIKI; Doduco: https://www.electrical-contacts-wiki.com/index.php?title=Silver_Based_Materials; 24.02.2020.
- [11] S. Berger, R. Ziebart, F. Talgner: Silber-Palladium – Eine außergewöhnliche Legierung für elektrische Kontakte mit besonderen Anforderungen; Anwenderkongress Steckverbinder 2019, Elektronik Praxis Akademie, Vogel Communications Group.
- [12] C.-M. Chen; S.-W. Chen: “Electromigration effect upon the Sn/Ag and Sn/Ni interfacial reactions at various temperatures”; in Acta Materialica 50(9), May 2002, p. 2461-2469.

Thanks to Stefan Thoss, Majorie Myers, Waldemar Stabroth, Christopher Muth and Claus Borhauer with their teams, without their work and support this development and success would not be possible any more.

TE Connectivity Germany GmbH makes every effort to ensure the accuracy of the information in this article, TE does not warrant that it is error-free, accurate, correct, reliable or up-to-date. TE reserves the right to change the information in this article at any time without notice. TE expressly disclaims all warranties with regard to the information contained in this paper, including any implied warranties of merchantability or suitability for a particular purpose. Unauthorized reproduction or distribution of single contents or complete pages is not permitted and is punishable by law. Only the production of copies and downloads for personal, private and non-commercial use is permitted.

Tin Free Solutions Against Whisker Growth in Press-Fit Applications

Dr. Erika Crandall¹, Dr. Frank Ostendorf, Martin Bleicher, Dr. Helge Schmidt, Dr. Isabell Buresch, Bart Kerckhof
TE Connectivity Germany GmbH, 64625 Bensheim, Germany

¹erika.crandall@te.com

Abstract

Lead (Pb) restrictions for electrical components, starting within the Automotive sector, led to a global shift towards the elimination of Pb in many electronics in general. This movement prompted industry to use pure tin (Sn) deposits in place of SnPb alloys. As a result, the growth of stress-induced, high aspect ratio Sn whiskers occurred, creating a plethora of short circuits and system failures throughout all sectors across the board. Although there now exist multiple mitigation strategies against Sn whisker growth, press-fit pin connections still hold one of the largest whisker risks today because of the unavoidable, high compressive stress exerted on the pin's finish after insertion. Nonetheless, the use of solderless press-fit pins is only increasing due to the numerous benefits gained with this very easy to implement, high reliability connection. Therefore, newly developed Sn-free surface finish solutions are being administrated specifically for press-fit applications in order to alleviate the whisker risk. This paper will discuss the idea/technique behind the new Sn-free solutions already being implemented on the market, as well as their advantages and disadvantages in OSP and iSn printed circuit boards (PCB).

1 Introduction

Tin (Sn), as a surface plating, has been utilized since the early 1800s for food preservation on canisters [1] and since then has become one of the more favorable platings of choice for electronic finishes due to the combination of its contact resistance, corrosion resistance, low cost and solderability. However, nothing is ever really perfect. One of the disadvantages of a Sn finish is the likelihood to grow whiskers.

Whiskers are nano-dimensional, metal, crystalline eruptions that grow from finished surfaces usually as a stress relief mechanism. The driving forces responsible for initiating whisker growth can come from many various factors, including but not limited to intrinsic (e.g. grain size/crystal orientation [2]) and/or extrinsic sources (e.g. irregular intermetallic compound formation [3]) as well as external applied stresses [4] (e.g. post-forming). In general, all factors that increase stress (i.e. stress gradients) or promote diffusion within the deposit, then the greater the whiskering tendency. They can grow up to several millimeters, even a few centimeters long, meaning long enough to branch over to a neighboring electrically conductive contact, which then often leads to short circuit failures and system malfunctions.

The ability of Sn to produce whiskers has been known since the early 1950s [5] and already by the late 1950s a solution was found to prevent the growth of threatening, long, high aspect ratio Sn whiskers in the form of a Sn alloy, with the alloy additive being lead (Pb) [6]. Typically, just 3% or more Pb by weight in Sn-Pb deposits [7] has shown to be a very successful whisker mitigator, in fact, probably the best universal solution known to mankind so far.

However, due to mandated regulations restricting the use of Pb, starting in 2003 from the European parliament and council with end-of-life vehicle guidelines [8] followed by RoHS (Restriction of Hazardous Substances Directive) in 2006 [9] expanding the restriction to electronic equipment in general, SnPb was no longer always an option. The fastest response and most economical approach to go forward was to simply remove the Pb in Sn-Pb and use pure Sn finishes [10],[11], leaving many applications prone to Sn whisker growth without a mitigating solution. This in combination with growing miniaturization trends in order to save on room and weight, especially in vehicles, means the probability for whisker induced failures rises.

Currently, for example in the Automotive sector, Pb is generally limited to 0.1% by weight in materials, with an overall average threshold of 60 grams/vehicle [12]. There are some exceptions to this (e.g. batteries), however most of the exceptions then require extra dismantling at end-of life if the 60 grams is exceeded, which is highly unsought. In such high reliability, extreme environment applications as Automotive, where Sn whiskers have already caused system malfunctions [13], this creates considerable concern. Since no other universal "one size fits all" Sn whisker mitigator currently exists, each individual contact where Sn-Pb was once used, must now come up with their own way to reduce the whisker risk for their corresponding application.

For compliant press-fit connectors this is no trivial task, as the unavoidable external stress applied on the pin's coating after insertion has shown to induce whisker growth [14]. The strong localized stress points between pin and plated through hole (PTH) can be clearly seen when referring to the elegant finite element modeling carried-out by Tranitz and Tarnovetchi [15] given in **Figure 1a**. This external stress on the surface, created at room temperature (RT) conditions, is in any

case the dominating source responsible for whisker generation in press-fit connections. The functional compressive radial force on a pressed-in pin can vary from ~45N-300N depending on the pin material thickness and PTH size. It is sufficient enough to produce Sn whiskers within days, as well as whiskers up to millimeters long, as shown in (Figure 1b).

However, despite this characteristic, press-fit pins have been increasingly incorporated in place of solder connections since as early as the 1970's [16],[17] due to multiple advantages such as faster processing times, additional flexibility in application design, as well as increased manufacturing and connection reliability [18]. Furthermore, with press-fit technology the electrical and mechanical connection to the printed board (PB) is achieved through pin insertion alone, eliminating the need for a soldering process, meaning no more thermal stress due to reflow and no harsh fluxes, creating a more environmental friendly procedure. The high reliability of press-fit connections is due to the efficient cold welding process between pin/PTH as a result of the firm pressure bringing the two surfaces close enough together so that the free electrons from the surfaces, which were generated as a result of plastic deformation during press-in, combine into one common electron cloud, connecting them together with the same mechanism as in the basic metal. The cohesion force is initially lower, but increases within the first hours as the system settles-in.

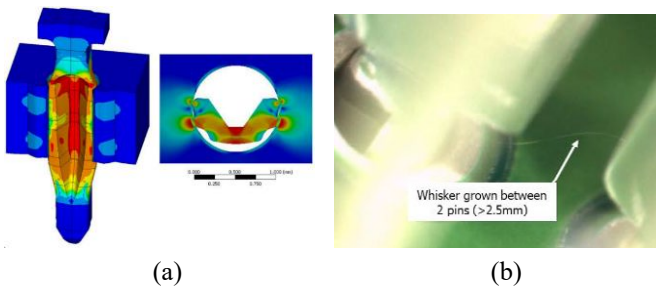


Figure 1: (a) Finite element model of the mechanical stress within a press-fit connection [15] and (b) a stereo microscope image of a Sn whisker spanning between adjacent pins.

Currently the usage of Pb in compliant press-fit pin finishes is one of the exceptions still being allowed in the automotive end-of-life regulations [8] due to the high whisker risk, but this exception may be withdrawn at any time, meaning new solutions are needed to ensure the future reliability of press-fit connections. Pure Sn is already frequently used in combination with a Ni barrier-layer [19], which has become a standard Sn whisker mitigation method for many applications. Due to pure Sn's high whiskering propensity, especially under press-fit conditions, long, threatening whiskers have still been observed to grow (Figure 1b). Therefore, many manufacturers are instead going 100% Sn free for press-fit applications. The idea here is very clear; if there is no Sn, then there cannot be Sn whiskers. However, Sn is not the only material known to whisker. In fact, there exists an entire webpage on NASA's whisker site dedicated just to "Other Metal Whiskers" [20], where literature on zinc, cadmium, silver, gold, etc. whiskers can be found, and

further materials are still being discovered as new surface finishes are being investigated for future applications. This is particularly true for press-fit applications due to the excessive stress conditions, and for that reason all materials need to be tested for whisker growth, independent of the surface finish's history to whisker or not.

The various Sn free solutions, which will be discussed here, are specifically tailored to relieve the risk of whisker induced failures for the high stress conditions of press-fit pin connections and are at this time not intended for other practices. Currently, the main Sn-free solution options include indium (In) and bismuth (Bi), in that order, and therefore they will be the focus throughout this paper with Sn as a comparative reference. Possible further future options, which are also being considered will be mentioned as well.

2 Experimental

All surface finishes were reel-to-reel, galvanic plated on a production line using signal Multispring (MS) pins with base material CuSn6. The In surfaces were plated externally, while Bi and Sn were deposited in-house. Properties of the compliant pin and various surface finishes tested here can be found in **Table 1** and **Table 2**. After visual inspection, the pins were inserted into their corresponding printed circuit boards (PCB) in preparation for the subsequent tests to follow. Immersion Sn (iSn) and organic solderability preservative (OSP) boards were tested in this study to ensure the compatibility of the Sn free platings for the more commonly used PCBs in Automotive. PCBs were 2x reflowed before pin insertion, which provides a few advantages: helps to prevent Sn whisker growth from the iSn PCBs, helps to ensure a reliable connection for the OSP PCBs, and this would be the normality in the practice. Details regarding the PCBs are listed in **Table 3**. The extreme minimum (min) and maximum (max) plated through hole (PTH) diameters were tested here for the state-of-the-art Sn free finishes to establish the reliability of the platings even in remote conditions. Sn was tested in nominal PTHs as a reference.

Table 1: Compliant Pin Properties

Pin Type	MULTISPRING
Base Material	CuSn6
Material Thickness (mm)	0.6
Max. Press-In Force (N)*	150
Min. Press-Out Force (N)*	30 (20 after environmental tests)

*Specified for iSn PCBs

Table 2: Surface Finish Properties

Platings	Bismuth (Bi)	Indium (In)	Tin (Sn)
Thickness (µm)	0.4 ± 0.2	0.7 ± 0.4	0.4-1.5
Ni barrier-layer (µm)	NA*	2 ± 1	0.8-1.3
Post-Treatment	NA	Heat Treated	NA

*Not required, however if used, then a Ni-Flash

Table 3: Printed Circuit Board Properties

Board Thickness (mm)	1.6 ± 0.14	
Finished PTH Diameter (mm)	min: 1.0 -0.01/+0.02	max: 1.09 -0.02/+0.01
PTH Cu Thickness (µm)	33-42	
Surface Finishes (µm)	iSn (1.00) and OSP (0.2)	

Figure 2 displays the basic test overview and pin count used per surface finish/PCB/PTH size combination, for each individual test branch. Press-in/out forces were recorded, microsections of the pressed-in pins were inspected for PCB deformation, and various environmental aging tests were carried-out. The contact resistance was initially measured after 24-48h of pressing-in using the four-point millivolt method (**Figure 3**) and then after each aging test. Details regarding the various aging tests are illustrated in **Table 4**. Note here that the test groups build on each other – for example, test group E has undergone thermal shock (TS), damp heat and 4-gas test. After each environmental test group was complete, 50 pin/PTHs were investigated for whisker growth.

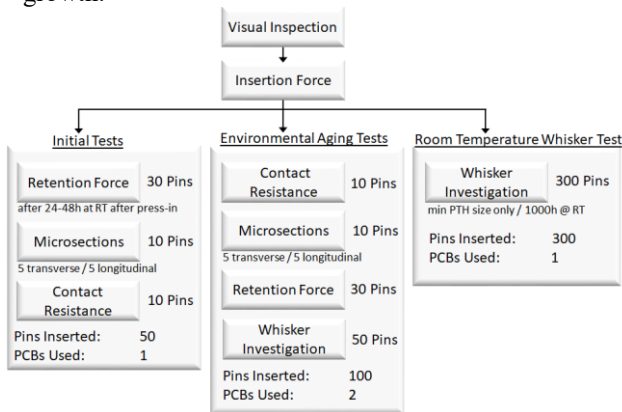


Figure 2: Test overview.

The RT whisker investigations were carried-out using 300 pins inserted in min PTH size on PCBs which were only 1x reflowed to test the resilience of the Sn free platings in the uttermost of conditions. The specimens were incubated at $25 \pm 10^\circ\text{C} / 50 \pm 25\%$ relative humidity (RH) conditions for 6 weeks and then examined using light microscopy. Since Sn whisker growth for press-fit connections is known to be most critical under RT conditions, the Sn plated samples were only tested at RT in combination with iSn PCBs as a worst-case scenario reference. However, the newer Sn free, Bi and In, finishes went through all environmental tests, since their whiskering characteristics are not as well known.

Visual inspections, microsections, pressing-in/out and contact resistance measurements were carried out in accordance to the IEC 60352-5 standard [21]. However, the aging tests were designated to account for the extreme environmental conditions inherent in automotive applications. All whisker imaging and length measurements were performed according to JEDEC Standard No. 22-A121A, by an external association with specially trained whisker investigators.

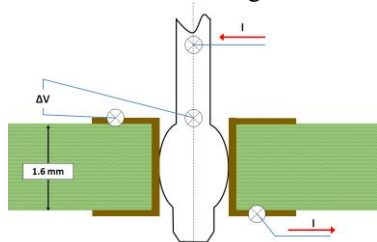


Figure 3: Standard [21] 4-point millivolt method used for contact resistance measurements.

Table 4: Environmental Aging Tests

Test Group (TG)	Aging Conditions	
B	Thermal Shock (TS)	$-40^\circ\text{C} / +125^\circ\text{C}$ (30min / 30min), 300 cycles
C	Vibration + Temperature after TS	Acc. ISO 16750-3, Ch. 4.1.2.1.2, sinusoidal and random in Z-axis, 22h
D	Damp Heat after TS	$+85^\circ\text{C} / 85\%\text{RH} - 504\text{h}$ $-10^\circ\text{C} / +65^\circ\text{C} / 93\%\text{RH} - 240\text{h}$ $+85^\circ\text{C} / 85\%\text{RH} - 504\text{h}$
E	4-Gas after Damp Heat	IEC 60068-2-60, method 4 $+25^\circ\text{C} / 75\% \text{RH} - 21$ days

3 Surface Finish Properties

Neither In nor Bi are known to possess high whiskering propensities in the practice, as Sn, zinc (Zn) [22] or cadmium [23] for example do. There are some publications in the literature regarding In and Bi whiskers, with In whiskers being more commonly recognized as Bi [20]. However, most of the “whiskering” literature for both In and Bi are not referring to common, natural growing whiskers from normal deposited finishes, but instead to “whiskers” which were purposely simulated to grow in lab under irregular conditions, for research purposes [24]. In fact, when it comes to literature on In or Bi in relation to whiskers, it is often dealing with the use of In or Bi as additives in Sn for whisker mitigation effects [25],[26]. But can they be used on their own as whisker mitigating solutions, especially in the highly compressive stress conditions created in press-fit connections? And what about the other properties needed for a reliable connection? A compliant pin’s finish needs to account for more than just whisker mitigation. Can In or Bi fulfill these as well?

The surface finish for a press-fit pin serves a few very important purposes necessary for the reliability of the electrical connection. It acts as a lubricant during press-in to help reduce insertion forces and minimize PCB/PTH damage as well as protects the copper-base substrate material from oxidation/corrosion. Of course, the material used also needs to be a non-toxic, environmentally friendly material or it will just end up on the same list as Pb, and it should ideally be a cost-effective material. Since, similar to Sn, there is currently no expected restrictive use for either In or Bi, as they are not known to possess any toxic characteristics as a surface finish for compliant pins, and since they are also both recyclable materials with the current state-of-the-art technology, there is no real environmental concerns regarding these aspects.

For an indication and comparison of their lubrication properties, nanoindentation measurements were carried-out on In, Bi and Sn films deposited on MS pins. The resultant hardness of In, Bi and Sn in the initially deposited state and after various aging environments is given in **Figure 4**. In initial condition, In appears to be the hardest of the finishes. This is most likely due to the detection of the harder InNi intermetallic compound (IMC) between the free In surface and Ni barrier-layer created during the post heat-treatment process required for In finishes, as seen in the scanning electron microscopy (SEM) images of the focus ion beam (FIB) cuts of In in

Figure 5b. Note: the remaining film seen here is the IMC. The pure In film has been sputtered away by the ion beam, leaving a noticeable gap between IMC and the protective platinum layer used for the FIB process. Bi and Sn do not have any IMC formation in initial condition (Figure 5c and d respectively).

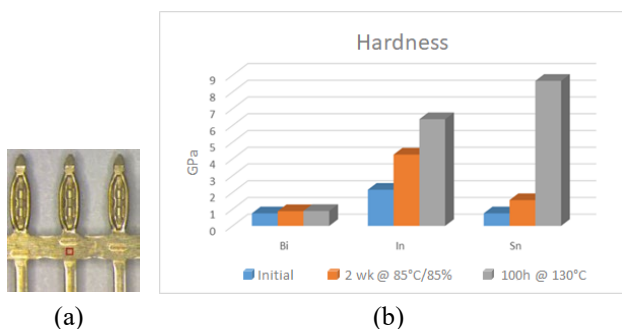


Figure 4: (a) position of nanoindentation measurements with (b) the hardness results of the deposited films on signal MS pins under various conditions.

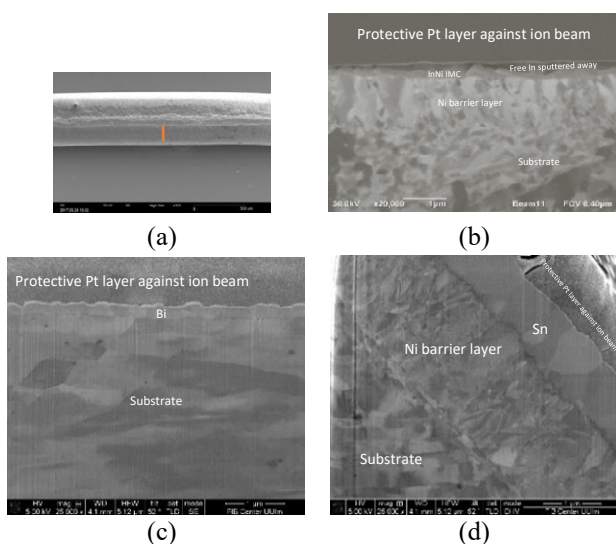


Figure 5: SEM images of (a) position of FIB cuts carried-out on (b) In plated (c) Bi plated and (d) Sn plated MS pins.

After the environmental exposures it is clear in Figure 4b that Bi’s hardness remains fairly constant while In’s and Sn’s increase, with Sn increasing the greatest after dry heat (100h @ 130°C) as a result of SnNi IMC formation, which although forms as an irregular NiSn₃ compound at RT conditions over time, is accelerated with higher temperature exposure into a more stable Ni₃Sn₄ phase [27]. Bi does not create an IMC with Cu [28], and can therefore, be used as its own surface finish and barrier layer in one, meaning it does not require a Ni layer.

Table 5 shows some further basic material properties, which are usually considered for electrical contacts.

Table 5: Material Properties [29]

	T_{melt} (°C)	ρ (ohm·m)	k (W/(m·K))
Sn	231.9	$11 \cdot 10^{-8}$	60.6
Bi	271.4	$2.2 \cdot 10^{-6}$ [1]	8
In	156.6	$8 \cdot 10^{-8}$	82
Zn	419.5	$5.48 \cdot 10^{-8}$	116

Using these properties, the predicted melting currents for In and Bi whiskers are given in **Figure 6** in comparison to Sn and Zn, at a whisker diameter of 1 μ m [30]. Larger enough potentials across a whisker can melt a whisker away, and therefore only create an intermittent electrical loss. As a result, whiskers tend to be of less concern in power and digital applications as to signal or analog applications, where whisker induced failures can be more permanent. Due to Bi’s higher resistivity, a Bi whisker may melt away faster than an In or Sn in similar situations, as a result of resistance heating, which could serve as an advantage in certain applications.

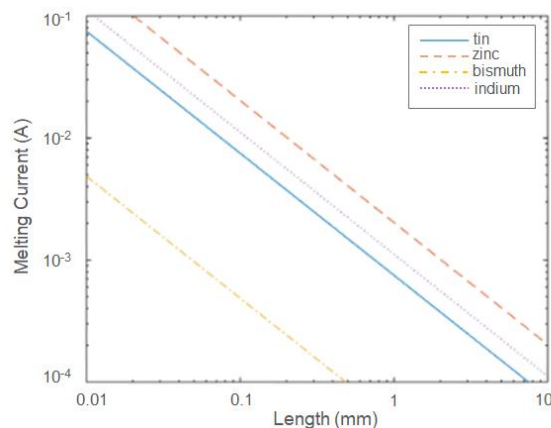


Figure 6: Prediction of melting currents for whiskers at various lengths composed of different materials, without convection or temperature dependence [30].

However, do these Sn free solutions, which are not known to regularly produce whiskers, even grow whiskers under press-fit conditions and what advantages/disadvantages do they bring to the application in reality compared to Sn? Having compared and discussed various properties of In and Bi with Sn, which correspond to the press-fit essentials, it’s time to delve into the experimental results.

4 Results

4.1 iSn PCBs - Initial & RT Tests

Insertion forces were recorded as In, Bi and Sn plated MS pins were pressed into 2x reflowed iSn PCBs (min and max PTHs for In and Bi, and nominal for Sn pins as a reference). After 24-48h at RT incubation, which is required for the cold welding process between pin and PTH, 30 pins from each PTH/pin finish combination were pressed-out for initial retention force measurements. The recorded insertion and retention forces are shown in **Figure 7**. In is always represented in blue, Bi in orange and Sn in green. All values, regardless of pin finish/PTH combination, resided well within the maximum recommended press-in force (150N) and minimum press-out force (30N). For CuSn6 signal MS pins in iSn PCBs, Bi had the highest insertion forces and In had the lowest, with Sn situated in the middle. The results for the retention forces of In and Bi are inverted from the insertion, with In having the highest retention

force gain of all finishes, while Sn and Bi lie within the same range. After the 24-48h RT incubation period, all max PTHs obtained higher retention values in comparison to the min. This is most likely a result from over-compression of the interior springs within the Multispring press-fit zone, due to being pressed into a PTH smaller than the specified limit, leading to a slight reduction in spring force. In any case, with all average retention forces laying between 80-140N, sound above the min 30N, it is clear that the cold welding process between the Sn free platings and the iSn PCBs was very successful.

In accordance with the IEC 60352-5 standard, both transverse and longitudinal cross-sections were investigated for avg. PTH deformation ($<70\mu\text{m}$), residual Cu thickness (min $8\mu\text{m}$) and jet effect ($<50\mu\text{m}$). Even with the extreme PTH diameters tested here for the Sn free finishes, all PCB deformation due to pressing-in remained within the suggested values given in the standard, with no functional damage inflicted on the iSn PCBs.

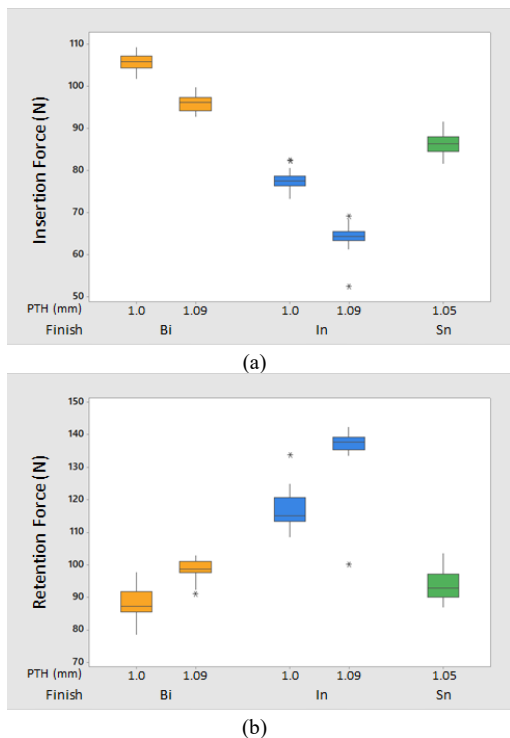


Figure 7: Initial (a) insertion and (b) retention forces after 24-48h @RT in iSn PCB.

An additional 300 pins from each surface finish were aged at RT conditions in 1x reflowed iSn PCBs with min PTHs, except for Sn which used nominal PTHs as the reference. Every pin was evaluated for whisker development after 6wk of incubation by an external company, with the results given in **Figure 8**.

After the first 6 weeks of incubation no whiskers were found on any of the PCBs. After 1000h of RT aging only 1 non-Sn whisker object of $100\mu\text{m}$ was found out of 600 pins, which was from a Bi pin. Out of the 300 In pins, only a total of 2 whisker objects were detected and both less than $100\mu\text{m}$ long. In comparison Sn grew multiple whiskers up to over $300\mu\text{m}$ long within the same time period.

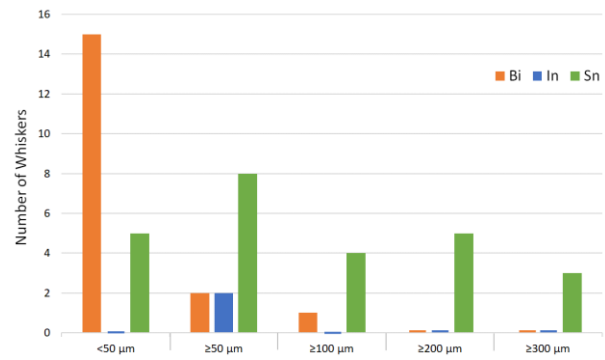


Figure 8: Whisker results after 6 weeks of RT incubation in iSn PCBs.

Since whiskers approximately $100\mu\text{m}$ and shorter are difficult to correctly identify under a light microscope, it is not 100% certain if these In and Bi whisker objects are really whiskers or just particles (e.g. slivers from pressing-in). However, these Sn free deposits already offer a promising outlook for whisker mitigation in press-fit applications.

As depicted in Figure 2, 10 pins of each variation were also measured for contact resistance. All avg. contact resistances for each pin finish/PTH combination lied under $130\mu\Omega$ with Sn having the highest resistances.

4.2 OSP PCBs – Initial, RT & Aging Tests

Initial insertion and retention forces after 24-48h at RT in min and max OSP PTHs were recorded and contact resistance measurements carried-out on the In and Bi plated pins. Separate pressed-in pins were subsequently aged under the various environmental conditions described in the test groups listed in Table 4. After the various aging sequences, retention forces and contact resistances were taken again. The results of the insertion, retention and resistance measurements before and after aging can be found in **Figure 9**. All insertion values for both finishes lie comfortably below the specified 150N and practical enough, the max PTHs obtained lower insertion forces. For MS pins in OSP PCBs In, however, has the higher insertion forces. In fact, the insertion values did almost a direct exchange between In and Bi from iSn to OSP, which is a good reminder that every press-in zone type, pin finish, and PCB technology need to be individual tested with each other.

The retention forces continue with the trend of the insertion forces for OSP, with In possessing distinct higher retention forces compared to Bi in initial condition and after aging. However, both retention forces dropped compared to iSn by $\sim 8\%$ and $\sim 60\%$ for In and Bi, respectively. This is not entirely surprising as OSP PCBs are specifically designed for soldered connections, as stated in the name (organic solderability preserve) and not for press-fit. Whatever amount of organic film still remains after reflow (2x) must be scrapped away during the press-in process so that the metal to metal connection between pin/PTH is achieved. The residual OSP coating can hinder the retention forces if some of the organic preserve still remains in various locations between pin/through hole.

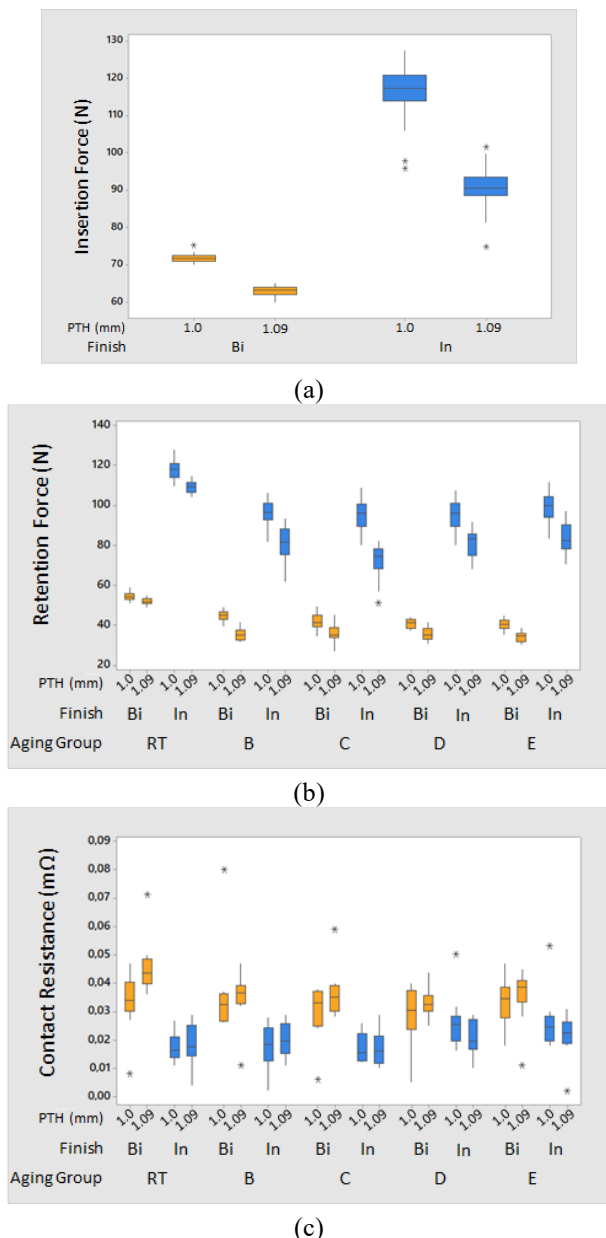


Figure 9: (a) Initial insertion forces as well as (b) retention forces and (c) contact resistances for In and Bi in OSP PCBs before and after environmental aging.

From Figure 7b and Figure 9b, it is clear that the surface finish alone can aid in higher retention forces depending on the material's inclination to react with a given PTH. Regardless of iSn or OSP PCB, In's retention force was always higher than Bi's, even when its insertion force was started off lower (iSn). This can be contributed to the affinity In has to react with the PTH materials, Sn and Cu, whereas Bi does not [28]. In creates IMCs with Sn and Cu already at RT conditions, whereas Bi and Sn have a eutectic phase, but no IMCs (similar to Sn and Pb), and as previously discussed, there are also no IMCs formed between Bi and Cu. The interaction of In vs Bi in iSn PCB at RT conditions, for an example, is depicted in **Figure 10**. Although Bi cold welds and acclimates itself with the iSn PTH, diffusing into Sn's grain boundaries, In forms an IMC with Sn, creating a stronger metallic bond between pin/PTH.

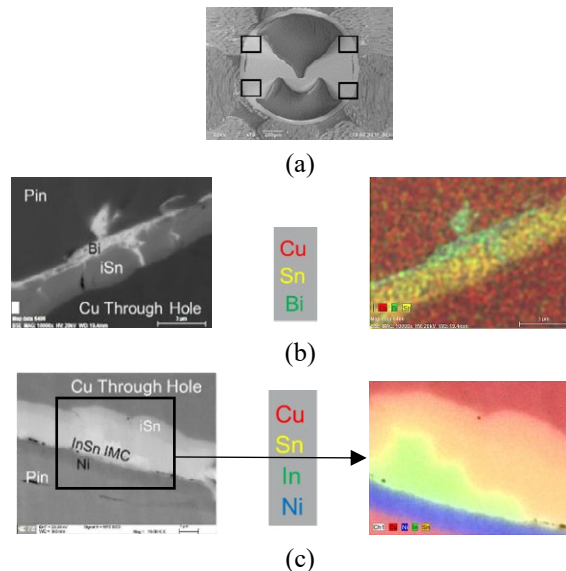
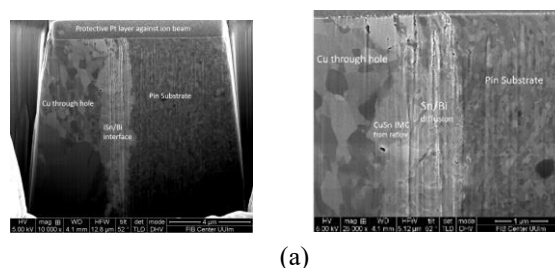


Figure 10: (a) Contact areas investigated in transverse cross-section with SEM and energy dispersive X-ray spectroscopy (EDX) (b) on Bi and (c) In plated pins pressed-in iSn PCB.

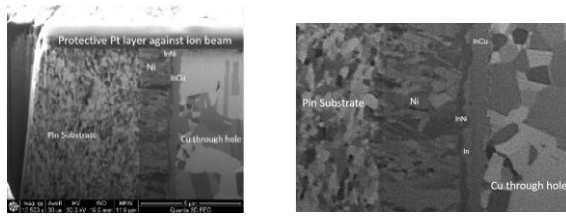
After thermal shock (TS) retention force values for both In and Bi drop slightly, most likely due to induced stresses as a result of coefficient of thermal expansion mismatch. The retention forces remain stable for the rest of the environmental exposures, even after vibration, suggesting that the Sn free finishes established successful, stable cold welding connections with the OSP PCBs. All the retention values in OSP passed the defined 30N and 20N after aging, which were specified for iSn PCBs. Exemplary pin/PTH interfaces after aging are given in **Figure 11**.

Another indicator for a successful pin/through hole connection and perhaps one of the most important qualities for a good electrical contact is a stable, reliable contact resistance. As seen in Figure 9c, after TS, vibration, damp heat and gas tests, no noticeable increase in contact resistance is found from In or Bi, with In consistently holding lower resistances compared to Bi. A slight increase is seen only in the In pins after damp heat of $<10\mu\Omega$ on average, which is an order of magnitude less than the accepted $500\mu\Omega$ given in the standard, demonstrating the high reliability achieved from the Sn free platings.

Transverse and longitudinal cross-sections were investigated for OSP PCBs as well in initial condition, and after each environmental test group for PTH deformation ($<70\mu\text{m}$), residual Cu thickness (min $8\mu\text{m}$) and any jet effect ($<50\mu\text{m}$). Similar to the results in the iSn PCBs, no deformation exceeded the allowed limits of the standard, even with the extreme PTH diameters and various aging tests, which all included thermal shock.



(a)

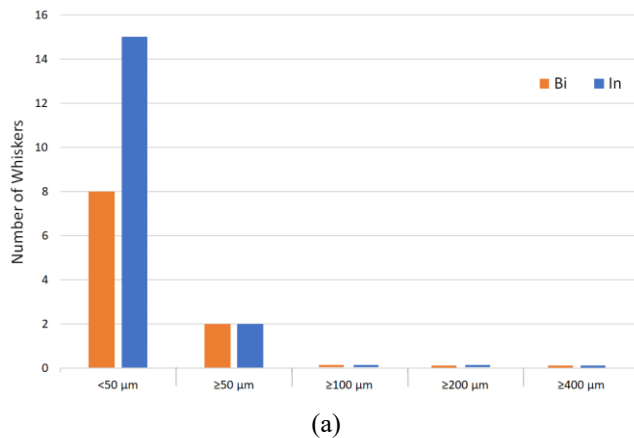


(b)

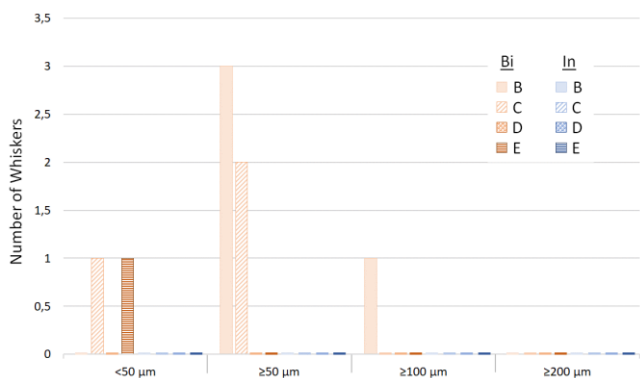
Figure 11: SEM images of FIB cuts through the pin/PTH interface (contact areas as shown in Figure 10a) after TS aging and then transverse cross-sectioning (a) of a Bi pin in iSn PCB and (b) a In pin in OSP PCB.

Last but definitely not least, whisker growth for In and Bi was investigated in OSP PCBs with min and max hole diameters at normal RT conditions as well as 50 pins of each after every environmental test group aging. The results for the min through hole PCBs are given in **Figure 12**. No whiskers over $100\mu\text{m}$ were observed at RT conditions, and after environmental aging only one Bi whisker object $>100\mu\text{m}$ was detected after TS. No In whiskers were found after any of the aging test groups.

Whiskers found in the max PTH size were even less. In fact, only one possible Bi whisker object $<100\mu\text{m}$ was detected in max PTH after TS. All other tests groups had no whiskers for In or Bi. It is evident that Sn free solutions for whisker mitigation in press-fit connectors have a very promising future.



(a)



(b)

Figure 12: Whisker results (a) after 6 weeks of RT incubation and (b) after tests groups B-E for In and Bi plated pins in min OSP PCBs.

5 Discussion & Conclusion

An In finish, as a press-fit solution, has already been on the market for a couple years without any known failures or recalls, and Bi may be coming out into the field in 2020. Although these two solutions are currently the most advanced in development, they are not the only Sn free solutions being considered for press-fit.

For example, Ni as a surface finish is also being considered [31]. The great advantage here is that even though Ni is used worldwide in various system, it is never been known to grow whiskers. The main disadvantage is that Ni is a much harder material, which often results in higher, more unstable insertion forces. Therefore, the intention here is to modify the surface Ni film by changing the grain size/structure of the film as well as perhaps incorporating co-deposited additives into the film (for a lubricating effect) by manipulating the galvanic Ni-electrolyte, so that the resultant surface is softer and compatible with press-fit connectors. The plan for this Sn free solution is to contain multiple different (2-3) Ni layers from varied electrolytes, with the possibility of an intermediate layer (e.g. to reduce the surface roughness) if deemed necessary.

Another Sn free solution possibility stems from the same idea as OSP PCBs. Instead of using a galvanic deposit as the pin's press-in lubricant and substrate oxidation preventer, just apply on a preservative. The greatest advantage here would be that there is then no coating to grow whiskers from. The disadvantage is the risk of preserve between pin/PTH, which could hinder the retention forces and lead to an increase in contact resistance. Another disadvantage would be monitoring and measuring the preserve's film thickness.

In any case, it is clear that Sn free finishes hold a strong presence for the way of the future in press-fit applications. As the In and Bi platings are designed for press-fit pin connections, the press-in force, press-out force, PCB deformation and contact resistance was thoroughly monitored and recorded throughout the experiment in accordance to the IEC 60352-5 international standard. The platings underwent multiple incubation tests ranging from RT conditions to a series of extreme environmental exposures including thermal shock, vibration, a damp heat climate sequence, and mixed flow gas. Both In and Bi lie well within the accepted standard values for all tests at every aging environment in iSn and OSP PCBs, demonstrating the high reliability of the finishes even throughout lifetime simulation exposures.

At the critical, RT conditions for whisker initiation in press-fit applications, 1200 Sn free pins (300 In and Bi each in iSn and 300 each in OSP) were investigated in min hole size (max induced stress) after 6wk of incubation, where only 1 Bi whisker object $\sim 100\mu\text{m}$ was found in iSn PCB. In comparison to Sn with a mitigation Ni underlayer and in nominal hole size, which grew multiple whiskers up to over $300\mu\text{m}$ long within the same time period. Taking into account the whisker occurrences ($\geq 100\mu\text{m}$), maximum length and possible impact of a bridging whisker due to its resistance, the whisker risk can be estimated between the Sn free solutions vs Sn using the results from iSn PCBs, as given in **Table 6**.

Though In and Bi are not a 100% whisker free technologies, they offer a new level of whisker risk reduction, which can reduce the possibility of whisker induced failures by orders of magnitude in comparison to Sn.

Table 6: Whisker Risk Estimation: Sn free vs Sn in iSn

Risk = $O \cdot L_M \cdot I$		Reference: Sn w/ Ni underlayer		
		Sn w/ Ni	Bi	In
O	Occurrence (>100µm)	4%	< 0.1%	< 0.1%
L_M	Max Length (µm)	376	93	70
I	Impact	100%	10%	139%
	Risk	1 = 100%	< 0.06%	< 0.6%

Values vary depending on pin, plating & PCB technology combination.

There are, of course, advantages and challenges to both solutions. For In, the free In on the surface can oxidize when directly exposed to condensation, which could lead to discoloration and/or blistering. This concern is easily remedied by applying sufficient packaging materials after final line inspection so to ensure the high functionality of the finish upon arrival at product's destination, which may incorporate extra costs. The price of In, in general, is notably higher than the price of Bi or Sn and the production process requires more energy and costs due to the necessary post heat-treatment. However, due to In's keen interaction with the PCB materials, In obtains very strong retention forces in initial condition and throughout aging, even higher than Sn.

The retention forces are lower for Bi in comparison to In since Bi does not create IMCs with Sn or Cu. However, this means that Bi also does not require a Ni underlayer, which reduces material and cost. Bi is also a more reasonably priced material, which helps reduce cost even further and Bi has low insertion forces, which reduces impact on PCBs.

Both In and Bi are environmentally friendly finishes, which is essential for their long-term acceptance and application within the electronics sector. They have shown to be very resilient against whisker growth under the high stressed conditions of press-fit pin applications, especially compared to Sn, in both iSn and OSP PCBs.

In this study all investigations were carried-out on CuSn6 signal MS pins only. Whenever incorporating a new surface finish, it is important that each press-fit zone variation is thoroughly tested with the new surface finish and PCB technology combination. Depending on the end application, the best corresponding Sn free solution can only then be chosen to significantly reduce its whisker risk.

REFERENCES

- Childs, Peter (July 1995). "The tin-man's tale". *Education in Chemistry*. Vol. 32 no. 4. Royal Society of Chemistry. p. 92. Retrieved 19 June 2018.
- J. H. Zhao, P. Su, M. Ding, S. Chopin, P. S. Ho, "Microstructure-based stress modeling of tin whisker growth", *IEEE Trans. Electron. Packag. Manuf.* 29, pp.265-273 (2006).
- Y. Zhang, C. Fan, C. Xu, O. Khaselev, and J. A. Abys, "Tin Whisker Growth – Substrate Effect Understanding CTE Mismatch and IMC Formation", *CircuitTree* 7, 70-82 (2004).
- H. Moriuchi, Y. Tadokoro, M. Sato, T. Furusawa, N. Suzuki, "Microstructure of External Stress Whiskers and Mechanical Indentation Test Method", *J. Electron. Mater.* 36, 220-225 (2007).
- K. G. Compton, A. Mendizza, S. M. Arnold, "Filamentary growths on metal surfaces – Whiskers." *Corrosion* 7 (10), 327-334 (1951).
- S. M. Arnold, "The growth of metal whiskers on electrical components", in *Proceedings of the IEEE Electronic Components Technology Conference*, 75-82 (1959).

- J.-L. Jo et al., "Least lead addition to mitigate tin whisker for ambient storage," *J. Mater. Sci.-Mater. El.*, vol. 24, no. 8, pp. 3108–3115, August 2013.
- Parliament and Council Directive 2000/53/EC, "on end-of life vehicles", *OJ L* 269, pp. 34, 21st October 2000.
- Council and Parliament Art. 95 EC, "Directive on the restriction of the use of certain hazardous substances in electrical and electronic equipment", *OJ L* 37, pp. 19-23, 13th February 2003.
- M. Warwick, "Implementing lead free soldering – European Consortium Research", *SMTA. J. Surf. Mount Tech.* vol. 12, no. 4, pp.1-12, October 1999.
- C. Xu, Y. Zhang, C. Fan, and J. Abys, "Understanding whisker phenomenon: the driving force for whisker formation". *Circuit Tree*, pp. 94-104, 2002.
- Commission Directive (EU) 2017/2096 of 15 November 2017 amending Annex II to Directive 2000/53/EC of the European Parliament and of the Council on end-of life vehicles, *Official Journal of the European Union*, L 299/24-30 (2017).
- H. Leidecker, L. Panashchenko and J. Brusse, „Electrical Failure of an Accelerator Pedal Position Sensor Caused by a Tin Whisker and Discussion of Investigation Techniques Used for Whisker Detection“, 5th International Tin Whisker Symposium, Sep. 14th, 2011.
- H.-P. Tranitz and S. Dunker, "Growth mechanisms of tin whiskers at press-in technology", *Continental Article*: 20130215, February 2013.
- H.-P. Tranitz and M. Tarnovetchi, Continental AG, "Whisker growth at press-fit connections", *Proceedings of the Albert Keil Kontakt Seminar*, Karlsruhe, Germany (2017).
- J. Mattsson, T. Callies, and B. Kerckhof, "Press-fit technology", TE Connectivity, White Paper 072014: <http://www.te.com/content/dam/te-com/documents/automotive/global/whitepaper-pressfit-072014.pdf>
- "Press-fit technology", ept Guglhör Peiting GmbH & Co. KG, 1999: <https://www.shoppui.com/import/datasheets/1479.pdf>
- IEC-1709, "Electronic components – reliability – reference conditions for failure rates & stress mode", June 2011.
- R. Schetty, "Minimization of Tin whisker formation for lead-free electronics finishing", *Circuit World* 27, 17-20 (2001).
- NASA Website: https://necpp.nasa.gov/whisker/other_whisker/index.htm
- IEC 60352-5, "Solderless connections – Part 5: Press-in connections – General requirements, test methods and practical guidance", International Electrotechnical Commission, Feb. 2012.
- J. Brusse and M. Sampson, "Zinc Whiskers: Hidden Cause of Equipment Failure", *IEEE Computer Society* (2004) 43-47.
- H. L. Cobb, "Cadmium whiskers", *Monthly Rev. Am. Electroplaters Soc.*, vol. 33, no. 28, pp. 28-30, January 1946.
- G. Sines, "Filamentary Crystals grown from the Solid Metal", *J. Phys. Soc. Jpn.* 15, pp. 1199-1210 (1960).
- L. Meinshausen, S. Bhassivasantha, B. S. Majumdar, and I. Dutta, "Influence of Indium Addition on Whisker Mitigation in Electroplated Tin Coatings on Copper Substrates," *Journal of Electronic Materials*, vol. 45 no. 1, pp. 791-801 (2016).
- K. Whitlaw and J. Crosby, "An Empirical Study into Whisker-Growth of Tin & Tin Alloy Electrodeposits", *AESF SUR/FIN® Proceedings*, pp. 136-147 (2002).
- J. Haimovich, *Intermetallic Compound Growth in Tin and Tin-Lead Platings over Nickel and Its Effects on Solderability*, 12th Annual Electronics Manufacturing Seminar, China Lake, California (1988) pp. 102-111.
- C. W. Bale, E. Bélisle, P. Chartrand, S. A. Decterov, G. Eriksson, A.E. Gheribi, K. Hack, I. H. Jung, Y. B. Kang, J. Melançon, A. D. Pelton, S. Petersen, C. Robelin, J. Sangster and M-A. Van Ende, *FactSage Thermochemical Software and Databases - 2010 - 2016*, Calphad, vol. 54, pp 35-53, 2016 <www.factsage.com>
- P. Desai, T. Chu, H. M. James, and C. Ho, "Electrical Resistivity of Selected Elements," *Journal of Physical and Chemical Reference Data*, Vol. 13, pp. 1069-1096 (1984).
- R. L. Jackson and E. R. Crandall, "The Effect of Convection on Electro-thermal Modeling of Whisker Shorting", *IEEE Holm Conference on Electrical Contacts*, pp. 262-269 (2019).
- U. Zeigmeister, Patent EP3375910 A2, Diehl Metal Applications GmbH, March 2018.

TE Connectivity, TE are trademarks licensed by the TE Connectivity Ltd. family of companies. © 2020 TE Connectivity. All Rights Reserved.

Microstructural evolution of Ag/MeO contact materials and influence on mechanical properties

Yinglu Tang, ABB Switzerland Ltd., Baden-Daetwil, Switzerland, yinglu.tang@ch.abb.com
Tim Voegtlin, ETH Zurich, Zurich, Switzerland, tim.voegtlin@gmail.com
Sam Bodry, ETH Zurich, Zurich, Switzerland, bodrys@student.ethz.ch
Moritz Boehm, ABB Switzerland Ltd., Zurich, Switzerland, moritz.boehm@ch.abb.com

Abstract

Poor adhesion between SnO₂ and Ag in Ag/SnO₂-based electrical contacts leads to crack formation, material loss and decreased lifetime. Addition of other metal oxides such as CuO and Bi₂O₃ besides SnO₂, improve the interface between the Ag matrix and SnO₂ particles. Here we study the microstructural evolution of Ag/CuO contact materials during sintering in comparison to that of Ag/SnO₂. The grain growth was investigated by interruption experiments followed by SEM and XRD analysis. Enhanced mechanical properties were observed in Ag/CuO systems which could possibly be attributed to the improved interface adhesion. This enhanced mechanical property could be beneficial for prolonged electrical lifetime.

1 Introduction

Ag/SnO₂ electrical contacts are widely used for electrical switchgear such as light switches, circuit-breakers and contactors [1-3]. However, due to the thermo-mechanical stresses induced during arcing, cracks form and propagate along the Ag/SnO₂ interface. This is facilitated by the low mechanical strength of the interface between SnO₂ and Ag [4]. This in turn can lead to unpredictable material loss and consequently a large scatter of the expected switchgear performance and lifetime. In order to improve the interfacial adhesion between Ag and SnO₂, small amounts of additive oxide powders (<1 wt%) are often mixed together with Ag and SnO₂, e.g. CuO. [5]. Here we investigate the reason of CuO as a good additive by studying the microstructure evolution of Ag/CuO system as a function of annealing time and temperature, in comparison to that of the Ag/SnO₂/Bi₂O₃ system as a reference.

2 Experimental details

Ag/CuO and Ag/SnO₂/Bi₂O₃ powders were prepared using powder metallurgy method. The particle size of initial metallic oxide (MeO) powder was measured by a Mastersizer 3000 from Horiba before mixing with Ag powder. The Mastersizer 3000 uses the technique of laser diffraction to measure the size of MeO particles by measuring the intensity of light scattered as a laser beam passes through a particulate sample dispersed either in water or ethanol. This data is then analyzed to calculate the size of the particles that created the scattering pattern. The powder size is listed in **Table 1**. The as-mixed Ag/MeO compositions are listed in **Table 2**.

	CuO	SnO ₂	Bi ₂ O ₃
Dv50 [um]	3.4	2.0	3.0

Tab. 1 Initial MeO powder size measured by Mastersizer 3000 laser particle size analyzer before mixing with Ag powder. Dv50 is the median for a volume distribution.

	Ag (wt %)	CuO (wt %)	SnO ₂ (wt %)	Bi ₂ O ₃ (wt %)
Ag/CuO	86	14	×	×
Ag/SnO ₂ /Bi ₂ O ₃	86	×	12	2

Tab. 2 Nominal compositions of Ag/MeO in comparison.

The powders were mixed with ZrO₂ balls (ball:mass ratio = 5:1) in a 3D mixer from Turbular for 48 h. The mixed powders were then pressed into green body, which is in the form of weakly bonded powder before it is sintered, using a die-pressure of 100 MPa. The green body was heated in air up to 600 °C in 4 h 48 min and then held at 600 °C for 30 min to eliminate the organic additives. Subsequently, the sample was heated at a heating rate of 15 °C/min to the target temperatures (800 °C, 850 °C, 900 °C) and held for a varying period (ranging between 0 min, 30 min, 2 h, 4 h). Afterwards the samples were quenched in air. A graphical illustration of the sintering profile is shown in **Figure 1**.

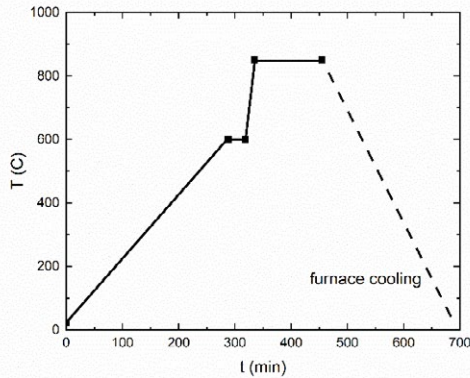


Fig. 1 Sintering profile of Ag/MeO electrical contacts (850 °C, 2 h). Dashed line means cooling time is not specified.

The obtained samples were then embedded in conductive resin and polished for Scanning Electron Microscopy (SEM) analysis. A magnification of 2000 x was chosen for all SEM images. Energy Dispersive Spectroscopy was used to analyse the elemental distribution with a working distance of 18.5mm and an emission voltage of 20kV. A mapping time of at least 20 minutes was applied for each sample. ImageJ software was used for particle size measurement analysis [6]. Color pictures obtained from EDS mapping were imported into ImageJ. The thresholding method was chosen to be “MaxEntropy”, with threshold color “B&W”, color space “YUV” and dark background. Afterwards the picture was converted to binary and processed by a watershed filter. Then a particle analysis with size range from 2 pixels up to infinity was performed. The average grain diameter is derived from the perimeter from the particle analysis.

Bar-shaped samples were prepared from green bodies (30mm*4mm*3.7mm, die-pressure of 100MPa) sintering at 850 °C, 2 h, as described in Figure 1. After sintering these samples were repressed at 750MPa for 10s for 3 to 6 times and then re-sintered at 450 °C for 2 h in order to achieve a relative density of at least 92 %. Fracture toughness of these bar-shaped samples was measured on a charpy test instrument.

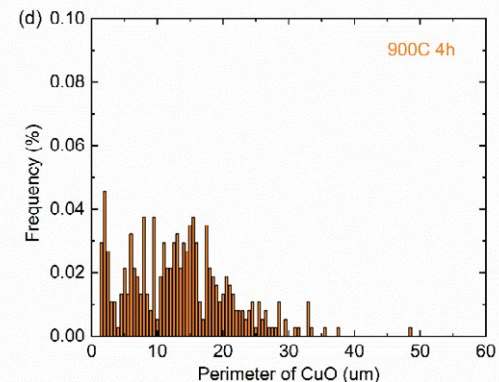
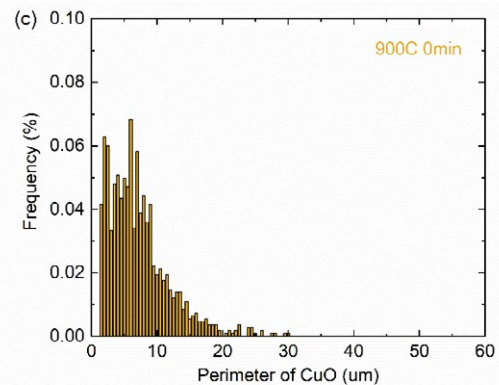
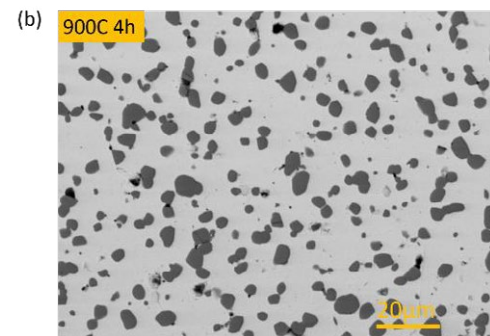
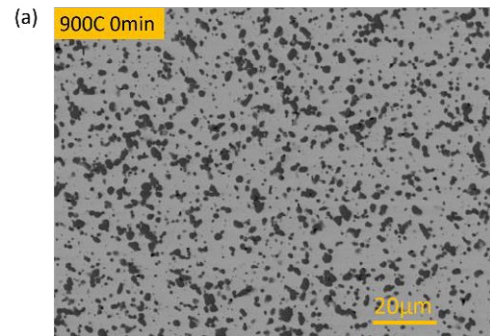
3 Results and discussion

3.1 Microstructural evolution in Ag/CuO system

SEM images with different magnifications (1000x, 2000x and 5000x) were taken in order to get a better overview of the particle size distribution of CuO particles. The number of CuO particles varies depending on the magnification. The derived D50 for a number distribution of the perimeter of CuO particle shows a standard deviation about 14% of the average D50. The

magnification is then chosen to be 2000x for all SEM images taken in this study to include a relatively large number of total oxide particles (> 350) with one image per sample.

It can be seen from **Figure 2** (a,b) that as the annealing time or temperature increases, the CuO grains tend to grow larger and the interspacing between grains increases. This trend also manifests in the grain size analysis as shown in Figure 2 (c-e).



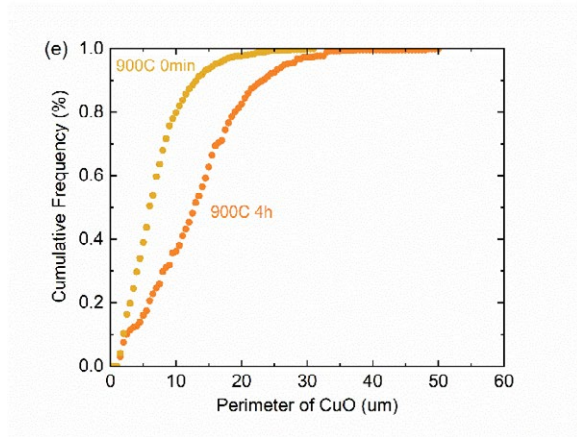


Fig. 2 Microstructure and CuO grain size distribution analysis with different annealing times (a, c) 0h; (b, d) 4h at 900 °C in Ag/CuO system. (e) shows an evolution of cumulative frequency of the perimeter of CuO. The images were taken with back-scattered electron detector. Grey phase is CuO and the white majority phase is Ag.

3.2 Microstructural evolution in Ag/SnO₂/Bi₂O₃ system

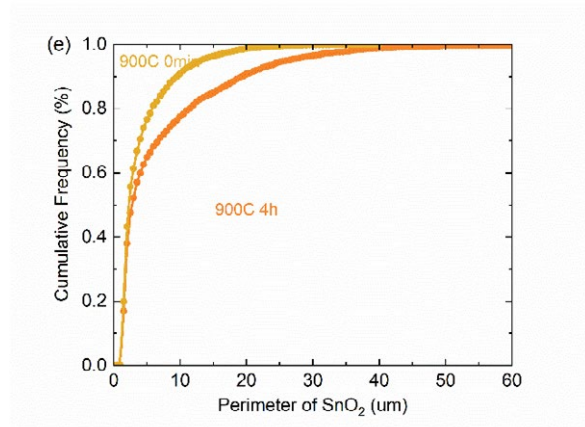
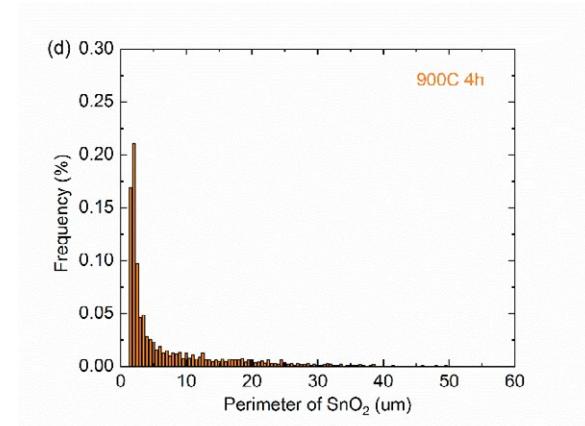
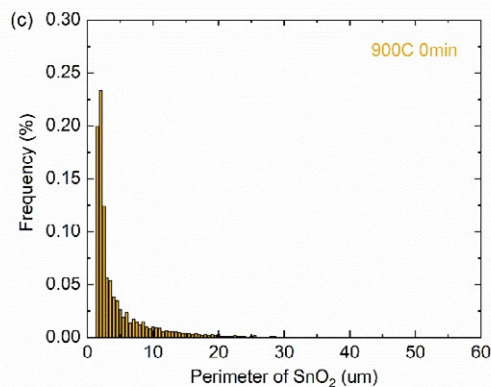
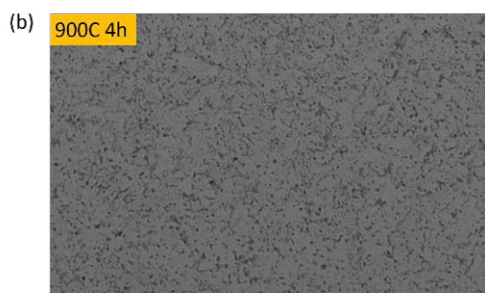
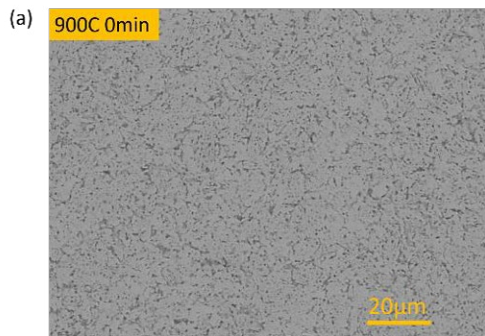


Fig. 3 Microstructure and SnO₂ grain size distribution analysis with different annealing times (a, c) 0h; (b, d) 4h at 900 °C in Ag/SnO₂/Bi₂O₃ system. (e) shows an evolution of cumulative frequency of the perimeter of SnO₂. The images were taken with back-scattered electron detector. Grey phase is SnO₂ and the white majority phase is Ag.

As we can see from **Figure 3**, in comparison to the Ag/CuO system which has a growth of 113% of the D50 perimeter of CuO, the growth in the D50 perimeter of SnO₂ in Ag/SnO₂/Bi₂O₃ is much less obvious, which is only 22%. This is shown in **Table 3**.

	D50 at 900 °C 0min [μm]	D50 at 900 °C 4h [μm]	D50 Growth (%)
CuO	1.91	4.06	113
SnO ₂	0.72	0.88	22

Tab. 3 D50 perimeter (in μm) of MeO particles after different sintering conditions.

3.3 Grain growth mechanism

In order to describe the grain growth of the MeO particles in Ag, the Ostwald ripening model was applied, in a similar manner as it was used previously to describe microstructural evolution in liquid phase sintered systems [7]. During particle coarsening, atoms from the

small precipitates dissolve into the matrix Ag, and diffuse through it, and reprecipitate at the larger precipitates, thereby making the larger precipitates grow at the expense of smaller ones.

$$d^3 - d_0^3 = K t \quad (\text{eq. 1})$$

$$K = \frac{8 \gamma C_\infty \Omega^2 D}{9 R_g T} \quad (\text{eq. 2})$$

Where d is the average grain diameter of all MeO grains, γ is the surface tension or surface energy of the inclusion phase, Ω is the molar volume of the inclusion phase MeO, C_∞ and D the solubility and diffusion coefficient of the diffusing species in Ag. Here we are assuming the grain growth is limited by the diffusion rate.

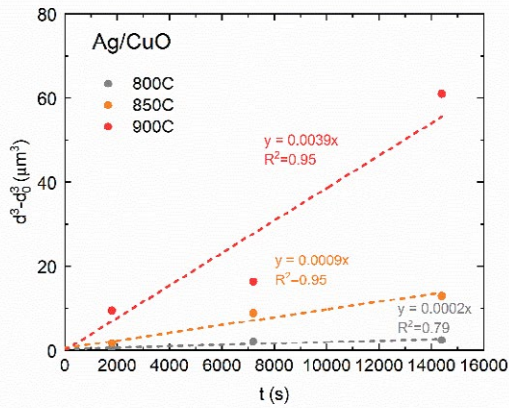


Fig. 4 Grain size evolution ($d^3 - d_0^3$) as a function of annealing time (t) for Ag/CuO material.

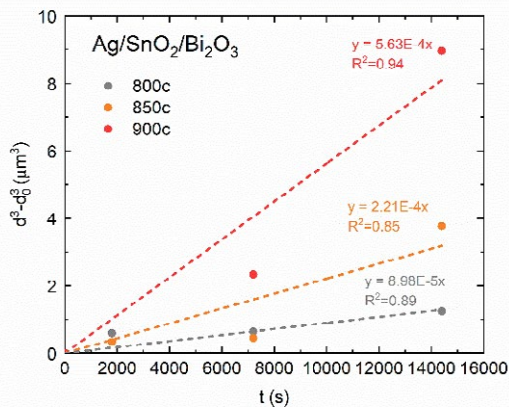


Fig. 5 Grain size evolution ($d^3 - d_0^3$) as a function of annealing time (t) for Ag/SnO₂/Bi₂O₃ material.

As a first order interpretation, a linear relationship was extrapolated between the cubic term of average grain diameter d and annealing time for each given temperature as shown in **Figure 4** and **Figure 5**. The slope of this linear relationship indicates the grain growth con-

stant K , which also increases as the temperature increases. This finding agrees with the microstructural evolution shown in **Figure 2** and **3**.

Comparing the grain growth constant K for Ag/CuO and Ag/SnO₂/Bi₂O₃ systems, we find K is much larger in Ag/CuO system. It is 6.9 times larger at 900 °C for Ag/CuO than Ag/SnO₂/Bi₂O₃. The different temperature dependence of K in **Figure 4** and **5** was compared, as shown in **Figure 6**.

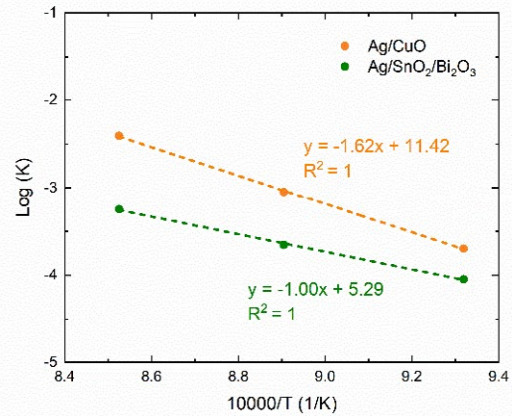


Fig. 6 Grain growth constant $\text{Log}(K)$ as a function of annealing temperature $10000/T$ for Ag/CuO and Ag/SnO₂/Bi₂O₃ material.

As can be seen from **Figure 6**, grain growth constant $\text{Log}(K)$ as a function of annealing temperature $10000/T$ can be approximated as $K = K_0 e^{-\frac{A}{T}}$. The difference in grain growth constant K gets larger as temperature increases when comparing the two systems. By analysing the parameters determining K , we found there is not much difference between the surface energy of CuO and SnO₂, which are in the range of (0.74, 2.28) J/m and (1.56, 2.71) J/m respectively depending on the crystallographic orientation [8-9]. The molar volume Ω of CuO is 12.61 cm³/mol compared to that of SnO₂, which is 21.68 cm³/mol. By comparing diffusion coefficients of Cu, Sn and O in Ag [10-11], we found that the diffusion of the Me atoms is much rate limiting ($D = E-9$ and $E-12$ cm²/s for Cu and Sn in Ag respectively) compared to that of O atoms ($D = 8.8E-3$ cm²/s). This could be attributed to the much larger molar mass of the Me atoms compared to that of an O atom. From previous phase diagrams, we find out the solubilities of Cu and Sn in Ag at 900 °C are about 3 wt% [12-13].

At 900 °C, the calculated diffusion coefficients for Cu atom and Sn atom in Ag matrix are 3.77E-11 cm²/s and 3.44E-12 cm²/s respectively. If we compare those values to literature, $D_{Cu \text{ in Ag}}(T = 1123K) = 10^{-9} \text{ cm}^2/\text{s}$, $D_{Sn \text{ in Ag}}(T = 1123K) = 10^{-12} \text{ cm}^2/\text{s}$. There is a large deviation for $D_{Cu \text{ in Ag}}$ as can be seen in **Figure 7**, which might be due to the different Cu concentrations

in Ag in the literature study and the work here. The large difference of diffusion coefficient between Cu and Sn in Ag (10 times according to our experimental results) could be the reason that there is so much difference in the grain growth rate in the Ag/CuO and Ag/SnO₂/Bi₂O₃ materials.

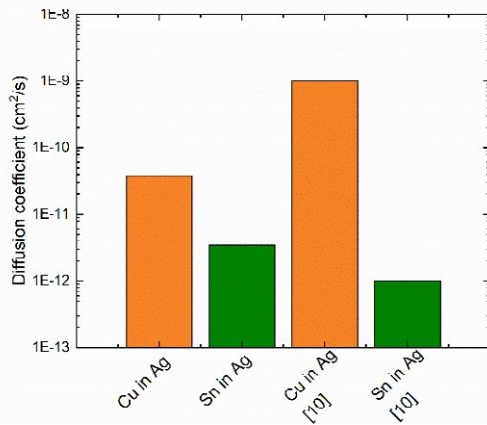


Fig. 7 Comparison of diffusion coefficients for Cu and Sn in Ag that is calculated with experimental results from this study (first two columns) and from reference [10] (last two columns) at 900 °C.

3.4 Mechanical properties

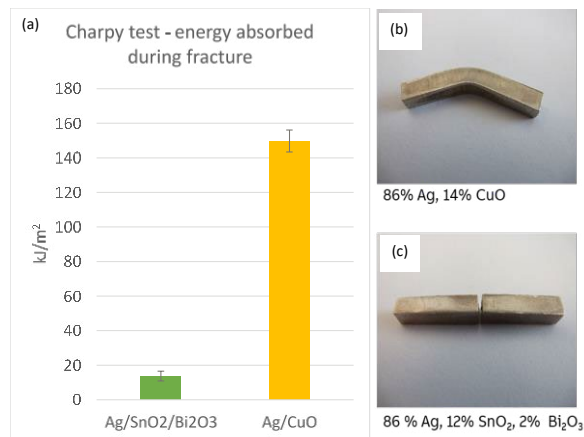


Fig. 8 (a) Charpy test result of both Ag/CuO and Ag/SnO₂/Bi₂O₃ material. (b, c) photos of sample after charpy test with the same hammering energy 2J. A higher hammering energy (5J) was used to get the data for Ag/CuO as shown in (a).

A significant improvement of fracture toughness can be observed in **Figure 8a**. The photos in Figure 8c and 8b of samples after charpy test also show a change from brittle fracture to more plastic fracture mechanism. There could be many reasons of such change, for example, the difference in the fracture resistant nature of

CuO and SnO₂, the MeO particle size and amount, and the interfacial bonding strength between Ag and MeO etc. While there is not much information about the fracture resistant nature of CuO and SnO₂, the weight percentage of MeO was kept as the same; the particle size of CuO is larger than that of SnO₂. After investigating the fracture surface of charpy tested samples, we found better interfacial adhesion between Ag and CuO compared to that of Ag and SnO₂, as shown in Figure 9 and 10. Compared to Ag/SnO₂/Bi₂O₃ where cracks propagate mostly along the interface between Ag and SnO₂, we observe much less interfacial crack resulted porosity in the Ag/CuO system. This agrees with the result of Li *et al* [14]. They found that the CuO and Cu₂O additives suppressed the growth of intergranular cracks in the Ag/SnO₂ materials by the formation of larger dimples around SnO₂ particles, which increases larger interfacial adhesion. Moreover, on the very top surface of the fractured Ag/CuO sample, cleaved CuO particles are also observed as shown in **Figure 9a** and **Figure 10a**, which indicates a stronger interface as well. It must be pointed out that these cleaved CuO particles were also observed on raw fractured surfaces without further processing. So, this eliminates the possibility of these cleavages formed due to preparation artefacts.

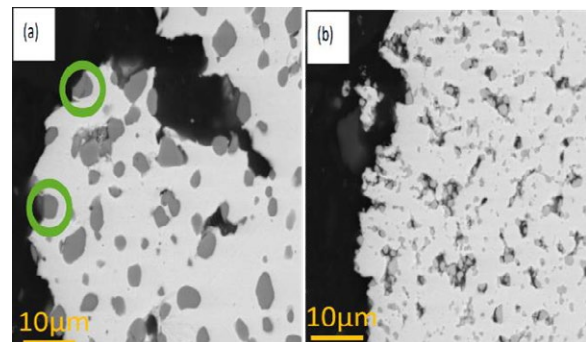


Fig. 9 SEM images of the cross section of fractured samples for (a) Ag/CuO and (b) Ag/SnO₂/Bi₂O₃ material respectively.

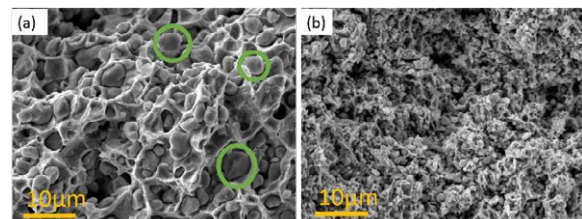


Fig. 10 SEM images of the raw fracture surfaces for (a) Ag/CuO and (b) Ag/SnO₂/Bi₂O₃ material respectively.

4 Conclusion

By studying the microstructural evolution of Ag/CuO contact materials during sintering in comparison to that of Ag/SnO₂/Bi₂O₃, we observed significant different

grain growth rates of MeO for the two systems, especially at temperatures >850 °C. This could be explained by the different diffusion rates of Cu and Sn atoms in Ag. The increased fracture toughness could be resulted from an improvement of interface adhesion between Ag/CuO compared to Ag/SnO₂/Bi₂O₃ as shown in the microstructure of fractured surfaces. This in turn could lead to increased electrical durability due to reduced fracture during arcing. Further electrical life testing with contact tips of the compositions studied here is undergoing.

5 Literature

- [1] B. Gengenbach, Ursijla Mayer, Roland Michal, and K. E. Saeger, "Investigation on the Switching Behavior of AgSnO₂ Materials in Commercial Contactors", *IEEE Transactions on Components, Hybrids and Manufacturing Technology* 8 (1) 58-62 (1985).
- [2] Chi H. Leung, Volker Behrens, "A Review of Ag/SnO₂ Contact Material and Arc Erosion", *Proceedings on International Conference on Electrical Contacts* 82-87 (2008)
- [3] T. Mützel and R. Niederreuther, "Advanced silver-tin oxide contact materials for relay application," *26th International Conference on Electrical Contacts (ICEC 2012)* 194-199, Beijing (2012). doi: 10.1049/cp.2012.0647.
- [4] D. Jeannot, J. Pinard, P. Ramoni and E. M. Jost, "Physical and chemical properties of metal oxide additions to Ag-SnO₂ contact materials and predictions of electrical performance," in *IEEE Transactions on Components, Packaging, and Manufacturing Technology: Part A* 17(1) 17-23 (1994). doi: 10.1109/95.296363.
- [5] Guijing Li, Huijie Cui, Jun Chen, Xueqian Fang, Wenjie Feng, Jinxi Liu, "Formation and effects of CuO nanoparticles on Ag/SnO₂ electrical contact materials", *Journal of Alloys and Compounds* 696 (5), 1228-1234, (2017). doi: 10.1016/j.jallcom.2016.12.092.
- [6] Rishi, Narinder Rana, "Particle Size and Shape Analysis using Imagej with Customized Tools for Segmentation of Particles", *International Journal of Engineering Research & Technology* 4(11) 247-250 (2015).
- [7] Thomas Vetter, Martin Iggland, David R. Ochsenein, Flurin S. Hänseler, and Marco Mazzotti, "Modeling Nucleation, Growth, and Ostwald Ripening in Crystallization Processes: A Comparison between Population Balance and Kinetic Rate Equation", *Crystal Growth & Design* 13 (11) 4890-4905 (2013). DOI:10.1021/cg4010714.
- [8] A. Beltra, J. Andres J. R. Sambrano, E. Longo, "Density Functional Theory Study on the Structural and Electronic Properties of Low Index Rutile Surfaces for TiO₂/SnO₂/TiO₂ and SnO₂/TiO₂/SnO₂ Composite Systems", *J. Phys. Chem. A* 112, 8943–8952 (2008).
- [9] Chiara Gattinoni, Angelos Michaelides, "Atomistic details of oxide surfaces and surface oxidation: the example of copper and its oxides", *Surface Science Reports* 70 (3) 424-447 (2015). DOI:10.1016/j.surfrep.2015.07.001
- [10] W. Gierlotka, Y.H. Chen, M.A. Haque, and M.A. Rahman, "Atomic Mobilities in the Ag-Cu-Sn Face-Centered Cubic Lattice", *Journal of Electronic Materials* 41(12) 3359-3367 (2012).
- [11] W. Eichenauer and G. Mueller, "Diffusion und Löslichkeit von Sauerstoff in Silber", *Journal of Metallurgy* 53, 321-324 (1962).
- [12] I. Karakaya, W. T. Thompson, "The Ag-Sn (Silver-Tin) system", *Bulletin of Alloy Phase Diagrams* 8, 340–347 (1987).
- [13] A. Kawecki, T. Knych et al., "Fabrication, properties and microstructures of high strength and high conductivity copper-silver wires", *Archives of Metallurgy and Materials* 57(4) (2013).
- [14] Guijing Li, Tianyang Yang et al., "Mechanical characteristics of the Ag/SnO₂ electrical contact materials with Cu₂O and CuO additives", *Journal of Alloys and Compounds* (817) 15, 152710 (2020).

On the correlation between performance, properties and microstructure of Ag/WC and AgW contact tips

Massimiliano Amato¹, Atanu Chaudhuri², Ato David³,
Cody Andelin³, Carlene Jerram³, Srinidhi Sampath², Linda Jacobs³

¹ELSB, ABB S.p.A. Italy,

² EL, ABB, India,

³ EL, ABB, USA

Email: massimiliano.amato@it.abb.com

Abstract

The performance of electrical protection devices strongly depends on contact tip materials: they should provide excellent anti-welding behavior, low contact resistance, low erosion rate and good arc root mobility. In order to guarantee good performance of the entire system, tips internal quality is fundamental. It could depend on manufacturing process, size of starting powders and a series of parameters controlled by the suppliers. Control procedures on contact tips are mandatory to anticipate failures due to low-quality issues.

In this paper, a Matlab based tool for metallographic inspection (MInT, Metallographic Inspection Tool) is presented: it automatically evaluates internal bulk quality of contact tips. Materials commonly used for low voltage circuit breaker contact tips (as AgW, AgWC) are included for MInT investigation. The analysis procedure can extract metallographic properties of the tip (such as dimensions and distribution of silver islands, porosities, mass composition). These quantitative outputs can be connected to performance during product tests. In this work, correlation between metallographic quality indexes and short circuit performances with a high level of agreement is also presented as an example. An attempt has been made to correlate the MInT output with the electrical properties (e.g. conductivity) of the contact tips.

1. Introduction

Low voltage (LV) circuit breakers (CB) must fulfil a list of requirements related to the protection of persons and electric network. The primary function of these devices is to identify a fault caused by overload or short-circuit and interrupt the current flow. The interrupting capacity of a CB strongly depends on the design of its mechanism and on contact materials [1]. The combination of both drives the ability of the whole device to extinguish the electric arc that will ignite during contacts opening [2]. Due to high thermal energy of the arc, the moving and fixed contacts are the components most exposed to damage. For this reason, the contact pair must be properly designed in order to withstand arc erosion: usually unsymmetrical contact pairs are used to reduce welding phenomena and to combine the advantages of different materials.

Silver-based refractory contact materials are usually chosen as arcing contacts in traditional CBs due to their low electrical resistance, high resistance against welding, high arc erosion resistance, good arc mobility and good arc extinguishing capability [1],[3],[4],[5]. The silver phase of the composite metal retains its high electrical and thermal conductivities, while the other components help to improve hardness and arc resistance properties. A proper combination of contact materials between moving and fixed contacts is crucial

to guarantee the interrupting performance. A material mating often used for LV CBs consists of silver-tungsten (AgW) or silver-tungsten carbide (AgWC) material for the moving contact and silver-graphite (AgC) for the fixed counterpart. AgW contacts are particularly resistant to arc erosion and show high conductivity, with typical silver content between 30%wt and 85%wt. AgWC represents a valid alternative to AgW if higher arc erosion resistance and hardness are required. In this case, silver content can vary in the range 40-60% wt. Silver-graphite is used as contact material because of its anti-welding and electrical resistance properties, with graphite content usually in the range 2-5% wt.

Visual inspection by means of metallographic images can help to check the internal quality of electrical contacts and identify possible manufacturing failures that can jeopardize the CB functionalities. In this paper, a tool (MInT, Metallographic Inspection Tool) developed by ABB has been used to automatically perform a quantitative analysis of contact tips quality. The results of this investigation have been directly correlated with short circuit switching performances on a CB from ABB. Finally, the outputs from MInT analysis have been used to extract preliminary data concerning material properties of the contact tips, such as conductivity. The latter depends also from impurities and additives solved in the silver matrix, usually not visible in microsections.

2. Methods and materials

2.1 Product under investigation

The device under test (DUT) is a four poles test setup (three phases and neutral) with significant features of a real Residual Current Circuit Breaker (RCCB) compliant with standard IEC 61008 [6]: it has been designed to demonstrate correlation between contact tip quality and short circuit performances. The DUT mainly consists of:

- sensing group to detect the electrical faults: in particular a current transformer to identify earth leakage currents;
- actuator to transmit a tripping signal to the mechanism, in the DUT an electro-mechanical relay;
- a mechanical assembly driven by the handle or the actuator, made of levers and springs that opens and closes the contacts;
- an arc chamber to extinguish the electrical arc following contact opening during short circuit operation.

The DUT is equipped with pairs of contact tips made of AgW or AgWC for the moving contact and AgC for the fixed one. In this paper, the investigation has been focused on Ag-based tips for the moving contact which is the most critical contact for short circuit failures: being on the cathodic side of the electric arc in the test set-up, it is subjected to higher temperatures and erosion due to ion bombardment [1]. Besides that, due to the typical design, the arc tends to stay longer on the moveable tip than the fixed tip. While the moving contact has been equipped with different Ag-based contact tips, the same fixed contact material (AgC 95-5, extruded with graphite fibers perpendicular to contact surface) has been used to avoid possible influences on the results.

The full test procedure for RCCB is described in the product reference standard IEC 61008 [6]. In particular, the short circuit sequence E has been chosen to compare different tips performances, because it has been considered the most arduous to be passed by contacts. The test sequence can be divided into two parts: the first one is in coordination with a Short-Circuit Protective Device (SCPD) and is intended to verify that the DUT is able to withstand the rated conditional short-circuit current (I_{nc}) without damage. The sequence of shots is Open-Close-Open (O-C-O). The second part wants to verify the DUT ability to make, carry and break short circuit current (I_m) without any other protection, while a residual current of 10 times the nominal differential current causes the CB to operate. The sequence of shots is CO-CO-CO. $I_{nc} > I_m$, where I_m is the greater between 10 times the nominal current of the DUT and 500 A. In this paper, all the tests have

been performed on samples with nominal current of 100 A, $I_{nc}=10$ kA protected by a 100 A fuse (first part of the sequence) and $I_m=1$ kA (second part of the sequence).

The shots at 10 kA are high thermal stress for the contact tips because of the high arc energy. If their quality is not sufficient, a high rate of failure due to welding between contact pairs can be observed in subsequent shots, where repulsion forces are lower due to smaller current intensities. They can cause partial opening between contacts and rebounds that could promote welding.

Figure 1 shows a comparison between a moving contact tip before and after the short circuit sequence.

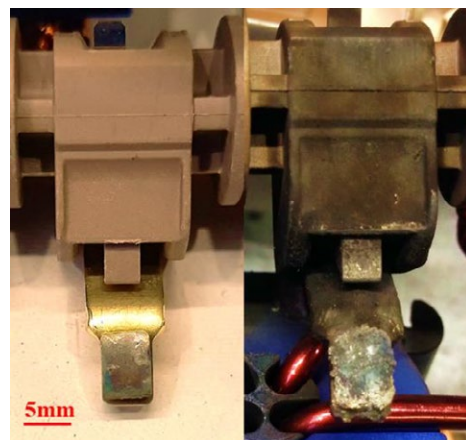


Figure 1 Example of contact tip before (left) and after (right) short circuit test.

The above-mentioned standard prescribes that a set of three samples must be tested for each test sequence: if no failure occurs, the test is passed. A single failure can be admitted: in this case another set of three samples can be tested, but no additional failures are permitted. If more than one failure is experienced on the first set of samples, the sequence is immediately failed. Typical failures related to contact tips that can occur during short circuit tests are:

- welding between moving and fixed contact tips after partial or total erosion due to the electric arc. In extreme cases, welding can occur directly between one tip and the counterpart contact carrier, if the contact tip has been completely eroded;
- sticking between moving and fixed contact tips. It is usually distinguished from a welding tips failure, because it happens at lower currents and results in a lower force acting between the tips;

- lack of electrical continuity at contact reclosing, due to complete erosion of electrical contacts by the arc;
- chipping of the moveable contact tip due to thermal shock.

All these failures can be directly connected to tip internal structure and/or composition. In particular, the first two can be linked to insufficient anti-welding properties, while the third can be related to low arc resistance and material hardness and the fourth to poor grain structure of the contact.

2.2 Tool for metallographic analysis

Visual inspection of contact microstructure can give valuable feedback about tip quality only if associated with quantitative outputs allowing objective comparison between tips. In the case of sintered Ag-based contact tips, the presence of large silver islands in the moving contact tip can facilitate welding phenomena and increase the short-circuit failure rate. On the back side used to attach the tip on the contact carrier, the tip should exhibit a good homogeneity, no voids and uniform silver infiltration in the knurled region. These conditions should allow an optimal welding of the tip on the contact carrier. Regarding porosities, they can affect electro-mechanical properties, such as electrical resistance and hardness. In the presented paper, impact of porosities on product performance has not been investigated.

Usually optical microscopes are equipped with tools for image analysis. MInT solution developed by ABB is a Matlab-based software and does not require special equipment to be run. Starting from the image file of a tip cross-section, the software tool can automatically identify silver islands thanks to different colour or grey level existing between silver and refractory phases. A consistent procedure should be established to capture multiple pictures from the same cross-section to build a more solid statistical base. In order to be more conservative, metallographies can be focused on the regions containing the largest silver islands. After their identification, the software extracts statistics regarding different microstructural parameters, such as metal islands maximum diameter, area, and orientation. Figure 2 illustrates the measurement of maximum axis length and area for a silver island as an example.

The outputs chosen as representative and quantitative criteria to accept or reject the contact tip depend on the performance required by the product. The cumulative area of silver islands as a function of their maximum axis length has been already presented as quality index for tip microstructure [5]. A plot of the Ag islands cumulative area is reported as an example in Figure 3 for an AgWC tip. The experimental data are plotted with circular markers. The cumulative area is normalized to

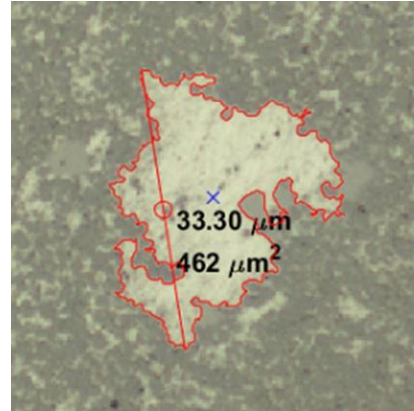


Figure 2 Measurement of maximum axis length and area for an Ag agglomerate in an AgW contact tip.

the total detected area of silver islands in the cross section. Four check-points are extracted by MInT, corresponding to the percentile values of 50%, 70%, 90% and 95%. For sake of clarity, an explanation of the plot in Figure 3 is presented here: 50% of the area covered by silver consists of islands with major axis length below 4.2 μm (1st column), 70% by Ag islands with maximum diameter up to 6.7 μm (2nd column) and so on. If no experimental major axis length data precisely corresponds to the prescribed percentile value, the closest value is considered.

Finer microstructure means that more smaller Ag islands are present: therefore, the first part of the curve should be more populated and show a higher slope, reaching the 100% of cumulative Ag area should by smaller values of major axis length.

In order to classify the contact tip quality, the experimental curve is compared to a specification limit curve which has been fixed considering both the expected silver distribution due to the sintering and infiltration process and the requirement to achieve good short circuit performance. The sintered grain structure is not random, but it is driven by smaller particles that tend to cluster [7]. Islands size distribution in the sintered materials is described by an exponential law, given by the Weibull distribution in the cumulative form:

$$F(d) = 1 - e^{\left(-\frac{d-d_0}{d_m}\right)^m}, \quad (1)$$

where $F(d)$ is the cumulative fraction of grains up to size d , d_0 is the location parameter, d_m is the scale parameter (the median size corresponding to half of the grains being smaller), m is the shape parameter that equals 2 for two-dimensional grain size measures (as in the here presented analysis) and 3 for three-dimensional grain size measure.

In MInT plot, $d_0=2$ μm because agglomerates smaller than this value have been filtered out to avoid possible artefacts. Therefore, d_m is the remaining variable to fit

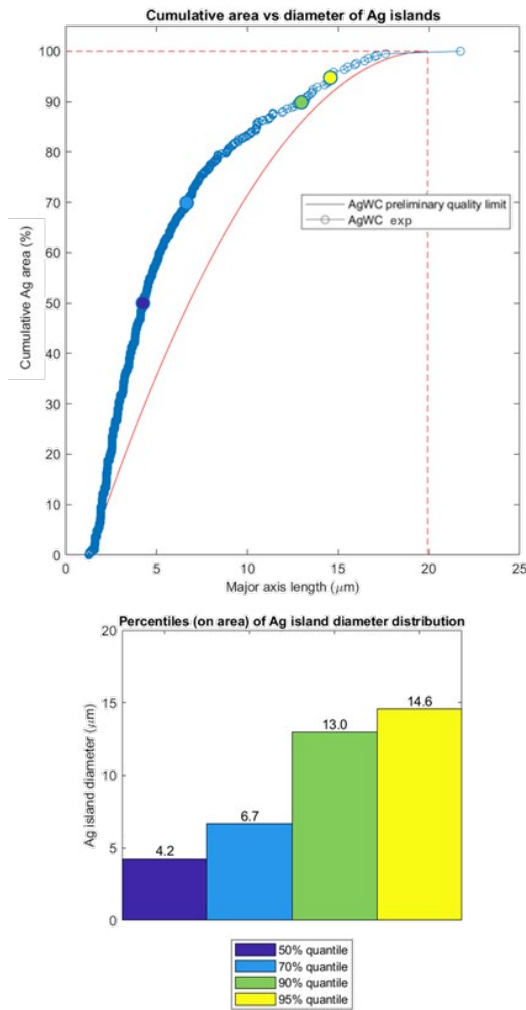


Figure 3 Cumulative area of silver islands as a function of major axis length (top) and corresponding percentiles values histogram (bottom).

experimental distribution of good tips. Its value has been obtained to reach a satisfactory agreement between tips that passed short circuit testing and MInT outputs. By varying the d_m value, the ending point of the curve corresponding to 100% of silver cumulative area changes accordingly. The x-coordinate of this point establishes the maximum allowed size for silver islands: from short circuit test, it has been fixed at 20 μm for AgWC tips and 30 μm for AgW contacts. The reason for this difference is due to the starting material properties and process parameters during sintering that result in smaller silver islands in AgWC contacts with respect to AgW. As a result, d_0 values used in MInT are 10 μm and 7 μm respectively for AgW and AgWC tips.

Two conditions are required to accept the sample: the experimental data must lie above the specification limit curve and the 95% data point must not exceed the maximum major diameter established by the specification curve, as in the case illustrated in Figure 3.

3. Short circuit results

3.1 Correlation with SC performances

AgW and AgWC contact tips from different suppliers and with different Ag island diameter distributions have been analysed by MInT and tested in short circuit (SC) sequence. In order to correlate contact microstructure to the macroscopic behaviour during operation, only failures connected to welding and sticking between contact pairs have been considered because those failure modes are suspected to be directly connected to non-homogeneous metal distribution and/or the presence of large silver islands. Other failure modes during SC tests on the DUT can be related to complete erosion of one of the two contact tips, leading to welding between carrier and the counterpart contact tip. This failure can be affected also by hardness of contact tip rather than only Ag islands distribution. The two quantities are interconnected, but this topic is not subject of this work.

Being the moving contact tips of the DUT manually assembled, parameters for a correct welding on the carrier have been found and the proper adhesion of the tips on the carrier has been checked by means of shear force tests.

The short circuit test sequence is repeated on six samples for each type of contact tip: it is passed if a failure equal or less than 17% is observed, corresponding to 1 failure out of 6.

3.1.1 Results on AgW contact tips

Analysis of four different batches of AgW contact tips (from A to D) will be presented in this section. Metallographic cross-sections are reported in Figure 4. All the images refer to the same level of magnification, therefore they can be directly compared. A first visual inspection highlights significant differences in bulk microstructures. A lower content of silver is immediately evident in tip A (AgW 25-75 wt%) with respect to the other samples (AgW 40-60 wt%).

Tips B and C are very similar at a glance, both showing a homogenous phase distribution. Sample C presents a higher tendency of silver islands to be interconnected: as a result, a larger median size of Ag islands is expected. Finally, tip D contains a lower number of Ag agglomerates but with larger dimension.

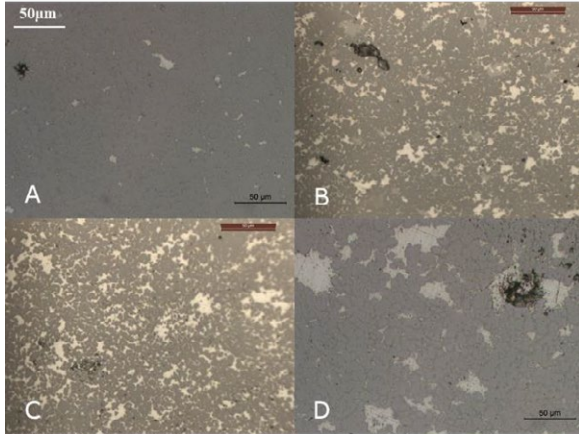


Figure 4 Metallographies of four different AgW contact tips (AgW 25-75 wt%, tip A; AgW 40-60 wt%, tips B-D).

A quantitative analysis of these preliminary observations is plotted in Figure 5. As illustrated in section 2.2, the cumulative area plot should lie above the specification limit curve and the 95% point below the maximum diameter value (30 μm for the AgW tips). According to a strict observation of these requirements, only tip A can be accepted. Tip B shows a 95% percentile in line with technical specifications but the experimental data falls in the rejection area of the graph. In this case, further and more detailed investigations should be considered to accept or reject this batch. Both tips C and D should be rejected because of a coarser distribution of silver islands and the presence of silver agglomerates that exceed maximum allowed dimensions and could promote welding between contacts.

Table 1 summarizes MInT outputs and compares them to their short circuit failure rate. For each tested contact type, the 95% size value is reported together with the comparison between experimental cumulative plot and quality limit curve. As a result, the final MInT assessment of tip quality is summarized. The last column reports the short circuit failure rate due to sticking/welding based on six samples. Values higher than acceptance thresholds are highlighted in bold (i.e. 95% diameter higher than 30 μm, short circuit failure rate higher than 17%).

MInT evaluation shows a good level of agreement with the results of the short circuit test: a fine and homogeneous distribution of silver islands results in successfully passing the short circuit test (tip A). Also, tip B presents an internal microstructure good enough to fulfil test requirements: even if the cumulative area line slightly lies below the acceptance curve (see Figure 5), metal phases are uniformly distributed and large silver agglomerates are absent. For tips C and D, metallographic analysis fully predicts higher failure rates in product tests.

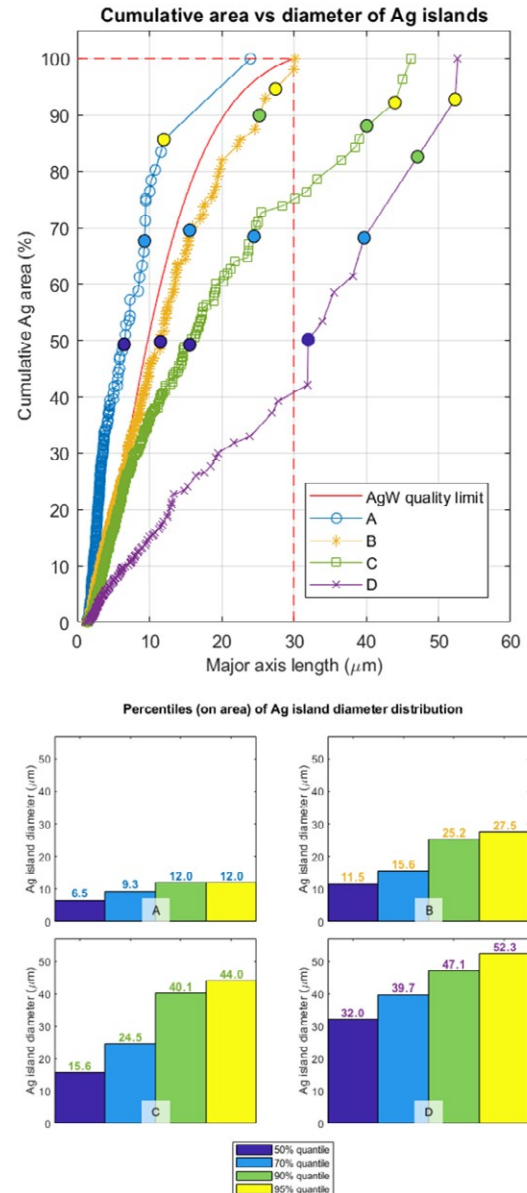


Figure 5 Cumulative silver area plot vs islands size (top) and extracted percentile values (bottom) for analysed AgW contact tips.

A remarkable result regards the difference between tips B and C. They have been produced by the same supplier and a first visual inspection of metallographic images (see Figure 4) could not properly distinguish between the two samples. MInT analysis has been able to quantitatively evaluate microstructural differences and anticipate possible failures in short circuit tests. In addition to this, with the two tips manufactured by the same supplier and having identical nominal composition, MInT analysis can be used also to detect process deviations occurring between batches.

Tip	Supplier	95% size (μm)	Above curve?	Accept?	% SC failure*
A (AgW 25-75 wt%)	1	12	y	y	17%
B (AgW 40-60 wt%)	2	27.5	n	n	17%
C (AgW 40-60 wt%)	2	44	n	n	33%
D (AgW 40-60 wt%)	3	52.3	n	n	67%

* over 6 samples

Table 1 Correlation between MInT outputs and short circuit failure rate for the tested AgW contact tips. In bold, specification out of technical requirements.

3.1.2 Results on AgWC contact tips

A similar analysis has been conducted on AgWC contact tips. Figure 6 shows metallographic images of six different AgWC contact tips (from E to L) having AgWC composition from 40-60 wt% to 60-40 wt%. Metallographies are taken with different levels of magnification, so a direct visual comparison could lead to erroneous results.

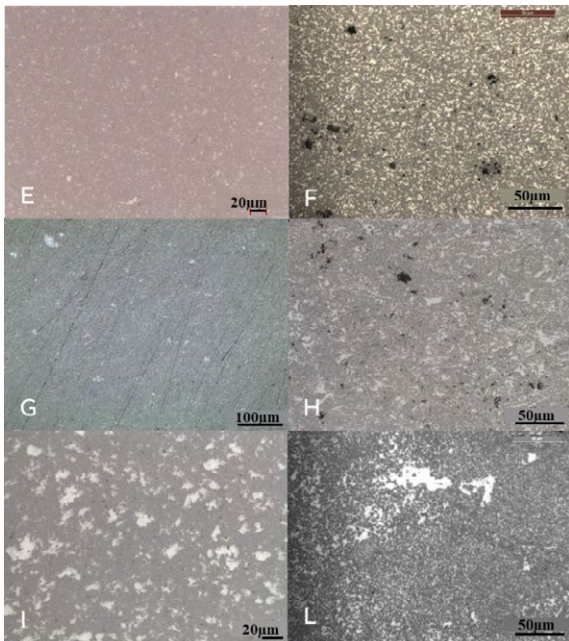


Figure 6 Metallographies of six different AgWC contact tips (AgWC 40-60 wt%, tip F; AgWC 50-50 wt%, tips E, G, I, L; AgWC 60-40 wt%, tip H). Images are taken with different levels of magnification.

Despite that, significant differences are evident: some tips present fine and homogeneous silver distribution (tips E, G), others higher median size of silver agglomerates but still uniform dispersion (tip F), others more inhomogeneous microstructure and larger silver islands (tips H, I). Tip L shows a fine and uniform distribution in the main part of the image, but some large Ag agglomerates are present. A direct and reliable comparison of these metallographies can be quite hard and subjective. MInT analysis points out clear differences. As presented in section 2.2, in this case the maximum

allowed diameter for Ag islands is 20 μm , more stringent than for AgW because of a finer expected microstructure.

Results of metallographic investigation are reported in Figure 7. First two tips E and F show an internal microstructure perfectly in line with technical requirements fixed by the AgWC quality limit curve: the silver phase is fine and uniformly dispersed. Tip G follows similar considerations reported in section 3.1.1 for tip B: even though the cumulative silver area curve partially lies below the specification line, the resulting microstructure could be considered fine enough to be accepted. The presence of few large Ag agglomerates partially deviates the final portion of the experimental curve from the ideal trend, but the 95% value meets the prescribed limit. MInT analysis confirms the first visual evaluation of a poor internal quality for tips from H to L. Tip L represents an interesting case to estimate the impact of few large Ag islands over a fine microstructure. The initial part of the cumulative silver island curve (size less than 10 μm and area percentage below 60%) is perfectly in line with the quality limit, as can be observed comparing the first percentile bars for tips E-G and L in Figure 7. This means that a large number of small silver islands is present. Beyond this point, the slope of the cumulative area plot for tip L decreases. The weight of large silver agglomerates is evident especially in the final part of the curve, where the largest silver islands contribute 5% each to the total cumulative area.

The correlation between tip quality evaluation made by MInT and short circuit failure rates is reported in Table 2. As for AgW contacts, the impact of contact microstructure on product performances has been correctly predicted by MInT. Tips E and L are made with the same nominal composition (AgWC 50-50 wt%) and have been produced by the same supplier. Despite this, the microstructure and product performance are significantly different. The microstructure analysis has been proven to quantitatively discriminate between manufacturing lots and may reflect deviations from the optimal sintering process.

Tip	Supplier	95% size (μm)	Above curve?	Accept?	% SC failure*
E (AgWC 50-50 wt%)	4	9.0	y	y	17%
F (AgWC 40-60 wt%)	5	13.8	y	y	17%
G (AgWC 50-50 wt%)	6	17.8	n	y	0%
H (AgWC 60-40 wt%)	7	27.5	n	n	50%
I (AgWC 50-50 wt%)	8	34.5	n	n	33%
L (AgWC 50-50 wt%)	4	42.6	n	n	67%

*over 6 samples

Table 2 Correlation between MInT outputs and short circuit failure rate for the tested AgWC contact tips. In bold, specification out of technical requirements.

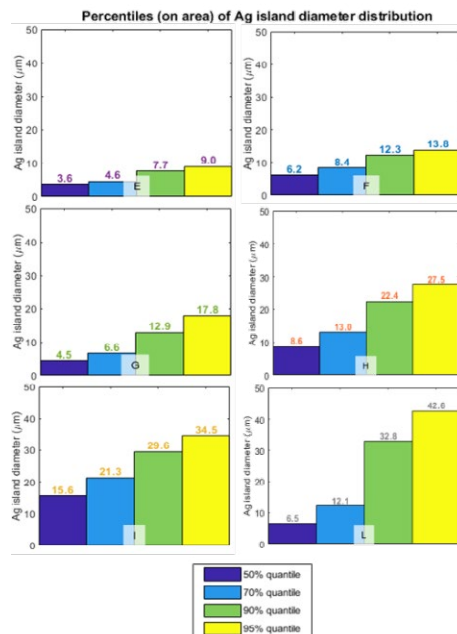
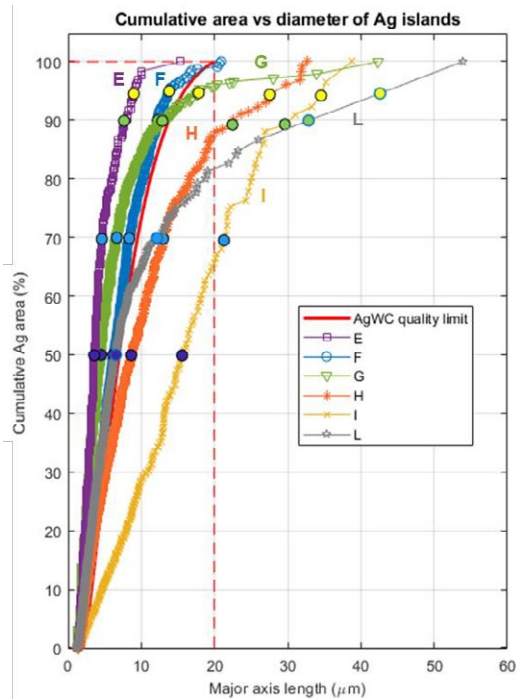


Figure 7 Cumulative silver area plot vs islands size (top) and extracted percentile values (bottom) for analysed AgWC contact tips.

3.2 Correlation with electro-mechanical properties

In section 3.1, it has been proven that MInT software is able to correlate the SC failure rate due to welding to the contact tip quality. As conductivity is a crucial electrical parameter, an attempt has been made to investigate the correlation between microstructural output of the MInT tool and the conductivity of the tips. Besides that, a correlation between microstructure quality and tip composition has been investigated. The analysis has been conducted for AgW tips of different Ag content ranging from 27 to 65 wt%. All the tips have been manufactured by same supplier (supplier 9). Cold blend-sintering and fire blend process have been used for manufacturing the tips. In fire blending process, cold blended powders of different materials are mixed in furnace to form alloyed powders. They are broken down again to desired powder size and used for contact tip manufacturing. This practice ensures better mixing of elements. For this investigation, it has been assumed that the Ag islands are the only contributor to the conductivity, neglecting the contribution from the tungsten.

Twelve AgW contact tips have been characterized in terms of electrical conductivity using an eddy current measurement method. Wet chemical analysis has been performed to determine the exact Ag content of each set of contact tips. From MInT analysis, Ag island size and island numbers at percentile cumulative area values have been considered as microstructural contribution factors (CF) that impacts conductivity.

As mentioned in section 2.2, based on the greyscale value of metallographic images, Ag and W are distinguished and further analysed in the MInT tool. For each contact tip set, at least three tips have been analysed with five images taken from the central region of each tip section (i.e. minimum fifteen images were analysed for each case). From the cumulative distribution plot of each image, the diameter of Ag islands corresponding to each of the percentile values of the cumulative plot has been identified. In the next step, the number of Ag islands has been similarly calculated for each percentile value.

The contribution factor has been defined by the following formula:

$$CF = \sum_i d_i n_i, \quad (2)$$

where $i=1-4$ is the index of the percentile value, d is the major axis length of Ag islands extracted from the cumulative plot and n the number of Ag islands covering the corresponding cumulative area percentage.

The CF as a function of electrical conductivity and Ag content is plotted in Figure 8 for different cold blend AgW contact tips. The correlation of these three parameters will be studied with more details once data is available for additional compositions. From the preliminary results presented here, it can be observed that the conductivity and Ag content is linearly dependent to the CF. The CF is higher for the tips with higher conductivity and Ag content and vice versa. Important to note is that all the tips contributing to the plot in Figure 8 are manufactured by the same supplier with the same process (cold blend), but with different Ag contents.

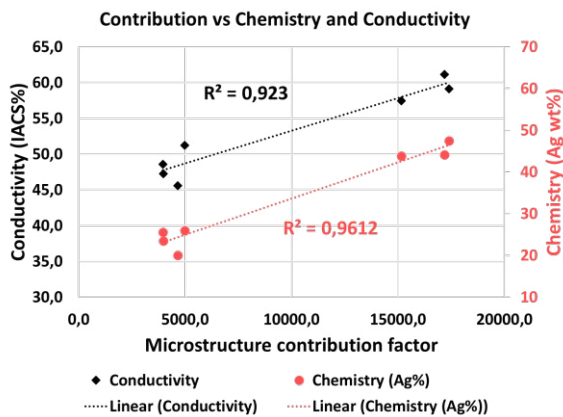


Figure 8 Contribution factor vs Conductivity (IACS%) and Ag composition plot for cold blend tips,

In Figure 9, composition and electrical conductivity are plotted against the CF including both process (cold and fire blend). It can be observed that the data points are more dispersed, compared to Figure 8. The conductivity and Ag content are higher for the fire blend tips

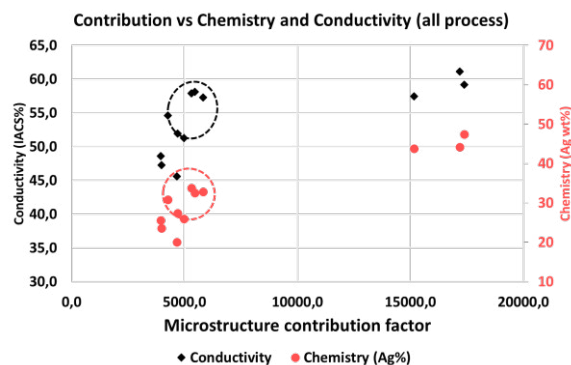


Figure 9 Contribution factor vs Conductivity (IACS%) and Ag composition for cold and fire blend process, the data from the fire blend process are marked with circle in the plot.

(marked with circle in plot) of similar CF with respect to cold blend process. Therefore, it seems that the manufacturing process can play a role on this correlation even for the tips with similar Ag content. Further investigation will be a topic for future works.

4. Conclusions

AgW and AgWC contact tips for LVCB have been analysed and tested in order to correlate internal microstructure with short circuit behaviour. Thanks to a metallographic inspection tool (MInT) developed by ABB, cumulative area of silver phase as a function of island size has been used to evaluate silver distribution. A high level of agreement between MInT evaluation and short circuit performances has been proven, making the presented procedure a solid solution for contact quality check. Failures due to large silver islands or non-homogeneous silver distribution can be reliably predicted. The described methods can be used not only to accept or reject contact tips, but also as support tool for designers to discuss technical requirements with suppliers and to identify specifications to be included in contact drawings. The future plan is to find the correlation between conductivity/composition and contribution factor or other MINT calculated predictor for different process route. Understanding this relationship can help to qualify tips or supplier based on the microstructure parameters of the different contact tips.

5. Literature

- [1] Slade, P. G.: Electrical Contacts, Principles and Applications, 2nd Edition. CRC Press, 2014.
- [2] Freton, P.; Gonzalez, J.-J.: Overview of Current Research into Low-Voltage Circuit Breakers. The Open Plasma Physics Journal, 2, 105-119, 2009.
- [3] Findik, F.; Uzun, H: Microstructure, hardness and electrical properties of silver-based refractory contact materials. Materials and Design 24, 489–492, 2003.
- [4] Mützel, T.; Braumann, P.; Niederreuther, R.: Development of Contact Material Solutions for Low-Voltage Circuit Breaker Applications. IEEE 56th Holm Conference on Electrical Contacts (2011), Charleston, SC (USA).
- [5] Mützel, T.; Kempf, B.: Silver Tungsten Carbide Contacts for Circuit Breaker Applications. IEEE 60th Holm Conference on Electrical Contacts (2014), New Orleans, LA (USA).
- [6] IEC 61008-1: Residual current operated circuit-breakers without integral overcurrent protection for household and similar uses (RCCBs).
- [7] Fang, Z. Z.: Sintering of Advanced Materials. Woodhead Publishing, 2010.

The Impact of Arcing (AC3) on the Contact Resistance Behavior of Ag/SnO₂

Mützel Timo, SAXONIA Technical Materials GmbH, Hanau, Germany, timo.muettel@saxonia-tm.de
Hubrich Christian, SAXONIA Technical Materials GmbH, Hanau, Germany
Tasch Johannes, SAXONIA Technical Materials GmbH, Hanau, Germany

Abstract

For medium and high power rated contactors silver tin-oxide (Ag/SnO₂) materials doped with different types of additives are state-of-the-art contact materials. AC3 endurance tests were performed with a commercially available contactor type (45 kW). By novel approach, arcing voltages during make and break operation throughout endurance testing as well as individual contact voltage drops during temperature rise test sequences were studied.

Focus of the studies was set on the evaluation of contact resistance for individual pairs of contacts and correlating it to individual arcing stresses during endurance switching (within a double-breaking device design). Several types of silver metal-oxides were examined and deeper insights into the interaction between contact material and device could be achieved. Experimental contact resistance results are further explained by post-switching analysis of the contacts via metallurgical routines.

1 Introduction

Electro mechanical contactors are industrial control elements for switching, mainly motor loads. For power ratings above 10 kW silver tin-oxide (Ag/SnO₂) is the state-of-the-art, RoHS conform contact material in use.

Miniaturization of switching devices and increasing power densities by novel device designs were technological drivers for material development over the last decades. These technology developments were covered by design to cost measurements including precious metal reduction requirements [1 – 3].

Following these developments temperature rise behavior of switching devices like contactors is becoming an increasingly important parameter. As contact materials contribute essentially via Joule heating generated by their contact resistance, which is in general significantly increased in switched condition, knowledge about the interaction of arcing and contact resistance is key for finding appropriate solutions.

In 1991 Rieder [4] concluded that “detailed further investigations are required to understand the mechanism of AC3 make-and-break erosion”. Corresponding studies were presented by the authors in [5] and will here be extended into the area of contact resistance behavior.

2 AC3 Test Parameters and Materials under Test

2.1 Test Parameters

Basis for the studies performed is the AC3 endurance test in accordance to IEC 60947-1 [6]. Whereas temperature rise in accordance to this standard is only required in advance of electrical endurance testing, we extended this test to higher practical relevance and included such test in switched condition. The measurement setup for studying individual arcing energies per contact pair was published by the authors in [5]. A 45 kW (AC3 power) rated contactor was chosen as test object and the applied, corresponding test parameters are summarized in **Table 1**.

Table 1 Test Parameters

parameter	value
voltage U (make/break)	400/67 V
current I (make/break)	486/81 A
power factor $\cos\varphi$	0.35
switching frequency	1,000 1/h
number of operations n	1,000,000
drive voltage	230 V (AC)
thermal current I_{th} (new device)	100 A
thermal current I_{th} (AC3 service life)	50 A

In switched conditions I_{th} was reduced to 50 A avoiding over-heating of the device during temperature rise tests, which could cause damages on plastic parts as well as reaching softening or even melting voltage of contact material, thus impacting the measured contact resistance results, if not completely destroying the entire device.

2.2 Contact Materials under Test

Contact materials based on silver tin-oxide are commonly applied for contactors rated 10 kW and above. Different types of additives are used to tailor this group of contact materials for specific application needs. **Table 2** is presenting an overview on tested materials.

Table 2 Contact Materials

material	additives	production method
Ag/SnO ₂ 88/12 SPW4	WO ₃	p.m.
Ag/SnO ₂ 88/12 SPW7	Bi ₂ O ₃ , WO ₃	p.m.
Ag/SnO ₂ 88/12 LC1	Bi ₂ O ₃ , In ₂ O ₃	p.m.
Ag/SnO ₂ 86/14 PMT3	Bi ₂ O ₃ , CuO	p.m.

All Ag/SnO₂ materials in this study were produced by powder metallurgy (p.m.) via

- blending of silver and metal oxide powders,
- isostatic compaction,
- sintering,
- extrusion, and
- hot cladding with fine silver and braze alloy layer.

The evaluated materials differ by total metal oxide content, 12 and 14 wt.-%, and additives applied. These were tungsten oxide (WO₃) in the case of SPW4 material and combinations of bismuth oxide (Bi₂O₃) with WO₃, indium oxide (In₂O₃) and copper oxide (CuO).

BrazeTec S 15 (BCuP-5) was used to build assemblies via an induction brazing process, including a subsequent ultrasonic inspection on bonding quality of all parts before test.

3 Switching Phenomena and Analysis

Braumann et al. showed the impact of contact make phenomena during AC3 endurance test on the service life [7, 8]. Especially the energy induced by the electric

arc during contact bounce phenomena was considered a major impact factor.

With the measurement set-up presented in [5], the authors were able to assign single sided bounce events to the relevant contact pair within a double breaking device design (contactor). **Figure 1** is showing the single sided bounce probability plot evaluated per complete contactor phase, followed by separated plot representations for all individual contact pairs.

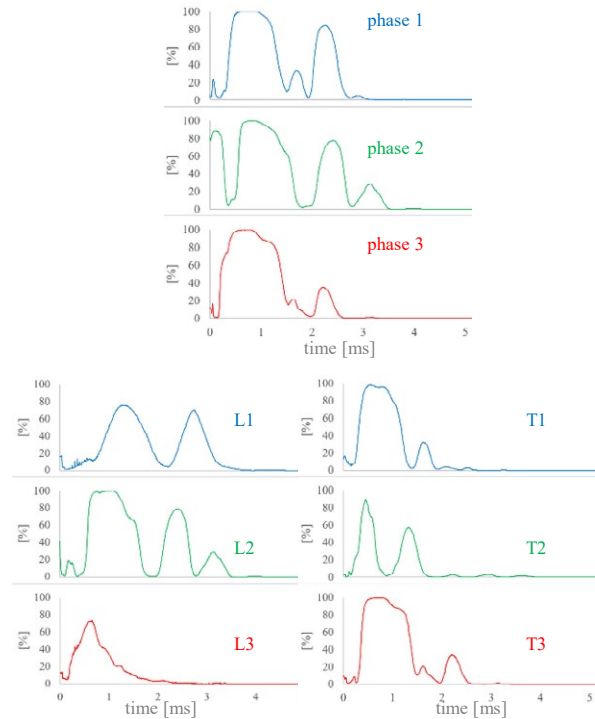


Fig. 1 Bounce probability plot per (double breaking) contactor phase and for all individual contact pairs

The single sided bounce probability in all phases reaches 100% around 1 ms after initial contact make within the particular phase and becomes 0% after 4 ms.

Splitting the probabilities up for individual contact pairs 100% is not reached any longer in all cases. Furthermore, especially contact pair L2 is showing a high probability for bounces later than 3ms after initial contact make. In contrast this probability is very low for contact T2, which is in series and therefore carrying the identical inrush current at make operation.

In accordance to [8] the energy transfer in the bounce arc W_{make} is given by:

$$W_{make} = U_{AC} \int_{t_{bounce}} i(t) dt \quad (1)$$

where U_{AC} represents the anode-cathode voltage drop, t_{bounce} the bounce time, and $i(t)$ the phase current.

Calculated arcing energies for individual L / T contact pairs within the phases and for the entire contactor phases are shown in **Table 3**

Table 3 Arcing Energies at Contact Make W_{make} [Ws]

	Phase 1	Phase 2	Phase 3
L	1.6	5.6	0.4
T	0.6	0.6	1.7
Total	2.2	6.2	2.1

Accordingly, the variation in bouncing statistics obtained for each phase's associated contact pairs accumulate to deviation in average arcing energies at contact make, that interfere with the specific contacts.

In addition, switching synchronization by using a 50 Hz control coil on the contactor, and phase sequence on contact make together with an isolated neutral need to be considered as they impact statistics and therefore plotted average values.

4 Temperature Rise Test and Contact Resistance Behavior

4.1 Temperature Rise Behavior

The temperature rise behavior of the contactors was investigated at thermal current I_{th} acc. to Table 1. The temperature was measured by thermocouples applied to the contactor terminals. In less than an hour stable temperature conditions are reached on the terminals of this device type. A full temperature cycle measurement consists of 24 one-hour cycles with dry switching in between to re-position the contacts to each other, that way increasing statistics on the temperature rise behavior by forming new a-spots. Temperatures for statistical analysis are taken in stable conditions directly before dry switching, whereby only the highest value out of the six terminal measurements is considered.

Such temperature rise test cycles are carried out in new conditions and every 200,000 operations within endurance test, leading to four measurement records in switched conditions (at $n = 1,000,000$ no temperature rise test is performed, as it is considered end of lifetime). As tests at $n = 0$ switching operations didn't reveal any differences between the different types of Ag/SnO₂, **Figure 2** is showing the statistical analysis of test results of all materials considering the four measurements in AC3 switched condition. The temperature rise represents the difference between terminal temperature and ambient temperature.

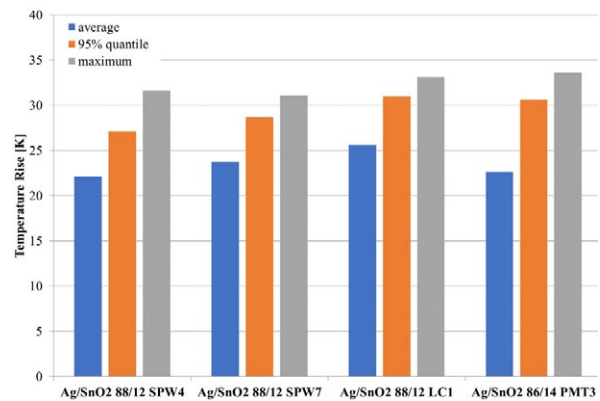


Fig. 2 Statistical temperature rise analysis on contactor terminals for different Ag/SnO₂ materials (details see text)

The absolute maximum values are on almost comparable level for all Ag/SnO₂ materials under test. On the 95% quantile level the two materials containing tungsten-oxide (SPW4 and SPW7) are insignificant lower in temperature rise compared to the others. The average values of the material containing indium-oxide (LC1) add up slightly above those of the other materials. Nevertheless, in general all materials under test seem to be on a fairly comparable level based on this type of temperature rise analysis.

4.2 Contact Resistance Behavior

Contact resistance measurements per individual contact pair were performed in parallel to above temperature rise measurements. Intention was to work out differences between the materials and to investigate contact resistance dominating effects by combining these measurements with those from arcing phenomena during AC3 endurance testing. **Figure 3** is an example for such contact resistance measurement cycles in switched condition, showing the contact resistance evolution for all six individual contact pairs over 24 hours, with a dry switching operation every hour.

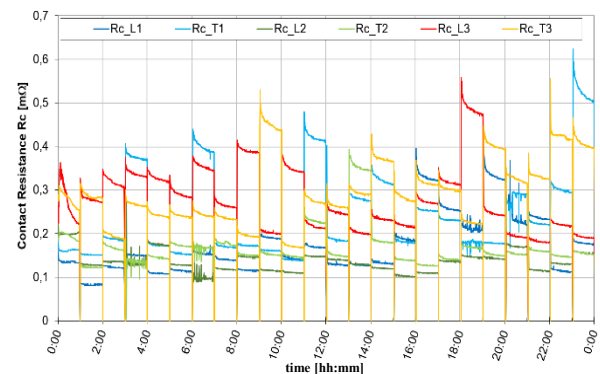


Fig. 3 Contact resistance measurement over time in switched conditions

Measured contact resistance values show significant deviation up to a factor of five, and this even within the identical contactor phase (e.g. phase 1) for individual contact pairs (L1 vs. T1). In addition, resistance values can vary strongly between consecutive single one-hour measurement cycles of identical contact pair, showing the statistical importance of such a dry switching procedure coming along with a reconfiguration of a-spots.

Contact resistances in general are declining and stabilizing over the one-hour measurement time after dry switching, along with the increasing but saturating temperature. The contact resistance values for each contact pair was stored for statistical analysis at the end of each one-hour cycle.

Combining all contact resistance measurement cycles in switched condition, a statistical analysis was carried out to compare the contact resistance performance for the different Ag/SnO₂ materials under test. **Figure 4** is comparing average, minimum and maximum values of contact resistances per contactor phase.

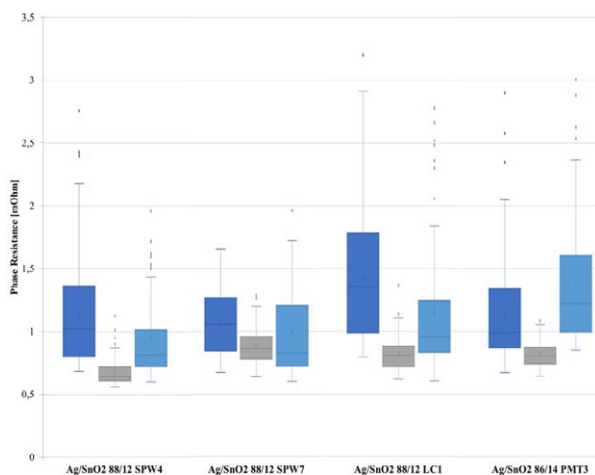


Fig. 4 Contactor phase resistance (3 parallel phases) for different Ag/SnO₂ materials in switched condition

Overall the Ag/SnO₂ materials show a rather comparable contact resistance behaviour, similar to the temperature rise test results from Figure 2. As phase resistances are plotted individually, a specific trend can be seen. Lowest average and maximum resistance values are found within phase 2 for all materials, whereas phase 2 comes along with highest arcing energies at contact make during AC3 endurance testing (see total values in Table 3, for example).

As Figure 3 showed that contact resistances may even vary drastically within the same phase, instead of phase resistance the individual resistance per contact pair will be subject to deeper analysis hereinafter. As a representative example, **Figure 5** shows the statistical analysis of contact resistance data related to specific indi-

vidual contact pair, obtained from all measurement cycles in switched conditions, for the material Ag/SnO₂ 88/12 LC1.

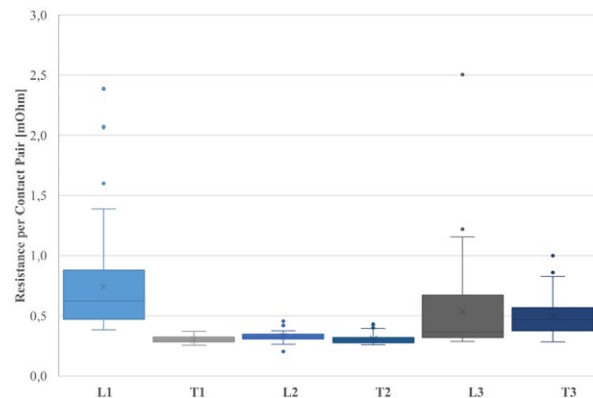


Fig. 5 Resistance per contact pair for Ag/SnO₂ 88/12 LC1 material in switched condition

In phase 2 and 3 the contact resistance values are stable and comparable within the phase, even though on a significant higher level in phase 3. Dramatic differences can be observed within phase 1, where the resistance for the L1 contact pair are more than 2 times higher compared to T1. As the differences in W_{make} for individual contact pairs are significantly smaller within phase 1 (comparable level as phase 3) than phase 2, this effect has to be withdrawn as the single root cause for low and stable contact resistances. Maybe mechanical effects driven by device design (e.g. contact normal force distribution on different phases) or effects generated by break arc need to be considered in addition.

5 Interpretation

A practical method for a combined examination of arcing energies at contact make and break, as well as their interaction with contact resistances after arcing was presented by the authors in [9]. Here, the ratio of arcing energies was applied as a basic criterion for evaluation.

This method can now be extended from arcing energies and contact resistances per phase to those of individual contact pairs, which is significantly improving the method as variances within a single phase, as shown before, can be very large.

Contact resistance measurement average and minimum values together with 95% quantiles over their corresponding ratio W_{make}/W_{break} for contact material Ag/SnO₂ 88/12 LC1 can be read from **Figure 6**. This includes measurements for all contact pairs and several contact resistance measurement sequences at different numbers of operations.

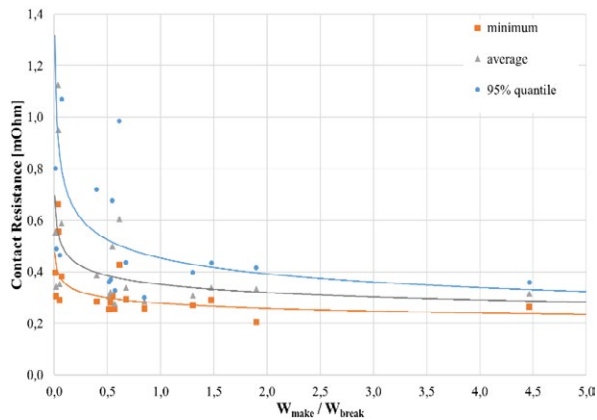


Fig. 6 Contact resistance for Ag/SnO₂ 88/12 LC1 over W_{make}/W_{break}

The trend from Figure 6 is representative for all tested Ag/SnO₂ material types. Ratios of W_{make}/W_{break} larger one, so-called make arc dominated regimes, show low and stable contact resistance values. Below a ratio of 1, in regimes dominated by break arcs, contact resistance values are scattering and show up to 4-times higher values. Therefore, to achieve low and stable contact resistances, decently high make arc energies, which are closely connected to the bouncing behaviour of the device, must come together with low arcing energies at contact break, which under AC3 are impacted by the contact opening velocity and of course synchronization effects.

Contact materials from the AC3 lifetime sequence were cross sectioned at end of the test ($n = 1,000,000$ operations) to explain the differences seen in the contact resistance values by microstructure features generated from the combine make and break arc load. As an example, Ag/SnO₂ 88/12 LC1 contacts from phase 1, providing most significant differences regarding contact resistance within a single phase (compare Fig. 5), are shown in **Figure 7** (T1) and **Figure 8** (L1), respectively.

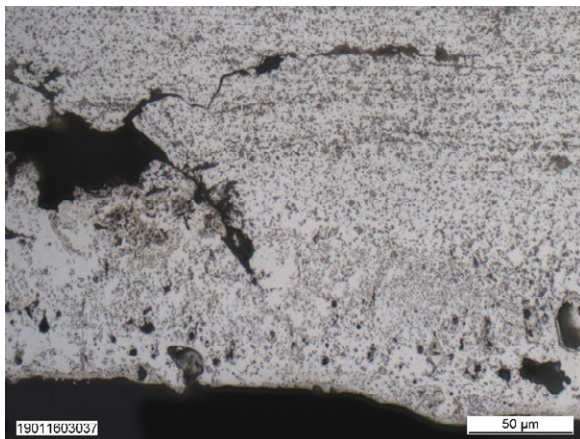


Fig. 7 Cross Section Ag/SnO₂ 88/12 LC1 after test

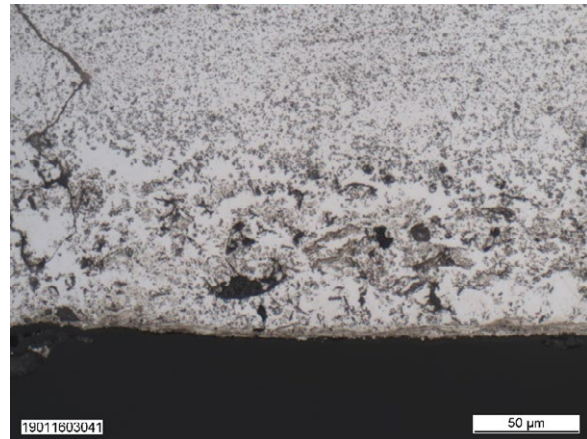


Fig. 8 Cross Section Ag/SnO₂ 88/12 LC1 after test

Both contacts show mechanical cracks from the 1,000,000 operations mechanical impact and thermo-mechanical stresses built up throughout test. The heat impacted area, estimated to a depth of around 150 μm from contact surface, is additionally providing pores from evaporated or mechanically ruptured material.

The significant differences regarding contact resistance can be explained by segregation effects that form a silver depleted and metal oxide enriched surface layer of approx. 5 μm under the arcing conditions of L1 contact pair, which can be summarized as a combination of low bounce arc energies at contact make combined with comparatively high break arc energies.

6 Summary and Conclusions

Miniaturization of switching and control devices is emphasizing their temperature rise requirements. AC3 endurance test in 45 kW contactors were performed and extended by temperature rise tests in switched condition. Different types of powder metallurgical Ag/SnO₂ contact materials (metal oxide content and types of additives) were studied regarding their temperature rise and contact resistance behavior.

Arcing energies at make and break as well as contact resistances during temperature rise test were monitored for every individual contact pair by a novel measurement approach. Significant differences between contact pairs within the same phase, regarding arcing energy loads as well as resulting contact resistances, were observed.

Compared to existing studies the performed experiments reveal not only arcing at contact make (W_{make}) is responsible for contact resistance appearing under AC3 switching, but also break arc effects need to be considered – and this for individual contact pairs within double breaking systems.

Furthermore, the ratio of arcing energies at contact make and break W_{make}/W_{break} is considered a relevant parameter for the formation of silver depleted surface layers and corresponding high contact resistances under AC3 load conditions. Here, especially break arc dominated switching regimes ($W_{make}/W_{break} < 1$) are critical.

In general, the wording “contact resistance behavior” or “contact resistance performance” should be used cautiously in relation to device tests, as boundary conditions for the contact materials may heavily vary and in many cases are even unknown.

7 Literature

- [1] Böhm, W.; Behrens, N.; Lindmayer, M.: The Switching Performance of an Improved Ag/SnO₂ Contact Material, 27th Holm Conference on Electrical Contacts, Chicago, IL, USA, 1981
- [2] Gengenbach, B.; Mayer, U.; Michal, R.; Saeger, K.E.: Investigations on the Switching Behaviour of AgSnO₂ Materials in a Commercial Contactor, 30th Holm Conference on Electrical Contacts, Chicago, IL, USA, 1984
- [3] Hauner, F.; Jeannot, D.; McNeilly, K.: Advanced AgSnO₂ Contact Materials with High Total Metal Oxide Content, 48th IEEE Holm Conference on Electrical Contacts, Orlando, FL, USA, 2002
- [4] Rieder, W.; Weichsler, V.: Make Erosion Mechanism of Ag/CdO and Ag/SnO₂ Contacts, 37th IEEE Holm Conference on Electrical Contacts, Chicago, IL, USA, 1991
- [5] Mützel, T.; Hubrich, C.: Effect of Additives on the Switching Performance of Ag/SnO₂ under AC-3 Conditions, 65th IEEE Holm Conference on Electrical Contacts, Milwaukee, WI, USA, 2019
- [6] IEC60947-1:2007: Low-voltage switchgear and controlgear - Part 1: General rules
- [7] Braumann, P.; Warwas, T.: Analyse des Einschaltvorganges von Motorschaltern für die Entwicklung von Kontaktwerkstoffen, Albert-Keil-Kontaktseminar, Karlsruhe, Germany, 1991
- [8] Braumann, P.; Koffler, A.; Schröder, K.-H.: Analysis of the interrelation between mechanical and electrical phenomena during making operations of contacts, 17th International Conference on Electrical Contacts, Nagoya, Japan, 1994
- [9] Mützel, T.; Niederreuther, R.: The Influence of Switching Arcs on Contact Resistance of Ag/SnO₂ Materials, 61st IEEE Holm Conference on Electrical Contacts, San Diego, CA, USA, 2015

Effect on Brush Electrification Mechanism Associated with Various Ag Content of Ag Graphite Brushes.

Naoki Fukuda, Yusuke Takada, Koichiro Sawa, Takahiro Ueno,
Nippon Institute of Technology, Saitama, Japan,
ueno@nit.ac.jp

Abstract

Sliding contact is a mechanism for the transfer of electrical current between stationary and moving parts. To date, slip ring systems have mainly been used to provide the excitation mechanism required by turbine generators. However, more diverse systems are now needed in the current clean energy setting. For example, the slip ring systems used in wind power generators must operate at low temperatures. In contrast, automotive alternators operate at high temperatures. Moreover, slip ring systems are also used in applications that require the transmission of electrical signals, such as radar antennae and computed tomography. In such cases, silver (Ag)–graphite brushes and noble metal slip rings are often used, because they are regarded as effective at reducing contact voltage drop, even in harsh environments.

In this study previously, a 20-hour slide experiment to determine the contact voltage drop and amount of wear characteristics of Ag-graphite brushes and silver – gold (Ag – Au) slip rings was reported.

In the present paper, contact voltage drop – brush current (V-I) characteristic tests were conducted using Ag – graphite brushes (Ag content of the coating were 50, 70, and 90 wt%), and noble metal-coated slip rings (plated with silver and gold) to determine the electrical effects of contact voltage drop. The V-I characteristics revealed linearity in all the silver content brushes.

1 Introduction

Sliding contacts enable the transfer of electrical current between stationary and moving conductors. Commonly used sliding contact arrangements include the brush and commutator system used in direct current (DC) machines, and the brush and slip rings system used in alternating current (AC) machines [1]. Recently, silver (Ag)–graphite brushes and noble metal-plated slip rings – which are effective in reducing contact voltage drop – have attracted a great deal of attention. However, their sliding contact and energization characteristics remain unclear.

In this study previously, in order to clarify the contact voltage drop characteristics (electrical characteristics) and brush wear characteristics, sliding experiments with Ag-graphite brushes (Ag contents 50, 60, 70, 80, and 90 wt%) and noble metal-plated slip rings (silver and gold (Ag – Au)-plated) were conducted. The brush current was 9.6 A, the sliding time was 20 h, and the brush had negative polarity. The experiments revealed the characteristics shown in **Figure 1**. Doing this, it was concluded that the optimum Ag content of the

brush for the effective reduction of contact voltage drop and resistance to brush wear is 60% – 80% [2].

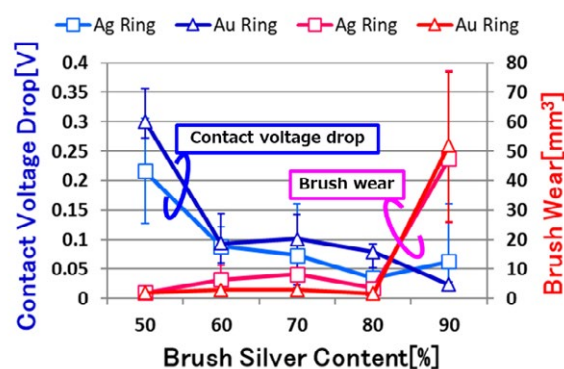


Fig. 1 Relationship between brush wear and contact voltage drop during the operation of silver (Ag) and gold (Au) slip rings and Ag – graphite brushes.

This time mainly, dominant factor to the contact voltage drop characteristics (electrical characteristics) shown in Figure 1. was discussed. Therefore contact voltage drop-brush current (V-I) tests were conducted to understanding electrical characteristics of noble metal-coated slip rings. The V-I characteristic is an important indicator to consider the temperature rise be-

tween the slip ring and the brush due to the brush current, and determines the reliability of the brush performance.

This paper shows the results of the V-I test of Ag-graphite brushes (Ag content 50, 70 and 90 wt%) and noble metal-coated slip rings (Ag-Au plating). As a result, the V-I characteristics were found to be linear, regardless of the Ag content of the brush. Also, the sliding surface temperature was estimated from contact voltage drop of V-I characteristics using $\phi-\theta$ theory. As a result, it was considered that the relationship between the heat of the brush current and the electrical characteristics was small. Therefore, the electrical characteristic of noble metal-coated slip rings was concluded that greatly affected by the inclusions between the brush and the slip ring. Finally, brush current allowance values in Ag-Au slip ring were estimated.

2 Conditions and Methods

2.1 Experimental Circuit

The sliding contact experimental apparatus is shown in **Figure 2**. The slip ring was driven by a three-phase induction motor with an inverter. The current from a DC power supply flowed through the positive brush and slip ring to the negative brush.

During the sliding tests, the contact voltage drop between the slip ring and the negative brush was recorded with a pen recorder and LabVIEW software using the circuit between the negative and auxiliary brushes.

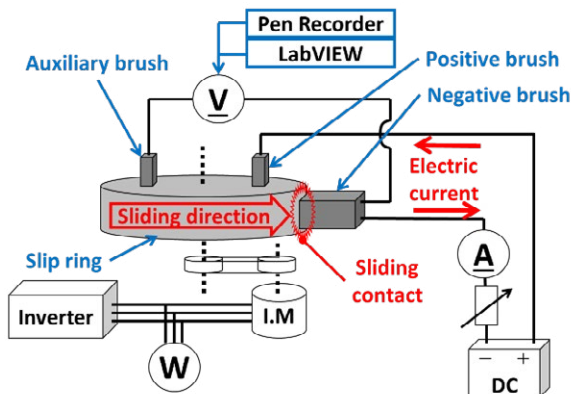


Fig. 2 Experimental circuit.

The brush and slip ring used are schematically represented in **Figure 3**. The slip ring was 100 mm in diameter and 20 mm thick. The negative brush was 10 mm high, 16 mm wide, and 36 mm long. The contact area was 160 mm².

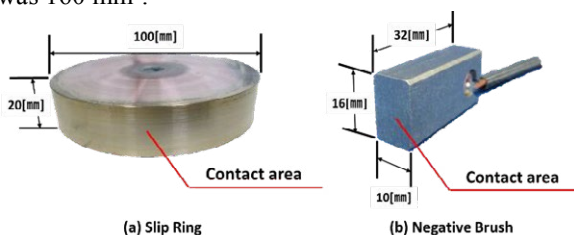


Fig. 3 Dimensions of the brush and slip ring.

2.2 Experimental Conditions

The experimental conditions are shown in **Table 1**. The Ag slip ring was plated with a 100- μ m-thick coating of silver, and the Au slip ring was plated with a 10- μ m-thick coating of gold. The graphite brushes were coated with Ag-graphite composites with silver contents of 50, 60, 70, 80, and 90 wt%.

Before each test, the surface of the negative brush was polished with #400 and #600 emery paper, and the slip ring was polished with a rubber stone. The pressure was adjusted to match the spring constant of the brush (2.45 N/cm²). The temperature of the room was maintained at 20°C using an air conditioner. The brush current changed from 0 to 30 A in steps of 5 A. The sliding speed of the slip ring was 2.67 m/s, and the sliding duration was 45 min.

Table 1 Experimental conditions.

Brush Current	0 – 30A
Sliding Time	45min (1min/Step)
Sliding Speed	2.67m/sec
Brush Pressure	2.45N/cm ²
Atmospheric Temperature	20°C(About 50% RH)
Test Brush	Silver Graphite Brush (Silver Content 50,70,90 wt%)
Test Slip Ring	Silver (100 μ m Coating) Gold (10 μ m Coating)
Surface Treatment	Brush: Emery Paper #600 Slip Ring: Rubber Stone
Polarity	Negative

2.3 Experimental Process

The experimental process is represented in **Figure 4**. First, the sliding surfaces of the brush and slip ring were polished. Next, the brush and slip ring were allowed to slide over each other for 6 h. At that point, the brush current was 9.6 A, the sliding speed was 2.67 m/s, the brush pressure was 2.45 N/cm², the brush had negative polarity, and the atmospheric temperature was 20°C.

Subsequently, a V-I characteristic test was conducted. In the V-I characteristics test, the brush current increased and decreased from 0A to 1A, 2A, 5A, after that, up to 30A, as shown in **Figure 5**. Each brush current changed every minute. The brush current increased and decreased three times in a row. The contact voltage drop at this time was recorded.

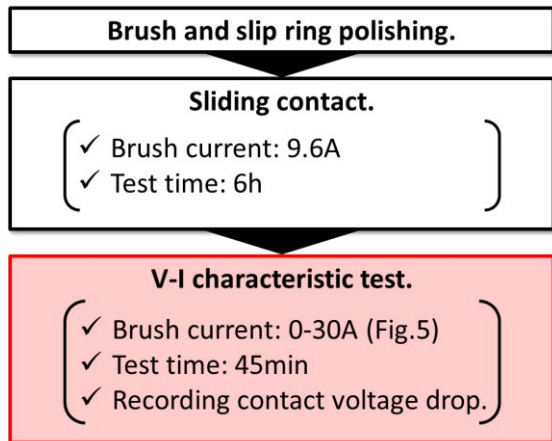


Fig. 4 Experimental process.

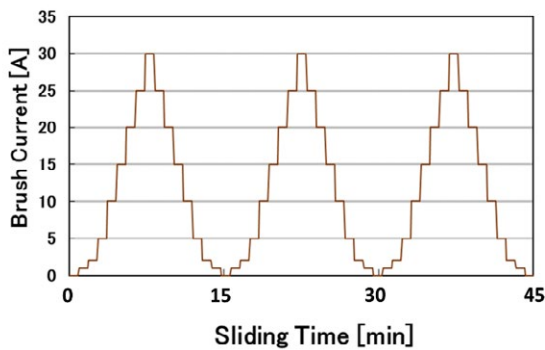


Fig. 5 Change in brush current over time.

3 Experimental Results

3.1 Change in Contact Voltage Drop Over Time

The change in the contact voltage drop with a changing brush current over time is shown in Figure 6 [3]. The solid lines represent the Ag slip ring and the broken lines represent the Au slip ring. The Ag and Au slip rings exhibited similar trends, with little differences in the contact voltage drop. The contact voltage drop was highest in the case of the 50% Ag brush, and the fluctuation range was wide. In contrast, the contact voltage drop was lowest in the case of the 90% Ag brush, and the fluctuation range was narrow.

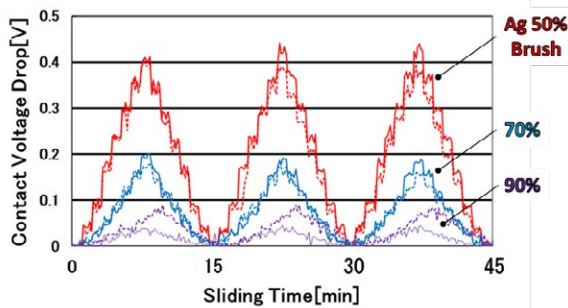


Fig. 6 Change in contact voltage drop over time.

3.2 V-I Characteristics

The V-I characteristics are shown in Figure 7 [3]. The solid lines represent the Ag slip ring and the broken lines represent the Au slip ring. In the brush current region of 0–30 A, the V-I characteristics of both the Ag and Au slip rings exhibited linearity with all the Ag brushes.

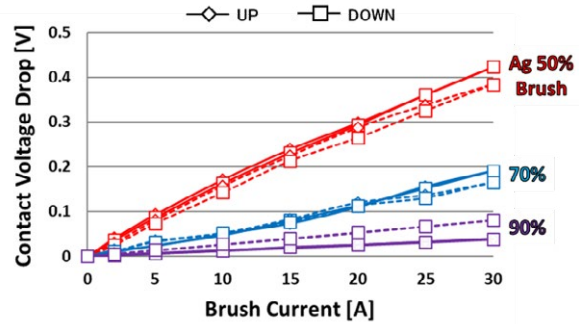


Fig. 7 Contact voltage drop–brush current (V-I) characteristics.

4 Discussion

4.1 Relationship between softening of Slip Ring by Brush current and linearity of V-I characteristics.

Figure 7 shows that the brush current and the contact voltage drop were proportional. This means that there was no extreme expansion (or reduction) of the a-spot with increasing (or decreasing) brush current. This suggests that softening of the brush and slip ring material due to the heat generated by the brush current was unlikely in the brush current range 0–30 A.

In general, the melting point of Ag is approximately 1233.95 K, and the melting point of Au is approximately 1336.15 K [4].

Next, the maximum temperature between the brush and the slip ring was estimated based on the V-I characteristics (Figure 6) using ϕ - θ theory (equation (1)). [5].

$$\theta_{max} = \left(\frac{V_c^2}{4L} + 300^2 \right)^{\frac{1}{2}} \dots \dots \dots (1)$$

where, V_c is the contact voltage drop and L is the Lorenz number ($= 2.4 \times 10^{-8} [K/V]^2$).

The results are shown in Figure 8. The solid lines represent the Ag slip ring and the broken lines represent the Au slip ring.

When the brush current was 30 A, the maximum temperature of the Au slip ring was 1276 K and the maximum temperature of the Ag slip ring was 1399 K with a 50% Ag brush. These temperatures exceed the melting points of Au and Ag. Therefore, it was expected that the V-I characteristics would soon be saturating due to the softening of the slip ring and the easy expansion of the a-spot. In the case of the 70% Ag brush, the

maximum temperature of the Au slip ring was 612 K and the maximum temperature of the Ag slip ring was 686 K, and in the case of the 90% Ag brush, the maximum temperature of the Au slip ring was 397 K and the maximum temperature of the Ag slip ring was 325. These temperatures were below the melting points of Au and Ag. Therefore, it is to be expected that even if the brush current had been further increased, the contact voltage drop would probably have increased linearly for a while.

Therefore, brush and slip ring softening is unlikely in the maximum temperature range of 300–1399 K (brush current 0–30 A) and it is considered that difficult to increase (or decrease) the a-spot. This suggests that the a-spot is approximately constant for change of brush current.

Furthermore, according to Ohm's law, the contact voltage drop is determined by the product of the contact resistance values as approximate constant and the brush current value as variable. Therefore, it is considered that V-I characteristics showed a linear.

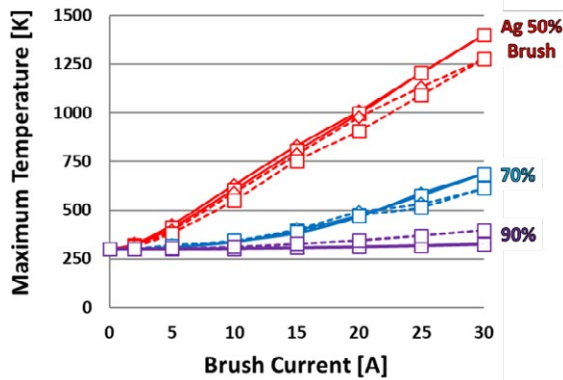


Fig. 8 Relationship between the maximum temperature and the brush current.

Furthermore, Ag and Au have low ionization tendencies and are difficult to oxidize. Therefore, an oxide film is also unlikely to affect the contact voltage drop characteristics.

In summary, the characteristics shown in Figure 1 (at a brush current of 9.6 A) are thought to be largely due to inclusions between the brush and slip ring (carbon (C) film and Ag powder from the brush).

4.2 Effect of Inclusions Between the Brush and Slip Ring

Figure 9 shows photographs and micrographs of the slip ring surface after contact for 20 h [6]. There was little difference between the characteristics of the Ag and Au slip rings, so only evaluated with Au slip ring. Black, streak-shaped C films were visible on the slip ring surfaces of the 50%–80% Ag brushes. The C films became thinner as the Ag contents of the brushes increased. In contrast, in the case of the 60%–90% Ag brushes, Ag powder formed on the slip ring surface. Furthermore, the thickness of the Ag powder tended to increase as the Ag contents of the brushes increased.

Next, the inclusions between the brush and the slip ring during the slide was investigated, based on the change in the contact voltage drop over time (Figure 10) [6]. The contact voltage drop of each Ag brush is the average of three values. The contact voltage drop values were lower than the voltage drop values owing to the bulk resistance of each Ag brush.

The contact voltage drop increased for approximately 10 h from the start of sliding with a 50% Ag brush, and the contact voltage drop also gradually increased from start to finish with 60%–80% Ag brushes. These results suggest that a C film formed on the slip ring surface, i.e., C intervened between the brush and the slip ring.

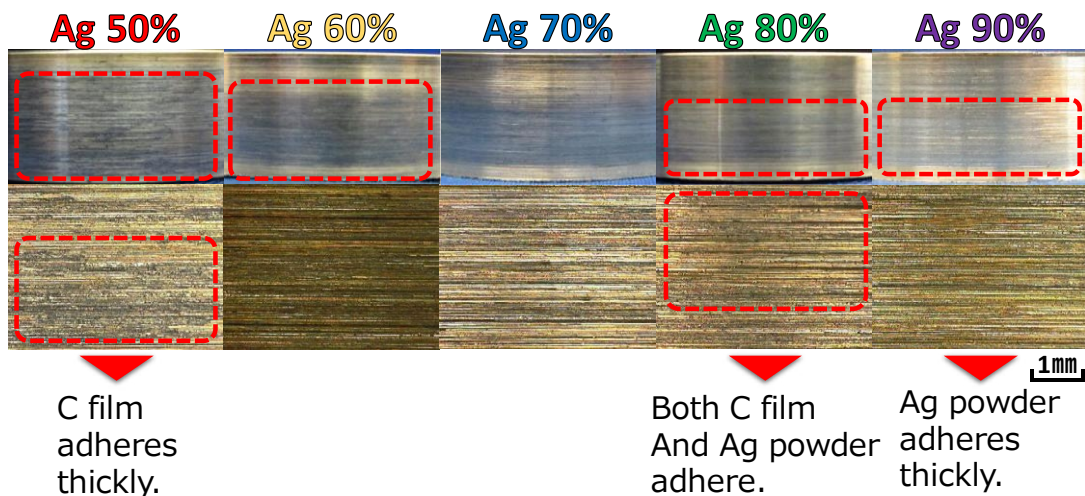


Fig. 9 Photographs and micrographs of the slip ring surface after contact 20h.

Therefore, C is considered to have prevented direct metal-to-metal contact (brush material to slip ring material)[7][8], and reduced the adhesive wear of the brush. The contact voltage drop also increased owing to the resistance of C.

However, in the case of the 90% Ag brush, there were no fluctuations in the contact voltage drop from start to finish. This suggests that the Ag powder ground the C film formed on the slip ring surface. As a result, the brush and slip ring material came into direct contact, resulting in chronic adhesive wear[7][8]. Therefore, wear to the 90% Ag brush increased rapidly, and the contact voltage drop decreased.

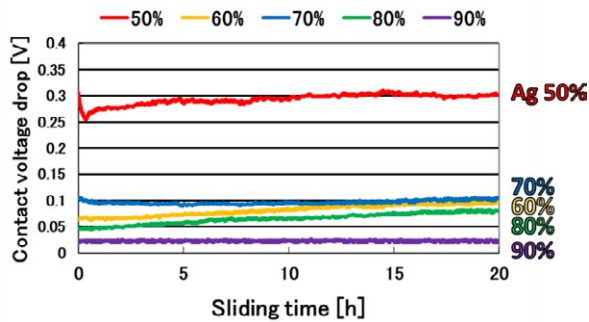


Fig. 10 Change of contact voltage drop with sliding time.

4.3 Estimation of the Brush Current Allowance for the Ag and Au Slip Rings

The brush current allowance values for the Ag and Au slip rings was estimated based on the relationship between maximum temperature and the brush current. (Figure 8). The results are shown in Figure 11. The horizontal axis presents logarithmic values.

The values from 0 to 30 A were actually measured. The values above 30 A were estimated by extrapolating from the 0–30 A values. The solid lines represent the Ag slip ring and the broken lines represent the Au slip ring.

In the case of the 50% Ag brush, the brush current allowance values were estimated to be 30 A for the Ag slip ring and 35 A for the Au slip ring.

In the case of the 70% Ag brush, the brush current allowance values were estimated to be 65 A for the Ag slip ring and 85 A for the Au slip ring.

In the case of the 90% Ag brush, the brush current allowance values were estimated to be 840 A for the Ag slip ring and 250 A for the Au slip ring.

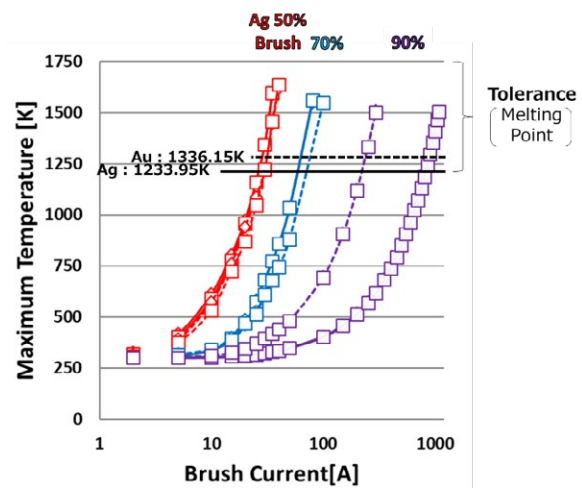


Fig. 11 Estimates of the brush current allowance values for the silver (Ag) and gold (Au) slip rings.

5 Summary

The conclusions from the present study can be summarized as follow:

- I. Both the Ag and Au slip rings exhibited similar trends, with little difference in the contact voltage drop. Moreover, the V-I characteristics of both the Ag and Au slip rings exhibited linearity.
- II. The contact voltage drop and brush wear characteristics at a brush current of 9.6 A (Figure 1) were greatly affected by inclusions between the brush and slip ring (C film and Ag powder from the brush).
- III. In the case of the 50% Ag brush, the C film prevented direct metal-to-metal contact, and suppressed the adhesive wear of the brush. However, the contact voltage drop increased. In contrast, in the case of the 90% Ag brush, the amount of brush wear increased because the brush and slip ring material were in direct contact with each other, and the contact voltage drop decreased.
- IV. The allowance values of the brush current were estimated to be 30–35 A for the 50% Ag brush, 65–85 A for the 70% Ag brush, and 250–840 A for the 90% Ag brush.

6 Acknowledgement

We thank Frank Kitching, MSc., from Edanz Group (www.edanzediting.com/ac) for editing a draft of this manuscript.

7 Literature

- [1] Toshinobu Ichiki: Theory and Actual of for Electric Machinery Brush. CORONA PUBLISHING CO.,LTD.: 1978
- [2] N. Fukuda: K. Sawa: T. Ueno: Contact Voltage Drop and Brush Wear Characteristics for Various Silver Content of the Silver Graphite Brush in Slip Ring System. IEEE Holm Conference on Electrical Contacts 2018, pp.521-525
- [3] N. Fukuda: Y. Takada: Y. Machida: A. Maruyama: K. Sawa: T, Ueno: V-I Characteristics in Silver Graphite Brush and Noble Metal Slip Ring. IEICE Society 2019, Electronics Lecture Proceedings2, p.2
- [4] The Japan Institute of Metals and Materials: Metal data book. 4th ed.: Maruzen Publishing Co., Ltd., p.11, 2004
- [5] R. HOLM: Electric Contacts Theory and Applications, 4th ed.: Springer, §13, 1967 pp.60-64
- [6] N. Fukuda: Y. Takada: R. Higa: K. Sawa: T. Ueno: Brush Wear Characteristics for Various Silver Content in Sliding Contact of Silver Graphite Brush and Noble Coated Slip Ring, IEICE Journal. (2015) Vol. J102-C No.6, pp.222-244
- [7] C. Holzapfel: P. Heinbuch: S. Holl: Sliding electrical contacts: Wear and electrical performance of noble metal contacts. IEEE Holm Conference on Electrical Contacts 2010, pp.543-550
- [8] E. Rabinowicz: S. W. Webber: The formation of frictional polymers on noble metal surfaces. Proc. 11th ICEC 1982, pp. 98-102

Electrical and mechanical wear of a graphite brush having varying silver content in a slip-ring system

Takahiro Ueno, Naoki Fukuda, Koichiro Sawa Nippon Institute of Technology, Saitama, Japan, ueno@nit.ac.jp

Abstract

The environments in which electrical brushes are used have become increasingly severe; e.g., wind turbine generators and automotive alternators. Furthermore, the brush–slip-ring system used for an electrical signal such as that of a radar system and that of computed tomography must have stable conductivity. Silver–graphite brushes and noble-metal slip rings with excellent conductive performance are therefore used. However, brush wear characteristics have not yet been determined for different silver contents of the silver–graphite brush. The present study conducted a sliding test using silver graphite brushes (with silver contents of 50, 60, 70, 80, and 90 wt%) and gold-coated slip rings, under a brush current of 9.6 A. Brush wear increased largely between silver contents of 80% and 90%. We applied the brushes with silver contents of 80 and 90 wt% and a copper slip ring under brush currents of 0 A, 10 mA, and 9.6 A and compared the wear characteristics of the two brushes. At a brush current of 9.6 A, the ratio of mechanical to electrical wear was about 1:2 for the 80% silver brush and about 3:1 for the 90% silver brush. In addition, it was found that brush wear was almost the same regardless of current flow in the sliding of a gold-plated slip ring and silver–graphite brush.

1 Introduction

A sliding-contact mechanism supplies a current from a stationary object to a rotating object. Generally, a slip-ring system is adopted to provide this mechanism. We therefore investigate the material wear and electrical properties of brush and slip-ring systems. Previous studies used copper as the slip-ring material. In the present study, we conducted a sliding test using silver–graphite brushes and a gold-coated slip ring. Few sliding tests have been conducted using a combination of a noble-metal slip ring and a silver–graphite brush [1][2][3][4].

The present paper reports on a sliding experiment conducted to investigate the amount of brush wear when using a gold-coated slip ring under the conditions of an energized state and non-energized state. Furthermore, the relationship between the silver content of the brush and brush wear is discussed.

2 Experimental Procedures and Conditions

2.1 Experimental Circuit and Process

Sliding contact was realized using the sliding test apparatus shown in **Figure 1**. The slip ring was driven by an induction motor with an inverter. The frictional coefficient was calculated by measuring the active power of the electric motor. In this experiment, the frictional coefficient was determined by the following equation.

$$\mu = \frac{W - W_0}{g \times n \times P \times N} \quad (1)$$

μ : Coefficient of Friction
 W : Motor Input Power with Test Brush
 W_0 : Motor Input Power without Test Brush
 g : 9.8m/sec²
 n : Number of Brushes
 P : Brush Pressure kg
 N : Sliding Speed m/sec

During a sliding test, the contact voltage drop between the slip ring and test brush was measured with LabVIEW software. The brush wear was measured as the weight difference before and after a sliding test. The shapes of the brush and slip ring used in the test are shown in **Figure 2**. The brush was 10 mm high, 16 mm wide, and 32 mm long. The slip ring was 20 mm thick and 100 mm in diameter. The contact area was 160 mm².

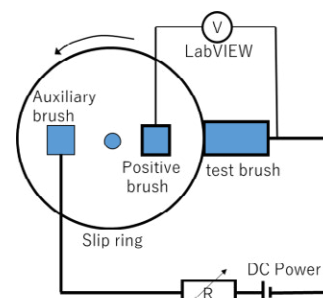
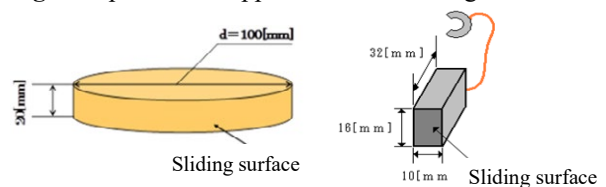


Fig. 1 Experimental apparatus in the sliding test



(a) Slip ring (b) Brush
Fig. 2 Schematic illustrations of the slip ring and brush

2.2 Experimental Conditions

The experimental conditions are given in **Table 1**. The slip ring was plated with a 10- μm -thick coating of gold. The graphite brushes were coated with silver-graphite composites with silver contents of 50, 60, 70, 80, and 90 wt%. Before each sliding test, the surface of the test brush was polished with #600 emery paper, and the slip ring was polished with a rubber stone. A spring coil provided brush pressure of 2.45 N/cm². A direct-current power supply generated brush current of 9.6 A. The sliding speed was 2.67 m/s while the sliding time was 20 h.

Table 1 Experimental conditions

Brush Current	0A, 9.6A
Sliding Time	20h
Sliding Speed	2.67m/sec
Brush Pressure	2.45N/cm ²
Test Brush	Silver Graphite Brush (Silver Content 50, 60, 70, 80, 90 wt%)
Test Slip Ring	Gold (10 μm Coating)
Surface Treatment	Brush: Emery Paper #600 Slip Ring: Rubber Stone
Polarity	Negative

3 Experimental Results

3.1 Characteristics under Energizing Conditions

This section describes brush wear characteristics, contact voltage drop characteristics, and frictional coefficient characteristics under the condition that current is applied [4].

3.1.1 Characteristics of the Brush Wear Length

Figure 3 shows the brush wear length characteristics for the brushes with various silver contents. The 90% silver brush showed a large amount of wear about 0.3 mm long. Conversely, brushes with 80% to 50% silver content showed little wear.

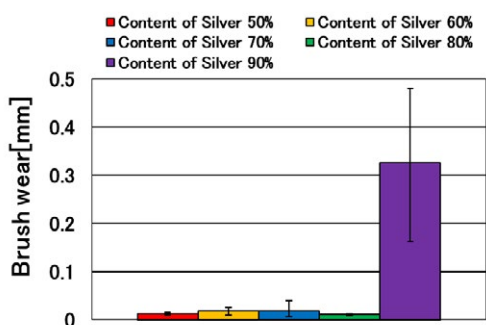


Fig. 3 Brush wear characteristics for brushes having various silver contents

The wear amount of the 90% silver brush was about 30 times that of the 80% silver brush. When the silver content of the brush was 80% or less, there was little change in brush wear with the silver content.

3.1.2 Relation between the Brush Wear and Contact Voltage Drop for Brushes Having Various Silver Contents

Figure 4 shows the change in the contact voltage drop relative to the experiment time. In this paper, we investigate using the average contact voltage drop for 5 hours before the end of the experiment.

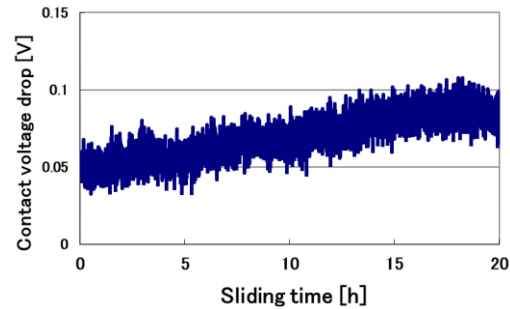


Fig. 4 Contact voltage drop relative to the experiment time (Silver content 80% brush)

Figure 5 shows the relationship between the brush wear amount and the contact voltage drop.

The brush wear suddenly changed between brush silver contents of 80% and 90%. In addition, the 50% silver brush showed little wear but had a large drop in contact voltage.

The contact voltage drop was higher for the 50% silver brush than for the other brushes. Meanwhile, the contact voltage drop was a low value of no more than 0.1 V for brushes having a silver content of 60% or more. This result reveals a trade-off relationship between the brush wear and contact voltage drop.

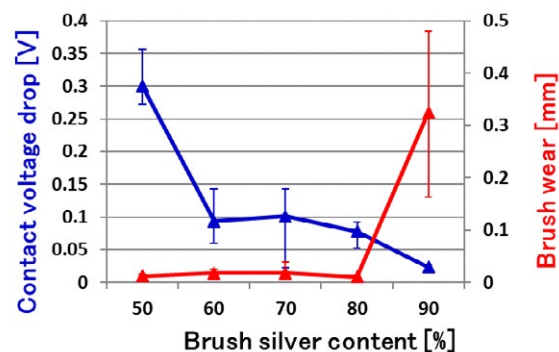


Fig. 5 Relationship between the contact voltage drop and brush wear length for various brushes

3.1.3 Relationship between the Brush Wear Length and Frictional Coefficient for the Condition of Current Flow

Figure 6 shows the relationship between the brush wear length and frictional coefficient. The brush wear

length was 0.3 mm for the 90% silver brush. However, the coefficient of friction tended to be lower for the 80% and 70% silver brushes. The frictional coefficient and brush wear length thus had a nonlinear relationship.

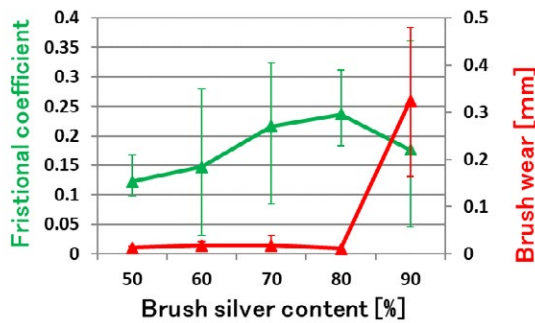


Fig. 6 Relationship between the brush wear length and frictional coefficient

3.2 Characteristics under Non-energizing Conditions

This section describes various characteristics of the sliding of the gold-coated slip ring and the silver-graphite brush in the non-energized state.

3.2.1 Characteristics of the Brush Wear Length under the Condition of No Current

Figure 7 shows characteristics of the brush wear length for brushes having various silver contents under the condition of no current flow. It is seen that wear sharply increased for the 90% silver brush under this condition. Furthermore, the wear length of the brush was almost equal to that when current was applied.

Conversely, brushes with silver contents ranging from 80% to 50% showed little wear. The wear amount of the 90% silver brush was about 30 times that of the other brushes.

The above results show that the use of a gold ring hardly causes electrical abrasion due the current supply.

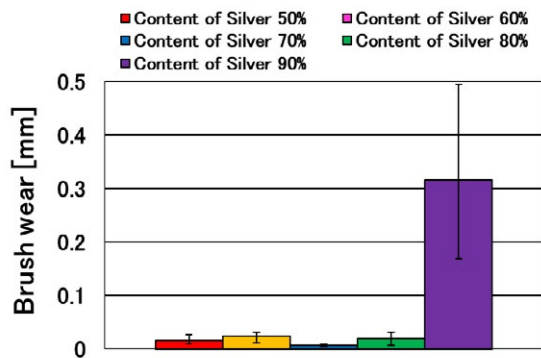


Fig. 7 Wear characteristics of brushes having various silver contents under the condition of no current

3.2.2 Relationship between the Brush Wear Length and Frictional Coefficient

Figure 8 shows the relationship between the brush wear length and frictional coefficient under the condition of no current. The wear was 0.3 mm for the 90% silver brush. However, the coefficient of friction tended to be lower than that for the other brushes. Furthermore, for all brushes, the coefficient of friction tended to be lower under the condition of no current than under the condition of current flow as shown in Figure 6.

It is seen that for the sliding of the gold ring and silver brush, there was almost no difference in the brush wear between current-energizing and non-energizing conditions.

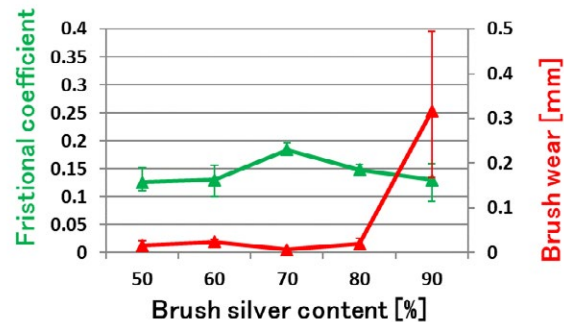


Fig. 8 Relationship between the brush wear length and frictional coefficient under the condition of no current

4. Discussion

4.1 Relationship between Brush Wear and Carbon Occupancy at the Brush Contact Surface

Figures 9 and 10 show the relationship between the carbon occupancy at the brush surface and brush wear. The horizontal axes indicate the carbon occupancy of the brush. It is seen that when the carbon occupancy was between 80% and 40%, the brush wear changed very little. However, brush wear increased sharply when the carbon occupancy fell below 40%.

It is therefore considered that the brush wear mode changes with the carbon occupancy of about 40% as a boundary regardless of whether there is a flow of current.

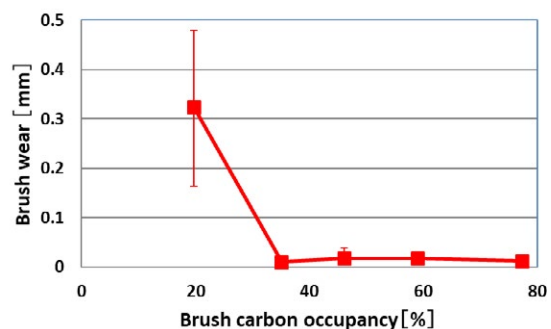


Fig. 9 Relationship between the brush wear and carbon occupancy at the brush contact surface under the condition of current flow

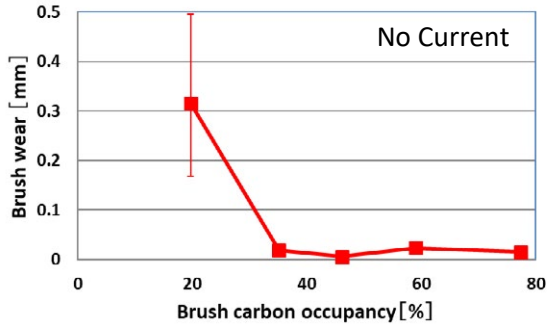


Fig. 10 Relationship between the brush wear and carbon occupancy at the brush contact surface under the condition of no current

4.2 Relationship between Brush Wear and Brush Current Conditions

Figure 11 compares brush wear between the conditions of current flow and no flow. The 90% silver brush had a high wear rate under both conditions. Abrasion sharply increased between silver contents of 80% and 90%, and the amount of abrasion was thus compared between conditions in this range.

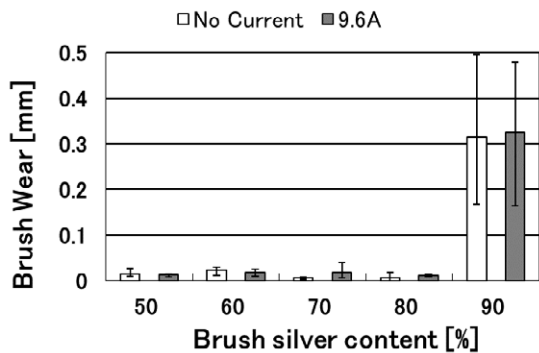


Fig. 11 Relationship between the brush wear and condition of current flow

Figures 12 and 13 compare the wear amount between 80% and 90% silver brushes.

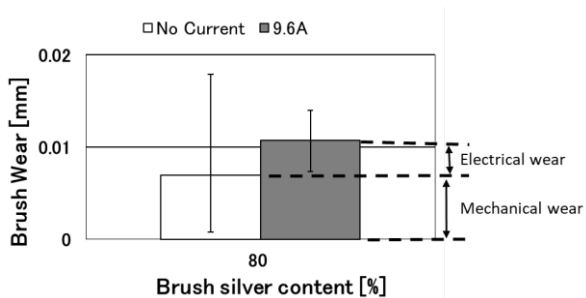


Fig. 12 Relationship between the brush wear and current condition when using a gold-plated slip ring (80% silver brush)

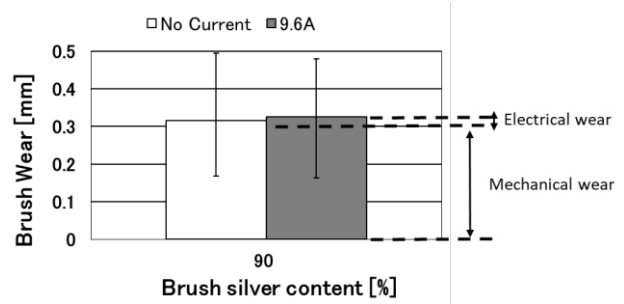


Fig. 13 Relationship between the brush wear and current condition when using a gold-plated slip ring (90% silver brush)

When the silver content was 80%, the brush wear length was an extremely small 0.01 to 0.02 mm. Furthermore, the brush wear was less during energization. The coefficient of friction was around 0.15 under the condition of no current and 0.23 under the condition of current flow.

The above results showed no clear correspondence between the coefficient of friction and the amount of wear. Meanwhile, in the case of the 90% silver brush, the wear amount was 0.3 mm, and it can be said that electric current hardly affects wear.

The results of past research on the wear characteristics of a copper slip ring and silver graphite brushes are shown in **Figure 14** [5][6][7].

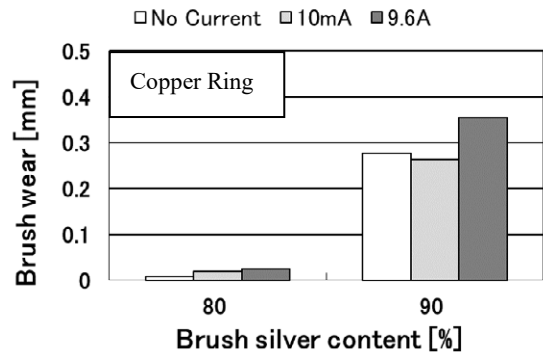


Fig. 14 Relationship between the brush wear and condition of current flow when using a copper slip ring

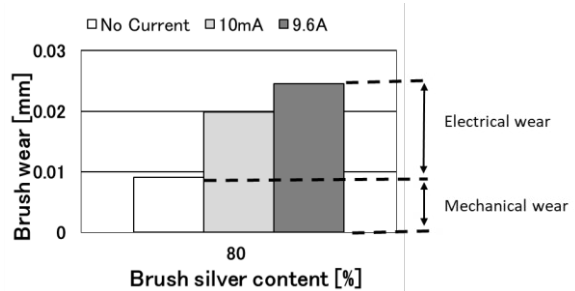


Fig. 15 Relationship between the brush wear and current condition when using a copper slip ring (80% silver brush)

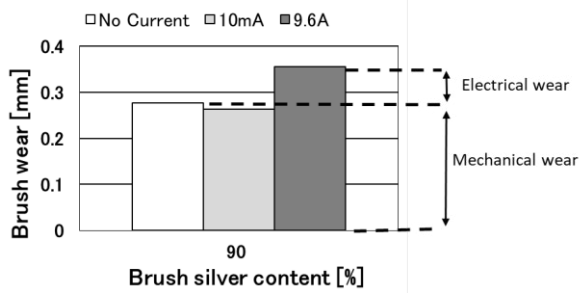


Fig. 16 Relationship between the brush wear and current condition when using a copper slip ring (90% silver brush)

Figures 15 and 16 show the ratio of electrical wear to mechanical wear.

In the case of sliding between the copper slip ring and silver graphite brush, brush wear was increased by energization. However, in the case of the 90% silver brush, brush wear due to energization was less than 80%. The ratio of mechanical wear to electrical wear was 1:2 when the silver content was 80% and 3:1 when the silver content was 90. These results show that the effect of energization on brush wear was extremely small in the sliding of the gold ring and silver-graphite brush.

In the case of the gold-plated slip ring, the ratio of mechanical wear to electrical wear was 1:0.5 for the 80% silver brush and 1:0.03 for the 90% silver brush; i.e., the electric effect was close to zero.

4.3 Analysis of the Sliding Surface After the Experiment

Figures 17 and 18 show the surfaces of the slip ring and brush after sliding with an applied current of 9.6 A.

Figures 19 and 20 show the surfaces of the slip ring and brush after sliding with an applied current of 0 A.

When the silver content was 80%, a thin carbon film formed on the surface of the slip ring. The surface roughness was $R_a = 1.38 \mu\text{m}$ for current of 9.6 A and $R_a = 0.56 \mu\text{m}$ for no current; i.e., the surface roughness at 9.6 A was about twice that at 0 A. A correlation between the surface roughness of the slip ring and brush wear is considered.

Meanwhile, when the silver content was 90%, a silver powder film adhered to the surface of the slip ring. The surface roughness was $R_a = 1.12 \mu\text{m}$ and $0.99 \mu\text{m}$ for energization and non-energization, respectively, which are similar values.

Brush wear can thus be reduced by setting the brush silver content to 80% or less. In addition, there is little electrical wear due to energization when a gold-plated slip ring is used.

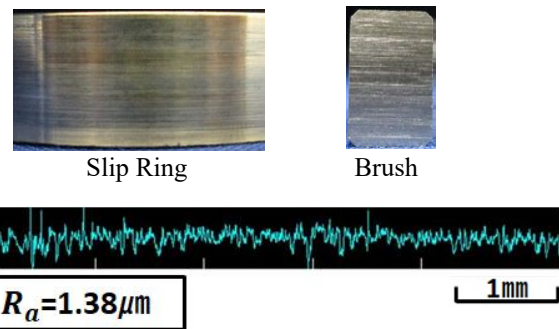


Fig. 17 Surface conditions after sliding (9.6 A, 80% silver)

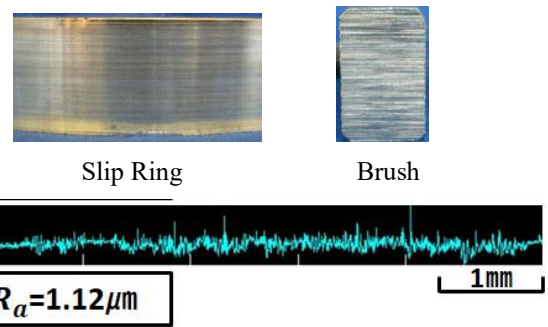


Fig. 18 Surface conditions after sliding (9.6 A, 90% silver)

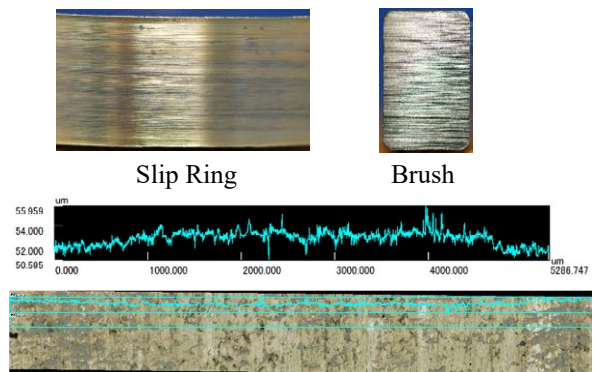


Fig. 19 Surface conditions after sliding (0 A, 80% silver)

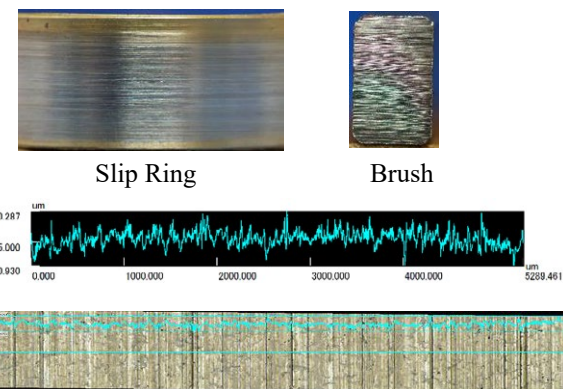


Fig. 20 Surface conditions after sliding (0 A, 90% silver)

4. Summary

The following conclusions are drawn from the results of the study.

I. In the sliding of the gold-plated slip ring and silver-graphite brush, the brush wear is hardly affected by the flow of current.

II. The brush wear mode changes with a carbon occupancy of about 40% regardless of the condition of current flow.

III. In the sliding of the 90% silver brush and gold-plated slip ring, the surface roughness of the slip ring and the amount of wear of the brush were hardly affected by the flow of current.

6 Acknowledgement

We thank Edanz Group (www.edanzediting.com/ac) for editing a draft of this manuscript.

7 Literature

- [1] Toshinobu Ichiki "Theory and Practice of Carbon Brushes", CORONA Publishing Co.,LTD. 1978
- [2] Erle I. Shobert II "CARBON BRUSHES" Chemical Publishing Company, Inc. 1965
- [3] Naoki Fukuda "Contact Voltage Drop Behavior in a Noble Metal Slip-Ring System with Silver-Graphite Brushes" ICEC2016, Edinburgh, (2016), No.06-05
- [4] Takahiro Ueno "Effect of the Content of an Ag/C Brush on the Contact Voltage Drop and Brush Wear of the Sliding Contacts Between a Silver-Coated Slip Ring and the Ag/C Brush" IEICE Journal, (2015), Vol. J98-C No.12 pp.478-480
- [5] Naoki Fukuda , Koichiro Sawa ,Takahiro Ueno, Contact Voltage Drop and Brush Wear Characteristics for Various Silver Content of the Silver Graphite Brush in Slip Ring System, 2018 IEEE Holm Conference on Electrical Contacts, 18396953, (2018),pp.521 - 525
- [6] Z.L. Hu, Z.h. Chen, J.T. Xia "Study on surface film in the wear of electrographite brushes against copper commutators for variable current and humidity" Wear 264, (2008),Issues1-2, pp.11-17
- [7] I.Yasae, A.Canakci, F.Arslan "The effect of brush spring pressure on the wear behaviour of copper-graphite brushes with electrical current" Tribology International 40(9), (2007), pp.1381-1386

Relationship between sliding surface roughness of slip ring and amount of brush wear in slip ring system

Yusuke Takada, Naoki Fukuda, Koichiro Sawa, Takahiro Ueno,
Nippon Institute of Technology, Saitama, Japan,
ueno@nit.ac.jp

Abstract

An electric sliding contact permits the transmission of electric power or signals from a stationary object to a moving (usually rotating) object. This mechanism is widely used in electrical equipment such as in AC generators and AC motors. However, the desire is to mitigate the abrasive resistance of the brush and improve electrical reliability. In an electric sliding contact, brushes and slip rings are used. They constitute the very important slip-ring system that is also used in large generators. Generally, steel is used for slip rings of large generators. However, little is known about characteristics of the steel slip-ring system. In this study, we investigated experimentally the influence of the roughness of the sliding surface of the steel slip ring. With the sliding surfaces of several slip rings polished with either rubber stone or emery paper of various grades, the brush wear was measured following a prescribed experiment. Our findings show that brush wear from the slip ring polished with emery paper #100 was maximal. Also, surface preparations with rubber stone and emery paper #1200 produced similar brush wear. The conclusion draw is that sliding surface roughness does affects the amount of brush wear.

1 Introduction

Electric sliding contact allows the supply of electric power and signal transmission from a stationary object to a moving object, one that is usually rotating. This mechanism is widely used in industry, for example, electric motors and generators. For direct current (DC) machines, a commutator and brush are used in the electric sliding contact; for alternating current (AC) machines, a slip ring and brush are used. In this latter instance, the slip ring and brush are generally referred to as the slip-ring system. Used for large generators, this system is an important mechanism and is designed in accordance with its usage in the environment and conditions. For low electric power, a slip ring made of noble metal is use to protect the deterioration of the signal. For high electric power, a slip ring made of steel is used so as to endure the high revolutions as well as the rapid signal excitation. With the slip ring being large in diameter, any gold or silver coating applied to the slip ring increases costs. For this reason, steel slip rings are used for large generators. However, their characteristics have not been fully clarified in the little literature that exist. We have therefore focused attention on these characteristics in this study.

Generally, the effect of roughness of the sliding surface on the amount of brush wear is significant. Furthermore, the mechanical wear without an applied current is known to be 1/100 to 1/1000 of the electrical brush wear with current.[1][2]. However, electric sliding contacts with current has not been well studied. In our study, sliding experiments were conducted using a steel slip ring and copper-graphite brush. Various slip rings of different sliding surface roughness were used. In their preparation, the sliding surfaces were polished

with either rubber stone or emery paper (EP) of different grades to examine the relationship between roughness of the sliding surface and brush wear.

2 About experiments

2.1 Experimental apparatus and circuit

In the experimental setup (Figs. 1 and 2), the slip ring was driven by a three-phase induction motor with an inverter. The brush current from the DC power supply (Constant current source) flows through the negative brush and slip ring to the positive brush. During sliding experiments, the contact voltage drop between the positive brush and the slip ring was measured using a pen recorder and Lab VIEW software while using the auxiliary brush. The active power of the induction motor was measured every 10 minutes during the first hour and hourly thereafter. The coefficient of friction was calculated using the active power of the induction motor.

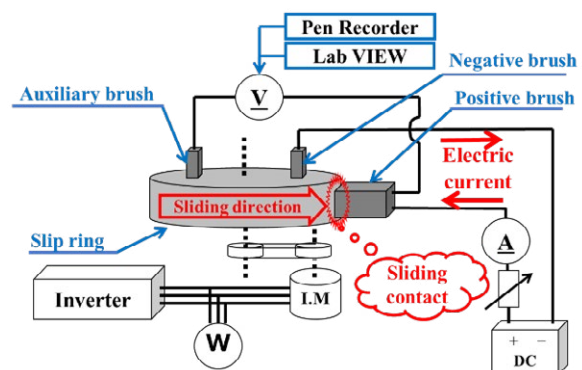


Fig. 1 Experimental apparatus and circuit with brush current of 10 A.

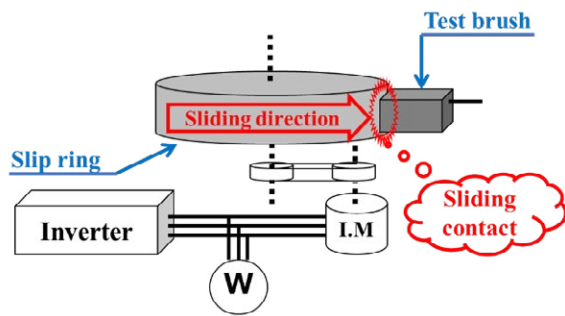


Fig. 2 Experimental apparatus and circuit with no brush current.

For each experiment, the size of the steel slip ring (Fig. 3) was 100 mm in diameter and 20 mm thick. Made of copper and graphite, the block-like brush was 16 mm high, 10 mm wide, and 35 mm long, the contact area being 1.6 cm². In addition, the copper content of brush is 70-80wt%. This copper content is commonly used for copper graphite brush. The sliding surface of the brush is curved around the circumference of the ring.

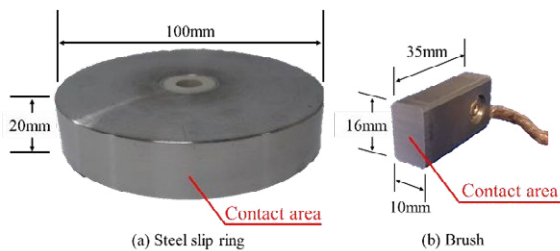


Fig. 3 Dimensions of the slip ring and brush.

2.2 Experimental conditions

Table 1 lists the experimental conditions.

Table 1 Experimental conditions

Brush Current	0[A], 10[A]
Sliding Time	Pre-operation: 5 h Main experiment: 50 h
Sliding Speed	5.24 m/s (1000 min ⁻¹)
Brush Pressure	3.92[N]
Test Brush	Copper-Graphite Brush
Test Slip Ring	Steel Slip Ring (S45C)
Surface Preparation	Brush: Emery Paper #600 Slip Ring: Rubber Stone, Emery Paper #100, Emery Paper #1200
Polarity	Positive
Atmosphere Temperature	20°C (About 50%RH)

Experimental runs consisted of using slip rings of different sliding surface roughness. The sliding surface was polished using either a rubber stone, EP #100, or EP #1200. The surface of the brush in all runs was polished using EP #600. The brush current from the DC

power supply was regulated at 10 A. The brush pressure was 3.92N (400gf). The sliding speed of the slip ring was 5.24 m/s. The duration of the sliding of the pre-operation was 5 hours and for the main experiment 50 hours. Over the course of the experiments, the room temperature was regulated by an air conditioner set at about 20°C.

3 Experimental Procedures

An outline of the experimental procedure is charted in Fig. 4. First, the surfaces of the slip ring and the positive brush were polished with a rubber stone or EP. The brush was weighed. Once inserted in the slip ring system, 5 hours pre-operation began. In addition, the pre-operation was performed at the same current value as in main experiment. After 5 hours, the apparatus was stopped, and the brush removed and reweighed. Next, the 50 hours run was performed after which the apparatus was stopped and the brush reweighed. After the experiment, we imaged the sliding surface. Also, because moisture normally adheres to the brush, we reweighed the brush after waiting 24 hours. We had decided that at various stages of the experimental procedure (before and after the 50 hours run) the condition of the brush in regard to moisture would be different. Hence, for consistency, a final weighing was delayed 24 hours for moisture to adhere to the brush.

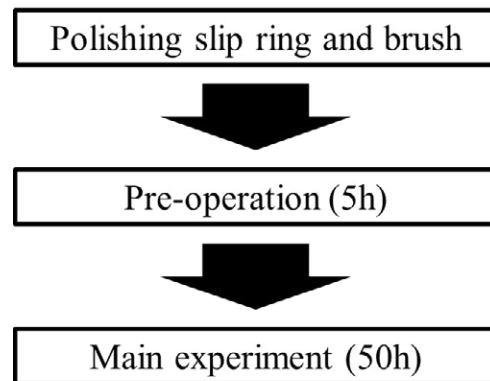


Fig. 4 Summary of experimental procedures.

4 Results

4.1 Contact voltage drop

The variation in time of the contact voltage drop was plotted for each preparation (Fig. 5). In this data, the voltage drop due to the brush bulk resistance is subtracted. Polishing the sliding surface with rubber stone or EP #1200 yielded little fluctuation in the contact voltage drop during the 50 hours experiment. In addition, the values of the contact voltage drop were about 0.3 V. Polishing with EP #100, produced an increase in the contact voltage drop throughout the running of the 50 hours experiment.

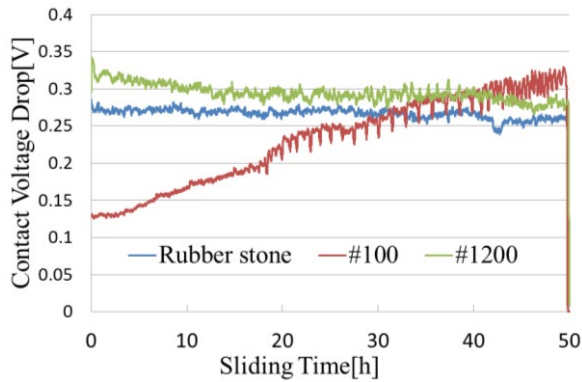


Fig. 5 Change over time of the contact voltage drop.

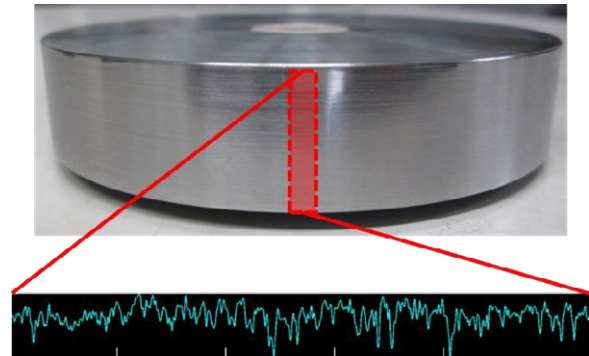


Fig.7 Measurement points of slip ring.

4.2 Brush wear sustained on each run

The amount of brush wear after 50 hours of sliding without a current (Fig. 6) was greatest for the surface polished using EP #100. Furthermore, the amount of that with EP #1200 was almost non-existent. With a 10-A current, the amount of brush wear was again greatest for the surface polished using EP #100; using rubber stone and EP #1200 gave similar values.

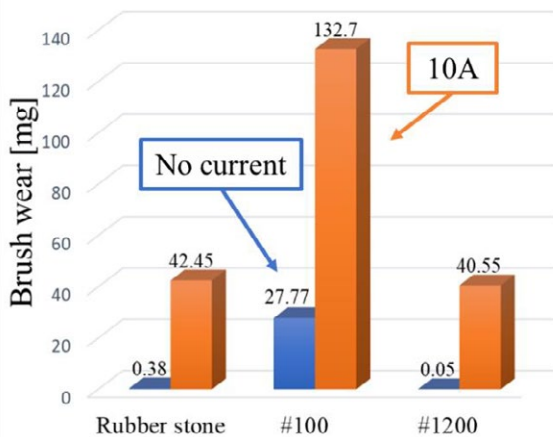


Fig. 6 Brush wear from sliding surfaces of different preparations for brush currents of 0 A and 10 A.

5 Discussions

5.1 Relationship between brush wear and roughness by brush current

We next conducted experiments with slip rings for which the sliding surface had different roughness. Before the experiment, we measured the roughness of the sliding surfaces using a laser microscope. In addition, the measurement points of the slip ring by the laser microscope is shown in Fig.7.

The relationship between the amount of brush wear and roughness of the sliding surface of slip ring are shown in Figs. 8 and 9, the former with a brush current of 10 A and the latter without a brush current applied.

With a brush current of 10 A, the roughness from EP #100 was also greatest, as for the brush wear. From polishing with rubber stone and EP #1200, there was a difference of about 0.2 μm in roughness, but the brush wear was seen to be only slight. Therefore, for a brush current of 10 A, there is a correlation between the amount of wear and roughness.

In the absence of a brush current, polishing with rubber stone and EP #1200 produced a difference of about 0.1 μm in roughness. In both instances, the amount of wear differed greatly, although there was no significant difference in roughness.

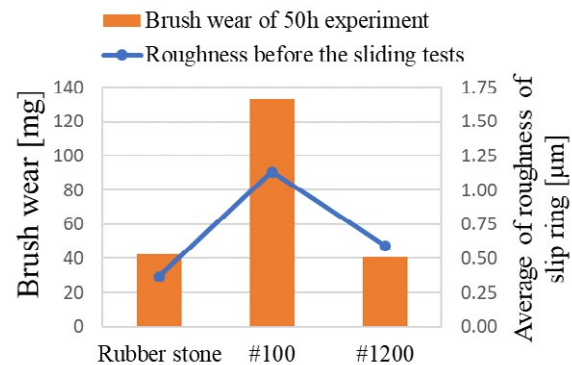


Fig. 8 Relationship between brush wear and roughness with a brush current of 10 A.

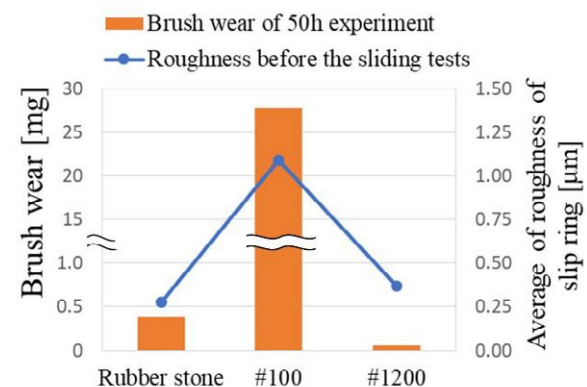


Fig. 9 Relationship between brush wear and roughness with no brush current applied.

5.2 Difference in roughness with no current

In experiments without a brush current, there was a difference in amount of brush wear for the sliding surface polished using rubber stone and EP # 1200. A laser-microscope image showing the roughness of the slip ring surface after the experiment is presented in Fig. 10.

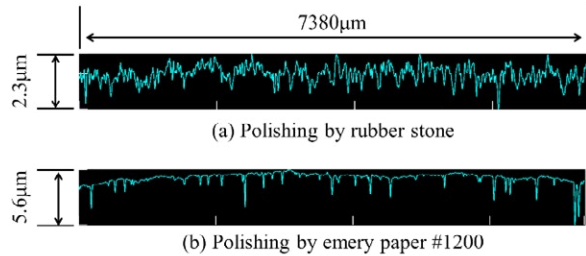


Fig. 10 Laser microscope images used in a roughness analysis.

Polishing the sliding surface using rubber stone produced a fine unevenness in the surface. In contrast, polishing using EP #1200 produced some deep grooves, nevertheless the sliding surface was smooth. To factors are believed responsible for the difference in roughness between the two preparations. The first is that although the deep grooves are dispersed, the average roughness was increased with their presence. Second, the sliding surface was slightly curved and hence the average roughness may have increased overall by the slight curvature.

5.3 Influence by film of sliding surface

After polishing with rubber stone and EP #1200, there was a large difference in the amount of wear depending on the presence or absence of brush current. The roughness of these two sliding surfaces were found to have similar values (Figs. 8 and 9). When the roughness of a sliding surface is low, we believe the electrical wear is much larger than the mechanical wear.

Photographs of the sliding surfaces of the slip rings taken after the experiments are shown in Fig. 11. In addition, a schematic of graphite being transported by the brush current is shown in Fig. 12 [3]. With a brush current of 10 A, graphite forms on the slip ring surface. At the sliding surface, graphite moves from the brush to the slip ring, thereby forming a graphite film on the surface of the slip ring. Furthermore, copper wears away in the sliding contact. As the brush was also worn, it is conceivable that the copper powder from brush wear suppresses any excessive build-up of a graphite film. In addition, it is conceivable that the current increases the temperature of the current-carrying spot on the real contact area. When current flows, Joule heat is generated [4]. Since the actual current-carrying spot was very small, the resistance value was increased, and the brush was locally softened by Joule heat. Therefore, the brush wear was promoted by current.

From Fig. 11, without a brush current, graphite does not adhere to the slip ring, implying that graphite had not formed on the surface of the slip ring and hence the metals of the surfaces made contact. Therefore, mechanical wear is believed to have been suppressed by the lubricity of graphite in the brush material [5].

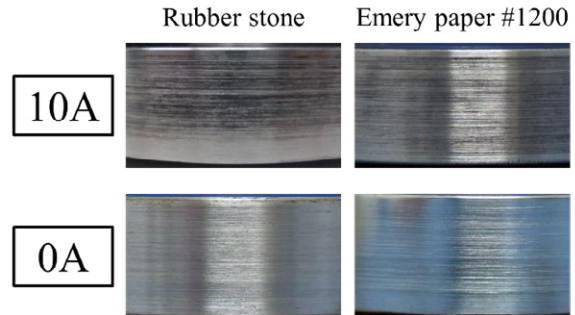


Fig. 11 Photographs of the sliding surface of the slip rings after the experiments.

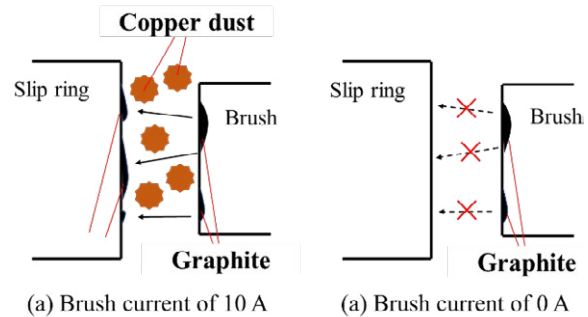


Fig. 12 Schematic of graphite moving under the influence of the brush current.

5.4 Relationship between coefficient of friction and roughness

The relationship between the coefficient of friction and roughness of the sliding surface is shown in Fig. 13. When there is no brush current, roughness and coefficient of friction are proportional. However, when the brush current is 10 A, the coefficient of friction for the surface prepared using EP #100, which has a high roughness, was not much different from the other two surfaces. This result suggests contact area and current are correlated.

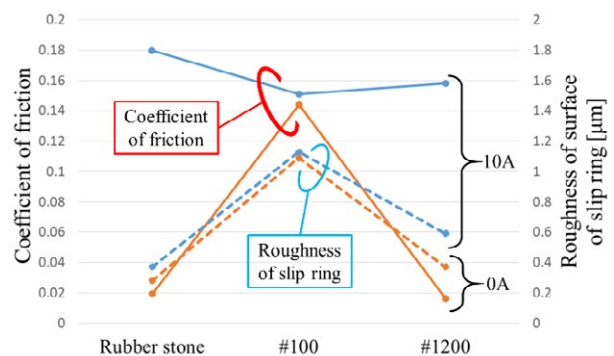


Fig. 13 Relationship between the coefficient of friction and roughness of the sliding surface.

Referring to the schematic of the sliding surface (Fig. 14), for the preparation with EP #100, the real contact points of the sliding surface is fewer because roughness is high. Conversely, preparations with rubber stone and EP #1200, the real contact points of the sliding surface is increased because roughness is low. The current is distributed by the numerous contact points of the surfaces. For that reason, with the preparation using EP #100, the current flowing through a single contact point increases. Therefore, copper is thought to be softened locally by the current and a small value was obtained for the coefficient of friction. In addition, the locally softened copper is sheared and worn down by the slip ring. That is, the amount of brush wear occurring during the 10 A experiment indicates that wear due to current is dominant.

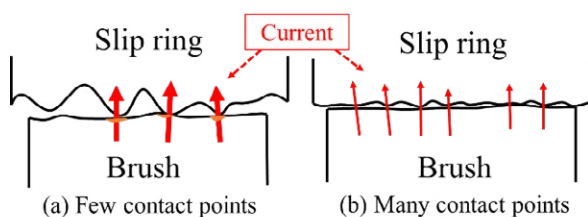


Fig. 14 Schematic of the sliding surface of a slip ring with and without a brush current.

6 Summary

The conclusions of this study are summarized in the following remarks:

1. Slip rings of different roughness exhibited a linear relationship between the amount of brush wear and the roughness of the sliding surface.
2. When a brush current of 10 A was applied and the surface roughness low (Rubber stone and Emery Paper#1200), although the coefficient of friction was increased, the brush wear was suppressed.
3. When a brush current of 10A was applied and the surface roughness high (Emery paper#100), the coefficient of friction was small because the copper of the brush had softened through the concentration of current at the contact point.
4. With no brush current and a surface roughness that was low (Rubber stone and Emery Paper#1200), the amount of brush wear was reduced by graphite from the brush forming a lubricant.
5. With no brush current and a surface roughness that was high (Emery paper#100), mechanical wear increased due to friction between the metal surface. The amount of brush wear also increased.

7 Acknowledgments

We thank Richard Haase, Ph.D, from Edanz Group (www.edanzediting.com/ac) for editing a draft of this manuscript.

8 Literature

- [1] Toshinobu Ichiki: Theory and practice of electric brushes. p. 49, 1978
- [2] J. Neukirchen: Kohlebuesten. p. 37
- [3] Ryuta Higa, Yusuke Takada, Naoki Fukuda, Koichiro Sawa, Takahiro Ueno: Sliding Characteristics of Fe Slip Ring in the Change of Silver Content of Silver-Graphite Brushes. IEICE Technical Report, vol. 118, no. 462, EMD2018-75, pp. 87-90, 2019
- [4] Yuki Amada, Takahiro Ueno, Koichiro Sawa, Noboru Morita, Kazuhiko Takahashi: Voltage Saturation Mechanism in V-I Characteristics for Natural Graphite Brush and Steel Slip-ring. IEEJ Transactions on Industry Applications, Vol.140 No.2 pp.117-127, 2019
- [5] Naoki Fukuda: Contact Voltage Drop and Brush Wear Characteristics for Various Silver Content of the Silver Graphite Brush in Slip Ring System. IEEE Holm, 2018

Raman Spectroscopic Analysis of Carbon Film on Frictional Surface of Contact Wire

Yoshitaka Kubota, Railway Technical Research Institute, Tokyo, Japan, kubota.yoshitaka.77@rtri.or.jp

Abstract

It has been presumed that lubricating carbon films are formed on the frictional surface of the contact wire when using carbon-based pantograph contact strips. However, there have, as of yet, been no reports including observation of such films, and the details of the film have not yet been clarified. In this study, we investigated the surface of a worn contact wire used on a commercial railway line, where metalized carbon contact strips had been applied. The results of Raman spectroscopic analysis revealed that both the intensity ratio of the D-band and G-band (I_D/I_G) and the half-height width of the G-band of the carbon film were decreased compared with those of the as-manufactured carbon substrate of the strip. This indicates that the carbon film contains graphite-like sp^2 -bonded structures. We also conducted wear experiments using the metalized carbon strip by sliding it against a copper ring under electric current. It was found that the structural change of the carbon was mainly promoted by the heat of the arc discharge that occurred between the contact strip and contact wire.

1 Introduction

On electric railways, electric multiple units or electric locomotives collect current from an overhead contact wire through pantograph contact strips (Fig. 1). Carbon materials have been widely used as contact strips because of their superior lubricating properties [1]. There have been many studies investigating the carbon film formed on copper slip-rings by carbon brushes [1], [3], and it has been presumed that lubricating carbon films are similarly formed on the frictional surface of contact wires by carbon contact strips. However, there have been no reports on the observation of such films so far, and the details of the film have not yet been clarified.

In this study, Raman spectroscopy was used to investigate the surface of a worn contact wire used on a commercial railway line. The results of the Raman spectroscopic analysis of the carbon film are presented and the thermal factors that cause the structural change of the carbon are discussed.

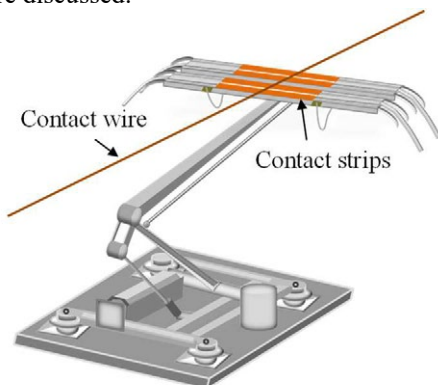


Fig. 1 Pantograph contact strip and contact wire

2 Materials and Raman Spectroscopic Analysis

2.1 Materials

2.1.1 Contact Wire

A contact wire used in a commuter rail line was investigated. Table 1 shows the wire characteristics. The frictional surface was examined by a Raman spectrophotometer (details are described in 2.2). Fig. 2 shows the frictional surface of the contact wire. A cross-section of the contact wire was examined with both a scanning electron microscope (SEM, JSM-7800F, JEOL, accelerating-voltage: 5kV) and using energy dispersive x-ray spectrometry (EDX, JSM-7800F, JEOL, accelerating-voltage: 15kV).

Material	Cu-0.3mass%Sn
Profile	Circular grooved, 170mm ²
Line	Commuter rail line in a metropolitan area
Wear rate	0.2nm/one pantograph passage

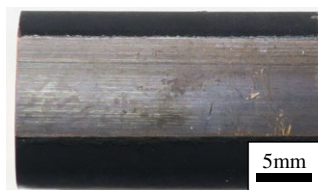


Fig. 2 Frictional surface of the examined contact wire

2.1.2 Pantograph Contact Strip

As a sample for reference, a metalized carbon contact strip (PC78A, Toyo Tanso Co., Ltd) was examined using Raman spectroscopy. PC78A is a Cu-impregnated carbon material that does not include graphite and is a mating material of the wire. The carbon substrate of PC78A is carbonized at 1200°C, which is lower than its graphitization temperature, as mentioned below. To preliminarily investigate the structural change of the carbon of the strip, the samples were carbonized at different temperatures (1200°C, 1600°C, 2200°C, and 2800°C). The results of this examination revealed that graphitization of the carbon substrate of PC78A occurs above 2000°C. Raman spectroscopy was conducted at 3 points on each sample.

2.2 Raman Spectrophotometer and Measurement Conditions

We applied Raman spectroscopy, one of several experimental techniques for analyzing the structure of carbon materials, to examine the carbon film on the wire. This method in particular is appropriate for thin films because the penetration depth of the laser is approximately 0.5 μm. An NRS-7100 laser Raman spectrophotometer (JASCO corp.) was used for measurement of the wire surface. Table 2 shows the measurement conditions.

Table 2 Raman spectroscopy measurement conditions

Wavelength of laser	532 nm
Power of laser	0.5 mW
Range of observed wave number	1490~150 cm ⁻¹
Measurement time and number of iteration	10sec×2times
Spot diameter of laser beam	1 μm

3 Wear Experiment

During the running of a pantograph, the sliding surface of a contact strip is heated by Joule heating, frictional heating, and arc discharge. Such factors cause a temperature rise in the strip and induce the structural change of the carbon. In this study, we investigated the effect of the three thermal factors on the structure of the carbon on the contact strip by conducting a wear experiment.

A block-on-ring machine was used as the wear experiment apparatus. Fig. 3 shows a schematic diagram of the apparatus. The Cu ring was composed of oxygen-free copper (99.96% Cu, HV(9.8N)86) and represented the contact wire. The experiment conditions are shown in Table 3.

The total Joule heating energy E_j , frictional work E_f , and arc discharge energy E_{arc} generated during sliding contact was calculated using the following equations:

$$E_j = \sum (I \times V) \Delta t \quad (1)$$

$$E_e = \sum (I_{arc} \times V_{arc}) \Delta t \quad (2)$$

$$E_f = \sum (F \times v) \Delta t \quad (3)$$

Here, I is the electrical current, V is the contact voltage, Δt is the sampling period, and I_{arc} and V_{arc} are the current and the voltage during arc discharge, respectively. Arc discharge was identified when contact voltage exceeded the threshold voltage (10 V). Finally, F is the frictional force, and v is the sliding speed.

To confirm the results, a second type of Raman spectrophotometer (Nicolet Almega XR, Thermo Nicolet; excitation wavelength: 532 nm) was also used to analyze the frictional surface of the worn test pieces.

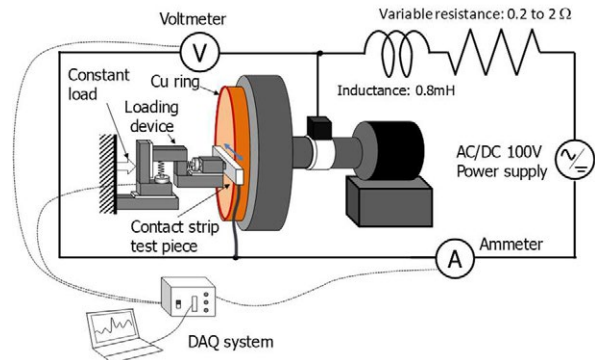


Fig. 3 Schematic diagram of the experimental apparatus

Table 3 Experimental condition

Items	1	2	3	4	5
Sliding speed	100 km/h	100 km/h	100 km/h	100 km/h	100 km/h
Contact load	14 N	54 N	14 N	14 N	98 N
Electric current	DC 100 A	DC 100 A	DC 300 A	DC 500 A	DC 500 A
Sliding distance	25 km	25 km	25 km	25 km	25 km

4 Results and Discussion

4.1 Carbon Film on Frictional Surface of Contact Wire

The SEM image and the results of the EDX analysis are shown in Figs. 4 and 5, respectively. As can be seen, a carbon film, with a thickness on the order of 1 μm, was confirmed to form on the frictional surface of the wire (Fig. 5). Fig. 5 also revealed that the carbon film deposited a layer of copper oxide. This result is similar to the carbon film formed on a copper collector ring sliding against a carbon brush [1].

The wear rate of the wire was approximately 0.2 nm per one pantograph passage (Table 1). The carbon film should therefore diminish over the course of several thousand pantograph passages if it undergoes no re-formation, indicating that the film is able to maintain a uniform thickness as a result of repeated breakage and re-formation. The carbon film on the wire is considered to be formed by material transfer from the carbon contact strip.

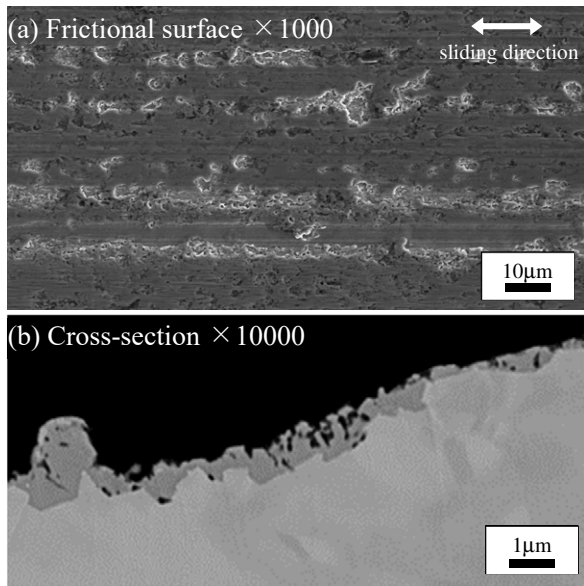


Fig.4 SEM image of frictional surface and cross-section of the wire

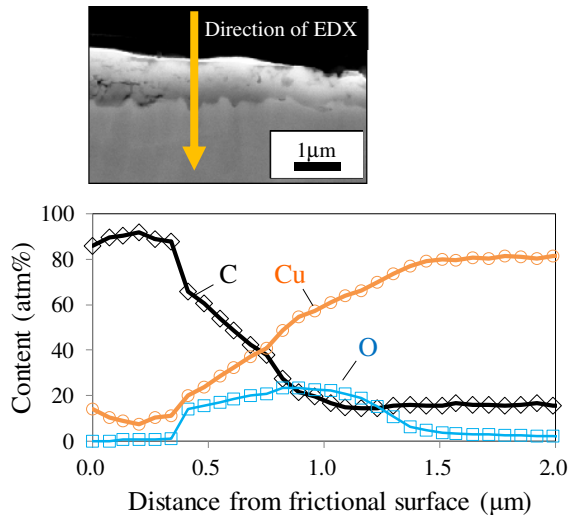


Fig.5 Result of EDX

4.2 Raman Spectroscopic Analysis of Carbon Film

Raman spectra of the contact strips carbonized at different temperatures and the frictional surface of the contact wire are shown in Fig. 6. The spectra of the carbon strip samples carbonized at 1200°C and 1600°C have two broad peaks, one at approximately 1360 cm⁻¹ (D-band) and the other at approximately 1580 cm⁻¹ (G-band). The spectra of the strips carbonized (graphitized) at 2200°C and 2800°C have these peaks as well as a small shoulder peak at approximately 1620 cm⁻¹. Altogether, in the spectra of the wire sample, broad D-band and G-band peaks and a small peak at 1620 cm⁻¹ (at 2200°C and 2800°C) were observed. The Raman spectra reported here are similar to those reported for coke samples carbonized at 1300°C and 1900°C [4].

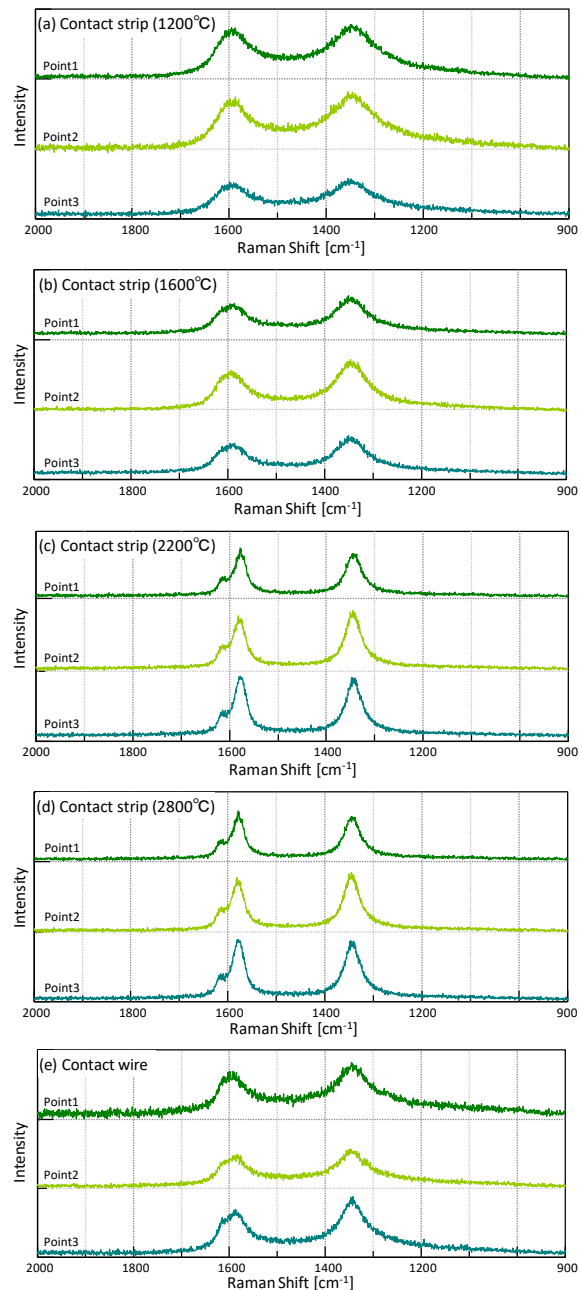


Fig. 6 Raman spectroscopy results

To quantitatively evaluate the structural change of the carbon, five peaks were separated from the Raman spectra, as shown in Fig. 7. From the separated peaks, We calculated the intensity ratio of the D-band and G-band (I_D/I_G), a measure widely used as an indicator of graphitization degree. We also calculated the full width at half maximum intensity (FWHM) of the G-band, and the bandwidth of the 1580 cm⁻¹ peak band at 1/2 height. Fig. 8 shows a characterization of the G-band by I_D/I_G ratio and FWHM [5]. Both the I_D/I_G ratio and FWHM of the G-band of the carbon film were lower than those of the as-manufactured carbon strip (carbonized at 1200°C). This indicates that the carbon film contains graphite-like sp²-bonded structures. The structural change of the carbon is considered to be caused by the temperature rise in sliding surfaces.

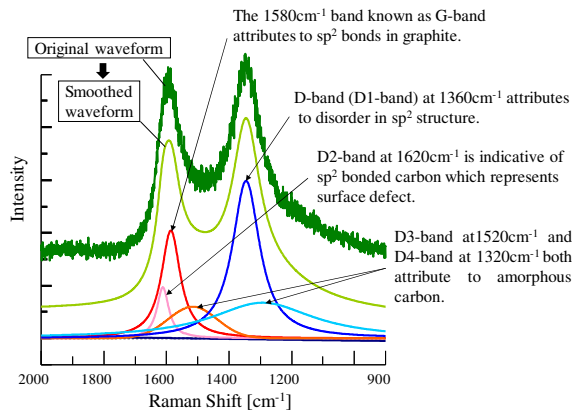


Fig. 7 Schematic of waveform processing and five separated bands

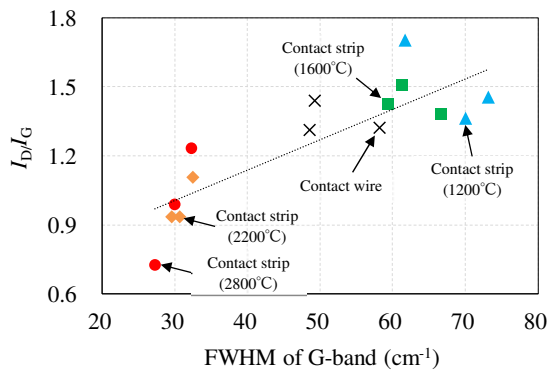


Fig. 8 I_D/I_G and FWHM of G-bands

4.3 Thermal Factors Affecting Structural Change of Carbon

Fig. 9 shows one example (condition 4) of the results of Raman spectroscopy for nine points on the worn surface of the contact strip test piece, and Fig. 10 summarizes the results. The dashed lines in Fig. 10 represent the results of the contact strip samples carbonized at different temperature. As mentioned above, the graphitization of the carbon occurs above 2000°C; therefore, the points at which the FWHM of the G-band is lower than 60 cm^{-1} represent the graphitized region. Joule heating and the frictional work were the largest factors in condition 5 (500 A and 98 N, respectively). Graphitization of the carbon, however, was not observed (Fig. 10). It is considered because no arc discharge occurred during the test in condition 5. Arc discharge occurred in conditions 1, 3, and 4, and graphitized points were observed on the worn surface of the strip in conditions 3 and 4.

Fig. 11 shows the relation between FWHM of the G-band and total Joule heating, frictional work, and arc discharge energy. The amount of arc discharge energy was smaller than that of Joule heating or frictional work. However, arc discharge energy did have a stronger correlation with the FWHM of the G-band (correlation coefficient $R = -0.73$, Fig. 11). These results strongly indicate that the structural change of the carbon was mainly promoted by the heating of the carbon electrode by arc

discharge. It has been reported that during arc discharge, the surface temperature of a carbon electrode exceeds 2400 K [6], a temperature sufficient for graphitizing the carbon. Meanwhile, neither the Joule heating nor the frictional heating gave rise to comparatively high temperatures.

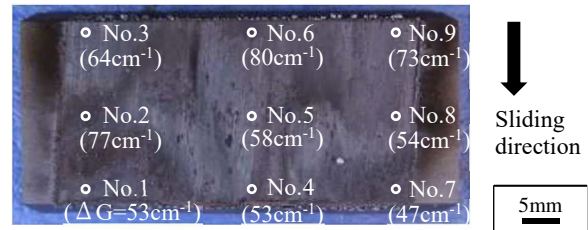


Fig. 9 Examined points and FWHM of the G-band on the worn surface of contact strip test piece

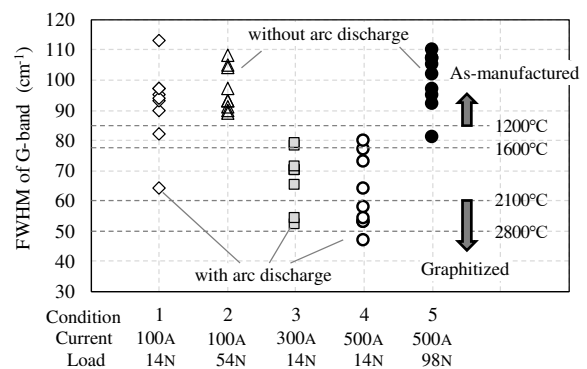


Fig. 10 FWHM of G-bands measured on the worn surface of contact strip test piece

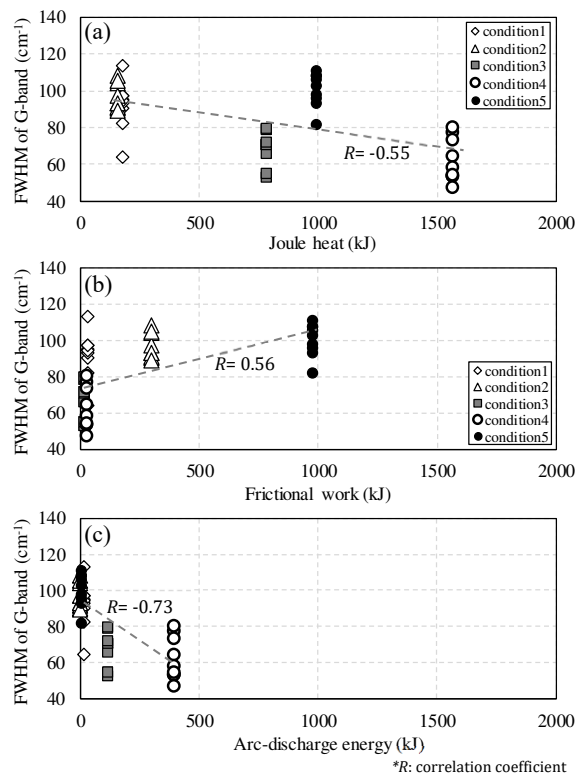


Fig. 11 Relation between FWHM of the G-band and (a) Joule heating, (b) frictional work, (c) arc discharge energy.

5 Conclusion

The frictional surface of a contact wire rubbed against a metalized carbon contact strip was examined using a SEM and Raman spectroscopy. In addition, a wear experiment was conducted using carbon strips under electric current. The main conclusions are as follows:

1. A carbon film with a thickness on the order of 1 μm was confirmed to form on the frictional surface of the contact wire. This film is considered to form due to material transfer from the carbon contact strip.
2. Our results indicate that the structure of the carbon film is different from that of the as-manufactured carbon contact strip, with the carbon film containing graphite-like sp^2 -bonded structures.
3. Our results indicate that the structural change of the carbon of the contact strip during running is mainly promoted by arc discharge rather than Joule heating or frictional heating.

6 Literature

- [1] D.L. Dixon: Development with Carbons for Current Collection, Railway Engineering Journal, 1973
- [2] C. Van Brunt, R.H. Savage: Carbon brush contact films, General Electric Review, Vol.47, No.16, 1944
- [3] E.F. Fullam, R.H. Savage: Carbon Film Formation and Commutator Brush - Wear As Revealed by the Electron Microscope, Journal of Applied Physics, Vol.19, No.7, pp.654-660, 1948
- [4] P. Puech, et al: Analyzing the Raman Spectra of Graphenic Carbon Materials from Kerogen to Nanotubes, Journal of Carbon Research, Vol.5, No.69, 2019
- [5] G. Katagiri: Raman Spectroscopy of Graphite and Carbon Materials and Its Recent Application (written in Japanese), Carbon, Vol.1996, No.175, 1996
- [6] F Liang, et al: Effect of arc behaviour on the temperature fluctuation of carbon electrode in DC arc discharge, Journal of Physics Conference Series, Vol.518, 2014

Tribology of electrical sliding contacts

Christian Holzapfel, Schleifring GmbH, Fürstfeldbruck, Germany, Christian.Holzapfel@schleifring.de

Abstract

In this study, a tribometer development is described that aims at understanding sliding electrical contacts that apply a wire-design principle. The tribometer was designed such that the contact configuration of a wire in a V-groove is reproduced. At the same time, design-related influences are minimized. This enables to establish the relationship between friction coefficient, temperature, speed, and contact resistance of two model systems applying PAO lubricants with low and high viscosity. In general, the contact resistance is higher for the high viscosity lubricant especially at low temperature. This behaviour is in general consistent with the friction coefficient measured at the same conditions. In this respect, full Stribeck curves at varying temperatures are discussed.

1 Introduction

Any sliding electrical contact can be interpreted in terms of a tribological system where in parallel an electrical current is transferred. Successful use of such systems in real contact applications demands a thorough understanding of the friction properties, wear and electrical behaviour. In order to understand these properties, in this study, tribometer tests are described where the friction properties are measured in parallel to the contact resistance. In this way a database of different contact systems is being built up. From this database pre-selection of material systems can be performed. In [1] further test strategies are described, that lead to full system level qualification of new contact systems for use in sliding electrical contacts.

Systems for sliding electrical contacts come in a variety of different design and materials solutions. Well-known are carbon brushes as well as so-called gold-wire systems. Overviews of such solutions are given in [2,3]. The gold- or more general wire-design principle, as well as relevant properties, is further detailed in [1] and references herein. In this technology one or several wires in-parallel are usually used in one or several V-grooves in order to transfer electrical energy. In this way, the wire alloy has to ensure both, the contact resistance as well as the contact force. Over life-time, wear and relaxation must be sufficiently low to guarantee a reliable contact. Such systems are successfully used for a large variety of industrial applications such as pitch control systems for wind power, bottle filling machines, pick and place machines, tooling machines, etc. Although these systems are well understood, there is a continuous demand for longer life-time, miniaturization, as well as low cost solutions (noble metal substitution or reduction of gold content). It should be noted that in these systems, in general, a liquid lubrication is being used in order to extend life-time [4]. However, the lubrication system being applied must be tailored to guarantee a reliable

contact and low wear rate at the same time. This apparent contradiction between low amount of lubricant (electrical performance) and high amount of lubricant (mechanical wear performance) is a demanding task for the variety of climatic conditions that need to be taken into account.

In [5] crossed bar experiments are described where material screenings are being performed and the pure contact resistance can be determined. However, in these tests, only longitudinal sliding with limited sliding distance can be performed. [6] use a rotating component test setup where also material screenings for wire and track coating alloys are being performed. In this setup, the friction coefficient was not directly measured in parallel. The same author used an oscillating setup for measuring the friction coefficient in a later study [7] but these tests were conducted without lubrication.

In this study a tribometer was developed that applies the real contact configuration (wire in V-groove). The contact resistance is measured using a 4-wire technique and in parallel the friction force is measured (and hence the friction coefficient can be determined). The tribometer is able of performing experiments at different temperatures between -20°C and $+70^{\circ}\text{C}$. In this way the Stribeck curve (friction coefficient as a function of sliding speed) at different temperatures can be derived. The main emphasis of the present paper is to first describe the experimental setup, second to detail the data acquisition strategy and third, to describe selected tests with two PAO model lubricants, one with low viscosity and one with high viscosity (factor 20 difference) and generalization of underlying trends. These tests apply standard gold wire alloys running on galvanic hard gold coatings. Hence, the main focus of the present study is to establish the general effects of liquid lubrication on friction coefficient and contact resistance in a model system.

2 Tribometer setup

The tribometer developed for this study is described in detail in [1] together with preliminary test data in the framework of a test strategy for full contact system qualification. Hence, the tribometer setup is here only detailed to an extent that allows understanding the principal settings. The tribometer aims at reproducing the real geometry of a wire-design slip ring by applying a track with a double V-groove (**Figure 1**). Two wires (0.38 mm diameter) are guided to the V-grooves using glass tubes and are pressed against the tracks using a pulling spring. Both wires are used in a trailing configuration. This means that the relative track movement is directed towards the end of the wire. In principal also a leading situation can be applied (opposite turning direction) but was not used in the present study. The track is made out of brass and can be coated with a suitable functional layer (e.g. hardgold coating). The wire consists of metallic alloy with suitable spring and contact properties (e.g. gold or silver alloys).

The setup for applying the normal force (guidance within glass tubes and use of pulling spring) is different to the real geometry where the contact force is generated by the wires itself (acting as a bending beam, [8]). However, for the tribometer, this modification was used in order to stabilize the dynamic behaviour of the system: Any sliding system is sensitive to some extent to frictional induced vibrations [9]. Previous studies have demonstrated this also for wire design slip ring systems [10]. The currently used setup is much stiffer than using the wires as force generating system element directly and hence, vibrations were not detected to play a significant role in the system at any speed and configuration. In this way, the effect of the viscosity of the applied lubrication schemes as well as the temperature effect on viscosity can be studied more clearly. Otherwise, a superposition of hydrodynamic effects as well as increased vibration amplitudes at high speed would have been difficult to be distinguished. In addition, the setup with a relatively long pulling spring ensures a constant contact force with a flat force-distance spring characteristic. Hence, e.g. any variation in the run-out, will not lead to a significant force variation.

The normal contact force can be varied within a range of 10 to 150 mN per wire. Speed can be varied between 0 and 1200 rpm corresponding to a track speed between 0 and 1.5 m/s. The test strategy (see below) consists of measuring oscillograms at constant speed and temperature as well as collecting Stribeck curves at different temperatures. The Stribeck curve is measured with increasing speed. Each test is performed for a total number of 5 million revolutions (total test time is 1 week). Wear is determined after testing by visually inspecting the wires and the tracks. In addition, the tracks are cross-sectioned in order to determine remaining coating thickness. Each test configuration is

at least tested two times in order to determine reproducibility.

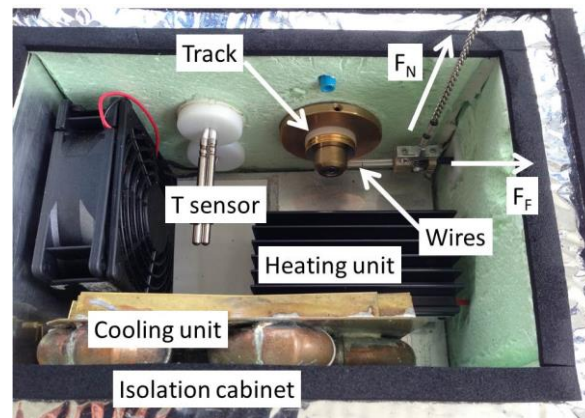


Fig. 1 Overview of tribometer. Two wires are pressed against a track with a double V-groove. The normal force F_N is applied by using a pulling spring. Force sensors for F_N and friction force F_F are outside of the image area. The tribometer is contained in an isolation cabinet and temperature can be varied between -20°C and $+70^{\circ}\text{C}$.

Based on the fact that two wires are being used, application of current during testing has to be applied in a way that the two contacts are applied in series and the measured contact resistance will always contain the contribution of two contact points. Moreover, a "contact" defined in this way will in reality also contain two physical contacts in parallel since a V-groove geometry is being used. For measurement of a single contact a circuit setup with layout as given in [11] would need to be applied. However, in this case three wires would have needed to be implemented within the setup.

Figure 2 shows the equivalent circuit diagram used in the present study.

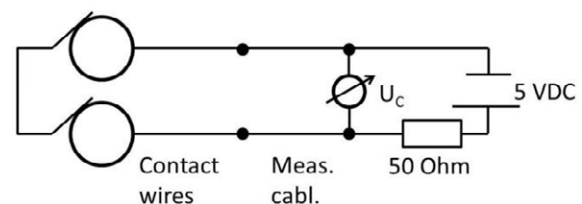


Fig. 2 Equivalent circuit diagram for electrical measurements used in this study. The contact voltage drop U_C is measured over two sliding contacts in series. A measurement current of 100 mA is generated using a constant voltage source. Thus, the calculated contact resistance contains contributions from two wire contacts (with two contact points within the V-groove). In the measurement of U_C some static contribution from the contact wires as well as a measuring cabling (meas. cabl.) is contained.

A measurement current of 100 mA (DC current) is generated using a constant voltage source of 5 VDC and applying a serial resistor of 50 Ohm. In general, the serial resistance is much larger than the contact resistance, and based on this fact, the current will be effectively constant. It should be noted that in the case that a constant current source is being used without a serial resistance the control behaviour of the current source will be critical. The currently applied setup circumvents this challenge.

The contact voltage drop U_C is measured in a 4-point setup. The common current and voltage path that is being measured also contains the two contact wires. They are contacted by a measurement cabling that leads to the common measurement points. The resistance of the cabling is constant. The static resistance contribution of the contact wires can be directly calculated from the length of the wires. For later representation of the contact resistance the values are corrected for the static contributions and all values are normalized for comparison reasons. For further details on the electrical evaluation see below. The bandwidth for measurement of U_C is 0-1 kHz.

3 Test strategy

The test strategy consists of performing each test for a minimum amount of life time in order to get a rough estimate of full life time potential. However, a full life time test with the tribometer for a large screening test sequence is not possible since typical life time of lubricated wire-design slip rings can be in excess of 50 million revolutions [1]. These tests, depending on the rotational speed, would last several months (accelerated speed) or even years (typical application speed). Hence, as a compromise, a life time target of 5 million revolutions was chosen for building up the contact system database. The testing procedure consists of measurements at -20°C , -10°C , 0°C , 25°C and 70°C at the beginning (0 rotations), in the middle (2.5 million rotations) and at the end of the test sequence (5 million rotations, test points 1, 2, and 3). At each of these test points, a full Stribeck curve (friction coefficient as a function of speed) is collected at -20°C , -10°C , 0°C , 25°C and 70°C . In parallel the contact resistance is measured. Both, friction coefficient and contact resistance will be displayed below in 3D diagrams as a function of speed and temperature. For data collection of the Stribeck curve, the speed is increased from 0 rpm to 1200 rpm during 120 s, then hold for 10 s followed by a decrease of speed to 0 rpm again within 120 s (data plotted below are always given for increasing speed). Immediately after this sequence, oscillograms representing 5 consecutive rotations at 20 rpm, 100 rpm and 500 rpm are collected. Typical time scales for temperature equilibration is ~ 2 hours. Between different test points and during tem-

perature equilibration a constant speed of 500 rpm is employed.

As discussed above, test reproducibility for each system (wire material, track material e.g. coating system, lubrication scheme, contact force) is checked by repeated test series (at least two tests are being performed). Results of the reproducibility verification can be found in the preliminary study in [1] and will not be repeated in the current work.

4 Results of example PAO with low viscosity

The main emphasis of the present work is elucidating of general trends between viscosity of lubricant, speed, temperature, and contact resistance. For this purpose, a standard gold wire setup and two model PAO lubricants are being used (one with a low viscosity and a second with a high viscosity with a difference of a factor of 20). In the current section the results for the PAO with low viscosity are discussed. In the next section, they can be directly compared to results for the PAO with high viscosity.

PAO can be used as sample lubricants for sliding contacts since they can be procured with widely different viscosity values. Hence, they can be regarded as model systems for understanding the influence of viscosity on sliding (friction and wear) as well as electrical properties (note that of course both effects are coupled with each other). For real applications they are not regularly used because of their lower temperature stability and potential decomposition over life time as compared to other synthetic base oils. The examples shown below, thus, must also be regarded as example of general behaviour and cannot be directly extrapolated to real field use. Such a qualification scenario for real applications must be subsequently followed-up by different test strategies and qualification scenarios [1].

In **Figure 3**, the temperature-dependent Stribeck curves of a PAO with relatively low viscosity are given. **Figure 4** contains the representation of the contact resistance for the same conditions.

The Stribeck curves in Figure 3 show an expected behaviour: With increasing speed within a mixed friction regime the friction coefficient initially decreases. No clear minimum of the friction coefficient as a function of speed can be identified at least for temperatures above 0°C . A clear hydrodynamic behaviour cannot be found within the speed range investigated in this study. However, the friction coefficient increases with decreasing temperature (hence increasing viscosity). Thus, from a friction point of view, high speed and low temperature appear to be the most critical running conditions. The electrical measurements overall show a relatively constant behaviour with a slight tendency of higher values at lower temperature and especially at test point 1 also at high speed consistent with the friction data.

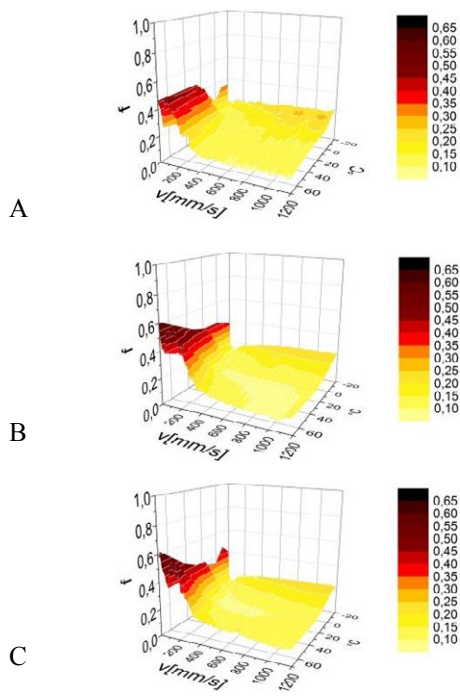


Fig. 3 PAO with low viscosity. Temperature-dependent Stribeck curves (f denotes friction coefficient) at A) test point 1, B) test point 2, and C) test point 3. Speed varies between 0 and 1200 rpm, temperature between -20°C and 70°C .

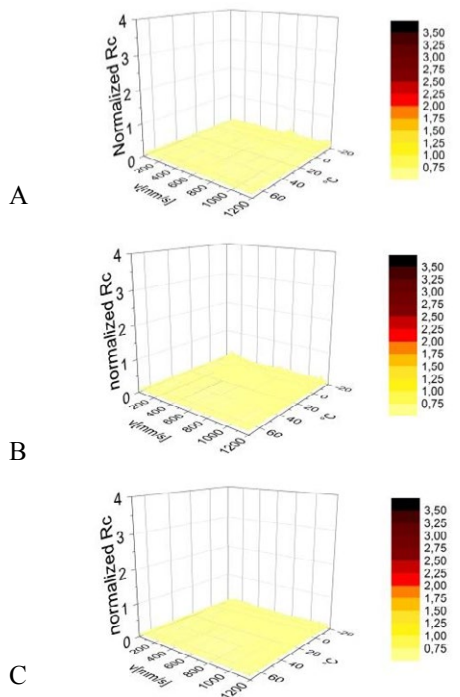


Fig. 4 PAO with low viscosity. Temperature-dependent normalized contact resistance curves at A) test point 1, B) test point 2 and C) test point 3. Speed varies between 0 and 1200 rpm, temperature between -20°C and 70°C .

For a more detailed understanding of the electrical behaviour, individual oscillograms are being shown in **Figure 5** and **Figure 6**. For interpretation of the oscillograms it must be noted that, since a single track is used, a design contribution is not present [10] and hence any variation in contact resistance is related to a change at the contact points or configuration along the circumference.

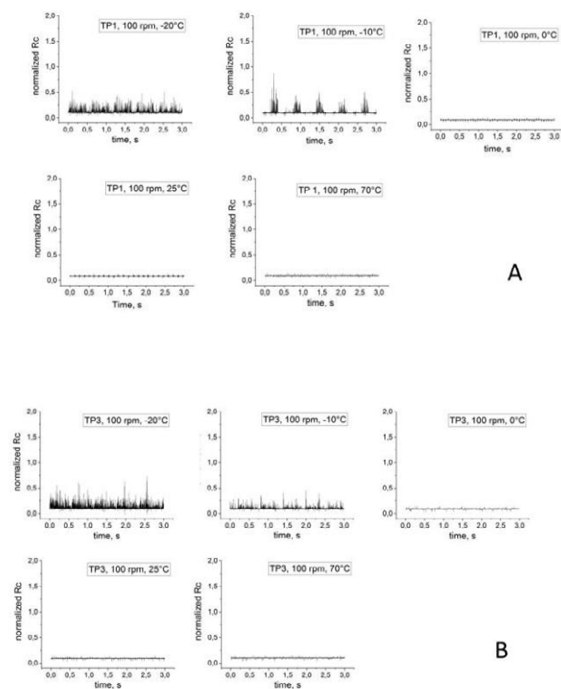


Fig. 5 PAO with low viscosity. Oscillograms at 100 rpm at -20°C , -10°C , 0°C , 25°C and 70°C . In A) the results at test point 1 (beginning of the test) and in B) the results for test point 3 after 5 million revolutions are shown (and hence evolution over life time).

Figure 5 aims at understanding the influence of temperature and life time at constant speed. Thus, only oscillograms at 100 rpm are being shown. As discussed in several earlier studies [1, and references herein] the time-dependent contact resistance (noise) can be described using a variety of different characteristic values (e.g. peak-to-peak variation). For the comparison shown in the present study, main emphasis is being placed on a qualitative comparison of full oscillograms. Although no quantitative value is given, the complete information contained in a full oscillogram can be visually compared. At 100 rpm for PAO with low viscosity the behaviour is relatively similar at beginning of the test (test point 1) and 5 million revolutions life time (test point 3), see Figure 5. There is a gradual decrease in the contact resistance variation (noise) with increasing temperature consistent with the friction behaviour in Figure 3. However, in

addition, it can be seen that during one rotation the scatter in contact resistance seems to be higher along the circumference initially and the distribution of noise becomes more homogeneous at the end of the test (compare corresponding oscillograms in Figure 5A and Figure 5B, e.g. at -10°C). This finding is interpreted by the distribution of the lubricant: At the beginning of the test the lubricant distribution seems to be less homogeneous along the circumference than at the end of test. Of course, also contamination or wear debris can play a role in this respect. However, all samples are thoroughly cleaned before the test and at least initially wear debris will not be present within the V-groove (for further discussion of wear, see below).

Figure 6 aims at understanding the influence of speed on the electrical behaviour. Here, oscillograms at 20 rpm and 500 rpm are being shown for test point 3.

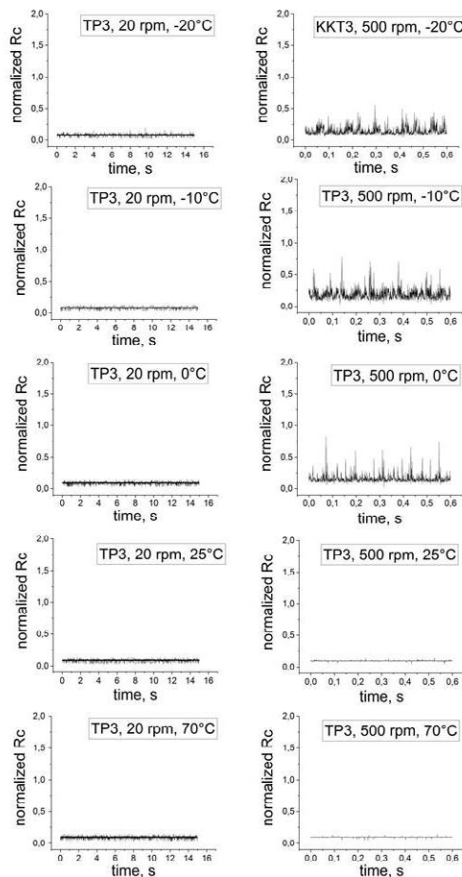


Fig. 6 PAO with low viscosity. Oscillograms at 20 rpm at -20°C , -10°C , 0°C , 25°C and 70°C (left column) and 500 rpm (same temperature conditions right column). Only results at test point 3 are being shown.

At 20 rpm, the influence of temperature on contact resistance is relatively minor (Figure 6, left column). Note that also for the friction behaviour at this low speed more constant friction behaviour is observed (Figure 3). The situation is different at 500 rpm (Figure 6, right column): here, in general at low temperatures, noise is higher. Interestingly the highest noise values itself would be found at 0°C rather than

at -20°C . This finding is different to the friction behaviour and implies that an understanding of the friction coefficient only is not sufficient for predicting the electrical performance.

The wear mechanism is similar as described in earlier studies applying similar contact materials and consists of material transfer from the track to the wire [12, 13]. Figure 7 shows the formation of transfer layers on a wire from the tribometer test with PAO with low viscosity. At the same time, the wear on the track is relatively low along the circumference and overall predicted life time would be significantly longer than 5 million revolutions.

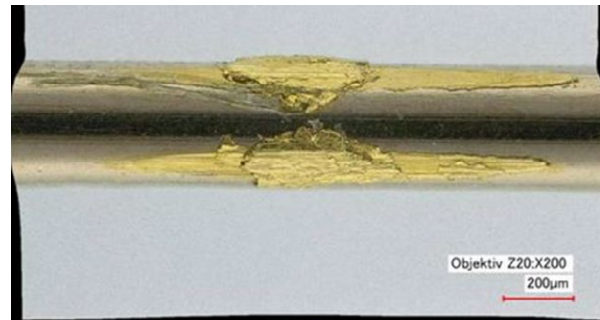


Fig. 7 Material transfer or prow formation after 5 million revolutions during tribometer test with PAO with low viscosity.

5 Results of example PAO with high viscosity

In the preceding section, the principal relationships between viscosity, friction, speed and electrical behaviour was established. In the following, a comparison is being made with corresponding results applying a PAO lubricant with very high viscosity. The difference in viscosity of the two model oils is a factor of 20 at room temperature. However, the viscosity index of the two lubricants is very similar and hence the relative difference in viscosity is nearly the same over the whole temperature range. **Figure 8** and **Figure 9** show the temperature-dependent Stribeck curves as well as the contact resistance curves with the same layout as given in Figure 3 and Figure 4.

The Stribeck curves shown in Figure 8 (high viscosity) show a similar behaviour as shown in Figure 4 (low viscosity). For the lubricant with high viscosity, absolute values seem to be slightly higher at the same conditions compared with the same values for the low viscosity PAO. Moreover, the temperature dependence is much more pronounced and in a section at constant speed the increase of friction coefficient with decreasing temperature is significantly steeper for the lubricant with high viscosity.

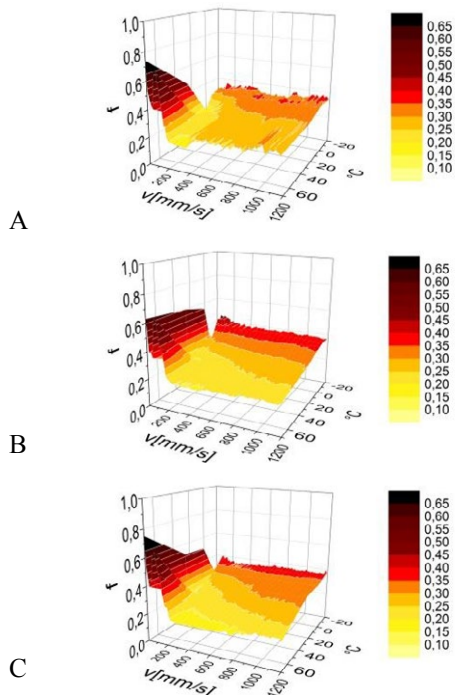


Fig. 8 PAO with high viscosity. Temperature-dependent Striebeck curves at A) test point 1 at beginning of testing, B) test point 2 at middle of testing and C) test point 3 at end of testing (5 million revolutions). Speed varies between 0 and 1200 rpm, temperature between -20°C and 70°C .

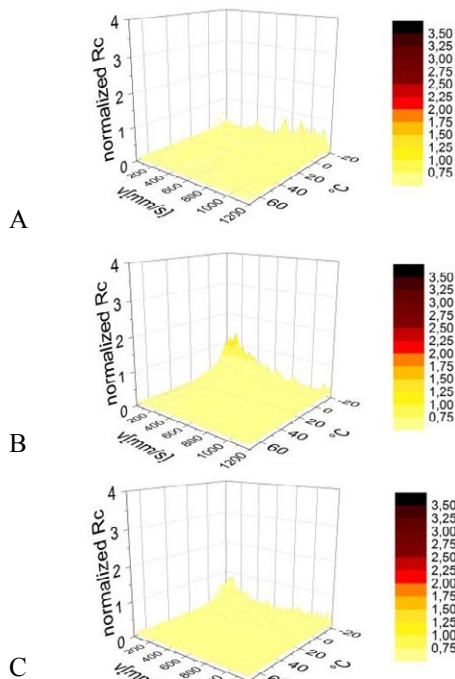


Fig. 9 PAO with high viscosity. Temperature-dependent normalized contact resistance curves at A) test point 1 at beginning of testing, B) test point 2 at middle of testing and C) test point 3 at end of testing (5 million revolutions). Speed varies between 0 and 1200 rpm, temperature between -20°C and 70°C .

Obviously, these differences also lead to a significant difference in the electrical behaviour (Figure 9): At least below 0°C the contact resistance rises with decreasing temperature and in a real application some challenges at low temperature might result. This effect can also be demonstrated by comparing the oscillograms for test point 3 at 20 and 500 rpm for the high viscosity lubricant in **Figure 10** with the same values for the low viscosity lubricant plotted in Figure 6 (see discussion below).

There is also some difference in the general behaviour for PAO with high viscosity with respect to the normalized contact resistance at test point 1 compared to the subsequent test points (Figure 9): At the beginning of life time (test point 1), the electrical behaviour shows higher values at low temperature and higher speed whereas after some life time the highest contact resistance is found at low temperature and low speed. In a repeated test this behaviour can be reproduced. These findings imply some redistribution in the oil film similar as discussed above. In addition, it is not necessarily the system at high speed that shows highest contact noise under all temperatures.

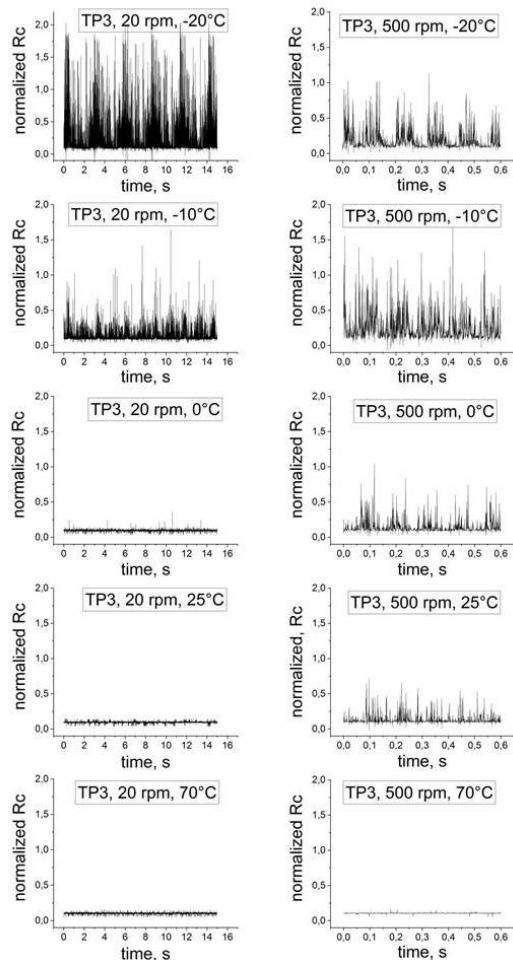


Fig. 10 PAO with high viscosity. Oscillograms at 20 rpm at -20°C , -10°C , 0°C , 25°C and 70°C (left column) and 500 rpm (same temperature conditions right column). Only results for test point 3 are being shown.

This becomes also apparent in the oscillograms shown in Figure 10: at 20 rpm the behaviour for PAO with high viscosity shows increasing noise with decreasing temperature. This leads to the appearance of very high noise especially at -20°C . Note also the large difference in normalized contact resistance as compared to the system with low viscosity PAO (Figure 6, note that all diagrams have the same y-scale settings). Interestingly, the absolute noise value measured as peak-to-peak value for the PAO lubricant with high viscosity at 20 rpm and -20°C is highest for all data shown in the present study. For high speed (500 rpm), the maximum of noise is at -10°C (but lower on an absolute scale). Here the peak in noise is shifted in temperature which means that both towards higher as well as lower temperature the scatter in contact resistance decreases. However, at temperatures $> 0^{\circ}\text{C}$ the noise is higher than at the lower speed (consistent with the low viscosity PAO).

In **Figure 11** the wear state of the wire after tribometer test with PAO with high viscosity is being shown. Comparing Figure 7 and Figure 11 reveal no obvious difference in the wear process or extent of wear. It should also be noted that in cross sections only minor wear is present. Hence, it cannot be concluded that e.g. the oil with the higher viscosity would necessarily have larger life time expectancy. However, in detail, tests would have to be performed for much longer life time for full qualification since e.g. the lubricant with lower viscosity might show a higher tendency for flowing out of the contact area. In addition, the lubricant with high viscosity will have more lubrication potential in the case of continuously occurring high temperature conditions.

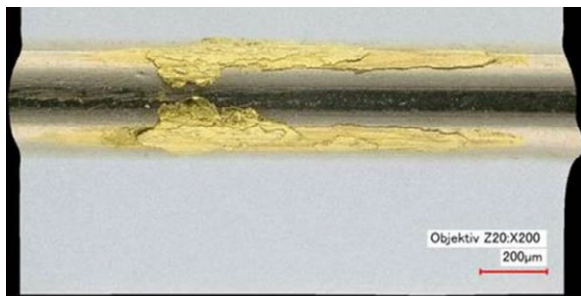


Fig. 11 Material transfer or prow formation after 5 million revolutions during tribometer test with PAO with high viscosity.

6 Conclusions

The present work describes a setup for a tribometer adapted for a wire-design sliding electrical contact system. During development of the tribometer the main emphasis was placed on a robust design that should exclude dynamic instabilities (frictional induced vibrations) in order to be able to deduce the general relationship between viscosity, speed, temperature and electrical contact resistance. Using data for

model PAO lubricants with high and low viscosity, respectively, it could be shown that in general the friction coefficient shows a well-defined Stribeck curve. From the electrical data it does not appear that at any condition a pure hydrodynamic behaviour occurred. In this case, full contact separation would lead to very high contact resistance or open circuit conditions. However, it must be noted that the temperature at the contact point will always be higher in a current carrying state locally influencing viscosity. In addition, for small separations caused by a lubricating film, also other conduction mechanisms such as tunnelling effects can occur. The data also show that during life time some redistribution of oil does take place. This effect leads to different behaviour at running-in and steady-stage. Unfortunately, at present, a direct imaging of oil layers at very low layer thickness ($< 1 \mu\text{m}$) showing the thickness of the film in a lateral distribution map is highly challenging and could not be performed for the samples investigated here. The data also show that, for a specific material system and a specific lubrication scheme, additional qualification tests are necessary. In general, noise values tend to be higher for high viscosity lubricants. However, the exact relationship of viscosity, speed, temperature and contact resistance is very system-dependent. In this respect, the tribometer setup did enable to establish a large database of different lubrication schemes that allows pre-selection of a suitable lubrication scheme for specific conditions tailoring electrical behaviour and life time for general as well as specific application scenarios.

7 Acknowledgement

The tribometer was jointly developed with the company Dr. Tillwisch GmbH Werner Stehr. We greatly acknowledge the expertise for tribology as well as always fruitful discussions with Werner Stehr und Susanne Beyer-Faiss.

8 Literature

- [1] C. Holzapfel, "Test categories for characterization of sliding electrical contacts", Proc. 65th IEEE Holm conference, pp. 309-316, 2019
- [2] P. G. Slade, "Electrical Contacts, principles and applications", CRC Press, Boca Raton, 2014
- [3] E. Vinaricky, "Elektrische Kontakte, Werkstoffe und Anwendungen", Springer, Berlin, Heidelberg, 2016
- [4] H. Chudnovsky, "Lubrication of electrical contacts", Proc. 51st IEEE Holm Conference, pp. 107-114, 2005
- [5] E. F. Smith III, A. Klein, "Screening contact materials for low speed slip ring assemblies", Proc. 39th IEEE Holm Conference, pp. 157-170, 1993

- [6] B. Gehlert, "Lebensdaueruntersuchungen von Edelmetall-Kontaktwerkstoff-Kombinationen für Schleifringübertrager", VDE Fachbericht 61, pp. 95-100, 2005
- [7] B. Gehlert, "Silberkontaktwerkstoffe für Schleifringübertrager", VDE Fachbericht 69, 2013
- [8] K. E. Pitney, "Ney contact manual, electrical contacts for low energy uses", the J. M. Ney Company, 1973
- [9] R. R. Babayan, G. T. Ismailov, "Influence of dynamic process in low current sliding contacts wear", Proc. 14th ICEC, pp. 39-42, 1988
- [10] C. Holzapfel, "Selected aspects of the electrical behavior in sliding electrical contacts", Proc. 57th IEEE Holm conference, pp. 325-333, 2011
- [11] C. Holzapfel, P. Heinbuch, S. Holl, " Sliding electrical contacts: wear and electrical performance of noble metal contacts", Proc. 56th IEEE Holm conference, pp. 543-550, 2010
- [12] M. Antler, "Tribological properties of gold for electric contacts", Proc. IEEE 18th Holm Conference, pp. 41-63, 1972
- [13] C. Holzapfel, C. Pauly, M. Engstler, F. Mücklich, "Electron Beam Characterization Techniques for the Study of Wear in Sliding Contacts", Proc. 61st IEEE Holm conference, pp. 227-234, 2015

Future of Electromechanical Switchgear

Frank Berger, TU Ilmenau, Ilmenau, Germany, frank.berger@tu-ilmenau.de

Abstract

The current development of the electrical networks towards a DC system imposes certain changes in the design and functionality of several network components. This paper aims to offer an overview of the challenges and the opportunities that are raised by the DC system over the electromechanical switchgear in order to identify its future path in the electrical network. The paper starts with a review process of the previous statements regarding the future of the low-voltage (LV) electromechanical switchgear. In the second part, the existing developments in the LV technology towards a mixed (centralized and decentralized) DC grid are presented. The third part presents the main influencing factors and the developments in the classic electromechanical switchgear as well as in the relatively new switchgear technologies represented by the hybrid and power electronic switches. Following, several questions concerning the standardization and the DC ageing behaviour of the insulating materials will be presented and discussed. The last part will present the conclusions of the current overview.

1 Introduction

The low-loss transmission and distribution of electrical energy and its resource-saving use has played an increasingly important role in recent years in the discussion regarding the future of electrical power engineering and thus also on the future of electromechanical switchgear technology.

The energy transmission and distribution technology based on high-voltage direct current transmission (HVDC) as well as the worldwide massive expansion of renewable generation plants, especially in the medium and low voltage range, require a wide range of studies on new network topologies that consider mixed AC and DC networks, microgrids as well as switching and protection devices adapted to the technical requirements imposed by them [1 - 3].

The observations on the future of electromechanical switchgear begins with a brief summary of previous forecasts on this subject.

2 Previous forecasts and factors influencing the development of electromechanical switchgears

Electromechanical switchgear, e.g. contactors, relays or circuit breakers, are among the oldest components of electrical power engineering. Their partial or complete replacement by power electronic components, e.g. thyristors, IGBTs or FETs has been discussed for a long time.

The switching characteristics of electromechanical and power electronic switches are being compared for more than 30 years [4]. The advantages of electromechanical switches are:

- the low power losses associated with the current carrying function,
- the safe and visible galvanic separation gap,
- the high breaking capacity,
- the small construction volume and the low cost of the devices
- the ability to withstand temporary overload.

A decade later, the development of the switching principles for low-voltage switchgear was envisioned by [5,9] along the following directions:

- an increased use of vacuum switching technology in low voltage,
- optimization of the AC and especially the DC extinguishing principles concerning a better switching capacity, the prevention of reignitions as well as the improvement of the current limitation in AC networks,
- improved methods and algorithms for early detection of short circuits in low-voltage networks,
- new methods for diagnosis and determination of the remaining service life of contactors and
- development and use of hybrid switching devices.

In [6], it is emphasized that innovations in low-voltage switchgear technology will secure the future of electromechanical switchgear. These innovations are:

- the introduction of vacuum switching technology in the low voltage range,
- better control of larger short-circuit currents through new current-limiting effects (e.g. conductive polymers, liquid current limiters),
- condition and remaining service life monitoring and display for selected switchgear,

- the control and adjustment of electromagnetic contactor drives,
- the arc fault detection and shutdown and
- power electronic switching by means of Si-MOSFETs and Si-JFETs.

In the Morton Antler Lecture held in 2016 and celebrating 50 years of the Holm Conference on Electrical Contacts the future trends for switches were expected in the following fields [7]:

- electronic sensing and tripping systems applied to switches of all types will expand,
- AgSnO₂ will be gradually the contact material for currents below 4 kA and Ag and AgNi will be for low current relays,
- higher voltage (> 100 V) DC switches with permanent magnets will produce a new range of compact relays for automotive and photovoltaic applications,
- MEMS switches will find a commercial application and may become hermetically sealed with a non-oxidizing gas.

A concluding remark of this anniversary lecture concerning the topic “switching with arc” was presented in the following generalized statement:

„Circuit switching using electrical contacts has not been superseded by electronic switching except for special operations. Electrical contacts plus electronic detection, sensing and tripping systems will be the partnership for the future”.

It must be mentioned that the most of the forecasts presented so far were obtained from scientific publications concerned with the future development and optimization of electromechanical switching devices based on the AC grid structure. This implies the existence of typical AC sources and consumers as well as the classical electrical energy flow from the high voltage grid via medium voltage grid towards the low voltage distribution network.

In the first decade of the new millennium, new challenges for electrical power distribution have been emerging.

Due to the growing population and increasing demand for electrical energy, the earth's fossil fuels will not be able to meet the increased demand for electrical energy as it can be concluded from analyzing Table 1 (IEA, World Energy Outlook 2014) and Figure 1.

Renewable energy generation plants (photovoltaic and wind power), sustained by appropriate storage media are future drivers of the electric networks and implicitly for the next generations of electromechanical switchgear.

Region	PwE (mil.)	ER (%)	Urban ER (%)	Rural ER (%)
Developing countries	1283	77	91	64
Africa	622	47	68	26
North	1	99	100	99
Sub-Sahara	621	38	59	16
Asia	620	84	95	74
China	3	100	100	100
India	304	80	94	67
Latin America	23	90	99	82
Middle East	18	88	98	78
OECD	1	100	100	100
WORLD	1285	82	94	68

PwE – Population without Electricity
ER - Electrification Rate

Table 1: Global status of electrification

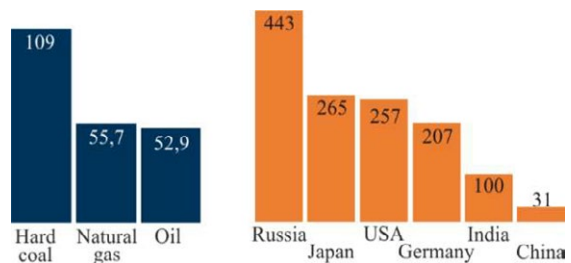


Figure 1: Fossil fuel reserves

DC distribution networks, DC on-board power supplies, electromobility and DC microgrids set new challenges for switching and protection devices and their corresponding protection criteria.

For these new challenges, an electromechanical switchgear requires a significantly improved DC switching capacity. Due to a series of advantages, nowadays, the hybrid and electronic switches seem to be a genuine alternative to the classic electromechanical switchgear.

The new requirements for the switching technology are specified in [8,10] on the basis of the new network architectures as follows:

- increased reliability,
- higher power values,
- integrated security,
- encapsulated switching arc, and
- the use of hybrid switches and power electronic switching devices.

In conclusion, it can be stated that the previous development of electromechanical switchgear was characterized by:

- developments meant to improve the switchgear itself (contact material, contact and extinguishing system, drive system)

- miniaturization,
- innovations (controlled drive, vacuum switching technology, current limitation, remaining service life, etc.),
- improvement of the price-performance ratio as well as
- new requirements for switchgear resulting from the development of electrical distribution networks, in particular those resulting from future DC low-voltage networks, see Figure 2.

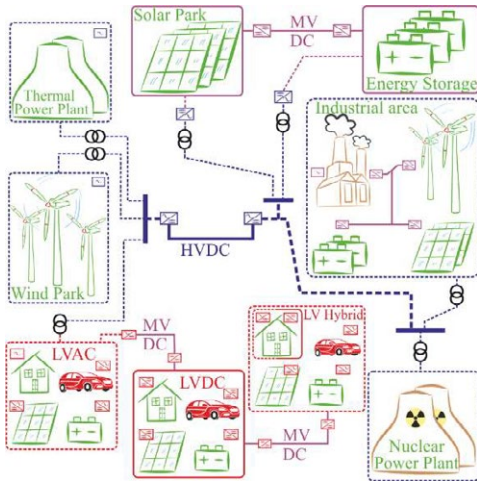


Figure 2: Typical structure of modern power systems

3 DC Low Voltage Networks

The existing development towards an increased number of DC low voltage networks results mainly from the following factors:

- the number of renewable energy generation plants with corresponding storage media is increasing globally,
- DC island grids or microgrids are easier to interconnect to form larger grid connections,
- the stability and regulation of DC grids requires less effort than for AC grids,
- the 3-wire layout imposed by three-phase current system usually results in a 2-wire layout for DC system (cost savings for cables or conductors).

These benefits, characteristic for a LVDC network, have been analyzed and implemented in test projects, for different applications. Exemplary in this regard are the envisioned LVDC networks for home applications, presented in Figure 3, or for computer centers as described in Figure 4.

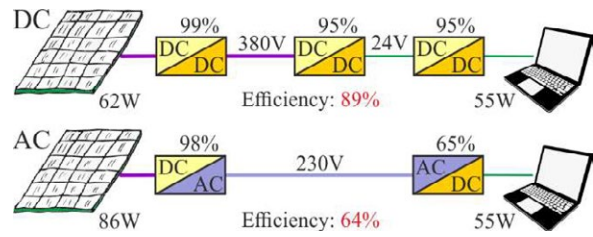


Figure 3: Comparison of efficiencies in AC and DC distribution for home applications [11]

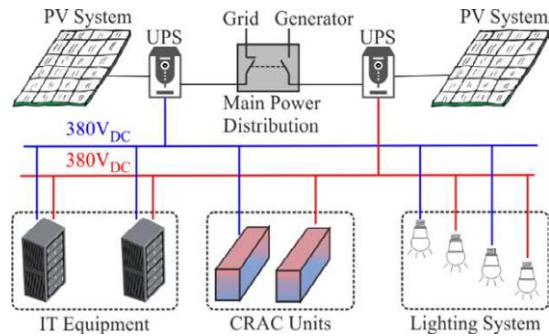


Figure 4: DC -Network for computer center

Common to all these new DC networks is that:

- the losses in the distribution of electrical energy are approx. 10...20% higher in AC systems than in DC systems, because DC-systems have no skin, proximity, hysteresis and dielectric losses,
- many applications, e.g. in the household, are based on DC voltage; the AC/DC conversion losses can be avoided by using a pure DC system and DC-DC conversion is more efficient than AC-DC conversion,
- the components used for household applications have a lower cost, size and weight due to the reduction of transformers.

The wide application of DC networks in the low-voltage range sets known and new challenges for switchgear and components. In the following these are mentioned:

- switching off the current when there is no current zero crossing,
- new switching requirements created by the very high di/dt values generated by the new electrical sources and by the new loads (IEC 60947-4-1 DC utilization categories with time constants up to 15 ms (DC-5)),
- material migration and erosion in electromechanical switches,
- new protection concepts caused, on the one hand by the new consumers, and on the other hand by connecting the DC grid to the existing AC grids,
- national and international standardization,
- profitability,
- acceptance by the population.

4 DC Switching Principles

Figure 5 shows a systematic representation of the DC switching principles that can be used from low voltage to high voltage [12].

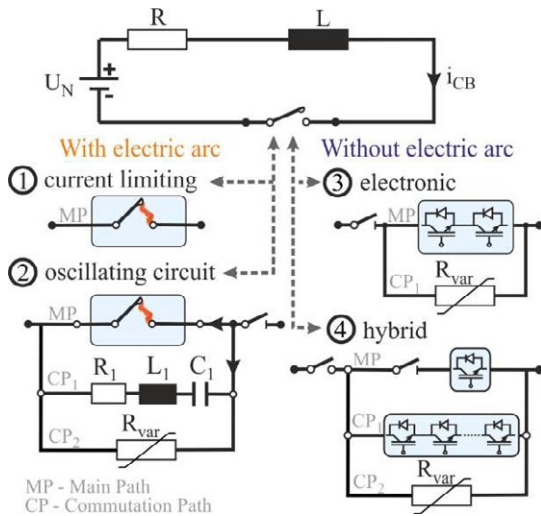


Figure 5: Systematization of the DC switching principles

Low-voltage switchgear is special due to the fact that, if the contact and extinguishing system is appropriately designed, electromechanical switchgear alone is capable of successfully switching off DC currents and providing galvanic isolation. At other DC voltage levels this cannot be achieved without special effort and additional switching elements.

The switching principle with electric arc based on the current limiting method uses several methods meant to increase the arc voltage above the network voltage in order to create the arc current zero crossing required for the arc quenching. The methods used to quickly achieve this purpose (e.g. arc splitting, arc elongation, etc.) are presented in Figure 6 as a schematic illustration. Their functionality is used in real switching devices through certain design and material features.

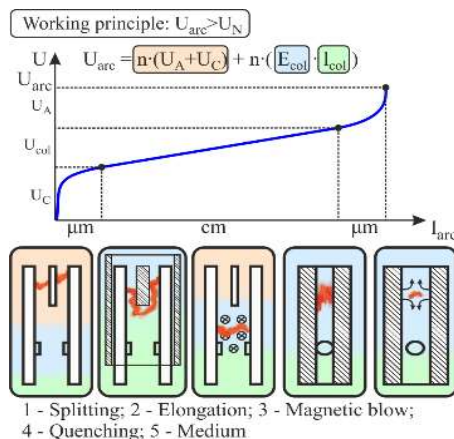


Figure 6: Arc quenching principle

The voltage characteristics obtained from experimental investigations on DC contactors using different arc quenching principles in the design of their contact and extinguishing system are shown in Figure 7 [13].

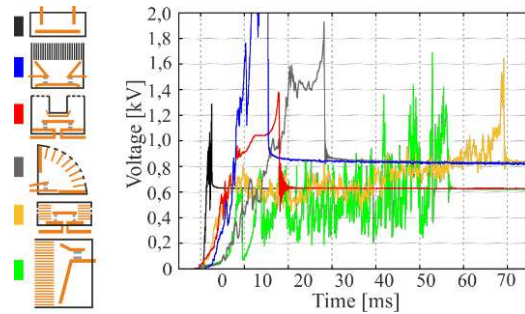


Figure 7: Arc voltage structure with different contactor designs

Depending on the design and the dimensions of the devices, a very different arc voltage structure in terms of time and magnitude can be recognized.

From these results it can be concluded that there is still considerable improvement potential in the classic switching principle to achieve the best possible DC switching behavior.

A further challenge involves minimizing the contact material migration phenomena occurring during DC switching operations. With respect to this, the main influences are analyzed in [14].

The switching principles with electric arc based on resonant switching have been intensively studied in the field of high-voltage [15] and medium-voltage technology. In the low voltage area there are currently only very few aspects considered.

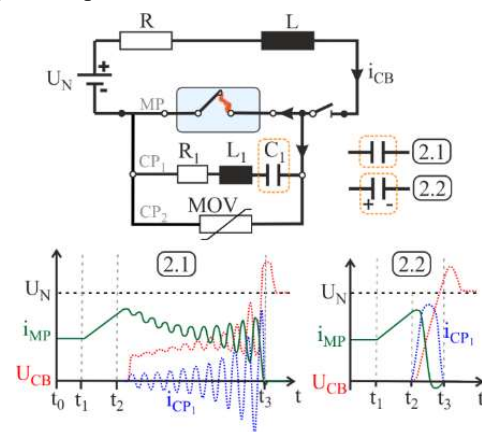


Figure 8: Arc quenching by means of passive and active resonance

The principles, presented in Figure 8, consist in creating a current oscillation between the main current path, where the mechanical switch is connected, and the elements (R_1 , L_1 , C_1) of the parallel path. The resulting

current will oppose the main current and decrease its value creating a current zero crossing, when the arc quenching will occur.

For dimensioning, however, the oscillating system formed between the circuit breaker, situated in the main path, and the RLC elements of the first parallel path must be considered.

Hybrid Switch

The switching principle of the hybrid switches consists of a parallel connection of an electromechanical switching device, found usually in the main current path, and power electronic components (MOSFET, IGBT, Thyristor) as well as overvoltage arresters (MOV) placed in parallel to the main current path [15 - 17].

Referring to the occurrence of a switch-off arc, a distinction is made between hybrid arrangements with and without arc formation [18 - 22].

In arrangements with arc formation, the fast and high arc voltage build-up serves to change, in a short time interval, the breaking current path from the main path to the power electronics path.

There are setups providing the switching voltage for the power electronics by using the arc voltage but most of the hybrid switches mentioned in the literature use an additional auxiliary voltage supply to control the power electronic elements.

Figure 9 shows a typical switching arrangement without auxiliary power supply. S1 is the main switch and the switches S2 and S3 serve for galvanic isolation.

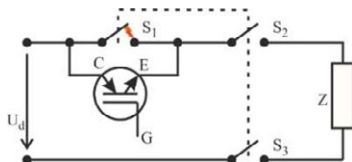


Figure 9: Hybrid Switch with arcing switching [16]

For the contact system of the mechanical switchgear, mostly circuit breaker, single and double break systems, placed in air or vacuum, are used. In some cases, a series connection of the contact system is realized.

The main task of the mechanical contact systems is to provide a low contact resistance path in the switched-on state and the build-up of a high arc voltage (e.g. very fast mechanical contact opening) with the corresponding high arc resistance required for a fast current commutation in the power electronic components, which then switches off the current in the μs or ms range. For the optimization of these processes, a decisive role is played by the contact material, by the arcing processes, by the metal bridge explosion or by the metal vapor arc created at very short distances after contact separation.

When compared to a classical breaker, it can be observed that the mechanical breaker in a hybrid configuration must provide a different functionality. The first aspect to account for is that the contact material is highly affected by short bouncing arcs with high di/dt values during the switch-on procedure and by very short arcs during the switch-off procedure. The second aspect that must be regarded during a switch-off procedure is the extremely small arc quenching period imposed in order to create a fast commutation of the current path. These two requirements provide a new set of physical characteristics for the contact materials as well as for the circuit breaker design in general.

If very short commutation times, in the μs range, are desired, hybrid switches arrangements without arc commutation are used, see Figure 10 [19].

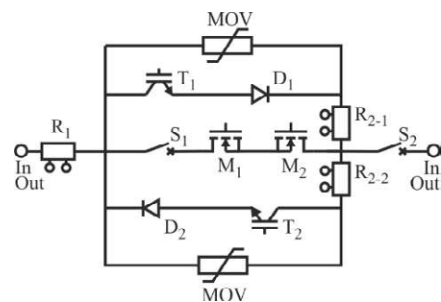
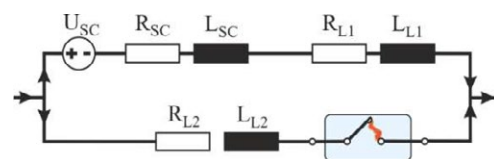


Figure 10: Hybrid Switch with arc-free switching

In these arrangements, a very low impedance power electronic component (e.g. SiC-MOS-FET) is used in the main path with the mechanical contact system S1. During the switch-off process the auxiliary electronics (MOSFET M1, M2) are switched off, while the mechanical switch S1 is still switched on. Due to the high resistance, the current commutates to the other paths, and the mechanical switch will be switched off without arcing. The switchgear S2 realizes the galvanic isolation. For such switching arrangements the optimization of the mechanical contact system must be accompanied by an optimization of the electrical properties of the commutation circuit (e.g. loop inductance).

In addition to the power electronic elements, the cabling and connection conditions of these elements with the mechanical contact system plays a decisive role. These arrangements can be optimized in terms of short commutation times by computer simulation of the corresponding equivalent circuit diagrams. Figure 11 shows such a basic equivalent circuit diagram.



U_{SC} - Semiconductor
 $R_{SC}; L_{SC}$ - Resistance and Inductance semiconductor
 $R_{L1}; L_{L1}$ - Resistance and Inductance loop 1
 $R_{L2}; L_{L2}$ - Resistance and Inductance loop 2

Figure 11: Equivalent circuit for current loop of switch-off operation

A successful function of the hybrid switches can only be achieved when no reignitions occur at the mechanical contact system.

The overvoltage caused by the switching process on the power electronics is usually limited by means of surge arresters. This voltage must be lower than the re-ignition voltage of the opened contact system.

Typical hybrid switch arrangements are additionally equipped with current measurement technology and algorithms for early detection of short circuits and monitoring of the hybrid switch itself. Successful switching tests have been achieved for the following parameters:

- U_{network} : 380 V DC,
- Current ratings: 50 ... 125 A,
- I_K up to 25 kA, Current limitation up to 1 - 3 kA,
- Switch-off times: ~ 10 ms ... 500 μs with time constant of the DC network of 10 ms ... 0.02 ms

Solid State Switch [23,24]

A typical layout of a Solid State Switch is presented in Figure 12. By using components with reduced on-stage losses (Wide Band Gap, R_{on} 2 ... 4 m Ω), 180 A could be switched off within 0.8 μs . In general, however, it has been found that despite already optimized power electronic components, the Solid State Circuit Breaker still have an on-state resistance R_{on} that is 100 ... 1000 times higher than the typical contact resistance of Electromechanical Switchgear.

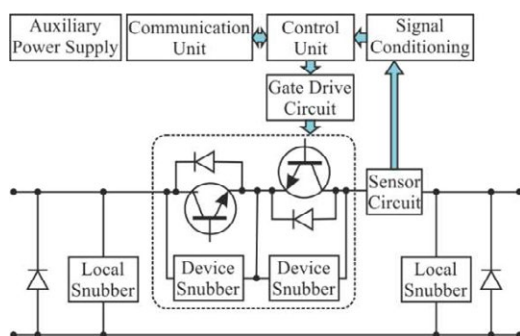


Figure 12: Solid State Circuit Breaker

Even so, it must be considered that the power semiconductors used in different Solid State Switches arrangements up to now were designed for other applications. Information from manufacturers of power electronic components indicates that nowadays, and in the future, power semiconductor elements will be developed and adapted for the switchgear functionality in order to substitute the electromechanical switching devices.

As an existing alternative to the Solid State Circuit Breaker, the Hybrid Switch is suggested.

Conclusions on the DC Switching Principles

In classic DC low-voltage networks, the electromechanical switchgear based on the arc quenching principles can fulfill the requirements for switching capacity well.

Due to the development of electrical networks with small time constants, where extremely high di/dt can be observed, the hybrid switches are gaining in importance according to the author.

A reasonable use of these switching devices in combination with other features, such as: early fault detection, monitoring or even power flow control within the networks, may provide the most economically feasible way to implement this new technology in the future DC low voltage networks.

5 Visible galvanic separation gap

Another important fact that must be considered in the analysis regarding the future of electromechanical switchgear is the visible galvanic separation.

A major advantage of electromechanical switchgear is that they can provide by default a visible galvanic gap. Power electronic components lack such characteristic because a temperature-dependent leakage current in μA range flows, even if a certain reverse voltage is applied. Galvanic separation is therefore not achievable. The international normative IEC 60364-5, "*Selection and Installation of Electrical Equipment, Switchgear and Control Devices*", states that "Semiconductors must not be used as isolating devices".

This means that switching arrangements with Hybrid Switches or Power Electronic Switches must additionally be equipped with an isolating switch to fulfil the requirements of galvanic separation.

Overview of regulations and activities for visible galvanic separation

In IEC 60947-3 standard on low-voltage switchgear and disconnectors, and in the IEC 60947-2 standard on low-voltage switchgear and circuit-breakers, a reference is made to the IEC 60947-1 standard on low-voltage switchgear and general specifications. These specifications further reference the IEC 61140 standard "Protection against electrical noise-common requirements for installations and equipment".

IEC 61140 specifies the requirements imposed for devices used for disconnecting electrical circuits and for protection against electric shock. That standard imposes that:

“The position of the contacts or other disconnecting devices in the disconnected position must either be visible from the outside or be clearly and reliably indicated.”

The devices for separation must meet two requirements:

“In new, clean and dry conditions with contacts in the open position, the device must resist a surge voltage applied between the input and output terminals.”

“The leakage current via the open contacts must not exceed the following values: 0.5 mA contacts when new, 0.8 mA contacts at the end of the agreed lifetime.”

The standard IEC 60204-1 on Electrical Equipment of Machines, also refers to the standard IEC 60947-1 ... 3. The specification IEC 60934 on Equipment Circuit-Breaker, specifies the minimum air gap of the opened contacts for the corresponding rated impulse withstand voltage.

The IEEE Switchgear Committee, the visible break discussion group, provided the following definition in 2018: “Visible break – a gap between conductors that can be visually verified and meets the dielectric withstand requirements in the relevant product standard.”

These regulations play an increasingly important role due to the growing use of power electronics (generation of transients) as switching elements in electrical networks.

6 Insulation

The further miniaturization of electromechanical switchgear and their compact design require safe insulation, galvanic separation and a long service life even at increased operating temperatures, e.g. 120 °C.

Recently, partial discharges have been observed in low-voltage switchgear, which considerably accelerate the aging of the insulating materials and can lead to insulation failure [25, 26].

When using the switchgear under DC voltage, it must be considered that the voltage stress is based on different physical principles compared to AC voltage, as described in Figure 13.

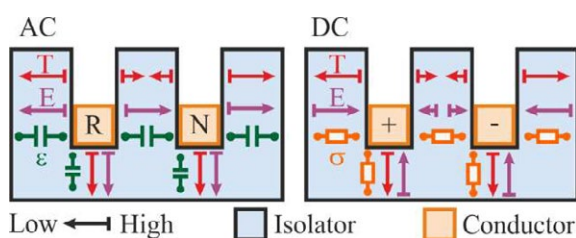


Figure 13: Difference in insulation material stress for AC and DC

For AC voltage stress, the geometric arrangement and the dielectric constant ϵ , showing a low temperature dependence, determine the field strength stress in the insulating material system (e.g. contact air gap, housing wall).

For DC voltage stress, the decisive material constant is the conductivity κ , which is for plastic/synthetic insulation material often specified with the following temperature (T) and electric field strength (E) dependency:

$$\kappa(T, E) = \kappa_0 \cdot e^{\alpha \cdot T} \cdot e^{\beta \cdot E}$$

This dependence on temperature leads to the so-called electric field strength inversion, i.e. the maximum field strength stress of the insulation system changes with the temperature distribution in the insulation arrangement. Areas which initially show the highest electric field stress are slowly relieved as the temperature increases inside the insulating material and modifies its electric conductivity. In this manner the cooler areas will present, under DC stress, the highest electric field stress. As a rule, temperature fluctuations and DC voltage stress results in larger insulation material areas with a higher field strength than in AC voltage stress. This has a significant influence on the ageing behavior of the insulating materials. The aging process has already been investigated for high-voltage and medium voltage cable constructions, and this research is currently being carried out for low-voltage cables and switchgear [27].

The situation is further aggravated by the fact that due to the diverse use of power electronic switching elements, in the DC networks there are no pure DC voltages but the so-called mixed voltages representing a superposition of the DC voltage with higher-frequency oscillation components.

7 Conclusion

Electromechanical Switchgear is a cost-effective, proven and continuously developed technology of the electrical power engineering that has been optimized for various switching applications. Due to worldwide developments and the changes that take place in the low-voltage grid new demands are being placed on the electromechanical switchgear. In addition to the existing optimizations required for the classic DC switching devices (i.e. improvement of the arc quenching phenomena, contact and insulating materials, etc.) nowadays it must be accounted that these switching devices are increasingly being used in hybrid switchgear arrangements. This fact creates a new set of requirements for the contact materials as well as for the circuit breaker design. Another important aspect that we must account for is the development of dedicated power electronic switching elements that, under certain conditions, may entirely replace the mechanical breaker.

The increased use of power electronic switching elements, in combination with and without electromechanical switchgear, will make it possible in the future to implement improved measuring and diagnostic functions in the switchgear. This will allow the execution of the protective functions in a quick and selective manner and even to regulate power flows within the low-voltage grid.

Even so, it can be concluded that the existing limitations of power electronic switching elements with regard to power loss, thermal and insulating stress, the lack of a visible galvanic isolation gap, standardization and cost will continue to make the electromechanical switchgear necessary in the future.

8 Literature

- [1] Dragicevic, T.; Wheeler, P.; Blaabjerg, F.: DC-Distribution Systems and Microgrid, The Institution of Engineering and Technology, London/UK, 2018
- [2] Streck, M.; Berger, F.: Mechanical Switching Devices in Low-Voltage DC-Nano and Microgrids: Imperative and Challenges, 2nd IEEE Intern. Conference on DC-Microgrids, Nürnberg/Germany, 2017
- [3] Hauer, W. u. a.: A Novel Low Voltage Grid Protection Component for Future Smart Grids, 51st Intern. Universities Power Engineering Conference (UPEC), Coimbra/Portugal, 2016
- [4] Schröder, K.-H.: The Future of Electrical Switching Contacts as Affected by Electronic Components, 14th Intern. Conference on Electrical Contacts, Paris/France, 1988
- [5] Berger, F. et. al.: Schaltprinzipien der Niederspannungsschaltgeräte, 15. Albert-Keil-Kontaktseminar, Karlsruhe/Germany, 1999
- [6] Branston, D.: Innovation in Low Voltage Switching Technology, 21st Intern. Conference on Electrical Contacts, Zürich/Switzerland, 2002
- [7] Slade, Paul G.: 50 Years of the Holm Conference on Electrical Contacts 1967 – 2016, Morton Antler Lecture, 62nd IEEE Holm Conference on Electrical Contacts, Clearwater Beach/USA, 2016
- [8] Theisen, P.: A DC Switching Renaissance Energy, Renewable Energy and Storage Switching Technologies for Control and Protection, 25th ICEC & 56th IEEE Holm Conference on Electrical Contacts, Charleston/USA, 2010
- [9] Lindmayer, M.: Low Voltage Contactors, Design and Materials Selection Considerations, 16th Intern. Conference on Electrical Contacts, Loughborough/UK, 1992
- [10] Schöpf, Th.: Interplay between electromechanical and solid state switching technologies for meeting cost, sustainability, and safety demands of various applications, Morton Antler Lecture, 54th IEEE Holm Conference on Electrical Contacts, Orlando/USA, 2008
- [11] Petri, E.: Niederspannungsgleichstromnetze LVDC, Vortrag Cluster Leistungselektronik, Erlangen, 2012
- [12] Berger, F.: Overview and Developing Directions for DC-Switching Technology, DAS 2016, 13th Intern. Conference on Development and Application System, Suceava/Romania, 2016
- [13] Jebramcik, J.; Berger, F.: Observations on switching characteristics of arc chutes in DC Contactors, 27th Intern. Conference on Electrical Contacts, Dresden, 2014
- [14] Weis, M.: „Charakterisierung und systemrelevante Auswirkungen der Materialwanderung in elektrischen Kontakten von Kleinschaltgeräten“, Dissertation, TU Ilmenau, 2011
- [15] Barnes, M et al: HVDC Circuit Breakers- A Review, IEEE Access, Vol.8, 2020, doi 10.1109/Access.2020.3039921
- [16] Meckler, P. et al.: Hybrid Switches in protective devices for low voltage DC-grids at Commercial used buildings, 27th Intern. Conference on Electrical Contacts, Dresden, 2014
- [17] Gao, L. u. a.: A DC-Hybrid Circuit Breaker with Buffer Capacitor and Vacuum Interrupters, 28th Intern. Symposium on Discharges and Electrical Insulation in Vacuum (ISDEIV), Greifswald/Germany, 2018
- [18] Meyer, J. M.; Rufer, A.: A DC Hybrid Circuit Breaker with Ultra-Fast Contact Opening and Integrated Gate-Commutated Thyristors (IGCTs)
- [19] Askan, K. et. al: Power Module for Low Voltage DC Hybrid Circuit Breaker, PCIM Europe, 2018
- [20] Askan, K. et. al: Design and Development of an Integrated Power Module Used in Low Voltage DC/AC Hybrid Circuit Breaker, PCIM Europe, 2018
- [21] Shungo, Z. et al: Development of an Arcless DC Circuit Breaker using a Mechanical Contact and a Semiconductor Device, 63rd IEEE Holm Conference on Electrical Contacts, Denver/USA, 2017
- [22] Yasuoka, K. et. al.: Contact Resistance and Arc-free Commutation Current of Tungsten-clad Copper Contacts for a Hybrid DC switch, 65th IEEE Holm Conference on Electrical Contacts, Milwaukee/USA, 2019
- [23] Shen, J.Z. et al.: Solid State Breakers for DC Microgrids: Current State and Future trends, 1st IEEE Intern. Conf. on DC-Microgrids, Atlanta/USA, 2015
- [24] Qu Lu, et.al.: Design and Analysis of a 375A/ 5kA Solid State DC Circuit Breaker Based on IGCT, IEEE Intern. Power Electronics and Application Conference and Exposition (PEAC), 2018
- [25] Weichert, et al.: On Partial Discharge/Corona Considerations for Low Voltage Switchgear and Control, 29th ICEC & 64th IEEE Holm Conference on Electrical Contacts, Albuquerque/USA, 2018
- [26] Fuchs, K. et. al.: Partial Discharges in Low Voltage Switchgears at Elevated Temperatures, 29th ICEC & 64th IEEE Holm Conference on Electrical Contacts, Albuquerque/USA, 2018
- [27] Stammberger, H.; Borchering, H: Project introduction: DC-Industrie2, https://dc-industrie.zvei.org/fileadmin/DC-Industrie/Praesentationen/DCI2_Project-presentation_en.pdf, 02.03.2021

The silver anti-tarnish affecting the electrical stability of automotive terminals

Maxime Porte, Aptiv, Nuremberg, Germany, maxime.porte@aptiv.com

Abstract

In the automotive industry, having the Ag surfaces covered with an anti-tarnish layer is a strict OEM requirement. Indeed, it has been reported that interfaces resistance increases over 1 Ohm can be attributed to failures of the anti-tarnish process. One major issue is that the usual anti-tarnish detection method as well as optical observations cannot prevent the risk of having low performing interfaces. It was been observed that in particular conditions, some passivation aggregates interfere the electrical interface almost independently of the normal force. Of course guidance are given how to evaluate if the interfaces could be subjected to future electrical degradation. Finally a discussion is re-opened on the risks of having permanent Ag surfaces without anti-tarnish.

1 Problem overview

1.1 Silver interfaces in the automobile applications

In the last years, the environment for the automotive connectors has become extremely harsh (temperature, current load and vibrations) and the demand in transmitted signal quality increased (higher frequency, functions more sensitive to resistance changes). Silver plated terminals have been introduced because of an excellent electrical conductivity, a higher temperature class, a really low surface oxidation and a cost competitiveness in comparison with the gold plated terminals [1]. Moreover when it is combined with a nickel under-layer silver plated terminals enable to reach the more severe requirements.

Today the silver plated interfaces can be found in main functions of the car like for example the electronic control units, sensors or safety circuit lines (**Figure 1.1**).

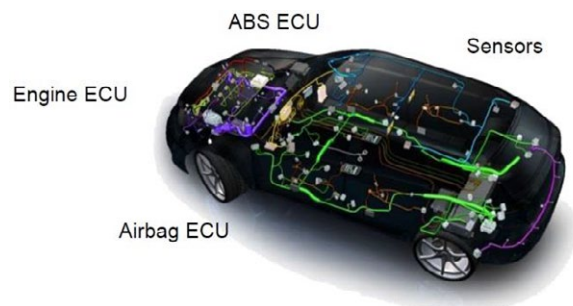


Fig. 1.1 Automotive applications for silver plated terminals (wiring scheme from a Delphi presentation).

For the automotive applications, the silver plated surface are combined with an anti-tarnish to limit surface aspect changes under an atmospheric exposure. It is also said that the Ag surface is passivated because it should not react anymore with the atmosphere. In fact,

silver plating can develop a dark, tarnish film when exposed to open air (**Figure 1.2**). The tarnish is mostly silver-sulfide, with some chlorides mixed in. High humidity and high air pollution levels can increase the growth rate of the tarnish layer. Luckily, silver tarnish is very soft, so it moves away from the contact area when terminals are plugged together. Silver plating can tarnish in days if left exposed in areas with normal air-flow [2].



Fig. 1.2 Typical silver plated tarnished tab

A common anti-tarnish often called a SAM (self-assembled monolayer) is supposed to form a film that is only one or two molecules thick in order to block the formation of the tarnish. The performance of the anti-tarnish with heat-aging is also quite unclear. It is assumed that the anti-tarnish volatilizes without leaving any insulating residue.

One qualification test consists in exposing the anti-tarnish to ammonium sulfide [3] and to measure the electrical resistance (according ASTM B667 specification for example). This test is usually done on coupons at room temperature (typical concentration of 0.2 ml of ammonium sulfide per liter of distilled water (**Figure 1.3**)). The acceptable contact resistance increase after his test are few milliohms maximum typically.

One common molecule called Octadecanethiol (ODT) is proposed by the plating supplier to cover the Ag surface with a monolayer. The linkage scheme is described in the **Figure 1.4**. The deposition can be done via several processes as immersion, electrodeposition, rolling or spraying. The ODT passivation solution is

prepared either with deionized water or with an organic solvent (alcohol based). For the immersion deposition the bath temperature has to be between 40 and 50°C. One motivation in the past year for using the alcohol based ODT solvent was to reduce the coefficient of friction of the surface. The concentration of ODT in the solvent is also adjustable. Some documentation and additional studies have been recently released by some suppliers [4].



Fig. 1.3 Ag plated coupons after ammonium sulfide test

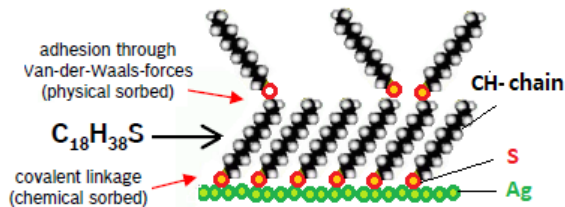


Fig. 1.4 ODT monolayer linkage scheme

1.2 Possible issues due to passivation

One new parameter of the problem comes from the fact that the electronic systems are always more complex and their sensitivity to voltage change increased. Because the usage of silver contacts has been enlarged, millions of silver plated terminals in the vehicles enable today to collect feedbacks from the field. This data should today help to consider if the risk assessment made years ago is still valid.

In addition, it appears that the definition, the processing and the control of the anti-tarnish hasn't been clearly specified between the OEM and the suppliers during the last years. The **Figure 1.5** shows two extracts of the two OEM pin and tab specifications.

Extract of the BMW drawing n° 1 383 799)

Anlaufschutz: Spezifikation Passivierung durch Thiole
 1.) Wirkstoff auf Basis Oktadekanthiol oder Hexadekanthiol oder Gemisch aus beidem
 2.) Geschlossen aufgebracht und homogen verteilt. Die Aufbringung mittels Sprühverfahren ist nicht zulässig
 3.) Nachweis der Wirksamkeit durch Ammoniumsulfid-Test oder Kaliumsulfid-Test oder Cyclovoltammetrie
 LUBRICATION: SPECIFICATION OF PASSIVATION BY THIOL
 1.) THIOL ON BASE OF OKTADKANTHIOL OR HEXADKANTHIOL OR A MIXTURE OF BOTH
 2.) CLOSED SURFACE AND HOMOGENEOUS DISTRIBUTED. APPLYING BY SPRAYING IS NOT PERMITTED.
 3.) PROOF OF EFFECTIVENESS BY AMMONIUM SULFIDE TEST OR POTASSIUM SULFIDE TEST OR *CYCLOVOLTAMMETRIE*

Extract of the Daimler drawing n° A 003 002 99 99)

Anlaufschutz: Spezifikation Passivierung durch Thiole
 1.) Wirkstoff auf Basis Oktadekanthiol oder Hexadekanthiol oder Gemisch aus beidem
 2.) Geschlossen aufgebracht und homogen verteilt
 3.) Nachweis der Wirksamkeit durch Ammoniumsulfid-Test oder Kaliumsulfid-Test oder Cyclovoltammetrie
 LUBRICATION: SPECIFICATION OF PASSIVATION BY THIOL
 1.) THIOL ON BASE OF OKTADKANTHIOL OR HEXADKANTHIOL OR A MIXTURE OF BOTH
 2.) CLOSED SURFACE AND HOMOGENEOUS DISTRIBUTED
 3.) PROOF OF EFFECTIVENESS BY AMMONIUM SULFIDE TEST OR POTASSIUM SULFIDE TEST OR *CYCLOVOLTAMMETRIE*

Fig. 1.5 OEM Pin passivation specification

If we tried to summarize the different opinions given in the literature and the customer feedbacks, the following matters or operating failures related to passivated silver contacts may be given (see **Figure 1.6**): first the some pins shown some discoloration (esthetic) or a partial tarnish after some time. It has been also noticed some change of coefficient of friction leading to mating force increases. In some case the anti-tarnish may have concentrated some external contaminant. More critical some interfaces are suspected to generate contact resistance fluctuation in the milliohm range but also stronger resistance increases.

This possible matters don't impact the customers at the same level of criticality. For example some defects may be detected earlier and a change of the component may be possible before its integration in the vehicle.

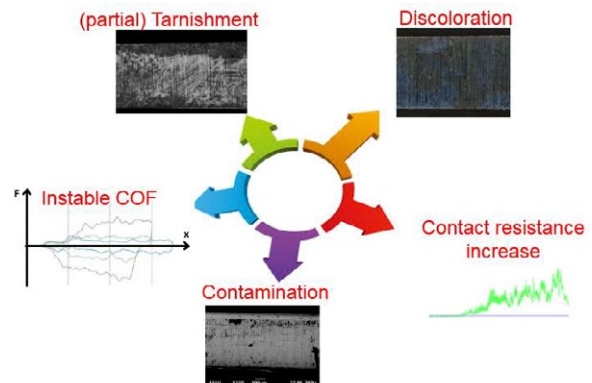


Fig. 1.6 Passivation matters and technical issues

1.3 Vehicle failure reported

Some customers reported cases of function failure of pressure sensors using silver plated terminals. This electrical failure impact vehicles produced and in the field since days and weeks. A first analysis by the OEM points out high contact resistance increases at the connector area then more precisely at the contact interface between the pins and the female terminals (no failure of the crimp area). The **Figure 1.7** represents the application circuitry:

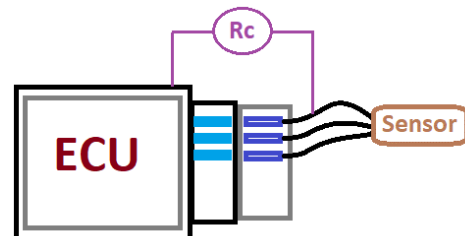


Fig. 1.7 Schematic of the sensor – ECU connectivity

Some contact resistances measurements have been conducted and the values are shown in the **Table 1.8**. This resistance measurements include the cables, the

terminals, the pins and soldered points to PCB. Values much over 1 Ohm are reported.

	Pin line n°1	Pin line n°2	Pin line n°3
Meas. 1	76	5129	36
Meas. 2	33	33	36
Meas. 3	33	58	40
Meas. 4	34	34	40
Meas. 5	41	94	45
Meas. 6	103	73	40

Table 1.8 Measured contact resistances between ECU and the cables.

Additional measurements have been conducted on the terminal crimp area. The results didn't show any resistance abnormality (see **Table 1.9**) and the crimp dimensions match the specifications.

	Pin line n°1	Pin line n°2	Pin line n°3
Meas. 1	19	19	22
Meas. 2	19	20	23

Table 1.9 Measured crimp contact resistances.

Not all measurement are shown in the paper, but it leads finally to the conclusion that a default in the pin / terminal contact interface is the cause of high and instable electrical resistances.

Some optical analysis of the contact points have been done. Surprisingly the pictures didn't show any specific degradation or wear. Just some organic material has been detected with the scanning electron microscope (see **Figure 1.10**). The correlation between the electrical measurements and the surface analysis is at that point not possible. Especially that the gap sizes and normal forces of the terminal are within the expected range.

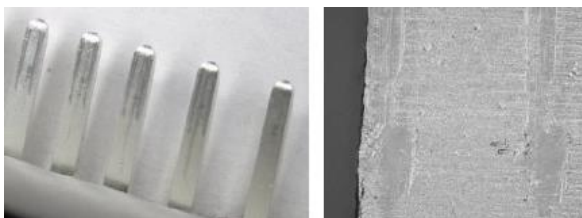


Fig. 1.10 Optical (left) and SEM (right) of the silver plated pins. The contact points appear functional.

1.3 Root cause analysis

The case reported in the previous paragraph highlights a need to see the problem with a more wider angle. A

root cause analysis through of a fishbone diagram is given in the **Figure 1.11**.

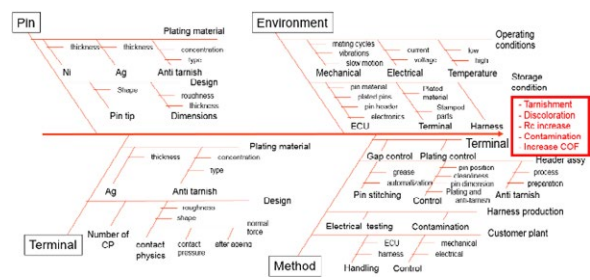


Fig. 1.11 Fishbone diagram related to the passivation at the interface of silver plated contacts.

2 Testing and Analysis

2.1 Influent parameters

The contact traces of the failed samples shown that the parameters related to the design of the terminal cannot have a major role. Nevertheless, two type of terminals will be used later on and the characterization of the surface via an indentation test device should be able to point out the impact of the contact force on the electrical stability of the interfaces.

The behavior of the passivated surface under aging conditions is unclear and this parameter will be investigated.

Two surface passivation will be considered, some samples will be made using a spray process and some others via a bath immersion processes. We will be also able to investigate the impact of the different concentration of ODT. One difference between both processes is that the immersion will use a water based solution and an organic based solvent will be used for the passivation spray process (supplier process restrictions). The **Figure 2.1** shows a scheme of plating cells around the passivation phase.

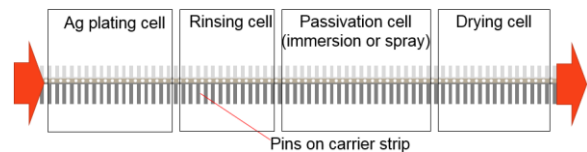


Fig. 2.1 Plating cells description.

Finally some contact traces will be created in order to investigate the mechanical resistance of the passivation under wear conditions.

2.1.1 Design of Experiment

From the Fishbone diagram, and taking in consideration the manufacturability efforts, the following variables have been taken for the Design of Experiment: terminals and coupons have been selected, an ODT concentration of 0, 0.1%, 0.5%, 1% and 10% and a deposition

of the anti-tarnish via an immersion and a spray process. The thermal ageing is set as 1 hour, 8 hours, 1 day, 7 days and 3 weeks associated with temperature changes between -40°C and +125°C.

As main outputs, the surfaces will be characterized, the contact resistances will be measured in contact pair condition and indentation force test measurements will be led (see Figure 2.2).

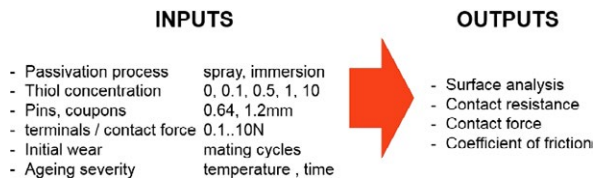


Fig. 2.2 Inputs / outputs parameters of the DoE

2.1.2 Test description

The Figure 2.3 describes how the samples are tested. First the surfaces will be checked with an optical microscope then with a scanning electron microscope in Back Scattering Imaging mode (BSQ). The BSQ mode or so call “chemical contrast mode” enables to identify low electro-conducting elements (dark colors).

Some of the samples are mated once in order to proceed to some contact electrical measurements. One lot of samples will stay mated during the full ageing phase and will be unmated only after the last contact resistance measurement. Another lot will be unmated before the ageing phase and will be mated for the final contact resistance measurements. One purpose of the first mating is to create initial contact traces that might highlight local surface disturbances. Final surface characterizations will be done and some electrical indentation tests are performed to evaluate the electrical conductivity of the films under variable contact forces.

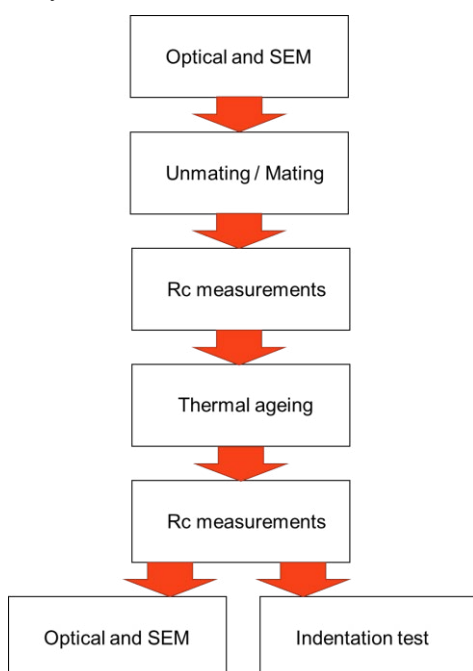


Fig. 2.3 Test sequence description

The Figure 2.4 show the preparation of the samples and the samples in the climatic chamber.



Fig. 2.4 Samples for the tests

2.2 Optical und SEM analysis

In this paragraph we will proceed to the characterization of the samples that have been passivated through an immersion process.

An optical and a SEM analyze has been perform on the samples before being set in the climatic chamber (Figure 2.5).

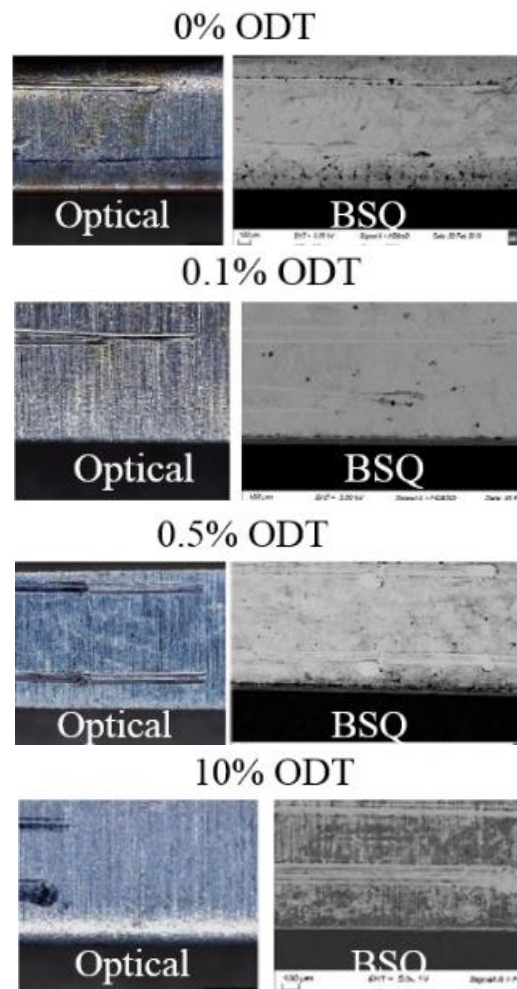


Fig. 2.5 Pins before ageing analyzed with optical and SEM. ODT concentration are 0, 0,1, 0,5 and 10% (immersion process).

The optical microscope do not enable to differentiate the samples beside the one without ODT that show already some traces of discoloration. The usage of the

SEM in BSQ mode enable to highlight several surface conductivity failure for the samples passivated with different ODT concentrations. The samples with 10% appear really dark that means really low surface conductivity.

After thermal ageing (3 weeks), the analysis doesn't show a big differences with the initial pictures (Figure 2.6). Nevertheless, a stronger magnification enables to point out crystals or an accumulation of organic compounds. In fact it looks that the homogeneity of the passivation film has been damaged.

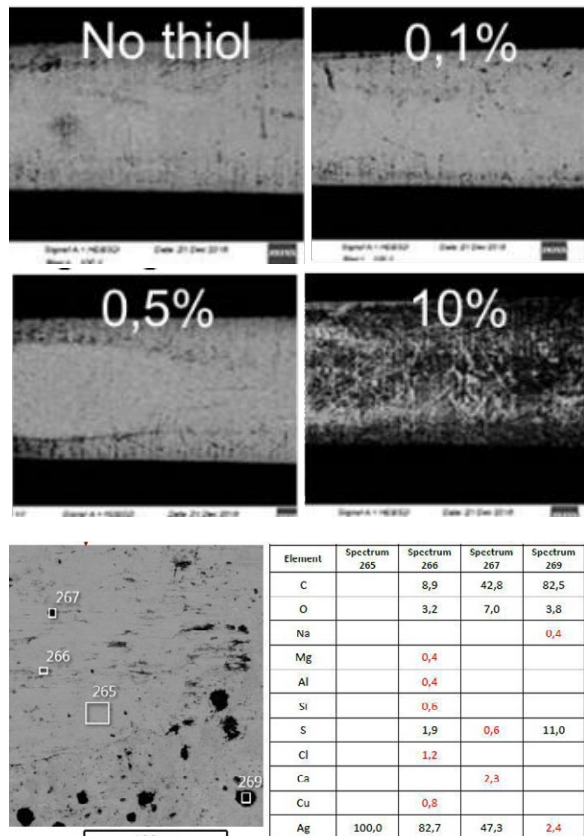


Fig. 2.6 Pins after 3 weeks ageing analyzed with SEM (BSQ mode). ODT concentration are 0, 0,1, 0,5 and 10% (immersion process).

The samples made with a sprayed process deposition (1% ODT and above) are with the optical microscope really different that the first ones. In fact we were able to notice a stronger accumulation of the organic material at the contact area (brown traces). It appears that a crystallization process occurred, several low conductive spots are detected quite homogenous on the surface (Figure 2.7). At that stage another hypothesis could be that a de-wetting occurred locally and that the thiol was missing in some locations generating further tarnishing. Once again the black spots are not visible with optical means.

It appear also possible that the relative movements due to the ageing thermal phases brought more ODT at the contact point area, then crystallize a film at the interface.

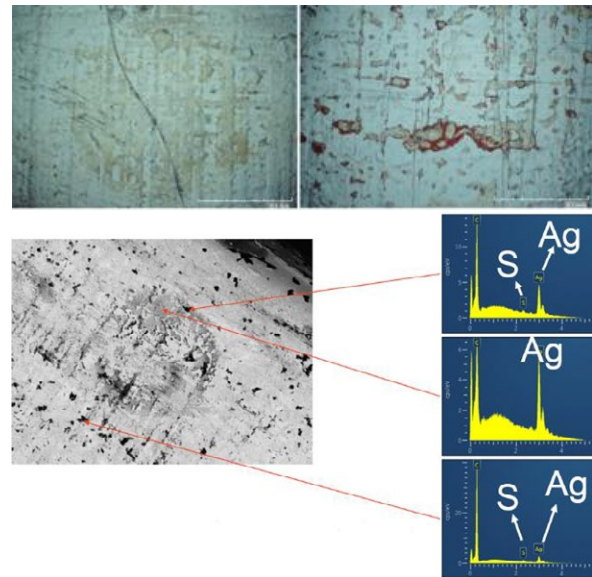


Fig. 2.7 Optical (upper pictures) and BSQ (lower pictures) analysis of an ODT sprayed sample after ageing.

2.3 Electrical results

Some electrical measurements have been carried out with the mated samples (Table 2.8). Same resistance variations have been noticed but the values are still within the OEM specifications. The variations are higher for the samples having coated with 0,5% (type D) and 10% ODT (type B). No difference can be made between the type of terminal used for the connection.

Group 1 (8 hrs Temperature cycle)

Terminal #	TYPE A		TYPE B		TYPE C		TYPE D	
	Mated	Unmated	Mated	Unmated	Mated	Unmated	Mated	Unmated
1	1.60	1.50	1.55	2.55	1.60	1.50	1.60	1.45
2	1.55	1.45	1.65	2.15	1.35	1.45	1.60	1.55
3	1.50	1.40	1.50	2.40	1.50	1.50	1.50	1.45
4	1.45	1.40	2.20	2.40	1.50	1.60	1.55	1.60
Min	1.45	1.40	1.50	2.15	1.35	1.45	1.50	1.45
AVG	1.53	1.44	1.73	2.38	1.49	1.51	1.56	1.51
Max	1.60	1.50	2.20	2.55	1.60	1.60	1.60	1.60
s	0.06	0.05	0.32	0.17	0.10	0.06	0.05	0.07

Group 2 (24 hrs Temperature cycle)

Terminal #	TYPE A		TYPE B		TYPE C		TYPE D	
	Mated	Unmated	Mated	Unmated	Mated	Unmated	Mated	Unmated
1	1.55	1.50	2.40	1.60	1.65	1.70	1.55	1.45
2	1.50	1.40	1.60	1.80	1.60	1.60	1.70	1.65
3	1.55	1.55	1.75	1.90	1.45	1.45	1.60	1.50
4	1.45	1.45	1.50	1.60	1.70	1.55	1.50	1.60
Min	1.45	1.40	1.50	1.60	1.45	1.45	1.50	1.45
AVG	1.51	1.48	1.81	1.73	1.60	1.58	1.59	1.55
Max	1.55	1.55	2.40	1.90	1.70	1.70	1.70	1.65
s	0.05	0.06	0.40	0.15	0.11	0.10	0.09	0.09

Group 3 (168 hrs Temperature cycle)

Terminal #	TYPE A		TYPE B		TYPE C		TYPE D	
	Mated	Unmated	Mated	Unmated	Mated	Unmated	Mated	Unmated
1	1.60	1.50	2.40	1.75	1.50	1.40	2.10	1.55
2	1.55	1.45	1.90	2.10	1.60	1.60	2.05	2.10
3	1.55	1.60	2.00	2.00	1.55	1.55	1.95	2.10
4	1.45	1.50	2.10	2.15	1.50	1.50	1.90	1.95
Min	1.45	1.45	1.90	1.75	1.50	1.40	1.90	1.55
AVG	1.54	1.51	2.10	2.00	1.54	1.51	2.00	1.93
Max	1.60	1.60	2.40	2.15	1.60	1.60	2.10	2.10
s	0.06	0.06	0.22	0.18	0.05	0.09	0.08	0.26

Group 4 (504 hrs Temperature cycle)

Terminal #	TYPE A		TYPE B		TYPE C		TYPE D	
	Mated	Unmated	Mated	Unmated	Mated	Unmated	Mated	Unmated
1	1.80	1.65	1.90	2.10	1.50	1.60	2.05	1.40
2	1.75	1.55	1.75	2.00	1.45	1.40	1.95	1.50
3	1.60	1.45	1.60	1.90	1.55	1.45	1.90	1.45
4	1.65	1.60	1.70	1.95	1.50	1.65	2.00	1.65
Min	1.60	1.45	1.60	1.90	1.45	1.40	1.90	1.40
AVG	1.70	1.56	1.74	1.99	1.50	1.53	1.98	1.50
Max	1.80	1.65	1.90	2.10	1.55	1.65	2.05	1.65
s	0.09	0.09	0.13	0.09	0.04	0.12	0.06	0.11

Fig. 2.8 Electrical measurement made on mated samples.

Additional electrical measurements have been conducted in order to evaluate if an aged passivation leads to contact resistance increases. The force indentation test method is used to record the contact resistance (4 wires) versus contact normal force. A sphere ($r=1\text{ mm}$) is tooled and renew for each experiment. A conductive silver paste is used to connect the wires to the male pins or coupons. The normal force is adjustable between 0,1 and 10N (see **Figure 2.9**).

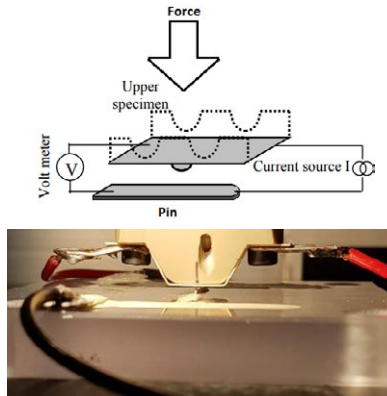


Fig. 2.9 Indentation force test setup

The samples aged for 7 days have been used for the measurements. The results of the measurements are shown in the **Figure 2.10**.

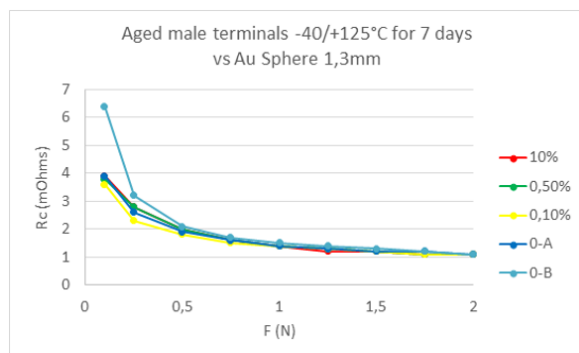


Fig. 2.10 Contact resistance versus contact force for samples with ODT made by immersion.

The electrical results don't show any resistance increase when tested under a normal force over 0,5N. Slight resistance increases (within the OEM requirements) are noticeable for the samples without ODT tested with low normal force ($<0,2\text{N}$).

Samples with sprayed ODT and aged show higher electrical contact resistance for all contact forces (**Figure 2.11**). Because of the humogen distribution of the ODT spots on the surface, we assume that the probe is always in contact with several of this low conductive spots.

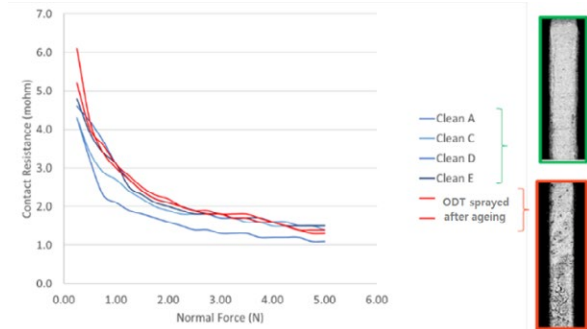


Fig. 2.11 Contact resistance versus contact force for samples ODT sprayed.

2.4 Next steps

The validation of a new design of experiment is currently on going. It takes in consideration others terminals and a new test methodology that may activate other failure modes. In fact as first results, it appears that some repetitive maneuvers of the terminals (out of the OEM specifications) may lead to higher resistance fluctuations.

It is also important to report that during the time of this investigations some questions related to the effective ODT concentration or the quantity of ODT on the surface has been investigated. Because of the molecular monolayer of ODT after solvent evaporation, the measurement of the film thickness is difficult in laboratory conditions and almost not feasible in industrial conditions. Some tries have been leaded via a chromatography spectrum analysis (**Figure 2.12**).

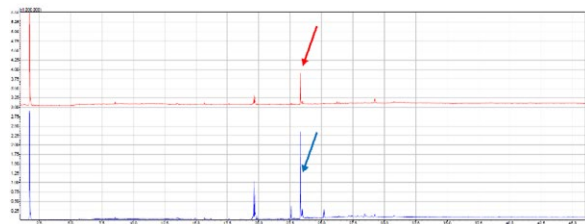


Fig. 2.12 chromatography spectrum analysis of samples coated with 2 different ODT concentration. In red a low concentration and in blue a higher ODT concentration.

It appears that a correlation between the analysis is possible when a reference sample is set. The calculation formula can be written as follow :

$$I_{\text{peak1}} / I_{\text{peak2}} = [\text{ODT}]_1 / [\text{ODT}]_2$$

Nevertheless no reference or specification can be set for using such analysis in production.

3 Conclusions

In this paper, we had the opportunity to investigate and to discuss the impacts of the superficial passivation film on the silver plated terminals. As main result, the ODT water based immersion process leads a more homogeneous film on the silver surface than the spray alcohol based process. The optical analysis of the surface is not sufficient to evaluate if the passivation is well set on the surface. A SEM analysis combined with chemical contrast analysis (BSQ) is in all cases required. In addition it appears that the resistance fluctuations are related to a high amount of highly resistive spots on the pin surface and the correlation between the contact pressure of the terminal with the resistance measurements at that stage is not demonstrated.

The state of the art of the passivated silver plated terminal need to be challenged, maybe just because some deviations between the OEM specifications exist and also because we could report some resistance fluctuations in the results of this design of experiment.

In case of no anti-tarnish on the silver surface short term impacts are noticeable like a surface discoloration and a higher tendency for cold welding leading to higher mating forces. Nevertheless, this inconvenient may be reconsidered in comparison with the electrical failures that an uncontrolled passivation layer can lead. Some discussions are currently ongoing to evaluate if it is possible to measure the ODT quantity of the anti-tarnish on silver in production.

In the meanwhile one solution consisting of having no anti-tarnish may be option to be discussed with the OEMs (at least for the non-sensitive automotive applications). This solution may require some product design adjustments to reduce the mating forces and/or cold welding effect to ensure that the parts are mountable in the vehicle without any additional assistance device (connector lever).

4 Literature

- [1] The Performance Implications of Silver as a Contact Finish in Traditionally Gold Finished Contact Applications. Marjorie Myers. Interconnection and Process Technology Tyco Electronics Harrisburg, USA . ICEC 2009..
- [2] Overview of the Use of Silver in Connector Applications. Marjorie Myers. Interconnection & Process Technology Tyco Electronics, Harrisburg, PA. February 5, 2009
- [3] W. Crossland, E. Knight, "The accelerated tarnish testing of contacts and connectors employing silver alloy contacts", HOLM conf. 1973.
- [4] E. Philipp, A, Vogt, E. Flegel, "Neue Methode zur Bestimmung und Charakterisierung der ODT-Belagung und deren Wirkung auf versilberte, Elektrische Kontaktflächen", 7. Symposium Connectors conference, VDE/VDI, Lemgo, 2019.

Study on the Arc Erosion Characteristic and Mechanism of AgSnO₂ Used in the Simulated Conditions of Automotive Relay

Li Jie, Yan Xiaofang, Bai Xiaoping, Zhang Mingjiang Zhang, Chen Yangfang,
Jin Yangdeng, Yang Changlin, Zhang Xiufang
Fuda Alloy Materials Co., Ltd., Wenzhou, Zhejiang, 325025, China
E-mail: lj@china-fuda.com Tel: +86-18357800054 Fax: +86-577-86909166

Abstract

Automotive relays, which are widely used in the control of automotive starting, preheating, air condition, lighting and other systems, play an important role in controlling electrical systems. When the relay is under lighting load, a surge current (5-10 times of the steady-state current) will be produced, which is easy to welding and leading to serious contact material transfer. When the electric contact is eroded seriously, the reliability of the contact will be decreased. This paper has focused on the study of the arc erosion performance of different electric contact materials under the simulated lighting load. Arc energy, arc time, welding force, rebounding times and other characteristic parameters of different AgSnO₂In₂O₃ electric contact materials, as well as arc erosion mechanism, were investigated by using electrical performance simulated device. It was expected to provide an important reference for the development and application of electrical contact materials.

Key words

Arc Erosion, Electric Contact, AgSnO₂, Automotive Relay

1 Introduction

Automobile relay is an important control element in automobile electrical system, which is widely used in the control of automobile starting, preheating, air conditioning, lighting, wiper, oil pumping, security, audio, navigation, automobile electronic instrument and fault diagnosis systems. The quality of automobile relay plays an important role in ensuring the safe operation of automobile [1].

When the relay is under lighting load, a surge current (5-10 times of the steady-state current) will be produced, which is easy to welding and leading to serious material transfer. When the relay is under inductive load, it is difficult to extinguish the arc due to the long arc time, leading to serious erosion. After the electric contact is eroded, it will lead to bad consequences such as the decrease of contact reliability and electric life. Therefore, it is very important to study the arc erosion performance of electrical contact materials.

Many scholars have studied the arc erosion performance of automotive relays [2-11].

N. Ben Jemaa has focused on transition from the anodic arc phase to the cathodic metallic arc phase in vacuum at low DC electrical level. It indicated that transfer direction was independent from metallic and gaseous-

phases. Besides, it showed that it was possible to distinguish the transition from the anodic to the cathodic arc by observing the evolution of the arc spots on the rivets [2].

Peter Braumann has investigated the influence of manufacturing process, metal oxide content, and additives on the switching Behaviour of Ag/SnO₂ in automobile relays. It was concluded that the use of Bi₂O₃ in place of WO₃ considerably reduced the welding forces, under lamp load the reduction of In₂O₃ content improved welding resistance, the additive Bi₂O₃ also reduced the specific erosion under motor load, a further optimization of erosion behaviour under motor load can be achieved by using high concentrations of the additive In₂O₃ [3].

W. Weise has researched thermodynamic analysis of erosion effects of silver-based metal oxide contact materials. It was showed that the an arc erosion would not depend on the type of oxide particles added to the silver base material [4].

In the practical application process of automotive relay, there are some problems, such as poor anti-welding properties and serious material transfer. In this paper, the erosion characteristics and mechanism of the arc will be investigated under the condition of simulated lighting load by studying on the simulated electrical properties between conventional materials and special materials, including rebounding times, rebounding en-

ergy, arc energy, arc time, welding force, contact surface morphology analysis after the test etc., hoping to provide an important reference for the research and design of the electric contact materials for DC relay.

2 Test Method and Process

2.1 Material preparation method and composition

Internal oxidation method is one of the most commonly used methods to prepare silver tin oxide electrical contact materials. The materials prepared by this method have a series of advantages, such as good arc wear resistance, good material transfer resistance, etc., which are widely used in the field of automotive relays.

In this test, conventional materials and special materials were prepared by internal oxidation process, and the properties of the two materials were compared as well. The specific composition is shown in Table 1. And then the above wires were made into rivets, and the electrical performance simulated test was carried out on the electrical performance simulated test device. Besides, the contact was assembled into automotive relay, and the electrical life test was carried out.

Table 1 Comparison on composition between conventional materials and special materials

Category	Content (wt.%)				Notes
	Ag	In ₂ O ₃	SnO ₂	Additives	
Conventional material	85.5	4	Remain	1	The additives types of the two materials were the same, while the additives content of the two were different.
Special material	85.5	4	Remain	2	

The internal oxidation process of this test was as follows: the raw material was melted, extruded and drawn to obtain the wire material of the required specification for internal oxidation, and the final product was obtained by internal oxidation, ingot pressing, extrusion and drawing. The specification of the final wire material was Φ 1.4[soft state].

Internal oxidation process including: melting → removing the oxide skin on the surface → AgSn extrusion → drawing and annealing → punching → internal oxidation → ingot pressing → sintering → recompression → extrusion → drawing and annealing.

The density, hardness, tensile strength, elongation, electrical resistivity and microstructure of the wire were measured by electronic balance densitometer, Vickers hardness tester, tensile machine, electrical resistivity tester and metallographic microscope, respectively.

2.2 Introduction of electrical performance simulated device

The above wires were made into rivets by cold heading machine, and the specifications of moving and static

contacts were R2.2x0.5+1.5x1.2SR15. Then the electrical simulated test was carried out.

The electrical performance simulated test device used in this test, which was mainly applied to simulate contact materials, was developed by Harbin Institute of Technology, China.

The typical actuation of electromechanical relay is provided by the electromagnetic force. In order to simulate the mechanical operation quite closely, the mechanical structure of the test rig is designed as shown in Fig.1. The whole experimental apparatus consists of three main modules, including the four degrees of freedom motion structure, the measurement unit and the software control part. The horizontal actuation of the moving electrode is realized by a micro electromagnet connected with an insulated pushing rod. The actuation travel could be set by a micrometres head. The movable contact is attached to the free end of the leaf spring (beryllium bronze strip). The relative distance between pushing rod and the normally open contact pair in 'X' direction is determined by the Muli-Axis stage 1. The stationary contact is connected with the force sensor by the stationary strip, whose position in 'X' direction can be controlled by using Muli-Axis stage 2, thus the contact gap and the final contact force are both adjustable. All the above mechanical parameters have a resolution of 10 μ m. The mechanical structures are secured on the vibration isolation platform.

The contact voltage is measured by the method of resistor division, which provides a test resolution of 30mV. The contact current is measured by Hall current sensor, which has the measurement range of 100A and the resolution of 50mA. The measurement of contact force is realized by a piezoelectric force sensor with the measurement range of 45N and the resolution of 1mN.

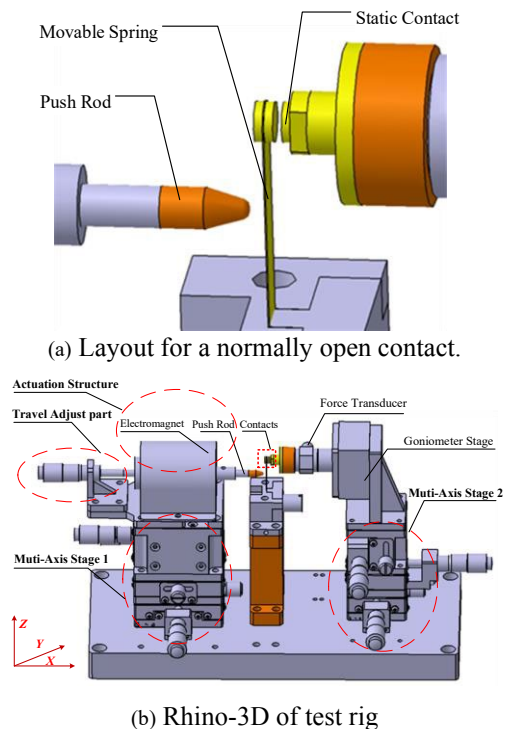


Fig. 1 Mechanical structure of test rig

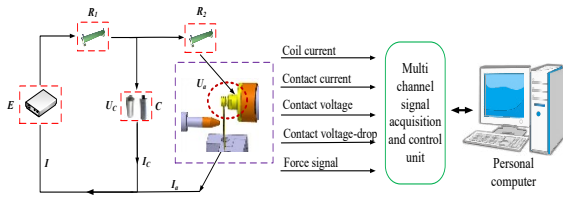


Fig. 2 Schematic of the experimental circuit

All above testing data including contact voltage, contact current and dynamic force are acquired by the commercial DAQ system (PCI1706, Advantech, Taiwan), which has a measurement resolution of 16 bits and a sampling frequency of 250kHz. The instrument is interfaced to a personal computer using serial port RS232. Data acquisition and logging process are controlled by a PC with the help of LabVIEW software specifically programmed for this purpose.

Table 2 shows specific parameters of electrical performance simulated and relay test.

Table 2 Specific parameters of electrical performance simulated and relay test

Category	Load type	Voltage (V)	Current (A)	Frequency	Times (Times)	Failure judgment	Notes
Simulated electrical performance test	Simulated lamp load	13.5V	Impact 90A	1s on 1s off	until failure	5 continuous times of welding force exceeding 30g	
Relay test			Steady state 20A			Voltage drop is greater than 1.35V	

3 Results and analysis

Firstly, the mechanical and physical properties of conventional materials and special materials were compared, as shown in Table 3. It can be seen that conventional materials have higher hardness, higher tensile strength and lower elongation.

After improvement, the hardness of special materials was 19HV lower than that of conventional materials, the tensile strength of special materials was about 62MPa lower than that of conventional materials, the elongation of special materials was 8% higher than that of conventional materials, and the electrical resistivity of special materials was $0.07 \mu\Omega \cdot \text{cm}$ lower than that of conventional materials. It should be noted that lower hardness can reduce the occurrence of contact rebounding and increase the contact stability.

Table 3 Comparison on mechanical and physical properties between conventional materials and special materials

Category	Hardness value (HV0.3)				Tensile strength (MPa)	Elongation (%)	Electrical resistivity ($\mu\Omega \cdot \text{cm}$)	Density (g/cm^3)	Notes
	Data 1	Data 2	Data 3	Average					
Conventional material	120	121	121	120.7	382	17	2.47	9.75	
Special material	102	101	101	101.3	330	25	2.40	9.75	

Fig. 3 shows the comparison on microstructure between conventional materials and special materials. It can be seen that the oxide particles size of conventional material was small, most of which were smaller than 1

μm , while the oxide particles size of special materials was relatively larger and the coarse oxide particles of $1 \mu\text{m}$ could be found.

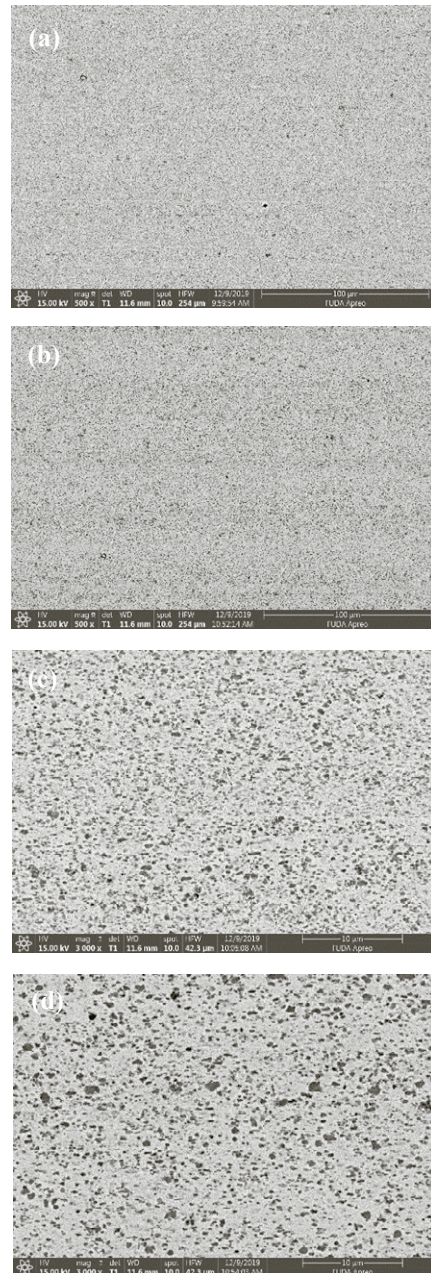


Fig. 3 Comparison on microstructure between conventional materials and special materials (SEM)

- (a) Conventional material, 500x,
- (b) special material, 500x,
- (c) Conventional material, 3000x;
- (d) special material, 3000x

It is noted that the principle of dispersion strengthening was that mechanical properties of materials could be improved by blocking the movement of dislocations with dispersed fine particles, such as hardness, tensile strength and so on. In this test, the oxide particle size of conventional materials was smaller, and special materials has more amount of the coarse oxide particles (about $1 \mu\text{m}$). According to the principle of dispersion

strengthening, the fine particles would increase the hardness, tensile strength and other properties of materials. Therefore, the hardness and tensile strength of special materials were lower than that of conventional materials, and the elongation was higher than that of conventional materials.

In addition, under the condition of the same oxide content, the smaller the oxide particles, the more oxide particles per unit volume, the longer the path to hinder the electron movement. The special materials have more coarse oxide particles, therefore, the resistivity of the special materials was lower than that of the conventional materials.

Comparison on simulated and relay electrical life results between conventional materials and special materials are shown in Table 4 and table 5.

It can be seen from table 4 that the 95% confidence interval of Weibull curve, the electric life of simulated electrical life of conventional materials and special materials were 146572 and 234612 times respectively, and the electric life of special materials was about 88000 times higher than that of conventional materials. It can be seen from table 5 that the 95% confidence interval of Weibull curve, the electrical relay life of conventional materials and special materials were 174153 and 254698 times respectively, and the electrical life of special materials was about 80, 000 times higher than that of conventional materials. Compared with table 4 and table 5, it indicates that the simulated and relay electrical life of special materials were superior to those of conventional materials, that is, the rule of simulated electrical life was the same as relay. Therefore, the data of simulated electrical properties test could be used to explain the difference between these two materials.

Table 4 Comparison on simulated electrical life results between conventional materials and special materials

Category	Electrical life (Times)	Shape parameter m	Scale parameter η	AD	μ_{10} Characteristic life (Times)			Significance of distribution P
					Lower limit	Confidence interval	Upper limit	
Conventional materials	138260	19.82	138680	0.325	139585	146573	153908	> 0.250
	135317							
	127549							
	146674							
	1288359							
Special materials	224796	49.31	229688	0.276	230279	234856	239977	> 0.250
	225414							
	234953							
	227505							
	228697							

Table 5 Comparison on electrical life results of relay between conventional material and special material

Category	Electrical life (Times)	Shape parameter m	Scale parameter η	AD	μ_{10} Characteristic life (Times)			Significance of distribution P
					Lower limit	Confidence interval	Upper limit	
Conventional materials	163327	23.96	166358	0.425	167314	174153	181272	> 0.250
	159689							
	174597							
	154123							
	163254							
Special materials	240567	65.07	250439	0.261	250795	254698	258661	> 0.250
	244102							
	253975							
	251609							
	241673							

Besides, it can be seen from Table 4 that the shape parameters m of conventional materials and special materials were both larger than 1, which indicating that the electrical life of the two materials was an increasing

loss failure period. The shape parameters of conventional materials and special materials are 138680, 229688 times respectively. Besides, the AD values of conventional materials and special materials were 0.325 and 0.276 respectively, indicating that the distribution of electrical life of special materials was better than those of conventional materials. The Weibull distribution parameters of electrical life of relays of conventional material and special material also showed similar rules.

It is noted that in this paper five groups of tests have been carried out respectively for simulated electrical life and relay electrical life, and the AD value were all greater than 0.25. The larger the number of sample groups was, the more accurate the fitting results were. However, the development trend of electrical life can be seen from the existing data, which was expected to provide some reference for scholars and other researchers.

In order to further understand the reasons for the differences of electrical properties between conventional materials and special materials in simulated electrical properties and relay tests, as well as to understand the characteristics of arc action more comprehensively, this paper selected the conventional materials and special materials with simulated electrical life of 138260 times and 224795 times to carry out the rebounding times, rebounding energy, arc energy, arc time, welding force, contact morphology analysis after burning and other comparisons.

Fig. 4 illustrates the comparison on rebounding times and rebounding energy between conventional materials and special materials in the electrical performance simulated test.

Fig. 4(a) and Fig. 4(b) show the rebounding times of conventional materials and special materials respectively. It can be seen that the rebounding times of conventional materials were mostly distributed between 4-9 times, and tend to be stable as the increase of test times. While the rebounding times of special materials were mostly distributed between 0-6 times, as the increase of test times there was a trend of first stabilizing and then increasing rapidly. After 180000 times, the rebounding times increased significantly and reached the maximum value before failure, about 35 times.

It can be seen from the rebounding energy curves in Fig. 4(c) and Fig. 4(d) that as the increase of electric life times the rebounding energy region of conventional materials was stable, which was consistent with the law of rebounding times, with the maximum rebounding energy of about 200mJ. While the rebounding energy of special materials tended to be stable firstly and then increased rapidly after 170000 times, which was the same as the law of rebounding times. For rebounding energy of after 170000 times, there was a rapid increase and the maximum value was about 1300mJ before failure.

It is noted that the hardness of conventional materials was about 20HV higher than that of special materials,

which was easy to make the contact rebound, thus the rebounding times and rebounding energy of conventional materials were higher than that of special materials.

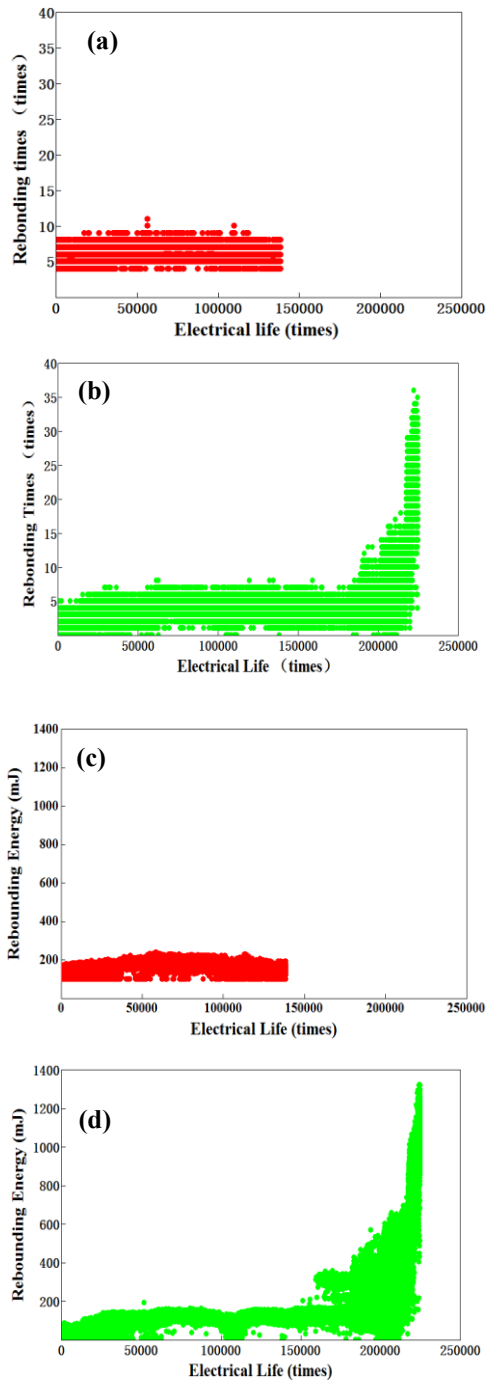


Fig. 4 Comparison on rebounding times and rebounding energy between conventional materials and special materials in electrical performance simulated test. (a) rebounding times of conventional materials, (b) rebounding times of special materials, (c) rebounding energy of conventional materials, (d) rebounding energy of special materials.

Fig. 5 shows the comparison on arc energy and arc time between the conventional materials and special materials in the electrical performance simulated test.

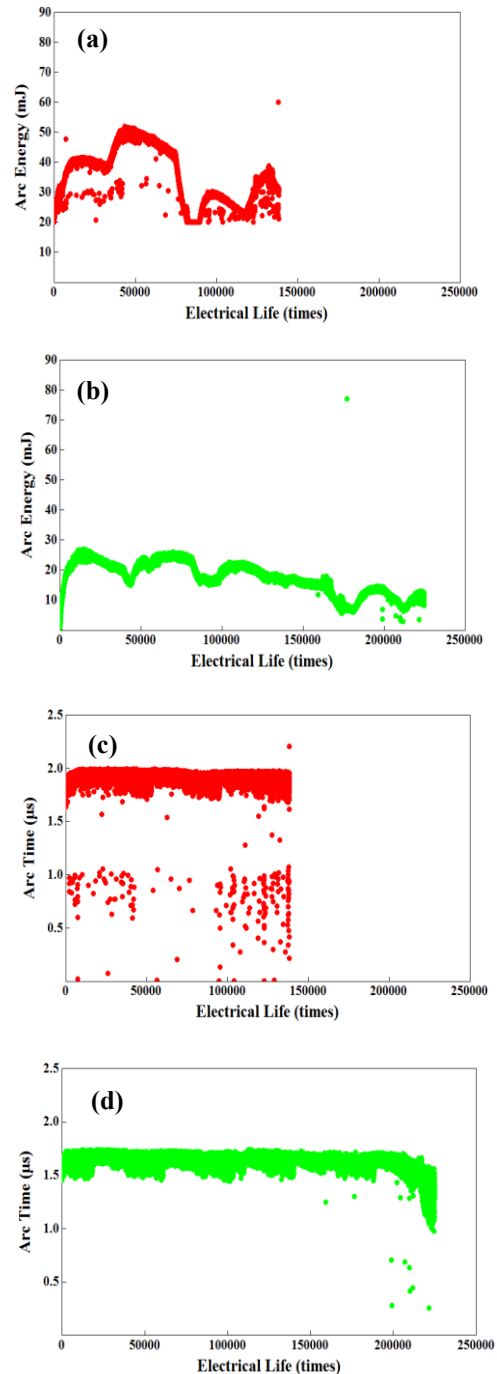


Fig. 5 Comparison on arc energy and arc time between conventional materials and special materials in electrical performance simulated test. (a) arc energy of conventional materials, (b) arc energy of special materials, (c) arc time of conventional materials, (d) arc time of special materials.

Fig. 5(a) and Fig. 5(b) show the arc energy of conventional materials and special materials respectively. It can be seen that the arc energy of conventional materials was higher than that of special materials, in which the arc energy range of conventional materials was about 20-50mJ and the arc energy of special materials was about 10-30mJ. Meanwhile, the arc energy of the two materials fluctuated obviously, which was caused

by the change of the final separation position of the contact.

Fig. 5(c) and Fig. 5(d) show the arc time of conventional materials and special materials respectively. It can be seen that the arc time of conventional materials was about 0.2s longer than that of special materials, and the arc time range of conventional materials and special materials were about 1.7-2.0 μ s and 1.5-1.75 μ s respectively.

Fig. 6 shows the comparison on welding force between conventional materials and special materials in electrical performance simulated test. It can be seen that the welding force of conventional materials was about 0.04N higher than that of special materials. As the increase of electrical life times, the welding force of special materials increased at about 100000 times (presumably due to the change of contact position) and then the welding force increased rapidly after 200000 times.

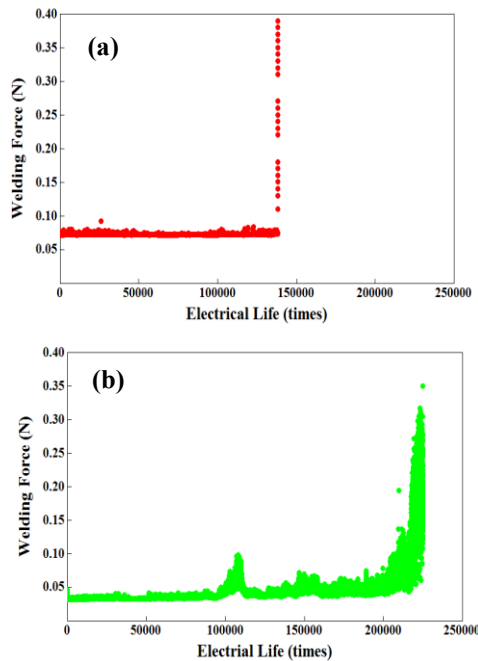


Fig. 6 Comparison on welding force between conventional materials and special materials in electrical performance simulated test.

(a) conventional materials, (b) special materials

Fig. 7 and Fig. 8 show the comparison on the macroscopic and microscopic appearance of the contact surface after the arc burning during the electrical performance simulated test.

It can be seen from the macroscopic appearance in Fig. 7 that the conventional materials showed obvious material transfer phenomenon, the moving contact presented obvious bulge while the static contact exhibited obvious pit.

It means that the materials were transferred from the static contact to the moving contact, accompanied by the splashing of materials, in which the static contact exhibited holes due to burning loss. While the surface

of the special materials after burning loss was relatively flat, and the static contact was burned seriously, mainly in the way of burning loss of static contact.

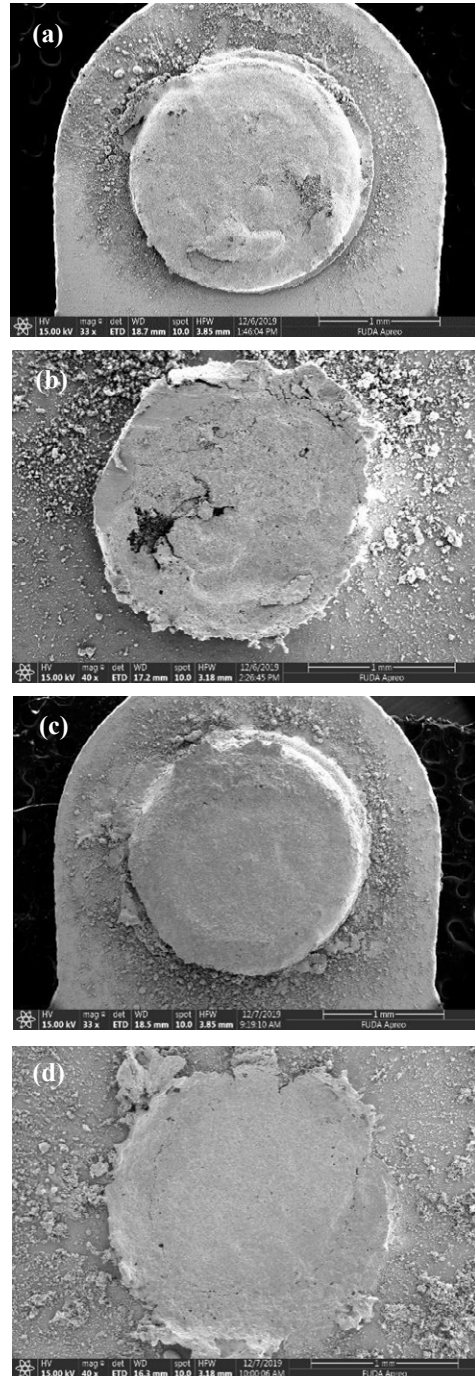


Fig. 7 Comparison on contact surface macro morphology after arc burning during electrical performance simulated test.

(a) moving contact of conventional material, 138260 failure;

(b) static contact of conventional material, 138260 failure;

(c) moving contact of special material, 224795 failure

(d) static contact of special material, 224795 failure

It can be seen from the micro morphology in Fig. 8 that the bulges and pits in conventional materials were

rough, while the contact position of special materials was smooth, showing the characteristics of re-solidification after high temperature melting.

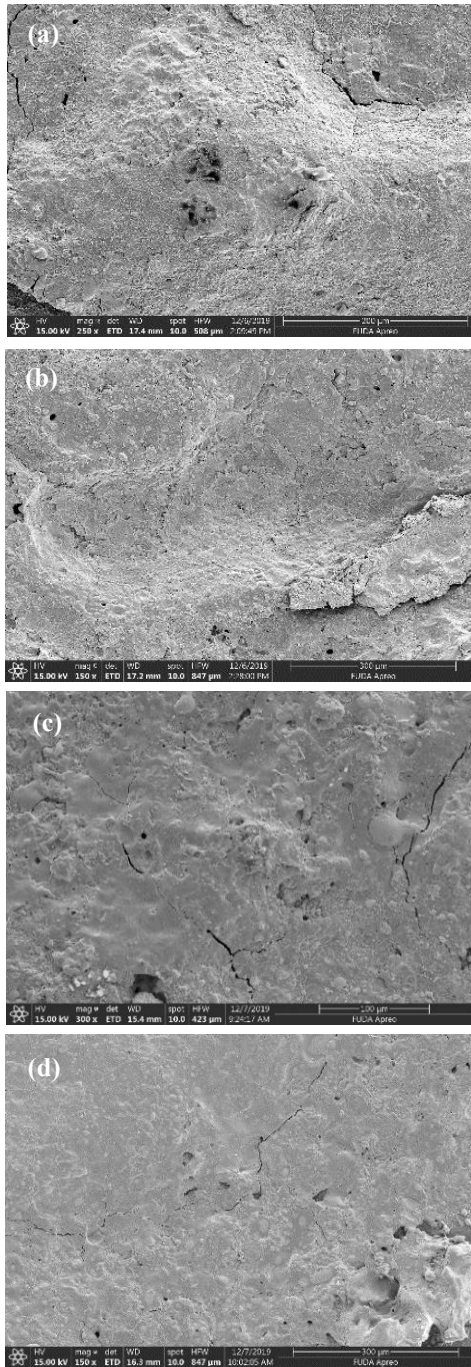


Fig. 8 Comparison on micro morphology of contact surface after arc burning during electrical performance simulated test

- (a) the moving contact of conventional material, 138260 failure;
- (b) the static contact of conventional material, 138260 failure;
- (c) the moving contact of special material, 224795 failure;
- (d) the static contact of special material, 224795 failure.

It can be concluded from Fig. 7 and Fig. 8 that the erosion of conventional materials by electric arc was mainly material transfer, while the erosion of special materials by electric arc was mainly static contact consumption.

In conclusion, the electrical life of special materials was longer than that of conventional materials. The failure mechanism of conventional materials was that the material transfer lead to the failure of welding. The direction of material transfer was from static contact to moving contact and the roughness of material transfer position was large. The failure mechanism of special materials was that the contact consumption was large, which lead to the failure of welding force exceeding the setting requirements, and the contact position was relatively smooth, showing characteristic of recrystallization by high temperature fusion. The low hardness of special materials could increase the stability of the contact process and reduce the rebounding times and rebounding energy. Besides, coarse oxide particles and high content of additives played an important role in reducing the arc energy, arc time and welding force, so special materials showed better electrical performance under simulated lighting load.

It is noted that low hardness and coarse particles played a significant role in improving contact rebounding and anti-welding properties. Therefore, for loads with large current impact, such as lighting load, low hardness and coarse particles were the direction of electric contact materials for the research and development in the future. At the same time, for the research and development of electrical contact materials under different load conditions, the balance between consumption resistance and anti-welding resistance by adjusting the content of additives needs to be studied further.

4 Conclusions

- (1) Compared with the physical and mechanical properties between conventional and special materials, the special materials exhibited lower hardness, lower tensile strength, lower electrical resistivity, higher elongation and more coarse oxide particles (particle size was about 1 μm).
- (2) The 95% confidence interval of Weibull curve shows that the simulated electrical life of conventional materials and special materials was 146572 and 234612 times respectively, and the electrical life of special materials was about 88000 times higher. Besides, the electrical life of relays showed the similar law.
- (3) The failure mechanism of conventional materials was that the material transfer led to the heavy welding failure finally, the direction of material transfer was from static contact to moving contact, and the roughness of material transfer position was large. While the failure mechanism of special materials was that the contact consumption was large, which led to the failure of welding force exceeding the setting requirements,

and the contact position was relatively smooth, showing the characteristics of re-solidification after high temperature melting.

(4) The lower hardness of special materials can increase the stability of contact process and reduce the rebounding times and rebounding energy. Meanwhile, coarse oxide particles and high additive content reduce the arc energy, arc time and welding force. Therefore, it shows more excellent electrical performance under simulated lighting load.

5 Literature

- [1] Zhenbiao L., Xixiu W., Meifang W.: The influence of short arc on the dynamic welding of automobile relay contact. *Low voltage electrical apparatus*, 2007(1): 10-13.
- [2] L. Morin, N. Ben Jemaa, D. Jeannot, H. Sone: Transition from the Anodic Arc Phase to the Cathodic Metallic Arc Phase in Vacuum at Low DC Electrical Level. *IEEE*. 2001: 88-93.
- [3] Peter Braumann, Andreas Koffler: The Influence of Manufacturing Process, Metal Oxide Content, and Additives on the Switching Behaviour of Ag/SnO₂ in Relays. *IEEE*, 2004: 90-97.
- [4] W. Weise, P. Braumann: thermodynamic analysis of erosion effects of silver-based metal oxide contact materials. *IEEE*. 1996: 98-104.
- [5] Verma A., Anantharaman T.: Internal oxidation of rapidly solidified silver-tin-indium alloy powders. *Journal of Materials Science*. 1992(27): 5623-5628.
- [6] Schimmel G., Kempf B., Rettenmayr M.: Exudation of Ag and Cu In Internal oxidized Ag-Sn-In-(Cu) Alloys. *Material Letters*. 2009:1521-1524.
- [7] Fuqi D., Ji Z., Zhihao R., Jian L.: Study on the arc erosion performance of AGW and AgSnO₂ contact materials under the condition of simulated automobile relay. *Electrical materials*. 2009, 1: 6-9.
- [8] Jie L., Wei W., Xiaoping B., Xiaofang Y., Heng W., Liqiang L.: Study on the effect of different indium content on arc erosion performance of AgSnO₂ contacts under simulated automobile relay conditions. *Electrical appliances and energy efficiency management technology*. 2016(3): 22-26.
- [9] Jie L., Xiaofang Y., Xiaoping B., Liqiang L., Suhua L., Wei W.: Effect of different In contents on hardness and microstructure of AgSnIn alloy during internal oxidation. *The Institute of Electronics, Information and Communication Engineers Technical Report*, 2013[C], 113(298): 95-98.
- [10] John J. Sher, Charles J. Luebke, Kevin L. Parker: RF Current Produced from DC Electrical Arcing. *ICEC*. 2012:1-6.
- [11] Liqiang L., Xiaofang Y., Wei W., Jifeng X., Ning Z.: The Investigation on the Production Process of AgSnO₂ Contact Materials by AgSn Powder Pre-oxidation. *ICEC*. 2012:362-367.

Thermal Equivalent Circuits: An Approach to Rate High-Power Connectors for Electric Mobility Applications

Dr. Michael Ludwig¹, Dr. Michael Leidner, Dr. Helge Schmidt, Dr. Frank Ostendorf
TE Connectivity Germany GmbH, 64625 Bensheim, Germany
¹michael.ludwig@te.com

Abstract

The evolution of electric cars raises challenging requirements for the electrical architecture, including connectors and charging inlets for high-voltage ($60\text{ V} < U_{DC} \leq 1500\text{ V}$) applications in automotive industry [1]. Electrical currents in the high-voltage backbone are continuously increasing whereas the time scales in which these currents take place are decreasing. State-of-the-art approaches to rate connectors are based on steady-state dynamics and neglect the environment. Therefore, a new selection criterium is required to evaluate connector performance. A simulation approach is presented here, considering the transient dynamics as well as the system integration. The method requires low computational power and is built using a modular approach. Thereby this method enables the system's architect to efficiently and effectively analyze the system performance, eliminate bottlenecks and optimize the design.

1 Introduction

One of the fundamental laws in physics connects heat generation to the electrical resistivity of a conductor, stating that a current I and a resistance R cause a heating described by the power P [2]:

$$P \propto I^2 \cdot R \quad (1)$$

This quadratic relationship between the electrical current and the power, as shown in **Figure 1**, is limiting the scalability of connectors for high power applications.

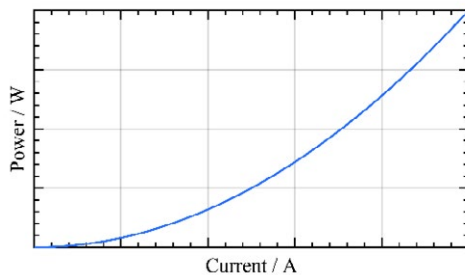


Fig. 1 Generated heat in dependency of an electrical current according to equation (1).

Hence all power losses are thermal losses, where P equals the heat flow $\dot{Q} = \frac{\delta Q}{\delta t}$ with Q being the heat and t being the time in which the heat is dissipated.

As all kinds of bodies are exhibiting a thermal mass, the temperature of a body does not instantly jump to its steady-state temperature, but rather exhibits an exponential behavior as shown in **Figure 2**.

In reverse, this means that a conductor can carry higher currents for shorter timescales without being heated above the steady-state temperature [3, 4]. This dependency is shown in **Figure 3**. Intuitively, this correlation is only valid within certain boundaries.

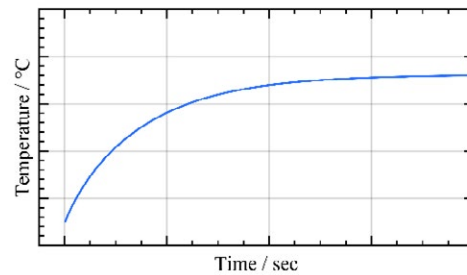


Fig. 2 Temperature of a body being subjected to heating with a constant rate of heat flow \dot{Q} .

This boundary at short time scales is pronounced for connectors especially and can be considered as an adiabatic limit.

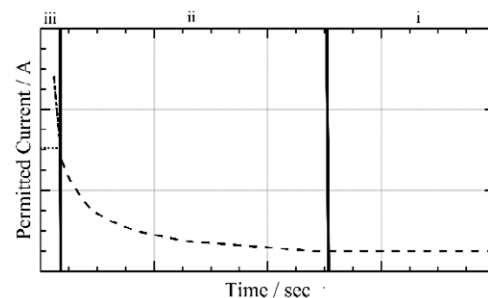


Fig. 3 The permitted current for a conductor depends on the exposure time of the current. For small time-scales this exponential curve is not valid anymore and a limitation takes place (shown by dotted line).

Based on these considerations three time-regimes can be identified, which exhibit different properties and are linked to different methodologies required to assess the suitability of high-power connectors:

- i. The steady-state regime: Within this time regime the connector is in its steady-state and does not heat anymore when all parameters remain constant. This parameter is historically used to choose components for specific applications based on the so-called derating curve, which puts the permitted current in relation to the ambient temperature.
- ii. The natural regime exhibits dynamics without reaching adiabatic conditions at any spatial point, and with any physical changes in the materials, e.g. contact melting or softening are not present. This time-scale plays an ever-increasing role of importance for high-power applications of modern electric vehicles: for example, applications like high-power charge, (HPC) in which currents of 400 – 500 A are applied for several minutes, or with high current peaks of > 1000 A for durations of milliseconds to seconds.
- iii. The adiabatic regime is closely linked to failure modes and must be considered when analyzing a connector for robustness or short-currents.

Within this paper the focus is put on the second regime.

2 Theory

Equivalent Circuits are well known from electrical engineering [5] but are not limited to this. The most pronounced benefits resulting from representation using equivalent circuits are the applicability of Kirchhoff's laws and the well-known mathematics, which can be used to solve the resulting linear equation systems. A variety of tools, based on SPICE simulation software or any software using state-space representation, can be used for this purpose [6, 7, 8].

Thermal equivalent circuits have been used to simulate semiconductors [9, 10] and conductors [11, 12, 13, 14] widely, also application to a gearbox has been described previously [15].

The thermal regime can be represented using thermal equivalent circuits (TEC) making use of the following analogy [16, 10]:

electrical regime		thermal regime	
El. Resistance	$R_{el} [\Omega]$	Th. Resistance	$R_{th} [\frac{K}{W}]$
El. Capacity	$C_{el} [F]$	Th. Capacity	$C_{th} [\frac{J}{K}]$
Potential	$U [V]$	Temperature	$T [K]$
Current	$I [A]$	Heat transfer	$\dot{Q} [W]$
Ohm's law	$I = \frac{U}{R_{el}}$		$\dot{Q} = \frac{T}{R_{th}}$

Table 1 Conversion of physical quantities from electrical to thermal regime.

In contrast to the electrical regime in which the sources, voltage or current, of the system are well defined and spatially located, the thermal world differs slightly: Besides external sources, e.g. hot surfaces, intrinsic

sources are also existing. These result from Joule heating, as it can be seen in equation 1, and are originating in every current carrying body as well as at interfaces. As a conclusion, each component, thermally represented by an equivalent circuit, can be described as shown in **Figure 4** making use of a “top-down approach” [6]. Each body consists of essentially three blocks:

- A source: An intrinsic heat-source caused by Joule heating. A non-conducting part, e.g. insulating, is not active.
- A thermal mass: The property of a body to store heat energy is represented by a capacitor which is connected to an initial temperature T_{Start} . In the case of interface resistances, e.g. crimp resistances, this block is vanishing.
- Thermal conduction: Each body can transport thermal energy, either by electrons as in the case for conductors, or by phonons for non-conductors. The resistance is split in two equal portions, separated by the link to the source and/or the capacity.
- The block interacts with neighboring parts and its surrounding interfaces. Heat can be exchanged in the direction of the electrical conduction or perpendicular. One example of perpendicular transport is the heat exchange with its surroundings via convection and radiation.

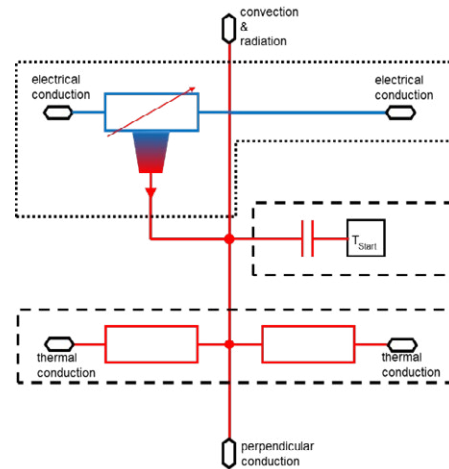


Fig. 4 Generic representation of a body using thermal equivalent circuits. The dotted box at the top highlights the electrical path and the heat source caused by Joule losses. The middle box (dashed box) indicates the thermal capacity of the body and the bottom dashed box represents the thermal conduction along the body.

2.1 Connector

Based on the generic block depicted in Figure 4, modified blocks can be used to describe any component of a connector. A combination of multiple of these blocks is making up a connector, as indicated in **Figure 5** for a simple unshielded connector with one cavity.

The contact resistance R_c must be considered carefully: In general, it consists of the bulk resistance of the contact spring R_{bulk} , the constriction resistance R_{constr} and the resistance resulting from tarnish films R_{film} [17].

$$R_c = R_{\text{bulk}} + R_{\text{constr}} + R_{\text{film}} \quad (2)$$

As the representation shown in Figure 4 spatially summarizes constriction resistance and bulk resistance, this simplification also limits the spatial and temporal resolution of the model. In the case of many small contact springs this approximation becomes more robust as $R_{\text{bulk}} \gg R_{\text{constr}}$.

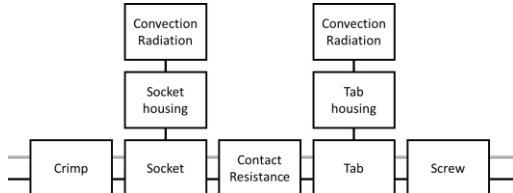


Fig. 5 Schematic representation of a connector using generic building blocks as shown in Figure 4. The grey line highlights the electrical path, the black line the thermal path.

2.2 System

One of the major intentions behind the approach is directly linked to the need of system simulations. Additional components, like cables and modules can also be described using generic thermal equivalent circuits as represented in Figure 4 and thereby extending simulation and calculation capabilities closely linked to inline connectors [18]. For reasons of validation and comparability in this paper, only a simple design without an aggregate is considered, cf. **Figure 6**.

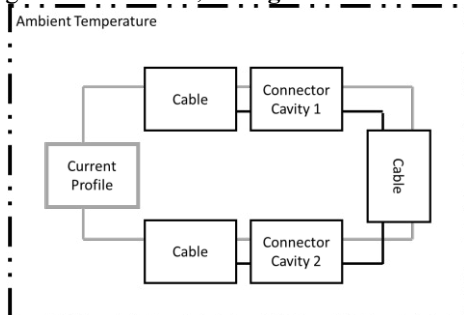


Fig. 6 System equivalent circuit containing blocks for cables and two connector cavities. The boundary conditions include a current profile and the interaction of all blocks with the ambient temperature.

This kind of representation can be modified and adapted to application specific conditions. The usage of current profiles based on data, recorded from test drives is one important benefit. Consideration of the application space, e.g. convection conditions, temperatures, close by heat-sources or radiators is a second major benefit.

2.3 Sub-Division

One major topic of simulation approaches considering spatially distributed objects is the need to decide on the suitable divisions of the geometries. In Finite Element Analysis (FEA) quantization is the main impact on the spatial resolution. When comparing the temperature

distribution along a conductor of length $L = 1.4$ m for FEA with a varying number of elements, the accuracy is limited by resolution (cf. **Figure 7**).

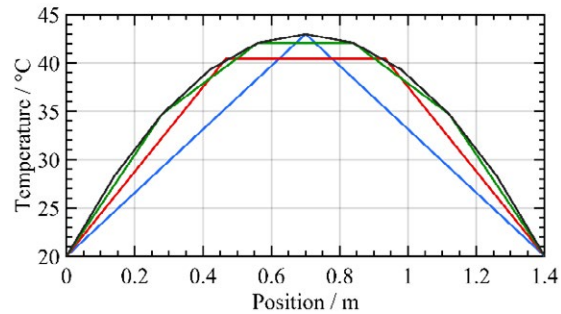


Fig. 7 FEA results for a copper conductor of length $L = 1.4$ m with a number of elements $N = 2$ (blue), $N = 3$ (red), $N = 5$ (green) and $N = 10$ (black) in steady-state.

Due to the nature of thermal equivalent circuits, the errors caused by division propagate differently in this approach. Separation of the same conductor, as simulated in Figure 7, shows that simulation accuracy shows a different temperature pattern compared to FEA (compare Figure 8).

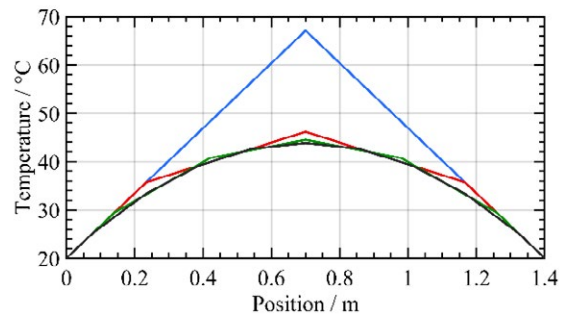


Fig. 8 Results for a copper conductor of length $L = 1.4$ m with a number of elements $N = 1$ (blue), $N = 3$ (red), $N = 5$ (green) and $N = 9$ (black) in steady-state, using thermal equivalent circuit simulation.

The reason behind is linked to the location of heat injection. In case of $N = 1$, the element, as shown in Figure 4, injects all heat in the center of the conductor. For higher values of N the number of “injection points” increases, resulting in a more distributed heat pattern. This relationship must be considered carefully when setting up a thermal equivalent model for a component. As a result, each cable, as shown in Figure 6, is made-up using a series connection of multiple short cable segments to overcome this issue.

2.4 Safety Factor

Derating curves are used to rate connectors in steady-state conditions. The approach relies on temperature measurements of the connector for various qualifica-

tion currents I_{Qual} as well as a fixed ambient temperature T_{amb} . The temperature rise ΔT follows equation (3):

$$\Delta T = k \cdot I_{\text{Qual}}^2 \quad (3)$$

The connector's application temperature is limited by a temperature T_{max} leading to:

$$\Delta T + T_{\text{amb}} \leq T_{\text{max}} \quad (4)$$

Combining equations (3) and (4) it can be derived that

$$I_{\text{rated}} \leq \zeta_{\text{SF}} \sqrt{\frac{T_{\text{max}} - T_{\text{amb}}}{k}} \quad (5)$$

Introducing a safety factor ζ_{SF} in this equation allows the inclusion of a safety margin and takes into account contact resistance and crimp/termination resistance degradation over lifetime and environmental impacts. The safety factor rates the current linearly: $\zeta_{\text{SF}} = I_{\text{rated}} / I_{\text{Qual}}$.

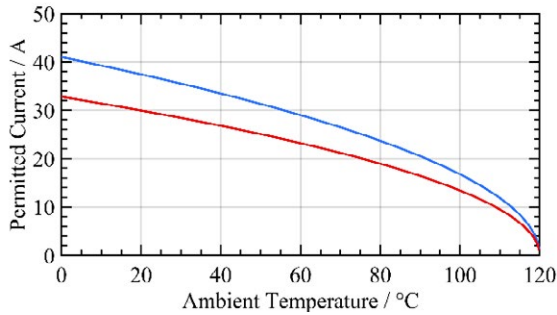


Fig. 9 Typical derating curve showing the maximum permitted current as derived from product qualification I_{Qual} (blue) and the rated current I_{rated} with a safety factor of $\zeta_{\text{SF}} = 0.8$ (red).

The method used to determine the derating curve, as shown in **Figure 9**, is given in the specification LV214 [19], widely applied in automotive industry. For high power applications a connector is equipped with a cable of length $L = 1.4$ m to each side of the connector. This setup needs to be considered in the following.

To introduce a safety factor for the thermal equivalent circuits, which is linked to ζ_{SF} , a couple of assumptions, simplifications and boundary conditions need to be considered.

The first assumption states that the connector is the electrical bottleneck in the test set-up and that the system is attached to cables of sufficient length. In this case “sufficient” implies that the cable, close to the termination, does not exhibit a spatial temperature gradient in steady-state.

The second important assumption refers to the heat dissipation. For the calculation a constant heat transfer coefficient \tilde{a} has to be derived which represents the situation in the test setup at steady-state on average. This simplification of $\tilde{a} = \text{const}$ neglects therefore the temperature dependency and the linked spatial temperature distribution in the cable T_{cable} , as $\tilde{a} = f(T_{\text{cable}}, T_{\text{amb}})$ and $T_{\text{cable}} = f(\vec{x})$. T_{amb} represents the ambient temperature.

As the temperature rise is caused by electrical resistance and current as stated in equation (1) the safety

factor ζ_{SF} impacting the current needs to be converted to a safety factor β_{SF} up-rating the electrical resistance R_0 . The generated heat is calculated using equation (6):

$$P_{\text{Qual}} = R_0 \cdot I_{\text{Qual}}^2 \quad (6)$$

Introduction of an acceptable resistance R_{acc} and usage of $I_{\text{rated}} = \zeta_{\text{SF}} \cdot I_{\text{Qual}}$ can be used to state equation (7):

$$P_{\text{acc}} = R_{\text{acc}} \cdot \zeta_{\text{SF}}^2 \cdot I_{\text{Qual}}^2 \quad (7)$$

With P_{acc} being the acceptable generated power. As $P_{\text{Qual}} = P_{\text{acc}}$, equation (8) can be derived

$$R_0 \cdot I_{\text{Qual}}^2 = R_{\text{acc}} \cdot \zeta_{\text{SF}}^2 \cdot I_{\text{Qual}}^2 \quad (8)$$

The electrical resistance R_0 is composed of constant components R_{const} , for example bulk resistances of the connector and bulk resistances of the cable, and degrading resistances R_{var} , these are linked to connection areas like crimp/termination and contact zones. Therefore, the safety factor to be considered only affects the degradable components.

$$R_{\text{acc}} = R_{\text{const}} + \beta_{\text{SF}} \cdot R_{\text{var}} \quad (9)$$

Insertion of equation (9) in equation (8) and solving for the safety factor yields:

$$\beta_{\text{SF}} = \frac{R_{\text{const}} \cdot (1 - \zeta_{\text{SF}}^2) + R_{\text{var}}}{R_{\text{var}} \cdot \zeta_{\text{SF}}^2} \quad (10)$$

As the number N of degradable connection resistances varies, the safety factor β_{SF} has to be made up out of N individual factors $\beta_{\text{SF},i}$ as well. The factors have to meet equation (11).

$$\beta_{\text{SF}} \cdot \sum_{i=1}^N R_{\text{var},i} = \sum_{i=1}^N \beta_{\text{SF},i} \cdot R_{\text{var},i} \quad (11)$$

In case of a uniform degradation of these resistances $\beta_{\text{SF},i}$ calculates to $\beta_{\text{SF},i} = \beta_{\text{SF}}$. The individual safety factor $\beta_{\text{SF},i}$ for the degradable resistances $R_{\text{var},i}$ physically describes a scaling factor describing the resistance change over lifetime. Therefore $\beta_{\text{SF},i} \geq 1$, whereas the safety factor ζ_{SF} , which is derating the current, is defined to be $\zeta_{\text{SF}} \leq 1$.

The resistances to be considered in equation (10) include the bulk resistances of the connector and need to take the cable into account. **Figure 10** visualizes the thermal interaction between connector and cable. Whereas the cable exhibits a spatial temperature dependence which is well known [18], at connector position the distribution has a significant jump to an increased temperature.

The cable impact is considered by usage of the characteristic length χ_c . This value represents the length of cable where thermal conduction resistance R_{th} equals the resistance for heat dissipation to ambient $R_{\text{th,dis}}$. When neglecting radiation this value is made up out of the sum of thermal resistance of isolation for radial heat flow $R_{\text{th,iso}}$ and convection resistance.

$$R_{\text{th,dis}} = R_{\text{th,iso}} + R_{\text{th,conv}} \quad (12)$$

The thermal resistance $R_{\text{th,dis}}$ of a cable with length l depends on the convection factor \tilde{a} , the thermal conductivity of the isolator λ_{iso} and the geometrical factors d , describing the thickness of the isolation of the cable

and D_i describing the inner diameter of the isolation (compare Figure 12):

$$R_{th,dis} = \frac{\ln\left(\frac{D_i + 2 \cdot d}{D_i}\right)}{\lambda_{iso} \cdot l \cdot 2 \cdot \pi} + \frac{1}{\tilde{a} \cdot l \cdot \pi \cdot (D_i + 2 \cdot d)} \quad (13)$$

Whereas the thermal resistance for conduction depends on the thermal conductivity of the conductor λ_{cond} .

$$R_{th} = \frac{4 \cdot l}{\lambda_{cond} \cdot \pi \cdot D_i^2} \quad (14)$$

The characteristic length can be derived using equation (15):

$$\chi_c = \sqrt{\frac{\ln\left(\frac{D_i + 2 \cdot d}{D_i}\right)}{\lambda_{iso} \cdot 2 \cdot \pi} + \frac{1}{\tilde{a} \cdot \pi \cdot (D_i + 2 \cdot d)}} \cdot \frac{4}{\lambda_{cond} \cdot \pi \cdot D_i^2} \quad (15)$$

The Temperature of the conductor at the characteristic length $T(x = \chi_c)$ equals $\sim 37\%$ of the peak temperature at the contact point. At a length of $x = 3.5 \cdot \chi_c$ the temperature equals $\sim 95\%$. Therefore, a system with cables of length $l \geq 3.5 \cdot \chi_c$ can be considered to have well defined boundary conditions.

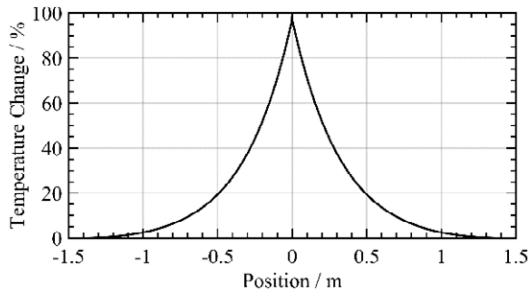


Fig. 10 Temperature increase within a simulation containing a simple connector made up out of 3 electrical resistances at $x = -1$ cm, 0 cm and 1 cm. The connector is attached to 1.4 m of cable on each side. The heat dissipation is dominated by the cable.

Based on these considerations the individual constant resistances $R_{const,i}$ represent the bulk resistances of the connector and the electrical resistances of 2 cables with a length of $l = \chi_c$. The electrical resistance $R_{el,ax,cyl}$ of the cable is calculated according equation (16).

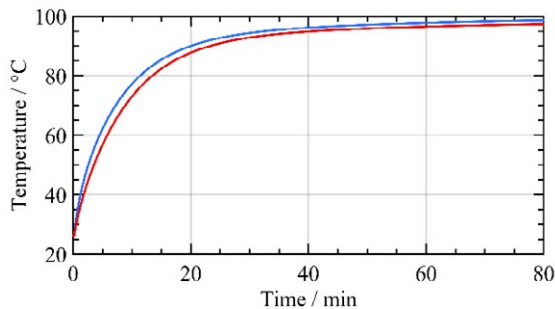


Fig. 11 Simulation results comparing contact point temperatures for the scenario considering ζ_{SF} (blue line) and β_{SF} (red line).

A comparison of contact point temperature using the safety factor $\zeta_{SF} = 0.8$ and $\beta_{SF} = 3.35$ as calculated using equation (10) is shown in **Figure 11**. The deviation between the two methods is linked to two issues:

- i. The safety factor β_{SF} depends on the characteristic length $\chi_c = f(\tilde{a})$ and therefore on convection. For simplification an average convection factor can be chosen which approximates convective heat transfer at steady state temperatures.
- ii. The electrical resistances of the cables $R_{const,i}$ to be included into calculation of β_{SF} are based on a cable length of $l = \chi_c$. This relation is connected to the simplified assumptions as mentioned before.

3 Parameter Determination

As the equivalent circuit of each generic block is linked to a specific component, a specific parameter set is also required describing the physical performance.

The parameter set is composed of the quantities shown in **Table 2**.

Component	Parameter	
El. Resistor	$R_{el} [\Omega]$	el. resistivity
	$\alpha_{el} [K^{-1}]$	linear temperature coefficient
Th. Resistor	$R_{th} [K/W]$	th. resistivity
	$\alpha_{th} [K^{-1}]$	linear temperature coefficient
Th. Capacitor	$C_{th} [J/K]$	th. capacity
Convection	$A [m^2]$	surface
	$\tilde{a} [\frac{W}{m^2 \cdot K}]$	heat transfer coefficient
Radiation	$A [m^2]$	surface
	$\varepsilon [-]$	radiation coefficient

Table 2 Components in thermal equivalent circuit and the parameter required to describe them.

The values for these parameters are depending on various physical quantities, which can be determined by different methods:

3.1 Calculation

By approximating complex geometries as simpler, well known geometries and by making use of the linked mathematics, preliminary values can be derived in early design stages. The conducting parts can be approximated by a cylinder geometry, whereas the insulating and housing parts can be described by a hollow cylinder (cf. **Figure 12**).

Thereby calculation of resistivity, surfaces and thermal capacity is simplified [20]. The electrical resistance in axial direction of the cylinder $R_{el,ax,cyl}$ results to

$$R_{el,ax,cyl} = \rho_{el} \cdot \frac{4 \cdot l}{\pi \cdot D^2} \quad (16)$$

with ρ_{el} being the specific electrical resistivity.

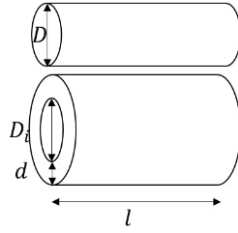


Fig. 12 Most geometries can be approximated by a cylinder with length l and diameter D or a hollow cylinder with inner diameter D_i and wall thickness d .

The axial resistances of the hollow cylinder can be calculated as follows:

$$R_{el,ax,hol} = \rho_{el} \cdot \frac{l}{\pi \cdot t \cdot (D_i + d)} \quad (17)$$

$$R_{th,ax,hol} = \rho_{th} \cdot \frac{l}{\pi \cdot t \cdot (D_i + d)} \quad (18)$$

ρ_{th} denotes the specific thermal resistivity of the linked material. In the case of the hollow cylinder, the radial heat transport mechanisms have to be considered [6]:

$$R_{th,rad} = \rho_{th} \cdot \frac{\ln\left(\frac{D_i}{2} + d\right) - \ln\left(\frac{D_i}{2}\right)}{2 \cdot \pi \cdot l} \quad (19)$$

The surface can be easily calculated by $A_{cyl} = l \cdot \pi \cdot D$ and $A_{hol} = l \cdot \pi \cdot (D_i + 2 \cdot t)$. The thermal capacity is then:

$$C_{th,cyl} = c_p \cdot \rho_m \cdot l \cdot \pi \cdot D^2 / 4 \quad (20)$$

$$C_{th,hol} = c_p \cdot \rho_m \cdot l \cdot \pi \cdot t \cdot (D_i + d) \quad (21)$$

with c_p being the specific heat capacity and ρ_m the density of the material.

3.2 Computer-Aided Design (CAD)

Values for the thermal capacity of more complex parts can be especially extracted from the CAD software as well, using $C_{th} = c_p \cdot \rho_m \cdot V$ with V being the volume of the part.

3.3 Reduced Order Modelling (ROM)

FEA can be utilized to derive values for the parameters for thermal capacity and resistivity as well. In contrast to simulations of complex systems and/or transient simulations which are time-consuming and costly, a ROM approach provides advantages. The following workflow has been established:

1. The CAD model is separated into model blocks, which correspond to the blocks used in the thermal equivalent circuit. Thereby the assembly is reduced into blocks, which can be simulated efficiently.
2. The blocks are individually simulated. Either the block is considered to contain a surface in which a heat flow \dot{Q} is injected and an opposing surface, which is kept at constant temperature T_{out} , and the temperature at the injection surface T_{in} is measured., or

3. alternatively, the two surfaces are kept at differing, but constant temperatures T_{out} and T_{in} , and the heat flux through the volume is measured.

When making use of this method the thermal resistance calculates to:

$$R_{th} = \frac{T_{in} - T_{out}}{\dot{Q}} \quad (22)$$

3.4 Lab Data

Data acquired in a laboratory environment offer an alternative, when samples are available. The methods available vary.

- The first method relies on electrical measurements and offers high accuracy but is limited to conductors. A direct current (DC) I is applied to the device under test (DUT) and this current is measured accurately, for example by measurement of the voltage drop over a precise shunt in series. Based on knowledge of the DC, the voltage drop U_{Drop} among various sections in the DUT can be measured accurately with standard equipment. The resistance calculates using Ohm's law to $R_{el} = U_{Drop} / I$. An approximation for the thermal resistivity can then be derived by applying Wiedemann-Franz law:

$$R_{th} = R_{el} / (L \cdot T) \quad (23)$$

with the temperature T and the Lorenz constant L .

- To measure the thermal resistivity of a non-conducting body a heat current \dot{Q} can be injected into a surface using a heating cartridge or resistance wire and by controlling voltage/current to

$$P = U \cdot I = \dot{Q} \quad (24)$$

The temperature has to be measured at the injection surface and the outgoing surface. To mitigate complexity arising from additional heat flux, as caused by convection, the DUT can be wrapped in bubble wrap. The thermal resistance can then be calculated according equation (22).

- The third experimental method does not aim to measure the parameters directly, but rather to measure the temperatures and then alter the parameter values in the model to match the experimental data. The basis for this is to have well defined boundary conditions in lab and a simulation environment which matches. This can be achieved by using bubble wrap to suppress convection and thereby simplify the TEC. A second supportive action is the introduction of defined cooling points in the electrical path. By water-cooling, four cooling spots for a connector can be made up out of two cavities and a constant temperature can be created at distinct locations. With these actions an enclosed system can be created with neglectable interactions to its surrounding, as shown in **Figure 13**. Within this setup, a number of temperature

sensors have to be integrated to measure the temperature at the various points of interest without having an impact on the setup itself.

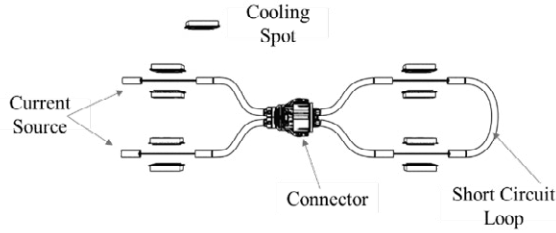


Fig. 13 Setup to measure temperatures in an enclosed system with suppressed interaction with surrounding.

3.5 Optimization

The mentioned methodology to match simulation results to empirical data requires a robust and efficient approach, since the number of parameters which can be adapted may easily reach an order of magnitude of $\sim 10^2$. To additionally ensure accuracy, the number of temperature sensors in simulation and in lab need to be sufficient – 40 temperature sensors are quite common. For the transient dynamics to be reflected, measurement series over hours shall be conducted with a resolution of seconds. The approach consists of:

1. Parameter estimation: Values for all parameters need to be initially estimated based on the methods mentioned above. This estimation needs to consider expectation values as well as physically reasonable limits.
2. Set all thermal capacities to 0 or open circuit.
3. Simulation now considers steady-state temperatures only. Steady-state temperatures from simulation $T_{sim,ss,i}$ are compared to measurement results $T_{meas,ss,i}$ in steady-state. Parameter values are varied inside the defined limits in order to optimize for minimization of ΔT_{ss} for all temperature measurement positions i :

$$\Delta T_{ss} = \sqrt{\sum_{i=1}^N (T_{meas,ss,i} - T_{sim,ss,i})^2} \quad (25)$$

4. The values for thermal resistances are kept constant and the values describing the thermal capacities are altered within their physical limits. Within this step the steady-state values are not used for optimization, but rather all values over the complete measurement duration t . The optimization target $\Delta T_{transient}$ is defined to be

$$\Delta T_{transient} = \sqrt{\sum_{i=1}^N \left(\sqrt{\sum_{\tau=0}^t (T_{meas,i}(\tau) - T_{sim,i}(\tau))^2} \right)^2} \quad (26)$$

4 Results

To prove the accuracy of the TEC, a simulation has been carried out and the result has been compared to lab data. Therefore, a tab has been crimped to a 1.4 m cable of 95 mm² and another tab was screwed to a cable shoe, crimped to 1.4 m of cable of the same diameter. The temperature was measured at the surface of the socket. At an ambient temperature of $T_{amb} = 32$ °C, a current of $I = 462$ A was applied. From the measurements, a temperature rise of $\Delta T_{meas} = 93$ K was measured. The simulation results, as shown in **Figure 14**, show a temperature rise of $\Delta T_{sim} = 92$ K.

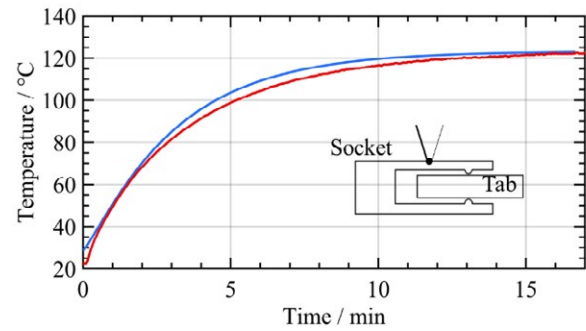


Fig. 14 Result for a socket/tab system connected to 95 mm² cable of a length of 1.4 m. Experimental data are shown in red, simulation results in blue. Parameter values have been derived from the voltage drop measurements and CAD data.

A benefit from the simulation is the accessibility of spatially buried structures, e.g. the contact spring itself. Zooming into the simulation results visualizes the instantaneous temperature rise of the contact spring, whereas the bulky materials are responding with a delay, as shown in **Figure 15**.

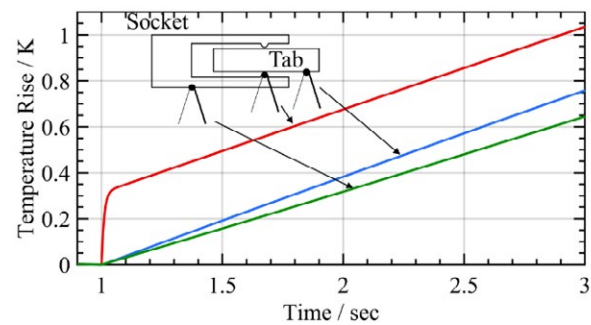


Fig. 15 Simulation results showing the transient heating of various connector locations upon a current pulse. The green line shows the temperature rise of the bulk socket, the blue line of the tab and the red line shows the temperature rise of the spring. The data results from the same simulation as shown in Figure 15.

Experimental data are not available due to spatial restrictions. Besides the spatial resolution and the ability to simulate the temperature of the contact spring, in general being the most sensitive part in the connector, transient analysis is also important. Within an electrified drivetrain a highly dynamic current profile is com-

mon, exhibiting peaks of high current and low duration. Thereby a situation is created, in which the components are subject to heat pulses, pushing the system into a kind of equilibrium over a long time while still causing short heat peaks, which mainly effect parts of low thermal mass. TECs can be used to simulate system performance upon such dynamic drive cycles and help identify bottlenecks in dependency of location and current profile (compare **Figure 16**).

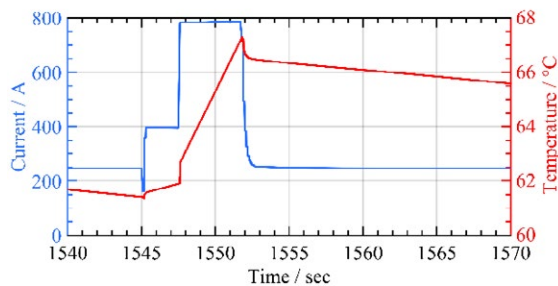


Fig. 16 Simulation using a dynamic mission profile. The current used for simulation is shown in blue, the temperature of the contact spring is shown in red.

5 Summary & Conclusion

Based on the well-known mathematics as applied to equivalent circuits, the same approach has been utilized to design thermal equivalent circuits for a connector system. The advantages of this method in relation to system simulation, modularity, simulation speed and complexity have been discussed, as well as the intrinsic issues linked to model segmentation.

The general layout of TECs for high-power connectors is defined by a guideline and applies to all connectors independent of cavities, design details or shielded/unshielded version [21]. Customization of connectors is achieved by connector specific parameter sets.

One major focus was put on the key requirements to consider safety factors throughout the simulation, which are valid and comparable to established standards. As all simulation models rely on the quality of the data used for parametrization, various methods to acquire values for the various parameters have been presented and discussed. The approach of thermal equivalent circuits offers an efficient and effective method to simulate connectors in general. The schematic representation of connectors is defined in a general manner, therefore specific connectors are specified by their adjacent parameter sets only [21]. Due to the versatile applicability of TECs, equivalent circuits can be defined and parametrized for components like shielded/unshielded wires [21] and cooled cables. Complex modules and aggregates can be represented in a simplified manner using TECs, allowing simulation of connectors in application specific conditions and include system impacts on the connector as well. The presented methodology exhibits a high accuracy of <5% for deviation between simulated and measured temperatures. The efficiency is linked to simplicity of the model and the low effort required to set up a model, the fast simulation

time and the versatility of simulation environments. Another benefit is the opportunity to link electrical domain simulations to thermal equivalent circuits when using a 1D physical simulation environment like MATLAB-Simscape™.

6 Literature

- [1] ZVEI - Zentralverband Elektrotechnik- und Elektroindustrie e.V., Voltage Classes for Electric Mobility, Frankfurt am Main, 2013.
- [2] H. Böhme, W. Keller and H. Löbl, "3.6 Stromleitungsanordnung," in *Taschenbuch Elektrotechnik Band 5: Elemente und Baugruppen der Elektroenergie-technik*, Berlin, 1986, pp. 765-781.
- [3] M. Gatzsche and e. al., "Validity of the Voltage-Temperature Relation for Contact Elements in High Power Applications," *Holm Conference on Electrical Contacts*, 2015.
- [4] T. Israel and e. al., "The Influence of Peak Current and ECR on the Transition Performance of High Power Connectors during Faults," *International Conference on Electrical Contacts*, 2018.
- [5] E. Philippow, *Taschenbuch Elektrotechnik - Band 1 Allgemeine Grundlagen*, Berlin: VEB Verlag Technik Berlin, 1986.
- [6] F. Huebner, H. Schmidt, S. Thies and K. Dvorsky, "Thermal Simulation of an Automotive HV Wiring Harness," *28th International Conference on Electric Contacts*, pp. 355-360, 6-9 June 2016.
- [7] M. Blauth, "Parametrisierte Modelle zur konstruktiven Auslegung optimierter elektrischer Steckverbinderkontakte," *Ilmenauer Beiträge zur elektrischen Energiesystem-, Geräte- und Anlagentechnik*, vol. 18, 2017.
- [8] N. Simpson, R. Wrobel and P. H. Mellor, "An Accurate Mesh-Based Equivalent Circuit Approach to Thermal Modeling," *IEEE Transactions on Magnetics*, vol. 50, no. 2, 2014.
- [9] Infineon, AN2015-10: Transient Thermal Measurements and thermal equivalent circuit models, Munich, Germany: Infineon Technologies AG, 2015.
- [10] H. Hantzsch, *Wärmeableitung bei Halbleitern*, vol. 161, Berlin: Militärverlag der Deutschen Demokratischen Republik, 1978.
- [11] I. Baker and F. de Leon, "Equivalent circuit for the thermal analysis of cables in non-vented vertical risers," *IET Sci. Meas. Technol.*, vol. 9, no. 5, pp. 606-614, 2015.
- [12] X. Dong, R. Summer and U. Kaltenborn, "Thermal network analysis in MV GIS design," in *20th International Conference on Electricity Distribution*, 2009.
- [13] F. M. Echavarren, L. Rouco and A. Gonzales, "Dynamic Thermal Modeling of Insulated Cables," in *CIGRE*, Paris, 2012.
- [14] F. C. van Wormer, "An Improved Approximate Technique for Calculating Cable Temperature," *Transactions of the American Institute of Electrical Engineers. Part III: Power Apparatus and Systems*, pp. 277 - 281, 1955.
- [15] C. Gramsch, A. Blaszczyk, H. Löbl and S. Grossmann, "Thermal Network Method in the Design of Power Equipment," in *Scientific Computing in Electrical Engineering*, Berlin, Heidelberg, Springer, 2007, pp. 213-219.
- [16] H. Schmidt, M. Leidner, S. Thoss and G. Heine, "Einfache thermische Modellierung von Steckverbindern," *Albert-Keil-Kontaktseminar*, pp. 63-72, Oktober 2017.
- [17] F. Lewellyn Jones, *The Physics of Electrical Contacts*, Oxford: Clarendon Press, 1957.
- [18] M. Blauth, F. Berger and J. Song, "A Systematic Approach for the Design of Electrical Connection Systems with Respect to the Current Carrying Capacity," *28th International Conference on Electric Contacts*, pp. 299-304, 6-9 June 2016.
- [19] *LV 214:2010-03 Kfz-Steckverbinder; Prüfvorschrift*, 2010.
- [20] F. P. Incropera, D. P. Dewitt, T. L. Bergman and A. S. Lavine, *Principles of Heat and Mass Transfer- 7th Edition*, 2017.
- [21] ZVEI - Zentralverband Elektrotechnik- und Elektroindustrie e.V., *Technischer Leitfaden: Thermosimulationsmodelle*, Köln, 2019.
- [22] J. H. I. Lienhard and J. H. V. Lienhard, *A Heat Transfer Textbook*, 2006.
- [23] VDI-Gesellschaft Verfahrenstechnik und Chemieingenieurwesen, *VDI-Wärmeatlas*, 11. Auflage, Berlin Heidelberg: Springer-Verlag, 2013.

TE Connectivity is a trademark owned or licensed by the TE Connectivity Ltd. family of companies. © 2020 TE Connectivity. All Rights Reserved.

Influence of the aging temperature on the hardness and the temperature-specific compressive yield point of bolted joints with copper and aluminium alloys conductors for vehicle electrical systems

Franck Stephane Djuimeni Poudeu,
franck_stephane.djuimeni_poudeu@daimler.com

Michael Beilner,
michael.beilner@daimler.com

Mercedes Benz AG, Stuttgart, Germany

Stephan Schlegel, Technische Universität Dresden, Dresden, Germany
stephan.schlegel@tu-dresden.de

Abstract

Bolted joints with busbars are often used for high current transmission. In order to ensure the long-term stability of these joints, the contact pressure between the busbars has to be higher than the specific minimum value over the complete expected service lifetime. For this, high assembly preload force is necessary. However, the temperature-specific compressive yield point of the used material limits the maximum applicable assembly preload force. Exceeding this limit will lead to an accelerated reduction of the preload force, and thus to an inadmissible increase of the joint resistance if the minimum pressure is underrun. Currently, the permissible assembly preload force is estimated based on the tensile yield point. Since the materials behave differently under tensile than under compressive loads, this estimation would lead to overload of the material if the tensile yield point is higher than the compressive yield point. There are currently only a few published research findings of temperature-specific compressive yield point of the busbar materials. Based on the determined temperature-specific compressive yield point, the investigated influence of the aging temperature on the hardness and the discussed temperature limit of the material, the permissible assembly preload force for the long-term stability of electrical contacts can be calculated.

1 Introduction

During the design of bolted joints the limiting surface pressure P_G under the head of the bolt or the nut must not be exceeded [1]. Exceeding this surface pressure during the assembly will result in an overstressing and a plastic deformation of the pressure-loaded area (therefore the limiting surface pressure of a material can be seen as the compressive yield point). This could accelerate the flowing and the creeping behavior of the material, which will lead to an accelerated reduction of the preload force.

Under mechanical load, metal deforms initially elastically and when the yield strength is exceeded, it deforms plastically. The yield strength depends on the the crystal structure, the microstructure of the material, the speed of the deformation and on the temperature. The flow stress is made up of two components. One component mainly depends on the microstructure of the material (also called athermal material resistance) and a second component, which is also characterized by the temperature and the rate of deformation (called the thermal material resistance). The higher the temperature, the lower is the thermal material resistance and the total yield stress [2]. This means that the temperature can lead to a reduction of

the compressive yield point P_G . Therefore, the influence of the temperature on the compressive yield point is investigated in this article. Depending on the aging temperature, the aging time and the technological history of the material, the microstructure can change due to the static recovery and the static recrystallization. This can lead to a loss of strength [3]. In [4] the decrease of the hardness of Cu-ETP and AlMgSi0.5 after the exposure to temperature of 160 °C and 180 °C, respectively, for more than 2,000 hours was demonstrated. This decrease of the hardness can be seen as an indicator for the loss of strength due to softening. Therefore, the time and the temperature dependency of the compressive yield point must be investigated. This determines the long-term behavior of the preload force, which is important for the long-term stability especially of the bolted joints in vehicle electrical systems. In order to show how the aging temperature can influence the preload force and the long-term stability of the electrical bolted joints, aging tests were carried out.

2 Investigation of the compressive yield point

In [5] the determination of the compressive yield point of metallic materials at room temperature is

specified. In this standard, the specimen must be cylindrical and the size must meet the following condition $1 \leq \frac{h_0}{d_0} \leq 2$ where h_0 is the specimen height and d_0 is the specimen diameter. However, recent findings have shown that the compressive yield point varies depending on the specimen height and the specimen diameter [6]. Therefore the compressive yield point, which is determined by this method, cannot be used to estimate the compressive yield point for busbars, since the busbars are mostly flat and the thickness-width-ratio is smaller than 1. Added to this, it is known that the material properties vary depending on the manufacturing process. Thicker materials are mostly just extruded while thinner materials are poured and rolled.

2.1 Experiment

To determine the real compressive yield point of the busbar it is necessary to use a specimen geometry, which can map the applications in the vehicle electrical system. Mostly busbar thicknesses h in the range of (1 to 5) mm are used. **Table 1** shows the investigated materials and geometries. All busbars are 30 mm wide with an R_z -value smaller than 10 μm . The two through holes with a diameter of $d_{h1} = 5.5$ mm and $d_{h2} = 9$ mm were selected according to DIN EN ISO 20273: 1992-02 [7]. The two selected diameters $D_{km1} = 10.5$ mm and $D_{km2} = 16$ mm of the upper steel pressure plate are the same with the under head diameter of the M5 and M8 bolt in accordance to ISO 8102.

Properties	AlMgSi0,5 T7 $h = 5$ mm	Cu-ETP R240			Cu-OFE R240 $h = 5$ mm
		$h = 1$ mm	$h = 2,5$ mm	$h = 5$ mm	
electrical conductivity κ at 20°C in $\text{m}/(\Omega\text{mm}^2)$	32,2 - 32,4	> 57	> 57	> 57	58,7
yield strength R_{p02} in N/mm^2	164,04	196	198	196	197
tensile strength R_m in N/mm^2	195,5	267	272	269	271
hardness H	-	79 HV	83 HV	81 HV	81 HV

Table 1 Material properties

Earlier studies in the area of the limiting surface pressure under the head of the bolt were carried out using different compression test setups and evaluation methods [8], [9], [10], [6]. Therefore, it is not possible to compare the determined values with each other or to use it as guide values during the estimation of the maximal assembly preload force. In this work following compression test setup and evaluation method were used.

The compression tests were done using a universal testing machine (Zwick*). The force was applied at the center of the upper steel pressure plate so that the specimen was loaded uniformly. During the test, the pressure force and the elongation is automatically recorded (**Figure 1**).

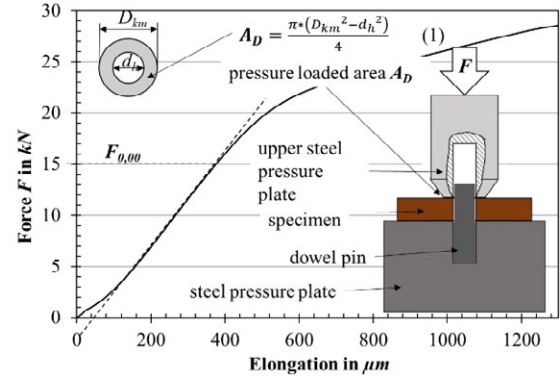


Fig. 1 Schematic representation of the test setup and the determination of the compressive yield point

The evaluation was carried out based on the recorded force-elongation-diagram. The linear part of the curve shows the elastic behavior of the material. At a force $F_{0,00}$ the material will deform plastically. To ensure the long-term stability of the bolted joint, no plastic deformation during the assembly is permitted. The limiting surface pressure P_G is calculated using this force and the pressure loaded area A_D .

$$P_G = \frac{F_{0,00}}{A_D} \quad (2)$$

This value only corresponds to the normal compressive stress σ_D (uniaxial stress state).

$$\sigma_D = \frac{F}{A_D} \quad (3)$$

Due to the friction, a tangential shear stress τ_t exist in a bolted joint additionally to the normal compressive stress.

$$\tau_t = \mu * \frac{F}{A_D} \quad (4)$$

μ is the friction coefficient. For this multiaxial stress state, the equivalent compressive stress σ_V can be calculated using the following equation [8], [10], [9].

$$\sigma_V = \sqrt{\sigma_D^2 + 3 * \tau_t^2} = \sigma_D * \sqrt{1 + 3\mu^2} \quad (5)$$

Internal investigations have shown that the friction coefficients of coated busbars are in the range of 0.08 to 0.3. In accordance to this, the equivalent compressive stress can be 1 to 10 % higher than the normal compressive stress. That means a minimum safety factor $S_{min} = 1.1$ needs to be considered during the estimation of the permissible assembly preload force.

*: <https://www.zwickroell.com/products/static-materials-testing-machines/>

2.2 Experimental results

2.2.1 Influence of the width of the busbar and the pressure-loaded area on the compressive yield point

In [6] it was indicated for cylindrical specimens that the compressive yield point depends on the height of the specimen and the outside diameter of the hollow cylinder. The smaller the specimen height or the larger the external diameter, the greater is the compressive yield point. The influence of the specimen height (thickness) could be confirmed for flat specimen with a thickness of 1 to 5 mm for Cu-ETP R240 at room temperature. By reducing the specimen thickness from 5 mm to 2.5 mm or respectively to 1 mm, the compressive yield point increases by approx. 5 % respectively by approx. 7 % (**Figure 2**). This can be explained by the cross-sectional enlargement as a result of the pronounced friction-related hindrance to transverse expansion on the pressure loaded area. This hindrance to transverse expansion is reduced from the pressure loaded area towards the center of the specimen [11]. This means that with increasing specimen thickness, the deformation and the heavily deformed zones increase and the compressive yield point is reached earlier.

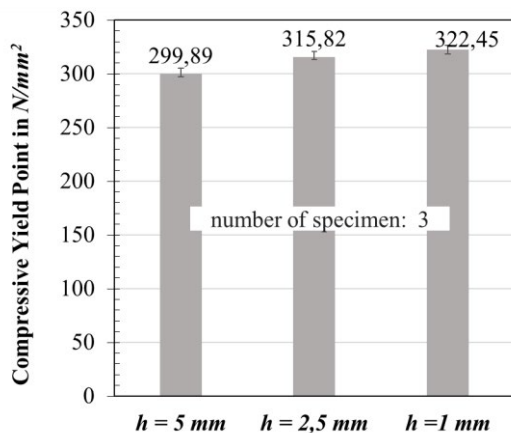


Fig. 2 Influence of the width of the busbar on the compressive yield point

In addition to the influence of the specimen thickness, the influence of the pressure-loaded area was also investigated, since the different bolt sizes used for screwing the busbars in the vehicles have different under-head diameters. With a through hole of $d_{h1} = 5.5$ mm and an effective under-head diameter of $D_{km1} = 10.5$ mm, a pressure loaded area of $A_D = 62.8$ mm² results. For $d_{h2} = 9$ mm and $D_{km2} = 16$ mm, the pressure loaded area A_D is 137.4 mm².

As can be seen in **Figure 3**, an influence of the pressure-loaded area was found, only in the case of Cu-ETP R240. The difference is approx. 8.8 %.

With C-OFE R240 and AlMgSi0.5 T7, the deviations are still within the spread of the measurement results and are therefore not considered significant (**Fig. 3**).

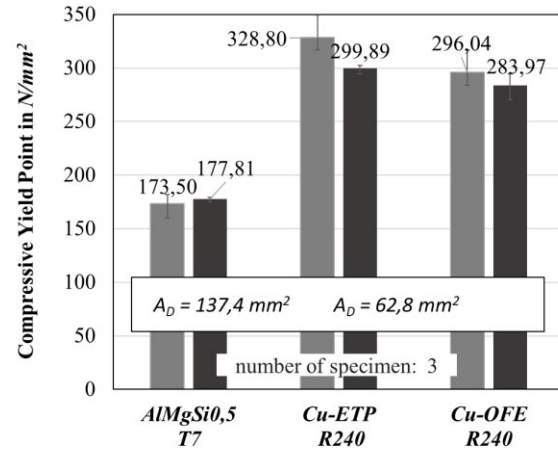


Fig. 3 Influence of the pressure loaded area on the compressive yield point

The measurement results discussed in this subsection indicate that the geometric factors (the specimen thickness and pressure-loaded area) have a marginal influence on the compressive yield point. The differences are in the range of less than 10 %, which corresponds to the minimum safety factor of 1.1.

2.2.2 Influence of the aging temperature on the hardness and the temperature-specific compressive yield point

To investigate the influence of the temperature on the compressive yield point, an upper steel pressure plate with a pressure loaded area of $A_D = 137.4$ mm² was used. The specimen thickness is 5 mm for all materials. The tests were carried out with the ZWICK testing machine, which was integrated in a heating cabinet. The desired temperatures were set on the heating cabinet and the specimen temperature was measured with a thermocouple. After completed heating, the compression tests were carried out at this desired temperature and then the next higher temperature was set.

The results show that the compressive yield point decreases linearly as the specimen temperature increases. With Cu-ETP R240 and Cu-OFE R240 the compressive yield point decreases by approx. 15 % respectively 13 % and with AlMgSi0.5 T7 by approx. 30 %, when the specimen temperature increases from 25 °C to 180 °C. If the specimen temperature is 120 °C, the compressive yield point of Cu-ETP R240 respectively of Cu-OFE R240 decreases by approx. 12.5 % respectively 6.7 % and for AlMgSi0.5 T7 the compressive yield point decreases by approx. 20.6 % (**Figure 4**).

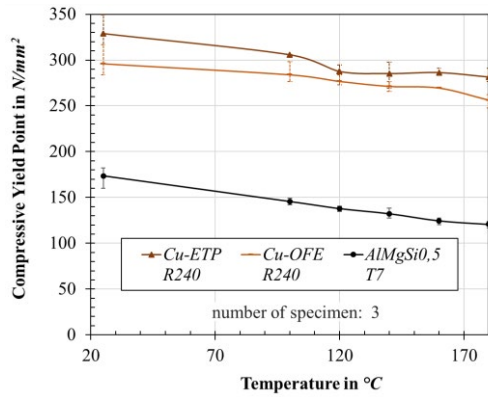


Fig. 4 Temperature-specific compressive yield point

It becomes clear that the temperature dependence of the compressive yield point of AlMgSi0.5 T7 is more pronounced than with the copper specimen. The decreasing of the compressive yield point is due to the decrease of the thermal flow stress component and the change in the relaxation and creep properties of the materials because of the simultaneous thermal and mechanical stress. It is expected that with such short-term thermomechanical loads (approx. 1 min), the relaxation and creep behavior of Cu-ETP R240 and Cu-OFE R240 is hardly changed. Longer holding times are necessary to record the influences of the change in compressive yield point due to relaxation and creep.

Due to the long-term temperature aging, the materials can soften depending on the aging temperature. That can cause the reduction of the compressive yield point and the hardness. In order to investigate this, the specimens were simultaneously stored in three different heating cabinet respectively at 140 °C, 160 °C and 180 °C for 2000 hours. After certain times, some specimens were taken from the heating cabinet and the compressive yield point and the hardness, respectively, were determined at room temperature and shown graphically (Figure 5 und Figure 6). The specimen thickness was 5 mm for all materials and the pressure-loaded area A_D was 62.8 mm². The results of the Cu-ETP R240 and of the Cu-OFE R240 show that all three temperatures lead to a decrease of the compressive yield point. However, the velocity of this reduction decreases with the time and with the aging temperature, so that the compressive yield point approaches an asymptotic value. After 2000 hours, the compressive yield point of the Cu-ETP R240 at 140 °C and 160 °C is still approx. 83.3 % and at 180 °C only 79.6 % of the initial value. With Cu-OFE R240, the compressive yield point at 140 °C and 160 °C is still approx. 86.2 % and at 180 °C 79.9 % of the initial value. Nevertheless, the hardness and the grain size of both materials were constant even at 180 °C. Therefore, this decrease of the compressive yield point cannot be explained with the softening of these two materials. A clear relationship between the hardness, the

grain size and the compressive yield point could therefore not be established.

With AlMgSi0.5 T7, an increase of the compressive yield point is observed at 140 °C and 160 °C for up to 250 hours of thermal load. This is due to the precipitation of Mg and Si molecules. It is suspected that the overaging was not completed during the heat treatment process. After 500 hours at 160 °C the maximum was already reached and at 140 °C the maximum was reached after 1000 hours. During the aging at 180 °C, a decrease of the compressive yield point was observed after 250 h. This suggests that the increase of the compressive yield point was completed earlier. That means that the speed of the increase of the strength of AlMgSi0.5 T7 increases with the aging temperature. Such an increase of the compressive yield point was also observed with EN-AW 6082 T6510 at temperatures of up to 300 °C [12]. In [13] the increase of the hardness of AlMgSi was observed at an aging temperature of up to 140 °C within 300 to 500 h. The subsequent decrease of the compressive yield point can be explained by the progressive softening. As a result of the temperature and the time, the grain size increases, which leads to a decrease of the strength. This could be confirmed by hardness measurements after 2000 hours (Fig. 6).

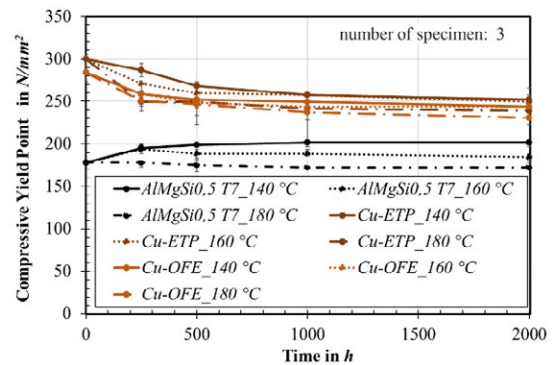


Fig. 5 Influence of aging temperature and aging time on the value of the compressive yield point at room temperature

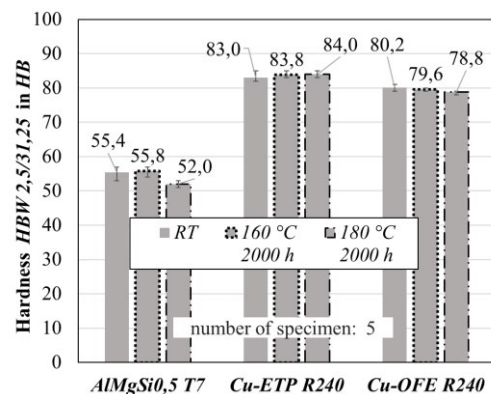


Fig. 6 Influence of aging temperature and aging time on the hardness at room temperature

3 Influence of the aging temperature on the preload force and on the long-term behavior of the electrical bolted contact

To investigate the influence of temperature on the preload force, a temperature cycle test (from -40 °C to 140 °C with a temperature gradient of 3 K/min over 50 cycles) was carried out. In principle, the constantly high temperature has the greatest effect on the long-term creep compared to a cyclic temperature load. However, because of the permanent temperature changes occurring in a vehicle during its service life, temperature change tests were preferred. This maps the creep behavior of the materials under thermomechanical stress and the self-loosening due to the permanent change of the stress in the entire system. These two mechanisms are also responsible for the decreasing of the preload force during the service life. For the temperature change test, two bolted joints with two busbars made of Cu-ETP R240 with a thickness of $h = 5$ mm and with an M8 8.8 bolt were prepared. In accordance to previous internal investigations, the assembly preload force of the two bolted joints was 10 kN. Another bolted joint with two busbars made of AlMgSi0.5 T7 with a thickness of $h = 5$ mm and with an M5 8.8 bolt was prepared. The assembly preload force was 5 kN. Therefore, the utilization factor of the yield point stress of these bolts was approx. 0.5. Force measurement sensor were placed between the bolt heads and the respective specimen to continuously measure the preload force. A steel washer with a pressure loaded area A_D of 53.4 mm² for the M5 variant and one of 119.9 mm² for the M8 variant were inserted between the force washer and the specimen. This results in a surface pressure p_1 of 93.6 N/mm² for the M5 variant and a surface pressure p_2 of 83.4 N/mm² for the M8 variant immediately after the assembly. This means that the compressive yield point of the respective material was not exceeded in all bolted joints neither at room temperature nor at 140 °C (Figure 4 and Figure 7). The contact surface of the busbars was not pretreated. One bolted joint made of Cu-ETP R240 and the bolted joint made of AlMgSi0.5 T7 were stored in a heating cabinet and subjected to the temperature change. The remaining bolted joint was stored at room temperature for the entire duration of the experiment.

It can be seen from Fig. 7 that the preload force of the bolted joints, which was stored in the heating cabinet, decreases with the highest speed within the first five hours. This is due to the leveling of the roughness peaks in all interfaces, because the local surface pressures are too high in the contact spots. In addition, the frictional engagement is reduced by the decrease of the thread and under-head friction with lowering the temperature [14]. This phase of time-

independent setting is followed by a phase that depends on the temperature and the time. In this phase, the velocity of the reduction of the preload force gradually decreases due to the progressive solidification due to the hindrance of the dislocation movements [15]. The preload force approaches an asymptotic value. However, this process can take several thousand hours as long as the equilibrium between creep or relaxation and material hardening is not achieved. After 280 h the specimens were cooled to room temperature. In the bolted joint made of Cu-ETP, which was stored in the heating cabinet, there was still 72.5 % of the assembly preload force. In the bolted joint made of AlMgSi0.5 T7 there was still 73.4 % of the assembly preload force. In the bolted joint made of Cu-ETP that has been stored at room temperature, the residual preload force is still approx. 97 % of the assembly preload force (Fig. 7). Further internal investigations over 1500 hours with similar specimens and similar conditions have shown that the preload force can decrease by more than 50 % if the compressive yield point was not exceeded during the assembly and by more than 70 % if the compressive yield point was exceeded. Therefore, it is not permissible to exceed the compressive yield point during the entire service life. Otherwise, an accelerated reduction of the preload force can be expected. This can cause the undershooting of the minimum surface pressure between the busbars, which is necessary for the long-term stability of the electrical bolted contact.

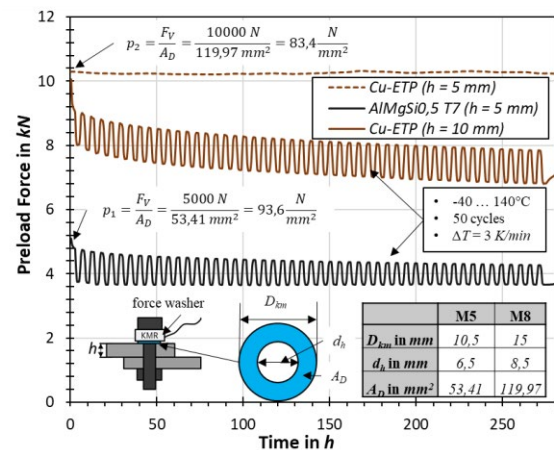


Fig. 7 Influence of temperature changes on the preload force

To determine the influence of the preload force on the electrical long-term stability of the bolted joint and to determine the minimum assembly preload force, five bolted joints made of two tinned Cu-ETP R240 busbars as well as of two tinned AlMgSi0.5 T7 busbars with respectively 2 kN and 4 kN were prepared. After the assembly the specimens were stored in a heating cabinet. They were firstly exposed at 160 °C for 1000 hours and then at

a thermal shock from -40 to 140 °C for 500 hours. The joint resistances were measured at room temperature every 500 hours. The performance factor k_u was used to evaluate the quality of the bolted joint. The performance factor is independent of the material and of the geometry and is the ratio between the joint resistance R_j and the material resistance R_{bus} (Figure 8). A bolted joint is considered as technically good if the performance factor is less than or equal to 1.5 [16].

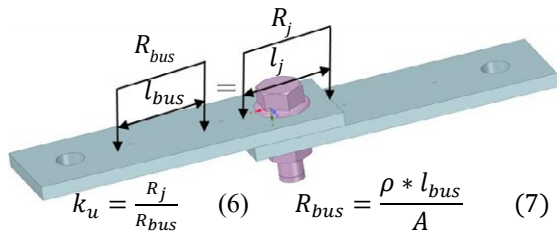


Fig. 8 Relation between joint resistance R_j and performance factor k_u

Immediately after assembly, the performance factor of all bolted joints was below 1.1 and therefore all joints were technically good. Over the entire loading time, the performance factor of all bolted joints, that were bolted with 4 kN, was almost constant and with little variation. It is assumed that the residual preload force (approximately 50 % of the assembly preload force) in the joint was still sufficient to ensure the long-term stability of the joint. With bolted joints, that were screwed with 2 kN, the performance factor increased significantly within 500 hours. After 1500 hours, the limit for the performance factor of 1.5 was exceeded clearly and with pronounced scatter for the Cu-ETP test series. With bolted joints of AlMgSi0.5 busbars, the mean value of the performance factors was still below 1.5, but the performance factor of some bolted joints were already above 1.5 (Figure 9).

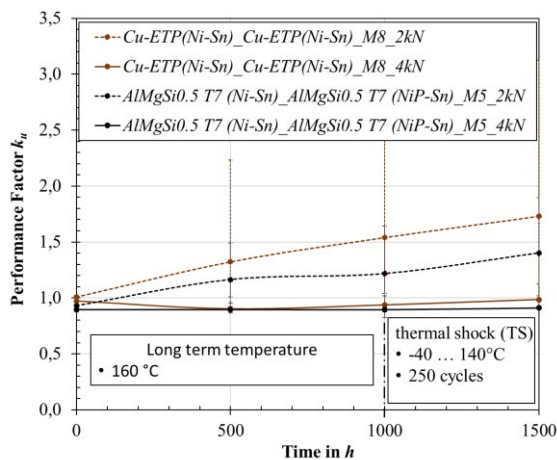


Fig. 9 Influence of the preload force and the temperature on the long-term behavior of the screw joint

The pronounced increase of the performance factor of the bolted joints, that were bolted with 2 kN, indicates that the residual preload force (approximately 50% of the assembly preload force) in the bolted joint was too low to guarantee long-term stability. In this force range, some of the a-spots formed during the assembly are not stable. These are partly destroyed during the reduction of the preload force. It is also assumed that the formed true contact area was not gastight due to the lower preload force. In this case, electrically insulating chemical reaction products formed due to the temperature can penetrate into the true contact area and reduce it. The joint resistance and the performance factor increases. This means that the assembly preload and the residual preload force are decisive for the long-term stability of the electrical bolted contact.

The assembly preload force must be selected so high that the residual preload force is always equal or greater than 2 kN during the entire service life. It must be taken care of not exceeding the compressive yield point. Otherwise, an accelerated reduction of the preload force can take place, which can lead to an earlier undershooting of the minimum preload force of 2 kN. This jeopardizes the electrical stability of the electrical bolted contact.

4 CONCLUSION

The long-term stability of a current-carrying bolted joint is heavily dependent on the surface pressure between the busbar, among other things. Depending on the coating materials and the geometry of the bolted joint, the residual preload force must not fall below a certain minimum preload force during the service life. To ensure this, greater assembly preload forces are necessary, which are limited by the temperature and time-dependent compressive yield point. In this paper, the compressive yield points of Cu-ETP R240, Cu-OFE R240 and AlMgSi0.5 T7 were examined. The effects of temperature on the preload force and on the long-term behavior of current-carrying bolted joints were also considered. The test results can be summarized as follows:

1. With increasing busbar thickness and with decreasing pressure loaded area, the compressive yield point decreases.
2. The compressive yield point decreases linearly with increasing temperature. With Cu-ETP R240 respectively Cu-OFE R240, a decrease of 12.5 % respectively 6.7 % and with AlMgSi0.5 T7 a decrease of 20.6 % of the values at 25 °C was found.
3. After the aging at 140 °C, 160 °C and 180 °C for 2000 hours, there was a maximum decrease of the compressive yield point of 20.4 % for Cu-ETP R240 and

20.1 % for Cu-OFE R240 of the initial value. With AlMgSi0.5 T7 it was 3 % of the initial value.

4. The hardness of Cu-ETP R240 and of Cu-OFE R240 remained constant. A hardness drop of 6.8 % was determined for AlMgSi0.5 T7.
5. For bolted joints made of tinned busbars with a cross-section of 30 mm * 5 mm, a minimum assembly preload force of 4 kN is necessary to ensure the long-term stability of the bolted joint.

In further investigations, the influences of constantly high temperature and vibrations on the preload force and on the long-term stability of current-carrying bolted joints will be examined. The minimum surface pressure of various contact pairings will also be examined.

5 Acknowledgement

All tests were carried out at Mercedes Benz AG, Sindelfingen, Germany.

6 References

- [1] Systematic calculation of highly stressed bolted joints Joints with one cylindrical bolt, VDI Standard 2230-1, 2015.
- [2] E. Macherauch and H.-W. Zoch, "Temperatureinfluss auf die Streckgrenze," in *Praktikum in Werkstoffkunde*, Vieweg+Teubner, 2011.
- [3] G. Gottstein, "Erholung, Rekristallisation, Kornvergrößerung," in *Physikalische Grundlagen der Materialkunde*, Springer, 2007.
- [4] Schlegel S., S. Großmann, M. Lakner, and T. Schoenemann, "Investigations on material structural changes on electrical joints at high contact temperature," *Proceedings of the 26th International Conference on Electrical Contacts*, pp.7-11, 2012.
- [5] Testing of metallic materials - Compression test at room temperature, DIN Standard 50106, 2016
- [6] C. Stolle, "Einflüsse auf die Veränderungen der Vorspannkraft unter Betriebsbedingungen bei Verschraubungen im modernen Leitchbau," *Forschungsvorhaben AIF 13639 N*, ifw Darmstadt, 2005.
- [7] Fasteners; clearance holes for bolts and screws ISO Standard 273,1979; german version, DIN EN ISO Standard 20273, 1992.
- [8] G. H. Junker, "Flächenpressung unter Schraubenköpfen", *Der Maschinenmarkt*, 1961.
- [9] M. Duchardt, "Bewertung des Vorspannkraftverlustes in Schraubenverbindungen unter kombinierter mechanischer und thermischer Beanspruchung". Zugl.: Darmstadt, Techn. Univ., Diss., Shaker, Aachen, 2013.
- [10] U. Arz, C. Berger, H. Müller, and K. Westphal, "Ermittlung der Grenzflächenpressung unter einachsialer kontinuierlicher Beanspruchung bei Raumtemperatur," in *Konstruktion*, 2002, 38-42.
- [11] Druckversuch. [Online]. Available: <https://www.tec-science.com/de/werkstofftechnik/werkstoffpruefung/druckversuch/> (accessed: Feb. 24 2021).
- [12] C. F. M Oechsner, „Rechnerische Beschreibung des Relaxationsverhaltens von Schraubenverbindungen unter leichtbaurelevanter Temperaturbelastung,“ *Forschungsvorhaben IGF 18670 N*, 2018.
- [13] T. Fuhrman, „Kontakt- und Langzeitverhalten von stromführenden Schraubenverbindungen mit vernickelten und versilberten Leitern aus Aluminiumwerkstoffen,“ *Dissertation*, Dresden, 2020.
- [14] K.-H. Kloos and W. Thomala, "Schraubenverbindungen": "Grundlagen, Berechnung, Eigenschaften, Handhabung", 5th Ed. Berlin, Heidelberg: Springer-Verlag, 2007.
- [15] Uilrich Wuttke, "Vorspannkraftabbau in Schraubenverbindungen unter Schwingungsbelastungen mit zusätzlicher Temperaturbelastung," *Forschungsvorhaben IGF 15320N*, Darmstadt, 2011.
- [16] H. Böhme, „Mittelspannungstechnik: Schaltanlagen berechnen und Entwerfen“, Huss-Medien, Verlag Technik, 2005.

Modelling the switching behavior of pyrofuses for the protection of electric cars based on measurement data

Dietmar Haba, Hirtenberger Automotive Safety GmbH, Hirtenberg, Austria, Dietmar.Haba@Hirtenberger.com

Abstract

The rapid development in electric car batteries allows steadily increasing operating currents with low power losses thanks to decreasing internal resistances. This challenges the electric protection on board: Accidental short-circuit currents can reach over 20 kA within milliseconds, bringing conventional protection systems to its technical limits, particularly at high on-board voltages. This problem limits the development of electric car architecture significantly. Pyrotechnically activated circuit breakers are a suitable solution. These *pyrofuses* actively cut a busbar triggered by an ignition signal. They respond very fast, have low resistance before activation and high resistance thereafter, good aging characteristics and high reliability. Other than melt fuses, the separation time hardly depends on the overcurrent, the temperature or the product's age. Moreover, the active triggering allows separating even without any overcurrent, e.g., after a car crash. Upon activation, a switching arc forms within the product. Depending on the current and the inductivity, up to 6 kJ of inductive energy must be dissipated for this arc to be extinguished, which transforms into high pressure and temperature. Development focuses on controlling this energy and limiting its harmful effects, thus providing a safer solution for steadily increasing demands.

1 Introduction

Both the technology and the market for battery-electric vehicles (BEVs) have made outstanding progress over the past ten years, and both keep progressing at high pace. Strong political support in many parts of the world makes sure that the technological transition from fossil fuels to batteries as the main energy storage for vehicles will stay the top priority of all automotive manufacturers for years to come. This change process is probably the most tremendous technological transformation automobile has ever experienced since its invention in the 19th century. Of course, such rapid development challenges many conventional solutions and in many ways demands entirely new solutions for existing problems. One example for such a challenging problem is the electric fault current protection.

1.1 Conventional protection

Conventionally, high-voltage vehicle board grids of BEVs are protected by a combination of melt fuses and contactors in series. Here, the contactors serve as the protection from overcurrents, i.e., fault currents below a certain value (e.g., 1000 A), while the melt fuses protect the system from higher currents, as they can occur in the case of a short circuit.

However, the rapid development in BEVs creates challenges that need entirely new solutions. In their endeavor to make BEVs competitive with fossil-fuel cars, automotive engineers are constantly working on enhancing the BEVs' range per battery charge while reducing their charging time. In order to do so, they are developing batteries with ever higher capacities and

lower power losses (i.e., lower internal resistances) that can be recharged with high currents of several 100 A. Both the increased capacities and the lower internal resistances lead to a further increase in short-circuit currents. Some BEVs can even use double the board voltage during charging (e.g., 800 V) to reduce the charging time by half without increasing the charging current. This higher voltage is an additional obstacle that can exceed the limits of conventional electric protection solutions.

In addition to these new challenges, conventional electric protection also suffers from its well-known drawbacks:

- Aging – Melt fuses are known to change their switching behavior significantly over lifetime.
- Controllability – The switch-off time of melt fuses is determined by the fault current height and thus cannot be defined by the system designer.
- Temperature dependency – As melt fuses need to reach a certain temperature before switching, the ambient temperature affects their switching behavior significantly.
- Power loss – The rather high internal resistance of melt fuses translates to high power loss, which not only reduces the BEV's range and overall energy efficiency, but also raises the temperature within the battery safety box, thus affecting all other component therein.

1.2 Pyrofuses

The problems described in section 1.1 lead to the development of an entirely new protection concept, the

pyrotechnically activated circuit breaker, often called *pyrofuse* (example in Fig. 1).



Fig. 1 Hirtenberger's CB500-2 as an example for a high-voltage pyrofuse. In this image, the conductor has a cross section of $16 \times 4 \text{ mm}^2$.

The general principle is depicted in the sectional view in Fig. 2: A pyrotechnic ignitor propels a piston, which cuts the middle part (called *blank*) out of a busbar and then prohibits its re-contacting.

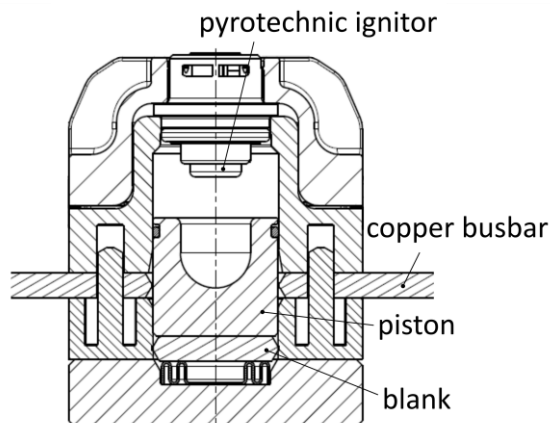


Fig. 2 Sectional view of a pyrofuse like the CB500-2 after activation

While these pyrofuses are well known in low-voltage systems ($\leq 60 \text{ V}$), they are relatively new products in high-voltage applications. The main advantage of a pyrofuse when compared to a melt fuse is that it separates the busbar on command, independently of the current. Pyrofuses can open the electric circuit without any fault current, even at current zero, e.g., in the case of a car crash. In addition, they have a very short separation time (usually $< 2 \text{ ms}$), low internal resistance (usually $< 50 \mu\Omega$), good aging behavior, hardly any temperature dependency and good reliability.

This work deals with the theoretical modelling of pyrofuse separation events and how it can be used to predict the pyrofuses' limitations.

2 Theory

2.1 Separation energy

When the current I_0 in an electric circuit with given inductance L is suddenly switched off, a transient electric arc forms across the separating contacts until the inductive energy $E_{\text{ind}} = I_0^2 L / 2$ is reduced to zero. This so-called *separation energy* represents a major challenge for pyrofuses.

For example, to switch off a 10 kA short circuit in an electric system with 20 μH system inductance, the pyrofuse must dissipate at least 1 kJ of energy. This is a physical necessity and cannot be prohibited. In BEVs, where batteries can store several 100 MJ of electric energy, 1 kJ might not sound like a lot. However, due to the extremely short time period in which the switching must take place, the dissipation power can be as high as 10 MW and more.

Moreover, the constant urge to reduce product size means that this high power must be dissipated in a very small volume, resulting in high temperature and pressure. In fact, the electric energy a pyrofuse must be able to dissipate roughly compares to the energy of an assault rifle cartridge, not taking into account the energy of the pyrotechnic ignitor itself. This is significant, as pyrofuses are significantly smaller than assault rifles, and they are mostly made of plastic components.

Due to the low heat capacity of air, the pyrofuse's solid components must absorb almost the entire separation energy. A significant proportion of this energy will be dissipated in the form of enthalpy of fusion or vaporization, thus melting and vaporizing some of the product's inner surfaces. A pyrofuse is usually mostly made out of electrically and thermally insulating plastics, so that these harsh conditions are a major challenge for the product's mechanical integrity. Moreover, the high temperature causes the plastics to pyrolyze, forming electrically conductive carbon black, which can result in an unacceptably low electrical resistance after separation. Venting openings in the pyrofuse can limit both pressure and temperature to some extent, as long as the exhausted gases do not harm other components nearby. In a nutshell, the separation energy is one of the most important factors limiting the capabilities of pyrofuses and determining the minimum product size.

2.2 Switching model

Fig. 3 shows a simplified model of an electric circuit with a pyrofuse during separation, with an electric arc forming within the pyrofuse. Tab. 1 lists the meanings of the variables used therein and in the rest of this work and their exemplary values.

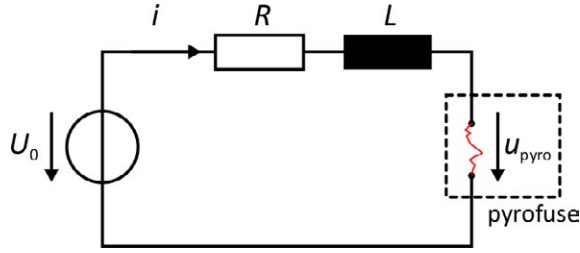


Fig. 3 RL-circuit with a pyrofuse during separation

Tab. 1 Used variables and their exemplary values

symbol	meaning	exemplary value
t	time	
i	current	
u_{pyro}	pyrofuse voltage	
R	system resistance	30 mΩ
U_0	source voltage	500 V
L	system inductance	20 μH
I_0	initial or prospective (short-circuit) current	$U_0/R \approx 16000$ A
τ	time constant	$L/R \approx 0,67$ ms

Note that these exemplary values depend strongly on the individual case. For example, if a short circuit occurs close to the battery, R and L are both significantly lower and I_0 , consequently, is significantly higher.

We define $t = 0$ as the moment when u_{pyro} becomes non-zero, i.e., when the pyrofuse starts affecting the electric circuit. To achieve that, it must be triggered a certain time period earlier. This aspect will be discussed in more detail in section 3.1.

Using Kirchhoff's voltage law, the voltages in Fig. 3 sum up to eq. (1), which can be re-arranged to give the current change in eq. (2).

$$U_0 = R \cdot i(t) + L \cdot \frac{di}{dt} + u_{\text{pyro}}(t) \quad (1)$$

$$\frac{di}{dt} = [U_0 - R \cdot i(t) - u_{\text{pyro}}(t)]/L \quad (2)$$

Thus, the voltage via the electric arc u_{pyro} must be higher than $[U_0 - R \cdot i(t)]$ to reduce the current $i(t)$. In order to reduce $i(t)$ to zero, u_{pyro} must necessarily be higher than U_0 and the higher $[u_{\text{pyro}} - U_0]$ is, the faster $i(t)$ will decrease.

For practical purposes, we can transform the differential equation eq. (2) into a difference equation by $di/dt \approx (i_{n+1} - i_n)/(t_{n+1} - t_n)$, to give eq. (3).

$$i_{n+1} = i_n + (t_{n+1} - t_n) \cdot [U_0 - R \cdot i_n - u_{\text{pyro},n}]/L \quad (3)$$

The conservative assumption is that $i_0 = I_0 = U_0/R$, hence assuming that a short circuit was present for a certain time ($> 3\tau$) before the pyrofuse was triggered, so that the induced magnetic field is fully developed. However, modern electronics can usually detect a short circuit and trigger the pyrofuse in less than 1 ms, so that

the pyrofuse can limit i well before it reaches its maximum. Then, i_0 can take on any value from zero to I_0 . (If $i_0 = I_0$, the starting value t_0 does not affect the outcome, as long as $t_0 \leq 0$. For this investigation, we chose $t_0 = -1$ ms.)

Using eq. (3), we can plot the current $i(t)$ during a separation with a pyrofuse if we know the corresponding arc voltage $u_{\text{pyro}}(t)$.

2.3 Simplified pyrofuse model

Fig. 4 shows the electric parameters in a pyrofuse's busbar, like that used in *Hirtenberger's CB500-2* (shown in Fig. 1). The cutting piston separates the busbar and displaces the blank by a certain distance $d(t)$.

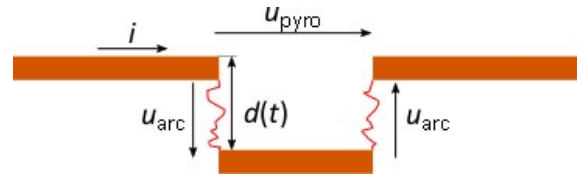


Fig. 4 Simplified pyrofuse busbar model during separation

Neglecting the copper's resistivity, u_{pyro} is the sum of the voltage drops via the electric arcs u_{arc} , which, in turn, is the sum of the anode drop voltage $U_{\text{drop,anode}}$, the cathode drop voltage $U_{\text{drop,cathode}}$ and the arc column voltage u_{col} . The combined anode and cathode drop voltage ($U_{\text{drop,anode}} + U_{\text{drop,cathode}}$) for copper for stable electric arcs is around 13 V [1]. In the model in Fig. 4, the cutting piston separates the conductor at two positions, so that the total anode and cathode drop voltage is around 26 V, i.e., well below typical values of U_0 (cf. Tab. 1). Thus, the two arc columns must provide the vast majority of the u_{pyro} that is necessary to reduce i to zero. The arc column voltage u_{col} strongly depends on many factors, among them current, atmosphere, pressure and temperature, and thus, time, but the most important factor is the length of the electric arc, i.e., $d(t)$.

3 Modelling switching behavior

For a constant product design, the copper blank movement course $d(t)$ is well reproducible and relatively independent from many noise factors. As u_{pyro} depends mostly on $d(t)$, it can be hypothesized that $u_{\text{pyro}}(t)$ is consequently also well reproducible, as long as the product design is kept constant. In a series of tests, we found that the $u_{\text{pyro}}(t)$ is, in fact, very well reproducible as long as the product is not altered internally.

For instance, **Fig. 5** shows i and u_{pyro} data of a *CB500-2*, switching off $I_0 = 12.5$ kA at $U_0 = 500$ V and $L = 20$ μH at three different temperatures. The courses of i and u_{pyro} are very similar in all three cases, which shows that the pyrofuse's switching behavior is well reproducible and very independent from the temperature.

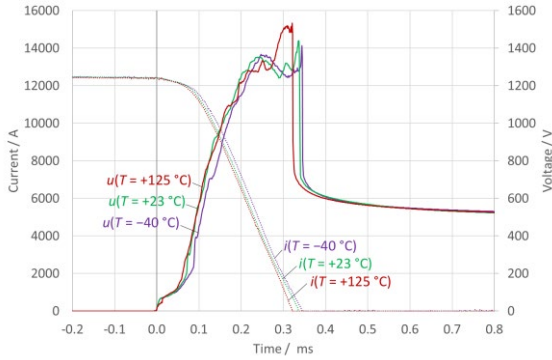


Fig. 5 Measured i and u_{pyro} for three different switching events, all with $U_0 = 500$ V, $L = 20$ μH and $I_0 = 12.5$ kA, at three different temperatures.

This low temperature dependency is one of the major advantages that pyrofuses can offer over alternatives like melt fuses and is key for automotive applications.

Fig. 6 shows $i(t)$ and $u_{\text{pyro}}(t)$ for five switching events with very different circuit parameters (i.e., U_0 , I_0 and L): While the courses of i depend strongly on the particular circuit parameters, the courses of u_{pyro} are, indeed, all rather similar until i drops below a certain value.

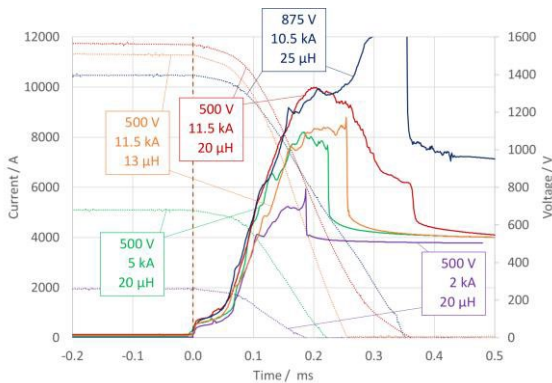


Fig. 6 Measured current i (dotted lines) and voltage u_{pyro} (full lines) for five switching events with strongly varying circuit parameters (U_0 , I_0 and L). While i varies strongly, the courses of u_{pyro} are all very similar.

In fact, we can assume that the voltage course is mostly given by the product design, neglecting all outer influences without making too much error. For example, the pyrofuse voltage during separation of a *CB500-2* can roughly be given by the empirical model eq. (4):

$$u_{\text{model}}(t, i) = \begin{cases} 0, & (t < 0) \\ 50 \text{ V} + 2000 \text{ V/ms}, & (0 < t \leq 0,05 \text{ ms}) \setminus (i = 0) \\ 150 \text{ V} + 8000 \text{ V/ms}, & (0,05 \text{ ms} < t < 0,20 \text{ ms}) \setminus (i = 0) \\ 1400 \text{ V}, & (t \geq 0,20 \text{ ms}) \setminus (i = 0) \\ U_0, & (t \geq 0) \cup (i = 0) \end{cases} \quad (4)$$

In other words, this simple model assumes that the voltage via the pyrofuse u_{pyro} is zero before activation, and then increases at different rates until it reaches its maximum at 1400 V. As soon as the current i equals zero,

u_{pyro} becomes U_0 instantaneously (this follows from eq. (1)). This model is plotted in the following figures for illustration.

The particular u_{model} in eq. (4) is valid only for the *CB500-2*, but similar models with adjusted values were used for various different pyrofuses and all of them agreed well with the respective measurement data. However, depending on the particular type of pyrofuse, a certain piece-to-piece variance and temperature dependency must be considered.

The claim that eq. (4) gives a good estimate of $u_{\text{pyro}}(t)$ for various values of U_0 , I_0 and L could be confirmed in various experiments. For example, **Fig. 7** shows voltage curves of a *CB500-2*, switching off various different short circuits. The model u_{model} fits the measured voltage curves of most measurements reasonably well. The exception is the measurement done with $I_0 = 20$ kA, where u_{pyro} deviates significantly from the model, probably because the separation energy was already bringing the product to its limits.

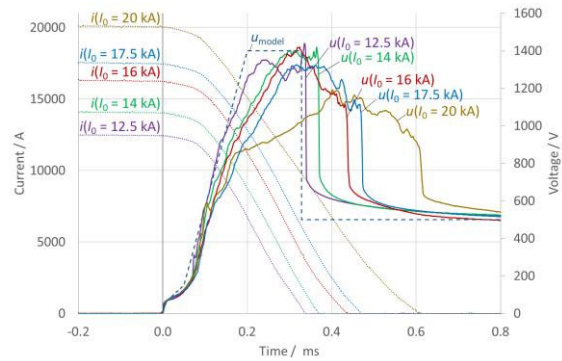


Fig. 7 Measured current i and voltage u_{pyro} during five different switching events, all with $U_0 = 500$ V and $L = 20$ μH , but very different I_0 . The model u_{model} fits u_{pyro} reasonably well, independently of I_0 .

By combining eq. (3) and eq. (4), we can furthermore calculate $i(t)$ from u_{model} and any values of I_0 , L and U_0 .

Fig. 8 shows the theoretically modelled course of i using the same circuit parameters as in Fig. 7.

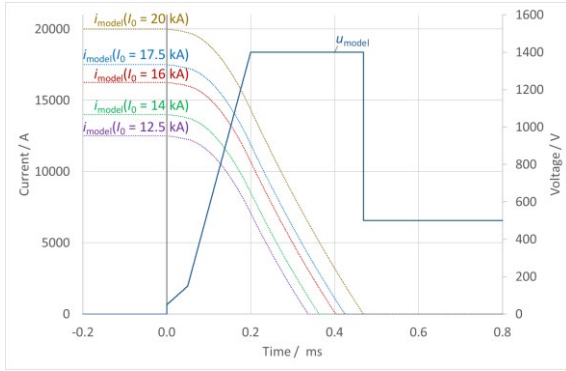


Fig. 8 The modelled current course i_{model} , which is calculated from u_{model} via eq. (3), agrees well with the measured data in Fig. 7.

With the exception of the data with $I_0 = 20$ kA, the curves are very similar to those in Fig. 7, showing the general usefulness of the model. The modelled separation times of these curves are very close to those measured (max. deviation 12 %).

The model also accurately displays the fact that u_{pyro} must be higher than U_0 to reduce $i(t)$. Thus, we can use it to estimate the product's limitation with regards to U_0 . For the *CB500-2*, U_0 must be below 1400 V, as shown in Fig. 9.

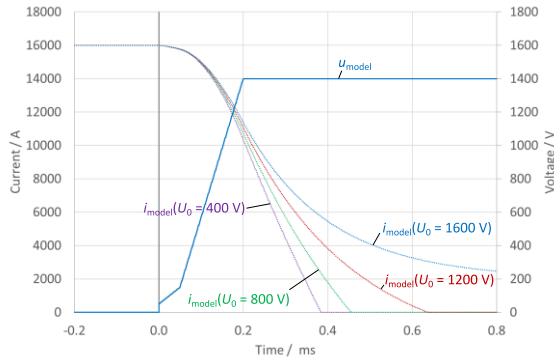


Fig. 9 Modelled current i during four switching events, all with $I_0 = 16$ kA and $L = 20$ μH , but very different U_0 ; $i(U_0 = 1600$ V) will never reach zero.

This model furthermore allows estimating the total dissipated electric energy $E_{\text{total}} = \int u(t) \cdot i(t) dt$. As mentioned, this energy is the most important challenge for pyrofuses, as it causes high temperature and pressure and possibly energy emission and thus determines the maximum possible short-circuit current that can be disconnected safely. While the inductive energy E_{ind} depends only on I_0 and L , the total energy to be dissipated also depends on U_0 and on $u_{\text{pyro}}(t)$, as can be seen in Tab. 2.

Tab. 2 Examples of calculated separation times and energies to be dissipated depending on the circuit parameters, assuming a pyrofuse that provides a u_{pyro} according to u_{model}

I_0 / kA	L / μH	U_0 / V	$t(i=0)$ / ms	E_{ind} / kJ	E_{total} / kJ
2	20	500	0.15	0.04	0.06
5	20	500	0.21	0.25	0.32
10	20	500	0.29	1.00	1.18
12.5	20	500	0.36	1.56	1.85
16	20	500	0.40	2.56	2.95
20	20	500	0.47	4.00	4.33
25	20	500	0.56	6.25	6.08
16	10	400	0.25	1.28	1.48
16	20	400	0.38	2.56	2.87
16	20	800	0.46	2.56	3.18
16	20	1200	0.64	2.56	3.43
16	20	1600	∞	2.56	∞

What E_{total} is acceptable depends on the individual product and the individual requirements, and must be determined in tests. For example, *Hirtenberger's CB1000* is designed to dissipate up to 4.2 kJ, while the *CB500-2* is usually tested with 1.9 kJ.

3.1 Prohibiting a short circuit

All these data were gathered under the conservative assumption that $i_0 = I_0 = U_0/R$, i.e., the short circuit was present for a significantly long time ($> 3\tau$) before the pyrofuse was triggered. As mentioned, a more realistic assumption is that the pyrofuse is triggered when the current is still increasing, thus prohibiting the short circuit from reaching its prospective value in the first place.

The presented equation eq. (3) can also model a switching event where the pyrofuse is activated while the short-circuit current is still increasing, by using $i_0 = 0$ and $t_0 = -t_{\text{delay}}$, where t_{delay} is the time delay after which the pyrofuse starts separating. For example, if the system electronics need 0.2 ms to detect a short circuit and to give a trigger signal to the pyrotechnics, the pyrotechnics need 0.5 ms until ignition, and it takes another 0.1 ms for the piston to cut the copper busbar, t_{delay} would be 0.8 ms. As Fig. 10 shows, the actual maximum short-circuit current would in that case be much lower than I_0 , so that significantly higher values of I_0 would be possible before E_{total} exceeds the product's limits.

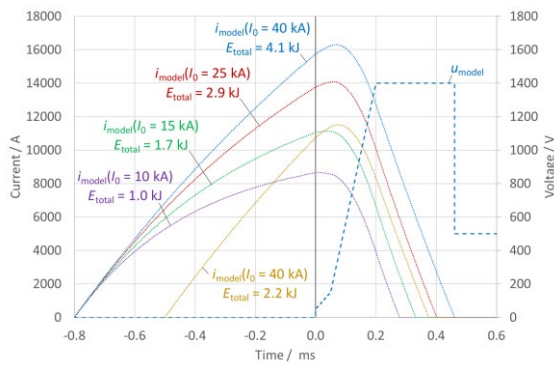


Fig. 10 Modelled current i during five switching events, all with $U_0 = 500$ V and $L = 20$ μ H, but very different I_0 . In these cases, the pyrofuse was triggered while the current was increasing.

The stated t_{delay} of 0.8 ms can be reduced further with suitable detection and triggering technology to less than 0.5 ms. As Fig. 10 shows, this has a significant effect on the resulting E_{total} , so that much higher I_0 can be switched off with a certain product.

3.2 Protecting the electric system

In its application, the main purpose of a pyrofuse is to protect other vehicle components from overcurrents, so that they do not overheat. The longer the separation takes, the higher is not only the heat created within the pyrofuse, but also that created in other components that are connected in series.

To test this, a contactor with 4 Ω resistance was connected in series with a *Hirtenberger CB500* pyrofuse and the latter was used to switch off a nascent short circuit. **Fig. 11** compares the modelled i -curves to the measured data with two different t_{delay} . As a *CB500* was used rather than a *CB500-2*, a modified model for the pyrofuse voltage course u_{model*} was used here. With this adjusted model, the course of i can once again be predicted quite well, although the model deviates somewhat from the measured data.

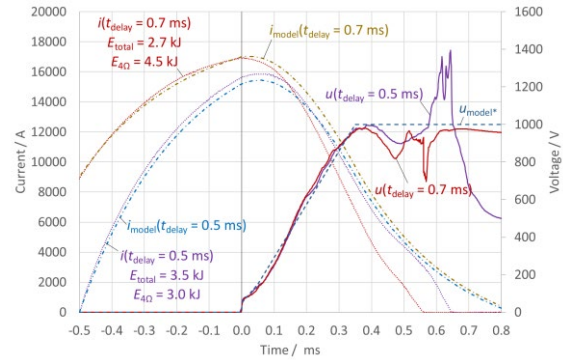


Fig. 11 Measured and modelled i and u_{pyro} during two switching events of a *CB500* with $U_0 = 880$ V, $L = 15$ μ H and $I_0 = 19$ kA, where the pyrofuse was triggered while the current was increasing, with different t_{delay} .

As U_0 was rather high (880 V) and u_{model*} is lower than u_{model} , the pyrofuse takes significantly longer to switch the current off than in Fig. 10. The data show again that the course of u_{pyro} is very well reproducible for a constant product design. In addition to E_{total} , Fig. 11 lists the energy $E_{4\Omega} = 4 \Omega \cdot \int i^2(t)dt$ that formed within the contactor with the 4 Ω resistance during the short circuit. The additional delay of 0.2 ms has a minor effect on the heat created within the pyrofuse during separation (E_{total}), but a high influence on the heat created in the hypothetical additional product ($E_{4\Omega}$, +50 % in this case).

In the case of $t_{delay} = 0.7$ ms, the resulting 4.5 kJ of heat energy was too much for the used contactor, resulting in its disintegration. This is why the measured i was lower than that modelled: The contactor's resistance rose significantly upon combustion, thus limiting the current. While we used a contactor in this example, the same principle can be applied to all system components that have to carry the short-circuit current. This shows how critical it is to keep t_{delay} as low as possible.

4 Conclusion

The switching behavior of the presented pyrofuses is almost independent from the ambient temperature and it can be modelled very well for a variety of electrical systems: As long as the product design is kept constant, the voltage course is well reproducible. From this voltage course, we can calculate the current course and the separation time as well as the total energy to be dissipated upon separation, which is crucial for estimating the capabilities of a pyrofuse.

It is crucial that the pyrofuse is activated with as little time delay as possible, ideally less than 0.5 ms, when a short circuit is forming. Otherwise, the high short-circuit currents will damage the other components in the system and the maximum possible prospective short-circuit current to be switched is severely reduced.

Pyrofuses are already a suitable alternative to melt fuses as an overcurrent protection in electric vehicles, thanks to their low internal resistance, reliability, good aging behavior and controllability, and, last but not least, their economic competitiveness.

Current work focuses on increasing the maximum possible separation energy of pyrofuses, while simultaneously limiting their sizes and costs, thus making them continuously more competitive with conventional protection solutions.

5 Acknowledgements

The author highly acknowledges the great theoretical and experimental support of his colleagues at Hirtenberger Automotive Safety GmbH. Special thanks go to H Weinkopf, L Marker, K Aigner, P Pörtl and L Muñoz.

6 Literature

- [1] E. Vinaricky: Elektrische Kontakte, Werkstoffe und Anwendungen, Grundlagen - Technologien - Prüfverfahren, 3. Aufl. Unter Mitarbeit von K.-H. Schröder und J. Weiser. Springer Vieweg, 2016

Where would we be without contacts?

Automotive trends and impact on electromechanical components

Uwe Hauck, TE Connectivity, Berlin, Germany, uwe.hauck@te.com;

Dr. Dominique Freckmann, TE Connectivity, Schaffhausen, Switzerland, dominique.freckmann@te.com

Abstract

Megatrends such as digitization, networking, and electrification have an enormous impact on electrical connectivity requirements for Automotive applications. In this paper, we highlight how these trends effect Automotive contacts such as high-speed data, power charging contacts, and switching contacts.

1 Introduction

1.1 What are Contacts?

Analogies from nature can be useful to illustrate technical issues. Most people naturally first think of contacts in terms of fellow human contact, which can be divided into two categories: family connections as well as social and professional networks. While the former is directly associated in a mostly permanent 1:1 connection, the latter are found in more dynamic, sometimes less tightly bound connections, that are increasingly linked together using digital tools.

Just as on the human level, we see a greater intermixing, and sometimes shifting, of the importance of these connections in technology. Correspondingly, we see in the technical world an increasing interconnection of analogue (the familial) and digital (the networks) worlds (domains). Digitalization is leaving its mark and changing our world faster than any technological trend before and it has the potential to help solve one of our biggest societal problems - the dramatic increase in resource consumption. Exponential increase of many global populations, along with the aging occurring within many of those populations, will require societies to adapt. These adaptations will bring about new ways of thinking, new socio-economic models, business models, and development of services that must be sustainable to meet the changing circumstances in the world.

1.2 Connectivity Trends in Automotive

In the mobility sector, electric vehicles have recently made enormous gains in importance because they enable drive system efficiency improvements and with the use of renewable energies, progress towards de-fossilization of mobility. Inherently, this use of battery elec-

tric drive trains also allows for the use of green hydrogen as an energy source which will increasingly play a role in several mobility sectors.

Though the focus of automated or autonomous driving technologies have once again attenuated, they have lost none of their long-term importance. Electric and automated driving used together can inherently enable new mobility concepts and open up new eco-systems inside and outside the vehicle. Connected vehicles, enabled by the use of additional sensor technology plus electrification, both considered individually and in various combinations, have and will continue to give rise to further business models.

The development of these new mobility formats brings together three very different industrial sectors: the legacy vehicle industry, the energy and electrical industry, and the digital economy. Each side has its own development dynamics, comes from different standardization regimes, and has a different view of product life cycles. Successful collaboration between these very different sectors will require the ability to keep the associated and steadily increasing complexity under control.

Recent years have seen a major shift of automotive actuator technology development from mechanical, to electrical to being on-demand driven. This has necessarily led to a rapid growth in the amount of electrical control and monitoring signal lines. A modern vehicle now has up to ~ 100 Electronic Control Units (ECU) with more than 3,000 contacts - reaching a level of complexity that can only be managed with great effort in product planning, development, and production. Recently, new architectural approaches are trying to counteract this increasing complexity by reducing the number of ECUs.

On the data side, we see a transition from today's decentralized arrangement in which each application has its own ECU, to consolidation within a zonal/ multi-

domain architecture where applications are grouped together according to their in-vehicle location, to a future central architectural configuration with overall central computer control from which almost everything is to be controlled (see **Fig. 1**).

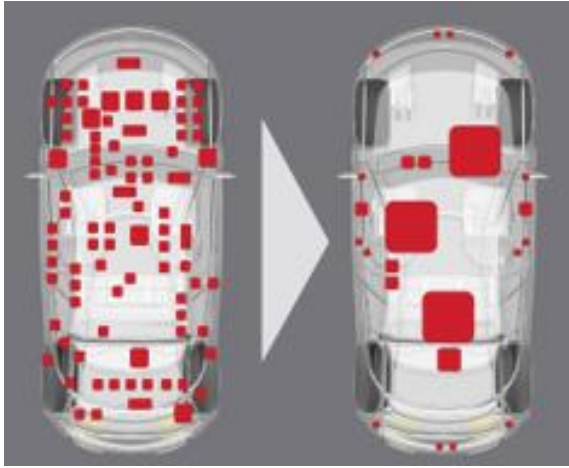


Fig. 1 Change of data architecture from current decentralized (left) to multi-domain (right)

A major reason for this complexity trend is the increasing software load in vehicle development which now accounts for 40% of development expenditure. For example, the software share of a modern luxury class vehicle is around 100 Million Lines Of Code (MLOC) (see **Fig. 2**). With the control distributed over the above-mentioned number of ECUs, the drive towards centralization can be clearly understood; particularly considering that the MLOC level may grow to 700 in the next few years as new applications are developed. On the power side, a similar industry-changing transformation is happening as the transition from a mechanical to an electrical drive system is occurring.

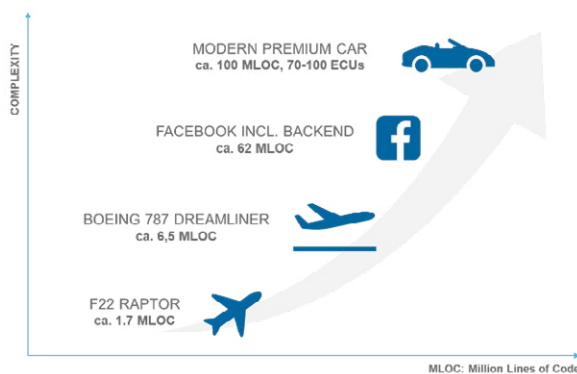


Fig. 2 Examples of increasing complexity regarding the underlying software (MLOC)

2 Electrical Contacts for Automotive Applications

We can divide contacts in automotive contact applications into the following five subcategories:

1. classic 12/14V board net contacts (pure signal, analog data, low power)
2. high-speed data contacts (digital communication)
3. power contacts (vehicle systems)
4. charging application contacts
5. switching contacts

Three examples will be used to explain how the megatrends of digitization, networking and electrification affect these contact classes in cars.

2.1 High-speed data

The most important trends are miniaturization and a constant increase in data rates for both differential and coaxial data transmission between electronic devices. Although the development of optical systems began early on, this transmission path type has not displaced copper in cars for two main reasons. First, the robustness requirements regarding handling and maintenance are more challenging for an optical data transmission path. This leads directly to higher cost as compared to copper-based transmission path development. Second, the data rates are not (yet) so high that copper in combination with sophisticated chipsets can no longer handle them. Therefore, in-vehicles coaxial, or whenever possible differential, transmission is achieved by optimizing the transmission paths. Copper lines are fully capable of executing data rates of 25 Gbit/s and more to be sufficient for (near) future infotainment and information management applications within a vehicle.

Two strategies are primarily being pursued to enhance the performance of copper transmission lines. First, reduction of losses and attenuation within the transmission path (insertion loss) can be achieved by reducing the cable lengths. Vehicle manufacturers have found ways to reduce the cable lengths from as high as 15 meters to just a few meters. Miniaturization is not only taking place in the devices and connectors. Short cables also allow for further reduced cable cross-sections, which always provides welcome savings. These advantage in terms of transmission rate and cost comes at the price of lower mechanical robustness of the thinner cables which must be addressed within the vehicle system. The second strategy is to optimize the contact designs along with their cable transition interfaces - decisive factors in reducing reflection losses. The increasing miniaturization of connectors is leading to ever smaller permissible manufacturing and assembly tolerances as well as reduced contact sizes that can only be processed using fully automatic processing methods. To optimize data transmission along a full channel, the

impacts of all components need to be well understood and balanced together as a system (see Fig. 3 and [1]).

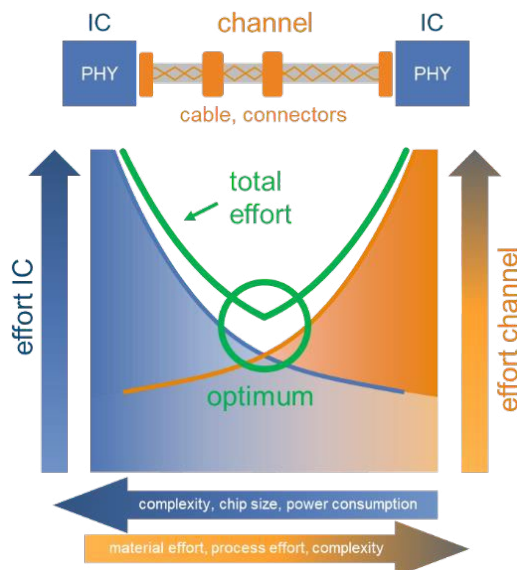


Fig. 3 Considerations for designing the physical layer of the full data transmission channel, including integrated circuits (IC), cables, and connectors [1]

Automation of wire harness production is a trend that also aims to further reduce failure rates. A necessary step, considering that traditional wire harness production is almost entirely done by hand. In the future, the previously mentioned architecture adaptations will make it possible to break down complex customer-specific harnesses into ever smaller independent segments to facilitate automatic production. This will require changes to connectors and contact designs such as gripper-compatible housing shapes, robust insertion zones, mechanical overload protection features, etc.

Fully automated harness production will also be important for the larger high-voltage components of the electrified powertrain. Similar design conditions apply here, except that additional physical parameters must be optimized in addition to the shielding quality. The most important parameter to manage is the electrical resistance. Greater resistance leads to greater power dissipation and heat generation. A sub-category with its own set of distinct requirements is the charging connector, which is considered next.

2.2 Power contacts for vehicle charging

A well-known and often discussed (psychological) barrier to the adoption of electric drive vehicles within the industry is range anxiety. The possible and reasonable range of an electric vehicle per charge depends to a large extent on how it will be used and the availability level of on-demand charging facilities. Western vehicle users are conditioned to own a multi-purpose vehicle; a vehicle for every conceivable use case. In Asia, this

expectation is less common, but there too, a compromise must be found between the amount of on-board energy available and the energy demand of the vehicle. Large batteries allow longer ranges but incur high costs and inefficiencies from the additional weight. Smaller batteries need to be charged more frequently, however -from a psychological perspective- might be expected to charge more quickly.

In addition to battery parameters such as cell chemistry, dimension, and capacity, a lot of attention is paid to the charging process. The goal is to have charging resemble the traditional vehicle refuelling process as much as possible. This means that there is pressure to maximize the current used to be able to charge the battery in the shortest possible time. This leads to charging current density increases. Due to the relationship $I^2 \times R$, there are quadratic increases in thermal losses with such current increases which leads to greater cable cross-section requirements.

An alternative approach is to increase voltage. To achieve similar or increasing charging energy (charging rate), doubling the voltage would allow the current needed to be halved while reducing thermal losses to a quarter – a significantly lower loss when compared to the current increase approach. Correspondingly, a significantly greater level of charging energy can be transferred at the same cable cross-section by using higher charging voltages. Currently, fast charging systems are in use that deliver well over 200 A charging current. Several car manufacturers have already announced 800 V charging processes, and even a voltage level ~ 1500 V is being discussed, which would result in charging power levels in the megawatt range! The requirements for new types of Direct Current (DC) charging contacts are getting correspondingly higher. And on the cable side, the copper cable cross-sections required for this 1500 V would be far above 90 mm² which is not easily installed due to the weight and the required large bending radii for such large flexible cables. Aluminium cable could lead to a reduction in weight but would require even larger cable cross-sections than copper.

As described, the electrical contact resistance of the charging contact over the application lifetime is one of the most important requirements. Achieving a separable connection electrical resistance close to that of a permanent connection is only possible with correspondingly high contact forces, large cross sections, and highly conductive materials and contact surfaces. Due to the frequent use that is required of customer charging interfaces, high contact forces are a hindrance for two reasons. First, contact surface wear levels increase with contact force. Second, high mating forces are not reasonable for the user. An additional difficulty factor for the case of the charging connector applications is that the applicable standard requires a level of

10,000 mating cycles, and for some customers far beyond that. Therefore, keeping the charging interface resistance low and consistent over the service lifetime of the connection can be a challenge. If the interface resistance increases during charging, the resulting connector temperature increase will be detected leading to system charging power level capability reductions being applied. This will lead to prolonged charging times, and at a worst case, interruption.

In addition, there are other sources of increased wear and tear variability on the charging interface such as debris and/or damage caused by customer dropped plugs, and the almost infinite combinations of different vehicles and charging stations interface designs. The standardization of the charging interface contact design has not been defined, only the interface geometry. Therefore, the contact pin on the vehicle side charged using a tulip infrastructure plug contact one time, can subsequently be charged using a lamella infrastructure plug contact the next time, and so on. With each mating cycle, this specific pin/plug combination with their mating histories creates a "fingerprint" with a different wear pattern. Consequently, in a growing DC charging network, fault transmission and propagation will also have to be addressed, including a customer-friendly diagnosis and repair strategy. This example shows that the additional automotive connectors interface design rules are no longer sufficient and there is room for innovation.

The potential risks of injury when charging at higher voltages must be considered to not only meet vehicle servicing requirements, but also take into consideration that the battery charging operation is an inherently Direct Current (DC) process. Contact safety of 'live' contacts cannot be achieved by the surrounding connector housing alone. High Voltage (HV) connector contact pins therefore often have captive finger protection features on their visible front end. Systems are designed to have additional safety features within the vehicle, such as interlocks, to be able to detect any conduction loop interruption if disconnection of a power interface under load occurs. In this way, the potential for arcing occurring in this case scenario can be prevented by a safety system disconnection of the power source from the HV vehicle electrical system prior to arc initiation. This disconnection should be reserved exclusively for the contacts intended for this purpose – those used in contactors.

2.3 Contactors

Contacts in contactors are used to implement electrical isolation of the energy storage device from the rest of the HV vehicle electrical system as needed. In the open state, they must ensure electrical isolation in accordance with the electrotechnical regulations, and in the

switched or closed state, they must enable safe transmission of power. A deep understanding of the application is required to be able to fully characterize both operating states. Modern energy storage systems in electric vehicles can have very low internal resistances and thus generate short-circuit peak currents of up to 30kA in the event of a fault, which can be limited by parasitic physical effects, but must be precisely understood in terms of their dynamics. The safety of the overall system is therefore based on a precise coordination of a multi-stage protection strategy at the level of the entire vehicle and the Battery Management System (BMS) with its administered individual components: HV fuse or pyro-switch and contactors, pre-charge relays, the battery sensor system and battery status detection. This ensemble must work together as an overall system over the wide range of current conditions such as open state, continuous, overcurrent, short circuit, and transients that can occur.

The normally open contacts of contactors, for example, must be designed to be able to switch in response to different current conditions (disconnection during charging, or recuperation, or during normal driving operation and its extreme cases such as short circuits). At first glance, this does not seem logical for an electrical contact, but it becomes understandable when the use of additional magnetic arc quenching devices is considered. Blast magnets oriented perpendicular to the contact current flow direction are used to deflect any arcs formed between the separating DC contacts and extend them to achieve an arc break condition faster. Physically, the direction of arc deflection is dependent on the current direction due to the polarized magnetic blowout field. Depending on the design and installation space, it can therefore be assumed that the switch-off capability varies depending on the direction of current. Therefore, the contact design must be accordingly optimized geometrically (see Fig. 4 and [2]). In automotive applications, additional influencing factors come into play such as shock and vibration.

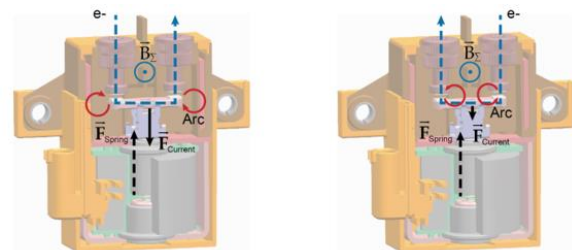


Fig. 4 Repulsion and attraction force of the current in the external magnetic field (left: discharge, right: charge [2])

High vehicular vibrational dynamics impose acceleration forces along all three axes of the contactor contact interface, alongside the applied contact force. Additionally, the effect of the operational current dynamics also needs to be considered (e.g., Lorentz forces can

lead to levitation). Under no circumstances may unintentional contact opening/bouncing be allowed to occur during operation since such short-time openings can lead to contact welding. For example, as contact surface materials can melt under the effect of an arc, if the contact comes to rest again against the opposite surface too quickly (e.g., a bounce) solidification leading to contact welding could occur. This risk is prevented by careful selection of contact material and force balance adaptation within the scope of the contactor specification.

Overall, the service life of a contactor is strongly dependent on its use cases. In addition to the number, direction, and strength of the switch-off operations; contact wear also depends on the contact chamber design and the arc extinguishing mechanism used. There is a complex mix of factors that must be thoroughly considered to enable safe as well as cost-effective long-term operation in a vehicle. For safety purpose, switching state detection and switching history are monitored by the BMS and increasingly accurate wear models are stored in the diagnostic routines. This is a good example of how the physical and logical layers in the vehicle can be better networked and how the ever-increasing computing power in central computers can be used in the future for real-time simulations and diagnostics in the vehicle.

2.4 Other Considerations

2.4.1 Semiconductor technology

When considering the growing demands, semiconductor technology should not be neglected. Power electronics are developing rapidly, and their large-scale industrial use creates a scaling opportunity for new semiconductor technologies. At higher costs, it is possible to obtain higher performance from converters by using silicon carbide (SiC) semiconductors. For example, their higher switching frequencies allow the size of components in power electronics to be reduced which leads to valuable installation space savings of up to 50% to compensate for the higher semiconductor costs. Functional integration of power electronics into the electric motor thus becomes easier and vehicle integration allows modular designs.

However, the possibility of achieving higher switching frequencies by using SiC also has an influence on the electromagnetic interference energies emanating from the power electronics directly via the line or via other geometries acting as antennas. This can lead to interference in other electronic functions. Therefore, the shielding effectiveness requirements for such unintended disturbances are becoming more stringent. Especially when it comes to improving the reliability of

safety relevant functions in the environment of automatic or autonomous driving. The shielding effectiveness enabled by the contact between connector shielding components and the housings on which they are mounted is becoming increasingly demanding. This is only made more difficult to achieve considering that the housings used are not made of preferred electrical conductor materials, but of alloys or even composite materials. Ensuring a permanently low impedance of the shield connection points is thus another technical challenge in the use of Alternating Current (AC) power in and around electric drive systems.

2.4.2 Thermosimulation

The development of models for contact systems for use in simulation environments is becoming increasingly important to be able to optimize materials used for specific vehicle applications, as well as ensure reliable function over the service lifetime. Linking electrical and thermal simulations is a logical step which allows for the direct analysis of the thermal consequences of applying the current profiles used in driving or charging operations along the complete power path. Possible instances of thermal overloads that could potentially lead to subsequent accelerated degradation and possible early failures can thus be identified and eliminated early in the design process. At the same time, oversizing of lines and components can be avoided since possible load scenarios can be compared with the planned operating strategy at any time.

An example illustrating the use of this simulation technique is optimization of energy transmission paths during the fast charging of a traction battery. The use of large conductor cross-sections in the charging path is often already sufficient enough to dissipate any accumulating current driven connector heating away from the contact zone. In the case of very short charging times, for high-capacity batteries or highly dynamic driving operations, high temperatures are to be expected in the contact zones. This heating must not lead to exceeding the critical limit temperatures of the materials and contact surfaces used at any time. Transients, which could occur during a fault condition, must also be considered in the dimensioning of the system design since short current peaks in small current-transmitting geometries or thin layers can represent an adiabatic load. In effect, the peak heat input at the contact zone during such an effectively adiabatic transient event is not dissipated by thermal conductivity. Therefore, calculating heat loss by evaluating an average value is not sufficient since such transient current peaks are too short for thermal dissipation to be a factor. Physically, these events can lead to accelerated aging or total failure of a connector.

Existing electrical power beam cross-section design tables for electrotechnical systems compensate for any

additional simultaneous occurrence of such load excursions by means of a correspondingly high safety margin. To optimize such an electrical design by applying system level simulation, uniform individual models of all components involved must be available to be able to dynamically calculate their electro-thermal behaviour throughout the network. As part of an industry-wide collaboration, the ZVEI published Technical Guideline TLF 0101 [3] describes this type of model structure and its parameter sets. The thermal behaviour is translated into electrical equivalent circuit diagrams by means of sources, sinks, resistances and capacitances. Connectors, conduction path lines, and other components can be represented at the component model and linked together in a wide variety of simulation environments (see Fig. 5).

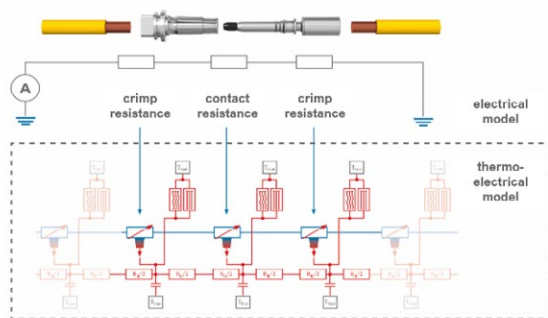


Fig. 5 Model for thermosimulation

This approach shows how specific knowledge in the field of contact physics can be made available in a user-friendly way that is closely representative of the application. In a form for use with development tools that are available throughout the industry.

3 Conclusions

Societal changes and economic goals drive megatrends such as electrification and digitalization and are accompanied by miniaturization and functional integration to achieve performance increases with decreasing material usage. This leads to an ever-increasing power and information density and requires reliable product designs that keep pushing to the physical limits.

Contacts are an excellent example of the increasing requirements. High operating temperatures, harsh environmental conditions as well as rising material costs, or even material bans, force constant innovations and a deep understanding of the application and the technical relationships between the product and its environment. Simulations can support the design process and enable faster and more advanced optimization of contacts and its systems.

In an ever-connected world, connectivity and with it the underlying contacts -which on an atomic level provide the basis for each traveling electron- are becoming increasingly important because so much more depends

on them. The robust and reliable physical foundation is the imperative basis for the progressively software-driven innovations in product enhancements and services, without which new ecosystems would not work.

4 Literature

- [1] Trend Paper „Driving the Data Fueled Future - Automotive Trends, Challenges, and Solutions for Data Connectivity“; TE Connectivity, 2020.
- [2] White Paper „EVC 250 Main Contactor“; TE Connectivity, 2020.
- [3] ZVEI „Technical Guideline 0101: Thermal Simulation Models“; ZVEI (German Electrical and Electronic Manufacturers’ Association), 2020.

TE Connectivity is a trademark licensed by the TE Connectivity Ltd. family of companies.

Qualification of Power Contacts in High-Voltage Products for IEC 115 °C Limit Temperature

Michael Gatzsche, Alberto Zanetti, Falk Blumenroth, Hitachi ABB Power Grids, Zurich, Switzerland, michael.gatzsche@hitachi-powergrids.com

Abstract

To ensure reliable long-term performance of high-voltage switchgear, IEC series 62271 prescribes material specific limit temperatures that may not be surpassed during continuous current type tests and during normal continuous operation, respectively. With the second edition of IEC 62271-1, published in July 2017, silver-plated contacts can now reach a limit temperature of 115 °C, which is 10 K higher than before. Silver-plated contacts are often used to implement sliding or plug-in connections in the nominal current path of High-Voltage Products like Gas-Insulated Switchgear (up to 8 000 A) and Generator Circuit Breakers (up to 50 000 A). In the present contribution we discuss how thermal design of high-voltage products can be adapted to utilize the new limit temperature for higher current ratings and how long-term performance of the contact systems are influenced by temperatures. We present measures to qualify contact systems for reliable long-term operation at 115 °C: Specifically, relaxation behaviour of spring-loaded elements based on copper alloys and steel as well as thermal stability of grease are verified by application-related long-term tests and extrapolation methods.

1 Introduction and Background

1.1 High Voltage Products and Contact Systems

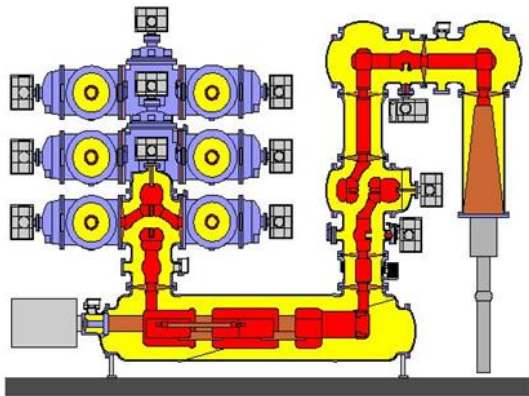


Fig. 1: High-voltage gas-insulated switchgear

Metal-enclosed gas-insulated switchgear (GIS) is an option for low-loss transmission and distribution of electrical power (Fig. 1). Due to the high electrical strength of the insulating gas SF₆ or more eco-efficient alternatives, these systems are very space saving. Rated Voltages up to 1 200 kV as well as rated currents up to 8 000 A are available. The most common contact system are power connectors with silver coated CuCr1Zr helical springs (“spiral contacts” Fig. 2) for quasi-stationary (bus-ducts) and dynamic (disconnecter, circuit breaker, ...) use. To ensure low plug-in and sliding

forces as well as high tribological lifetime (up to 10 000 close-open operations), lubrication in the form of grease is applied.

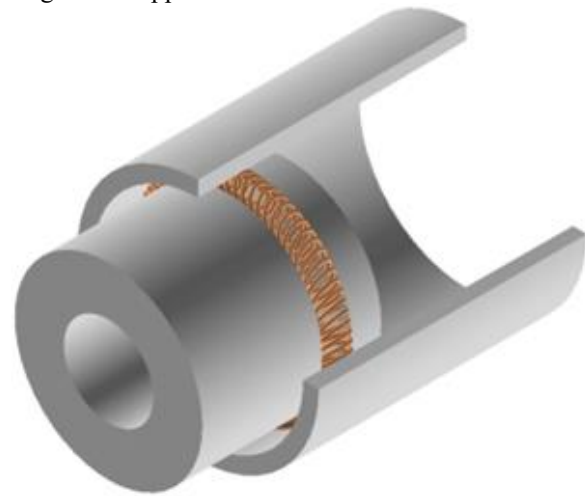


Fig. 2: Contact system using spiral contacts

Generator circuit breakers (GCBs, Fig. 3) are typical components that can be found in power plants. The key role of GCBs is to protect the power generation system by switching the circuit between generator and transformer in a power plant. The use of a GCB is widespread because it offers many advantages for the operation of power plants such as simplified and more flexible procedures and higher reliability and availability [1]. These breakers are subjected to lower voltages (up to 31.5 kV) compared to the GIS equipment, but they experience for most time of their operating lifetime very high nominal currents (up to 50 000 A). For this application the contact systems are different compared to the ones of the GIS. The most used contacts for GCB are finger contacts with a spring to build up the desired

contact force. The springs for such application are normally made from steel. The contact systems for GCBs are normally dynamic contact systems, with different speeds ranging from slow (around 1-2 mm/s) to very fast (4-5 m/s). To transport reliably such very high currents it is crucial to minimize the thermal losses, thus the contact resistance must be as low as possible.

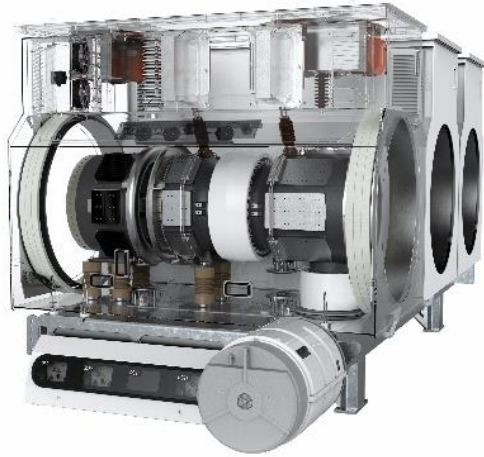


Fig. 3: Generator circuit breaker (GCB)

From user perspective, common key requirements for GIS and GCB are absolute reliability and a long service life: 40 years and more without exchange of active parts in the current path. Thus, contact systems must provide connection resistances in the single digit $\mu\Omega$ -range; being stable over decades and over up to 20 000 plug-in cycles. The service life in the range of decades provides a challenge from a qualification standpoint, with R&D cycles that are in the range of a few years or shorter.

1.2 Standardization and Long-Term Performance of Contact Systems

To ensure reliable long-term performance of contact systems, material specific limit temperatures are defined in standards. For high voltage devices, IEC series 62271 is most relevant. With the second edition of IEC 62271-1, published in July 2017 [2], silver-plated contacts can now reach a limit temperature of 115 °C, which is 10 K higher than in the previous edition [3]. This change is expected to follow in the GIS and GCB product standards [4], [6] as well as in Chinese standardization (GB/T and DL).

Temperature limits in standardization derive from the fact that degradation mechanisms of electrical contacts accelerate with increasing temperature [7]. For contacts systems that allow relative movement and/or separation of the contact partners in operation, chemical reactions at the surface, i. e. oxidation and formation of insulating oxide surface films are most critical. Thus, the limit temperature depends on coating material and ambient medium: A bare copper contact may reach a

maximum temperature of 75 °C in an oxidizing gas (e. g. air) while when operated in a non-oxidizing gas (e. g. SF₆) a bare copper contact is allowed to reach 115 °C [2]. The highest limit temperature is allowed when using silver-plated contacts (115 °C in both oxidizing and non-oxidizing gases).

Limit temperatures may not be surpassed during continuous current type tests. During normal continuous operation, these temperatures would be reached at maximum ambient temperature when operated with rated current for several hours (thermal steady state).

A successful continuous current type test alone is not enough to qualify a high-voltage product for reliable long-term operation. It is the responsibility of the manufacturer to ensure that all materials and designs are long-term stable at the operating temperatures. The increase of the contact temperature limit from 105 °C to 115 °C subjects the contact system and adjacent components to higher thermal stress. With respect to the contact system, two key degradation processes can be identified [10]:

- reduction of contact force due to relaxation of spring elements
- aging of the lubricant (grease) and resulting degradation of tribological performance

Based on an estimation in [7], the 10 K increase in operating temperature is expected to accelerate aging by a factor 2 to 3.

1.3 Thermal Design of High Voltage Products

There is an incentive towards using higher limit temperatures: Higher temperature means more heat transfer, which in turn allows higher power loss and current density in the conductors. Designing high voltage products, higher current densities enable more compact devices (using less material) or higher current ratings (using the same amount of material).

2 Qualification of Power Contacts for 115 °C

2.1 Mechanical and Electrical

The mechanical and electrical qualification tests are focused on the temperature induced reduction of contact force and its possible effect on the connection resistance. We exemplarily show procedure and results of a contact system with copper based (CuCr1Zr), spring loaded spiral contacts (Fig. 2). Similar tests and evaluations are conducted on systems with contact force being created via steel springs.

Model contact systems using two flat pressure plates contacted via two spiral contacts have proven well suited for long-term tests, allowing both a measurement of contact force and contact resistance (Fig. 4), [8], [9], [10], [11]. In the present investigation, we thermally aged model contact systems in an oven for 6 400 h (9 months). The contact force at nominal deflection was regularly measured at the cooled down connections using a 10 kN material test machine (Fig. 4) by slowly decreasing deflection (Fig. 5). Connection resistance has been measured using a 200 A_{DC} microohm meter. Two different spiral contact suppliers (“spiral sup A/B”) as well as two different greases (“grease 1/2”, see section 2.2.1) and non-lubricated references (“no grease”) have been investigated (4 samples for each combination).

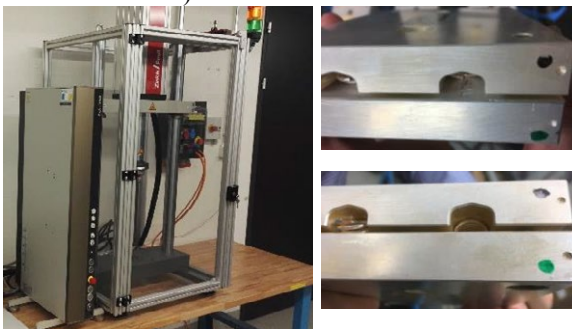


Fig. 4: Material test machine and flat model connection with spiral contacts

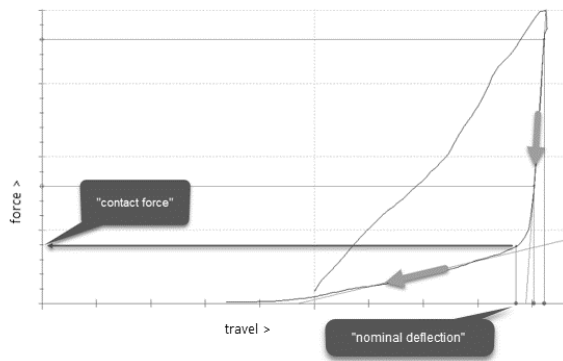


Fig. 5: Procedure for contact force measurement

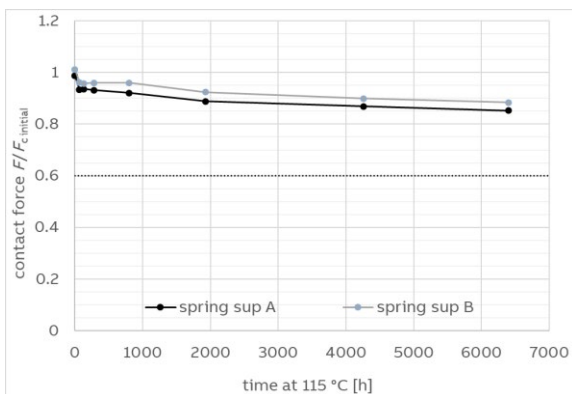


Fig. 6: contact force of spiral contacts during thermal aging at 115 °C for 6400 h (standard deviation below 3 % in all cases)

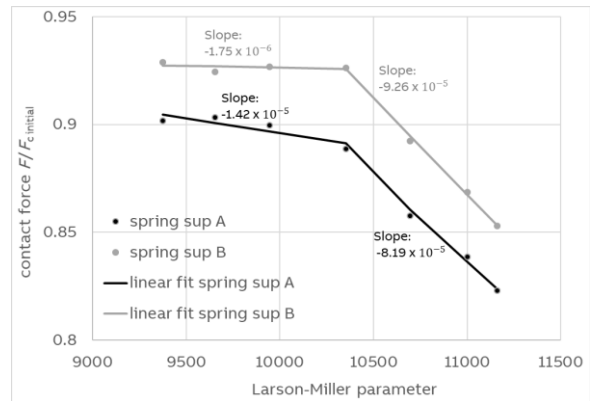


Fig. 7: Larson-Miller transformation of data in Fig. 6 with linear fit

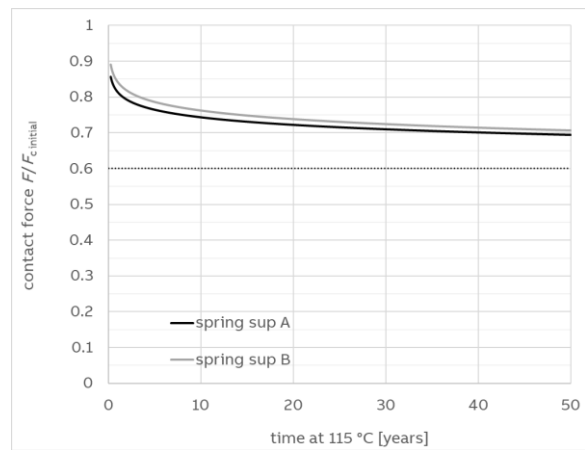


Fig. 8: Contact force for spiral contacts being continuously operated at 115 °C for 50 years, based on data from Fig. 6, extrapolated via Larson-Miller method (Fig. 7)

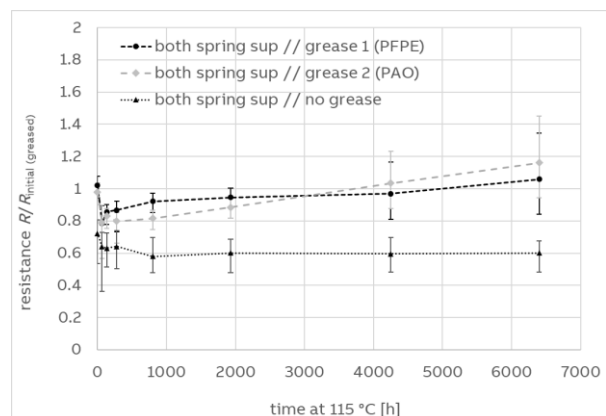


Fig. 9: Connection resistance of spiral contact during thermal aging at 115 °C, range of all 8 samples per group plotted (cf. Fig. 6)

Heating to 115 °C, the spiral contacts initially lose around 5 % contact force (first measurement after 64 h). Subsequently the rate of force reduction significantly decreases. After 6400 h, remaining contact force is above 85 % of initial value. Both tested spiral contact suppliers show equal mechanical performance (Fig. 6).

To extrapolate the data to typical GIS or GCB service life, the Larson-Miller Parameter is used [12]. This approach consists in transforming the time t in the force-time plot to a time and temperature dependent parameter P :

$$P = \frac{T}{K} \left(\log_{10} \frac{t}{h} + 20 \right)$$

In the resulting Larson-Miller plot, periods with a continuous force reduction process can be identified as straight lines. In case no change in process occurs, force reduction can be extrapolated towards higher P using linear fit (Fig. 7). Retransformation of the linear fit to time t yields force reduction for several decades of service life (Fig. 8). Similar extrapolations have been carried out for copper-based contact systems of lamella type [9] as well as busbars [13]. For the spiral contacts in the present investigation, after prospected 50 years of continuous operation at 115 °C, more than 70 % of initial contact force remains (Fig. 8).

At 70 % of its initial value, the contact force is expected to still be high enough to create low resistance connection after an open-close operation. In [10], tests were performed on different silver based spring loaded contact systems up to 180 °C and yielded a reduction of spring force down to 60 % of initial level, without an increase of resistance, even after open-close operations. Resistance measurements at the model connections of the present investigation (Fig. 9) also exhibit a stable resistance, especially at the non-lubricated samples. A slight increase of connection resistance at the greased samples can be attributed to thermally induced changes in the grease (evaporation, see section 2.2.1), but is not seen as critical, especially since the effect will be considerably less pronounced at a real contact system with significant relative movement of the contact partners (see section 2.2.2.).

In summary, we evaluate the investigated spiral contacts to be mechanically and electrically fit for operation at 115 °C for 40 years and more.

2.2 Tribological

When the two parts of a sliding electrical contact systems must be operated, a tribological system is created. The tribological properties of the system are influenced from: the materials, the surface finish, the force applied and the lubrication. All these parameters influence the wear of the system. In this specific application, the need for the very low electrical contact resistance, leads to the need of using quite high contact forces [14]. High contact forces and high opening speed requires a good lubrication in order to keep the wear of the system low, so that the target for reliability and lifetime of the breakers can be met. To assess the influence of the new 115 °C on the tribology of the used contact systems, different tests are carried out.

2.2.1 Grease evaporation

Lubrication is a crucial aspect for a tribological system, and even more important for contact systems. The lubricant used in electrical contacts must reduce the friction between the two surfaces, but it shall not create an insulating layer that will lead to a raise of the contact resistance. To assure the correct operation, and a long lifetime of the products, the correct grease needs to be chosen and used. One important aspect of a grease for high temperature use, is the evaporation rate. A low evaporation rate of the grease will help to maintain the tribological properties of the system at a level that will assure the correct functioning of the contact system. To assess the suitability of the grease a test for the evaporation is carried out. The test consists on the exposure of greased aluminium plates to a constant temperature of 115 °C in air. The plates are greased with a thin film of grease, in the same way as the electrical contacts are greased in the production. This approach is chosen because of the importance of testing a system in a meaningful way, meaning as close as possible to the real application. For this test 2 different greases are chosen: one is a perfluoropolyether (PFPE) based grease (grease 1) and one is a poly-alpha-olefin (PAO) based grease (grease 2).

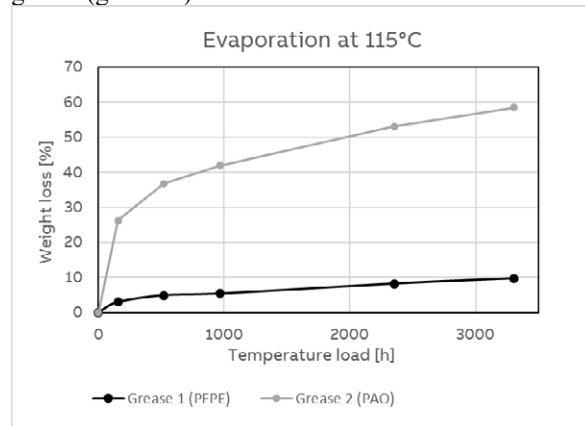


Fig. 10: Grease evaporation in air at 115 °C.

Heated to 115 °C, both greases lose weight (Fig. 10). The loss is quite fast in the beginning and tends to decrease the rate of evaporation with time. This behaviour is explained by the loss of the more volatile species present in the grease in the first stage. After this phase, further loss of weight is slower (1000 hours to 3000 hours), and after all volatile species has evaporated the weight is almost stable. Although the two greases show the same general trend for the weight loss, it is possible to see the grease 1 (PFPE) has a much better resistance to the evaporation at 115 °C compared to grease 2 (PAO). After 3500 hours, the loss in weight of the grease 1 is only 10%, while for the grease 2 this is 6 times bigger. The difference in evaporation together with the mechanical tests shows that the PFPE based grease is a good candidate for the use to fulfil the new IEC standard.

2.2.2 Mechanical lifetime

The tribological properties of aged grease are tested by mean of a special setup that was built for the purpose. It is a high speed (4 m/s) testing device that recreates a stress for the contacts and grease like the real application in a GCB arcing chamber. The contact forces are comparable to the one in the real application, and they can be set between 15 N and 40 N. The differences compared to the real application are: oxidizing atmosphere (air) instead of SF₆, operation at room temperature. The moving part is a silver-plated copper plate, that is greased with a thin layer of special grease. The ageing of the grease is performed beforehand by storing the greased plate in the oven at 115 °C in air. The testing device can perform 500 strokes in 8 minutes and the length of the stroke is 40 mm. The test is considered as passed when 20 000 COs (closed-opened operations) can be reached without an excessive wear of the contacts (no copper visible), and the contact resistance within a $\pm 20\%$ range of the value taken as initial reference. The contact resistance is measured by 4-point probes method with a measuring current of 50 A_{DC}, using a micro-ohmmeter.

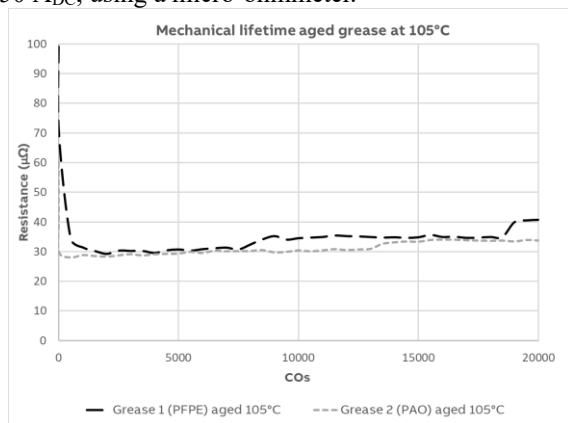


Fig. 11 Mechanical lifetime tests with grease aged at 105°C.

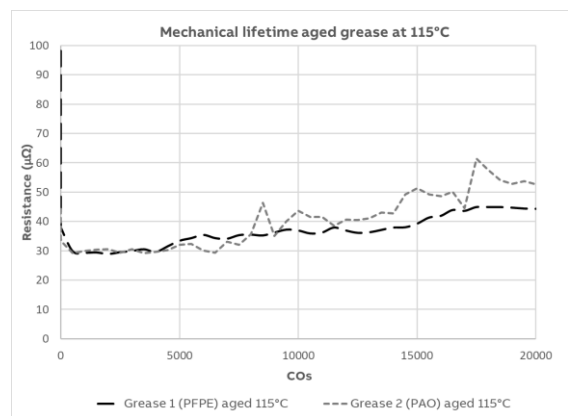


Fig. 12 Mechanical lifetime tests with grease aged at 115°C.

The initial drop of the resistance during the first CO (Fig. 11 and Fig. 12) confirms, that a slight increase of

contact resistance caused by the thermally aged grease film (as seen in spiral contact test, Fig. 9) is not critical for application in high power contact systems, because excess grease will be removed by friction and wipe in the system. Looking at the complete 20 000 CO test series (105 °C: Fig. 11 and 115 °C: Fig. 12) it is clear that the increase in temperature influences the wear rate and integrity of the contact system. The wear of the contact, and hence a certain instability of the contact resistance, settled in for grease 2 aged at 115°C already after 7000 COs (Fig. 12), while for the same grease aged at 105°C the wear and resistance are stable for the complete test (Fig. 11). Even though grease 1 (PFPE) shows a slightly higher resistance than grease 2 (PAO) when aged at 105°C, the PFPE oil-based grease shows better performance at 115°C, with a more stable contact resistance over 20 000 COs. The contact resistance increases also in this case, but the final value is still acceptable. There is a good correlation between what we observed on the evaporation (Fig. 10) of the grease and the performance of aged grease during mechanical lifetime tests. The high mass loss when exposed at 115°C has clearly a detrimental impact on the lifetime and stability of the contact resistance, hence the grease 1 is a more suitable candidate for 115°C applications. The tests described in the present work are carried for an initial screening of possible greases, but more in-depth analysis is carried out on the best candidates, aiming to understand the physical and chemical processes that cause the different performances. After these lab assessments and tests on small scale test rigs, the greases are then tested in the real products, in experiments closer to the real service conditions. The final decision on the best grease to be used is taken after development tests on large scale and type tests on the products that can be safely and reliably operated at up to 115°C.

3 Conclusions

Going from 105 °C to 115 °C limit temperature for silver plated contact systems allows more compact design and higher current ratings in high voltage products such as GIS and GCB. Components of the contact system, most notably spring elements and grease will be subjected to higher thermal stress. Tests allowing an extrapolation of force reduction behaviour as well as thermal stability of grease have been identified as key to qualify contact systems for the higher service temperature. Tests are being performed and show that contact materials, designs and lubrication for high power plug-in connections are available for continuous operation at 115 °C and a service life of 40 years and more. It is recommended to perform similar tests for all systems that shall be operated at 115 °C.

4 Acknowledgments

We thank Marco Rohner and Andreas Wetzel for executing the long-term tests and Shams Taha for her support in data evaluation and presentation.

5 Literature

- [1] M. Palazzo and O. Fritz, “A novel monitoring system for generator circuit breakers to increase the availability of power plants,” in CEPSI, 2016, p. 8.
- [2] IEC 62271-1, Edition 2.0, 2017-07 “High-voltage switchgear and controlgear – Part 1: Common specifications for alternating current switchgear and controlgear”
- [3] IEC 62271-1, Edition 1.1, 2011-08 “High-voltage switchgear and controlgear – Part 1: Common specifications”
- [4] IEC 62271-203 Edition 2.0 2011-09 “High-voltage switchgear and controlgear – Part 203: Gas-insulated metal-enclosed switchgear for rated voltages above 52 kV”
- [5] IEEE Power & Energy Society, Substations and Switchgear Committees: IEEE Std C37.122™-2010 “IEEE Standard for High Voltage Gas-Insulated Substations Rated Above 52 kV”
- [6] IEC/IEEE 62271-37-013 Edition 1.0 2015-10 “High-voltage switchgear and controlgear – Part 37-013: Alternating-current generator circuit-breakers”
- [7] IEC/TR 60943 Edition 2.1 2009-03 “Guidance concerning the permissible temperature rise for parts of electrical equipment, in particular for terminals”
- [8] Blumenroth, Falk: Zum Langzeitverhalten von Steckverbindungen mit Schraubenfedern in Anlagen der Elektroenergie-technik. Aachen: Shaker, 2010
- [9] Lücke, Nils: Zum Langzeitverhalten elektrischer Steckverbindungen mit Kupfer-Beryllium-Kontakt-lamellen : TUDpress, 2014
- [10] Gatzsche, Michael: Elektrisch-thermisches Betriebs- und Langzeitverhalten hochstromtragfähiger Kontaktelemente. Aachen : Shaker, 2016
- [11] Gatzsche, Michael; Lücke, Nils; Großmann, Stefan; Ledermann, Tom; Freudiger, George: Impact of the temperature-induced reduction of joint force on the long-term behavior of contact elements with material-allocated electrical and mechanical function. In: 28th International Conference on Electrical Contacts (ICEC 2014), 2014
- [12] Larson, Frank R.; Miller, James: A time-temperature relationship for rupture and creep stresses, 1952
- [13] Schlegel, Stephan: Langzeitverhalten von Schraubenverbindungen mit Stromschienen aus Reinkupfer in der Elektroenergie-technik unter besonderer Berücksichtigung der Temperatur. Dresden, Technische Universität Dresden, Fakultät, Dissertation, 2011
- [14] Slade, Paul G., “Electrical Contacts: Principles and Applications” , CRC Press, 2014

Recommendations for Testing the Short Circuit Behaviour of Power Plug-In Connectors

Toni Israel, Technische Universität Dresden, Germany, toni.israel@tu-dresden.de
 Stephan Schlegel, Technische Universität Dresden, Germany, stephan.schlegel@tu-dresden.de
 Steffen Großmann, Technische Universität Dresden, Germany, steffen.grossmann@tu-dresden.de
 Tom Kufner, Stäubli Electrical Connectors AG, Allschwil, Switzerland, t.kufner@staubli.com
 George Freudiger, Stäubli Electrical Connectors AG, Allschwil, Switzerland, g.freudiger@staubli.com

Abstract

Worldwide, there is a growing demand for the flexibility of power plug-in connectors, especially in transportation electrification (e.g. electrical technologies for automotive, electric propulsion for ships or electric aircraft technologies), renewable energy distribution and Industry 4.0. Stäubli and TU Dresden have been researching the short circuit behavior of this kind of power connectors for years. An important part are type tests for connectors according to standards. In this publication, the boundary conditions and the allowed deviations from them are analyzed taking into account the characteristics of connectors, especially with contact elements. Generally, the test duration and waveform should fit to the real world or rated values as close as possible. The waveform, especially the peak current at the beginning of the short circuit, greatly influences the heating of the connector. This also influences the reduction in contact force. In type tests, often the Pt -criterion is used to adjust the tested short circuit current and its duration. But, the Pt -criterion may only be used with caution for altering the test duration. Its boundary conditions are not generally fulfilled for electrical connections. So, with a change in the tested duration of the short circuit the thermal stress for the system will also change, which is shown in this publication. As a possible work around, this paper proposes an P^t -criterion which is able to change the short circuit duration in a relatively wide range while keeping the thermal stress for the contact system almost constant.

1 Short Circuit Tests

1.1 Nomenclature

Short circuit tests for connectors and equipment, which contains connectors, can be found in IEC 62271-1 (High Voltage Switchgear), IEC 60309-1 (Low Voltage Switchgear) and IEC 61439-1 (electrical connectors).

The nomenclature of the peak short-circuit current and the steady short-circuit current is not uniform in standardization [1], [2], [3]. Therefore, in this publication, the following nomenclature, based on high voltage electrical equipment, is used:

rated value	tested value
rated short time withstand current $I_{sc r}$ (RMS)	tested short time withstand current $I_{sc test}$ (RMS)
rated duration of short circuit $t_{sc r}$	tested duration of short circuit $t_{sc test}$
rated peak withstand current i_{pr}	tested peak withstand current $i_{p test}$

Table 1: Nomenclature

1.2 The P^t criterion

Assuming an infinitely long conductor with a uniform cross-section and neglecting the heat dissipation by convection and radiation (adiabatic heating), the final temperature after a short time current can be calculated analytically (cf. [4]). Typically, these conditions apply for short time load under 5 s in electrical power engineering. Additionally, the following boundary conditions apply:

1. No radial heat transport
2. No heat conduction along the conductor

$$\vartheta_{\max}(t = t_k) = \frac{1}{\alpha} \left(1 + \alpha (\vartheta_0 - 20^\circ\text{C}) \right) \cdot \left(\exp \left(\frac{k I_{sc}^2 \alpha \rho}{c A^2} t_{sc} \right) - 1 \right) + \vartheta_0 \quad (1)$$

Where c is the heat capacity, A is the cross sectional area, k is the skin effect factor, α is the resistance temperature coefficient, ρ is the specific electrical resistance, ϑ_{\max} is the maximum temperature at the end of the short circuit and ϑ_0 is the temperature at the start of the short circuit. If the conductor material, cross-section and boundary conditions are not changed, the temperature rise $\Delta\vartheta$ at the end of the short circuit is

basically only a function of the short circuit current and the short circuit duration:

$$\Delta\vartheta = f(I_{sc}^2 t_{sc}) \quad (2)$$

If the test current and test duration are changed while this I^2t value is kept constant, then the final temperature of the homogeneous conductor does not change. This I^2t criterion is therefore used in several test standards.

1.3 Test samples

Plug-in connectors with contact elements are an excellent test object for short circuit tests, because the electrical and mechanical properties of the contact elements and thus the electrical and mechanical contact behavior can be precisely measured before and after the short circuit. This is not easily possible with compression connections or bolted connectors.

A model contact system consisting of two conductors of Cu-ETP and a contact element "MULTILAM LA-CU" is investigated. Both the conductor and the contact element are silver plated.

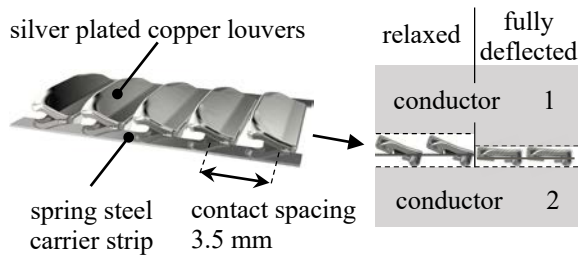


Fig. 1 Cross section of the investigated contact system with MULTILAM LA-CU.

A single louver of this contact element has a joint resistance of less than $300 \mu\Omega$, a rated continuous current of up to 60 A, a contact force of approximately 7 N and a rated $I_{scR} = 800$ A for $t_{scR} = 1$ s.

The contact elements are tested mounted within a flat arrangement, as well as mounted within a round plug-in connector with a nominal diameter of 40.7 mm. (Fig. 2).

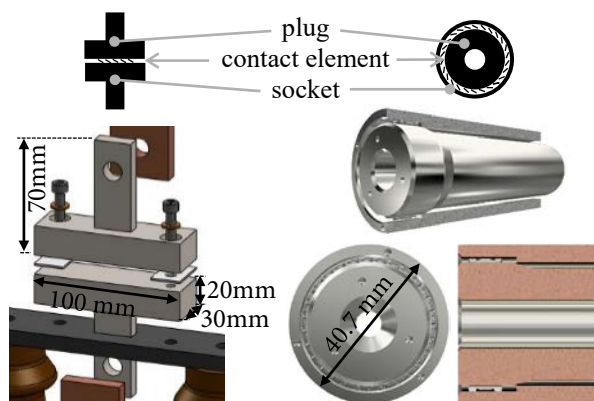


Fig. 2: Flat (left) and round (right) model connector.

1.4 Experimental setup

Three different test stands were used. In all test stands, the following data was measured:

- temperature with infrared camera OPTRIS PI 640
- connection resistance before and after the short circuit with a microohmmeter WIE LoRE / TI
- contact force with material test machine (Zwick)

The first test stand is a low voltage (LV) AC test stand for testing moderate short circuits up to 8 kA. The short circuit current can be adjusted continuously with an adjustable transformer (Fig. 3).



Fig. 3 LV short circuit test stand with continuous current regulation.

The second test stand uses a medium voltage (MV) high current transformer to test connections with short circuit currents up to 90 kA peak and 35 kA RMS for a maximum of 1 s (Fig. 4).

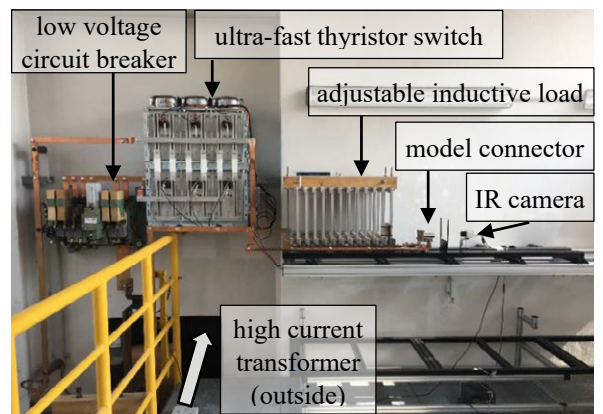


Fig. 4 MV short circuit test stand for testing electrical equipment.

The third test stand is a DC test stand designed and operated by Stäubli Electrical Connectors AG (Fig. 5). A 15 kA DC Generator stresses the contact element. The contact force and electrical resistance of the contact element are measured continuously with a force test machine and a digital multimeter (DMM). The temperature of the contact element is measured with an infrared camera.

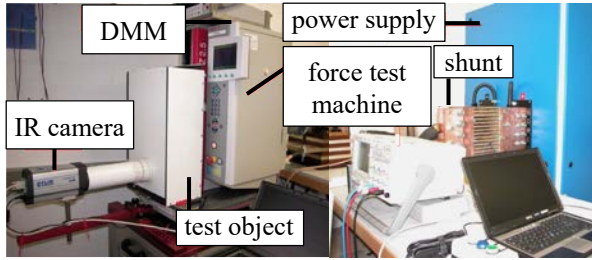


Fig. 5: LV DC short circuit test stand.

2 Calculation of the temperature rise

The calculation of the temperature rise is explained in detail in [5].

Holm applied the Kohlrusch relation [6] to contact problems by using the model of two semi-spheres with the electrical resistance ρ , which are connected by a contact point with the radius a . Between the outer shells of the two semi-spheres, the contact voltage drop U_c exists due to current flow. Assuming the Wiedemann-Franz law is valid and T_1 and T_2 are the absolute temperatures at the opposite sides of the contact interface, the temperature of the contact point can be calculated analytically [7], where L is the Lorenz number:

$$T_{\max} = \sqrt{\frac{U_c^2}{4L} + \frac{1}{2}(T_1^2 + T_2^2) + \frac{L}{4U_c^2}(T_1^2 - T_2^2)^2} \quad (3)$$

If the boundaries of both semi-spheres are heated up to the same temperature ($T_1 = T_2$), eq. (3) simplifies to the well-known correlation:

$$T_{\max} = \sqrt{\frac{U_c^2}{4L} + T_1^2} \quad (4)$$

Eq. (3) is used to implement the contact behavior into a numeric transient electric-thermal model. This was built in ANSYS Workbench rev. 17 and is enhanced with the User Programmable Feature type *usercnp* written in FORTRAN. This feature describes the contact behavior and considers joule heating, the overtemperature inside the a-spots, the electromagnetic forces and the softening behavior of the silver coating.

An exemplary temperature rise during the rated 1 s short circuit of the MULTILAM LA-CU is shown in Fig. 6. It can be seen that the standard behaviour of the FE-program calculates temperatures which are much higher than the measured temperatures because the increase of a-spot size due to softening of the coating is not implemented.

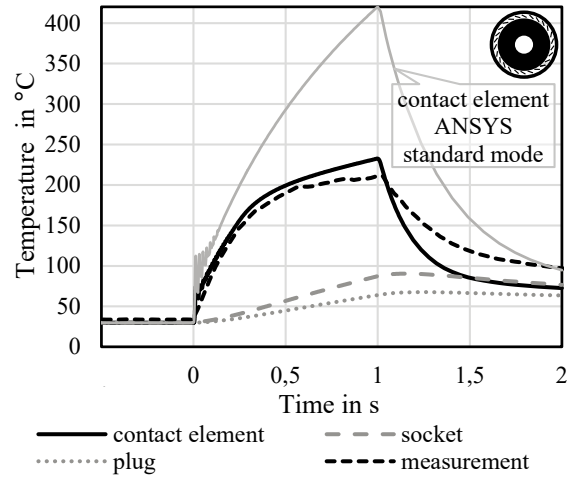


Fig. 6 Temperature of the contact element, plug and socket during a 1 s short circuit (starting at $t = 0$ s).

3 Influences on the short circuit behavior in testing and real world application

The fault current which stresses the connector has different waveforms depending on the type of equipment and grid type in which it is used (Table 2). In chapter 3.1 and 3.2 the influence of exemplary waveforms on the heating and the damage of the connector is discussed.

	waveform	chapter
AC grid – single halve wave current		3.1
AC grid–short circuit far from generator	low peak current	3.2
	high peak current	
DC grid		

Table 2: Fault types and short circuit waveforms

Additionally, in chapter 3.3 it is shown how pre-heating a connector to its operating temperature before the short circuit influences the heating and mechanical damage. After that, in chapter 3.3 it is discussed to which extent a variation of the test duration does change the thermal load for the connector.

3.1 Influence of the peak current

Tests with single 50 Hz half-waves showed that the higher the tested peak withstand current i_p is, the lower

the contact resistance R_c will be after the short circuit in comparison to the value before the short circuit R_{c0} (Fig. 7). If the peak current is high enough, the contact spots may partially melt and may adhere to the plug and socket (Fig. 8). If, after the separation, the coating is damaged and teared of the contacts, this is considered to be a failure (Fig. 9).

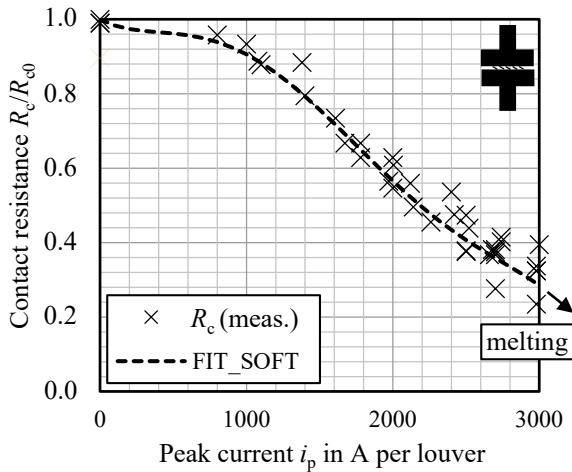


Fig. 7 Measured contact point resistance before (R_{c0}) and after short circuit (R_c) depending on peak current (at 20 °C), $t_{sc} = (10...12)$ ms [8].

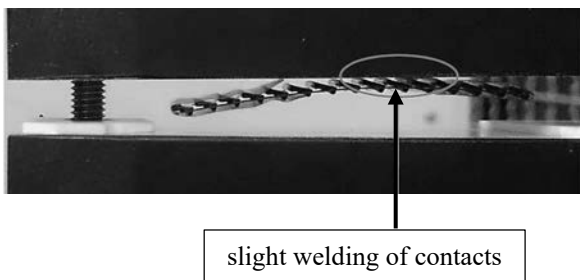


Fig. 8 Example of a slightly welded contact which adheres to the upper conductor. In this investigation, the contact element can easily be separated manually.

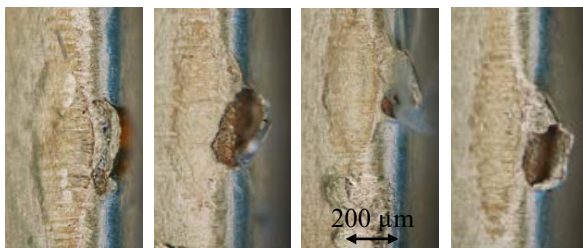


Fig. 9 Example of the contact points after a peak current > 3 kA per louver and after separation of the sample from plug and socket.

3.2 Comparison between AC and DC tests

If the a-spots did not soften during the initial peak (for low peak currents, e.g. peak factor $\kappa = 1$ or DC), the power losses inside the contact points are higher than for $\kappa = 1.8$ until the softening temperature is reached in

the contact points. This leads to a measurable increase in the maximum temperature at the end of the short circuit (Fig. 10). In the test with alternating current and $\kappa = 1.8$, the peak current was applied with a separate peak current test before the 3 s short circuit.

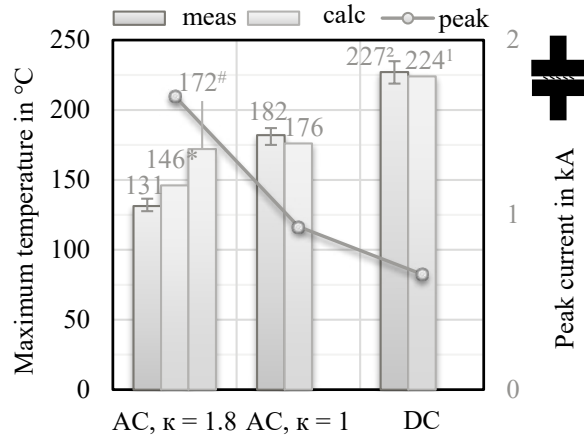


Fig. 10 Maximum temperature and peak current for the MULTILAM LA-CU for 3 s short circuit with $I_{sc} = 660$ A [8]. ^{1,2}lubricated samples with higher contact resistance which is considered in the calculation: *calculation was done with the contact resistance which was measured directly before the 3 s short circuit, corresponding to the separated peak current test #calculation was done with a combined peak- and short circuit current

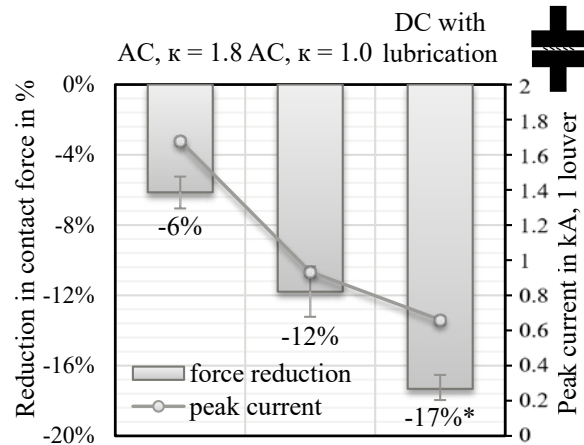


Fig. 11 Reduction of joint force is greater for low peak currents for 3 s short circuit with $I_{sc} = 660$ A. Mean value and span width are plotted [8].

These findings apply for tests with newly installed contact elements. If the contact system was pre-stressed to elevated temperatures, the contact resistance may drop to relatively low values and the difference when testing with low or high peak currents can be less significant.

3.3 Pre-heating

In the recommended standards, the connectors are stressed while staying at room temperature. In real world application, a fault may occur when the

connector is under a heavy load situation. To reproduce this, tests were carried out in which the connector was pre-heated with a heating sleeve to (100...110) °C.

Due to the pre-heating, the resistance of the whole connector drops by approximately 31 % compared at room temperatures (Fig. 12). Even if the increased resistance at higher temperature is not corrected, the overall resistance of the connector is still 8 % lower than the resistance at room temperature before heating. This is due to the reduced hardness of the silver coating at elevated temperatures and thus the a-spots increase significantly.

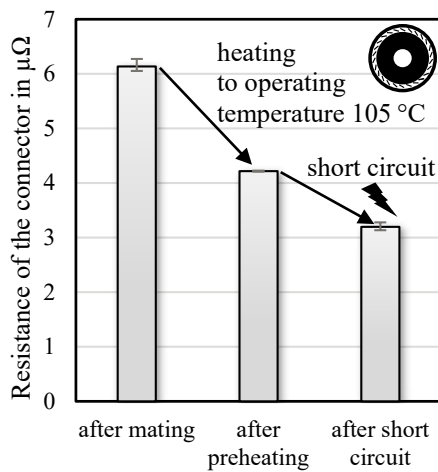


Fig. 12 Resistance of the connector at 20 °C after mating, heating to operating temperature and after short circuit.

Due to the higher starting temperature, pre-heating leads to higher maximum temperatures and slightly higher mechanical damage (Fig. 13). But, the influence of pre-heating on the mechanical damage is much lower than the influence of the peak current or the variation of the short circuit duration according to $I^2t = \text{constant}$.

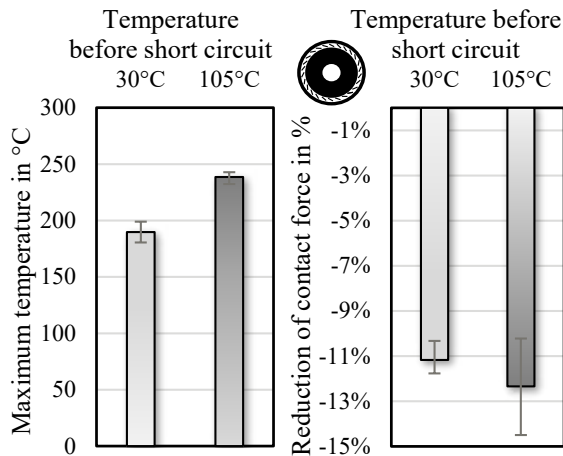


Fig. 13 Comparison of short circuit behaviour with pre-heated (100...110) °C connector and at room temperature after a 1 s short circuit with $I_{sc} = 800$ A .

3.4 Variation of the test duration

The recommended standards allow a variation of the test duration according to $I^2t = \text{constant}$. In [9], short circuit tests have been done on round connectors. In these tests, the temperature rise during the short circuit could not be observed, so additional short circuit tests were done with a specially built round connector which allowed the direct measurement of the temperature of the contact elements (Fig. 2, [5]).

With a contact system, the assumptions for eq. (1) are not generally fulfilled, since the conductor cross-section is not uniform, but reduced in the contact area. Also, the contact resistances are not considered in the formula. As a result, the constrictions heat up more than the connecting conductors. There is a heat flow from the contact area into the connecting conductors (Fig. 14). Also, a typical short circuit is longer than the thermal time constant of the a-spots, which is in the order of μs , and also often longer than the thermal time constant of the contact elements, which are in the range (0.1...1) s.

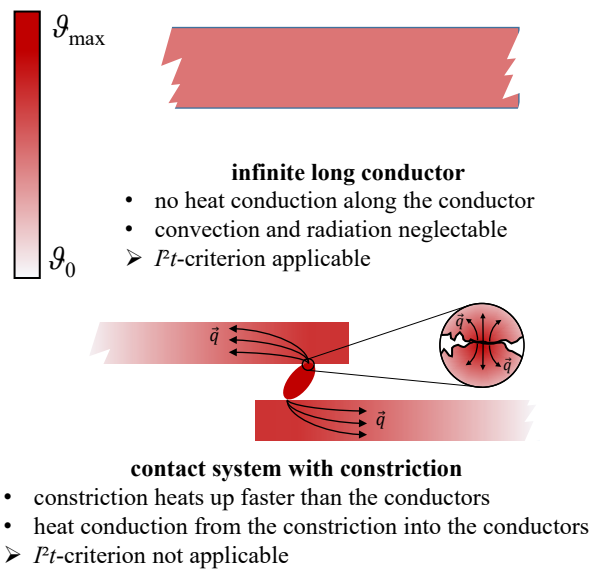


Fig. 14 Heat flow in a contact system (cf. [9]).

In [9], [10] it was shown by calculation and measurement on high-current connector that a test current set on the basis of the I^2t criterion leads to a changed thermal load on the system. If the short-circuit duration is extended from $t_{sc,r} = 1$ s to $t_{sc,test} = 2$ s and the short-circuit current is reduced by the factor $\sqrt{2}$, so that I^2t remains constant, this leads to a significantly lower maximum temperature of 110 °C at $t_{sc,test} = 2$ s compared to 200 °C at $t_{sc,r} = 1$ s and thus to less mechanical damage. The dependence of the transmissible I^2t on the short circuit duration was also determined by other authors [11], [12].

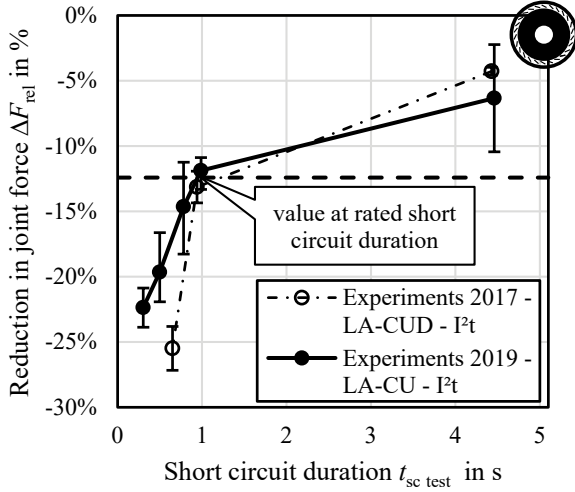


Fig. 15 Reduction of contact force depending on short circuit duration for two different contact elements using the I^2t criterion, with data from [9].

LA-CUD shows a more significant impact on the duration of the short circuit which is due to the different structural design in comparison with LA-CU.

4 Recommendations for testing and dimensioning of electrical connectors

Obviously, the I^2t criterion for setting a test current or for calculating permissible short circuit currents beyond the rated value is only conditionally suitable. If the I^2t -criterion is used, then in order to qualify a connector for a rating of $I_{sc r}$, $t_{sc r}$ and $i_{p r}$, the test current ($I_{sc test}$, $t_{sc test}$ and $i_{p test}$) has to fulfill conditions 1 and 2 in **Table 3**. Generally, connectors should not be tested with longer short circuit durations and lower currents than rated because the thermal stress will be lower.

condition 1	condition 2
$I_{sc test} \geq I_{sc r}$ if $t_{sc test} \geq t_{sc r}$ or $I_{sc test} \geq I_{sc r} \sqrt{\frac{t_{sc r}}{t_{sc test}}}$ if $t_{sc test} \leq t_{sc r}$	$i_{p test} \geq i_{p r}$

Table 3: Conditions for testing power connectors.

Instead, the $I^x t$ -criterion can be used, which allows to adjust the test duration and current with a comparable thermal stress for the connector. This requires a deeper investigation of the thermal behavior of the connector, which is shown in chapter 4.1 - 4.3.

4.1 Calculating the permissible test current

It must be clarified whether there is a more suitable criterion for setting the short circuit current for different test durations. For this, it is assumed that the

current should not to be adjusted with the exponent 2, but with an exponent x which has to be calculated.

$$I^x t = const. \quad (5)$$

$$I_{sc1}^x t_{sc1} = I_{sc2}^x t_{sc2} \quad (6)$$

In order to be able to calculate the exponent x , two short circuit parameters I_{sc1} and t_{sc1} as well as I_{sc2} and t_{sc2} for which the thermal stress in the contact system are comparable are needed. Subsequently, the exponent can be calculated directly.

$$x = \frac{1}{\log_{\frac{t_{sc2}}{t_{sc1}}} \frac{I_{sc1}}{I_{sc2}}} = \frac{\ln \frac{t_{sc2}}{t_{sc1}}}{\ln \frac{I_{sc1}}{I_{sc2}}} \quad (7)$$

In order to calculate the short circuit current $I_{sc test}$ for the contact system for a time period $t_{sc test}$, the following equation can be used.

$$I_{sc test} = I_{sc r} \left(\frac{t_{sc r}}{t_{sc test}} \right)^{\frac{1}{x}} = I_{sc r} \sqrt[x]{\frac{t_{sc r}}{t_{sc test}}} \quad (8)$$

Taking into account the rated short-circuit currents for $t_{sc r} = 1$ s and $t_{sc r} = 3$ s of the investigated contact element, the exponent $x \approx 6$ was determined. The test currents calculated according to the $I^x t$ -criterion (eq. (8)) and the $I^2 t$ -criterion are shown in **Fig. 16**.

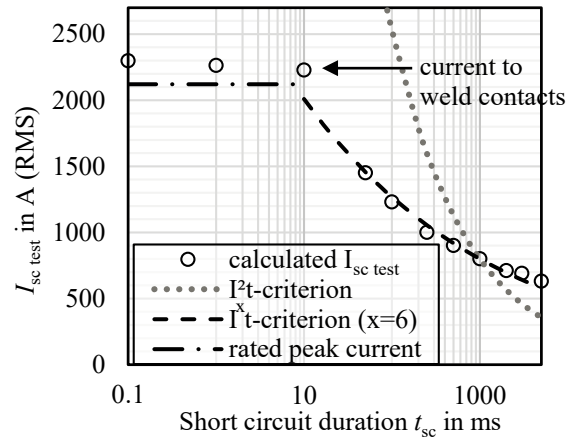


Fig. 16 Calculated permissible short circuit current depending on test duration and value according to $I^2 t = constant$.

Also, the short circuit currents $I_{sc test}$ which heat the contact element to approximately the same temperature for a given test duration $t_{sc test}$ than at the rated test duration have been calculated [13] and are shown in **Fig. 16**. The curve which was calculated using the $I^x t$ criterion shows a good agreement with the values calculated in the FE model. The deviation of both methods is negligible in the investigated contact systems. The values of the 1 s and 3 s short circuits can also be used for very good extrapolation up to short

circuit durations of 0.05 s. As shown in Fig. 16, there is a maximum current which the connector is able to withstand before the contacts weld. This peak withstand current limit does not increase much for short circuits shorter than 10 ms. However, if the pulse width is reduced below 100 μ s, the thermal capacity of the a-spots may be utilized [14, Ch. 4.4; 5.3.5]. Instead of using a FE-model, the welding current limit can be estimated using analytical models [8], [14, Ch. 5.3.2].

4.2 Verification

Short circuit tests were done with the calculated test current $I_{sc\ test}$ to verify the results. In Fig. 17, the measured temperatures are shown. They are comparable to the temperature measured at the rated test duration which are in the range (200...240) $^{\circ}$ C [15].

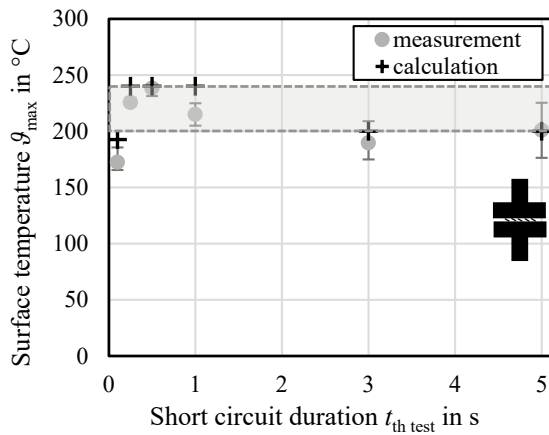


Fig. 17 Maximum temperature during the short circuit depending on short circuit duration using the I^2t -criterion [10].

In Fig. 18 the force reduction due to the short circuit for experiments done using the I^2t - and I^2t -criterion is shown. The experiments with I^2t -criterion have a comparable force reduction in the range (0.5...3) s. Below $t_{sc\ test}$ 0,5 s, mostly the contact points are heated which does not result in a force reduction.

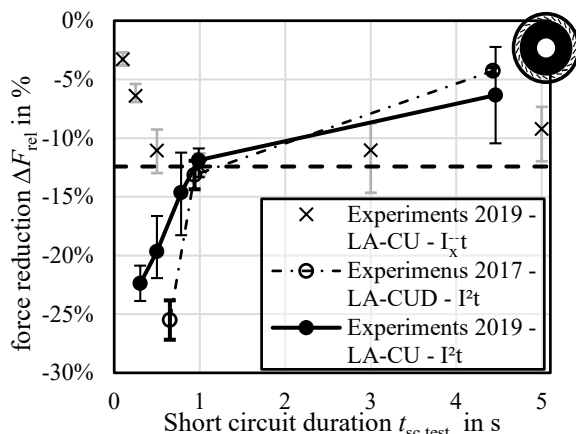


Fig. 18 Force reduction depending on short circuit duration using the I^2t and I^2t criterion [9], [10].

The I^2t -criterion allows interpolation between the specified values and in the range (0.1...5) s also extrapolation for very short or very long short-circuits.

4.3 Other contact systems

The calculation of the permissible short-circuit currents can be omitted for known contact systems if the manufacturer has already determined the permissible short circuit currents experimentally. In the literature there are a few specifications for permissible short-circuit currents of connectors [11], circuit-breaker contacts [16] and other contact elements [17] depending on the short-circuit duration. For these systems, the parameter x was calculated using eq. (7).

system	x	comment
MULTILAM ML-CUX	4.4	contact element [17]
MULTILAM LA-CUD	6.0	contact element [17]
MULTILAM LA-CUT	4.4	contact element [17]
Ag contact points	9.8	$F_K = 300$ N, peak current [16]
Cu contact points	8.7	$F_K = 300$ N, peak current [16]
high current connector ¹	2.3	slotted socket connector, calculated values [11]

¹ Harting HAN HC. Rated continuous current $I_r = 600$ A. Equation (3) and softening were neglected.

Table 4: Application of the I^2t criterion to other contact systems.

The exponent x is a measure for the metallic cross-section in the contact area in relation to the connecting conductors as well as for the thermal time constant of the system. The larger the parameter x is, the smaller is the thermal time constant of the system and the more "sensitive" the system reacts to short, high loads.

5 Summary

Performing reproducible tests of the short circuit behavior of electrical connectors may be a challenging task. Generally, the test duration and waveform should fit to the real world or rated values as close as possible.

For example, the I^2t -criterion may only be used with caution for altering the test duration. Its boundary conditions are not generally fulfilled for electrical connections. So, with a change in the tested duration of the short circuit the thermal stress for the system will also change. This is especially critical for very short test durations since the joule heat cannot dissipate during short impulses, which may lead to a failure of the system. Instead, the I^2t criterion is proposed for altering the short circuit duration. This is able to change

the short circuit duration in a relatively wide range while keeping the thermal stress for the contact system almost constant. When using connectors with contact elements, the I^2t -criterion can easily be used since the manufacturer typically provides the needed data to calculate it. For other connector types, the I^2t -criterion needs to be evaluated by calculation or measurement. In future standards for connectors, the I^2t -criterion may only be used for a change of short circuit duration by +/- 10 %. If the tester needs to change the test duration even more, the I^2t -criterion may be used. Otherwise, the thermal load for the system is practically unknown and the type test does not really show if the connectors is sufficient for the rated short circuit current and duration.

Also, tests with different waveforms of the current were done. AC tests with high peak currents lead to a reduction in the thermal stress compared to DC tests because the contact resistances are greatly reduced during the peak current in the first half-wave of current flow. Pre-heating the connector before the test also reduces the contact resistance significantly. But, the higher starting temperatures nullify this effect to a certain degree and the maximum temperatures are higher than when testing at room temperature. However, the mechanical damage is about comparable to tests at room temperature. The tests in this paper were done on arrangements typical for low- and high voltage switchgear. But, the findings also apply to high current connectors which are used for electrical transportation. These also have to withstand fault currents, for example connectors for charging and in the wire assembly of electric vehicles. In future standards for testing equipment which contains connectors, such as low- and high voltage switchgear or connectors for electrical transportation, these findings should be implemented.

6 Literature

- [1] DIN EN 61439-1 VDE 0660-600-1:2012-06, "Niederspannungs-Schaltgerätekombinationen – Teil 1: Allgemeine Festlegungen." VDE Verlag.
- [2] DIN EN 62271-1 VDE 0671-1:2018-05, "Hochspannungs-Schaltgeräte und -Schaltanlagen – Teil 1: Gemeinsame Bestimmungen." VDE Verlag.
- [3] DIN EN 61238-1:2004-03, "Pressverbinder und Schraubverbinder für Starkstromkabel für Nennspannungen bis einschließlich 36 kV (Um = 42 kV)." VDE Verlag.
- [4] H. Böhme, *Mittelspannungstechnik: Schaltanlagen berechnen und entwerfen*, 2nd ed. Berlin: Huss-Medien, 2005.
- [5] T. Israel, S. Schlegel, S. Großmann, T. Kufner, and G. Freudiger, "Modelling of Transient Heating and Softening Behaviour of Contact Points during Current Pulses and Short Circuits," presented at the 65th IEEE Holm Conference on Electrical Contacts, Milwaukee, USA, 2019.
- [6] F. Kohlrausch, "Ueber den stationären Temperaturzustand eines elektrisch geheizten Leiters," *Annalen der Physik*, vol. 306, no. 1, pp. 132–158, 1900, doi: 10.1002/andp.19003060107.
- [7] R. Holm, *Electric Contacts: Theory and Application*, 4th ed. Berlin Heidelberg: Springer-Verlag, 1967.
- [8] T. Israel, S. Schlegel, S. Großmann, T. Kufner, and G. Freudiger, "The Influence of Peak Current and ECR on the Transmission Performance of High Power Connectors during Faults," presented at the International Conference on Electrical Contacts, Albuquerque, 2018.
- [9] M. Gatzsche, T. Israel, N. Lücke, S. Großmann, T. Kufner, and G. Freudiger, "Grenzen der Gültigkeit des I^2t Kriteriums beim Prüfen der Kurzschlussfestigkeit von Kontaktsystemen," in *Elektrische und optische Verbindungstechnik 2017*, Lemgo, Mar. 2017, pp. 185–196.
- [10] T. Israel, S. Schlegel, S. Großmann, T. Kufner, and G. Freudiger, "Zum elektrisch-thermisch-mechanischen Verhalten von silberbeschichteten Hochstrom-Steckverbindern – Das I^2t -Kriterium bei der Kurzschlussprüfung von Steckverbindern Teil II," presented at the Symposium Connectors 2019, Lemgo, 2019.
- [11] G. Staperfeld and A. Brenner, "PULSE CURRENT BEHAVIOUR OF HIGH CURRENT CONNECTORS," Nürnberg, 1998, p. 5.
- [12] B. T. McCuistian, H. Davis, and K. Nielsen, "Pulsed current threshold of Multilam," in *Digest of Technical Papers. 12th IEEE International Pulsed Power Conference. (Cat. No.99CH36358)*, Jun. 1999, vol. 2, pp. 677–679 vol.2, doi: 10.1109/PPC.1999.823603.
- [13] T. Israel, S. Schlegel, S. Großmann, T. Kufner, and G. Freudiger, "Zum elektrisch-thermisch-mechanischen Verhalten von silberbeschichteten Hochstrom-Steckverbindern – Das I^2t -Kriterium bei der Kurzschlussprüfung von Steckverbindern Teil II," presented at the Symposium Connectors 2019, Lemgo, 2019.
- [14] T. Israel, "Verhalten von Hochstrom-Steckverbindungen mit Kontaktelementen bei kurzer Strombelastung," Dissertation, Technische Universität Dresden, Dresden, 2020.
- [15] T. Israel, M. Gatzsche, S. Schlegel, S. Großmann, T. Kufner, and G. Freudiger, "The Impact of Short Circuits on Contact Elements in High Power Applications," in *63rd IEEE Holm Conference on Electrical Contacts*, Denver, CO, USA, Sep. 2017, pp. 40–49, doi: 10.1109/HOLM.2017.8088061.
- [16] Hilgarth, Günther, "Über die Grenzstromstärken ruhender Starkstromkontakte," *ETZ*, vol. 78, no. Ausgabe A, pp. 211–217, 1957.
- [17] Stäubli Electrical Connectors AG, "MULTILAM Technical Overview. MULTILAM Technology." 2019.

Calculations and metallographic investigations on the growth of Al₂O₃-layers in bimetallic contacts

Marcella Oberst, Technische Universität Dresden, Dresden, Germany, marcella.oberst@tu-dresden.de
Stephan Schlegel, Technische Universität Dresden, Dresden, Germany, stephan.schlegel@tu-dresden.de
Steffen Großmann, Technische Universität Dresden, Dresden, Germany, steffen.grossmann@tu-dresden.de

Abstract

In electrical power engineering and in electromobility, bimetallic joints can occur when e.g. the coated terminals of the lithium-ion battery are connected to the bare aluminum used as conductor inside the vehicle. The resistance of such detachable, current-carrying connections consisting of a bare aluminum contact member and one of bare copper or a coated contact member with a cover layer of tin or silver increases significantly over time. Previous research showed that the failure is due to the formation of Al₂O₃ in the contact interface. In this paper, the film growth is investigated more closely by supplementing the resistance measurements with metallographic investigations. Different mathematical models are developed that describe the film growth and aim to predict a connection's resistance behavior over time. The growth is considered in lateral direction, decreasing the area of metallic contact, as well as in axial direction causing quasimetallic areas to rise in resistance and eventually become insulating. The entirety of the apparent contact area is considered in a macroscopic model as well as single a-spots in a microscopic model. The results yielded by the models were compared to the measured values of the long-term behavior of connections of different material combinations.

1 Introduction

In order to achieve the highest possible range and acceleration, electric vehicles are optimized regarding their weight. For the electrical conductors, this results in the application of aluminum wherever it is possible. Compared to copper, aluminum has a higher current-carrying capacity at the same weight, even though the necessary diameter is bigger. The current-carrying components that need to be connected with one another inside the vehicle may therefore consist of bare aluminum, but also other materials such as bare copper, silver-, tin-, or nickel-coatings may be found. At the high temperatures allowed for these connections of up to 180 °C according to LV 2015-1: 2013-2, the bimetallic contacts often deteriorate quickly [1], [2]. This results in dangerously high temperatures at the contacts and ultimately in their failure.

The findings from experiments on the long-term behavior of connections between silver and aluminum as well as copper and aluminum are evaluated using already existing theories on the formation of oxygen layers. A new model is developed that should improve the understanding of the processes in the different material combinations and enable the prediction of the long-term behavior of the connections.

2 Previous Research

In the past, different aging mechanisms such as fretting and the formation of intermetallic compounds were

assumed to be responsible for the witnessed rise in resistance of Al-Cu- and Ag-Al-connections [1], [3], [4]. Pfeifer characterized the intermetallic phases that occur in these two systems at temperatures < 200 °C regarding their specific electrical resistances. Together with long-term experiments on current-carrying connections with constant and cycling load and metallographic investigations, she proved that intermetallic compounds and mechanical stress alone cannot cause the fast deterioration observed in connections of these material combinations. Instead, she suspected oxygen and the formation of aluminum oxide Al₂O₃ to have a major impact on the connections' long-term behavior. [5] This thesis was proven by conducting experiments on bolted joints with busbars in ambient air and repeating them in a N₂-atmosphere (Fig. 1). The resistance of the joints did not increase in the N₂-atmosphere. Aging mechanisms such as the formation of intermetallic compounds, force reduction and fretting do not seem to have a major impact on the long-term behavior of the bimetallic connections in the absence of oxygen. [6], [7], [8]

In order to enable calculations on the oxidation of Al-Cu- and Ag-Al-connections in ambient air, a special test setup was developed. It consisted of two cylinders of which one was flat and the other conically reduced with a diameter of 500 μm (Fig. 2). They were pressed together by two spring pins with a force of 12.5 N, eliminating force reduction as a possible aging

mechanism. The pressure in the contact interface was approximately 64 N/mm^2 . [6], [7], [8]

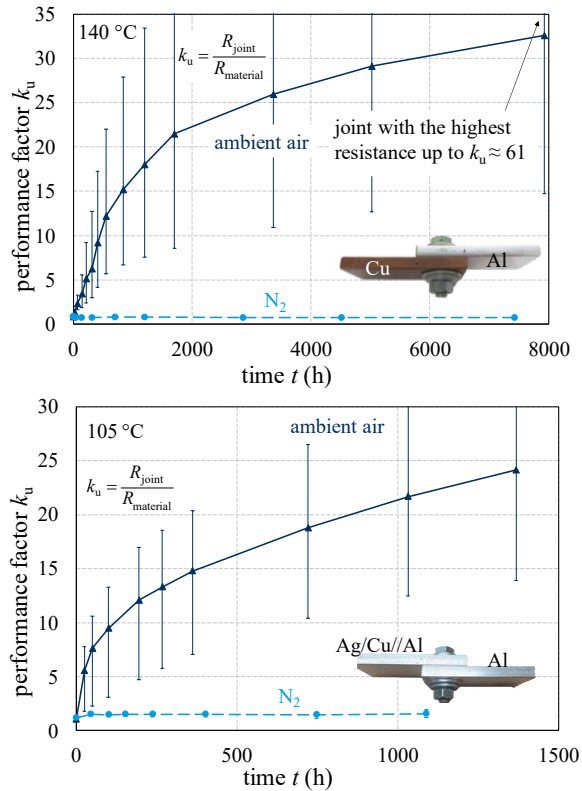


Fig. 1: Long-term tests on bolted joints with busbars in ambient air and in a N_2 -atmosphere: a) Al-Cu joints [6], b) Ag-Al joints [7]

The gilded spring pins at the end of the cylinders were also used for injecting the current for the resistance measurements. Two further spring pins were installed 10 mm from the interface to measure the voltage drop. The measured resistance therefore included not only the contact resistance, but also the material resistance R_M of the cylindrical conductors on the length of 20 mm. In order to be able to evaluate only the contact resistance, the material resistance was calculated using the finite element method in ANSYS. For each test series, five connections were investigated. The setup was stationary in a heating cabinet throughout the experiments in order to prevent fretting motions. [6], [7], [8]

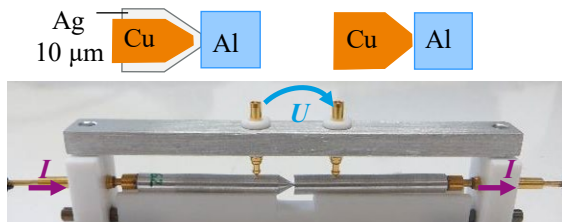


Fig. 2: Test setup for the experiments on bimetallic connections [6], [7]

The measurements were performed with a micro-ohmmeter Type “LoRe” by Werner Industrial Electronic with a reduced measurement current of approx. 1 A and a constant source voltage of 4.1 V. The

resulting voltage drop across the connection was $< 10 \text{ mV}$ for the Ag-Al-connections and $< 2 \text{ mV}$ for the Al-Cu-connections. Applying the Kohlrausch-relation [9] to this setup shows that the measurement current causes an additional rise in temperature of $< 0.1 \text{ K}$ for Al-Cu- and $< 2 \text{ K}$ for Ag-Al-connections. This is negligible compared to the temperature of (90; 115) °C the connections were stored at in the heating cabinet.

While other aging mechanisms were eliminated, the formation of intermetallic compounds between the two contact members cannot be prevented. However, its influence can be calculated according to [8] and deducted from the measured resistances. For the Al-Cu-connections after 4,000 h at 90 °C the rise in resistance caused by intermetallic compounds would be less than $0.1 \mu\Omega$ and for the Ag-Al-connections after 4,000 h at 115 °C it would be $1.7 \mu\Omega$. Compared to the measured resistances these increases are not significant (Fig. 3). [6], [7]

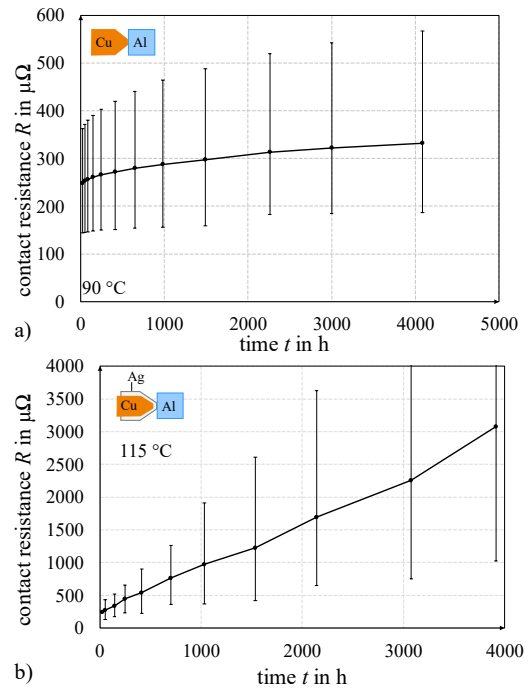


Fig. 3: Long-term tests on the test setup with two cylinders in a heating cabinet: a) Al-Cu-connections [6], b) Ag-Al-connections [7]

3 Existing Models

Based on *Takano* and *Mano*'s theoretical approach to calculate the lifetime of static Cu-contacts [10], different approaches to model the long-term behavior of current-carrying connections have been developed. Two models will be presented in the following section, one for the formation of an oxide layer in the contact interface and one for the calculation of the contact resistance over time caused by a diffusion-based aging mechanism. The results they yield are compared to the resistances measured in experiments on Ag-Al- and Al-Cu-connections.

3.1 Diffusion of oxygen

Izmailov used the differential equation of diffusion into a cylindrical region to describe the entrance of oxygen into an a-spot. It yields the oxygen concentration C along the radius of the a-spot as a function of the parameter Dt/r^2 with D being the temperature-dependent diffusion coefficient, t the time and r the distance from the center of the a-spot with radius a (Fig. 4). Outside of the a-spot, the oxygen concentration is C_0 . [11]

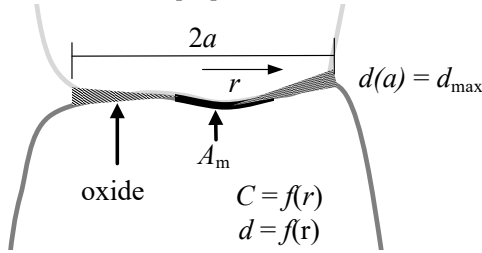


Fig. 4: a-spot with a location-dependent thickness of the oxide layer

For $0.01 < Dt/r^2 < 1$ the equation can be approximated:

$$C = C_0 \left[1 - \frac{2}{\exp\left(\frac{4Dt}{a^2(1-r/a)}\right) + 1} \right] \quad (1)$$

Assuming that the oxide layer has grown to its maximum thickness at $r = a$, its thickness along the radius can be calculated using the following equation:

$$d = d_{\max} \left[1 - \frac{2}{\exp\left(\frac{4Dt}{a^2(1-r/a)}\right) + 1} \right] \quad (2)$$

For Al_2O_3 on technically pure aluminum at temperatures up to 200°C in normal laboratory humidity conditions, the maximum oxide layer thickness is $d_{\max} \approx 25 \text{ \AA}$ [12]. In order to apply eq. (2) to calculate the oxide layer thickness, the diffusion coefficient of oxygen as well as the a-spot radius need to be known. The volume diffusion coefficient for oxygen through silver has been determined for temperatures $> 400^\circ\text{C}$ and a model to calculate the diffusion also at other temperatures was deduced by Baird [14]. For the maximum allowed temperature of connections with a silver-coated contact member according to DIN EN 62271-1: 2018-05, the diffusion coefficient would be $D_V(115^\circ\text{C}) = 1.6 \cdot 10^{-10} \text{ cm}^2/\text{s}$. The continuous distribution for an a-spot with an exemplary radius of $a = 5 \text{ \mu m}$ depicted in Fig. 5 is only a mathematical model. As layers with a thickness of less than the diameter of one atom are not possible, it cannot be an accurate description of the actual layer growing in the interface. At normal pressure and a temperature of 25°C , Al_2O_3 has a lattice constant of 4.7 \AA [13]. With the calculated diffusion coefficient

only the outer 0.05 \mu m of the diameter would reach a layer thickness $> 4.7 \text{ \AA}$ after one year at 115°C .

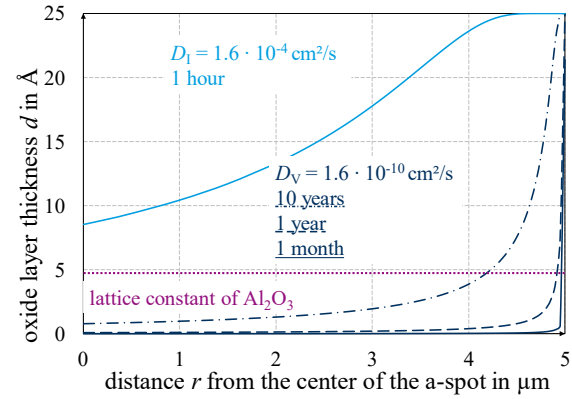


Fig. 5: Oxide layer thickness along the radius of an a-spot with $a = 5 \text{ \mu m}$ at different times and with two different diffusion coefficients

The experiments that have led to that coefficient were performed at temperatures $> 400^\circ\text{C}$, considering volume diffusion as dominant diffusion mechanism. At lower temperatures, grain boundary diffusion becomes relevant as well. On top of that, the diffusion along the phase boundary is expected to be even faster at the relatively low temperature of 115°C . For this interface diffusion, the diffusion coefficient is supposed to be $10^5 \dots 10^7$ times higher [11]. Hence, the calculations were repeated with the original $D_V \cdot 10^6 = D_I$. After one hour, the layer thickness in the center of the a-spot would already be 8.5 \AA (Fig. 5). After ten hours a constant thickness of 25 \AA would be reached over the entire contact area.

For a constant film thickness on the quasimetallic area A_q , the film resistance R_F can be calculated according to Slade [15]:

$$R_F = \frac{d}{A_q} \left(\frac{h}{e} \right)^2 \frac{2}{3\sqrt{2m\phi}} \exp\left(\frac{4\pi d}{h} \sqrt{2m\phi}\right) \quad (3)$$

m and e are the mass and charge of an electron, respectively, and h is Planck's constant. ϕ describes the height of the potential barrier that needs to be tunneled. For a layer of Al_2O_3 between two aluminum contact members a value of $\phi \approx 2 \text{ eV}$ is given in the literature [16]. To calculate the film resistance over time, the medium oxide layer thickness can be evaluated with eq. (2) and inserted into eq. (3).

3.2 Long-term behavior of the contact resistance

In a different approach by Dzejtser, the resistance over time of a connection aging due to the diffusion of oxygen into the contact can be calculated for an equilibrium distribution of the a-spot radii. [17]

$$R = \frac{R_0}{\left(1 - \frac{2D}{\bar{a}^2 d_q / d_{\max}} t\right) \left(1 - \sqrt{\frac{2D}{\bar{a}^2 d_q / d_{\max}} t}\right)} \quad (4)$$

The initial resistance of the connection R_0 and its average a-spot radius \bar{a} are required for the calculation. Beside that, the diffusion coefficient D , the maximum oxide layer thickness d_{\max} , and the maximum layer thickness that can still be tunneled $d_q \approx 10 \text{ \AA}$ [17] must be known. Assuming $\bar{a} = 5 \text{ \mu m}$, the change in resistance over time was calculated with the previously used diffusion coefficient $D_V = 1.6 \cdot 10^{-10} \text{ cm}^2/\text{s}$. After 4,000 h at 115 °C the resistance would have risen only by 7 % (Fig. 6). It is likely that the diffusion coefficient is several orders of magnitude higher due to surface effects. With $D_I = 1.6 \cdot 10^{-4} \text{ cm}^2/\text{s}$, the resistance would reach 106 R_0 within 1 h. Additionally, an intermediate D_{V-I} , increasing the volume diffusion coefficient by 10^2 , is depicted. It causes the resistance to reach almost 4 R_0 within 4,000 h.

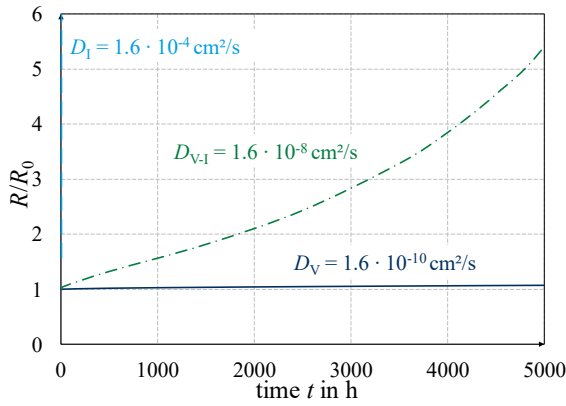


Fig. 6: Dimensionless resistance over time of a connection aging due to the diffusion of oxygen into the contact interface with $\bar{a} = 5 \text{ \mu m}$

4 Model of the oxidation in the contact interface

When the resistance of a connection rises over time due to oxidation, the growth of the oxide can be divided into two directions of growth. Firstly, the oxide grows in areas in which it has already been present previously. This growth in axial direction (Fig. 7a) causes the film resistance R_F to increase. Secondly, the oxide will grow into areas in which it has not been present before (Fig. 7b). This will reduce the metallic contact area A_m and therefore increase the constriction resistance R_C . The oxide growth in both directions (Fig. 7c) can be described using eq. (2) and its influence on the resistance using eq. (4).

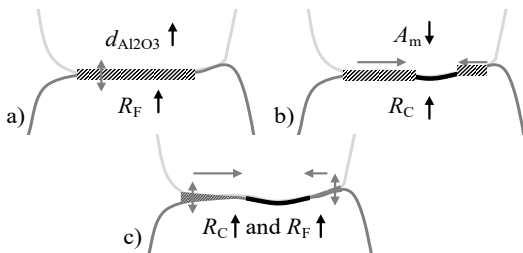


Fig. 7: Growth of the oxide layer in an a-spot in a) axial direction, b) radial direction, c) both directions

However, it is problematic that neither the radius of the a-spots nor the exact diffusion coefficient for the diffusion along the phase border in the contact interface are known. Therefore, the following sections aim to describe the aging with a different approach and compare the results of all three models with the resistances measured in previous experiments [6], [7].

4.1 Ag-Al

A test series in a N_2 -atmosphere was used in order to determine the constriction resistance of the connection. As neither of the contact members was exposed to oxygen before the joining or during the aging, the entire contact resistance was constriction resistance. Since the resistance changed notably when the connections were heated for the first time, the resistance after 24 h was used. After the subtraction of the material resistance, the constriction resistance $R_C = 43.8 \text{ \mu}\Omega$ was obtained.

If the a-spots are far enough apart, the following equation can be used to calculate the constriction resistance of a bimetallic connection between aluminum and silver:

$$R_C = \frac{\rho_{Al} + \rho_{Ag}}{4 \sum_{i=1}^n a_i} \quad (5) [18]$$

In order to estimate the size and number of the a-spots in the connection, the number of a-spots n and their mean radius \bar{a} are determined so that the results fit the assumption that the metallic contact area makes up 3 % of the apparent contact area [19]. The best fit is achieved for $\bar{a} = 7 \text{ \mu m}$ and $n = 39$. The condition for neglecting the interaction term between the a-spots, $s/a \gg 1$, with s being the distance between the a-spots, is fulfilled with this distribution.

In a single a-spot, an oxide-layer of the film thickness of the lattice constant of one Al_2O_3 -molecule would cause the resistance to rise from 1.7 m Ω to 16.7 m Ω according to eq. (3). Therefore, the current flow through the quasimetallic contact area can be neglected compared to the flow through the metallic contact area. With this assumption, the contact resistance over time can be modeled using only the constriction resistance. For calculating the progressing oxidation, two approaches regarding the oxide growth can be pursued: On the one hand, it can be assumed that each of the n a-spots will get smaller over time (Fig. 8a). This would require all of the a-spots to have the same access to the oxygen independent of their position along the radius of the apparent contact area. On the other hand, it can be assumed that the a-spots closer to the edge of the apparent contact area would fail first, as the oxygen does not reach all a-spots equally fast (Fig. 8b). These

two approaches will be examined separately in the following sections.

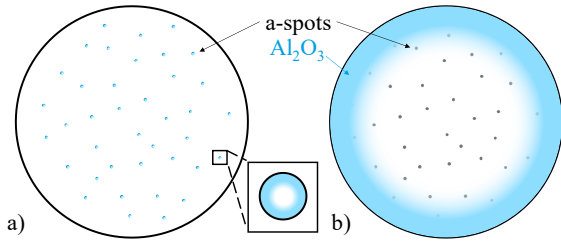


Fig. 8: Point contact with a radially growing oxide layer, a) microscopic growth: reduction of the radius of each a-spot, b) macroscopic growth: failure of entire a-spots from the outside in

4.1.1 Macroscopic approach

The macroscopic approach is based on the assumption that the oxide film grows from the outside in over the entire contact area. The a-spots that are the furthest from the center of the contact fail first. The reduction of the radius of a single a-spot is neglected. The entire a-spot is considered to be either film-free or insulating. This results in n discrete values for the contact resistance depending on the number of a-spots that are still intact (Fig. 9). In the experiments, the resistance of the connections in atmospheric air rose to more than five times the resistance of the connections in the N₂-atmosphere within the first 24 h at 115 °C. In order to match the calculation to the measurements, only two a-spots would remain. The measured curve cannot be described well with the approximations that have been made. While the a-spots failing first barely have any effect on the resistance, the last remaining a-spots cannot describe the resistances measured at $t > 700$ h.

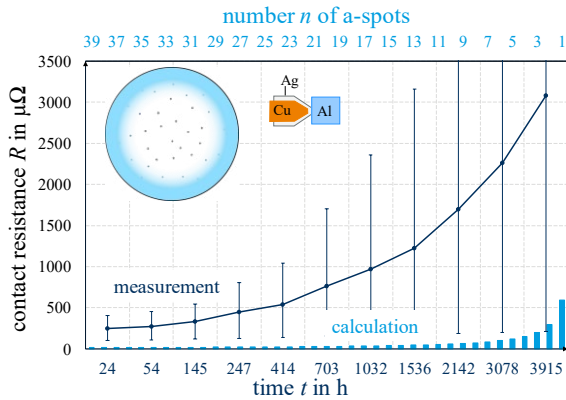


Fig. 9: Measured contact resistance depending on the time and calculated contact resistance depending on the number of a-spots in an Ag-Al-connection

4.1.2 Microscopic approach

The microscopic approach considers the decrease in radius of every single a-spot under the assumption that they all are equally accessible for the oxygen. The increase in resistance within the first 24 h would be caused by a reduction of the a-spot radius to 1.25 μm compared to the 7 μm in the N₂-atmosphere (Fig. 10).

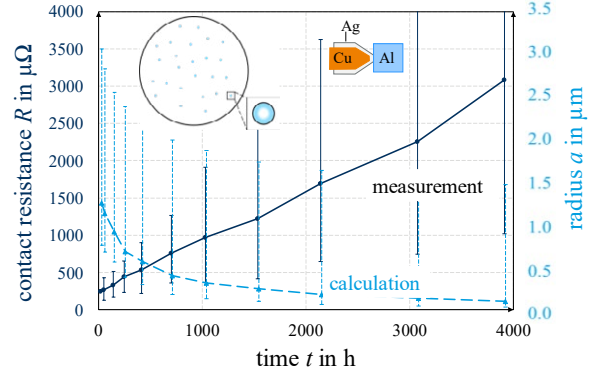


Fig. 10: Measured contact resistance and calculated radius of the a-spots assuming a uniform growth of the oxide layer on all 39 a-spots in an Ag-Al-connection

While the contact resistance over time increases approximately in a linear fashion, the decrease in radius of the a-spots slows down gradually. Instead of the radius of the a-spots, the thickness of the oxide that has grown from the edge of the a-spot inwards in axial direction can be depicted (Fig. 11).

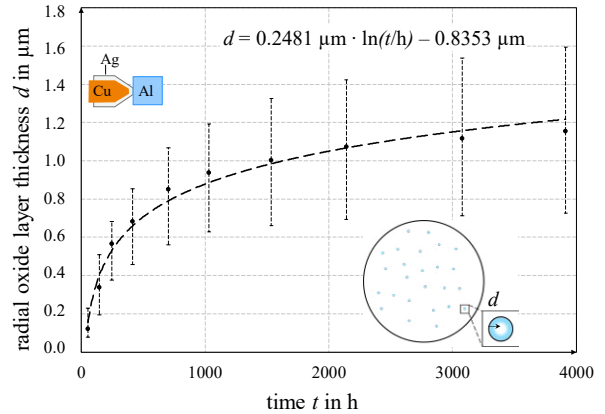


Fig. 11: Radial growth of the oxide layer in an a-spot starting at $t = 24$ h at 115 °C in an Ag-Al-connection (mean value and span)

This reveals an approximately logarithmic growth of the oxide layer. This kind of growth indicates that not a constant diffusion coefficient through the oxide layer is determining the oxidation rate. It depends on the probability of the existence of free paths along which the particles can move. With an increasing layer thickness, the probability for the existence of these paths decreases and the oxidation rate slows down. [20] In order to transfer the results to other connections, the uniform pressure of 64 N/mm² in the apparent area of contact A_s needs to remain the same as in the evaluated experiments. The number of a-spots with $\bar{a} = 7$ μm can be estimated for a different apparent contact area.

$$n = 198.6 \text{ mm}^{-2} \cdot A_s \quad (6)$$

Knowing the contact resistance after 24 h at the operating temperature, the remaining metallic radius of the a-spots can be calculated.

$$a(24 \text{ h}) = \frac{\rho_{\text{Ag}} + \rho_{\text{Al}}}{4nR(24 \text{ h})} \quad (7)$$

With these two values, the contact resistance over time can be calculated. The model is currently limited to a temperature of 115 °C and a uniform pressure in the contact interface. Due to the necessary approximations, it can only be used for estimations of the long-term behavior of Ag-Al-contacts, but should be seen as an approximation equation.

$$R = \frac{\rho_{\text{Ag}} + \rho_{\text{Al}}}{4n [a(24 \text{ h}) - (0.2481 \mu\text{m} \cdot \ln(t / \text{h}) - 0.8353 \mu\text{m})]} \quad (8)$$

4.1.3 Comparison to the existing models

In section 3.1 a model for the diffusion of oxygen according to *Izmailov* was presented. Using the diffusion coefficient $D(115 \text{ °C}) = 1.6 \cdot 10^{-10} \text{ cm}^2/\text{s}$ [14], the mean oxide layer thickness for one a-spot with $a = 7 \mu\text{m}$ was determined via eq. (2). With the film resistance R_F according to eq. (3) the resistance of one a-spot and the entire connection consisting of $n = 39$ a-spots was calculated. The resistance would remain almost constant over 4,000 h at 115 °C with the given diffusion coefficient (**Fig. 12**).

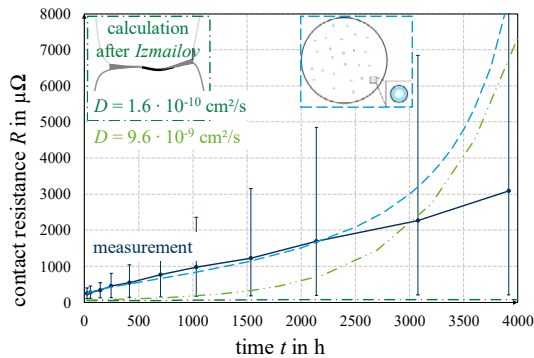


Fig. 12: Comparison between the measurement and the calculations according to the models presented in sections 3.1 and 4.1.2

As the diffusion coefficient is expected to be higher by several orders of magnitude at the phase border between the two materials, it was increased in order to achieve a better correspondence between the measured and the calculated values. The calculation with a diffusion coefficient increased by the factor 60 approaches the measured values better. However, it cannot be seen as a good fit. At $t < 3,000 \text{ h}$ the calculated values are significantly below and at $t > 3,000 \text{ h}$ significantly above the mean value of the measured resistances. In contrast, the model presented in the previous chapter approaches the measured resistances within the first 2,000 h very well. Afterwards, the differences between the model and the measurement increase. For the model according to *Dzejtser*, presented in section 3.2, the resistance over time with $\bar{a} = 7 \mu\text{m}$ and $D(115 \text{ °C}) = 1.6 \cdot 10^{-10} \text{ cm}^2/\text{s}$ was calculated. This would result in a change in

resistance of only $10 \mu\Omega$ over 4,000 h (**Fig. 13**). To achieve a better fit, the diffusion coefficient was increased by the factor 10^3 .

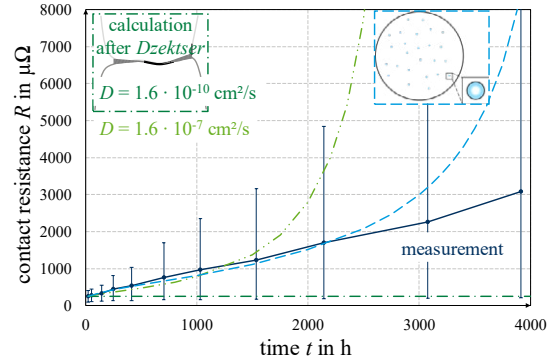


Fig. 13: Comparison between the measurement and the calculations according to the models presented in sections 3.2 and 4.1.2

During the first 1,000 h, the calculated values with the increased diffusion coefficient match the measured resistances rather well. Afterwards, the calculation increases considerably faster than the measurement. The deviations between all three calculation models and the measured resistances at $t > 3,000 \text{ h}$ indicate that different processes superimpose each other. One mathematical relation cannot describe them accurately. A possible reason might be that the diffusion mechanisms change over time. In the beginning, diffusion along the phase boundary determines the growth rate of the oxide. Due to the barrier effect of the oxide layer, these relatively fast diffusion paths might be blocked and slower diffusion processes e.g. along the grain boundaries would then dominate the growth.

Metallographic investigations were performed in order to gain further insight into the way the oxygen progresses into the contact interface. An EDX-mapping (energy dispersive x-ray spectroscopy) was conducted on the FIB-cut (focused ion beam) of an Ag-coated sample that had been stored at 115 °C for 4,000 h (**Fig. 14a**). It would have been expected that accumulations of oxygen could be seen at the grain boundaries. However, either there was no higher oxygen concentration or the resolution was not sufficient to detect it (**Fig. 14b**).

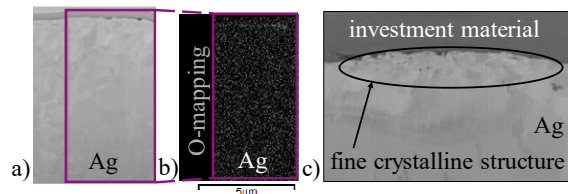


Fig. 14: Metallographic investigations on an Ag-coated contact member: a) FIB-cut with b) EDX-mapping of the oxygen, c) section of a FIB-cut with recrystallized microstructure

In the FIB-cut, it could be seen that areas that had experienced mechanic deformation during the joining

had recrystallized (Fig. 14c). The resulting, fine structure could facilitate the diffusion along the grain boundaries.

4.2 Al-Cu

The experiments on five connections with a bare aluminum and a bare copper contact member at 90 °C over 4,000 h have shown that the oxidation proceeds slower in this material combination than in Ag-Al-connections [1]. As the force applied via the spring pins and the hardness of the softer contact member were the same as in the Ag-Al-connections, the assumption of $n = 39$ a-spots was adopted for this system as well.

4.2.1 Macroscopic approach

Due to the slower rise in resistance, the macroscopic model can approximate the measurement better at first. After 24 h a remainder of six a-spots would reproduce the measured resistance (Fig. 15). However, the failure of further a-spots would cause a rise in resistance that is higher than the measured, small increase. Overall, the discrete resistances of this theory are not a suitable fit for reproducing the measured values.

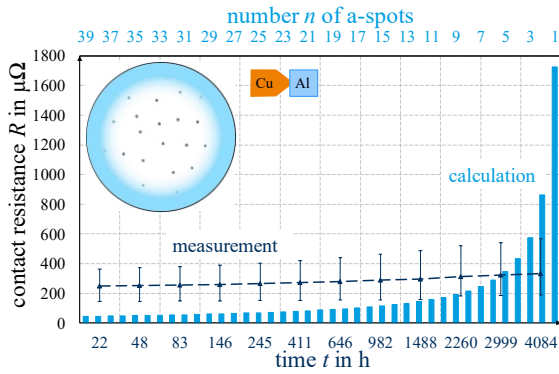


Fig. 15: Measured contact resistance depending on the time and calculated contact resistance depending on the number of a-spots in an Al-Cu-connection

4.2.2 Microscopic approach

With the microscopic approach, the radius of a single a-spot would be 1.25 μm after 24 h at 90 °C (Fig. 16).

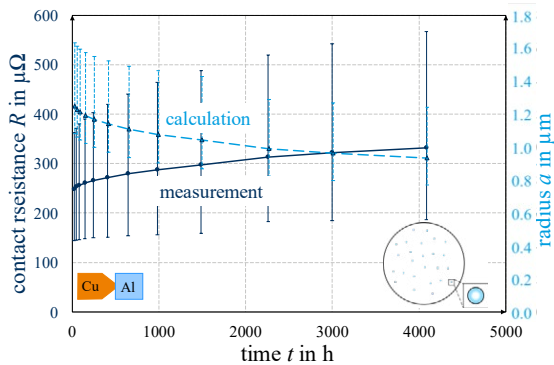


Fig. 16: Measured contact resistance and calculated radius of the a-spots depending on time assuming a uniform growth of the oxide layer on all 39 a-spots in an Al-Cu-connection

The increase in resistance slows down over time. The radial growth of the oxide layer after the first heating over time shows a parabolic oxide growth in this material combination (Fig. 17). This type of relation is typical for diffusion processes.

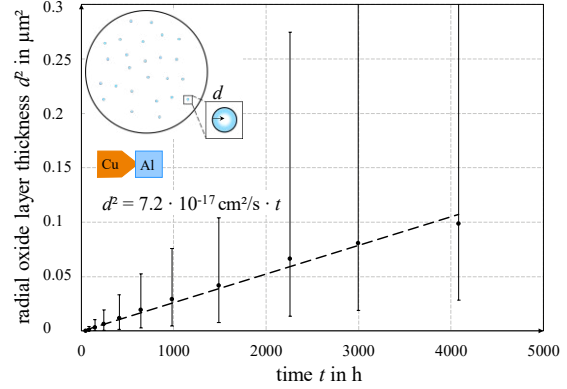


Fig. 17: Radial growth of the oxide layer in an a-spot starting at $t = 24$ h at 90 °C in an Al-Cu-connection (mean value and span)

A growth constant of $k = 7.2 \cdot 10^{-17} \text{ cm}^2/\text{s}$ can be determined for a temperature of 90 °C. Taking into account the span of the results, the growth constant that would be necessary to fit the minimum and maximum values were determined as $k_{\min} = 1.9 \cdot 10^{-17} \text{ cm}^2/\text{s}$ and $k_{\max} = 2.6 \cdot 10^{-16} \text{ cm}^2/\text{s}$. With eq. (6), the number of a-spots in any connection with the softer contact being aluminum and a uniform pressure of 64 N/mm² in the apparent contact area can be determined. In eq. (7) ρ_{Ag} has to be replaced by ρ_{Cu} for this material combination. Hence, the mean value of the contact resistance over time for an Al-Cu-connection at 90 °C can be calculated as follows:

$$R = \frac{\rho_{\text{Cu}} + \rho_{\text{Al}}}{4n \left[a(24 \text{ h}) - \sqrt{7.2 \cdot 10^{-17} \frac{\text{cm}^2}{\text{s}} t} \right]} \quad (9)$$

4.2.3 Comparison to the existing models

For comparing the measurement to the models after *Izmailov* and *Dzektser*, there is no previously known diffusion coefficient that can be used for the calculation. Instead, the diffusion coefficient is determined for which the calculated resistances fit the measured values as far as possible. For the mean values, it is $D = 4.2 \cdot 10^{-16} \text{ cm}^2/\text{s}$ and considering the span it would be $D_{\min} = 5.6 \cdot 10^{-17} \text{ cm}^2/\text{s}$ and $D_{\max} = 6.7 \cdot 10^{-16} \text{ cm}^2/\text{s}$. With the calculation after *Izmailov*, the measured values cannot be approximated well (Fig. 18). Compared to the exponential growth of the resistance in this model, the measured values are too low in the beginning and too high later on. The intersection point between the calculated and the measured curve can be shifted by assuming a different diffusion coefficient.

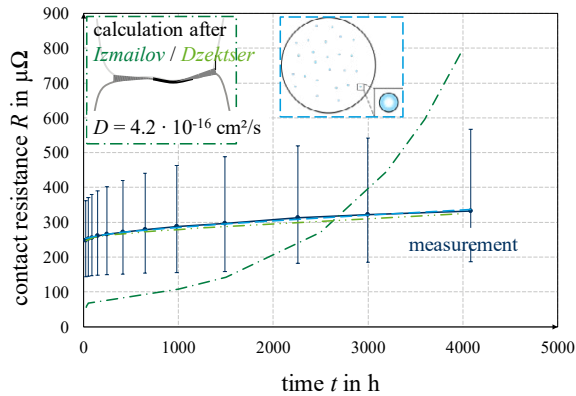


Fig. 18: Comparison between the measurement and the calculations according to the models presented in sections 3.1, 3.2 and 4.2.2

In contrast, the model after *Dzejtser* and the model developed in chapter 4.2.2 both match the mean value of the measured resistances quite well. The diffusion process of the oxygen along the interface between aluminum and copper determines the long-term behavior of the connections of this material combination. Eq. (4) and (9) can both be used in order to estimate the resistance of a connection with a bare aluminum and a bare copper contact member over time.

5 Summary

- For Ag-Al- and Al-Cu-connections, models describing the aging of the connections caused by the growth of an Al_2O_3 -layer in the contact interface were developed. Both models are limited to connections with a uniform pressure in the contact interface. The results were compared to previously existing models.
- In Ag-Al-connections different processes seem to be taking place within the connection that cannot be described accurately yet. Neither the previously existing, nor the newly developed model can approximate the measured resistances closely for $t > 3,000$ h.
- The long-term behaviour of Al-Cu-connections at 90°C can be described well with the determined diffusion coefficient for eq. (4) or the growth constant for eq. (9). In order to calculate the aging of connections at other temperatures, further investigations are necessary.
- The diffusion mechanisms for the entrance of the oxygen into the different material combinations and the diffusion coefficients for the different kinds of diffusion require closer investigation.
- Fritting seems unlikely in the investigated connections due to their steady rise in resistance. As leaps in resistance have been witnessed in other connections, experiments are currently conducted with a variable source voltage. Examining the breakthrough of Al_2O_3 may also help gain insight into the thickness of the oxide layer.

The authors would like to thank Mrs. Willing and Mrs. Bretzler of fem in Schwäbisch Gmünd for their work on the metallographic investigations and the helpful discussion of the results.

6 Literature

- [1] M. Braunović, “Evaluation of Different Platings for Aluminum-to-Copper Connections”, IEEE Transactions on Components, Hybrids, and Manufacturing Technology, Vol. 15, No. 2, April 1992.
- [2] A. Ramonat, “Untersuchungen zum elektischen. Kontakt- und Langzeitverhalten von Füge-technologien mit zylindrischen Leitern aus Al”, TU Dresden, 2019.
- [3] P. Slade, “Electrical Contacts: Principles and Applications”, 2nd Ed., CRC Press, Boca Raton, 2014.
- [4] R. Schneider, “Langzeitverhalten geschraubter Stromschienenverbindungen in der Elektroenergie-technik”, TU Dresden, 2012.
- [5] S. Pfeifer, “Einfluss intermetallischer Phasen der Systeme Al-Cu und Al-Ag auf den Widerstand stromtragender Verbindungen im Temperaturbereich von 90°C bis 200°C ”, TU Dresden, 2015.
- [6] M. Oberst, S. Schlegel, S. Großmann, “On the Aging of Electrical Joints with a Copper and an Aluminum Contact Member”, presented at the 65th IEEE Holm Conference, Milwaukee, WI, USA, Sept. 15-18, 2019.
- [7] M. Oberst, S. Schlegel, S. Großmann, “Influence of Oxygen on the Aging of Electrical Joints with one bare and one coated Aluminum contact Member,” presented at the 29th International Conference on Electrical Contacts, Albuquerque, NM, USA, Oct. 14-17, 2018.
- [8] M. Oberst et al., “Impact of the Formation of Intermetallic Compounds in Current-Carrying Connections”, IEEE Transactions on Device and Materials Reliability, Vol. 20, No. 1, pp. 157-166, March 2020.
- [9] R. Holm, “Electric Contacts: Theory and Application”, 4th ed., Springer Verlag, Berlin, New York, 2000.
- [10] E. Takano, K. Mano, “Theoretical Lifetime of Static Contacts”, IEEE Transactions on Parts, Materials and Packaging, Vol. 3, No. 4, pp. 184-185, Dec. 1967.
- [11] V. Izmailov, “Conductivity of long-term closed electrical contacts”, 10th International Conference on Electrical Contacts, Budapest, Hungary, 1980.
- [12] I. Olefjord, A. Nylund, “Surface Analysis of Oxidized Aluminum – 2. Oxidation of Aluminum in Dry and Humid Atmosphere Studied by ESCA, SEM, SAM and EDX”, Surface and Interface Analysis, Vol. 21, pp. 290-297, 1994.
- [13] J. H. Gieske et al., “Pressure Dependence of the Elastic Constants of Single Crystalline Aluminum Oxide”, Physica Status Solidi, Vol. 29, No. 1, pp. 121-131, 1968.
- [14] J. K. Baird et al., “Diffusion of Oxygen in Silver”, Journal of Physics and Chemistry of Solids, Vol. 60, pp. 891-894, 1999.
- [15] P. Slade, “Electrical Contacts”, 2nd Edition, CRC Press, Boca Raton, 2014.
- [16] D. Meyerhofer, S. A. Ochs, “Current Flow in Very Thin Films of Al_2O_3 and BeO ”, Journal of Applied Physics, Vol. 34, No. 9, pp. 2535-2543, September 1963.
- [17] N. Dzejtser et al., “On the Life-Time of Stationary Contacts”, 16th International Conference on Electrical Contacts, Loughborough, UK, Sep. 7-11, 1992.
- [18] R. Holm, “Electric contacts: theory and applications”, 4th Edition, Springer Verlag, Berlin, 2000.
- [19] M. Braunović, “Electrical contacts: Fundamentals, Applications and Technology”, CRC Press, New York, 2006.
- [20] U. R. Evans, “Laws Governing the Growth of Films on Metals”, Trans. Electrochem. Soc., Vol. 83, pp. 335-342, 1943.

Volumetric erosion of a structured electrical contact surface using X-Ray Computed Tomography.

J.W. McBride, University of Southampton, UK, jwm@soton.ac.uk

T.G. Bull, University of Southampton, UK.

K.J. Cross, TaiCaan Technologies Ltd, Southampton, UK. Kevin.Cross@taicaan.com

Abstract

The use of 3D optical scanning methods is well established for the evaluation of volumetric wear on electrical contact surfaces. A longstanding limitation of these methods has been the accuracy to which the underlying form of the surface prior to the wear process is determined. Electrical contact surfaces are never perfectly flat, in many applications the underlying surface is nominally spherical or a freeform surface. This paper introduces newly developed methods to enhance the capability of resolving volumetric wear on a surface with complex shape (form). These methods are applicable to a wide range of applications, but the focus here is on arcing electrical contacts. The paper investigates wear on a nominally spherical AgNi contact used in low voltage switching applications and compares this to the wear on a surface modified using an electron beam process to create a highly structured surface; under the same switching conditions. The spherical contact is analysed using a new 3D optical metrology solution using a data fusion method, which combines both metrology data and surface photographic image data. The 3D optical scanning data is then compared with surface data from X-Ray computed tomography (X-CT) of the structured electrical contact surface.

1 Introduction

This paper focuses on wear related to arcing devices although the methods discussed are applicable to other electrical contact applications and to other types of surfaces. Many studies over the last 30 years have investigated mass transfer processes linked to arcing in switching contacts. **Figure 1** shows example results of such a study, [1]. It shows that the transfer between the anode and cathode surfaces in a 64 V DC resistive switching circuit related to the current level (0-16 A). With the transfer between the anode and cathode reversing above 3A, linked to the onset of a gaseous arc. The results in [1] showed one of the first applications of 3D surface data, with the data collected using a stylus profiling system. The onset of optical methods for the 3D surface profiling [2] generated a number of studies on the volumetric wear of electrical contacts [2-8]. Showing two key advantages over the stylus methods; firstly, the contact surfaces do not need to be removed from the support to evaluate the surfaces; secondly the ability to differentiate between wear both above and below a set datum, as shown in **Figure 2**.

The detection of wear on a complex surface can be applied in many applications and in all cases, there are a number of fundamental issues; (1) the precision of the measurement system, (2) the accuracy of the volume algorithms, and (3) the methods used to identify the underlying surface form, examples include; (a) Flat, (b)

Spherical, (c) cylindrical, (d) toroidal, (e) free-form, (f) structured surfaces no recess, and (g) structured surfaces with recesses.

1.1 Arc Wear Transport between Electrical Contact Surfaces

The wear process in electrical contacts with arcing is very complex, as reflected in the number of research publications in the field, [9]. The key issue is that the wear is a complex interaction of many variables, here separated into 5 categories, as shown in **Table 1**. Because of the complexity it is often difficult to determine underlying phenomena, with the results only relating to the specific conditions used. To reduce the complexity, control of the independent variables is used. For example, the data in **Figure 1**, is for a fixed DC voltage, with a resistive load, with a single material and constant opening velocity; thus controlling 2 of the variable categories. The remaining categories will have a significant influence on the resulting wear, it is therefore important to clearly define these.

In this study, we investigate a controlled experimental condition with modern surface scanning instruments to provide information around the interaction of anode and cathode surfaces.

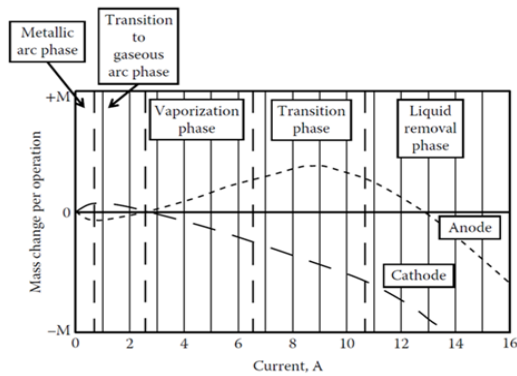


Fig.1 Mass Transfer, 60 VDC Break only, Ag MeO contacts, constant velocity (0.1m/sec) [1].

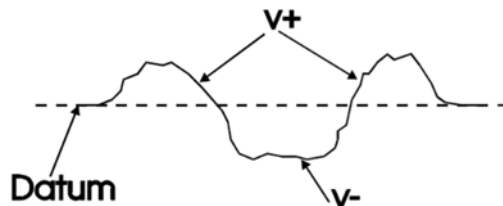


Fig. 2 Volume above and below a fixed datum surface.

1	Circuit conditions	Supply voltage V (AC DC), I, Load type.
2	Device design	Contact velocity, number of bounces on closure, interaction with magnetic fields, surrounding enclosure materials.
3	Experiment condition	Make only, Break Only, Point on Wave, Make and Break
4	Electrical contact material	Ag, Ag/Ni, Ag MO, etc
5	The environment	Temp, Pressure, humidity, vibration levels.

Table 1. Factors influencing the wear and erosion of electrical, contact switching surfaces.

2 Experimental Methods and Data Resolution

2.1 Test Fixture

A model relay mechanism is used, as shown in **Figure 3**, with two commercial contact rivets, Ag/Ni, (80/20). The lower contact is a fixed cathode; the moving contact has a maximum contact gap pre-set of 0.3mm. The moving contact is in the normally open condition and actuated by a standard (14 V) relay coil. The circuit conditions used are, 14.8 V (DC), 10.2 A, resistive load, the contacts are switched for 3000 operations with both make and break cycles. Two surface types are used; in Experiment (1), a standard rivet contact; and in

Experiment (2) the same material as (1), modified to a predefined structured surface, shown **Figure 4**.

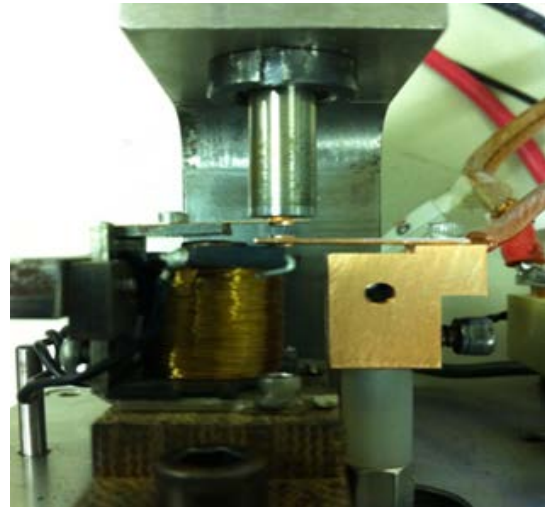


Fig. 3. The experimental test set up, with a fixed cathode (lower) and moving anode contact (upper), actuated by the relay coil.



Fig. 4 Ag/Ni contact processed by electron beam processing, to create a highly structured surface.

2.2 The Structured Electrical Contact Surface

The structured electrical contact surface used in Experiment (2) is shown in **Figure 4**, it was modified using an electron beam processing method, [10]. The darkened area in the figure is the location of the arc related wear. When the electron beam comes into contact with the surface it melts and vaporises the material. Providing that the beam does not penetrate the surface, the vapour pressure of the molten material causes the material to be expelled from the hole formed. This material is deposited around the perimeter of the hole. A series of electro-magnetic coils are used to focus the electron beam and then deflect it around the material in a rapid and controlled manner, allowing this process to

be carried out at many sites consecutively. In this study the resultant surface is the same material as the commercial Ag/Ni rivet, (80/20) with the same overall dimensions. The surface exhibits a structure with a very high degree of surface roughness as shown in **Figure 4**.

2.3 Optical and X-Ray Surface Metrology Hardware and Software

The optical 3D surface metrology instruments used in this study is the TaiCaan Technologies XYRIS 2020. This is a calibrated metrology instrument. It is a new class of instrument (released in 2020), which combines an ability to measure surfaces with significant slope, with the ability to view the samples via microscope and scan over large areas, (100 x 100 mm), with 0.1 μm resolution. Two optical sensors have been used in this paper, the XYRIS 2020 L and H, where the L refers to a low gauge range sensor with a resolution of 0.01 μm and the H sensor is a high gauge range with a resolution of 0.025 μm .

X-Ray Computed Tomography (X-CT) has been used for many years in medical applications. Recent developments in metrology have seen increasing use of the method for precision metrology in engineering applications, [11-13]. The systems are not calibrated, and as such the optical data produced from the XYRIS 2020 H/L can be used to give an indication of the accuracy of the X-CT system. The system used is a Nikon 225 kVp Nikon/Xtek HMX, with the commercial software VGStudio Max 2.1 used to generate the surfaces. The data has 8-bit image resolution and a spatial resolution of, 4.8 μm in X, Y and Z, (voxel resolution). The point cloud data produced requires a further step in processing to detect the surface and to then render the surface. The render settings used within VGStudio Max 2.1, are, (1) to select a sample of the background and a sample of the volume of interest, (2) use the ISO standard which automatically detects the surface from a histogram, and the (3) select the meshed data to very precise with no simplification.

Both XYRIS and X-CT systems have commercial software tools, which enable the generation of the 3D data for processing. The data format used is a standard 3D point cloud format (STL) for the X-CT system. The XYRIS system generates both STL format data and a standard metrology format surface (2.5D) data (*.tai). Both formats are imported into @BEX [14], for analysis of the dimensional and volumetric data.

2.4 Defining the accuracy of the volumetric wear as a function of the metrology systems and software

There are a number of critical factors in defining the accuracy of volume measurements;

1. The accuracy of the measurement process. The system (XYRIS 2020 H) has a volume resolution of (X,Y,Z,) 0.1 μm , 0.1 μm , and 0.025 μm . If we use the term VOXEL as used in XCT to define volume resolutions, and assume Z to be the same as X,Y then the XYRIS Voxel size is 0.1 μm . The Voxel size of the X-CT system is correspondingly 4.8 μm , or approximately 50 times larger than the optical method. For both systems the resolution does not directly relate to accuracy of the systems. The accuracy is a function of systematic and other errors. For the X-CT this is very complex and undefined. The accuracy of the XYRIS 2020 is defined; with the repeatability in X and Y of 0.150 μm , and a noise floor in Z, 0.024 μm , (for the L sensor). The corresponding value for the H sensor is, a noise floor in Z of 0.084 μm . These combined to define the volumetric accuracy of the system used as 172 nm^3 (for the H sensor). Both the resolution and the accuracy are significantly higher when compared to the data in [1-7].

2. The X-CT system has a second stage of errors associated with the surface generation processes, which adds a further level of complexity to a system which has already poorly defined accuracy.

3. The accuracy of the software approach used to determine the volume. Some existing commercial software packages used to define volume have been shown to have errors of 9% when compared to reference data sets. Care must be used when selecting the appropriate methods. The software package used here is @BEX (TaiCaan Technologies) with a defined software error on a reference surface of <0.003%.

4. The accuracy of the form fitting methods used to remove the underlying form. The results of the volumetric wear are highly sensitive to selection of the area and the fitted surface. This is discussed in the results of experiment (1). The form fitting of a surface and the link to before and after studies leads to an introduction of the topic of data registration, [11], discussed briefly below.

2.5 The Characterisation of a Structured Electrical Contact Surface

Regular surfaces can be described by a number of parameters the most common of which are the two 2D amplitude roughness parameters, Ra and Rq; the former is the arithmetic mean value of a rough surface and the latter is the Root Mean Square or standard deviation of the surface. The 2D parameters are matched by the standard 3D amplitude parameters Sa and Sq. These values both R and S are taken relative to a nominal form fit and waviness filter (Gaussian). These parameters are crude descriptors proving no indication of the

nature of the surface, as this requires both spatial and amplitude information, along with some function describing the functionality of the surface, which in turn will be related to the application of the surface.

To allow the combination of both amplitude and spatial data a hybrid parameter is used we define as Sap. This areal parameter, (S type) and has been developed for the optimisation of electrode surfaces where the surface area is a key design parameter. For an ideal smooth plane surface, the texture ratio (Sap) is 1.

$$\text{Texture Ratio} = \frac{3D \text{ Surface Area}}{\text{Projected Surface Area}}$$

The texture ratio parameter is similar to the Sdr parameter as defined by ISO25178 – Developed Interface Area Ratio – which describes how much the texture increases the surface area from a 2D. For an ideal plane surface the value is 0.

$$S_{dr} = \frac{3D \text{ Surface Area} - \text{Projected Surface Area}}{\text{Projected Surface Area}}$$

2.6 Data Registration to detect surface changes.

Data registration is a process where before and after (wear study) data is registered such that surfaces can be subtracted to determine the wear relative to the know datum. The registration problem is mathematically complex and a subject of major interest in a range of applications, [11]. In this work the surfaces were not measured before testing; in this case the underlying form is assumed to be a known geometric form, i.e. flat, spherical, etc. [1-7]. The natural contact rivets used are not high precision components and as such there will be errors in the underlying form evaluation as these are not perfectly spherical, as discussed below.

3 Results and Discussion

3.1 Experiment 1. Standard Electrical Contact, Ag/Ni 80/20, 3000 operations make and break.

Figure's 5 and 6 show the cathode and anode surface, measured using the XYRIS 2020H. The righthand colour scales show the height range and the height data distribution. It shows that the H sensor range allows the capture of both the base and the pip and crater wear.

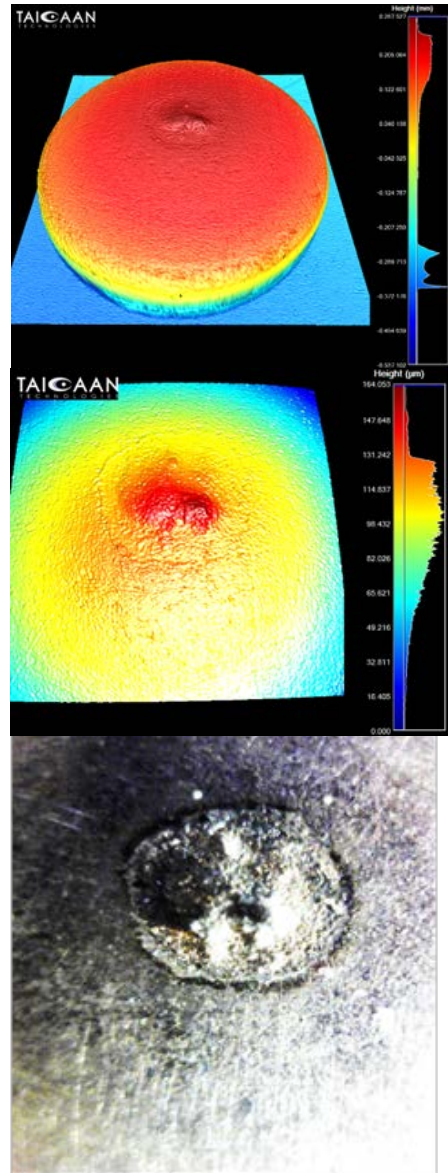


Fig. 5 Cathode; 14.8 V (DC), 10.2 A resistive load, 3000 switching operations with both make a break cycles. Ag/Ni. (80/20), (a) upper, 2.6 mm x2.6 mm, colour scale (0-0.78mm) (b) middle, 1.5mm x 1.5mm, colour scale (0-0.164mm) (c) lower, microscope image.

	Exp. 1 (Cathode)	Exp.1 (Anode)	Exp. 2 (Anode)
Volume (Above)	2.86	0.271	0.582
Volume (Below)	-0.093	-3.701	-3.513
Volume Change	2.767	-3.43	-2.931

Table 2. Volumetric data Exp. 1 as shown in Fig's 5-8, and Exp. 2 in Fig. 9, all x10⁻³ mm³.

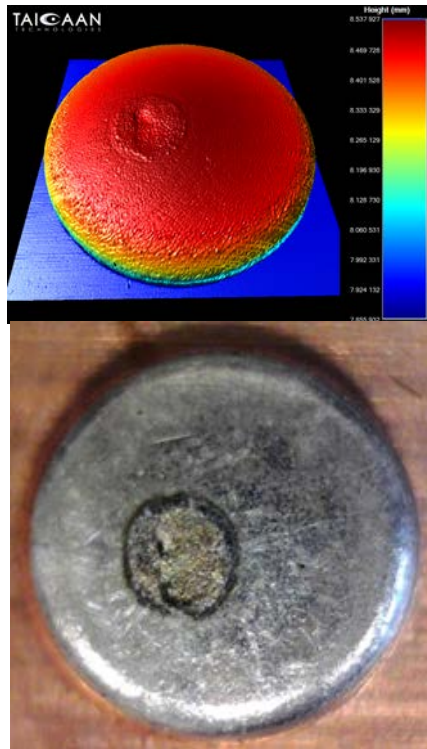


Fig.6 Anode Surface; 14.8 V (DC), 10.2 A resistive load, 3000 switching operations with both make a break cycles. Ag/Ni. (80/20); (a) upper, 2.6 mm x 2.6 mm, colour scale (0-0.68 mm) (b) lower, microscope image.

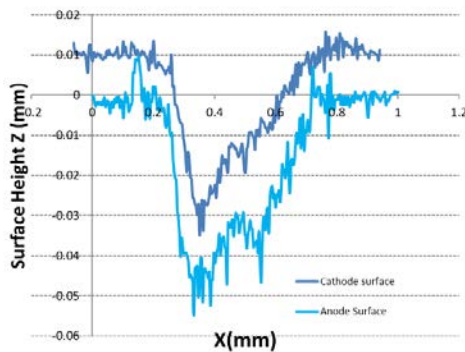


Fig.7 Cross section data through the pip and crater formation in Fig's 5 and 6, with the surfaces separated by 1 μ m.

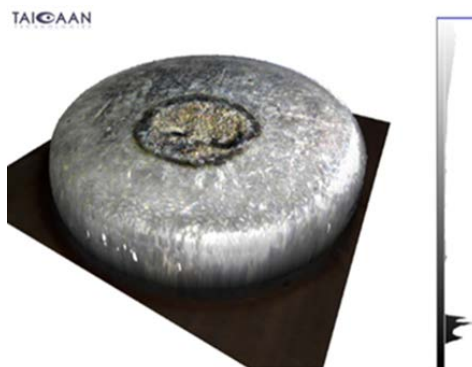


Fig.8 2D data superimposition. (a) Combining 2D data from Fig 5 and Fig 6.

The analysis of the volume information in **Figure's. 5 & 6**, follows an established 3 step methodology.

- Step 1; apply a 2D 80 μ m gaussian filter to the measured data, showing the changes in surface roughness only. This allows the identification of the wear region.
- Step 2; remove the region and fit a sphere to the residual surface. Replace the wear region to the levelled residual data.
- Step 3; remove the datum surface, using the region identified in Step 1 and determine the volume above and below the datum.

The results of the volumetric erosion are shown in **Table 2**. As evidenced by the difference in the net cathode gain and the net anode loss, some material is lost to the environment. This is observation is further confirmed in **Figure 7**, which shows a cross section of the wear region with the cathode surface inverted onto the anode surface. It shows a close match, but it is clear that the material gained on the cathode is less that the material lost from the anode. This suggests that material is lost to the environment as shown by the volume differences. **Table 3** shows the roughness parameters of the undamaged surface, and the evaluation of the hybrid *Sap* parameter, (1.094). To show the sensitivity to the form fitting process, the position of the datum surface can be adjusted in software, to show a shift of 1 μ m, reduces the negative wear volume by 15%. This emphasizes the sensitivity of the datum surface definition to any analytical evaluation of the volumetric data. To overcome this limitation would require a data registration process, [11].

Figure 8 shows the application of data fusion with the anode surface height rendered with the photographic colours. This technique allows the user to define regions of wear which are not apparent in the 3D data. An example is the region surrounding the wear crater in Figure 6, which shows a darkened area.

	XYRIS H (Optical) Exp. 1	XYRIS L (Optical) Exp. 2	Nikon (X-CT) Exp. 2
Ra	1.545 μ m	52.015 μ m	45.781 μ m
Rq	1.96 μ m	58.95 μ m	53.187 μ m
Rz	13.91 μ m	237.93 μ m	225.31 μ m
X 4 peak	N/A	0.635 mm	0.639 mm
S a/p	1.094 (0.5 mm)	2.41* (1 mm)	1.924 (1 mm)

Table 3 Metrology data comparison, Experiment 1 and 2.* the optical data requires smoothing using Median filters

3.2 Structured cathode surface with regular anode surface, Ag/Ni 80/20, 3000 operations make and break

The electron beam modified electrical contact surface, (cathode or fixed contact) is shown in **Figure 9**. It shows a highly structured surface measured with the X-CT system, with a cross section, showing recessed surface, i.e. where there is an overhang and where top down optical sensing would not be able to show the corresponding hidden surface. The data shows the height data from the X-CT measurement and associated surface rendering process as described above. The features in the surface as shown in the cross section correspond to holes in the surface with a typical depth of 0.16 mm. The resultant surface shows a number of peaks and a wear area apparent in the microscope image after the switching operations, in **Figure 4** (the darkened area), but not apparent in the 3D X-CT data.

The corresponding data from the optical system (XYRIS 2020 L) is shown in **Figure 10**, in this case for both the cathode surface and the anode surface. The optical measurement of the cathode surface is with higher resolution when compared to the X-CT data, but because of the line of sight issue, is unable to show the recessed surfaces.

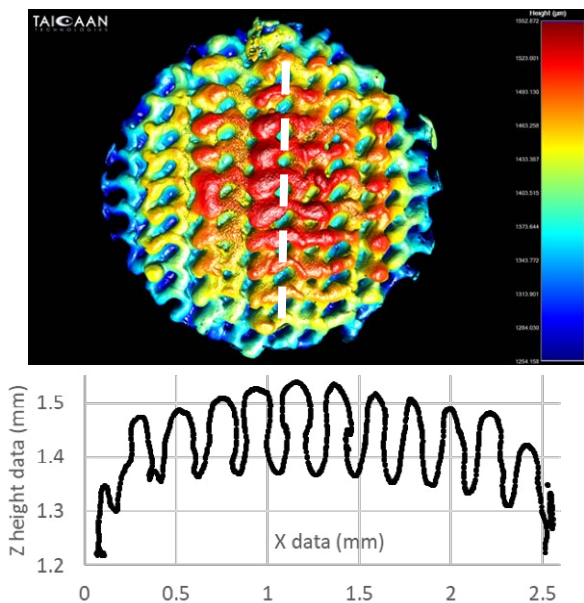


Fig 9. Structured cathode surface, using X-CT and surface generation, with cross section, through the white line. Colour scale (1.25-1.55 mm)

3.3 Characterisation of the Surfaces.

The roughness values for the surfaces are shown in **Table 3**. It is noted, that the method used to generate the values in **Table 3**, are subject to systematic user errors. The relative positions of the cross section and the selected area are hand selected but are as close as possible. These are determined using both the Ra and Rq values associated with the selected cross sections. The

data is relative to a selected form, in Experiment 1 this is a circle fit, while in Experiment 2 it is a 3rd order polynomial fit. The results shows the expected Ra for the undamaged regular surface is of the order of 1-2 μm , while the corresponding roughness for the structures surfaces is of the order 40-55 μm . It is noted that the Ra values is an arithmetic mean and that the hidden surfaces (with lower amplitude) will contribute to the lower Ra when compared to the Ra from the optical system, where there is no hidden data. The similar values for, the overall height Rz (after form fitting), and the distance between the top 4 peaks suggest that the accuracy of the X-CT system is well matched with the calibrated XYRIS 2020 system.

To enable the application of the Sap parameter on both X-CT and optical surface data, we need to define the reference projected area. In this data a 1mm radius is used. The areas are selected by eye, and because of the nature of the surface this implies a possible systematic error. The results in **table 3**, show that for the selected areas the optical data has a slightly higher surface area. This is probably the consequence of the higher data resolution, since the higher data resolution on a rough surface will by it nature generate a higher surface area. To remove outliers associated with the optical data, a Median filter (3 x 3) has been applied, while no filter has been applied to the X-CT surface data.

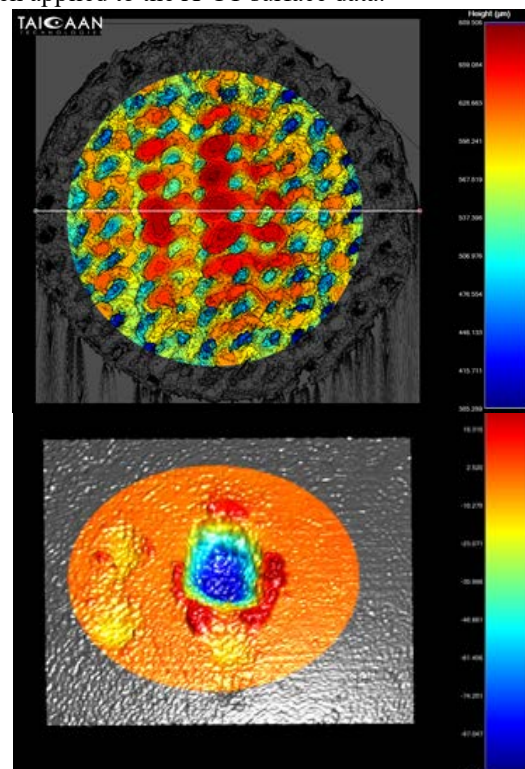


Fig 10. XYRIS data with selected 1 mm radius used for S (a/p) parameter, (upper), colour scale (0.38-0.68mm) while the lower surface is the anode modified using the 3 stage process, and showing the area selected for the volume in Table 2, colour scale (-0.1 to +0.028 mm).

The anode wear region in **Figure 10**, has been processed following the same 3-stage process in experiment 1, and the resulting volume shown in **Table 2**. This shows a small reduction in the wear volume (from 3.43 to $2.93 \times 10^3 \text{ mm}^3$) when compared to the data in experiment 1. There is no evidence of corresponding wear on the structured cathode surface.

It is noted, that with only one experimental sample the reduction in wear is not a important observation. The main result is that using the methods developed in this paper, we are able to generate the wear volume with a well defined accuracy.

4 Conclusions

There are a number of new develops presented in this paper.

1. A new data rendering method is shown which allows surface 3D data to be superimposed on microscope images to provide additional data particularly on a surface where there is no clear change in volume but a darkening of the surface is apparent.
2. The results show that the complexity of the volume fitting methods and the requirement of the application of data registration methods. The current established 3-step method is prone to user error. It has been shown that a small change of 1 μm in the position of the flat surface datum can result in a 15% change in the measured volumes.
3. A new texture parameters is introduced and used in the analysis of a structured cathode surface. The parameter has been used in the evaluation of the structured surface.
4. The paper introduces the application of electron beam forming to create a structured surface.
5. Finally X-CT is used and compared with the established optical methods in the evaluation of the structured surface. It is shown that the X-Ray method is able to show surfaces not visible with conventional optical methods (recesses), and the data processing methods used allow the recessed surfaces to be included in the characterisation of the surface.
6. Initial results are presented on the evaluation of wear in samples measured using both techniques. Initial result show that the spatial data in the X-CT results are good (X dimension in Table 3), the roughness data are not similar. The lower voxel resolution of the X-CT data leads to a smoothing of the surfaces. Further investigations are required.
7. The wear observed in experiments with the structured surface is slightly lower on the unstructured anode surface, with no observable wear measured on the cathode surface.

Acknowledgements.

The authors would like to thank Ang Zong-Zi (William), a student at the University of Southampton, for undertaking the X-CT study; to Jerry Witter and Zanka Chen of Electrical Contacts Plus (USA) for the supply of the contact materials and hoasting switching experiments. The stuctured surfaces were processed by Dr B. Dance of TWI, UK. (<https://www.twi-global.com/media-and-events/connect/2000/may-june-2000/a-thousand-holes-every-second>).

Referenecs

- [1] J. Swingler ; J.W. McBride, "The erosion and arc characteristics of Ag/CdO and Ag/SnO₂ contact materials under DC break conditions", IEEE Trans. CPMT, Vol 19, Issue 3, Sept 1996, pp404-415.
- [2]. McBride J.W, Maul C, "The 3D measurement and analysis of high precision surfaces using con-focal optical methods", IEICE transactions on electronics, Volume 87, Issue 8, (2004) pp 1261-1267.
- [3]. McBride J.W, "The Volumetric Erosion of Electrical Contacts", IEEE Transactions on Components and Packaging Technology, Vol 23, No 2, June 2000, pp 211-221.
- [4] McBride, J.W. "A review of surface erosion measurements in low voltage switching devices". In, Proceedings of Twenty First International Conference on Electrical Contacts, Zurich, Switzerland, Sep 2002, pp 462-470.
- [5] McBride, J.W. "A review of volumetric erosion studies in low voltage electrical contacts". IEICE Transactions on Electronics, E86-C, (6), 2003, pp 908-914.
- [6] McBride, J.W., Sumption, A.P. and Swingler, J. (2004) On the Evaluation of Low Level Contact Erosion. In, Electrical Contacts, 2004. Proceedings of the 50th IEEE Holm Conference on Electrical Contacts and the 22nd International Conference on Electrical Contacts, 20-23 Sep 2004.pp, 370-377.
- [7] Zhang, D., McBride, J.W. and Hill, M. (2004) A feature extraction method for the assessment of the form parameters of surfaces with localised erosion. Wear, 256, (3-4), 243-251.
- [8] Hasegawa M, Izumi K, Kamada Y, "New algorithm for volumetric analysis of contact damages with laser microscope data", International Conference on Electrical Contacts, 2006, pp 337-342.
- [9] McBride J.W, Chapter 13, "Low Current Switching", 2nd Edition "Electrical contacts (Principles and applications), Ed. Slade. P.G, 2014, pp 731-784.
- [10] B. A. Dance, Buxton BG, An introductiuon to surfi-sculpt technology - new opportunities, new

- challenges, Proceedings of the 7th International Conference on Beam Technology (2007), pp. 75-84
- [11] McBride J.W, Cross K.J, Bull T.G, “Optical metrology for the morphological characterization of surfaces: limitations, innovations, registration, and new directions”, Optical Metrology and Inspection for Industrial Applications VI 11189, 111890S, SPIE China, 2019.
 - [12] J.J Lifton, A. A. Malcolm, J. W. McBride, (2015), “On the uncertainty of surface determination in X-ray computed tomography for dimensional metrology”, Measurement Science and Technology. 26 (3), 2015, 03500.
 - [13] JJ Lifton, AA Malcolm, JW McBride, “An experimental study on the influence of scatter and beam hardening in x-ray CT for dimensional metrology”, Measurement Science and Technology 27 (1), 2015, 015007.
 - [14] BEX®, surface analysis software, from TaiCaan Technologies Ltd, www.taicaan.com

Silver based contact system enabling extremely low and stable contact resistance in mini thermal cut off devices

Dr. Werner Johler, Littelfuse Europe GmbH, Lenzburg, Switzerland wjohler@littelfuse.com
Jack Bu, Littelfuse Electronics, Shanghai, PRC, JBu2@littelfuse.com
Kevin Liang, Littelfuse Electronics, Shanghai, PRC KLiang@littelfuse.com
Steven Hu, Littelfuse Electronics, Shanghai, PRC SHu3@littelfuse.com

Abstract

Li-ion batteries are widely used in mobile electronic devices. Battery evolution with thinner, smaller but higher density, creates more cell hazards, as the lithium-ion cell is designed with materials that are flammable and degradable, and mechanical and electrical shocks can lead to thermal runaway. Efficient and reliable protection of the batteries is a must to keep consumers safe. Thermal cut off devices are widely used to protect Li-ion batteries from thermal runaway. Whenever the battery temperature reaches a critical temperature level, the TCO must reliably interrupt the current. As battery capacities of mobile devices increase and fast charging of batteries becomes a standard feature, the conducting and breaking capacity must increase and contact resistance of the TCO must become lower and stay stable during the entire service life.

A silver-based contact system was developed and optimized for the use in a resettable mini thermal cut off device, providing low ($\leq 2\text{m}\Omega$) contact resistance and variation of resistance, for the use at low voltage ($\leq 10\text{V}$) and operating currents of $\leq 10\text{A}$.

By optimizing the contact force to a level of 30cN , optimizing the contact shape, enabling relative movement during contact closing, providing tight protection of the contact system from environmental influences, and applying an asymmetric contact system of $\text{AgNi}0.14$ and $\text{AgNi}10$ contact material, a contact resistance of less than $2\text{m}\Omega$ in a very narrow range of $\leq 1\text{m}\Omega$ was achieved.

The good performance was also confirmed during dry and humidity storage at $85\%\text{r.H.}/60^\circ\text{C}$ and application testing.

Keywords: Resettable mini thermal cut off devices, TCO, low voltage switching, reliability of silver-based contact systems at low loads.

1 Introduction

In the past decade, the usage of mobile electronic devices has increased dramatically. In 2019, approx. 164 million Laptops and Notebooks, 139 million Tablet PC's, 1.697 billion mobile and smart phones and over 140 million of other different wearable electronic devices such as smart watches, fitness bands, headphones etc. were sold. Most of these devices are equipped with Li-ion batteries. In order to guarantee safe and reliable function of these widely used consumer devices, the batteries must be protected from well-known failure modes such as overcharging, thermal runaway, overheating etc.. For most of the multi-cell devices, electromechanical, resettable mini thermal cut off devices (TCO) are used. The miniature design of these electromechanical devices requires electrical contacts which can carry up to 20A and are able to switch rated currents up to 25A . The most critical requirement is a very low and stable contact resistance over the lifetime of the electronic device to avoid Li-ion cell power losses and device self-heating.

1.1 Protection of Li-ion Batteries

Portable consumer electronics such as Notebook PCs, Tablets and Smartphones need the battery manufacturers to offer higher density and larger capacity Li-ion battery cells for compact, lightweight and more functional devices, and longer battery life. Battery evolution with thinner, smaller but higher density, creates more cell hazards, as the lithium-ion cell is designed with materials that are flammable and degradable, and mechanical and electrical shocks can lead to thermal runaway.

The lithium-ion cell materials are stable at lower temperature but can breakdown at higher temperatures. If a Li-ion cell starts to enter thermal runaway, the results can be disastrous, and the potential dangers of lithium-ion batteries have become hot news recently.

Battery problems in some smartphones and notebooks have highlighted that even the largest companies may see problems with lithium-ion batteries, so the need for protection circuits to maintain the voltage and current within safe limits of the Li-ion batteries is one of the primary limitations. One of the latest approaches for

providing a safety circuit to lithium-ion battery packs is the use of the Mini-breaker, which is a resettable Thermal Cut Off (TCO) device designed to provide accurate and repeatable overcurrent and overtemperature protection. Today, mini breakers are commonly used to protect the Li-ion battery cells of notebook PCs, tablet computers and smartphones (Fig.2).

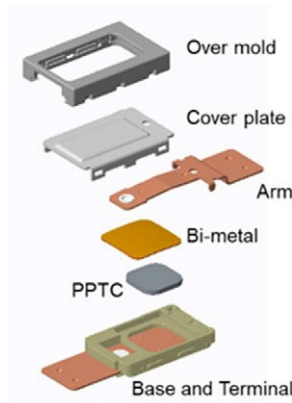


Fig. 1 Design of a Mini Resettable Thermal Cut-Off Device [2]

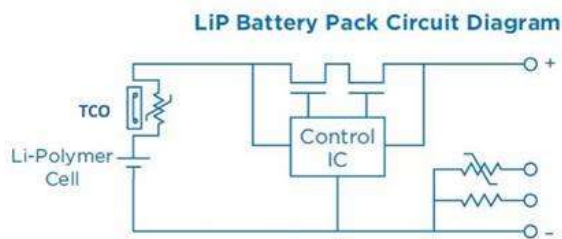


Fig. 2 Protection of a Li-Polymer Cell

1.2 Resettable Thermal Cut-Off devices (TCO) and their design

A typical design of a resettable thermal cut off device is given in Fig.1. The available sizes are as small as 4.75x2.8x0.8mm and can carry up to 18A at 23°C and up to 13A@60°C. The TCO consists of a moveable spring with a contact (arm), a base with a terminal and a fixed contact. Underneath the moveable arm, a bi-metal disk and a PPTC (Positive Polymer Temperature Coefficient) is placed. The entire structure is covered with a cover and over-molded with a low outgassing plastic material, in this case with LCP (Liquid Crystal Polymer).

In normal condition (Fig.3a) the current flows through the electrical contacts during charging and discharging of the battery. When the temperature increases the bi-metal disk flips and pushes the arm upwards and opens the electrical contact. The current is diverted into the PPTC which trips and keeps the bi-metal disk heated and latched until the overtemperature/failure situation discontinues (Fig.3b).

The contact resistance of the electrical contact is much lower than the resistance of the PPTC, so the power

losses in closed conditions are very low. PPTC resistance should be as high as possible to minimize the leakage current in tripped condition, typically less than 0.2 A@3VDC.

The trip temperature is mainly determined by the set and reset temperature of the bimetal disk. It is important that the resistance of the electrical contact is low and stable during the entire lifetime of the battery pack, so the trip temperature of the TCO is not influenced by the resistive losses. The typical UL current rating is 25A@12VDC [16].

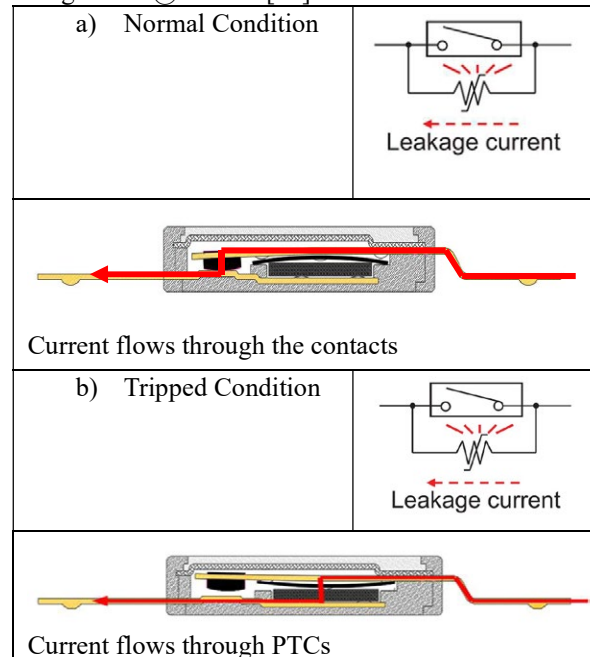


Fig. 3 Function of a Resettable Thermal Cut off Device [3]

1.3 Contacts for high current low voltage applications

When low and very stable contact resistance is required over lifetime in low power switching devices, typically gold plated contacts are used. When high current is transmitted over closed contacts, there is an inherent risk of contact welding. Welding contacts are completely unacceptable for a safety related device and would hinder the device function in a failure situation where reliable power interruption is needed.

As gold or gold plated contacts are not an option, the application of silver-based contacts seems to be the only possible option to achieve very low contact resistance of less than 2mΩ.

Generally, the application of silver-based contacts is not recommended for low voltages and currents [5, 6, 7, 11]. Multiple grades of Ag based contact materials are available on the market. Pure silver, silver alloys, silver composite and silver metal oxide materials are applied in switching devices.

- Pure silver has the highest electrical and thermal conductivity and therefore low contact resistance, can be formed easily in manufacturing [5], but has

low contact welding resistance and a high affinity to sulphide formation. Typically, not used for switching devices which must switch more than 2A.

- Ag alloys such as AgNi0.15 and AgCu3 are widely used. Their conductivity is almost as good as Ag99.99 but their hardness is higher and both alloys have replaced Ag99.99 due to significantly better contact properties. These materials are typically used up to approximately 16A switching current.
- Silver composite materials – AgNi. As Ni is not soluble in Ag over 0.15%, higher Ni contents are produced by powder metallurgy. The sintered AgNi billets are extruded into wires and the Ni is distributed into the silver matrix. Ni contents between 10 and 20% are most common. The high density of this material results in good arc erosion resistance for switching currents up to 100A [5].
- Silver-Metal Oxide Materials – AgCdO, AgSnO2. This group of powder metallurgical produced materials provide the best switching performance, but have lower conductivity and do not provide the same resistance stability during lifetime of the switch [8, 9]

In order to achieve a very low contact resistance of 1mΩ, a minimum contact force of 20cN is required for Ag99.99 contacts [3, 4]. When Ag alloys or Ag composite materials are used, even higher contact forces will be necessary. Considering manufacturing tolerances and spring relaxation, a 50% higher force will be needed to keep the resistance stable for lifetime. Besides the contact force, the shape of the contacts is important too. B. Jemaa [11] reported that a larger radius resulted in lower contact resistance values at lower contact force.

As silver-based contacts are sensitive to tarnishing of the contact surfaces, there are 2 possible solutions to avoid this:

- Ensure good quality contact after each closing
Several authors [7, 12, 13] described the advantage of relative movement between the contact pieces during closing of the contacts. Relative movements between the contact pieces destroy tarnishing films and enable pure metallic contacts, which is absolutely required when very low contact resistance values are mandatory. Fritting of the contacts (electrical breakdown of tarnishing films) will not result in low enough contact resistance as the contact voltage of fritted contacts is in the range of the melting voltage of the contact material, which is 370mV for Ag99.99 [7]
- Protect the contacts from tarnishing
Ideally the contacts should be enclosed in a gastight housing filled with an inert gas, such as N₂. Long time storage of Ag based contact materials and switching devices performed by Jöhler [7] showed that dust proof housings protect Ag contacts sufficiently from contact corrosion and contact resistance increase.

Taking all the aspects into consideration and driving for metallic contacts after each closing of a switching device [15], designs with low and stable contact resistance based on silver-based contacts are possible.

2 Miniature Thermal Cut-Off devices (TCO)

Resettable thermal cut-off devices are resettable circuit breakers that are sensitive to over-current and over-temperature conditions. In fault conditions the TCO will remain open until the fault is removed or power cycled.




Items	MHP-TAM15	MHP-TAT18	MHP-TAC15	
Pictures				
Dimensions [mm]	L*W*H 5.8*3.8*1.15 max	L*W*H 5.8*3.8*1.10	L*W*H 4.75*2.8*0.8	
Hold Current	72	5A @60°C	9A @60°C	5A @60°C
	77	6A @60°C	10A @60°C	6A @60°C
	82	15A@25°C 7A @60°C	18A@25°C 11A @60°C	15A@25°C 7A @60°C
	85	8A @60°C	12A @60°C	8A @60°C
	90	9A @60°C	13A @60°C	9A @60°C
Contact Rating	DC9V/25A ; 6000cycles	DC9V/30A ; 6000cycles	DC12V/25A ; 6000cycles	

Table 1: TCO's and their characteristics [2]

2.1 Requirements

To ensure battery safety, designers try to mitigate against cell thermal runaway, whereby the increase in cell temperature may cause fire or harmful gas exhaust. Therefore, the trip temperature of a TCO device is a key specification to battery pack manufacturers. When a TCO device trips, it immediately cuts the power to the cell and allows the cell to cool.

The TCO should meet following requirements:

- Smallest possible size e.g. minimum real estate to fit on the balcony of the Li-ion cell
- Accurate protection temperature with ±5 °C accuracy
- Trip temperatures from 72 to 90°C
- Minimum 10°C hysteresis between trip and reset temperature
- Support fast charging with a current rating of up to 18A at room temperature
- Highest possible current ratings of up to 15A even at an elevated temperature of 60°C.
- Low resistance down to 2mΩ - 5mΩ
- Very stable resistance during entire lifetime, ideally not more than 1mΩ variation over lifetime
- Leaded format to allow the device to be welded to the positive terminals of the battery cells.

2.2. Basic Design

The basic design of a typical resettable TCO is given in Fig.1.

2.3. Design Challenges

Major design challenges have been the ongoing reduction of device size, combined with the ability to hold and switch even higher currents.

- Challenge 1 – Device resistance

The maximum resistance should not exceed 2mΩ.

The terminals have a major contribution – approx.

50% – to the entire terminal to terminal resistance.

Most commonly CuSn8 is used as material for the terminals, as this material combines good overall performance at reasonable cost level. When resistance values less than 5mΩ are required, Cu materials with higher conductivity such as pure copper or high-performance Cu alloys such as C15100 or similar materials must be applied to minimize cross sections of the conductive parts and provide good spring characteristics at the same time.

Material	Electrical Resistivity [μΩcm]	Electrical Conductivity [MS/m]	Thermal Conductivity [W/m.K]
Cu-ETP (C11000)	1,72	>58	390
CuSn8 (C52100)	13,3	>7.5	67
CuNiSiMg (C70250)	4,00	25	190
CuZr 0,1 (C15100)	1,82	55	360
CuCrAgFeTiSi (C18080)	2,17	46	320
CuSnCrZn (C18045)	2.23	44	301

Table 2: Comparison between pure copper and commonly used copper alloys [5]

Material	Electrical Resistivity [μΩcm]	Electrical Conductivity [MS/m]	Hardness [HV10]
Ag 99,99	1,67	60	30-90
AgNi0.15	1,72	58	40-100
AgCu3	1,92	52	45-115
AgNi10	1,82-1,92	52-55	50-100
AgSnO92/8	1,92-1,96	55-95	220-300

Table 3: Comparison of Ag based contact materials [5]

- Challenge 2 – Low and stable contact resistance

As the size of the device should be as small as possible and stable over the entire lifetime of the TCO, the selection of contact material is limited. Only

Ag99.99, AgNi0.15 or AgNi10 can be taken into consideration and meet the cost target. Furthermore, the design must provide a contact force higher than 20cN.

- Challenge 3 – Size reduction

Size reduction can be achieved by higher performing materials used in the design, an optimized design and in handling manufacturing tolerances well design optimization and well-controlled manufacturing tolerances. Over-molding, and other innovative assembly technologies, provides high stability and enables further size reductions.

- Challenge 4 – Precision of trip and rest temperature

The precision of the trip and reset temperature mainly depends on the precision of the bimetal disk, as well as the overall manufacturing tolerances.

In the following the focus will be in how to solve challenges 1 and 2.

3 Test Parameters and Results

Multiple design optimizations were made to achieve smaller size, higher hold current, as well as lower and more stable contact resistance (Table 4).

	Base		Spring		Contact force [cN]
	Base	Base Contact	Spring	Spring Contact	
Base-line	C18045 0.1mm	AgNi10	C18045 0.1mm	AgNi10	18
Ver.1	C11000 0.1mm	AgNi10	C15100 0.1mm	AgNi10	18
Ver.2	C15100 0.12mm	AgNi10	C15100 0.12mm	AgNi10	23
Ver.3	C15100 0.12mm	AgNi 0.15	C15100 0.12mm	AgNi 0.15	23
Ver.4	C15100 0.12mm	AgNi 0.14	C15100 0.12mm	AgNi 0.14	23
Ver.5	C15100 0.12mm	AgNi 0.14	C15100 0.12mm	AgNi 0.14	30
Ver.6	C15100 0.12mm	AgNi 0.14	C15100 0.12mm	AgNi 0.14	36
Ver.7	C15100 0.12mm	AgNi 0.14	C15100 0.12mm	AgNi 0	30
Ver.8	C15100 0.12mm	AgNi10	C15100 0.12mm	AgNi 0.14	30
Ver.9	C15100 0.12mm	AgNi 0.14	C15100 0.12mm	AgNi10	36

Table 4: DOE to optimize the performance of TCO. Terminal material and dimension, contact material and contact force was optimized

3.1 Test Parameters

The following parameters were investigated and compared:

- Terminal and spring material and thickness
 - C11000
 - C18045
 - C15000
 - Contact material
 - AgNi 10
 - AgNi 0.14
 - AgNi 0.15
 - Contact force
 - 18 cN
 - 23 cN
 - 30 cN
 - 36 cN
 - Measurement conditions: $U \leq 4V / I \leq 100mA$
- The parameter combinations investigated are given in Table 4.

3.2 Results

3.2.1 Terminal material and dimension

Impact of the conductivity of the terminal and spring material is shown in Fig. 3. Change of the base and spring material to higher conductive material reduces the median resistance by approx. $0.4m\Omega$, but still exceeds the critical $2m\Omega$ limit. Increasing the thickness of the terminal and spring material by 20% reduces the median value of the resistance by approx. $0.3m\Omega$. C11000 has

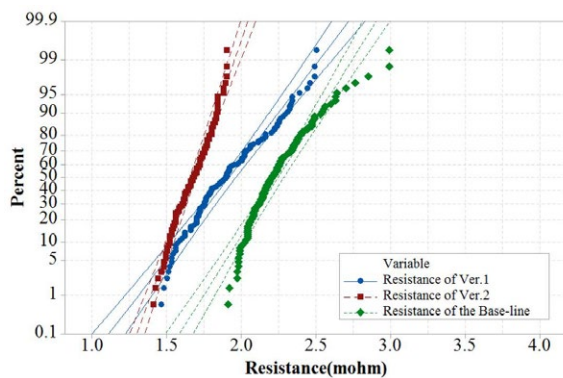


Fig. 3: Impact of Terminal and spring material and thickness of material C11000/C15100 compared with C18045. Thickness 0.1 and 0.12mm

the best conductivity. However, processing during stamping, contact riveting and over-molding were difficult due to the softness of the material, so C11000 was excluded from further investigations.

3.2.2 Contact material

The optimum contact material for the TCO application must provide the lowest possible resistance, ideally a

very narrow distribution and provide stable contact resistance during the lifetime of the device. In Fig. 4 the distribution of the contact resistance of the 3 contact materials taken into consideration is presented. AgNi10 offers the narrowest resistance distribution, but lower conductivity of AgNi10 and higher median value than the AgNi0.14 and AgNi0.15 alloys. Although AgNi0.14 and AgNi0.15 show lower contact resistance, the distributions are not very favourable and show a double-peak. 25% of the AgNi0.15 and 5 % of the AgNi0.14 contact resistance measurements showed a different characteristic than the remaining values. The results indicate that AgNi0.14 and AgNi0.15 provide lower resistance, but for the price of a higher contact resistance variation. The results achieved are unacceptable for the application in TCO's.

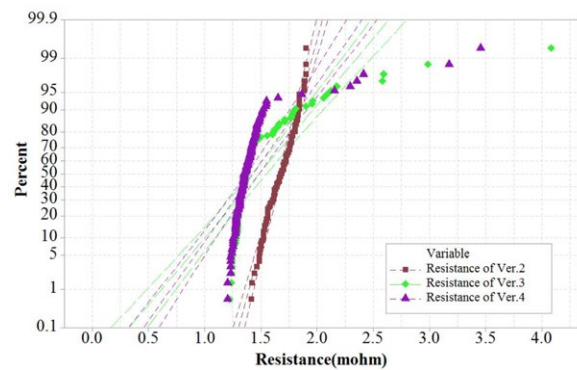


Fig. 4: Impact of contact material (AgNi10, AgNi 0.15, AgNi0.14). Contact force 23cN

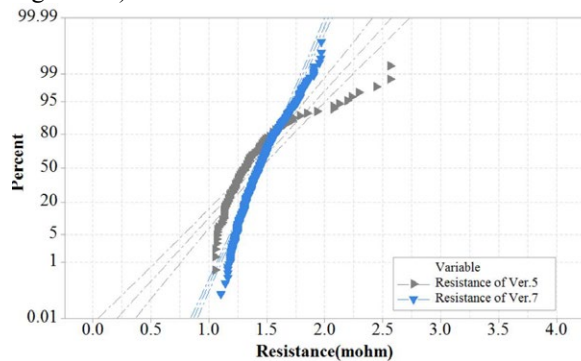


Fig. 5: Impact of contact material (AgNi0.14 - AgNi0.14, AgNi10 - AgNi0.14). Contact force 30cN

As the symmetric contact material arrangements did neither provide the required absolute value of contact resistance, nor the required narrow distribution, the lower resistance of AgNi0.14 and the higher stability of AgNi10 were combined in an asymmetric arrangement, and the contact force was increased to 30cN. The results are given in Fig.5 and provided the results needed. The asymmetric arrangement gives a low median value of resistance and a narrow resistance distribution.

Asymmetric contact material combinations have the potential disadvantage that the resistance and the

switching performance might have a polarity dependence. Fig.6 show the resistance distribution

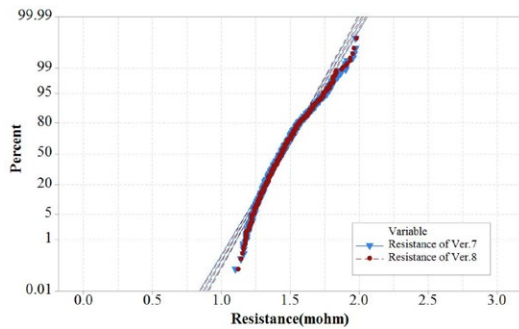


Fig. 6: Impact of contact material - Polarity AgNi10-AgNi 0.125, AgNi0.125- AgNi10. Contact force 30cN.

3.2.3 Contact Force

For Ag based contact materials, higher contact force would always be an advantage when very low contact resistance values are needed. Theoretically a contact force of at least 25cN is necessary to achieve the required contact resistance of 1mΩ. In miniaturized designs, higher contact force is quite difficult to achieve and contradictory to the smaller size of the device. In Fig.7 the impact of the contact force – 30 and 36cN - to the resistance distribution is given for AgNi0.14 symmetric and the asymmetric AgNi0.14 – AgNi10 combination.

For the symmetric AgNi0.14 arrangement (Ver.5 and 6), there is a positive impact on the 20% higher contact force, but the resistance distribution is still not improving significantly and showing resistance values higher than 2mΩ. For this contact material the higher contact force would not solve the problem (Fig.7).

For the contact material combination AgNi0.14 – AgNi10 (Ver. 7 and 9), there is minor reduction of the contact resistance, but the impact of the increase of contact force is not as big as the choice of the contact material combination.

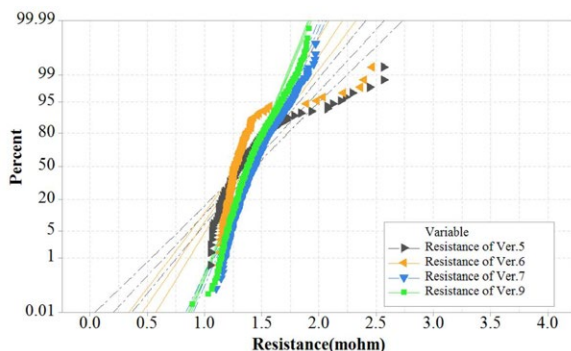


Fig. 7: Impact of contact force. AgNi0.14 symmetric, AgNi10-AgNi0.14. Contact force 30 and 36cN.

3.3 Long term stability

Out of the 9 versions, the versions with the best results in long-term stability of the resistance were further investigated. As the overall device performance at a contact force of 30cN was better than at 36cN, the long-term stability tests were focusing on Ver.7.

Long term stability was judged with following tests

- Vibration
 - Test parameters:
 - Sine-wave
 - Amplitude: 1.5mm
 - Frequency: 10Hz – 55Hz – 10Hz in 1 minute
 - Directions: X, Y, Z
 - Duration: 2 hours in each direction, totally 6 hours
 - Robustness during welding
 - Leads are attached with a laser welding process, with significant external force going to the TCO
 - Long term storage
 - 23°C
 - 85%rH/60°C

3.3.1 Vibration

All TCO's will experience vibration during the life of the component, during transportation as well as during use in the mobile devices. The results of the vibration test are given in Fig.8. The results before and after vibration are almost identical and way below the requested 2mΩ limit.

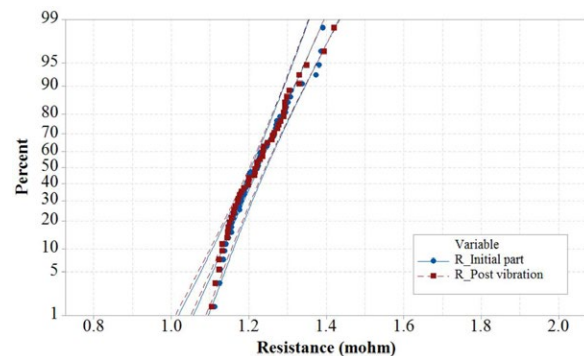


Fig. 8: Contact resistance distribution before and after vibration test (Ver.7).

3.3.2 Robustness during welding

When TCO's are assembled to the battery pack of a mobile device, the first step is welding Nickel leads to the terminals of the device (Fig.9). During the laser welding process, the TCO is subjected to significant mechanical force and heat.

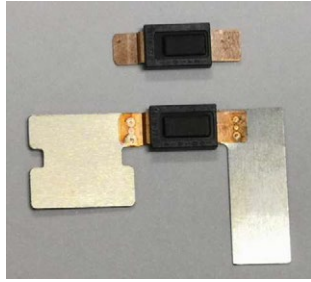


Fig. 9: Impact of welding process on Contact resistance stability

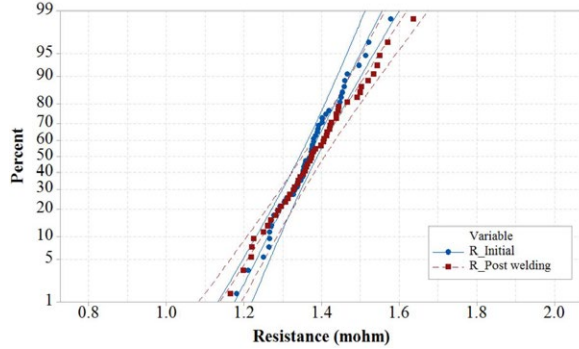


Fig. 10: Impact of welding process on Contact resistance stability

3.3.3 Long time storage

In **Fig. 11** and **12**, the results for long term storage at room temperature and at 85%rH/60°C are presented. For both test conditions no change of resistance can be observed. Resistance is well below the limit of 2mΩ, stable and well-distributed.

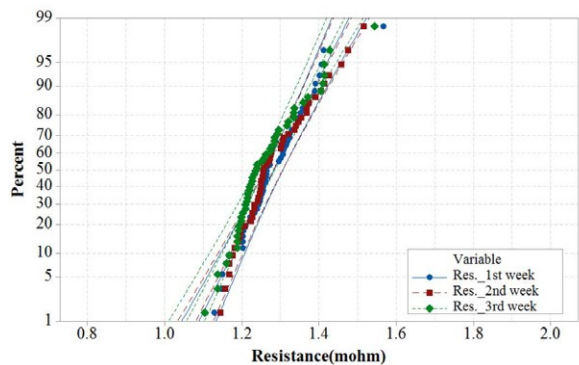


Fig. 11: Contact Resistance stability during long time storage at 23°C

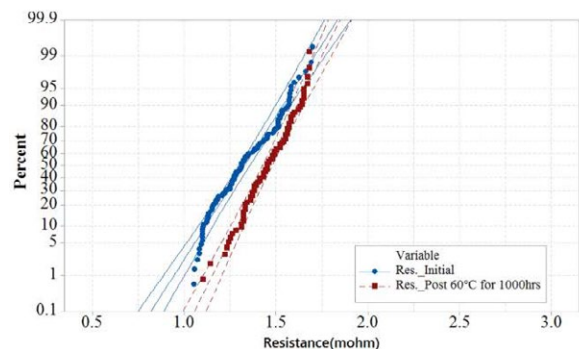


Fig. 11: Contact Resistance stability during long time storage at 85%rH/60°C for 1000hrs

3.4 Discussion

When contact systems with very low resistance are required in small designs, silver-based contacts are the only cost-effective approach. When the voltage applied is relatively low, the contact force cannot be increased due to the size of the device, and the requirements are high as described for TCO's, all optimization opportunities must be considered to achieve a technical and commercially reasonable solution.

For highly reliable solutions, the contacts must be protected from environmental influences, whereas a tight housing is sufficient for most applications under normal conditions. Optimum contact shape and a relative movement during contact closing is important. In this paper the effect of contact material and contact force was investigated.

Theoretically a contact force of >25cN is required to achieve a contact resistance of <1mΩ. The results show the positive effect of a higher contact force to achieve a low contact resistance with minimum variation, but the effect is by far not as big as the selection of the optimal contact material **Fig.4, 5 and 7**.

While AgNi10 showed very stable resistance values (**Fig.3, 4 and 5**) with low variation, it is very difficult to achieve very low contact resistance values with the force budget available for the TCO design, due to reduced conductivity of AgNi10.

AgNi0.14 and AgNi0.15 showed the lowest median values of the resistance, but always a few outliers were observed (**Fig. 4, 5 and 7**). This is caused by locally excess Ni which was precipitated along the grain boundaries. This excess Ni is oxidizing and results in higher contact resistance values. This effect was not observed on AgNi10, where the Ni is dispersed in the silver matrix.

Best results were achieved when the advantages of AgNi10 and AgNi0.14 were combined. The asymmetrical combination provided the stability of AgNi10 and the low resistance of AgNi0.14. This system showed very good results at the force available (30cN) and during all storage and aging tests (**Fig.6, 7, 8, 10 and 11**).

4 Summary

Detailed investigations were performed to design and test a silver-based contact system for a mini resettable thermal cut off device. To achieve low and stable contact resistance of less than 2mΩ, the following findings were implemented in the design of the TCO:

- Contact force should be as high as possible. Based on the size of the design, 30cN was the highest force possible to achieve overall good device performance and good manufacturability.
- Lowest conductivity contact material provides the lowest median contact resistance, but not the best distribution. AgNi0.15 and AgNi0.14 have the tendency to have outliers in the resistance distribution,

which makes these materials less suitable for stable resistance requirements.

- For AgNi0.15, the Ni content has a major impact on resistance stability. Reducing the Ni content only by 0.01% improves the contact resistance stability.
- Best compromise between low and stable resistance was achieved by an unsymmetrical contact system with a fixed contact made from AgNi0.14 and a moveable contact made from AgNi10.
- Contact Resistance during application testing and long-term storage was stable.

Overall it was shown that a silver-based contact system can be applied in a low voltage and low power application by optimizing contact force, protecting the contact system well from environmental impacts and optimizing the contact material. The required low contact resistances of less than 2mΩ with very low resistance variations can be achieved.

5 Literature

- [1] IDC Report August 2018
- [2] MHP Datasheet, <https://www.littelfuse.com/products/battery-mini-breakers/metal-hybrid-protection/mhp-tac.aspx>
- [3] Protecting Rechargeable Li-Ion and Li-Polymer Batteries, Littelfuse, https://www.littelfuse.com/~media/electronics/application_notes/littelfuse_protecting_rechargeable_li_ion_and_li_polymer_batteries_in_consumer_portable_electronics_application_note.pdf
- [3] P. Slade (editor): Electrical Contacts – Principles and Applications, Marcel Dekker Inc., 1999
- [4] E. Vinaricky (Hrsg.): Elektrische Kontakte, Werkstoffe und Anwendungen, Springer Verlag Berlin, 2002.
- [5] AMI DODUCO Data Book of Electrical Contacts, 2010.
- [6] W. Johler: Einsatz von Silber und Werkstoffen auf Silberbasis für Kontakte bei niedrigen Kräften und Spannungen, Literaturbericht TU Wien (1984), 29S.
- [7] W. Johler: Zuverlässigkeit von Silberkontakten mit und ohne Hauchvergoldung im Kleinlastbereich, Dissertation TU Wien, 1988, 67S.
- [8] W. Johler, W. Rieder, T. Strof: Untere Einsatzgrenzen für Kontaktwerkstoffe auf Silberbasis, 10. VDE Seminar Kontaktverhalten und Schalten“, Karlsruhe, VDE Fachbericht 40 (1989) S. 61-70.
- [9] W. Rieder, T. Strof: Relay Lifetests with Contact Resistance Measurements after each Operation, Proc. IEEE Holm Conference 1990, pp. 73 – 78.
- [10] J. Munies, J.Y. Mousson: Effect of Measurement on low Level Contact Resistance, Proc. Holm Conference on Electrical Contacts, 1983, pp.165-168.
- [11] N.B. Jemaa: Contacts Conduction and Switching in DC Levels, Proc. IEEE Holm Conference 2002, pp. 1 – 15.
- [12] M. Hasegawa, T. Yamamoto, K. Sawa: Significant Increase of Contact Resistance of Silver Contacts by Mechanical Switching Actions; Proc. Holm conference 1991, pp. 176 – 182.
- [13] R.D. Malucci: The Effects of Whipe on Contact Resistance of Aged Surfaces, IEEE Holm Conference 1994, pp. 131 – 144.
- [14] J. Urbig: Kontaktwiderstände an ruhenden Kontakten in Abhängigkeit von der Kontaktkraft und von der Zeit, Nachrichtentechnik- Elektronik 24 (1974) S. 305 - 307.
- [15] H. Brun, W. Johler, A. Windisch: Reliable Switching of Minimum Contact Loads, Proc. Proc. 53rd Relay and Switch Technology Conference, 2005, pp. 15-1 – 15-12.
- [16] UL 2055, Standard for Household and Commercial Batteries, Ed. 2, 2004.
- [17] J. Weiser: Elektrische Kontakte in Kleinschaltern und Relais, 7. VDE Seminar Kontaktverhalten und Schalten, Karlsruhe, 1983 S. 1 – 13.

Research on the Corrosion Phenomenon of Iron Parts in the Internal Micro-environment of Relay

Qingxing Su, Changliu Jiang, Ningyi Lu, Lei Yi
Xiamen Hongfa Electroacoustic CO., LTD, Xiamen, 361021, China
E-mail: suqingxing1120@126.com

Abstract

With the higher reliability of relay products, more attention has been paid to the influence of varied micro-environment caused by the production of arc during the operation. In this paper, the corrosion phenomenon of iron parts of relays after electrical life test has been analyzed. It is confirmed that the formation of acidic substances is the primary cause of the corrosion of iron parts. Here the acidic substances are the reaction production of water vapor (H_2O) and compounds of nitrogen and oxygen (N_xO_y) produced in air under the action of arc. According to the corrosion mechanism, the various internal micro-environment of relays during the electrical life test has been simulated, and a rapid method for the evaluation of the corrosion resistance of the iron parts has been carried out.

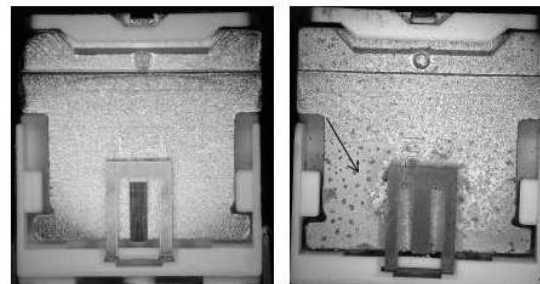
1 Introduction

Metal corrosion refers to the deterioration caused by chemical changes in the environment. According to the reaction mechanism, metal corrosion can be classified as chemical corrosion and electrochemical corrosion. Chemical corrosion is based on chemical reaction in dry atmosphere or non-electrolyte environment. Electrochemical corrosion is based on the formation of two electrodes of metal and electrolyte to form corrosive primary battery. Metal corrosion can be classified as localized corrosion and total corrosion according to its morphology. Localized corrosion forms of spot corrosion, galvanic corrosion, crevice corrosion, abrasion corrosion, etc. The mechanisms of different corrosion forms are different^[1]. The causes of metal corrosion include environmental factors (external factors) and material factors (internal factors).

Xiaofeng Zhu^[2] analyzed that the main reason for the corrosion of relay components in the switch box is the high temperature and high humidity. The most important factor affecting the corrosion of metal is humidity. Chongfeng Liang^[3] analyzed the harm of humidity to electrical equipment and the corrosion mechanism in humid environment. Kai Liu^[4] analyzed the harm of condensation in terminal box to power equipment corrosion, and studied the condensation mechanism.

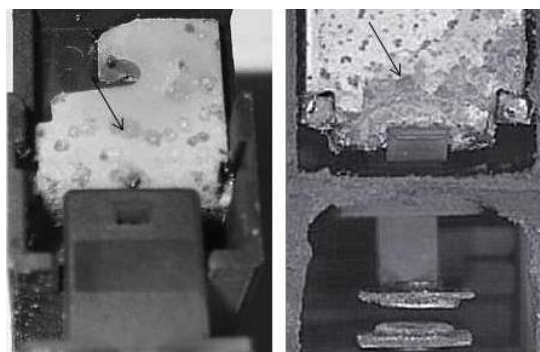
The corrosion of the iron parts in relay to a certain extent will bring harm to the relay as Fig.1. It will affect the appearance of the relay, resulting in the reduction of the over travel (OT) and the excessive actuation voltage. With the higher reliability of relay products, people pay more and more attention to the influence of varied micro-environment caused by the

production of arc during the operation. Therefore all important parameters have to be taken into consideration to get a full and complete understanding of the problem.



(a) Not corroded iron of Relay A1

(b) Corroded iron of Relay A2



(c) Corroded iron of Relay B

(d) Corroded iron of Relay C

Fig.1 Different relay corrosion after electrical life test

In this paper, through the systematic analysis of the corrosion form and composition of iron parts in relay after the electrical life test, we confirmed that the formation of acidic substances is the primary cause of the corrosion of iron parts. The acidic substances are the reaction production of water vapor (H_2O) and N_xO_y produced by N_2 and O_2 in a relay

under the arc action. According to the corrosion mechanism, the various internal micro-environment of relays during the electrical life test has been simulated, and the fast evaluation method of the corrosion resistance of the iron parts is explored.

2 Test method

After electrical life test of the relay samples from different quality of iron parts, the corrosion type, products and content were analyzed by SEM-EDS, FT-IR, ICP-OES, IC and other instruments. In order to further accelerate the corrosion resistance of different iron parts, the fast evaluation method of corrosion resistance of relay iron parts is discussed by using the combined testing environment of different temperatures and humidity.

2.1 Analysis of the components of corrosion products

2.1.1 SEM-EDS analysis of corrosion on relay iron surface

As shown in Fig.2, SEM-EDS detected higher content of N and O and lower content of Ni in the serious corrosion area (position 1) than that in the slight corrosion area (position 2). In the area of position 3, it is mainly Ni, while N is not founded and the content of O and Fe is a little.

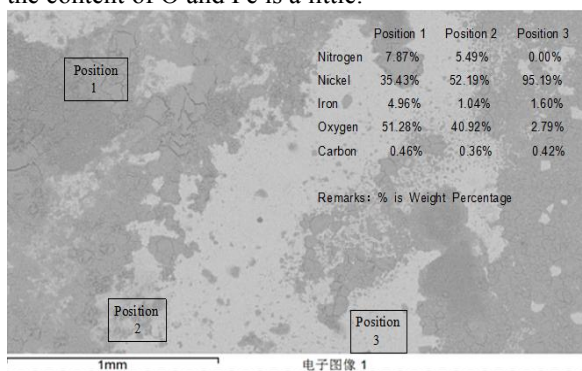


Fig.2 SEM-EDS detected higher content of N and O elements in the corrosion area than in the normal area.

2.1.2 FT-IR analysis of corrosion on relay iron surface

Four relays named A, B, C and D were tested 100,000 operations under the same electrical life condition (NO contacts, 250Va.c., 16A, $\cos\Phi=0.75$, 1s ON: 9s OFF). As shown in Fig.4, there were obvious peaks near the infrared spectrum 1350 cm^{-1} on the surface of armature of A, B and C. It was inferred that these relays contained nitrate. However, no obvious corrosion was found on the armature surface of relay D, and no obvious peak was found near the infrared spectrum 1350 cm^{-1} . It was inferred that the armature surface contains very small amount

of nitrate if not absent. The results of the infrared spectrum 1350 cm^{-1} at the corrosion site of relay iron parts are consistent with the results of SEM-EDS which has the higher content of N and O.

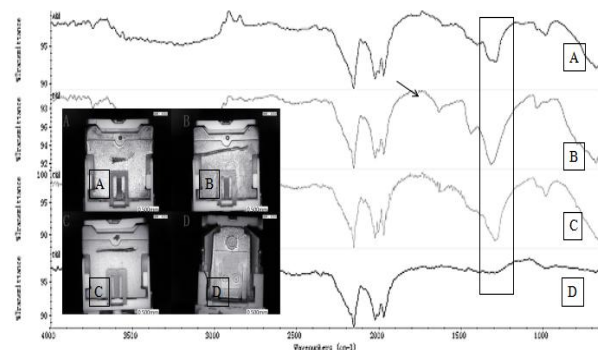
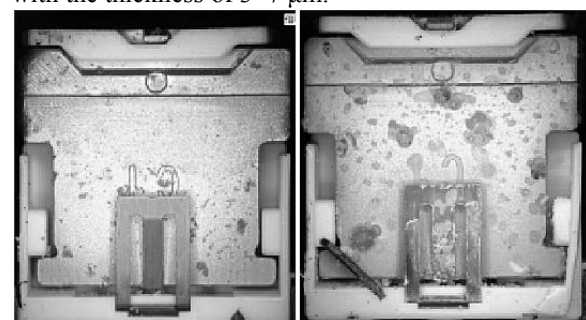


Fig.3 There are obvious peaks near 1350 cm^{-1} in the corrosion site where may contains nitrate by FT-IR.

2.1.3 ICP-OES analysis of corrosion on relay iron surface

Put relay E (Fig.4. a) and F (Fig.4. b) armature after electrical life test (NO contacts, 250Va.c., 16A, $\cos\Phi=0.75$, 1s ON: 9s OFF) into a clean beaker. Add ultra pure water to a certain scale. Vibrate and clean the corrosion products of armature surface by ultrasonic cleaning equipment. Transfer the corrosion solution to the volumetric flask and filter it. Analyze the content of Ni, Cu and Fe in the filtered corrosion solution by ICP-OES. There are more content of Ni, Cu and Fe in serious corrosion of Relay F armature than that in slight corrosion of Relay E as shown in Fig.4.

The matrix materials of armature of relay E and F is Fe. The inner layer coating is Cu with the thickness of $1\sim 3\ \mu\text{m}$. The outer layer coating is Ni with the thickness of $3\sim 7\ \mu\text{m}$.



(a) Relay E	(b) Relay F
Electric life 100,000 times	Electric life 100,000 times
Slight corrosion	Serious corrosion
Ni: 0.36 mg/l	Ni: 2.28 mg/l
Cu: 0.12 mg/l	Cu: 0.36 mg/l
Fe: N.D.	Fe: 0.06 mg/l

Fig.4 Analysis concentration of Ni, Cu and Fe in the solution of armature surface corrosion by ICP-OES.

2.1.4 IC analysis of anionic concentration in the solution of iron corrosion products

Higher concentration of NO_x^- (NO_3^- and NO_2^-) was detected in relay F than relay E as shown in Fig.5. While NO_3^- and NO_2^- were not detected in the corrosion solution of relay G without electrical life test. After 100,000 operations under the same electrical life test of relay H from competitor, there is no obvious corrosion on the surface of iron parts, but 1.45mg/l NO_x^- was detected in the iron corrosion solution. It was shown that the production of nitrogen oxides (NO_x) is related to the electrical life test. The armature of relay H from competitor is plated with Ni with the thickness of 3~7 μm . The obvious difference between competitor iron and the iron in E、F or G is that the former has very few Si (<50 $\mu\text{g/g}$), but the latter has excessive Si (1000~2000 $\mu\text{g/g}$). The excessive Si may aggravate the grain boundary corrosion of iron parts.

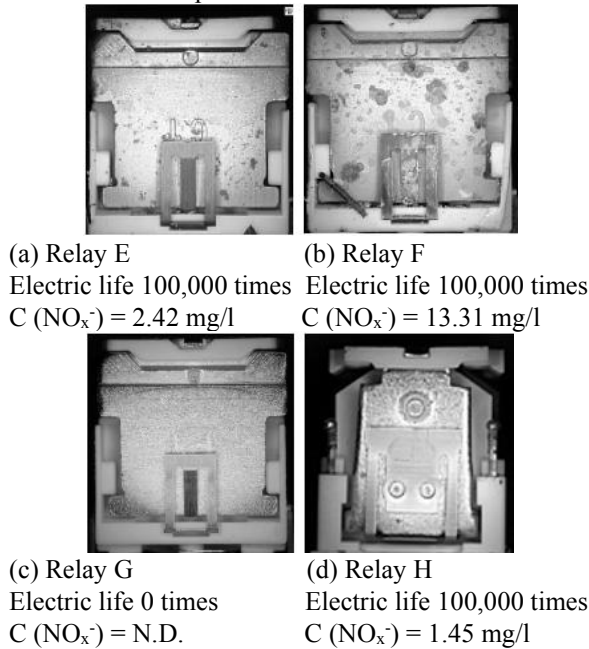


Fig.5 IC analyses anionic concentration in solution of iron corrosion products from different relays

2.2 Electrical life test of different temperatures and humidity

The same batch of relays were put into three different temperatures and humidity for electrical life test to 100,000 times. The results show that the corrosion degree of iron parts is the most serious in high humidity as Fig.6.

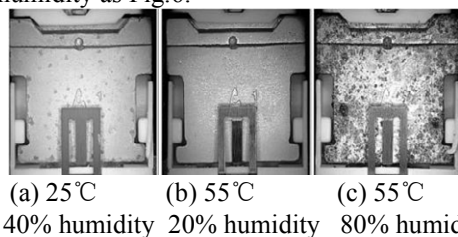


Fig.6 Life test in different temperatures and humidity

3 Results and discussion

3.1 Discussion on the form of corrosion products of iron

3.1.1 Iron corrosion is divided into five categories according to the severity

Observe the relay after electrical life test according to the corrosion degree of iron surface from light to heavy (Fig.7). Corrosion can be divided into five categories according to severity: no corrosion (Fig.7.a) → beginning corrosion (Fig.7.b) → light corrosion (Fig.7.c) → medium corrosion (Fig.7.d) → heavy corrosion (Fig.7.e).

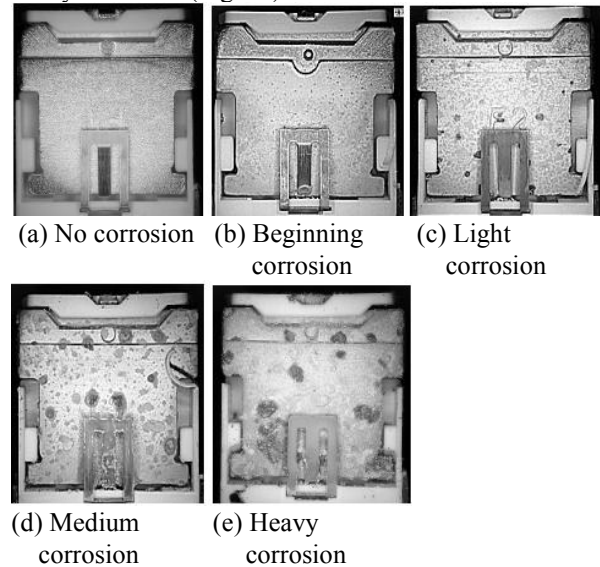
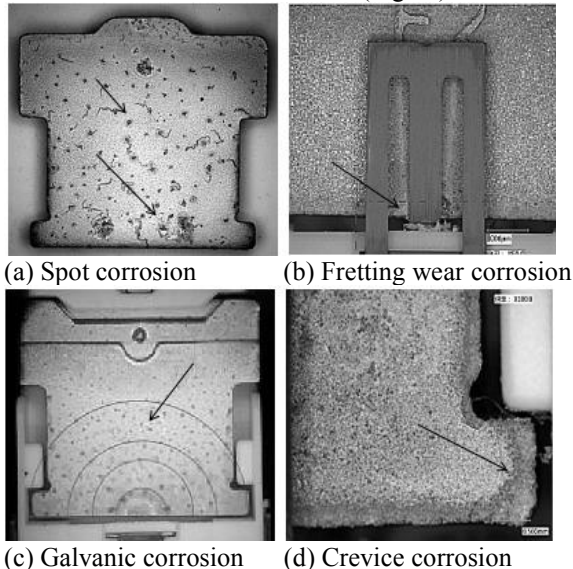


Fig.7 The photograph of the corrosion according to severity

3.1.2 Classification of iron corrosion according to micro mechanism

The metal corrosion can be divided into spot corrosion, fretting wear corrosion, galvanic corrosion, crevice corrosion and other types. Spot corrosion focuses on a small area of metal surface and penetrates into the metal interior^[1]. Spot corrosion usually starts from a defective part of the metal material, then the loss of metallic luster → localized spot corrosion → spot corrosion gradually spread → comprehensive corrosion. Fig. 8a shows the spot corrosion morphology. Fretting wear corrosion is the result of the synergistic effect of fretting wear and corrosion as Fig. 8b. Fretting refers to the relative movement with periodic small amplitude, then micropores or spots appear on the surface of metal coating. In addition, the corrosion of corrosive substances makes the fretting wear position susceptible to produce more corrosion. Galvanic corrosion is also known as contact corrosion or dissimilar metal corrosion. When two different metals or alloys are in contact, the corrosion rate of the metal with a negative potential in the solution increases (armature plated

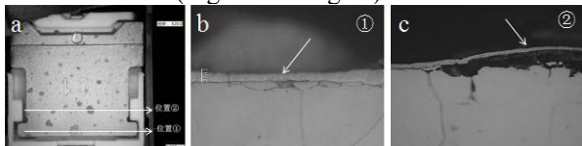
with Ni, anode), while the metal with a positive potential is protected as cathode in compression spring (Fig.8c). Crevice corrosion is a form of localized corrosion, which occur at the joint of metal and metal or metal and nonmetal (Fig.8d).



(a) Spot corrosion (b) Fretting wear corrosion
(c) Galvanic corrosion (d) Crevice corrosion
Fig.8 Morphology of different corrosion mechanism

3.1.3 Spot corrosion is the main form of localized corrosion of relay iron parts

44 relays out of 50 with the corrosion form were spot corrosion. It is indicated that spot corrosion is the main form of localized iron corrosion. The Ni plating layer under the armature corrosion position of the relay with spot corrosion became thinner (Fig.9b), and Fe matrix was corroded (Fig.9c). The corrosion extends along the metal grain boundary to the depth of the iron base (Fig.9b and Fig.9c).



(a) Corrosion morphology of the armature surface of Relay I after electrical life test (NO contacts, 250 Va.c., 16 A, cosΦ = 0.75, 1s ON: 9s OFF).
(b) The Ni coating at position ① became thin.
(c) The Ni coating at position ② became thin and bulged.

Fig.9 Corrosion morphology of the relay iron section

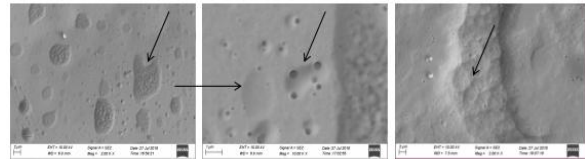
3.1.4 Discussion the production condition of spot corrosion of relay iron parts

When the iron coating is damaged due to defect (Fig.10), spot corrosion will occur on the metal with cathode coating on the surface, such as Ni coating of iron parts. Then the iron matrix under the damaged area and the undamaged area of iron coating will form a activation-deactivation corrosion cell. The deactivation surface (iron coating) is a cathode, and the area is much larger than the activation area. The

corrosion develops to the deep iron matrix and forms small holes.

Spot corrosion also occurs in the medium with special ions, such as uneven adsorption of NO_3^- and NO_2^- compounds on the surface of iron parts^[1].

Spot corrosion also occurs above a critical potential, which is called spot corrosion potential. When the iron parts are in corrosion solution and the corrosion potential exceeds the spot corrosion potential, uniform spot corrosion will occur.

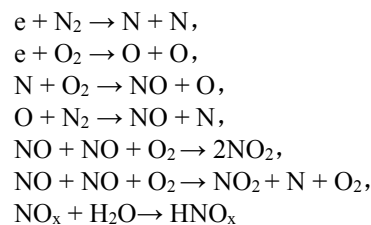


(a) Corrosion on iron surface (b) Surface holes of iron parts (c) Surface pits of iron parts
Fig.10 Corrosion and defects on the surface of iron

3.2 Discussion on the composition of corrosion products of iron parts

3.2.1 The mechanism of HNO_x produced by lightning

HNO_x is one of the main sources of acid rain^[5]. A large number of authors have done a lot of analysis and research on the mechanism of HNO_x produced by lightning^[6]. The main chemical reaction theories are as below^[7]:



3.2.2 Discussion on the mechanism of HNO_x produced in relay

For the relay, the arc is similar to the lightning in the atmospheric environment. But the relay cavity is relatively small, so the concentration of NO_x and HNO_x generated inside relay may be relatively large.

The results of SEM-EDS, FT-IR, ICP-OES and IC analysis of the corrosive products further confirmed that: under the action of relay arc, the N_2 and O_2 of internal relay will produce NO_x , and generate HNO_x with internal environment moisture. The main corrosion type of relay iron parts after the electrical life is the electrochemical corrosion reaction between the Ni coating and HNO_x .

The causes of iron corrosion have external environmental factors and internal material factors. The following is a brief discussion.

3.3 Discussion on the environmental factors affecting corrosion of iron

3.3.1 The relationship between corrosion rate of iron and the thickness of water film on the surface

Water can react with NO_x to produce HNO_x , but also provide a medium for iron corrosion. When the relay works and the surrounding humidity is high, the water film is easy to form on the surface of the iron parts, because the temperature difference inside the relay will change. The relationship between the corrosion rate of iron parts and the thickness of water film formed on the surface is shown in Fig.11^[8]

In zone I, there are several molecular layers of adsorbed water film on the metal surface, the thickness of which is less than 10nm. No continuous electrolyte is formed, and the corrosion rate of metal is very low.

In zone II, when the humidity exceeds the critical value, the thickness of the water film on the metal surface is between 0.01 μm and 1 μm . Due to the rapid diffusion of oxygen, the corrosion rate of the metal is multiplied.

In zone III, with the further increase of water film thickness, a visible liquid film will be formed. At this time, due to the barrier of the liquid film, the diffusion of oxygen becomes difficult, so the corrosion rate of the metal is correspondingly reduced.

In zone IV, when the thickness of water film increases gradually to form water drop, the thickness of water film is more than 1 mm. The corrosion rate is similar to that of metal immersed in liquid.

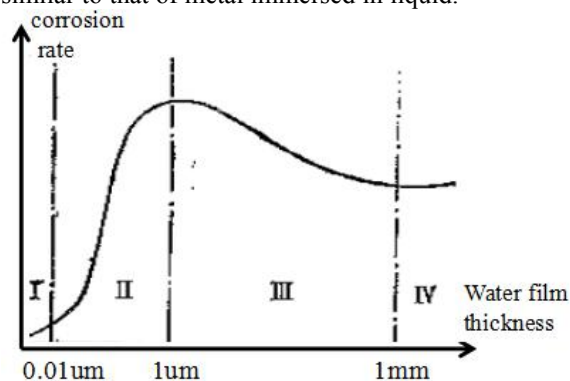


Fig.11 Relationship between thickness of water layer on metal surface and corrosion rate^[8]

When the thickness of water film on the surface of the iron parts is in the area II and III, the iron are prone to corrosion. At this time, the corrosion speed is related to the thickness of the water film. Therefore, the analysis of relay iron environment can further promote understanding corrosion of relay iron parts.

3.3.2 Discussion on the mechanism of increasing iron corrosion in high humidity environment

When water molecules are adsorbed on the surface of the iron parts, they can react with water chemically. At this time, the condensation of water on the surface of iron is called chemical condensation. When the relative humidity is between 70% and 80%, HNO_x will agglomerate on the surface of iron and react with Ni coating. The formation of electrolyte nickel nitrate aggravates the corrosion of iron parts.

When the relative humidity of metal storage environment is lower than its critical value, the temperature has little effect on the corrosion rate. However high the temperature is, because the environment is dry, the metal is not easy to corrode. When the relative humidity reaches the critical value of metal corrosion, the influence of temperature plays a significant role. At this time, when the temperature increases by 10 $^{\circ}\text{C}$, the corrosion rate increases by about two times^[3].

The main effect of temperature is that cause condensation on the metal surface and accelerate the corrosion, when the temperature is greatly reduced. Large temperature difference between day-night and in-outdoor temperature will make the condensation happen. If the condensation happens periodically, iron parts will corrode seriously, when not coated properly.

3.4 Discussion on material factors affecting corrosion of relay iron

3.4.1 Discussion on spot corrosion resistance of iron coating

Spot corrosion occurs above a critical potential, when the iron parts are in the corrosion solution. The corrosion potential exceeds the spot potential, uniform spot corrosion will occur. When two different metals contact, the corrosion rate of the metal with negative potential increases, while the metal with positive potential is protected.

For the common coating of relay iron parts, the potential of Cu electrode is +0.337, Sn is +0.007, Ni is -0.25, Fe is -0.44. Cu is relatively the most positive, and the corrosion resistance is the strongest, followed by Sn, Ni, and finally Fe. Therefore, generally, the outer layer of Cu plated iron parts has strong corrosion resistance.

3.4.2 Discussion on the influence of defects of iron coating on corrosion

There are quality defects on the surface and inside the coating of some iron parts (Fig.12). These defects will weaken the protection ability of the coating and cannot effectively prevent the oxygen and water in the air from being immersed. For example,

the high humidity environment discussed in the previous will accelerate the corrosion of iron parts. In addition, the nitric acid compound produced during the operation of the relay will agglomerate on the surface of the iron parts, and the corrosion will occur first at the defective part of the coating.

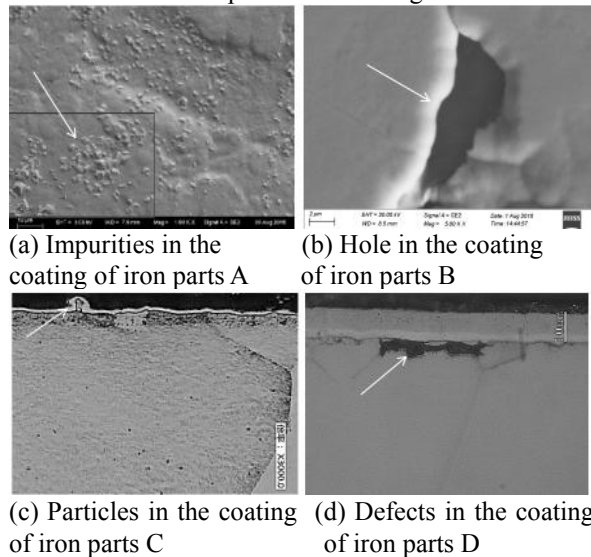


Fig.12 Defects in the coating quality of iron parts

3.5 Discussion on evaluation method of coating quality of iron parts

The internal micro-environment of relay is complex, so a constant test environment is needed to evaluate the corrosion resistance of iron coating.

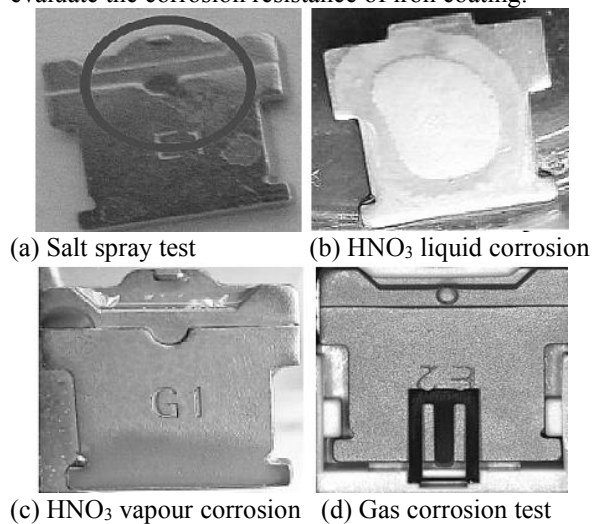


Fig.13 Comparison of evaluation methods for coating quality of relay iron parts

Salt spray test method (Fig.13 a), in which the mechanism of Cl^- corrosion of iron parts is completely different from that of HNO_x corrosion. The speed of nitric acid liquid corrosion of iron parts is fast (Fig.13b), but the method belongs to comprehensive corrosion, and there is no small difference in corrosion. The speed of HNO_3 vapour is fast (Fig.13c), but the temperature and humidity are uncontrollable, and the edge of iron parts surface is prone to condense. Gas corrosion test box method is fast, the temperature,

humidity and the concentration of NO_x can be effectively controlled, so the surface of iron parts is uniformly corroded as shown in Fig.13 d.

4 Conclusion

(1) The observation of corrosion form shows that spot corrosion is the most important form of iron corrosion, and spot corrosion often occurs on the surface or internal defects of the iron coating.

(2) The analysis of corrosion products shows that the corrosion of relay iron parts after electrical life test is mainly the electrochemical corrosion of Ni coating and HNO_x electrolytic medium. N_2 and O_2 in the relay generate NO_x under the action of arc, and generate HNO_x in combination with water vapor.

(3) The combination test of different temperature and humidity shows that high humidity environment is the most important environmental factor affecting the corrosion of iron parts inside the relay.

(4) The method of gas corrosion test chamber to evaluate the quality of iron coating is effective.

5 Literature

- [1] Dejun Yang , Zhuoshen Shen. Metal corrosion [M]. Beijing: Metallurgical Industry Press, 1999.
- [2] Xiaofeng Zhu, Weihua Tang, Hanlin Liu. Study on corrosion mechanism of siemens series knife switch relay and moisture-proof treatment of mechanism box [J], science and Technology Plaza, 2015, 10 (13): 50-59.
- [3] Chongfeng Liang, Wei Wang, Tao Yang. Discussion on key problems of moisture-proof electrical equipment [J]. Clean and air conditioning technology, 2012, 12 (4): 8-12.
- [4] Kai Liu, Gongze Zhang. Discussion on formation mechanism and prevention measures of condensation in terminal box of substation [J]. Journal of Jiangxi Electric Power Vocational and technical college, 2014, 27 (3): 2014.
- [5] Junjun Zhou, Xiushu Ying. The mechanism of NO_x produced by lightning and the estimation of NO_x produced by lightning in inland China [J]. Plateau Meteorology, 2002, 21 (5), 501-506.
- [6] Ping Yuan, Xueyan Zhao. Theoretical study on NO production by lightning [J]. Journal of Northwest Normal University, 2009, 45 (3), 33-36.
- [7] Feifei Wang, Shuran Li, et al. NO_x produced by arc discharge and its oxidation to ammonium sulfite [J]. Journal of environmental engineering, 2015, 9 (1), 281-285.
- [8] Yingjun Pan, Heng Zhang, Jing Liu. Materials environment [M]. Metallurgical Industry Press, 2004.

Reliability Improvement of Gold Plated Contacts in Card Edge Connector of Power Cabinet

Yilin Zhou Mengqing Wang Nan Tian Yunjie Shi
Beijing University of Posts and Telecommunications, Beijing 100876, China
ylzhou@bupt.edu.cn

Abstract

A power cabinet adopts an electric contact structure between the gold fingers on printed circuit board (PCB) and the card edge connector to transfer the current with dozens to hundreds of amperes. The wear of the gold plating on the contacts during insertion and withdrawal causes the degradation of the contact resistance due to the oxidation of non-noble underplating and substrate materials especially under a relatively high temperature environment. Therefore, it is of great significance to improve the sliding wear resistance of the gold plating so as to prevent corrosion and improve the long-term reliability of card edge connectors. In this paper, through sliding simulation and orthogonal experiments, the influences of the thickness of gold plating on both sides of contacts, the types of substrate copper alloy, the normal force, the ambient temperature and the sliding cycles on the sliding wear were studied. The influence of the corroded products in the wear tracks of gold fingers on PCB on electrical contact reliability was studied by the repeated sliding tests after accelerated temperature and humidity tests of the worn contact pairs. The design and usage suggestions on the material selection and working conditions were put forward for the contacts between the gold fingers on PCB and the card edge connector in the power cabinet.

Keywords—gold plating; card edge connectors; gold fingers on PCB; reliability

1 Introduction

The power cabinet of communication equipment undertakes the function of converting high-voltage AC input to DC output with low-voltage and high-current. There are two commonly used board-to-board electric connection methods between the functional circuit boards and the backboard with current input in the power cabinet. One is the power blade connector welded on the circuit boards; the other is the electric connection between the gold fingers on the PCB and the card edge connector on the backboard. The power blade connectors have many advantages, such as high reliability, low insertion and withdrawn force, high carrying current, but this kind of connector takes up more space than the gold fingers on PCB mating with the card edge connector. In order to improve the power per unit volume (power density) of the power cabinet, the gold fingers on PCB and the card edge connector are more frequently adopted to transfer the current with dozens to hundreds of amperes.

For the mating structure of the gold fingers on PCB and the card edge connector, the gold plating on the contacts may be worn during insertion and withdrawal, which causes the degradation of the contact resistance due to the oxidation of non-noble underplating and substrate materials during their service period [1]. If the current-carrying capacity needs to be improved

further, the electric contacts will be exposed in a relatively high temperature environment, which deteriorates the corrosion on the worn contacts. Therefore, it is significant to improve the wear resistance of the gold plated contacts so as to prevent further corrosion and improve the long-term reliability of card edge connectors.

To improve the corrosion resistance of contacts, gold plating was adopted as the finish on the electric contacts, whose thickness was usually 0.4~0.8 μm in the market of electronic connectors, but it was sometimes increased even to several micrometers in harsh environment in the industry [2]. However, limited by the high cost of gold, too thick gold plating cannot be accepted to most applications. It was found that Au/Ni plating has effectively mitigated the bond strength and electrical connect failure caused by the reliability of bond pads [3]. Many researches were carried out to keep the long term reliability of electric contacts with the reduction of gold thickness, such as a NiPdAu (electroless Ni, electroless Pd, and immersion Au) plating combination was selected as an alternative for 0.4 μm electroless Ni and immersion Au with an electroless Au top finish (ENIG+EG) for microelectronic package substrates, which reduced about 85% in Au thickness [4]. To balance the cost, electric performance, and reliability of gold plated socket contact tips and substrate lands, the optimizing the gold thicknesses of substrate lands was studied in the range of 0.06 to 0.4 μm . An empirical model that

relates the contact resistance to mechanical force and plating thickness was derived from the simulation tests [5]. To keep protection ability of thin gold plating on contacts, the wear resistance of gold plating have to be improved, so that the harder contact materials, such as the hard gold, nickel intermediate plating, and hard substrate copper alloy are widely adopted [6]. Some researches show that composite plating with dispersed nanoparticles on a metal matrix has been developed as a new coating technology to improve wear resistance [7]. The previous study showed that the thickness of gold plating on the flat coupons had the most significant effect on the stability of sliding contact resistance compared with the normal force and the thickness of gold plating on the probe with a hemisphere tip during sliding. The sliding life increased linearly with the thickness of gold plating on the coupons, since the source of gold to keep stable contact resistance was the gold plating on the coupons, which was the key factor on sliding contact life. A properly selected medium normal force, such as 1N might supply a longer sliding life comparing with the normal force of 0.5N and 1.5N [8].

For the mating structure of the gold fingers on PCB and the card edge connector, the thickness of gold plating on both contact sides, the substrate materials, the normal force, and repeated mating times decide the endurance life of the gold plated contacts. When the current is increased, higher local temperature will cause oxidation of underplating and substrate exposed from the worn gold plating and the change of relative humidity will also affect the corrosion process [9], which influence the reliability of the connectors in service.

In this paper, the influence of the thickness of gold plating on both sides of contacts, the types of substrate copper alloy, the normal force, the ambient temperature and the sliding cycles on the performance of the gold plated contacts were studied by sliding tests. The environmental reliability of the gold plated contacts was evaluated by repeated sliding tests on the corroded wear tracks of gold plated coupons after accelerated temperature and humidity test of the worn contact pairs. The design and usage suggestions on the material selection and working conditions were put forward for the contacts between the gold fingers on PCB and the card edge connector in the power cabinet.

2 Experimental Design

The electric contact between a gold finger on PCB and a card edge connector is simulated by a coupon and a probe with a hemisphere ($\Phi 3\text{mm}$ diameter). A sliding test system was used to simulate the wipe during the reciprocated insertion and withdrawal between the gold fingers on PCB and the card edge connector. The orthogonal design was adopted to study the influence of the thickness of gold plating on both sides of

contacts, the types of substrate copper alloy, the normal force, the ambient temperature and the sliding cycles on the sliding electrical performance and sliding wear. The effects of the corroded products on electrical contact reliability was studied by two steps. The first step is to accelerate the corrosion of the worn gold plated contacts after sliding tests by an alternating temperature and constantly high humidity test. Then the second step is to carry out the repeated sliding tests on the wear tracks of gold plated coupons after corrosion, and the contact resistance performance can be used to evaluate the long term contact reliability of the gold fingers on PCB and a card edge connector.

2.1 Materials

The substrate material for the probe is beryllium copper, and that for the coupon is pure copper or C18070 copper alloy. C18070 is selected for the comparison with pure copper, which is composed of 0.3%Cr, 0.1%Ti, 0.02%Si, and Cu, and has 85%IACS and hardness of 150-190HV. 2-3 μm nickel is the underplating, which is covered by gold plating for both the probes and the coupons. The thickness of gold plating is selected as 0.38 μm , 0.76 μm , and 1.27 μm . The material information is listed in **Table 1**.

Table 1 The materials of the probes and the coupons

Samples Materials	Probes	Coupons	
	Substrate	BeCu	Cu
Intermediate layer	Ni (2-3 μm)		
Top finish	Au (0.38 μm , 0.76 μm , 1.27 μm)		

2.2 Orthogonal experiment design

According to usual working conditions of card edge connectors in the power cabinet, the contact normal force was set at 50g, 100g, 300g, and the local environmental temperature was set at 25°C, 45 °C, 65 °C respectively. The sliding cycles were considered as 50, 120, and 250. Including the thickness of gold plating on the probes or coupons, there are four influencing factors, so that an orthogonal experimental design with four factors and three levels, $L_9(3^4)$, was used to study the effects of normal force, sliding cycles, thickness of gold plating, and the temperature on the sliding contact resistance and sliding wear, as listed in **Table 2**. Then the range analysis was applied for the rank of the significance.

2.3 Experimental systems

A sliding test system was used to simulate the sliding between the contact pairs, as shown in **Fig. 1**. The sliding distance was 1 cm, the sliding frequency was set at 1Hz. The four-point method was used to measure the sliding contact resistance. The constant current was 100mA, the open circuit voltage was 1V. The

Table 2 Orthogonal experimental design

Levels	Normal force (g)		Cycles		Au Thickness (μm)		Temperature ($^{\circ}\text{C}$)	
	1	2	1	2	1	2	1	2
1	1	50	1	50	1	1.27	1	25
2	1	50	2	120	2	0.76	2	45
3	1	50	3	250	3	0.38	3	65
4	2	100	1	50	2	0.76	3	65
5	2	100	2	120	3	0.38	1	25
6	2	100	3	250	1	1.27	2	45
7	3	300	1	50	3	0.38	2	45
8	3	300	2	120	1	1.27	3	65
9	3	300	3	250	2	0.76	1	25

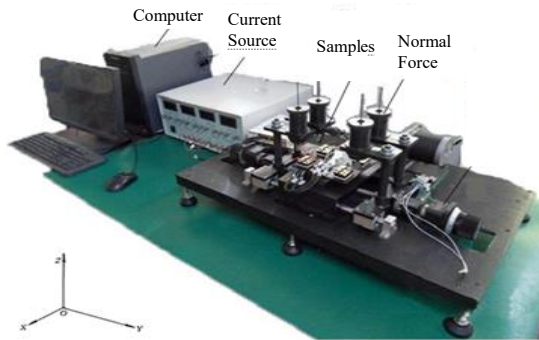


Fig. 1 A sliding test system

sliding contact resistance was tested for 40 times evenly in each sliding cycle, and the average contact resistance of each cycle was used to draw the sliding contact resistance curve. Each experimental condition was repeated by three times.

The wear morphology of both probes and coupons after sliding was taken photos by an optical microscope (OM). The wear tracks on the coupons were measured by a three-dimensional profiler to gain the depth and width of the wear tracks, then the cross section area can be calculated to evaluate the wear resistance.

A programmable temperature and humidity test chamber was used for the accelerated corrosion of worn connectors to simulate the service of the connectors in the fields. The humidity was set at a constant 93%RH, but the temperature alternated between 25 $^{\circ}\text{C}$ and 85 $^{\circ}\text{C}$, as shown in Fig. 2. Alternated temperature can increase the condensation of water on the worn contacts to push corrosion. It takes 8 hours for each cycle, and there are a total of 10 cycles, which is 80 hours.

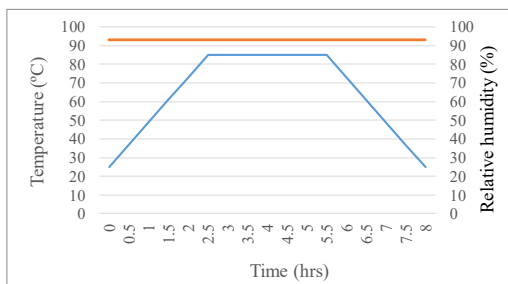


Fig. 2 Temperature and humidity test profile

3 Experimental Results

According to the experimental design in Table 2, three groups of orthogonal experiments were carried out. The group 1 was the combination of four factors, the normal force, sliding cycles, thickness of gold plating on the coupons with copper substrate, and the temperature; the group 2 was the combination of the normal force, the sliding cycles, the thickness of gold plating on the probes, and the temperature; the group 3 was the combination of the normal force, the sliding cycles, the thickness of gold plating on the coupons with the C18070 copper alloy substrate, and the temperature. The sliding contact resistance, morphology of wear tracks, and the wear extent were analyzed respectively for three groups of orthogonal experiments.

3.1 Sliding contact resistance

The sliding contact resistance curves of three groups of orthogonal experiments are shown in Fig. 3-5 respectively. All the sliding contact resistance of these tests are lower than 10m Ω . As the sliding cycles increase, the contact resistance decreases slightly to about 4-6m Ω . It is shown that the sliding contact resistance can keep low and stable within the usual application conditions of card edge connectors in the power cabinet.

3.2 Sliding wear morphology

The morphology of the wear tracks on the probes and coupons in the three groups of orthogonal experiments are shown in Fig. 6-8 respectively. For three groups of the orthogonal experiments, it is seen from each group that as the sliding cycles increase from 50 to 120 and to 250, the thickness of gold plating reduces from 1.27 μm to 0.76 μm and to 0.38 μm , the width and depth of the wear tracks on the coupons are aggravated markedly, such as the condition 1 to 3 in Fig. 6-8. It is obvious that the normal force increasing from 50g to 100g, and to 300g can also deteriorate the wear by comparing the condition 7-9 (300g normal force) with the condition 4-6 (100g normal force) and the condition 1-3 (50g normal force) in Fig. 6-8.

The difference of the test conditions between the orthogonal experiments of the group 1 and the group 2 is the thickness of gold plating. For the group 1, the thickness of the gold plating on the probe is 0.76 μm , but that on the coupon is changeable, with 0.38 μm , 0.76 μm , and 1.27 μm three levels. On the opposite, for the group 2, the thickness of the gold plating on the coupon is 0.76 μm , but that on the probe is changeable, with 0.38 μm , 0.76 μm , and 1.27 μm three levels. By comparing the wear morphologies of the same orthogonal conditions in Fig. 6 and Fig. 7, it is shown that most of the contact pairs in the group 2 have better

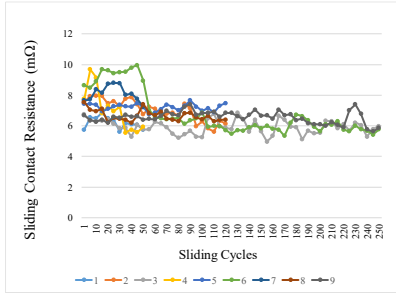


Fig. 3 The sliding contact resistance curves of the orthogonal experiments of the group 1.

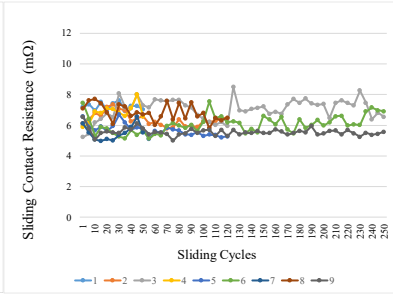


Fig. 4 The sliding contact resistance curves of the orthogonal experiments of the group 2.

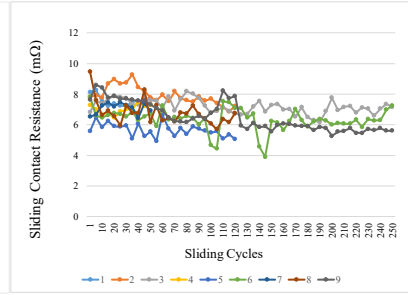


Fig. 5 The sliding contact resistance curves of the orthogonal experiments of the group 3.

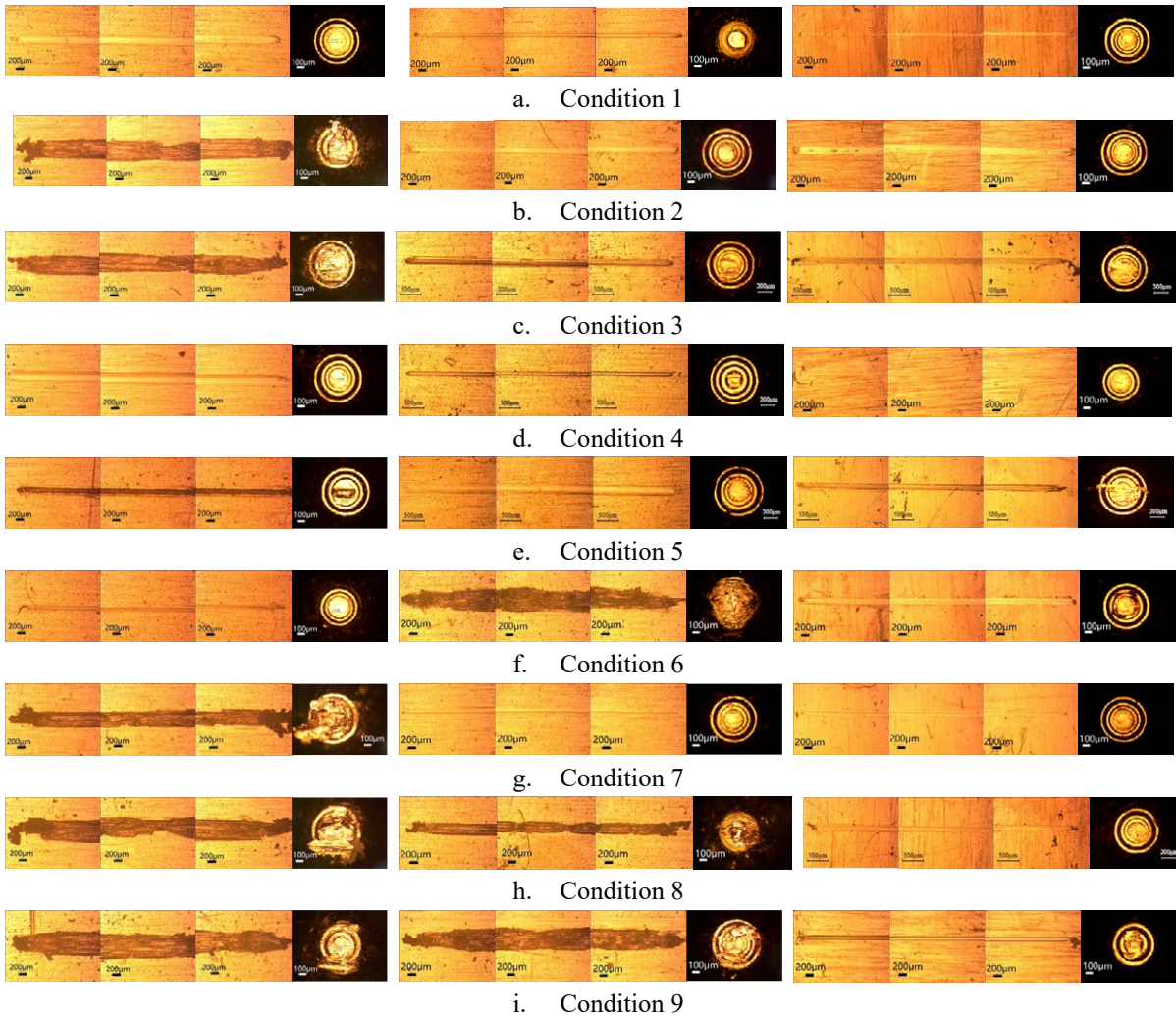


Fig. 6 The sliding wear morphology of the probes and the coupons in the orthogonal experiments of the group 1.

Fig. 7 The sliding wear morphology of the probes and the coupons in the orthogonal experiments of the group 2.

Fig. 8 The sliding wear morphology of the probes and the coupons in the orthogonal experiments of the group 3.

wear resistance. The reason is that the thickness of gold plating of the coupons in the group 2 is an intermediate value, $0.76\mu\text{m}$, the thicker gold plating on the coupons has stronger wear resistance than that on the probe.

The difference between the orthogonal experiments of the group 1 and the group 3 is the substrate material of

test coupons. For the group 1, the substrate material of the coupon is pure copper, but that in the group 3 is the C18070. The wear resistance is markedly improved by the C18070 instead of the pure copper substrate under every test conditions.

3.3 Wear extent

To compare the wear resistance quantitatively, the cross section area was supposed as a rectangular and calculated by the width timing the depth of the wear tracks on the coupons. The average cross section areas of sliding tracks on the coupons of three groups of orthogonal experiments are listed in **Table 3**. The comparison of the wear extent between the group 1 and the group 2 is shown in **Fig. 9**.

Table 3 The average cross section area of sliding tracks on the coupons of three groups of orthogonal experiments

Orthogonal conditions	Group 1	Group 2	Group 3
1	225	175	25
2	300	300	70
3	675	684	420
4	396	396	80
5	1760	252	165
6	308	17000	280
7	8250	187	30
8	12500	270	132
9	19950	19950	200

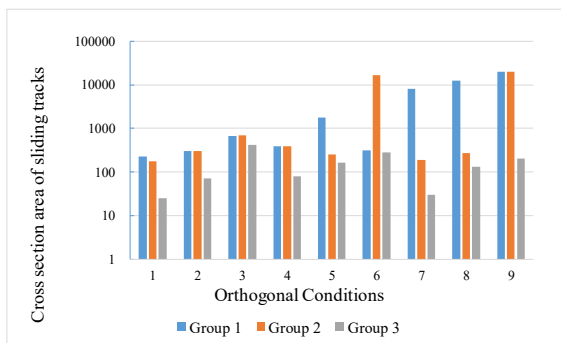


Fig. 9 The cross section areas of sliding tracks on the coupons of the group 1 and 2 of the orthogonal experiments.

It is shown that the wear resistance of the test condition 1-3 has similar extent, but that of the test condition 5-8 has obvious difference between the group 1 and the group 2 orthogonal experiments. For the condition 4 and 9, the four factors have same levels for the contacts in the group 1 and 2, so the wear result is same. For the condition 1-3, the normal force is 50g, no matter what sliding cycles, the thickness of gold plating, or the temperature, the wear extent of the group 1 and the group 2 are similar, which means the wear resistance of the gold plated contacts mainly depends on the normal force. For the condition 5 and 6, the normal force, the sliding cycles, and the temperature are same for both the group 1 and 2, only the thickness of gold plating on the coupons and the probes is different. For the condition 5 in the group 1, the probe with 0.76µm gold plating mated with the coupon with 0.38µm gold plating, but for the condition 5 in the group 2, the probe with 0.38µm gold

plating mated with the coupon with 0.76µm gold plating, so the reason that the samples in group 2 shows better wear resistance is the marked effect of the gold plating thickness of the coupon on the wear resistance. For the condition 6 in the group 1, the probe with 0.76µm gold plating mated with the coupon with 1.27µm gold plating, but for the condition 6 in the group 2, the probe with 1.27µm gold plating mated with the coupon with 0.76µm gold plating, the reason that the group 1 shows better wear resistance is also the stronger wear resistance of the gold plating thickness on the coupons than that on the probes. For the condition 7, the thickness of gold plating on the coupon is 0.38µm for the group 1 and 0.76µm for the group 2, so the wear of the group 1 is much severer than that of the group 2. For the condition 8, the normal force increases to 300g, the gold plated probe was worn severely, which caused wear track wider on the coupon, even the thickness of the gold plating on the coupon is 1.27µm for the group 1. But the thicker gold plating on the probe was worn not so much severely in the group 2, so that the wear track on the coupon is narrower than that on the coupon in the group 1, as comparing in Fig. 6h and 7h.

The comparison of the wear extent between the group 1 and the group 3 is shown in Fig. 10. When the substrate material of the coupons changes from pure copper to C18070, the wear resistance is markedly improved, especially for the condition 7-9 with higher normal force of 300g, as shown in **Fig. 10**.

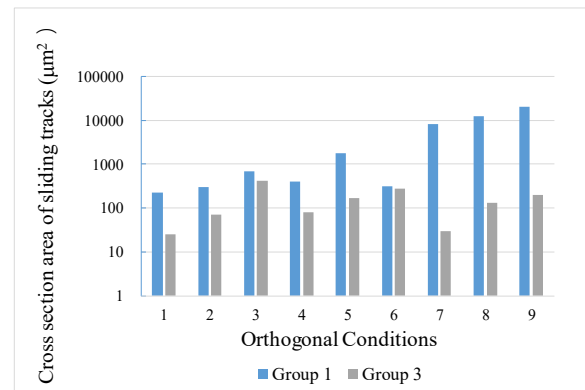


Fig. 10 The cross section areas of sliding tracks on the coupons of the group 1 and 3 of the orthogonal experiments.

3.4 Analysis of the Influence factors

Based on the orthogonal design of sliding tests with four influencing factors and three levels in Table 2 and the wear extent of three groups of test results listed in Table 3, the significance of the four factors on the wear resistance of sliding contacts was ranked by analysis of the range. For the group 1, the rank of influencing factors is the normal force >> temperature > sliding cycles > thickness of gold plating on the coupons; for the group 2, the rank of influencing factors is the sliding cycles >> thickness of gold plating on the

probes \approx normal force \approx temperature; for the group 3, the rank of influencing factors is the sliding cycles \gg thickness of gold plating on the coupons \approx temperature $>$ normal force.

The effect trends of these four influencing factors on wear extent for three groups of orthogonal experiments are shown in Fig. 11. For the group 1, the normal force shows the most significant effect on the wear resistance, especially higher than 100g, so that it is not suggested to use too high normal force for gold plated fingers mating with the card edge connector. For the group 2, the thickness of the gold plating on the coupons is an intermediate value, 0.76 μ m, the wear resistance is improved comparing with contacts with thin gold plating on the coupons. At this time, the sliding cycles is key factor to decide the wear extent. The wear extent becomes obvious severely after 120 cycles. For the group 3, the wear extent is much slightly than those of the group 1 and 2. Even though the wear is aggravated by increasing the sliding cycles, it is still much mild, so that C18070 is a good selection for the substrate material instead of pure copper.

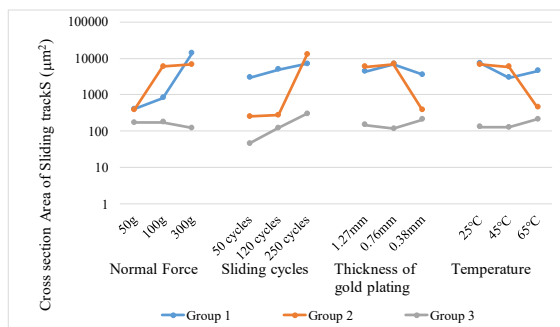


Fig. 11 The effects of the influencing factors on wear extent for three groups of the orthogonal experiments.

3.5 Reliability Analysis

The worn areas on the contacts due to the insertion and withdrawal while the PCB are assembled with the connectors may be corroded during service, so the creep of the corroded products and the repeated insertion and withdrawal might induce the corroded products into the contact interfaces to cause

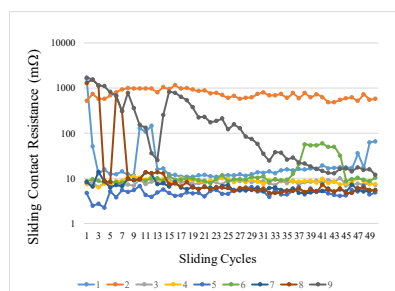


Fig. 12 The sliding contact resistance curves of the group 1 in the repeated sliding tests after accelerated corrosion.

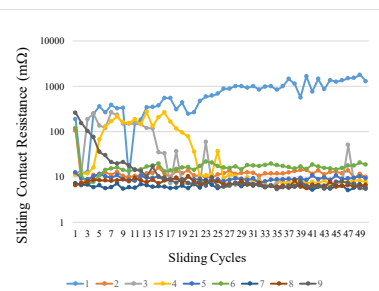


Fig. 13 The sliding contact resistance curves of the group 2 in the repeated sliding tests after accelerated corrosion.

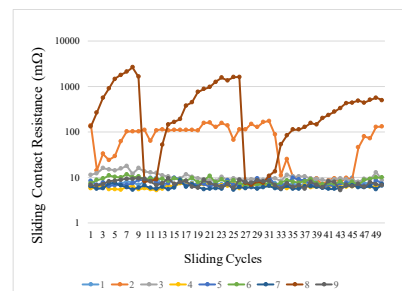


Fig. 14 The sliding contact resistance curves of the group 3 in the repeated sliding tests after accelerated corrosion.

degradation or even failure of electric contact. After the sliding experiments, all the samples of the different groups had different degrees of wear, so the underplating or the substrate material was exposed more or less. To evaluate the reliability of gold fingers on PCB mating with gold plated card edge connectors for long term application, an accelerated corrosion and a repeated sliding test were used. The worn coupons and probes were firstly stored under high humidity and alternating temperature for 10 cycles (80 hours) to push the formation of the oxidation with the profile of the test curves in Fig. 2. Then, the probes after sliding wear were used to slide on the original sliding tracks on the coupons for 50 cycles. Samples under different sliding conditions were subjected to the normal force set by the original sliding experiments, which simulate the insertion and withdrawal in the field application of the gold plated fingers on PCB mating with gold plated card edge connectors after long term application.

The sliding contact resistance curves of three groups repeated sliding tests after accelerated corrosion are shown in Fig. 12-14 respectively. Some initial contact resistance is higher than 100m Ω , but as the wear cycles increase, the contact resistance gradually drops below 10m Ω ; some initial contact resistance is not high, but the contact resistance increases in the sliding process; some contact resistance always fluctuates above 100m Ω ; some contact resistance always keeps low and stable.

4 Discussion

4.1 Sliding performance of the gold plated contacts

In terms of sliding contact resistance of gold plated contacts, it is very stable and the final average value is around 6-8m Ω during 250 cycles no matter what thickness (0.38-1.27 μ m) of gold plating or what the substrate materials (pure copper, C18070, BeCu) under the normal force with 50~300g and the temperature with 25~65 $^{\circ}$ C, as long as there is a little gold remained in the contact interfaces.

From the wear extents of the samples in the group 1 and 2, it is shown that with the increase of normal force from 50g to 300g and the increase of sliding cycles from 50 to 250, the contact wear becomes more and more severe, the cross section area of the wear tracks on the coupons increases from $200\mu\text{m}^2$ to $20000\mu\text{m}^2$. The thickness of gold plating on the coupons shows more positive effects on the wear resistance of gold plated contacts, which can be proven by comparing the morphologies of wear tracks on the coupons under condition 5-7 in Fig. 6e-g and Fig. 7e-g, and the cross section area of the sliding tracks under condition 5-7 in Fig. 9.

Since the hardness of the C18070 is higher than pure copper, the contacts in the group 3 shows stronger wear resistance comparing with those in the group 1, which means if substrate material has higher hardness, it will markedly improve the endurance under the working conditions even with the normal force of 300g, the temperature of 65°C and the sliding cycles of 250. But C18070 cannot have been yet used as a substrate on PCB limited by the process.

4.2 Influencing factors on the wear resistance

For the gold plated probes ($0.76\mu\text{mAu/Ni/BeCu}$) mating with Au plated coupons with pure copper substrate (Au/Ni/Cu), the range analysis of orthogonal experiments in the group 1 shows that the normal force is the most significant factor. The normal force increasing from 100g to 300g will greatly increase the wear of the gold plated contacts. Therefore, it is recommended to control the normal force to be below 100g for Au-Au sliding material combination. For the gold plated probe (Au/Ni/BeCu) mating with gold plated coupons with pure copper substrate ($0.76\mu\text{m Au/Ni/Cu}$), the range analysis of orthogonal experiments in the group 2 shows that the sliding cycles is the most significant factor. When the sliding cycles increases from 120 to 250, the sliding wear increases greatly, and the width and depth of the sliding tracks increase significantly. This is related to the transition point of the wear from the coupon side to the probe side [10]. Therefore, it is recommended that the number of sliding cycles should be controlled below 120. The influence of thickness of gold plating on the probe on sliding wear was the second most obvious. The increase in the thickness of the gold plating on the probe delays the transition point of the wear from the coupon side to the probe side, but the transition still occurs within 120~250 cycles. The gold plating on the probe contact is quickly worn out and the sliding tracks on the coupons become wider. Therefore, it is suggested that it's not necessary to increase the thickness of gold plating on the probe, the key point is reducing the sliding cycles to be less than 120 to improve the reliability.

For the gold plated probe ($0.76\mu\text{mAu/Ni/BeCu}$) mating with gold plated coupons with C18070 substrate (Au/Ni/C18070), the range analysis of orthogonal experiments in the group 3 shows that the sliding cycle is also the most significant factor. But even the sliding cycle increases to 250, the wear of the contacts is still milder than those of the gold plated contacts with pure copper substrate in the group 1. Therefore, it is proven that gold plated probe ($0.76\mu\text{mAu/Ni/BeCu}$) mating with gold plated coupons with C18070 substrate (Au/Ni/C18070) can be used under the conditions of normal force of 300g and the temperature of 65°C , 250 sliding cycles, even when the thickness of the gold plating on the coupon is $0.38\mu\text{m}$.

The effect of the temperature on sliding contact resistance is not marked, which is caused by the time for sliding tests is too short to show the effects of the temperature on the corrosion acceleration of worn contacts. The effect of the temperature on wear resistance is also limited since the temperature is too low to cause the contact materials to be softened.

The wipe caused by the reciprocating insertion and withdrawal of card edge connectors was simulated by sliding tests between the probe and the coupons, but the effect of the "angle of attack" on the wear extent when initial contact is made during the mating is not discussed, which needs further investigation.

4.3 Reliability of card edge connectors

The high humidity and alternating temperature test is used to accelerate corrosion of the worn gold plated contacts, which simulates the environment effect on the worn contacts of connectors for long term exposure in the practical filed. The sliding tests are repeated on the corroded wear tracks, which corresponds to the repeated insertion and withdrawal for the gold fingers on PCB and card edge connectors after a period of service.

The high sliding contact resistance is caused by the corroded products on the wear tracks. If the corroded products can be crashed by the probe under a certain normal force or be removed during sliding, the contact resistance can drop to be lower than $10\text{m}\Omega$; but the corroded products can be induced into the contact interfaces from the wear tracks due to the tangential force during sliding, then the contact resistance will increase. According to the repeated sliding tests after corrosion in Fig. 12-14, the contact resistance of about 90% samples is low or reduces to be low in tens of sliding cycles, which means most the gold plated contacts can be recovered by repeated insertion and withdrawal if the contact resistance is increased by environmental corrosion. But there is still a proportional of unreliable contacts to be concerned.

5 Conclusion

To study the reliability improvement of the gold plated contacts in the gold fingers on PCB and the card edge connectors with increased power density for long term service, the wear extent and sliding contact resistance before and after the corrosion were studied by the simulation experiments. The sliding contact resistance of gold plated contacts (0.38~1.27 μm gold plating) is around 6-8m Ω during 250 cycles under the normal force of 50~300g and the ambient temperature of 25~65 $^{\circ}\text{C}$. As the increase of normal force from 50g to 300g and the increase of sliding cycles from 50 to 250, the contact wear becomes more and more severe. The thickness of gold plating on the coupons shows more positive effects on the wear resistance of gold plated contacts than that on the probes. When the substrate pure copper of the coupon is replaced by C18070, the wear resistance is markedly improved.

Compared with thickness of the gold plating and the temperature, the normal force and sliding cycles have more obvious effects on the wear extent. Therefore, it is recommended to control the normal force to be below 100g and sliding cycles to be below 120 for gold plated contacts. For the higher normal force of 300g, the higher temperature of 65 $^{\circ}\text{C}$, and the longer sliding cycles of 250, the harder substrate material is recommended.

The corroded products on the worn contacts can be removed by tangential force during sliding, but they can also be induced into the contact interfaces at the same time. There is an unreliable possibility of the gold fingers on PCB mating card edge connectors for long term service, which needs to be concerned.

6 Acknowledgement

The authors are thankful for the support of National Natural Science Foundation of China (No. 61674017).

7 References

- [1] Sawa, K.; Watanabe, Y.; Ueno, T.: Effect of Lubricant on Sliding Conditions in Au-Plated Slip-Ring System for Small Electric Power Transfer. The 60th IEEE Holm Conference on Electrical Contacts, New Orleans, LA, 2014: 1-6.
- [2] Lee, D.; Chen, C.; Lee, J.; Yao, L.; Chen, C. C.; Lin, A.: Evaluation of the Metal Coating Porosity of Gold Finger for Secure Digital Memory Card by Way of Flower of Sulfur Test Methodology. The 12th International Microsystems, Packaging, Assembly and Circuits Technology Conference, Taipei, 2017: 263-267.
- [3] Cao, Y.; Yao, X.; Zeng, Y.; Yang, B.; Ming, X.: Effect of Ni/Au Plating on the Interconnection Reliability of Bond Pad. The 18th International Conference on Electronic Packaging Technology, Harbin, 2017, 169-172.
- [4] Meyyappan, K.; Murtagian, G.; Kurella, A.; Pathangey, B.; McAllister, A.; Parupalli, S.: Corrosion Studies on Gold-Plated Electrical Contacts. IEEE Transactions on Device and Materials Reliability, Vol. 14, No. 3, 2014, 869-877.
- [5] Meyyappan, K.; Kurella, A.; Pathangey, B.; McAllister, A.; Abraham, A.; Murtagian, G.: Optimizing Gold Thickness of Land Grid Array Pads for Cost, Performance and Reliability of Connectors. The 60th IEEE Holm Conference on Electrical Contacts, New Orleans, LA, 2014: 1-9.
- [6] Antler, M.; Feder, M.: Friction and Wear of Electrodeposited Palladium Contacts: Thin Film Lubrication with Fluids and with Gold, IEEE Transactions on Components, Hybrids, and Manufacturing Technology, Vol. 9, Issue: 4, Dec., 1986, 485-491.
- [7] Yamaguchi, M.; Araga, S.; Mita, M.; Yamasaki, K.; Maekawa, K.: Wear Resistance of Laser-Sintered Gold-Nickel Composite Film for Electrical Contacts. The 65th IEEE Electronic Components and Technology Conference, San Diego, CA, 2015: 1967-1972.
- [8] Zhou, Y.; Hong, C.; Liu, L.; Xu, L.: Sliding Performance of Electrical Contact Pairs with Unsymmetrical Thick Gold Plating. The 58th IEEE Holm Conference on Electric Contacts, 2012.
- [9] Pompanon, F.; Fouvry, S.; Alquier, O.: The Effects of Relative Humidity on the Fretting Wear Behavior of Silver-plated Electrical Contacts. The 64th IEEE Holm Conference on Electrical Contacts, Albuquerque, NM, 2018: 302-309.
- [10] Antler, M.: Sliding Wear of Metallic Contacts, IEEE Transactions on Components, Hybrids, and Manufacturing Technology, Vol. 4, Issue: 1, Mar 1981, 15- 29.

Influence of red phosphorous flame retarded plastic materials on relay contacts and electronic components

Dieter Volm, Bernhard Fauth, Panasonic Electric Works Europe AG, Robert-Koch-Straße 100, 85521 Ottobrunn, Germany, dieter.volm@eu.panasonic.com, Thomas Herrle, Panasonic Industrial Devices Europe GmbH, Am Temmelacker 2, 85276 Pfaffenhofen, Germany

Abstract

The influence of phosphorous containing substances outgassing from plastic materials flame retarded with red phosphorous on electronic components is discussed. These substances might cause increased contact resistances in relays. Also corrosion phenomena of components on printed circuit board assemblies (PCBAs) can be traced back to the influence of red phosphorous. In the outgassing of red phosphorous and the corrosion process humidity plays a crucial role which leads to the formation of different phosphorous acids and gaseous phosphine.

The influence of three differently flame retarded polyamide (PA) choke coil bobbins on the contact resistances of an unsealed relay in their vicinity is investigated. Two sets of choke coils are flame retarded with red phosphorous whereas one set is flame retarded with a different but also phosphorous containing flame retardant. A contact resistance increase while operating in humid environment and under changing temperatures can only be observed for one coil bobbin set flame retarded with red phosphorous. Phosphorous containing substances can also only be found on the contact surfaces of the relay in the vicinity of this coil bobbin set.

In a further example the corrosive effect of the outgassing products of red phosphorous is shown which leads to short circuits between different terminals of ICs mounted on a PC-board but only in a humid environment.

1 Introduction

Plastic materials are widely used in the electrical industry in switches, circuit breakers, relays, contactors, connectors as well as IT-equipment or household appliances, for example. A primary purpose of the plastic is thereby the electrical insulation of current-carrying parts. The plastic material has to provide the necessary safety to protect the users from accidental contact with electricity.

Besides the electrical properties of the used plastic materials the flammability is an additional safety concern. In electronics unforeseen shorts, unintended electrical connections or overheating devices can finally ignite a fire. The purpose of the plastic is to retard the outbreak and spread of a fire by being temperature stable, flame resistant and self-extinguishing.

In order to achieve these tasks the plastic materials have to be in accordance with standards issued by normative organizations like UL, (Underwriters Laboratories), IEC (International Electrotechnical Commission), EN (European Standardization Organization) and VDE Association of German electrical Engineers. Most important is the vertical burning test of UL94 with a Bunsen burner flame and the glow wire test IEC60695-2-10. It is more and more important in the electrical and electronics industry that the used plastics are self-extinguishing and achieve an UL94 V-0 flammability classification or pass the glow wire test at 960°C (GWT960). Many plastic materials can attain

these properties only if they contain flame retardant additives [1].

Most prominent flame retardants are the bromine containing class. These flame retardants are widely used in the electrical and electronic industry where they cover more than 50% of the applications. Among this class are polybromodiphenyl ethers (PBDEs), polybrominated biphenyls (PBBs) and tetrabromobisphenol-A (TBBPA) which is most commonly used in epoxy laminates for printed circuit boards. Also hexabromocyclododecane (HBCD), brominated polystyrols, brominated phenols and tetrabromophthalic acid anhydride belong to the brominated flame retardant class [2].

However, in the past environmental and health concerns came up about some brominated flame retardants which led to the ban of PBDEs and PBBs by the RoHS- (Restriction of Hazardous Substances) and WEEE- (Waste from Electrical and Electronic Equipment) directives since these substances were found to be toxic. This raised the need to replace these substances.

Such substitutes which have already been in use depending on the underlying plastic material and application are, for example, mineral based like aluminium- or magnesium hydroxide, melamine based and phosphorous based flame retardants. Among the phosphorous containing class phosphate esters, phosphonates, phosphinates, ammoniumpolyphosphate and red phosphorous can be found [2].

Besides the environmental and health implications of flame retardants also their implications on electrical components and whole PCBAs have already been long

discussed and investigated [3]. Namely some of them tend to gas out and have corrosive effects on metal parts or just cause deposits on electrical contacts of relays or switches which accumulate in the course of time leading to increased contact resistances.

The outgassing of substances is often associated to increase with increasing temperatures. However, it is reported for red phosphorous flame retarded plastics that applications passed qualification tests at elevated temperatures but nevertheless failed in the field [4].

Therefore, in the following the influence of red phosphorous as flame retardant on electrical contacts and electronic components and the importance humidity plays in this process is discussed.

2 Red phosphorous as flame retardant

The use of phosphorous based flame retardants is quite common also outside of the electronics industry comprising a worldwide market share of 24% [5].

2.1 Mode of operation of red phosphorous

Phosphorous inhibits the combustion process of plastic materials by multiple reaction steps. During the exposure to high temperatures, the phosphorous or phosphorous compounds are transformed to phosphoric acid by thermal decomposition. An esterification of the phosphoric acid forms a protective carbonaceous layer which is heat resistant at higher temperatures. This protective layer impedes the transport of oxygen to the burning zone.

Another believed mechanism is the reaction of phosphorous with radicals such as hydrogen (H) or hydroxide (OH) to reduce the energy of the flame in the gas phase similar to bromine based flame retardants [5].

2.2 Structure of red phosphorous

Red phosphorous is one of three allotropic forms of elemental phosphorous meaning that the three different forms have different physical structures but similar chemical properties. The other forms are white and black phosphorous. Red phosphorous can be generated by heating white phosphorous above 250°C under air exclusion or by exposure of white phosphorous to light which is a very slow process. Red phosphorous is typically amorphous and not toxic.

2.3 Application of red phosphorous as flame retardant

Red phosphorous has been used in plastic materials for almost thirty years being most common in the electronic industry. Generally, red phosphorous has a very

high flame retarding ability. The contents of red phosphorous particles varies from 5-40% by weight depending on the application. The maximum diameter of the phosphorous particles varies between 75 to 250 µm. The particle distribution depends on the processing technique. The preferred diameter range is between 10 to 40 µm [5].

Due to the very high flame retarding ability only few amount of red phosphorous has to be added to the plastic to be effective leaving the mechanical and electrical properties of the underlying plastic material largely preserved. The lowest contents can go down to 5%.

This is also the reason why the plastics can be reinforced with higher glass fibre contents. All that makes red phosphorous as flame retardant very cost efficient and has made it to the “state of the art” flame retardant solution in polyamide (PA), especially PA66 [1][6].

2.4 Implications of red phosphorous

However, the same mechanism of producing phosphoric acids at elevated temperatures which leads to the flame retardant properties of red phosphorous might cause corrosive effects due to the generated acids.

In dependence of the environmental conditions like temperature and humidity the red phosphorous inside the plastic starts to disproportionate to form phosphorous acids of different oxidation states and phosphine (PH₃). The phosphorous acids can further react with the underlying plastic material, for example polyamide, to form adipic acid [7]. All these generated substances can be released and gas out in the surrounding environment. The produced acids can also attack the underlying plastic material itself and alter its physical and electrical characteristics [5] or even damage it [8].

2.5 Stabilization of red phosphorous

Therefore, efforts are made to measure the amount of outgassing products and to stabilize the red phosphorous to minimize the release of these phosphorous acids and phosphine [7][4]. The first stabilizers consisted of silicon oil or a combination of ammonium bisulfate, paraffin oil, and pentaerythritol. Later, as the application of red phosphorous was also introduced to epoxy the red phosphorous particles were coated with a thermosetting resin such as formaldehyde-, melamine- or phenol based compositions. The advantages of thermosetting coatings are improved coverage, better wettability and increased resistance of the melt proof coatings to industrial processes [5]. Additional improvements in the stabilization were achieved by a dual coating process of the red phosphorous particles. The initial coating consists of aluminium hydroxide and/or

zinc hydroxide followed by an additional thermoset resin.

3 Failure analysis and analytical methods

Nevertheless, there are still applications where red phosphorous as flame retardant causes various failures of electronic components with which the PCBA- and the electronic components manufacturers have to struggle.

3.1 Implications in failure analysis

In the failure analysis the whole application has to be taken into account and not just the failed component to definitely track the failure down to the red phosphorous flame retardant. The reason is that the red phosphorus is often not contained in the plastic of the failed component itself but in the plastic of some component in the surrounding or in the housing of the whole PCBA. Often red phosphorous flame retarded plastics can be recognized by their inherent red colour. However, not all these plastics have a red colour. So it is difficult to tell if a plastic material contains red phosphorous even if elemental phosphorous can be found in the plastic material since also other phosphorous based flame retardants might have been used. Additionally, it is also difficult to tell if the red phosphorous is stabilized or not and if yes to which degree.

Also the environmental conditions, especially temperature and humidity, have to be considered. Under some environmental conditions no failures might occur in a certain application whereas under different environmental conditions the same application might fail.

3.2 Analytical methods

The most important analytical equipment besides, of course an optical microscope (Leica DVM 6), used in this investigation was a Hitachi SU3500 scanning electron microscope (SEM) together with a Bruker XFlash 6|30 EDS (electron dispersive spectroscopy) system. On the one hand contaminations can be observed visually with the SEM and on the other hand elemental compositions can be analysed using the EDS system. Furthermore, a Nicolet 5700 Fourier Transform Infrared (FTIR) spectrometer with an attached Nicolet Centaurus microscope was used to identify chemical compounds.

Last but not least a Shimadzu GCMS-QP2010plus gas chromatograph mass spectrometer (GC/MS) was used

to study the temperature dependent outgassing of substances using a pyrolysis unit.

In the following these methods are used to investigate different examples of failures caused by red phosphorous and the underlying environmental conditions, especially, the influence of humidity.

4 Contact resistance increase of unsealed relays due to red phosphorous

Initially, a typical failure of an open vent hole type relay on a PC-board in the vicinity of a component flame retarded with red phosphorous is discussed. From our experience, for sealed relays with closed vent hole no failures related to red phosphorous have been found so far. The red phosphorous containing component was a big power supply having a red polyamide (PA) housing **Figure 1.1**. The application was in the field for about one year before the first failures in form of increased contact resistances occurred.

The failed relay contacts were investigated by optical microscopy where crystalline structures could be found on the contact surfaces **Figure 1.2**.

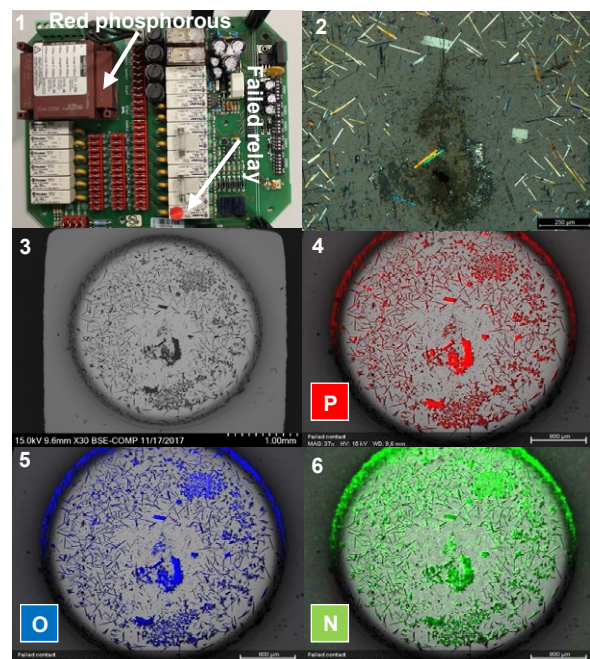


Fig. 1 1: PCBA with relays and a power supply flame retarded with red phosphorous. 2: Crystals of ammonium phosphate on relay contact. 3: SEM image of affected contact surface showing contaminations. 4-6: Elemental EDS-mapping of the contaminations showing the found elements phosphorous (P), oxygen (O) and nitrogen (N).

A SEM-EDS investigation shows that the crystals mainly consist of oxygen (O), phosphorous (P) and nitrogen (N) **Figures 1.3-6, 2**. A FTIR-analysis shows that the crystals consist of ammonium phosphate

$(\text{NH}_4)_3\text{PO}_4$ respectively ammonium hydrogen phosphate $(\text{NH}_4)_2\text{HPO}_4$ **Figure 2**. These substances are built under certain environmental conditions, like temperature and humidity, by a chemical reaction of the red phosphorous flame retardant and the nitrogen containing polyamide matrix of the power supply housing. The generated ammonium (hydrogen) phosphate reaches the relatively cold relay contacts in the gaseous phase and crystallizes on the contact surfaces [9].

This does not necessarily lead to a contact resistance failure immediately since the contaminations might not be thick enough at the contact point. However, due to a self-centring process more and more ammonium (hydrogen) phosphate reaches the contact point and finally leads to the contact resistance failure.

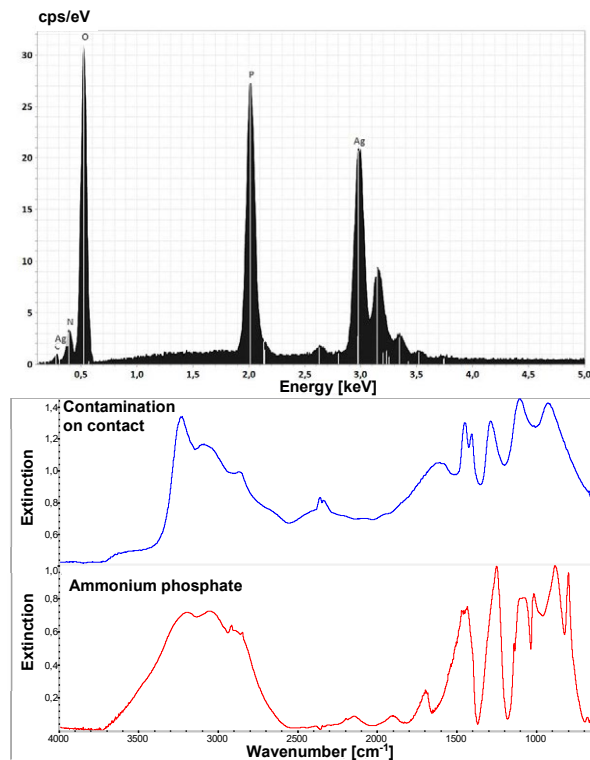


Fig. 2 *Top: EDS-spectrum of the contaminations on the relay silver (Ag) contacts showing especially nitrogen (N), oxygen (O) and phosphorous (P). Bottom: FTIR-spectrum of the contaminations on the failed relay contacts (blue curve) showing good agreement with the spectrum of ammonium phosphate (red curve).*

The ammonium phosphates are hygroscopic and dissolve in surrounding humidity building droplets on the relay contact surfaces. These droplets coalesce due to the mechanical shock of the switching relay to form a liquid film on the contact surfaces. This liquid, saturated solution flows into the capillary of the closed relay contacts. When the relay contacts open a large drop of the liquid is left at the contact points [10].

As humidity decreases a dense, solid layer of ammonium (hydrogen) phosphate is left at the contact points which, when thick enough, finally leads to the contact resistance failure. This shows that the environmental conditions, especially humidity, are very important in the dissolution process of the red phosphorous out of

the plastic matrix as well as in the transportation process of the phosphorous containing products to the spot where they finally cause the failure.

5 Comparison between differently phosphorous flame retarded choke coil bobbins

In the following this influence of the environmental conditions of red phosphorous flame retarded materials on the performance of relay contacts in their vicinity is studied in more detail on the basis of an application example. After qualification tests contact failures on the normally closed signal load contact of a relay on a PCBA could be observed. A SEM-EDS analysis of the contacts showed phosphorous (P) which led to the conclusion that some phosphorous containing plastic caused these failures as in the example of section 4. Polyamide choke coils on the original PCBA with a red coloured coil bobbin in which phosphorous could be detected by SEM-EDS were suspected to be the failure origin. However, the supplier of the choke coils claimed that the coil bobbins show no outgassing.

5.1 Electrical experiment

Therefore, in order to investigate the failure mechanism in the qualification test systematically in more detail, an experimental series was designed investigating three different samples of choke coil bobbins where samples A and B have a red coloured and sample C has a black coloured polyamide (PA) bobbin:

Sample	Description
A	Red PA coil bobbin
B	Red PA coil bobbin
C	Black PA coil bobbin

Samples A and B are flame retarded with red phosphorous, whereas sample C is flame retarded with a different but also phosphorous containing substance. Other phosphorous containing flame retardants are, for example, phosphate esters, phosphates, phosphonates, phosphinates and ammonium polyphosphate where in polyamides preferably phosphinates are used [2].

For the experiments two unsealed relays together with the different choke coil samples A-C were put in a box to simulate the housing of the real PCBA **Figure 3**.

In three experiments the influence of different environmental and test conditions on the three different choke coil bobbins was investigated:

Experiment	Description
1	Temperature cycle without humidity
2	Temperature cycle with constant humidity
3	Temperature cycle with constant humidity and additionally powdered choke coils

5.1.1 Experiment 1

In the first step of the experimental series the box was put into a climatic chamber and the temperature was cycled from 20°C to 105°C within two hours where the minimum and maximum temperatures were each kept for 20 minutes. The normally closed contacts of the relays were switched at a load of 12V and 12mA 59s on and 1s off. All these parameters are according to the actual qualification test representing the real application.

The contact resistances of the relays were monitored by the voltage drop at a microcontroller input at every switching cycle. This measurement circuit is shown in **Figure 3**. The complete test duration was about six days.

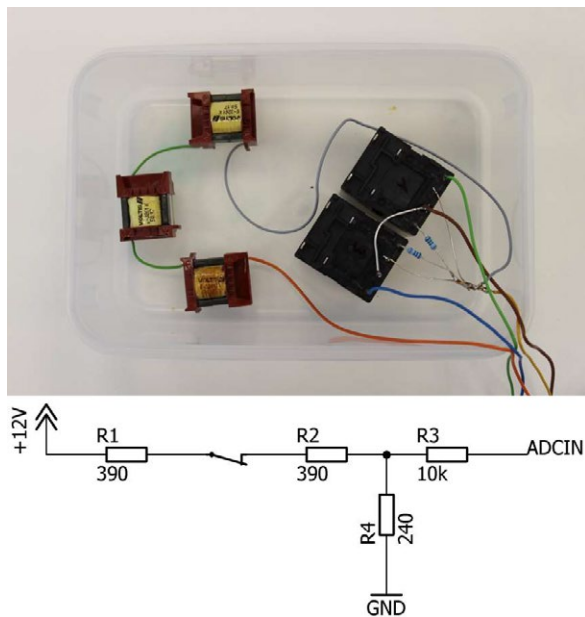


Fig. 3 *Top:* Three choke coils of sample A in the box together with two unsealed relays. *Bottom:* Measurement circuit to detect normally closed contact resistance failures of the relays.

In this first step of the experiment without applying any humidity no contact resistance failures could be detected for neither of the samples A-C **Figure 4**.

5.1.2 Experiment 2

In the second step of the experiment additionally to the temperature cycle a constant ambient relative humidity of 50% as in the actual qualification test was applied in the climatic chamber leaving all other parameters of the test unchanged. Also in this experimental step no contact resistance failures could be detected for neither of the samples A-C **Figure 4**.

5.1.3 Experiment 3

In the third step of the experiment additionally the choke coils were powered with a constant current of 500mA as in the real application enlarging the local

temperature at the choke coils and setting free additional humidity stored in the plastic coil bobbins and windings of the choke coils. In this experimental step massive contact resistance failures could be detected after about two days, but only for sample A. However, also sporadic failures could be detected earlier **Figure 4**. Note that also after two days not every switching cycle caused a failure. There were switching cycles in between where the contact resistance was fine.

No contact resistance failures could be detected for the relay contacts in the box together with samples B and C.

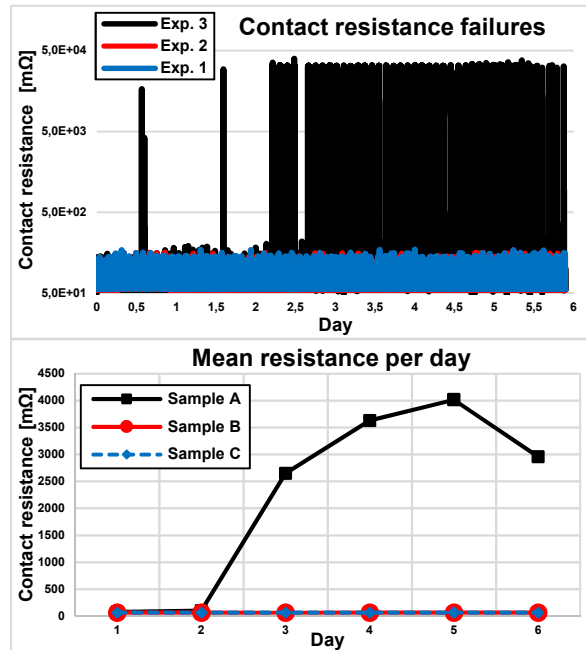


Fig. 4 *Top:* Contact resistance failures of a relay monitored during the different experiments without humidity, with an additional constant relative humidity of 50% and with additionally powered choke coils for sample A. Contact resistance failures could only be observed with powered choke coils. *Bottom:* Comparison of the mean contact resistance per day calculated from the measurement data between relays together in the box with samples A, B and C. Significant contact resistance failures could only be observed for relays in the box together with samples A (lines are only a guide to the eye).

A corresponding comparison of the mean resistance per day calculated from the measurement data for a relay together in the box with samples A, B and C is shown in **Figure 4**. Significant contact resistance failures could only be observed for relays in the box together with samples A. The results of the different experiments are summarized in the table below:

Sample	Experiment		
	1	2	3
A	No failures	No failures	Failures
B	No failures	No failures	No failures
C	No failures	No failures	No failures

It is not amazing that no failures could be detected for sample C since this was not flame retarded with red phosphorous. However, it is somehow puzzling that only for sample A contact resistance failures could be found since also sample B was flame retarded with red phosphorous.

5.2 GC/MS measurements

In order to investigate this phenomenon in more detail a GC/MS analysis of the outgassing products and behaviour of the three different coil bobbin samples was performed while increasing the temperature of the pyrolysis unit.

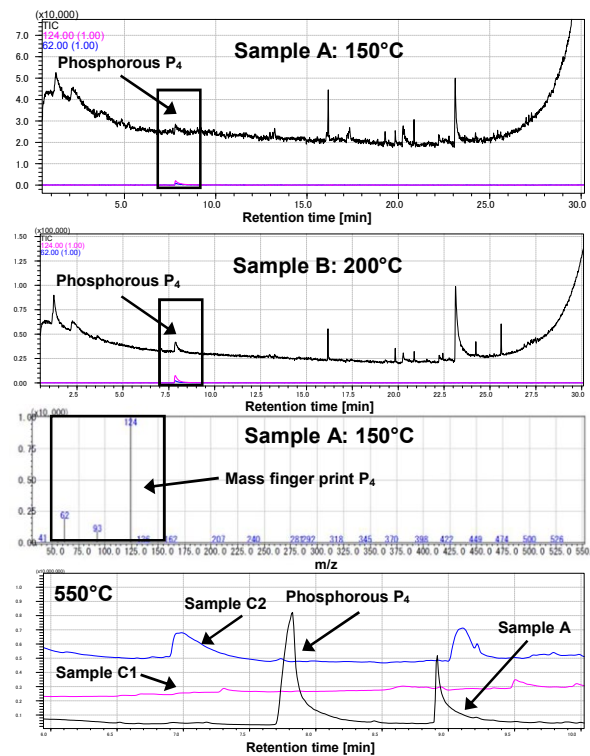


Fig. 5 GC of the three different choke coil bobbin samples A-C showing outgassing of P_4 only for sample A at 150°C and for sample B at 200°C. No outgassing of P_4 could be detected for sample C up to 550°C and even higher. The corresponding mass spectrum shows the typical mass spectrum of P_4 , here for sample A.

For sample A an outgassing of phosphorous in form of P_4 could be detected at a temperature of 150°C **Figure 5**, whereas for sample B P_4 could only be detected at a temperature of 200°C.

For sample C no outgassing of P_4 could be found up to a temperature of 550°C where the polyamide plastic material is completely incinerated.

5.3 SEM-EDS measurements

At the end of the tests the relay contacts were examined by optical microscopy and SEM-EDS **Figures 6, 7**. Contaminations could only be found on the contacts of a relay inside the box with samples A out of the third experiment. The contaminations mainly consist, as in

section 4, of nitrogen (N), oxygen (O) and phosphorous (P) **Figure 7**.

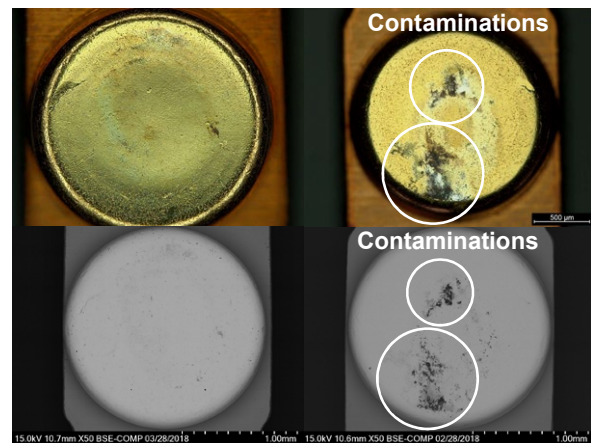


Fig. 6 Optical microscope (top) and SEM (bottom) images of relay contacts of a relay in a box without (left) and with (right) red phosphorous containing samples C and A, respectively. Contaminations could only be found on contacts of a relay inside the box with red phosphorous containing samples A (right images).

The contaminations accumulate at the contact point in the humidity assisted self-centring process already discussed in section 4.

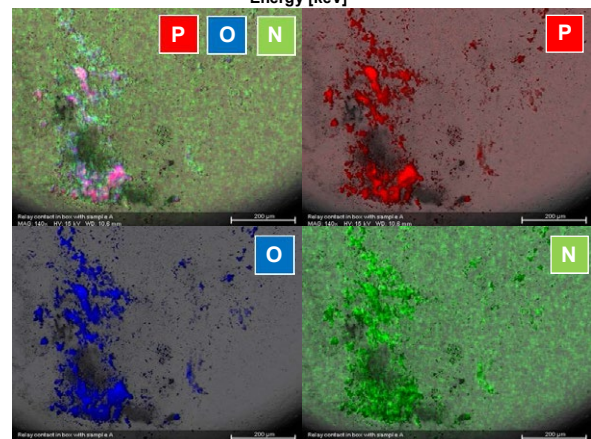
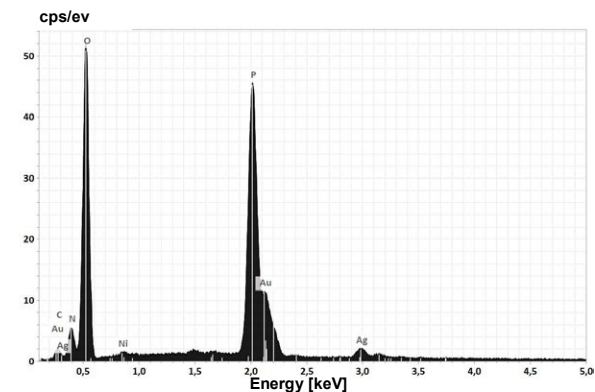
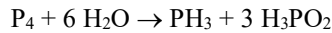


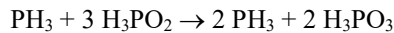
Fig. 7 **Top:** EDS-spectrum at a contaminated spot showing that the contaminations mainly consist of nitrogen (N), oxygen (O) and phosphorous (P). The found silver (Ag) and gold (Au) is from the relay contact. **Bottom:** Elemental EDS-mapping of the contaminations showing phosphorous (P), oxygen (O) and nitrogen (N).

5.4 Results and discussion

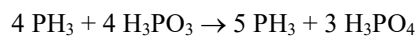
The found phosphorous P_4 by GC/MS for samples A and B is the starting point for the reaction of P_4 with humidity and the disproportionation of the red phosphorous into phosphine (PH_3) and phosphorous acids mentioned in [7].



The phosphinic acid (H_3PO_2) can further react to phosphine and phosphonic acid (H_3PO_3) at elevated temperatures:



The phosphonic acid can further react to phosphorous acid (H_3PO_4):



This corresponds to the findings above where the choke coil supplier claimed a not outgassing of the coil bobbins and the findings in the first experimental step only cycling the temperature. When humidity was added and the choke coils were powered simultaneously, which enhanced the local temperature through self-heating of the coils and the evaporation of intrinsic humidity, contact resistance failures could be found in the presented experimental setup.

These experiments which were repeated for verification could prove that on the one hand the red phosphorous flame retardant caused the failure in the application and on the other hand revealed an alternative solution by using differently flame retarded choke coils. Also the strong impact of the environmental parameters like temperature and humidity and the parameters of the whole application could be demonstrated. Furthermore, an influence of the content of red phosphorous, the red phosphorous particle sizes or the degree of stabilization may play an important role and is very interesting to study in future experiments. This example also shows the difficulties in the failure analysis to definitely track down the failure to the red phosphorous flame retardant.

6 Corrosion of chip terminals caused by red phosphorous

Besides failures caused by deposits of outgassing products due to red phosphorous also corrosion on metals can occur which is also strongly humidity dependent. PCBAs in a, this time black instead of red, polyamide (PA) housing flame retarded with red phosphorous were subjected to different qualification tests while the electronic was powered. One branch of the test was just a test at a constant temperature of $85^\circ C$ and the second branch was a test at a constant temperature of $85^\circ C$ and a constant relative humidity of 85%. Failures in form of short circuits on some devices or even burnt devices only occurred on PCBAs out of the test where humidity was involved.

In the optical microscope investigation greenish residues could be found on the chip terminals which formed shorts between them as shown in **Figure 8**.

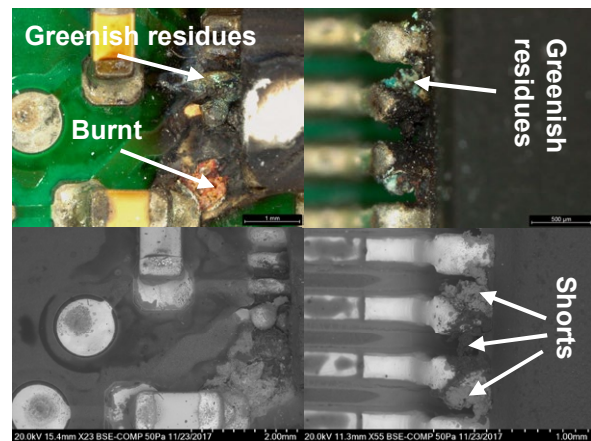


Fig. 8 *Top:* Optical microscope images of a burnt driver (left) and shorts between terminals of a microcontroller (right). *Bottom:* The corresponding SEM-images are shown.

In the SEM-EDS-investigation oxygen (O) and phosphorous (P) could be found for the residues on the terminals of the corresponding chips **Figure 9**. This leads to the conclusion that the failures were indeed caused by the red phosphorous contained in the plastic housing of the PCBA.

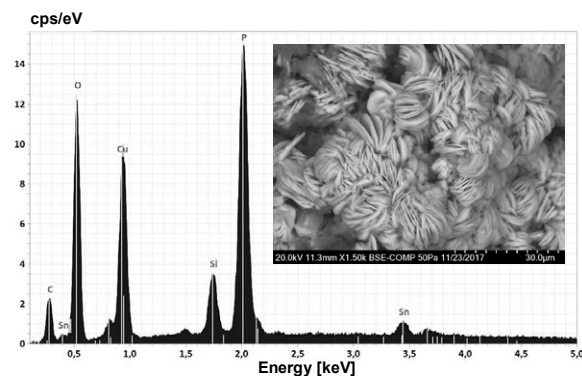


Fig. 9 *EDS-spectrum of residues on the terminals (inset) of the microcontroller showing lots of oxygen (O) and phosphorous (P).*

As already discussed in section 2.4 the red phosphorous dissolves with humidity to phosphorous acid which condenses on the chip terminals and attacks the underlying copper material. The generated salts like copper phosphate $Cu_3(PO_4)_2$ form the greenish residues and the conductive bridges between the chip terminals. Since the PCBA was powered the generation of shorts might have also been supported by electrochemical migration [5].

7 Summary

Above various examples were reported where red phosphorous as flame retardant in plastics caused different kinds of failures. In all these examples humidity

played a major role in the dissolution process of the red phosphorous out of the underlying plastic as well as in the transportation process to the location where the failure happened.

For unsealed relays in which the dissolved phosphorous substances can intrude mostly increased contact resistances led to a failure of the devices. Here the humidity enhanced the transport of the phosphorous substances to the contact point by the capillary effect.

The corrosive effect of red phosphorous was also discussed in which the generation of phosphorous acids out of the plastic material assisted by humidity played a crucial role. In the presented example the corrosion led to shorts between chip terminals and even to burnt devices.

All these examples show that it is very important in the design of PCBAs to keep the implications of red phosphorous as flame retardant in mind.

The example with the red phosphorous flame retarded power supply from section 4 was an application from the field whereas the examples from sections 5 and 6 were still in the qualification state.

This shows that appropriate qualification tests are also important to bring potential failures to light prior to the release of the application to the field. As shown in above examples the choice of the environmental conditions in this qualification tests like temperature and especially humidity and also the parameters of the application itself during the test are fundamental.

8 Acknowledgements

We like to thank Franz Winkler for the electrical measurements.

We also like to thank Tatsuo Aratani and Sora Matsuda from Panasonic Laboratory in Ise for the GC/MS measurements.

9 Literature

- [1] Uske K., Roth M.: Less Is More (Flame Retarded Polyamides Based on Red Phosphorous), *Kunststoffe international* 1-2/2015 pp. 77-79 (www.kunststoffe-international.com/960505)
- [2] The European Flame Retardants Association, Flame Retardants (Frequently Asked Questions), www.flameretardants-online.com/images/itempics/2/9/1/item_18192_pdf_1.pdf
- [3] Göttert B., The Influence of Various Flame-Retardant Additives in Polybutylene Terephthalate on the Resistance Behavior of AuAg8 Contacts, 14th International Conference on Electric Contacts, Paris (F), June 20-24, 1988
- [4] Seubert J.: Kunststoff-Prüfung für elektrolytische Korrosion (Resistente PBT und PA für elektrische Leistungsmodule), *Plastverarbeiter* 12 2014, pp. 52-54

- [5] Hillman C., Red Phosphorous Induced Failures in Encapsulated Circuits, *DfR Solutions White Paper*, 2002
- [6] Uske K., Ebenau, A.: A Plea for Red Phosphorous, *Kunststoffe international* 9/2013 pp. 130-133 (www.kunststoffe-international.com Document Number: PE111459)
- [7] Uske K., Roth M., Minges Ch.: Prevention of Contact Corrosion (Stabilizing Flame Retarded Plastics against Plate-Out), *Kunststoffe international* 9/2015 pp. 68-70 (www.kunststoffe-international.com/1090223)
- [8] Chen Z. et al., *RSC Adv.*, 2019, 9, 24935
- [9] ACL GmbH, Erhöhter Übergangswiderstand bei Kontakten in Polyamidgehäusen, Newsletter no. 33
- [10] Vogel G., Failure mechanisms of electromechanical relays on PCBAs - PART II, *EDFAAO* (2018) 2: 4-8

The Effect of Relative Humidity on the Diffusion of Brass Elements Through Tin Plating

Bradley M. Schultz, Rodney I. Martens, Suvrat Bhargava
TE Connectivity, Corporate Technology, Middletown, PA, 17057, USA, bradley.schultz@te.com

Raymond Landon
TE Connectivity, Commercial Solutions Appliance Business Unit, Middletown, PA, 17057, USA, raymond.landon@te.com

Abstract

The diffusion of zinc from brass substrates through tin plated layers leading to surface discoloration is a well-known issue. Cost pressure is driving investigation of brass substrate alloys containing larger zinc content such as yellow brass (C27400), which is a potential substitute for cartridge brass (C26000) due to the decreased amount of copper (Cu) wt.% and comparable electrical and mechanical properties. However, the increased zinc (Zn) wt.% may pose a risk of increased Zn grain boundary diffusion through the tin (Sn) plating, leading to discoloration of the surface during storage. Using a temperature/humidity-controlled climate chamber, this study investigates effects of base metal, Sn plating thickness, exposure time, and relative humidity (RH) on the discoloration of the surface, the surface elemental composition, and electrical performance of Sn plated brass. Exposure conditions were 85 °C with relative humidity levels ranging from 15 to 90%. To quantify visual appearance, a colorimeter was used to determine that increasing the relative humidity has the largest statistical impact on the surface discoloration of the Sn parts, and that below RH levels of 60%, little discoloration is seen after 10 days exposure. RH and Sn thickness were the most significant factors for observable Zn at the surface as measured by Energy Dispersive Spectroscopy (EDS). Only under the higher humidity levels was there a statistically significant effect of substrate composition on Zn at the surface. There was no statistically significant impact on the electrical contact resistance of the Sn plated brass under the most severe conditions evaluated. Results indicate that to delay discoloration of the Sn surface and Zn grain boundary diffusion, samples should be stored in a dry environment, use a thicker Sn layer, or incorporate barrier layers.

1 Introduction

General discoloration of Sn plated brass surfaces following Zn diffusion and oxidation is well known [1]. As discussed in the literature, Zn diffuses to the surface through Sn grain boundaries and oxidizes to present an optically darkened surface. The surface concentration of Zn is higher with exposure to elevated temperatures, and significantly higher under elevated humidity [2]–[6]. The diffusion of Zn through Sn to the surface can be mitigated or delayed with the addition of a copper or nickel barrier layer between the brass and Sn or with a thicker Sn layer. However, for many low-cost applications, these solutions are cost prohibitive.

Motivated by the rising cost of copper (Cu), the need to reduce costs has driven the investigation of using alternate substrate materials for connector terminals. Historically, C26000 cartridge brass (70% Cu/30% Zn), has been used for many terminal applications. However, over the last two decades, the price of

copper has doubled and at one point, tripled [7]. To reduce material costs, lower copper content C27400 yellow brass (63% Cu/37% Zn) was identified as a potential replacement. As shown in Table 1, C27400 has similar mechanical and electrical properties to C26000, which make it a reasonable substitute for many applications (Table 1).

While property comparison would indicate C27400 is equivalent to C26000, the increased Zn wt.% leads to a potential concern of an increase in Zn grain boundary diffusion through the Sn plating (Fig 1).

Table 1- The mechanical and electrical property comparisons of C26000 and C27400.

Property	C26000 [8]	C27400 [9]
Zn wt.%	~30%	~37%
E (GPa)	110	110
σ_y [soft] (MPa)	145	179
Electrical Conductance (%IACS)	28%	27%
T_m (°C)	954	920
CTE @ 20 °C ($10^{-6}/K$)	20.0	20.5

A potential issue with the increased Zn content is the formation of the beta phase in the dual phase C27400 alloy [10]. The addition of a Zn-rich beta phase creates a more heterogeneous distribution of the Zn throughout the microstructure of the plated material, potentially creating locations for increased diffusion. Resnick *et al.* experimentally showed that the beta brass phase has more rapid diffusion than the alpha brass phase [11]. Diffusion of Zn to the surface, especially in uncontrolled storage conditions, leads to discoloration which may raise aesthetic concerns from end users. While evaluation of material exhibiting discoloration has shown no deterioration in electrical contact performance [12], further investigation is needed to fundamentally understand the effect of storage conditions and the impact, if any, of the increased Zn wt.% in the lower cost C274000 alloy on discoloration.

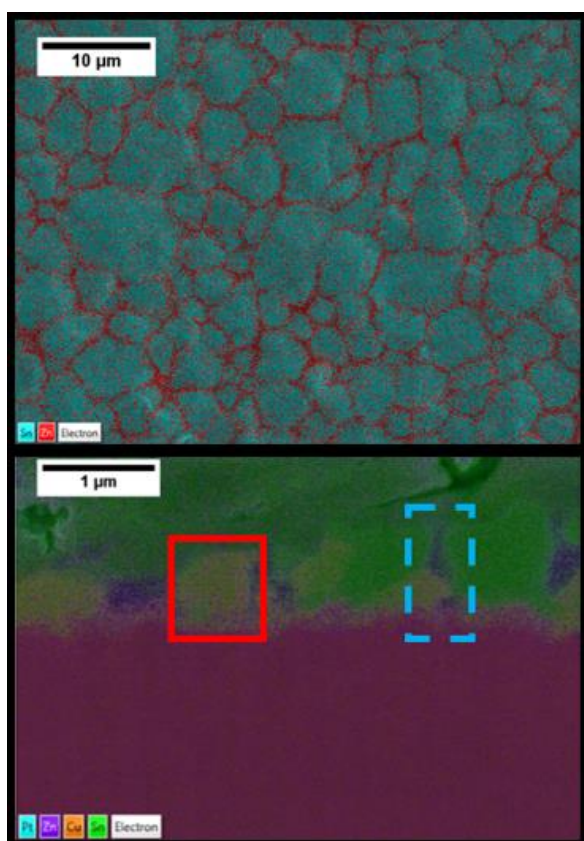


Fig 1- (top) Energy dispersive x-ray spectroscopy (EDS) of the Sn surface on a Sn plated brass coupon. Results show zinc (red) diffusing through the grain boundaries of the Sn (blue) to be exposed at the surface. (bottom) EDS of a cross-section cut of the Sn-plated brass. The red box (solid) displays a Sn_xCu_y intermetallic forming at the interface of the Sn plating and brass substrate. The blue box (dashed) displays the Zn diffusing through the grain boundaries to the surface.

This study investigates the visual and electrical contact performance impact of humidity on Zn diffusion through electroplated Sn layers. C26000 and C27400 alloy coupons are plated with 1 μm and 3 μm thick Sn layers and exposed to relative humidity (RH)

percent ranging from 15 to 90% with temperature held constant at 85 °C. The surface of the coupons was characterized to determine the amount of brass constituents at the surface, visual appearance, and functionality in terms of electrical contact resistance. These results will help define storage conditions recommendations for Sn plated brass components.

2 Methodology

2.1 Sample Preparation

Test coupons were created from C26000 and C27400 brass strip, 5 cm wide x 0.45 mm thick. The continuous strip was plated on a production reel-to-reel line with a whisker mitigated methanesulfonic acid (MSA) Sn bath. Nominal Sn thicknesses of 1 and 3 μm were targeted, with actual Sn thickness ranging from 0.8-1.5 μm and 2.7-3.3 μm , respectively as measured via X-ray fluorescence (XRF) and verified with focused ion beam (FIB) cross section. Individual samples were created by shearing the strip in 40 mm increments. All samples were hermetically sealed with desiccant after plating to minimize environmental exposure prior to accelerated aging.

2.2 Accelerated Laboratory Testing

From literature [2], it is known that elevated humidity has the most significant impact on discoloration, while elevated temperature has a lesser impact. Coupons were placed in three temperature/humidity chambers for different amounts of time, ranging from 1 to 10 days. The temperature was fixed at 85 °C, while the relative humidity ranged from 15 to 90%. For a relative humidity (RH) of 15%, 30%, and 45%, the samples were placed in a Tenney BTRC temperature humidity chamber. For 60% and 90% RH, the samples were placed into a Thermotron model SE-600-5-5. Samples at 75% RH were placed in an ESPEC model ESX-3CW temperature humidity chamber.

2.3 Sample Characterization

Upon removal from the chambers, samples were immediately characterized to minimize the effect of ambient aging or other exposure that may impact oxidation or surface discoloration. Characterization processes for visual appearance, elemental composition, and electrical contact resistance are discussed below.

2.3.1 Visual Appearance

All coupons were imaged in a photography light box to create consistent light conditions for optical photographs as well as for quantifying the color of the coupons. To objectively measure the color properties of the coupons, a FRU WR10QC Colorimeter was used to measure the values based on the CIELAB scale. The CIELAB color space describes color in three values: 1)

'L*', which represents the lightness of the samples from black (0) to white (100), 2) 'a*', which represents color from green (-) to red (+), and 3) 'b*', which represents color from blue (-) to yellow (+). The use of a colorimeter allows for a consistent, quantitative analysis of visual appearance. Fig 2 illustrates how colorimeter results can give a more quantitative and accurate differentiation as compared to subjective visual comparison. For this paper, the lightness or L* parameter is used for comparison as the purpose of the study is to determine how reflective Sn surfaces become matte and discolored/darkened.

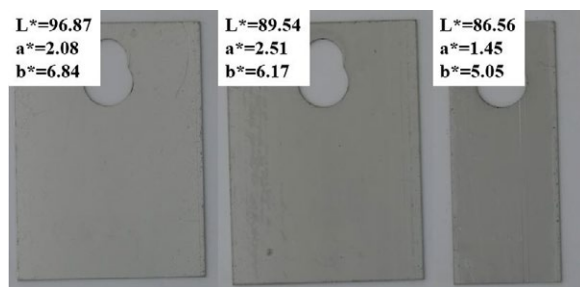


Fig 2- Optical photographs of exposed coupons with corresponding CIELAB properties. The L* value quantifies the “darkness” of the samples.

2.3.2 Electron Microscopy/Electron Dispersive Spectroscopy/Focused Ion Beam

To acquire magnified images of surface morphology and to quantify the elemental composition of the Sn surface, scanning electron microscopy (SEM) and electron dispersive spectroscopy (EDS) was performed using a Hitachi SU-6600 SEM with an Oxford Instruments X-Max EDS system with a 50 mm² detector window. All coupons were mapped at 2500x at 20 keV at a location that was representative of the entire sample. The data was used to compare the Sn, Zn, and Cu wt.% of each sample at the surface to quantify the impact of humidity and aging on the diffusion of Zn and Cu. Cross-sections of select aged coupons were examined with a FEI Nova 600 NanoLab focused ion beam (FIB) system with an Oxford Instruments ULTIM MAX EDS system with a 65 mm² detector window.

2.3.2 Electrical Contact Resistance

To assess the functional implications of humidity and aging on the electrical resistance of the Sn plated brass, contact resistance measurements were performed with a custom fabricated contact resistance probe [13]. Readings were taken at 200 g normal force under dry circuit conditions with and without wipe at the interface.

3 Results and Discussions

3.1 Impact of Humidity on the Color of Sn Plated Brass

Using the measurements collected from the colorimeter, the lightness values were statistically analyzed using a standard least squares model with JMP 15™. A full factorial model was used to determine the effects and interactions of %RH, exposure time, Sn thickness, and base metal on the lightness of the coupons. The ranked model results are shown in Table 2.

Table 2- Standard least squares model parameter significance for coupon lightness. Only parameters that are statistically significant with a p-value < 0.01 are displayed.

Source	LogWorth	p-Value
%RH	49.72	0.00000
%RH*Sn Thickness	8.81	0.00000
%RH*Days	8.15	0.00000
Days	7.07	0.00000
Sn Thickness	6.08	0.00000
%RH*Base Metal	3.86	0.00014
Base Metal	2.70	0.00199

In Table 2, ‘LogWorth’ statistic is used to illustrate significance of the main factors and interactions as it allows for a higher resolution analysis of very low p-values. Values greater than 2 Table 2 are deemed significant with a p-value of < 0.01 since $-\log_{10}(0.01) = 2$.

Based on the statistical model, relative humidity has the largest influence on the lightness of the Sn plated brass coupons. The 2nd order interactions of %RH/Sn thickness and %RH/days have a larger influence on the lightness than the main factors of days and Sn thickness. These results indicate that dry storage conditions are critical to minimize darkening of Sn plated brass components. It is of note that base metal is the least significant factor as compared to relative humidity, exposure time, and Sn thickness. As such, this parameter was eliminated from the variability analysis in Fig 3.

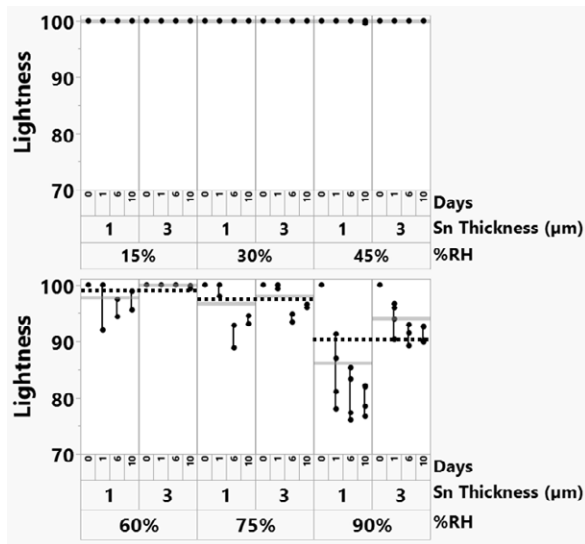


Fig 3- Variability chart of the largest influencers on the lightness value. The x-axis is three overlapping parameters of relative humidity, Sn thickness, and amount of days. The black dashed horizontal lines are the means for each relative humidity group. The solid grey horizontal lines are the means for each Sn thickness in each relative humidity group.

Multiple trends can be observed from the results in Fig 3. First, lower relative humidity levels have no impact on the lightness. The 45% RH/1 μm /10-day coupons are the first conditions where any measurable change in lightness occurs. Starting with 60% RH, there is a noticeable decrease in the means of the lightness values as indicated by (dashed black). Based on Table 2, base metal barely rises to statistical significance with a p-value of 0.0019, but if the lower humidity conditions of 15%–45% RH were removed, the significance of the base metal increases.

The next observable trend is the impact of Sn thickness on the lightness value. Similar to the impact of RH, there is no change in lightness with the thickness of Sn at lower RH, but at 60% RH, the lightness for 1 μm Sn thickness decreases at an increased rate as compared to 3 μm Sn (solid grey). Even though the 3 μm Sn exhibits a lighter surface as compare to the thinner 1 μm Sn, it does decrease. As would be expected, this result elucidates that thicker Sn does not stop the problem of discoloration, it merely delays it.

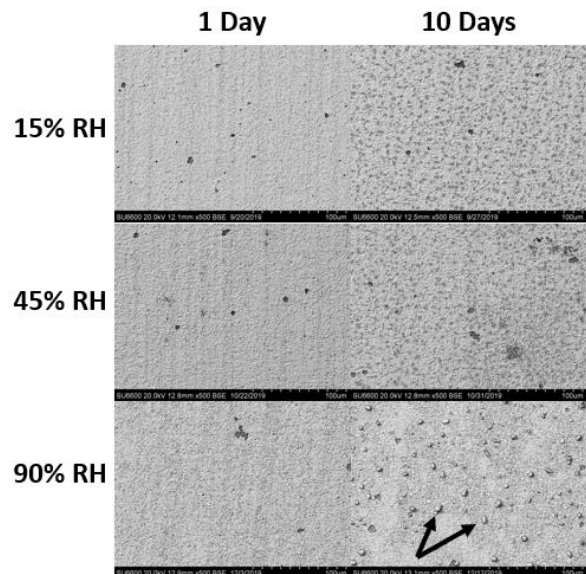


Fig 4- BSE images of the Sn-plated brass samples as a function of increasing relative humidity and amount of days. All images are of coupons with C27400 substrate and 1 μm of Sn. Each image is 250 μm wide. An observed change in microstructure occurs, along with the growth of Sn whiskers (indicated by arrows).

Regarding the impact of exposure time, an unexpected trend occurs. As exposure time increases, there is an initial decrease in lightness, but the values then stay level or increase at 10 days. Increased RH levels and exposure time leads to an increase in Zn diffusion to the surface, specifically at the grain boundaries, which will be described more in detail in section D.2. As the RH and exposure time continues however, the levelling or increase in lightness is due to the growth and formation of Sn whiskers (as indicated in Fig 4) which registers as a lighter surface since the Sn whiskers are reflective. It has been observed in previous work that exposing Sn to similar environments leads to Sn whisker formation [14], [15]. Clearly, longer exposure times in extreme environments drive more discoloration and aesthetic issues in Sn-plated brass components.

3.2 Impact of Humidity on the Surface Composition of Sn Plated Brass

Using electron dispersive spectroscopy (EDS), the Sn, Cu, and Zn content was characterized and statistically analyzed on the lightness values in section D.1 above. Accelerating voltage of 20 keV was used for all measurements. As EDS is not a surface sensitive technique, the term ‘observable’ is used to acknowledge that the penetration depth of the measurement may include some signal from the substrate material.

Table 3 ranks the significance of the four main factors of Sn thickness, Base Metal Type, Exposure time and Relative Humidity with respect to Sn, Cu, and Zn composition. The parameter of base metal is not statistically significant when examining Sn and Cu wt.%,

hence is removed from those analysis. It is more significant for the case of Zn wt.% and is included for that case.

Table 3- Ranking of Sn/Cu/Zn content versus main factors. The ‘LW’ represents the LogWorth value. ‘*’ indicates the parameter is not statistically significant.

		Sn wt. %	Cu wt. %	Zn wt. %
Sn Thickness (µm)	Rank	1 st	1 st	2 nd
	p-value	0.000	0.000	0.000
Base Metal	Rank	8 ^{th*}	11 ^{th*}	3 rd
	p-value	0.288*	0.414*	0.000
Days	Rank	2 nd	2 nd	4 th
	p-value	0.000	0.000	0.000
%RH	Rank	3 rd	5 th	1 st
	p-value	0.000	0.000	0.000

Fig 5 displays the EDS results for Sn wt.% at the coupon surface. The initial offset at 0 days of exposure is due to the penetration depth of the electron beam for the EDS analysis, where some substrate is included in the analysis. As shown in Fig 1, Cu forms an intermetallic with the Sn at the plating/substrate interface and the Zn diffuses through the grain boundaries to the surface. This happens in both the 1 and 3 µm Sn, but due to the penetration depth of the electron beam for the EDS analysis, the 1 µm Sn allows for more of the intermetallics to be observed. If more time were to pass, the thickness of the Sn_xCu_y intermetallics would continue to grow and the Sn wt.% would decrease for the 3 µm Sn thickness as well.

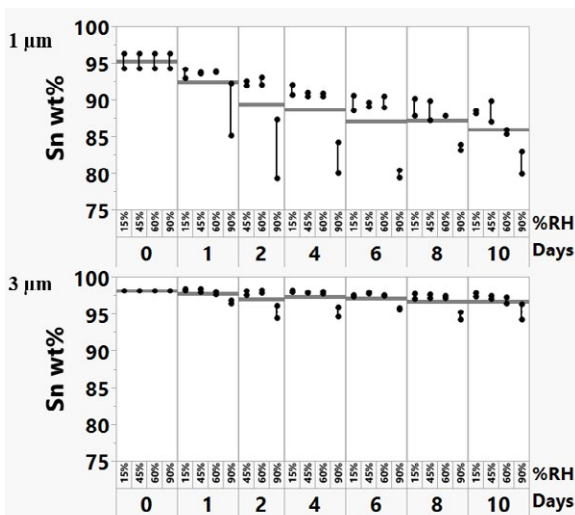


Fig 5- EDS results for the Sn wt.% for each sample. Samples with a Sn thickness of 1 µm are shown in the upper plot, while 3 µm are in the lower plot. The horizontal lines represent the group means for amount of days.

The exposure time and relative humidity were also statistically significant with respect to Sn wt.% at the surface. As shown by the horizontal lines in Fig 5, the means decreased as exposure time increased. This

trend was more observable in the 1 µm thickness. Additionally, increased relative humidity decreased the Sn composition. Up to 60% RH, change in the Sn wt.% is minimal, but at higher levels there is an evident drop, most notably at 90% RH. The decrease in observable Sn is potentially caused by an increase in intermetallics formed at the interface or the growth of Sn whiskers allowing for a more rapid and less blocking path for Zn diffusion through the grain boundaries.

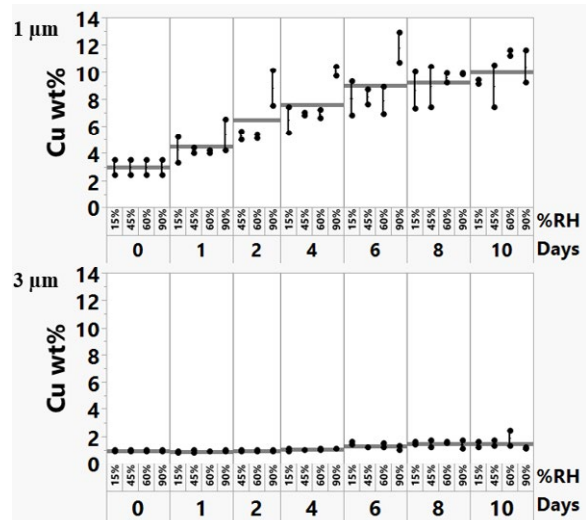


Fig 6- EDS results for the Cu wt.% for each sample. Samples with a Sn thickness of 1 µm are shown in the upper plot, while 3 µm are in the lower plot. The horizontal lines represent the group means for amount of days.

The observed Cu wt.% was inversely proportional to the Sn wt.%. For the 1 µm thickness, regardless of base metal, the amount of copper increases as exposure time increases. The relative humidity, although statistically significant, did not have as large an impact. From the results displayed in Fig 6, it can be observed that the 3 µm thick Sn layer has an insignificant increase in Cu wt.% across all days and %RH, while the 1 µm layer shows a significant increase in observed Cu. As noted above the Sn_xCu_y intermetallics are forming in both 1 and 3 µm, but due to the thicker layer of Sn, the penetration depth of the EDS measurement is not capturing the intermetallic layer. [16], [17]. A visual representation of the intermetallics observed in the EDS can be observed in Fig 7.

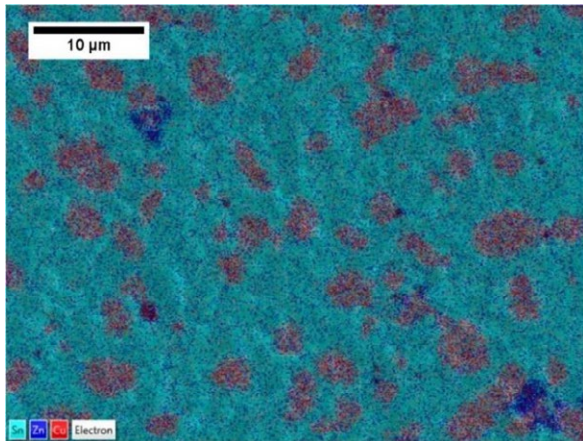


Fig 7- EDS surface scan of a 1 μm Sn plating on C26000 brass. The blue is the Zn diffusing to the surface. The red spots indicate Sn_xCu_y intermetallics.

As shown in Fig 8, relative humidity has the largest statistical impact on Zn wt.%, however, there is not a significant increase in Zn wt.% at humidity levels below 60%. At both 75% and 90%, for both C26000 and C27400, there is a significant increase in the Zn signal initially, and a decrease. This is most likely due to Sn whiskers growth as the Sn whiskers are pure Sn, resulting in a larger measured Sn signal near the surface.

Unsurprisingly, Sn thickness has the largest impact on what composition EDS detects at the surface. As for the Zn and Cu, the two elements leave the brass in different diffusing modes. Cu leaves the brass by forming intermetallics with Sn at the interface between the plating and the brass. These intermetallics increase as the relative humidity exposure and the amount of days increases. However, Zn diffuses out of the brass to the surface of the Sn. This diffusion occurs via the Sn grain boundaries, which can be seen in Fig 1. Zn diffusion is relatively minimal at RH levels below, 60%, but increases significantly at 75% and above. For the C27400 material, observed Zn wt.% levels were higher than C26000 due to the increased Zn content, but this statistical significance is overwhelmed by the import of humidity levels as shown in table 3.

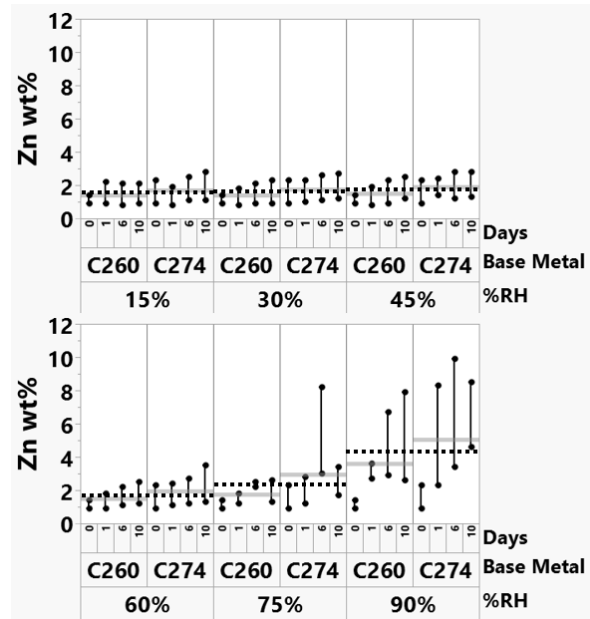


Fig 8- EDS results for the Zn wt.% for each sample with 1 μm Sn. The samples with 3 μm Sn showed identical trends, but with lower Zn wt.%. The dashed black horizontal lines represent the group means for relative humidity and the solid grey horizontal lines represent the group means for base metal.

3.3 Impact of Humidity on the Electrical Contact Resistance of Sn Plated Brass

To characterize the functional performance of the coupons after exposure to accelerated conditions, Low-Level Contact Resistance (LLCR) values were measured under dry-circuit conditions. Reference test probes comprised of 6mm diameter hemispheres plated with 1.5 μm nickel and 0.76 μm cobalt-hardened gold. UNS C51100 phosphor bronze was used as the substrate material for the reference probes. For each coupon, nine LLCR measurements were recorded as a function of the normal load (without wipe) and then with a wipe distance of 530 μm at 200 g normal load. Fig 9 presents the LLCR values measured for coupons with different tin layer thicknesses and substrates after exposure to various humidity levels for 10 days. The values measured without wipe using a 200 g normal load are presented on the bottom, and the values measured after a 530 μm wipe 200 g normal load are presented on the top. When measured without wipe, the coupons exposed to even 90% relative humidity for 10 days do not show any appreciably increased LLCR values in comparison with the control or the coupons exposed to lower humidity levels for the same duration. As expected, the LLCR values measured with wipe are typically lower than those measured without wipe. But more importantly, the LLCR values measured for coupons exposed to 90% relative humidity and coupons exposed to lower humidity levels remained comparable, with any differences, measured between the means of the LLCR populations, remaining under 1 m Ω .

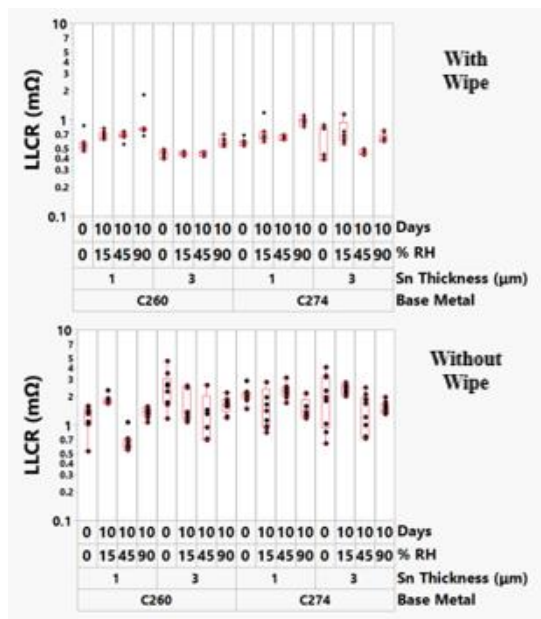


Fig 9- LLCR values measured for coupons exposed to various humidity levels for 10 days with a 530 μm wipe at 200 g normal load (top) and without wipe at 200 g normal load (bottom).

4 Conclusions

This study investigated the impact of relative humidity, Sn plating thickness, exposure time, and base metal composition (C26000 vs C27400) on the discoloration, surface composition, and electrical contact performance of Sn plated brass coupons.

Using a colorimeter using the CIELAB color scale to quantitatively assess the appearance of the Sn surface, it was determined relative humidity is the most significant factor in delaying darkening of the Sn plated surface. Comparatively, the substrate alloy had minimal impact on the surface color. While a thicker Sn layer will delay the darkening of the surface, there will eventually be discoloration over time. In general, discoloration can be delayed by dryer storage conditions, thicker plating layers, or incorporating barrier layers.

The observable surface composition as determined by EDS evolves over time with respect to relative humidity. However, the most significant parameter on the surface composition was the Sn thickness. Clearly, a thicker Sn layer delays diffusion as it is a longer diffusion path.

Using an electrical resistance contact probe, it was determined that there was no significant change in electrical resistance between an as plated coupon and one that was exposed to the most severe conditions in this study (90% RH/10 days). This indicates the darkening of the surface via Zn diffusion is more of an aesthetic issue than a functional or reliability concern with respect to making electrical contact to the surface.

Based on these results, storage conditions rather than substrate materials have the largest impact on visual appearance of Sn plated brass components.

Ongoing work will further investigate Zn diffusion in Sn plated brass coupons in a yearlong longitudinal study where coupons are placed in various controlled and uncontrolled field environments around the world.

5 Acknowledgements

The authors would like to acknowledge Thomas Clark for procuring the metal used for this experiment. The authors would also like to thank Jerry Zhou and Bill Qiu for plating the brass coupons. Finally, the authors would like to thank Dr. Erica Crandall, Dr. Isabell Buresch, Dr. Gregory Pawlikowski, and Mr. Robert Doss for insightful conversations.

6 References

- [1] S. C. Britton and M. Clarke, "Effects of Diffusion from Brass Substrates into Electrodeposited Tin Coatings on Corrosion Resistance and Whisker Growth," *Trans. IMF*, vol. 40, no. 1, pp. 205–211, 1963.
- [2] B. C. Scott, "Zinc Diffusion in Tin Coatings on Brass," *Trans. Inst. Met. Finish.*, vol. 65, no. 90, 1987.
- [3] S. C. Britton and M. Clarke, "Detection of Zinc Diffusion into Tin Coatings on Brass," *Trans. Inst. Met. Finish.*, vol. 36, 1959.
- [4] M. A. Ashworth, "An Investigation into zinc diffusion and tin whisker growth for electroplated tin deposits on brass," *J. Electron. Mater.*, vol. 4, no. 3, pp. 1005–1016, 2014.
- [5] I. Buresch, "Yellowishing of tin coatings at elevated temperatures," *27th Int. Conf. Electr. Contacts, ICEC 2014 - Proc.*, pp. 175–180, 2014.
- [6] C.-Y. Yu, K.-J. Wang, and J.-G. Duh, "Interfacial reaction of Sn and Cu-xZn substrates after reflow and thermal aging," *J. Electron. Mater.*, vol. 39, no. 2, pp. 230–237, 2010.
- [7] InfoMine, "Historical Nickel Prices and Price Chart," 2017. [Online]. Available: <http://www.infomine.com/investment/metal-prices/nickel/all/>.
- [8] Aurubis, "Technical Datasheet C26000." pp. 1–3, 2018.
- [9] Aurubis, "Technical Datasheet C27400." pp. 1–3, 2018.
- [10] W. D. Callister and D. G. Rethwisch, *Materials Science and Engineering, An Introduction*, 9th ed. 2014.
- [11] R. Resnick and R. Balluffi, "Diffusion of Zinc and Copper in Alpha and Beta Brasses," *J. Met.*, 1955.
- [12] T. E. Connectivity, "502-127005 Performance Test, 250 Series FASTON Receptacle," 2012.
- [13] M. Myers, M. Leidner, H. Schmidt, and H. F.

- Schlaak, "Extension and Experimental Verification of a New 'First Contact' Method to Model Performance of Multilayer Contact Interfaces," in *Proceedings of the Fifty Fourth IEEE Holm Conference on Electrical Contacts*, 2008, pp. 66–73.
- [14] E. R. Crandall, G. T. Flowers, P. Lall, and M. J. Bozack, "Whisker growth under controlled humidity exposure," *Electr. Contacts, Proc. Annu. Holm Conf. Electr. Contacts*, pp. 49–54, 2011.
- [15] E. R. Crandall, *Factors Governing Tin Whisker Growth*. Springer, 2013.
- [16] M. Dittes, P. Obermdorff, and L. Petit, "Tin Whisker formation - results, test methods and countermeasures," *53rd Electron. Components Technol. Conf.*, pp. 822–826, 2003.
- [17] J. Gong, C. Liu, P. P. Conway, and V. V. Silberschmidt, "Evolution of CuSn intermetallics between molten SnAgCu solder and Cu substrate," *Acta Mater.*, vol. 56, no. 16, pp. 4291–4297, 2008.

Simulations of switching devices with the example of a circuit breaker: the knowns, the unknowns, and the way ahead.

Henrik Nordborg, Roman Fuchs, Mario Mürmann,
OST Eastern Switzerland University of Applied Sciences, Rapperswil, Switzerland

Abstract

Numerical simulations of gas discharges have long been considered too challenging for routine use in product development. There are two reasons for this: the complex physics involved and the lack for suitable software tools. The physical complexity requires us to be judicious in the choice of models as we are constantly forced to compromise between speed and accuracy. The challenge is to find approximations good enough for specific applications and there will never be one universal simulation model for all kinds of arc discharges.

The lack of suitable software tools is partly due to lack of interest from software vendors and partly due to the difficulty of coupling the equations involved. Whereas the flow equations are best solved using a finite volume formulation, the electromagnetic equations are best solved using finite elements. Currently, the perfect algorithm for coupling the equations only exists on paper.

Despite these difficulties, significant progress has been made in recent years. This paper tries to outline the state-of-art in simulations of electric arcs and gas discharges with a detailed discussion of the approximations made and their impact on convergence and accuracy. We emphasize that arc simulations, if correctly used and interpreted, are useful tools for product development today. In particular, simulations can deliver results that are only indirectly related to the arcing process, such as pressure build-up and mechanical stresses on enclosures.

In addition, we argue that a paradigm shift will be required to develop better software simulation tool. Rather than first developing theoretical models and implementing them, we need to start by establishing an efficient computational framework and fill in the details later. An efficient and parallelizable code is required to validate the simulations in rigorous manner.

1 Introduction

Numerical simulations are an essential part of modern product development, promising to shorten development times and optimizing products. This is only natural, given that all products are designed in CAD and the 3D geometries are always available. Given the increasing availability of computing power, new algorithms for numerical optimization, and developments in adaptive manufacturing, numerical simulations are more important and promising than ever.

In many areas, the use of numerical simulations has become standardized, and a lot of excellent software tools exist. This is true for rigid-body dynamics, structural mechanics, thermal and electromagnetic simulations, and fluid dynamics. Unfortunately, many phenomena important to switching devices are missing on this list. This is mainly due to the extreme physical conditions present in arc discharges, with high temperatures and large electric fields. Not only do these require the coupling of various simulation disciplines, such as fluid dynamics, electromagnetic field simulations, and transient structural mechanics, they also require detailed knowledge about material properties, which can be difficult to obtain. This is particularly true for the electrical contacts, where the interaction of the gas discharge

with a metallic surface leads to a number of interesting but not necessarily desirable effects, such as contact erosion and evaporation of metal into the plasma.

The fact that arc simulations are challenging does not make them less relevant to product development. It does mean however, that one must be much more cautious about what, when, and how to simulate, and that the simulation of switching devices has to be considered a long-term research effort, which probably has to be initiated with in collaboration with a university to be successful.

Before going into the physical and technical details, I would like to start with some general remarks relevant to all complex simulations. First, one needs to understand that simulations are engineering tools, which are used to answer specific questions. To paraphrase Einstein, simulations should be as simple as possible, but not simpler. There is no point in building a simulation model which captures every aspect of the system, even if it were feasible. Only by focusing on the question at hand, it is possible to understand the requirements on the model for the problem at hand.

Development engineers have long understood the usefulness of good numerical models. Recently, the rumor of their usefulness has reached marketing departments, who have decided to rename them Digital Twins. However, the learning effect from developing such models

is often underappreciated. The main benefit of numerical simulations is not that they relieve us from the responsibility to think, but that they require us to think in detail about the product we try to design. It might be possible to build a switching device using a trial-and-error approach without detailed understanding of all the physical processes, but it is not possible to develop a simulation model this way.

We also must discuss topics of accuracy, verification, and validation. Unfortunately, complex non-linear physical effects cannot be computed with the same accuracy as simpler linear problems. Achieving good agreement between experiments and simulations can therefore be very time consuming, if not impossible. In many cases, it is only possible to validate parts of the model using simplified experiments. As a result, one sometimes has to be satisfied with simulations getting the trend right, rather than achieving perfect quantitative agreement.

Finally, we come to the topic of speed and stability of the numerical solver, a topic which has been ignored for far too long by the research community. Developing good models for arc simulations involves a lot of trials and errors and requires a large number of simulations to be performed and compared with experiments. For this to be manageable, the numerical solvers must be fast, stable, and accurate. In our view, far too little effort has been spent on understanding the numerical properties of arc simulations and to develop better and faster simulation tools. Since the structure of the equations is known, it is possible to develop a general framework for solving them without knowing all the details. Access to a suitable Open Source code for this kind of simulations, which could be developed by a consortium of power device manufacturers with government funding would provide a significant boost to the industrial use of gas discharges for various applications.

2 Physical Modeling

An ideal switching device would have zero resistance as long as a current is flowing through it, and an infinitely high resistance immediately after current zero. Since such a device does not exist, we use electrical arcs, which are extremely non-linear resistors negative with differential resistivity. The easiest way to understand the role of an arc is to model its resistivity using a Cassie-Mayr model [1]

$$\frac{dR_a}{dt} = \frac{R_a}{\tau} \left(1 - \frac{UI}{P} \right) \quad (1)$$

where R_a is the arc resistance, I is the current, and U is the arc voltage. The advantage of the arc is that its cooling power, which is denoted P , can be manipulated in various way, using a gas flow as in self-blast breakers, extending the length of the arc, or introducing splitter plates [2]. As soon as the cooling power is larger than the electric power UI , the resistance of the arc will

grow exponentially with a time constant τ , eventually leading to its extinction. The goal of good circuit breaker design is typically to maximize the cooling power and minimizing the time constant.

The basis for the simulation of switching devices is the physical modeling of a gas discharge. This means that we consider an ionized gas at high temperature exposed to an electric field. The degree of ionization depends both on the temperature and the electric field strength. In most industrial applications, we can assume the plasma to be collision dominated, making it possible to introduce an electrical conductivity $\sigma(p, T)$ depending only on pressure and temperature. We can also assume that the plasma is charge neutral, meaning that any relevant volume of the plasma will contain the same number of positive and negative charges. Another way of formulating this statement is to state that the Debye length

$$\lambda_D = \sqrt{\frac{\epsilon_0 k_B T}{n q^2}}, \quad (2)$$

where n is the charge density and T the plasma temperature, is short compared to all physically relevant length scales. This is not true close to the electrodes, where a different modeling approach will be required. The advantage of assuming charge neutrality is that the gas discharge can be modeled as a simple electrically conducting fluid, where the electrical conductivity $\sigma(p, T)$ couples the flow equations with the equations for the electromagnetic field. A typical result is shown in in Fig. 1. The details of this model, which is typically referred to as magnetohydrodynamics, will be provided below. As it only uses one temperature for all species, the model describes a thermal plasma. An excellent review on the topic has been written by Gleizes *et al.* [3].

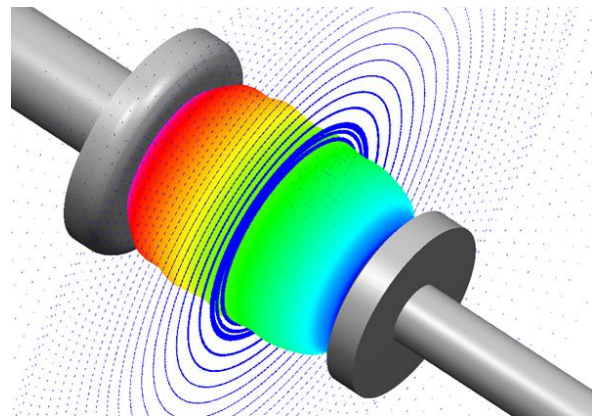


Fig 1. A typical electric arc between two electrodes. The color represents the electric potential, and the arrows show the azimuthal magnetic induction B .

A detailed simulation of an arc can easily be coupled to a circuit model to determine its behavior under operation of the switching device. In other words, our goal is to replace the resistance from the Cassie-Mayr equation with a detailed simulation. This allows us to understand how the cooling power and the time constant of the arc can be influenced by careful product design.

2.1 Fluid Dynamics

The derivation of the Navier-Stokes equations for fluid dynamics can be found in many excellent textbooks [4, 5]. They describe the conservation of mass, momentum, and energy, and can be written

$$\frac{\partial \rho}{\partial t} + \nabla \cdot (\rho \mathbf{u}) = 0 \quad (3)$$

$$\frac{\partial (\rho \mathbf{u})}{\partial t} + \nabla \cdot (\rho \mathbf{u} \otimes \mathbf{u}) = \nabla \cdot \boldsymbol{\sigma} + \mathbf{j} \times \mathbf{B} \quad (4)$$

$$\begin{aligned} \frac{\partial (\rho e)}{\partial t} + \nabla \cdot (\rho \mathbf{u} e) = \\ \nabla \cdot (\boldsymbol{\sigma} \mathbf{u}) + \mathbf{j} \cdot \mathbf{E} - \nabla \cdot \mathbf{q} - \nabla \cdot \mathbf{q}_{rad} \end{aligned} \quad (5)$$

The equations describe a fluid with density ρ and flow velocity \mathbf{u} . The specific energy of the fluid is given by

$$e = e_{in}(p, T) + \frac{1}{2} u^2$$

with $e_{in}(p, T)$ being the internal (thermodynamic) energy of the gas, as a function of pressure and temperature. The stress tensor contains the pressure, viscous shear forces, and the effects of turbulence as provided by a suitable turbulence model,

$$\boldsymbol{\sigma} = -p\mathbf{I} + \mu(\nabla \mathbf{u} + \nabla \mathbf{u}^T) - \frac{2}{3}\mu(\nabla \cdot \mathbf{u})\mathbf{I} + \boldsymbol{\sigma}_{Re} \quad (6)$$

Here, μ represents the dynamic viscosity, \mathbf{I} is the identity tensor, and $\boldsymbol{\sigma}_{Re}$ is the Reynolds stress tensor from turbulence modeling. Finally, heat is transported through the plasma through heat conduction, including both the molecular and turbulent parts,

$$\mathbf{q} = -(\lambda + \lambda_{Re})\nabla T,$$

and radiation \mathbf{q}_{rad} as will be described below. The full set of Navier-Stokes equations, including the turbulence models and radiation are implemented in a number software packages. It is important to use a software which can handle highly compressible flow. The coupling to the electric field can be implemented using the appropriate source terms in the momentum and energy equations. The main difficulties are the following:

1. It is necessary to perform simulations of compressible gas dynamics with real-gas data. These data need to be available at extremely high temperatures and pressure and for different gas compositions.
2. The turbulence of the gas must be modelled. There is no reason to believe that standard turbulence models will work under the extreme conditions present in gas discharges.
3. Radiative heat transfer must be computed in a participating medium with a very complex absorption spectrum.

2.1.1 Real gas properties and mixing rules

As was mentioned above, all arcing phenomena must be simulated using compressible gas dynamics due to the high temperatures and pressures. Furthermore, as the temperature increases, the gas molecules will dissociate and become ionized, leading to significant changes in the material properties. This can be clearly seen in the specific heat $c_p(p, T)$, which shows large peaks associated with the dissociation of the gas, as shown in Fig. 2. For the purpose of accuracy and numerical stability, it is important to implement the material properties in a thermodynamically consistent manner, so that the thermodynamic relations between density, enthalpy, specific heat, and the speed of sound, are exactly satisfied. This can be accomplished by using some form of differentiable interpolation functions, such as cubic splines or polynomials.

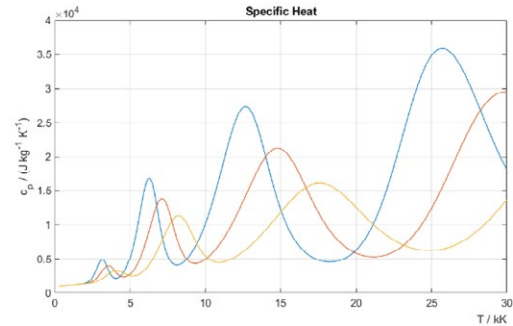


Fig. 2 Specific heat c_p of air as a function of temperature. The data was obtained from A. B. Murphy [6]

As it is not possible to measure gas properties at the conditions present in arcs, they must be calculated from first principles. Thus, we start from a cold gas consisting of molecules and compute the composition, the thermodynamics properties, and the transport coefficients, taking dissociation and ionization processes into account. The theory for doing so is well established, but the calculations are rather involved, requiring a lot of data to be processed [7–9].

A more fundamental problem is how to deal with gas mixtures. The problem is that by mixing two gases and heating them up, we might create new species that are not present in either of the two separate gases. For example, a mixture of SF_6 and copper vapor can contain new molecules, such as CuF_2 . It is therefore not possible to simply combine the properties of the original gases using mixing rules. Rather, a multi-dimensional lookup table with thermodynamics properties as a function of pressure, temperature, and the various concentrations, needs to be generated, e.g.,

$$\rho = \rho(p, T, C_{Cu}, \dots). \quad (7)$$

Obviously, the more different materials are involved, the more laborious does this approach get.

Determining the relevant gas or plasma properties for arc simulation applications is an important task. After

all, we know that the gas properties are essential for the switching performance of circuit breakers. The topic has received renewed interest with the demand to replace SF₆ in high-voltage applications [10, 11].

2.1.2 Turbulence modeling

Turbulence modeling is an underappreciated topic in gas discharge simulations. Most simulations still use a standard turbulence model based on Reynolds-averaged Navier-Stokes (RANS). There is absolutely no reason to believe that this would be a good idea, as these models are developed for stationary flows and are calibrated for very different flow simulations [12].

The purpose of the turbulence model is to account for the flow patterns (often referred to as eddies) which are too small to be resolved by the time step and mesh used in the simulation. These eddies are important, as they significantly increase the viscosity, heat conductivity, and diffusivity of the plasma. Consequently, the effect of turbulence is added to the transport equations, i.e., for the viscosity we have

$$\mu \rightarrow \mu(p, T) + \mu_t \quad (8)$$

where the second represents the turbulent or eddy viscosity. Analogous formulas apply to the diffusivity and heat conductivity. In the case of RANS, only the time averaged effect of turbulence is calculated, meaning that the approximation is only valid when the turbulent length scale is much shorter than all other relevant time scales. Furthermore, it is assumed that the effect of turbulence is isotropic and that the eddies are neither influenced by the flow direction nor the electromagnetic field. All these assumptions are questionable in an arcing device.

A second class of turbulence models are Large Eddy Simulations (LES), which resolve the large eddies whilst using a simple modeling for the smaller ones. In contrast to the RANS models, LES does not require any additional equations to be solved. On the other hand, a significantly finer mesh is required.

There has not been much research devoted to the systematic study of turbulence in arc simulations. The reason is probably simple: validating the turbulence model would require very detailed data from well-controlled experiments. These data are currently not available.

2.2 Simulation of electromagnetic field

The full set of Maxwell equations can be written

$$\nabla \times \mathbf{H} = \mathbf{j} + \frac{\partial \mathbf{D}}{\partial t} \quad (9)$$

$$\nabla \times \mathbf{E} + \frac{\partial \mathbf{B}}{\partial t} = 0 \quad (10)$$

$$\nabla \cdot \mathbf{D} = \rho \quad (11)$$

$$\nabla \cdot \mathbf{B} = 0 \quad (12)$$

Computing the divergence of the first equation, we obtain the continuity equation for the electrical current

$$\frac{\partial \rho_e}{\partial t} + \nabla \cdot \mathbf{j} = \nabla \cdot \left(\epsilon_0 \frac{\partial \mathbf{E}}{\partial t} + \sigma \mathbf{E} \right) = 0. \quad (13)$$

Comparing the two terms in the second bracket, we see that second term dominates for time scales larger than

$$t_D = \frac{\epsilon_0}{\sigma} \quad (14)$$

Thus, as long as the conductivity is sufficiently large, we can safely ignore the displacement current and only assume charge conservation,

$$\nabla \cdot \mathbf{j} = 0. \quad (15)$$

The remaining equations are typically solved by the introduction of electromagnetic potentials, with

$$\mathbf{B} = \nabla \times \mathbf{A} \quad (16)$$

$$\mathbf{E} = -\nabla \phi - \frac{\partial \mathbf{A}}{\partial t} \quad (17)$$

The remaining equation to be solved is

$$\begin{aligned} \nabla \times \left(\frac{1}{\mu_0} \nabla \times \mathbf{A} \right) = \\ -\sigma \nabla \phi - \sigma \frac{\partial \mathbf{A}}{\partial t} + \sigma \mathbf{u} \times (\nabla \times \mathbf{A}) \end{aligned} \quad (18)$$

Assuming the $\nabla \cdot \mathbf{A} = 0$, we can write this as

$$\frac{\partial \mathbf{A}}{\partial t} = \frac{1}{\sigma \mu_0} \Delta \mathbf{A} - \nabla \phi + \mathbf{u} \times (\nabla \times \mathbf{A}) \quad (19)$$

This is a diffusion equation for the magnetic vector potential, with a diffusion constant of

$$D = \frac{1}{\sigma \mu_0} \quad (20)$$

From this, the characteristic time and velocity scales are found to be

$$t_s = \sigma \mu_0 L^2 \quad (21)$$

and

$$u_s = \frac{1}{\sigma \mu_0 L} \quad (22)$$

where L is the characteristic length scale of the arc. As long as we are only interested in time scales $t \gg t_s$, we can drop the transient term. If $u \gg u_s$, we can drop the velocity-dependent term. Both these conditions are typically valid for smaller arcing devices.

The problem with solving the electromagnetic equations this way is that they are not valid in the limit of vanishing conductivity. It is therefore necessary to introduce an artificial minimum conductivity in the cold gas, making it impossible to simulate the process of dielectric breakdown or the extinction of the arc. Furthermore, choosing the minimum conductivity too small will make the equation $\nabla \cdot \mathbf{j} = 0$ very ill conditioned, leading to numerical difficulties. A better electromagnetic model would have to relax the requirement of charge neutrality.

Solving the Maxwell equations in the presence of ferromagnetic materials is difficult due to the requirement that

$$\mathbf{n} \cdot (\mathbf{B}_1 - \mathbf{B}_2) = 0 \quad (23)$$

and

$$\mathbf{n} \times (\mathbf{H}_1 - \mathbf{H}_2) = 0 \quad (24)$$

at the interface between two domains. Since $\mathbf{B} = \mu\mathbf{H}$, satisfying both these conditions requires the use of special electromagnetic edge elements when discretizing the equations [13]. This makes the implementation of arc simulations somewhat difficult, as the electromagnetic fields must be computed using finite elements, whereas the flow equations are solved using finite volumes. An alternative approach could be to use finite elements in the solid domain and finite volumes both for the flow and the electromagnetic equations in the flow domain.

2.3 Radiative Heat Transfer

Due to the high temperatures in gas discharges, a large fraction of the power is dissipated as radiation. The modeling of thermal radiation is based on the spectral radiance

$$I_\nu(\mathbf{r}, \mathbf{s}) = I_\nu(\mathbf{r}, \phi, \theta) \quad (25)$$

which measures the amount of radiation with frequency ν at point \mathbf{r} travelling in the direction \mathbf{s} . The physical unit is $[I_\nu] = \text{W}/\text{m}^2 \cdot \text{sr}$. The spectral radiance is typically computed from a simplified version of the radiation transfer equation (RTE)

$$\mathbf{s} \cdot \nabla I_\nu = \kappa_\nu (I_\nu^b - I_\nu), \quad (26)$$

where $I_\nu^b(T)$ is the irradiance from a gas in local thermal equilibrium,

$$I_\nu^b(T) = \frac{2h}{c^2} \frac{\nu^3}{e^{h\nu/k_B T} - 1}. \quad (27)$$

and κ_ν is the absorption coefficient. The equation (26) can be solved for a single frequency ν using the discrete ordinate method, which is implemented in most flow solvers. A less accurate but computationally less demanding approach is the P1 method[14].

The net emission from each point in space can be written $\nabla \cdot \mathbf{q}_{rad}$ with

$$\mathbf{q}_{rad}(\mathbf{r}) = \iint \mathbf{s} I_\nu(\mathbf{r}, \mathbf{s}) d\Omega d\nu \quad (28)$$

this net emission can be added as an energy sink to the energy equation, as discussed above.

The main difficulty with computing the effect of radiation is the strong frequency dependence of the absorption coefficient, as shown in Fig. 3. Since it is not possible to solve the RTE for every frequency, it becomes necessary to divide the absorption spectrum into bands with averaged absorption coefficients. The question is

how to select the bands and how to perform the averaging, given the large absorption peaks. Physically, the problem is the following: A large value of the absorption coefficient κ_ν means that radiation is absorbed on a length scale $l_\nu = 1/\kappa_\nu$. If this length is much shorter than any relevant length scale, it does not really matter how short it is. In other words, it makes sense to renormalize the peaks in the spectrum according to

$$\kappa_\nu \rightarrow \kappa_\nu^R = \frac{1}{h} (1 - e^{-\kappa_\nu h}), \quad (29)$$

where h is some suitably chosen length scale. The renormalized spectrum will look be the original one, but without the largest peaks. Choosing $h = 3R$, where R is the arc radius, leads to good results. [15, 16]

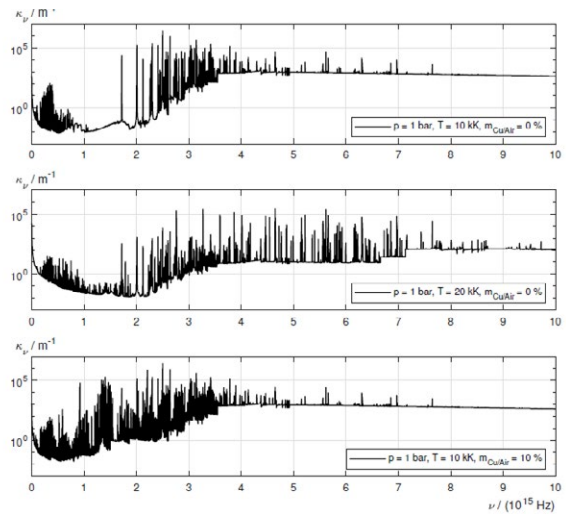


Fig. 3 Absorption spectrum κ_ν for air and air with 10% mass ratio of copper [17].

2.4 Electrodes and Walls

A key aspect of arc simulation is the interaction of the arc with the electrodes and walls. In both cases, detailed modeling of the processes is neither possible nor desirable, as everything happens on length scales which are too short to be resolved by a reasonable mesh. It is therefore useful to implement a 2D model, which can be implemented as a boundary condition on the surface.

2.4.1 Arc Root Models

The physical processes taking place at the electrodes are too complex to be included into a simulation directly, even if suitable physical models were available [18, 19]. Fortunately, as we only need an arc root model for the simulation of the thermal plasma, we do not need to know all the details. We only need to know the voltage drop, the energy balance, and the possible evaporation of electrode material. In other words, the task is to develop an integral model for a thin sheath close to the electrode.

A crucial part of this model is the voltage drop $U(j)$ as a function of current density and temperature. Methods

for doing so were developed by Rümpler and others [20, 21] and we have used similar models [17, 22].

$$\frac{U}{U_0} = \frac{(j/j_0) + \gamma(j/j_0)^2}{1 + (j/j_0)^2} \quad (30)$$

where

$$U_0 = 28.6 \text{ V}, j_0 = 2.10e6 \text{ A/m}^2, \gamma = 0.175 \quad (31)$$

Similar models for the voltage drop can be used to model the effect of splitter plates, where the introduction of a splitter plate leads to the creation of two new arc roots, thereby increasing the arc voltage.

The arc root model also influences the motion of the arc and more systematic research would be needed to clarify this behavior.

The voltage drop introduces an additional energy source at the surface, which needs to be included in the energy equation.

Accounting for metal vapor is important, as it has a significant impact on both the electrical conductivity of the plasma and the absorption spectrum, apart from the thermodynamic effects [20, 21]. Typically, an erosion rate can be defined as a function of the current density, and the energy required needs to be handled as an energy sink at the electrode surface.

2.4.2 Ablation

Ablation of wall material is vital for the pressure buildup in high-voltage breakers but is also important in low-voltage switching devices. The standard approach is to use the incoming radiative heat flux and the latent heat of the wall material to define a mass source at the wall. [22, 23]. This leads to increased pressure buildup and cooling of the arc.

2.5 Computational Considerations

Simulations of arc discharges are challenging. The task of simulating a compressible turbulent gas flow with radiation transport is comparable to the challenges facing researchers working in combustion modeling, where simulations are routinely run on large meshes using LES and significant computing power. Fortunately, because flow simulations can be easily parallelized, the use of large meshes does not present an obstacle [24].

Solving the Maxwell equations in complex geometries is computationally expensive, especially in presence of ferromagnetic materials. The reason is that the corresponding system of equations is ill conditioned, limiting the scalability of the simulation. New algorithms that solve this problem have only been recently developed but have not yet been implemented in simulation tools [25, 26].

Ideally, one would want to solve the electromagnetic and flow equations on the same mesh in the entire flow domain. Since the electrical conductivity varies on the same length and time scales as the flow parameters, such as temperature and pressure, it makes no sense to try to use a coarse mesh for the electromagnetic part. Furthermore, the electromagnetic algorithm needs to

work efficiently in the limit of vanishing conductivity. Fortunately, we can safely assume that the plasma cannot be magnetized, meaning that we have $\mu = \mu_0$ for the permeability. Our experience shows that the electromagnetic fields can be computed accurately using a finite volume solver in this case. The finite element formulation of the electromagnetic fields is only required in the electrodes. Unfortunately, no simulation tool exists to exploit this fact.

3 State-Of-The-Art

Despite the difficulties of arc simulations, as described on the previous pages, significant progress has been made in recent decades. Many companies have built up significant simulation capabilities mainly, based on the use of commercial simulation tools. One common approach is to use a combination of ANSYS-Fluent for the flow equations, which is coupled to some electromagnetic solver. The approach works sufficiently well to model current-voltage characteristics and pressure buildup in various switching devices. The simulations have been successful both in low-voltage [27–29] and high-voltage devices [30, 31].

In the last couple of years, our research group has built up significant experience in simulating electrical arcs using the commercial software tools Star CCM+ from Siemens PLM. This combines a state-of-the-art flow solver with solvers for the electromagnetic fields, both using finite volumes and finite elements (cf. Fig. 4)

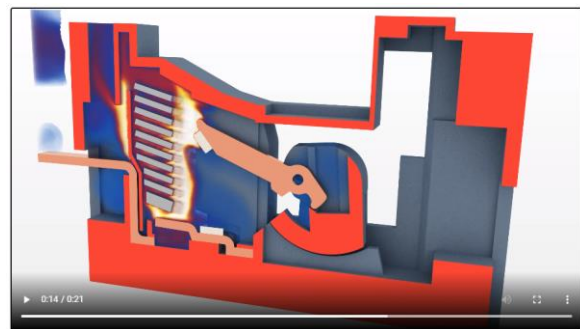


Fig 4. Simulation of a model low-voltage circuit breaker using Star-CCM+. More details can be found here: <https://blogs.sw.siemens.com/simcenter/plasma-arcs-circuit-breakers/>

This allows for the implementation of arc simulations based on existing functionality. Essentially, only the material properties and arc root models need to be implemented. Since most of the work was done in collaboration with private partners, only parts of the work have been published [32, 33].

4 Outlook

The numerical simulation of gas discharges in switching devices has been a research topic for more than two decades. Looking back, significant progress has been made and we are now at a point where such simulations can be used for product development. The accuracy is still far from optimal and the simulation times are still too long. Nonetheless, arc simulations today provide valuable insights into the operation of switching devices.

On the other hand, progress has clearly been hampered by short-term thinking. In contrast to other industrial sectors, there has not been a coordinated effort to develop arc simulation capabilities using publicly funded research projects driven by industrial consortia. Changing this will require a different mindset in the industry. First, an efficient and publicly available research code for gas discharge simulations needs to be developed. This code could be based on other open-source tools and would allow researchers to experiment with the physical modeling. In addition, the code would provide insights into the numerical issues related to arc simulations.

Second, improving the physical modeling will require numerous systematic experiments performed under controlled laboratory conditions. Experiments in complex geometries contain too many unknown parameters to allow for systematic improvement of the models. Experiments will be needed to investigate turbulence, radiation transfer, ablation and erosion models, and material properties.

The ongoing decarbonization of our society will only be possible through increased electrification. Both the integration of renewable energy into the power grid and the rise of electromobility will require new solutions and many more electrical contacts at different current and voltage levels. In addition, the use of electric arcs for other applications, such as waste treatment and metallurgy, is on the rise. In this respect, we are only at the beginning of fascinating research journey.

5 Acknowledgment

The research reported here has been funded by various agencies as reported in the corresponding publications. We gratefully acknowledge support from the Eastern Switzerland University of Applied Sciences.

6 References

[1] O. Mayr, "Beiträge zur Theorie des statischen und des dynamischen Lichtbogens," *Archiv für Elektrotechnik*, vol. 37, no. 12, pp. 588–608, 1943, doi: 10.1007/BF02084317.

- [2] T. Christen and N. Ranjan, "Generalized Mayr Model for Arcs in MV Switches with Splitter Plates," *IEEE Trans. Power Delivery*, p. 1, 2021, doi: 10.1109/TPWRD.2021.3060145.
- [3] A. Gleizes, J. J. Gonzalez, and P. Freton, "Thermal plasma modelling," *Journal of Physics D: Applied Physics*, vol. 38, no. 9, pp. R153–R183, 2005, doi: 10.1088/0022-3727/38/9/R01.
- [4] J. D. Anderson, *Modern compressible flow: With historical perspective / John D. Anderson, Jr*, 3rd ed. Boston, London: McGraw-Hill, 2003.
- [5] J. H. Ferziger, M. Perić, and R. L. Street, *Computational methods for fluid dynamics*. Cham, Switzerland: Springer, 2020.
- [6] A. B. Murphy, "Plasma data for air (private communication)".
- [7] Y. Cressault and A. Gleizes, "Thermodynamic properties and transport coefficients in Ar–H₂ – Cu plasmas," *J. Phys. D: Appl. Phys.*, vol. 37, no. 4, pp. 560–572, 2004, doi: 10.1088/0022-3727/37/4/008.
- [8] Y. Cressault, R. Hannachi, P. Teulet, A. Gleizes, J.-P. Gonnet, and J.-Y. Battandier, "Influence of metallic vapours on the properties of air thermal plasmas," *Plasma Sources Sci. Technol.*, vol. 17, no. 3, p. 35016, 2008, doi: 10.1088/0963-0252/17/3/035016.
- [9] A. B. Murphy, "Calculation and application of combined diffusion coefficients in thermal plasmas," *Sci. Rep.*, vol. 4, 2014, doi: 10.1038/srep04304.
- [10] S. Tian *et al.*, "Research status of replacement gases for SF₆ in power industry," *AIP Advances*, vol. 10, no. 5, p. 50702, 2020, doi: 10.1063/1.5134727.
- [11] W. Chunlin, W. Yi, S. Hao, D. Jiawei, N. Chunping, and Y. Fei, "Thermophysical properties calculation of C₄F₇N/CO₂ mixture based on computational chemistry — A theoretical study of SF₆ alternative," in *2017 4th International Conference on Electric Power Equipment - Switching Technology (ICEPE-ST)*, Xi'an, 102017, pp. 255–258.
- [12] P. Davidson, *Turbulence: An introduction for scientists and engineers / P.A. Davidson*. Oxford: Oxford University Press, 2015.
- [13] J.-M. Jin, *Theory and computation of electromagnetic fields*. Hoboken, New Jersey: Wiley; [Piscataway, 2015.
- [14] M. F. Modest, *Radiative Heat Transfer*. [S.l.]: ELSEVIER ACADEMIC PRESS, 2021.
- [15] H. Nordborg and A. A. Iordanidis, "Self-consistent radiation based modelling of electric arcs: I. Efficient radiation approximations," *Journal of Physics D: Applied Physics*, vol. 41, no. 13, p. 135205, 2008, doi: 10.1088/0022-3727/41/13/135205.
- [16] P. Kloc, V. Aubrecht, and M. Bartlova, "Numerically optimized band boundaries of Planck mean

- absorption coefficients in air plasma,” *J. Phys. D: Appl. Phys.*, vol. 50, no. 30, p. 305201, 2017, doi: 10.1088/1361-6463/aa7627.
- [17] R. Fuchs, “Numerical Modeling and Simulation of Electrical Arcs,” Seminar for Applied Mathematics, ETHZ, Zürich, 2020.
- [18] P. Zhu, J. J. Lowke, and R. Morrow, “A unified theory of free burning arcs, cathode sheaths and cathodes,” *J. Phys. D: Appl. Phys.*, vol. 25, no. 8, pp. 1221–1230, 1992, doi: 10.1088/0022-3727/25/8/011.
- [19] R. Morrow and J. J. Lowke, “A one-dimensional theory for the electrode sheaths of electric arcs,” *J. Phys. D: Appl. Phys.*, vol. 26, no. 4, pp. 634–642, 1993, doi: 10.1088/0022-3727/26/4/016.
- [20] P. Kloc, V. Aubrecht, M. Bartlová, and O. Coufal, “Radiation transfer in air and air-Cu plasmas for two temperature profiles,” *Journal of Physics D: Applied Physics*, vol. 48, no. 5, p. 55208, 2015, doi: 10.1088/0022-3727/48/5/055208.
- [21] A. Gleizes and Y. Cressault, “Effect of Metal Vapours on the Radiation Properties of Thermal Plasmas,” *Plasma Chem Plasma Process*, 2016, doi: 10.1007/s11090-016-9761-y.
- [22] C. Rümpler, H. Stammberger, and A. Zacharias, “Berücksichtigung gasender Kunststoffe bei der Simulation des Schaltlichtbogens,” *VDE*.
- [23] E. Doméjean, P. Chévrier, C. Fiévet, and P. Petit, “Arc - wall interaction modelling in a low-voltage circuit breaker,” *J. Phys. D: Appl. Phys.*, vol. 30, no. 15, pp. 2132–2142, 1997, doi: 10.1088/0022-3727/30/15/003.
- [24] C. J. Rutland, “Large-eddy simulations for internal combustion engines – a review,” *International Journal of Engine Research*, vol. 12, no. 5, pp. 421–451, 2011, doi: 10.1177/1468087411407248.
- [25] R. Hiptmair, “Multigrid Method for Maxwell's Equations,” *SIAM J. Numer. Anal.*, vol. 36, no. 1, pp. 204–225, 1998, doi: 10.1137/S0036142997326203.
- [26] J. Smajic, M. K. Bucher, C. Jager, and R. Christen, “Treatment of Multiply Connected Domains in Time-Domain Discontinuous Galerkin \mathcal{H}^1 – \mathcal{H}^1 Eddy Current Analysis,” *IEEE Trans. Magn.*, vol. 55, no. 6, pp. 1–4, 2019, doi: 10.1109/TMAG.2018.2890525.
- [27] C. Rümpler *et al.*, “Advances in design of miniature circuit breakers for pressure load,” in *Albert-Keil-Kontaktseminar*, Karlsruhe, 2017.
- [28] C. Rümpler, H. Stammberger, and A. Zacharias, “Low-Voltage Arc Simulation with Out-Gassing Polymers,” in *2011 IEEE 57th Holm Conference on Electrical Contacts (Holm 2011)*, Minneapolis, MN, USA, pp. 1–8.
- [29] L. Ghezzi, “Modeling and Simulation of Low Voltage Arcs,” Ph. D. Dissertation, Technische Universiteit Delft, Delft, The Netherlands, 2010.
- [30] M. T. Dhotre, X. Ye, M. Seeger, M. Schwinne, and S. Kotilainen, “CFD simulation and prediction of breakdown voltage in high voltage circuit breakers,” in *2017 IEEE Electrical Insulation Conference (EIC)*, Baltimore, MD, USA, 62017, pp. 201–204.
- [31] F. Reichert, A. Petchanka, P. Freton, and J. J. Gonzalez, “Modelling and Simulation of SF6 High-Voltage Circuit-Breakers - an Overview on Basics and Application of CFD Arc Simulation Tools,” *PPT*, vol. 4, no. 3, pp. 213–224, 2017, doi: 10.14311/ppt.2017.3.213.
- [32] R. Fuchs, M. Mürmann, and H. Nordborg, “Towards an Efficient Arc Simulation Framework,” *PPT*, vol. 4, no. 1, pp. 79–82, 2017, doi: 10.14311/ppt.2017.1.79.
- [33] M. Mürmann, A. Chusov, R. Fuchs, A. Nefedov, and H. Nordborg, “Modeling and simulation of the current quenching behavior of a line lightning protection device,” *J. Phys. D: Appl. Phys.*, vol. 50, no. 10, p. 105203, 2017, doi: 10.1088/1361-6463/aa560e.

Remarks Concerning Arc Roots in CFD Modeling of Switching Arcs

Manfred Lindmayer¹, TU Braunschweig, Braunschweig, Germany, M.Lindmayer@tu-braunschweig.de

Abstract

This paper reviews arc root models used to represent the processes at anode and cathode of arcs in a simplified way. From the electrical potential distribution, there are the voltage falls V_A and V_C across thin sheaths in front of both electrodes. Their product with the current and current density, respectively, characterize the power (power density) generated in these areas. The powers (power densities) that flow to the electrodes and thus determine their heating and erosion are often expressed by equivalent voltages V_{eqA} , V_{eqC} . A frequent approach to model arc roots within computational fluid dynamics (CFD) models of switching arcs is to replace the root region within the CFD volume by a thin layer adjacent to the electrodes of voltage drops $V_A(J)$, $V_C(J)$, depending on the current density there. An equivalent “contact resistance” is an alternative. The power generated in this region is the product of voltage and current density. Its partition between the electrodes and the arc column then follows the rules of the CFD differential equations (“Navier-Stokes” equations). However, the physics of the fall regions is completely different, with charge carriers freely falling without collisions, and hitting the electrodes. It is therefore better to separate both effects. For this, the knowledge of V_A , V_C , V_{eqA} , and V_{eqC} is necessary. After a summary of the methods used so far by the author’s own research group, experimental work is considered to determine the required values, and additionally the current density at the roots. Two ways can be differentiated: Comparison of experiments with simulations of fall regions, and with simulations of the electrode heating. Based on voltage data from the literature, a modified model of the power flows in the electrode fall regions is derived. It also holds for zero length of the arc column. Finally, an implementation into CFD programs suitable for complete simulations is suggested.

1 Problem, Objectives

A low-voltage switching arc consists of three essential regions [1]: The main area is the so-called arc column. Its length lies in the millimeter to centimeter range, and it can be treated in simulations as a fluid continuum following the rules of Computational Fluid Dynamics (CFD). They describe the balances of mass, momentum, and power in the form of second order partial differential equations. Often it is justified to assume the plasma of the column to be in thermal equilibrium, allowing identical temperatures for all particles (electrons, ions, neutral molecules and atoms) [2-4]. Then the properties of this “single fluid” depend on the local temperature and pressure. Under special conditions, the plasma is treated as a “two fluid” model, with different temperatures for the lightweight electrons and the heavier ions and neutrals [5]. Immediately adjacent to anode and cathode the regions of the anode and cathode falls (“sheaths”) extend over a thickness of around one mean free path, i.e. across micrometer length. The physical processes there are completely different from the CFD case. Particles freely fall across the fall regions and hit the electrodes, as well as the ends of the column facing both electrodes. Equivalent to the three regions, the arc voltage (V_{arc}) consists of the voltage fall along

the column (V_{col}) plus the anode fall and cathode fall voltage drops (V_A , V_C). In analogy power losses and power generation, respectively, take place in these three regions. The aim of complete simulations of switching arcs can be twofold: The temporal development of arc voltage in interaction with the electric circuit determines the switching success. On the other hand, the power flowing to the contacts, the insulating walls, or the splitter plates (“deion plates”) provides information about the thermal stress and the thermal erosion of these parts.

Often the powers flowing in the arc are expressed in terms of voltages [6, 7]. For a current $I = \text{const}$ across all three parts the powers are proportional to the voltage. Similarly, power densities and current densities are linked by the appropriate voltage.

Fig. 1 demonstrates this. It is assumed that the power generations (power densities) in both the anode and cathode falls (p_A , p_C) split up each into one “equivalent” part flowing toward the electrode (p_{eqA} , p_{eqC}) and toward the column (p_{colA} , p_{colC}), see Fig. 1a. Fig. 1b shows the corresponding voltages. Additionally, Fig. 1c depicts for both arc roots an example of characteristics fall voltage vs. current density [3, 8, 9], here from [9]. They will be explained later.

¹ The author is indebted to Rockwell Automation Switzerland GmbH for the cooperation in the field of low-voltage switching

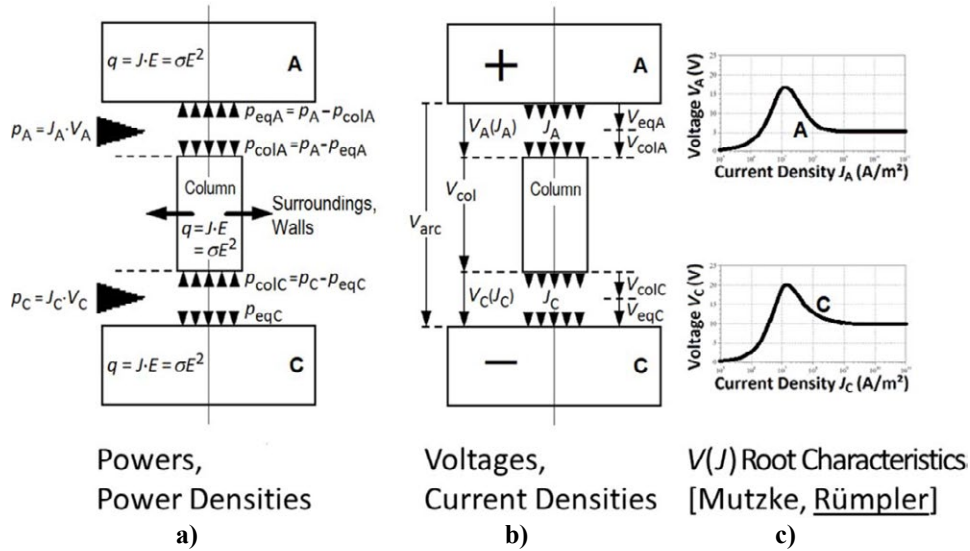


Fig. 1 Power Flows (a) and Voltages (b, c) in Switching Arcs

There have been complete simulations where the system of CFD equations has been solved together with equations from cathode and anode fall theories [5, 10-13]. For a more simplified consideration concerning the arc roots, it is sufficient to take Fig. 1 as starting point. Besides characteristics like Fig. 1c, the knowledge of the fall voltages V_A , V_C , and the equivalent portions to the electrodes V_{eqA} , V_{eqC} is required. The corresponding power densities can then be applied as boundary conditions for a CFD simulation of the plasma column, as well as a coupled power simulation of the electrode heating. For pure contact erosion simulations [14], only solid body heat transfer simulation and the knowledge of V_{eqA} , V_{eqC} are necessary. Then the root diameters and power densities there must also be known.

2 Literature Survey on Arc Root Models for Simulations

As an initial overview, **Fig. 2** [15] shows the components of power balances in the fall regions and at the adjacent metallic electrodes. Investigations published so far differ in which processes have been used to derive the simplified characteristic values for the simulation of fall regions.

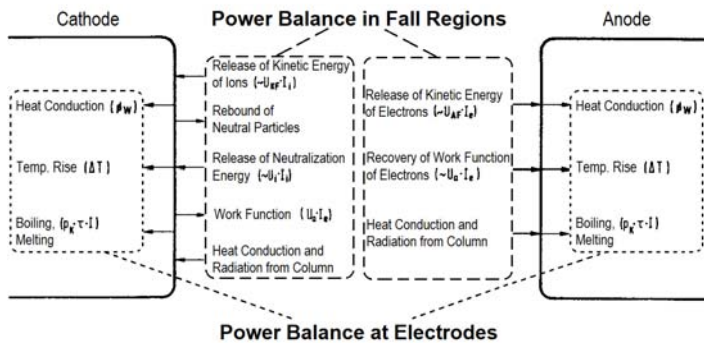


Fig. 2 Power Balance of Arc Roots [15]; see also [16]

2.1 Author's Working Group at TU Braunschweig

One of the earliest representations of arc roots within CFD simulations is a purely thermal one [2, 17]. At the interface (boundary) between the plasma column and the electrode the total current I is subdivided to the interface area by weighting factors depending on the local temperature. They resemble the emission current density of thermionic or thermo-field emission at cathodes. This leads to the root center where the electrodes are hottest, and to a continuous decrease of the current density away from this point. The voltage distribution along the arc and the "fall voltages" close to the electrodes become then a consequence of the CFD calculation coupled with current flow.

A later model [1, 3, 8], also taken by others in a similar way [9], starts with the nearly constant and current-independent anode and cathode voltage drops, without consideration of the electrode temperatures. To enable modelling of the splitting-up process at metallic splitter plates [18], it is useful to apply a steady Voltage = $f(\text{Current Density})$, $V = f(J)$, characteristic with zero voltage at zero current density. Two different types of characteristics were investigated, **Fig. 3**:

A monotonically rising voltage curve $V_1(J)$ of (1-exp)-shape up to a constant value V_∞ , and a curve shape with an initial "ignition peak" V_i , followed by an asymptotic decrease toward this fall voltage V_∞ . Fig. 1c shows examples of the latter case from [9]. Here the end values are different for both polarities, 10 V for cathode, and 5 V for anode. In model [1, 3, 9, 18] they were assumed identical = 10 V for both polarities. The $V(J)$ characteristics are either applied on a thin discretized layer, e.g. 0.1 mm thick, or as a "contact resistance" of zero thickness between column and electrode [8].

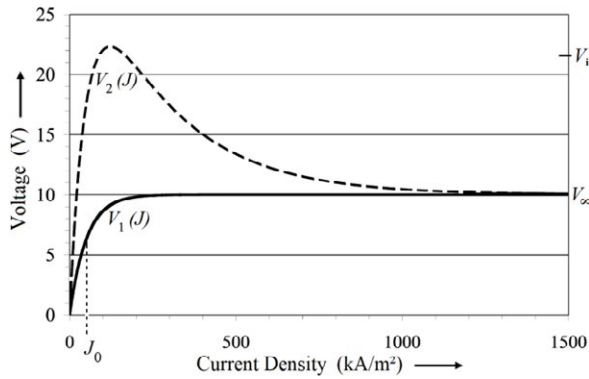


Fig. 3 $V(J)$ Characteristics of Electrode Falls [3]

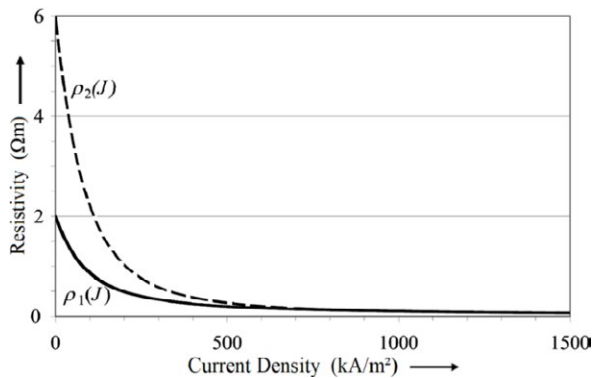


Fig. 4 Equivalent $\rho(J)$ Characteristics of Electrode Falls for 0.1 mm Sheath Thickness [3]

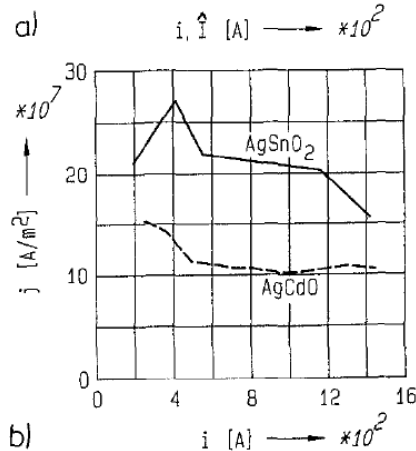
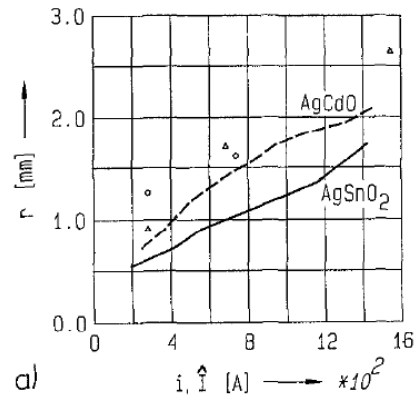


Fig. 5 Arc root radius and apparent current density
Electrode diameter 16 mm
— film camera
○ crater, AgSnO₂ △ crater, AgCdO

Fig. 5 From [19]

Fig. 4 shows the equivalent resistivity ρ vs. current density J curves for the same cases.

While the characteristic values of arc root parameters in the next sections predominantly refer to pure copper or copper compounds as contact material, Fig. 5 shows measured arc root diameters and current densities, Fig. 6 minimum arc voltages ($V_A + V_C$) for silver compound materials like AgCdO (obsolete) and AgSnO₂ [19]. The current densities are roughly constant and equal for both polarities, 10^8 A/m² for AgCdO, $2 \cdot 10^8$ A/m² for AgSnO₂. The sum of fall voltages rises only moderately with the current.

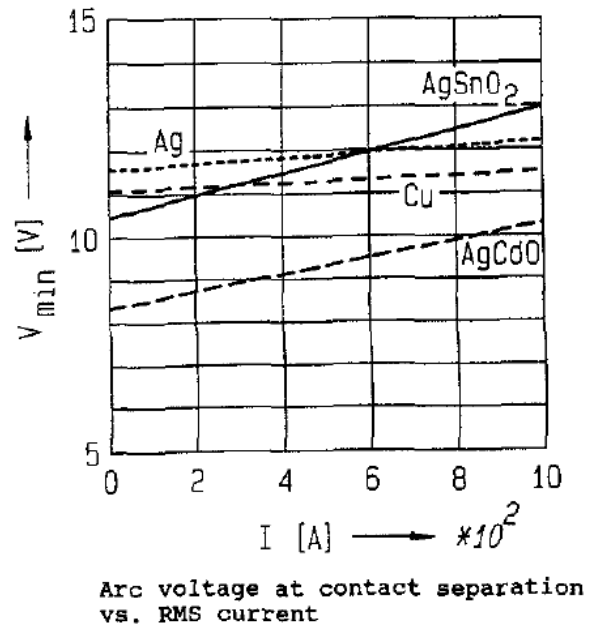


Fig. 6 From [19]

2.2 Other Researchers' Results

2.2.1 Detailed Physical Models of Arc Roots

In a number of research projects, in addition to the fluid dynamics simulation (CFD) of the arc plasma ("column"), the physical processes of power flow as well as particle movements have been taken into account for the anodic and cathodic arc roots. For arcs like welding arcs with thermionic cathodes, Lowke et. al. [10] postulate that the cathodic situation is determined by ambipolar diffusion. In addition to the rotationally symmetric 2D CFD plasma model, they discretize their cathode model in 1D. Wendelstorf [5] develops for similar applications a complete two-temperature CFD model for the quasi-neutral arc column, linked to the complex processes at both electrodes by so-called transfer functions. Purandare et. al. [12] try to describe the particle, current and power flows in the electrode regions by systems of algebraic equations. In [13] they also take into account the thermo-field emission and the secondary electron

emission by ion bombardment of the cathode. The FEM Multiphysics simulation program Comsol [14] provides a “Plasma Module”, from which the “Equilibrium DC Discharge Interface” looks suitable for simulations of thermal arcs. With reference to [11], it contains boundary couplings for both polarities. The author’s experience with this program, however, is ambiguous. While 2D geometries with current flow perpendicularly to the x - y plane could be handled easily [21, 22], trials with 3D geometries failed because of convergence problems.

2.2.2 Results from Experiments and Simulations

This section describes research work, where typical values of electrode characteristics, like V_A , V_C , V_{eqA} , V_{eqC} , or the current and power densities, respectively, have been determined from experiments in comparison with theoretical models. Both theoretical calculations of the heat propagation into the contact material and the power acting on the contacts from the fall mechanism can be utilized and compared with optical arc shape measurements or arc traces on the contacts. Teste et. al. [23] have gained their results from comparison of arc craters with results of heat propagation simulations within the Cu contacts, including material melting and vaporization. Fig. 7 shows their summary.

$$9 \text{ V} \geq V_{eqC} \geq 5.4 \text{ V},$$

$$12.6 \text{ V} \geq V_{eqA} \geq 9 \text{ V},$$

$$7 \times 10^9 \text{ W m}^{-2} \geq Q_C \geq 6 \times 10^9 \text{ W m}^{-2},$$

$$6.5 \times 10^9 \text{ W m}^{-2} \geq Q_A \geq 5.5 \times 10^9 \text{ W m}^{-2}.$$

Fig. 7 Characteristic Values from [23]

Sharakovsy et. al. [24] have received such values from experiments with magnetically driven arcs. Landfried et. al. [7] have concentrated on copper electrodes with cathode polarity only.

Abbaoui et. al. [25] have investigated the context of erosion losses with the theoretical energy fluxes from the fall regions for 40 A millisecond arcs on silver electrodes. Their theoretical estimations are summarized in Fig. 8. The cathodic current and thermal power densities lie orders of magnitude above those known for low-voltage switching arcs, and more resemble those of cathodic micro-spots in vacuum discharges. Therefore they are put in square brackets in the summary table of next chapter.

Yokomizu et. al. [26] have studied the fall voltages ($V_A + V_C$) of axially blasted arcs on tungsten-based as well as Cu and Fe contact materials. The current has no influence, and the gas plays only a minor role.

Anode

	first limit	second limit
$J_a(A/m^2)$	5×10^8	1×10^9
$r_a(m)$	159.6×10^{-6}	112.8×10^{-6}
$P_{thermal}(W/m^2)$	5.315×10^9	1.063×10^{10}

Cathode

	first limit	second limit
$J_c(A/m^2)$	2.5×10^{11}	5×10^{11}
$r_c(m)$	7.14×10^{-6}	5.05×10^{-6}
$P_{thermal}(W/m^2)$	7.62×10^{11}	1.52×10^{12}

Fig. 8 Estimations of Electrode Values from [25]

3. Summary of Characteristic Values

Fig. 9 summarizes characteristic values of voltages as well as current and power densities in the electrode regions. The values in curly brackets mark data in the references concluded from other literature. For square brackets see the section above, related to [25]. Fig. 10 shows the conditions for Fig. 9. The relevant values and their means that can be used as a recommendation, are highlighted dashed in Fig. 9.

Lit.	V_{eqA} (V)	V_{eqC} (V)	ΣV_{eq} (V)	V_A (V)	V_C (V)	ΣV (V)	J_A (A/m^2)	J_C (A/m^2)	P_{eqA} (W/m^2)	P_{eqC} (W/m^2)
[23]	9-12.6	5.4-9				18-24			(5.5-6.5) $\cdot 10^9$	
[24]	10.4- 13.7	6.8-10.8	18-24.3			18-27	(4.1-5.1) $\cdot 10^8$	9.3-12.7		
[16]	7.1-7.2	5.1-6		2.3-3.3	8.9-9.9	11.2-13.2				
[9]				{5}	{10}					
[7]		6.7-10.7						(0.8-3.5) $\cdot 10^8$		(0.6-2.5) $\cdot 10^9$
[25]				3	12.3		(5-10) $\cdot 10^8$	{(2.5-5) $\cdot 10^{11}}$	(5-10) $\cdot 10^9$	{(8-15) $\cdot 10^{11}}$
[26]				{3}	{(13.3-14.5)}	{16.3-17.5}				
[19]						10.5-13 ^{a)} 8-10.3 ^{b)}	Similar $\cdot 10^8$	2 $\cdot 10^8$ ^{a)} $\cdot 10^8$ ^{b)}	AgSnO2	
	Mean Values $V_{eqA} = 9 \text{ V}, V_{eqC} = 6 \text{ V}$			Mean Values $V_A = 3 \text{ V}, V_C = 12 \text{ V}$						

Fig. 9 Summary of Characteristic Arc Root Values

Lit.	
[23]	100-2500 A, OFHC-Cu, 0.1 mm,
[24]	25-1000 A, $B=0.13$ -0.95 T, 1-40 atm, Cu, 1.5-3 mm
[16]	5-30 A, Cu, 0-12 mm
[9]	$\hat{I}=1$ -3 kA, Simulations with Air + Cu Vapor
[7]	60-70 A, 2-5 ms, 3.5 mm, Cu, only Cathode
[25]	40 A, <20 ms, Ag, 1-50 cm/s
[26]	10 A-20 k A; Cu/W, Cu, Fe, W; 0.2-3 mm; SF6, Argon, Air. For W ΣV by 2V lower
[19]	100-1000 A a) Ag/SnO2, b) Ag/CdO, c) Cu, d) Ag

Fig. 10 Conditions from Fig. 9

4. Consequences for Modeling

4.1 General

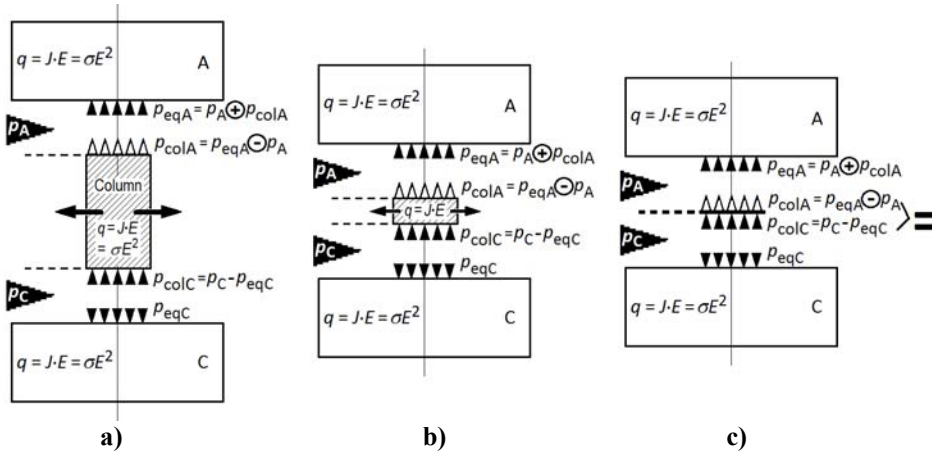


Fig. 11 Modified Power Flow Schemes according to Eqns. (1) and (2)

We assume for simplicity that the current-carrying cross-section is constant along the whole arc path including the arc roots (1D simplification). Then the voltages V_A , V_C , V_{eqA} , V_{eqC} , V_{colA} , V_{colC} are synonyms for the corresponding power densities (Fig. 1). We first stay with Fig. 1, where the power input from the electrode sheaths p_A , p_C is split up into one portion going to the metallic electrode, and a second portion toward the column. Based on the recommended values of Fig. 9, and with the equations in Fig. 1 we then get

$$\begin{aligned} V_{colA} &= V_A - V_{eqA} = -6V, & (1) \\ V_{colC} &= V_C - V_{eqC} = 6V, & (2) \end{aligned}$$

meaning that their algebraic signs are opposite, or that the power flow of identical magnitude on the cathodic side goes to the column, and on the anodic side away from it. This situation is represented in **Fig. 11** by reversed white arrows on the anode side and by the encircled algebraic signs in the appropriate equations. Fig. 11 also shows that these findings are consistent with the concept that the situation in the arc root regions should not change when the arc length, and hence the column length, are varied. When the column length is reduced to zero from Fig. 11a to c, there is no more column left, meaning that there is no more volume and/or area for power dissipation by radiation and heat conduction to the vicinity (lateral arrows in Fig. 11a, b). The ‘‘column power density’’ just goes through from the cathodic to the anodic side.

4.2 Implementation Example

Fig. 12 shows an implementation of the preceding perceptions into CFD programs. The simulation space is separated between the metallic parts – contacts, splitter plates, etc., which must not necessarily be connected – with a temperature T_m , and one or several plasma part(s) with temperature T_p . For the plasma, all Computational Fluid Dynamics (CFD) equations have

to be solved, for the metal only heat conduction is necessary. Plasma and metal are coupled by boundary conditions of location-dependent normal power densities p_n .

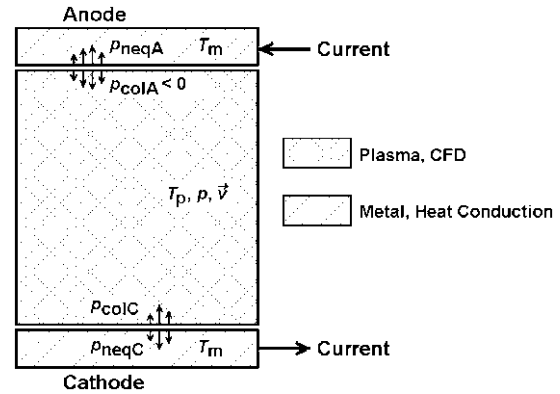


Fig. 12 Implementation into CFD Program

On the anodic side of the electrode(s)

$$p_{neqA} = j_{nA} \cdot V_{eqA}, \quad (3)$$

and on the cathodic side

$$p_{neqC} = j_{nC} \cdot V_{eqC}, \quad (4)$$

go into the metal.

j_n are the location-dependent normal current densities on the electrode – plasma interface. Due to the high difference in conductivity between metal and plasma, they are practically identical with the total local current densities j . Their local distributions and magnitudes are not necessarily identical between anode and cathode, but they follow within the course of the complete simulation.

On the plasma part(s),

$$p_{colA} = j_{nA} \cdot V_{colA}, \quad (3)$$

and

$$p_{\text{colC}} = j_{\text{nC}} \cdot V_{\text{colC}}, \quad (4)$$

Since V_{colA} is negative and V_{colC} is positive, p_{colA} leaves (= cools) the column, p_{colC} enters (= heats) it.

For the simulation of current and voltage distribution, as well as magnetic field and resulting forces, only one unified body is taken. The $V(J)$ characteristics at the metal/plasma interfaces or equivalent “contact resistances” can be applied as internal boundaries.

5 Summary

For simplified models of switching arcs where the correlation between the current densities and the power densities

at the electrodes is represented by equivalent voltages, these values are required. This paper studies and summarizes research results from the literature with such data. While the mean voltage drop $V_C = 12$ V at the cathode is higher than at the anode with $V_A = 6$ V, the situation with the equivalent voltages, i.e. the proportionality factor between current density and power density, is opposite:

$$V_{\text{eqA}} = 9 \text{ V} > V_{\text{eqC}} = 3 \text{ V} \quad (5)$$

This means that the cathodic boundary of the column is heated, while the anodic one is cooled by the same power. This paper ends with an implementation example for CFD programs, where the metallic parts and the plasma are separated into two spaces with different temperature variables, coupled by boundary conditions at the metal/plasma interfaces.

6 Literature

- [1] Lindmayer, M.: Lichtbogensimulation – ein Überblick. 20. Fachtagung “Kontaktverhalten und Schalten” Karlsruhe 2009. VDE-Fachbericht 65, pp. 113-123, VDE-Verlag Berlin 2009
- [2] Karetta, F.: Dreidimensionale Simulation wandernder Schaltlichtbögen. PhD Thesis TU Braunschweig 1998. ISBN 3-18-325021-7
- [3] Mutzke, A.M.: Lichtbogen-Simulation unter besonderer Berücksichtigung der Fußpunkte. PhD Thesis TU Braunschweig 2009. ISBN 978-3-86853-034-6
- [4] Rütger, J.: Weiterentwicklung und Vereinfachung eines Simulationsmodells für Schaltlichtbögen in Löschblechkammern. PhD Thesis TU Braunschweig 2014. ISBN 978-3-8439-1793-3
- [5] Wendelstorf, J.: Ab Initio Modeling of Thermal Plasma Gas Discharges (Electric Arcs). PhD Thesis TU Braunschweig 2000.
- [6] Boucadoum, R., Barbet, A., Dessante, Ph., Landfried, R., Leblanc, T., Teste, Ph.: Simple 1D Model of a Short Gap DC Electric Arc in Aeronautical Pressure Conditions. 62th IEEE Holm Conference on Electrical Contacts, Clearwater Beach 2016
- [7] Landfried, R., Leblanc, T., Kirkpatrick, M. Teste, Ph.: Assessment of the Power Balance at a Copper Cathode Submitted to an Electric Arc by Surface Temperature Measurements and Numerical Modeling. IEEE Transactions on Plasma Science, Vol. 40, No 4, 2012
- [8] Reiß, J., Lindmayer, M., Kurrat, M.: Modellierung von Elektrodenfallgebieten mithilfe einer nichtlinearen Spannungs-Stromdichte-Kennlinie. ANSYS Conference & 28th CADFEM User's Meeting, Aachen 2010
- [9] Rümpler, Ch.: Lichtbogensimulation für Niederspannungs-Schaltgeräte. PhD Thesis TU Ilmenau 2009
- [10] Lowke, J.J., Morrow, R., J Haidar, J.: A Simplified Unified Theory of Arcs and their Electrodes. J. Phys. D: Appl. Phys. 30 (1997) pp. 2033–2042
- [11] Lowke, J.: A Unified Theory of Arcs and their Electrodes. Journal de Physique IV Colloque, 1997, 07 (C4), pp.C4-283 - C4-294.
- [12] Purandare, K.R., Ahmed, N.: Modeling of the Near Electrode Physics for Simulation of Arc. 59th IEEE Holm Conference on Electrical Contacts, Newport 2013
- [13] Singh, A.K., Nairn, A. Atharparvez, A.M.: Numerical Simulation of Arc Splitting Process in a L V Switching Device Considering Thermo-Field Emission Mechanism. 61st IEEE Holm Conference on Electrical Contacts, San Diego 2015
- [14] Lindmayer, M.: Simulation von Erwärmung, Abbrand und mechanischer Beanspruchung elektrischer Kontakte beim Schalten. 20. Fachtagung “Kontaktverhalten und Schalten” Karlsruhe 2009. VDE-Fachbericht 65, pp. 147-153, VDE-Verlag Berlin 2009
- [15] Erk, A., Schmelzle, M.: Grundlagen der Schaltgerätektechnik. Springer-Verlag Berlin, Heidelberg, New York 1974
- [16] Rieder, W.: Plasma und Lichtbogen. Vieweg Verlag, Braunschweig 1967
- [17] Karetta, F., Lindmayer, M.: Simulation of the Gasdynamic and Electromagnetic Processes in Low Voltage Switching Arcs. 42th IEEE Holm Conference on Electrical Contacts, Chicago 1996
- [18] Lindmayer, M., Marzahn, E., Mutzke, A.M., Rütger, Th, Springstubbe, M.: The Process of Arc-Splitting between Metal Plates in Low Voltage Arc Chutes. 22nd International Conference on Electrical Contacts / 50th IEEE Holm Conf. on Electrical Contacts, Seattle 2004
- [19] Lindmayer, M., Sun, M.: Arc Stress and Erosion Losses of Contact Materials at Currents up to 1000 A. 16th International Conference on Electrical Contacts, Loughborough/UK 1992
- [20] COMSOL AB, Stockholm (2018). *Introduction to COMSOL Multiphysics and Documentation* within COMSOL 5.4
- [21] Lindmayer, M.: Simulation of Switching Arcs under Transverse Magnetic Fields for DC Interruption. IEEE Transactions on Plasma Science 44 (2016) pp. 187-194
- [22] Lindmayer, M.: Cooling Mechanisms of Switching Arcs under Transverse Magnetic Fields in Comparison with Arcs without Magnetic Blast. IEEE Transactions on Plasma Science 46 (2018) pp. 444-450
- [23] Teste, Ph., Leblanc, T., Rossignol, J., Andlauer, R.: Contribution to the Assessment of the Power Balance at the Electrodes of an Electric Arc in Air. Plasma Sources Sci. Technol. 17 (2008)
- [24] Sharakhovskiy, L.I., Marotta, A., Borisyuk, V.N.: A Theoretical and Experimental Investigation of Copper Electrode Erosion in Electric Arc Heaters: II. The Experimental Determination of Arc Spot Parameters. J. Phys. D: Appl. Phys. 30 (1997) pp. 2018–2025
- [25] Abbaoui, M., Lefort, A., Sallais, D., Benjemaa, N.: Theoretical and Experimental Determination of Erosion Rate due to Arcing in Electrical Contacts. 52nd IEEE Holm Conference on Electrical Contacts, Montreal 2006
- [26] Yokomizu, Y., Matsumura, T., Henmi, R., Kito, Y.: Total Voltage Drops in Electrode Fall Regions of SF₆, Argon and Air Arcs in Current Range from 10 to 20 000 A. J. Phys. D: Appl. Phys. 29 (1996) pp. 1260–1267

Arc Evolution Process Considering the Motion of Moving Contact in DC Circuit Breaker

Jianning Yin¹, Qian Wang², Tian Tian³, Xingwen Li³

¹ School of Electrical Engineering, Xi'an University of Technology, Xi'an, China

² School of Sciences, Xi'an University of Technology, Xi'an, China

³ State Key Laboratory of Electrical Insulation and Power Equipment, Xi'an Jiaotong University, Xi'an, China
qianwang@xaut.edu.cn

Abstract

Direct current (DC) circuit breaker is a crucial component for controlling and protecting the DC power system, especially in photovoltaic power generation system. It should switch off the DC load current. The motion process of the moving contact (arm) greatly affects the arc voltage and arc evolution process. Therefore, this paper focuses on the arc evolution process considering the motion of moving contact in a DC circuit breaker. A 2-D magneto-hydrodynamic (MHD) model of a miniature circuit breaker is built. Based on this model, the temperature distribution and airflow field distribution are obtained. The arc evolution process with two different structures is analyzed. At the same time, the results with arm motion and without arm motion are compared and analyzed. In addition, the related experiments are carried out. It turns out that the arc evolution considering arm motion is closer to the experimental results.

1 Introduction

With the development of the photovoltaic power generation system, energy storage system and the electric vehicles, the DC power supply and distribution system receive more and more attention [1,2]. The direct current circuit breaker is a crucial component for controlling and protecting the DC power distribution network.

In order to interrupt the load current, the arc must be extinguished in the arc chamber. The DC arc is more difficult to break than an AC arc because the current does not have a natural zero. Therefore, the circuit breaker usually makes the arc current be zero by increasing the arc voltage above the supply voltage. In order to increase the arc voltage, an external magnetic field and gassing material are usually used to make the arc quickly enter the splitter plates in low-voltage circuit breakers [3-8]. However, the effect of external magnetic field and gassing material are not very effective with smaller current. Therefore, the motion of an arc can probably be accelerated by the change of contact structure. The tilting contact structure is proposed in [9]. The motion of moving contact (arm) will affect the motion process of arc. Therefore, this paper focuses on the arc evolution process considering motion of the moving contact and the calculation results with arm motion and without arm motion are compared.

In this paper, a 2-D MHD model considering arm motion is built. The effect of a permanent magnet is replaced by an external magnetic field. The self-generated magnetic blast field of arc is calculated using magnetic vector potential method. The ablation of electrode and splitter plates are not considered. The arc temperature and gas flow field distribution are obtained by simulation. The arc motion process of tilting contact structure and non-tilting contact structure are analyzed.

2 Numerical Geometry and Method

2.1 Numerical geometry

The computational domain for the fluid of two structures are shown in **Figure 1**. The non-tilting contact structure is shown in Figure 1 (a) and the tilting contact structure is shown in Figure 1 (b).

The extinguishing arc chamber of a DC miniature circuit breaker includes the moving contact (arm), static contact, arc runner, splitter plates and arc domain. The main difference between two structures are structures of moving and static contact. The current density is applied in " I_{in} " as shown in Figure 1. The electric potential is set to zero in " I_{out} ". The current is $I=3.2A$ at $t=0s$, and drops to 0 at $t=35ms$ in the calculation.

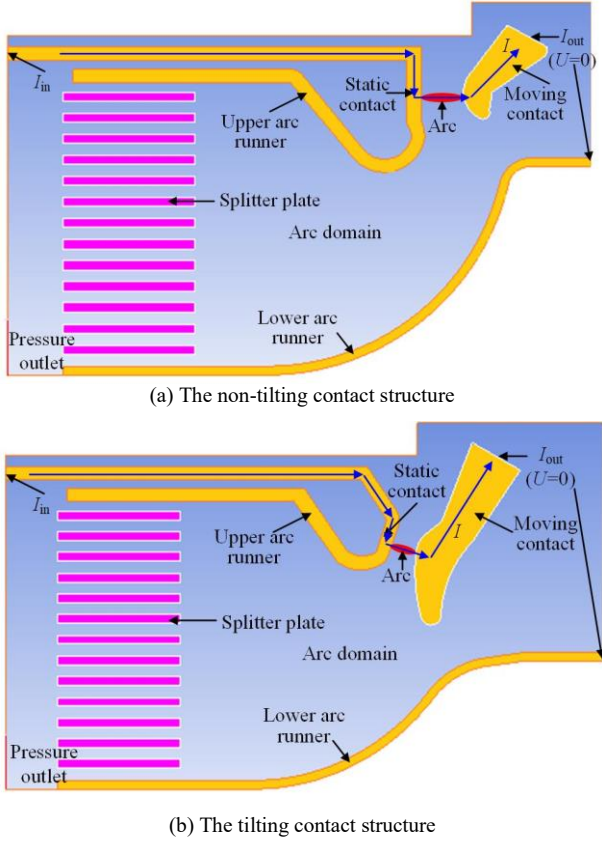


Fig. 1 Numerical geometry for fluid domain

2.2 Technology of dynamic mesh

The moving contact will rotate and separate from static contact when interrupting the load current. The arc is ignited between static contact and moving contact. The motion process of moving contact is very important to interruption of arc. However, the challenge connected with the modeling of low voltage circuit breaker is the representation of the contact arm motion. For the representation of moving objects in the soft ANSYS Fluent [10], several technology of dynamic mesh update methods are described in following [10,11].

2.2.1 Smoothing method

When smoothing is used to adjust the mesh of a zone with a moving and deforming boundary, the interior nodes of the mesh move, but the number of nodes and their connectivity remain unchanged. In this way, the interior nodes “absorb” the movement of the boundary.

2.2.2 Dynamic layering

In prismatic (hexahedral and/or wedge) mesh zones, dynamic layering can be used to add or remove layers of cells adjacent to a moving boundary, based on the height of the layer adjacent to the moving surface. The dynamic

mesh model in ANSYS Fluent allows to specify an ideal layer height on each moving boundary. The layer of cells adjacent to the moving boundary is split or merged with the layer of cells next to it.

2.2.3 Remeshing method

ANSYS Fluent agglomerates cells that violate the skewness or size criteria and locally remeshes the agglomerated cells or faces. If the new cells or faces satisfy the skewness criterion, the mesh is locally updated with the new cells (with the solution interpolated from the old cells). Otherwise, the new cells are discarded and the old cells are retained.

According to the motion process of the moving contact in a miniature circuit breaker, the remeshing method is used in the arc domain. Therefore, the elements of the arc domain are formed into triangular mesh. The rigid body is used with the moving contact and the rotation speed is set to 166 rad/s in the calculation.

The position of the moving contact shown in **Figure 1** is the initial position. The contact moves to maximum position at $t=3\text{ms}$.

2.3 Governing equations

The arc plasma can be modelled by N-S equations for mass, momentum and energy conservation to describe the gas dynamic processes [12].

(1) Mass balance equation:

$$\frac{\partial \rho}{\partial t} + \nabla \cdot (\rho \vec{V}) = 0 \quad (1)$$

(2) Momentum balance equation:

$$\frac{\partial (\rho v_k)}{\partial t} + \nabla \cdot (\rho v_k \vec{V}) = \nabla \cdot (\eta \nabla v_k) - \frac{\partial p}{\partial x_k} + (\vec{J} \times \vec{B})_k \quad (2)$$

(3) Energy balance equation:

$$\frac{\partial (\rho h)}{\partial t} + \nabla \cdot (\rho h \vec{V}) = \nabla \cdot \left(\frac{\lambda}{c_p} \nabla h \right) + S_h \quad (3)$$

$$S_h = \sigma E^2 - q_{\text{rad}} + q_{\eta} \quad (4)$$

Where, σE^2 is the Joule heat, which represents the energy injected into the arc plasma, and $\vec{J} \times \vec{B}$ is the Lorentz force density. The radiation energy source term is calculated using the net emission coefficient (NEC) method due to the calculation accuracy in arc core [13]. The radiation energy source term q_{rad} can be defined by:

$$q_{\text{rad}} = 4\pi \varepsilon_n \quad (5)$$

Where, ε_n is the net emission coefficient [14].

The air plasma's physical properties depend strongly on temperature and pressure [13]. The material of moving and static contact, arc runner is cooper and the splitter plates are ferromagnetic materials. In order to take the form process of new arc root, a 0.1mm sheath with a nonlinear resistance completely surrounding the splitter

plates and contacts (arc runner) is applied. The local value of the nonlinear resistance is chosen according to a specific voltage-current density characteristic [12].

3 Simulation Results and Analysis

The temperature and airflow field distribution of a miniature circuit breaker are obtained by the simulation and the DC arc evolution process will be analyzed in the following.

3.1 Arc Motion Process

The temperature distributions of two different contact structures considering arc motion are shown in **Figure 2** and **Figure 3** respectively.

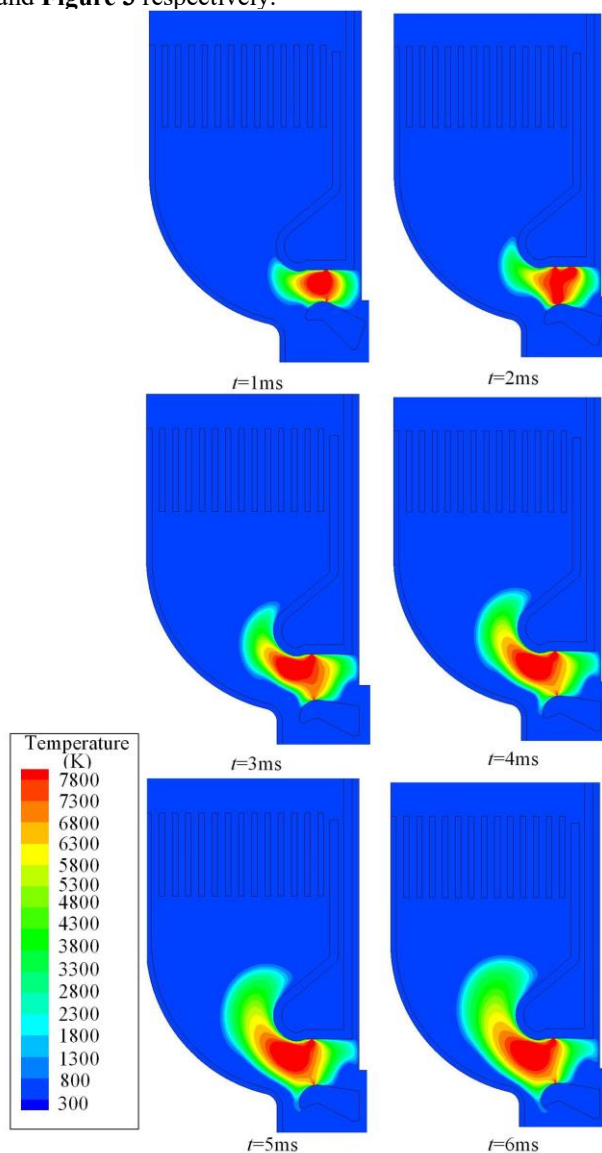


Fig. 2 Temperature distribution sequences of the non-tilting contact structure

The arc initiation process of arc is not considered in this calculation due to its complexity. Therefore, there is a distance between the moving contact and the static contact at $t=0\text{ms}$ and the distance is 2mm. The calculation begins with a stationary temperature distribution between two contacts. The initial position is shown in Figure 1.

The arc column begins to expand and diffuse with the rotation of moving contact. For the non-tilting contact structure, the arc column moves along the upper arc runner. However, the arc root moves slowly as shown in Figure 2. The arc column moves slowly after a hesitation time of 3ms. The temperature of arc core is higher than tilting contact structure during the whole motion process.

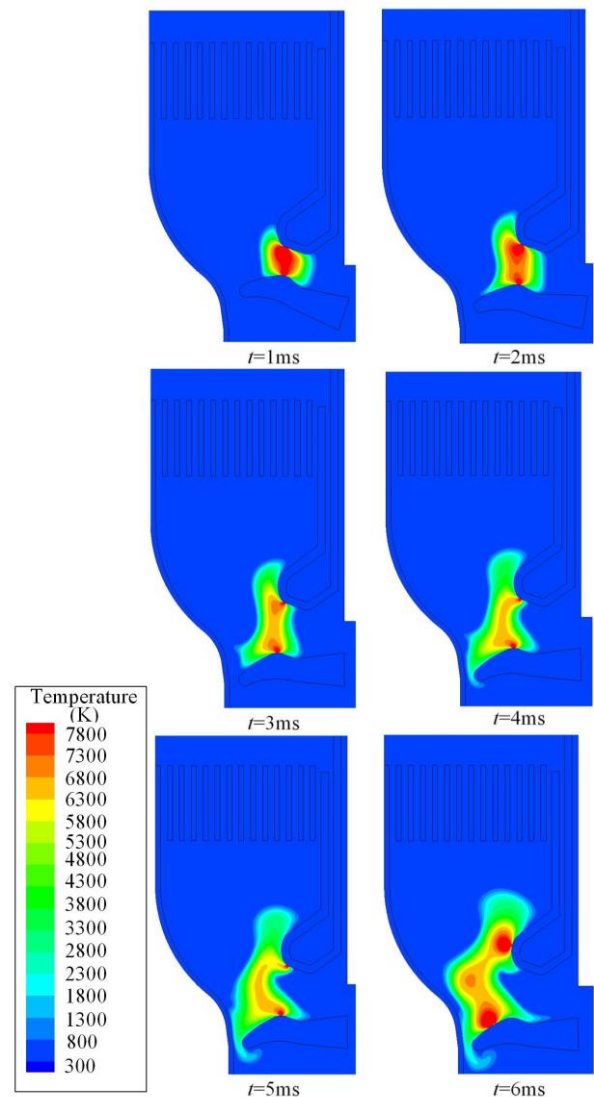


Fig. 3 Temperature distribution sequences of the tilting contact structure

For the tilting contact structure, the arc column expands with the motion of moving contact. At the same time, the arc roots move along the contact with a higher speed,

especially after $t=3\text{ms}$. Comparing the calculation results of the two structures, it can be seen that the arc temperature is lower in the tilting contact structure. This can be explained by the fact that the nozzle structure is formed between moving contact and static contact [9].

To further analyze the differences between the two structures, the airflow field distributions are obtained and shown in **Figure 4**. The motion velocity at $t=2\text{ms}$ of the tilting contact structure is higher than that of the non-tilting contact structure. Moreover, it can be observed that a significant vortex appears under the moving contact in the tilting contact structure. The existence of a vortex will increase the convection effect and thus reduces the arc temperature.

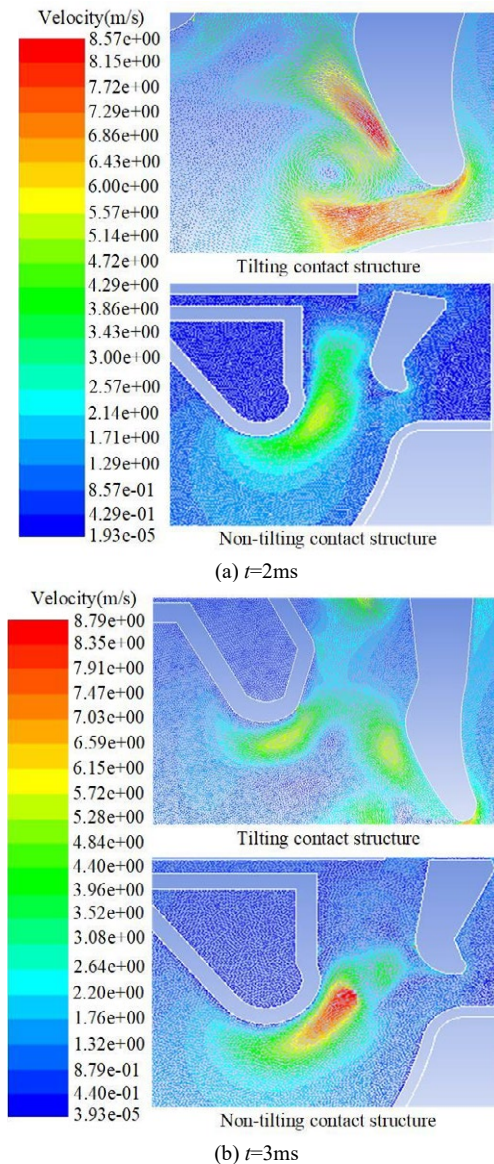


Fig. 4 Airflow field distribution sequences of two structures

It is found that the airflow diffuses to both sides along the moving and static contact at $t=3\text{ms}$ in the tilting contact structure. However, the airflow channel is more concentrated in the non-tilting contact structure. This also explains the lower temperature in the tilting contact structure.

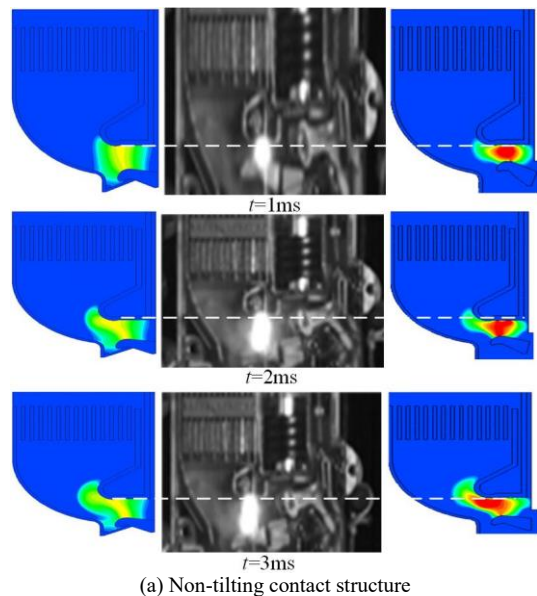
Although the airflow velocity is higher at $t=3\text{ms}$ in the non-tilting contact structure, it is not conducive to energy dissipation because the arc column is more concentrated.

3.2 Comparative analysis of calculation results

The simulation for motion of a moving contact is difficult. Therefore, the motion of the moving contact is ignored in reference [9]. The comparison of calculation and experimental results are shown in **Figure 5**.

The arc shape of calculation results is represented by temperature distribution in Figure 5. The legend is the same as in Figure 2 (Figure 3). And the arc shape obtained by experiment is represented by arc image. Therefore, the physical quantities are not appeared in Figure 5.

It can be seen that the temperature is lower when the motion of the moving contact is not considered. It appears that the front and rear have moved further but the position of the hot core is not much different. This is due to the airflow channel is wider and the velocity of arc front and rear is higher. It is better for arc cooling. For the arc shape, the experimental results agree better with calculation result when the motion process of moving contact is considered as shown in Figure 5. And the evolution process of the arc is closer to the experimental results. Therefore, the motion process of moving contact must not be ignored in simulation.



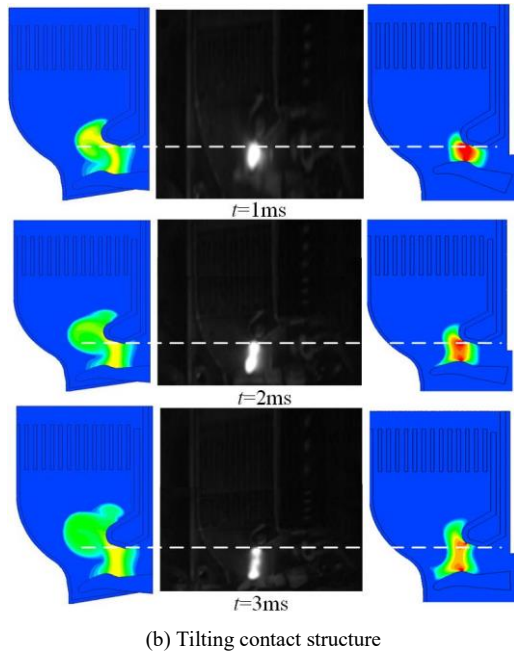


Fig. 5 Comparison of calculation and experimental results. (Left: calculation without arm motion; Middle: experiment; Right: calculation with arm motion)

we calculate the arc voltage according to the arc current and circuit parameters in experiment. The supply voltage is 1050V. The resistance and the inductance are 328Ω and 328mH respectively. The arc voltage and arc current curves are shown in **Figure 6**.

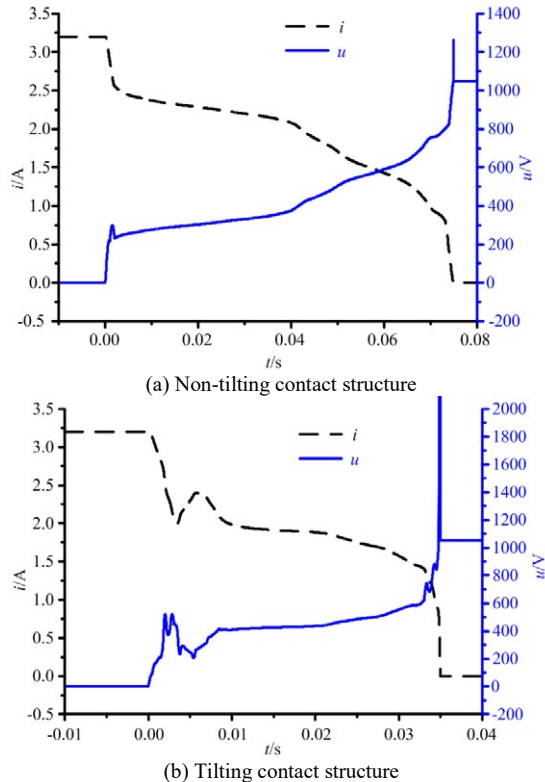


Fig. 6 The curves of arc voltage and current

It is noted that the arc voltage rises faster in tilting contact structure and the arcing time is lower. The main mechanism is that a nozzle structure is formed between the moving contact and the static contact of tilting contact structure. The arc velocity will be accelerated by nozzle structure.

4 Conclusion

Based on the two-dimensional (2D) magneto-hydrodynamic (MHD) method, the simulation model of a miniature circuit breaker is built. The motion process of moving contact is considered by the method of dynamic mesh.

The temperature and the gas flow field distribution are obtained by simulation. It can be concluded that:

1) For non-tilting contact structure, the arc column moves along the upper arc runner with motion of the moving contact. However, the arc roots move slowly. For the tilting contact structure, the arc column expands with the motion of the moving contact. At the same time, the arc roots move along the contact with a higher speed.

2) The airflow diffuses to both sides along the moving and static contact in the tilting contact structure. However, the airflow channel is more concentrated in the non-tilting contact structure. Therefore, the temperature is lower in the tilting contact structure.

3) The temperature is lower when the motion of the moving contact is not considered. In this case the temperature is lower due to a wider airflow channel and higher velocity of the arc which is beneficial to arc cooling.

4) The evolution process of the arc is closer to the experimental results when the motion process of the moving contact is considered. Therefore, contact motion should be included in the simulation as the results are closer to the experiment.

5 Acknowledgement

This work was supported by the Research Fund of Xi'an University of Technology (104-451119032).

6 Literature

- [1] Hendrik Köpf, Ernst-Dieter Wilkening, Christoph Klosinski, Michael Kurrat. Breaking Performance of a Circuit Breaker influenced by a Permanent Magnetic Field at DC Voltages up to 450V, 27th International Conference on Electric Contacts

- (ICEC), June, Dresden, Germany, 2014, pp. 126-131.
- [2] P. Meckler, F. Gerdinand, R. Weiss, U. Boeke, and A. Mauder. Hybrid switches in protective devices for low-voltage DC grids at commercial used buildings, 27th International Conference on Electric Contacts (ICEC), June, Dresden, Germany, 2014, pp. 120–125.
- [3] A. Vassa, E. Carvou, S. Rivoirard, L. Doublet, C. Bourda, N. Ben Jemaa, D. Givord. DC-arc blowing under pulsed magnetic field, 26th International Conference on Electric Contacts (ICEC), May, Beijing, China, 2012, pp. 23-29.
- [4] A. Iturregi, B. Barbu, E. Torres, F. Berger, and I. Zamora. IEEE Transactions, Plasma. Science. Vol. 45, No. 1, Jan. 2017, pp. 113-120.
- [5] L. Yun, L. Zhenbiao, W. Ke, and W. Ronghua, Experimental study on arc duration under external transverse magnetic fields in a DC 580 V circuit, 26th International Conference on Electric Contacts (ICEC), May, Beijing, China, 2012, pp. 30-34.
- [6] M. Lindmayer. IEEE Transactions, Plasma. Science. Vol. 44, No. 2, Feb. 2016, pp. 187–194.
- [7] M. Lindmayer. IEEE Transactions, Plasma. Science. Vol. 46, No. 2, Feb. 2018, pp. 444–450.
- [8] C. Rümpler, H. Stammberger, A. Zacharias. Low-voltage arc simulation with out-gassing polymers, 57th IEEE Holm Conference on Electrical Contacts (HOLM), Sep, Minneapolis(MN), USA, 2011, pp. 1-8.
- [9] Y. Nan, L. Wang, J. Zhu, Yijun Deng, Fang Liu, Jianning Yin, Tian Tian, Xingwen Li. Analysis of Interrupting Characteristic of DC Circuit Breaker With Different Structures, 65th IEEE Holm Conference on Electrical Contacts (HOLM), Sep, Milwaukee, USA, 2019, pp. 122-127.
- [10] ANSYS, Inc. ANSYS Release 15, Help system, Canonsburg, PA, USA, 2014.
- [11] R. Ch, N. V.R.T. Plasma Physics and Technology, Vol. 2, Sep. 2015, pp. 261-270.
- [12] J. Yin, Q. Wang, X. Li, and H. Xu. IEEE Transactions. Components, Packaging and Manufacturing Technology, Vol. 8, No. 8, Aug. 2018, pp. 1373–1380.
- [13] Y. Naghizadeh-Kashani, Y. Cressault and A. Gleizes. Journal of Physics D: Applied Physics, Vol. 35, Nov. 2002, pp. 2925-2934.
- [14] A. B. Murphy. Plasma Chemistry and Plasma Processing, Vol. 15, Vo. 2, Feb. 1995, pp. 279-307.

Surge protection device digital prototyping

Olga Schneider¹, Arnd Ehrhardt¹, Bernd Leibig¹, Sebastian Schmausser¹,
Andrey Aksenov² and Elena Shaporenko²

¹ DEHN SE + Co KG, Hans-Dehn-Straße 1, 92318 Neumarkt, Germany, olga.schneider@dehn.de

² Capvidia NV, Technologielaan 3, 3001 Leuven, Belgium

Abstract

The market requirements for surge protection devices (SPD) call for improvements of their technical parameters, characterized by; higher impulse currents, higher short-circuit currents and at the same time reduced size. This leads to a significantly increased level of complexity for the tools used in design, simulation, and production. Another very crucial business aspect is time to market, forcing shorter development cycles. Implementing the SPD digital prototyping workflow into design cycle reduces both the development time and development costs. This paper presents virtual spark gap model development steps and simulation results of the real physical processes occurring in a spark gap-based SPD device. The virtual spark gap simulation is based on the full compressible Navier-Stokes equations, the energy conservation law, the radiation heat transfer and Maxwell equations. Presented simulation results include arc behaviour, gas flow dynamics and electromagnetic forces. The results are validated using a high-speed camera for arc visualization and compared with experimental data. This virtual simulation technology shows the ability for the further increase of product reliability, performance and size optimization.

1 Introduction and background

To ensure high quality products, it is necessary to consider market requirements, which are constantly becoming more complex for SPD products. In line with market trends, performance characteristics, such as impulse and short-circuit currents, are becoming higher and the size of the product needs to get smaller. These requirements force the design team to increase their efforts to add more physical design loops in the SPD standard development process, see Fig. 1a. In each loop of the standard workflow, a physical test must be executed at the laboratory. This is a very time-consuming process and puts a lot of strain on expensive and highly loaded laboratory resources. The digital prototyping is an ideal concept to reduce these efforts.

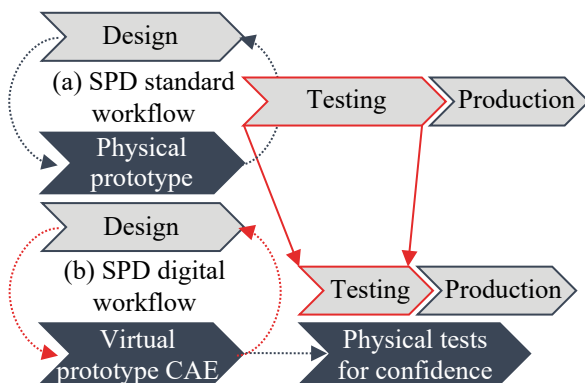


Fig. 1 Product design process and comparison of the SPD standard workflow (a) with the SPD digital workflow (b).

The SPD digital workflow (Fig. 1b) is based on virtual testing, which includes design and downstream computer-aided engineering (CAE) simulation. Computer simulation enables product optimization without the need for physical tests in the laboratory. Physical tests are only necessary to ensure confidence in the final design. Comparison of the digital workflow with the standard workflow (see Fig.1) shows that the digital process can reduce the time required for product development and provide significant cost savings.

The content of this paper is focused on the SPD digital prototyping based on spark gaps. Modern lightning and overvoltage arresters are mainly integrated into low-voltage installations, such as DIN-rail devices. SPD devices are installed directly at the entry point of the power and data lines onto the building or installations. These devices provide potential equalization and protection of electrical and electronic equipment against high-energy, conducted and field-based interference. After the lightning current arrester has operated due to an overvoltage, impulse currents flow to earth. In case of spark-gap-based lightning current arresters, an arc discharge occurs, and the separation gap is ionized. The impulse current is followed by the mains current controlled by the mains voltage. Spark gaps with arc splitters or deionization chambers have a high follow current extinguishing capability and follow current limitation in case of both alternating and direct currents. The important requirements for modern lightning protection systems [1, 2] are divided into the following main topics. SPD devices must be able to safely extinguish the prospective short-circuit current in the system several times. Effective encapsulation of arresters is required to prevent the release of hazardous ionized

gases, especially under loads with high lightning impulse currents. Particularly relevant is a space-saving rule that uses the horn principle with asymmetrical shapes. Therefore, along with the physical properties of the plasma, the electrodynamic spark gap processes and hot gas control play a crucial role in product development to determine whether the arc will be able to extinguish in time to keep the device operational. The optimization of the geometric and gasdynamic parameters can only be achieved in combination with the plasma physical processes. Due to the complex multiphysical processes, digital prototyping is highly useful for the further development of modern SPD devices.

The basic principle of the lightning current arrester with its most important components, including the essential spark gap processes, is shown in Fig. 2.

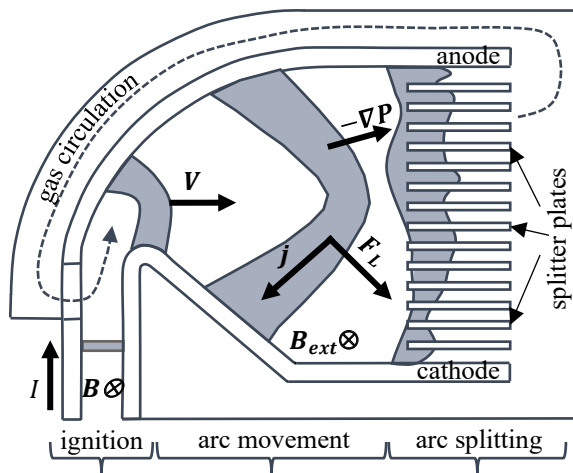


Fig. 2 Schematic diagram of the lightning current arrester and spark gap processes.

The lightning protection device consists of two electrodes and an extinguishing chamber. The distance between these electrodes increases in a horn-shaped and asymmetric way from the ignition area over the arc movement area to the arc splitting chamber. The chamber has many ferromagnetic splitter plates with a V-shaped recess. In the practical implementation [1, 2] the splitter plates are fixed in a plastic support with exhaust openings, so that the gases released from the chamber are directed through special channels in the housing. The outer casing of the device is fully encapsulated to prevent interference with the environment. The overvoltage triggers the lightning current arrester. The electrical current flows from the anode to the cathode as the electric field intensity reaches values higher than the breakdown electric intensity of the gas [3]. The electrical arc occurs in the ignition area between the diverging electrodes. The electrical arc in the lightning arrester is supported by two sources. Impulse current is the ignition source, which can be triggered by 10/350 μ s or 8/20 μ s waveforms and then accompanied by the mains following current. During ignition a high pressure is generated by intense gas heating. Due to the pressure gradient and Lorentz force, the arc moves in the direction of the splitter plates, see Fig. 2. Some

lightning protection devices include ferromagnetic concentration plates, which create an additional magnetic field to increase the Lorentz force. During the splitting process, the arc starts to stretch around the splitter plates and the voltage rises for forming the arc roots on the plates. When the current flowing through the plates reaches the total current, the arc splits into small parts.

In order to describe these spark gap processes, the three-dimensional virtual spark gap model for SPD digital prototyping is developed. The model is based on the FlowVision computational fluid dynamics (CFD) code [10]. The mathematical model reflects the real physical processes of spark gap formation and is based on the compressible Navier-Stokes equations, the energy conservation law, Maxwell equations for electric and magnetic fields and the radiation heat transfer equations.

There are many publications about arc numerical models [4, 5, 6, 7, 8], where arc simulation frameworks consist of two or more separate solvers working on different numerical domains. These frameworks require additional software for solvers synchronization and their data exchange. In this work, the arc model is based on the magnetohydrodynamic approach (MHD), where the gas flow solver and the electromagnetic equations are solved conjointly on one simulation domain, which uses the finite volume method (FVM).

For the simulation of the arc motion and splitting processes, the arc root model at the gas-solid interfaces must be taken into account. Generally, voltage drop is modelled by introducing an effective electrical conductivity [4, 5, 8] in a computational cell adjacent to the metal surface. This approach leads to a mesh-dependent solution.

In this paper, the modified arc root model based on boundary conditions is described. In addition, this paper presents the results of a simple design shape optimization using the developed virtual 3D spark gap model based on local thermal equilibrium assumption and modified arc root model parameters. The simulation results are compared with the experimental data to verify the proposed model.

2 Physical tests for confidence

A high-speed camera is used to obtain arc information through videos with high temporal and spatial resolution. To make this possible, the spark gaps are modified to make the inner processes optically accessible. These preparations are carried out without affecting the functionality of the equipment to ensure comparability. In addition to the high-speed camera, various lenses, optical filters and evaluation software are used to obtain information. This enables examinations of the general arc behaviour, the contour of the arc, and the arc root movement. This experimental method can be used for validation of digital spark gap results.

2.1 Spark gap effects

The high-speed camera captures the events with the voltage and current development over time. Fig. 3 depicts the comparison of two measurements with the same parameters. The current pulse with $I_{8/20} = 500$ A is used for ignition. The prospective short-circuit current has the same value $I_p = 500$ A. The red (dashed) curve shows good behaviour, whereas the blue curve shows a re-ignition event. As a result, there is a drop in the spark gap voltage and a plateau in the arc current.

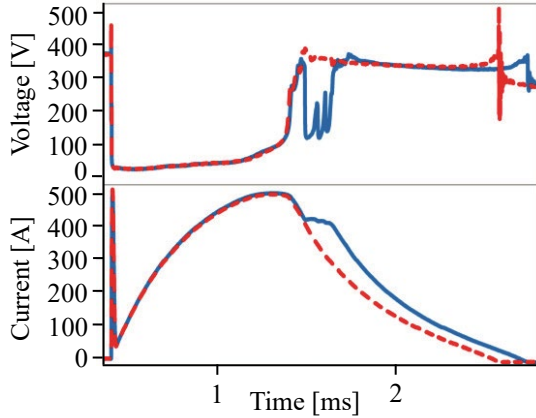


Fig. 3 Comparison of two measurements.

Additionally, this event is recorded with the high-speed camera at the resolution of 336 x 240 px, the framerate of 15 kfps, and the exposure time of 1 μ s. By using the camera's trigger signal, the recorded frames can be assigned to the correct position in the timeline, and thus it is possible to observe where the arc is before and after the re-ignition event (Fig.4).

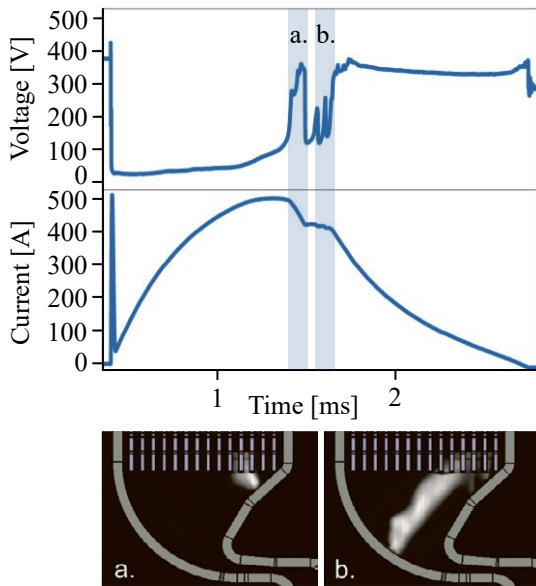


Fig. 4 Visualization of the re-ignition event by frame assignment.

However, such recordings are not able to deliver the physical parameters – e.g. temperature or pressure –

that lead to spark gap effects like this. In the previous example, the re-ignition leads to an increase in specific let-through energy of 13 %. Re-ignition events at current rise can even cause a much higher energy the spark gap has to handle. Hence, understanding spark gap effects is highly relevant for product development as they strongly influence the physical parameters of the device. Digital prototyping offers a possibility to obtain this understanding.

3 Spark gap digital workflow

3.1 Numerical model

CFD code FlowVision is used for the simulating arc ignition, propagation and splitting in the surge protection devices. The software provides automatic mesh generation with local adaptation based on the sub-grid geometry resolution method (SGGR) [9]. The numerical method for calculating the Navier-Stokes equations is based on the finite volume method (FVM) and solves flows with any Mach number in the computational domain [10]. Moreover, this software includes the parallel code architecture with mixed parallelism - simultaneously shared and distributive memory.

3.1.1 Governing equations

The arc phenomenon in gas is characterised by the wide range of physical effects. The most important of these are such as shock waves, ionisation, gas flow with transonic and supersonic velocities, radiation and conjugate heat exchange, the formation of a magnetic field and the generation of ponderomotive and Lorentz forces [12]. These physical effects are described by the following system of governing equations.

Mass conservative law (continuity equation):

$$\frac{\partial \rho}{\partial t} + \nabla \cdot (\rho \mathbf{V}) = 0. \quad (1)$$

Moment conservation law (Navier-Stokes equation):

$$\frac{\partial \rho \mathbf{V}}{\partial t} + \nabla \cdot (\rho \mathbf{V} \otimes \mathbf{V}) = -\nabla P + \nabla \cdot \hat{\boldsymbol{\tau}} + \mathbf{F}_L. \quad (2)$$

Energy conservation law:

$$\frac{\partial (\rho H)}{\partial t} + \nabla \cdot (\rho \mathbf{V} H) = \frac{\partial P}{\partial t} + Q_{rad} + Q_{Joule} + \nabla \cdot \left(\frac{\lambda}{C_p} (\nabla H - \mathbf{V} (\nabla \cdot \mathbf{V})) \right), \quad (3)$$

here $\hat{\boldsymbol{\tau}} = \mu \left(2\hat{\mathbf{S}} - \frac{2}{3} (\nabla \cdot \mathbf{V}) \hat{\mathbf{I}} \right)$ is the viscous stress tensor, ρ is the density, t is the time, \mathbf{V} is the gas velocity, P is the pressure, H is the total enthalpy, μ is the viscosity, $\hat{\mathbf{S}}$ is the shear rate tensor, $S_{ij} = \frac{\partial v_i}{\partial x_j} + \frac{\partial v_j}{\partial x_i}$ and $\hat{\mathbf{I}}$ – the unit tensor.

The Maxwell steady-state equations for magnetic and electric fields at low magnetic Reynolds numbers and

for electroneutral media has the form shown in the below equations.

Electric charge conservation law (electric current continuity):

$$\nabla \cdot \mathbf{j} = 0. \quad (4)$$

The equation for magnetic induction, induced by electrical current:

$$\nabla \times \mathbf{H} = \mathbf{j}. \quad (5)$$

Gauss law (no magnetic charges):

$$\nabla \cdot \mathbf{B} = 0. \quad (6)$$

Electric current density \mathbf{j} is specified by Ohm's law and Hall effect

$$\mathbf{j} = \sigma(\mathbf{E} + \mathbf{V} \times (\mathbf{B} + \mathbf{B}_{ext})), \quad (7)$$

where \mathbf{E} is the electric field strength and σ is the conductivity. Magnetic induction \mathbf{B} and magnetic field strength \mathbf{H} are linked by the material condition

$$\mathbf{B} = \mu_a \mathbf{H}, \quad (8)$$

where μ_a is the absolute magnetic permeability. External magnetic field \mathbf{B}_{ext} is an artificial magnetic field that is not simulated but can be set up.

For solving the equations (4-7), the electrical potential ϕ and the magnetic vector potential \mathbf{A} are represented as

$$\mathbf{E} = -\nabla\phi, \quad (9)$$

$$\mathbf{B} = \nabla \times \mathbf{A}. \quad (10)$$

Substituting (9-10) into (4-7), the equations for the electric potential can be written in the form

$$-\nabla \cdot (\sigma \nabla \phi) + \nabla \cdot \sigma (\mathbf{V} \times (\mathbf{B} + \mathbf{B}_{ext})) = 0 \quad (11)$$

and for the magnetic potential

$$\nabla \times \left(\frac{1}{\mu_a} \nabla \times \mathbf{A} \right) = \mathbf{j} \quad (12)$$

The electric force for the equation (2) is defined by Lorentz and the ponderomotive forces

$$\mathbf{F}_L = \mathbf{j} \times \mathbf{B} - \frac{1}{8\pi} \mathbf{E}^2 \nabla \varepsilon \quad (13)$$

here ε is the dielectric permeability of the media. Joule heating in the equation (3) is calculated by

$$Q_{Joule} = \mathbf{j} \cdot \mathbf{E}. \quad (14)$$

For the modeling the heat transfer by radiation, so-called P1 model is used

$$\nabla \left(-\frac{4}{3} \frac{1}{\alpha + \beta} \nabla E_r \right) = 4\alpha (\sigma_{rad} T^4 - E_r), \quad (15)$$

where σ_{rad} is Stefan-Boltzmann constant, T – the temperature, E_r – the radiation energy density, α and β are the absorption and scattering coefficients for medium. The radiation term in the energy equation (3) equals

$$Q_{rad} = 4\alpha n^2 (E_r - \sigma_{rad} T^4) \quad (16)$$

and n is the refraction index.

Usually this whole system of governing equations is solved in separate codes [4, 5, 6, 7, 8] - the hydrodynamic subsystem (1-4) and (15) in CFD codes, and the Maxwell equation subsystem (11-12) in other codes. In this work, all systems are solved simultaneously in one code on the same computational mesh. This approach provides more stable solution due to the possibility of

using the method of Newton iterations to solve all strongly coupled governing systems.

3.1.2 Modified arc root model

In a thin layer of plasma near the metal (anode or cathode), the condition of plasma electroneutrality is violated. Shielding of the interface with charges leads to a voltage jump at the metal-plasma interface with nonlinear current density-voltage characteristics [5]. Fig. 5 shows typical current density-voltage characteristics.

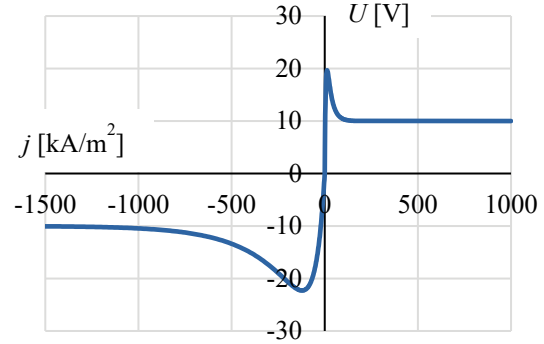


Fig. 5 Current density-voltage characteristics of the electric potential drop between plasma and metal.

As a usual, voltage drop is modelled by introducing an effective electrical conductivity [4, 5, 8] in a cell adjacent to the metal surface. This approach leads to a mesh-dependent solution, the current along the surface could be different than in the real case. In this paper, special boundary conditions are implemented. In this case it is assumed that the layer of voltage drop is very thin and can be neglected. Consider the interface between two substances with the voltage drop $U2$ and $U1$ from the left and right sides of the interface (Fig. 6).

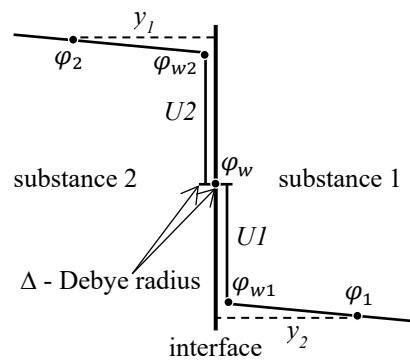


Fig. 6 Schematic diagram of the voltage drop model

Values ϕ_i, y_i, σ_i in Fig. 6 are the electric potential, the distance from the interface and the conductivity for points $i = 1, 2$ near both sides of the interface. According to the continuity condition of the normal current density to the interface it leads to

$$j_n = \sigma_1 \frac{\phi_{w1} - \phi_1}{y_1} = \sigma_2 \frac{\phi_2 - \phi_{w2}}{y_2}, \quad (17)$$

where $\phi_{w1} = \phi_w + U1$ and $\phi_{w2} = \phi_w - U2$.

For the equation (11) the boundary values ϕ_{w1} and ϕ_{w2} can easily be found, where $U1$ and $U2$ are the nonlinear

functions of the current density. The calculation of electric potential is done in two steps. Firstly, the normal current density to the interface is calculated from the previous time step and use for calculating the voltage drop and ϕ_{w1} . After that, the equation (11) is calculated. For stabilization and accuracy of the simulation, some iterations of these steps can be required.

3.2 Design

Two SPD designs are investigated in this work using digital spark gap prototyping. A goal of the study is to compare functionality of these different designs.

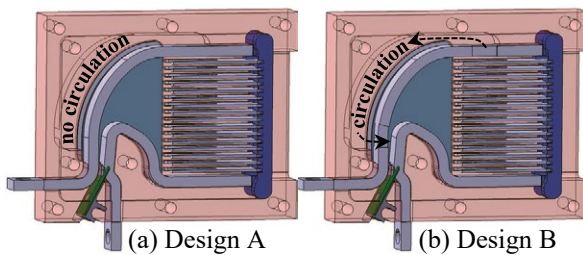


Fig. 7 SPD designs: (a) without gas circulation and (b) with gas circulation.

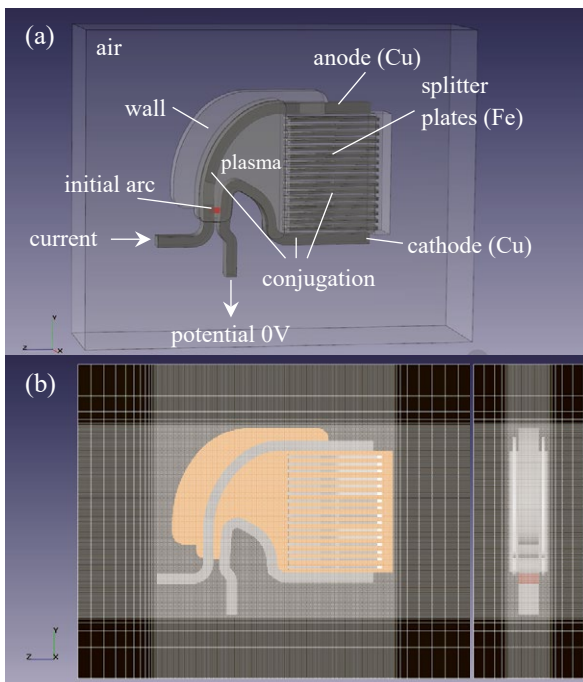


Fig. 8 Simulation model: (a) initial and boundary conditions and (b) computational grid.

As shown in Fig. 7, each geometry consists of two diverging electrodes in the horn and asymmetrical shapes and 16 splitter plates with the V-shaped recess. There is a difference between these two designs. The second geometry includes a channel for gas circulation through the upper electrode, as shown in Fig. 7b.

The upper electrode has openings so that the hot gas from the arc zone flows through the electrode into the special gas channel and back into the arc zone. Compared to the second geometry, the first design (Fig. 7a) has no circulation zone inside and the upper electrode is closed, has no openings. Fig. 8a describes the simulation model, initial and boundary conditions.

The SPD design (Fig. 7b) is imported into the MHD simulation domain, where the thermodynamic and transport properties of the air plasma, the material properties of copper for the electrodes and steel for the splitter plates are considered. These properties are given in the literature [4, 5]. In addition, the splitter plates include non-linear ferromagnetic properties ($\mu_a > 1$) for steel. The geometry takes the position in the centre of a large air box. It is assumed that the magnetic field induced by the electrical arc vanishes on the faces of this box. The additional volume to the magnetic field can be estimated according to the approximation that the magnetic field strength around the current-carrying conductor decreases outwards by $1/r$ [4]. The spark gap simulation includes heat transfer and electromagnetic conjugation between plasma, electrodes, splitter plates and air. At plasma-solid interfaces, the voltage drop is specified as a function of the current density (Fig. 5). The cathode roots are treated with the ignition voltage of 22.3 V at the current density of 130 kA/m² and the anode roots have the ignition with 19.6 V at 13 kA/m², whereby the anode is positive and the cathode negative. The modified arc root model is applied here.

Reference temperature of 300 K and reference pressure of 101325 Pa are specified as initial conditions. The ignition of impulse current is not simulated directly in this work. Instead, the arc ignition is carried out by setting the initial temperature 9700 K at the ignition point (Fig. 8a red cylinder) with radius 0.5 mm and thus the corresponding electrical conductivity. The external magnetic field $(-0.05, 0, 0)$ T is applied in the arc run area. The resulting force acts in addition to the Lorentz force and accelerates the arc from the ignition position in the y-direction. This force accelerates the arc of the mains-frequency current in roughly the same way as the impulse current 8/20 μ s with 10 kA. The spark gap is applied to the voltage of 230 V with the prospective current of 3.7 kA and ignited with the impulse current at the phase angle of 90°. These current characteristics are used in the presented spark gap prototyping approach and the input current corresponds to the experimental values according to Fig. 9. The shape of the outlets in the virtual tests are simplified for both designs and the free outlet boundary is used. The presented MHD model is solving on one computational domain. The computational grid is unstructured mesh with about 1.3 mln. cells, where the maximum cell edge size is 6 mm and the minimum size is 0.25 mm.

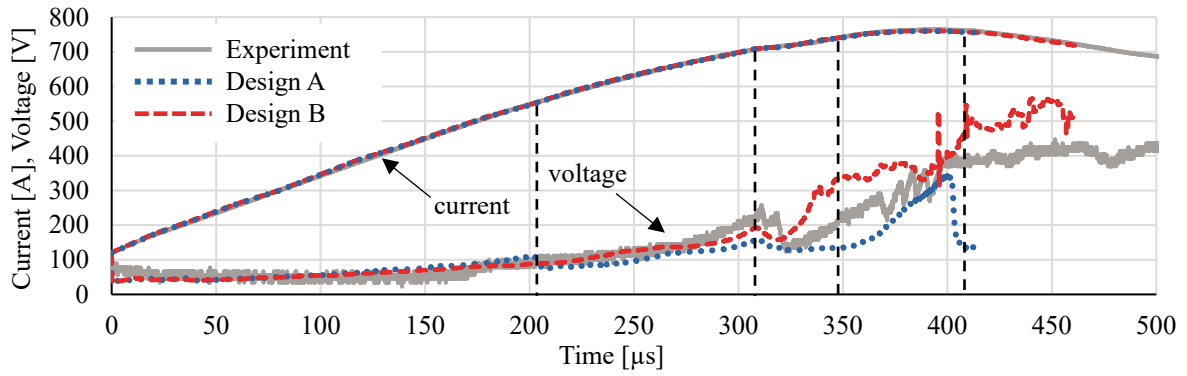


Fig. 9 Comparison of measured and calculated voltage and current.

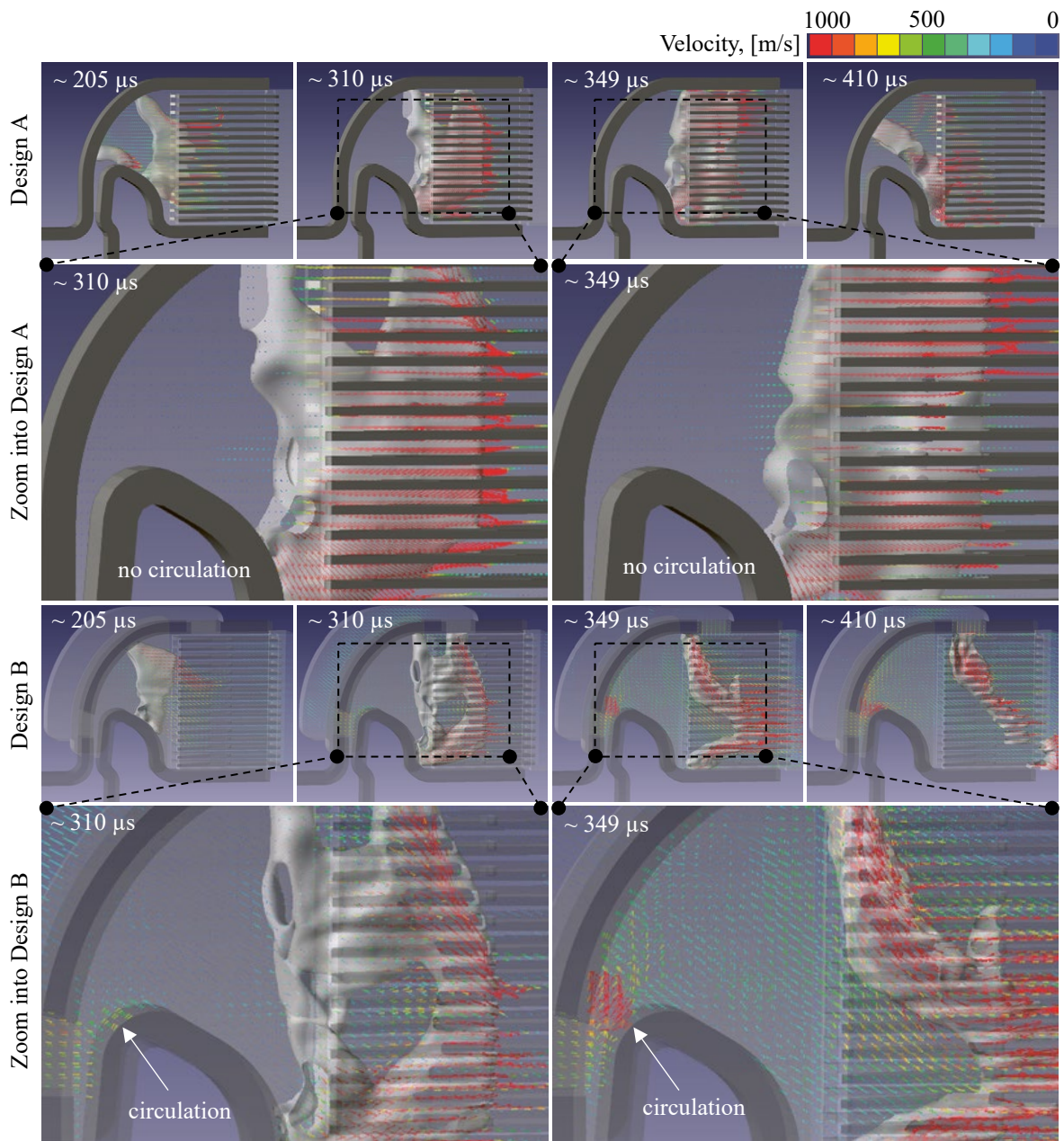


Fig. 10 Velocity distribution (vectors) visualises gas circulation and current density isosurface ($1.5 \times 10^7 \text{ A/m}^2$) shows arc shape in time for Design A and Design B.

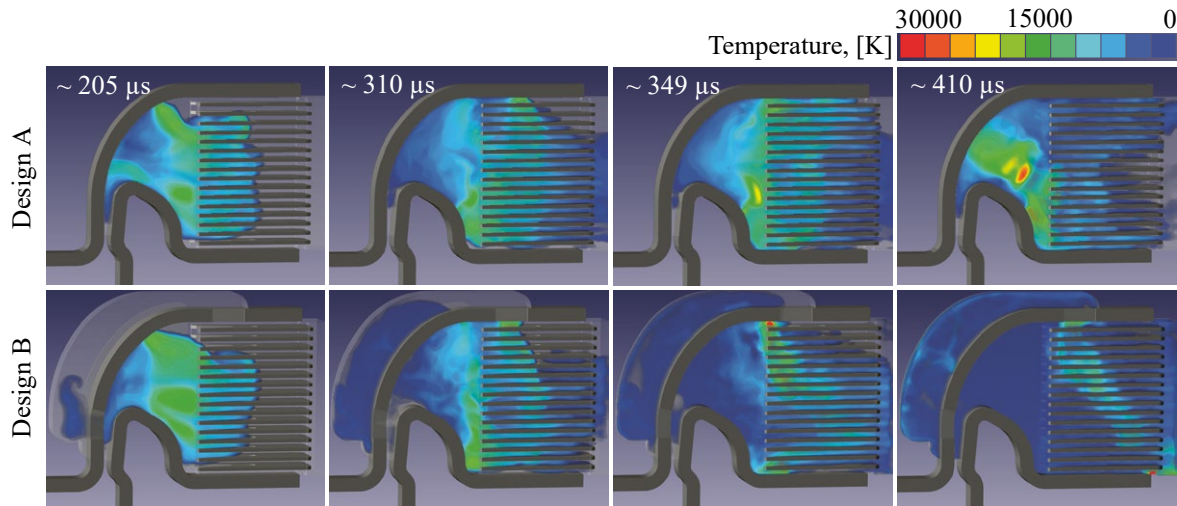


Fig. 11 Temperature distribution in time for Design A and Design B.

4 Results

As shown in Fig. 7, two SPD designs differ in the shape of the upper electrode. Design B has holes in the upper electrode, allowing the gas to circulate inside the SPD product. Design A has no circulation due to the closed electrode shape and the gas cannot flow into the circulation channel.

In Fig. 9, the calculated arc voltages for Design A and Design B are compared to the measurement values. The measurement was carried out on Design B. The arc movement visualization at time steps 205, 310, 349 and 410 μs , as shown in Fig. 10, is used to analyse the voltage profiles for the virtual and physical tests in Fig. 9 in detail. The results for A and B show that the arc movement process towards the splitter plates takes about 310 μs . Between 310-349 μs , the arc for Design B starts to split on the plates and spreads through these plates from about 400 μs . Compared to the experiment (Fig. 9), the results for Design B are in good agreement with the voltage measurement values.

Additionally, the simulation results for Design B show the gas circulation over time (Fig. 10). The velocity visualisation at time 349 μs demonstrates that the gas flows back into the arc area and accelerates the arc splitting process, see Fig. 10 (Zoom into Design B). According to Design A without circulation at time 349 μs , the arc lies close to the plates and does not split at them. In this case, the gas acceleration behind the arc is practically absent, as shown in Fig. 10 (Zoom into Design A).

At time 205 and 410 μs in Fig. 10, the arc in Design A jumps back deep into the arc area and re-ignition effects are observed. The position and shape of the re-ignited arc at 410 μs agree well with the high-speed camera image in Fig. 4b. The re-ignition affects the voltage profiles as it is shown in the experimental curve

in Fig. 4 and in the virtual test for Design A at time 205 and 410 μs shown in Fig 9. The voltage curve drops steeply towards low voltage values. The virtual test for Design A, Fig. 9 also achieves good agreement between experiment and numerical calculation up to 400 μs , but the arc does not split at the splitter plates because of re-ignition, therefore Design A does not satisfy the spark gap requirements.

Fig. 11 shows the temperature distribution over time for Design A and Design B. At time 205 μs , 349 μs and 410 μs , it is clearly seen that the temperature behind the arc in Design B is much lower than in Design A. It is in the range of 300-6000 K, while for Design A the temperature behind the arc at these times is in the range of 6000-17000K. Due to the high temperature in Design A, the re-ignition effect happens very often during the arc movement. Therefore, the gas circulation inside the product helps to lower the temperature and prevent the arc re-ignition.

At time 310 μs , the temperature distribution shown in Fig.11 and the arc shape shown in Fig.10 are almost the same for both designs. In Design B at time 310 μs , shown in Fig. 10 (Zoom into Design B), gas recirculation towards the arc area starts to develop, therefore the gas speed is still very low. The voltage profiles at time 310 μs shown in Fig. 9 demonstrate that the experimental and calculated voltages have almost the same peak shapes. This means that at the 310 μs analysed time the small re-ignition takes place. The re-ignition phenomena are caused due to the high temperature behind the arc and the relatively still cold, almost immobile air between the iron splitter plates.

Comparing the results in time frame 310 μs with time 349 μs , as shown in Fig. 10 (Zoom into Design B), the gas velocity in Design B increases. The gas circulation accelerates and supports the arc splitting process. Furthermore, the circulation cools the gas in the arc area, so that the arc generates less re-ignition and thus less energy in the device.

5 Conclusion

In this paper, two SPD designs were investigated using the developed digital spark gap prototyping model. The following conclusions can be drawn. The virtual spark gap model based on the 3D MHD approach and the modified arc root model has been implemented and validated. The presented MHD model works on one computational domain using FVM. The arc root model is based on boundary conditions, which leads to mesh-independent solution. The investigation of two SPD designs has shown that gas circulation within the spark gap helps to cool the temperature behind the arc, accelerate the arc splitting process and prevent re-ignition. The virtual test with the SPD design including gas circulation agrees well with the experiment, where arc movement and arc splitting are completed. Thus, this design fully satisfies the spark gap requirements. Based on these results, the presented virtual spark gap technology has great potential for further increasing product reliability, performance and size optimisation.

6 Literature

- [1] Ehrhardt A., Beier St.: New Deion Chamber for Encapsulated Switchgear, 27th International Conference on Electrical Contacts, June 22 – 26, 2014
- [2] Ehrhardt A., Schreiter St., Strangfeld U. and Rock M.: Encapsulated lightning current arrester with spark gap and deion chamber, 19th FSO, Brno, 2011
- [3] Chen F., Chang J.: Lecture Notes on Principles of Plasma Processing, Los Angeles: Plenum/Kluwer Publishers, 2002
- [4] Rütter J.: Weiterentwicklung und Vereinfachung eines Simulationsmodells für Schaltlicht bögen in Löschblechkammern, Dissertation, TU Braunschweig, 2014
- [5] Mutzke A.: Lichtbogen-Simulation unter besonderer Berücksichtigung der Fußpunkte, Dissertation, TU Braunschweig, 2009
- [6] Rümpler Ch.: Lichtbogensimulation für Niederspannungsschaltgeräte, TU Ilmenau, 2009
- [7] Fuchs R., Mürmann M., Nordborg H.: Towards an efficient arc simulation framework, *Plasma Physics and Technology* 4(1):79–82, 2017
- [8] Benz P, Lichtbogenlauf in einem Leistungsschalter, Presentation, Simulation Conference Schweiz, 2017
- [9] Rong M., Yang F., Wu Y., Murphy A. B., Wang W., and Guo J.: Simulation of arc characteristics in miniature circuit breaker, *IEEE Trans. Plasma Sci.*, vol. 38, no. 9, pp. 2306–2311, 2010
- [10] Aksenov A, Dyadkin A, Pokhilko V. Overcoming of Barrier between CAD and CFD by Modified Finite Volume Method, Proc. 1998 ASME Pressure Vessels and Piping Division Conference, San Diego, ASME PVP-Vol. 377-2., 1998. pp 79-86
- [11] Aksenov A.A., Zhlyukov S.V., Savitskiy D.V., Bartenev G.Y., Pokhilko V.I. Simulation of 3D flows past hypersonic vehicles in FlowVision software, *Journal of Physics: Conference Series*, Volume 653, No. 012072, 2015
- [12] Schmidt, George (1979). *Physics of High Temperature Plasmas*, second edition. Academic Press

Numerical arc simulations of radiatively-induced PMMA nozzle wall ablation

Roman Fuchs, HSR University of Applied Sciences Rapperswil,
IET Institute for Energy Technology, Rapperswil, Switzerland, rfuchs@hsr.ch

Abstract

An axially-blown arc in a PMMA nozzle is analyzed with numerical simulations. Previous experiments showed that wall ablation is observed for current values larger than a threshold and absent otherwise, and it has recently been found that PMMA is optically thick in the ultraviolet (UV) frequency range. An appropriate definition of radiation bands for the UV range has recently been published that allows for evaluating irradiance on the nozzle surface. In this contribution, it is shown that copper vapor affects the spatial temperature profile of the arc column and increases wall irradiance towards the upstream nozzle section. A caloric estimate for radiation-induced wall ablation is presented, which sheds some light on the experimental findings.

1 Introduction

An axially-blown electrical arc is considered in a convergent-divergent nozzle made of PMMA (poly-methyl methacrylate). The experimental setup was developed as the main functional element for a cost-efficient design of a high voltage direct current (HVDC) circuit breaker. [13] Subsequent work analyzed the electric field in the nozzle. [2, 3] In [4] it was found that the amount of ablated wall material was related to the differential resistance, and mass loss of the PMMA nozzle was measured only for currents larger than 350 A. However, the effect could not be explained by the measurements due to many unknown factors.

The experimental setup was investigated by numerical simulations in a magneto-hydrodynamic (MHD) framework focusing on the gas flow conditions and the energy budget. [5] The numerical results agreed reasonably with previous measurements although the solid bodies were modeled as adiabatic, and wall ablation as well as electrode erosion were neglected. It was found that the arc column is surrounded by a cold gas layer, so that the experimentally observed wall ablation must be due to radiative heat transfer from the plasma to the nozzle surface.

Recent work focused on radiative properties of polymers that are required for arc simulations. [1] It was found that PMMA is transparent in the visible range but opaque in the ultraviolet (UV) range, that is, for wavelengths shorter than 420 nm. Moreover, band-averaged absorption coefficients have been reported that are a key input for numerical simulations of electrical arcs.

This study is aimed at refining the numerical model [5] towards the experimentally measured results [4]. For that, copper vapor due to electrode erosion shall be included and tested for its effect on observable quantities by a parametric study. Moreover, the process

of wall irradiation and its ablation shall be investigated, based on the recent findings of radiative properties of PMMA.

The paper is structured as follows. Section 2 describes the model and the effects included in this numerical analysis. It also presents an estimate for a minimum irradiance required such that wall ablation is observable. The results are presented in section 3, by comparing arc voltage to measured values and the effects of copper erosion on the temperature distribution along the arc axis. We also show the irradiation on the nozzle wall for the UV range. Conclusions are summarized in section 4.

2 Numerical Model

2.1 Geometry

The geometric setup is taken from [4] and described in the following using the nozzle throat and its axis as a reference (see **figure 1**). The inlet section has a radius of $R_{in} = 25$ mm. The nozzle has conical sections of 70 mm length with half-angles 15° upstream and 10° downstream, respectively. The throat radius is $R_{th} = 10$ mm and connects the two sections with a rounded edge of radius 10 mm. Copper rods are used as electrodes with 5 mm diameter and inserted into the nozzle axially at positions $x_A = -30$ mm and $x_B = 50$ mm. The inlet is located at $x = -230$ mm and the outlet at $x = 300$ mm. The geometry allows to perform this study with axial symmetry.

The computational domain has a radius of 100 mm and it is discretized with polyhedral cells. The grid is refined between the electrode tips to a size of 0.25 mm. The downstream section is refined well beyond the nozzle exit with cell diameters of 0.5 mm to resolve the shock fronts appropriately. Prism layers are specified on all body interfaces to ensure a perpendicular mesh, since this helps to ensure convergence of the electric potential solver; their height is specified to be 0.1 mm.

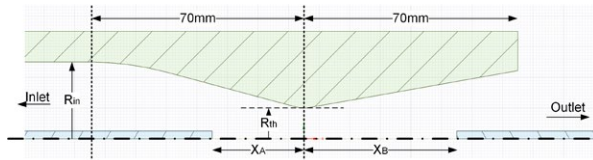


Figure 1: Axisymmetric view of the PMMA nozzle and electrodes.

2.2 Model equations and framework

The aim of this study is to evaluate thermal irradiation on the nozzle surface that is exposed to the electrical arc. Therefore, we are looking for a numerical and coupled solution in steady state of the Navier-Stokes equations for gas flow, Maxwell's equations for electromagnetism, and the radiative transfer equation accounting for radiative heat transfer. The model is implemented in the numerical framework of Simcenter STAR-CCM+ (version 2019.3.1) [12].

Because the arc is located at the symmetry axis, the magnetic field has a negligible effect and is discarded; as a consequence, the electromagnetic equations reduce to the Gauss law for electric field. The upstream electrode (cathode) is stressed with a current value I , while the downstream electrode (anode) is fixed to zero potential. The electrical conductivity of the plasma is characterized by temperature, pressure, and copper mass fraction, and provided to the software in tabulated format.

The inlet pressure $p = 8.4$ bar is specified in absolute scale and the outlet pressure is set to ambient conditions. This results in supersonic flow conditions downstream of the nozzle throat, and shock fronts will form at the anode tip and nozzle exit. Turbulent flow conditions are accounted for by the standard $k-\epsilon$ model. Ohmic heating is included as energy source term. The thermodynamic and transport properties of air-copper plasma were provided by Murphy. [8, 9]

The radiative transfer equation is solved numerically by the Discrete Ordinate Method. The frequency domain is discretized into bands (see **table 1**) according to the ionisation energy levels of atomic nitrogen (see [11]) and the UV frequency band definitions in [1]. Mean absorption coefficients are computed from spectral data provided by Kloc [6] with Planck-averaging in each band, and supplied to the software in tabulated format and as functions of temperature, pressure, and copper mass fractions (see **figure 2**).

A detailed model would account for heat conduction from the plasma to the solid bodies, their erosion, and also include an arc root model for the detailed physics at the plasma-electrode interface (see, e.g., [11]). However, as we are looking for a steady state solution, the thermal inertia is discarded which would lead ultimately to solid bodies at evaporation temperature. This situation is resolved and simplified: the electrodes are excluded from the energy balance and adiabatic boundary conditions applied. Nevertheless, we account for electrode erosion with a mass species source term $\Phi = g_j$

Band	$\lambda_l/\mu\text{m}$	$\lambda_u/\mu\text{m}$	Radiation category
1	30000.0	4542.3	IR
2	4542.3	856.5	
3	856.5	700.0	
4	700.0	420.0	Visible
5	420.0	290.0	UV
6	290.0	194.7	
7	194.7	113.1	
8	113.1	102.0	
9	102.0	85.2	
10	85.2	30.0	

Table 1: Definition of radiation band boundaries.

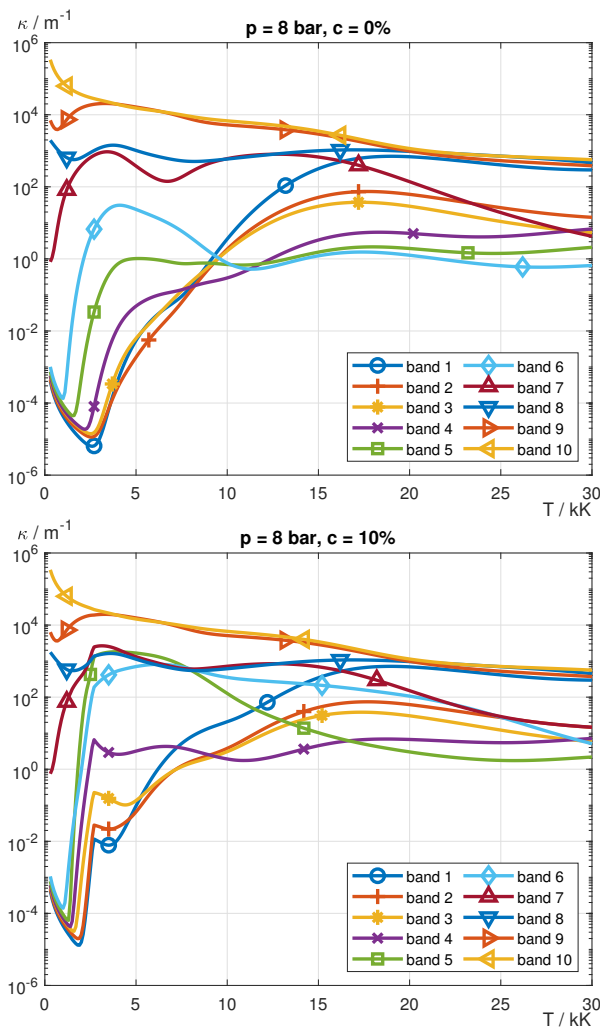


Figure 2: Mean absorption coefficients at 8 bar and for copper mass fraction 0% (above) and 10% (below).

that is proportional to current density j and a constant erosion rate g (units: μgC^{-1}). As in [11], the erosion rate discriminates between anode and cathode by a factor of two: $g_a = 0.5g_c$. A drawback of this approach is that the electrode surface temperature will be significantly higher than copper evaporation temperature.

Similar modeling issues are observed for the nozzle domain. The solid domain must be included in the energy balance because we aim to evaluate the irradiation on the nozzle surface. With this aim, we set the absorption coefficient as well as the nozzle surface emissivity to zero so that the body is optically transparent and therefore heating effects are suppressed; as a consequence, we do not model any evaporation of PMMA. This aspect is justified by the recent results that those polymer vapors have negligible effects on the total radiative energy balance when exposed to high current arcs. [1] Moreover, if ablation was included, the ablated vapors would be transported along the nozzle surface and likely not be mixed into the arc column. Therefore, it would only affect the gas flow conditions which could be mimicked by a source term for air species.

The simulations run for 1500 iterations. It takes about 1000 to 1200 iterations until the initial conditions disappeared and the quantities of interest converged. Despite of the nonlinear coupling among the gas flow, electromagnetism and thermal radiation, the residuals systematically reduced by three orders of magnitudes.

2.3 Estimate on radiation-induced wall ablation

This section presents a caloric relation on the irradiance E_w required to heat the nozzle wall and trigger its ablation in a time interval $[0, t]$.

Let us consider a cylindrical tube with inner wall radius r_w and axial length l irradiated uniformly. We also assume that the absorption coefficient κ and mass density ρ of the tube material are given.

Let us consider the radiative intensity $I(s)$ into the tube wall along a straight line perpendicular to its surface, with $s = 0$ at the inner tube wall. Moreover, let us assume that the tube wall is cold such that its emission is negligible. From the radiative transfer equation, we find that the radiative intensity decays exponentially on the scale of its optical depth τ ,

$$I(s) = I(0)e^{-\tau}, \quad \tau = \int_0^s \kappa(x) dx. \quad (1)$$

We may assume that the absorption coefficient is constant along this path, which yields $\tau = \kappa s$. We choose s such that the radiative intensity has decayed by two orders of magnitude, i.e., $\tau = -\ln(10^{-2}) = 4.6$. Using this value for optical depth, we define the heated tube volume as

$$\begin{aligned} V &= \pi l ((r_w + s)^2 - r_w^2) \\ &= 2\pi l \left(r_w + \frac{1}{2}s \right) s \approx A_w s, \end{aligned} \quad (2)$$

assuming that the material layer thickness s is small compared to the wall radius, and denoting the irradiated wall area by $A_w = 2\pi l r_w$. This volume has mass $m = \rho A_w s$, and the absorbed energy until time t is equal to

$$Q = E_w A_w t. \quad (3)$$

On the other hand, the required heat to increase the temperature of a mass m from ambient temperature T_0 to vaporization temperature T_v and its latent heat of evaporation L_v is equal to

$$Q = m(\Delta h + L_v), \quad (4)$$

where $\Delta h = h(T_v) - h(T_0)$ denotes the difference in specific enthalpy of the solid material. Therefore, the minimum value for wall irradiation E_w required to induce wall ablation in time t is given by:

$$E_w = \frac{Q}{A_w t} = \frac{\rho s}{t} (h(T_v) - h(T_0) + L_v). \quad (5)$$

To be specific and relate to the measurements in [4], in which the nozzle was exposed for $t = 10$ ms to high current arc, we note that the mass density of PMMA is $\rho = 1.18 \text{ g cm}^{-3}$ and its melting temperature $T_v = 160^\circ\text{C}$. We find data for the enthalpy difference $\Delta h = 211 \text{ kJ kg}^{-1}$ [10] and the latent heat of evaporation $L_v = 330 \text{ kJ kg}^{-1}$ [7], and use an absorption coefficient $\kappa = 1 \times 10^4 \text{ m}^{-1}$ from the UV range [1]. With this data, we calculate that the irradiation affects a material layer of thickness $s = 0.46 \text{ mm}$, and a minimum irradiance for radiatively induced ablation

$$E_w = 3 \times 10^7 \text{ W m}^{-2}. \quad (6)$$

3 Results & Conclusions

Figure 3 provides an overview of the gas flow field. It shows the temperature field for current $I = 1400 \text{ A}$ and erosion rate $g_c = 40 \mu\text{gC}^{-1}$. We see that the arc temperature in the convergent section is larger than downstream of the throat. We observe flow expansion in the divergent section, and the shock fronts at the anode tip and after the nozzle exit. The increased temperature at the cathode and upstream of the nozzle is due to radiative heat transfer from the arcing zone and that we solved for the steady state. A more detailed analysis of the temperature in the arc column follows in figure 5.

Figure 4 shows the arc voltage as a function of current and erosion rate. We see that the arc voltage reduces with arc current and agrees rather well with the results reported in [4] for low to intermediate currents. This is an improvement to previous numerical results [5] which used rounded electrode tips and the $k - \omega$ turbulence model, in particular for the lowest current values. We also note that including electrode erosion leads to slightly larger arc voltage, and its effect being more pronounced as current increases.

Figure 5 shows the arc center temperature profile in axial direction. At low currents ($I \leq 300 \text{ A}$), we see that

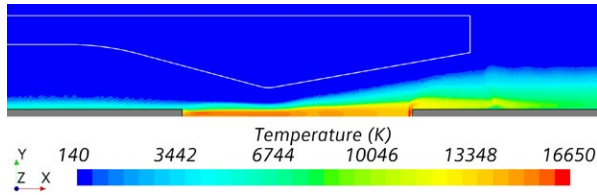


Figure 3: Temperature field for $I = 1400\text{ A}$ and $g_c = 40\mu\text{g C}^{-1}$.

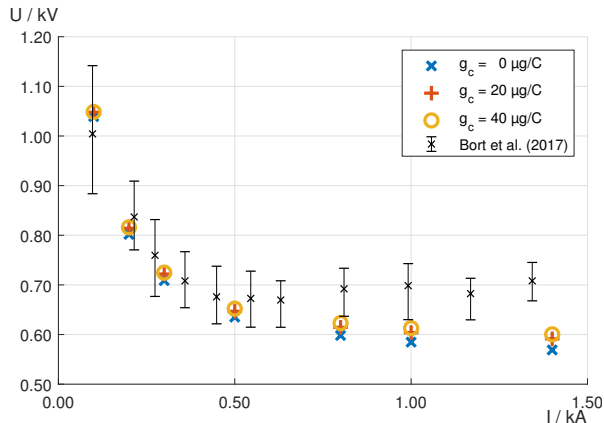


Figure 4: Arc voltage as a function of current and erosion rate.

copper vapor reduces the arc center temperature only in a region close to the upstream electrode tip, whereas for larger currents the temperature profile is reduced for longer distances downstream.

The temperature profiles reveal further details that are independent of arc current and characteristic to the gas flow field in the nozzle. A few millimeters after the cathode tip ($x = -25\text{ mm}$), we note a temperature maximum; this is due to the gas flow being directed towards the nozzle axis enhancing effectively convective heat transfer from the arc column and leading to a constricted arc column. At $x = 15\text{ mm}$, we note a dip in the temperature profile which is a result of the expanding flow downstream of the throat. At the anode tip, we see a sharp increase in temperature because of a bow shock that is formed by the supersonic flow. Finally, we see that the temperature profiles are rather uniform in the convergent upstream section, whereas a negative slope is observed in the downstream divergent section.

This last observation may be of interest for further developments in the design of the geometric setup. It is interesting to note that these findings on the temperature profile correspond to results on the electric field, both numerically [5] and experimentally [3].

Figure 6 shows the boundary irradiance, i.e., the radiant flux received per unit area on the nozzle wall, summed for all radiation bands with wavelengths in the UV range (i.e., for band numbers 5 to 10). We note that irradiance increases with electrode erosion rate. For low currents, we see that irradiance is larger in the upstream section than it is downstream. For larger currents ($I \geq 500\text{ A}$) we discriminate on the erosion rate:

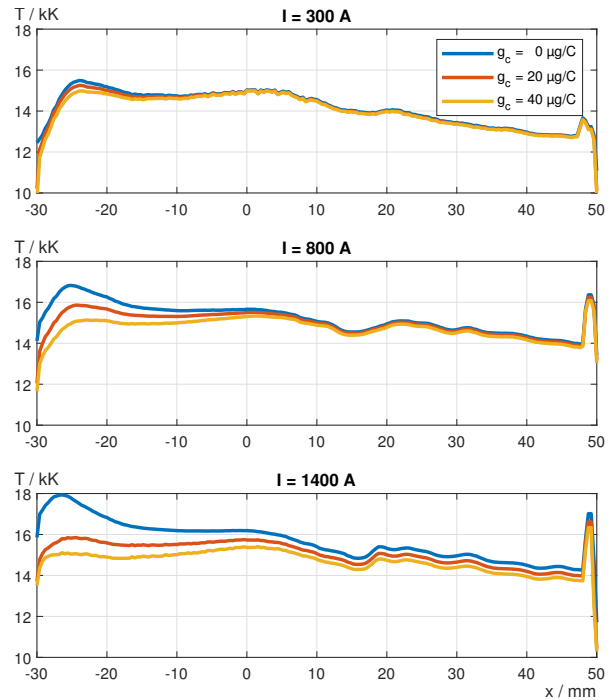


Figure 5: Arc center temperature at axial positions.

if electrode erosion is neglected ($g_c = 0$), we see that irradiance is larger downstream compared to the same distance upstream of the nozzle. On the other hand, if electrode erosion is included ($g_c > 0$) irradiance remains larger in the upstream section for positions $|x| \leq 25\text{ mm}$.

From these findings on arc voltage, arc center temperature, and boundary irradiation, we conclude that copper vapor enhances radiative heat transfer from the plasma column to its ambient and, as a consequence, reduces the plasma temperature in the upstream section (see also **figure 5**). Although copper-contaminated plasma is more conductive than pure air at otherwise identical temperatures and pressures, the total effect of reduced arc temperature dominates and leads to larger arc voltage (see **figure 4**).

In section 2.3 we developed an expression for radiation-induced wall ablation (see eq. (6)). A closer look at **figure 6** reveals that the criterion $E_w \leq 3 \times 10^7\text{ W m}^{-2}$ is fulfilled for current $I \leq 300\text{ A}$ independently of the erosion rate, and coincides with the observations in [4]. It is therefore concluded that those observations are due to fact that PMMA is opaque in the UV range (as found in [1]). However, the hypothesis on the criterion for radiation-induced wall ablation should be tested with further experiments.

Figure 7 shows the wall irradiance for all bands in the two cases of $I = 100\text{ A}$ and $I = 1400\text{ A}$. The thick line shows the sum of irradiance of all bands in the UV range, and it is the same as in **figure 6**. We highlighted the bands that contribute most for the two cases. For low current it is band 7 and 2 that contribute most along the full arc column. This picture changes for larger current: we observe that band 7 has the largest contribution only in the downstream section, whereas band 6 has the

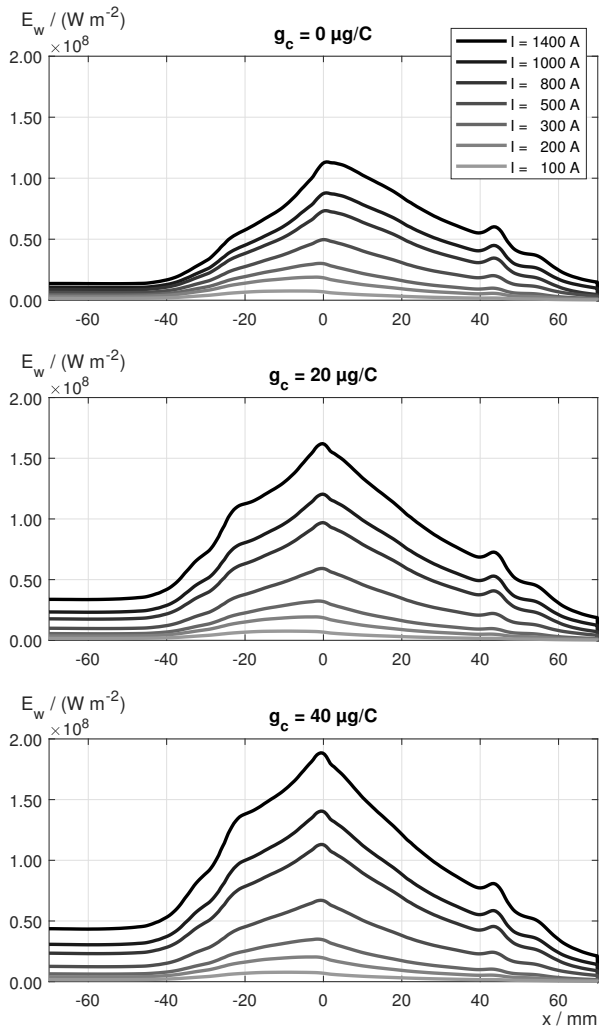


Figure 6: Sum of band-integrated boundary irradiance in UV ranges. The vertical sequence of curves are the same as in the legend.

largest contribution upstream. We also read from the figure that the UV bands cover about 2/3 of the total wall irradiance in both cases. It is concluded that the band definition in **table 1** will be useful for further studies on PMMA ablation, and it would be useful if measurements of optical properties of PMMA are extended to shorter wavelengths.

Figure 8 shows the radiant flux, i.e., the surface integrated value of boundary irradiance, onto the nozzle wall for frequencies in the UV regime. We clearly see that the radiant flux increases with current. Moreover, we see that the total irradiance is enhanced by the erosion rate for currents larger than 300 A. This may be another indication for the observations in [4] that ablation occurs only for currents above a certain threshold.

4 Summary

Numerical results have been presented on an axially-blown arc in a PMMA nozzle. The computational model was refined by including copper erosion and defining the

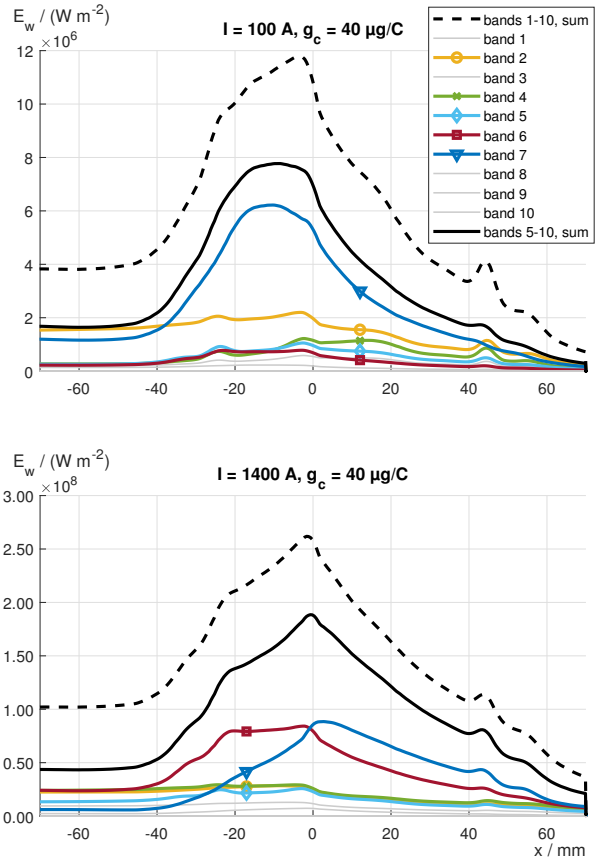


Figure 7: Band-integrated boundary irradiance, total irradiance (dashed line), and irradiance of UV-bands (thick line).

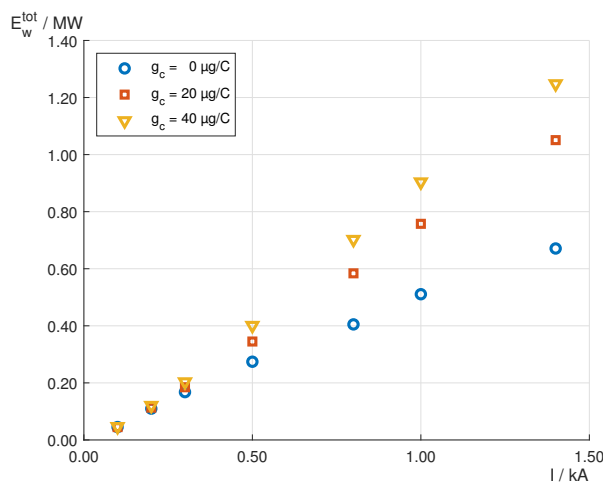


Figure 8: Total radiant flux on nozzle wall in UV range.

radiation bands to allow for analysis of wall irradiation in the UV range, because PMMA is optically thick for those wavelengths. An estimate for radiation-induced wall ablation has been developed and tested with previous results of measurements and the actual data obtained from these simulations. Additionally, a detailed analysis of the temperature profile in the arc column and the band-averaged wall irradiance has been provided. It has been found that copper erosion leads to higher arc voltage and lower arc center temperature particularly in the upstream section because it enhances radiative transfer to its ambient. It has also been found that copper erosion affects the spatial distribution of irradiance as evaluated on the nozzle wall, in particular that the upstream section is more intensely irradiated if copper vapor is present. Finally, it has been found that irradiance in the UV range covers about 2/3 of the total wall irradiance.

Further work may refine the computational model in various aspects. For instance, heat conduction to the solid bodies and their evaporation would lead to a more complete and consistent model and might help for more accurate arc voltage at large currents.

The estimate for radiation-induced wall ablation shall be tested with other testcases. For instance, the experiments by [4] should be repeated with a shorter or longer time for high arc current, since this will affect the wall irradiance E_w required to observe ablation as shown by eq. (5). The numerical simulations may also be repeated for other inlet pressures and compared to further results in [4].

References

- [1] M. Becerra and J. Pettersson. Optical radiative properties of ablating polymers exposed to high-power arc plasmas. *Journal of Physics D: Applied Physics*, 51(12):125202, 2018. ISSN 0022-3727. doi: 10.1088/1361-6463/aaaeda.
- [2] L. S. J. Bort and C. M. Franck. Effects of nozzle and contact geometry on arc voltage in gas circuit-breakers: 2016 IEEE International Conference on High Voltage Engineering and Application : 19-22 September 2016, Chengdu, China. pages 1–4, 2016. doi: 10.1109/ICHVE.2016.7800700.
- [3] L. S. J. Bort and C. M. Franck. Determination of Axial Electric Field Distribution in Blown Arcs With Differential Method. *IEEE Transactions on Plasma Science*, 47(1):714–720, 2019. ISSN 0093-3813. doi: 10.1109/TPS.2018.2880950.
- [4] L. S. J. Bort, V. Freiermuth, and C. M. Franck. Influence of ablation on differential arc resistance. *Plasma Physics and Technology*, 4(2):145–148, 2017. doi: 10.14311/ppt.2017.2.145.
- [5] R. Fuchs and H. Nordborg. Energy budget of electrical arcs in a gas-blast circuit breaker. *Nafems World Congress 2019*, 2019.
- [6] P. Kloc, V. Aubrecht, and M. Bartlová. Effective plasma radius for planck mean absorption coefficient: 129425. In *Proceedings of the 21st International Conference on Gas Discharges and their Applications*, pages 89–92, 2016.
- [7] P. J. Lindstrom and W. G. Mallard. Nist chemistry webbook: Nist standard reference database number 69, 30.01.2020. URL [https://webbook.nist.gov/cgi/inchi/InChI%3D1S/C5H8O2/c1-4\(2\)5\(6\)7-3/h1H2%2C2-3H3](https://webbook.nist.gov/cgi/inchi/InChI%3D1S/C5H8O2/c1-4(2)5(6)7-3/h1H2%2C2-3H3).
- [8] A. B. Murphy. Transport coefficients of air, argon-air, nitrogen-air, and oxygen-air plasmas. *Plasma Chemistry and Plasma Processing*, 15(2): 279–307, 1995. ISSN 0272-4324. doi: 10.1007/BF01459700.
- [9] A. B. Murphy. A comparison of treatments of diffusion in thermal plasmas. *Journal of Physics D: Applied Physics*, 29(7):1922–1932, 1996. ISSN 0022-3727. doi: 10.1088/0022-3727/29/7/029.
- [10] M. Pyda. Poly(methyl methacrylate) (PMMA) Heat Capacity, Enthalpy, Entropy, Gibbs Energy: Datasheet from “The Advanced THERMAL Analysis System (ATHAS) Databank – Polymer Thermodynamics” Release 2014 in SpringerMaterials. URL https://materials.springer.com/polymerthermodynamics/docs/athas_0010.
- [11] C. Rümpler. *Lichtbogensimulation für Niederspannungsschaltgeräte*. Dissertation, TU Ilmenau, Ilmenau, 2009.
- [12] Siemens PLM Software. STAR-CCM+. URL <https://www.plm.automation.siemens.com/global/en/products/simcenter/STAR-CCM.html>.
- [13] M. M. Walter. *Switching arcs in passive resonance HVDC circuit breakers*. Phd thesis, ETH Zurich, 2013.

Simulation-based Development of a Line Lightning Protection Device

Mario Muermann, HSR University of Applied Science, Rapperswil, Switzerland, mario.muermann@hsr.ch,
Alexander Chusov, Streamer-Electric, Saint Petersburg, Russia, alexander.chusov@streamer-electric.com,
Roman Fuchs, HSR University of Applied Science, Rapperswil, Switzerland, roman.fuchs@hsr.ch,
Henrik Nordborg, HSR University of Applied Science, Rapperswil, Switzerland, henrik.nordborg@hsr.ch

Abstract

Overhead lines can be protected from lightning strikes via so-called multi-chamber systems or 'line lightning protection devices (LLPDs)'. These systems divert the lightning energy to ground by the use of multiple spark gaps. After the lightning strike, the electrically conducting gaps need to be reverted to insulating behavior, which is achieved by suitable plasma and gas flow.

Existing designs are used up to line voltage ratings of about 35 kV, whereas higher voltage ratings are desirable. However, one cannot simply scale this design to significantly higher voltage ratings due to weight and space requirements. In this paper an approach is presented, which allowed for a new LLPD design development up to voltage ratings of 110 kV exploiting slightly different physical phenomena compared to existing designs. We were able to identify key parameters for the device's performance and behavior within an electrical test circuit by analytical calculations. On the basis of these findings, we designed a new discharge chamber as the basis of a multi-chamber system forming a new type of LLPD. This design was used as input to numerous numerical simulations and was further optimized with respect to line protection performance. The designed chambers will be produced and tested by experiments at the high-voltage laboratory at HSR in the near future.

This work has been done in the framework of a close collaboration of HSR with Streamer-Electric and is partly funded by Swiss Innovation Agency 'Innosuisse'.

1 Introduction

Overhead lines are exposed to all weather conditions and need to be designed to withstand lightning strikes and lightning induced overvoltage. This is done by installation of so-called Line Lightning Protection Devices (LLPDs), which are produced and distributed by Streamer-Electric in Chur, Switzerland and Saint Petersburg, Russia [1]. These devices consist of a series of discharge chambers, that divert the lightning energy to ground by the use of multiple spark gaps. After the lightning strike, the electrically conducting gaps also ground the line voltage and need to be reverted to insulating behavior, which is achieved by suitable plasma flow within the gap structure [2] [3]. A suitable chamber design is therefore absolutely crucial in order to achieve a reliable operation and to meet performance requirements [4].

Technically, the lightning overvoltage causes an electrical breakdown in the gaps. The resulting current is fed by the lightning current and the follow current from

the power station. As a result, the air inside the chambers is heated, leading to further formation of plasma and a significant pressure build-up. As soon as the lightning current expires in the range of microseconds, the heating mechanism collapses and the plasma is blown out of the chamber due to the developed high-pressure gradients, resulting in insulating the spark gaps and therefore in desirable performance. This kind of operation is also called 'Impulse Quenching' [2] [4]. However, the level of follow current determines, whether the residual heating after the lightning strike causes a self-establishing current due to persistent ohmic heating in the plasma or if Impulse Quenching is achieved. In case of high follow current levels, one must await the next current zero crossing to achieve quenching behavior. This kind of quenching is called 'Zero Quenching' [2] [4].

Since the line's voltage level determines the follow current level, existing LLPD designs are used up to line voltage ratings of about 35 kV only. In case of higher voltage ratings, the heat input might lead to damage or

to self-establishing currents. Nevertheless, the development of LLPDs for voltage ratings up to 110 kV is highly desirable [5] and is presented in the framework of this paper.

Due to weight and space limitations, one cannot simply scale existing designs to significantly higher voltage ratings. Therefore, we developed a new design based on the amount of know-how regarding the physical phenomena in existing LLPDs and with the help of various numerical simulation techniques. Since the chamber's technical performance strongly depends on the voltage and current rating besides the thermodynamical plasma properties, the choice of boundary conditions, which are applied to the LLPD design, must also be done with great care. The latter is determined by the interaction between plasma physics, chamber geometry, and surrounding electrical line components.

Electric arc simulations are in general challenging, since these require a lot of knowledge about the involved physical phenomena, such as compressible flow, radiation, material ablation amongst others. In addition, the interaction between the electric circuit representing the overhead line and the electric arc has to be taken into account.

In a first step, we were able to identify key parameters for the device's performance and behavior within an electrical test circuit by understanding the interaction between circuit and electric arc. This approach is documented in section 2.

After key parameter identification, we used these parameters to develop a new chamber design with the help of CAD-Systems, which was used afterwards as an input for detailed three-dimensional numerical simulations including the electric circuit as boundary conditions. Details on this project stage can be found in section 3. Note, that this development work is still ongoing, thus the presented approach is not to be understood as final.

The simulation results are presented and discussed in section 4 and in section 5.

Based on numerous simulations, prototypes of single chambers will be produced. Validation experiments are planned and will be carried out in the near future.

This work has been done in the framework of a close collaboration of HSR with Streamer-Electric and is partly funded by Swiss Innovation Agency Innosuisse.

2 Circuit Model

Prototypes of existing LLPDs have been tested in the electric circuit shown in figure 1. This circuit approximates the physical behavior of an overhead line [2]. The LLPD in this circuit is represented by the resistance R_{LLPD} . The capacitor C_0 and the inductor L_0 build an oscillating circuit with a resonant frequency of $f \approx 50$ Hz. Thus, these components represent the power station. The inductor L_1 accounts for line induct-

ance, the capacitor C_f and resistance R_f represent capacitance effects of the line. The current source $I_{Lightning}$ introduces the lightning current into the circuit and is represented by a 8-50 μ s-pulse with a peak

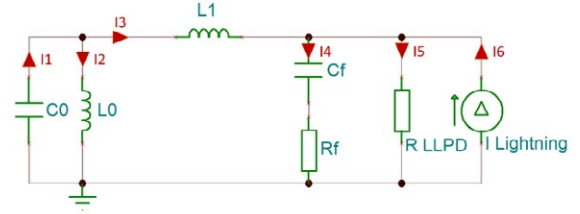


Fig. 1: Electric Circuit, that is used as a testing environment for LLPDs. The component data are as follows: $C_0 = 350 \mu F$, $L_0 = 22 mH$, $L_1 = 11 mH$, $C_f = 125 nF$, $R_f = 50 \Omega$.

value of 30 kA. Its transient data is shown in figure 2. From the circuit's perspective, the multiple electric arcs in the LLPD represent a highly dynamic ohmic re-

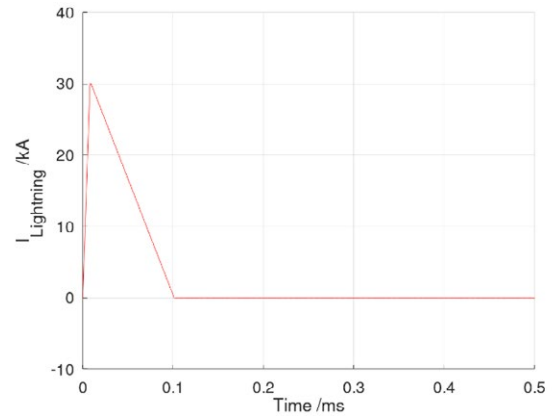


Fig. 2: Lightning current curve as boundary condition in the electric circuit.

sistance. Its transient behavior can be roughly estimated. Therefore, the electric circuit representing the overhead line was formulated as a system of ordinary differential equations, forming an initial value problem. Here, the LLPD's resistance curve was used as an input parameter. Different choices of resistance curves lead to valuable insights into the system's dynamics.

$$\dot{I}_1 = \dot{I}_2 + \dot{I}_3$$

$$L_0 \ddot{I}_2 = I_1 / C_0$$

$$-L_0 \ddot{I}_2 + L_0 \ddot{I}_3 - R_f \dot{I}_4 = I_4 / C_f$$

$$R_f \dot{I}_4 - R_{LLPD} \dot{I}_5 = I_4 / C_f$$

$$\dot{I}_4 + \dot{I}_5 = \dot{I}_3 - \dot{I}_6$$

The ODE-system was solved with the initial vector \vec{I}_0 using the ode45-solver of the software package Matlab and Octave, respectively.

$$\vec{I}_0 = \begin{pmatrix} I_{1,0} \\ I_{2,0} \\ \dot{I}_{2,0} \\ I_{3,0} \\ \dot{I}_{3,0} \\ I_{4,0} \\ I_{5,0} \end{pmatrix} = \begin{pmatrix} 0 \\ 0 \\ 110 \text{ kV}/L_0 \\ 0 \\ 110 \text{ kV}/L_1 \\ 0 \\ 0 \end{pmatrix}$$

Within this approach, we used different transient ohmic resistance functions for the new LLPD in order to study the dynamic quenching behavior of the system. In this manner, reasonable ohmic resistance curves for the LLPD in question were identified, that allowed for reliable quenching. Finally, the desired resistance curves had to be translated into suitable LLPD design ideas in a next step (see also section 3).

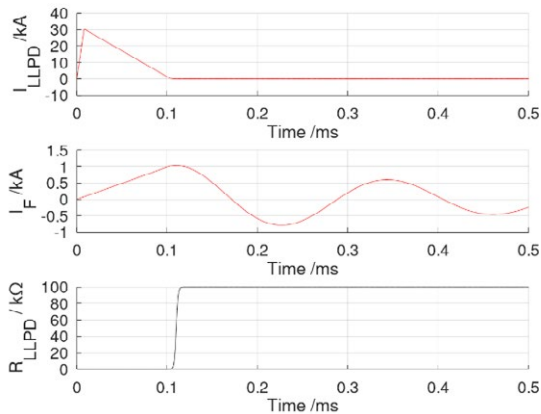


Fig. 3: Obtained data for the LLPD's current (top), follow current (middle) and electric LLPD's resistance (bottom). The latter was used as input for the circuit simulation. The ohmic resistance during the lightning stage was chosen to $R_{LLPD,0} = 0.1 \Omega$.

Clearly, an ohmic resistance curve, that is shown in figure 3 (bottom), seems desirable in general, since it allows to divert the lightning energy effectively to ground due to a negligible initial resistance value during the lightning stage ($R_{LLPD,0} = 0.1 \Omega$). After been exposed to the lightning strike at around $100 \mu\text{s}$, the rapidly increasing resistance blocks the current path to ground, leading to perfect performance. However, as the resulting relative high follow current indicates in figure 3 (middle), quenching is unlikely to happen under that circumstance. The low LLPD's resistance value during the lightning stage doesn't allow for a high electric potential between line inductance and LLPD. Therefore, almost the whole grid voltage is placed across the line inductance, resulting in an increase of follow current during the first $100 \mu\text{s}$ up to a value of roughly 1 kA. This relative high follow current rating is in reality acting upon the LLPD's plasma as ongoing

heat input at $t = 100 \mu\text{s}$, counteracting the cooling mechanisms inside the spark gaps or chambers and preventing quenching. Thus, the desired ohmic resistance curve is hardly achievable. The amount of heat input per chamber can only be lowered by additional chambers, resulting in violating the acceptable maximum number of chambers due to the resulting device's weight and size.

A more promising approach consists of the combination of the Impulse Quenching and the Zero Quenching technique, respectively. By manipulating the LLPD's resistance in a way, such that the follow current is mostly negative during the lightning stage, we can initiate an artificial current zero crossing right after the

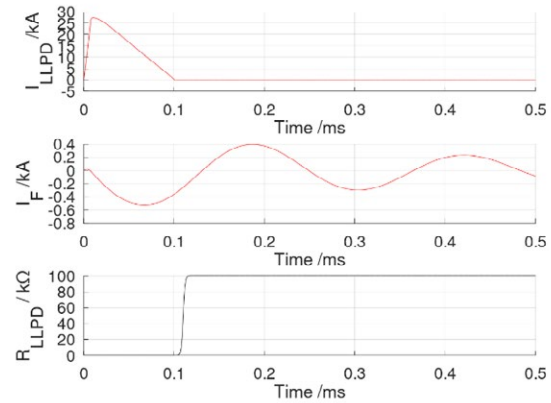


Fig. 4: Obtained data for the LLPD's current (top), follow current (middle) and electric LLPD's resistance (bottom). The latter was used as input for the circuit simulation. The ohmic resistance during the lightning stage was chosen to $R_{LLPD,0} = 10 \Omega$.

lightning strike. This can be realized using an initial resistance of $R_{LLPD,0} = 10 \Omega$ during the lightning stage. This way, a small time-frame with almost no heat input into the LLPD is introduced, that is supposed to allow for rapid plasma cooling due to developed pressure. The corresponding transient resistance and current curves are shown in figure 4. The current zero crossing's point of time is determined mainly by the initial

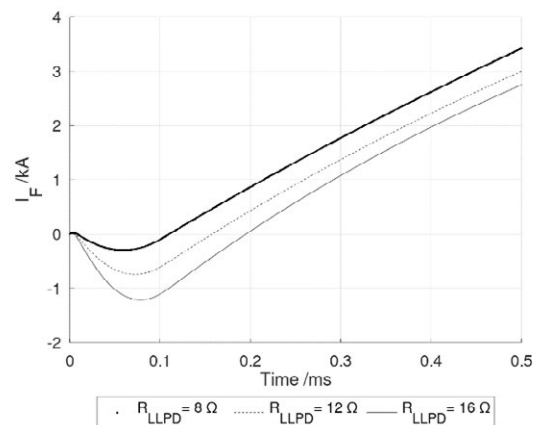


Fig. 5: Comparison of current zero crossing times for different initial arc resistance values.

arc resistance during the lightning stage as can be seen in figure 5.

As a result of this approach, we derived the following desirable LLPD properties:

- Initial resistance of $\approx 10 \Omega$.
- Fast increase of arc resistance at the stage of current zero crossing.

3 Full Simulation Model

Based on the circuit model investigations, we developed several design ideas for a new LLPD, that seemed suitable for 110kV-overhead lines. As a constraint, the LLPD shall consist of a series of identically designed chambers. Thus, a multiple spark gap is established. Hence, the LLPD development is broken down into the development of a suitable single chamber design consisting of a pair of electrodes and an air-filled current path between them. The overall LLPD resistance R_{LLPD} is then easily calculated based on the resistance of one chamber R_C and the total number of chambers n_C as:

$$R_{LLPD} = n_C \cdot R_C$$

Figure 6 shows a chamber design, that is currently used in ongoing simulations and a prototype version will be produced and tested in HSR's high-voltage laboratory. In case of success, a full LLPD prototype will be compiled by a series of chambers and then be tested at Streamer-Electric's high-voltage facilities. The chamber's geometry is designed, such that the resulting

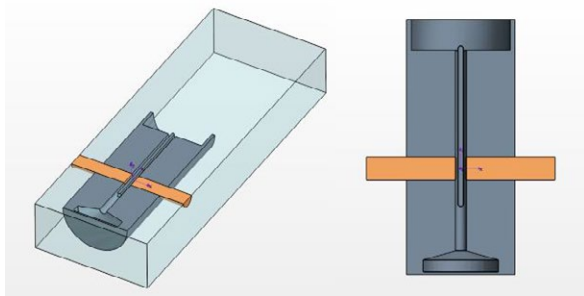


Fig. 6: Cross sectional view including surrounding air-box and top view of a single chamber design consisting of a pair of electrodes and the chamber itself.

LLPD exhibits a minimum resistance of $\approx 15 \Omega$, which allows for artificial current zero crossing. The electrodes are separated by an inner wall, forming small channels, that mainly set the overall initial electric resistance. Further, we aim for a suitable but not harmful pressure build-up within the chamber. This is done by introducing an air reservoir in the chambers' back side, which will be flooded by hot plasma during the lightning stage. At that stage, the plasma is supposed to mix with the reservoir's cold air supported by turbulent flow, leading to a controllable temperature and pressure build-up. Finally, after the lightning strike at the stage of current zero crossing, the pressure has to be released

in a rapid manner, that allows for cooling air flow. Finally, the initially electric conducting area between the electrodes shall be filled with cold air again.

Clearly, the amount of energy, that is introduced into the chamber, in combination with small channels lead to locally high-pressure peaks, which the chamber has to withstand. The right choice of the materials and the manufacturability are therefore further unknowns in the ongoing development process. At the current working stage, we focus on prototype simulations in order to identify key features of suitable chamber designs.

As mentioned in section 1, the simulation of electric arcs is generally challenging due to numerous physical phenomena, that cannot be neglected and that need to be coupled. On the one hand, we have a compressible fluid, that is heated and then chemically converted into a plasma with changing material properties. The Navier-Stokes equations have to be solved in order to obtain the flow and heat situation. The heat transfer is determined by radiation, convection and diffusion. On the other hand, electrodynamic effects are present, that are described by Maxwell's equations, such that both equation systems have to be coupled. The formation of a plasma can be regarded as turning an insulator into an electric conductor surrounded by magnetic flux during the presence of electric currents. The magnetic flux distribution determines the Lorentz Force, which in turn acts as a momentum source in the Navier-Stokes equations. Although not done in the presented work, additional external magnetic fields or permanent magnets as well as moving parts can also be taken into account in the simulations.

Traditionally, software packages mostly kept focus on the calculation of the Navier-Stokes equations (CFD) or the Maxwell's equations (EMAG), so that an external coupling mechanism between the two had to be established. We used the software package Star-CCM+ from Siemens PLM, that allows for combination of both solvers within one software [6].

Star-CCM+ offers suitable models, that can be activated for our situation. The discretized model consists of ≈ 700000 finite volume cells representing the insulating chamber, the conducting electrodes and the air volume around and inside the chamber (see also figure 6). Note that due to symmetry, we only simulated one half. Through application of electric current into one electrode and grounding the other, current starts to flow through the chamber and the inner air is heated, forming additional electrically conducting plasma. The current is in turn calculated dynamically by integrating the model as a dynamic resistance into the electric circuit solver.

The following physical phenomena and models are taken into account in our simulations:

- Compressible, supersonic flow
- Turbulent flow using $k-\epsilon$ -model
- Chemical plasma composition represented by material data tables as functions of temperature and pressure, respectively
- Radiation using a 2-Band DO-Model
- Ohmic heating
- Electric circuit
- Electric potential calculation

Clearly, simplifications to the model have to be made in order to reach acceptable calculation times without losing too much accuracy. Due to the high-voltage level applied to the chambers, arc root voltages are neglected as well as magnetic forces in the simulations. Further, contact erosion and wall material ablation is only included, such that the chamber's and electrode's wall temperatures are limited to their respective boiling temperatures. Thus, we expect the heat transfer mechanisms to be sufficiently realistic. However, the possible addition of electrode and chamber material molecules into the plasma is neglected. Nevertheless, due to the small timescale, this approach seems to be appropriate. The mechanical chamber deformation due to the pressure levels was not taken into account due to lack of material data for this timescale. However, from existing LLPDs we know, that suitable chambers can withstand short pressure level peaks of ≈ 100 bar in the range of microseconds.

The material data for the plasma consists of pressure and temperature dependent tables assuming local thermal equilibrium (LTE), that are shown exemplary as functions of temperature at $p = 1$ bar in figure 7.

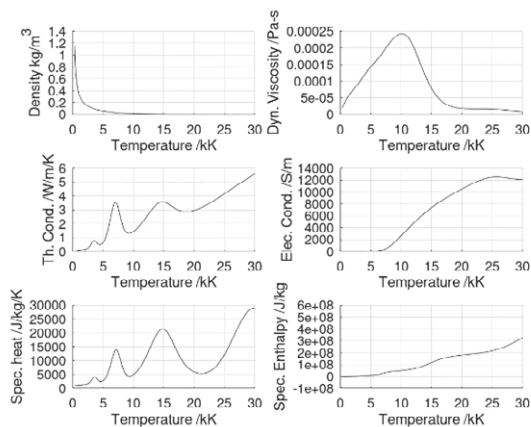


Fig. 7: Material properties of air as a function of temperature at $p = 1$ bar.

The model's boundary conditions can be summarized as follows:

- The exterior surrounding air faces act as pressure outlet.
- Chamber- and electrode-faces act as no-slip walls for the air or plasma, respectively, and

their temperatures are limited to their boiling temperatures to roughly account for material ablation.

- One electrode's outer face is electrically grounded.
- The outer face of the other electrode is set to a dynamically calculated electric current, which considers the surrounding electric circuit and the whole series of chambers, forming one LLPD.
- Radiative emissivity is set to $\epsilon = 0.8$ at chamber and electrode walls.
- A total number of 60 chambers is used in series for the whole LLPD, whereas only one needs to be simulated.

As initial condition, the plasma's electric conductivity in the area between the electrodes is artificially set to $\sigma = 1 \cdot 10^4$ S/m for the first 10 μ s, since we are not able to simulate the electric breakdown itself. By this approach, the lightning current path is determined.

4 Simulation Results

The simulation results generally indicate promising chamber performance with respect to the targets, that are defined in section 2. The simulated LLPD's current, the follow current and the LLPD's resistance are shown in figure 8 and can be compared directly to the data expected by the circuit model in figure 4. In the circuit model, the resistance curve was predefined to obtain chamber requirements. From 3D simulations, we see that this curve seems to be more or less realizable.

In addition to the current and resistance results, the voltage curves for the LLPD's voltage, the voltage

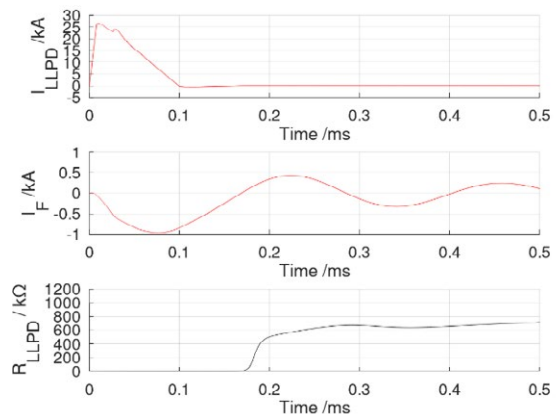


Fig. 8: Simulated data until $t = 0.5$ ms for the LLPD's current (top), follow current (middle) and electric LLPD's resistance (bottom). This data was obtained using full 3D simulation.

across the line inductance L_1 and the grid voltage across the capacity C_0 are shown in figure 9.

The development of the electric conductivity and the absolute pressure is shown in figure 10 and in figure 11, respectively. It can be seen that the lightning current forms an arc inside the chamber. After $\approx 10 \mu\text{s}$, the plasma starts to fill the reservoir at the chamber's back side, where it mixes with cold air by turbulent flow. This causes a cooling effect in addition to mainly radiative cooling effects at the chamber surface. Thus, relative cold plasma is accumulated in the reservoir leading to a pressure build-up during the lightning stage. At the same time, the pressure is also increasing in the arc region, preventing the plasma to flow out of the chamber's outlet at the front side. However, after $\approx 0.1 \text{ ms}$ the lightning current has vanished and the (negative) follow current remains, heading towards the artificial zero crossing. At that stage, the ohmic heat input collapses, allowing for pressure release in the reservoir and therefore the expanding hot plasma is flowing from the reservoir to the chamber's outlet while suffering additional cooling by the gas expansion. Since the electric conductivity is decreasing with decreasing temperature, the electric resistance increases dramatically at that stage as desired by the investigations made in section 2.

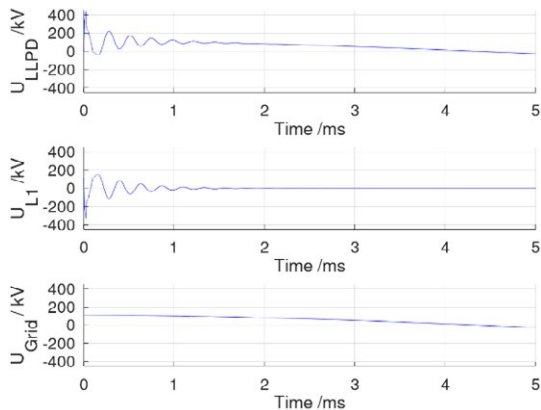


Fig. 9: Simulated data until $t = 5 \text{ ms}$ for the LLPD's voltage (top), voltage across inductivity L_1 (middle) and grid voltage across capacity C_0 (bottom). This data was obtained using full 3D simulation. The LLPD's voltage can be regarded as the line voltage provided to the consumer (see also figure Fig. for electric component notation). Note, that the disturbance due to the lightning strike vanishes.

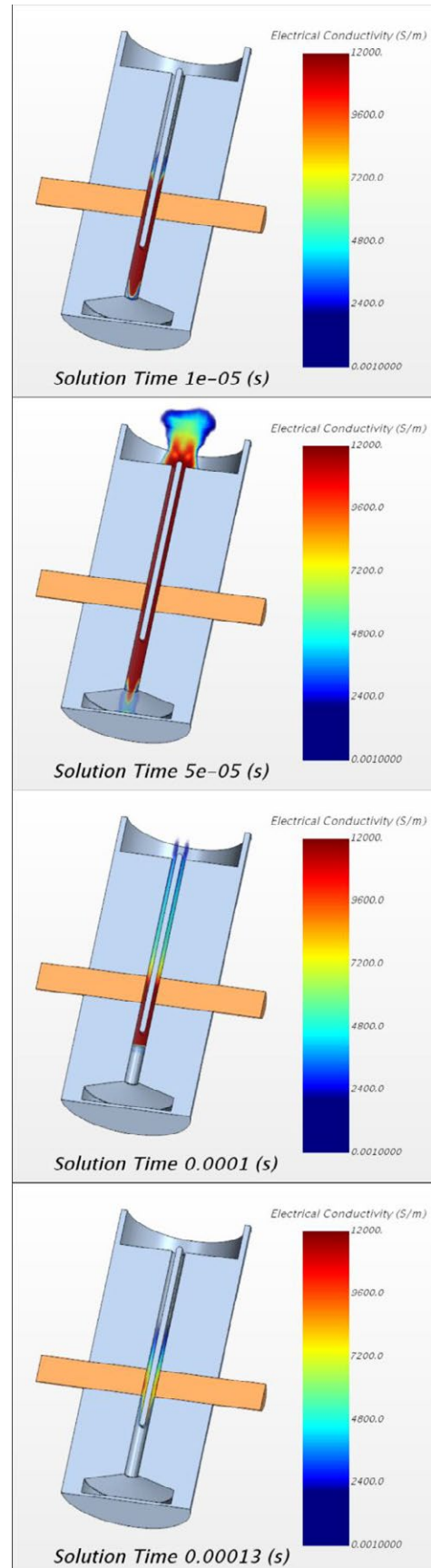


Fig. 10: Development of electrical conductivity during the first 0.13 ms . The quenching process at $\approx 0.1 \text{ ms}$ is clearly noticeable (see text for further details).

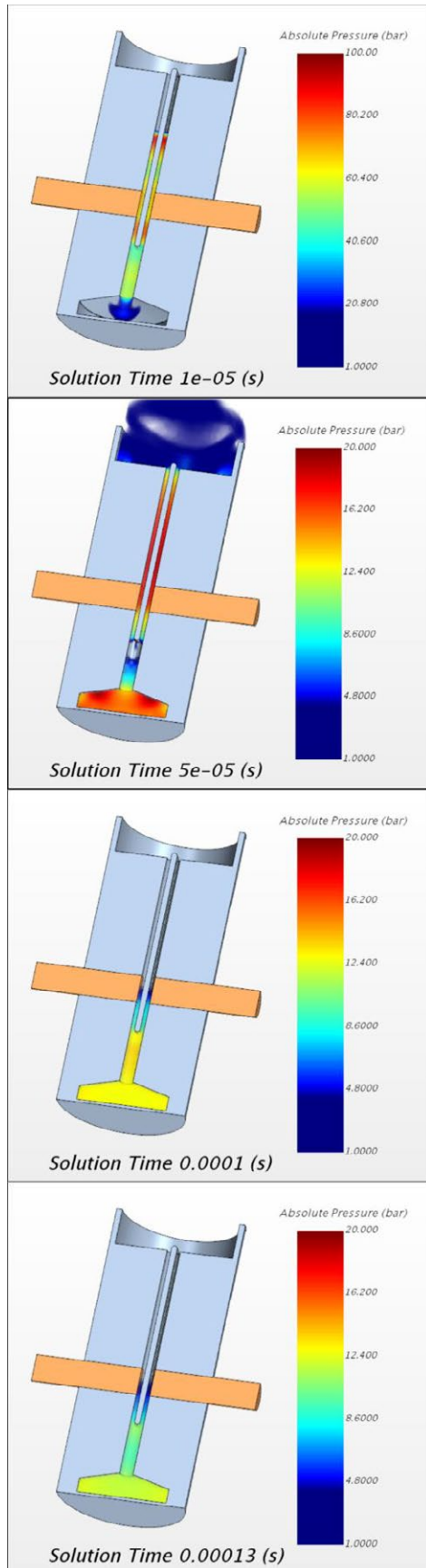


Fig.11: Development of absolute pressure during the first 0.13 ms. The pressure build-up in the reservoir can be seen clearly (see text for further details).

5 Discussion

The simulations allowed for valuable insights into the chamber's and therefore into the LLPD's electric and thermodynamic behavior and also into the interaction with the surrounding electric circuit. Further, with the simulation environment we were able to test upcoming ideas and strategies in short time, which in turn enabled a significant knowledge build-up.

However, due to the simplifications made, the presented results and insights have validity limitations. The reasons can be summarized as follows:

- The mechanical deformation determines the pressure levels inside the chamber but is not considered in the simulation due to lacking mechanical data for the short timescales, where equilibrium assumptions cannot be made.
- Despite the fact, that additional vapors influence the plasma properties [7] [8], the material data does not reflect material ablation as well as contact erosion.
- Thermal radiation plays a major role in electric arc's heat transfer mechanisms but can only be considered in numerical simulations in a simplified manner [8].
- Additionally, the total number of 60 chambers in the simulation might be too much for the device's real suitability.

By comparing performance and simulation data of already existing LLPDs to former and current simulation results, we are nevertheless confident, that the presented approach is suitable regarding the development of new LLPDs. The gained insights and the knowledge build-up are undoubtedly valuable for further development tasks. Clearly, prototypes must be produced and tested, not only to validate the simulations, but also to reveal possible manufacturability issues and to choose appropriate materials from a technical and also an economic point of view. Even in case of failures in pending prototype experiments, design optimizations and improvements can still be made with the help of a simulation approach.

6 Literature

- [1] G. V. Podporkin, E. Y. Enkin, V. V. Zhitenev, R. I. Zainalov, V. E. Pilshikov, and D. O. Belko. Development of shield-type multichamber lightning arrester for 35kv ohl. In *2015 International Symposium on Lightning Protection (XIII SIPDA)*, pages 88-93, Sep. 2015.
- [2] G. V. Podporkin, V. E. Pilshikov, E. S. Kalakutsky, and A. D. Sivaev. Overhead lines lightning protection by multi-chamber arresters and insulator-arresters. In *2014 International Conference on Lightning Protection (ICLP)*, pages 1243-1249, Oct 2014.
- [3] V. Y. Frolov, D. Y. Ivanov, G. V. Podporkin, and A. D. Sivaev. Development of mathematical model of processes in multi-chamber arrester for identification of criteria of arc extinction. In *2017 International Symposium on Lightning Protection (XIV SIPDA)*, pages 240-243, Oct 2017.
- [4] Mario Muermann, Alexander Chusov, Roman Fuchs, Alexander Nefedov, Henrik Nordborg. Modeling and simulation of the current quenching behavior of a line lightning protection device. *Journal of Physics D: Applied Physics*, 50(10):105203, feb 2017.
- [5] G. V. Podporkin, E. Y. Enkin, E. S. Kalakutsky, V. E. Pilshikov, and A. D. Sivaev. Development of multi-chamber insulator-arresters for lightning protection of 220 kv overhead transmission lines. In *2011 International Symposium on Lightning Protection*, pages 160-165, Oct 2011.
- [6] Roman Fuchs, Mario Muermann, and Henrik Nordborg. Towards an efficient arc simulation framework. *Plasma Physics and Technology*, 4(1):79-82, 2017.
- [7] Y Cressault, R Hannachi, Ph Teulet, A Gleizes, J-P Gonnet, and J-Y Battandier. Influence of metallic vapours on the properties of air thermal plasmas. *Plasma Sources Science and Technology*, 17(3):035016, jul 2008.
- [8] Nadezda Bogatyreva, Milada Bartlová, Vladimír Aubrecht and Petr Kloc. Radiation transfer in arc plasmas. 4(3):253-256, september 2017.

Research on virtual prototyping technology of dynamic characteristics on the example of hermetically sealed electromagnetic relay

JiaxinYou, Rao Fu, Xiangdong Feng, Bo Li and Huimin Liang
Harbin Institute of Technology, Harbin, China, hitra@hit.edu.cn

Abstract

With the development of FEM and other modern numerical analysis methods, simulation analysis methods for hermetically sealed electromagnetic relays (HSER) have developed rapidly. A much more precise simulation analysis can be obtained for the design and analysis of static, dynamic, thermal and mechanical properties of relays in recent year. Taking the simulation method of dynamic and static characteristics of HSER as an example, the application of virtual prototyping technology (VPT) in electromagnetic relay is studied. Firstly, the VPT calculation model of static characteristics for a relay is established, and the attractive force and static data table of HSER are obtained. On the basis of the establishment of flexible part, the VPT model of dynamic characteristics is established. Finally, the parameters of the relay, such as the make time, release time, make voltage, release voltage, dynamic contact resistance, bounce characteristics of make spring and bounce characteristics of release spring, are calculated. The quantitative analysis from design to performance for a relay is realized. Based on this, the VPT model is applied to a certain type of relay. In the parameter design of a HSER, the performance improvement and optimization of relay are realized.

1 Introduction

The dynamic characteristics of electrical appliances is related to the life of electrical apparatus, so it is necessary to calculate the dynamic characteristics of electrical apparatus. With the application of the finite element method, the calculation of the dynamic characteristics of electrical apparatus becomes more simple, efficient and low cost.

As early as the 1990s, finite element method (FEM) was applied to the calculation of electrical dynamic characteristics [1-4]. With the development of FEM, Harbin Institute of technology uses FEM software to optimize the design of sealed electromagnetic relay characteristics such as dynamic characteristics, overload capacity and thermodynamic characteristics [5,6], which improves the efficiency of optimization design and reduces the cost of manufacturing prototype. The concept of virtual prototyping technology (VPT) in electromagnetic relay is established, and its application is studied[7-9]. In addition, the finite element software can also be used to build VPT and improve the reliability of electrical apparatus in design process even in parameter design [10].

In this paper, based on VPT, the performance of a typical hermetically sealed electromagnetic relays (HSER) is improved and optimized.

2 Virtual prototyping technology

2.1 Technological process

In order to analysis the changes brought by the improvement of the contact system more accurately, an improved dynamic calculation model need to be established, which can be used to evaluate the effort of the improved design.

There are mainly two issues need to be paid attention in the process of model establishment. The first one is that, the calculation of electromagnetic force influenced by electromagnetic parameter. The other one is that, the motion parameters of armature influenced by electromagnetic force. For the first problem, it can be solved by the voltage balance equation. While for the second one, it can be solved by Darren Bell's motion equation.

Although there are many ways to calculate the dynamic characteristics of electromagnetic mechanisms, the core is to solve the differential equations by numerical methods.

Although there are many ways to calculate the dynamic characteristics of electromagnetic mechanisms, the core is to solve the differential equations by numerical methods.

$$\begin{cases} \frac{d\psi(i, x_{mov}, t)}{dt} = u - iR(t) \\ \frac{dv_{mov}}{dt} = \frac{F_E(i, x_{mov}, t) - F_f(x_{mov})}{m} \\ \frac{dx_{mov}}{dt} = v_{mov} \end{cases} \quad (1)$$

where $\psi(i, x_{mov}, t)$ represents the magnetic chain of excitation coil(Wb), v_{mov} represents the armature moving speed(m/s), u represents the rated voltage of the coil (V), $R(t)$ represents the resistance of the coil (Ω), i represents the current of the coil(A), t represents the temperature of the coil(K), $F_E(i, x_{mov}, t)$ represents the electromagnetic force(N), $F_f(x_{mov})$ represents the counter force(N), m represents the quality of the armature (kg), x_{mov} represents the displacement of the armature (mm).

Based on the dynamic calculation software, the process of rigid-flexible coupled mechanical systems modeling is showed in Fig. 1.

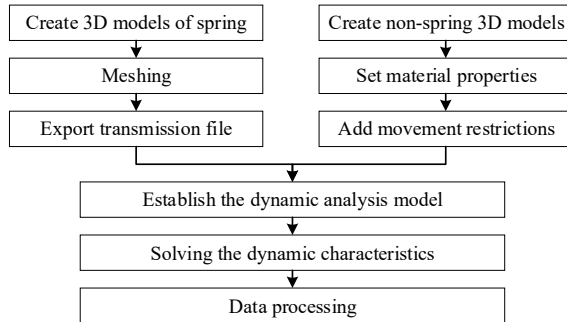


Fig. 1 Flowchart of FEM

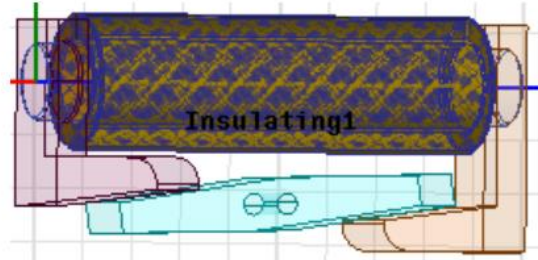
In dynamic characteristic simulation, the whole model of the typical relay needs to be established in ADAMS, and the interface program with MATLAB is derived. Then a joint simulation circuit diagram is set up in Simulink, which includes the electromagnetic simulation data used by linear interpolation. The software module is included, which can invoke ADAMS in the circuit diagram, so as to realize the joint simulation model. Due to the output data of MATLAB, the characteristic parameters of electromagnetic relay can be obtained. Finally, the simulated data could be processed.

2.2 Static analysis VPT for HSER

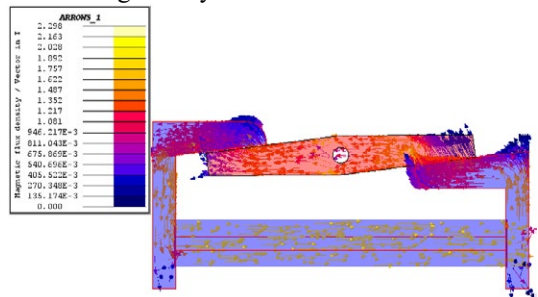
After the solid model is established, several different subnet nodes are established in Flux, each subnet node is set with different subnet density, and then the points in the model are divided into these subnet nodes according to the needs of the actual problems, so as to realize the subnet of different density for different regions of the model, which can not only save the calculation time but also be more convenient to observe the reality test results.

The electromagnetic system model established in Ansoft maxwell is shown in Figure 2. The voltage range of the relay is 0 to 27V, and the angle range is 0 to 4.57

degrees. In order to establish a more accurate simulation model, and to take into account the static analysis and calculation time, the simulation voltage step is set to 1V and the angle step is set to 0.24052 degrees. After the simulation script setting, the model is simulated and the preliminary results are obtained.



a) Electromagnetic system model



b) Vector map of magnetic induction intensity

Fig. 2 Static analysis magnetic induction intensity distribution

Export the calculated data in Excel format in flux and process the data with MATLAB software, and draw the relationship diagram among voltage, electromagnetic torque and rotation angle, as shown in Fig. 3.

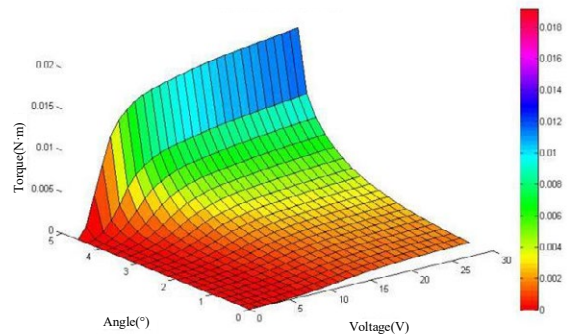


Fig. 3 Static analysis results

2.3 Dynamic analysis VPT for HSER

From the above results, we can see the trend among voltage, angle, electromagnetic torque and flux. From Fig. 3, it can be seen that the electromagnetic torque is positively related to the voltage and the angle of rotation. The three-dimensional graphs of voltage, rotation angle and electromagnetic torque can clearly characterize the change relationship between the three.

By assembling the rigid body model established in Adams and the flexible body model established in FEM software, the relay HSER's original structure model is showed in Fig. 4.

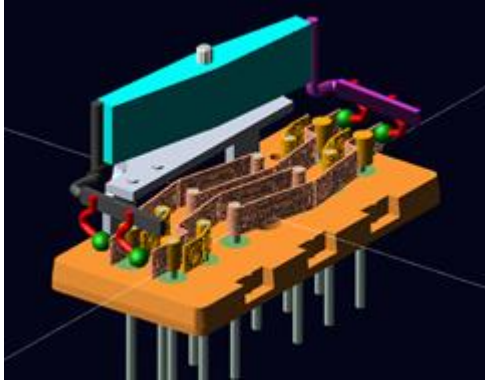


Fig. 4 Dynamic model of HSER

2.4 Calculation result of VPT

After confirming that the model setting is correct, the dynamic simulation analysis is carried out. The analysis results can be divided into two parts: the make process and the release process.

The analysis results are shown in the figure below, including coil voltage waveform, armature displacement.

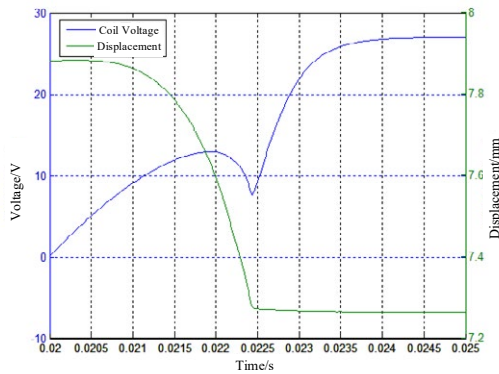


Fig. 5 Coil voltage and armature displacement curve

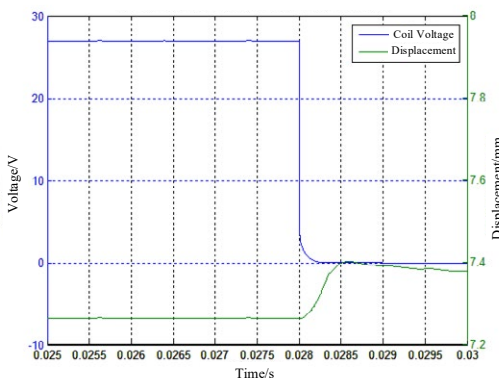


Fig. 6 Coil voltage and armature displacement curve during release

According to the analysis in Fig. 5, the simulation calculation value of the movement speed of the armature is close to the measured value, and the trend of the speed is the same. The make time is about 2.25ms, which is close to the measured average value of 2.35ms. It shows that the accuracy of dynamic simulation

model is high and it can be used in dynamic characteristic analysis.

According to Fig. 6, the release time of armature is about 0.5ms, and the breaking speed of dynamic closing and static spring is 314.9mm/s, which is close to the measured value.

3 Parameter design

The structure of HSER relay is relatively complex, and its structural dimension parameters and assembly parameters are numerous. It is impossible to calculate the influence of each parameter on the output parameters when considering the parameter design. Therefore, it is necessary to preliminarily screen the input parameters, select some parameters that have a significant impact on the system, and select some parameters that have a very small impact on the system output parameters. Numbers can be excluded from parameter design.

The most intuitive way to measure the impact of a parameter on the system output is to study the impact of this parameter on the output parameter when it fluctuates within a certain range. Take HSER electromagnetic system as an example, select several parameters of armature and yoke in the electromagnetic system, determine the variation range of these parameters according to the drawings, and then calculate the influence of parameters on the output parameters within these variation range. This kind of influence quantification, defined as the contribution rate of input parameters to output parameters, can be used to quantify the influence degree of design parameters on output dynamic parameters. Finally, through this method, five key parameters are obtained, including three for electromagnetic system and two for contact spring system. Three key parameters in electromagnetic system: coil resistance, yoke width and armature width.

There are two key parameters in the contact spring system: normal open(NO) spring stiffness, armature over-travel.

In the process of selecting the key parameters, the change of some parameters in the calculation model of electromagnetic system will greatly affect the magnetic circuit, so when the magnetic circuit structure changes obviously, such as the obvious influence on magnetic flux leakage, the accuracy of the finite element calculation model of static magnetic field needs special attention in the calculation process. When it is applied to the parameter robust design, the fast calculation model and other methods need to carry out appropriate results inspection and calculation compensation in the process of using. Therefore, the virtual prototype model based on the finite element static magnetic field calculation is used in the parameter design of the electromagnetic system. This problem also exists in the calculation model of contact spring system based on the variable energy method. After weighing the calculation effi-

ciency and accuracy, it is determined that the size parameters in the electromagnetic system structure will fluctuate within the reasonable range of technology. The parameter robust design in the contact system will take the calculation method of dynamic characteristics of the electromagnetic system as the main calculation mode through indirect indicators.

According to the main performance public relations point of HSER overload capacity, the main measurement standards are the kinetic energy of NC spring and the kinetic energy of NO spring. According to the variation range of five key parameters of electromagnetic system and contact spring system, the value level is determined, and combined with tolerance, based on orthogonal test and Taguchi robust design theory, the internal and external direct product table is constructed, and the test scheme is as follows.

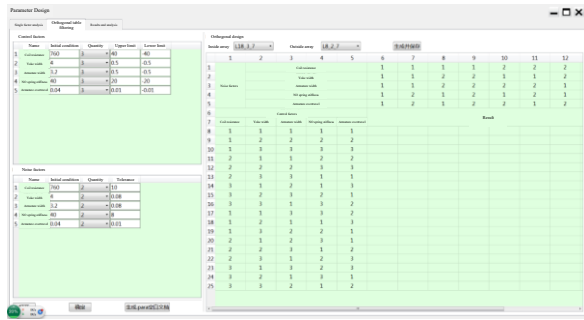


Fig. 7 Orthogonal design by inside and outside array
The 1, 2 and 3 of coil resistance correspond to 710, 750 and 790 Ω. The 1, 2 and 3 of yoke width correspond to 3.42, 3.92 and 4.42mm. The 1, 2 and 3 of armature width correspond to 2.62, 3.12 and 3.62mm. The 1, 2 and 3 of NO spring stiffness correspond to 12, 32 and 52N/mm. The 1, 2 and 3 of armature correspond to 0.02, 0.03 and 0.04mm.

According to the combination of parameter values, modify the values of the above five parameters in the calculation model in turn and carry out simulation, corresponding to the results of 2 dynamic output parameters in all tests. Some results are as follows.

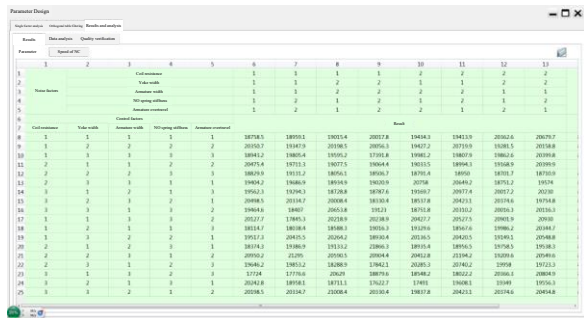


Fig. 8 Simulation results of angular velocity at armature of static closing and breaking speed

Using the result data to calculate the sensitivity and signal-to-noise ratio, the analysis of variance is carried out respectively, and then the significance of 5 input parameters corresponding to 2 output parameters is determined. The results are as follows:

Tab. 2 Result of significance of input factors on kinetic energy of NC spring

	Signal-to-noise ratio 1	Signal-to-noise ratio 2	Signal-to-noise ratio 3	conclusion of significance
coil resistance	19639.5	19537	19481.8	other
yoke width	19484.4	19658.6	19515.3	other
armature width	19474.4	19612.5	19571.4	other
NO spring stiffness	85.9853	85.7618	85.6682	significant
armature overtravel	85.7766	86.0193	85.6195	significant

Tab. 3 Result of significance of input factors on kinetic energy of NO spring

	Signal-to-noise ratio 1	Signal-to-noise ratio 2	Signal-to-noise ratio 3	conclusion of significance
coil resistance	10607.2	9616.16	10126.9	other
yoke width	10577.2	9866.47	9906.56	other
armature width	11254.1	9341.27	9754.92	other
NO spring stiffness	9496.07	10921.5	9932.64	Adjustable
armature overtravel	-83.0404	-78.1757	-79.515	significant

4 Result comparison

From the above calculation and analysis, it can be seen that among the five key parameters of the electromagnetic system, the NO spring stiffness and the armature overtravel have obvious nonlinear properties for the kinetic energy of NO spring. The armature overtravel has obvious nonlinear properties for the kinetic energy of NO spring, and the NO static spring stiffness has obvious linear properties for the kinetic energy of NO spring.

It can be concluded that the optimal level of the input parameters to the kinetic energy of the dynamic spring at the static end is 12212, and the optimal level of the kinetic energy of the dynamic spring at the dynamic end is 22212. Because the coil resistance has no significant effect on the two output parameters, and the impact on the collision kinetic energy of the dynamic and static spring is slightly greater than the impact on the breaking kinetic energy of the static and dynamic spring, it is considered that the best scheme is to choose level 2. That is to say, the level selection combination of the new scheme is 22212. The parameter values of the two schemes before and after design are shown in Tab. 4.

Tab. 4 Comparison of parameter values of two schemes before and after parameter design

parameter Name	Coil resistance	Yoke iron width	Armature width	NO spring stiffness	Armature overtravel
Original scheme	800	4	3.2	60	0.03
New scheme	760	4	3.2	20	0.04

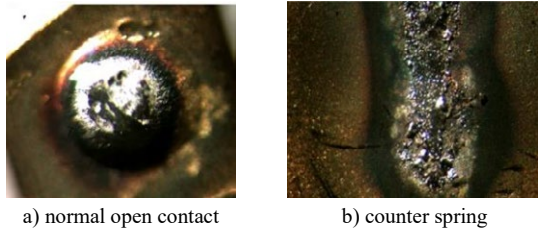


Fig. 9 surface topography of contact before parameter design.

The contact morphology after the overload test is shown in Fig. 9. Compared with the improved product passing over load, the reed of the original design is seriously eroded, some even melted, which proves the progress of the design and the effectiveness of the VPT parameter design.

5 Conclusion

The quantitative analysis from design to performance for a relay is realized. Based on this, the VPT model is applied to a certain type of relay. In the parameter design of a HSER, the performance improvement and optimization of relay are realized.

6 Literature

- [1] Y. Kawase, O. Miyatani, T. Yamaguchi and S. Ito, "Numerical analysis of dynamic characteristics of electromagnets using 3-D finite element method with edge elements," *IEEE Trans. Magn.*, vol. 30, no. 5, pp. 3248-3251, Sept. 1994.
- [2] Y. Kawase, S. Tatsuoka, T. Yamaguchi and S. Ito, "3-D finite element analysis of operating characteristics of AC electromagnetic contactors," *IEEE Trans. Magn.*, vol. 30, no. 5, pp. 3244-3247, Sept. 1994.
- [3] W. Yan, L. Rao, Q. Yang, Y. Li, X. Shen and J. Wang, "Finite element dynamic analysis for the electromagnet of AC contactor," *IEEE Trans. Magn.*, vol. 27, no. 5, pp. 4133-4135, Sept. 1991.
- [4] M. A. Juds and J. R. Brauer, "AC contactor motion computed with coupled electromagnetic and structural finite elements," *IEEE Trans. Magn.*, vol. 31, no. 6, pp. 3575-3577, Nov. 1995.
- [5] R. Wanbin, L. Huimin and Z. Guofu, "Thermal analysis of hermetically sealed electromagnetic relay in high and low temperature condition," *Electrical Contacts - 2006. Proceedings of the 52nd IEEE Holm Conference on Electrical Contacts*, Montreal, QC, 2006, pp. 110-116.
- [6] H. Yu, H. Liang, K. Bo, X. Ye and G. Zhai, "Virtual Prototype and Optimal Design of Short Circuit Current Capability of Magnetic Latching Relay," *2018 IEEE Holm Conference on Electrical Contacts*, Albuquerque, NM, 2018, pp. 124-129.
- [7] Z. Guofu, W. Qiya, Y. Wenying and L. Huimin, "Permanent-Magnet Equivalent Model of Calculating Relay's Static Attractive Torque Characteristics by Finite Element Method," *IEEE Transactions on Magnetics*, vol. 48, no. 9, pp. 2467-2471, Sept. 2012.
- [8] Z. Guofu, W. Qiya and R. Wanbin, "An Output Space-Mapping Algorithm to Optimize the Dimensional Parameter of Electromagnetic Relay," *IEEE Transactions on Magnetics*, vol. 47, no. 9, pp. 2194-2199, Sept. 2011.
- [9] J. You, B. Li, S. Zheng, Y. Ruan, S. Wang and H. Liang, "Break Kinetic Energy-based Overload Dynamic Model for a Small Hermetically Sealed Relay," *2019 IEEE Holm Conference on Electrical Contacts*, Milwaukee, WI, USA, 2019, pp. 223-226.
- [10] S. Yamada, K. Ishikawa, Q. Yu, R. Ramadoss and L. Almeida, "Tri-state multi-contact lateral MEMS relay with high mechanical reliability," *2006 International Conference on Electronic Materials and Packaging*, Kowloon, 2006, pp. 1-13.

Robust and Efficient Software-based 3D Clearance and Creepage Analysis

Dr. Michael Martinek, e-laborate Innovations GmbH, Nuremberg, Germany, martinek@e-laborate.net

Abstract

In almost every component in the field of automotive, power electronics or mechatronics, engineers have to fulfil strong requirements regarding clearance and creepage distances in order to avoid shortages between different electric circuits. Determining all possible safety violations manually is not only time-consuming, but also highly inaccurate and can lead to severe product failures, especially when compactness of an assembly is an additional design rule. After a decade of research, scientists at the university of Erlangen-Nuremberg have developed methods to perform an automatic 3D clearance and creepage analysis on the CAD data of electric assemblies. These methods have already been successfully implemented in various software products [1],[2], which significantly assist an engineer to robustly detect and to eliminate all safety violations in an early product stage. The fast and exact computation of clearance and creepage paths also allows a product designer to regularly check his design during development and, thus, to find the perfect compromise between safety and compactness. This is particularly important for components such as electrical switchgear, connectors, electric engines, power converters or high-voltage battery systems used for e-mobility, where space is limited and safety is an inevitable requirement.

1 Introduction

Wherever circuits with higher operational voltages are forced to coexist close to each other, the risk of hazardous shortages caused by clearance or creepage currents is extremely high. Industry standards such as IEC 60664 [3] or UL 840 [4] define rules as to the minimum acceptable distance between electric circuits with respect to clearance and creepage distances in order to reduce this risk. These distances have been established by means of experiments and depend on various parameters such as voltage difference, pollution degree, insulation class or height above sea level. However, despite knowing the distance to be fulfilled between two different networks, there are two problems an engineer is facing: first, the industry standards are often not clearly formulated, leaving room for different interpretations and second, the shortest path of a clearance or creepage current is impossible to measure exactly on complex 3D assemblies without a corresponding tool. As the requirements are ever increasing, so is the need for automatic methods for computing exact clearance and creepage paths. Especially in e-mobility, components must be more and more powerful while still being compact as space in an electric vehicle is extremely limited. In this paper, we will address this topic by providing ideas to eliminate degrees of freedom arising from different interpretations of the industry standards and introducing software methods for computing exact clearance and creepage paths on 3D data. These methods arose from over five years of research at the Uni-

versity of Erlangen-Nuremberg and have been implemented by the company e-laborate Innovations in commercial software products [1],[2].

The rest of this paper is organized as follows: In Section 2, we will briefly describe the existing industry standards for clearance and creepage while Section 3 addresses the math behind these complex measurements and reveals various inconsistencies in the existing industry standards. Section 4 describes a method for the efficient and exact computation of clearance and creepage by means of software and Section 5 provides an insight of future improvements of these methods.

2 Industry Standards for Clearance and Creepage

The behavior of a current which does not take the way it is supposed to go is actually quite unpredictable. However, regulation authorities such as IEC or UL have derived definitions which try to give an engineer concrete rules as to avoid clearance and creepage failures in his design. These rules have been formulated in standard tables, which map a set of various parameters such as operational voltage difference, pollution degree or insulation class to a distance value expressed in mm or inch.

Such tables reformulate the electric problem to a pure geometric problem as one simply needs to measure the shortest clearance and creepage path in his model only to compare it with the corresponding value in the table in order to tell whether there is a violation or not. However, “simply” is by far the wrong word for this task as

the solution to this geometric problem is almost impossible to solve for complex models as the following Section 3 will point out.

Additionally, the clearance and creepage currents are allowed to take shortcuts through potential-free elements such as screws or spring, which adds a significant amount of complexity to the exact determination of shortest paths. An example of such a shortcut is shown in **Figure 1**.

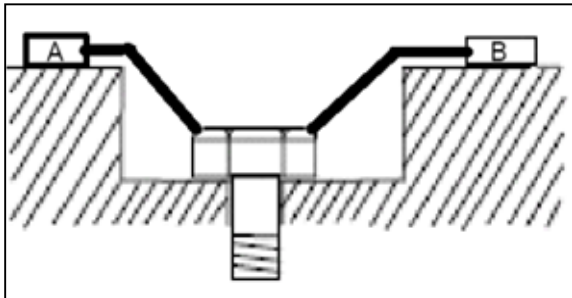


Fig. 1 Sketch of a clearance path at a screw. The path is shorter than the direct line between A and B as the way within the screw does not count to the total length.

3 The Geometry behind Creepage and Clearance Paths

The industry standards render two different geometric distance metrics for clearance and creepage, which need to be measured separately.

3.1 Clearance Metric

The clearance is defined as shortest path between two electric nets through air.

In simple situations, where the shortest path between two electric networks is obviously a straight line, a manual measurement of exact clearance might be possible. However, as soon as the geometry gets a little more complex, there is no chance to get the optimal path just by using a thumb or a ruler. Consider the situation from **Figure 2**, where just a single step of a staircase lies between the source and the target.

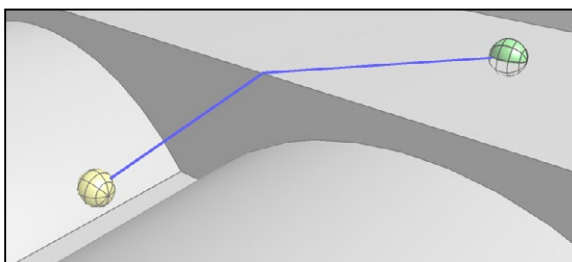


Fig. 2 Example of a clearance path over a single convex edge

Without any further help, one could hardly determine the exact point P at which the clearance breaks at the convex edge.

Even for a computer, the exact computation of shortest paths through air is actually an impossible task, as the problem is known to be NP complete for three dimensions, meaning that the number of operations is growing exponentially with the distance. However, the fact that clearance distances are relatively short compared to the dimensions of the entire model allows to perform computer-aided checks for violations. It might not be possible to compute the shortest clearance between from one end of a large model to the other end as this would take centuries even with the world's most powerful computer, but it is feasible to determine whether there is a clearance violation between two circuits or not as this only requires to compute the minimum acceptable distance around one circuit. If no other circuit is located within this distance, there is no violation.

3.2 Creepage Metric

The creepage is the shortest distance between two electric nets on the surface of insulators. If this was the entire definition, the creepage would be the geodesic distance and dozens of algorithms exist for an efficient computation of such. However, there are two additional aspects which make the math behind creepage paths much more complex and unsolvable with classic algorithms. These will be described in the following subsections.

3.2.1 The Groove Width Parameter

According to Industry standards, the creepage is allowed to jump for a certain distance x , which may be between 0.25mm and 2.5mm depending on the pollution degree. This parameter is also referred to as “groove width” as it allows the path to jump over a groove if it is smaller than x , as shown in **Figure 3**.

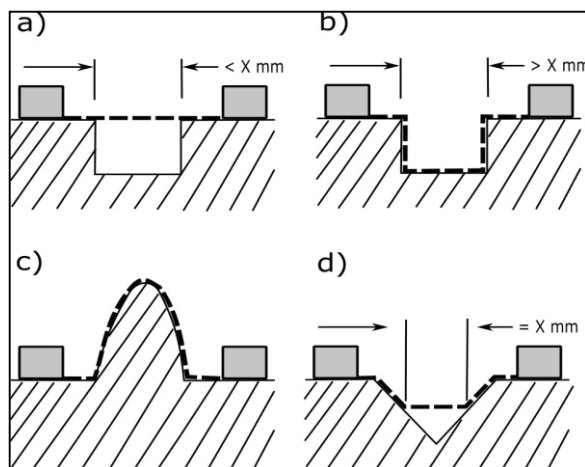


Fig. 3 The course of a creepage paths in various geometric situations according to industry standards.

The groove width parameter is subject to various different interpretations of the industry standards. While **Figure 3d)** shows a jump over a non-convex edge, the subfigures **b)** and **c)** do not include such jumps at the corners despite the fact that they could also foreshorten the path.

Many engineers derive from the sketches in **Figure 3** that the creepage can only jump over edges with an angle less than 90 degree while on edges where the angle is greater or equal 90 degree, the creepage has to go all the way down to the corner. This interpretation creates a highly discontinuous metric, making it impossible to define deterministic algorithms for computing such distances. We therefore hold the opinion that if one allows the creepage to jump a certain distance x , it should do so whenever it leads to a shorter path. Therefore, the sketches **b)** and **c)** in **Figure 3** should look like the ones in **Figure 4**.

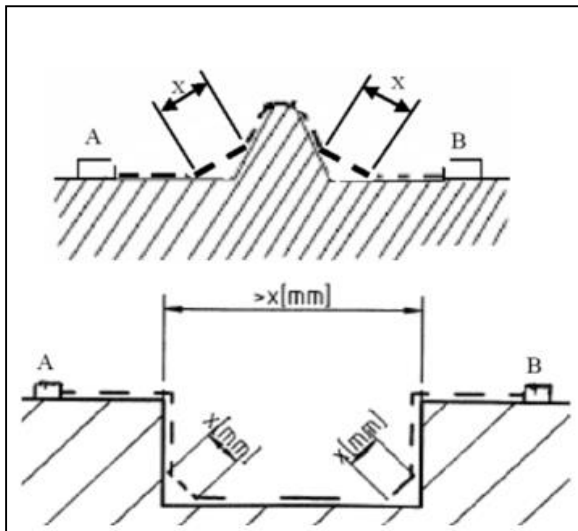


Fig. 4 Modified sketches of creepage paths. The path exploits the jump x whenever it can lead to a shorter path

This formulation creates a unique definition and a continuous distance metric for creepage. However, the exact computation of the optimal jumps remains a very complex task, especially in three dimensions. In the 2D sketches from the industry standards, it seems pretty straight-forward how the jumps must look for an optimal foreshortening at the non-convex corners, but these sketches are not very helpful when it comes to real three-dimensional situations. Consider **Figure 5** as an example.

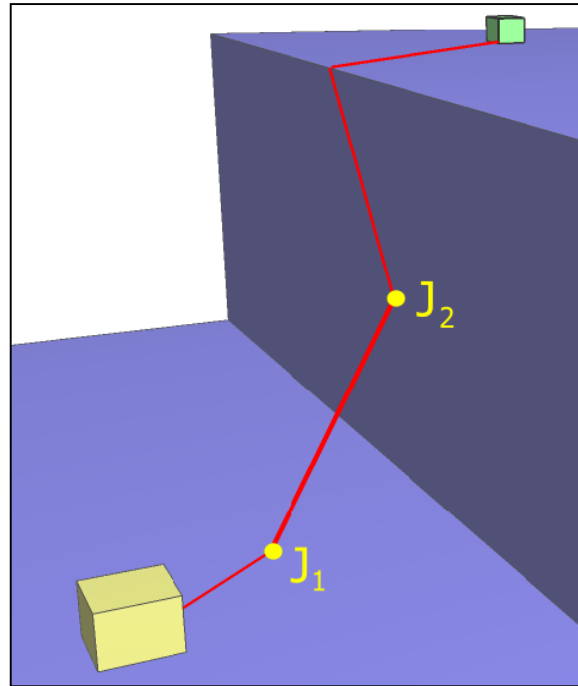


Fig. 5 Example of a creepage path taking a jump over a non-convex edge.

Now where exactly does the creepage jump and how are the angles at the respective jump points J_1 and J_2 such that the path is the global minimum among all possible paths? Just to get an idea of the complexity of this rather simple situation, **Figure 6** show the computation parameter required to determine the exact jump points J_1 and J_2 .

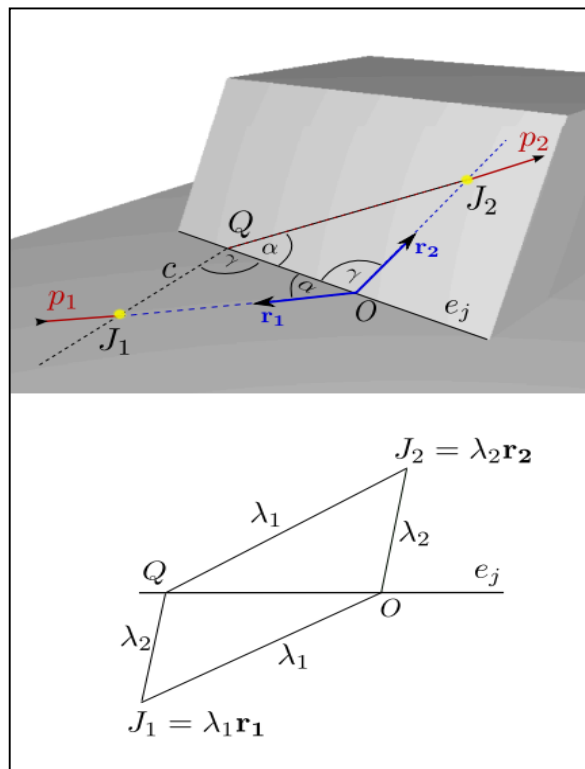


Fig. 6 Sketch illustrating the computation of the optimal jump points J_1 and J_2 according to an incoming path p_1 approaching a non-convex edge e_j .

While the point O and the vectors r_1 and r_2 are known for an incoming path p_1 , the required parameters λ_1 and λ_2 compute to:

$$\lambda_1 = \frac{x}{\sqrt{1+A-2\cos\beta}} \text{ and } \lambda_2 = \frac{x}{\sqrt{1+A^{-1}(1-2\cos\beta)}}$$

With $A = \cos^2\alpha \cdot \cos^2\beta + \sin^2\alpha$

Where α is the angle between p_1 and the edge e_j and β is the angle between the two surfaces on which J_1 and J_2 are located. Needless to say that the one path which follows this quotation is impossible to guess manually and it required sophisticated software to determine the minimum path shown in **Figure 5**, which is yet a very simple scenario. In complex designs, the creepage can make an entire sequence of jumps, making the room for error in a manual measurement even larger.

3.2.2 Creepage over Materials with different CTI Values

As the tables from **Figure 1** implies, the minimum acceptable creepage distance depends on the material group of the underlying insulator. There are four different material groups defined by corresponding ranges of the Comparative Tracking Index (CTI), which are shown in **Table 1**. Additional Information about CTI values can be found in [8].

Group	Range
I	CTI \geq 600
II	400 \leq CTI < 600
IIIa	175 \leq CTI < 400
IIIb	100 \leq CTI < 175

Tab. 1 Definition of material groups by means of CTI ranges.

The CTI value is a measure for the quality of insulators. The higher the value, the better the insulation, which explains why the acceptable creepage distances are shorter for lower groups. However, what if the creepage paths goes over different insulation groups, as shown in **Figure 7**.

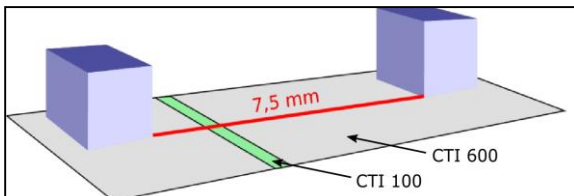


Fig. 7 Creepage path over materials with different insulation classes.

Let the acceptable creepage be 5mm for CTI 600 and 10mm for CTI 100. If the insulation in **Figure 7** was all 600, the design would be OK, while for 100, we would have a violation. But how should be interpret the combined situation as displayed in the figure? Industry

standards suggest to take the worst case for the entire path, rendering a violation as we need to fulfil 10mm. We think that this approach can be massively optimized as we will described later in **Section 5** while in this section, we only want to address the geometric aspects of creepage paths and the geometry of the path from **Figure 7** is always the same independent of the underlying CTI value. However, there are also situations where the entire course of the path can change due to different CTI values, as shown in **Figure 8**.

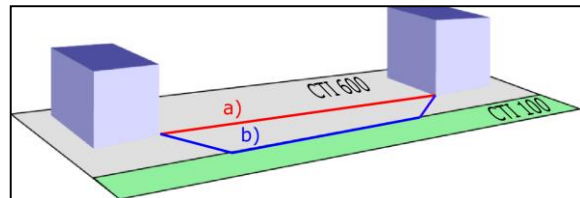


Fig. 8 Another creepage path over different insulation classes. Path a) is 7.5mm and path b) is 9.5mm. While a) is ok according to industry standards, path b) would be a violation despite the fact that it is longer

Path a) is obviously the shortest one and the industry standard suggests that this path is OK as it fulfils the required 5mm on CTI 600. However, path b) would be a violation as it requires 10mm due to partly traveling on CTI 100.

Thus, we actually should not search for the path with the minimum distance when dealing with different insulation classes, but the path with the minimum resistance. But what exactly are the geometric properties of such a path? As proven in [5], it turns out that the path of minimum resistance follows Snell's Law of refraction at the border between two different insulations, whereas the refraction index is derived from the ratio of minimum acceptable creepage distances of the two insulation classes.

Again, such paths are impossible to determine without the help of a powerful software. Even the current state of the art software products [1],[2] are not yet capable of handling the scenario from **Figure 8** correctly as this requires a whole new approach for measuring paths. **Section 5** describes, how we will solve this problem in the future.

4 Software-based Clearance and Creepage Analysis

The exact measuring of minimum clearance and creepage paths is inevitable for telling if an assembly conforms to the industry standard or not. However, the previous section has pointed out the impossibility of determining the shortest paths in complex geometries manually. Thus, there has always been a strong demand for a software to solve this particular geometric problem.

4.1 Previous Work

Kaguera and Shimada [7] formulated the problem already in 2002, but failed to implement a solution despite announcing one in their “future work” section. PTC released the “Spark Analysis Extension” [6] in 2009, which promised to compute exact 3D clearance and creepage paths. However, the method was too inefficient for larger assemblies and could not handle the creepage jumps properly.

Our proposed method has undergone a research project at the University Erlangen-Nuremberg between 2010 and 2014, where the important mathematical fundament for an efficient solution was established [5]. This was the basis for the first commercial software products to allow for a robust and efficient clearance and creepage analysis on real CAD data [1],[2]. The rest of this section describes important aspects of the entire analysis workflow using the software described in [1].

4.2 Preparation of the CAD Data

This subsection describes mandatory preparation steps before an automatic analysis can be performed. All of these steps can be fully performed within the software.

4.2.1 Assigning Meta Information

First of all, the software must know which elements are conductive and which are insulating. This can be done by an intuitive assignment of CTI values for parts and surfaces. As an optional step, it can also perform automatic optimizations for certain part types such as springs (see **Figure 9**).

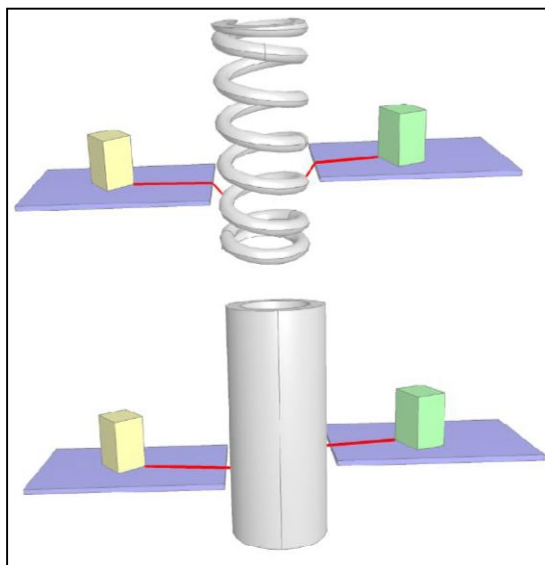


Fig. 9 Creepage path which takes a shortcut through a spring. “AutoCrear” can automatically replace the spring by a cylinder in order to obtain the worst case scenario under all possible rotations

4.2.2 Combining Mechanical and Electrical Data

Each layer of a printed circuit board (PCB) is internally checked regarding clearance and creepage distances with simple 2D methods. However, circuits on the PCB must also be checked against the peripheral mechanic elements, which requires a 3D computation. “AutoCrear” provides an interface to ECAD data by means of an odb++ import, where a 3D model of the PCB is automatically created, as illustrated in **Figure 10**.

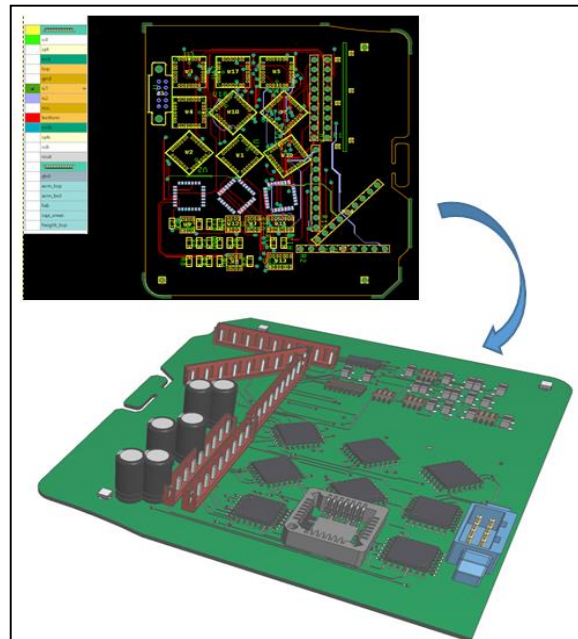


Fig. 10 AutoCrear can generate a 3D model out of the 2D layer information of a PCB.

The generated 3D model features all the material and network information from the ECAD system and can be assembled with the mechanics in order to allow for a combined analysis.

4.2.3 Defining Electric Nets

Electric circuits are the main entities of a clearance and creepage analysis as they are eventually the sources and targets of a path. The software automatically detects electric networks by means of the geometric adjacency of conductive elements. The nets can be assigned a type in order to distinguish between live, grounded, or potential-free nets. As for PCB, the nets are automatically obtained from the odb++ import.

4.2.4 Specifying Analysis Parameters

Basically, one can already compute the shortest clearance and creepage paths between the net pairs according to the information specified so far. However, in order to get an automatic interpretation of the paths, the program must know the minimum acceptable distances between the nets. This can be obtained either manually

or automatically by applying a pre-defined standard table, which map the operational voltage difference and the insulation class onto the corresponding distance value [3],[4]. Additionally, altitude correction can be applied automatically so that the results for clearance can be seen for all relevant altitudes.

4.3 Performing and Evaluating an Analysis

Once all the analysis parameters are set, the program can perform an automatic computation of all clearance and creepage paths within the critical section of each circuit pair according to the distance metrics described in Section 3. Figure 11 shows various results of such a computation.

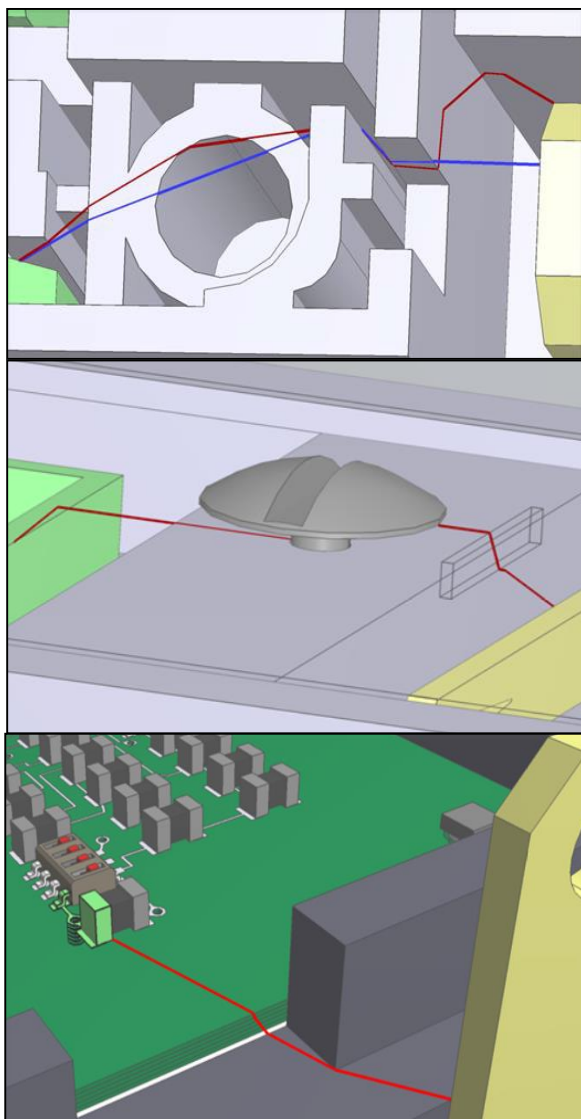


Fig. 11 Various example results of clearance (blue) and creepage (red).

The time for an entire analysis may vary between a few seconds and several hours depending on the complexity of the assembly and the distance to be computed.

The resulting path can be visualized in a special 3D viewer including functions to quickly identify paths in the interior.

If desired, one can generate an automatic analysis report, which is an important aspect of safety documentation. Customers or certification authorities often demand such a document and they will be much more impressed by receiving a systematically generated report which contains exact results rather than a hand-made drawing with rough approximations.

5 Future Work

In the future, we will establish a new approach to determine and evaluate creepage paths, which eliminates the problems described in Section 3.2.2. As described in said section, especially in Figure 8, it is not always meaningful to determine the path with minimum distance in order to detect violations, we rather need to find the path with minimum resistance when materials with different insulation classes are involved.

Also, the approach suggested by industry standards to take the worst involved CTI value for the entire path can create absurd situations as illustrated in Figure 12.

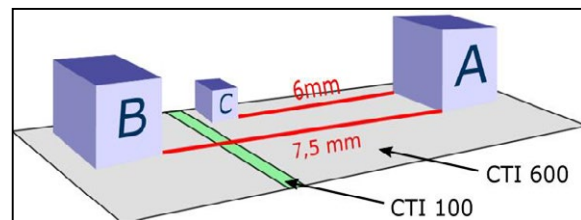


Fig. 12 Creepage paths on different CTI values. The pairs AB as well as AC must fulfil a distance of 5mm on CTI 600 and 10mm on CTI 100

While the net pair A and C are considered to be OK as the required 5mm on CTI 600 are fulfilled, the nets A and B render a violation despite the fact that B is even further away from A. Intuitively, AB should actually be safer than AC but by no means is this reflected by the classical approach.

In order to eliminate such a discontinuous behavior, the idea is not to measure the distance of a path but the percentage of fulfilment of the acceptable minimum distances on each insulation class. In the example of Figure 12, the path between A and B travels 7mm on insulation class I and 0.5mm on insulation class IIIb. As the acceptable distances for creepage are 5mm and 10mm, respectively, we have a fulfilment of 140% in insulation class I (7mm where we only need 5mm) and an additional 5% on insulation class IIIb (0.5mm where we need 10mm) resulting in a total value of 145%. The path between A and C renders a value of 120% which reflects the intuition much better.

Another advantage of this new violation measure compared to the classical distance-based approach is the fact that the software would indeed find the path of minimum resistance. In the example from **Figure 8**, path b) would be computed as the worst creepage path instead of path a), allowing to detect the violation at hand.

6 Summary

Meeting the standards regarding minimum acceptable clearance and creepage paths is an important aspect in the development of electric assemblies, especially when compactness of the design is an additional requirement. Traditional methods, which are based on manual measurements and rough approximations are not only time consuming but also inaccurate and can thus lead to product failures in service as safety violations can easily be missed. New software-based approaches [1],[2] to measure clearance and creepage paths are capable of computing exact results under consideration of complex aspects such as groove width for creepage or the fact that currents can take shortcuts through conductive-free elements. The knowledge of the minimum paths not only allows for a robust detection and target-oriented elimination of violations, it also can assist an engineer to design the assemblies as compact as possible. The standalone solution “AutoCrear” [1] also allows for an efficient import of both, MCAD and ECAD data in order to perform a combined analysis between mechanical elements and PCBs. In the future, the method for creepage computation will be further improved in order to eliminate the existing discontinuities arising from current industry standards.

7 Literature

- [1] e-laborate Innovations GmbH. AutoCrear – The State of the Art Solution for automatic Creepage and Clearance Analysis. www.AutoCrear.com, 2017
- [2] PTC Inc. Clearance & Creepage – Automate your clearance and creepage analysis. www.ptc.com/en/products/cad/creo/clearance-and-creepage, 2017
- [3] IEC 60664-1:2007: Insulation coordination for equipment within low-voltage systems - Part 1: Principles, requirements and tests, VDE Verlag, Vol. 2, 2007
- [4] UL 840: Insulation coordination including clearances and creepage distances for electrical equipment, UL standards catalogue, 2015
- [5] Martinek M.: Advanced Distance Metrics Defined on Complex Geometries. PhD Thesis, FAU Erlangen-Nuremberg, 2015
- [6] PTC Creo Spark Analysis Extension, Data Sheet, <http://www.cad-corner.be/site/files/files/Datasheets/PTC%20Creo%20Spark%20Analysis%20Extension.pdf>
- [7] Kageura M. and Shimada K.: Finding the Shortest Path for Quality Assurance of Electric Components. Proceedings of DETC'02, Jan 2002, pp. 1-22
- [8] "Tech Brief Comparative Tracking Index" (PDF). Retrieved January 29, 2018. <https://multimedia.3m.com/mws/media/1289893O/tech-brief-comparative-tracking-index-test.pdf>

Investigations into the Mechanical Behaviour of Aluminium Conductors in Connectors for Plastic-Insulated High-Voltage Cables with large Cross-Sections using the Finite Element Method

Michael Hoischen, South Westphalia University of Applied Sciences, Soest, Germany,
hoischen.michael@fh-swf.de

Shem George Varghese, South Westphalia University of Applied Sciences, Soest, Germany,
Shem.George.Vargese@gmail.com

Robert Bach, South Westphalia University of Applied Sciences, Soest, Germany,
bach.robert@fh-swf.de

Abstract

The climate protection targets require a feed-in of renewable energies such as wind power. Special conditions, regarding the temperature dependence of the dielectric system properties of cable insulation and accessories, apply here for HVDC (High-voltage direct current) cables. Due to the limited transportable length of power cables, especially with large conductor cross-sections, it is necessary to connect several cable sections in order to cover long distances. It is not sufficiently known, how to connect the cable ends in order to achieve a permanent reliable connecting system and the availability of the entire cable route. To achieve this, it is necessary to understand the criteria, under which a conductor connector can be optimized. Therefore, a depth simulation of the contact behaviour of a single-core conductor in a screw connector with regard to the resulting power dissipation is necessary. Accordingly, it will be determined which factors are decisive for the optimization. In particular, the mechanical behaviour of different aluminium alloys, used as conductor material, is investigated. It will be shown which mechanical changes are necessary, in order to describe the contact pressure, contact surface and thus the contact resistance in more detail.

1 Introduction

High-voltage cables are used especially in urban areas but also to transport large quantities of electrical energy over long distances. Due to the portable length of cable drums, it is necessary to connect the cables with a joint and the connector inside. A special field of application is energy transmission by HVDC. Transporting high direct currents safely via cable connections, is of special importance.

Due to the cable sizes, only small sections can be transported, which in turn must be joined. With a conductor cross-section of up to 3000 mm² and a rated current of over 2000 amperes, the connection must be designed in such a way that it does not endanger the safety of the entire system. The contact resistance, in particular, is decisive here in order to keep the power dissipation and thus the heat emission low.

In order to guarantee this, certain mechanical prerequisites have to be considered. Later in this paper, the mechanical limitations for generating an electrical contact is examined in more detail. The penetration depth, the contact pressure generated between connector and conductor, as well as, the contact area generated are investigated.

Figure 1 shows a screw connector with a 240 mm² solid wire aluminium conductor and a high voltage connector with a 1000 mm² solid wire aluminium conductor.

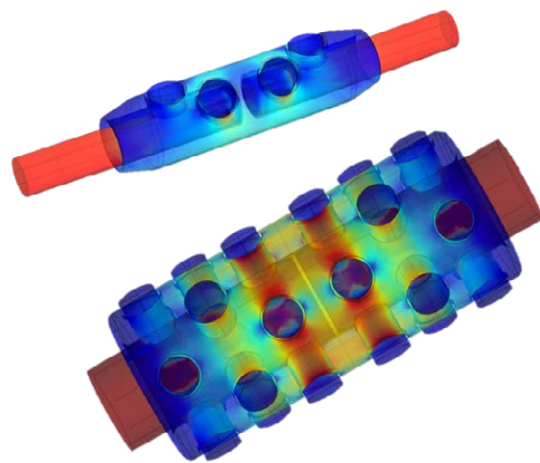


Fig. 1 Medium-voltage and high-voltage screw connector

2 Theoretical background

In order to infer the quality of an electrical connection, screw connectors for medium and high voltage are examined in the following. Since there are a large number of parameters in the screw joint system under investigation, influencing the joint resistance, the following parameters will be examined in more detail: Aluminium alloys, applied contact pressure, connector internal geometry, contact area produced, number of screws and screw arrangement.

2.1 Contact resistance

Maintaining a very low transition resistance is the most important prerequisite for ensuring the long-life and reliability of bolted connections for power cables. This is influenced by the contact pressure achieved, the material combination and the current distribution within the connector. The contact resistance in a typical metal-to-metal contact, can be divided mainly into electrical contact resistance and thermal contact resistance [1]. The major factors affecting the electrical contact resistance are as follows:

- Surface roughness
- Shape of contact surfaces
- Contact pressure between metals in contact
- Used metal type

As far as the type of metal used is concerned, materials with high electrical conductivity such as copper or silver give considerably lower electrical resistances. Even metal surfaces finished to optimal flatness, will have peaks or hills at the microscopic level as shown in **Figure 2**. When these metal surfaces are brought into contact under low contact pressure, the electrical current will experience higher resistance at these isolated points, thus increasing contact resistance. Moreover, the current density will also increase at these points. However, as contact pressure increases, these peaks flatten out, thus increasing the metal to metal contact area and reducing contact resistance [2].

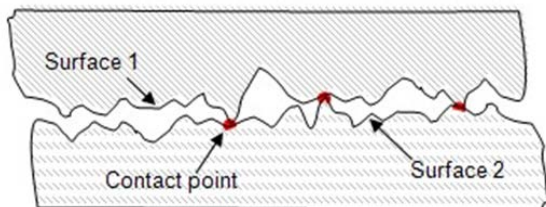


Fig. 2 Microscopic contact surface for metal-to-metal contact [3]

2.2 Contact mechanics

Contact mechanics is a fundamental discipline of the tribology, which mainly deals with the interaction of solid surfaces. In a typical metal-to-metal contact, the surfaces are almost uneven. Contact problems between metals are strongly non-linear and lead to plastic deformation [4].

The main drawback with contact problems is the uncertainty in contact area. Based on the loads, material type, surface roughness and boundary conditions, the surfaces can come in contact and then suddenly become contactless or be separated by a large gap. The contact areas are highly unpredictable and behaves in an abrupt manner. This is the biggest challenge in metal to metal contact. Moreover, from an electrical point of view, the rise in conductor temperature, makes it even more complicated. Analytical solutions, associated with contact problems, are highly limited. Therefore, Finite Element Method (FEM) approach is widely used as an industry standard to predict the behaviour of bodies under contact [4, 5, 6].

2.3 Stress-strain curve

The resistive property of deformable bodies is of high importance while dealing with contact mechanics. This is illustrated in terms of stress-strain curve obtained from various experiments such as tensile and compression testing. The stress-strain curve (see **Figure 3**) gives a clear indication about the behaviour of materials under load.

Stress is described as the force acting per unit area [7].

- Stress = Force / Cross sectional area,
 $\sigma = F / A$

Strain is defined as the change in unit length of a material under tensile/compressive testing [7].

- Strain = Change in length / Original length,
 $\epsilon = \Delta L / L$

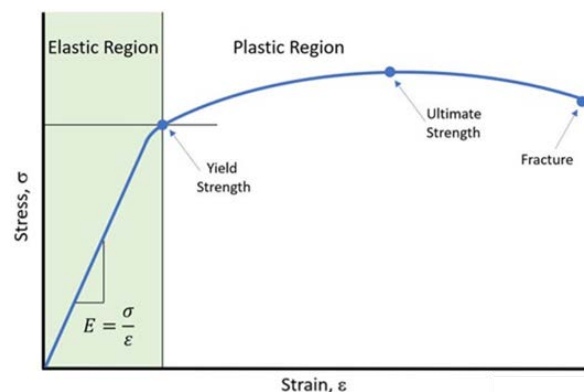


Fig. 3 Stress-Strain-Curve [8]

2.4 Contact resistance vs. contact pressure

Investigations show that both electrical and thermal resistances are primarily a function of the contact pressure and surface condition between a metal-to-metal contact [2]. At low contact pressure, only the hills or peaks touch the material surface. As the pressure increases, the peaks become flatter and both the electrical and thermal contact resistance decreases. This phenomenon is called "spreading resistance". Another type of resistance caused by oxide layers or impurities on metal surfaces is called "interfacial resistance". Studies show that the presence of oxide layers prevents metal-to-metal contact [9]. At high contact pressures, these oxide layers are broken up and ensure metal-to-metal contact. The contact pressure, at which these oxide layers break up, depends on the properties of the oxide layer and the underlying material. Soft metals such as aluminium consist of thin, brittle oxide layers that can break open easily. If the material and the oxide layer have the same mechanical strength (e.g. iron), the oxide layers deform with the metal and thus prevent metal-to-metal contact. Experimental investigations show that the contact resistance values achieved for lubricated and non-lubricated surfaces are comparatively similar and have little effect [10]. The contact pressure between the metals in contact plays an important role in regulating the contact resistance. A low contact resistance is decisive for the reduction of energy losses and the durability of screw connections. The contact resistance depends on many factors, such as the connector, the conductor and bolt material. From a theoretical point of view, the metal surface roughness and the shape of the contact surfaces influence the contact pressure and the contact area between the metals. This paper focuses on the effect of material thickness on contact pressure and contact area, in which the influence of conductor material, connector design, bolt type and number of bolts on contact pressure and the contact area is examined.

3 Aluminium conductors

Due to its excellent mechanical and electrical properties, aluminium is one of the most common metals used for the production of electrical cables. Aluminium surfaces quickly form a corrosion-resistant oxide layer (Al₂O₃), when exposed to oxygen. This thin oxide layer is formed immediately when exposed to air and is about 2-4 nm thick. Although the oxide layer protects the material from corrosion, this is not desirable for electrical connections. The non-conductive oxide layer worsens the electrical conductivity and also increases the contact resistance. Therefore, connecting an oxidized aluminium conductor increases the contact resistance between the aluminium conductor and the connector body. To avoid such problems, the oxide layer

must be removed or broken before connecting. Brushing the aluminium conductor surface prior to assembly is one of the most commonly used methods. In addition, if an oxide inhibitor is used immediately, contact grease is also used. Contact grease consists of fine, abrasive material such as corundum. Under pressure the grease particles have an abrasive effect on the conductor surface and break up the non-conductive oxide layer. In addition to removing the oxide layer, the contact grease prevents the penetration of moisture and oxygen. In some commercially available screw connectors, the connector body contains transverse or longitudinal grooves. These grooves break into the aluminium oxide layers of the conductor when plugged in, thus ensuring the metal-to-metal contact and reducing the contact resistance [11, 12].

3.1 Aluminium alloys

The prime focus of this study is to find out the most ideal aluminium alloy that can be used as conductor material. The ideal one will be selected based on the following parameters:

- Electrical conductivity of the alloy
- Maximum contact pressure achieved between conductor and the bottom connector surface
- Contact area between conductor and connector surface

As the strength of the alloy increases, the greater the ability to adapt to the deformation and thus the increase in contact pressure. The simulations are performed by using different aluminium alloys as conductor material (see **Table 1**).

Table 1 Aluminium Alloy Comparison Chart [14]

Aluminium Alloy	Maximum Contact Pressure	Contact Area	Electrical Conductivity
1060-H18	264 MPa at 1 mm	1241 mm ² at 1 mm	61 % IACS
1350-H19	423 MPa at 1.25 mm	1230 mm² at 1.25 mm	61 % IACS
6101-T6	440 MPa at 1.25 mm	1190 mm ² at 1.25 mm	57 % IACS
6201-T81	671 MPa at 1.5 mm	1141 mm ² at 1.5 mm	52.5 % IACS
8176-H24	355 MPa at 1.25 mm	1179 mm ² at 1.25 mm	61 % IACS

Table 1 shows the simulation results of the most commonly used aluminium alloys by HV cable manufacturers and their relevant properties. The design of the connector remains the same, only the conductor material is changed in order to investigate how the contact pressure and contact area varies based on different aluminium alloys. The selection of the appropriate aluminium alloy, considers the alloys with the highest electrical conductivity, among which, the 1350-H19 has the highest maximum contact pressure per square millimetre. The main chemical composition of the selected aluminium alloy 1350-H19, are given as follow in % weight: *Al: 99.5; Fe: 0 - 0.4; Si: 0 - 0.1* [14]. Therefore this aluminium alloy is chosen as conductor material for further simulations. Its ability to achieve good contact pressure and area values in combination with excellent electrical properties makes it the most suitable alloy for conductor material [13].

4 Connector design

Seven different connector variants for 240 mm² and five variants for 500 mm² and 1000 mm² round solid conductors were investigated as model. The connector inner surface was modified in two variants (round and V-shaped), and the screw arrangement and number of screws was also varied. Only the combinations with the best results of contact pressure and area are presented in **Figure 4**, in which two variants for 240 mm² conductors are shown.

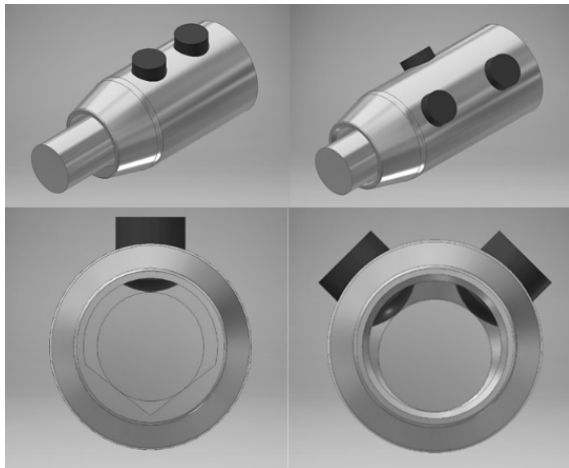


Fig. 4 Connector-Design-Variation 1 (left) & Variation 2 (right)

4.1 Simulation results for 240 mm²

The results of the simulations for a 240 mm² aluminium conductor are shown below. The results for the previously mentioned geometries are shown. **Figure 5** indicates the value of contact pressure and the area at a bolt

displacement of 2.25 mm in radial direction, for a connector with a V-shaped inner surface and two non-staggered bolts (Variation 1).

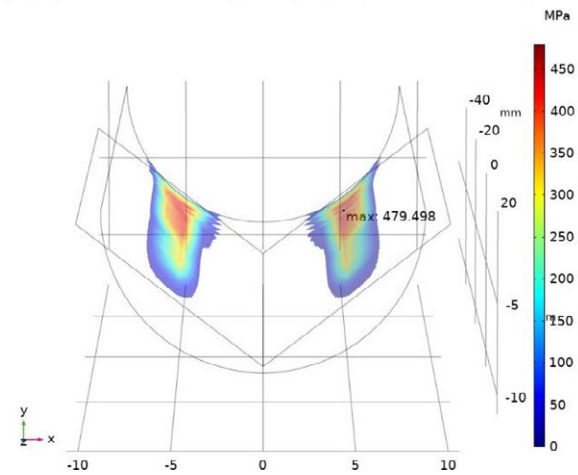


Fig. 5 Contact Pressure & Area from Variant 1 (V-shape / two bolts in a row)

As shown in **Figure 6**, a maximum contact pressure of 532 MPa is achieved at a bolt displacement of 1.5 mm. Further displacement of bolts results in the reduction of contact pressure.

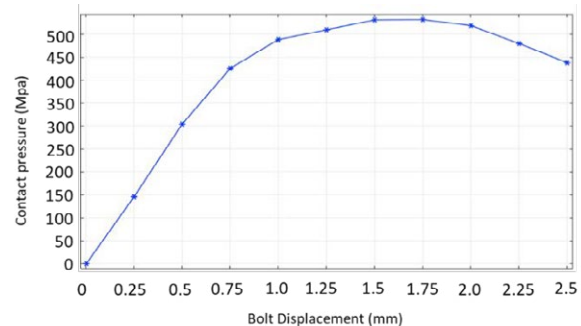


Fig. 6 Contact Pressure vs. Bolt Displacement (Variant 1)

Figure 7 shows that the contact area is 1346 mm² with a bolt offset of 1.5 mm. The contact area fluctuates at a low rate, which is to be expected for contact problems within metals.

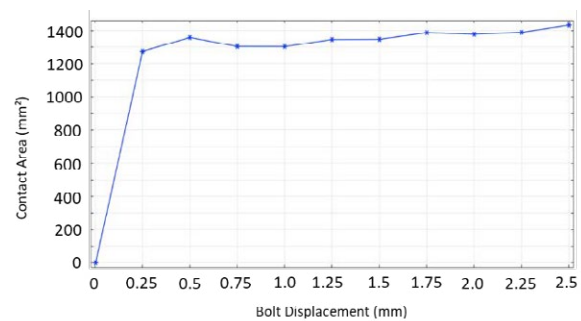


Fig. 7 Contact Area vs. Bolt Displacement (Variant 1)

Figure 8 shows the contact pressure for a connector design with a round connector inner surface and an off-set arrangement of 3 bolts. The contact pressure shown is achieved with a bolt penetration of 2.25 mm.

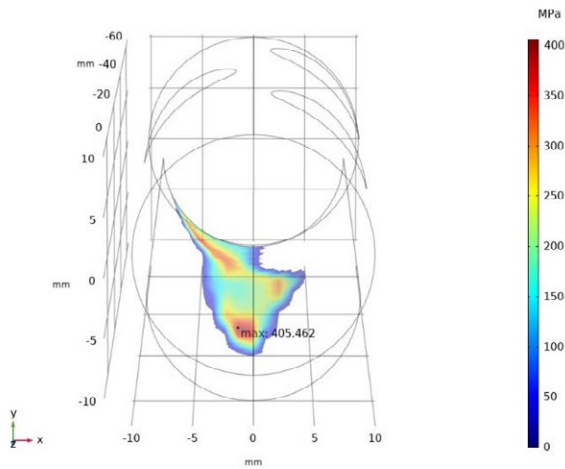


Fig. 8 Contact Pressure & Area from Variant 2 (Round / three bolts displaced)

As shown in **Figure 9**, a maximum contact pressure of 442 MPa is achieved at a bolt displacement of 1.5 mm. Further displacement of bolts results in the reduction of contact pressure.

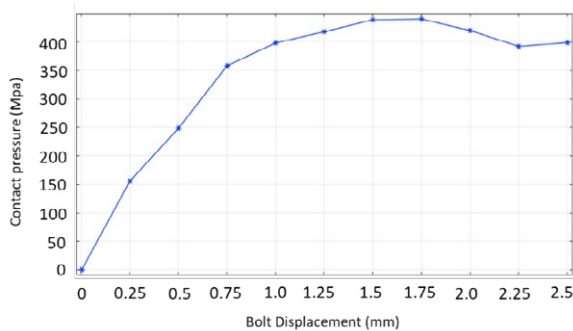


Fig. 9 Contact Pressure vs. Bolt Displacement (Variant 2)

The contact area is 1343 mm² with a bolt offset of 1.5 mm (see **Figure 10**). The area is highly unstable and fluctuates in an unpredictable manner, as can be seen in the range of 1.25 mm to 2.0 mm bolt displacement.

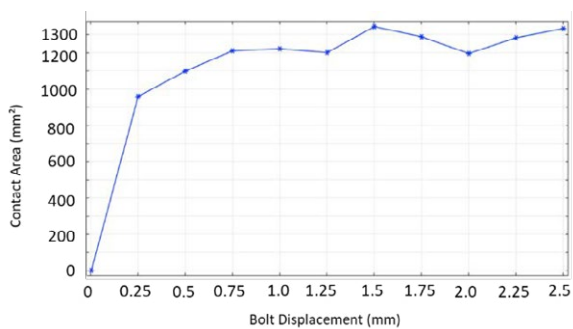


Fig. 10 Contact Area vs. Bolt Displacement (Variant 2)

Design variants with V-shaped inner surface achieves the maximum contact pressure. V-shaped inner surface helps to increase the contact area in comparison to circular (round) inner surfaces. However, most of the commercially available screw connectors consists of a circular inner surface. Therefore, the use of V-shaped connector design must be validated from an electrical point of view to check its suitability. The unpredictability of contact area after reaching a specific bolt displacement is especially visible in **Figure 10**. The contact area increases and decreases in an unstable manner. As discussed, the fluctuation in contact area is mainly due to the bolt position and the unpredictability of contact areas in metal to metal contact. Other design variants with angled bolts show similar behaviour with respect to contact area.

Contact pressure range are as follows:

- For variants with *circular inner* surface: **357 MPa to 442 MPa**
- For variants with *V-shaped inner* surface: **528 MPa to 532 MPa**

4.2 Simulation results for 500 mm² and 1000 mm²

The results show almost the same characteristics in comparison to 240 mm² conductors. Increasing the number of bolts helps to achieve the maximum contact pressure at a small bolt displacement. Design variants with V-shaped inner surface achieves the maximum contact pressure similar to that of 240 mm² connectors. It is evident that the contact pressure decreases as the conductor cross-section increases.

Contact pressure for 500 mm²

- V-shaped inner surface: **510 MPa**
- Circular shaped inner surface: **381 - 410 MPa**

Contact pressure for 1000 mm²

- V-shaped inner surface: **501 MPa**
- Circular shaped inner surface: **346 - 401 MPa**

The contact area increases with increase in conductor cross-section, which is self-explanatory. However, 500 mm² and 1000 mm² connector designs with angled bolts (30°, 45°, 135°, etc.) shows unstable contact areas compared to connector designs without any angled bolts which has only slight deviations in contact area. The contact area increase and decreases in an unpredictable manner. The deviation in contact area is mainly due to the position of bolts and also due to the unpredictability of contact areas in metal to metal contact as discussed in the literature review.

In comparison with the 240 mm² conductor, the bigger cross-sections have almost the same characteristics. Design variants with V-shaped inner surface achieves

the maximum contact pressure similar to that of 240 mm² connectors. Also it is evident that as conductor cross-section increases, the achieved contact pressure decreases.

5 Conclusion and outlook

The contact resistance between the aluminium conductor and the connector body should be kept very minimal, in order to ensure efficient transmission of power. High-contact resistance leads to power loss in the form of heat, which might result in connection breakdown. Studies indicate that contact resistance between metals reduce with increase in contact pressure. The main focus of this investigations is to study the major factors which affects the contact pressure and area between aluminium conductor and connector body. Screw connector designs with various combination of conductor material, bolt type and numbers, etc., were simulated and studied.

The following results can be summarised from the investigations:

1. The correct ratio between conductivity and mechanical strength is a prerequisite for the lowest possible connection resistance.
2. The contact resistance depends on the contact pressure, which in turn has a maximum value depending on the geometry.
3. This maximum depends on the following parameters:
 - a. Contact area of the elements to be connected
 - b. Penetration depth of the contact bolts
4. The required penetration depth varies with the number of contact bolt.
5. The size of the contact surface becomes unstable with offset screw angulation.

Further investigations are aimed at evaluating the findings on a real connector system. For this purpose, the material properties of the connector and conductor must be determined as accurately as possible. In addition, further simulations will be carried out to electrically simulate the arrangements that have already been mechanically investigated in order to investigate their resistance.

In addition, a measuring principle is being developed which is intended to reproduce the resistance values determined in the simulations. Furthermore, the influence of temperature, the force reduction and the transition from elastic to plastic deformation must be investigated in more detail.

6 Literature

- [1] Thermopedia, (2011): Thermal Contact Resistance; Available: <http://www.thermopedia.com/content/1188/>, Last accessed January 15, 2020
- [2] R.E. Ott: Termal and Electrical Resistance of Metal Contacts, PDXScholar, vol. 325, pp. 1-28, 1967
- [3] Spotwelding Consultants, Inc., (2020): Fundamentals of Capacitive Discharge Resistance Welding; Available: <https://www.spotweldingconsultants.com/capacitive-discharge-welders/dual-pulse-ins.htm>, Last accessed January 15, 2020
- [4] H. Ghaednia, R. Jackson, A. Rostami and H. Lee: Contact Mechanics, Researchgate, pp. 93-110, November 2013
- [5] F. Pennec, H. Achkar, D. Peyrou, R. Plana, P. Pons and F. Courtade: Verification of contact modelling with Comsol Multiphysics software, ResearchGate, pp. 1 - 6, 2014
- [6] H. Ghaednia, X. Wang, S. Saha and Y. Xu: A Review of Elastic-Plastic Contact Mechanics, ResearchGate, vol. Vol. 69, pp. 1 - 4, November 2017
- [7] S-cool, (2018): Definitions of Stress, Strain and Youngs Modulus; Available: <https://www.s-cool.co.uk/a-level/physics/stress-and-strain/re-verse-it/definitions-of-stress-strain-and-youngs-modulus>, Last accessed January 15, 2020
- [8] Altair Engineering, Inc., (2020): Material properties, Available: <https://www.simsolid.com/faq-items/material-properties/>, January 15, 2020
- [9] R. W. Wilson: The Contact Resistance and Mechanical Properties of Surface Films on Metals, Research Laboratory on the Physics and Chemistry of Surfaces, pp. 625 - 638, 1955
- [10] K. Dieter Haim: Reliability of mechanical connectors for medium voltage cables, 21st International Conference on Electricity Distribution, vol. Paper 0290, pp. 1-4, 2011
- [11] D. H and B. M: Role and Characterization of Surfaces in the Aluminium Industry, de Physique IV Colloque, vol. C6, pp. C6-163-C6-174., 1997
- [12] Helukabel GmbH (2011): Aluminium as a Conductor Material; Available: <http://helukabel-group.com/>, Last accessed July 15, 2019
- [13] The Aluminium Assosiation 2019: Aluminium Alloys 101; Available: <https://www.aluminium.org/resources/industry-standards/aluminium-alloys-101>, Last accessed May 20, 2019
- [14] Iron Boar Labs Ltd. (2019): MakeItFrom.com, Available: <https://www.makeitfrom.com/material-properties/1350-H19-Aluminum>, Last accessed March 20, 2020

An improved method to identify the evolution of rough surface contact by the elliptical asperity

Wanbin Ren¹, Chao Zhang¹, Fubiao Luo², Zhen Wei²

1. School of Electrical Engineering and Automation, Harbin Institute of Technology, Harbin, 150001, China

2. G&A Electronics Ltd. Co., Guilin, 541002, China

Email: renwanbin@hit.edu.cn

Abstract

The accurate estimation of real contact area is important to evaluate the contact resistance for engineering rough surfaces. In this work, an improved contact analysis method for calculating the real contact area of rough surface is proposed. Firstly, an elliptical asperity is introduced to represent the asperity peak with a large aspect ratio feature, which is different from the traditional spherical asperity. Subsequently, the real contact area and contact load under progressive indentation depth are identified by combining the Hertz theory for the fractal rough surface. Furthermore, a 3D finite-element model of rough surface is built and the mechanical simulation results are compared with the analytical methods. And the proposed method based on elliptical asperity compared with spherical asperity is more effective and shows a good agreement with the numerical simulation.

Keywords: surface topography, elliptical asperity, real contact area, contact resistance, finite-element method.

1 Introduction

It is well known that the real contact area between rough surfaces is only a small fraction of the nominal contact area for a wide range of contact loads [1-2]. This not only causes much higher contact pressures and contact temperatures locally [3-4], but also induces additional electrical and thermal resistance at the interface [5-6]. Accordingly, the accurate estimation of the real contact area is necessary to better understand the behaviors of materials in contact.

The most ideal way to directly obtain the sizes and distributions of the real contact area between rough surfaces is in-situ observation during the loading process by using the visualization techniques [7-10]. However, the common experimental methods remains highly challenging due to the lower lateral resolution (about 0.2 mm) [11] for the ultrasonic technique and higher requirement of one transparent contact pair for the optical method. As for the finite element method, the computational time is very high for tens of hours or even several days since the meshes for the concerned rough surface must be enough dense to capture the whole details in the contact process.

Nowadays, the deterministic 3D contact method is becoming more popular to evaluate the evolution of real contact area with convenient acquisition for the height information of the rough surface [12-15]. The general process for the deterministic 3D contact method is shown in Fig. 1. Firstly, the height distributions of engineering rough surfaces could be obtained by the scanning instruments to characterize the surface topography digitally. Then, these height information is used to reconstruct the rough surface by fitting the discrete points locally to asperity-peaks. Subsequently, the mechanical deformation and electrical performance

for each possible asperity are conducted based on the Hertz theory and Holm conductivity. Finally, the total contact load, the size and distribution of the real contact area and contact resistance are output to analyze the contact behaviors of rough surfaces. It is noted that the second step, i.e. reconstruction of the rough surface by the asperity-peaks, is the most critical one in four steps. And the level of what could be considered as asperity-peaks mainly depends on our ability to identify and quantify them. The evaluation of the contact characteristics is also directly determined by the identification of the shapes and relevant parameters for the asperity-peaks. Though some literatures have proposed identification methods for determining the asperity-peaks, only the sphere-peaks are identified and there is no further contact analysis conducted [16-17].

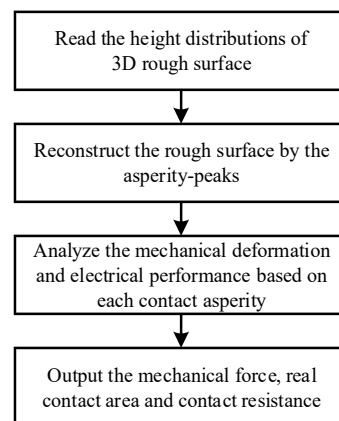


Fig. 1 The general four steps for the deterministic 3D contact method.

The purpose of this paper is to propose a method for identifying the evolution of rough surface contact by introducing the elliptical asperity. For this purpose, a determination process for the elliptical asperity-peak in 3D is presented in detail. Then, the real contact area

and contact load are identified by combining the Hertz theory for the fractal rough surface. Subsequently, a 3D finite-element model of rough surface is built and the mechanical simulation results are compared with the analytical methods. The comparison results show the proposed method based on elliptical asperity is more effective.

2 Determination of Elliptical Asperity-peak in 3D

The 3D topography of engineering surfaces could be measured by using different scanning instruments, such as stylus profilometers, optical interferometers and AFM [18]. And the surface measurement results would consist of a number of discrete points with height information, which are spaced by a certain distance apart. Fig. 2(a) shows a top view of the schematic surface consisting of discrete dots. And the asperity-peak (denoted as **AP** for asperity point) is defined as a point which is higher than its nearest-neighbor finite points (denoted as **NP** for neighboring point). The most widely used spherical asperity-peak determination method in the literature are the 5- and 9-point square definitions [19-20]. And Greenwood suggested using the 9-point sphere-peak method (*9PSP method*) in 3D to avoid the possibility of finding false asperity-peak by using the 5-point one [16]. The 3D schematic view of the 9-point sphere-peak in 3D is shown in Fig. 2(b). However, there would be some asperities with a large aspect ratio on the rough surfaces, even for isotropic surface. Thus, the sphere-peak assumption becomes invalid and might cause inaccurate evaluation of rough surface. Therefore, it is necessary to introduce ellipsoid-peak to determine the properties of ellipsoid-asperity exactly.

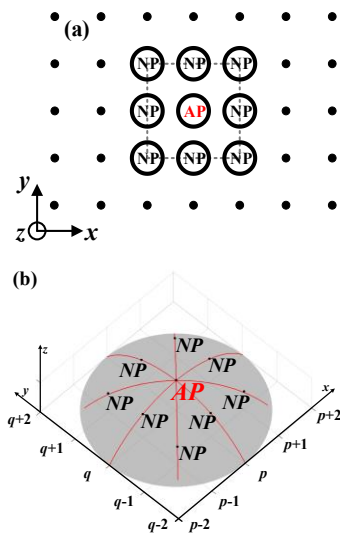


Fig. 2 The schematic graph of (a) the top view of the 9-point sphere-peak. (b) 9-point sphere-peak in 3D. **AP** and **NP** represent the asperity point and neighboring point, respectively.

The general identification process for elliptical asperity-peak is as follows: Firstly, it is necessary to identify the asperity point **AP** with the highest height locally due to the fact that the higher point is always more likely to be in contact during the actual loading process [1]. Then, if the highest **NP** around **AP** is also higher than the seven nearest-neighboring points (except for **AP**) around it, we further define this point as a sub-asperity point which is denoted as **SAP**. Thus, the height order of involved points is $AP > SAP > NPs$. In addition, if the **NP** which locates in line with determined **AP** and **SAP**, is the second highest one in eight original **NPs** and also higher than the seven nearest-neighboring points (except for **AP**) around it, then it also could be recognized as another **SAP**. Once some **SAP** is determined, then other possible **SAP**(s) would be further identified only along the directions of identified **AP** and **SAP**. And this identification process would continue until there is no **SAP** identified. It is noted that the core of this identification process is to determine the numbers and relative directions of the sub-asperity points (**SAPs**). There are multi-points (more than 9 points) to reconstruct an elliptical asperity-peak compared with the traditional *9PSP method* due to the introduced point **SAP**. Thus, the determination process mentioned above is called multi-points ellipsoid-peak method (*MPEP method*).

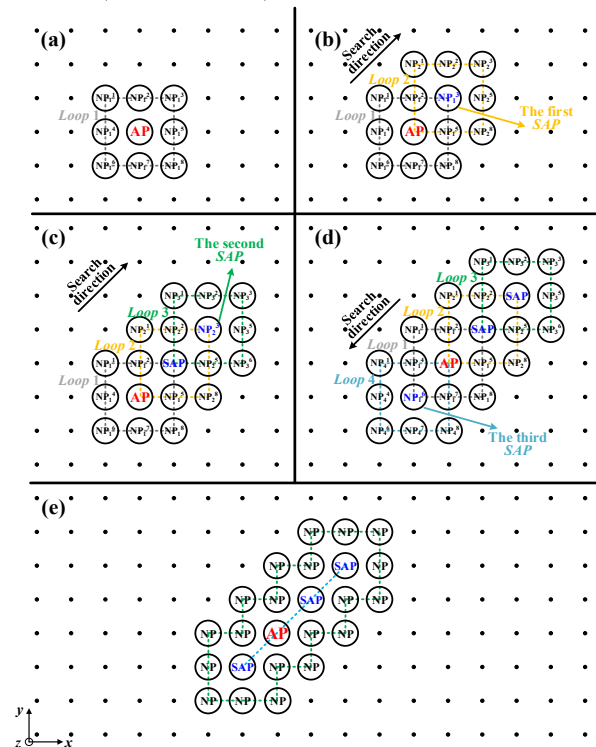


Fig. 3 Determination process for three identified **SAPs**. (a) One **AP** surrounded by eight **NPs** in **Loop 1**. (b) The point NP_1^3 in **Loop 2** is defined as the first **SAP**. (c) The point NP_2^3 in **Loop 3** is identified as the second **SAP**. (d) The point NP_1^6 in **Loop 4** is identified as the third **SAP**. (e) The identified **AP**, three **SAPs** and twenty **NPs**.

Table 1. The detailed corresponding relationship between the superscript of *NP* and the relative direction to the centre point.

The superscript of <i>NP</i>	The relative direction to the centre point
1	Top left
2	Top
3	Top right
4	Left
5	Right
6	Bottom left
7	Bottom
8	Bottom right

In order to describe this determination process clearly, an example with three identified *SAPs* is illustrated in Fig. 3. There is one *AP* surrounded by eight *NPs* within *Loop 1* in Fig. 3a. The subscript and superscript of *NP* represent the *i*th loop and the relative direction to the centre point of the corresponding loop, respectively. The numbers of the superscript of *NP* and the correspondingly relative directions to the centre point are described in detail in Table 1. In this example, we assume that the point NP_1^3 is the highest one compared with the other seven *NPs* in the *Loop 1*. Next, if the NP_1^3 also has the highest height compared with the seven nearest-neighboring points (except for *AP*) around it in *Loop 2*, the point NP_1^3 is further defined as the first *SAP* in Fig. 3b. Then, if the NP_2^3 which is the centre point in *Loop 3* also has the highest height compared with the seven nearest-neighboring points (except for the first *SAP*) around it in *Loop 3*, the point NP_2^3 is further defined as the second *SAP* in Fig. 3c. And if the point NP_3^3 is not the highest one in the next loop, then the identification of *SAP* along the top right direction is terminated. Thus, the direction of the major axis of the elliptical asperity peak has been determined. Subsequently, if the centre point NP_1^6 is the second highest point in *Loop 1* and also the highest one compared with the seven nearest-neighboring points (except for *AP*) around it in *Loop 4*, then this point could be taken as the third *SAP* along the bottom left direction in Fig. 3d. And if the point NP_4^6 is not the highest one in the next loop (except for the third *SAP*), then the identification of *SAP* along the bottom left direction is also terminated. Thus, there are one *AP*, three *SAPs* and twenty *NPs* in the whole identification process as shown in Fig. 3e and these points could be equivalent to a 3D elliptical asperity-peak. Therefore, the axis radii in three orthogonal directions of the ellipsoid-peak could be calculated by the least-square fitting to all *AP*, *SAPs* and *NPs*. Then, the identified ellipsoid *i* could be characterized by the obtained axis radii a_i , b_i , c_i and height z_i . Fig. 4 shows the 3D fitting case of the ellipsoid-peak corresponding to the Fig. 3e.

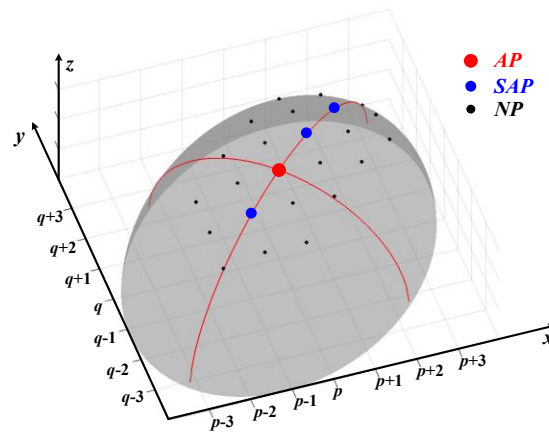


Fig. 4 The 3D schematic view of ellipsoid-peak in 3D corresponding to the case in Fig. 3e.

3 Contact Model of 3D Rough Surfaces

3.1 Deformation of single asperity

When a rough surface is in contact with a flat surface, there are only some higher discrete asperities bearing the load. And the possible contact asperities are identified by the aforementioned identification process. Therefore, it is necessary to primarily analyze the deformation of the single asperity. Fig. 5 shows representatively an elastic half-ellipsoid with three orthogonally axial radii r_x , r_y and r_z contacting with an elastic plane with smooth surfaces. The equivalent curvature radius r_e of contact position is $r_e = (r'r'')^{1/2}$, where $r' = r_x^2/r_z$ and $r'' = r_y^2/r_z$ are the principal curvature radii in the *x-z* and *y-z* planes. When the interference is δ between half-ellipsoid and elastic plane under the normal load P , the initial contact point is extended to an ellipse with semi-major axis a and semi-minor axis b ($b < a$). And the eccentricity of the produced ellipse is defined as $e = \sqrt{1 - (b^2/a^2)}$. The relationship between contact load P , contact area A and interference δ are written as [21]

$$P = \left(\frac{4}{3}\right) E r_e^{1/2} \delta^{3/2} \cdot F(e) \quad (1)$$

$$A = (\pi r_e \delta) \cdot A(e) \quad (2)$$

where $E^* = ((1-\nu_1^2)/E_1 + (1-\nu_2^2)/E_2)^{-1}$ is a constant consisting of Young's modulus and Poisson's ratio of the involved materials.

And the contact load coefficients $F(e)$ and contact area coefficients $A(e)$ are

$$F(e) = \frac{\pi}{e\sqrt{2}} K(e)^{-3/2} \left\{ \left[\left(\frac{a}{b}\right)^2 E(e) - K(e) \right] \cdot [K(e) - E(e)] \right\}^{1/4} \quad (3)$$

$$A(e) = \frac{2\left(\frac{b}{a}\right) \left\{ \left[\left(\frac{a}{b}\right)^2 E(e) - K(e) \right] \cdot [K(e) - E(e)] \right\}^{1/2}}{e^2 K(e)} \quad (4)$$

where $K(e)$ and $E(e)$ are the complete elliptic integrals of the first and second kind, respectively.

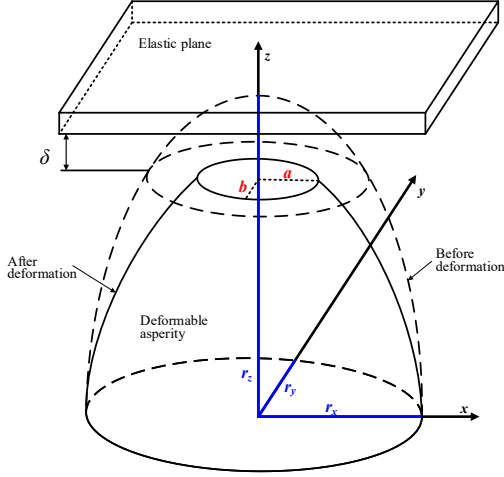


Fig. 5 The contact schematic diagram of an elastic flat with an elastic asperity.

If the axial radii satisfy $r_x = r_y = r_z = r$, then this ellipsoid becomes to a sphere with curvature radius r . Thus, the elliptical a -spot becomes a circular one and the coefficients $F(e) = A(e) = 1$ in Eqs.(5) and (6). Fig. 6 shows the results of illustrative calculations of the dependence of coefficients $F(e)$ and $A(e)$ on the eccentricity e . When the eccentricity e is 0.972, the bearing load increases to 1.1 times compared with a circular a -spot. When the eccentricity e reaches up to 0.991, the contact area decreased to 0.9 times. This demonstrates that the two coefficients $F(e)$ and $A(e)$ are affected significantly by high values of e . And the contact force would be underestimated and the contact area would be overestimated if the elliptical a -spot is simplified to a circular one.

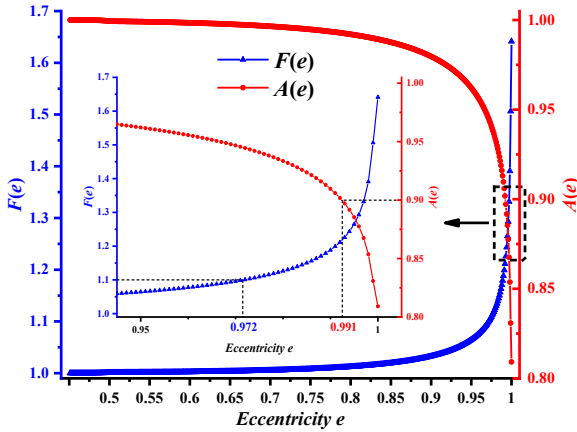


Fig. 6 Evolution of the coefficients $F(e)$ and $A(e)$ for contact load and contact area in terms of the eccentricity e .

3.2 Contact model of rough surface based on the elliptical asperity

It is well known that there are only some paralleled asperities bearing the load when two rough surfaces contact. Thus, an improved method to model rough surfaces contact could be proposed by applying the *MPEP* determination process for possible asperities mentioned above. It is assumed that all the asperities deform elastically during the whole loading process. And

the interaction effects between asperities during deformation process are neglected for simplicity. To illustrate how to model contact between rough surfaces based on the elliptical asperity in more detail, a recursive procedure is developed and the flow chart of this process is given in Fig. 7. Firstly, the obtained 3D point cloud data of rough surface topography consisting of the positions and heights are read. Then, the identified local maximum heights are marked as *AP*, and the corresponding positions and total numbers n are recorded. Next, continue to find out the possible *SAP* around *AP* and record its direction and position. Furthermore, if there is *SAP* around the *AP*, the identified *AP*, *SAP*(s) and *NPs* would be fitted to an ellipsoid by the least-square method. Otherwise, the *AP* and *NPs* would be fitted to a sphere by the least-square method. Subsequently, the bearing load and contact area of identified ellipsoid or sphere i could be calculated according to the Eqs.(1) and (2) under the given Young's modulus E and indentation depth δ . Thus, the total contact load P_j and contact area A_j are updated. When the deformation δ reaches to the prescribed displacement of δ_c , the calculation ends.

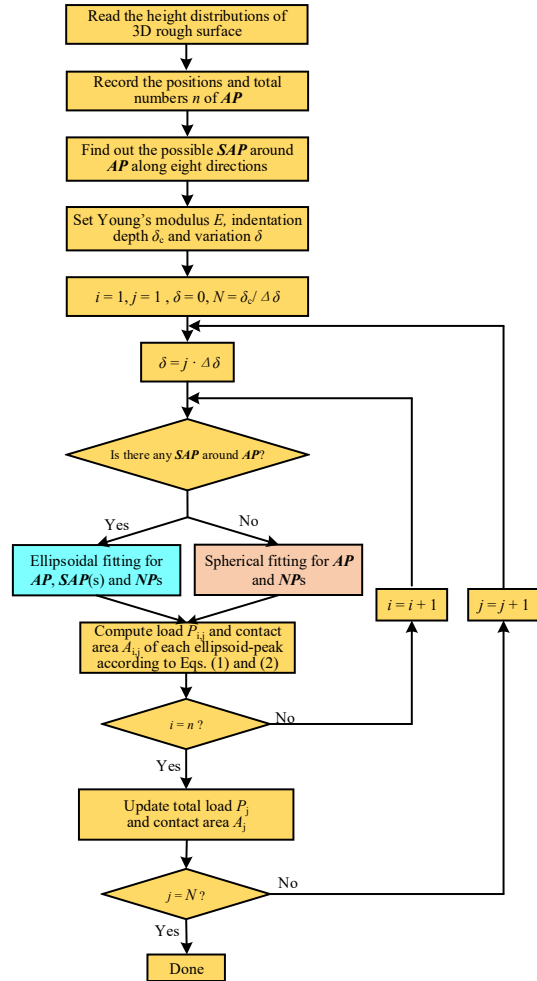


Fig. 7 Flow chart of iterative procedure for rough surface contact model based on the elliptical asperity.

4 Results and Discussion

4.1 Reconstruction of rough surface

In order to validate the identification effects on the properties of the asperity-peaks (shapes, numbers, radii and heights) for rough surfaces by using the proposed equivalent method, the 3D self-affine fractal rough surface independent of scale is selected. The three-dimensional fractal surface topography could be generated using a modified two-variable Weierstrass-Mandelbrot function which is described as [22]

$$z(x, y) = L \left(\frac{G}{L}\right)^{D-2} \left(\frac{\ln \gamma}{M}\right)^{1/2} \sum_{m=1}^M \sum_{n=0}^{m-1} \gamma^{(D-3)n} \times \left\{ \cos \varphi_{m,n} - \cos \left\{ \frac{2\pi \gamma^n (x^2 + y^2)^{1/2}}{L} \cos \left[\tan^{-1}(y/x) - \frac{\pi m}{M} \right] + \varphi_{m,n} \right\} \right\} \quad (5)$$

where L is the sample length, G is the fractal roughness, D is the fractal dimension ($2 < D < 3$ for 3D rough surface). The fractal roughness G is a height scaling parameter independent of the frequency and the magnitude of the fractal dimension D determines the contribution of high- and low-frequency components in the surface function $z(x, y)$. Other parameters and corresponding detailed definitions in Eq.(5) are described in Ref[23]. Fig. 8(a) shows a representative $0.5 \times 0.5 \text{ mm}^2$ fractal surface with $G = 10^{-13}$ and $D = 2.4$, simulated from Eq.(5) using $M = 10$, $\gamma = 1.5$, $L = 500 \mu\text{m}$, and $L_s = 1 \text{ nm}$. The lateral data resolution is $\Delta x = \Delta y = 1 \mu\text{m}$. And a $21 \mu\text{m} \times 21 \mu\text{m}$ part of the simulated rough surface shown in Fig. 8(b) is further chosen to verify the identification accuracy for the numbers and properties of the asperity-peaks on the rough surface. It is noted that there are many local points with higher heights in Fig. 8(b). And these points would play an important role when analyzing the mechanical and electrical behaviors in contact.

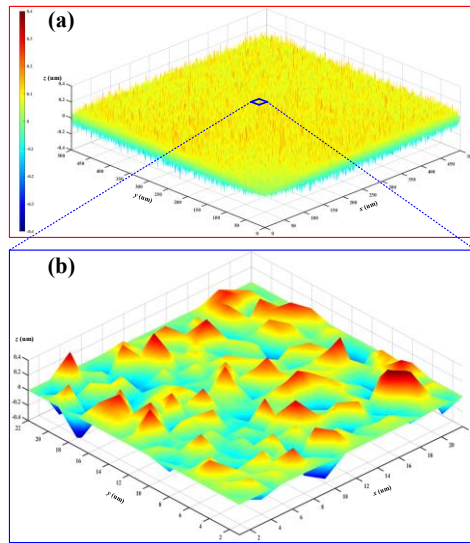
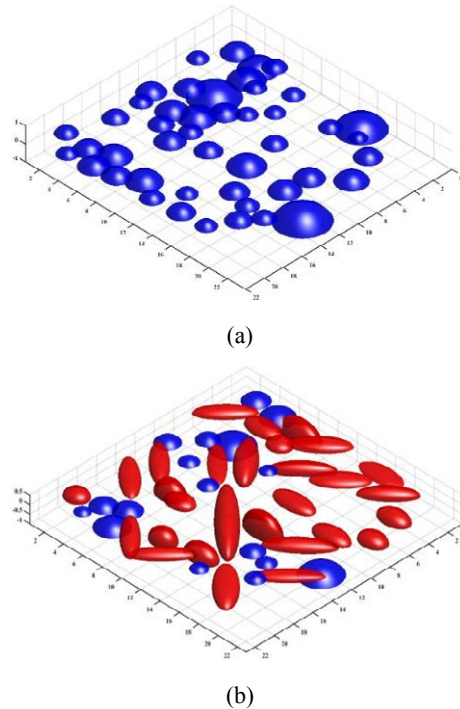


Fig. 8. The simulated three-dimensional fractal rough surfaces ($M = 10$, $\gamma = 1.5$, $L = 500 \mu\text{m}$, $L_s = 1 \text{ nm}$, $G = 10^{-13} \text{ m}$ and $D = 2.4$). (a) $500 \mu\text{m} \times 500 \mu\text{m}$ rough surface. (b) A local $21 \mu\text{m} \times 21 \mu\text{m}$ rough surface.

Table 2 Total numbers N , average curvature radii r and average heights h of identified asperity-peaks

Asperity parameters	Determination method	<i>9PSP method</i> (Only sphere-peak)	<i>The proposed MPEP method</i> (Considering ellipsoid-peak)
	Numbers N		46
Curvature radius r (μm)		1.912	4.437
Heights h (μm)		0.342	0.272

The results of the total numbers N , the average curvature radii r and the average heights h for the *9PSP method* and the *MPEP method* introduced in Section II are represented in Table. 2. The number of determined asperity-peaks is 46 (about 9.5% of the total 484 points) for both two methods. However, there are 29 ellipsoid-asperities and 17 sphere-asperities for the *MPEP method* when further considering the existence of ellipsoid-peak. And the proposed method determines the higher average curvature radius of $4.437 \mu\text{m}$ and the lower peak-height of $0.272 \mu\text{m}$. Fig. 9(a) and (b) show the relative positions and height distributions of the identified 3D asperity-peaks for the *9PSP method* and *MPEP method*, respectively. To highlight the differences between two methods, the identified ellipsoid-peaks by the *MPEP method* are marked as red in Fig. 9(b). The 3D solid model based on the local point cloud is also reconstructed using the Pro/ENGINEER commercial software shown in Fig. 9(c). The comparison results indicate the asperity-peaks identified by the *MPEP method* and *9PSP method* are in good agreement with the 3D surface topography. And the *MPEP method* has a more accurate characterization especially for the ellipsoid-peaks.



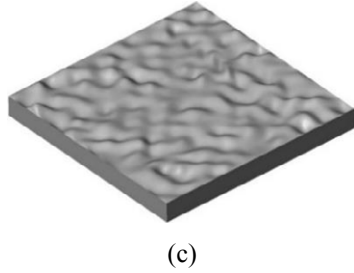


Fig. 9. The identified three-dimensional distributions for (a) *9PSP method* and (b) *MPEP method*. (c) The solid model generated by the Pro/ENGINEER software.

4.2 Evaluation of rough surface contact

For further validating the deformation of asperities on the rough surfaces during loading process, the commercial program COMSOL Multiphysics 5.3a version is used to perform simulations by solving mechanical contact equations through FEM. Based on the extracted topography of rough surface with fractal dimension $D = 2.4$, 3D finite element contact model is developed. Fig. 10 illustrates two parts of this model in which a $21\mu\text{m} \times 21\mu\text{m} \times 2.5\mu\text{m}$ elastic cube with smooth surfaces and a $21\mu\text{m} \times 21\mu\text{m} \times 2\mu\text{m}$ elastic cube with a fractal rough surface are built. The material properties are listed in Table 2 for the smooth and rough cubes. The upper and lower surfaces are defined as target surface and source surface, respectively. Both of two bodies are meshed with 3D traditional tetrahedral elements. Specially, the zone near contact surfaces is highly meshed with the finest elements with the maximal size of $0.25\mu\text{m}$ to get the more accurate results, and the sizes of elements increases gradually with increasing distance from the contact surfaces as shown in Fig. 10. The base surface of the cube with rough surface is fixed, and no displacement is allowed in the x - and y - planes. The displacement load is vertically applied to the top surface of the cube with smooth surface using a single $0.01\mu\text{m}$ step with 50 sub-steps. As for the FE simulation results, contact load F and real contact area A are calculated by integrating the built-in variables “solid.Tn” and “incontact_p1” for the smooth surface, respectively. And the contact resistance R_c is obtained by the global evaluation of the built-in variable “ec.R11”.

Table 2 Material properties in FEM

Material	Elastic modulus (GPa)	Poisson's ratio
Copper for the smooth surface	110	0.35
Gold for the rough surface	70	0.44

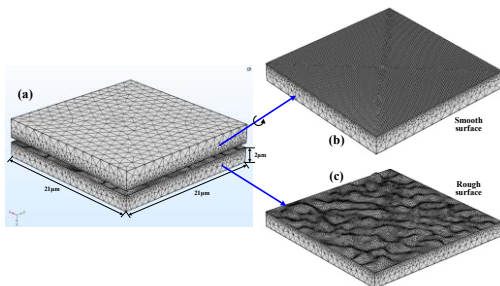


Fig. 10 Three-dimensional finite element simulation model. (a) The contact models of rough surface. (b) The surface mesh of the smooth surface cube. (c) The surface mesh of the rough surface cube.

The distribution of contact stresses on rough surface corresponding to $\delta_c = 0.5\mu\text{m}$ by the FE simulation is shown in Fig. 11(a). As expected, higher contact stresses are always at the centre of each contact asperity. And there are many ellipse-shape contact a -spots in the simulation contact stress map. Three representative deformation of asperities are extracted when the indentation depth δ are $0.4\mu\text{m}$, $0.45\mu\text{m}$ and $0.5\mu\text{m}$ as shown in Fig.11(b), (c) and (d), respectively. With the indentation depth increasing which is corresponding to the increasing contact load, the contact shapes of asperities ①, ② and ③ all extend to ellipse with different directions of major axis. This could be attributed to the deformation of ellipsoid-peaks which is not similar to the spherical one. And this unequal deformation also demonstrates that it is reasonable to introduce the ellipsoid to simulate the asperity-peak with a large aspect ratio feature in some direction. And the proposed *MPEP method* has a better performance in identification accuracy than traditional sphere-peak method, i.e. 9-point method.

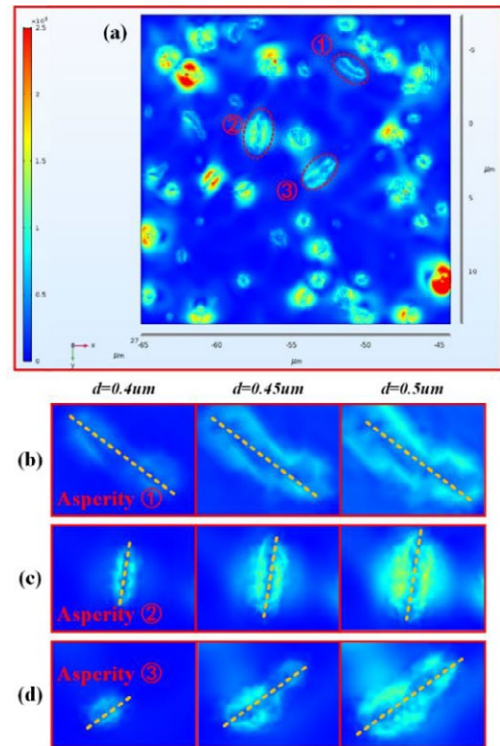


Fig. 11. The contour map of contact stresses on the rough surface by FEM. (a) Distributions of contact stresses under displacement load of $0.5\mu\text{m}$ for $21\mu\text{m} \times 21\mu\text{m}$. Deformations of (b) asperity ①. (c) asperity ②. (d) asperity ③ under displacement load of $0.4\mu\text{m}$, $0.45\mu\text{m}$ and $0.5\mu\text{m}$.

The revolutions of contact load F , real contact area A and contact resistance R_c versus the indentation depth δ between rough surface and flat surface are represented for two methods and FE simulation in Fig. 12.

The calculated contact area and contact load both increase during the whole $0.5\mu\text{m}$ loading process for two methods and the tendency is similar to the simulation results shown in Fig. 12(a) and 12(b). And the results for the proposed *MPEP method* show better agreement with FE simulation compared with that of the 9-point method. The contact area and contact load increase significantly when the indentation depth exceeds $0.05\mu\text{m}$ for the pure sphere-peak method (9-point method). However, both the results of the proposed method and FE simulation show a significant growth after $0.2\mu\text{m}$. And the calculation results by the 9-point method are always higher than that of the *MPEP method* and FE simulation and show a faster increase rate. When the indentation depth reaches up to $0.5\mu\text{m}$, the contact area and contact load for the 9-point method are about 1.8 times and 1.3 times than that of simulation results, respectively, while the results of the proposed method is lower than 1.1 times. And the calculations of 9-point method deviate from that of the proposed method and FE simulation with further loading. The main reason for this phenomenon is that there are only equivalent sphere-peaks for the 9-point method. And this method would overestimate the heights of asperities due to less strict identification as shown in Table 1. Then, when the indentation depth is smaller, there would be some higher asperities in contact with the plane and this falsely estimate the contact area and contact load initially. For the proposed method, the calculation results for contact load and real contact area have the similar increasing trend with FE simulation before the indentation depth reaches $0.25\mu\text{m}$ and becomes higher as the loading process continuing. The contact resistance decreases nonlinearly with the indentation depth increasing for two methods and FE simulation shown in Fig. 12(c). The results for the *9PEP method* are the lowest one due to the overestimation of real contact area. When the indentation depth is smaller than $0.16\mu\text{m}$, the contact resistance for the proposed *MPEP method* shows better agreement with FE simulation results. However, an obvious deviation occurs between these two results with the indentation depth further increasing. This could be attributed to the fact that all the asperities identified by the proposed method are assumed to be discrete and the interactions especially the combinations between neighboring asperities are neglected when loading.

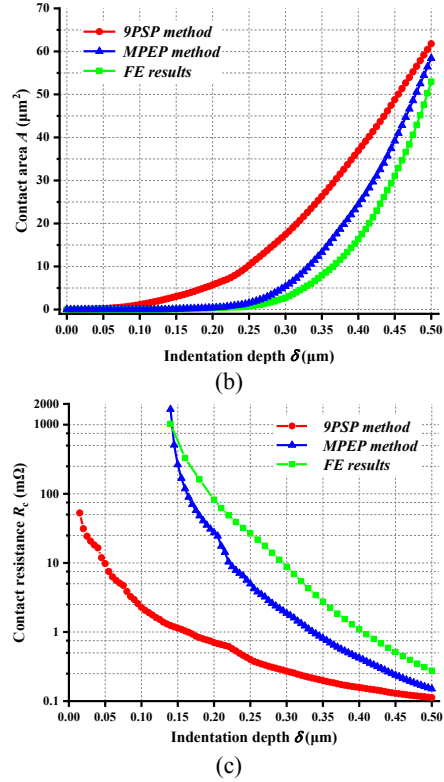
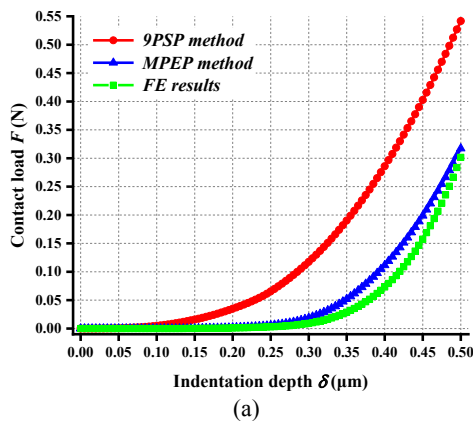


Fig. 12. Analytical and FE simulation results for the rough surfaces. (a) Indentation depth vs contact load. (b) Indentation depth vs contact area. (c) Indentation depth vs contact resistance.

It is obvious that the real contact area is the mixture of the elliptical a -spots and spherical a -spots as shown in Fig. 11(a). Thus, the total contact resistance contains the constriction resistance of each elliptical a -spot and spherical a -spot. For the i th elliptical a -spot, the constriction resistance associated with semi-axes a_i and b_i presented by Holm could be written as [24]

$$R_{ci} = \frac{\rho}{2\pi} \int_0^\infty \frac{d\mu}{[(a_i^2 + \mu^2)(b_i^2 + \mu^2)]^{1/2}} \quad (6)$$

where $\rho = 1.92 \times 10^{-8} \Omega \cdot \text{m}$ is the average resistivity of the contact members. It is noted that Eq.(6) degrades into the classic $R_{ci} = \rho/2a_i$ when the elliptical a -spot becomes to the spherical one. For a large number of small a -spots, the calculation for the contact resistance when no interactions between a -spots are considered as follows

$$R_c = \left(\sum_{i=1}^N \frac{1}{R_{ci}} \right)^{-1} \quad (7)$$

The variations in the numbers of contact a -spots N , contact area A , contact resistance R_c as functions of the indentation depth δ between rough surface and flat surface in the whole $0.5\mu\text{m}$ loading process for the proposed *MPEP method* are shown in Fig. 13. When the indentation depth is smaller than $0.205\mu\text{m}$ (corresponding to the point A), there is only one elliptical asperity in contact. After that, the numbers of contact a -spots increases from 1 to 4 with the total contact area

increasing and the calculated contact resistance decreasing nonlinearly. With the numbers of contact a -spots further increasing, the total contact area increases and the calculated contact resistance decreases linearly in the log-log domain with slopes of 121.3 and -5.08 after point **B**, respectively. This demonstrates that the calculation results of the proposed *MPEP method* could accurately capture the evolution of the contact area and contact resistance with the loading process continuing.

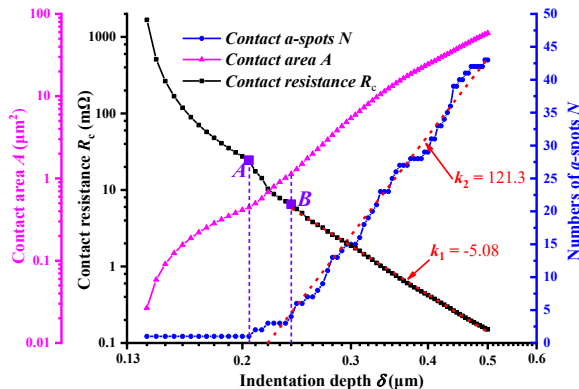


Fig. 13. Variations in numbers of contact a -spots N , contact area S and contact resistance R_c as functions of the indentation depth during the whole $0.5\mu\text{m}$ loading process.

5 Conclusions

This paper proposed an improved method by introducing the elliptical asperity to predict the evolution of contact area and contact resistance for rough surfaces based on the purely elastic deformation of asperities. A determination process for the ellipsoid-peak with a large aspect ratio feature in some direction which is different from the traditional sphere-peak is described in detail. And the real contact area and contact load under progressive indentation depth are identified by combining the Hertz contact theory for the fractal rough surface. The analytical results for the proposed *MPEP method* show good agreement with the simulation results using the FE method during the loading process compared with the traditional sphere-peak method. However, a slight deviation appears for a larger contact load due to the combinations of neighboring asperities. Overall, the presented method is also advantageous in comparison with the *9PEP method* and FEM due to its accuracy and efficiency.

ACKNOWLEDGMENT

The authors express their gratitude for the kind support provided by The National Natural Science Foundation of China (Contract Number 51377029 and 51777039).

References

- [1] J. A. Greenwood and J. B. P. Williamson, "Contact of nominally flat surfaces," Proc. R. Soc. London A. Vol. 295, No. 1442, Dec. 1966, pp. 300–319.
- [2] T. R. Thomas, "Rough Surfaces," Longman Group Limited, NY, 1982.
- [3] M. Kalin, "Influence of flash temperatures on the tribological behaviour in low-speed sliding: a review," Mater. Sci. Eng. A. Vol. 374, No. 1-2, Jun. 2004, pp. 390–397.
- [4] R. L. Jackson, "A multi-scale model for contact between rough surfaces," Wear. Vol. 261, No. 11-12. Dec. 2006, pp. 1337-1347.
- [5] J. J. Salgon, F. RobbeValloire, J. Blouet, and J. Bransier, "A mechanical and geometrical approach to thermal contact resistance," Int. J. Heat Mass Transf. Vol. 40, No.5, Mar. 1997, pp. 1121-1129.
- [6] G. Anciaux and J. F. Molinari, "A molecular dynamics and finite elements study of nanoscale thermal contact conductance," Int. J. Heat Mass Transf. Vol. 59, Apr. 2013, pp. 384-392.
- [7] M. Pau, "Estimation of real contact area in a wheel-rail system by means of ultrasonic waves," Tribol. Int. Vol. 36, No. 9, Sep. 2003, pp. 687–690.
- [8] A. Ovcharenko, G. Halperin, I. Etsion and M. Varenberg, "A novel test rig for in situ and real time optical measurement of the contact area evolution during presliding of a spherical contact," Tribol. Lett. Vol. 23, No. 1, Jul. 2006, pp. 55–63.
- [9] J. Swingler, "The resolution dependence of measured fractal characteristics for a real un-dismantled electrical contact interface," Wear. Vol. 268, No. 9-10, Mar. 2010, pp. 1178-1183.
- [10] S. E. Rohde, A. I. Bennett, K. L. Harris, et al. "Measuring contact mechanics deformations using DIC through a transparent medium," Exp. Mech. Vol. 57, No. 9, Nov. 2017, pp. 1445–1455.
- [11] R. Dwyer-Joyce and B. Drinkwater, "In situ measurement of contact area and pressure distribution in machine elements," Tribol. Lett. Vol. 14, No. 1, Jan. 2003, pp. 41–52.
- [12] B. Buchner, M. Buchner, and B. Buchmayr, "Determination of the real contact area for numerical simulation," Tribol. Int. Vol. 42, No. 6, Jun. 2009, pp. 897–901.
- [13] J. Jamari, M. B. de Rooij and D. J. Schipper, "Plastic deterministic contact of rough surfaces," J. Tribol. Vol. 129, No. 4, Oct. 2007, pp. 957–962.
- [14] M. N. Webster and R. S. Sayles, "A numerical model for the elastic frictionless contact of real rough surfaces," Vol. 108, No. 3, Jul. 1986, pp. 314–320.
- [15] A. Söderberg and S. Björklund, "Validation of a simplified numerical contact model," Tribol. Int. Vol. 41, No. 9-10, Sep. 2008, pp. 926–933.
- [16] J. A. Greenwood, "A unified theory of surface roughness," Proc. R. Soc. Lond. A. Vol. 393, 1984, pp. 133-157.
- [17] M. Kalin and A. Pogačnik, "Criteria and properties of the asperity peaks on 3D engineering surfaces," Wear. Vol. 308, No. 1-2, Nov. 2013, pp. 95-104.
- [18] D. Whitehouse, "Surfaces and Their Measurement," Hermes Penton, London, 2002.
- [19] D. J. Whitehouse and M. J. Phillips, "Sampling in a two-dimensional plane," J. Phys. A. Vol. 18, No. 13, 1985, pp. 2465–2477.
- [20] K. Yanagi, S. Hara and T. Endoh, "Summit identification of anisotropic surface texture and directionality assessment based on asperity tip geometry," Int. J. Mach. Tools Manuf. Vol. 41, No. 13-14, Oct. 2001, pp. 1863–1871.
- [21] K. L. Johnson, "Contact Mechanics," Cambridge University Press, NY, 1985.
- [22] M. Ausloos and D. H. Berman "A multivariate Weierstrass-Mandelbrot function," Proc. R. Soc. A-Math. Phys. Eng. Sci. Vol. 400, No. 1819, 1985, pp. 331-350.
- [23] W. Yan and K. Komvopoulos, "Contact analysis of elastic-plastic fractal surfaces," J. Appl. Phys. Vol. 84, No. 7, Oct. 1998, pp. 3617-3624.
- [24] R. Holm. "Electric Contacts: Theory and Application," New York, NY, USA: Springer-Verlag, 1967, pp. 14-16.

Elastic Rough Surface Contact and the Root Mean Square Slope of Measured Surfaces

R. L. Jackson^a, Y. Xu^b, S. Saha^a, K. Schulze^a

^aDepartment of Mechanical Engineering, Auburn University, Auburn, AL, 36849, USA
jackson@auburn.edu

^bSystems Power and Energy, School of Engineering, University of Glasgow, UK

Abstract

This study investigates the predictions of the real contact area for perfectly elastic rough surfaces using a boundary element method (BEM). Sample surface measurements were used in the BEM to predict the real contact area as a function of load. The surfaces were normalized by the root-mean-square (RMS) slope to analyze if contact area measurements would collapse onto one master curve. If so, this would confirm that the contact areas of manufactured, real measured surfaces are directly proportional to the root mean square slope and the applied load. The data predicts a complex response that deviates from this behavior. The variation in RMS slope and the spectrum of the system related to the features in contact are further evaluated to illuminate why this property is seen in some types of surfaces and not others.

1 Introduction

The surfaces of electrical connectors are rough, and when brought together, what is actually touching is a fraction of the surface area. The contact spots occurring between the peaks or asperities act as bottlenecks of the electrical current conducted between the surfaces. This results in spreading resistance to occur between the contacting surfaces. Many rough surface contact models exist to predict the spreading resistance [1-8].

The real area of contact between rough surfaces is often assumed to only be a function of the average pressure normalized by the equivalent elastic modulus and the RMS slope [9, 10]. The idealized surfaces are often modeled as a set of asperities of different scales and sizes based on geometric shape (e.g. Archards' bumps on bumps) or as self-affine fractals [10, 11]. When using the same idealized surface the majority of contact models developed from these assumptions converge, more or less, on to a single contact area vs applied pressure plot (Cite Contact challenge). A similar master curve is replicated experimentally by producing several self-affine fractal surfaces (via 3D-printing) of varying roughness and performing in situ contact measurements (Bennett, McGhee). However, not all models and experimental measurements produce the same results. Campana and Muser [12] noted a 20% variation between the contact area as a function of the pressure normalized by the RMS slope of real measured and random rough surfaces. The RMS slope is calculated by squaring the slope at each point on a rough surface,

taking the mean value of these, and then taking the square root of the mean. Putignano et al. used deterministic modeling of elastic rough surface contacts to find the proportion between the normalized contact area and average pressure to be approximately 2 [13]. Additionally, a recent analysis of generated fractal surfaces suggests that the contact area is not solely dependent on the root mean squared gradient but must also factor in the bandwidth or Nayak parameter, α [14]. These discrepancies may tie back to the original surfaces many of the current models are based upon. Greenwood and Williamson [15], Whitehouse and Archard [16], McCool [17] and others have observed that some real surfaces have nearly Gaussian distributions in surface heights and are highly random, but they are never perfectly Gaussian nor perfectly fractal. Sayles and Thomas also showed that many different surfaces appeared to follow a self-affine fractal structure, but just approximately [18]. Recent work by Zhang and Jackson have found discrepancies between different mathematical theories of fractals and the parameter extraction methods employed [19, 20].

Here we examine the relationship between contact experiments with real (measured), imperfect surfaces and the contact mechanics literature [21, 22] using a boundary element method. If the theories mentioned above are correct, using surfaces that each have the same RMS slope we should expect to see full collapse of the contact area over the pressure data. If they do not, it suggests that additional parameters should at least be considered to refine contact results and emulate manufactured surfaces. An examination of the hierarchy of the surface features on the surface will be explored to preliminarily assess the key parameters.

This said, other models already exist that suggest the rough surface contact is dependent on many rough surface contact parameters and not the RMS slope alone.

Table 1: Properties of surfaces in [23] as measured.

Parameter	Surface 1	Surface 2	Surface 3
σ (μm)	0.4057	0.6513	15.01
m_o ($10^{-12}/\text{m}^2$)	0.1646	0.4242	225.3
m_2	0.0286	0.1143	8.03
m_4 ($10^{12}/\text{m}^2$)	0.01904	0.07683	3.560
B_{max}	0.019	0.0283	0.1958

2 Methods

The same measured surfaces used in Jackson and Green [23] are again employed here to consider the effectiveness of RMS surface slope on normalizing the contact area to pressure function. Their measured surface properties are listed Table 1. The properties of the original surfaces are given in Table 1. σ is the root mean square roughness and m_n are the spectral moments of the surface. B is the ratio of the amplitude to wavelength ratio taken from a Fourier transform of the surface, and B_{ave} is the average value and B_{max} is the minimum value. Finally, \bar{g} is the root mean square slope or gradient, which is of course related to m_2 by

$$\bar{g} = \sqrt{m_2}$$

Table 2: Properties of surfaces in after normalization.

Parameter	Surface 1	Surface 2	Surface 3	Surface 4	Surface 5
σ (μm)	0.2282	0.2293	0.5241	0.4133	0.7838
m_o ($10^{-12}/\text{m}^2$)	0.05207	0.05257	0.2748	0.1708	0.6144
m_2	1.000	1.000	1.000	1.000	1.000
m_4 ($10^{12}/\text{m}^2$)	79.41	76.88	61.72	65.14	2.584
α	4.135	4.042	16.96	11.12	1.588
B_{ave}	0.0158	0.0158	0.0165	0.0136	0.0168
B_{max}	0.0329	0.0307	0.0257	0.0237	0.0224
\bar{g}	1.000	1.000	1.000	1.000	1.000

The 1001 nodex1001 node surfaces in [23] were reduced to 512x512 in the current work so that an existing boundary element method [24, 25] and code can be used to solve the contact problem. Two additional experimentally measured surfaces are added and also considered (Surfaces 4 and 5). They were also scaled to be 100 micrometers in width on each side. Plots of all the surfaces are in the Appendix.

Next, the surface heights of each were scaled by a single factor such that all the surfaces had an RMS slope of unity. This same factor also adjusts the roughness by the same proportion. The resulting surfaces have the parameters listed in Table 2. Note that the values of m_2 and \bar{g} are both now unity due to the normalization. In addition, many of the other parameters are now within an order of magnitude.

The effective elastic modulus (E^*) between the surfaces is also set to unity. The surfaces are considered to be perfectly elastic in nature. As mentioned previously, a boundary element model is used to predict the real contact area of the surfaces as they are effectively brought into contact with a frictionless rigid flat surface.

3 Results and Discussion

As shown in Figure 1, the real area of contact curves as function of normalized pressure do not collapse onto one curve. The five surfaces immediately start to diverge after the surfaces are put into contact and do not begin to converge until they reach a dimensionless contact pressure of 2 which is associated with over 90% of the surfaces in contact. Surface 2 had the strongest response as a function of applied pressure and Surface 1 and 5 had the weakest responses over different ranges. Although the differences may visually appear small, they are as large as 50% in some locations on the curves. The differences in the results might be due to the anisotropic and random nature of real measured surfaces that preclude perfectly fractal, self-affine surfaces.

The differences might therefore be explained by how the structure of the surface changes as the scales are traversed. The spectrum of the surfaces are plotted in Figs. 2-3. A spectrum is a description of a

signal's (here a surface) amplitude at different harmonic scales, or wavelengths (frequency is the inverse of wavelength and defines the number of peaks per length). In this work the spectrum was calculated using a Fast Fourier Transform. Here the spectrums are plotted in two ways: first the spectrums are plotted simply as the amplitude as a function of the wavelength (see

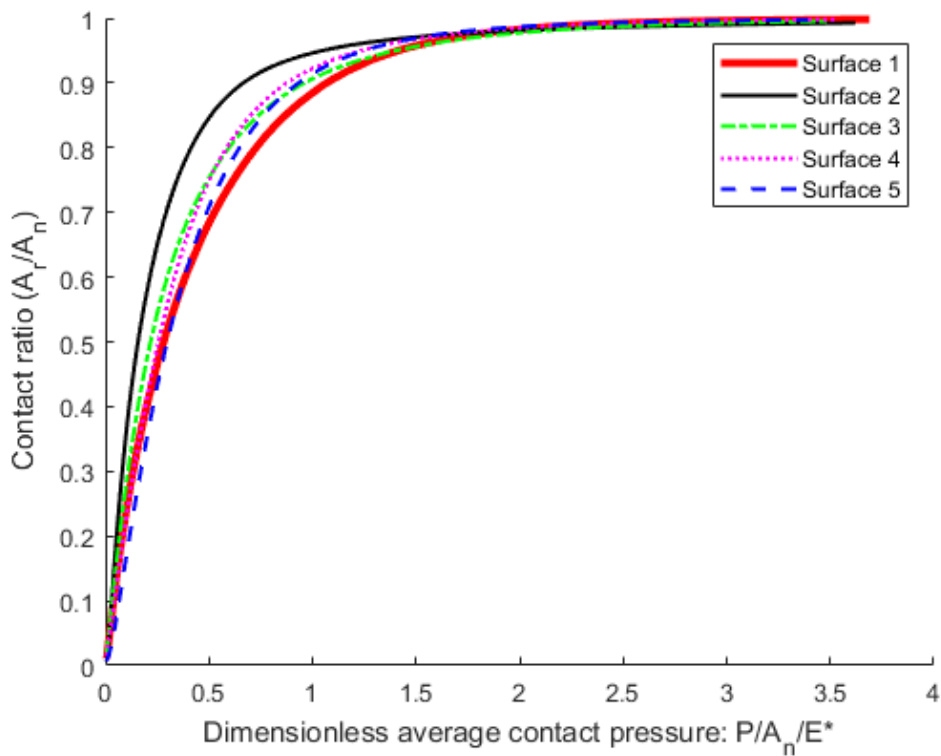


Fig. 1 Real contact area for each surface from BEM predictions

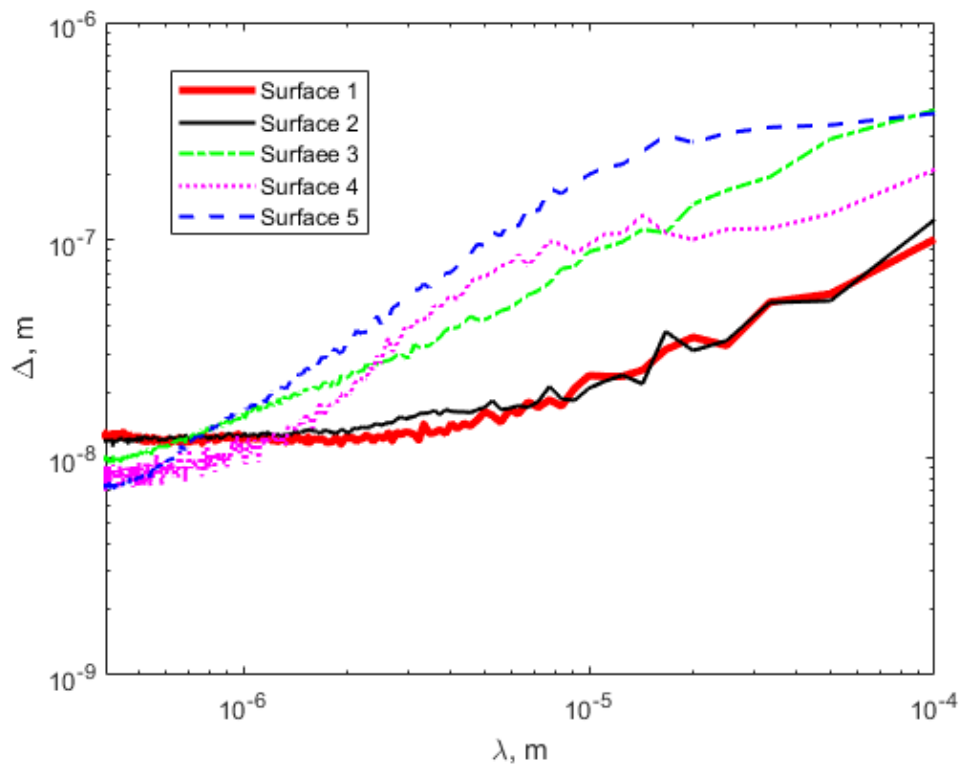


Fig. 2 Spectrum of each surface.

Fig. 2), next they are plotted by normalizing the amplitudes of the Fourier series by the wavelength at each scale (see Fig. 3). In previous literature the aspect ratio (amplitude to wavelength ratio) has been assigned the symbol, B [5, 26]. If B were constant across all scales,

this indicates that a surface's asperities (the peaks on a rough surface) have the same aspect ratio or shape across all scales. This structure would indicate a self-similar fractal surface. Figure 3 demonstrates that the normalized amplitude for each surface is divergent

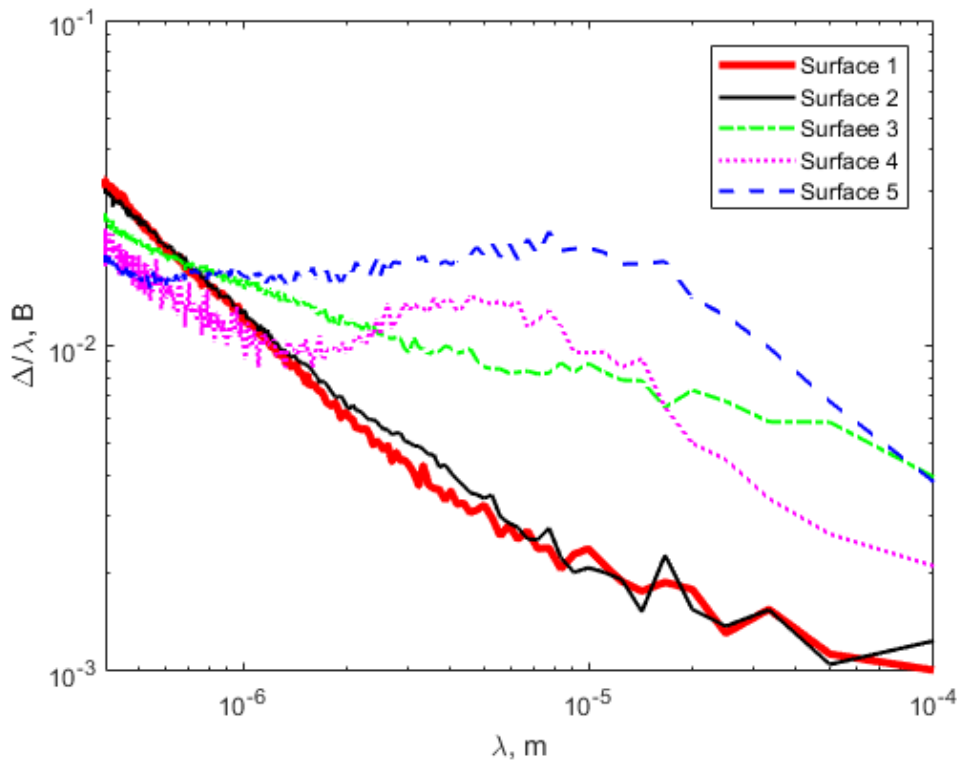


Fig. 3 Normalized spectrum of each surface.

from each other for wavelengths exceeding 10^{-6} m and non-constant at all length-scales. For most of the surfaces the ratio B appears to increase as the scale (wavelength) decreases. Surface 5 does have a shoulder in the data spanning between 300 nm and 10 μ m wavelength which you would expect in a self-similar structure.

However, a completely self-affine fractal surface would not experience the drop off seen at higher wavelengths, and would be represented by a straight line without deviation. The deviation seen here for normalized amplitude for the five RMS-equal surfaces indicates a likely vector for the divergence between traditional models and real surfaces.

To further explore the potential link between variable RMS roughness and surface contact response, the RMS slope (g) is plotted as a function of the surface height in Figure 4. For a certain truncation height (h) only the portion of the surface taller than h is used to calculate the RMS slope (g). As shown in Fig. 4, the RMS slope (g) varies based on the truncation height (h). Since only the taller peaks on the surface will be in contact at lighter loads and rest of the surface will only move into contact as the load increases, it stands to reason that the RMS surface roughness will only be dependent upon the surface area currently in intimate contact. In this way RMS surface roughness will vary throughout the loading of a real surface. We can call the RMS slope of the contacting surface the effective RMS slope. The data in Fig. 4 shows that the effective RMS slope will start at a higher value for lightly loaded

contacts and decrease gradually until approaching the RMS slope of the entire surface for heavier loads as expected. The effective RMS slope appears to approach the RMS slope of the entire slope at an h value of approximately $-\sigma$ or -2σ which is just after passing the mean height of the surface. The trends for each surface are complex, containing plateaus but are roughly monotonic. It is likely that this variation in the slope during loading is a direct cause of disparity between contact response of real, imperfect surfaces and computational models, and is a result of these natural surfaces lack of perfectly self-affine features.

Contact theories incorporating self-affine features remain one of the most critically important tools we use to understand how surfaces will generally behave when creating an interface. It is not surprising that the data set that is most nearly self-affine (surface 5) sat in-between all the other data sets at appreciable loads. However, there is always room for refinements. Moving forward it would be interesting to compare and evaluate the many existing rough surface contact mechanics models when real surface measurements are employed.

4 Conclusions

This work considers five different measured rough surfaces that are scaled such that they all have an equal RMS slope. A BEM method is used to predict the

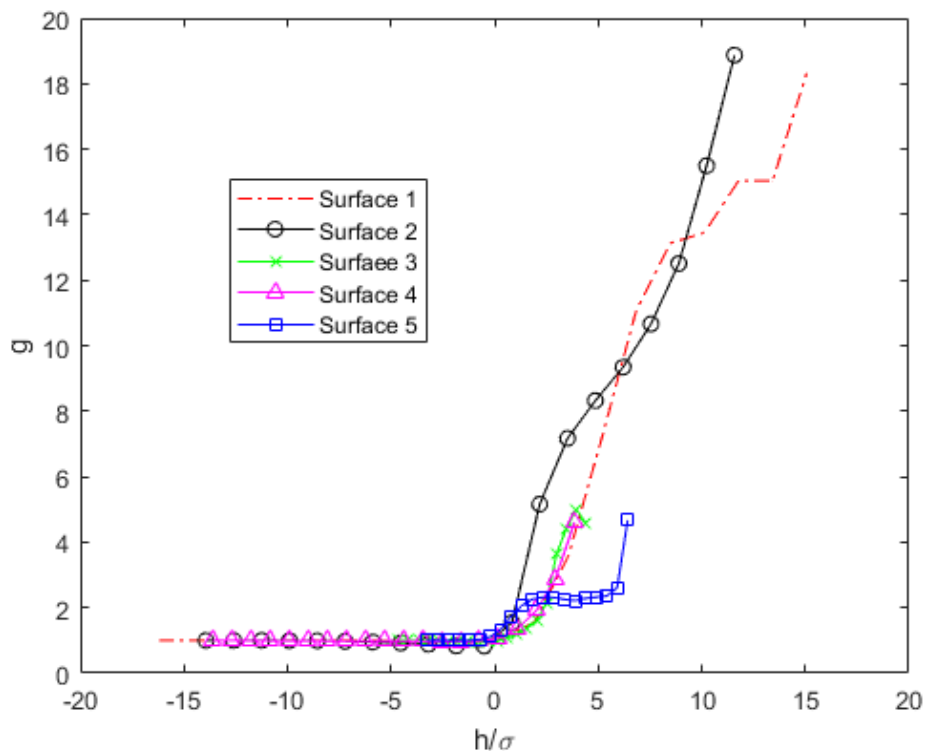


Fig. 4 Surface RMS slope as a function of truncation height.

real area of contact for these surfaces as a function of load. Based on some existing theories, the predicted real area of contact versus load curve of these surfaces should collapse onto one unified curve. However, they do not. This work also provides several possible reasons for this deviation. Measured surfaces are not perfect self-affine fractals that many of these theories are based on, and therefore this is probably why the theories do not hold for measured surfaces. The spectrums of the measured surface clearly show that they are not perfect fractals because the curves are not linear. In addition, it is also shown by using a truncation approximation that the RMS slope of the surface portion actually in contact (the real area of contact) can actually change non-linearly with load and area of contact. This too provides an explanation as to why the real contact area vs. load curves do not collapse.

5 Literature

1. Ciavarella, M., et al., *Elastic contact stiffness and contact resistance for the Weierstrass profile*. *J. Mech. Phys. Solids*, 2004. **52**(6): p. 1247-1265.
2. Greenwood, J.A., *Constriction Resistance and the Real Area of Contact*. *Brit. J. Appl. Phys.*, 1966. **17**(12): p. 1621-1632.
3. Kogut, L. and K. Komvopoulos, *Electrical contact resistance theory for conductive rough surfaces*. *Journal of Applied Physics*, 2003. **94**(5): p. 3153.
4. Wilson, W.E., S.V. Angadi, and R.L. Jackson. *Electrical Contact Resistance Considering Multi-Scale Roughness*. in *IEEE Holm Conference on Electrical Contacts*. 2008. Orlando, FL.
5. Wilson, W.E., S.V. Angadi, and R.L. Jackson, *Surface Separation and Contact Resistance Considering Sinusoidal Elastic-Plastic Multi-Scale Rough Surface Contact*. *Wear*, 2010. **268**(1-2): p. 190-201.
6. Barber, J., *Incremental stiffness and electrical contact conductance in the contact of rough finite bodies*. *Physical Review E*, 2013. **87**(1): p. 013203.
7. Kogut, L. and I. Etsion, *Electrical conductivity and friction force estimation in compliant electrical connectors*. *Tribology Transactions*, 2000. **43**(4): p. 816-822.
8. Jackson, R.L., E.R. Crandall, and M.J. Bozack, *Rough surface electrical contact resistance considering scale dependent properties and quantum effects*. *Journal of Applied Physics*, 2015. **117**(19): p. 195101.
9. Bush, A.W., R.D. Gibson, and T.R. Thomas, *The elastic contact of a rough surface*. *Wear*, 1975. **35**(1): p. 87-111.
10. Persson, B.N.J., *Elastoplastic contact between randomly rough surfaces*. *Physical Review Letters*, 2001. **87**(11): p. 116101.

11. Archard, J.F., *Elastic Deformation and the Laws of Friction*. Proc. R. Soc. Lond. A 1957. **243**: p. 190-205.
12. Campaná, C. and M.H. Müser, *Contact mechanics of real vs. randomly rough surfaces: A Green's function molecular dynamics study*. EPL (Europhysics Letters), 2007. **77**(3): p. 38005.
13. Putignano, C., et al., *The influence of the statistical properties of self-affine surfaces in elastic contacts: A numerical investigation*. Journal of the Mechanics and Physics of Solids, 2012. **60**(5): p. 973-982.
14. Yastrebov, V.A., G. Anciaux, and J.-F. Molinari, *The role of the roughness spectral breadth in elastic contact of rough surfaces*. Journal of the Mechanics and Physics of Solids, 2017. **107**: p. 469-493.
15. Greenwood, J.A. and J.B.P. Williamson, *Contact of Nominally Flat Surfaces*. Proc. R. Soc. Lond. A, 1966. **295**(1442): p. 300-319.
16. Whitehouse, D.J., Archard, J. F., *The Properties of Random Surfaces of Significance in their Contact*. Proc. R. Soc. Lond. A, 1970. **316**: p. 97-121.
17. McCool, J.I., *Relating Profile Instrument Measurements to the Functional Performance of Rough Surfaces*. ASME J. Tribol., 1987. **109**(2): p. 264-270.
18. Sayles, R.S. and T.R. Thomas, *Surface Topography as a nonstationary Random Process*. Nature, 1978. **271**(2): p. 431-434.
19. Zhang, X. and R.L. Jackson, *An analysis of the multiscale structure of surfaces with various finishes*. Tribology Transactions, 2017. **60**(1): p. 121-134.
20. Zhang, X., Y. Xu, and R.L. Jackson, *An analysis of generated fractal and measured rough surfaces in regards to their multi-scale structure and fractal dimension*. Tribology International, 2017. **105**: p. 94-101.
21. Ghaednia, H., et al., *A review of elastic-plastic contact mechanics*. Applied Mechanics Reviews, 2017. **69**(6): p. 060804.
22. Vakis, A.I., et al., *Modeling and simulation in tribology across scales: An overview*. Tribology International, 2018. **125**: p. 169-199.
23. Jackson, R.L. and I. Green, *On the Modeling of Elastic Contact between Rough Surfaces*. Tribology Transactions, 2011. **54**(2): p. 300-314.
24. Xu, Y. and R.L. Jackson, *Boundary element method (BEM) applied to the rough surface contact vs. BEM in computational mechanics*. Friction, 2019. **7**(4): p. 359-371.
25. Xu, Y. and R.L. Jackson, *Statistical models of nearly complete elastic rough surface contact-comparison with numerical solutions*. Tribology International, 2017. **105**: p. 274-291.
26. Jackson, R.L., *An Analytical Solution to an Archard-type Fractal Rough Surface Contact Model*. Trib. Trans., 2010. **53**(4): p. 543 - 553.

Appendix:

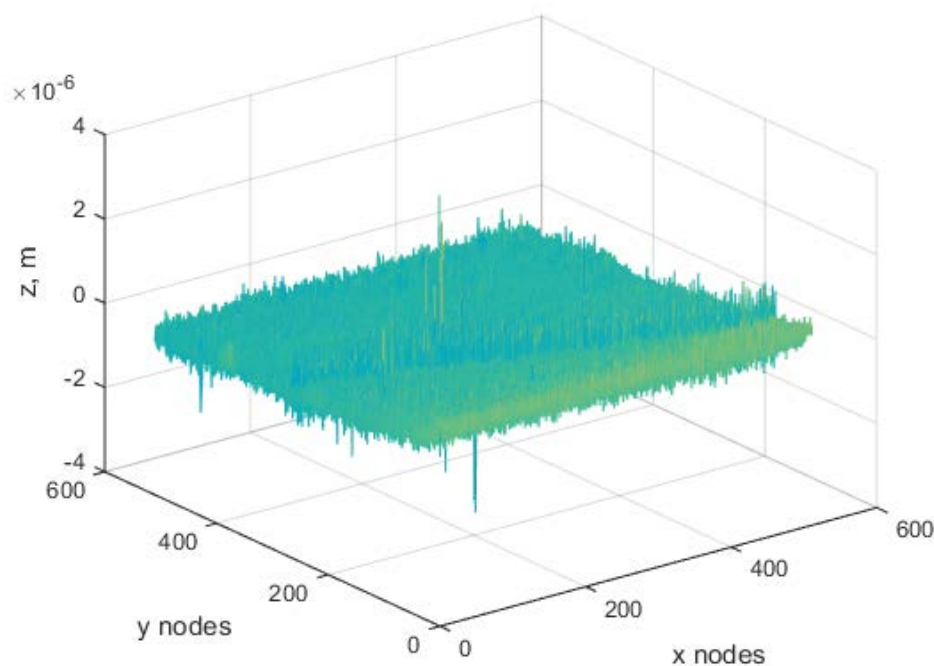


Figure A1: 3-D plot of Surface 1

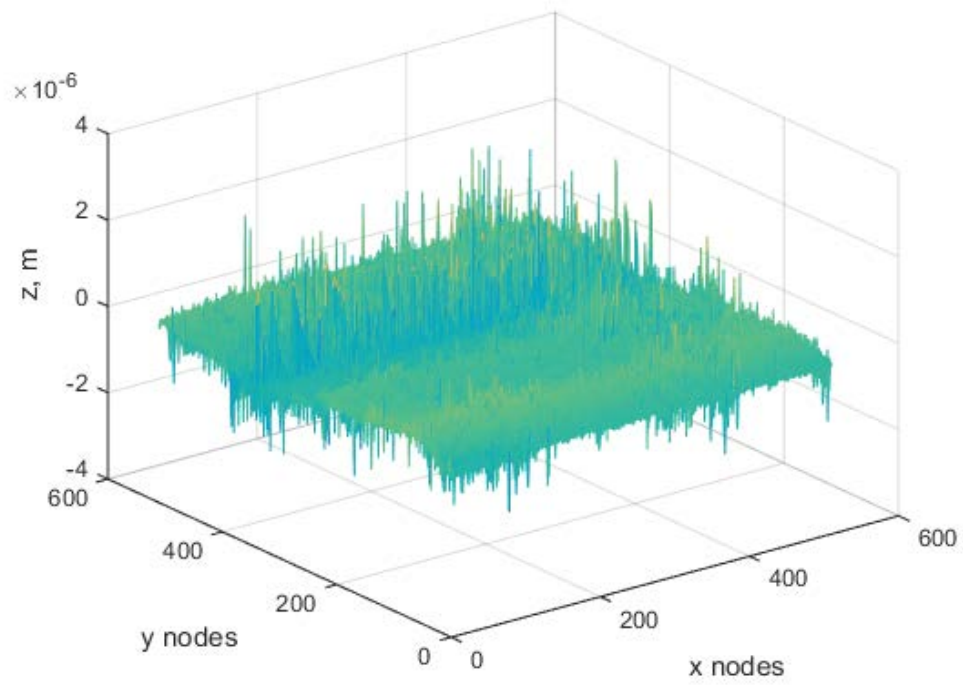


Figure A2: 3-D plot of Surface 2

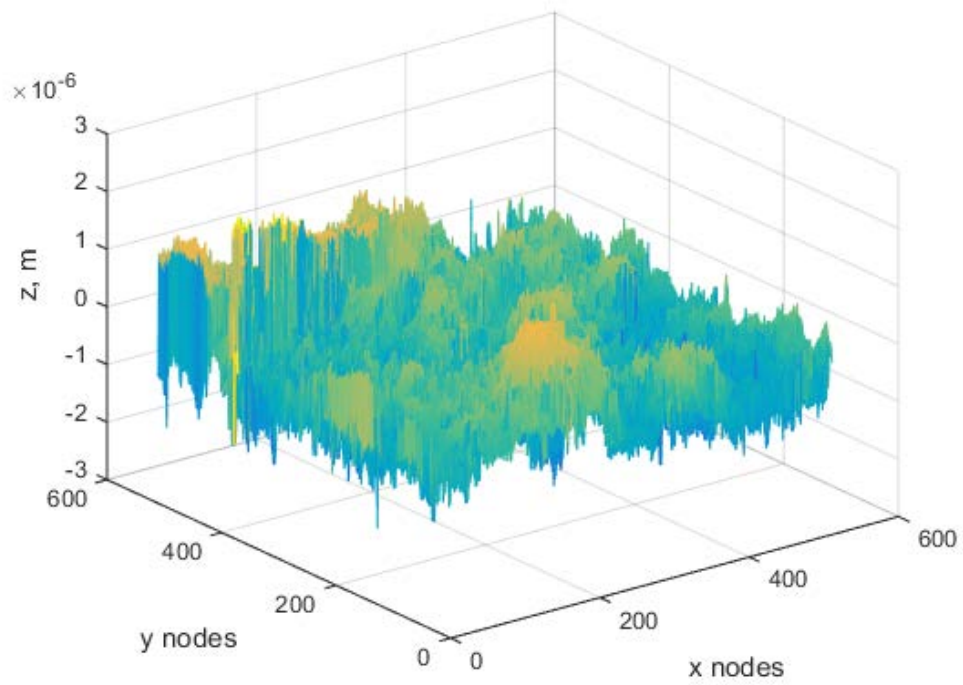


Figure A3: 3-D plot of Surface 3

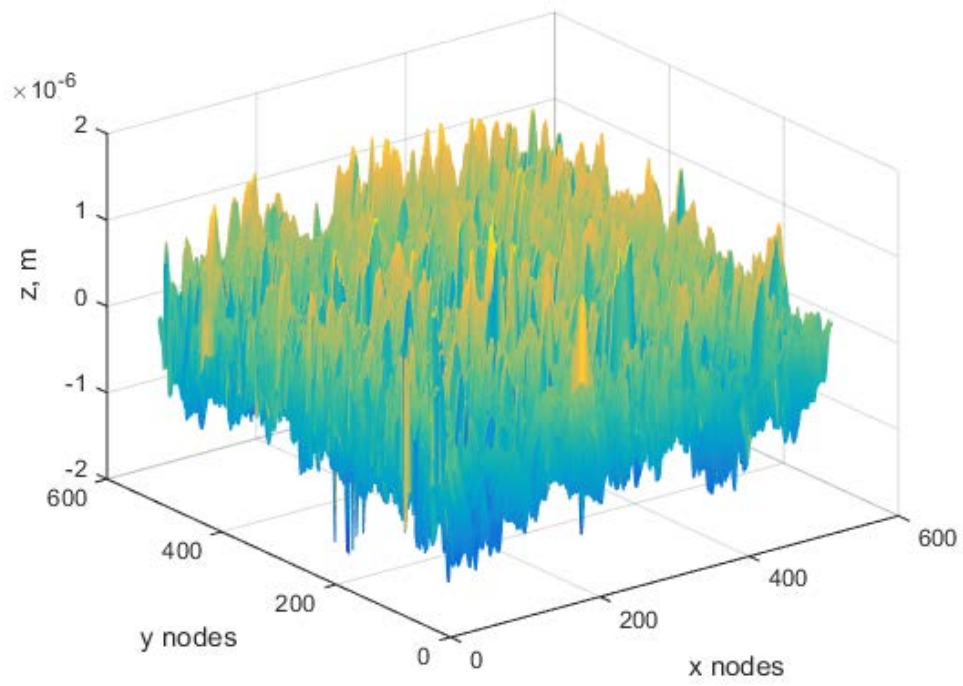


Figure A4: 3-D plot of Surface 4

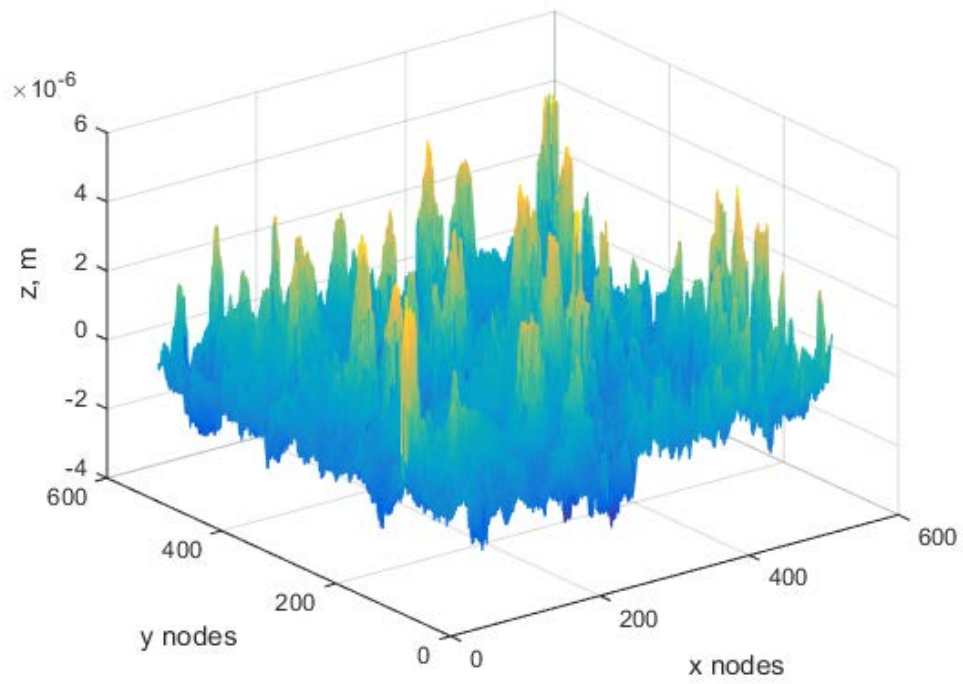


Figure A5: 3-D plot of Surface 5

Press-fit Whiskers Risk Assessment by Simulation

Marius Tarnovetchi, Vitesco Technologies, Timisoara, Romania, marius.tarnovetchi@vitesco.com

Francois Le-Rest, Continental AG, Toulouse, France, francois.le-rest@continental-corporation.com

Hans-Peter Tranz, Continental AG, Regensburg, Deutschland, hans-peter.tranz@continental-corporation.com

Abstract

The press-fit technology is a solder-less electrical connection which offers many advantages to the conventional soldering technology. Since the restriction of lead usage in electronic equipment, also the surface finish of press-fit contacts has been migrated to pure tin finishes. The press-fit technology, by definition, relies for the electrical contact in the mechanical contact pressure between Pin and Printed Circuit Board (PCB). The presence of free tin in the transition area of the contact, with an undesirable mechanical stress condition, may grow into long whiskers, which can lead to electrical short circuits or parasitic current flows. The present work describes a method based on finite element analysis (FEA) to evaluate the stress field in the contact area of the Pin to the PCB, and to assess the risk for whiskers for the given Pin - Plated Through Hole (PTH) combination.

Key words: whiskers, tin, press-fit, FEA, finite element analysis, simulation, risk assessment.

1 Introduction

1.1 Background

Tin whiskers are electrically conductive, crystalline structures of tin that under specific environmental and mechanical conditions may grow from the surfaces where tin is used as protective layer. If long enough, they may cause a short circuit to the adjacent circuit elements with a different electrical potential, eventually leading to catastrophic failures [1].

Despite the comprehensive research in the field of tin whiskers, the phenomena behind the whisker growth is yet not fully understood but seems to be related to the compressive stress in the superficial layer of the tin-plated parts. As reported, the whiskers are caused by the formation of inhomogeneous intermetallic phases [2,3].

In the press-fit technology for electronic contacts, there are several studies for tin whiskers describing the growth mechanisms and the severity of whiskering for different geometrical shapes of the existing press-fit zones [4,5].

Preconditions for the tin whiskers' formation are not only the presence of free tin and available space for whiskers to grow (gap larger than 1 μm), but the exceed of certain mechanical stress values and local stress gradients. Studies on general whisker theory indicates that the excess of compressive stresses larger than -8 to -15 MPa in combination with stress gradients beyond -35 to -50 MPa/ μm , lead to whisker formation [2,6].

The scientific knowledge of the established whisker theory on mechanical stress and stress gradients was

transferred to the press-fit technology. Finite element analyses have been performed to determine the likelihood and the critical positions for whiskering, considering the global and local stress results for the given press-fit zone - plated through hole combination. [7].

1.2 Motivation

The main purpose of the finite element simulation is to determine the local deformation of the PCB hole when the pin is inserted and the stress gradient on the surface of the PTH.

As shown in **Figure 1**, to capture whisker-size effects, the study [7] was using a domain discretization with 1 μm elements size in the contact region of the pin - plated hole.

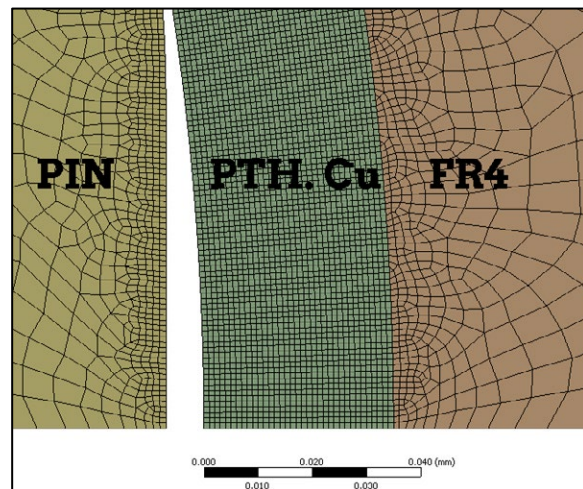


Fig. 1 – Pin-PTH top view mesh with 1 μm element size in the contact area

Due to the size of the finite element model and the long calculation time, the described technique [7] consisted in performing a coarse 3D simulation of the press-fit connection, followed by a transversal 2D cut of the domain in the highest stress region. The 2D model was calibrated to reassemble an equivalent stiffness with the 3D model. **Figure 2** shows the stress distribution of the press-fit connection of the 3D analysis (left) and the 2D cut model (right).

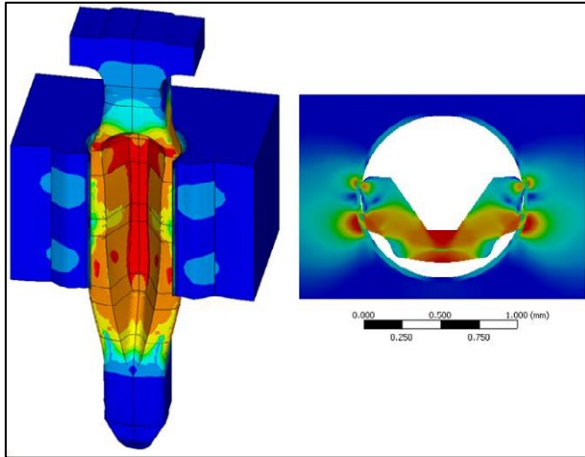


Fig. 2 – Stress plot of the press-fit connection

The drawback of this method is the subjectivity of picking the correct position in vertical direction for the 2D cut and the stiffness calibration from 3D to 2D. It may work for specific press-fit zones without difficulties, but it may require artificially induced elements for stiffness compensation of various pin geometry features, such as cavities or holes.

The current work describes an evolution of the 2D cut method [7] using the submodeling technique in the contact zone. Similarly, a coarse 3D simulation is performed to retrieve the global deformation and stress state, followed by a local 3D cut of the volume of interest, where a finer mesh is going to be used. All this to avoid the expense of a large-size mesh model of the complete Pin - PTH assembly.

The advantage is having a stiffness-balanced local model with a fine enough mesh that can capture the micrometric scale effects of whiskering.

2 Simulation Model

2.1 Method

The submodeling is an easy and efficient method to get accurate results from a finite element model without having the hassle of a fully meshed model with super-small elements. The method dates from the early days of FEA when the computing power was limited and the engineers did not have the luxury to refine the mesh in the areas of concern, not even thinking of creating a full-size fine-mesh model. The way it was accomplished implied that a local refined-mesh model was

realized only in the area of interest, and a coarse-mesh model for the whole structure. The displacements from the coarse model were applied as boundary conditions to the refined model. The method is based on St. Venant's principle: "... the difference between the effects of two different but statically equivalent loads becomes very small at sufficiently large distances from load."

As the computers got more powerful, to the areas of interest was just applied a mesh refinement in the full part model, and the use of submodeling technique decayed in the simulation communities. As of today, the localized mesh refinement is still the best option for localized stress analysis [8].

In the simulation of a press-fit connection there are some major drawbacks for either of the two methods:

- A fully fine-mesh model of a volume of $2 \times 2 \times 1.6$ mm with $1 \mu\text{m}$ mesh size would require more than 1 billion elements, inappropriate for the current available computing power. A fine mesh only at the interface Pin-PTH may still require over 20 million elements, not very attractive for optimization studies.

- The submodel must be carefully constructed, as the area of interest is exactly at the interface Pin-PTH, where contact elements must be used. The cut boundary conditions must be carefully chosen to avoid degree-of-freedom constraints applied directly to the contact elements.

The current FEA study was made using ANSYS Workbench 2019 R3, but the method is not limited to the software selection, the only prerequisite being the capability of interpolating nodal results from one model to another.

1.2 Geometry

The 3D geometry of the current study is shown in **Figure 3**, consisting in a generic "Eye of the Needle" pin (left) assembled in ANSYS SpaceClaim with a generic 6-layer copper 1.6 mm thick PCB (right).

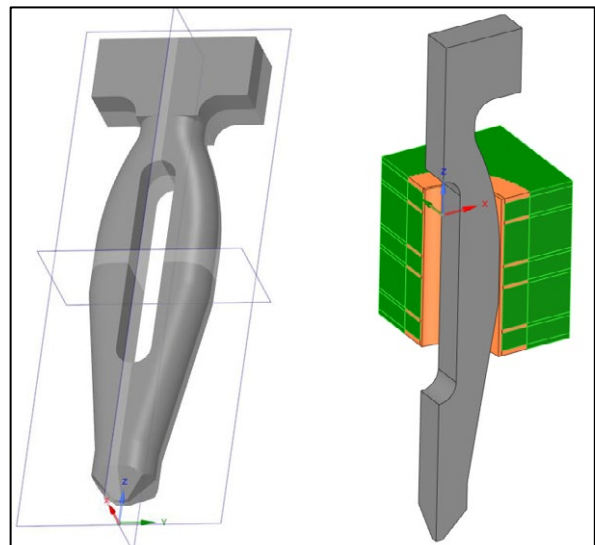


Fig. 3 – Pin geometry (left) and the assembly Pin-PCB (right)

As the Computed Aided Design (CAD) model represents an ideal pin, symmetrical to the vertical planes XZ and YZ, the FEA model will take advantage for the model size reduction, by using only a quarter of it.

2.3 Material Properties

The material properties in any finite element analysis are crucial for the accuracy of the results. For the stress analysis of press-fit connections, we are mainly interested in the elastic moduli, yield strength, tangent moduli and ultimate strength, respectively.

The copper and the dielectric layers of the PCB are modelled discretely and use a generic set of material properties based on supplier test data. As the interest is the impact of the press-fit pin to the plated through hole stress, the construction and the material properties of the PCB are kept fixed among these studies.

The pin though, sees a wide range variation in elasticity properties. Although its base material is a Copper-Tin alloy, the chemical composition differs from supplier to supplier, implying also a different mechanical behavior. Even more, for the same part number, a supplier may use several alloys with similar, but different properties. Therefore, for any press-fit connection simulation it is advisable to characterize the pin mechanical behavior under compression loads.

2.3.1 Pin Elasticity Test

A standard test method [9] was developed a for the pin elasticity, to characterize its compressive behavior.

The test is performed using a compression tool of semi-cylindrical shape, according to the through hole diameter, as shown in **Figure 4 left**. The amount of displacement and elasticity recovery characteristics are measured taking into consideration the maximum and minimum diameter of the through hole, **Figure 4 right**.

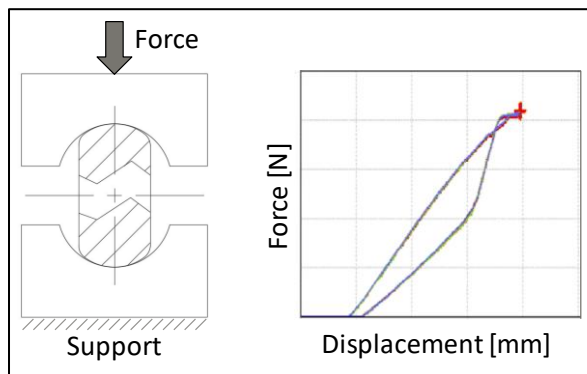


Fig. 4 – Compression test setup (left) and test data (right)

Understanding the Force - Displacement diagram is the key in the calibration of the simulation model. To emphasize it, the same test curve is shown now in **Figure 5**, where the following points are marked:

- The start of the compression, usually when the force exceeds a minimum threshold value set to the equipment.
- The point where the stress reaches the proportional limit of the material. Up to this point, the stress is proportional to the strain, according to the Hooke's law. The gradient of the AB segment indicates the elastic modulus of the pin material. From here, the force is ramping towards point C", the pin exhibiting both elastic and plastic deformation.
- The point where the pin's material reaches the yield strength; very important when later analyzing the plastic deformation of the pin. From here, the pin is deforming mainly in plastic domain and is ramping towards point D with the tangent modulus of the material.
- End of the compression displacement, when the tool has reached its final diameter. It is advised to perform the test in both conditions, minimum and maximum hole diameter, to check that the pin is appropriate for the standard hole tolerances.
- The compression tool retracts, the pin deforming elastically. This point can be used to verify the plasticity calibration, as the segment AE represents the permanent plastic deformation of the pin.

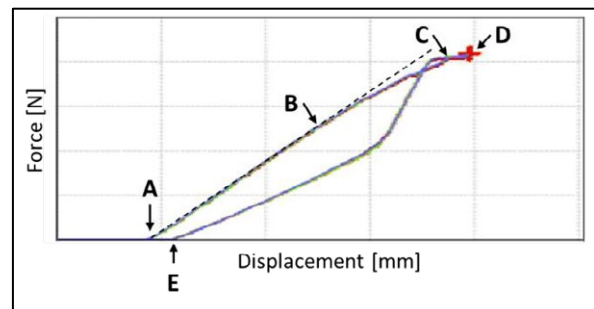


Fig. 5 – Compression characteristic diagram

Although looking straight forward, the results diagram of this case shows a glitch of the test data, as the returning path DE intersects the pressing path AD. For the current calibration of the FEA model, only the AD path was used, but for deeper understanding of the phenomena, this result is under investigation. It is the perfect example of FEA engineers questioning test data and test engineers not trusting the simulation results.

2.3.2 Simulation of Pin Elasticity Test

The elasticity test setup is replicated with a simulation model, using a bilinear plasticity model for the pin material. As the geometry of the investigated pin is symmetrical, only a quarter of the model was discretized in FEA, as shown in **Figure 8**. The elements size should be fine enough to capture the plastic strains, but not exaggeratedly small.

The intent is to calibrate the elastic modulus, the yield strength and the tangent modulus, and a good starting point is to use datasheet material properties.

Firstly, is used only the elastic behavior of the material, to calibrate the compression rate to the slope of the BC segment of the test data. When the fit is good enough, the plasticity in the model is enabled and the yield strength and tangent modulus are alternately adjusted until reaching the desired accuracy of the compression diagram. The integration time step should be adequately chosen to capture the plasticity starting point. Note in **Figure 6** the current calibration, with solid blue line the test data, and the calibrated FEA model with orange dotted line. Both, the elasticity and plasticity slopes of the test data were matched, and the pin generated the same reaction force at the end of the compression, as in the physical test.

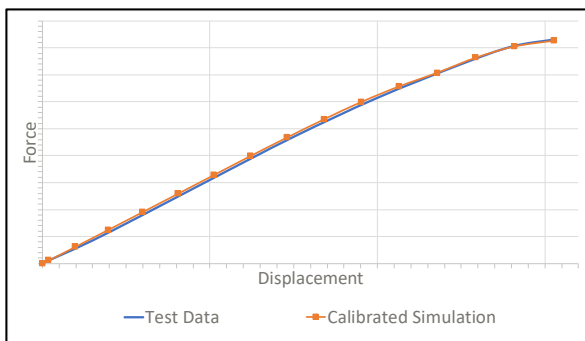


Fig. 6 – Calibration data

Some remarks and lessons learned from personal experience and other distinguished fellow analysts [10] regarding the correlation of a simulation model to a test result:

- The test is not always right!
- Too much correlation can ruin you!
- Correlation metrics are bad!

If the calibration process seems not to go in the expected direction, think what other parameters may influence your result: elements order, friction coefficients, boundary conditions, geometrical simplifications. Check also if the CAD model resembles the real geometry of the pin. A 3D-scan overlapped to the existing CAD model may show unexpected differences. Cross-sections are always welcomed to verify the symmetry of the insertion, the contact lengths, the state of deformation, and the way the pin indents the PTH.

3 Pin Insertion Simulation

A coarse mesh model may be the only currently viable option to reach simulation convergency for the pin insertion into the PCB plated hole. The challenges are coming from the non-linearities involved, such as contact elements, material plasticity and large deformations.

The results give valuable insights about the stress level and deformation, as shown in **Figure 7**.

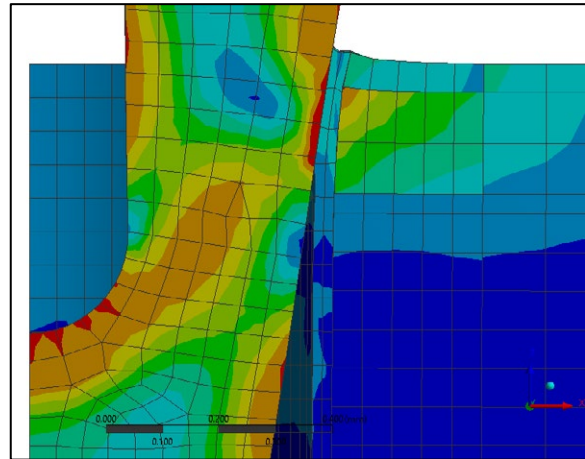


Fig. 7 – Stress plot during the insertion phase

The authors consider that developing a simulation method for the pin insertion with a micrometric-size mesh in the contact area, the next step in simulation-based whisker risk assessment. The target is to include also the longitudinal effects of the insertion force.

4 Pin Compression Simulation

To overcome the issues of the pin insertion simulation described in **Paragraph 3**, an alternative method was developed, more robust, but changing the perspective of applying the stress field in the Pin - PTH assembly. Instead of inserting the pin, a transversal compression is applied to the pin by the PCB, similarly to the elasticity test described in **Paragraph 2.3.1**.

As the press-fit connection is mainly realized by radial mechanical forces, the longitudinal insertion force is neglected for the moment.

The simulation model is setup in the same manner as the pin elasticity test, replacing the compression tool with the PCB model. As shown in **Figure 8 left**, the mesh size was kept in the optimal balance, targeting the correct plastic deformation and computational speed, having in mind that a submodel for local stress analysis will follow. In **Figure 8 right**, is shown the displacement applied to the PCB to compress the pin until the designated hole diameter (minimum or maximum tolerance case).

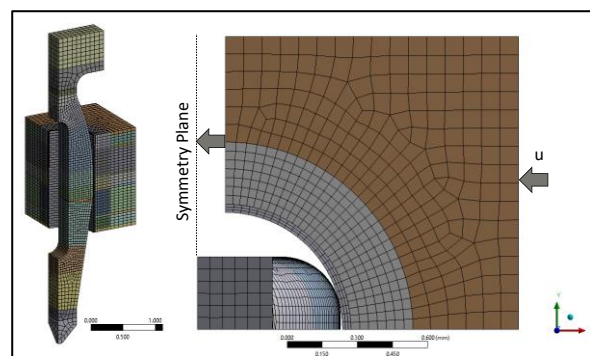


Fig. 8 – Compression FEA model (left) and boundary conditions (right)

The solution of the coarse model shown in **Figure 9** matches the observations from physical cross-sections of “Eye-of-the-Needle” pins: the deformation is low, without excessive indentation in the PTH surface.

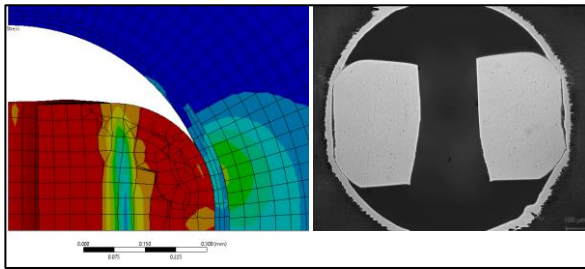


Fig. 9 – Cross-section deformation, simulation (left) vs. physical test (right)

The pin deformation is shown in **Figure 10**, pointing with red color the areas which exceed the material’s yield strength and exhibit permanent plastic deformation.

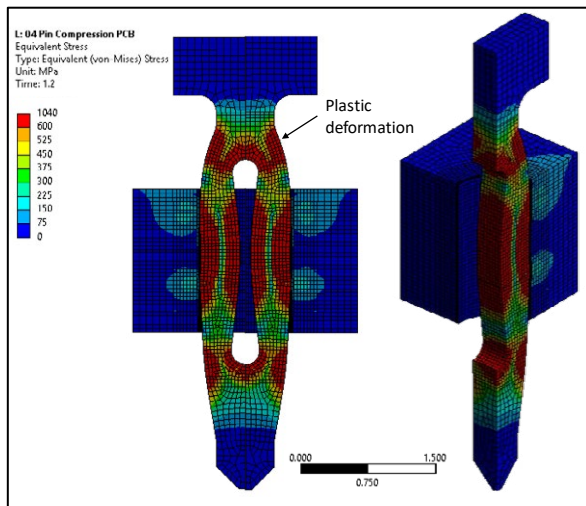


Fig. 10 – Equivalent stress plot

Reviewing the contact status pressure plot in **Figure 11 left** and the minimum principal stress (compressive) on the PTH in **Figure 11 right**, there is the clear indication of the actual contact area, and we can easily identify the best suited locations for the submodel boundaries.

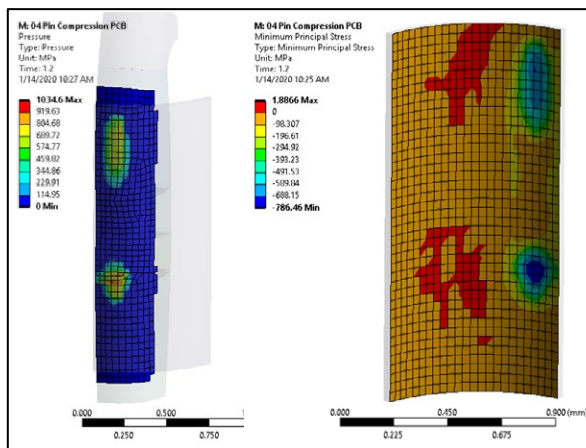


Fig. 11 – Pin contact pressure (left) and PTH compressive stress (right)

As shown in **Figure 12**, using a geometrical model derived from the full model, and defining a micrometric-size mesh, the displacements from the full model are interpolated on the cut boundary conditions of the Submodel.

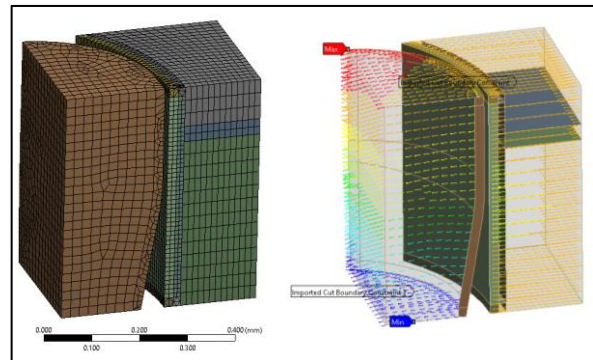


Fig. 12 – Submodel mesh (left) and interpolated boundary conditions (right)

Figure 13 shows the contact status (left) at the interface Pin-PTH and the contact pressure (right). This is a good indication for the stress gradient analysis, as the critical location for whiskering is at the boundary of the contact patch. Regarding the contact pressure, to be recognized that the -8 to -15 MPa compressive stress limit for general whisker growth [2,6] is by far exceeded in the case of press-fit connections.

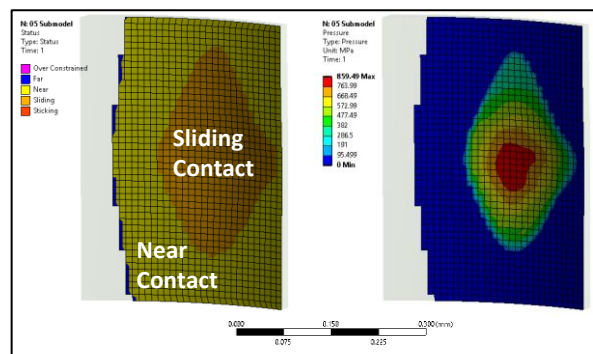


Fig. 13 – Contact status (left) and contact pressure (right)

To analyze the tangential stress gradient, a cylindrical coordinate system (x =radial, y =tangential, z =vertical) was defined on the PTH axis. **Figure 14** plots the stress

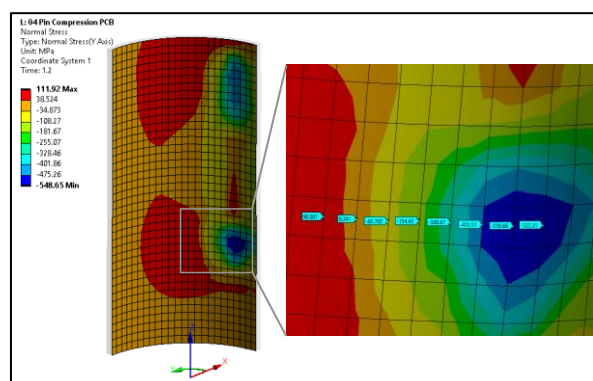


Fig. 14 – Stress plot in tangential direction on the PTH surface

in tangential direction. For stress analysis, nodal paths were defined through the location of maximum compressive stress (dark blue area) in horizontal (azimuthal, Y) and vertical (Z) directions.

The graphs on **Figure 15** reveal a maximum compressive stress gradient of $-5.43 \text{ MPa}/\mu\text{m}$ for a $40\mu\text{m}$ mesh size. This mesh size is proper for global press-fit connection stress analysis but too coarse to capture whisker-size effects. To capture whisker-size effects, the elements size must be comparable to the whisker diameter, typically $1\text{--}2 \mu\text{m}$ [7].

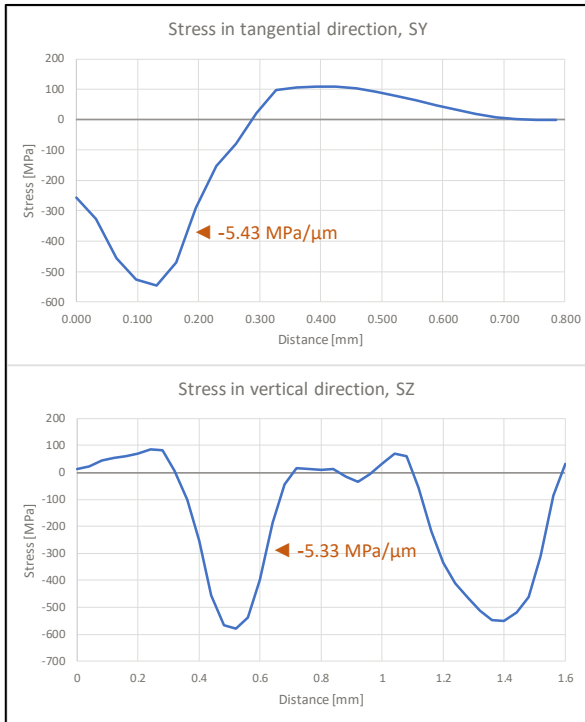


Fig. 15 – Nodal stress results on tangential (top) and vertical (bottom) direction respectively

The beauty of the submodeling method is that it allows creating multiple submodels, in different regions of the structure, and even more, cascading submodels, having sequential steps of mesh refinement. For this analysis, the mesh size was reduced from $40 \mu\text{m}$ to $10 \mu\text{m}$ and finally $2 \mu\text{m}$, as shown in **Figure 16**.

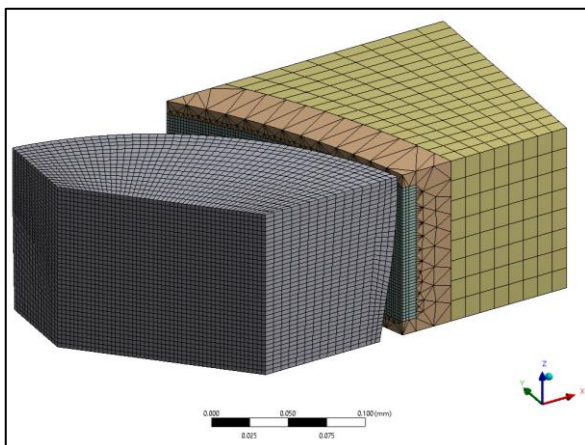


Fig. 16 – Second-level submodel

Similarly, to the global model, in a cylindrical coordinate system was defined a horizontal (azimuthal, Y) nodal path, in the high stress area of the PTH surface. In **Figure 17** we identify for the $2 \mu\text{m}$ mesh size, two locations of high stress gradient, closely to the pin's mid-plane (location A), and towards the exit of the contact area (location B).

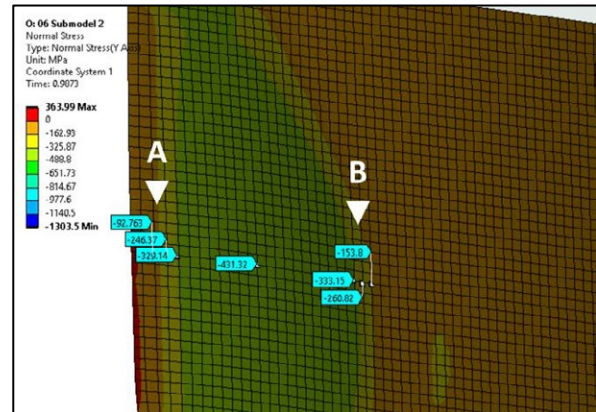


Fig. 17 – Stress plot in tangential direction on the PTH surface

Plotting the nodal stresses onto the defined path we can see in **Figure 18** that the minimum principal stress (S3) is exceeding, as expected, the normal stress in tangential direction (SY). As a parenthesis, this is a common fault in strain-gauge measurements when measuring only axial strains and overlooking the principal strains.

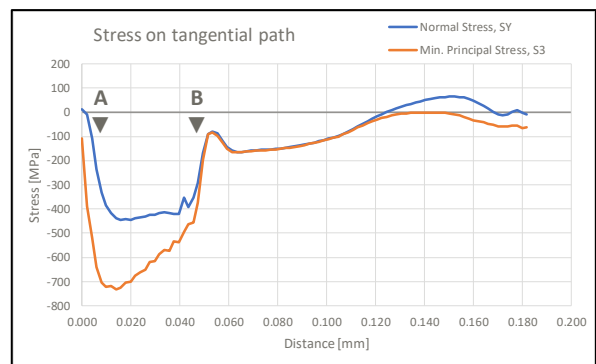


Fig. 18 – Nodal stress results in tangential direction on the PTH surface

Analyzing the gradients for both stresses, the tangential and minimum principal respectively, we see in **Table 1** that the simulated values are larger than the considered limit of -35 to $-50 \text{ MPa}/\mu\text{m}$ [7] and therefore the risk of whisker formation for the current studied geometry seems to be confirmed.

Table 1 - Compressive Stress Gradient

Stress Gradient [MPa/ μm]	Location A	Location B
Tangential, dSY/dx	- 65.5	-62.3
Min. Principal, $dS3/dx$	-142.0	-90.5

5 Conclusions

The submodeling method applied to the press-fit pin connection analysis is very attractive regarding the accuracy of the stress results, the cascading refinement option and the efficiency of the calculation time. It is a step beyond the 2D cut method developed for the local deformation and stress analysis of the plated through hole [7]

Being only a transversal compression, the current simulation setup does not include the longitudinal effects of the insertion force, especially at the entrance side of the PTH, where whiskers are more likely to be seen. The authors of this article consider the vertical insertion simulation with a micrometric size mesh as a next step in our continuous research in simulation-based whisker risk anal.

6 Literature

- [1] NASA Tin Whisker (and Other Metal Whisker) Homepage: <https://nepp.nasa.gov/whisker/background/index.htm>
- [2] M. L. Sobiech, Whisker formation on Sn thin films, Dissertation an der Universität Stuttgart, 2010.
- [3] T. Kato, C. A. Handwerker, J. Bath, Mitigating Tin Whisker Risks, Wiley, 2016.
- [4] H.-P. Tranitz, S. Dunker: Growth Mechanisms of Tin Whiskers at Press-in Technology. Proceedings of IPC APEX EXPO, San Diego, 2012.
- [5] H.-P. Tranitz, T. Schmidt, P. Jaeckle, T. Gottwald, H. Woldt, H. Eicher, W. Neef, R. Vodiunig, U. Pape: Einpresstechnik in Cu/OSP-Oberflächen – eine Variante mit Zukunft?, PLUS 05, 2015.
- [6] M. Sobiech, J. Teufel, U. Welzel., E.J. Mittemeijer, W. Hügel, Stress relaxation mechanisms of Sn and SnPb coatings electrodeposited on Cu: avoidance of whiskering, Journal of Electronic Materials (2011) 40: 2300.
- [7] H.-P. Tranitz, M. Tarnovetchi, Whisker growth at press-fit connections, Proceedings of the Albert-Keil-Kontaktseminar, 2017
- [8] E. Miller, Submodeling in ANSYS Mechanical: Easy, Efficient, and Accurate, PADT, Inc. – The Blog, August 2013
- [9] IPC-9797, Press-Fit Standard for Automotive Requirements and Other High-Reliability Applications, May 2020
- [10] G. Goetchius, The Seven Immutable Laws of CAE/Test Correlation, Sound & Vibration Magazine, June 2007

The mathematical model of a short arc at the blow-off repulsion of electrical contacts during the transition from metallic phase to gaseous phase

S.N. Kharin, T. Nauryz, Institute of Mathematics and Mathematical Modeling, Almaty, Kazakhstan, staskharin@yahoo.com

Abstract

The mathematical model describing the dynamics of temperature field in electrical contacts at the initial stage of a blow-off repulsion is presented. It is based on the Stefan problem for the disk of a short arc and two spherical domains for the liquid and solid zones. All coefficients in the equations such as the thermal and electrical conductivities, density, thermal capacity are dependent on the temperature. The analytical solution of this problem is obtained using the similarity principle. The results of calculation are compared with the data obtained in published papers and with the experimental data.

1. Introduction

Mathematical modeling of the electrical arc is very important to understand its dynamics and to estimate arc parameters because experimental methods give as a rule only the resulting information about arcing and arc erosion because of a fleeting process. General models describing phenomena in the arc plasma are based on the systems of partial differential equations of the magneto-hydrodynamics (MHD) [1] – [4]. These models are too complicated for the practical investigation of the arc dynamics in electrical contacts. The non-stationary model presented in the paper [5] describes temperature and electromagnetic fields in a short electrical arc taking into account near-electrode phenomena. However, its application is also not so simple.

The arc appearing at blow-open contact repulsion has specific particular qualities conditioned by the electromagnetic and metallic vapor pressure. The non-stationary model of the dynamics of repulsion is presented in the paper [6]. It was found that the metallic vapor pressure plays a very important role in the process of the repulsion. However, this model has two drawbacks. Firstly, in this model there was no heat equation for the arc, and secondly, all the coefficients appearing in the model, such as thermal and electrical conductivities, heat sources, heat capacitance etc. were assumed constant. However, for a high current the temperature dependence of all these coefficients is very essential, thus this model should be corrected, and this idea is the main aim of this paper.

2. Mathematical model

At the initial stage of the blow-off repulsion, when the arc is burning in the metal-dominated phase with following transition to the gas-dominated phase, it can

be considered as a short arc, i.e. the occupied by the arc domain D_A has the form of a thin disk which radius $r = r_A(t)$ is much greater than the thickness $h = h(t)$ (Fig. 1)

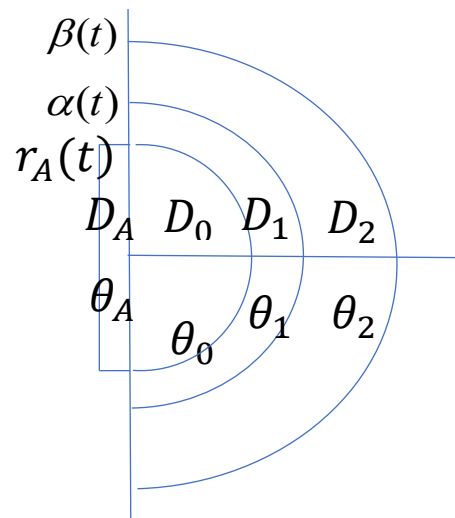


Fig.1. The axial contact cross-section of the spherical domains. D_A - the disk occupied by the arc, D_0 - the Holm sphere of the ideal conductivity, D_1 - the sphere of metallic vapours, D_2 - the sphere of liquid metal, $r > \beta(t)$ - the solid zone

The equation for the temperature field of the arc $\theta_A(r, t)$ can be written in the form

$$c_A(\theta_A)\gamma_A(\theta_A)\frac{\partial\theta_A}{\partial t} = \frac{1}{r}\frac{\partial}{\partial r}\left(\lambda_A(\theta_A)r\frac{\partial\theta_A}{\partial r}\right) + \frac{j^2}{\sigma(\theta_A)} - W_r(\theta_A) - P(r, t) \quad (1)$$

Here $c_A(\theta_A)$, $\gamma_A(\theta_A)$, $\lambda_A(\theta_A)$, $\sigma_A(\theta_A)$ are the coefficients of the arc heat capacity, density, thermal and electrical conductivity correspondingly,

$$j = \frac{I(t)}{\pi r_A^2(t)}$$

is the arc current density, $W_r(\theta_A)$ and $P(r,t)$ are the volumetric arc power radiation and power losses due to the arc heat conduction into contacts.

The temperature dependence of the coefficients [7] is presented in Fig. 2 and Fig. 3

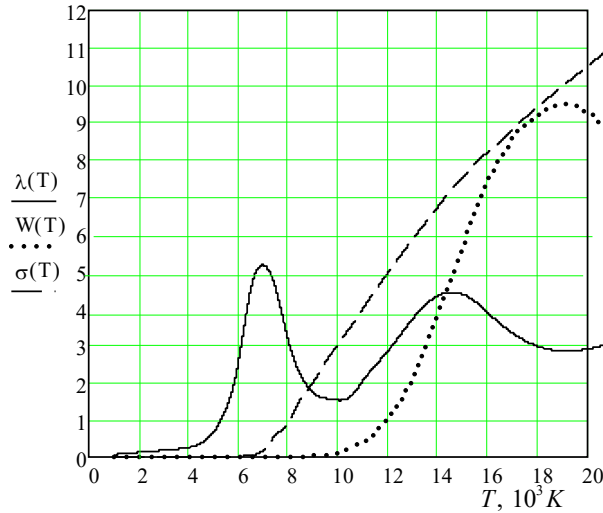


Fig. 2 Temperature dependence of the thermal and electrical conductivity and radiation losses for the arc burning in air

λ (W/mK), σ ($10^3 \Omega^{-1}m^{-1}$) and W_r ($10^9 W/m^3$)

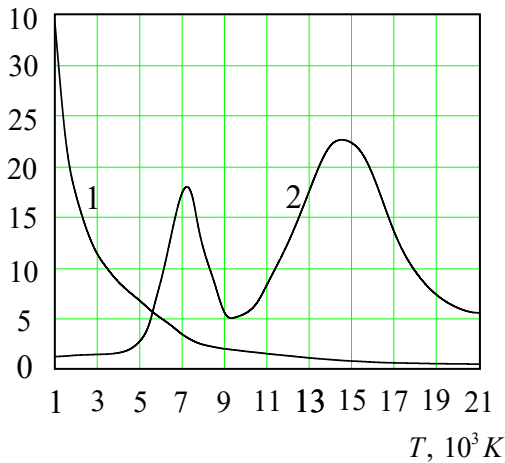


Fig. 3 Temperature dependence of γ and c for the arc burning in air. 1 — γ , $10^2 kg/m^3$

2 — c , $10^3 J/kg \cdot K$

The metallic arc phase continues up to the time $t = t_{gi}$, when the temperature maximum at the center of the arc disk reaches the value of the gas ionization (approximately about 7000 K

$$\theta_A(0, t_{gi}) = \theta_{gi} \quad (2)$$

Thus, for the equation (1) we consider the domain

$$D_A : 0 < t < t_{gi}, \quad 0 < r < r_A(t) \quad (3)$$

for the temperature range

$$\theta_{mi} < \theta_A(r, t) < \theta_{gi} \quad (4)$$

where θ_{mi} is the temperature of the metallic vapor ionization (approximately about 5000 K)

As can be seen from Fig. 2, the arc radiation $W_r(\theta_A)$ can be neglected in the temperature range (4) and we should take into account only the power losses $P(r, t)$ due to the arc heat conduction into the zone of metallic vapour D_1 via the zone of the ideal thermal and electrical conductivity D_0 introduced by R. Holm [8].

This loss can be calculated using the formula

$$P(r, t) = - \frac{2\lambda_1}{h(t)} \frac{\partial \theta_1}{\partial r} \Big|_{r=r_A(t)} \quad (5)$$

It was shown in the paper [6] that the contact gap, i.e. the arc disk thickness $h(t)$, increases in the initial stage of the metallic arc phase at the blow-off repulsion due to the summary action of electromagnetic and vapor forces according to the expression

$$h(t) = h_0 \sqrt{t} \quad (6)$$

where the constant h_0 depends on the current amplitude I_0 .

For the considered time interval $0 \leq t \leq t_{ig}$ it is possible to approximate the alternative current $I(t) = I_0 \sin \omega t$ by the expression

$$I(t) = k \sqrt{t} \quad (7)$$

Where

$$k = \frac{I_0 \sin(\omega t_{ig})}{\sqrt{t_{ig}}} \quad (8)$$

Substituting the expressions (5) – (8) into the equation (1) we get

$$c_A(\theta_A) \gamma_A(\theta_A) \frac{\partial \theta_A}{\partial t} = \frac{1}{r} \frac{\partial}{\partial r} \left(\lambda_A(\theta_A) r \frac{\partial \theta_A}{\partial r} \right) + \frac{k^2 t}{\pi^2 r_A^4(t) \sigma(\theta_A)} - \frac{2\lambda_{1b}}{h_0 \sqrt{t}} \frac{\partial \theta_1(r_A(t), t)}{\partial r}, \quad (9)$$

$$D_A : 0 < r < r_A(t), \quad 0 < t < t_{ig}$$

where

$$\lambda_{1b} = \lambda_1(\theta_1(r_A(t))) = \lambda_1(\theta_{mi})$$

At the initial time the domain D_A collapses into a point $r = r_A(0) = 0$, where the temperature should be equal to the threshold of metal ionization temperature θ_{mi} :

$$\theta_A(0, 0) = \theta_{mi} \quad (10)$$

This temperature remains the same value on the boundary of the disk for $t > 0$:

$$\theta_A(r_A(t), 0) = \theta_{mi} \quad (11)$$

The arc heat flux passes through the sphere of ideal conductivity D_0 without any power losses and enters into vapor zone D_1 through the spherical surface $r = r_A(t)$ which temperature is the same like (11):

$$\theta_1(r_A(t), 0) = \theta_{mi} \quad (12)$$

The phenomena occurring in the vapor zone are too complicated for mathematical modeling in the frame of our approach, thus let us consider this zone as the thermal resistivity between the arc zone D_A and the liquid zone D_2 with a linearly decreasing temperature

$$\theta_1(r, t) = \theta_{mi} - \frac{r - r_A(t)}{\alpha(t) - r_A(t)} (\theta_{mi} - \theta_b) \quad (13)$$

$$r_A(t) \leq r \leq \alpha(t)$$

The temperature fields of the liquid zone D_2 and the solid zone D_3 satisfy the heat equations

$$c_i(\theta_i) \gamma_i(\theta_i) \frac{\partial \theta_i}{\partial t} = \frac{1}{r^2} \frac{\partial}{\partial r} \left(\lambda_i(\theta_i) r^2 \frac{\partial \theta_i}{\partial r} \right)$$

$$i = 2 \rightarrow \alpha(t) < r < \beta(t) \quad (14)$$

$$i = 3 \rightarrow \beta(t) < r < \infty$$

The Stefan conditions hold on the interfaces of the phase transformations:

$$\theta_2(\alpha(t), t) = \theta_b \quad \theta_2(\beta(t), t) = \theta_3(\beta(t), t) = \theta_m$$

$$-\lambda_b \frac{\partial \theta_2(\alpha(t), t)}{\partial r} = L_b \gamma_b \frac{d\alpha}{dt}$$

$$-\lambda_2 \frac{\partial \theta_2(\beta(t), t)}{\partial r} = -\lambda_3 \frac{\partial \theta_3(\beta(t), t)}{\partial r} + L_m \gamma_m \frac{d\beta}{dt} \quad (15)$$

Here L_b, L_m are specific heats of evaporation and melting,

$$\lambda_b = \lambda(\theta_b),$$

$$\lambda_2 = \lambda(\theta_m) \quad \text{for liquid},$$

$$\lambda_3 = \lambda(\theta_m) \quad \text{for solid}$$

$$\gamma_b = \gamma(\theta_b), \quad \gamma_m = \gamma(\theta_m)$$

The last boundary condition for the solid zone is

$$\theta_3(\infty, t) = 0 \quad (16)$$

At the initial time all zones collapse into a point:

$$r_A(0) = \alpha(0) = \beta(0) = 0 \quad (17)$$

The solution of the above-formulated problem can be found using the similarity principle (See Appendix 2).

3. Numerical calculation

The arc temperature at the transition from metallic phase to the gaseous stage, which changes in the range $4000K - 7000K$, was calculated for the parameters of the blow-off repulsion presented in the paper [6], which are shown in Fig. 4.

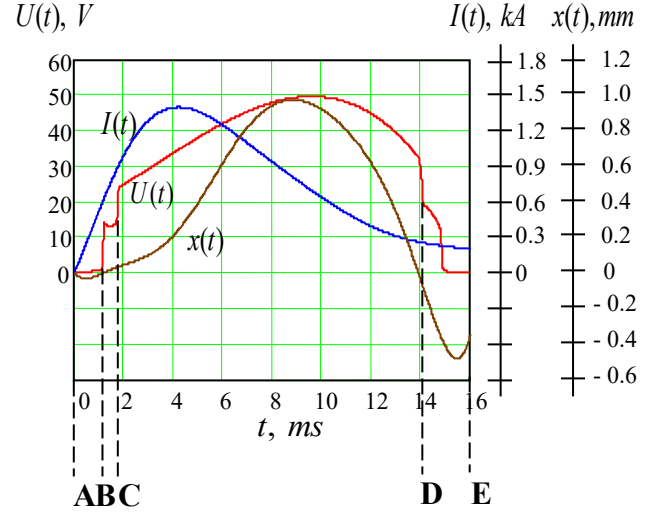


Fig. 4. Dynamics of voltage $U(t)$, current $I(t)$, and contact displacement $x(t)$

The metallic and transition stages last from 0 to 4 ms (ABC zone). During this stage the temperature increases up to $5000^\circ K$, and the function $M(T)$ in the expressions (32) and (37), which is the quantity inverse to the thermal diffusivity of the air) decreases more than twice, as can be seen from Fig. 5 and Fig. 6.

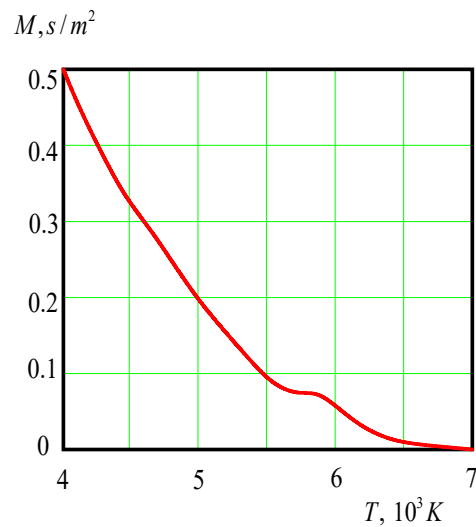


Fig. 5. The temperature dependence of $M(T)$ [7]

The results of the numerical solution of the problem (21) – (29) of the appendix 2 is presented in the Fig.6

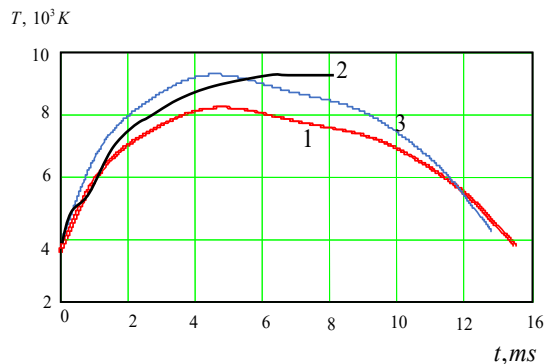


Fig.6.Dynamics of the arc temperature
 1 - experimental data [6] ,
 2 – calculation by the non-linear model,
 3 – calculation by the linear model [9]

One can see that presented in this paper non-linear model gives better approximation to the experimental data in the considered transition time interval than the linear model, however outside this interval it cannot be applied. The results of calculation of the radii of zones indicated in Fig. 1 are shown in Fig. 7.

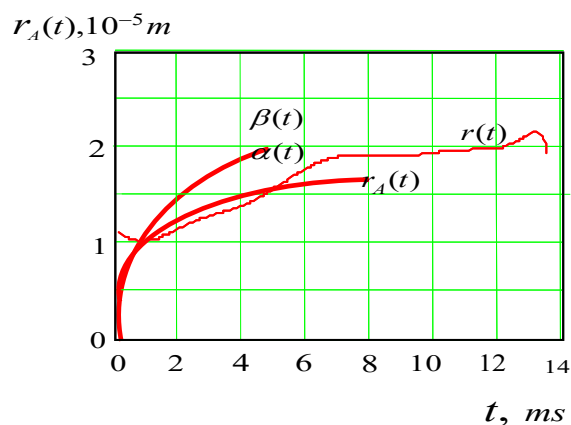


Fig.7. Dynamics of the arc radii.
 $r(t)$ is the arc radius calculated in [9]

Thus, the average value of the arc radius at the transition arc stage is equal approximately $1.5 \cdot 10^{-5} m$ that in a good agreement with experimental data [10].

4. Conclusion

1. The non-linear mathematical model of a short arc temperature at its transition from metallic to gaseous stages describes the dynamics of the blow-off repulsion of electrical contacts in a good agreement with experimental data.
2. The dynamics of increase of the radii of interfaces between zones of the phase transformations can be described by the self-similar law
3. Generalizing of this model for the gaseous arc stage is possible by the replacement of the

one-dimensional model of the arc disc for the two-dimensional model of the arc cylinder.

5. Literature

- [1] E. Tomas, I. Browne, Circuit Interruption , Marsel Dekker, New York, 1984
- [2] P. Slade, Electrical Contacts. Principles and Applications, CRC Press, Second Edition, 2014
- [3] Frank Karetta, Manfred Lindmayer, Simulation of the gas-dynamic and electromagnetic processes in low voltage switching arcs, IEEE Transactions on Components Packaging and Manufacturing Technology, Part A, 21(1), 1998, pp. 95-103
- [4] Xiayu Liao, Xue Zhou, Kai Bo, Guofu Zhai, 3-D Hydrodynamic Model of Metal Droplet Sputtering and Molten Pool Formation Under Electric Arc, Proc. Of 29th ICEC and 64th IEEE Holm Conference on Electrical Contacts, 2018, pp. 56-60
- [5] S.N. Kharin, Mathematical Model of the Short Arc Phenomena at the Initial Stage, Proc. 43-th IEEE Holm Conf. on Electrical Contacts, Philadelphia, USA, 1991, pp 289-305
- [6] S.N. Kharin, H. Nouri, M. Bizjak, Effect of Vapour Force at the Blow-open Process in Double-break Contacts, IEEE Transactions on Components and Packaging Technologies, March 2009, Vol. 32, № 1, 2009, pp. 180-190
- [7] V.S. Engelsht, Mathematical modelling of the electrical arc, ILIM Edition, Frunze, 1983 (Rus.)
- [8] R. Holm, Electric Contacts. Theory and Application, Fourth Edition, Springer-Verlag, Berlin, New York, 2000
- [9] S. N. Kharin, H. Nouri, B. Miedzinski, Phenomena of Arc Root Immobility in Electrical Contacts, Proceedings of the 58th IEEE Holm Conference on Electrical Contacts, Portland, OR, USA, 2012, pp. 11-15
- [10] Luc Nedelec, Contribution a l etude des Arcs electriques et de leurs consequences sur les materiaux de contacts: Application aux commutateurs automobiles, Docteur These, Univ. de Rennes, 1997
11. O.B. Bron, L.K. Sushkov, Plasma flows in the electric arc of the circuit-breakers, "Energia" Edition, Leningrad, 1975 (Rus.)

**Appendix 1. Temperature dependence of the coefficients for the arc
burning in nitrogen [7]**

Temperature θ, K^0	Density $\gamma, kg / m^2$	Viscosity $g / m \cdot s$	Radiation $W_r, 10^3 W / sm^3$	Enthalpy J / g	Heat conductivity $W / m \cdot K$	Heat capacity $J / kg \cdot K$	Electrical conductivity $\Omega^{-1} \cdot m^{-1}$
300	1.1400	0.0179	0	311	0.026	1050	0
500	0.6340	0.0257	0	526	0.039	1100	0
1000	0.3420	0.0400	0	1091	0.065	1160	0
1500	0.2280	0.0506	0	1686	0.094	1220	0
2000	0.1710	0.0694	0	2316	0.126	1300	0
2500	0.1370	0.0810	0	2976	0.152	1340	0
3000	0.1130	0.0920	0	3656	0.180	1380	0
3500	0.0978	0.1040	0	4355	0.210	1415	0
3700	0.0924	0.1090	0	4641	0.226	1450	0
4000	0.0853	0.1160	0	5090	0.255	1540	0
4500	0.0755	0.1270	0	5942	0.369	1870	0
5000	0.0668	0.1380	0	7085	0.657	2700	0
5500	0.0575	0.1520	0	8960	1.278	4800	2
5700	0.0541	0.1580	0	10080	1.645	6400	6
6000	0.0495	0.1680	0	12352	2.550	8750	14
6500	0.0419	0.1810	0	17890	4.500	13400	50
7000	0.0335	0.1950	0	25590	5.160	17400	179
7500	0.0273	0.2080	0.001	34257	4.525	16700	590
7700	0.0253	0.2120	0.002	37377	4.000	14500	700
8000	0.0233	0.2170	0.005	41315	3.130	11750	915
8500	0.0210	0.2270	0.010	46377	2.200	8500	1550
9000	0.0192	0.2330	0.025	49685	1.730	5450	2010
9500	0.0180	0.2390	0.060	52470	1.575	5050	2550
10000	0.0167	0.2430	0.100	55083	1.525	5470	3030
10500	0.0156	0.2420	0.240	58063	1.620	6450	3500
11000	0.0144	0.2370	0.420	61763	2.050	8350	4000
12000	0.0123	0.2100	1.000	72213	2.850	12550	4950
13000	0.0102	0.1720	2.150	87343	3.720	17710	5860
14000	0.0085	0.1170	3.800	107248	4.330	22100	6720
14500	0.0077	0.0940	4.700	118423	4.420	22600	7150
15000	0.0071	0.0760	5.650	129635	4.370	22250	7500
15500	0.0066	0.0610	6.650	140473	4.170	21100	7910
16000	0.0060	0.0490	7.400	150473	3.875	18900	8180
17000	0.0053	0.0330	8.550	166573	3.325	13300	8800
18000	0.0049	0.0250	9.200	177948	2.975	9450	9410
19000	0.0045	0.0210	9.460	186273	2.850	7200	9960
20000	0.0043	0.0180	9.260	191891	2.900	5950	10500
21000	0.0040	0.0170	8.650	197403	3.070	5500	11030
22000	0.0038	0.0170	8.050	203203	3.270	6100	11500
23000	0.0036	0.0170	7.680	210003	3.525	7500	11960
24000	0.0034	0.0160	7.550	218928	3.825	10350	12260
26000	0.0030	0.0150	8.250	248478	4.400	19200	12350
28000	0.0026	0.0130	9.800	296478	5.000	28800	12160

Appendix 2. Solution of the problem

According to the similarity principle we represent the solution in the form

$$\theta_A(r, t) = u_A(\eta), \quad \theta_i(r, t) = u_i(\eta), \quad i = 1, 2 \quad (18)$$

where

$$\eta = \frac{r}{2a\sqrt{t}}$$

$$r_A(t) = a\sqrt{t}, \quad \alpha(t) = \alpha_0\sqrt{t}, \quad \beta(t) = \beta_0\sqrt{t}$$

Then we get

$$\frac{\partial \theta_A}{\partial t} = -\frac{1}{2t} \eta \frac{du_A}{d\eta},$$

$$\frac{1}{r} \frac{\partial}{\partial r} \left[r \lambda(u_A) \frac{\partial \theta_A}{\partial r} \right] = \frac{1}{4a^2 t} [\lambda(u_A) u_A''(\eta) + \lambda'(u_A) \cdot u'(\eta)^2 + \frac{\lambda(u_A)}{\eta} u_A'(\eta)] \quad (19)$$

$$\frac{1}{r^2} \frac{\partial}{\partial r} \left[r^2 \lambda(\theta_i) \frac{\partial \theta_i}{\partial r} \right] = \frac{1}{4a^2 t} [\lambda(u_i) u_i''(\eta) + \lambda'(u_i) \cdot u_i'(\eta)^2 + \frac{2\lambda(u_i)}{\eta} u_i'(\eta)] \quad (20)$$

and the equation (9) takes the form

$$\lambda_A(u_A) u_A''(\eta) + \lambda_A'(u_A) u_A'(\eta)^2 + \left[\frac{\lambda_A(u_A)}{\eta} + 2a^2 c_A(u_A) \gamma_A(u_A) \eta \right] u_A'(\eta) + \frac{4k^2}{\pi^2 a^2 \sigma_A(u_A)}, \quad 0 < \eta < 1/2 \quad (21)$$

Similarly, the equations (14) can be written in the form

$$\lambda_i(u_i) u_i''(\eta) + \lambda_i'(u_i) u_i'(\eta)^2 + 2 \left[\frac{\lambda_i(u_i)}{\eta} + a c_i(u_i) \gamma_i(u_i) \eta \right] u_i'(\eta) = 0 \quad (22)$$

$$i = 2 \quad \rightarrow \quad \frac{\alpha_0}{2a} < \eta < \frac{\beta_0}{2a}$$

$$i = 3 \quad \rightarrow \quad \frac{\beta_0}{2a} < \eta < \infty$$

Thus, the problem is reduced to the solution of the ordinary differential equations (21), (22). The boundary conditions (12), (15) for these substitutions transform into expressions

$$u_A'(0) = 0 \quad (23)$$

$$u_A(1/2) = \theta_{mi} \quad (24)$$

$$u_2(\alpha_0/2a) = \theta_b \quad (25)$$

$$u_2(\beta_0/2a) = u_3(\beta_0/2a) = \theta_m \quad (26)$$

$$u_3(\infty) = 0 \quad (27)$$

$$u_2'(\alpha_0/2a) = -\frac{L_b \gamma_b}{\lambda_b a} \quad (28)$$

$$-\lambda_2 u_2'(\beta_0/2a) = -\lambda_3 u_3'(\beta_0/2a) + \frac{L_m \gamma_m}{a} \quad (29)$$

The problem (21) – (29) can be solved using the Runge-Kutta method. Sometimes, for an analytical analysis of the temperature dynamics, it is more convenient to reduce this problem to the system of the integral equations. In particular, the equation (21) after the substitution

$$\lambda_A u_A(\eta) = V_A(\eta) \quad (30)$$

can be written in the form

$$V_A'(\eta) + L_A(\eta)V_A(\eta) = N(\eta) \quad (31)$$

where

$$L_A(\eta) = \frac{1}{\eta} + 2a^2 M_A(u_A)\eta \quad (32)$$

$$M_A(u_A) = \frac{c_A(u_A)\gamma_A(u_A)}{\lambda_A(u_A)}$$

$$N_A(\eta) = -\frac{4k^2}{\pi a^2 \sigma_A(u_A)} \quad (33)$$

The equation (31) is equivalent the non-linear integral equation

$$V_A(\eta) = \exp\left[-\int_0^\eta L_A(s)ds\right] \int_0^\eta N_A(s) \exp\left[-\int_0^s L_A(s_1)ds_1\right] ds \quad (34)$$

Similarly, the equations (22) can be written in the form

$$V_i'(\eta) + L_i(\eta)V_i(\eta) = 0, \quad i = 2, 3 \quad (35)$$

where

$$V_i(\eta) = \lambda_i u_i(\eta) \quad (36)$$

$$L_i(\eta) = \frac{1}{\eta} + 2a^2 M_i(u_i)\eta \quad (37)$$

$$M_i(u_i) = \frac{c_i(u_i)\gamma_i(u_i)}{\lambda_i(u_i)}$$

or in equivalent form of integral equations

$$V_2(\eta) = \lambda_b \theta_b - \exp\left[-\int_\eta^{\beta_0/2a} L_2(\eta)d\eta\right] \quad (38)$$

$$V_3(\eta) = \lambda_b \theta_b - \exp\left[-\int_{\beta_0/2a}^\eta L_2(\eta)d\eta\right] \quad (39)$$

The integral equations (34), (38),(39) are the equations of the Volterra type, and if the kernels of integral operators are differentiable, then these operators are contraction and the solution can be obtained by the iteration method

Optimization of current carrying connections under STC test conditions

Bogusław Samul, Hitachi ABB Power Grids Research, Krakow, Poland,
boguslaw.samul@hitachi-powergrids.com;

Jörg Ostrowski, ABB Corporate Research, Dättwil, Switzerland, joerg.ostrowski@ch.abb.com;

Remigiusz Nowak, Hitachi ABB Power Grids Research, Krakow, Poland,
remigiusz.nowak.@hitachi-powergrids.com

Abstract

The short time current (STC) test is one of the most challenging tests for power devices. Components on the current path need to withstand a few seconds of operation under a very high short circuit current (e.g. 3s 80kA). STC tests are necessary but expensive and can significantly increase the cost of the design process of a power device. The integration of computer simulations into the design process can significantly reduce both the design cost (by reduction of physical tests to the absolute minimum) as well as the device cost (by optimization of material usage and implementation of easily manufacturable shapes). This paper deals with coupled electro-thermal transient simulations of examples of current carrying components with special attention afforded to their bolted contact area. The influence of the shape and mass of a conductor on the temperature of the contact was investigated. Both electrical and thermal contact resistances were included in the analysis together with skin and proximity effects related to the AC current flow. ABB inhouse simulation software has been developed and used for the simulation process. The goal of the analysis was to optimize the shape of the conductor to have the lowest possible mass and manufacturing cost whilst still successfully passing the STC test.

1 Problem description

1.1 Introduction

STC – short time current tests are mandatory for power devices. Details of the test, such as the current characteristics, the test duration and the pass criteria are described by international and local standards, e.g. in [1], [2]. Ohmic losses are generated in the bulk components on the current path (typically made of aluminum or copper alloys) and on the joints (contacts) between them. Different types of contacts may be distinguished from one another:

- Bolted contacts,
- Spring/lamella contacts,
- Sliding (e.g. finger) contacts,
- Mixed.

Due to the high current ratings of the STC test there is a risk of mechanical (cracks) and/or thermal (melting/welding) failures of the tested device. Problems are mainly observed at the electrical contacts because of their mechanical weakness and the significant local density of the ohmic losses. STC testing is complex and expensive due to the requirements of the power sources. When a failure occurs the test object is usually destroyed or damaged such that it may not be reused in further testing. A numerical simulation approach to STC allows a significant reduction of development time and cost. It enables the virtual testing of dozens of

design variations in a reasonable time, allowing only a few of the most promising designs to be selected and physically tested. This significantly reduces the risk of failure. This paper focuses on the thermal behavior of the tested objects. An example model that includes three aluminum alloy components connected with steel bolts was chosen as the investigation object. These kind of components and connections are widely used in HV GIS devices like grounding switches, disconnectors and breakers.

Previously, Ostrowski et al. [3] have investigated how statistical variation in electrical contacts influence the probability of an STC test being passed. This paper can be treated as a continuation of the mentioned work, with specific focus being given to the thermal resistances and the mass distribution in the vicinity of the contact, under the assumption that the electrical resistance of the connection is known.

1.2 Simulation model

The investigated device is presented in **Figure 1**, while the contacts and the location of the current inlets and outlets are presented in **Figure 2**.

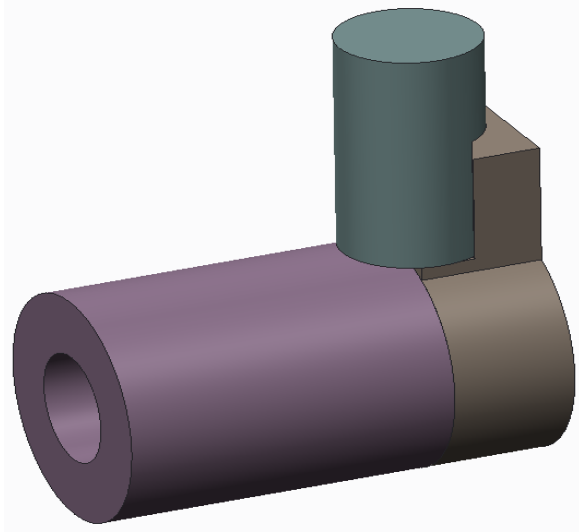


Fig. 1 Current path of HV device

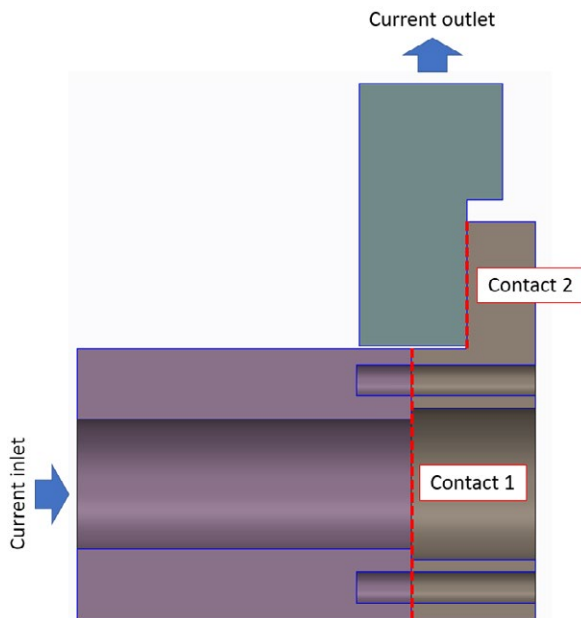


Fig. 2 Components joints/contacts

The simulated test conditions are collected in **Table 1**.

Current (RMS)	80kA
Frequency	50Hz
Test duration	3s
Electrical contact resistance for Contact 1	1.2 μΩ
Electrical contact resistance for Contact 2	1.5 μΩ
Ambient temperature	20°C
Initial temperature of test object	20°C

Table 1. Test conditions

All components of the simulated device were made of EN AW-6082 aluminum alloy. The material properties of this alloy which are relevant for the analysis are given in **Table 2**.

Specific electrical resistance	0.04 μΩm
Linear thermal coefficient or resistivity increase	0.0036 1/K
Density	2700 kg/m ³
Specific heat capacity	896 J/kg K
Thermal conductivity	170 W/mK
Melting temperature	615 °C / 888 K

Table 2. EN AW-6082 aluminum alloy properties

1.3 Thermal contact resistance

All mechanical joints on the electrical current path can be characterized by an electrical and a thermal resistance (ECR and TCR respectively). The complexity of the exact determination and the statistical fluctuations of ECR was presented in [3]. In case of TCRs the problem is even more complicated as the measurement procedure is very complex and, in contrary to the current path resistance, their measurement is not required by the standards.

In theory the TCR (the same as ECR) is formed between two contacting solids and is caused by the fact that the surface of each body is not perfectly flat. Rather it can be imagined as a wavy structure, where the actual contact between two bodies occur only at some small areas (less than 2% of total contact area) [4]. The rest of the contact area is filled with the surrounding medium, for example air or electrically insulated by oxide or impurity layers. Due to this resistance an additional temperature drop can be observed in the vicinity of a contact. Although the TCR itself is related to the simple conduction heat transfer mechanism, the theoretical calculation of its exact value between two contacting surfaces is challenging, as it depends on variety of parameters. In addition to readily-available information such as the geometry of the contact, thermal conductivity of contacting solids and fluid gap, more specific information such as [5]:

- surface condition (roughness, asperity slope, surface waviness),
- interstitial gap thickness
- hardness or yield pressure of the contacting asperities of solid surfaces, which affects the plastic deformation of the highest peaks of the softer solid,

is also necessary. Despite the general complexity of TCR calculations, some approaches of its theoretical approximation can be found in literature. A relatively simple formulation, previously proposed by Cooper [6], Mikic [7] and Yovanovich et al [8], takes the general form (1)

$$\frac{1}{TCR} = a \cdot k_s \frac{m}{\sigma} \left(\frac{P}{H_c} \right)^b \quad (1)$$

where k_s – thermal conductivity of the interface, P – contact pressure, H_c – surface microhardness of the

softer of the two surfaces, m – asperity slope of the interface, σ – RMS value of surface roughness of the surfaces that are in contact. a and b are constants which vary between the models [6]-[8].

More recently, Bahrami et. al [9] proposed a formula where in addition to solid contact resistance, also a resistance of interstitial gas was included (2-4)

$$R_s = \frac{0.565H \cdot (\sigma/m)}{k_s F} \quad (2)$$

$$R_g = \frac{Y}{k_g A_g} \left[1 + \frac{M}{Y} + \frac{0.304 \frac{\sigma}{Y}}{1 + \frac{M}{Y}} - \frac{2.29 \left(\frac{\sigma}{Y}\right)^2}{\left(1 + \frac{M}{Y}\right)^2} \right] \quad (3)$$

$$TCR = \left(\frac{1}{R_s} + \frac{1}{R_g} \right)^{-1} \quad (4)$$

At the same time Tomimura et. al. [10] introduced the so-called Unit Cell model for TCR calculations which also included a resistance of solid and interstitial fluid resistance (4)

$$\frac{1}{TCR} = \frac{1}{\frac{\delta_1 + \delta_2}{\lambda_1 + \lambda_2}} \cdot \frac{p_m}{H_{min}} + \frac{\lambda_f}{\delta_1 + \delta_2} \cdot \left(1 - \frac{p_m}{H_{min}} \right) \quad (5)$$

In equation (2) F describes the force acting on a surface as a results of its contact with another surface. H is the surface microhardness which may be calculated using the methods described in [9]. In equation (3) k_g denotes the thermal conductivity of the gas, A_g is the gap heat transfer area and d represents the distance between two parallel contacting surfaces. The values of M and Y define the gas parameter and the mean surface plane separation value [10].

δ_i, λ_i (where $i = 1, 2$) and λ_f in equation (5) are the maximum surface roughness, the thermal conductivity of both contacting surfaces and the interstitial fluid thermal conductivity respectively. p_m and H_{min} describes the mean nominal contact pressure and hardness value – see [10] for details.

It may be noted that each of the given equations requires specific information about the contact condition in order to approximate thermal resistance. Even when all of the required parameters are available, the TCR values calculated by the equations can differ significantly (even more than 60%). This further highlights the complexity of TCR determination.

One of the simplest ways to approximate the TCR value, based on the calculated ECR is the application of Wiedeman-Franz law which states that for metals where a dominant part of heat and electric conduction is carried by free electrons, the ratio of electrical to thermal conductivity is proportional to the temperature [11]. The proportionality factor here is a Lorenz number $L = 2.44 \cdot 10^{-8} \text{ W}\Omega\text{K}^{-2}$. This law yields a simple relation between TCR and ECR

$$TCR = \frac{ECR}{LT} \quad (6)$$

In the conducted calculations it was decided to use equation (6) for a calculation of thermal contact resistance. Taking advantage of its simplicity and keeping in mind significant differences in TCR vales calculated by more complex equations it was considered as a reasonable choice that provides satisfactory accuracy of the calculations. In addition, eq. (6) is always a “worst case” approach since in reality, there are parallel conducting paths through the gaps, as represented in eqs. (3)-(5), which will lower the TCR.

1.4 Simulation environment

In order to ensure proper and accurate virtual STC testing it is necessary to implement the following physical phenomena into the simulation procedure:

- Two way coupling between the electro-magnetic (EM) and the thermal (TH) solver
- Integration of the ECRs in the EM solver to ensure the correct calculation of the current and loss distribution, in both the bulk materials and on the contacts
- The integration of TCRs in the TH solver to ensure the proper calculation of the heat conduction and the temperature distribution

An inhouse ABB Simulation Toolbox was selected as it incorporates all of the above mentioned aspects in one single and robust environment.

The computation of the ohmic loss distribution is conducted by the Full Maxwell Module. It computes the Maxwell equations in the frequency domain in a formulation that is based on the electric field \mathbf{E} , i.e. it solves the equation

$$\mathbf{curl} \ 1/\mu \ \mathbf{curl} \ \mathbf{E} + i\omega(\sigma(T)\mathbf{E} + i\omega\epsilon\mathbf{E}) = 0 \quad (7)$$

Herein μ is the permeability, i is the imaginary unit, ω is the angular frequency, σ is the electrical conductivity that depends on the temperature T and ϵ is the permittivity. This equation is numerically solved with a Galerkin Finite Element Method (FEM). The ECRs are integrated by utilizing a discontinuous local scalar electric potential.

The temperature is also computed using an FEM method for the transient heat conduction equation

$$\rho c_p \partial_t T - \mathit{div}(k \cdot \mathit{grad} T) = P \quad (8)$$

with the mass density ρ , the heat capacity c_p , the thermal conductivity k , and the ohmic loss density $P = \sigma \cdot \mathbf{E}^2$ that results from the electromagnetic solution. The temperature dependency of the involved thermal material parameters is negligible and much smaller than the dependency of the electrical conductivity. The heat exchange between the parts and the environment is not of high importance because the overall process is so fast that only a small amount of the generated heat is lost. As a result it is possible to simulate the process as an adiabatic process. However, we instead used heat trans-

fer coefficients at the surface of the parts to approximate this cooling. The boundary used for this purpose may be given as

$$k \cdot n \cdot \text{grad } T = h \cdot (T_b - T) \quad (9)$$

with the exterior normal n , the heat transfer coefficient h , and the environmental temperature T_b .

Electromagnetic and thermal phenomena occur over very different timescales. The frequency of the current is 50 Hz thus the variations of the electromagnetic field primarily occur in the milliseconds range. For the thermal part the typical timescale of any variation is much larger, in the range of a tenth of a second, because it takes some time for the heat to be conducted and dissipated. Thus the electrical conductivity of bulk material does not change much during one electromagnetic period (detailed investigation of single contact spots is not covered by this study). This is why the electromagnetics are computed in the frequency domain, whilst the thermal phenomena are calculated in the time domain. The electrical conductivity is updated when the local change exceeds a predefined value.

The simulation method was verified with STC test for HV GIS grounding switch and was described in [12], where device failure was observed after 2 seconds of test while according to simulation melting temperature was reached after 1,7s.

Since the time of verification additional feature of thermal contact resistance was added to the simulation software. Benchmark model was then recalculated and provided even better correlation with the test.

2 Results

2.1 Results for the base design

The coupled transient electro-thermal analysis of the base design showed that the temperature in the area of Contact 2 exceed the aluminum alloy melting temperature of 888K after 2.1s, reaching 1071K (at the end of the test). This indicates that the device would fail the STC test with a high level of probability.

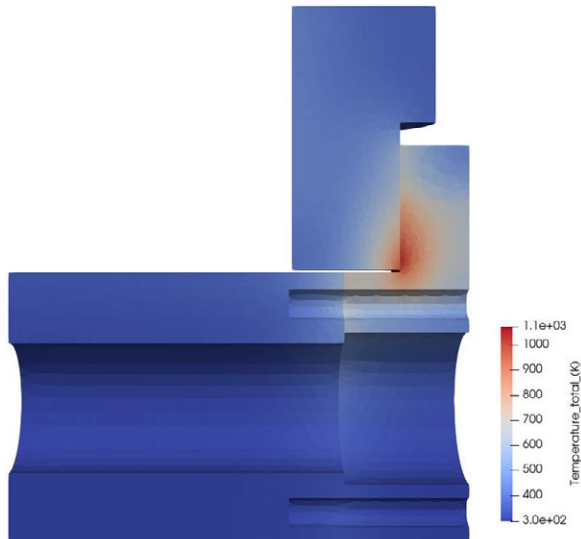


Fig. 3 Temperature distribution on base design at the end of the test (after 3 seconds) – cross-section view

The risk of failure during the testing of such an arrangement is so high that a redesign of the device was necessary. The detailed temperature distribution at the end of the test (after 3s) is presented in **Figure 3**, the volume with a temperature exceeding the melting point is shown in **Figure 4** and the temperature of the hotspot during the test in **Figure 5**.

The temperature at Contact 2 not only exceeds the melting point of aluminum alloy but is also non uniform on both sides of the contact. This effect is caused by the TCR and clearly shows that neglecting the TCR in the numerical analysis can significantly reduce the hotspot temperature. This may subsequently result in an under dimensioning of the current carrying components and failure during the test.

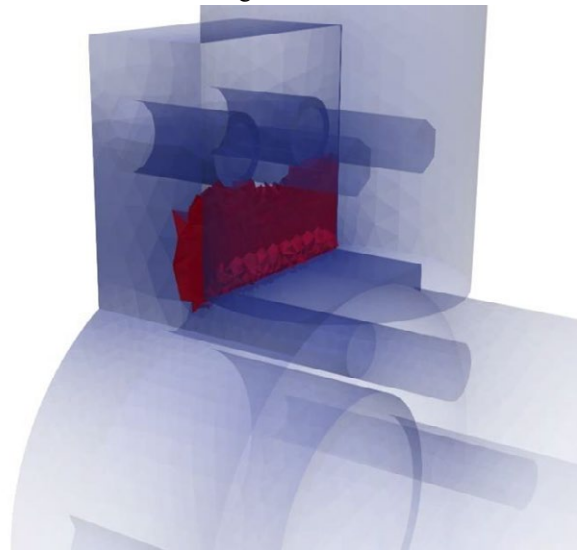


Fig. 4 Molten aluminum volume (marked with red color)

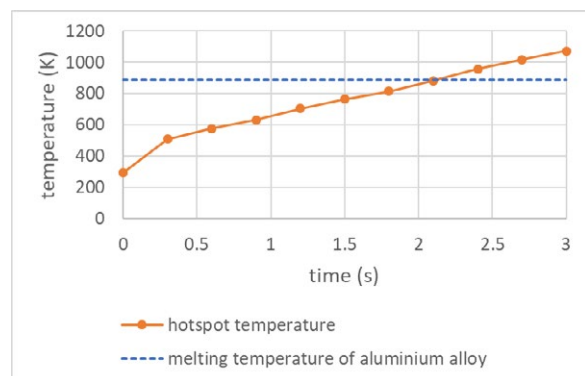


Fig. 5 Hotspot temperature vs. time

2.2 Design improvements

The design of the investigated device was changed to reduce the hotspot temperature below the melting point. It was decided to use 10% safety margin, resulting in a limit of 800K limit for the hotspot temperature, that margin should cover negative effects like local

overheating in contact spots and non-uniform distribution of resistance on contact surface.

The shape and size of high voltage electrical power devices is determined by the electric field distribution (insulation requirements), the thermal management (losses generation and heat dissipation), mechanical properties, manufacturing and cost.

The mentioned parameters determine the boundaries for the device optimization. To represent this kind of criteria the following boundaries/assumptions have been incorporated to the optimization study:

- Only the middle part can be modified (insulation requirements)
- The contact resistance cannot be changed for mechanical reasons
- The material of any component cannot be changed due to manufacturing, supply chain and cost reasons.

In addition to those limitations the final design should also be easy to manufacture and lightweight.

The ohmic losses that are generated by the current due to the bulk material resistivity are accumulated in the material, conducted from hotter to colder areas, and transmitted to the environment via convection and radiation. Due to the short duration of the test and the high loss generation, the transmission to the environment is significantly smaller than the heat accumulation in the material. As a result, the temperature of the hotspot can be diminished by reducing the losses or by increasing the heat capacity or preferably both together. Two possibilities were considered due to manufacturing and electric field limitations: A change in the axial direction and a change in the symmetrical side direction. The virtually tested designs are presented in **Figure 6**.

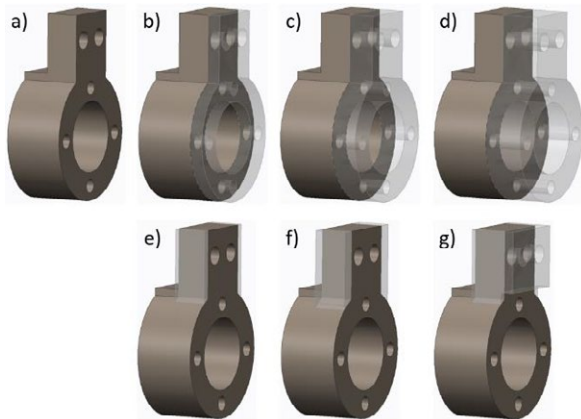


Fig. 6 Calculated designs of connecting component a) original design, b) +10mm axial, c) +20mm axial, d) +30mm axial, e) 2x 5mm side, f) 2x 10mm side, g) optimal design - mixed 2x 5mm side and +10mm axial (reduced to contact area)

The influence of the design changes on the hotspot temperature is presented in **Figure 7**.

The increase of the connector length provides a significant improvement for the first added 10 millimeters of

material, but after 20mm the effect saturates. Only an increase of the length by more than 30mm reduced the hotspot temperature to an acceptable level around 800K. Such a design change also results in a significant increase of the volume (and mass) of the component by 76%. This is unacceptable due to cost limitations.

The alternative design based on the addition of material to the side of the contact area (increasing of width) had much better effects. For example the version with 2x 10mm increase yielded temperatures below 800K with a mass increase of only 10%. However, this kind of modification would also lead to problems during the device assembly, possibly necessitating a redesign of the enclosure, which could again increase the overall costs of device. The final design change is a combination of axial and side changes. 5mm of material was added to the sides of the contact and 10mm in axial direction, but only in area of contact (see Figure 6g). Using this approach the temperature requirements were achieved with only a small increase of the material mass (14% only) together with a compact shape that is easy to manufacture and to assemble.

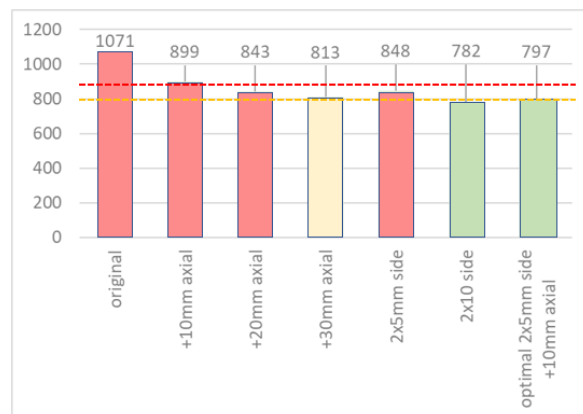


Fig. 7 Hotspot temperature (K) at the end of the test after 3s. Red line – melting point 888K, orange line – temperature limit 800K.

3 Conclusions and next steps

Numerical simulation can significantly improve the design process of electrical devices. With the proper approach that includes the most important physical effects, even such a complex test as short time current test can be represented virtually. The associated costs are significantly lower than in experimental based design. This publication shows that virtual testing helps to find weak points in the design of high current conductors. It allows a wide range of different designs to be evaluated to find the component that is cheapest and easiest to manufacture, which will pass the STC test with high probability.

This investigation showed that even with restricted design options related to contact parameters (ECR and TCR) and dimensions, it is possible to propose solutions that are very likely to pass the STC test. The key to reduce the contact temperature is to increase the heat

capacity by adding material in a close proximity to the connection point. This reduces the ohmic losses, increases the heat accumulation (in a short distance from the hot-spot) and leads to a more uniform temperature distribution on both sides of the joint.

The presented results are an example of a step by step manual investigation of different designs. The next step would be to implement an optimization algorithm (preferably freeform) to automatically search for optimal design, and/or to create a reduced order model for a connector based on DoE results.

4 Literature

- [1] IEC 62271-1, Ed. 2.0 High-voltage switchgear and controlgear: Common specifications for alternating current switchgear and controlgear.
- [2] IEC 62271-102: 2018, HV switchgear and controlgear: Alternating current disconnectors and earthing switches
- [3] Ostrowski, J.; Gatzsche, M.; Buffoni M. and Samul B.: A statistical approach to electro-thermal simulations with contacts, IEEE Holm Conference, Milwaukee USA, 2019.
- [4] Mantelli M.T.H. and Yovanovich M.M.: Spacecraft Thermal Control Handbook, chapter 16
- [5] Cengel, Y. A.: Heat Transfer: A practical Approach, Reno: McGraw-Hill, 2002.
- [6] Cooper M.; Mikic B. and Yovanovich M.: Thermal contact conductance, International Journal of Heat and Mass Transfer, vol. 12, pp. 279-300, 1969.
- [7] Mikic B.: Thermal contact conductance: Theoretical considerations, Int. Journal of Heat and Mass Transfer, vol. 17, pp. 205-214, 1974.
- [8] Yovanovich M.M.; Culham J. R. and Teertstra P.; Calculating interface resistance, Electronics cooling, pp. 1-9, 1997
- [9] Bahrami M.; Culham J. R. and Yovanovich M. M.: Thermal Joint Resistances of Conforming Rough Surfaces with Gas-Filled Gaps, J. Thermophysics and Heat Transfer, vol. 18, pp. 318-325, 2004
- [10] Tomimura T.; Takahashi Y.; TaeWan D.; Shigyo K. and Koito Y.: Simple evaluation method for temperature drop at contact interface between rough surfaces under low contact pressure conditions, IOP Conf. Series: Materials Science and Engineering, vol. 61, pp. 1-12, 2014.
- [11] Holm R.: Electric Contacts: Theory and Applications. Berlin: Springer, 2000
- [12] Ostrowski J.; Gatzsche M. and Samul B.: Simulation of short time current tests of industrial devices, SCEE conference, Italy, 2018

Series Arc Fault Modelling in Photovoltaic Resistive Systems

Silei Chen¹, Jing Wang², Xingwen Li³

¹School of Electrical Engineering, Xi'an University of Technology, Xi'an, P.R.China

²Shenzhen Power Supply Bureau, Shenzhen, P.R.China

³State Key Laboratory of Electrical Insulation and Power Equipment, Xi'an Jiaotong University, Xi'an, P.R.China

xwli@mail.xjtu.edu.cn

Abstract

Series arc fault modelling provides an effective simulation approach for understanding arc fault characteristics in photovoltaic (PV) systems. However, the measured arc fault signals are synthetic results between arc faults and many system interference factors, which makes the modelling process complicated. This paper aims at providing an effective arc fault model for the simulation research in PV resistive systems. In this paper, various arc fault data are acquired through the designed experiment platform firstly. Then the establishment direction is summarized for the arc fault modelling in PV resistive systems. Next, the series arc fault model is proposed by combining the U-I model and pink noise model. Finally, the simulation analysis of series arc fault is carried out in PV resistive systems. By comparing with the obtained experimental data, the effectiveness of the arc fault model is verified.

1 Introduction

With the increasing demand of renewable energy, photovoltaic (PV) power generation system has been applied worldwide. With more and more PV arrays connected to power system, the safe operation of PV system has become the focus [1]. However, series arc faults often occur in PV systems due to loose connectors and disconnected socket switches [1]. The occurrence of PV series arc fault endangers the normal operation of PV components and devices, causing safety threats to the around surroundings and people. Therefore, it is very important to detect and extinguish arc faults in time. However, PV series arc faults may bear the interference from many system factors including the wire and parameters of the load side. The increase of cable length would attenuate the arc noise signal in the frequency band of $10\sim 10^5$ Hz [2]. Then the interaction relationship between the PV arc fault and load is still unclear, requiring the study of the effective arc fault model. Furthermore, the arc fault model could be used to imitate complex arc fault conditions, which is helpful for the reliability development of arc fault detection algorithm in PV resistive systems.

At the beginning of the 20th century, researchers began to study the arc fault models in power systems. So far, arc fault models are generally divided into three types: the dynamical state model, the stationary state model, and the high-frequency component model [3]. In the

1940s, Cassie and Mayr established a dynamical state model from the perspective of energy conservation and heat balance principles [4]. Yao proposed a V-I model including transient and stable arc processes in 2014, which is applicable to the most common arc faults in power systems [5]. It could well simulate the arc characteristics, which is similar to the real arc characteristics in the time domain. Uriarte found that the dynamic component of arc voltage was similar to hyperbola through analyzing a large number of arc fault experimental data [6]. They used the sum of two hyperbolic approximate equations to represent the arc voltage, which is called a heuristic arc model. This modeling process is complex. Besides, the simulation performance of time-domain arc fault waveform is not significantly improved by comparing with the V-I model [7]. Therefore, the heuristic model is not the best method to simulate the arc fault waveform in the time domain. Due to the chaotic nature of the arc, the zero-mean Gaussian noise was used to describe the voltage fluctuation of the arc fault [8]. According to recent studies, the practical arc fault noises are closer to pink noises instead of white noises in the frequency domain [9][10]. Therefore, there are some limitations for zero-mean Gaussian noises to well display the arc fault noise distribution.

In this paper, various arc fault experiments are carried out with different current levels and arc gap lengths in the PV resistive system. Then the arc fault model is proposed to be accorded with the variation tendency of the arc fault current and spectrum. Based on MATLAB

platform, the proposed arc fault model is simulated in the PV resistive system. Through comparing the experimental and simulated results, the effectiveness of the proposed arc fault model is verified.

2 Arc fault experimental data and modelling directions

2.1 Experimental setup and method

To understand arc fault characteristics in the PV resistive system, series arc fault tests are conducted several times. As shown in Fig. 2.1, arc fault generator (AFG) is put on the incoming bus in front of the resistor to acquire the arc fault condition [11]. As shown in Fig. 2.2, two rod-type electrodes made of copper are used to get normal connections [12]. The system power supplies including the PV array and PV simulated source have the nonlinear V-I output characteristic curve, which are connected to the loop under the control of the switch. While the PV simulated source acts as a power supply, the arc fault current would be influenced by switching noises from the ac/dc rectifier and dc/dc converter. While the real PV array acts as a power supply, the arc fault current is relatively pure without switching noise interferences.

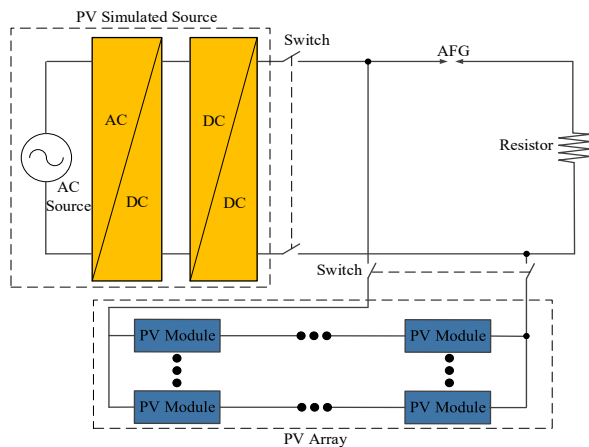


Fig. 2.1 Experiment schematic of PV series arc fault test [11].

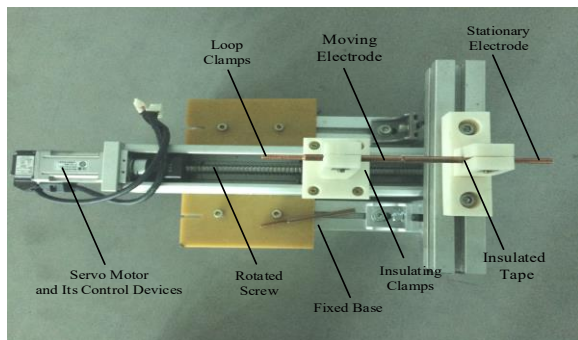


Fig. 2.2 Arc fault generator [12].

Through applying the pull-apart method according to UL1699B standard, arc fault starts to ignite and the

whole PV system steps into fault state [13]. The precisely sampled loop current signal is the core of the PV series arc fault detection, which measured by two kinds of current sensors at the same time. One is measuring the current signal with the dc component based on the Hall effect, having the bandwidth of 1MHz. The other one is measuring the current signal without the dc component based on the principle of the current transformer, having the bandwidth of 500kHz. They are applied to conduct the time-domain and frequency-domain analysis separately [14]. Arc voltage, PV voltage, and resistor voltage signals are measured by high voltage probes. After each experiment, the surface of electrodes is rubbed smooth to ensure that the arc gap length is the required value.

2.2 Typical arc fault electrical signal

When the switches of the PV simulated source or the PV array closes, an off-grid PV system is formed with the composition of the resistor. Due to the lack of inverter, the system does not have the adjustment ability of maximum power point tracking (MPPT) algorithm. Therefore, the initial operating point of the off-grid PV system depends on the set resistance. While the initial operating point is set in the non-linear operating area, the measured PV voltage and loop current signals will display the non-linear system output property. In this experiment, the resistance is 29Ω . Then an arc fault is introduced by separating the electrodes during the normal system operation, the measured electrical signals are shown in Fig. 2.3.

In stage I, the two electrodes of AFG are tightly closed and the PV resistive system is in the normal operating state. Since there is no arc, the arc voltage is zero. The output voltage of the PV array is almost applied to the resistor. All electrical signals seem to be relatively stable in the PV system.

In stage II, the electrodes are uniformly pulled apart by the motor at the speed of 2mm/s until the arc gap length reaches 3.2mm. When the electrodes are pulled apart, the arc voltage rapidly rises to about 20V. At the moment of the initial arc ignition process, the loop current decreases sharply. During the transient process of arc fault, the arc voltage increases with the longer arc gap length. The inserted arc fault gradually decreases the loop current, causing the decrease to the resistor voltage. On the other hand, the decreased loop current force the increase of the PV voltage under the control of the nonlinear output characteristic curve of PV array, which in turn would have the influence on the loop current. In the end, the arc gap length reaches the set value of 3.2mm. For the lack of MPPT adjustments, all four electrical signals come into the stable state in the end.

In stage III, the PV system is forced to stop after acquiring the enough arc fault waveform. Then the resistor voltage, loop current and arc voltage drop

sharply to zero. The PV voltage reaches the open-circuit point value of the PV array.

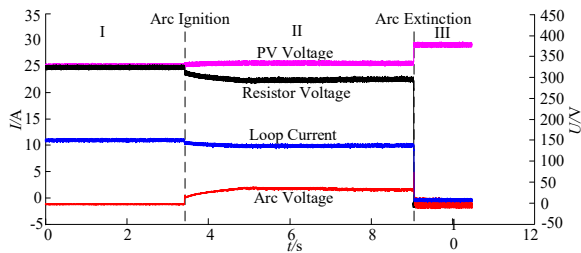


Fig. 2.3 Electrical signals in the PV resistive system (Loop current is measured with the dc component).

According to the measurement results of the current transformer, the loop current measuring without the dc component is shown in Fig. 2.4. In stage I, the arc fault has not yet been ignited, in which the PV system also operates normally. The non-zero value is derived from background system noises. At the beginning of stage II, the suddenly occurred arc fault forms significantly larger pulse. With the influence from arc fault noises, the amplitude of the signal fluctuation would increase. Compared with the transient process, the stable arc fault with longer arc gap length generally displays the larger amplitude. After the PV system stops operating in stage III, the arc fault current decrease to the smallest value among three stages.

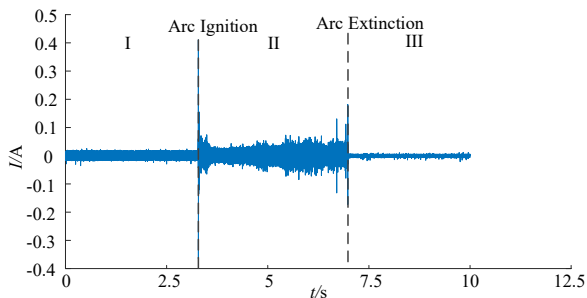


Fig. 2.4 Loop current is measured without the dc component.

2.3 Establishment direction of arc fault model

The time-domain description of the arc fault model should be accorded with the variation tendency of electrical signals shown in Fig. 2.3. For the arc fault generated by pulling the electrodes apart, the arc fault current displays the continuously decreasing tendency at the beginning in the time domain. Corresponding arc voltage should increase to the expected value. After the arc gap length keeps constant, the arc fault signals display the relatively stable tendency in the time domain.

As for the frequency characteristics of arc faults, most literatures focus on the frequency band below 100kHz with the sampling frequency of 250kHz [3]. On the basis of above experimental results shown in Fig. 2.4, the loop current is analyzed by short-time Fourier

transform (STFT) shown in Fig. 2.5. This arc fault spectrum result is the guidance for the frequency-domain description of the arc fault model. After the arc fault occurs, the spectrum would display the increasing amplitude in the frequency domain. These extra arc fault noises are the key to the large fluctuation of the time-domain current waveform in stage II of Fig. 2.4 [3][15]. Based on the experimental results, the arc noise itself displays $1/f$ phenomenon from around 50kHz to 150kHz in the PV resistive systems. The measured arc fault noise amplitude increases from zero to about 50kHz due to the high-pass effect of the current sensor. The sudden increasing pulse in amplitude of the spectrum is caused by the external switching processes from the ac/dc rectifier and dc/dc converter in the PV simulated source. The arc fault noise displays the similar amplitude to the normal spectrum after 150kHz, which would not provide significant differences for the arc fault identification. Therefore, the arc fault spectrum has the power spectral density inversely proportional to the frequency.

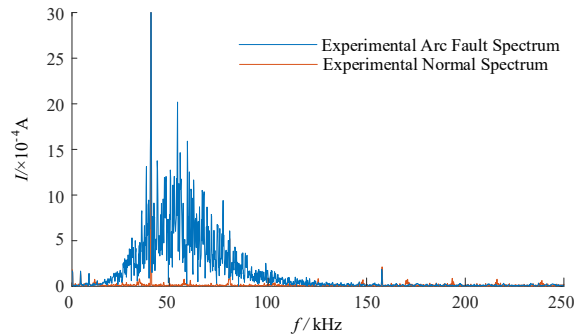


Fig. 2.5 Spectrum of the loop current during the normal and arc fault states in Fig. 2.4.

3 Simulation and verification of photovoltaic series arc fault

The proposed PV series arc fault model combines the modified Paukert model with the built pink noise model [14]. Through a large number of experiments, parameters of the modified Paukert model are obtained by statistical fitting methods, the equation is as follows:

$$V_{arc} = \frac{32.83 + 12.79L_{arc}}{I_{arc}^{0.223 + 0.02445L_{arc}}} \quad (1)$$

where L_{arc} is the arc gap length, I_{arc} and V_{arc} are the current and voltage separately. A digital filter could be designed with auto-regressive moving average model (ARMA) to generate the desired pink noise from the white noise. The arc noise model is built by further processing the generated pink noise through the high-pass and low-pass filters.

3.1 Simulation analysis of series arc fault in photovoltaic resistive systems

In order to verify the imitate accuracy of the proposed arc fault model, the model is connected to a PV resistive system, as shown in Fig. 3.1. The system consists of the PV array, the proposed arc fault model and the resistor. The output voltage of PV array is controlled by the input parameters setting of the temperature and solar irradiance.

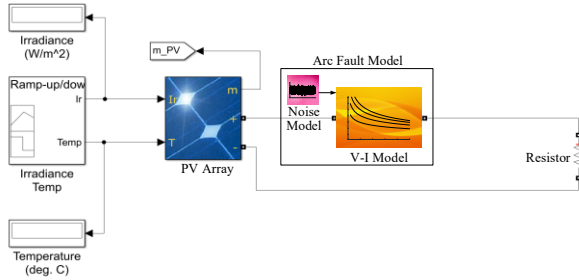


Fig. 3.1 Simulation of series arc faults in the PV resistive system.

3.2 Effectiveness verification of arc fault model through obtained experimental data

In order to verify the effectiveness of the arc fault model for simulation, the imitation effectiveness of the V-I model is firstly discussed. As shown in Fig. 3.1, the PV system works normally at 334V while the resistor is 29.5Ω. The arc fault is introduced to the PV system at 2.4s. The current and voltage signals of the dynamically burning arc process are continuously recorded through the MATALAB simulation analysis, which are shown in Fig. 3.2.

Before the arc ignites, both the normal current and voltage waveforms are relatively stable. They acquire the similar variation tendency to the experimental waveforms. It could be seen the current drops rapidly and the voltage rises up sharply at the moment of the arc fault ignition. This proves that the inserted arc fault gives the similar result to the experimental waveform. During the arc transition, the 3.2mm-long arc gap is formed by continuously increasing the arc gap L_{arc} from zero to 3.2mm at a speed of 2mm/s. Then the arc gap remains at 3.2mm, and the arc fault burns steadily from 4s. With the increasing arc gap length, the arc current decreases and the arc voltage increases smoothly. Then the arc gap reaches the maximum set length, forming the relatively stable arc voltage and current. However, the fluctuation of the stable arc voltage amplitude is within the normal range. In summary, the dynamically varying current level and arc gap length decides the arc voltage output. Comparing with the experimental arc fault electrical signals, it shows that the variation tendency of

simulated electrical signals are generally consistent with the experimental results in the time domain.

Four points are selected to describe the relative error between simulated and experimental data shown in Fig. 3.2. I_{init} and U_{init} mean the final decreased arc fault current and increased voltage value separately when the arc ignites. $I_{sustain}$ and $U_{sustain}$ means the initial arc fault current and voltage separately when the arc start to burn steadily.

For each group of four arc gap length conditions, arc fault experiment and simulation are carried out at three current levels. By comparing the experimental waveform with the corresponding simulated waveform, the relative error of four selected points are calculated shown in Fig. 3.3. All the relative error of the four points are less than 10%. Meanwhile, the relative error of the initial and sustaining current simulation is less than 4%, which proves the loop current is better simulated. Therefore, the well performance of the proposed V-I arc fault model is verified in simulating arc faults with different arc gap lengths and current levels.

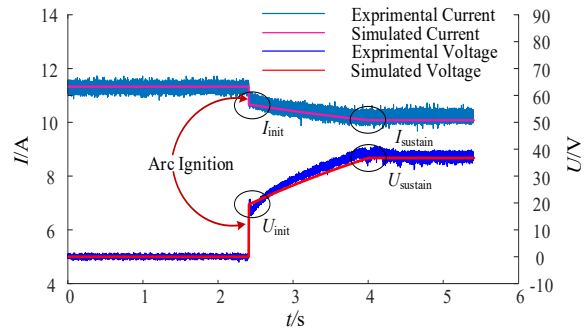


Fig. 3.2 The simulation and experiment comparison of arc fault current and voltage in time domain.

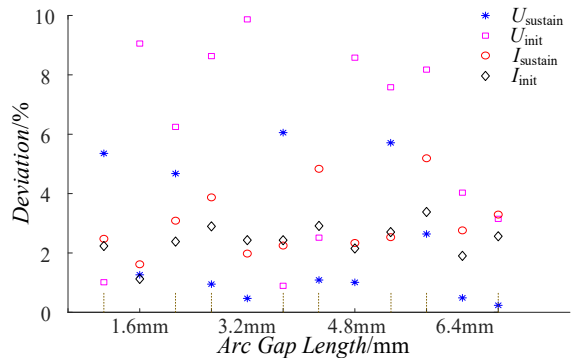


Fig. 3.3 Time-domain relative error analysis between simulation and experiment with different arc gap lengths and current levels.

Based on the high-pass filter designed by the MATLAB platform, the STFT spectrum of the proposed arc noise model is obtained shown in Fig. 3.4. At first, the simulated spectrum presents a process of oscillatory rising from 0 to 50kHz. After 50kHz, the simulated spectrum descends gradually. After about 150kHz, the decrease is significantly smaller than the spectrum from 50 to 150kHz. In general, the simulated

arc noise and the experimental arc noise show a consistent variation trend in the frequency domain. Therefore, the well performance of the proposed pink noise model is verified in simulating practical arc fault noises.

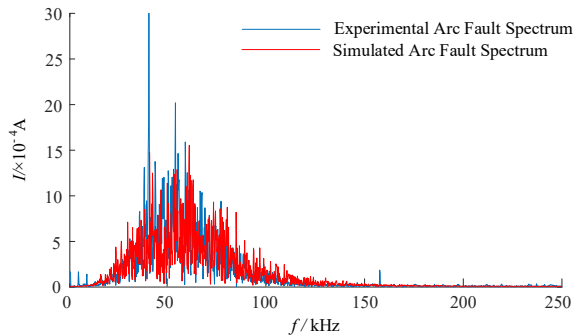


Fig. 3.4 Frequency-domain comparison between simulated and experimental spectrum results with different arc gap lengths and current levels.

Through applying the STFT analysis method introduced in Fig. 2.5, more arc fault data are considered to conduct the spectrum analysis. As shown in Fig. 3.5, the variation range of the arc fault spectrum is acquired for each frequency band. The arc fault noise is varying especially in the frequency band from 50kHz to 75kHz. With the decreasing amplitude value in higher frequency band, the variation range becomes smaller. Similarly, the simulated arc fault noise gives larger fluctuation in the frequency band of 50~75kHz than the higher frequency band. The global level of arc fault noises depends on the power of input white noises. The varying range is related to parameters of high-pass and low-pass filter.

The proposed arc fault model could also be used to simulate the arc fault characteristics in the PV system with converters and inverters [14]. The inverter is made up various power electronic devices and the MPPT control strategy, which would produce the background system noise during the normal operation period. After the comparison analysis, it is found that system noises would have the influence on high-frequency arc fault features. Noises from the power electronic equipment would interfere arc fault behaviors in the low and switching frequency bands.

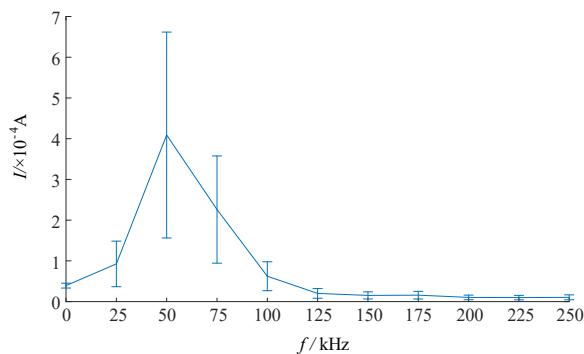


Fig. 3.5 The variation range of the arc fault spectrum.

4 Conclusions

In this paper, an arc fault model that could be applied to PV resistive systems is proposed based on the analysis of arc fault conditions. This model combines the modified Paukert model with the built pink noise model. In the established PV resistive system, the arc fault experiments are carried out with different arc gap lengths and current levels. Four test points are proposed, and the comparison between experimental and simulation results shows that the proposed modified Paukert model has good fitting results in the time domain. The simulation result of the arc noise model shows that the simulation and the experiment have the similar variation trend from 0 to 250kHz in the frequency domain.

5 Acknowledgement

This work was supported by the Key Science and Technology Project of China Southern Power Grid Corporation (090000KK52180116) and the Research Fund of Xi'an University of Technology (256081916).

6 References

- [1] C. Strobl and P. Meckler, "Arc faults in photovoltaic systems," *56th IEEE Holm Conference on Electrical Contacts (HOLM)*, 2010, pp. 1-7.
- [2] F. Reil *et al.*, "Comparison of different DC Arc spectra—Derivation of proposals for the development of an international arc fault detector standard," *39th IEEE Photovoltaic Specialists Conference (PVSC)*, Tampa, USA, 2013, pp. 1589-1593.
- [3] S. Lu, B. T. Phung, and D. Zhang, "A comprehensive review on DC arc faults and their diagnosis methods in photovoltaic systems," in *Renewable & Sustainable Energy Reviews*, vol. 89, pp. 88-98, Jun 2018.
- [4] S. Lim *et al.*, "Simulation analysis of DC arc in circuit breaker applying with conventional black box arc model," *2015 3rd International Conference on Electric Power Equipment – Switching Technology (ICEPE-ST)*, Busan, 2015, pp. 332-336.
- [5] X. Yao *et al.*, "Characteristic study and time-domain discrete-wavelet-transform based hybrid detection of series DC arc faults," in *IEEE Transactions on Power Electronics*, vol. 29, no. 6, pp. 3103-3115, June 2014.
- [6] F. M. Uriarte *et al.*, "A DC arc model for series faults in low voltage microgrids," in *IEEE*

- Transactions on Smart Grid*, vol. 3, no. 4, pp. 2063-2070, Dec. 2012.
- [7] Y. Kim and H. Kim, "Modeling for series arc of DC circuit breaker," in *IEEE Transactions on Industry Applications*, vol. 55, no. 2, pp. 1202-1207, March-April 2019.
 - [8] X. Yao, L. Herrera and J. Wang, "Impact evaluation of series dc arc faults in DC microgrids," *2015 IEEE Applied Power Electronics Conference and Exposition (APEC)*, Charlotte, NC, 2015, pp. 2953-2958.
 - [9] N. L. Georgijevic *et al.*, "The detection of series arc fault in photovoltaic systems based on the arc current entropy," in *IEEE Transactions on Power Electronics*, vol. 31, no. 8, pp. 5917-5930, Aug. 2016.
 - [10] Q. Xiong *et al.*, "Detecting and localizing series arc fault in photovoltaic systems based on time and frequency characteristics of capacitor current," in *Solar Energy*, vol. 170, pp. 788-799, Aug 2018.
 - [11] S. Chen *et al.*, "Hardware Implementation of series arc fault detection algorithm for different DC resistive systems," *2019 IEEE Holm Conference on Electrical Contacts (HOLM)*, Milwaukee, WI, USA, 2019, pp. 245-249..
 - [12] S. Chen, X. Li, and J. Xiong, "Series arc fault identification for photovoltaic system based on time-domain and time-frequency-domain analysis," in *IEEE Journal of Photovoltaics*, vol. 7, no. 4, pp. 1105-1114, Jul 2017.
 - [13] T. Zgonena, L. Ji, and D. Dini. "Photovoltaic DC arc-fault circuit protection and UL Subject 1699B," *Photovoltaic Module Reliability Workshop*, Golden, CO. 2011.
 - [14] S. Chen *et al.*, "Time-frequency distribution characteristic and model simulation of photovoltaic series arc fault with power electronic equipment," in *IEEE Journal of Photovoltaics*, vol. 9, no. 4, pp. 1128-1137, Jul 2019.
 - [15] J. Johnson *et al.*, "Photovoltaic DC arc fault detector testing at Sandia National Laboratories," *2011 37th IEEE Photovoltaic Specialists Conference (PVSC)*, Seattle, WA, 2011, pp. 3614-3619.

Thermal simulation based on fluid-solid coupling method demonstrated on an Automotive Relay

Wang Qiya, Zhang Zhengbin, Xiamen Hongfa Automotive Electronics Co., Ltd., Xiamen, China, 1001242@hongfa.cn

Abstract

The temperature rise of automotive relays, to a certain extent, restricts the development of miniaturization and weight reduction. Therefore, it is important to have a better understanding of the temperature field of automotive relays. A simulation method of temperature field is proposed by using computational fluid dynamics (CFD) software that is based on heat conduction differential equation, fluid motion control equation and radiation heat transfer equation. The temperature rise data gained from calculation and by measurement shows good agreement, which verifies the feasibility of the simulation method. The method is applied to analyse the heat transfer laws of the relay under different ambient temperatures and load current levels, which establishes the foundation of the thermal design and optimization of automotive relay. This method can be used for thermal analysis and optimization of other types of relays, too.

1 Introduction

Automotive relay is a low-voltage switch designed for low-voltage DC system. It used for control, protection, conversion and regulation in vehicle system, it is one of the most widely used switching appliances in low voltage DC system [1]. As the customer has more and more request about the automotive relay, such as working on the high ambient temperature like 125°C, miniaturization and reduction of weight. To meet these high requirements, the temperature rise must be well controlled. So, study on the temperature field and the law of heat dissipation is important for the design and optimization of automotive relay [2-3].

The temperature field analysis of switchgear by numerical calculation software shortens the research and development time compared with the traditional experimental method, and one can more intuitively understand the overall temperature distribution of switchgear [4-5]. In recent years, many researchers in China have done a lot of temperature field simulation on low voltage switchgear by using numerical calculation software. The electromagnetic-thermal coupling of AC solenoid valve was analysed by ANSYS in document [6]. The electromagnetic-thermal coupling of electromagnetic relay was analysed by Flux and Simulink in document [7]. The transient temperature field of DC relay was analysed by ANSYS in document [8]. The steady state temperature fields of DC relay were analysed by ANSYS in documents [9] and [10]. So far, all existing literatures adopt the finite element method to analyse the temperature field of relay based on the differential equation of heat conduction. When considering the heat boundary conditions of convection and radiation, only empirical formula is used to convert the heat dissipation coefficient to impose on the outer wall of the model, without considering that the heat boundary

conditions are restricted by the interaction between the fluid and the wall. It is difficult to get the temperature field distribution which is consistent with the reality, since the heat transfer laws of radiation and convection inside and outside the relay are unable to simulate well.

In the light of the above problems, using CFD simulation tool which bases on heat conduction differential equation, fluid motion control equation and radiation heat exchange equation, a fluid-solid coupling simulation method of temperature field of automotive relay is presented in this paper. This method can simulate the relay temperature field under three heat transfer laws: conduction, convection and radiation. The simulation results are compared with the temperature rise test, and the results verify the feasibility of the simulation method.

After that, this method is used to obtain the heat dissipation ratio of the whole relay and the coil, and analyse the heat dissipation laws under different ambient temperatures and load currents, which lay the foundation for the subsequent thermal design and temperature rise optimization of the automotive relay.

2 Automotive relay's thermal analysis

2.1 Structure of automotive relay

The investigation object of this paper is a plug-in automotive relay. Because it is an asymmetric structure, it is necessary to carry out three-dimensional modeling analysis on the whole relay. The relay structure is shown in Figure. 1.

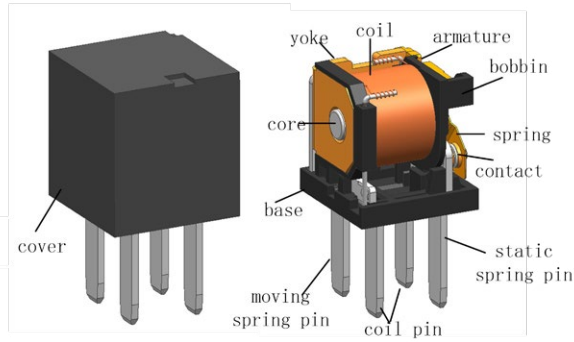


Fig. 1 The model of automotive relay

2.2 Heat source of automotive relay

Most of the automotive relays belong to water tight relays. On the one hand, the heat source and main components are concentrated in the internal space, and with small thermal conductivity parts in it like plastic parts; on the other hand, the internal sealing space is narrow, which will cause the heat is not easy to dissipation, resulting in high temperature rise inside the relay and the pin. The temperature is very high inside the relay and outside terminals due to the heat is difficult to dispersion. Normally the heat source of automotive relays consists of resistance loss and arc heating [11]. The resistance loss mainly includes: 1) Joule heat of relay coil ; 2) Joule heat of contact resistance of load circuit during conduction. The arc heating is caused by contact opening and closing. In the case of long-term stable current-carrying this part of heat can be ignored. Therefore, this paper mainly considers the Joule heat caused by resistance loss.

When the automotive relay works, the coil is energized by rated DC voltage, and the current flows into the coil to produce joule heat. The formula for calculating the heating power is as follows:

$$P_{coil} = \frac{U_{coil}^2}{R_{coil}} \quad (1)$$

In the formula(1) U_{coil} —coil voltage , R_{coil} —coil resistance.

When the load circuit of the relay is on, the contact resistances between the contact and the contact, between the contact and the spring, between the spring and the armature, between the spring and the moving pin and between the yoke and the spring will generate the Joule heat due to the load current. The formula calculating the heating power is as follows:

$$P_{cont} = I_{load}^2 R_{cont} \quad (2)$$

In the formula (2), I_{load} —load current, R_{cont} —contact resistance.

Using the above formula, according to the measured coil resistance and contact voltage drop, the heating power consumption of automotive relay under different test conditions can be calculated.

2.3 Heat transfer principle

When a certain temperature difference is generated in a certain space, the heat transfer will occur. According to the principle of heat transfer, there are three basic modes: heat conduction, convection and radiation. The heat transfer process is often carried out in one of these three basic ways or in two or three ways at the same time. The process of heat transfer can be divided into conduction heat dissipation, convective heat dissipation and radiation heat dissipation according to the characteristics of heat medium [12].

1) Conduction heat dissipation exists in any substance. Its essential phenomenon is the transfer of energy between particle and particle due to the existence of temperature difference. The formula describing the transfer law of heat conduction differential equation is

$$\frac{\partial T}{\partial t} = \frac{\lambda}{\rho c} \left(\frac{\partial^2 T}{\partial x^2} + \frac{\partial^2 T}{\partial y^2} + \frac{\partial^2 T}{\partial z^2} \right) + \frac{\theta}{\rho c} \quad (3)$$

In the formula (3), T is temperature, ρ is the density of matter, c is the Specific heat capacity of matter, λ is thermal conductivity of matter, θ is the heat generated by an internal heat source in the unit volume within a unit time.

2) Convective heat dissipation refers to the heat exchange between fluid and solid when the fluid (gas or liquid) flows through the solid surface. The heat transfer phenomenon is often the combination of heat convection and heat conduction under different conditions. The heat transfer law is described by the fluid control equations (conservation equations of mass, momentum and energy) [13].

According to the CFD software to calculate the Rayleigh number of this type of automobile relay model, the Rayleigh number of is 1.58×10^6 , which is much smaller than the Rayleigh number of 1×10^8 using the turbulent model, so this paper uses the laminar flow model of natural convection to simulate the thermal convection of the relay.

3) Radiation heat dissipation refers to the process of electromagnetic wave energy transfer excited by the change of thermal motion state of microscopic particles in an object. The difference between radiation heat dissipation and conduction and convective heat dissipation is that it does not need to consider whether there is a temperature difference between the object and the fluid in the heat transfer path, but only considering the temperature level on the radiation surface of the object. According to the law of Stefan-Boltzmann, the radiation heat transfer law is described with the radiation heat transfer equation

$$P_{rad} = \sigma \varepsilon (T^4 - T_0^4) \quad (4)$$

In the formula (4), P_{rad} is radiation power; σ is Stefan-Boltzmann constant, $5.67 \times 10^{-8} \text{W}/(\text{m}^2 \cdot \text{K}^4)$; ε is surface emissivity of objects. In this paper, the surface emissivity of black plastic parts is different from that

of other components. T and T_0 are absolute surface temperatures of radiation emitter and radiation receiver, respectively. The radiation model used in this paper is the discrete ordinate (DO) radiation transfer model, which uses the DO method to discrete the direction change of radiation intensity. The solution of the problem is obtained by solving a set of radiation transfer equations covering the whole solid angle in the discrete direction to simulate the radiation relationship between objects.

For the automotive relay, the internal heat is transferred from the inside of the relay to the outer surface of the relay under the combined actions of the conduction, radiation and convection of the sealed air. And finally, it emits into the external space environment under the actions of external air convection and radiation heat transfer.

3 Numerical simulation and experimental verification

3.1 Numerical simulation of temperature field

According to the above analysis of heat source and transfer law, the temperature field simulation of automotive relay is carried out by using CFD simulation software. The flow chart of temperature field simulation of automotive relay is shown in Figure 2.

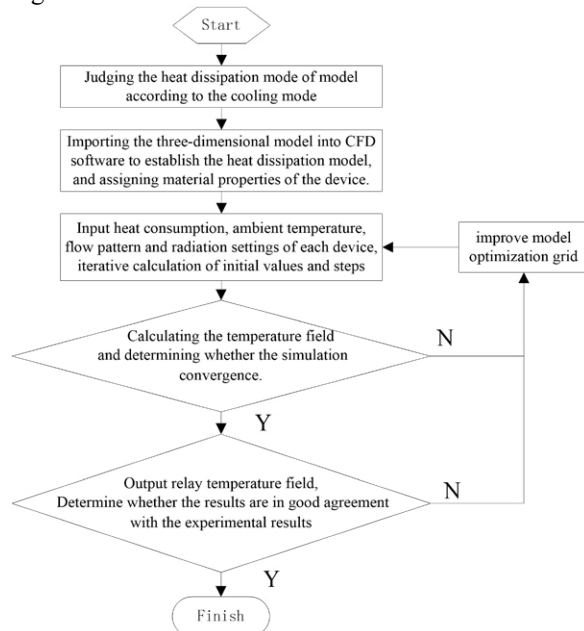


Fig. 2 Flow chart of temperature field simulation of automotive relay

Firstly, the steady state temperature field under natural cooling of the automotive relay is simulated by natural convection and radiation in this paper. The physical property parameters of air, such as density, thermal conductivity, kinetic viscosity and constant pressure heat capacity, affect the natural convective

heat dissipation. These parameters vary according to the temperature [14]. In order to simulate the natural convection accurately, the variations of air physical parameters with temperature in the literature [15] are mainly used in this paper. The nonlinear variation of these parameters and temperature is embedded in CFD software.

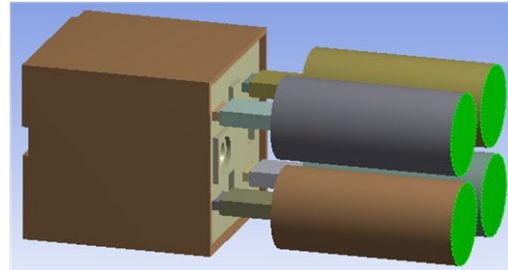


Fig. 3 Solid model of simulation

The solid simulation model is shown in Figure 3. The cylinders of pins are used to simulate the function of wires which are welded pins during test. Density of heat flow rate is added at the bottom of the cylinder according to the convection and radiation of wire which are mentioned to calculate in literature [16].

In the simulation and calculation, the finite volume method and the wall function are used by the CFD simulation software to discrete the convection-solid coupling model to solve the parameters such as temperature, gas flow rate, gas pressure and so on. Therefore, the quality of meshes plays a decisive role in the convergence and accuracy of temperature field calculation [17]. Because the three-dimensional model of the automotive relay is more complex, the Mesh-HD hexahedral mesh type is used in this paper. And local mesh refinement is carried out by adopting a non-continuous grid division mode to ensure that the meshes closely fit the model and the CFD simulation calculation amount is reduced (in Figure 4).

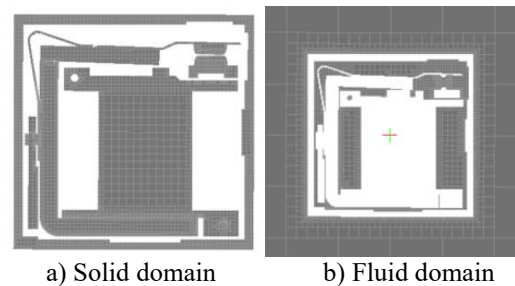


Fig. 4 Mesh section of automotive relay CFD model

Finally, the boundary conditions are set according to the different heat dissipation conditions, such as the laminar flow boundary under natural convection, radiation boundary, and so on. Heat consumption of each device and convergence criterion is also set for thermal calculation. Because in the actual temperature rise test, the relay is in the constant temperature test chamber with constant temperature and no forced air, and the volume of the relay is far smaller than the

working area of the test chamber, it can be considered that the influence of the wall of the test chamber on the temperature rise of the relay is small. The relay is considered in the infinite space. Therefore, the six faces of the calculation domain are set to the opening, so that the solid-free space of the calculation domain is filled with air without forced air flow.

When the ambient temperature is 23 °C, the coil voltage is 13.5 V and the load current is 30 A, the simulated contour image of the temperature field of the automotive relay is shown in Figure 5.

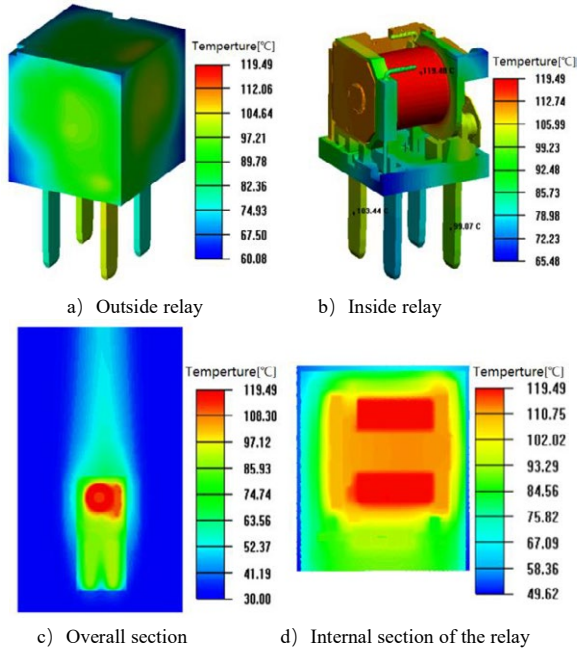


Fig. 5 Temperature field of automotive relay

3.2 Experimental verification of temperature rise results

In order to verify the accuracy of the simulation results, according to the technical standard [19], the temperature rise test of 12 relays of the same type is

carried out by means of direct current stabilized power supply, natural convection high temperature box and direct current electronic load and other equipment's. Due to the different installation position of the automotive relay and the load condition, it is required that the automotive relay functions normally with different ambient temperature and load current [18]. Therefore, this paper mainly simulates and verifies the temperature rise at different ambient temperatures (23 °C, 85 °C, 125 °C) with load current 30A and different load current (10 A, 20 A, 30 A) with ambient temperature of 125 °C, in which the coil voltage is set to 13.5 V DC voltage.

The temperature rises of the moving and static spring pins are measured by using a resistance method and a thermocouple. Taking into account the differences of the performance of relays themselves, the average value of the temperature rise of the 12 relays is taken as the measured value, and the temperature rise test chart is shown in Figure 6.



Fig. 6 Diagram of temperature rise test

When 13.5 V DC voltage is applied at both ends of the coil, 30 A DC and different load loop current (10 A, 20 A, 30 A) are applied to the load loop at different ambient temperatures (23 °C, 85 °C, 125 °C) and the ambient temperature is 125 °C, respectively. The temperature rise values of coil, moving spring and static spring pins' simulation and test are compared with that in Table 2 and Table 3.

Table 2 Comparison of simulation and test temperature rise at different ambient temperatures (load current is 30 A)

Ambient temperature / [°C]	Temperature rise of coil / [°C]			Temperature rise of moving spring terminal / [°C]			Temperature rise of static spring terminal / [°C]		
	Simulation value	Test value	Error / [%]	Simulation value	Test value	Error / [%]	Simulation value	Test value	Error / [%]
23	89.48	90.96	1.63	73.44	74.57	1.51	69.07	68.38	1.01
85	79.40	78.39	1.29	64.62	62.07	4.11	61.30	58.46	4.86
125	68.51	73.62	6.94	52.66	55.56	5.22	51.37	56.19	8.58

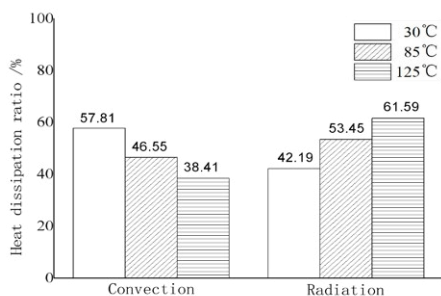
Tab.3 Comparison of simulation and test temperature rise at different load currents (ambient temperature is 125°C)

Load current / [A]	Temperature rise of coil / [°C]			Temperature rise of moving spring terminal / [°C]			Temperature rise of static spring terminal / [°C]		
	Simulation value	Test value	Error / [%]	Simulation value	Test value	Error / [%]	Simulation value	Test value	Error / [%]
10	44.56	43.44	2.58	24.03	22.88	5.03	23.20	22.06	5.17
20	53.1	56.05	5.26	38.37	36.87	2.09	36.68	34.64	5.95

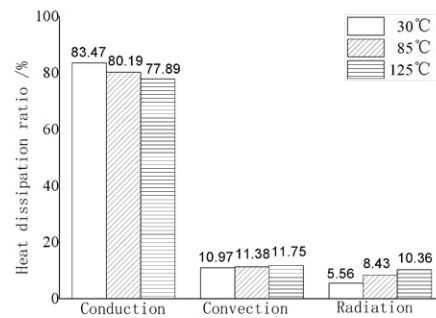
Since the contact resistance consists in the closed contacts, contact and spring, spring and armature, spring and terminal and also the riveting between yoke iron and terminal, the measured contact resistance is the sum of all the contact circuit. Therefore, it is impossible to accurately apply the heat consumption of the contact resistance at each place. Meanwhile the individual difference of relay and the error of measuring equipment itself will also cause certain error. However, from the Tab. 2 & Tab. 3, the error between simulation and measurement is less than the limitation 10 % of the allowable error of engineering. Therefore, in this paper, the fluid-solid coupling method is used to analyze the automotive relay, which is feasible and meets the requirements of engineering accuracy.

4 Heat dissipation analysis of Relay

For the fluid-solid coupled heat transfer, the thermal boundary conditions are determined dynamically by the heat exchange process rather than predetermined. It overcomes the problem that only the heat boundary conditions of convection and radiation are converted into the corresponding heat dissipation coefficient and regarded as constant in the traditional finite element temperature field simulation of relay, but not considering that the corresponding heat boundary conditions are often different because of the different environmental temperature and load conditions. For different ambient temperatures, Figure 7 shows the figures of heat dissipation ratio of relay and coil, and Figure 8 shows the pictures of whole relay gas flow field under different ambient temperatures by CFD software based on the temperature field analysis model constructed above. Figure 9 shows the figures of heat dissipation ratio of relay and coil, and Figure 10 shows the airflow field of relay at different load current levels, respectively.



a) Relay



b) Coil

Fig. 7 Heat dissipation ratios of the relay and the coil at different ambient temperatures (coil voltage 13.5 V, load current 30 A)

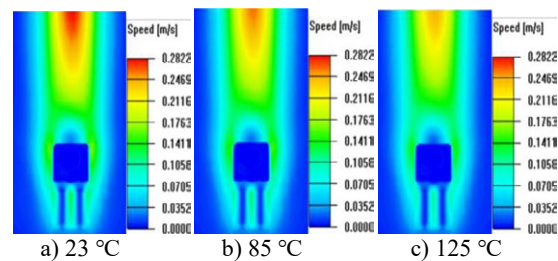
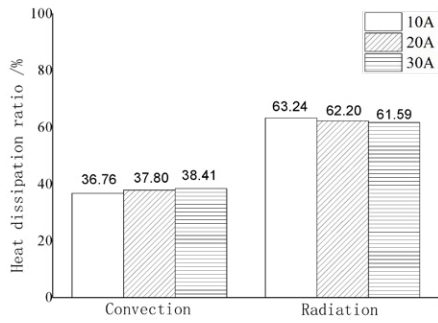
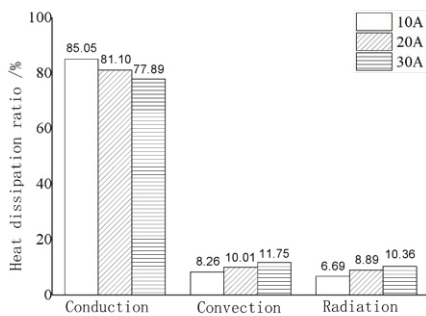


Fig. 8 Airflow field of relay at different ambient temperatures (coil voltage 13.5 V, load current 30 A)

From the Figure 7a) we can find that, with the increase of ambient temperature, the proportion of convective heat dissipation of relay decreases gradually, and the proportion of radiation heat dissipation increases gradually. This is because when the ambient temperature rises, the relay temperature rise falls, reducing the density difference of the air around the relay, resulting in a drop in the air velocity around the relay (This phenomenon can also be found from the nephogram of the airflow field in Figure 8). The decrease of air flow velocity leads to the weakening of convective heat dissipation intensity. In addition, according to the radiation heat dissipation formula, the overall radiation heat dissipation ability of relay increases with the increase of ambient temperature.



a) Relay



b) Coil

Fig. 9 Heat dissipation ratios of the relay and the coil at different load currents (ambient temperature 125 °C, coil voltage 13.5 V)

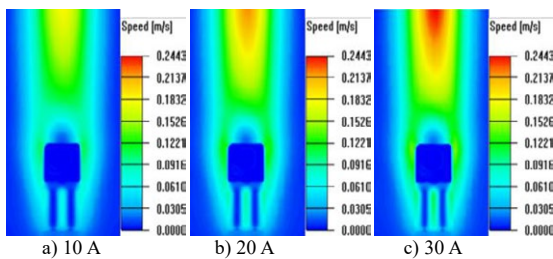


Fig. 10 Airflow field of relay at different load currents (ambient temperature 125 °C, coil voltage 13.5 V)

From the Figure 9a), it is found that, with the increase of load current, the proportion of convective heat dissipation in relay increases gradually, while the proportion of radiation heat dissipation decreases gradually. This is because when the load current increases, the temperature of the relay rises, which increases the density difference of the air around the relay and makes the air velocity around the relay (It can be seen in the picture of air flow field in Fig.10). Therefore, the increase of air velocity leads to the enhancement of convective heat dissipation. Meanwhile, according to the radiation heat dissipation formula, the absolute temperature of the relay increases with the increase of load current. It leads to the gradual enhancement of the thermal radiation ability.

Because the intensity of convective heat dissipation is greater than that of radiation heat dissipation, the proportion of convective heat dissipation increases and the proportion of radiation heat dissipation decreases gradually as a whole. However, the range of change is much smaller than that in Fig.7a).

It can be seen from Fig. 7b) and Fig. 9b) that the heat transfer mode of the coil is mainly conduction heat dissipation, and the proportion of convection and radiation heat dissipation is small. This is because the coil is inside the relay, the internal space of the relay is relatively small, the internal air flow velocity is low, the convective heat conduction is dominated by the heat conduction of air, and the air is a bad heat conductor, which leads to the low proportion of coil convective heat dissipation. Meanwhile, the absolute temperature difference between the internal components of the relay is small, so the proportion of radiation heat dissipation of the coil is also low.

On the other hand, the proportion of coil conduction heat dissipation decreases with the increase of ambient temperature or load current, while the proportions of convection and radiation heat dissipation increase with the increase of ambient temperature or load current. This is because in these two cases, the absolute temperature of the inner components and air of the relay increases, the thermal conductivity of the coil decreases with the increase of the absolute temperature of the coil, while the thermal conductivity of the air increases with the increase of the absolute temperature of the air, which leads to the decreasing of conduction proportion and the increasing of convection proportion; According to the radiation heat dissipation formula, the radiation heat dissipation of the coil will increase with the increase of the absolute temperature in the inner space of the relay, so the radiation proportion increases. Generally speaking, the internal heat transfer mode of relay is mainly conduction heat dissipation, accounting for about 80 %, convection and radiation accounting for about 10 % respectively.

From the Fig.8 and Fig.10, in the condition of natural convection, the maximum velocity of air caused by temperature rise under different ambient temperatures and loads is about 0.28 m/s.

5 Conclusion

In this paper, through the simulation of an automotive relay, the following conclusions are drawn.

1) A simulation method of temperature field of automotive relay based on fluid-solid coupling is proposed. This method can simulate the heat transfer of conduction, convection and radiation of automotive relay well.

2) For heat dissipation of the whole relay, the convective heat dissipation decreases with the increase of ambient temperature, and the radiative

heat dissipation increases with the increase of ambient temperature. At 85 °C ambient temperature, both of them about 50 % proportion of the total heat dissipation. With load increases, the convective heat dissipation proportion increases slightly, and the radiative heat dissipation proportion decreases slightly.

3) For the coil, conductive heat dissipation is dominant, about 80 %, both convection and radiation are about 10 %. Conductive heat dissipation decreases with the increase of ambient temperature and load, and convection and radiation increase with the increase of ambient temperature and load.

4) In the condition of natural convection, the maximum flow velocity is less than 0.3 m/s, which is caused by the temperature rise of the relay.

6 Literature

- [1] Zhai Guofu, Cui Xinglei, Yang Wenying. Overview for Development of Research and Technologies of Electromagnetic Relays[J]. *Electrical & Energy Management Technology*, 2016(02):1-8.
- [2] Xu Zhihong. Theoretical basis of electrical appliances[M]. Beijing: Science Publishing House, 2014.
- [3] Yanyan L, Fanbin M, Baoli L, et al. Study on the reliability test of automotive relays under temperature cycling condition[C]// 26th International Conference on Electrical Contacts (ICEC 2012), China, Beijing, 2012:61-66.
- [4] Zhang Kai, Chen Li-An, Huang Liuliu. Simulation Study on Temperature Field of Solid Insulated Switchgear Based on Finite Element Method[J]. *High Voltage Apparatus*, 2018,54(12):76-81.
- [5] Liu Gang, Li Yang, Chen Yuan, et al. Calculation and experiment verification on temperature distribution and radial temperature of overhead transmission line based on electromagnetic-thermal coupling fields[J]. *Power System Protection and control*, 2018,46(07):7-13.
- [6] Lin Shuyi, Xu Zhihong. Simulation and Analysis on the Three-dimensional Temperature Field of AC Solenoid Valves[J]. *Proceedings of the CSEE*, 2012,32(36):156-164.
- [7] Yang Wenying, Guo Jiuwei, Wang Ru, et al. Establishing and Calculating Methods of Electromagnetic-Thermal Coupling Model of Relay's Electromagnetic Mechanism[J]. *Transactions of China Electrotechnical Society*, 2017, 32(13):169-177.
- [8] Wu Yan, Liu Guojin. Thermal Field Simulation of Miniature Automotive Relays Based on Ansys[J]. *Electrical & Energy Management Technology*, 2015(02): 27-31+37.
- [9] Li Dan Zhang Dairun Yang Lin. Simulation research on thermal analysis of electromagnetic relays[J]. *Electrical Engineering*, 2018,19(03):26-30.
- [10] Su Xiuping, Lu Jianguo, Liu Guojin, et al. Thermal Field Simulation Analysis of Miniature DC Electromagnetic Relays[J]. *Transactions of China Electro-technical Society*, 2011,26(08):185-189.
- [11] Liang Panwang, Li Zhenbiao, He Zhengjie, et al. Transient Thermal Analysis of Sealed Electromechanical Relay in Repeated Short-Term Operation System[J]. *Transactions of China Electrotechnical Society*, 2011,26(01):57-62.
- [12] Wang Baoguo. *Heat Transfer Theory*[M]. Beijing: Mechanical Industry Publishing House, 2009 .
- [13] Pawar, Joshi, Kishor, et al. Application of Computational Fluid Dynamics to Reduce the New Product Development Cycle Time of the SF6 Gas Circuit Breaker[J]. *IEEE Transactions on Power Delivery*, 2012, 27(1):156-163.
- [14] Li Bing, Xiao Dengming, Zhao Su, et al. Temperature Rise Numerical Calculation of the Second Generation Gas Insulated Transmission Line[J]. *Transactions of China Electrotechnical Society*, 2017,32(13):271-276.
- [15] Liu Guangqi, Ma Lianxiang, Liu Jie. Physical property data manual of chemical industry [M]. Beijing: Chemical Industry Publishing House, 2002.
- [16] Barcikowski F, Lindamayer M. Simulations of the heat balance in low-voltage switchgear[C]. *Proceedings of 20th International Conference on Electrical Contacts*, Stockholm Sweden, 2000: 323-329.
- [17] Wang Zijian, Yan Fei, Hou Zhijian, et al. Thermal Field Characteristics of High Voltage Film Capacitors in Thermal Stability Test[J]. *Transactions of China Electrotechnical Society*, 2016,31(17):207-216.
- [18] Yanyan L, Jianguo L, Fanbin M, et al. Study on the reliability test and failure analysis of automotive relays at high temperature [C]. 26th International Conference on Electrical Contacts (ICEC 2012), China, Beijing, 2012:105-109.
- [19] IEC61810-1. Electromechanical elementary relays-Part 1: General requirements[S]. Switzerland: International Electrotechnical Commission, 2008.

Study on Thermoelastic Deformation of Bimetal Sheets in Miniature Circuit Breakers

Minglei Dai¹, Yunkun Deng², Xingwen Li¹

¹The State Key Laboratory of Electrical Insulation and Power Equipment, Xi'an Jiaotong University, Xi'an, 710049, People's Republic of China.

²Yunnan Electric Power Research Institute, Yunnan Power Grid Co., Ltd, Kunming, 650217, People's Republic of China.
xwli@mail.xjtu.edu.cn

Abstract

The overload protection of a miniature circuit breaker is mainly accomplished by the deformation caused by the heating of the bimetal sheet, which affects the performance of the miniature circuit breaker directly. Accurate calculations of thermal distribution and deformation degree of the bimetal sheet are significant to the design of miniature circuit breakers. In this paper, the temperature change and deformation process of the bimetal sheet at various instants are studied. Firstly, a finite element model of the bimetal sheet is built. Then the heating process of the bimetal sheet under different current values is simulated. The transient temperature distribution and the real-time displacement curve of the bimetal sheet are obtained. Meanwhile, the corresponding experimental research is completed. The maximum errors of temperature and deformation are 2.8 K and 0.026 mm respectively and the relative errors are 6.4% and 2.8% respectively. The correctness of the simulation method is verified. The simulation model can provide an empirical basis for the optimal design of a circuit breaker.

1 Introduction

Low voltage circuit breakers are mainly applied in low voltage distribution lines or electrical equipment. It is important for the control and protection of power systems. Nowadays, with the higher requirements for electrical protection, heat tripping problems of circuit breakers have been troubling production quality. To correctly design bimetal materials and improve required performances, the materials are the key to the problem. At present, the manufacturers conduct thermal analysis through experiments. This increases the product design cost and prolongs the life cycle. One main aim of the application of the simulation method in switchgear design is to cut the costs for experimental investigations and to shorten the development cycle. Therefore, if we can use virtual prototyping technology in the product design stage, the design cost and production cycle will be reduced. Therefore, it serves important practical value and development prospects to study the thermal analysis of bimetal sheets.

In recent years, different simulation techniques of temperature rise have emerged continuously. The thermal conduction model is usually used for the power equipment with a plastic shell. In this model, the convection and thermal radiation of the equipment shell surface are equivalent to the heat transfer coefficient. The equipment only takes into the thermal conduction process consideration. Kawase carries out simulation analysis on the temperature distribution of the thermal relay by using the finite element method [1]. Barcikowski found

that the convective and radiative heat transfer process inside the MCB was relatively small, and the effect on the steady-state temperature rise can be ignored [2]. Paulke focused on the analysis of the thermoelectricity process of conductor contact point [3]. It provided the theoretical basis for the thermal analysis of the switching device contact point. According to the actual structure and size of the circuit breaker, Frei further refined the model and carried out a finite element simulation calculation [4].

This paper studies the transient temperature change and deformation process of different types of bimetal sheets at different environments. To obtain the transient temperature distribution and real-time displacement curve of the bimetal sheets, this paper also measures the key component temperature rise of the bimetals by using a temperature rise experiment and makes comparisons with the simulation result.

2 Simulation model and simulation method

2.1 Calculation of thermal conductivity

In thermal analysis, the thermal conductivity of the metal conductor determines the temperature distribution of the whole model. The thermal conductivity of each material always changes with the purity of the metal, temperature, pressure and material structure. Generally, temperature plays a decisive role. In engineering calculations, the relationship between thermal conductivity and temperature of materials is [5]:

$$\lambda = \lambda_0(1 + b\theta) \quad (1)$$

where λ_0 is the thermal conductivity of the material at 0°C, θ is the temperature of the material, and b is a constant.

According to the theory of heat transfer, with the increase of temperature, the thermal conductivity of copper alloy and aluminum alloy changes little. Therefore, in engineering calculations, the thermal conductivity can be considered as constant within a certain temperature range [6]. The thermal conductivity of red copper is $400 \text{ W}\cdot\text{m}^{-1}\cdot\text{K}^{-1}$. Cast aluminum is $144 \text{ W}\cdot\text{m}^{-1}\cdot\text{K}^{-1}$.

2.2 Calculation of heat dissipation coefficient

The heat transfer mechanism in the model is heat conduction, convection and radiation. Generally, heat transfer is determined by the material and thermal convection depends on the geometry and surface of the object [7]. In the investigated circuit breaker, the bimetal sheet is wrapped by the air inside the plastic shell. Therefore, we need to calculate the convective heat transfer coefficient of bimetal to simulate the heat transfer between bimetal sheet wall and air. Convective heat transfer belongs to natural convective heat transfer in limited space, which is related to the temperature of medium [8]:

$$q = \alpha_{con} \cdot A_0 \cdot (T_f - T_0) \quad (2)$$

where α_{con} is the convective heat transfer coefficient of bimetal surface. A_0 is the convective heat transfer area of bimetal surface. T_0 is the ambient temperature and T_f is the surface temperature of the material.

The convective heat transfer coefficient of the surface is also related to the characteristics of the surrounding fluid [9]. In engineering calculations, the correlations of natural convection experiments are widely used:

$$G_r = \frac{g\beta l^3 \Delta T}{\nu^2} \quad (3)$$

$$N_u = C(G_r P_r)^n \quad (4)$$

$$\alpha_{con} = N_u \frac{\lambda}{l_c} \quad (5)$$

where G_r is the Grashof number. P_r is the Prandtl number. N_u is the Nusselt number. g is acceleration of gravity. ΔT is temperature difference between wall and room temperature. l is characteristic length of the object. ν , λ and β are coefficient of thermal expansion of air, kinematic viscosity, thermal diffusivity and thermal conductivity respectively. C is a constant.

Radiation is also a major way of heat dissipation. According to Stefan Boltzmann's law, the calculation formula of heat radiation and the coefficient of heat radiation are following [10]:

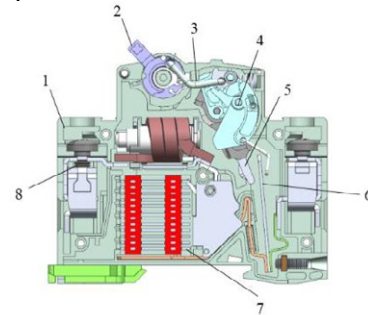
$$q_i = \sigma F_{ij} \varepsilon_i A_i (T_f^4 - T_0^4) \quad (6)$$

$$\alpha_{rad} = \frac{q_i}{A_i (T_f - T_0)} \quad (7)$$

where F_{ij} is a material coefficient. When calculating the radiation and heat dissipation of the outer surface of the shell and the conductor, the value is 1. ε_i is the emissivity. The metal material has a emissivity of 0.3. The insulation material has a emissivity of 0.8. σ is the Boltzmann constant. The value is $5.67 \times 10^{-8} \text{ W}\cdot\text{m}^{-2}\cdot\text{K}^{-4}$. A_i is the radiation heat dissipation area.

2.3 Establishment of simulation model

Figure 2.1 shows the miniature circuit breaker model. On the top is the operating mechanism of the circuit breaker, including handle, connecting rod, lock catch and rotating plate. On the left sides of the circuit breaker are coil, push rod and arc extinguishing grids for short circuit protection of the circuit breaker. The bimetal is located on the right side of the circuit breaker. The left side of the bimetal is connected with the moving contact through a conducting wire and the right side is connected with the right external wire through the copper strip.



1-Shell, 2-Handle, 3-Connecting rod, 4-Rotating plate, 5-Moving contact, 6-Bimetallic strip, 7-Grating, 8-Screw

Figure 2.1 Diagram of the miniature circuit breaker

When the temperature of bimetal rises, the bimetal will bend to the right. When the right lever is contacted and the thermal thrust reaches a certain value, the circuit breaker will trip. The thermal thrust of bimetal sheet is shown in the formula below.

$$F = \frac{k\Delta T b \delta^2 E}{4L} \quad (8)$$

where F is thermal thrust. ΔT is temperature rise of the bimetal sheet. b is width of the bimetal sheet. δ is thickness of the bimetal sheet. E is modulus of elasticity of the bimetal sheet. L is length of the bimetal sheet. k is a constant, depending on the material of the bimetal sheet.

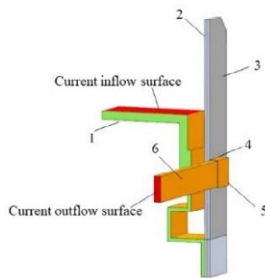
The temperature rise inside the circuit breaker is not considered in this paper. This paper focuses on the temperature rise of the bimetal. Because there are many parts in the circuit breaker, it is simplified to the bimetal model. Figure 2.2 shows a simplified model. The bimetal sheet is 35.5 mm long, 6 mm wide and 0.8 mm thick. The long side of the welding point is 4.1 mm.

The short side is 3.8 mm and the thickness is 1.1 mm. The thickness of contact resistance is 0.1 mm. The resistivity and thermal conductivity of contact resistance are calculated by formula[11]. The contact resistance between the welding point and bimetal sheet is $1 \mu\Omega$.

$$\rho = \frac{R \cdot s}{l} \quad (9)$$

$$\lambda = \frac{L \cdot T}{\rho} \quad (10)$$

where λ is the thermal conductivity. ρ is the electrical resistivity. R is the resistance measured in the experiment. s and l are the cross-sectional area and height of the contact resistance. L is the Lorentz coefficient and the value is $2.8 \times 10^{-8} (V/K)^2$. T is the temperature.



1-Conductive sheet, 2-Passive layer, 3-Active layer, 4-Contact resistance, 5-Welding point, 6-Wire
Figure 2.2 Diagram of the simplified circuit breaker

Figure 2.3 shows the simulation process. Firstly, the bimetal geometry is simplified by SolidWorks software and the bimetal simulation's geometry is obtained. Then, the geometry is imported into the ANSYS APDL module. The material properties of each component are set and the finite element mesh is generated. Figure 2.4 shows the finite element mesh. Finally, according to the ambient temperature and current of bimetal, the heat dissipation coefficient of each part is obtained. Given the boundary conditions of the model, the thermal simulation is carried out to obtain the results of temperature and deformation. We set the ambient temperature, current input surface, current output surface, and add a fixed constraint at the bottom of the bimetal. Then, the convective heat transfer coefficient of bimetallic sheet is set. We can get the temperature and deformation results of bimetal under different conditions.

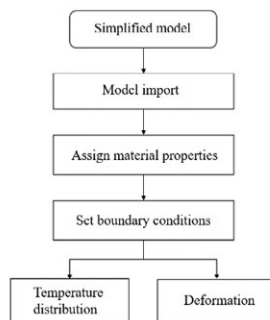


Figure 2.3 Simulation flow chart

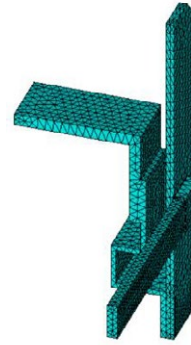


Figure 2.4 The finite element mesh

3 Calculation results of bimetal temperature rise

3.1 Simulation result

There are three kinds of bimetal parameters used in the simulation, which are taken from 63 A rated current circuit breaker, 40 A rated current circuit breaker and 32 A rated current circuit breaker respectively. Table 2.1 shows the main material parameters.

Table 2.1 Table of the miniature circuit breaker

Type	Flexivity ($10^{-6}/^{\circ}\text{C}$)	Mdulus of Elasticity ($\cong \text{N}/\text{mm}^2$)	Resistivity ($\Omega \cdot \text{m}$)	Density (g/cm^3)
63 A	33.8	1.45×10^5	4.8×10^{-8}	8.15
40 A	27.6	1.22×10^5	6×10^{-8}	8.2
32 A	28.1	1.22×10^5	10.5×10^{-8}	8.2

The temperature rise results of bimetals are obtained by ANSYS software. We set material properties of the model material properties of the model, the ambient temperature, current input surface, current output surface, and adding a fixed constraint at the bottom of the bimetal. The temperature distribution and the maximum displacement of different bimetals under different conditions can be obtained. Figure 3.1 shows the temperature distribution of bimetals of 63 A circuit breaker when the ambient temperature is 16°C and the current is 51 A. Figure 3.2 shows the maximum displacement at the same conditions.

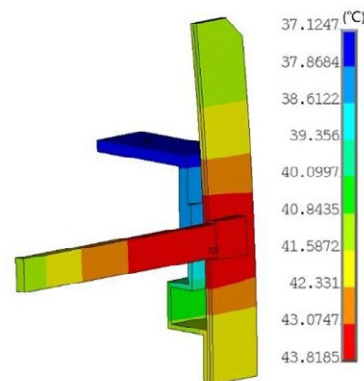


Figure 3.1 Diagram of temperature distribution

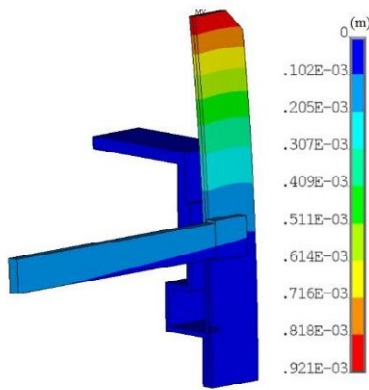


Figure 3.2 Diagram of deformation distribution

It can be seen that bimetal has the highest temperature at the welding point and the highest temperature is 43.8 °C. The rule of temperature distribution on the bimetal is that the bimetal near the welding point has the highest temperature. And the farther away from the welding point, the lower is the conductor temperature. The temperature near the welding point on wire is higher, and the temperature far away from the welding point is lower. The temperature on the copper sheet is the lowest. The maximum displacement of bimetal sheet is 0.921 mm, and the maximum displacement points are at the top of bimetal.

The specifications of three kinds of circuit breakers used in this paper are different. The degree of deformation required is also different. For 32 A rated current circuit breaker, switching can be realized when the deformation is 0.9 mm. For 40 A rated current circuit breaker, switching can be realized when the deformation is 1 mm. For 63 A rated current circuit breaker, switching can be realized when the deformation is 1.2 mm.

Figure 3.3 and Figure 3.4 show the maximum temperature rise and maximum displacement of bimetals of three specifications at different times. In the simulation, the current of 63 A rated current breaker is 51 A, that of 40 A rated current breaker is 51 A, and that of 32 A rated current breaker is 40 A. It can be seen that with the increase of time, the temperature and the maximum deformation of bimetal increase continuously. At 1200 s, the stable temperature and the maximum deformation are achieved.

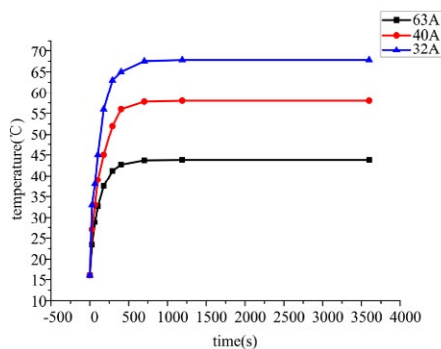


Figure 3.3 Diagram of instantaneous temperature

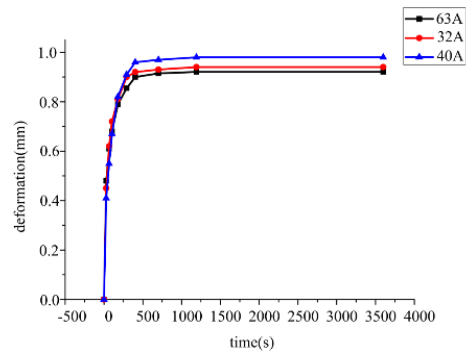


Figure 3.4 Diagram of instantaneous deformation

3.2 Experimental result

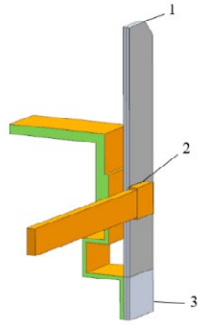
In order to verify the simulation model, the corresponding temperature rise experiment of bimetal is completed. In the experiment, the transformer provides a stable AC voltage and the experimental current is measured by a current coil. A thermocouple is used to measure the temperature rise. In order to measure the deformation of bimetallic sheet, the manufacturer provides a kind of miniature circuit breaker with transparent shell for experiment. Figure 3.5 and Figure 3.6 show the experimental device and the measured specimen. The current of 63 A rated current breaker is 51 A. The current of 40 A rated current breaker is 51 A. The current of 32 A rated current breaker is 40 A, and the temperature measuring points are shown in Figure 3.7.



Figure 3.5 The experimental device



Figure 3.6 The measured specimen



1-Measurement point 1, 2-Measurement point 2, 3-Measurement point 3

Figure 3.7 Measurement points of experiments

Figure 3.8 and Figure 3.9 show the comparison of instantaneous temperature rise and deformation results at measuring No.2 point of three kinds of circuit breakers. The temperature rise simulation results of three types of bimetals are consistent with the experimental measurement values, which shows the correctness of the simulation method. The maximum temperature error of 63 A circuit breaker at No.2 measuring point is 2.8 K and the relative error is 6.4%. The maximum error of deformation is 0.026 mm and the relative error is 2.8%. The maximum temperature error of 40 A circuit breaker is 0.9 K and the relative error is 1.3%. The maximum error of deformation is 0.009 mm and the relative error is 0.9%. The maximum temperature error of 32 A circuit breaker is 0.9 K and the relative error is 1.5%. The maximum error of deformation is 0.048 mm and the relative error is 4.8%. The accuracy of simulation can be improved by introducing more details inside the circuit breaker. Because the bimetal model is simplified in the simulation, the bimetal model can be improved and more details can be introduced in the future work.

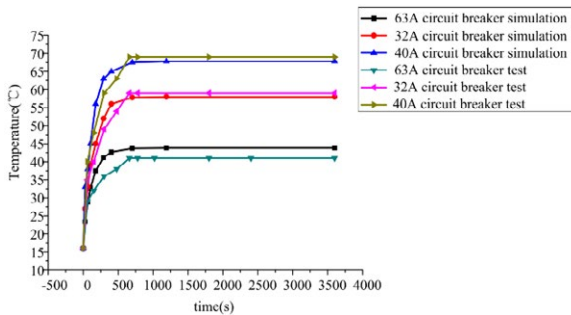


Figure 3.8 Diagram of temperature comparison

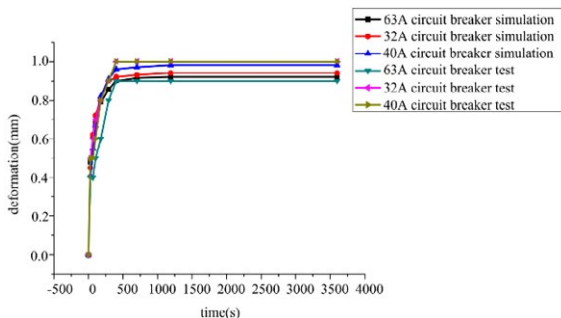


Figure 3.9 Diagram of deformation comparison

Figure 3.10 shows the temperature comparison of the 32 A circuit breaker at different measuring points. It can be seen that the temperature error at No.2 measuring point is the largest and the value 0.9 K. The error at No.1 measuring point is 0.6 K. The error at No.3 measuring point is 0.1 K.

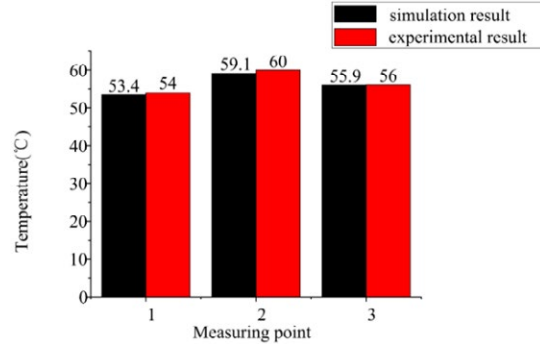


Figure 3.10 Comparison of 32 A circuit breaker results

Figure 3.11 shows the temperature comparison of the 40 A circuit breaker at different measuring points. It can be seen that the temperature error at No.2 measuring point is the largest and the value is 2.8 K. The error at the measurement point 1 is 1.8 K. The error at No.3 measuring point is 1.5 K.

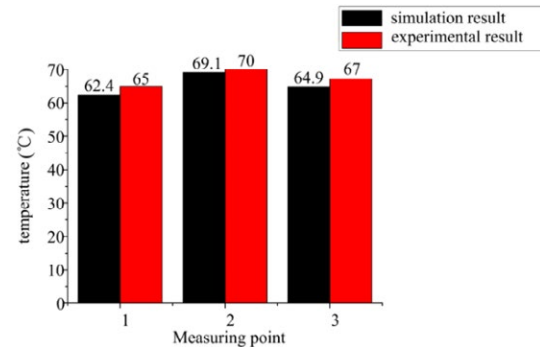


Figure 3.11 Comparison of 40 A circuit breaker results

Figure 3.12 shows the temperature comparison of the 63 A circuit breaker at different measuring points. It can be seen that the temperature error at No.1 measuring point is the largest and the value is 2.6 K. The error at No. 2 measuring point is 0.9 K. The error at No.3 measuring point is 2.1 K.

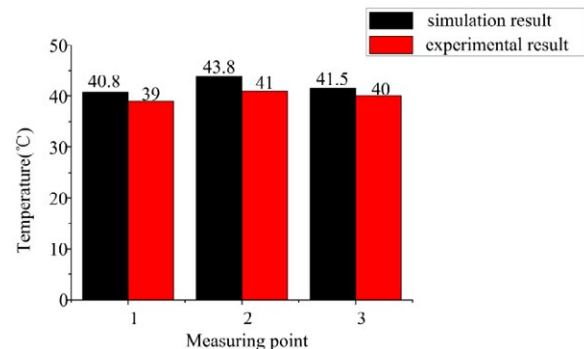


Figure 3.12 Comparison of 63 A circuit breaker results

4 Summary

Based on the bimetallic simulation and temperature rise experiment, this paper mainly studies the temperature change process and deformation process of bimetals at different times. The following conclusions can be drawn: In this paper, the thermal simulation model of bimetal is established, and the heating process of bimetal is simulated. At the same time, the corresponding experimental research is completed to verify the model. The maximum absolute error of temperature is 2.8 K and the relative error is 6.4%. The maximum error of deformation is 0.026 mm and the relative error is 2.8%. The calculated steady-state temperature distribution is in good agreement with measurements. The temperature and deformation of bimetallic sheet can be calculated by the finite element model. The deformation of bimetal sheet under different working conditions can be calculated conveniently by adjusting the boundary conditions. The error between simulation and experiment may be caused by the lack of refinement of the circuit breaker model. The simulation accuracy can be improved by building a more refined circuit breaker model.

5 Acknowledgement

The current work is supported by the Science and Technology Program of China Southern Power Grid Co. Ltd.(YNKJXM20180011).

6 Literature

- [1] Kawase, Y. Ichihashi, T. and Ito, S.: Heat analysis of thermal overload relays using 3-D finite element method. *IEEE Trans. on Magnetics*, vol. 35, no. 3, pp. 1658-1661, May 1999.
- [2] Barcikowski, F. and *Numerische Berechnungen zur Wärme-und Antriebsauslegung von Schaltgeräten.*: Göttingen, Germany: Technische Universität Braunschweig, 2003.
- [3] Paulke, J. Weichert, H. and Steinhuser, P.: Thermal simulation of switchgear. *IEEE Trans. Compon. Packag. Technol.* vol. 25 no. 3 pp. 434-439 Sep. 2002.
- [4] Frei, P. U. and Weichert, H. O.: Advanced thermal simulation of a circuit breaker. *Proceedings of the 50th IEEE Holm Conference on Electrical Contacts and the 22nd International Conference on Electrical Contacts* Electrical Contacts, 2004, Seattle, WA, USA, 2004, pp. 104-110.
- [5] Yang, J. Yin, F. Wang, W. and Shi, X.: Numerical simulation on temperature field for arc spray rapid prototyping. *2011 Second International Conference on Mechanic Automation and Control Engineering*. Hohhot, 2011, pp. 4195-4198.
- [6] Shi, X. Ni, J. and Zheng, Y.: 3-D numerical simulation and computation for transient temperature field of drum brake. *2011 International Conference on Electric Information and Control Engineering*. Wuhan, 2011, pp. 4701-4704.
- [7] Patankar, S. *Numerical heat transfer and fluid flow*. Hemisphere Publishing Corporation, 1980.
- [8] Sparrow, E. M. Stretton, A. J.: Natural convection from variously orientated cubes and from other bodies of unity aspect ratio. *Int. J. Heat Mass Transfer* 28 (1985), P. 741-752.
- [9] Singh, S. Summer, R. Kaltenborn, U.: A novel approach for the thermal analysis of air insulated switchgear. *21st International Conference on Electricity Distribution*, 2011:0495-0499.
- [10] Kaltenborn, U. Dong, X.: Dynamic thermal simulation of gas insulated switchgear. *21st International Conference on Electricity Distribution*, 2011:0492-0496.
- [11] Pradille, C. Bay, F. Mocellin, K.: An experimental study to determine electrical contact resistance. *2010 Proceedings of the 56th IEEE Holm Conference on Electrical Contacts (HOLM)*, 2010: 5 pages.

SF₆ alternative gases and future switching arc research

[«Invited Presentation, ICEC 2020 Switzerland, Christian M. Franck»]

In the past decades, circuit breakers in medium and high voltage networks have been dominated by vacuum and SF₆ gas technology, respectively. The increasing awareness of the high global warming potential of SF₆, the related national and international regulation and legislation efforts, and the consequential increasing objection to use this technology have triggered substantial R&D-efforts to find environmental friendly alternatives. This invited presentation will give an overview on the ongoing and planned activities and recent advancements associated with finding alternative high voltage circuit breaker technologies [1].

In contrast to the harmonized and standardized use of SF₆, the proposed and investigated alternatives are numerous and include various gases as well as vacuum. Pre-standardization initiatives (e.g. Cigre working groups (WG)) try to identify common grounds and suitable measures for comparison. WG B3.45 (“Applications of Non-SF₆ Gases or Mixtures in Medium and High Voltage Gas Insulated Switchgear”) collected the needs for adaptations or new requirements for the safe, reliable and sustainable application of non-SF₆ gases and gas mixtures in gas-insulated switchgear [2]. D1.67 (“Electric Performance of New Non-SF₆ Gases and Gas Mixtures for Gas-Insulated Systems”) collected the state-of-the-art about the electrical behaviour of the different novel insulation gas mixtures. As a satisfactory comparison was not possible based on the available literature, the group also designed and performed an international round-robin test initiative focussing on the electric strength. A3.41 (“Interruption and switching performance with SF₆ free switching equipment”) summarizes information with focus on the switching performance with novel gas mixtures. Also here, the present state-of-the-art does not allow for a satisfactory comparison.

Thus, the High-Voltage Laboratory of ETH Zürich proposed to start “investigations and measurements of basic experiments that allow an unbiased comparison of properties of alternative gas mixtures relevant for switching” [3]. Here, “basic experiments” refers to the fact that the investigations shall be performed under realistic stresses, but not on real breakers and not with type-test conform test circuits. “Comparison” refers to the plan that empirical experimental investigations shall be performed to show differences, but that it is not necessarily the goal to explain differences. “Properties relevant for switching” indicate that basic dependencies shall be studied, but not direct switching performance. To go beyond the state-of-the-art and to be of practical relevance for users, focus is also laid on “unbiased” investigations. For this, the freedom of academic research at a technical university is combined with a wide basis of financial supporters, backed with suggestion of tests by a large group of switching experts. Currently, 19 representative utilities and manufacturers support these activities.

One of the innovative “experimental tools” to investigate the interruption performance is a flexible pulsed current source with which sophisticated current shapes can be generated and which enables advanced tests, e.g. the determination of dissociation, ablation and erosion rates of gas molecules, nozzles and arcing contacts, respectively.

References:

- [1] C. M. Franck, A. Chachereau, J. Pachin “SF₆-Free Gas-Insulated Switchgear: Current Status and Future Trends”, IEEE Electrical Insulation Magazine 37(1), 7-16 (2021).
- [2] CIGRE working group: B3.45 “Application of non-SF₆ gases or gas-mixtures in medium and high voltage gas-insulated switchgear” investigated various aspects of non-SF₆ gases use in substations (Technical Brochure 802, 2020)

- [3] C. M. Franck, J. Engelbrecht, M. Muratovic, P. Pietrzak, P. Simka, Current Zero Club Members of Gas Inner Circle "Comparative tests for non-SF6 switching gases", in preparation for the Special issue of the Journal "B&H Electrical Engineering", Cigre 2021.

Electric Arc Reconstruction from Magnetic Field

Jinlong Dong, Xi'an Jiaotong University, Xi'an, China, djl.1989@stu.xjtu.edu.cn

Luca Di Rienzo, Politecnico di Milano, Milan, Italy, luca.dirienzo@polimi.it

Guogang Zhang, Xi'an Jiaotong University, Xi'an, China, ggzhang@mail.xjtu.edu.cn

Jianhua Wang, Xi'an Jiaotong University, Xi'an, China, jhwang@mail.xjtu.edu.cn

Abstract

The knowledge of current density distribution gives important information for the study of the electric arc in low-voltage circuit breakers. At present, available experimental approaches to investigate the electric arc behavior include electrical measurements, optical and magnetic diagnostic techniques where electric arc shapes and movement can be obtained by these approaches. However, non-invasive experimental methods able to obtain the electric arc current density cannot be found in literature. This paper presents a non-intrusive diagnostic technique which is able to reconstruct the three-dimensional electric arc current density from its magnetic field measurements by solving a magnetic inverse problem. This inverse problem is known to be ill-posed and therefore Tikhonov regularization is used together with the L-curve method to deal with the ill-posedness. Zero-divergence condition on the current density and boundary conditions are incorporated into the formulation of the inverse problem with the help of Whitney elements. A magnetic field measurement system is developed based on a Hall effect magnetic sensor array and a data acquisition board. The sensor array is composed of 64 mono-axial analog-bipolar sensors distributed in eight columns and eight rows. The data acquisition board consists of eight analog-to-digital converters with a maximum sampling rate of 200 kHz and a 16-bit resolution. Experimental tests are carried out using the proposed method in order to study the arc dynamics. The three-dimensional arc current density reconstruction are obtained with the experimental magnetic field data. The reconstructions are compared with the optical images of the arc by using an optical diagnostic technique based on a charge-coupled device camera.

1 Introduction

The current interruption in low-voltage circuit breakers (LVCBs) is characterized by an electric arc. When a fault current occurs in an electrical circuit, the contact opening ignites an electric arc, which slides between two electrodes due to the electromagnetic force and gas flow and finally is extinguished in splitter plates. The electric arc current density gives us very important information to investigate the temperature distribution, the erosion ratio of electrodes and the interactions of the electric arc with nearby sidewalls. It helps to understand the complex physical behavior of the electric arc plasmas in LVCBs during the transient arcing process.

Nowadays, available experimental approaches to investigate the electric arc behavior in a circuit breaker include total current and voltage measurements, optical and magnetic diagnostic techniques.

The first approach is based on current and voltage measurements during the transient arcing process which are then post-processed in order to analyze the arc dynamics [1], [2]. However, processing electrical quantities as well as their time derivatives is not enough to obtain details of the arc plasma, such as the trajectory

of the arc movement and of the arc current density distribution.

Optical diagnostic techniques include optoelectronic cameras [3], fast charge-coupled device (CCD) cameras [4], optical fiber arrays [5], spectrum analysis [6]. The electric arc commutation and movement can be well studied from two-dimensional (2D) optical images in a light pattern. However, optical methods require the use of transparent walls in the experimental device, which would have dramatic influences on the physical properties of the arc plasma [7]. Optical methods are therefore intrusive. Moreover, they can obtain information on the light pattern of the arc which does not perfectly coincide with its current density.

On the other hand, magnetic diagnostic methods are non-intrusive approaches. In [8], [9] the arc phenomenon in LVCBs is studied based on magnetic field measurements where the electrodes and the arc column are assumed to be a succession of 2D rectilinear and thread-like segments of current. Moreover, these methods can only reconstruct the position of the arc in an approximate way. At present, non-intrusive experimental methods able to obtain the 3D electric arc current density cannot be found in literature.

This work focuses on a non-intrusive magnetic diagnostic technique able to reconstruct the 3D electric

arc current density from its magnetic field measurements by solving a magnetic inverse problem.

Different formulations of the magnetic inverse problem of the arc current density reconstruction are presented and numerically analyzed in [10]-[13] and the one in [13] leads to the most accurate reconstructions. In this paper, we present the experimental set up and 3D current density reconstructions obtained from experimental magnetic field measurements using the formulation [13].

2 Experimental setup

The experimental set-up includes a pulsed current source for arc generation, a simplified arc chamber, current and voltage transducers to measure the total current and the arc voltage, a magnetic field measurement system, and a complementary optical diagnostic method based on a CCD camera (Fig. 1).

2.1 Pulsed current source

In order to produce the arc, we use an oscillating discharge into a low-resistance inductance L_0 of a bank of capacitors, of total capacity C_0 and initially charged at a desired voltage U_c . The circuit can generate a half-wave of approximately $f_0 = 50$ Hz sinusoidal current in order to simulate a low-voltage single-phase network, with a peak current I_p varying depending on the value of U_c , i.e., $I(t) = I_p \cdot \sin(2\pi f_0 t)$. The maximum value of the charging

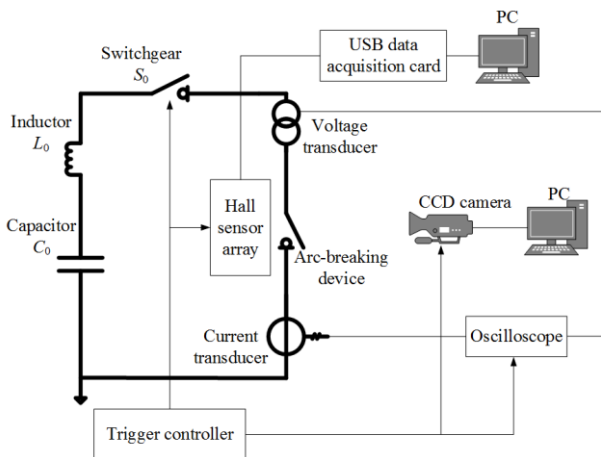


Fig. 1 Diagram of the experimental system. voltage U_c is 1000 V, with its corresponding peak current I_p equal to 9000 A.

2.2 The Simplified Arc Chamber

The arc chamber is composed by two parallel copper electrodes (anode and cathode, Fig. 2), a typical geometry used in modeling and experimental activities when

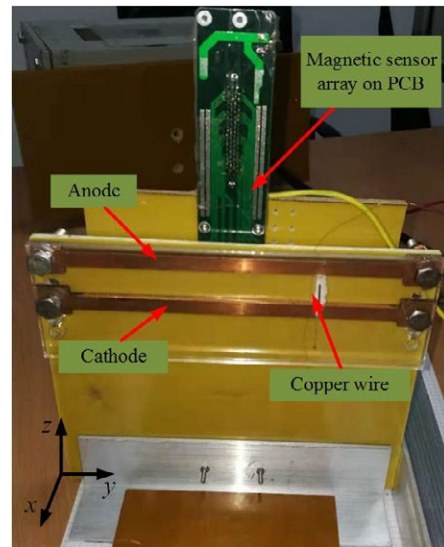


Fig. 2 Magnetic field measurement system and arc-breaking device.

studying low-voltage electric arcs [4]. In real circuit breakers the arcing process is composed by three stages: arc ignition and commutation, arc movement, and arc splitting. In the first two stages the arc is far enough from the splitters so that their influence can be neglected and the described arc chamber is representative.

The electrodes are 240 mm long (y -axis), 10 mm wide (z -axis) and 5 mm thick (x -axis). They are enclosed between two walls, one of which is transparent, in order to keep the arc confined in the chamber. The air gap between the electrodes is 30 mm. The left side of the chamber is open, allowing a free gas flow, while the right side is closed. The transparent wall is used in order to allow the light transmission so that the complementary optical diagnostic technique based on the CCD camera imaging can be used.

The electrodes are connected by a copper wire with a diameter equal to 0.1 mm. During the experiments, as soon as the switchgear S_0 is closed, the current starts flowing and the electric arc is ignited because of the explosion of the copper wire. Then, the arc stretches and moves from one side to the other along the y -axis, due to gas blowing and magnetic forces. The time delay of the arc ignition is approximately in the range of 0.5-1 ms after the switching of S_0 .

2.3 The Magnetic Field Measurement System

The magnetic field measurement system is composed of a matrix of 64 Texas Instruments DRV5053 Hall effect magnetic sensors mounted on a PCB [14], as shown in Fig. 3. The Hall sensor array covers an area of 39.5 mm \times 39.5 mm and are uniformly distributed in eight columns and eight rows, with a distance of 3.5 mm between each other. Each analog Hall-effect sensor is housed in a 2.92

mm \times 1.30 mm SOT package and its measurement range is ± 9 mT. The sensors are mono-axial, i.e. only the component of the magnetic flux density perpendicular to the device can be sensed. The array is placed at 10 mm from the side wall of the arc-chamber.

The PCB is connected to the data acquisition card via a SCSI-68 connector. A high-performance multi-function data acquisition board is used for sampling and buffer the 64 single-ended analog signals synchronously. The core components of this card includes eight AD7606 analog-to-digital converters and a FPGA chip. The maximum sampling rate of AD7606 reaches 200 kHz with a 16-bit resolution. The FPGA module serves as a control unit. The analog outputs of the sensors are converted into digital signals by AD7606, and then buffered in a RAM. Finally, the measurement data are sent to the computer through a USB interface.

The arc voltage between the two electrodes is measured by a differential voltage probe and the total current flowing through the arc column is measured by a current transducer based on a Hall effect sensor.

In addition, a CCD camera is used to obtain the optical images of the electric arc during the arcing process. The spatial resolution of the CCD camera is 512 \times 64 pixels, focused on a 240 mm \times 50 mm area of the cross section on yOz plane such that the completely arc chamber can be recorded. The exposure time of the camera is 5 μ s. The recording speed is 10⁴ frames per second. The obtained optical images will be compared with the electric arc current density reconstructions by the proposed magnetic diagnostic method.



Fig. 3 Texas Instruments DRV5035-VA Hall-effect magnetic sensor array mounted on PCB.

3 Methodology

3.1 Governing Equations

We consider the geometric model of the arc chamber as shown in Fig. 4. Displacement current is neglected according to magnetoquasistatic approximation. In this work, no magnetic materials are considered.

Given a current density $\mathbf{J}(\mathbf{r},t)$, the corresponding magnetic field is described by Ampere's and Gauss laws, complemented by the constitutive relation for linear and isotropic materials, as follows

$$\nabla \times \mathbf{B}(\mathbf{r},t) = \mu(\mathbf{r})\mathbf{J}(\mathbf{r},t), \quad (1)$$

$$\nabla \cdot \mathbf{B}(\mathbf{r},t) = 0. \quad (2)$$

where \mathbf{H} is the magnetic field, \mathbf{B} is the magnetic flux density, \mathbf{r} is the position vector, μ is the permeability, and t is time. The boundary conditions for the current density read

$$\mathbf{n} \cdot \mathbf{J}(\mathbf{r},t)|_{S_j} = 0, \quad (3)$$

$$\int_{S_G} \mathbf{n} \cdot \mathbf{J}(\mathbf{r},t) dS = \pm I_{tot}(t), i=1,2, \quad (4)$$

on the boundary $\partial\Omega = S_j \cup S_{C1} \cup S_{C2}$. I_{tot} is the total current and \mathbf{n} is the outward normal unit vector of the boundary. As shown in Fig. 4, S_{C1} and S_{C2} are the terminal sections of the upper and the lower electrodes. The surface integration in (4) is $-I_{tot}$ (resp., $+I_{tot}$) for S_{C1} (resp., S_{C2}). S_j is the remaining surface of the model with no current flowing through.

Magnetic flux density is then given by Biot-Savart's law

$$\mathbf{B}(\mathbf{r}) = \frac{\mu}{4\pi} \int_{\Omega} \frac{\mathbf{J}(\mathbf{r}') \times (\mathbf{r} - \mathbf{r}')}{|\mathbf{r} - \mathbf{r}'|^3} d^3\mathbf{r}'. \quad (5)$$

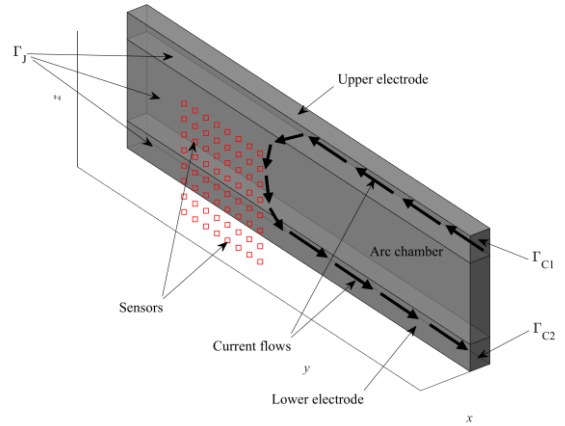


Fig. 4 Geometric model of the simplified arc chamber and location of the sensor array.

3.2 Discretization with Whitney Elements

We discretize current density with the help of Whitney elements [13], [15]. The problem's domain Ω is discretized with a tetrahedral mesh of N nodes, E edges, F faces, and V volumes. The shape function spaces are defined using the Whitney forms, and W^0 , W^1 , W^2 , and W^3 as the nodal, edge, face, and volume function spaces, respectively. The physical quantities represented using Whitney basis functions have a dimension of N , E , F , and V in spaces W^0 , W^1 , W^2 , and W^3 respectively. The relations between these spaces are given by De Rham's diagram [15]

$$\begin{array}{ccccccc}
W^0 & \xrightarrow{\text{grad } w_n} & W^1 & \xrightarrow{\text{curl } w_e} & W^2 & \xrightarrow{\text{div } w_f} & W^3 \\
\Downarrow & & \Downarrow & & \Downarrow & & \Downarrow \\
\mathbb{R}^N & \xrightarrow{[G]} & \mathbb{R}^E & \xrightarrow{[C]} & \mathbb{R}^F & \xrightarrow{[D]} & \mathbb{R}^V
\end{array} \quad (6)$$

where w^n , w^e , and w^f are the shape functions in W^0 , W^1 , and W^2 , respectively. One remarkable property of Whitney elements is that the physically relevant continuity conditions across element boundaries are automatically satisfied and need not to be imposed by extra conditions. The behavior of one face shape function in a tetrahedral element is shown in Fig. 5.

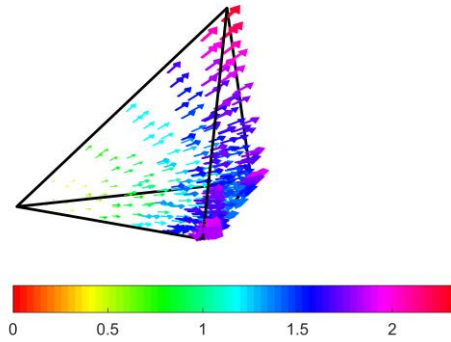


Fig. 5 Face shape functions for a tetrahedral element.

Using Whitney elements, current density \mathbf{J} can be appropriately represented in Whitney space W^2 as a linear combination of face shape functions

$$\mathbf{J} = \sum_{i=1}^F \mathbf{w}_i^f [J]_i, \quad (7)$$

where $[J]$ is the vector of the degrees of freedom for \mathbf{J} . The face shape functions \mathbf{w}^f are different from zero in two adjacent tetrahedrons sharing face f . The degrees of freedom in $[J]$ are the fluxes flowing through their corresponding faces, i.e., the i^{th} element of $[J]$ is the current flux across the i^{th} face. The integral of the face shape function over its corresponding face is one and is zero over all the other faces. Face shape functions have normal continuity, i.e., when passing from one tetrahedron to its adjacent tetrahedron both sharing the face, the normal component of the current density is continuous. Therefore, by representing the current density in Whitney space W^2 , the normal continuity for the current density can be automatically satisfied.

The measurement data collected by the sensor array are ordered in a vector $[B]$, where the i^{th} element of $[B]$ is the magnetic flux density measured by the i^{th} sensor. We denote with N_s the number of the magnetic sensors, here $N_s = 64$. Then, by discretizing (5), the magnetic inverse problem reads

$$[K][J] = [B], \quad (8)$$

where $[K] \in \mathbb{R}^{N_s \times F}$ is the kernel matrix (or lead-field matrix). Using Biot-Savart's law in (5), the generic element of kernel matrix $[K]$ which corresponds to the i^{th} sensor and j^{th} face shape function \mathbf{w}_j^f is calculated by

$$[K]_{ij} = \frac{\mu}{4\pi} \int_{\Omega} \mathbf{d}_i \cdot \frac{\mathbf{w}_j^f(\mathbf{r}_s) \times (\mathbf{r}_i - \mathbf{r}_s)}{|\mathbf{r}_i - \mathbf{r}_s|^3} d^3\mathbf{r}_s, \quad (9)$$

where \mathbf{r}_i is the position vector of i^{th} sensor, \mathbf{r}_s is the integration point, and \mathbf{d}_i is the vector of the orientation of i^{th} sensor.

From (1) it follows that current density is a zero-divergence vector field, i.e.

$$\nabla \cdot \mathbf{J}(\mathbf{r}, t) = 0. \quad (10)$$

In W^2 we can introduce the faces-to-volumes incidence matrix $[D] \in \mathbb{R}^{V \times F}$, which can act as the discrete equivalent of the divergence operator. Thus, the divergence-free condition for the current density in (10) can be represented in the discrete form in space W^2 by

$$[D][J] = [0]^{V \times 1}. \quad (11)$$

The boundary condition defined in (3) implies a zero current flux flowing through surface S_j , i.e., $\mathbf{n} \cdot \mathbf{J}|_{S_j} = 0$. Thus, we set

$$[J]_i|_{f_i \in S_j} = 0 \quad (12)$$

for every face element f_i located on boundary S_j . In addition, from (4) it follows that for the face elements located on S_{C1} and S_{C2} , the sum of the current flux over the area of the terminal sections are the total current, so that

$$\sum_{f_i \in S_{C1}} [J]_i = -I_{tot}, \quad \sum_{f_i \in S_{C2}} [J]_i = I_{tot}. \quad (13)$$

3.3 Common Mode Approach

Following [13], the reconstruction of the electric arc current density can be significantly improved with the help of a common mode approach. We split the total current density \mathbf{J} into a known common mode current density component \mathbf{J}_s with its terminal current being equal to the prescribed total current I_{tot} and into an unknown reduced component \mathbf{J}_m representing the internal current loops in the problem domain, i.e. the current density can be written as the superposition of the known component and an unknown one

$$\mathbf{J} = \mathbf{J}_s + \mathbf{J}_m, \quad (14)$$

or in vector form

$$[J] = [J_s] + [J_m], \quad (15)$$

We denote $[B_s]$ and $[B_m]$ as the contribution to the magnetic measurements produced by $[J_s]$ and $[J_m]$, respectively, i.e., $[B_s] = [K][J_s]$ and $[B_m] = [K][J_m]$. Owing to the linearity of the Biot-Savart operator, we can rewrite the inverse problem of (8) as

$$[K][J_m] = [B_m] = [B] - [B_s]. \quad (16)$$

Instead of solving for the total current density \mathbf{J} in W^2 , we can solve for the reduced unknowns \mathbf{J}_m in W^2 , i.e. the magnetic inverse problem is finally to solve (16).

The known common mode current density is supposed to be known in Ω and must be zero outside Ω , and it does not need to have a physical meaning. Moreover, \mathbf{J}_s should be normally continuous in the whole region, i.e. appropriately represented in W^2 and has a zero divergence, i.e. $\nabla \cdot \mathbf{J}_s = 0$. Then from (10) and (14), the divergence of the reduced current density component is also zero, i.e.

$$\nabla \cdot \mathbf{J}_m = \nabla \cdot (\mathbf{J} - \mathbf{J}_s) = 0 \quad (17)$$

$$[D][J_s] = 0 \quad (18)$$

The common mode current density can be defined as the solution of a stationary electrokinetic problem by imposing a uniform conductivity distribution σ_{cm} in the arc chamber with $\sigma_{cm} \ll \sigma_e$, where σ_e is the conductivity of the electrodes. Hence, we solve the following equation

$$\nabla \times (\sigma(\mathbf{r})\mathbf{J}(\mathbf{r}, t)) = 0, \quad (19)$$

complemented by the boundary conditions given in (3) and (4) and the zero-divergence condition given in (10). Noting that the total current $I_{tot}(t)$ is known (measured by the current transducer), we can calculate the common mode current density $\mathbf{J}_s(t)$ by solving (19) and its corresponding magnetic flux density $\mathbf{B}_s(t)$ using (5). Moreover, the common mode current density takes care of the boundary condition (4). Thus, the reduced electric vector potential needs only to satisfy the zero boundary condition, i.e.

$$[J_s]_i \Big|_{f_i \in S_j \cup S_{C1} \cup S_{C2}} = 0 \quad (20)$$

3.5 Tikhonov Regularization

Due to the reduced space available to locate the sensors near the chamber, the number of sensors is typically much smaller than the number of unknowns where $N_s < F$, i.e., the inverse problem is strongly underdetermined. Moreover, matrix $[K]$ can be considered as the kernel matrix of the Fredholm equation of the first kind. Thus, the magnetic inverse problem is known to be ill-posed in nature. The measurement noise in $[B]$ would be amplified, leading to an unstable or even useless solution. To deal with the ill-posedness, we use Tikhonov regularization to obtain a least-squares solution

$$[J_m^{reg}] = \arg \min_{[J_m]} \left\{ \|[K][J_m] - [B_m]\|_2^2 + \lambda^2 \|[J_m]\|_2^2 \right\} \quad (20)$$

where $\lambda > 0$ is the regularization parameter which is chosen by using the L-curve method [16]. The final solution of the reconstructed current density is given by

$$[J_{rec}] = [J_m^{reg}] + [J_s]. \quad (21)$$

4 Experimental results

4.1 Current Density Reconstruction

The experimental tests are carried out with a 150 V initial charging voltage of the capacitors. The values of the peak current are in a range of 500-700 A during the tests. Fig. 6 shows some examples of the reconstructed current density during different experimental tests compared with the optical images.

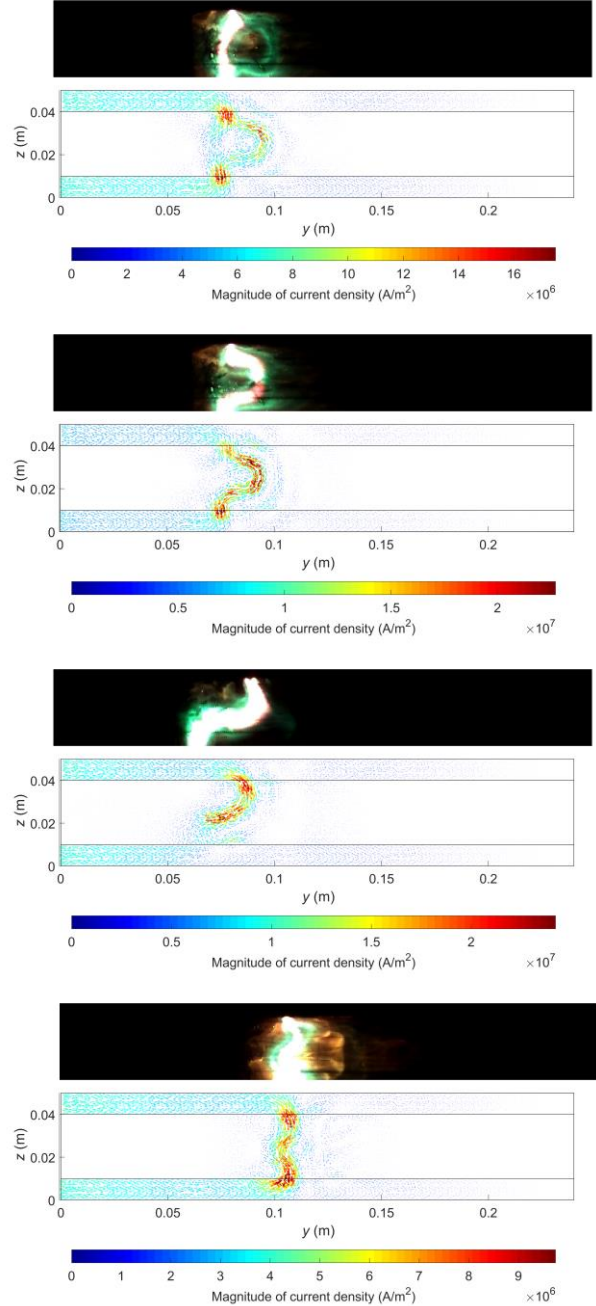


Fig. 6 Example of 2D projections of the reconstructed electric arc current density in different experimental tests compared with the optical image.

The tetrahedral mesh used for the discretization of the geometric model includes 1281 nodes, 6794 edges, 10088 faces, and 4574 volumes. Since the number of the unknowns is equal to the number of the edges, the inverse problem is strongly underdetermined.

At present, a 3D reference known current density is not accessible experimentally. One option is to compare the reconstruction with an optical image of the electric arc obtained by a CCD camera, carrying out a qualitative study. Alternatively, the error in the reconstruction of the arc current density can be evaluated quantitatively from numerical simulations as in [10]-[13].

From the current density reconstructions with experimental magnetic field measurement data, good agreement in terms of the arc shapes and positions can be observed, indicating the feasibility and capability of the proposed approach to describe the main characteristics of the electric arc with enough resolution. As can be noted the most important advantage of the proposed approach is its non-invasive nature and that there is no need to assume the arc is symmetrical or fills the full width of the electrode which are commonly used for both experimental and numerical investigation of the arc dynamics.

4.2 Diagnostics of the Dynamic Arcing Process via the Current Density Reconstructions

The current density reconstruction leads to a novel non-intrusive diagnostic method to study the arc dynamics. With the proposed approach, the dynamic behavior of the electric arcs during the transient arcing process can be studied in terms of the reconstructed current density.

Fig. 7 shows the measured arc current and arc voltage waveforms measured by the transducers during one test. The switchgear S_0 is closed at t_0 after which the current increases. The electric arc is ignited at instant t_{arc} . The

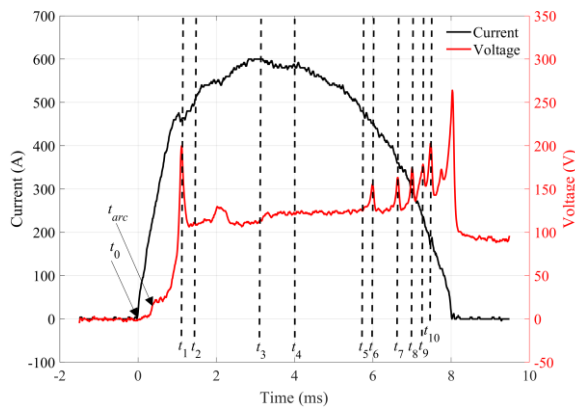


Fig. 7 Arc current and voltage waveforms.

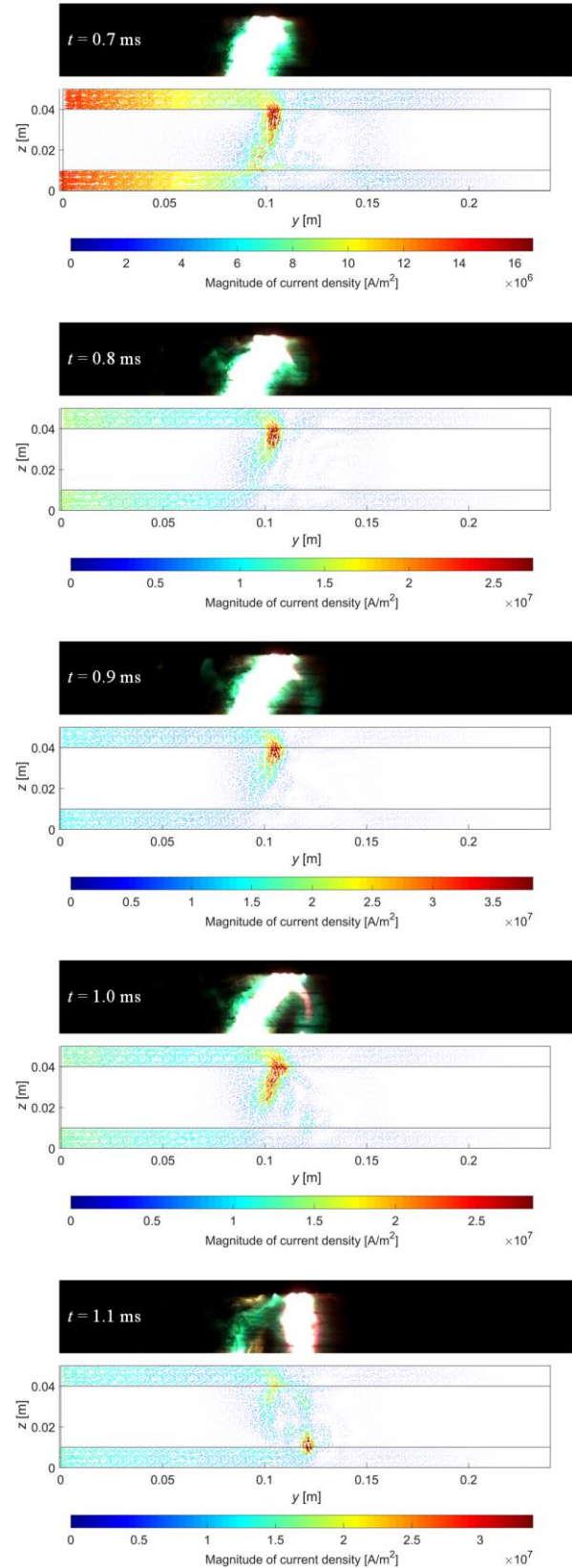


Fig. 8 Reconstructions of the electric arc current density during the period of 0.7 ms-1.1 ms.

total time duration of the discharging process is about 8 ms and that of the arcing process is about 7.5 ms.

Firstly, we focus on the period of 0.7 ms-1.1 ms and the arc current density reconstructions are shown in Fig. 8. At instant t_1 , a jump of the cathode arc root can be noted. Meanwhile, a peak of the arc voltage is also observed from the voltage waveform. The characteristics of the arc motion are related to the total current and the voltage of the electric arc, especially the peaks in the arc voltage waveform. The cathode root does not move continuously along the cathode. During this period, the total arc current

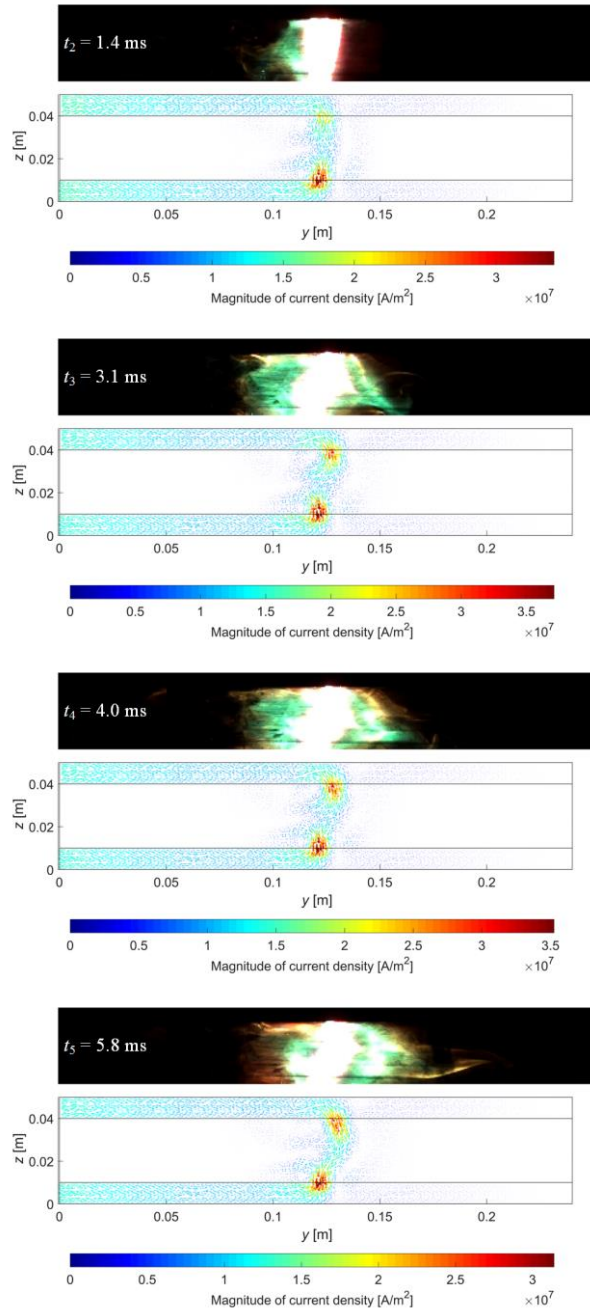


Fig. 9 Reconstructions of the electric arc current density at time instants t_2 - t_5 .

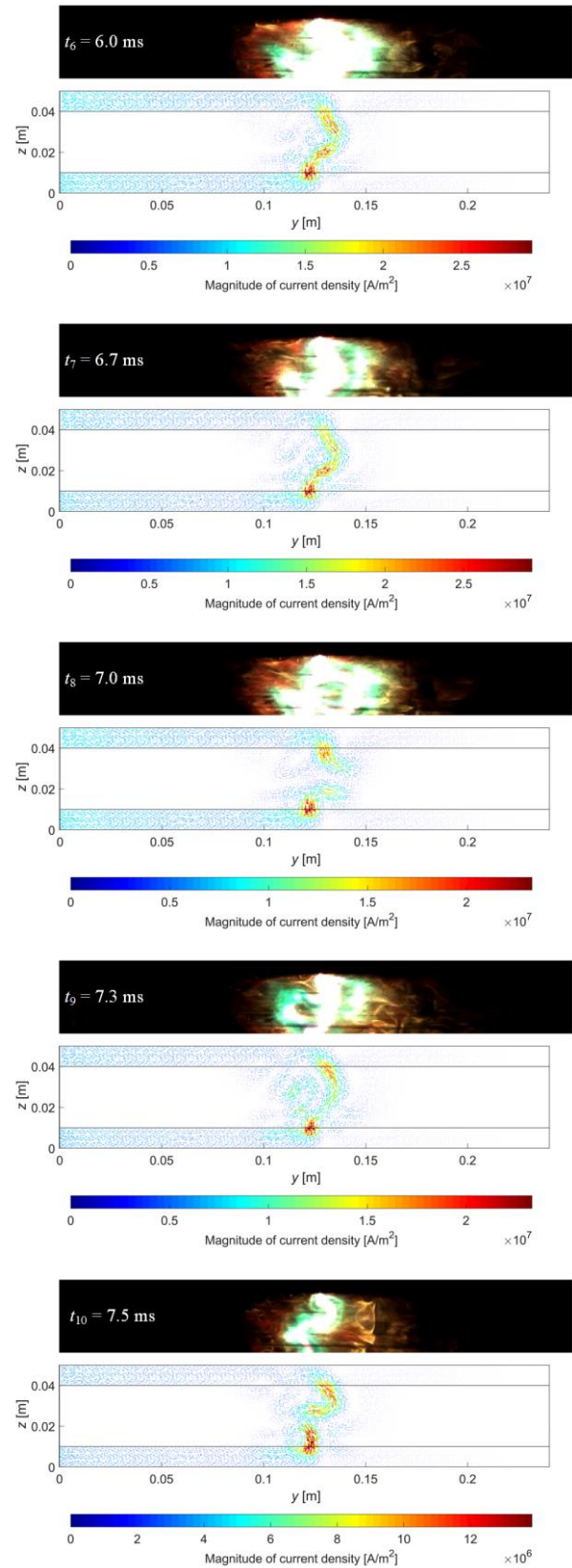


Fig. 10 Reconstructions of the electric arc current density at time instants t_6 - t_{10} .

increase rapidly. The value of the current density near the area of the anode root increase significantly and the anode attachment stays in a constricted mode. However, the current density near the cathode root become smaller since the cathode attachment transfers from a constricted mode to a diffuse mode. Then, a new cathode root and a new discharging channel appear as we can see from the reconstructions at $t = 0.9$ ms and $t = 1.0$ ms. Finally, the discharging channel transfers from the old one to the new one at $t_1 = 1.1$ ms.

After this jump of the cathode arc root, the arc keeps burning in a relatively stable mode between the electrodes from t_2 to t_5 , with its arc voltage staying at about 120 V. Fig. 9 shows the arc current density reconstructions at time instants t_2 - t_5 , from which we can see that the arc column stays almost in the same shape. During this period, the total arc current is approximately in a range of 450-600 A. Therefore, the energy fedded into the arc is high enough to sustain the wall-stabilized arcing process and the arc shapes do not change significantly. High levels of current density are found in the regions of the arc roots touching the electrodes, indicating that both anode and cathode attachments stay in the constricted mode.

However, during time interval t_6 - t_{10} , the total current keeps decreasing, and then the arc column becomes to change its shape, as shown in Fig. 10. The arc column stretches into curved shapes. The total resistance of the arc column is approximately proportional to its length. Thus, more voltage peaks can be seen from the voltage waveform during this period.

5 Conclusion

A non-invasive magnetic diagnostic method is proposed in order to study the arc dynamics in a low voltage arc chamber. It can reconstruct the three-dimensional electric arc current density, with great benefit to the study of the arc phenomenon. The method is implemented by means of a magnetic field measurement system based on an 8×8 Hall effect magnetic sensor array, which is shown to guarantee enough resolution to describe the main characteristics of the arc dynamics. A complementary optical diagnostic method based on a CCD camera is used for comparison.

6 References

- [1] D. Shin, I. O. Golosnoy, and J. W. McBride, "Experimental study of reignition evaluators in low-voltage switching devices," *IEEE Trans. Compon. Packag. Technol.*, vol. 8, no. 6, pp. 950-957, Jun. 2018.
- [2] G. Velleaud, A. Laurent, and M. Mercier, "A study of the kinematics of a low-voltage breaking self-blown arc: analysis of the derivative of the anode-cathode voltage," *J. Phys. D: Appl. Phys.*, vol. 22, no. 7: 933-940, Jul. 1989.
- [3] H. Manhart, W. Rieder, and C. Veit, "Arc mobility on new and eroded Ag/CdO and Ag/SnO₂ contacts," *IEEE Trans. Comp., Hybrids, Manusf. Technol.*, vol. 12, no. 1, pp. 48-57, Mar. 1989.
- [4] F. Yang, Y. Wu, M. Rong, H. Sun, A. B. Murphy, Z. Ren, and C. Niu, "Low-voltage circuit breakers — Simulation and measurements," *J. Phys. D: Appl. Phys.*, vol. 46, no. 27, pp. 1-16, Jun. 2013.
- [5] J. W. McBride, A. Balestrero, L. Ghezzi, G. Tribulato, and K. J. Cross, "Optical fiber imaging for high speed plasma motion diagnostics: Applied to low voltage circuit breakers," *Rev. Sci. Instrum.*, vol. 81, pp. 1-6, May 2010.
- [6] D. Hong, G. Sandolache, J. M. Bauchire, F. Gentils, and C. Fleurier, "A new optical technique for investigations of low-voltage circuit breakers," *IEEE Trans. Plasma Sci.*, vol. 33, no. 2, pp. 976-981, Apr. 2005.
- [7] J. J. Shea, "Gassing arc chamber wall material effect on post current-zero recovery voltage breakdown," *IEEE Trans. Compon. Packag. Technol.*, vol. 27, no. 1, pp. 42-50, Mar. 2004.
- [8] C. Brdys, D. Cajal, J. P. Toumazet, F. Gary, A. Laurent, and C. Arnoux, "Study of the arc behavior in low-voltage circuit breaker by means of optical and magnetic measurements," *Eur. Phys. J. Appl. Phys.*, vol. 49, no. 2, pp. 1-6, 2010.
- [9] P. Toumazet, C. Brdys, A. Laurent, and J. L. Ponthenier, "Combined use of an inverse method and a voltage measurement: estimation of the arc column volume and its variations," *Meas. Sci. Technol.*, vol. 16, no. 7, pp. 1525-1533, Jun. 2005.
- [10] L. Ghezzi, D. Piva, and L. Di Rienzo, "Current density reconstruction in vacuum arcs by inverting magnetic field data," *IEEE Trans. Magn.*, vol. 48, no. 8, pp. 2324-2333, Aug. 2012.
- [11] J. Dong, G. Zhang, Y. Geng, and J. Wang, "Current distribution reconstruction in low-voltage circuit breakers based on magnetic inverse problem solution considering ferromagnetic splitters," *IEEE Trans. Magn.*, vol. 54, no. 10, pp. 8001509:1-9, Oct. 2018.
- [12] J. Dong, G. Zhang, Y. Geng, and J. Wang, "Influence of magnetic measurement modeling on the solution of magnetostatic inverse problems applied to current distribution reconstruction in switching air arcs," *IEEE Trans. Magn.*, vol. 54, no. 3, pp. 8000704:1-4, Mar. 2018.
- [13] J. Dong, L. Di Rienzo, O. Chadebec, and J. Wang, "Application of Whitney elements for the reconstruction of electric arc current density in low-voltage circuit breakers," *COMPEL*, vol. 38, no. 3, pp. 1036-1047, 2019.
- [14] Texas Instruments. (Dec. 2015). *DRV5053 Analog-Bipolar Hall Effect Sensor*. [Online]. Available: <http://www.ti.com/product/drv5053>
- [15] A. Bossavit, "Whitney forms: A class of finite elements for three-dimensional computations in electromagnetism," *IEE Proc. A. Phys. Sci. Meas. Instrum. Manage. Edu.-Rev.*, vol. 135, no. 8, pp.493-500, Nov. 1988.
- [16] P. C. Hansen and D. P. O'Leary, "The use of the L-curve in the regularization of discrete ill-posed problems," *SIAM J. Sci. Comput.*, vol. 14, no. 6, pp.1487-1503, Nov. 1993.

Model-based Design of Circuit Protection in DC Grids

Christian Strobl, E-T-A Elektrotechnische Apparate GmbH, Altdorf, Germany, christian.strobl@e-t-a.de

Abstract

For DC grids, specific protective devices have to be designed depending on the application and on nominal voltage. Not only the basic functionality of switching direct current has to be taken in account, also a general concept depending on the topology of the grid and on the control of the converters has to be set up. Methods of factorial analysis using simplified equivalent circuits are helpful to establish an overall protection concept and to adapt the parametrization of the devices.

1 Introduction

For stationary direct current (DC) grids with semiconductor-based converter stages, circuit breakers and switches have to be redeveloped – in many application cases a revision of conventional AC-switchgear is not expedient.

Depending on system topology, on transient inrush characteristics, on maximum sustained short circuit current and furthermore on converter control dynamics, specific requirements for protective and switching devices can be set up. For that purpose, a factorial analysis based on component, line and fault models delivers basic information about current and voltage characteristics in cases of normal operation and in cases of faults. Not only short circuit and overcurrent fault events have to be analyzed. In the case of controlled load components with constant or only slowly changing power demand, serial faults and gradual malfunction of subcomponents might also lead to a rise in current in the affected branch.

Comparing normal operation and faulty modes, suitable tripping characteristics have to be defined in order to ensure a fast and selective de-energizing of faults and to avoid false tripping. For that reason not only the characteristics of single devices have to be specified, but an overall system protection concept has to be set up, which may also include additional features like power monitoring. Methodologies and parametrization of protective devices have to be coordinated to ensure optimum performance between all system components.

In the following, several issues regarding different designs for circuit protection devices will be discussed and compared. Then modeling concepts and specific signal analysis methods using simplified equivalent circuits for the DC-grid are introduced. They can be used to select the suitable switching methodology and to define the appropriate tripping characteristics for each circuit breaker in the case of a

distributed grid including loads with constant power demand.

Finally, some practical aspects for DC applications with a special focus on load shedding, power management and remote monitoring capability will be discussed.

2 Electronic, Mechanical and Hybrid Switching Devices

Normative directives regarding personal safety and system protection depend on nominal system voltage. It is defined whether galvanic isolation has to be guaranteed after switching off a certain branch of the grid if a protective device has tripped due to a recognized fault or was remotely triggered [1, 2]. For that reason, electronic devices based on power-semiconductors are state of the art especially in cases of extra-low nominal system voltage (< 120 V DC). In cases of higher voltages usually mechanical or hybrid components are needed.

For electronic devices suitable semiconductors have to be selected in order to withstand maximum permanent current and to show a low on-resistance. Current measurement methods delivering an adequate identification of faulty modes have to be included. Depending on the characteristics of the measured current signal, different strategies can be defined to clear a fault. In cases of low overcurrent e.g. current limiting mode can be selected. However, an instantaneous shut off is initialized if a sudden rise of the current signal over a threshold value can be detected. Supervised teach-in or unsupervised model-based machine learning methodologies can be included for a specific adaption of parameter values to system characteristics [3, 4].

Mechanical switching devices have to be designed in order to clear DC switching arcs within a short time of few ms. Due to a missing zero crossing of current like in AC, the arcs have to be split up using specifically designed arcing chambers with splitter plates. Permanent magnets are also useful in order to force an arc from the contact system towards the switching

Topics of this work were supported in part by the Bundesministerium für Wirtschaft und Energie (BMWi.IIC6), Germany, under grant 03EI6009A (project “DC-Schutzsystem”).

chamber especially for lower current amplitudes with only a small self-excited magnetic flux [5].

Hybrid devices (**Fig. 1**) combine the advantages of electronic and mechanical devices providing short reaction times on faults and low on-resistance due to a mechanical bypass (ME_p in **Fig. 2**) of the semiconductor electronics (SC). Specific strategies have to be implemented for the interaction of both subcomponents: In order to prevent contact surface erosion, switching at nominal or at lower overcurrent amplitudes is mainly performed by semiconductor devices. However, the parallel mechanical subcomponent takes over if very high amplitudes are expected, which would destroy the electronics. Depending on nominal voltage, a second mechanical switch (ME_s) in series is needed to ensure galvanic isolation. ME_s is set up as a first-to-make and last-to-break contact and is therefore switching at zero current.

Also overcurrent protection can functionally be included into a hybrid switch or hybrid relay in several ways. For ME_p a mechanical overcurrent circuit breaker can be applied operating in coordination with the semiconductor switch. As an alternative, a relay is used for ME_p and internal or external current measurements are evaluated in order to trip the hybrid device if an overcurrent of a specific amplitude and duration can be measured. Specific tripping characteristics have to be implemented according to a given characteristic tripping curve, which is adapted for the specific application.

3 Precise and Selective Protection against Faults in DC-Grids

In modern DC applications grid architectures show great diversity. Often several voltage levels are used. E.g. in more and more telecommunication or datacenter installations DC 380/400 V is common for transmission over a longer distance and for primary distribution, whereas -48 V or -60 V is the nominal voltage for secondary distribution [6].

Usually AC/DC or DC/DC converters powering higher distribution levels (source converter SC_0 in **Fig. 3**) are operating with output voltage control including output current limitation. If the loads are characterized with constant or varying power demand, secondary load converters (LC) provide the optimum load operating point for a specified range of input voltage. As long as the load is operating in a quasi-stationary mode, the load converter input shows constant power sink characteristics with input current limitation. All converter devices include input and output filters, which mainly consist of capacitors between the lines and common mode chokes.

Even though the converters include self-protection functionality during operation, each branch is



Fig. 1 Hybrid relay HVR10 (with nominal voltage of 1000 V, nominal current up to 300 A, breaking capacity of 2000 A) [7].

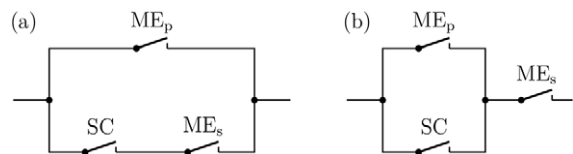


Fig. 2 Different principal designs of hybrid switches using a semiconductor device (SC), a mechanical switch (ME_p) in parallel and further a mechanical switch (ME_s) in series in order to ensure galvanic isolation, if needed [8].

equipped with an overcurrent protective device, usually located at the distribution unit. It has to limit prospective overcurrent and short circuit current or to switch off the affected branch in case of a fault. Therefore its task is to provide a selective de-energizing of a potential fault, keeping alive the unaffected branches. Electronic devices or mechanical circuit breakers (CB) – latter also ensuring galvanic isolation – are state of the art for that purpose. In recent years, also hybrid devices have been developed [7].

Especially if high overcurrent or prospective short circuit current can be expected due to a high overall grid capacitance, and if further a steep current rise may occur in the case of a fault, devices based only on semiconductor switching may fail. Mechanical devices or sub-devices have to be used instead or have to be combined with the power-electronics resulting in hybrid breaker functionality. As mechanical switchgear usually takes several milliseconds for breaking the contacts, a specific selectivity analysis has to be performed depending on the application, in order to avoid false tripping of unaffected branches.

To limit the inrush current involved by the input capacitance of the load converter and its filter, often pre-charging circuits are used [5]. Depending on nominal voltage and current values, active switch-mode methods using the semiconductors in electronic protective devices, thermistors or additional resistors, which are bridged after a certain time-span, can be applied. Where technical or financial reasons do not allow the use of pre-charging devices or methods, transient inrush current values are much higher than sustained current rating. For that reason the selection and parametrization of precisely operating overcurrent protection devices is a challenging task.

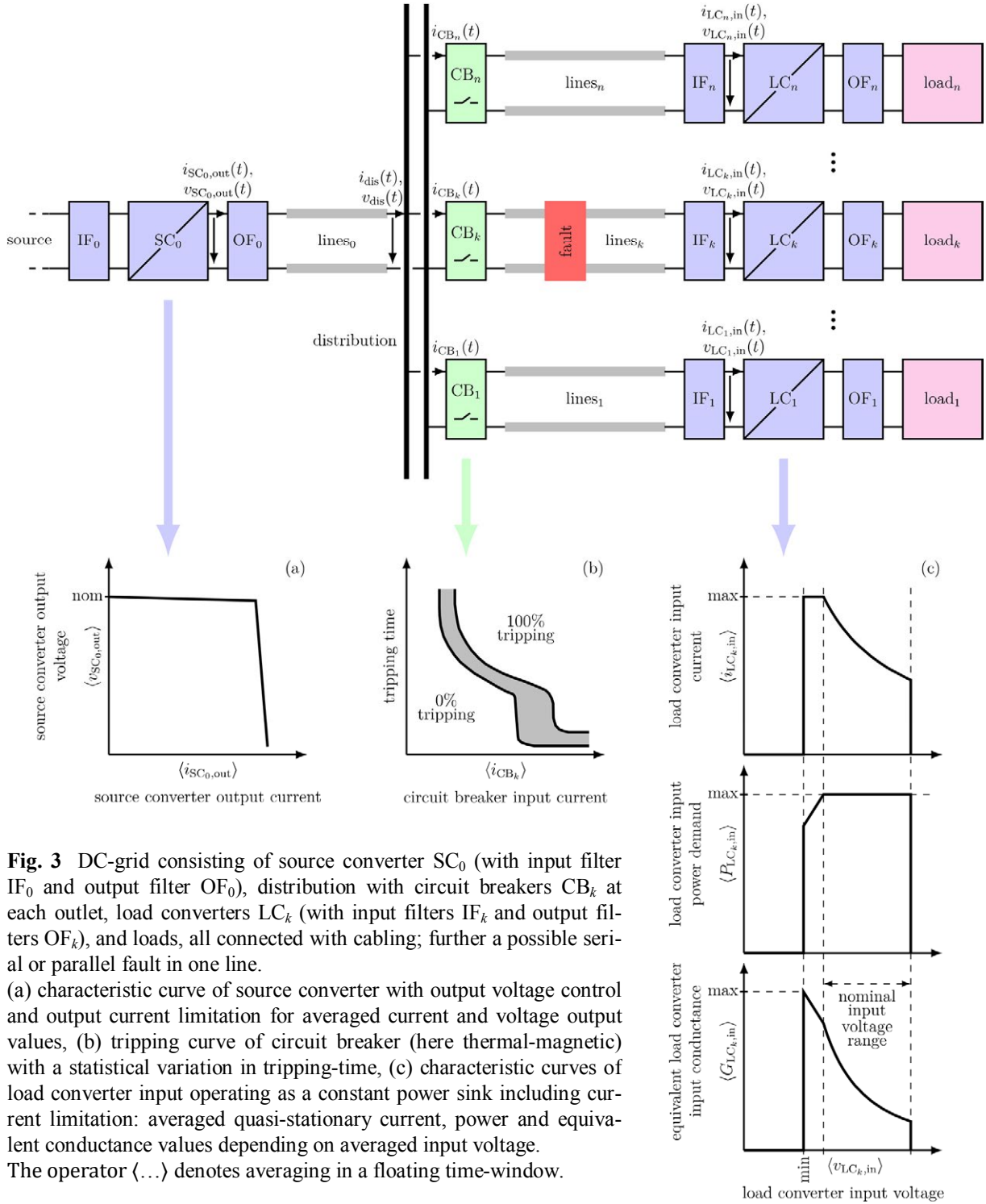


Fig. 3 DC-grid consisting of source converter SC_0 (with input filter IF_0 and output filter OF_0), distribution with circuit breakers CB_k at each outlet, load converters LC_k (with input filters IF_k and output filters OF_k), and loads, all connected with cabling; further a possible serial or parallel fault in one line. (a) characteristic curve of source converter with output voltage control and output current limitation for averaged current and voltage output values, (b) tripping curve of circuit breaker (here thermal-magnetic) with a statistical variation in tripping-time, (c) characteristic curves of load converter input operating as a constant power sink including current limitation: averaged quasi-stationary current, power and equivalent conductance values depending on averaged input voltage. The operator $\langle \dots \rangle$ denotes averaging in a floating time-window.

4 Modeling Methods

Concerning all possible applications in DC grids, it is not possible to give general design suggestions for protective devices. In order to surpass basic functionality given by standards, model based methods are helpful to adapt or select devices for an enhanced system performance of a specific application. Usually the designer of system protection does not know all specific technical details about the used converters. In most cases only input and output ranges of voltage and current and maximum transmitted power

are given. Depending on the application, only the basics on converter topology and control dynamics are described in datasheets. Typical value ranges of input capacitance can be estimated, for a more precise determination the input or output impedance has to be measured by applying high-frequency test-signals or by analyzing signals recorded during trial switching events. Also, in most cases the exact cable lengths are not known and prior knowledge about cable resistance and inductance is unprecise. In order to facilitate the selection and tuning of the devices to avoid false tripping in the case of inrush

current and to operate selectively in distributed grids, several methods of factorial analysis regarding the main equivalent parameters of grid components can be used. In the following, transient system modelling based on continuous or discrete time domain during inrush and faults as well as quasi-stationary grid modelling is presented. In the following examples, the grid models are parametrized for data-center or telecom applications, but can also be used for grids with different system voltages or power demand.

4.1 Modeling of Inrush Behavior and of Grids with Parallel Fault Events

As a first simplification for modelling the current inrush in the case a branch is activated, stable voltage conditions at the distribution unit due to high valued connected grid capacitance are assumed.

The lines of a branch numbered with k usually can be modelled using distributed resistance and inductance. Distributed cross-capacitance and conductance of the cables can be neglected due to low values. For that reason line resistance and inductance are concentrated to equivalent elements R_{lines_k} and L_{lines_k} for a given length l_{lines_k} of a uniform cable (Fig. 4a).

Instead of complicated load input filter circuits only the dominant resulting capacitance C_{IF_k} is used for the simplified linearized model circuit. Common mode chokes as well as equivalent capacitor series resistance and low-valued EMC-filter components are disregarded.

For modelling an inrush current behavior for a faultless branch, which is switched on at time $t = 0$ using an electronic switch, a mechanical breaker or a relay at the distribution unit, a resulting equivalent circuit can be used. In the model an ideal switch can be combined with a time-dependent switching resistance $R_{CB_k}(t)$ for that purpose. It can be set to a constant variable for an approximate calculation. For mechanical switchgear more elaborate models including bouncing effects and arcs can be used instead.

During the switching operation the equivalent load converter conductance $G_{LC_k,in}(t)$ starts at zero. It shows

a sudden step up to a high value, when the converter starts to work at minimum input voltage, and then declines with a rising voltage level at the input filter capacitor.

As already stated, in many applications converter control dynamics are not known exactly by the user. If (i) the load converter is based on a buck topology without a conductive serial path through initially deactivated converter semiconductors and blocking diodes, (ii) its minimum voltage input level is not too low and further (iii) its control dynamics can be assumed to be quite slow compared to transient effects caused by passive line and filter components, then its conductance can be disregarded for the principal simulation of the first time span of the inrush process.

If, on the other hand, converter control is very fast and its minimum voltage input level quite low, the power demand soon rises to an approximately constant level. In that case inrush current modeling must be based on a time-dependent conductance $G_{LC_k,in}(t)$.

For a rough estimation in order to define the parametrization of a suitable protective device, also a linearized circuit model can be calculated using the maximum expected conductance $G_{LC_k,in,max}$, which can be estimated with given nominal power and minimum input voltage disregarding converter losses.

If linearizations can be used and parameter estimations are given, the inrush current behavior which results after activating the switch can be calculated as

$$i_{CB_k}(t) = v_{SC_{0,out,nom}} \mathcal{L}^{-1} \left(\frac{sa_1 + a_0}{s^3 b_3 + s^2 b_2 + sb_1} \right) \quad (1)$$

with the abbreviations

$$\begin{aligned} a_1 &= C_{IF_k}, \\ a_0 &= G_{LC_k,in}, \\ b_3 &= C_{IF_k} L_{lines_k}, \\ b_2 &= C_{IF_k} (R_{CB_k} + R_{lines_k}) + L_{lines_k} G_{LC_k,in}, \\ b_1 &= (R_{CB_k} + R_{lines_k}) G_{LC_k,in} + 1. \end{aligned} \quad (2-6)$$

The operator \mathcal{L}^{-1} denotes inverse Laplace-Transform and s is the frequency variable in Laplace-domain.

If no parameter estimations are given, trial switching

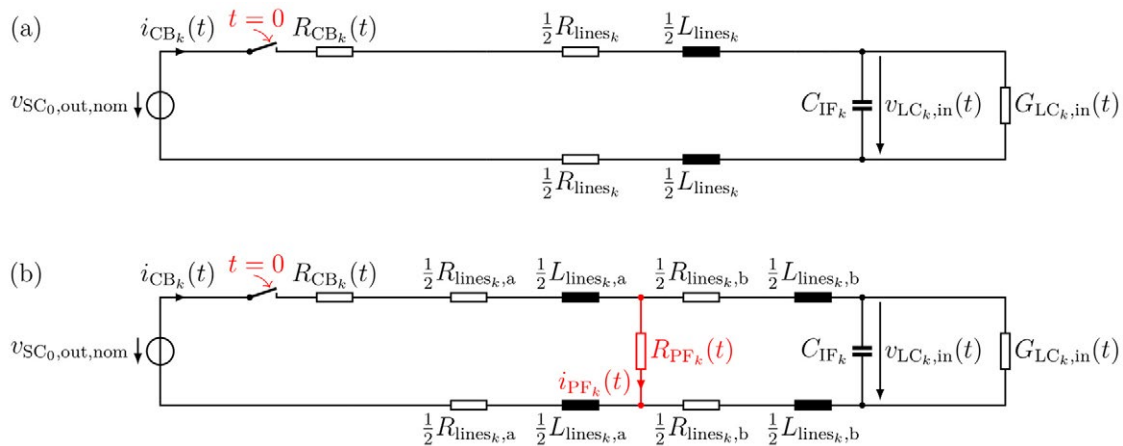


Fig. 4 Equivalent circuit for activating controlled load (a) without or (b) with parallel fault within the cabling.

events can be performed and the values of equivalent elements can be estimated from the measurements in time-domain by system identification methods [3, 4].

With this parametrized model several cases with varying cable length can be calculated as a factorial analysis. Based on the results, circuit breaker characteristics can be adjusted (i) in order not to false-trip in the case of normal inrush, (ii) but to trip at start-up, if there is an already existing parallel fault in the cabling (Fig. 4b), and (iii) to trip in the case of a fault event occurring during steady-state operation.

In Fig. 5 approximations of inrush current have been calculated for a test circuit without and with an additional pre-charging resistor of 4Ω including a potential parallel fault for various fault resistivity and location (for further parameter data see Fig. 5). Based on a linear model in continuous time-domain, different cases between zero and a maximum average equivalent load converter conductance have been performed. The current signal value range for conductance values between these two limits is depicted.

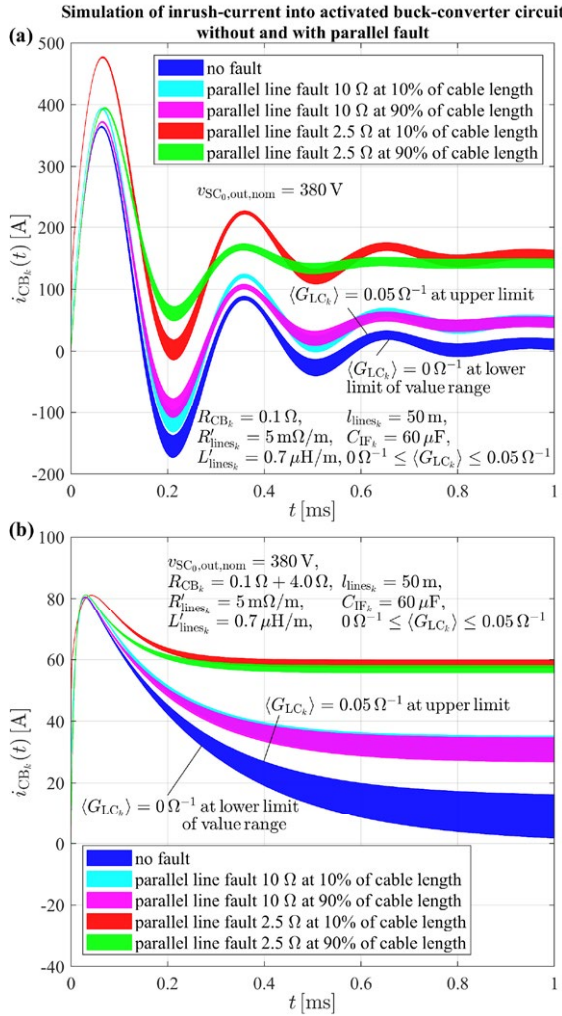


Fig. 5 Estimation of inrush current with potential parallel fault in cabling of test circuit for different fault conditions, (a) without and (b) with additional pre-charging resistor of 4Ω , stable voltage at distribution unit assumed (without circuit protection).

Fig. 6 shows current signals for fault events occurring during steady-state conditions. In this case the calculation has been performed with a model in discrete time-domain based on an average load converter power demand of 5 kW for very slow as well as for very fast converter control dynamics (main time-constant $T_{LC_k, in}$).

As being shown in both examples, the current signals are quite similar for different conductance values or control dynamics, respectively. Hence it is obvious for common component parametrization that resistivity and location of a potential fault have a more significant impact on inrush current characteristics than actual converter conductance resulting from converter control dynamics, even if capacitor values are very small. If a suitable circuit protection has to be selected or parametrized for such circuits, load-side control dynamics are of less relevance than filter parametrization as well as nominal voltage and current input data.

A further application example has been analyzed for the case of a parallel fault; see Fig. 7 for parametrization and results, again Fig. 3 for notation. An idealized high-power source converter with an output filter including resistive, inductive and capacitive equivalent elements R_{OF_0} , L_{OF_0} and C_{OF_0} is feeding a long main line with a sufficient cable cross section. At the distribution unit three feeder cables with different lengths are connected. The input filters of the idealized load converters with very fast control circuits are assumed to be mainly capacitive and can be modeled with C_{IF_k} . To decouple the load units and to provide selective fault detection, higher values in the mF-range are used for these capacitors. The load converters operate within an input voltage range with a lower limit of 320 V and are assumed to switch off immediately, if this limit is reached.

Starting with steady-state initial conditions with the

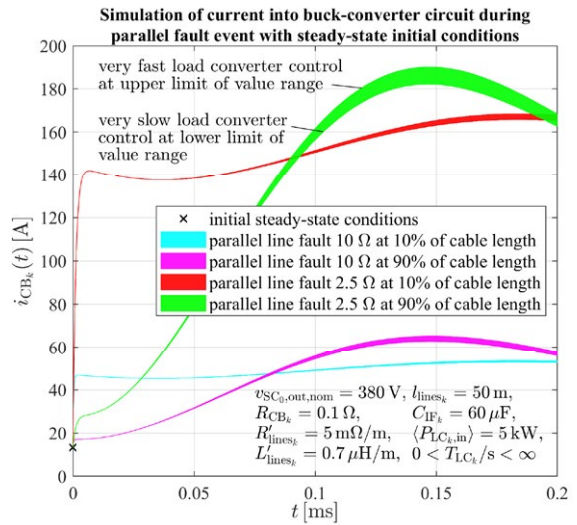


Fig. 6 Estimation of current in case of a parallel fault in cabling of test circuit for different fault conditions with steady-state initial conditions during normal operation, stable voltage at distribution unit assumed (without circuit protection).

power demands $P_{LC_{k,in}}$ at the load converters, a parallel fault with a constant fault resistance of R_{PF_1} is assumed in feeder cable 1 at 10% of cable length. For a model-based circuit analysis in case of a fault, potential overcurrent circuit protection is not activated in the model circuit.

Simulation of currents and voltages in grid with 3 controlled loads during (a) parallel fault event in feeder line to load 1 with steady-st. init. conditions

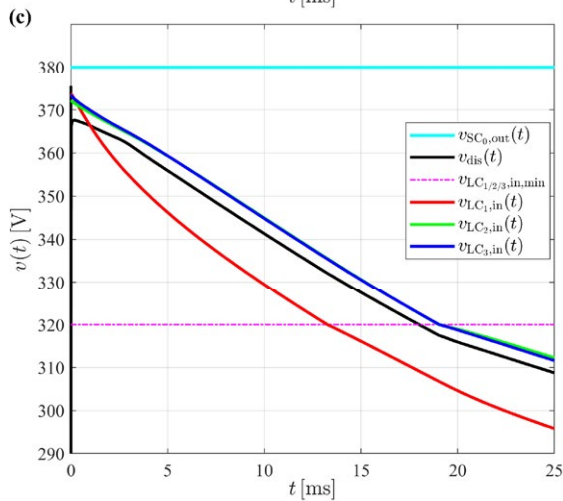
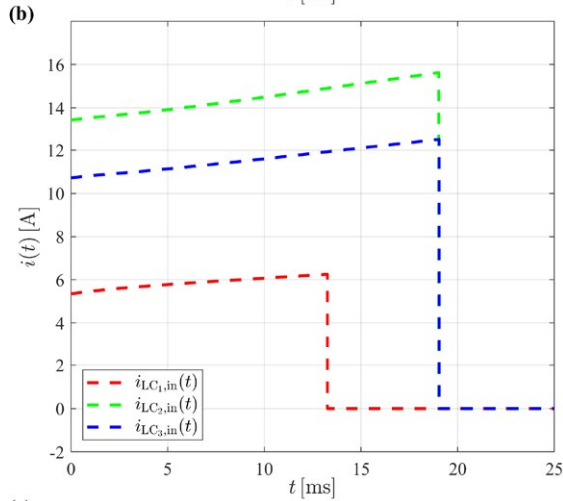
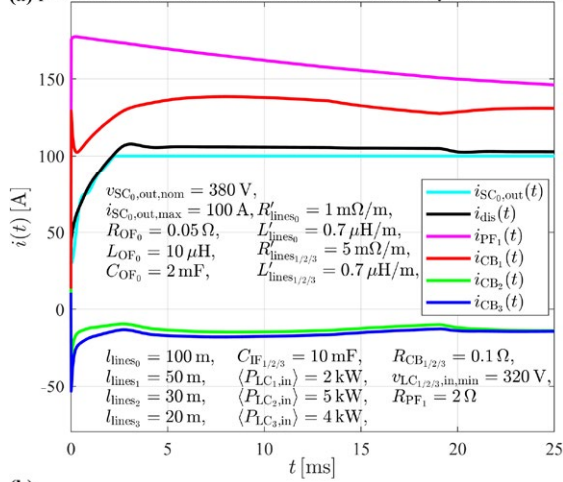


Fig. 7 Estimation of current and voltage behavior in distribution grid with three controlled load units in case of a parallel fault event in feeder line 1 (without circuit protection, load converters with self-protection).

Immediately after occurrence of the fault, backward currents also in lines 2 and 3 fed by the load side capacitors can be observed (Fig. 7a). Due to the discharge of all capacitors and due to the voltage drop in the cabling, the voltage levels at the distribution unit and at the load inverter inputs are decreasing (Fig. 7c). At first the load converter of the faulty line switches off when reaching its lower input voltage limit (320 V), then shortly afterwards the converters of the other both lines (Fig. 7b).

For the design of suitable circuit breakers, a fast switching off the fault affected line after detecting overcurrent (< 15 ms) has to be guaranteed in order to keep the other loads alive. Well parametrized and fast circuit breakers based on mechanical, hybrid or electronic devices have to be selected for this purpose.

As a further intermediate result it can be stated: For a selective system protection against parallel faults not only the specific line parameters and loads have to be taken into account. In fact, an overall analysis of signal transients has to be performed for different cases of fault events and compared with inrush behavior. Only by applying these results it is possible to select devices, which trip selectively in the case of faults and avoid false tripping during normal operation. If signal behavior during faults and during normal operation is too similar, a singular fault handling will not be possible only with mechanical devices. An overall fault detection using online measurements of all branches simultaneously has to be implemented instead.

4.2 Modeling of Grids with Serial Faults

Also potential series faults have to be considered for the operation of DC grids. Series arc faults may occur in the case of a cable break or loose contacts, depending on system voltage, nominal operating current, line inductances and converter capacitances. Due to the hot plasma temperature arcs may lead to serious damage. Applying arc fault sensors based on high frequency pattern recognition or model based methods analyzing the arc ignition event, arc faults can be detected and de-energized within a short time ($\ll 100$ ms) [9].

Not only a sudden event like a cable break, but also a local rise of contact resistance e.g. in a connector might lead to a serious arc fault. In the time frame before an arc might ignite due to the melting of contact material, also a rise of current should be observable, if controlled loads with constant or slowly changing power demand are used. For the case of contact resistance increase being significant, but slower than converter control dynamics, a steady-state analysis is helpful to analyze, whether converter self-protection or overcurrent protection devices are suitable to clear the fault in an early stage.

As a further example, a model-based simulation for a serial fault in a distribution grid was performed. The components were mainly parametrized as in the last

example, but at other operation points, again following the notation in Fig. 3.

Constant source converter output voltage and a small series output filter resistance R_{OF_0} are assumed. The idealized load converters operate as constant power sinks in normal operation mode within given input voltage ranges. All load converter filter resistances should be negligible.

Then the following equations hold for average steady-state values, if one or more upper bounds for the currents resulting from the lower input voltage limits are not reached

$$\begin{aligned} \langle v_{SC_0,out} \rangle &= \langle i_{SC_0,out} \rangle R_{lines_0} + \langle v_{dis} \rangle, \\ \langle i_{SC_0,out} \rangle &= \sum_{k=1}^n \langle i_{CB_k} \rangle, \\ \langle v_{dis} \rangle &= \langle i_{CB_k} \rangle \langle R_k \rangle + \frac{\langle P_{LC_k,in} \rangle}{\langle i_{CB_k} \rangle}, \quad k = 1, \dots, n, \\ \langle R_k \rangle &= R_{CB_k} + R_{lines_k} (+ \langle R_{SF_k} \rangle), \quad k = 1, \dots, n. \end{aligned} \quad (7-10)$$

$P_{LC_k,in}$ is the load converter power demand, R_{SF_k} the

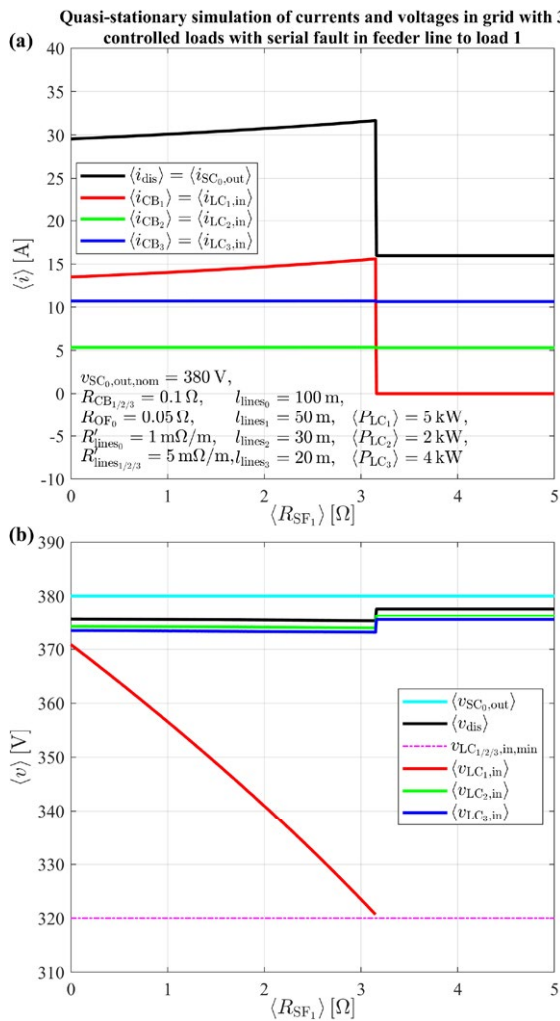


Fig. 8 Estimation of quasi-stationary current and voltage values in distribution grid with three controlled load units subject to resistivity of serial fault in feeder line 1 (without circuit protection, load converters with self-protection).

resistance of a potential serial fault in the feeder line k . The operator $\langle \dots \rangle$ denotes averaging in a floating time window and represents quasi-stationary conditions for a slow change of parameters.

For a total number of $n=3$ loads the quasi-stationary states are considered for a slow increase of the resistance of a serial fault in line 1.

Fig. 8a shows a significantly increasing current in the faulty feeder line 1 dependent to fault resistance, whereas the current signals in the other feeder lines are affected only slightly due to low cable resistance of the main line.

As the load converter input voltage at the faulty line decreases simultaneously (Fig. 8b), this converter switches off at low input voltage (minimum input voltage of 320 V). The other load converters keep on operating with a higher input voltage due to lower voltage drops in the source converter output filter and the main cable.

The exemplary results can be generalized: If (i) load converters with self-protection are used, provoking an immediate switch off in the case of low input voltage or too high input current, (ii) the upper current limit of the source converter exceeds the sum of the maximum load converter input currents and further (iii) cables with sufficient cross sections and low resistivity are installed, then serial faults with low dynamics in the feeder lines will mainly affect voltage and current behavior only in the faulty line.

5 Generalized and Sophisticated Grid Protection

Depending on the range of potential operating points of the load converters and on the passive equivalent components in filters and lines, even with modelling tools it will be a difficult task to design suitable mechanical circuit breakers. Their characteristic tripping curves representing the behavior of thermal and magnetic actors have to be adjusted in order to protect from different kinds of faults independently and to be unaffected from inrush and sudden load change effects.

In an actual project called “DC-Schutzsystem” it is a subject of research, whether a more sophisticated and flexible approach makes sense to achieve an improvement in total system safety and performance. In order to meet this objective, it could make sense to split up the sensoric and the actuatoric sub-functionalities of independent breakers and further to combine all data measured within the total grid or within sub-grids for an overall and generalized evaluation. Using current and voltage sensors in electronic devices for each output, online data measurements have to be collected in centralized microcontroller units preferably located in distribution devices.

Signal processing, system identification and pattern recognition methods are applied to the overall data stream in order to collect knowledge on actual system parametrization. With these model-based methods in addition to the basic functionality of the protective devices, refined fault identification procedures operating in real-time mode can be implemented for a better discrimination of different kinds of faults from inrush and load-change events depending on large-signal operating points [3, 4]. Also additional data from other protective devices, like arc-fault sensors based on AC small-signal measurements, residual current sensors and surge protective devices can be included, if provided with real-time capability or with a short time delay [7].

If an occurring fault and the corresponding line are identified within a short time-span, a fast mechanical, electronic or hybrid switching device is activated in order to switch off the affected load or sub-grid selectively and to avoid total system breakdown.

Based on this overall concept and depending on load types and characteristics, priority load shedding can additionally be implemented for different power applications, e.g. in telecommunication systems or in data centers. If mains supply is impaired or regenerative generation in a stand-alone micro-grid is decreasing due to weather conditions or to diurnal cycle, and further battery buffer capacity has to be spared, specific less important loads can be switched off for some time.

If, in another application case, DC as well as AC supplies are installed due to required high supply reliability, a specific switching device can be used to change between DC and AC connections depending on regenerative generation and battery status (**Fig. 9**). By ensuring a fast switching procedure in accordance with load input capacitance, any impairment of load operation is avoided.

Not only load shedding and a change between sources can be realized by analyzing total power demand and supply. Also a matured and sophisticated power and facility management can be set up using the recorded data stream for long term remote monitoring purposes, for the detection of gradual malfunction and for the derivation of predictive maintenance concepts. Unsupervised or supervised machine learning methods might be helpful in this context.

6 Conclusion and Further Work

A short overview in transient and quasi-stationary system modelling of DC distribution grids has been given. Using factorial analysis and based on exemplary test circuits, the behavior of current and voltage signals show significant dependencies to parameters of passive equivalent components and to basic large-signal converter parameters in the case of fault events and current inrush during start-up. Only with a specific



Fig. 9 Prototype of fast switching device to change between 380 VDC and 270 VAC supplies (continuous operating current 16 A DC, 20 A AC).

analysis of total connected grid components, an efficient fault protection can be set up using independent protective devices. A significant improvement is achievable applying a generalized system protection approach based on a centralized processing of all available sensor data.

For further phases of the actual research project “DC-Schutzsystem” it is planned to parametrize and to refine the principal system models according to existing DC test circuits with different converter architectures and control procedures including pre-charging circuits.

7 Literature

- [1] IEC 60364-4-41: Low-voltage electrical installations – Protection for safety – Protection against electric shock.
- [2] DKE-VDE, Low Voltage DC German Standardization Roadmap Version 2, 2018.
- [3] C. Strobl, L. Ott, J. Kaiser, K. Gosses, M. Schäfer, and R. Rabenstein, “Refined Fault Detection in LVDC-Grids with Signal Processing, System Identification and Machine Learning Methods”, 29th International Conference on Electrical Contacts, Together with 64th IEEE Holm Conference on Electrical Contacts, Albuquerque, USA, 2018.
- [4] C. Strobl, M. Schäfer, R. Rabenstein, “System Identification Methods for Refined Fault Detection in LVDC-Microgrids”, IEEE 3rd International Conference on DC Microgrids (ICDCM), Matsue, Japan, 2019.
- [5] H. Köpf, “Schalten von Gleichströmen in automobilen HV-Bordnetzen bis 500 V, unter Berücksichtigung der Lichtbogenwanderung im Doppelkontaktsystem”, Verlag Dr. Hut, München, 2019.
- [6] ETSI EN 300 132-2 V 2.5.1 (2016-10).
- [7] J. Kaiser, C. Strobl, H. Mann, H. Muhm, M. Klimpel, F. Schork, M. März, “A Comprehensive Approach for Safety in DC-Microgrids”, IEEE 3rd International Conference on DC Microgrids (ICDCM), Matsue, Japan, 2019.
- [8] IEC 60947-4-3 ED3.
- [9] C. Strobl, “Arc Fault Detection in DC Microgrids”, IEEE 1st International Conference on DC Microgrids (ICDCM), Atlanta, USA, 2019.

Influencing Factors for the Ultrasonic Compacting Process of Insulated Litz Wires for Electric Drives

Johannes Seefried, Andreas Riedel, Andreas Lohbauer, Hendrik Baessler, Alexander Kuehl and Joerg Franke
Institute for Factory Automation and Production Systems (FAPS),
Friedrich-Alexander-Universität Erlangen-Nürnberg (FAU), Nuremberg, Johannes.Seefried@faps.fau.de

Abstract

The increasing demand for new electric drive concepts in the automotive sector leads to innovations in the development and production of these drives. Due to the demand for steadily higher drive speeds, litz wires, also called stranded wires, offer various advantages in terms of loss reduction. These losses include current displacement due to the skin- and proximity effect in the wire at higher frequencies. However, these litz wires complicate the process step of contacting the winding ends. For example, during this contacting process it is necessary to connect a high number of individual wires electrically conductively and mechanically with each other. However, these individual wires must be stripped simultaneously during the process. One possibility to implement this process step is the ultrasonic compaction process. By applying and damping ultrasonic oscillations, the individual wires can be thermally stripped and also welded together. However, a wide range of influencing parameters must be validated for this process. These include relevant process parameters as well as properties of the litz wires used. Among other things, the properties can be divided into the type of insulation, the number of individual wires and their diameter. Within this publication, the essential process parameters are identified and evaluated in terms of the quality of the compaction by using suitable methods for measuring the node resistance.

1 Introduction

To push the development of the electrification in the automotive industry, new optimization possibilities for increasing the efficiency and performance of electric motors are continuously being researched. A crucial field of action is the design of the winding in the stator. From a manufacturing point of view, the use of hairpin winding enables the production of a stator in a short process time due to its easier assembling process. In this technology, the winding of the stator consists of rectangular enamelled copper wires bent into a U-shape, which are inserted into the lamination stack of the stator. Subsequently, the free ends of the hairpins are joined together in the contacting process to form the complete winding. As a result, the area of the stator slot is almost completely filled and thus enables to obtain higher power densities. [1] [2]

However, when realizing higher rotating speeds, current displacement losses occur in the solid copper wires due to the increase of the frequency in the winding. To reduce these current displacement effects, the solid copper wires can be replaced by twisted litz wires. Additionally, the twisting of the litz wires enables the heat losses of the copper wires to be conducted from the centre of the stator slot to the slot flanks, which results in higher heat dissipation and a better thermal connectivity. In order to ensure a high filling factor, the litz wires are pressed to shaped litz wires. The challenge

when using shaped litz wires is to electrically and mechanically connect the individual wires at their free end to form a solid conductor unit. The process of laser beam welding offers great potential, because of the very good automation capability, high process stability, accessibility and very low tool wear. However, it is not possible to close all cavities between the individual wires of the shaped litz wire by fusing the individual wires with the laser beam and removing the insulation layer in advance. Remaining insulation residues inevitably lead to the formation of pores or to a complete destruction of the welded joint due to outgassing during the welding process. Therefore, it is necessary to compact the individual wires of the shaped litz wire ends into a solid node and to remove the wire insulation from the node prior to laser beam welding. In addition, the compacting technology offers the advantage that additional connecting elements are not required and exact mounting dimensions can be achieved. [3][4][5]

2 State of the Art

The quality of the compaction is crucial for increasing the performance of the electric motor and ensuring the required lifetime. Among others, the following processes are available for compacting the ends of the shaped litz wires. The selected processes offer the possibility of compacting the shaped litz wires without any prior chemical, thermal or mechanical stripping.

2.1 Compacting by means of resistance heating

The compacting of conventional non-insulated litz wires by means of resistance heating is based fundamentally on the formation of a material bond using thermal and mechanical energy. The mechanical energy for compacting the litz wires is applied by two electrodes. At the same time, a current is applied to the litz wire by these electrodes, which leads to Joule heating and a firmly bonded connection. [6]

However, since shaped litz wires for electric motors consist of insulated individual wires, it is not possible to supply a current without further modifications. Similar to the hot crimping process, electrically conductive sleeves are therefore required which allow a Joule heating. This heating finally leads to a stripping of the wires of the shaped litz wire. The simultaneous mechanical force of the electrodes additionally pushes the insulation residues out of the node. Therefore, the process described is basically well suited for shaped litz wires, but always requires a conductive sleeve. [7]

For the sake of completeness, it should be mentioned that, beside the process of classical resistance compacting, there are already initial approaches for pressing the litz wires with hot punches. This would eliminate the disadvantage of additionally required sleeves. However, the process aims solely at compacting the litz wires without welding the individual wires. Nevertheless, the preconditions for a subsequent laser beam welding process would also be fulfilled in general. [8]

2.2 Compacting by means of ultrasonic

The ultrasonic compacting of litz wires is a special variant of ultrasonic welding. According to DIN 1910-100, ultrasonic welding belongs to the group of pressure welding processes. [9]

Using a generator, a high-frequency alternating current is generated and transmitted to an ultrasonic transducer, which generates a mechanical ultrasonic oscillation. The oscillations are adapted by an acoustic transformation element and transmitted to the sonotrode. The welding tool system consists of sonotrode, anvil, end plate and sideshifter and forms the compaction chamber where the litz wire is placed on the sonotrode. To avoid damage to the welding tools, the welding tools should not collide. On the one hand, the gap between the sonotrode and the tools must be sized so that the oscillating sonotrode and the tool elements do not collide. On the other hand, the gap must be small enough so that the individual wires do not get stuck in the gap. [10][11]

The compacting process starts by pushing the individual wires to the defined weld seam width b_s by moving the sideshift in horizontal direction by a stepper motor. Subsequently, the anvil moves pneumatically in horizontal direction until it reaches the sideshift with the set dimension of the weld seam width b_s . The anvil and

the end plate start to move simultaneous vertically downwards until the set welding dimension S_M or the welding energy E_s , depending on the selected welding mode, is reached. This compresses the inserted litz wire by the welding pressure p_s . During this process, the sonotrode starts to oscillate mechanically in the longitudinal direction of the litz wire with the amplitude A_s , which leads to a relative movement between the individual wires. The individual wires are plastically deformed to form a solid unit whereby the process takes place below the melting temperature of the wires. However, the process temperatures that can be achieved are also suitable for the thermal stripping of the shaped litz wires during the compaction process. The resulting melting residues of the insulation are also pushed out of the node by the compacting process and the relative movements. [12]

Characteristic of an ultrasonic compacted litz wire is a grooved surface which is caused by the welding tools. These require a grooved contour for the mechanical coupling of the oscillation so that a relative movement can be generated between the individual wires. Depending on the application, despite a low amplitude of 5 to 50 μm of the relative movement between the parts to be joined, a high relative speed of 0.8 to 2.0 m/s results due to the high frequency of 20 to 65 kHz. This results in very short welding times of 0.1 to 3.0 s. Figure 1 shows the ultrasonic compacting of a litz wire. [10][11][12]

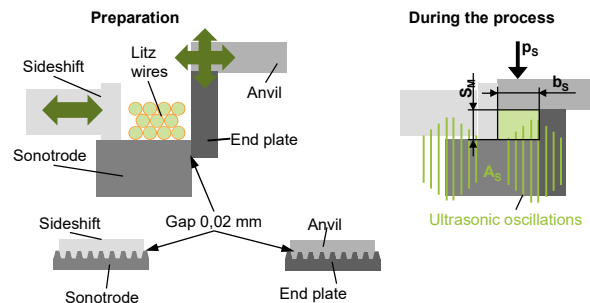


Fig. 1 Ultrasonic compacting of a litz wire according to [12]

Compared to resistance compacting, ultrasonic compacting must be highlighted under the aspect of the process energy consumption, as only about 10 % of the energy consumption of resistance compacting is required per connection. Furthermore, no additional semi-finished products such as sleeves are required for insulated shape litz wires. However, due to the lower process heat it is not possible to achieve such high compression ratios compared to resistance compacting. [6][10]

The contacting of the enamelled insulated wires of the shaped litz wires by means of compacting processes offers potential and challenges. The high process parameters required to remove the enamel insulation, especially during ultrasonic compacting, lead to a strong deformation of the free litz wire ends as well as to wire

breaks next to the compacting zone caused by a damping of the ultrasonic oscillations as shown in Figure 2.



Fig. 2 Litz wire with broken individual wire (black circle)

Especially with regard to a full contact of all individual wires and the resulting closing of all cavities between the individual wires, it is necessary to completely remove the insulation layer of the wires from the weld by the compacting process. In order to minimize current displacement effects at higher frequencies, the nominal wire diameter of the shaped litz wires has to be reduced. As a result, the number of wires per shaped litz wire increases in order to keep the copper filling factor constant, which means that the amount of insulation in the compacting zone increases as well. Therefore, it is the task of compacting to create a strong mechanical and electrical connection, which provides optimal conditions for the subsequent process steps such as laser beam welding. Furthermore, due to the concept-related high number of contacts per stator, the process time and tool wear of the litz wire compacting machine must be taken into account.

Based on the described problems during the compacting process, various factors which are influencing the process of ultrasonic compacting are evaluated in the following section of this paper.

3 Experimental evaluation of influencing factors on the ultrasonic compacting process

The objective of the experiments is to analyze and validate the influence of different shaped litz wire variations and the corresponding process parameters for the ultrasonic compacting process. In this context, the process of ultrasonic compacting has to be optimized in order to create an optimal compacting for the subsequent process steps in the stator production chain. The methods used to qualify an optimal compaction are explained in detail below.

3.1 Requirements and qualification of the compaction

The most important requirement for the compacting of the litz wire is the complete electrical contacting of all individual wires of the shaped litz wire. For this reason, the aim is to achieve the highest possible number of contacted wires n_K . It is possible that during the welding process individual wires may break due to a strong oscillation stress. The number of broken wires n_B must be minimized in order to achieve a wide current distribution and a homogeneous heat distribution in the shaped litz wire. The second factor to be considered when evaluating the quality of the compaction is the node resistance R_K in the compacted node. The node

resistance R_K should be minimized in order to keep the electrical power loss to a minimum. Condition for a low node resistance R_K is also the complete contacting of all individual wires and a complete removal of the insulation layer from the compaction node. In a simplified view, the total resistance of a compacted shaped litz wire is composed of the two resistances of the node points R_K and the resistance of the individual wires R_{EL} as shown in Figure 3.

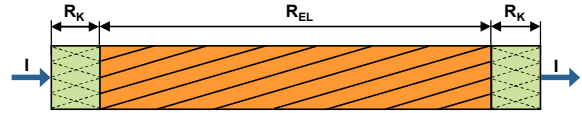


Fig. 3 Resistance of a compacted shaped litz wire

In order to enable the measurement of the node resistance R_K independent of the influences of the entire shaped litz wire, the measurements were carried out with a measurement device mounted perpendicular to the direction of the real current flow I as shown in Figure 4. The measurement is performed by using Kelvin pins and a four-wire measurement as well as the use of a delta-mode current direction reversal. The measuring current used is 105 mA. A measured value determined consists of the average value of 10 consecutive measurements.

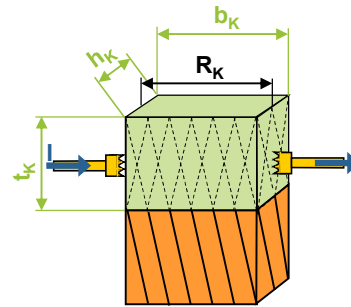


Fig. 4 Measurement of the node resistance R_K

The node resistance R_K can be determined according to equation 3.1 by the specific resistance of copper ρ , node width b_K , node depth t_K and node height h_K as well as contact resistance R_U between Kelvin pin and litz wire.

$$R_K = \rho \times \frac{b_K}{t_K \times h_K} + R_U \quad (3.1) [13]$$

The contact resistance R_U of the Kelvin pins is currently considered negligible in relation to the significantly higher node resistance. It depends on a number of influencing factors such as impurity layers. For its determination, the use of a standard with defined resistance is planned for upcoming investigations. The theoretical reference node resistance $R_{K,Ref}$ for a pure copper body is approx. $2.45 \mu\Omega$.

To determine the removal of the insulation layer from the node, the mass difference Δm was recorded by weighing the shaped litz wire before and after the compacting process with a precision scale. The reference mass difference Δm_{Ref} was calculated on the basis of

completely stripped individual wires. For this purpose, the insulation layer was removed from the individual wires using a chemical stripper.

In addition, the quality of the compacted section is analyzed by producing microsections of selected test samples in order to obtain conclusions on the removal of the insulation layer.

The node width b_K and height h_K are also measured, since the shape and dimensional accuracy of the compacted shaped litz wires is decisive for the subsequent process chain of stator production.

3.2 Evaluation of the influencing factors and the achievable compacting quality

Since there is only a limited amount of information available about the application case with regard to the settings of the process parameters, both the important machine dependent influencing factors as well as the litz wire dependent influencing factors are evaluated in preliminary tests. In this way, information on the relevance of the influencing factors should be determined. Figure 5 shows the essential factors influencing the ultrasonic compacting of shaped litz wires. In addition, there are of course further influences such as environmental conditions, which will not be considered in the context of this paper.

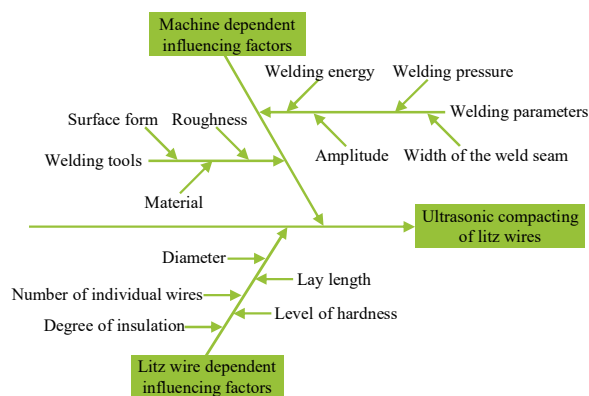


Fig. 5 Machine and litz wire dependent influences during ultrasonic compacting of shaped litz wires

The experiments are carried out with the ultrasonic litz wire welding machine TelsoSplice 3 from Telsonic AG. The TelsoSplice 3 works with a frequency of 20 kHz at a power of 3 kW. The node depth t_K of the processing surface is 12 mm.

The TelsoSplice 3 offers several welding modes for switching off the ultrasonic oscillations at the end of the process. During the experiments, the welding mode of energy welding is set, in which the process ends when a set welding energy E_S is reached. Alternatively, this can also be controlled by the parameters of welding dimension S_M or welding time. The welding pressure p_S is responsible for ensuring the coupling of the ultrasonic oscillations into the shaped litz wire. The oscillation amplitude A_S determines the intensity of the fric-

tion between the individual wires to be connected during the compacting process. These three influencing factors must always be considered in conjunction with each other in order to enable successful compaction. The weld seam width b_S was constantly set to the value 2.9 mm for all experiments in order to not exceed the maximum permissible node width of 3.0 mm.

The litz wires are manufactured in-house for experimental purposes with the aid of specific equipment. The different litz wires are twisted in a Z-twist with a length of lay of 105 mm and pressed with a force of 50 kN. The experimental litz wires are named according to the principle nominal wire diameter d_{Cu} in mm / number of individual wires n / degree of insulation (e.g. 0.8 mm / 10 individual wires / insulation grade 2). The degree of insulation is standardized according to DIN EN 60317-0-1. It specifies the range of the layer thickness of the insulation of a wire. Depending on the nominal wire diameter d_{Cu} , this standard specifies values for the minimum increase through the insulation as well as for the maximum allowed outer diameter of the wire for the three grades 1, 2 and 3. The thickness of the insulation increases with the grade number. Table 1 shows that the larger the nominal copper wire diameter d_{Cu} of a individual wire, the smaller the proportion of the insulation layer for the same copper wire cross-section A_{Cu} . [14]

Tab. 1 Produced litz wire variations for experiments

Litz wire	0.8/10/2	0.5/25/2	0.355/50/2	0.355/50/1
d_{Iso} [mm]	0.881	0.563	0.407	0.383
A_{Cu} [mm ²]	5.027	4.909	4.949	4.949
A_{Iso} [mm ²]	1.069	1.315	1.556	0.811

Figure 6 shows the different variations of shaped litz wires produced.

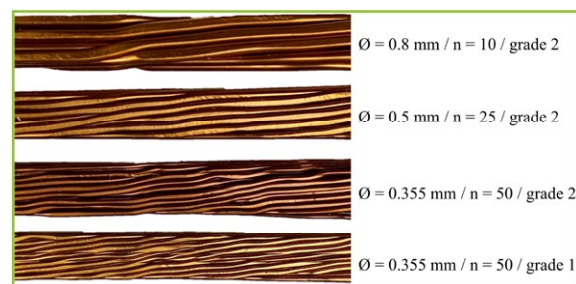


Fig. 6 Shaped litz wires samples

In order to optimize the parameters of the process and to reduce the experimental effort at the same time, the influencing variables welding energy E_S , amplitude A_S , welding pressure p_S and nominal wire diameter d_{Cu} are investigated by means of a full factorial experimental design. For these experiments, shaped litz wires with insulation grade 2 are used first. Table 2 summarizes the factor levels of the test design. The factor levels +1 and -1 define the upper and lower limits of the respective parameter. In order to ensure that the individual wires are contacted in all litz wire variations, the litz

wires are compacted with two process cycles in a row. From a theoretical point of view, there is the potential to influence the target variables node resistance R_K and mass difference Δm more positively with the use of two compacting processes than with one compacting process alone.

Tab. 2 Factor levels for insulation grade 2

Factor	-1	+1
Welding energy E_S [J]	2532	4468
Amplitude A_S [%]	75	85
Welding pressure p_S [bar]	2.5	3.5
Nominal wire diameter d_{Cu} [mm]	0.355	0.8

The investigation of the main and interaction effects of the full factorial experimental design shows that the process parameters nominal wire diameter d_{Cu} and welding pressure p_S have a highly significant influence on the number of contacted wires n_k . When looking at the main effect diagram in Figure 7, the strong causal relationship between an increasing welding pressure p_S of up to 3.5 bar and the increasing number of contacted wires n_k can be clearly seen. The influence of a larger nominal wire diameter d_{Cu} of 0.8 mm on the target number of contacted wires n_k can be seen even more clearly.

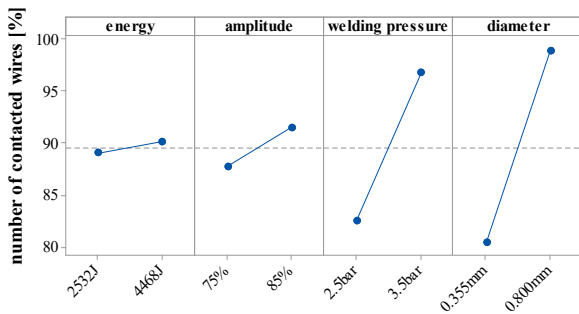


Fig. 7 Main effect diagram for number of contacted wires n_k

In combinations with a nominal wire diameter d_{Cu} of 0.8 mm and a welding pressure p_S of 3.5 bar, no individual wires of the shaped litz wires break, resulting in 100 % contacted wires n_k . On the other hand, combinations with a nominal wire diameter d_{Cu} of 0.355 mm do not allow complete contacting of all wires of the shaped litz wires. This is due to the facts that, on the one hand, the risk of breaking the individual wires increases with a reduction of the nominal wire diameter d_{Cu} and, on the other hand, the frictional forces between the individual wires lead to a wire break with increasing amplitude A_S . Figure 8 shows the influence of the examined parameters on the number of broken wires n_B .

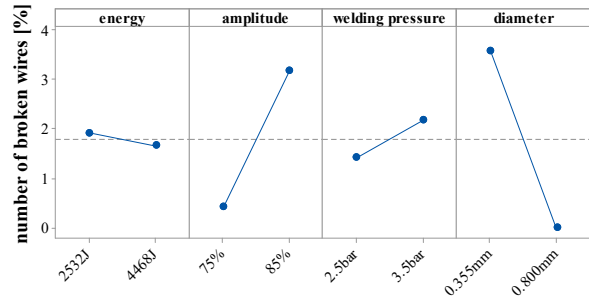


Fig. 8 Main effect diagram for number of broken wires n_B

The evaluation of the interaction effects shows that with the combination of a nominal wire diameter d_{Cu} of 0.355 mm and an amplitude of 85 %, the number of broken wires n_B is on average 6.3 %. In contrast, the experiments with a low amplitude A_S of 75 % and a high welding energy E_S of 4468 J as well as a high welding pressure p_S of 3.5 bar with a nominal wire diameter d_{Cu} of 0.355 mm lead to an average number of contacted wires n_k of 98.7 %. This result shows that with a sufficiently high welding energy E_S or welding time, even the friction intensity of a low amplitude A_S removes sufficient insulation to bring nearly all wires with a nominal wire diameter d_{Cu} of 0.355 mm with insulation grade 2 into contact without breaking wires.

When evaluating the effects affecting the node resistance R_K for shaped litz wire variations with insulation grade 2, only the effects for the nominal wire diameter d_{Cu} of 0.8 mm can be statistically evaluated. Since, in experiments with factor step combinations with a nominal wire diameter d_{Cu} of 0.355 mm and a low welding pressure p_S of 2.5 bar, the low welding pressure p_S was not sufficient to remove or break up the insulation of the individual wires so that all individual wires are in contact and a current flow through the litz wire node can occur. The evaluation of the main effects of the experiments with a nominal wire diameter d_{Cu} of 0.8 mm in Figure 9 shows a tendency to assume that factor level combinations with a high welding energy E_S of 4468 J and/or a welding pressure p_S of 3.5 bar result in a low node resistance R_K .

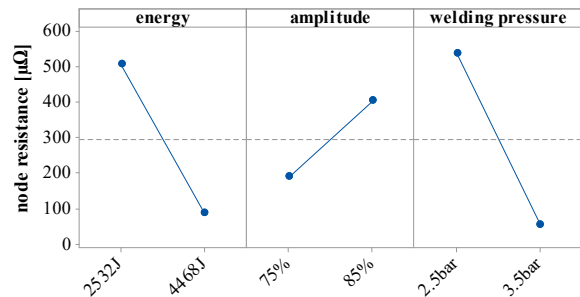


Fig. 9 Main effect diagram for node resistance R_K

With regard to the correlation between nominal wire diameter d_{Cu} and node resistance R_K , it can be seen that with a larger wire diameter d_{Cu} of 0.8 mm, considerably smaller node resistances are achieved than with a

smaller wire diameter d_{Cu} of 0.355 mm. The test samples with a wire diameter d_{Cu} of 0.8 mm have measured node resistances of up to $44 \mu\Omega$, which is higher than the theoretical reference node resistance $R_{K,Ref}$ of $2.45 \mu\Omega$. In comparison, with a wire diameter d_{Cu} of 0.355 mm, the lowest node resistance is R_K $972 \mu\Omega$. This result is also due to the higher insulation volume for the wire diameter d_{Cu} of 0.355 mm. For this purpose, Figure 10 shows a comparison of microsections located at the center of the compacted area.

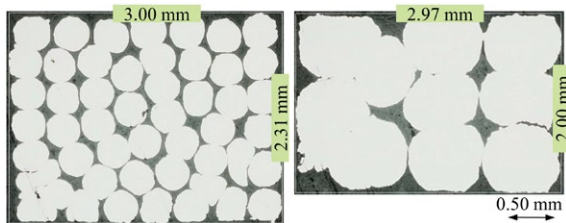


Fig. 10 Comparison of microsections between litz wire variation 0.355/50/2 (left) and 0.8/10/2 (right)

In order to determine the influence of the degree of insulation on the target values number of contacted wires n_k and the node resistance R_K more precisely, a second experimental plan is carried out with the shaped litz wire variant 0.355/50/1. As Table 1 shows, the ultrasonic oscillations only have to pass through almost half as much insulation A_{Iso} as in the case of the shaped litz wire variant 0.355/50/2. The setting of the welding energy E_S remains constantly at 5000 J for the series of experiments, so only the influence of the control parameters amplitude A_S and welding pressure p_S will be investigated at this point.

Again, an increasing amplitude A_S of up to 85 % results in the highest linear influence on the number of broken wires n_B . As Figure 11 shows, the welding pressure p_S hardly influences the number of broken wires n_B .

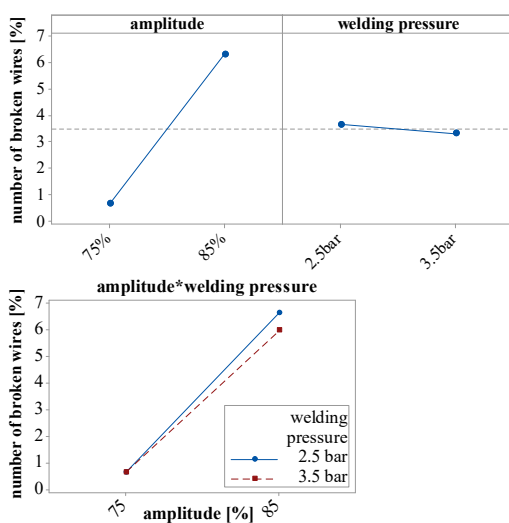


Fig. 11 Main and interaction effect diagram for number of broken wires n_B at insulation grade 1

To contact almost 100 % of the individual wires, a high welding pressure p_S of 3.5 bar is also required. However, due to insulation grade 1, in contrast to insulation

grade 2, 96 % of the wires can be contacted even with a welding pressure p_S of 2.5 bar in combination with a low amplitude A_S of 75 %, as shown in Figure 12.

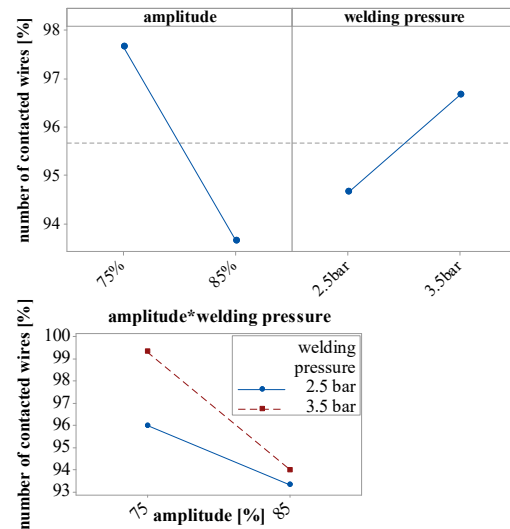


Fig. 12 Main and interaction effect diagram for number of contacted wires n_k at insulation grade 1

As a result, as shown in Figure 13, an increase in welding pressure p_S of up to 3.5 bar results in the lowest average values for the target value of the node resistance R_K of $126 \mu\Omega$ on average.

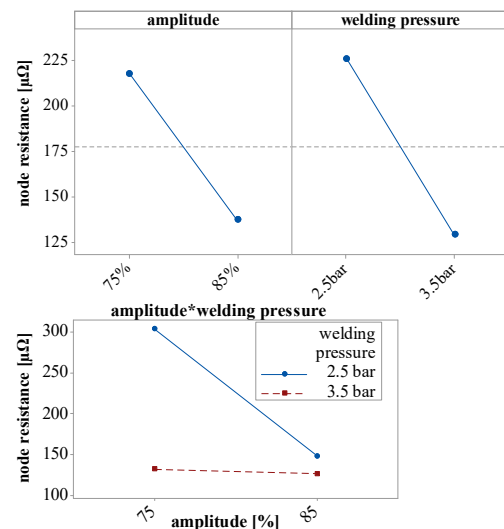


Fig. 13 Main and interaction effect diagram for node resistance R_K for insulation grade 1

Compared to insulation grade 2, the node resistance R_K for litz wires with a nominal wire diameter d_{Cu} of 0.355 mm and insulation grade 1 can be reduced. In addition, Figure 14 shows that the small cavities between the individual wires and the resulting low node height h_K in the shaped litz wire with insulation grade 1 (right microsection) indicate that the individual wires are much more compacted. However, for the subsequent process of laser welding of two shaped litz wires, the cavities must be minimized even further. Even small cavities bear the danger of a direct coupling of the laser beam into a cavity which leads to an enormous keyhole

effect. The sudden energy coupling can result in the destruction of the litz wire.

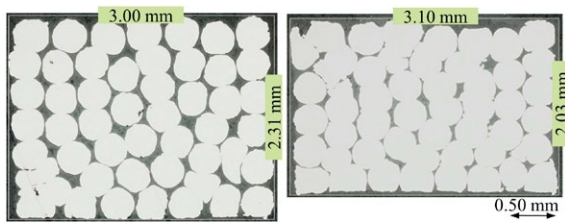


Fig. 14 Comparison of microsections between litz wires 0.355/50/2 (left) and 0.355/50/1 (right)

Furthermore, the evaluation of the target value mass difference Δm shows that no influencing factor has an approximately significant influence on the target value in both experimental designs. Nevertheless, it can be concluded that an increase in any factor also increases the mass difference Δm . However, the comparison between the mean values of the measured mass differences Δm and the reference values of the theoretical mass difference Δm_{Ref} shows that a high proportion of the insulation material still remains in the compaction.

In order to completely remove the insulation residues, especially with smaller nominal wire diameters d_{Cu} , and to completely close the cavities in the compaction process without increasing the process parameters, further initial tests are being carried out with SST litz wires (SST = Special Surface Treated). With these types of litz wires, the individual wires have no enamel insulation, so a higher fill factor is achieved by using additional copper wires. However, the complete litz wire is surrounded by a non-conductive tape, which is removed from the joining zone with cutting tools before compacting. The used SST litz wire has 62 individual wires with a nominal wire diameter d_{Cu} of 0.355 mm. The individual copper wires are covered with a thin insulating oxide layer. In addition to the natural oxide layer on the copper surface, this oxide layer is produced, among other processes, by a multiple heat treatment of the litz wires. In order to be able to successfully compact this version using ultrasonic, a welding energy E_s of 5000 J is used. The amplitude A_s can be reduced to 65 %, most likely due to annealed and therefore softer wires. The welding pressure p_s can also be lowered to 2.2 bar. These parameters enable the SST litz wires to be completely compacted with the existing ultrasonic welding system without the risk of cable breaks. An economic comparison of the SST litz wires with the litz wires analyzed in this paper cannot yet be considered due to the in-house production of the litz wires used.

4 Conclusion and Outlook

This paper shows the influencing factors for the ultrasonic compaction process of insulated litz wires for electric drives. To minimize the current displacement effects at higher frequencies, the basic aim is to reduce the nominal wire diameter of the shaped litz wires as much as possible. However, reducing the individual wire diameter of a litz wire increases the risk of breakage if the parameter settings are set too high during the compaction process. On the other hand, if the parameter settings are too low, not all individual wires will be contacted with each other. The aim of the experiments was therefore to identify the influence of the litz wire dependent parameters and machine dependent parameters in order to validate optimal process parameters. The litz wires differed from each other in terms of the nominal wire diameter, the number of individual wires and the degree of insulation. The maximum cross-section of the litz wire was 3.0 mm x 2.7 mm. The process investigation showed that combinations with a large nominal wire diameter and a high welding pressure contact all individual wires without breaking any individual wires. In contrast, combinations with a smaller nominal wire diameter do not ensure a complete contact of all wires of the shaped litz wires. This is due to the fact that the risk of breaking the individual wires increases as the nominal wire diameter decreases and the amplitude additionally increases. With regard to the relationship between the nominal wire diameter and the node resistance, it was found that with a larger nominal wire diameter, considerably lower node resistances could be achieved than with a smaller wire diameter due to the thinner insulation layer. Further investigations of litz wire variations with small nominal wire diameter and insulation grade 1 showed that it is also possible to fully contact all individual wires without breaking any individual wires and thus realizing a low node resistance. However, microsections showed that the cavities between the individual wire could not be completely closed in any variant of the litz wires. For this reason, final tests were carried out with SST litz wires. The first results show that, due to the lack of an insulating layer, the compaction results are much better. The achievable node resistances are in the range of 13 $\mu\Omega$. It can therefore be assumed that the oxide layers will be sufficiently broken up by the ultrasonic compaction to achieve an electrical contact between the individual wires.

5 Literature

- [1] Gläbel, T. et al.: Process Reliable Laser Welding of Hairpin Windings for Automotive Traction Drives. International Conference on Engineering, Science, and Industrial Applications (ICESI), Tokyo, 2019.
- [2] Riedel, A. et al.: Challenges of the Hairpin Technology for Production Techniques. International Conference on Electrical Machines and Systems (ICEMS), Jeju, 2018.
- [3] Stöck, M.: Steigerung der Leistungsdichte und der Wirtschaftlichkeit von Elektromotoren für atomotive Fahrtriebe. Eidgenössische Technische Hochschule (ETH) Zürich, Dissertation, 2016.
- [4] Gläbel, T.; Franke, J.: Kontaktierung von Antrieben für die Elektromobilität. In: ZWF Zeitschrift für wirtschaftlichen Fabrikbetrieb 112 (2017), Nr. 5, S. 322–326.
- [5] Stenzel, P.: Großserientaugliche Nadelwickeltechnik für verteilte Wicklungen im Anwendungsfall der E-Traktionsantriebe. Friedrich-Alexander-Universität Erlangen-Nürnberg, Meisenbach KG, Dissertation, 2017.
- [6] Broda, T.: Kompaktieren und Schweißen von Kupfer- und Aluminiumlitzen mit konduktiver Widerstandserwärmung. VS-Sondertagung Widerstandsschweißen, 22, S. 115-125, Duisburg, 2013.
- [7] Seefried, J. et al.: Experimental Evaluation of Tool Geometries for the Ultrasonic Crimping Process for Tubular Cable Lugs, IEEE Holm Conference on Electrical Contacts, Milwaukee, 2019.
- [8] Winkle, D.: Verfahren zum Kompaktieren von Einzeldrähten, BMW AG, DE102015201711 (A1), 2015.
- [9] Deutsches Institut für Normung, DIN 1910-100:2008-02: Schweißen und verwandte Prozesse - Begriffe - Teil 100: Metallschweißprozesse mit Ergänzungen zu DIN EN 14610:2005. Beuth Verlag GmbH, Berlin, 2008.
- [10] Golde, H.-D.: Ultraschall-Metallschweißen: Funktionsweise und Anwendung einer hochwertigen Verbindungstechnik, Verl. Moderne Industrie, Landsberg/Lech, 1995.
- [11] Wodara, J.; Herold, H.: Hg. Fachbuchreihe Schweißtechnik Band 151: Ultraschallfügen und –trennen. Verlag für Schweißen und verwandte Verfahren. DVS-Verlag GmbH, Düsseldorf, 2004
- [12] Ostermeier, A.: Verbindungen mit Ultraschallverdichten: Einmal kalt gepresst bitte – nicht gecrimpt!, Elektronik Praxis, 02/2017, S. 19 – 22, Würzburg, 2017.
- [13] Häberle, G. D.: Tabellenbuch Elektrotechnik - Tabellen, Formeln, Normenanwendung, Verlag Europa-Lehrmittel, Haan-Gruiten, 2015.
- [14] Deutsches Institut für Normung. DIN EN 60317-0, Technische Lieferbedingungen für bestimmte Typen von Wickeldrähten. Beuth Verlag GmbH, Berlin, 2008.

Abbreviations

Δm_{Ref}	mass difference	mg
A_{Cu}	copper wire cross-section	mm ²
A_{Iso}	insulation cross-section	mm ²
A_{S}	amplitude	%
b_{K}	node width	mm
b_{S}	set weld seam width of the machine	mm
d_{Cu}	nominal wire diameter	mm
E_{S}	welding energy	J
h_{K}	node height	mm
n	number of individual wires	
n_{B}	number of broken wires	
n_{k}	number of contacted wires	
p_{S}	welding pressure	bar
R_{EL}	resistance of the individual wires	$\mu\Omega$
R_{K}	node resistance	$\mu\Omega$
$R_{\text{K,Ref}}$	theoretical reference node resistance	$\mu\Omega$
$R_{\text{Ü}}$	contact resistance	$\mu\Omega$
S_{M}	set welding dimension of the machine	mm
SST	Special Surface Treated	
t_{K}	node depth	mm
ρ	specific resistance of copper	$\Omega \text{ mm}^2/\text{m}$

Acknowledgment

The corresponding author Johannes Seefried thanks Andreas Riedel, Andreas Lohbauer and Hendrik Baessler for the collaborative realization of this publication. Andreas Lohbauer and Hendrik Baessler are responsible for assisting in carrying out the compacting experiments and for the qualification of the contact points. Andreas Riedel assists in the selection of the litz wire configuration. The authors thanks Alexander Kuehl and Joerg Franke for counselling and reviewing the publication.

Experimental Setup of a Process Chain for Contacting Litz Wires for Electrical Drives

Andreas Riedel, Johannes Seefried, Alexander Schmidt, Alexander Kuehl, Joerg Franke
Institute for Factory Automation and Production Systems (FAPS),
Friedrich-Alexander-Universität Erlangen-Nürnberg (FAU), Nuremberg, andreas.riedel@faps.fau.de

Abstract

The main objective in the development of electric drives is the continuous effort to increase the performance. One possibility to achieve this is the use of shaped litz wires. However, shaped litz wires present major challenges regarding the contacting process. In the preparation of the contacting process, the individual conductors of the litz wires must be completely stripped without residues and brought into a defined geometry. This preliminary process step is also known as compacting. The compacting process is the basis for the subsequent contacting of the litz wires with each other or with contact elements. One process for contacting the litz wires is laser beam welding. In the context of this publication, the process chain consisting of ultrasonic compacting and laser beam welding is evaluated. The focus is put on the possible variations of the litz wire topologies, which differ in single wire diameter, number of wires and degree of insulation. Depending on this, parameters for the two processes are elaborated. To evaluate the results, electrical and mechanical testing of the litz wire connections is carried out. In addition, different approaches for the qualification of the compaction quality, in particular the evaluation of insulation residues, are considered.

1 Introduction

Strict limits on carbon dioxide emissions implemented by the European Union as part of the environmental legislation, lead to a strong increase in the number of registrations of electrified vehicles. Thus the automotive industry is faced with major challenges of improving these, both in technical and economic terms. The main focus is set on the electric drive train. In order to be competitive, manufacturers aim to improve the power density and efficiency of electric drives while reducing weight, the required installation space and costs at the same time [1]

There has been a rapid progress in the development of electrified drives for years. Currently there is a major optimization potential, especially from the process point of view. Due to the increasing number of drives for electrified vehicles, the use of new manufacturing processes for larger quantities is suitable. The development of novel winding processes and technologies is of particular importance. [2]

Novel winding technologies with shaped litz wires enable the production of windings with functions that are specifically designed to meet the diverse technical and economic requirements of the electric drive. An essential point is the electrical conductivity of the winding, which determines the power density. To reduce losses like the skin and proximity effect, research is currently investigating the possible use of litz wires in stators for electric vehicle drives. Thereby the copper filling factor can be increased compared to conventional winding processes such as needle winding. Litz wires therefore

have a great potential to improve the power density of the electric motor. [3]

The main challenge when using litz wires is the automation of the entire production chain. This is particularly important for contacting the ends of the conductors, as copper is a highly thermally conductive material. On the other hand, the structure of the litz wire does not have good joining properties due to its construction with single wires and cavities. For this reason, in this publication the procedure for identifying suitable contacting parameters for litz wires for use in the electric drive will be described.

2 Challenges of litz wire contacting

The welding of shaped litz wires requires specific characteristics for the contacting. In contrast to flat wires, it is not sufficient to contact exclusively the contact zone between two conductors. The welding of litz wires requires additionally the detection of each single conductor within a litz wire during the welding process in order to achieve a complete contact. Another challenge that occurs when welding litz wires is the presence of cavities in the contact area. If a laser beam hits a cavity between two individual conductors within a litz wire, this influences the quality of the contact. In addition, the insulation of the individual wires and a possible taping of the litz wire influence the contacting process. Due to the challenges mentioned above, in this study the focus is set on litz wires, in which on the one

hand the interspaces between the cavities are minimized and on the other hand the insulation of the individual wires is removed. The previous process step of compacting is suitable for this. For compacting litz wires, the processes of resistance and ultrasonic compacting are suitable. If a bandage exists, it can be removed automatically by means of a laser beam. The stripped and compacted litz wire is the starting point for this investigation. [3, 7]

2.1. Method for contacting litz wires

The production of litz wire windings requires the use of innovative joining processes. The main objective of the joining process is to produce the optimal connection in regards to electrical conductivity and mechanical resistance. There is a difference between a connection of each individual wire within a litz wire (“compacting”) and a connection between two litz wires (“connecting”).

Contacts can basically be made by crimping, soldering and welding processes. Crimping means that the two strands are mechanically pressed together by means of a connecting element. The most innovative crimping method is ultrasonic crimping, which supplements crimping with the principle of ultrasonic welding. The combination of these processes makes it possible to use the punch and die not only for joining through plastic deformation, but also for the implementation of ultrasonic waves. This reduces the mechanical stress on the electrical conductors significantly. [4]

However, the crimp sleeve is an additional component that increases the winding head height on the one hand and the total weight of the winding on the other hand. For these reasons, only the soldering and the welding processes are considered in the following.

2.1.1. Soldering process

According to ISO 857-2, brazing is defined as a joining process that uses a molten solder whose liquidus temperature is below the solidus temperature of the base material. The material of the solder is always different from the material of the workpiece. In the industrial application, brazing processes such as flame brazing are mainly used to contact litz wires. In this process, the joining surfaces are heated up to the soldering temperature of the solder. Then the flux is activated and the solder is applied to the soldering point until the two litz wires are sufficiently moistened. Finally, the flux residues are removed to prevent corrosion damage. [5]

An alternative method is resistance soldering. Thereby, the joining section is heated up by current flow. This brazing process is used for small workpieces with short seams, however, in most cases special equipment is required. Compared to resistance welding, this process offers the advantage that the component is not heated up as much. [13]

2.1.2. Welding methods

Welding technologies are the most widespread joining methods in industrial applications. They are divided into press joining and fusion welding processes. [10] For welding litz wires resistance welding, ultrasonic welding and laser beam welding are suitable. [7]

During the resistance welding, the two litz wires are melted in the contact zone and welded together. During this process heat conduction in the litz wires leads to a major heat loss. As resistance welding is a cost-effective process it is suitable for mass production. Compared to the other two welding processes, however, heat conduction leads to an extremely high thermal load on the electrical conductors. In addition, the limited accessibility of litz wires mounted in the stator is a critical factor for resistance welding. [6, 7]

Figure 1 shows the principle design of an ultrasonic welding system for contacting two litz wires. These are inserted in the device and then pressed against the spotting plate by the movable sideshift with low force. The anvil then closes to prevent a movement of the strands during the welding process. The sonotrode transmits the contact pressure required for welding as well as the high-frequency oscillations by oscillating longitudinally to the anvil. [11]

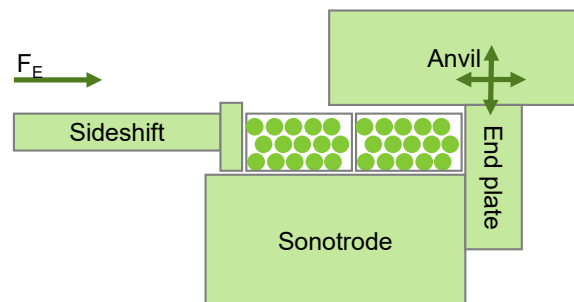


Fig. 1 Design of an ultrasonic welding system according to [11]

Additionally, ultrasonic welding offers the possibility to connect wires directly to busbars or metal sheets. [5]

The laser beam welding of litz wires requires a high energy input. Therefore, the process version laser beam deep welding is suitable, which has a very high power density. When the laser beam enters the conductor, a vapor capillary is formed. This causes the volume of the melt to rise sharply, since the laser beams are reflected many times. The vapor capillary is formed because the heat cannot be removed from the component quickly enough. [5]

The process of laser beam welding depends on a large number of adjustment variables. These include the welding speed, the laser power, but also the selected welding geometry and the welding direction.

2.2 Comparison of the contacting methods

Crimping processes require an additional connecting element which influences the winding head height and the total weight of the winding. Soldering methods are only conditionally suitable for mass production and are also only slightly process stable. For this reason, only the welding methods for contacting the litz wires are considered in the following. In contrast to the other two welding methods, laser beam welding is contactless. This enables the copper strands to be contacted in areas that are difficult to access. As the distances between the pairs of conductors to be contacted in the stator are minimal, this is a significant advantage for that field of application. In addition, the high power density and the targeted heat input of the laser enable short process times and low thermal stress on the copper conductors. Laser beam welding is therefore ideally suitable for the given requirements of contacting litz wires mounted in a stator. [7]

Table 1 shows the advantages and disadvantages of the presented contacting methods.

Tab. 1 Comparison of contacting technologies [7]

technology	status	automation capability	flexibility	tool wear	process stability	accessibility	cycle time
crimping	established	++	-	+	+	0	+
thermo-crimping	established	+	+	-	0	-	0
ultrasonic crimping	innovation	+	+	+	+	-	+
soldering	established	-	++	++	-	+	0
resistance welding	established	+	0	-	0	0	+
ultrasonic welding	established	+	0	++	+	-	+
laser welding	innovation	++	+	++	++	++	++

3 Influencing factors in laser beam welding of litz wires

The influencing variables in laser beam welding are divided into the controllable input variables and the disturbance variables that cannot be controlled (directly). The combination of the input and disturbance variables results in the target variables. These are measurable, whereby quantitative measurement results are always preferable. Figure 2 shows a black box of laser beam welding, which summarizes the most important parameters of the mentioned categories.

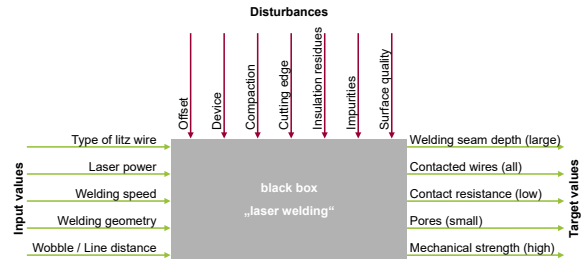


Fig. 2 Influences and target values of the laser welding process

The influencing factors can be divided into four categories. On the one hand, the laser system influences the quality of the contacting. This variable can be regulated by the laser control. The most important interaction within the input variables is the relationship between the laser power and the welding speed. This means that a higher power and a lower speed leads to a higher energy input into the wire surface.

The influence of the device for contacting the litz wires, the previous process steps in stator production and the structure of the wires themselves cannot be directly controlled. The task of the device is to prevent the offset (height and side). The upstream process step of cutting the wire influences the result of the welding due to the characteristic of the cut edge as well as the process step of compacting. Particularly relevant in this case is the compaction, i.e. the minimization of air spaces within the litz wire as well as the complete removal of the insulation of the individual wires in the contacting zone. Contamination particles can also be negative influences on the contacting process.

The two most important target values are a high mechanical strength of the welding joint and a low electrical conductor resistance. These two factors mainly depend on the fact that all wires of the two litz wires are contacted with each other and that air inclusions in the weld bead are minimized. The degree of fulfilment of these parameters also increases with increasing welding depth.

The measurement of the target variables can be done in different ways. The easiest measuring method is the optical inspection, which analyses the displacements and tilting of the welding bead as well as the number of contacted single wires.

The compaction can be determined with micrographs. Computer tomographic examinations allow the identification of pores and cavities in the weld bead. Insulation residues can be determined by fluorescence measurements. The most important measuring method is the electrical resistance measurement. Figure 3 shows the four-point measurement used in this parameter study schematically.

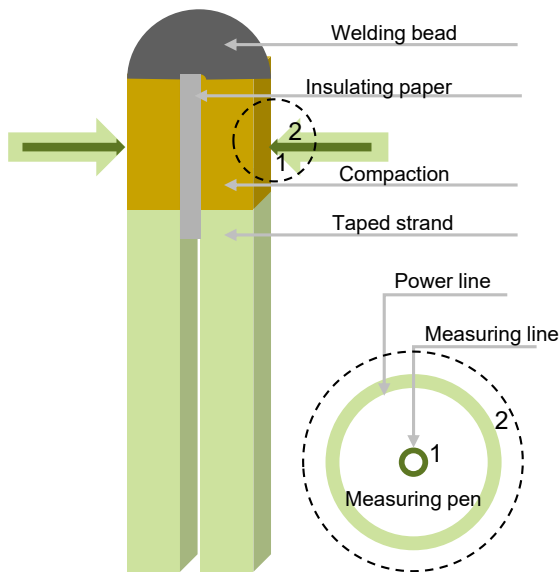


Fig. 3 Four-point measurement to check the electrical resistance

The four-point measurement determines the electrical resistance via the welding bead by applying a current of 105 mA via the current conductors. At the same time the applied voltage is tapped. The two green arrows represent the used Kelvin pen. This consists of two independent contact zones. Via the outer contact ring the litz wires are energized, via the inner one the voltage difference can be determined.

Important boundary conditions are that the contact pins are in full contact with the stripped and compacted surface and also that the two litz wires are insulated against each other. For this purpose, an insulating paper is used in this test setup, which is also used in the stator as groove base insulation paper. This is necessary because otherwise the current cannot only flow through the welding bead but also through the compaction.

4 Laser beam welding of litz wires

Before determining suitable parameters for the laser beam welding process, various basic conditions must be defined. On the one hand, preliminary process steps in stator production, such as compacting, influence the quality of the contacting. On the other hand, it is necessary to define the most important parameters for the laser beam welding process and their interactions. Furthermore, the structure of the shaped litz wires differs.

4.1. Process steps with influence on laser beam welding

Three preliminary process steps have a decisive influence on the quality of the connection during laser beam welding of litz wires. The first of these three process steps is the straightening and cutting process, whereby

the aim is to achieve a cut edge that is as flat as possible. An uneven or irregular cut edge will cause the welding bead to tilt during the laser beam welding process. In addition, the tape surrounding the litz wire should be removed as completely as possible before contacting, because the laser beam would burn the strip and thereby affect the welding process. The third and most important preliminary process step is the ultrasonic compacting process. This process is a modification of the ultrasonic welding described in chapter 2.1.2. However, compacting is not designed to join two litz wires. The process serves exclusively to compact the individual wires within the litz wire. In this case, a higher degree of compaction within the litz wire provides better preconditions for the laser beam welding. The upper limit for compacting are broken wires. Furthermore, in this process step the insulation of the individual wires is removed by friction within the litz wire. The lower the amount of residual insulation on the individual wires after the compacting process, the lower the probability of pore formation in the welding bead. [7, 8]

After the laser beam welding process, the quality of the contacts must be tested mechanically and electrically. Figure 4 summarizes the process steps that influence the laser beam welding.

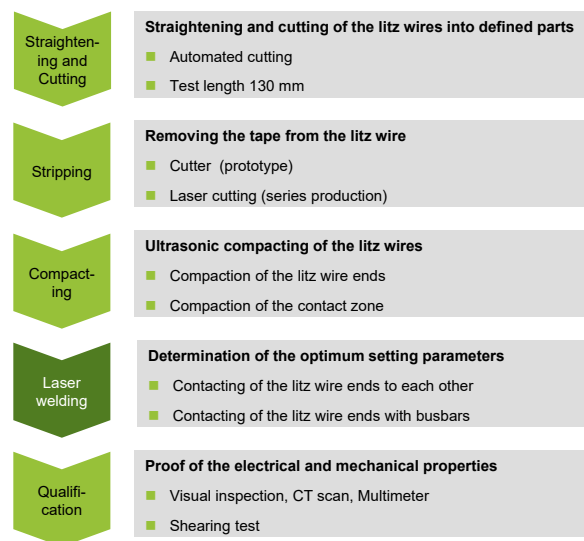


Fig. 4 Process steps with influence on the contacting [8]

4.2. Parameters of the laser welding system

The two most decisive parameters for the laser beam welding process are the laser power and the welding speed, resulting in the line energy. Figure 5 shows that the weld depth increases with increasing power and decreasing welding speed. In addition, the process range increases as well. If the power is selected too high, pores and weld spatter occur. [7]

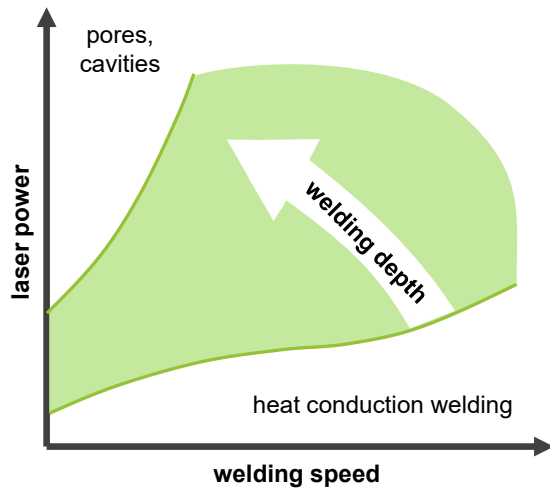


Fig. 5 Welding depth depending on laser power and welding speed according to [12]

Another parameter of the laser is the welding geometry. Basically, three different geometries are possible, which are summarized in Figure 6.

Name	Setting parameters	Welding geometry
Several lines	Line 1: Laser power 50 % Line 3: Laser power 100 % Line 2: Laser power 50 %	
Spiral	1: Line distance (a) in mm 2: Frequency (f) in 1/s 3: Geometry speed (v) in mm/s Formula: $v = a \times s$	
Zigzag	1: Line distance (a) in mm 2: Frequency (f) in 1/s 3: Geometry speed (v) in mm/s Formula: $v = a \times s$	

Fig. 6 Illustration of different welding geometries

The first geometry uses three horizontal lines, whereby both the number and the direction of the movement of the welding lines are basically adjustable. In addition, the welding can be done by means of spiral or zigzag movement. In this case, the smaller the distance between two lines and the higher the frequency, the lower the geometry speed. The general aim is to achieve the shortest possible process time, which enables a reliable welding result.

4.3. Defining the litz wires for the experiments

The stator slot defines the outer dimensions of the litz wires. However, the number of individual wires within a litz wire as well as their insulation and the choice of taping of the litz wire is adjustable. For this series of experiments, the variations of litz wires, as shown in Table 2, are tested. [9]

Tab. 2 Tested variations of litz wires [9]

Factor	Litz wire 1	Litz wire 2	Litz wire 3
Coating	enamel (grade 0)	SST	SST
Number of single wires	55	62	65
Single wire diameter	0.355 mm	0.355 mm	0.355 mm
Copper filling factor	low	medium	high

The SST (Special Surface Treated) variation differs from insulation by its lower thickness, consisting of an oxide layer, but also offers less resistance to electrical voltages. The number of individual wires should be chosen as high as possible, as this improves the electrical properties of the litz wire.

5 Methodical approach for the identification of optimized process parameters

The next series of experiments serves to define the range of possible parameters in terms of process windows and to determine the relationships between the factors. The overall objective is to determine reproducible welding parameters for laser beam welding of litz wires in the stator of electric drives. This requires a focus on the parameters that have a significant influence on contacting and that lead to constant results. These primarily include the laser power and welding speed as well as the interactions between these factors. The more significant a factor is, the earlier it is taken into account.

The experiments are carried out using a kind of funnel model, whereby each experimental loop aims to narrow down the optimal parameters in more detail. The result is therefore not only the basis for the qualification, it also indicates a value range that allows a reliable production of the contacts. The following figure 7 illustrates the systematic approach.



Fig. 7 Systematic approach of the experiments

Before carrying out the experiments, the influencing factors are divided into variable and fixed parameters. For the fixed parameters, the optimal settings are identified during the experiments, while for the variable parameters the extreme values are defined at first. This means that for variable parameters, process windows instead of values are identified. These extreme values form the process limits for contacting the litz wires. The selection of values within the process window is then carried out using quantitative or qualitative evaluation methods.

The target of the first test loop is to determine possible process windows for the laser power and welding speed. For this purpose, all other factors are fixed. For the experiments, a litz wire type 3 with 65 individual wires and SST coating and a welding geometry with three lines has been selected. Figure 8 shows the four determined process windows. The process windows become wider with increasing laser power and welding speed. In addition, only the top two process windows determined provide very good results. Due to the large number of experiments, the basis for the evaluation of the first test loop is the optical test, in which the position of the weld bead and a complete and mechanically stable connection are tested.

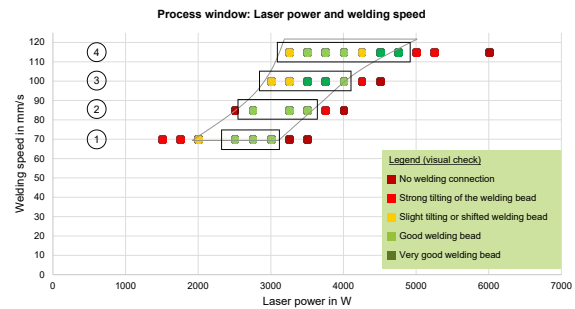


Fig. 8 Process windows related to laser power and welding speed

The second test loop serves to evaluate the determined process windows and to confirm the assumption that the upper two process windows are better suitable for contacting litz wires. For this purpose, samples with a repetition number of $n=5$ are produced from the centre of each process window and compared by means of four-point resistance measurement and visual inspection. Target values are a low electrical resistance and a welding bead that is neither tilted nor displaced and encloses all wires of the two welded litz wires. The resistance measurement is carried out three times in each case and then the average value is calculated to reduce the influence of measurement errors. Table 3 summarizes the results of the resistance measurement. As previously, process windows 3 and 4 show the best results, which confirms the visual inspection. It should be considered that these are preliminary tests. There might still be insulation residues on the individual wires in the litz wire. Eliminating these is subject to further research.

Tab. 3 Electrical resistance of the samples of each process window

Process window	1	2	3	4
Result 1 ($\mu\Omega$)	65.4	44.9	51.8	58.7
Result 2 ($\mu\Omega$)	62.3	92.7	81.5	71.6
Result 3 ($\mu\Omega$)	74.1	74.5	52.4	55.5
Average ($\mu\Omega$)	67.3	70.7	61.9	61.9
Std. deviation ($\mu\Omega$)	6.1	24.1	17	8.5

In the third experimental loop, the influence of the wobble geometry is investigated. For this purpose, samples with the three different welding geometries presented in section 4.2 are prepared and compared with each other. The evaluation is again carried out by visual inspections and resistance measurements. The required cycle time is also important for the welding geometry. This is to be chosen minimally, therefore the welding speeds of the selected geometries are also compared. On the basis of the optical inspection and the resistance measurements, only the geometry of several lines is considered in the following.

In the last test loop, the selected welding geometry must be optimized. According to the third test loop, the geometry “several lines” is the most suitable geometry

for the selected litz wire type and the process windows investigated. Optimization potentials of this geometry are the number of welding lines, the position of the welding lines as well as the distance of the welding lines to each other. Figure 9 shows three possible arrangements for the welding lines. For the number of welding lines, again, the target value - minimum cycle time - applies. Consequently, the lowest possible number of welding lines must be selected, with which the contacting of the litz wires is possible. For the litz wire type the geometry of three lines is preferred.

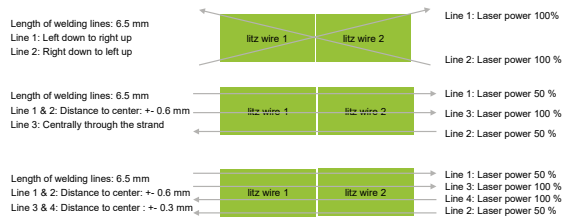


Fig. 9 Possible variants for the welding geometry “several lines”

The result of the previous series of measurements is the optimum setting of the laser welding system for the contacting of stranded wires. At the same time, the result is the basis for a statistical test plan in which different strand types can be compared with each other using the determined settings. On the other hand, it also provides the basis for the necessary qualification of the contacting. This must have a very high level of process stability. In addition, the statistical design of experiments enables the identification of interaction effects between the variable setting parameters.

6 Results of the tests

The four test loops show that good contacts can be produced with different welding geometries as well as with different parameter combinations of laser power and welding speed. When conducting the experiments, it is important to focus on the target variables. The four target parameters considered in this test series are low electrical resistance, complete contacting of all wires with a well-positioned weld bead, minimization of pores and blowholes and a minimum process time. The result of the test series is the optimum setting for an application. The tested litz wire type has the best manufacturing properties with the welding parameters in table 4.

Tab. 4 Optimum parameter settings for litz wire 3

Factor	Value
Laser power	3500 W
Welding speed	100 mm/s
Welding geometry	Three lines
Feed direction	Horizontal
Number of passes	1
Start / End ramp	None

The interpretation of this result implies that the adjustment variables used to achieve the above mentioned target variables are partly contradictory. A higher laser power leads to a lower electrical resistance due to the resulting increase in welding depth, but at the same time the risk of pore formation increases. This connection was already illustrated in Figure 5. For this reason, the interactions between the settings and the target variables must be investigated more closely by means of statistical design of experiments.

In contrast to the test series carried out, the statistical design of experiments does not aim to develop optimal parameters. It enables the identification of the interactions between the setting variables and their influence on the target variables. Furthermore, it serves as proof of the process stability. This is another target, which is of particular importance. In addition, a regression equation can be calculated with the help of a statistical experimental design, which allows the change of individual parameters and their effect on the target variables to be determined statistically. However, the proof of interaction effects as well as of process stability requires the use of highly accurate measuring instruments, because the informative value of the statistical experimental design depends on the standard deviation of the measurement results. Within the framework of this test series, it is not possible so far to achieve a sufficiently low standard deviation.

7 Summary and outlook

The laser beam welding of litz wires is subject to a variety of requirements. Therefore, it is important to define all influencing and target parameters before carrying out the experiments. The most important influencing variables are the laser power, the welding speed and the welding geometry. The main target parameters are low electrical resistance, low pore formation in the welding bead, the position of the welding bead and the mechanical stability of the welded joint. A specific test series can then be carried out according to these sizes and the specified boundary conditions of the laser welding system as well as the material and manufacturing properties of the selected litz wires. The objective is to determine the optimum parameter sets for laser beam welding. In order to reduce the experimental effort, only the main influencing variables should be designed in a variable way and should be restricted more and more by means of a funnel-shaped structure. The qualification of the parameter study requires the use of statistical design of experiments because only in this way the interaction effects of the influencing variables on the target variables can be identified. However, the continuous limitation of the variable parameters to the optimum settings is not generally valid, but applies exclusively to the tested litz wire type and its material properties and dimensions. Other material and

coating combinations require different parameter combinations of laser power and welding speed. For other conductor cross-sections, alternative welding geometries and other distances and directions of movement are required. The relationships between the most suitable number of welding lines, their vertical distance from one another and their direction of movement in relation to the selected conductor cross-section must be determined in further investigations. The same applies to the selection of the conductor material, the coating and the diameters of the individual wires. The qualification of the parameters, i.e. the proof of process stability, requires on the one hand the use of statistical design of experiments and on the other hand the use of high-precision measuring instruments which are designed for the specific requirements of copper litz wires. In particular, resistance measuring instruments with measuring accuracies in the nano-ohm range and measuring devices that enable precise resistance measurement of the compacting zone, the contacting area and the conductor resistance are essential for proving process reliability and must therefore be developed. The same applies to the detection of insulation residues. Due to the litz topology, the experimental setup and the methodics of the fluorescence measurement, as it is used for flat wires, cannot be adopted, thus further research on this topic is required.

8 Literature

- [1] Heidt, C.: Entwicklung und Bewertung von Maßnahmen zur Verminderung von CO₂-Emissionen von schweren Nutzfahrzeugen : im Auftrag des Umweltbundesamtes. UBA-FB 2672
- [2] Kampker, A.: Elektromobilproduktion. Berlin: Springer Viewieg, 2014.
- [3] Stöck, M.: Steigerung der Leistungsdichte und der Wirtschaftlichkeit von Elektromotoren für automotiv Fahrantriebe. Eidgenössische Technische Hochschule (ETH) Zürich. Dissertation
- [4] J. Seefried, T. Gläsel, M. Zürn, and J. Franke. "Evaluation of monitoring approaches for the ultrasonic crimping process of tubular cable lugs". In: 7th International Electric Drives Production Conference (EDPC), Würzburg, 2017, S. 212-217
- [5] Mayr, A.: Verbindung von Kupferlackdrähten mit feinadrigen Litzen. FVA Infotagung, Würzburg, 2019
- [6] Merkblatt DVS 2952: Widerstandsschweißen in der Elektrotechnik und Feinwerktechnik – Kompaktieren, Schweißen und Hartlöten von Kupferlitzen. DVS - Deutscher Verband für Schweißen und verwandte Verfahren, 2018
- [7] T. Glaessel, J. Seefried, and J. Franke, "Challenges in the manufacturing of hairpin windings and application opportunities of infrared lasers for the contacting process," in 2017 7th International Electric Drives Production Conference (EDPC): December 5th-6th, 2017, Würzburg, Germany: proceedings, Würzburg, 2017, pp. 1–7.
- [8] A. Riedel et al., "Challenges of the Hairpin Technology for Production Techniques," 2018 21st International Conference on Electrical Machines and Systems (ICEMS), Jeju, 2018, pp. 2471-2476.
- [9] A. Riedel, A. Roessert, A. Kuehl and J. Franke, "Calculation of the Copper Filling Factor of Electric Traction Drives including Graphical Representation" 2019 22nd International Conference on Electrical Machines and Systems (ICEMS), Harbin, 2019
- [10] DIN 8580: Manufacturing processes - Terms and definitions, division. Beuth Verlag, Berlin, 2020
- [11] Ostermeier, A.: Verbindung mit Ultraschallverdichten: Einmal kalt gepresst bitte – nicht gecrimpt!, Elektronik Praxis, 02/2017, S.19 – 22, Würzburg, 2017
- [12] Industrial Laser Solutions, Laser welding of copper, <https://www.industrial-lasers.com/welding/article/16485604/laser-welding-of-copper>
- [13] Fahrenwaldt, H.: Praxiswissen Schweißtechnik – Werkstoffe, Prozesse, Fertigung. Wiesbaden: Viewieg + Teubner, 2011

Acknowledgment

The corresponding author Andreas Riedel thanks Johannes Seefried and Alexander Schmidt for the collaborative realization of this publication. Alexander Schmidt assisted in the implementation of the contacting experiments and their qualification. Johannes Seefried supported in the choice of the litz wire configuration. The authors thank Alexander Kuehl and Joerg Franke for consulting and reviewing the publication.

Investigations on Different Joining Techniques Regarding Current-carrying Joints with Normal Conducting Material and YBCO Coated Conductors at low temperatures

Katrin Bäuml, Schneider Electric, Regensburg, Germany, Katrin.baeuml@se.com

Abstract

Due to the further development of metal coated, thin film high temperature superconductors (HTS) which operate at the temperature of boiling liquid nitrogen (LN_2 , $-195,8\text{ }^\circ\text{C}$) a wide field of application arises. To apply HTS in electrical devices, stable current-carrying joints between normal- and superconducting materials as well as joints between HTS are needed. To develop and evaluate these current-carrying joints it is necessary to measure and investigate the electrical and mechanical behaviour of the conductors themselves and their joints at the temperature of LN_2 .

This paper presents different joining techniques to establish current-carrying joints for low temperature applications. In a low temperature test rig, the joint resistance R_V was measured at initial state and in current increasing tests the power losses P_V were evaluated. Besides the electrical characterization, tensile tests were performed, to verify the mechanical strength of the joints. Based on the real geometric requirements of an inductive superconducting fault current limiter (iSFCL), the characterization of the HTS conductor was analysed in a parallel circuit, too. In addition, the iSFCL was modelled in a simulation environment with the „Electromagnetic Transients Program“ EMTP-ATP and loaded with real network parameters. Based on these results, the measuring results were assessed.

1 Introduction

The long-term behaviour and aging of electrical joints at high temperatures (above $80\text{ }^\circ\text{C}$) was investigated in many experiments. As electrical devices, applying superconductors are becoming more important, electrical joints, stable to operate in LN_2 have to be established and investigated related to their electrical and mechanical behaviour at an operating temperature of boiling LN_2 . An outstanding material property of HTS is their quasi zero resistance below a critical temperature of about $\vartheta_c \approx -185\text{ }^\circ\text{C}$. When loaded with DC the resistance and respectively the power losses are zero, loaded with AC it comes to so called AC - power losses. These losses had to be quantified for the following 12 mm wide YBCO coated conductors, which are schematically shown in **Figure 1**, and joints of these materials:

- HTSL Var1: AMSC
($50\text{ }\mu\text{m}$ substrate, $50\text{ }\mu\text{m}$ copper and $3\text{ }\mu\text{m}$ silver coating)
- HTSL Var2: Super Power SCS12100-CF
($100\text{ }\mu\text{m}$ substrate, $2\text{ }\mu\text{m}$ silver over layer and $40\text{ }\mu\text{m}$ copper stabilizer)
- HTSL Var3: Super Power SF12100
($100\text{ }\mu\text{m}$ of substrate and $2\text{ }\mu\text{m}$ of silver over layer)

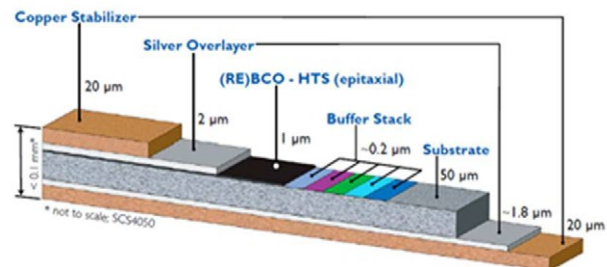


Fig. 1. Schematic view of a YBCO coated conductor [1]

For establishing a proper electrical joint with these three different types of YBCO coated conductors the surfaces of the copper coated conductors were cleaned with ethanol and treated with a non-woven web. Thus, oxide layers were removed, the pollution layer resistance R_F lowered and the roughness was increased. The silver coated surfaces were only cleaned with ethanol and a fine non-woven web to not destroy the thin silver layers. As the European Union is working at present on different guidelines like RoHS (Restriction of Hazardous Substances) [2] to ban cadmium and lead for industrial application, this study has focused on alternative joining techniques to the currently applied Pb- and Cd-solders. Therefore, techniques as clamping,

adhesive bonding and soldering with reactive nanometer multilayers (RMS) with stacks of Al/Ni were examined.

The clamp consists of two copper blocks whose sides, facing the conductors, were covered with an insulating foil to prevent electrical contact between the block and the conductors. As the conductor dimensions are very small, care has to be taken not to compress the material too much. The optimum torque was found with $M = 12,5 \text{ Nm}$.

Regarding adhesive bonding, a two-component non-conductive room temperature curing adhesive was used for these tests. As most electrically conducting adhesives which include silver components tend to embrittle at such low temperatures, this new investigated adhesive showed very good properties at low temperatures. A mating force of $F = 3.5 \text{ kN}$ was found as the best compromise between joint resistance R_V , tensile force F_Z and conductor stress while adhesive bonding.

When using reactive nanometer multilayers (RMS) for soldering, the thermal energy is provided by activating the atomic diffusion in a reactive nanometer multilayer system (Al-Ni). This results in a very short-term and localized heat input which can be used to melt the solder applied to both sides of the reactive multilayer. The technique enables joining with minimal thermal stress for the components. For the tests, RMS films with an $80 \mu\text{m}$ Al-Ni RMS stack with Sn solder were used. For RMS soldering there is a significant relationship between the mating force F , the joint resistance R_V and the tensile force F_Z . The best results were achieved with a mating force of $F = 3.5 \text{ kN}$.

The detailed joining processes of these three techniques are already reported in [3].

The electrical joint resistivity R_V will be reflected at state of the art joining techniques of YBCO coated conductors [4], [5], [6], [7] which reach joint resistance values even below $R_V < 100 \text{ n}\Omega \text{ cm}^2$ [6]. In addition, the industrial application in an inductive superconducting fault current limiter (iSFCL) will be evaluated.

2 Electrical Characterisation

2.1 Measurement principle

First, the material resistance $R_{L,45}$ of the YBCO coated conductors is measured at a distance of 45 mm. A 4 - point measurement method is used with potential tappings. The material resistance $R_{L,15}$ is calculated at a distance of 15 mm:

$$R_{L,15} = 1/3 R_{L,45} \quad (1)$$

Then, the YBCO coated conductors as well as the joints between normal and superconducting material are joined with an overlapping length of 15 mm with the face-to-face method (Figure 2). Again, the resistance $R_{V,45}$ is measured at 45 mm.

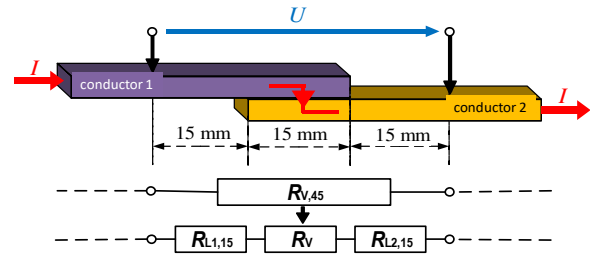


Fig. 2. Measurement principle at jointed conductors

The joint resistance R_V is calculated from the measured values:

$$R_V = R_{V,45} - (R_{L,15} + R_{L,15}) \quad (2)$$

As most applications in the energy supply sector work with AC loads, all measurements have been performed at AC currents of $I_{AC} = 100 \text{ A}$.

2.2 Test results

From each variant of joining technique, 6 samples have been built and measured in an AC application, as this is the operating condition of networks. These results are compared in Figure 3 for the YBCO coated conductor joints and are reflected concerning non-jointed continuous HTS conductors, too.

All samples have been measured 4 times. The shown values in Figure 3 represent the mean values from these measurement series. A deviation of the resistance values of maximal 2% was recorded during the tests.

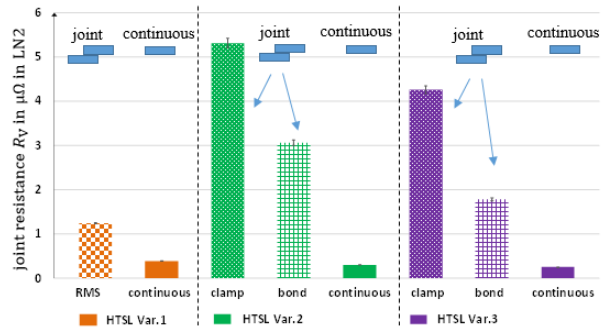


Fig. 3. AC joint resistances R_V of YBCO coated conductors compared to the resistance R of non-jointed HTS conductors

The most obvious observation is, that all joining techniques are resulting in a higher joint resistance R_V compared to the non-jointed continuous HTS conductors. This behaviour is different compared to normal conductors, like copper conductors. A joint within a superconducting material is therefore degrading the resistance behaviour.

Nevertheless, best joining results were received with the RMS soldered joint variants due to the establishing substance-to-substance bond between the two joining

partners. The complete joining surface is bonded together in this case and available for the current flow. The highest resistance values were measured with the clamped joining method. As the YBCO coated conductors show a high rigidity, the surface pressure during joining and thereby the formation of micro-contacts is reduced. To receive low resistance values with clamping technology, a lot of micro-contacts are essential to provide a proper current flow in the joining area. With adhesive bonded joints, care has to be taken, not to compress the YBCO coated conductors too much. The formation of micro-contacts for the proper current flow is the difference of clamping and adhesive bonding compared to the RMS soldering technique [8], [9], [10].

RMS soldering was only possible with the HTS Var.1 from AMSC. With HTS Var.2 and Var.3 from SuperPower, it came after the soldering process to dissolution of the over- and stabilization layers.

Compared to state of the art joining techniques, joint resistance values even below $R_V < 100 \text{ n}\Omega \text{ cm}^2$ could be reached [6]. Even if the presented joint resistance values R_V were measured in the range of few μohms , it has to be highlighted that these results were received with AC current load, where already a certain resistivity of the YBCO coated conductor itself could be measured as shown in the “continuous” bar of Figure 3.

In the detailed view of **Figure 4**, the bypass circuit of a superconducting fault current limiter (iSFCL) is shown [11]. To realise this bypass circuit, the YBCO coated conductors have to be joined to normal conductors for current commutation in case of a short-circuit or failure event.

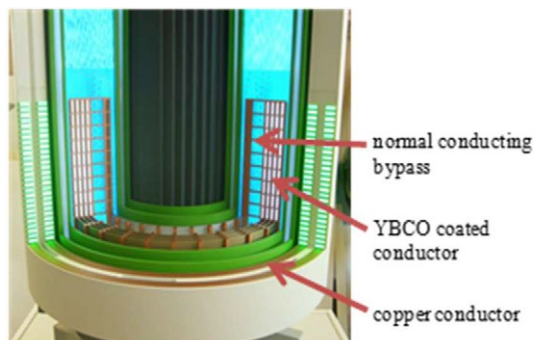


Fig. 4. Detailed view of a superconducting fault current limiter (iSFCL)

Based on this application, a low temperature test rig including a bypass circuit (**Figure 5**) was developed, to demonstrate the commutation behaviour from superconducting to normal conducting material in case of a failure. The YBCO coated conductors are joined to copper conductors and silver coated copper conductors with respect to their surface material. The established material combinations are indicated in **Figure 6**.

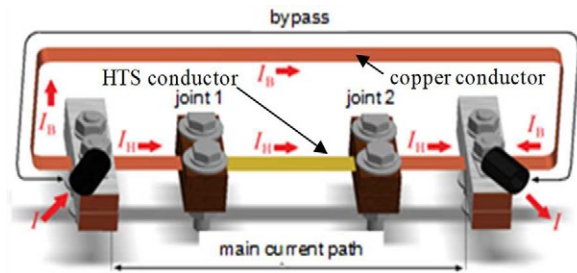


Fig. 5. Schematic illustration of the bypass test circuit

Figure 6 shows the joint resistances $R_{V,SL-NL}$ for the different joining techniques for the combined joints. Although the real network conditions are AC applications, the later on explained current rise test in the presented investigation is performed as a DC current test. Therefore, the joint resistance values $R_{V,SL-NL}$ were measured already with both, DC and AC current.

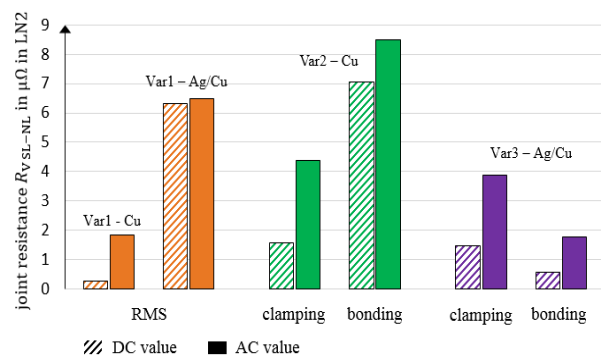


Fig. 6. Comparison of joint resistances $R_{V,SL-NL}$ of RMS soldered, clamped and adhesive bonded conductors

Best results are reached with the RMS soldering in a DC application, which results in $R_{V,SL-NL} = 0,26 \mu\Omega$. Installing superconducting devices in the network, AC applications have to be taken into account. Therefore, good results were reached with the adhesive bonding $R_{V,SL-NL} = 1,78 \mu\Omega$ as well as with the RMS soldering technique $R_{V,SL-NL} = 1,84 \mu\Omega$.

The reason for low resistance values with RMS soldering is related to the connection between the two joining partners. RMS soldering leads to a metallic continuously joint whereas adhesive bonding leads to form or force closure of the joining partners.

The difference between RMS soldering of HTS-Cu and HTS-Ag/Cu is due to differences in contacting the normal conductors' surface. After the soldering process, it came to dissolution of the silver layer, which results in a higher resistance $R_{V,SL-NL}$.

Installing a clamped HTS Var.3-Cu joint in the main current path of the bypass circuit, like shown in Figure 5, [3], and performing a current rise test (**Figure 7**), the bypass circuit worked as investigated in [12].

This test was performed with DC current to avoid the electromagnetic influence of time varying currents on the accuracy of the voltage measurement. Initially, the current I is flowing in the superconductor (green line) with a current ratio of $I_H/I \approx 0,8$. When the critical current I_c is reached, the superconductor quenches and the current I_H is immediately commutated according the resistance ratio to the normal conducting copper bypass (blue line). This commutation process took place within $\Delta t = 50$ ms. When raising the current I further, only the bypass current I_B is increasing. So, in case of a failure current, the superconductor is protected by the bypass circuit. The normal conducting bypass is essential to not destroy the superconductor due to thermal overheating. After lowering the current I , after $t = 125$ s, the superconductor recovers automatically and finally takes again over the current I_H at $I = 164$ A which led again to the initial current ratio of $I_H/I \approx 0,8$ in the bypass circuit.

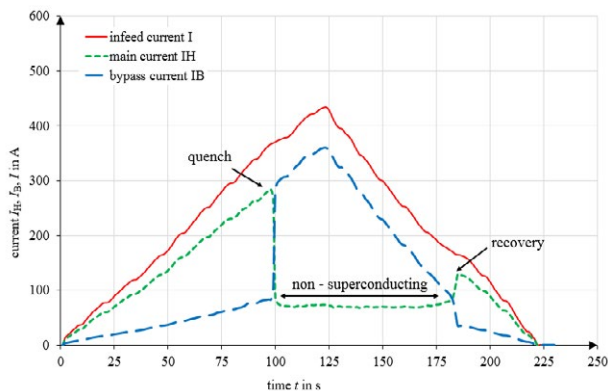


Fig. 7. Behaviour of a clamped superconducting joint in parallel to a normal conducting copper bypass

Regarding an application in an iSFCL, this behaviour means, that the current in a network is not completely interrupted but limited to the resistive value of the applied YBCO coated conductors. This reduced value can than be interrupted by a circuit-breaker.

3 Mechanical Characterisation

Short-circuits, which may occur in electrical networks, cause also mechanical stress to the installed components. Therefore, the investigated joining techniques were tested regarding their mechanical strength, too.

3.1 Test set-up

In order to investigate the maximal permissible tensile force F , a tensile testing machine was used together with a LN_2 tight Styrofoam. With this test set-up, the YBCO coated conductor and especially the joint area could be fully covered in LN_2 .

Like the electrical characterization, the joined conductors were compared to the tensile forces F determined with non-joined continuous conductors. In addition,

the comparison is shown between room temperature (RT) and LN_2 .

3.2 Test results

The expectation is, that at low temperatures, the maximal tensile force F is increasing. This is due to the face-centered cubic crystal structure of the investigated metals and could be observed at tensile tests with joined normal copper conductors.

Testing the adhesive bonded and RMS soldered YBCO coated conductors showed a different behaviour as displayed in **Figure 8**. At room temperature (RT) the maximal tensile force F was measured with 1200 – 1400 N for the variants Var.2 and Var.3. With Var.1, only $F = 750$ N could be reached. This can be explained with the thinner substrate layer compared to Var.2 and Var.3. As mainly the substrate layer is crucial for the mechanical strength of the YBCO coated conductors, a thinner layer is resulting in a lower mechanical strength.

In LN_2 , a different behaviour can be observed. Only for Var.1, an increase in the tensile force F could be observed in LN_2 due to the mechanically strong RMS soldered substance-to-substance bond. Both adhesive bonded variants Var.2 and Var.3 show a similar performance. Their maximal tensile force in LN_2 is reached at $F = 640$ N, which is the limit for the used adhesive in LN_2 environment. The adhesive bonded joints broke due to cohesion fracture. Tensile tests on continuous non-joined YBCO coated conductors could be stressed up to a force of $F = 1800$ N which is quite similar to what was reported under [13], [14].

With the clamped joint variants, no tensile tests were performed. As the clamp was fixed by screws, it is always the conductor itself to brake prior to the joint.

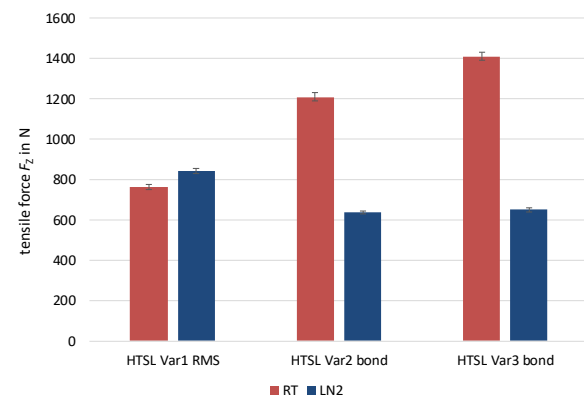


Fig. 8. Comparison of the maximal tensile forces F of the different joining technologies at RT and in LN_2

For the application of the investigated joining techniques in a real device, not the maximal tensile force F is essential but the force at the 0,2% elastic limit (**Figure 9**). If the conductors and their joints are only stressed up to this limit, no permanent deformation will occur, which is essential for a long-term use in a device. From the recorded force-deflection diagrams, the

acceptable force at the 0,2% elastic limit was determined.

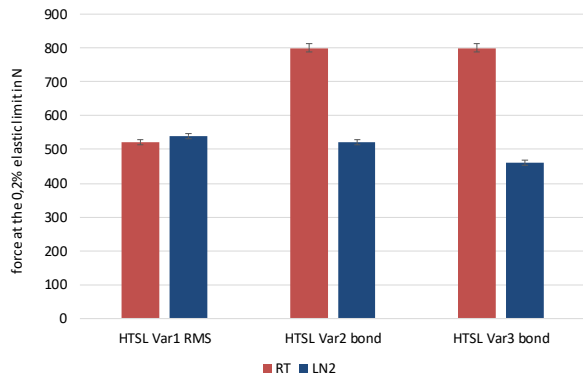


Fig. 9. Comparison of the forces at the 0,2% elastic limit of the different joining technologies at RT and in LN₂

In principle, the same behaviour could be observed compared to the tensile force measurement, just at lower values. The force limit for the adhesive bonded Var.3 is even further decreasing in LN₂ environment. With the used adhesive, a better connection to the copper surface of Var.2 is possible than to the silver surface of Var.3.

4 Network Integration

Finally, the investigated YBCO coated conductor joints are reflected regarding real network requirements. This is done based on an inductive superconducting fault current limiter (iSFCL) [15] which is installed in a 12 kV medium voltage network and is aimed to couple an industry network with an utility network (Figure 10).

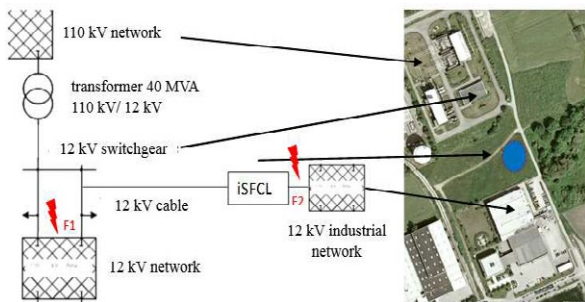


Fig. 10. Installation site of an iSFCL coupling two networks

As the existing 12 kV switchgear is limited to a short-circuit current rating of $I_{SC} = 25$ kA, the additional short-circuit current infeed from the industrial network in case of a failure at location F1, has to be limited to a maximum peak short-circuit current of $I_P = 12,5$ kA_p.

4.1 Modelling an iSFCL in EMTP-ATP

In order to evaluate the requested behaviour, the network is simulated with the “Electromagnetic Transients Program” EMTP-ATP. First, the three-phase network branch of the industry network is modelled without the iSFCL (Figure 11).

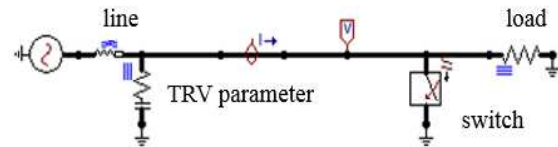


Fig. 11. 3-phase network branch of the industry network modelled in EMTP-ATP

The line and TRV parameter are simulated according the values given in IEC 62271-100 [16]. The rated current of the network is $I = 1250$ A.

The short-circuit event is initiated via a switch. Then, the 3-phase voltage is breaking down, whereas the short-circuit current reaches a peak value of $I_P = 25$ kA_p (Figure 12). Due to the pure ohmic load and the X/R ratio of a cable network, the maximum peak short-circuit current is reached, when initiating the short circuit in the voltage zero crossing.

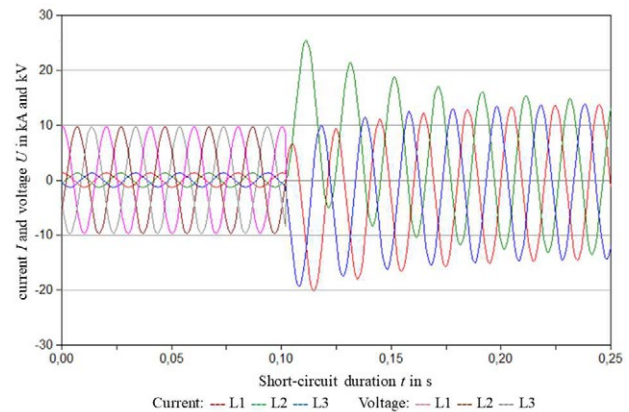


Fig. 12. Unlimited short-circuit current and voltage in the industry network branch

To limit this peak short-circuit current, the iSFCL is modelled and integrated in the above shown network branch. For better overview, only a 1-phase branch is shown in Figure 13.

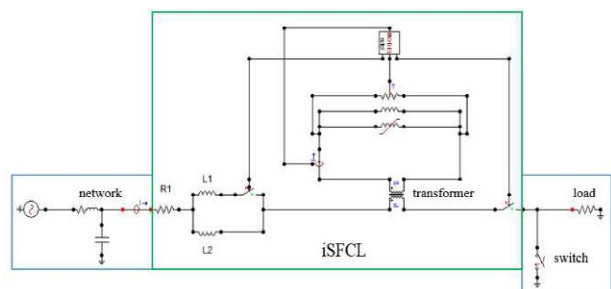


Fig. 13. 1-phase network branch including iSFCL

The iSFCL is based on the transformer principle and modelled with a transfer ratio of 64:1 between primary and secondary side. The resistance R1 is representing the losses of the normal conducting primary winding. Two operational modes, realised with the inductive parallel circuit of L1 and L2, simulate either the superconducting state, where the total inductance of the parallel circuit is active or the resistive state, where only the inductance of L2 is active. A TACS operated switch is foreseen to change between these two operational modes. The iron core was simulated with the „nonlinear current-dependent inductor TYPE 98“. To operate the TACS elements, MODELS was used. An input parameter to MODELS is the secondary current. Is the secondary current higher than the critical current I_C of the YBCO coated conductors, the related TACS element changes to high resistive state. These critical current values are taken from the HTS suppliers. Furthermore, the inductive parallel circuit is operated with this input value as described before.

When initiating the short-circuit event by closing the switch, the voltages breaks down. Furthermore, in **Figure 14**, the unlimited short-circuit current (blue line) is compared to the limited short-circuit current (green line). It was found, that with the chosen design, the limitation requirement was even exceeded. A limited peak short-circuit current of $I_p = 8 \text{ kA}_p$ was reached.

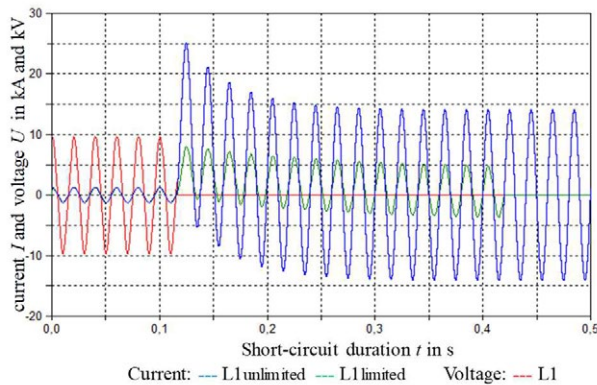


Fig. 14. Comparison of limited (green) and unlimited (blue) short-circuit current and voltage in the industry network branch

Before the short-circuit event, there is no difference between the rated current in the industry network with or without the iSFCL. This shows, that the iSFCL has no negative effect on the normal operation of the network.

4.2 Evaluation of the electrical parameters

In contrary to normal conductors, the quality factor of YBCO coated conductors can't be determined, as superconductors don't show a material resistance R_M . The measured resistance R_{AC} is related to the power loss during current carrying process. The evaluation of the electrical parameters is therefore based on the

measured power losses P_V at a current of $\hat{I} = 100 \text{ A}$ and at the quench.

High power losses at normal operation at $\hat{I} = 100 \text{ A}$ are limiting the current carrying capability of the YBCO coated conductors. At the resistive quench mode, high power losses result in higher cooling efforts. Therefore, the lower the measured power losses, the better for the application in a real electrical device like the iSFCL. In **Table 1**, where an overview of the measured power losses of the continuous conductors as well as of the joint conductors is shown, the preferred joining techniques and conductors are marked in bold. Best results were reached with the RMS soldering technique, as it leads to a metallic continuously joint whereas adhesive bonding leads to form or force closure of the joining partners. For the application in a real electrical device, RMS soldering is the preferred solution.

material	continuous conductors		clamping		adhesive bonding		RMS soldering	
	$\hat{I} = 100 \text{ A}$	Quench	$\hat{I} = 100 \text{ A}$	Quench	$\hat{I} = 100 \text{ A}$	Quench	$\hat{I} = 100 \text{ A}$	Quench
values in mW	P_{VAC}	P_{VAC}	P_{VAC}	P_{VAC}	P_{VAC}	P_{VAC}	P_{VAC}	P_{VAC}
Var1	6	45	-	-	-	-	-	-
Var2	4	78	-	-	-	-	-	-
Var3	3	51	-	-	-	-	-	-
Var1-Var1	-	-	-	-	-	-	10	69
Var2-Var2	-	-	28	363	17	255	-	-
Var3-Var3	-	-	18	170	10	112	-	-

Tab. 1 Overview of the measured power losses P_V of YBCO continuous and joint coated conductors

The same result is found for the joints between YBCO coated conductors and normal conductors (**Table 2**). Due to the normal conducting part, the power losses are much higher than for the pure superconducting joints.

material	continuous conductors		clamping		adhesive bonding		RMS soldering	
	$\hat{I} = 100 \text{ A}$	Quench	$\hat{I} = 100 \text{ A}$	Quench	$\hat{I} = 100 \text{ A}$	Quench	$\hat{I} = 100 \text{ A}$	Quench
values in mW	P_{VAC}	P_{VAC}	P_{VAC}	P_{VAC}	P_{VAC}	P_{VAC}	P_{VAC}	P_{VAC}
Cu-Var1	-	-	-	-	-	-	153	956
Ag-Var1	-	-	-	-	-	-	160	1072
Cu-Var2	-	-	160	1970	424	5514	-	-
Ag-Var3	-	-	140	1240	215	2030	-	-

Tab. 2 Overview of the measured power losses P_V of YBCO coated conductors and normal conductors

Nevertheless, also in this case, the RMS soldering technique using YBCO coated conductor Var.1 is the preferred solution for application in an iSFCL. Regarding the joints between superconductors and normal conductors, the power loss P_V at quench mode is of special interest. In this mode, the current is commutated from the superconductor to the normal conductor (Figure 7). The lower the power losses in this mode, the better regarding the necessary cooling efforts in an iSFCL cryostat.

5 Conclusion

Three alternative Pb-free joining techniques, clamping, adhesive bonding and RMS soldering, were presented and their short-time usability for LN₂ applications was tested and confirmed. Their different joint resistances R_V were compared regarding AC applications, where the RMS soldering techniques showed the best results with the lowest joint resistances R_V , due to a proper metallic continuity joint between the two joining partners. This substance-to-substance bond within the complete joining surface is available for the current flow. Compared with the other two joining techniques, only the micro contacts are available for the current transportation. This results in higher joint resistances R_V for clamping and bonding.

This result was found for the superconducting joints as well as for the combination of superconducting and normal conducting joints. The joints were applied in a parallel bypass circuit and tested related to their commutation behaviour. At the example of a clamped joint installed in the bypass circuit the proper functioning was shown.

In addition, the maximal tensile force F , as well as the force at the 0,2% elastic limit was determined for the different joining techniques. Again, in LN₂ environment, the RMS soldering technique showed the best results. The investigated adhesive has a limit of $F = 640$ N at low temperatures. With the investigated mechanical strength of the YBCO coated conductors and their joints, an example of applicability in a real fault current limiter was shown.

With the simulation tool EMTP-ATP an iSFCL was modelled. The measured commutation behaviour could also be investigated theoretically. Furthermore, an outlook of application possibilities was given, as the RMS soldering technique showed good technical values for an implementation in a real electrical device.

An important point which has still to be investigated is the long-time behaviour of the presented techniques. Although, the presented resistance values R_V are higher compared to conventional soldering techniques using lead, cadmium or indium solders [4], [5] the presented techniques show promising properties which will be further investigated and improved.

Acknowledgment

The adhesive bonding and RMS soldering of the conductors were performed in cooperation with the Institute of Manufacturing Technology of the Technische Universität Dresden. The authors would like to thank Maurice Langer (LOT), Evelyn Hofmann and Theresa Kühne (both FTM).

6 Literature

- [1] Super Power Inc. [Online] <http://www.superpower-inc.com/content/2g-hts-wire>, (27.02.2016)
- [2] ZVEI [Online] <http://www.zvei.org/Themen/GesellschaftUndUmwelt/Seiten/RoHS-Richtlinie.aspx>, (02.01.2020)
- [3] Bäuml, K., Großmann, S.: Investigations on Different Joining Techniques Regarding Electrical Joints with Normal Conducting Material and YBCO Coated Conductors, *IEEE Trans. Appl. Supercond.*, vol. 26, no. 3, Art. no. 6602605, 2015.
- [4] Shin, H-S., Dedicataria, M.: Comparison of the Bending Strain Effect on Transport Property in Lap- and Butt-Jointed Coated Conductor Tapes, *IEEE Tran. Appl. Supercond.*, vol 20, no. 3, pp. 1541-1544, March 2010
- [5] Baldan, C., Oliveira, U., Shigue, C., Filho, E.: Evaluation of Electrical Properties of Lap Joints for BSCCO and YBCO tapes, *IEEE Tran. Appl. Supercond.*, vol 19, no 3, pp. 2831-2834, June 2009
- [6] Kim, Y., Bascunan, J., Lecrevisse, T., Hahn, S., Voccio, J., Park, D., Iwasa, Y.: YBCO and Bi2223 Coils for High Field LTS/HTS NMR Magnets: HTS-HTS Joint Resistivity, *IEEE Tran. Appl. Supercond.*, vol. 23, no. 3, 6800704, June 2013
- [7] Ueltzen, M., Martinek, I., Syrowatka, F., Floegel-Delor, U., Riedel, T.: Soldered ohmic contacts to superconductors for high-current applications, *Physica C* 372-376, 1653-1656, 2002
- [8] Böhme, H.: *Mittelspannungstechnik*, Huss-Medien GmbH, Verlag Technik, Berlin, 2005, ISBN 3 341 01495 0
- [9] Bergmann, R.: *Zum Langzeitverhalten des Widerstands elektrischer Stromschienenverbindungen*, VDI Verlag GmbH, Düsseldorf, 1996, ISBN 3 18 319521 6
- [10] Braunovic, M., Konchits, V., Myshkin, N.: *Electrical Contacts*, CRC Press, Boca Raton, 2007, ISBN 987 1 57444 727 9
- [11] U. Kaltenborn, F. Mumford, A. Usoskin, S. Schmidt, T. Janetschek: Inductive Shielded Superconducting Fault Current Limiter – An Enabler of Smarter Grids, CIRED conference, paper no. 0955, Frankfurt, 2011
- [12] Usoskin, A., Mumford, F., Dietrich, R., Handaze, A., Prause, B., Rutt, A., Schlenga, K.: Inductive Fault Current Limiters: Kinetics of Quenching and Recovery, *IEEE Tran. Appl. Supercond.*, vol. 19, no. 3, pp. 1859-1862, June 2009
- [13] Hojo, M., Yoshida, Y., Sugano, M., Adachi, T., Inoue, Y., Shikimachi, K., Hirano, N., Nagaya, S.: FATIGUE BEHAVIOUR OF YBCO COATED CONDUCTOR WITH Cu LAYER AT 77K, 17th Int. Conf. on Composite Materials, *Supercond. Sci. Technol.*, 21 054006, 2009

- [14] Ochiai, S., Okuda, H., Sugano, M., Osamura, K., Prusseit, W.: Influences of Electroplated Copper on Tensile Strain and Stress Tolerance of Critical Current in DyBCO-Coated Conductor, *IEEE Tran. Appl. Supercond.*, 22(1), 2012
- [15] Bäuml, K., Kaltenborn, U.: POSSIBILITIES OF INTEGRATING RENEWABLE GENERATION TO THE DISTRIBUTION GRID BY FAULT CURRENT LIMITERS, CIRED Workshop, paper 137, Lisbon, 2012
- [16] DIN EN 62271-100:2018-04, Hochspannungs Schaltgeräte und -Schaltanlagen – Teil 100: Wechselstrom Leistungsschalter, Beuth Verlag, <http://www.beuth.de>, (13.01.2020)

Analysis of HDMI 2.1 Mated Connector Contact Boundary Impedance Impacts on a High-speed Digital System Performance

Youngwoo Kim, Daisuke Fujimoto, and Yu-ichi Hayashi
Nara Institute of Science and Technology, Ikoma, Japan, youngwoo@is.naist.jp

Abstract

In this paper, analysis of the high definition multimedia interface (HDMI) mated connector contact boundary impedance impacts on a signal integrity of high-speed digital system is conducted. For the HDMI 2.1 mated connectors, tight electrical specifications are proposed to ensure signal-integrity of the high-speed digital system. The connector specifications are defined for the mated condition therefore, most of connector companies develop mated plug-receptacle connectors together. However, in real applications, HDMI 2.1 plugs and receptacles from different developers can be mated. In this analysis, we report severely high impedance at connector contact boundary which fails to meet specification passed the system so called “eye-diagram” simulation test with enough margin. The eye-diagram test is based on a measured S-parameter of the cable and connector. Since certified connectors are used and eye-diagram tests are passed, those cases can exist in real market but failing mated connector specification which can cause severe radiation. Therefore, impacts of connector boundary impedance on system performance must be carefully conducted and reported.

1 Introduction

The high definition multimedia interface (HDMI) plays an important role in audio-video and computer markets. In late 2017, specification of the HDMI 2.1, which uses four high-speed differential channels operating at 12 Gbps/channel is introduced and expected to be a key technology for the growing 8K market [1]. For the HDMI 2.1 mated connectors, tight electrical specifications are defined: differential characteristic impedance, insertion loss and attenuation-to-crosstalk ratio exist to ensure signal-integrity of the high-speed digital system. The connector specifications are defined for the mated condition only therefore, most of connector companies develop mated plug-receptacle connectors together. However, in reality, HDMI 2.1 plugs and receptacles from different manufacturers can and will be mated.

In this study, we focus on cases when certified HDMI 2.1 plug and receptacle from different manufacturers are mated and failed to meet impedance specification at the contact boundary were observed. Due to different mechanical structures between original plugs or receptacles, electrical performances are also affected. In some cases, even though severely high impedance at connector contact boundary were observed, which fails to meet specification, the combination passed the system “eye-diagram” test. The eye-diagram test judges the signal integrity of the interconnection by accumulating all received data patterns [2]. In the HDMI 2.1 cable and connector assembly, there exist various electrical parameter specifications. If one of the tests failed, an alternative eye-diagram test can be conducted of the second option. For the system level

eye-diagram compliance test set-up, we considered HDMI 2.1 connectors, cable, PCB used for interconnections, equalizer and appropriate bit patterns based on the standard compliance test specification [3]. As guided in the specification, we made the standard eye-diagram simulation set-up using the circuit simulator, Keysight ADS. S-parameter touchstone file based on measurement for connectors, cable and other interconnections are included in the standard eye-diagram simulation set-up. We validated that some HDMI 2.1 mated connectors and cables with more than 140 Ω impedance which violated the standard specification, 90 to 110 Ω passed the system eye-diagram specification.

Since certified connectors are used and the eye-diagram tests are passed, those cases can exist in real applications but mated connectors failing the specification can cause signal integrity issues, severe electromagnetic interference (EMI) radiation [4]-[5]. Therefore, impacts of connector boundary impedance on system performance should be carefully conducted furthermore and reported to the community working on the standards.

2 Realization of the standardized “Eye-diagram” Compliance Test Set-up for HDMI 2.1

In this section, the realization of standardized eye-diagram compliance test set-up for a HDMI 2.1 system is explained. An “eye-diagram” is important indicator used to judge signal integrity of a high-speed digital system [6]. We used Keysight ADS ChannelSim to realize the eye-diagram compliance test set-up. In **Figure 1**, the overall block-diagram of the test set-up is shown.

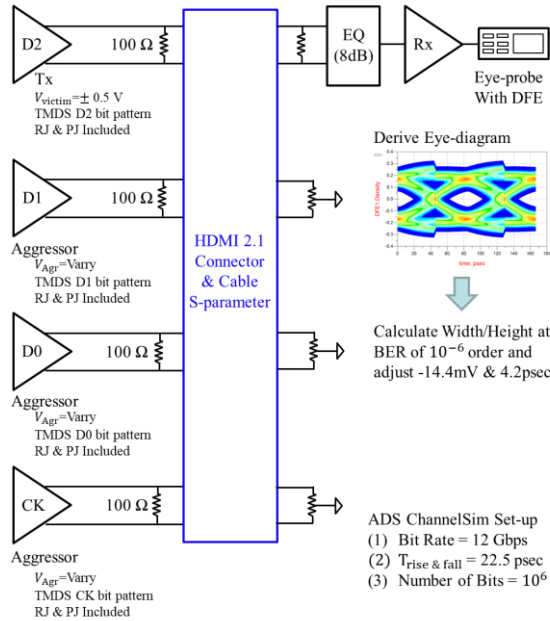


Fig. 1 Block-diagram of the HDMI 2.1 eye-diagram test including measured S-parameter touchstone file of connector and cable.

Since this is a standardized test, the transmitter and receiver must be universal. Therefore, instead of a specific circuit model such as input/output buffer information specification (IBIS) or IBIS algorithmic modelling interface (IBIS-AMI), an ideal driver model provided by the Keysight ADS ChannelSim is used. Since there are our high-speed differential channels: CK, D0, D1 and D2, four different driver models are used with different bit patterns for each driver. For bit patterns, transition minimized differential signalling (TMDS) bit patterns are used based on our previous study [6].

To realize the standardized set-up, we must use equalizer and worst cable model (WCM) provided by the standardization forum first. It is important to find the aggressor channels' input voltage swing values (peak-to-peak amplitude) and periodic jitter value to make the output eye-diagram barely passing the eye-diagram width and height when the WCM is used. Especially, by adjusting the input voltage swings of the aggressors, it is possible to control the amount of cross-talk induced to the target victim channel. In Fig. 1, the block-diagram is depicted for the case when the differential channel D2 is a victim channel. Therefore, the other differential channels CK, D0, and D1 are marked as an aggressor, which induces cross-talk to the victim channel that we are monitoring the eye-diagram.

In **Figure 2(a)**, the actual set-up that we realized using the ADS is shown. We also set proper values for the random jitter and decision feedback equalizer (DFE) [7]. For the differential channel CK and D2, we found that input voltage swings for the aggressors should be $V_{agr} = \pm 0.64$ V to make the output eye-diagrams at the victim receiver barely passing the specifications which

are 100 mV opening voltage and 29.167 ps at 12 Gbps. For the differential channel D0 and D1, we found that $V_{agr} = \pm 0.50$ V is the condition to make the output eye-diagrams of D0 and D1 barely passing the specification. In **Figure 2(b)**, simulated eye-diagrams for the WCM are shown with eye-diagram height and width. From the contour, width and height are derived by calculation at the bit error rate (BER) level of 10^{-6} order. Finally, adjustments of -14.4 mV and -4.2 ps for height and width are conducted. Note that the slope of the specification mask (100 mV/29.167 ps) is the same as that of the adjustment values (14.4 mV/ 4.2 ps). Since the eye-diagrams for the WCM are barely passing the specification, we validated that the set-up we realized is satisfying condition of the standard.

In the following section, we substitute the WCM into an actual connector and cable model which exceeds the contact boundary impedance specification severely.

3 Analysis of HDMI 2.1 Connector and Cable with Bad Contact Boundary Impedance

3.1 A Time-domain Reflectometer (TDR) Impedance Analysis

In this section, we conduct same eye-diagram test by replacing the WCM with actual HDMI 2.1 cable and connector models. The "target" cable and connector model includes a channel with extremely high contact boundary impedance violating the connector specification. The connector itself is certified, however, we cross mated different certified receptacles and plugs to find cases which are violating the specification. Before replacing the WCM with the target connector and cable model's measured S-parameter touchstone file, we conducted a time domain reflectometer (TDR) impedance analysis. In **Figure 3(a)**, TDR impedance analysis set-up using the measured S-parameter touchstone file is depicted. Additional Balun (an electrical device that converts between a balanced signal and an unbalanced signal) and ideal transmission line models are included to provide better convergence at the beginning of the transient analysis. For the channel under TDR analysis, we realized equivalent circuit model shown in Fig. 3(a) and injected step response with amplitude of 1 V and rise time of 75 ps. In front of the differential port of the Balun, we terminated 100 Ω and monitored voltages at the either end of the termination. Then, using equation (1), we can calculate the differential TDR impedance. It is important to terminate 50 Ω for the remaining 12 ports.

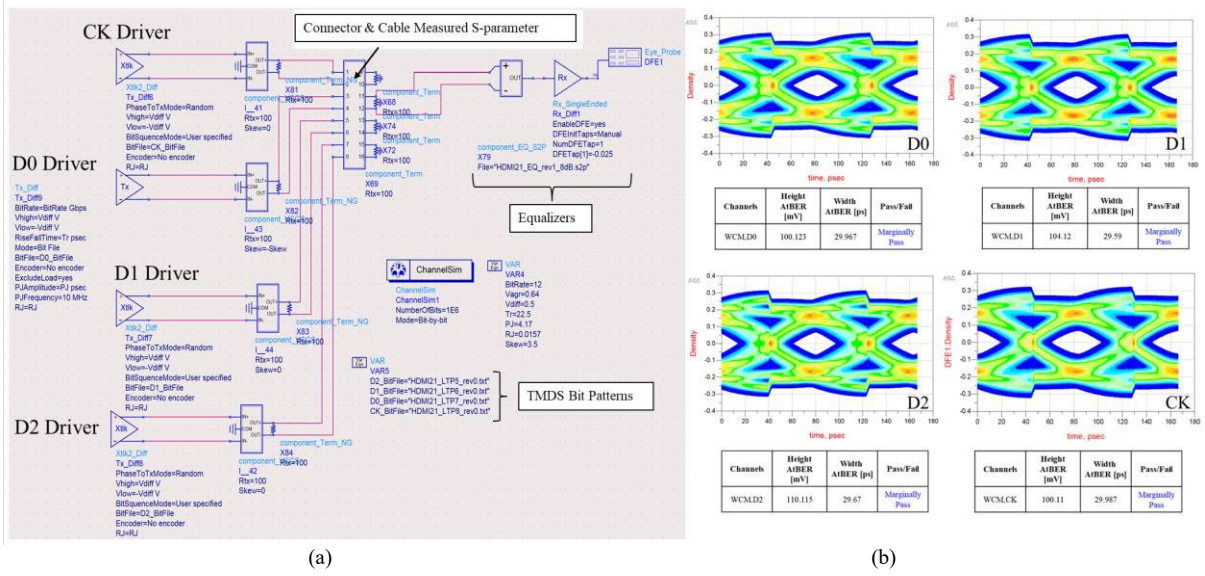


Fig. 2 (a) Set-up realized using the Keysight ADS. (b) Eye-diagram simulation results of four differential channels including connector and cable of WCM.

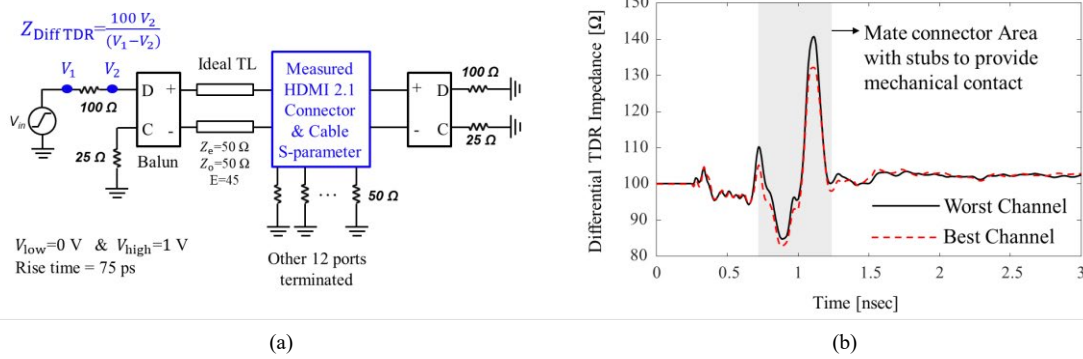


Fig. 3 (a) Equivalent circuit model to derive differential TDR impedance using measured S-parameter touchstone file. (b) Plotted differential TDR impedances for best and worst channel.

$$Z_{\text{DiffTDR}} = 100 (V_2 / (V_1 - V_2)) \text{ } [\Omega] \quad (1)$$

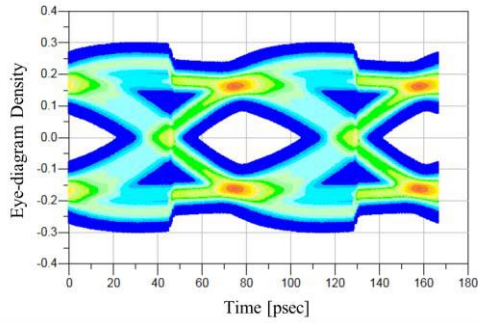
In **Figure 3(b)**, plotted differential TDR impedances for best and worst channel are shown. In this connector and cable model, the connector contact boundaries where stub terminals exist showed extremely high differential TDR impedance. Note that specification is $100 \Omega \pm 10 \Omega$. For single excursion of $\pm 15 \Omega$ is allowed if the excursion duration is less than 150 ps. In this case, even for the best channel exceeded the specification boundary significantly. In the following subsection, we use the same connector and cable model and conduct the eye-diagram test which is important for the signal integrity performance analysis of the high-speed digital system.

3.2 Eye-diagram Test Results using Connector and Cable Model with Bad Contact Boundary Impedance

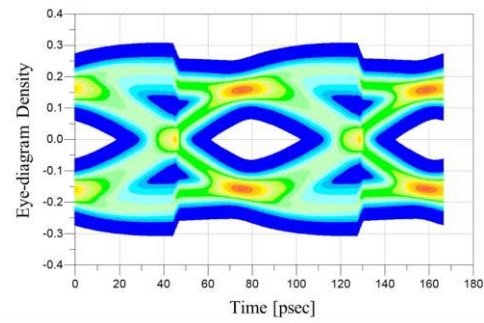
In this sub-section, we replaced the WCM model shown in Fig. 1 with the connector and cable model

with bad contact boundary impedance. In **Figure 4**, analysis results for the channel with the lowest impedance peaking profile (best channel among channels in the connector and cable model with bad contact boundary impedance) are shown. After deriving the eye-diagram which is shown in (Fig. 4(a)), we calculated the BER contours. Among BER contours, we selected the BER contour with the order of 10^{-6} and adjusted to -14.4 mV opening voltage and -4.2 ps width. As can be seen from Fig. 4(b), channel with peaking of 130Ω differential impedance passed the system level eye-diagram test with lot of room.

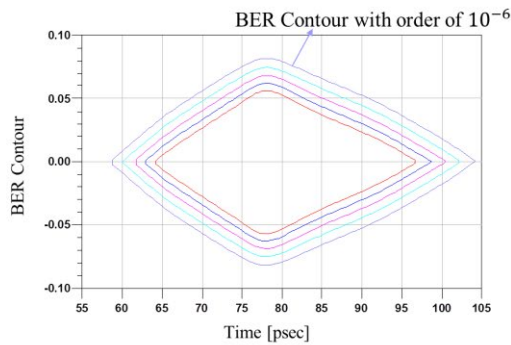
In **Figure 5**, analysis results for the channel with highest impedance peaking profile (worst channel in the connector and cable model with bad contact boundary impedance) are shown. In this case, due to increased differential TDR impedance around 140Ω , eye-diagram shown in Fig. 5(a) is even worse compared to that shown in Fig. 4(a). As a result, the BER contours shown in Fig. 5(b) have a smaller opening and width compared to the contours in Fig 4(b). However, the result is still passing the eye-diagram test.



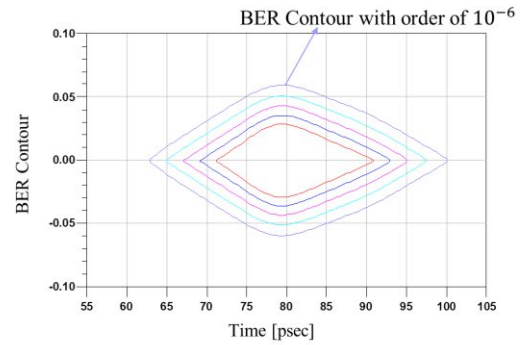
(a)



(a)



(b)



(b)

Channels	Height AtBER [mV]	Width AtBER [ps]	Pass/Fail
Bad Cable, Worst Channel	163 mV – 14.4 mV = 148.6 mV	41.44 ps – 4.2 ps = 41.24 ps	Passing with lot of room
Spec	100 mV	29.167 ps	

Channels	Height AtBER [mV]	Width AtBER [ps]	Pass/Fail
Bad Cable, Worst Channel	118.2 mV – 14.4 mV = 103.8 mV	37.5 ps – 4.2ps = 33.3 ps	Still passing
Spec	100 mV	29.167 ps	

Fig. 4 Analysis of the best channel. (a) Eye-diagram test result is plotted. (b) Calculated eye-diagram height and width at BER contour with order of 10^{-6} are compared with the specification mask.

Fig. 5 Analysis of the worst channel. (a) Eye-diagram test result is plotted. (b) Calculated eye-diagram height and width at BER contour with order of 10^{-6} are compared with the specification mask.

In the HDMI 2.1 standard specification, there exist many signal integrity (SI) and electromagnetic compatibility (EMC) criteria for connectors and cables. This is because the high-speed channels are operating at 12 Gbps and at this data rate, without consideration of the SI and EMC, many noise coupling issues can be generated. However, even if some test fails, if the system-level eye-diagram test based on measure S-parameter passes, then the mated connector and cable set is regarded as a specification compliant. However, in this study, we found and validated that due to cross-matching of the various certified connectors, some combination showed extremely bad impedance at the contact boundary but still passing the eye-diagram test with lot of room.

The alternative eye-diagram is especially useful for active cables since current electrical parameter tests are not applicable for the active cable. However, for the passive cables, we worry that assembled connector and cable sets with bad electrical parameters use the second option eye-diagram test to acquire standard certification. Therefore, it is better to allow only electrical pa-

rameter tests for the passive connector and cable assembly sets and allow the eye-diagram test or active cables such as optical cables not to cause confusion.

Based on current research, serious considerations of mandating both eye-diagram test and TDR impedance in the standard specification is needed. In the near future, we will investigate relationship between other electrical parameters and the eye-diagram test.

4 Conclusion

In this paper, we conducted analysis of HDMI 2.1 mated connector boundary impedance impacts on a high-speed digital system performance. In this study, we focus on cases when certified HDMI 2.1 plug and receptacle from different manufacturers are mated and fail to meet the impedance specification at the contact boundary. In some cases, even though severely high impedance at the connector contact boundary which fails to meet specification, the combination passed the system-level eye-diagram test which is based on measured S-parameter of the connector and cable assembly.

For the first time, we validated that connector with extremely bad differential TDR impedance passed the standard eye-diagram test. The standard eye-diagram test set-up is realized based on the specification and the WCM provided by the standard forum. The proposed set-up showed marginally passing eye-diagram results when the WCM is used.

After validating the set-up using the WCM, we replaced the WCM with the connector and cable model with extremely bad TDR impedance profiles at the contact boundary. We validated that the eye-diagram test solely cannot screen out the connector and cable with bad impedance profiles. Therefore, serious considerations of mandating both eye-diagram test and TDR impedance in the standard specification is needed.

Acknowledgements

This work was supported by JSPS KAKENHI Grant Number 8K18050 and KAKEN Kiban-A JP19H01104. Also, we would like to appreciate Dr. Baegin Sung of Invecas Inc. for providing key ideas for this research. Lastly, we appreciate prof. Joungho Kim of KAIST for technical supports.

5 Literature

- [1] HDMI 2.1 Standard Specification, 2017. (<https://hdmiforum.org>)
- [2] Y. Kim et al., "Statistical Eye-diagram Estimation Method Considering Power/Ground Noise Induced by Simultaneous Switching Output Buffers," in *IEEE Trans. Electromagn. Compat.*, Early-access, pp. 1-11, Mar. 2020.
- [3] HDMI 2.1 Compliance Test Specification, 2019. (<https://hdmiforum.org>)
- [4] J. Fan, *et al.*, "Signal integrity design for high-speed digital circuits: Progress and directions," *IEEE Trans. Electromagn. Compat.*, vol. 52, no. 2, pp. 392–400, May 2010.
- [5] D. Oh *et al.*, "High-speed Signaling: Jitter Modeling, Analysis and Budgeting", 1st ed. Prentice Hall, 2012
- [6] Y. Kim *et al.*, "Statistical Analysis of Simultaneous Switching Output (SSO) Impacts on Steady State Output Responses and Signal Integrity", in *Proceedings of the EMC Compo*, Haining, Hangzhou, China, October 22, 2019.
- [7] J. Park *et al.*, "A Novel Stochastic Model-Based Eye-Diagram Estimation Method for 8B/10B and TMDS-Encoded High-Speed Channels," in *IEEE Trans. Electromagn. Compat.*, vol. 60, no. 5, pp. 1510-1519, Nov. 2017.

Innovative switching concept to shutdown circuit currents in DC-operating systems up to 1000VDC / 30kA or 3600VDC / 12kA based on ultrafast Powerfuse (PF) technology without outgasing.

Dr. Peter Lell, PyroGlobe GmbH, Hettenshausen, Germany, p.lell@pyroglobe.de

Abstract

In almost all technology areas direct current replaces the alternating current circuits at voltages far over 100V. In order to avoid unquenchable electric arcs, the switching of DC-circuits is now the most important issue. These DC-circuits must be galvanically separated from the rest of the electrical system in case of thermal overload or a short circuit condition, as it may occur after an accident or in other emergency situations, or to switch-away short circuit loops, as it is important i.e. in electromobility or control-cabinets. In existing protecting circuits, melting fuses and mechanical circuit breakers have been the choice for overcurrent protection at higher voltages. But challenging new applications have brought conventional current breaking devices to their limits. Mechanical circuit breakers and fuses are too slow to prevent the starting of an electrical arc, nor can they quench these arcs once started. In this article we outline the newest development of cutters for active and passive triggering with pyrotechnic-driven-elements, so called Powerfuses. Powerfuses are actively controllable via a current pulse and can switch-off currents of 30kA at 1000VDC or 12kA at 3600VDC in the range of a few milliseconds. The principle of Powerfuses, their applications and the last test-results are shown and discussed.

1 Introduction

In nearly all technical fields of operations the use of high voltage DC high currents is now up-to-date and there is an exchange of power systems and distributions from AC to DC with good and bad consequences!

The worst consequences are the no more existing zero-crossing of the DC-current and the generating of a switching arc at the switching over about 20VDC [1].

So special switching systems have to be designed with respect to switching time, small dimensions and the designed usage in different environments.

2 Field of application and the basic requirements

For all fast switching of DC currents at voltages from 0VDC to 3600VDC in the temperatur range of -40°C to $+130^{\circ}\text{C}$ at environment pressure ranges between about 100bar till 10mbar.

Dependent on the used EED (electro explosive device) the switching starts between 20 μsec and 60 μsec after the trigger impulse finishes between 0,1 and 3 ms respectiveley to the inductance of the switched circuit and the voltage and the current at the beginning of the switching.

The loop resistance of the smallest powerfuse PF-HV-A25 is about only 30 μOhm .



Fig. 1 The powerfuse PF-HV-A25 over 5mm cross-section paper.

2.1 Safety switching of short circuit currents in battery systems

Today lithium-ion batteries are used in many systems for e-mobility, on ships, on aeroplanes, server or transmission stations. They are made mainly of easily flammable materials. Consequently, any damage due to overheating as a result of excessively high current charging or discharging, or by external mechanical damages can be extremely critical. Therefore such systems have to be secured by protective devices.

For e-cars or e-busses the maximum current can be up to 30kA at 1200VDC in short circuit situations that must be switched safely, at e-aeroplanes the switching task can be up to 10kA at 4000VDC.

2.2 Safety disconnecting in power networks on earth, ships and aeroplanes

The task is to disrupt a malfunctioning system from the other network, so the other systems and devices used in the network can continue their task.

Normally no overvoltage or overcurrent must be switched, but at low currents at high voltages, often!

2.3 Safety switching of overloaded semiconductor switches in power switching stations

Here the switching must be very very fast because the currents after a damage of overloaded semiconductor switches can very drastically increase after a damage.

The reason for this are the very low inductancies and resistances occurring here.

3 The basic design of the PF and operating principle

The basic operation principle of the powerfuse is the internal detonative disrupting of the switching area of a conducting tube (switching tube, conducting element) and the compressing of one or both of its separated contacts after the disrupting by a sabot.

So a fast initial gap can be made in the connector and an increasing distance between the separated parts of the connector, after.

So an initial high countervoltage can be realized in order to break the current instantenously and to force it fast to zero.

The electric arc is famished by an extinguishing fluid, generated at the moment of disrupting the conducting tube.

The next figures shows a moment short after the disrupting, the pictures are taken from an existing video:

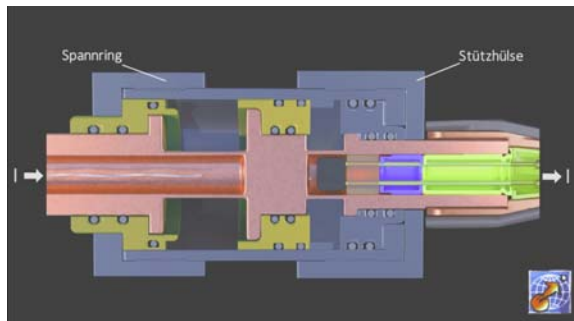


Fig.2 The powerfuse PF-HV-A25 just before ignition, the current flows over the central connector tube made of copper (Cu); the tube is isolated electrically by the isolator1 (left) and the sabot (middle in the fig.)

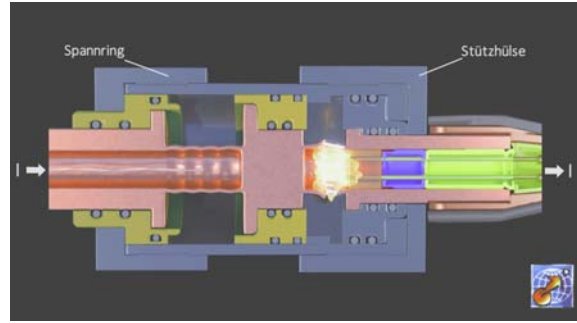


Fig.3 The powerfuse PF-HV-A25 short after ignition, the central connector tube is disrupted by the external triggered mini-detonator inside the tube, the arc starts inside between the separated connectorparts.

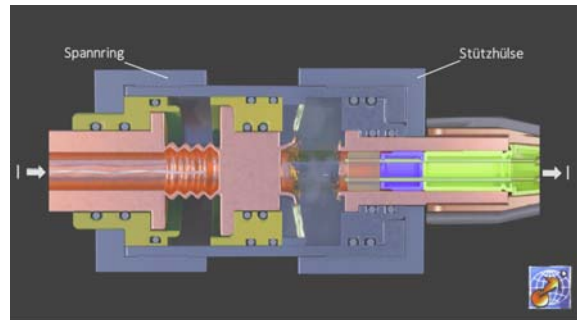


Fig.4 The powerfuse PF-HV-A25 after about 50% of the complete separation time; the arc switched from one connector to the housing inside, the left connectorpart is compressed, the gap between both separated connectorparts is grown.

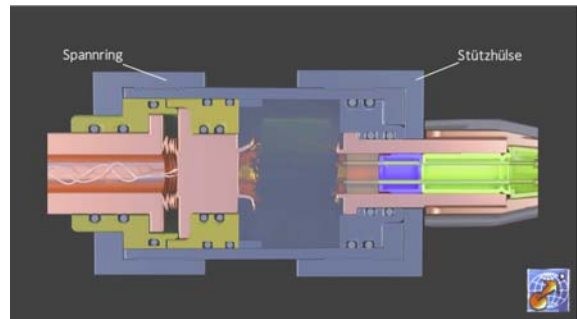


Fig.5 The powerfuse PF-HV-A25 at the end of the switching, the left part of the separated connector tube is compressed fully, the gap between both separated parts of the connector / contact is now maximum, the pressure inside the device is very high and helps so preventing late arcing.

3.1 Basic design

The connectortube, named switching tube in the Fig.6 is fitted in a steel housing. Its left side is isolated against the housing by the isolator, its right side has electrical contact with the housing.

The switching tube is divided to the named folding area and the switching area.

3.3 Parallel- and serial connection with other powerfuses or other power circuit breakers

With the parallel connection of two powerfuses neither the reliability of the switching system can be doubled, nor the capability of energy consumption. The reason for this: If both powerfuses are switched together the arc will act first in one of the separating powerfuses and will take the main current because of the extremely low resistance of the arc there - after the second separating powerfuse will take only a low current.

With the serial connection of two powerfuses the switchable voltage can be doubled because of the existing of two gaps after triggering. So at every gap act half of the voltage loaded to this serial system.

Additionally the consumptable energy of the system can be doubled now.

But the best method for the serial switching of two powerfuses is to trigger the second powerfuse about 4 to 6ms after the first powerfuse: So the first powerfuse can be overloaded heavily with high current, with high voltage and with high circuit inductance - till all its extinguishing media will be exhausted - after the second powerfuse switches only at low currents and secures so a really good isolation resistance after its acting!

For special tasks it is possible and useful to build a serial connection between a powerfuse and a mechanical or semiconductor switch. But this is applicable only for a mechanical or semiconductor switch which can be overloaded for 4 to 6 ms. Such a system is good for continuous / operational switching by the mechanical or semiconductor switch and for emergency situations.

3.4 Passive triggering and switching

The powerfuse is principally suitable for passive switching i.e. triggering, so it can act as a "normal fuse":

If the tube in the switching area is heated up to the melting point of the used material, the arc starts and vaporises the extinguishing media around it, pressure is generated and the sabot will be pressed like it will act after an active triggering.

The same action starts if the used EED is coated with a thermal sensible material or the tube is filled with such a material near the EED

Fig.10 shows a passive switching after 5,6sec and Fig.11 a passive switching after 25,4sec with another switching tube.

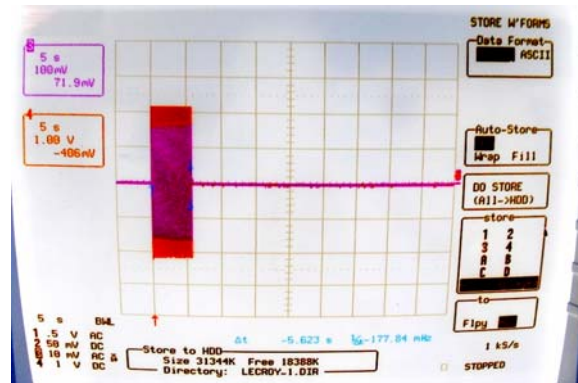


Fig.10 Passive switching of the PF after 5,6sec at 3000A continuous current load, tube No.1.

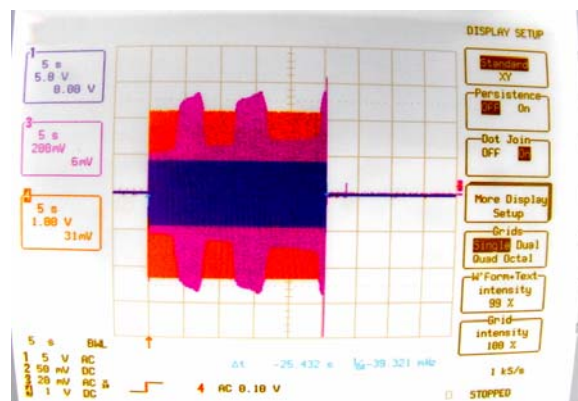


Fig.11 Passive switching of the PF after 25,4sec at 3000A continuous current load, tube No.2.

4 The test equipment

Several equipments of several laboratories were used in order to develop, optimize and qualify the powerfuse. They are shown in a short overview now.

4.1 Capacitor bank at PyroGlobe GmbH, Hettenshausen [2]

For all testing for development and optimization of the powerfuse a capacitor bank is used.

The main device exists of 2 modules of 6 capacitances each (Fig.12), each capacitor has its own ignitron (Fig.13).

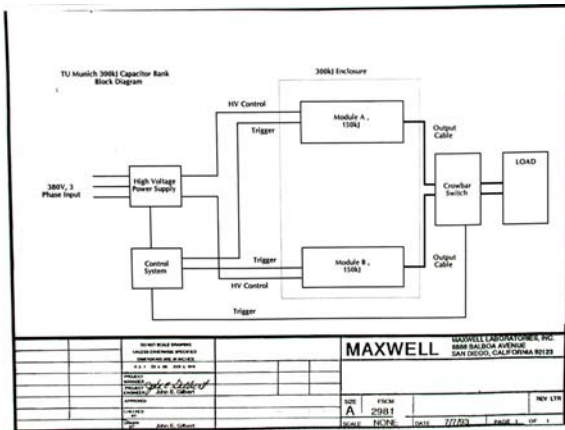


Fig.12 Block diagram of the C-bank at PyroGlobe

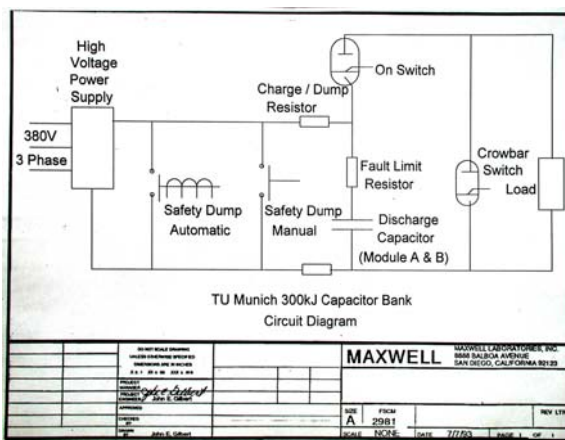


Fig.13 Circuit diagram of one module of the C-bank at PyroGlobe

The output of all 12 ignitrons are leaded by coaxial cables, parallel conducted on two great ignitrons for crowbar purposes (not used for the powerfuse) and then connected to a collector, shown in Fig.14.

Connected to this collector is a battery of threaded bars made of stainless steel in series, then removable inductances and the testing block at least, Fig. 14.

The main device has a capacity of 6mF and is chargeable up to 10kV.

In order to have more i.e. longer current flow 6 external capacitors are addable to the main device. Each of these external capacitors has a capacity of 9,5mF and is chargeable to 2,7kV (Fig.15).

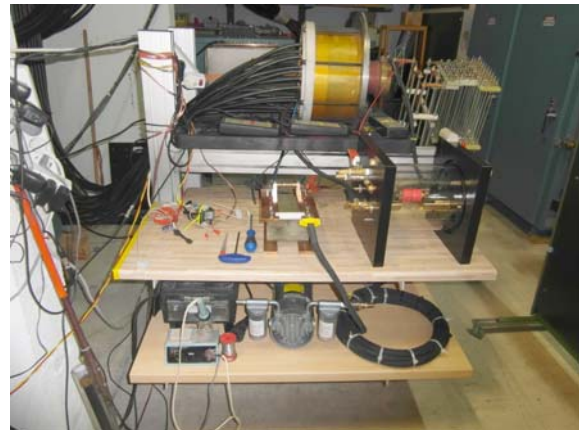


Fig.14 Collector of the capacitor network (middle behind), the resistor device (behind right), the testing block (middle in front of), the vacuum chamber (middle right), the vacuum pump (middle in front of) and one of several external removables inductances.



Fig.15 Main capacitor block (blue casing) and 3 external capacitors added on each side of the main device.

4.2 DC laboratory AIT in Vienna

For qualification purposes the DC laboratory AIT (Austrian Institut of Technology) in Vienna was used. Here the energy was taken from the three-phase hi-voltage power system, is transformed and rectified to the wanted voltage.

Again the current is adjusted by a resistor bridge (left in Fig.16), the wished inductivities can be switched in.

Because the rectifying is done near the work bench, the inductivity of the shorted circuit can be 16μH at the minimum.

Today the maximum voltage is 3kV, the maximum current about 30kA, the minimum voltage 150V, and again the power is switched by ignitrons.

Fig.17 shows a typical oscillogramm of the testing of the powerfuse.



Fig.16 The work bench of the AIT laboratory. Left the resistor and inductance device, middle behind the connectors of the trafostation and middle in front the work table.

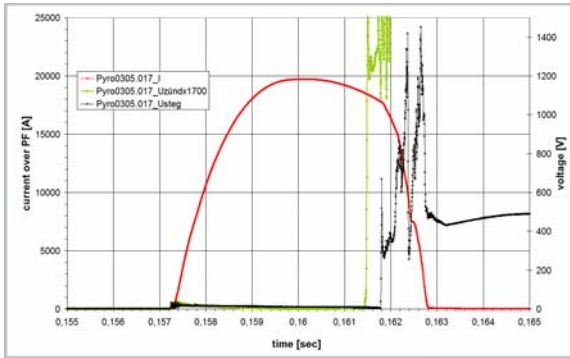


Fig.17 Current over a powerfuse, ignition voltage and voltage over the switched tube of the powerfuse as function of time, recorded at a typical testing at AIT.

4.3 Comparison of the both testing facilities AIT and PG

The AIT can provide a better battery simulation as the capacitor bank at PyroGlobe because of the nearly constant voltage over the switching, so all qualification tasks in the field of automotive should be done at the AIT.

Because the voltage of the capacitor bank sinks during the switching the amount of energy flowing into the powerfuse is a function of current and voltage at every time segment.

So the energy flow into the powerfuse cannot be foreseen so good and can be calculated strictly only by integration of the voltage over the switching tube multiplied by the current at every moment!

With a capacitor bank the tests can be made faster, cheaper and cause not so high damage if the switching is not good.

The facility at PyroGlobe is better for the testing of inductivities smaller than $15\mu\text{H}$ (down to $3\mu\text{H}$) and voltages over 3 kV.

4.3 Typical parts before and after ignition

The following pictures show some typical parts of the powerfuse and parts after the triggering and after the delaboration of the triggered powerfuse:

Fig.18 shows one of the used mini-detonators (EED), Fig.19 a composition of switching tube with isolator, sabot and closure, here made of plastics (actual the closure is made of steel).



Fig.18 One of the used mini-detonators with a M9x1 thread for the switching / connecting tubes of the powerfuse.

Fig.19 shows above the tube undesintegrated, below after the ignition of the EED:

The sabot is completely covering the folding area till the isolator and the gap is about 15mm wide, existing now.



Fig.19 The switching tube made of copper before (above) and after triggering the internal EED (below); the folding area ist completely covered by isolator and sabot.



Fig.20 Separated tube part 1 after ignition and delaboration with a rest amount of extinguishing media 1, photographed top down.



Fig.21 Like Fig.20, photo is taken 80° to axis.



Fig.22 Separated tube part 1 (right) and part 2 in the housing (left) after ignition and delaboration of another powerfuse filled with extinguishing media 2, photographed top down; no copper particle is broken!



Fig.23 Separated tube part 1 of Fig.21 after ignition and delaboration, photographed more inclined; no copper particle is broken!

5 Basic results

The first tests were done with the C-bank of PyroGlobe, later these tests were verified by tests at the AIT-laboratory in Vienna, after the optimization of the device was undertaken at the C-bank of PyroGlobe again.

5.1 0VDC to 1000VDC switching

Fig.24 shows a typical situation with tests in a DC laboratory:

The red curve is the current flowing through the switching tube of the tested powerfuse, the green is the ignition current and the black graph is the voltage over the switching tube.

After ignition of the EED there is a time delay of 20 till 200µsec depending of the used EED and the used ignition current. Then a primary countervoltage is generated decreasing with switching time.

The highest countervoltage is generated short before the current is cut completely. It can be up to 3 times the generator voltage depending on the switching time, the resistance and the inductance (rule of Lenz) of the switched circuit.

After that the voltage over the interrupted switching tube is the generator voltage of the powersystem of the test bench.

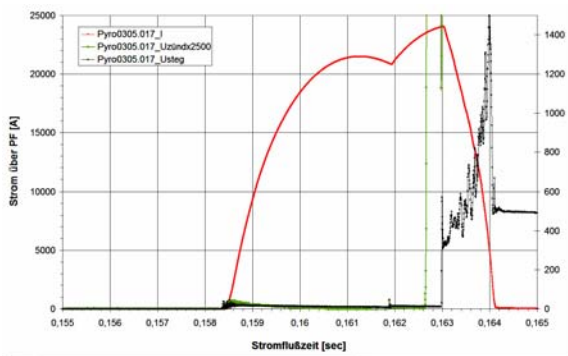


Fig.24 Testing at the AIT laboratory in Vienna with constant power of 490V and 25μH inductivity, switching at 24kADC; the switching time was 1,1ms.

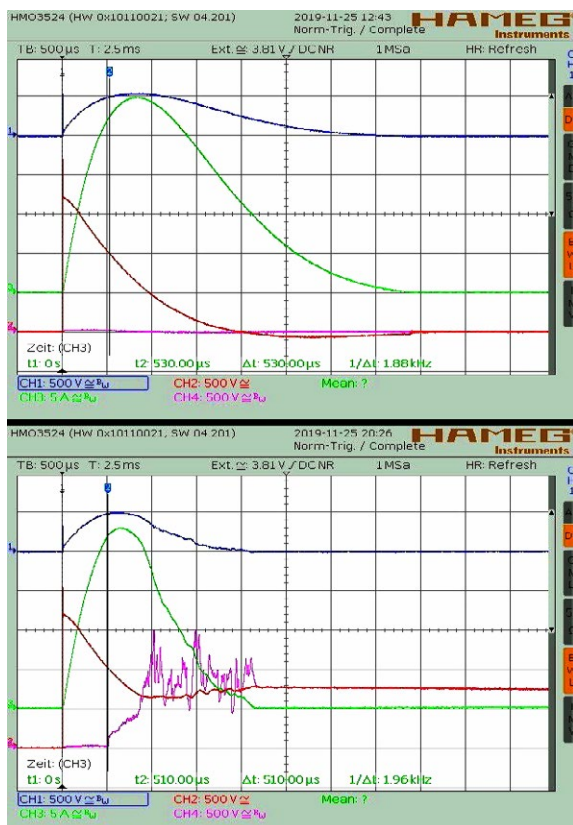


Fig.25 Switching test at 1020V and 22000 ADC with a switching time of 1,7ms. Above the situation without triggering, below after triggering. Current I = green curve, voltage over the tube = violet curve, voltage at the position of the collector = brown graph, voltage over the resistance of the circuit = the blue curve.

For comparison reasons or for optimization purposes of the powerfuse and its parts the flowing energies during the separating process can be used.

Fig.26 shows that the energy flowing out of the generator is divided into the energy consumed by the resistance of the circuit and the powerfuse itself.

Dependent on the used extinguishing media the consumed energy by it must not exceed a certain amount

in order to secure a good isolation resistance between the separated parts of the switching tube i.e. contacts after the ignition.

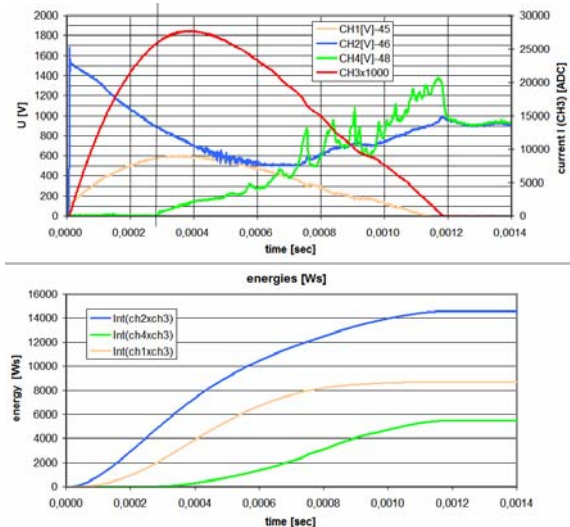


Fig.26 Calculating the energy situation during a switching (V1110) at 870V, 26,5kA, 10μH, 21mOhm with a isolation resistance of 15GOhm at 5kV, switching time was 980μsec!

Diagram above:

Current I = red curve, voltage over the tube = green curve, voltage at the position of the collector = blue graph, voltage over the resistance of the circuit = the orange curve.

Diagram below:

Energy flowed into the powerfuse = green curve, energy flowed out of the collector into the test setup = blue graph, energy consumed by the resistance of the circuit = the orange curve.

5.2 Switching over 1000VDC

When switching a circuit at voltages over 1000VDC the switching times becomes more and more longer and the break in the graph of the current is now more and more a round buckle so as if the current is undecided to decrease or flowing its way along...

Fig.27 shows the switching of a single powerfuse at 3200V and 8200ADC with an inductance of the circuit of 22μH.

The initial countervoltage is low in comparison with the driving voltage and there is no longer a really higher countervoltage at the end of the switching.

The consequence of this is a longer switching time with more energy flowing into the powerfuse as it would be necessary and degenerating the extinguishing media more as it would be other.



Fig.27 Switching test at 3200V and 8200 ADC with a switching time of 2,6ms; Current I = green curve, voltage over the tube = violet curve, voltage at the position of the collector = brown graph, ignition current = the blue curve.

5.3 The great influence of the inductance and the resistance of the switched circuit

Fig.26 shows the great influence of the resistance of the circuit to be switched. The higher the circuit resistance, the lower is the energy which has to be handled by the powerfuse.

So a given feasibility of a switching device without the declaration of the minimum possible resistance at a given voltage and current in the moment of triggering this switch make no sense, one would compare apples with nuts!

The inductance of the circuit is the main driving factor for the overvoltage and the generated energy feeding the arc.

After the rule of lenz the decreasing of the magnetic field in the inductance should be stopped in the moment of breaking the circuit, so a voltage is generated to drive the current in the same direction as the current generating the existing magnetic field short before the breaking.

The magnetic field stores so a lot of energy which must be changed in other energies in any way, it cannot be switched off simply! The amount of energy in this magnetic field is proportional to the square of the generating current.

Again a given feasibility of a switching device without the declaration of the maximum possible inductance of the circuit at a given voltage and current in the moment of triggering this switch make no sense.

5.4 Switching in hazardous areas

The powerfuse is sealed completely, so no outgasing happens during the switching act or after, there is only the outgasing known from o-rings.

The housing of the powerfuse is coated by an shrinking tube, so its weak heating up after the ignition will generate only low temperature differences of 10 to 30 degrees, there is no activating temperatur for the initiation of fire or explosions.

5.5 Switching on low pressure situations

The same for the usage under low pressures in the surrounding of the powerfuse. Only the decreasing of the isolating ability of the low pressured gas outside the PF has to be considered. So one has to prevent an arcing outside the switched powerfuse i.e. by isolating plates over the isolated contact part of the PF or to bring the PF completely in an isolating cup, that can be open on one front surface.

5.6 Physics in the powerfuse, a short overview

The physical situation in the powerfuse from the moment of ignition is that of a chemical reactor:

Temperatures generated through the arc short acting between 1000 and 3000 °C, pressures up to 400 bar and a initial existing shock wave from the mini detonator generates a thermal plasma in the housing.

So all molecules of the extinguishing media are broken up to their simple elements on all places the arc is contacting. Same with the solids in the powerfuse: They will be vaporized partly after the contact of the arc or/and be changed in their basic elements.

This has to be considered in the selection of the plastics, the housing material and the extinguishing media in order to have a good isolation resistance after the condensing of the vaporized materials.

6 Literature

- [1] R. Holm: Electrical Contacts, Springer-Verlag, 1967
- [2] Permanent loan of the Capacitor bank from the division of space technology of the Technical University of Munich, Prof. Dr. Walter, to PyroGlobe GmbH, Hettenshausen.

7 Patents and patent applications

Patent applications and patents concerning the powerfuse are listed on the next page. The list is not completely, some applications were made in China and Japan, too. Only the german titels are given.

DE101393601	Pyrosicherung ohne Wirkung nach außen bei Fremd- und Eigenauslösung
DE1020141078535	Elektrisches Unterbrechungsschaltglied, insbesondere zum Unterbrechen von hohen Strömen bei hohen Spannungen
DE1020141108256	Elektrischer Schalter, insbesondere für hohe Spannungen und/oder hohe Ströme
DE1020141108256	Elektrischer Schalter, insbesondere für hohe Spannungen und/oder hohe Ströme
DE1020161241768	elektr. Unterbrechungsschaltglied, insbes. Zum Unterbrechen von hohen Strömen bei hohen Spannungen
DE102017123021	elektr. Unterbrechungsschaltglied, mit passiver Unterbrechungsauslösung, insbes. zur Unterbrechung von hohen Strömen bei hohen Spannungen.
DE102018100686.1	elektr. Unterbrechungsschaltglied mit Reaktivbeschichtung in der Reaktionskammer
DE102018103018.5	Unterbrechungsschaltglied mit Haupt- und Nebenschlußstrompfad
DE102019102858-2	Verfahren und Vorrichtung zum dauerhaften Trennen eines Stromkreises mit induktiver Last durch zeitversetztes Schalten zweier in Reihe geschalteter Schalter
DE1020191044510	elektr. Unterbrechungsschaltglied mit einem rohrförmigen Trennelement mit variierender Wandstärke
DE1020191044537	elektr. Unterbrechungsschaltglied mit einem rohrförmigen oder stabförmigen Stauchbereich mit variierendem Querschnittsdurchmesser
DE501099786	Pyrotechnisches Sicherungselement
EP15742175	Elektrisches Unterbrechungsschaltglied, insbesondere zum Unterbrechen von hohen Strömen bei hohen Spannungen
EP17787320-5	elektr. Unterbrechungsschaltglied, insbes. Zum Unterbrechen von hohen Strömen bei hohen Spannungen
EP201573078	Elektrisches Schaltglied, insbesondere zum Schalten hoher Ströme
EP201573102	elektr. Unterbrechungsschaltglied mit einem rohrförmigen oder stabförmigen Stauchbereich mit variierendem Querschnittsdurchmesser
GM2020161069319	elektr. Unterbrechungsschaltglied, insbes. Zum Unterbrechen von hohen Strömen bei hohen Spannungen
GM202017106260-0	elektr. Unterbrechungsschaltglied mit passiver Unterbrechungsauslösung, insbes. Zur Unterbrechung von hohen Strömen bei hohen Spannungen
GM202017106261-9	elektr. Unterbrechungsschaltglied, insbes. zum Unterbrechen von hohen Strömen bei hohen Spannungen
GM202018100172.8	elektr. Unterbrechungsschaltglied mit Reaktivbeschichtung in der Reaktionskammer
GM202018100728	Unterbrechungsschaltglied mit Haupt- und Nebenschlußstrompfad
P10296442434	Elektrisches Schaltglied, insbesondere zum Schalten hoher Ströme
PCT/DE2015100218	Elektrisches Unterbrechungsschaltglied, insbesondere zum Unterbrechen von hohen Strömen bei hohen Spannungen
PCT/DE2017100844	elektr. Unterbrechungsschaltglied, insbes. Zum Unterbrechen von hohen Strömen bei hohen Spannungen
PCT/DE2018100812	elektr. Unterbrechungsschaltglied, mit passiver Unterbrechungsauslösung, insbes. zur Unterbrechung von hohen Strömen bei hohen Spannungen.
PCT/DE2019100010	elektr. Unterbrechungsschaltglied mit Reaktivbeschichtung in der Reaktionskammer
PCT/DE2019100124	Unterbrechungsschaltglied mit Haupt- und Nebenschlußstrompfad

Author Index

Aksenov, Andrey	486
Amato, Massimiliano	303
Andelin, Cody	303
Anderson, Doyle	260
Anheuser, Michael	80
Anspach, Frederik	141
Bach, Robert	520
Baessler, Hendrik	599
Baeuml, Katrin	615
Bartonek, Michael	149
Bauer, Felix	274
Behrens, Volker	210
Beilner, Michael	378
Berger, Frank	80, 347
Bhargava, Suvrat	458
Bleicher, Martin	289
Blumenroth, Falk	398
Bodry, Sam	297
Boehm, Moritz	297
Boening, Mike	87
Boening, Sabine	87
Brezard-Oudot, Aurore	194, 260
Bu, Jack	428
Bull, Thomas	420
Bund, Andreas	202
Buresch, Isabell	281, 289
Böhm, Moritz	99
Cai, Yide	9
Carvou, Erwann	52, 178
Chaudhuri, Atanu	303
Chen, Silei	121, 562
Chusov, Alexander	500
Claaßen, Lars	141
Comby-Dassonneville, Solène	29
Comte, Damien	194, 260
Crandall, Erika	289
Cross, Kevin	420
Dai, Minglei	575
Dandl, Christian	241
David, Ato	303
Delachaux, Thierry	99

Deng, Yunkun	575
Di Rienzo, Luca	583
Djuimeni Poudeu, Franck Stephane	378
Dong, Jinlong	583
Dorraki, Naghme	111
Dr. Schweigkofler, Martin	186
Drebenstedt, Christian	60
Dyck, Tobias	202
Ehrhardt, Arnd	157, 486
Eicher, Michael	241
Eisenbart, Miriam	274
Elmiger, David	37
Fares Karam, Antoine	194, 260
Fauth, Bernhard	450
Feng, Xiangdong	508
Franchini, Anthony	194, 260
Frank, Christian	581
Franke, Joerg	607
Franke, Jörg	599
Franke, Steffen	74
Freudiger, George	404
Fu, Rao	508
Fu, Yinghua	9
Fuchs, Roman	494, 500
Fujimoto, Daisuke	623
Fukuda, Naoki	317, 323, 329
Gao, Pengyu	172
Gatzsche, Michael	398
Gauthier, Jean-Pierre	95
George Varghese, Shem	520
Gonzalez, Diego	74, 87
Gortschakow, Sergey	74, 87
Grossmann, Steffen	412
Großmann, Steffen	404, 615
Gruber, Andreas	241
Haba, Dietmar	385
Habrych, Marcin	105
Hafenstein, Eric	219
Hasegawa, Makoto	45
Hauck, Uwe	392
Hauer, Wolfgang	149
Hayashi, Yu-ichi	623
Herrle, Thomas	450
Herrmann, Johannes	234

Hilty, Frédéric	234
Hoerburger, Markus	254
Hogger, Reinhard	241
Hoischen, Michael	520
Holzappel, Christian	339
Hu, Steven	428
Huang, Yinming	135
Hubrich, Christian	311
Hugon, Robert	24
Humbert, Jean Baptiste	24
Israel, Toni	404
Jackson, Robert	534
Jacob, Peter	166
Jacobs, Linda	303
Jerram, Carlene	303
Jiang, Changliu	436
Jiang, Duanlin	9
Jie, Li	362
Johler, Werner	428
Kerckhof, Bart	289
Kharin, Stanislav	549
Kim, Youngwoo	623
Klotz, Ulrich	274
Koeppel, Joshua	219
Kubota, Yoshitaka	334
Kuehl, Alexander	599, 607
Kufner, Tom	404
Kurrat, Michael	141
Lalet, Gregory	178
Landon, Raymond	458
Le-Rest, Francois	542
Lees, Philip	219
Leibig, Bernd	486
Leidner, Michael	226, 370
Lell, Peter	628
Li, Bo	508
Li, Xingwen	121, 480, 562, 575
Liang, Hong	172
Liang, Huimin	508
Liang, Kevin	428
Lindmayer, Manfred	37, 474
Liu, Jiaomin	172
Lohbauer, Andreas	599
Lu, Ningyi	436

Ludwig, Michael	370
Luo, Fubiao	526
Luo, Yanyan	172
Mainka, Marcel	186
Martens, Rodney	458
Martinek, Michael	513
Mashimo, Keiji	268
Mavuni, Mack	178
McBride, John	420
Meley, Jean-Pierre	95
Methling, Ralf	74
Miedzinski, Bogdan	105
Muermann, Mario	500
Muetzel, Timo	311
Myers, Marjorie	226
Niayesh, Kaveh	111
Noel, Sophie	260
Nordborg, Henrik	466, 500
Nowak, Remigiusz	556
Noël, Sophie	194
Oberst, Marcella	412
Ostendorf, Frank	226, 289, 370
Ostrowski, Joerg	556
Ou, Chomrong	129, 135
Papillon, Anthony	95
Polnik, Bartosz	105
Porte, Maxime	355
Ramzi, Asma	52
Reil, Christian	80
Ren, Wanbin	9, 526
Riedel, Andreas	599, 607
Rock, Michael	60
Roelfs, Bernd	254
Sachs, Sönke	226, 281
Saha, Swarna	534
Sampath, Srinidhi	303
Samul, Boguslaw	556
Sasaki, Hirokazu	268
Sawa, Koichiro	68, 317, 323, 329
Schach, Alexis	52
Scherf, Lavinia	99
Schlegel, Stephan	378, 404, 412

Schmausser, Sebastian	486
Schmidt, Alexander	607
Schmidt, Hans-Peter	80
Schmidt, Helge	226, 281, 289, 370
Schmölzer, Thomas	99
Schneider, Olga	486
Schultz, Bradley	458
Schulze, Kyle	534
Schweitzer, Patrick	24
Seefried, Johannes	599, 607
Shaporenko, Elena	486
Shi, Yunjie	442
Shimoyamada, Atsushi	268
Slade, Paul	1
Song, Jian	248
Spies, Tony	219
Spoerrler, Alexander	254
Staborth, Waldemar	226
Stammberger, Hartwig	149
Strand, Marius	111
Strobl, Christian	591
Su, Qingxing	436
Sun, Zihang	172
Suzuki, Kenji	68
Sütterlin, Ralf-Patrick	99
Takada, Yusuke	317, 329
Tang, Yinglu	297
Tarnovetchi, Marius	542
Tasch, Johannes	311
Tian, Nan	442
Tian, Tian	480
Tokumitsu, Seika	45
Toran, Jeffrey	194, 260
Torrealba, Ana	194, 260
Tranitz, Hans-Peter	542
Ueno, Takahiro	317, 323, 329
Uhrlandt, Dirk	87
Verdier, Marc	29
Vieth, Patrick	141
Voegtlin, Tim	297
Volm, Dieter	450
Volpi, Fabien	29
Wagner, Reinhard	241
Wang, Jianhua	583

Wang, Jing	121, 562
Wang, Jingqin	172
Wang, Mengqing	442
Wang, Qian	480
Wang, Qiya	568
Wapniarski, Stanislaw	105
Weber, Serge	24
Wei, Zhen	526
Werner, Frank	74
Wibberg, Bruno	254
Wielsch, Thomas	186
Wilkening, Ernst-Dieter	141
Wisniewski, Grzegorz	105
Wolfram, Sven	157
Wosik, Julian	105
Würtele, Ralph	186
Xiaofang, Yan	362
Xiaoping, Bai	362
Xu, Yang	534
Yasuoka, Koichi	129, 135
Yi, Lei	436
Yin, Jianning	480
Yinming, Huang	129
Yoshida, Kiyoshi	68
You, Jiaxin	508
Yu, Shun	74
Yuan, Haomiao	248
Yuan, Xuebing	116
Zanetti, Alberto	398
Zeller, Peter	16
Zhang, Chao	526
Zhang, Guogang	583
Zhang, Maosong	162
Zhang, Xu	9
Zhang, Zhengbin	568
Zhao, Hu	116
Zhao, Jingying	172
Zhou, Yilin	442
Zhu, Yiqing	162

